NEUROMODULATORY CONTROL OF BRAINSTEM FUNCTION IN HEALTH AND DISEASE

EDITED BY: Brian R. Noga, Mikhail Lebedev, Ioan Opris and Gordon S. Mitchell

PUBLISHED IN: Frontiers in Neuroscience, Frontiers in Systems Neuroscience, Frontiers in Human Neuroscience, Frontiers in Physiology, Frontiers in Neural Circuits, Frontiers in Behavioral Neuroscience, Frontiers in Cellular Neuroscience, Frontiers in Neurology and Frontiers in Pharmacology



frontiers Research Topics



frontiers

Frontiers eBook Copyright Statement

The copyright in the text of individual articles in this eBook is the property of their respective authors or their respective institutions or funders. The copyright in graphics and images within each article may be subject to copyright of other parties. In both cases this is subject to a license granted to Frontiers.

The compilation of articles constituting this eBook is the property of Frontiers.

Each article within this eBook, and the eBook itself, are published under the most recent version of the Creative Commons CC-BY licence. The version current at the date of publication of this eBook is CC-BY 4.0. If the CC-BY licence is updated, the licence granted by Frontiers is automatically updated to the new version.

When exercising any right under the CC-BY licence, Frontiers must be attributed as the original publisher of the article or eBook, as applicable.

Authors have the responsibility of ensuring that any graphics or other materials which are the property of others may be included in the CC-BY licence, but this should be checked before relying on the CC-BY licence to reproduce those materials. Any copyright notices relating to those materials must be complied with.

Copyright and source acknowledgement notices may not be removed and must be displayed in any copy, derivative work or partial copy which includes the elements in question.

All copyright, and all rights therein, are protected by national and international copyright laws. The above represents a summary only. For further information please read Frontiers' Conditions for Website Use and Copyright Statement, and the applicable CC-BY licence.

ISSN 1664-8714
ISBN 978-2-88963-575-7
DOI 10.3389/978-2-88963-575-7

About Frontiers

Frontiers is more than just an open-access publisher of scholarly articles: it is a pioneering approach to the world of academia, radically improving the way scholarly research is managed. The grand vision of Frontiers is a world where all people have an equal opportunity to seek, share and generate knowledge. Frontiers provides immediate and permanent online open access to all its publications, but this alone is not enough to realize our grand goals.

Frontiers Journal Series

The Frontiers Journal Series is a multi-tier and interdisciplinary set of open-access, online journals, promising a paradigm shift from the current review, selection and dissemination processes in academic publishing. All Frontiers journals are driven by researchers for researchers; therefore, they constitute a service to the scholarly community. At the same time, the Frontiers Journal Series operates on a revolutionary invention, the tiered publishing system, initially addressing specific communities of scholars, and gradually climbing up to broader public understanding, thus serving the interests of the lay society, too.

Dedication to Quality

Each Frontiers article is a landmark of the highest quality, thanks to genuinely collaborative interactions between authors and review editors, who include some of the world's best academicians. Research must be certified by peers before entering a stream of knowledge that may eventually reach the public - and shape society; therefore, Frontiers only applies the most rigorous and unbiased reviews.
Frontiers revolutionizes research publishing by freely delivering the most outstanding research, evaluated with no bias from both the academic and social point of view. By applying the most advanced information technologies, Frontiers is catapulting scholarly publishing into a new generation.

What are Frontiers Research Topics?

Frontiers Research Topics are very popular trademarks of the Frontiers Journals Series: they are collections of at least ten articles, all centered on a particular subject. With their unique mix of varied contributions from Original Research to Review Articles, Frontiers Research Topics unify the most influential researchers, the latest key findings and historical advances in a hot research area! Find out more on how to host your own Frontiers Research Topic or contribute to one as an author by contacting the Frontiers Editorial Office: researchtopics@frontiersin.org

NEUROMODULATORY CONTROL OF BRAINSTEM FUNCTION IN HEALTH AND DISEASE

Topic Editors:
Brian R. Noga, University of Miami, United States
Mikhail Lebedev, Duke University, United States
Ioan Opris, University of Miami, United States
Gordon S. Mitchell, University of Florida, United States

Citation: Noga, B. R., Lebedev, M., Opris, I., Mitchell, G. S., eds. (2020). Neuromodulatory Control of Brainstem Function in Health and Disease. Lauanne: Frontiers Media SA. doi: 10.3389/978-2-88963-575-7

Table of Contents

06 ***Editorial: Neuromodulatory Control of Brainstem Function in Health and Disease***
Brian R. Noga, Ioan Opris, Mikhail A. Lebedev and Gordon S. Mitchell

11 ***Noninvasive Focused Ultrasound Stimulation Can Modulate Phase-Amplitude Coupling Between Neuronal Oscillations in the Rat Hippocampus***
Yi Yuan, Jiaqing Yan, Zhitao Ma and Xiaoli Li

18 ***Histamine Increases Neuronal Excitability and Sensitivity of the Lateral Vestibular Nucleus and Promotes Motor Behaviors via HCN Channel Coupled to H2 Receptor***
Bin Li, Xiao-Yang Zhang, Ai-Hong Yang, Xiao-Chun Peng, Zhang-Peng Chen, Jia-Yuan Zhou, Ying-Shing Chan, Jian-Jun Wang and Jing-Ning Zhu

31 ***Neuronal Correlates of Functional Coupling Between Reach- and Grasp-Related Components of Muscle Activity***
Shashwati Geed, Martha L. McCurdy and Peter L. E. van Kan

49 ***Mapping and Analysis of the Connectome of Sympathetic Premotor Neurons in the Rostral Ventrolateral Medulla of the Rat Using a Volumetric Brain Atlas***
Bowen Dempsey, Sheng Le, Anita Turner, Phil Bokiniec, Radhika Ramadas, Jan G. Bjaalie, Clement Menuet, Rachael Neve, Andrew M. Allen, Ann K. Goodchild and Simon McMullan

65 ***Evaluation of the Cortical Silent Period of the Laryngeal Motor Cortex in Healthy Individuals***
Mo Chen, Rebekah L. S. Summers, George S. Goding, Sharyl Samargia, Christy L. Ludlow, Cecília N. Prudente and Teresa J. Kimberley

76 ***Deep Brain Stimulation Improves the Symptoms and Sensory Signs of Persistent Central Neuropathic Pain From Spinal Cord Injury: A Case Report***
Walter J. Jermakowicz, Ian D. Hentall, Jonathan R. Jagid, Corneliu C. Luca, James Adcock, Alberto Martinez-Arizala and Eva Widerström-Noga

83 ***LFP Oscillations in the Mesencephalic Locomotor Region During Voluntary Locomotion***
Brian R. Noga, Francisco J. Sanchez, Luz M. Villamil, Christopher O'Toole, Stefan Kasicki, Maciej Olszewski, Anna M. Cabaj, Henryk Majczyński, Urszula Sławińska and Larry M. Jordan

100 ***Dopamine and the Brainstem Locomotor Networks: From Lamprey to Human***
Dimitri Ryczko and Réjean Dubuc

110 ***Parameter Optimization Analysis of Prolonged Analgesia Effect of tDCS on Neuropathic Pain Rats***
Hui-Zhong Wen, Shi-Hao Gao, Yan-Dong Zhao, Wen-Juan He, Xue-Long Tian and Huai-Zhen Ruan

123 ***Hypotensive Response to Angiotensin II Type 2 Receptor Stimulation in the Rostral Ventrolateral Medulla Requires Functional GABA-A Receptors***
Laura Légat, Sofie Brouwers, Ilse J. Smolders and Alain G. Dupont

133 ***Rapid Alleviation of Parkinson's Disease Symptoms via Electrostimulation of Intrinsic Auricular Muscle Zones***
Yusuf O. Cakmak, Hülya Apaydin, Güneş Kiziltan, Ayşegül Gündüz, Burak Ozsoy, Selim Olcer, Hakan Urey, Ozgur O. Cakmak, Yasemin G. Ozdemir and Sibel Ertan

149 ***Astrocyte Activation in Locus Coeruleus is Involved in Neuropathic Pain Exacerbation Mediated by Maternal Separation and Social Isolation Stress***
Kazuo Nakamoto, Fuka Aizawa, Megumi Kinoshita, Yutaka Koyama and Shogo Tokuyama

159 ***Frontal Connectivity in EEG Gamma (30–45 Hz) Respond to Spinal Cord Stimulation in Minimally Conscious State Patients***
Yang Bai, Xiaoyu Xia, Zhenhu Liang, Yong Wang, Yi Yang, Jianghong He and Xiaoli Li

167 ***Corrigendum: Frontal Connectivity in EEG Gamma (30–45 Hz) Respond to Spinal Cord Stimulation in Minimally Conscious State Patients***
Yang Bai, Xiaoyu Xia, Zhenhu Liang, Yong Wang, Yi Yang, Jianghong He and Xiaoli Li

168 ***Inappropriate Timing of Swallow in the Respiratory Cycle Causes Breathing–Swallowing Discoordination***
Naomi Yagi, Yoshitaka Oku, Shinsuke Nagami, Yoshie Yamagata, Jun Kayashita, Akira Ishikawa, Kazuhisa Domen and Ryosuke Takahashi

179 ***Integration of Descending Command Systems for the Generation of Context-Specific Locomotor Behaviors***
Linda H. Kim, Sandeep Sharma, Simon A. Sharples, Kyle A. Mayr, Charlie H. T. Kwok and Patrick J. Whelan

198 ***Modulation of Neurogenesis Through the Promotion of Energy Production Activity is behind the Antidepressant-Like Effect of Colonial Green Alga,* Botryococcus braunii**
Kazunori Sasaki, Mahmoud B. Othman, Mikihide Demura, Makoto Watanabe and Hiroko Isoda

207 ***A Meta-Analysis of Adenosine A2A Receptor Antagonists on Levodopa-Induced Dyskinesia* In Vivo**
Wen-Wen Wang, Man-Man Zhang, Xing-Ru Zhang, Zeng-Rui Zhang, Jie Chen, Liang Feng and Cheng-Long Xie

216 ***Influence of Brain Stem on Axial and Hindlimb Spinal Locomotor Rhythm Generating Circuits of the Neonatal Mouse***
Céline Jean-Xavier and Marie-Claude Perreault

230 ***Age-Related Changes in Neuromodulatory Control of Bladder Micturition Contractions Originating in the Skin***
Harumi Hotta, Harue Suzuki, Kaori Iimura and Nobuhiro Watanabe

241 ***Effect of Different Movement Speed Modes on Human Action Observation: An EEG Study***
Tian-jian Luo, Jitu Lv, Fei Chao and Changle Zhou

256 ***Altered Neuromodulatory Drive May Contribute to Exaggerated Tonic Vibration Reflexes in Chronic Hemiparetic Stroke***
Jacob G. McPherson, Laura M. McPherson, Christopher K. Thompson, Michael D. Ellis, Charles J. Heckman and Julius P. A. Dewald

271 ***Reticulospinal Systems for Tuning Motor Commands***
Robert M. Brownstone and Jeremy W. Chopek

281 ***Inspiratory-Activated Airway Vagal Preganglionic Neurones Excited by Thyrotropin-Releasing Hormone via Multiple Mechanisms in Neonatal Rats***
Lili Hou, Min Zhang, Xingyi Zhang, Zhenwei Liu, Pengyu Zhang, Dongying Qiu, Lei Zhu and Xin Zhou

299 ***Post-stroke Hemiplegic Gait: New Perspective and Insights***
Sheng Li, Gerard E. Francisco and Ping Zhou

307 ***TASK1 and TASK3 are Coexpressed With ASIC1 in the Ventrolateral Medulla and Contribute to Central Chemoreception in Rats***
Xia Wang, Ruijuan Guan, Xiaomei Zhao, Danian Zhu, Nana Song and Linlin Shen

317 ***Differential Dopamine D1 and D3 Receptor Modulation and Expression in the Spinal Cord of Two Mouse Models of Restless Legs Syndrome***
Samantha Meneely, Mai-Lynne Dinkins, Miki Kassai, Shangru Lyu, Yuning Liu, Chien-Te Lin, Kori Brewer, Yuqing Li and Stefan Clemens

331 ***Parameters of Surface Electromyogram Suggest That Dry Immersion Relieves Motor Symptoms in Patients With Parkinsonism***
German G. Miroshnichenko, Alexander Yu Meigal, Irina V. Saenko, Liudmila I. Gerasimova-Meigal, Liudmila A. Chernikova, Natalia S. Subbotina, Saara M. Rissanen and Pasi A. Karjalainen

348 ***The Role of Long Noncoding RNAs in Central Nervous System and Neurodegenerative Diseases***
Chang-Wei Wei, Ting Luo, Shan-Shan Zou and An-Shi Wu

359 ***Optogenetic Activation of A11 Region Increases Motor Activity***
Kathrin Koblinger, Céline Jean-Xavier, Sandeep Sharma, Tamás Füzesi, Leanne Young, Shane E. A. Eaton, Charlie Hong Ting Kwok, Jaideep Singh Bains and Patrick J. Whelan

374 ***Electroacupuncture Inhibits Visceral Nociception via Somatovisceral Interaction at Subnucleus Reticularis Dorsalis Neurons in the Rat Medulla***
Lingling Yu, Liang Li, Qingguang Qin, Yutian Yu, Xiang Cui, Peijing Rong and Bing Zhu

383 ***Upregulation of AT_1 Receptor Mediates a Pressor Effect Through ROS-SAPK/JNK Signaling in Glutamatergic Neurons of Rostral Ventrolateral Medulla in Rats With Stress-Induced Hypertension***
Liping Jiang, Xuan Zhou, Hongyu Yang, Ruijuan Guan, Yanlei Xin, Jijiang Wang, Linlin Shen, Danian Zhu, Shulan Ma and Jin Wang

394 ***Non-invasive High Frequency Median Nerve Stimulation Effectively Suppresses Olfactory Intensity Perception in Healthy Males***
Ashim Maharjan, Mei Peng and Yusuf O. Cakmak

408 ***Adjustment of Synchronization Stability of Dynamic Brain-Networks Based on Feature Fusion***
Haifang Li, Rong Yao, Xiaoluan Xia, Guimei Yin, Hongxia Deng and Pengfei Yang

423 ***Activation of Brainstem Neurons During Mesencephalic Locomotor Region-Evoked Locomotion in the Cat***
Ioan Opris, Xiaohong Dai, Dawn M. G. Johnson, Francisco J. Sanchez, Luz M. Villamil, Songtao Xie, Cecelia R. Lee-Hauser, Stephano Chang, Larry M. Jordan and Brian R. Noga

frontiers in Neuroscience

EDITORIAL
published: 11 February 2020
doi: 10.3389/fnins.2020.00086

Editorial: Neuromodulatory Control of Brainstem Function in Health and Disease

Brian R. Noga[1]*, *Ioan Opris*[2]*, *Mikhail A. Lebedev*[3,4,5] *and Gordon S. Mitchell*[6]

[1] Miller School of Medicine, University of Miami, Miami, FL, United States, [2] Department of Biomedical Engineering, University of Miami, Coral Gables, FL, United States, [3] Department of Neurobiology, Duke University, Durham, NC, United States, [4] Center for Bioelectric Interfaces of the Institute for Cognitive Neuroscience, National Research University Higher School of Economics, Moscow, Russia, [5] Department of Information and Internet Technologies of Digital Health Institute, I.M. Sechenov First Moscow State Medical University, Moscow, Russia, [6] Center for Respiratory Research and Rehabilitation, Department of Physical Therapy, University of Florida, Gainesville, FL, United States

Keywords: brainstem, neuromodulation, locomotion, neurotransmitters and motor control, autonomic function, spinal cord injury, movement-related disorders, pain

Editorial on the Research Topic

Neuromodulatory Control of Brainstem Function in Health and Disease

The brainstem plays a crucial role in the control of locomotion, posture, balance, arousal (alertness, awareness, and consciousness), sensory information processing, respiration, autonomic functions (including control of blood pressure, heart rate, bowel, and bladder), and is responsible for the regulation of multiple reflexes including coughing, swallowing, and vomiting. It is controlled by the executive centers in the brain originating from cortical areas and subcortical regions, including the basal ganglia nuclei and the diencephalon, as well as, feedback loops from the cerebellum and spinal cord. A modulatory control of brainstem output can be accomplished by affecting single neurons and consequently, the operation of neuronal microcircuits and behavior. This is accomplished by altering cellular excitability, synaptic transmission (release probability, postsynaptic receptor responsiveness, thus altering synaptic strength, and efficacy) and network properties. Such dynamic control provides flexibility to the brain systems to adapt their outputs in synchrony to the functional requirements/demands of the individual to achieve the desired behavioral goal in a changing environment. Classical ionotropic transmitters: glutamate/acetylcholine, glycine/GABA (gamma-amino butyric acid) are responsible for the primary excitation and inhibition of the "anatomical network." In addition, transmitters such as the monoamines (serotonin, dopamine, or noradrenaline), acetylcholine, glutamate and GABA can alter electrical and synaptic properties of neurons by acting on metabotropic (G protein-coupled) receptors which affect signal transduction pathways.

This special topic on *Neuromodulatory Control of Brainstem Function in Health and Disease*, highlights recent advances in our understanding of the intrinsic and extrinsic neuromodulatory systems affecting brainstem function and means to control them. Two hundred twenty-five authors contributed 35 articles to this Research Topic. The contributions are summarized below in 9 thematic categories: (i) motor control, (ii) neurotransmitters and motor control, (iii) cardiovascular, respiratory and other autonomic functions, (iv) movement-related disorders, (v) pain, (vi) other disorders, (vii) non-invasive stimulation approaches for modulation of brainstem function, (viii) brain computer/machine interfaces (BCI), and (ix) non-stimulation approaches.

OPEN ACCESS

Edited and reviewed by:
James W. Grau,
Texas A&M University, United States

***Correspondence:**
Brian R. Noga
bnoga@miami.edu
Ioan Opris
ioanopris.phd@gmail.com

Specialty section:
This article was submitted to Neural Technology, a section of the journal Frontiers in Neuroscience

Received: *16 December 2019*
Accepted: *21 January 2020*
Published: *11 February 2020*

Citation:
Noga BR, Opris I, Lebedev MA and Mitchell GS (2020) Editorial: Neuromodulatory Control of Brainstem Function in Health and Disease. Front. Neurosci. 14:86. doi: 10.3389/fnins.2020.00086

MOTOR CONTROL

A group of experimental studies performed in a variety of animal models provide new insights into specific brainstem circuits involved in locomotion, posture, and voluntary (reach-to-grasp) movements.

Opris et al. examined the distribution of locomotor-activated neurons along the brainstem, combining c-Fos immunohistochemistry and cellular phenotyping. Locomotion was induced by electrical stimulation of the mesencephalic locomotor region (MLR). Of the putative anatomical correlates of the physiologically defined MLR [the cuneiform nucleus (CnF) and the pedunculopontine nucleus (PPN)], only neurons within the CnF showed significant Fos labeling, supporting the idea that the CnF is the anatomical correlate of the MLR. Local field potentials (LFPs) are thought to coherently bind cooperating neuronal ensembles during the production of different behaviors and may be useful as biomarkers to target brain regions for deep brain stimulation (DBS). Noga et al. recorded LFPs within previously identified MLR sites during voluntary locomotion. In low threshold MLR stimulation sites, onset and speed of locomotion was best correlated to the appearance and power of theta rhythms. The results demonstrate that theta band activity may be a suitable biomarker to identify functional MLR sites. The MLR is but one node or integration center involved in the descending control of spinal locomotor circuits and the operational node used at any one time is context dependent. By integrating work from the locomotion and animal behavioral domains, Kim et al. examined the neural circuits for context-specific control of locomotion, as well as approach and avoidance behaviors affecting onset and offset of locomotion. Special emphasis was given to the descending modulatory control of spinal locomotion centers from the MLR and the diencephalon. Using optogenetic stimulation, Koblinger et al. demonstrate that cells within the dopaminergic A11 region of the posterior diencephalon can enhance motor activity which may lead to locomotion.

Efficient locomotion depends upon proper control of both hindlimb and trunk muscles. The control of trunk musculature by the brainstem was examined by Jean-Xavier and Perreault using calcium imaging to discern activation of axial and hindlimb motoneurons during pharmacologically induced locomotion in the isolated neonatal mouse brainstem-spinal cord preparation. Removal of the brainstem resulted in an increase in locomotor rhythm frequency and a concurrent reduction in motoneuron burst durations, suggesting that the brainstem plays a central role in the control of trunk activity during walking.

The reticular formation is important for the integration of descending inputs controlling movement. The review by Brownstone and Chopek examines the areas of the pontomedullary reticular formation that control posture, walking and sleep and their role in the activation and inhibition of movement.

Precision reach-to-grasp movements require coordination of proximal and distal muscles controlling shoulder, arm and hand. The role of the cerebellum in reach-to-grasp movements was investigated by Geed et al. The results indicate that there is a correlation of activity between similar functional ensembles within the cerebellar nucleus interpositus and its target, the magnocellular red nucleus, which act synergistically to control complex coordinated movements.

NEUROTRANSMITTERS AND MOTOR CONTROL

Another group of papers highlight the role of the neurotransmitters dopamine, noradrenaline, serotonin, and histamine in modulating the electrical and synaptic properties of brainstem neurons during motor control.

Reticulospinal neurons are known to convey the descending command for the initiation of locomotion with stimulation of the MLR. Opris et al. show that stimulation of the MLR also activates serotonergic and catecholaminergic neurons of the pons/medulla, in addition to reticulospinal neurons. The study provides anatomical and functional evidence for spinal monoamine release during evoked locomotion. Koblinger et al. provide evidence for the existence of a new catecholaminergic neuron subtype within the A11 region, that contributes to the control of motor activity. Their data suggests that this catecholaminergic motor circuit forms part of the diencephalic locomotor region. Dopaminergic neurons modulate locomotion via their projections to the basal ganglia which ultimately affect the brainstem locomotor networks. Ryczko and Dubuc review new findings that indicate dopamine neurons project to the MLR in many vertebrate species. They summarize studies demonstrating that dopamine is released in the MLR and modulates neuronal activity there by acting on D1 receptors.

There is increasing evidence for the involvement of histamine in the modulation of motor responses. Li B. et al. show that histamine, acting on the H2 receptor, increases the excitability, and sensitivity of lateral vestibular neurons and contributes to improved central vestibular-mediated motor behaviors.

CARDIOVASCULAR, RESPIRATORY, AND OTHER AUTONOMIC FUNCTIONS

Several studies discuss new findings concerning the neuromodulatory control of respiratory, vestibular, cardiovascular and micturition systems.

Opris et al. discuss how these systems are coupled during MLR-evoked locomotion. Airway resistance is modulated by vagal preganglionic (AVP) neurons, which are regulated by thyrotropin-releasing hormone (TRH). Hou et al. show that TRH regulates inspiratory-activated AVP neuronal activity by: (i) modulating the response to excitatory and inhibitory inputs; (ii) activation of an excitatory postsynaptic slow inward current; and (iii) production of a gap junction-mediated oscillatory pattern of activity. Central chemoreception of changes in hydrogen ion concentration within the brain help to regulate respiration and acid-base homeostasis. Wang X. et al. show that local pH changes within the ventrolateral medulla modulate breathing not only by acid-sensing ion channels (voltage-independent proton-gated cation channels) but by a novel mechanism utilizing TWIK-related acid-sensitive potassium channels.

When swallowing occurs at an inappropriate time during inspiration, it increases the possibility of aspiration which can cause dysphagia. Yagi et al. investigated respiratory and swallowing activity in patients with dysphagia vs. normal subjects. Their results show a direct correlation between breathing–swallowing discoordination and the severity of dysphagia.

Sympathetic premotor neurons of the rostral ventrolateral medulla (RVLM) play an important role in the generation of vasomotor sympathetic tone. Dempsey et al. mapped the inputs to the spinally projecting RVLM neurons and found that the majority of inputs originate within the brainstem. These are likely to control respiratory-sympathetic coupling. Angiotensin II is a powerful vasoconstrictor that interacts with glutamate and GABA within the RVLM to modulate blood pressure. Légat et al. found that selective stimulation of angiotensin II type 2 receptors within the RVLM in normotensive rats increases local GABA levels and decreases blood pressure. Jiang et al. found that angiotensin II also mediates the pressor effect through a specific intracellular signaling mechanism in the glutamatergic neurons of the RVLM in rats with stress-induced hypertension.

The brainstem has a crucial role in micturition. Segmental afferent input from the skin of the perineum is known to inhibit bladder contractions due to its effects on signal transmissions between the brain and spinal cord. Hotta et al. examined the hypothesis that an overactive bladder in old age may be due to a malfunction in this inhibitory mechanism. Their results show that while the inhibitory mechanism is present in aged rats, there is evidence for reduced responses in Aδ- and C-low-threshold mechanoreceptors that can explain the weak inhibition observed in older rats.

MOVEMENT-RELATED DISORDERS

A group of studies focused on movement-related disorders provide valuable insight into gait impairments, muscle weakness, postural control and motor excitability in disorders resulting from focal ischemic stroke, hemiparetic stroke, post-stroke hemiplegic gait, Parkinson disease (PD), or restless legs syndrome.

Gait impairments are common after stroke due to the development of spasticity and paresis. Li S. et al. provide a new perspective and insight into hemiplegic gait. Damage to the motor cortex and the corticospinal tracts leads to muscle weakness. Descending brainstem and intraspinal circuits controlling posture and locomotion are disinhibited causing hyperexcitability and spasticity. These changes lead to a reorganization of the spatiotemporal patterns of activation of limb and trunk muscles during gait. They propose that post-stroke hemiplegic gait is the result of the mechanical consequences of this reorganization. This new perspective has important clinical implications for the management of hemiplegic gait. Changes in the descending neural drive (like those in focal ischemic stroke) have the potential to alter the spinal motor excitability, that may increase in the chronic hemiparetic stroke state, inducing the exaggerated stretch-sensitive reflexes. To infer the sources of spinal motor excitability in individuals with chronic hemiparetic stroke, McPherson et al. examined tonic vibration reflexes during voluntary muscle contractions. Their findings indicate that the increased excitability of motor neural ensembles innervating the paretic limb may come from neuromodulatory and ionotropic mechanisms.

In Parkinson Disease, DBS of the PPN or the subthalamic nucleus significantly improves motor symptoms and postural instability. As a treatment alternative to DBS, Cakmak et al. used intrinsic auricular muscle zone stimulation to modulate the activity of these motor centers. Clinically significant improvements in motor function were observed following stimulation indicating that such approach may be useful as a minimally invasive approach to treat PD. Ryczko and Dubuc provide a review of the involvement of dopaminergic neurons in the activation of neurons within the MLR and ultimately reticulospinal neurons, for the control of spinal locomotion. The potential involvement of dopaminergic neurons in the pathology of PD is discussed. On the other hand, the long-term use of levodopa (L-dopa) for the treatment of PD results in multiple adverse effects including drug-induced dyskinesias. Adenosine may alleviate L-dopa induced dyskinesias (LID) but the mechanism of this effect is unknown. Wang W-W. et al. conducted a metanalysis of the efficacy of adenosine A2A receptor antagonists in reducing LID. They found that although these drugs have efficacy in animal models of LID, more studies are warranted to establish this approach. In another study of PD (Miroshnichenko et al.) found that motor symptoms of PD (elevated muscle tone) were relieved with dry immersion of subjects (wrapped in a waterproof film) in water to deprive muscles of the sensory stimuli that activate reflexes. The results indicate its potential use as a rehabilitation strategy for PD patients.

Restless legs syndrome (RLS) is a sensorimotor disorder characterized by an increased urge to move the legs when they are at rest. RLS may be successfully treated using agonists that target the inhibitory dopamine D3 receptor subtype. Although there is little evidence in RSL patients of D3 receptor dysfunction, there is evidence that a mutation in the MEIS1 gene (which has been linked to an altered phenotype of dopaminergic neurons) increases the risk for developing RLS. Meneely et al. assessed the effects of dopaminergic treatment and spinal cord dopamine receptor expression in two different dopaminergic receptor knockout models of RLS. Their results suggest that the two models are complimentary and are best used to explore different aspects of RLS related sensory and motor dysfunction.

PAIN

A variety of neuronal systems within the brainstem are involved in the processing and modulation of pain signaling. These include the periaqueductal gray (PAG) and the monoaminergic nuclei, which comprise the descending pain inhibitory system. These nuclei are interconnected with higher brain centers involved in pain or nociceptive processing. A number of papers evaluated the effectiveness of different stimulation strategies aimed at reducing pain/nociception. Their results provide further evidence for the effectiveness of DBS, transcranial direct current stimulation

(tDCS), and electroacupuncture (EA) for the treatment of chronic neuropathic pain.

Chronic neuropathic pain (CNP) is a major problem following SCI and few therapeutic approaches (from pharmacological to non-pharmacological) bring relief to CNP patients. Jermakowicz et al. reported the case of a patient with severe CNP (from the incomplete paraplegia), treated with bilateral DBS of the midbrain periaqueductal gray (PAG). Their results show that DBS of the PAG had a major effect on the severity of CNP and reversed the neurological abnormalities associated with pain. The findings further suggest that activation of endogenous pain inhibitory systems linked to the PAG, may remove CNP in many patients with SCI.

In a different study, Wen et al. evaluated the prolonged analgesic effects of tDCS of primary motor cortex (M1) on chronic neuropathic pain in rats. The reported anti-nociceptive effects of tDCS had a longer analgesic effect and depend on the intensity and time of stimulation. These findings are important to the clinical application of tDCS.

To relieve visceral pain, Yu et al. applied an efficient treatment—electroacupuncture. To document the effect, they recorded neuronal firing in the medullary subnucleus reticularis dorsalis of anesthetized rats. Their findings revealed that EA induced an inhibiting effect on visceral nociceptive signals, likely due to the somato-visceral interaction within these neurons.

OTHER DISORDERS

Several brainstem reticular nuclei are involved in the control of sleep/wakefulness (consciousness) and in the control of nausea. Two papers provide insight into different strategies for the neuromodulation of disorders of consciousness and nausea.

Spinal cord stimulation may be used to treat patients with disorders of consciousness. Examining the effects of spinal stimulation on the connectivity/network properties of patients with minimally conscious state, Bai et al. confirmed that this strategy can affect gamma cortical activity, producing instant global effects (large scale connectivity and network alteration), as well as long-lasting local effects. The data indicates that the stimulation effects on consciousness may be the result of an altered frontal cortical-thalamo-cortical network function.

Median nerve stimulation (MNS) is known to alleviate the symptoms of nausea and vomiting. In a clinical trial, Maharjan et al. investigated the effect of MNS on human olfactory function, a major sensory modality for inducing vomiting and nausea. They show that only high frequency MNS can suppress odor perception. This method may be useful to treat nausea and malnutrition accompanying different health conditions.

NON-INVASIVE STIMULATION APPROACHES FOR MODULATION OF BRAINSTEM FUNCTION

Two experimental studies explore the utility of non-invasive stimulation approaches to modulate brainstem function: transcranial magnetic stimulation (TMS), based on the electric current induced by a change in magnetic field and focused ultrasound stimulation (FUS) using low intensity, low frequency ultrasound.

Chen et al. used TMS to evaluate the excitability of the laryngeal motor cortex and its responses to neuromodulation by measuring motor evoked potentials and the cortical silent period (cSP). Their results support the feasibility of using TMS for measuring laryngeal muscles responses during vocalization and thus provide a new tool for understanding the neural control of voice production.

Neuronal oscillations coordinate neural ensembles by coupling the firing of multiple neurons through phase-amplitude coupling (PAC). PAC is closely linked with cognitive brain functions and may be used to measure cortical excitability as well as network interactions. Yuan et al. examined the relationship between the intensity of ultrasounds and the PAC index in the rat brain. They demonstrated that FUS can be used to modulate neural firing with tremendous spatial precision leaving open the possibility that this method may be useful for improving cognitive abilities.

BRAIN COMPUTER/MACHINE INTERFACES (BCI)

A brain computer interface (BCI) is a neural control system that provides a communication pathway between a computer, the brain and an external device/actuator. An interesting BCI is based on the concept of mirror neurons. A "mirror neuron" represents a special type of neuron that "mirrors" the behavior of an observer, assuming the observer was itself acting. The components of the human mirror neuron system activate subcortical systems and "sensorimotor" cortices (occipital or parietal) when a subject performs or observes an action. Engaging the mirror system in such a fashion can be used as a therapeutic strategy for rehabilitation after brain injury or disease. An "action observation" produces "event-related desynchronization" (ERD) suppressions in the human brain by activating regions of the "mirror neuron system." Luo et al. examined the mirror system's response in different cortical regions to the speed of action observed by adjusting the movement speed of a robotic arm. Results indicate the possibility to construct BCIs based on patterns of action observation.

Li H. et al. built an EEG brain functional network with dynamic connections and used its special characteristics to derive synchronization features. These were used to interpret processing during a memory paradigm and examine differences between healthy controls and mental patients. The results provide new insights into the pathology of brain disorders.

NON-STIMULATION APPROACHES

Finally, a group of studies explore the utility of non-stimulation approaches to modulating brainstem function, examining the

role of astrocytes in the locus ceruleus in pain resulting from emotional dysfunction, the antidepressant-like effect of algae on dopaminergic function and the regulation of gene expression by long non-coding RNAs in the pathophysiology of central nervous system diseases.

Emotional dysfunction joined by early life stress has been shown to increase the perception of pain. Nakamoto et al. examined the role of astrocytes in emotional dysfunction in mice under maternal separation and social isolation as a source of life stress. Their results show that astrocyte activation in the locus coeruleus is involved in the increase of neuropathic pain caused by maternal separation.

Algae have been shown to have a variety of beneficial effects on health. Sasaki et al. assessed its antidepressant effect using a forced-swimming test rodent model of depression. They found that an extract of the colonial green alga *Botryococcus braunii* enhanced the expression of genes involved in neurogenesis, energy metabolism and dopamine synthesis. They suggest that the antidepressant-like effect of this alga is due to enhanced dopaminergic function.

The review by Wei et al. describes the varied roles for long non-coding RNAs, and how they may be involved in the development of the etiology and pathophysiology of central nervous system diseases.

In conclusion, the Research Topic on *Neuromodulatory Control of Brainstem Function in Health and Disease* contributed with valuable insight into the multitude of functions involving the brainstem.

AUTHOR CONTRIBUTIONS

All authors listed have made a substantial, direct and intellectual contribution to the work, and approved it for publication.

FUNDING

This work was supported by The Craig H. Neilsen Foundation (190550), NIH NINDS (R01NS46404 and R01NS089972) and the Department of Defense (SCI140238) to BN, by the Center for Bioelectric Interfaces (NRU HSE), RF Government grant, ag. No 14.641.31.0003 to ML and NIH grants NIH SPARC OT2OD023854, R01 HL148030, and R01 HL147554 to GM.

ACKNOWLEDGMENTS

We would like to thank all authors and reviewers for their contributions to this Research Topic. We would also like to thank the Frontiers team for professional help with this Research Topic.

Conflict of Interest: The authors declare that the research was conducted in the absence of any commercial or financial relationships that could be construed as a potential conflict of interest.

Copyright © 2020 Noga, Opris, Lebedev and Mitchell. This is an open-access article distributed under the terms of the Creative Commons Attribution License (CC BY). The use, distribution or reproduction in other forums is permitted, provided the original author(s) and the copyright owner(s) are credited and that the original publication in this journal is cited, in accordance with accepted academic practice. No use, distribution or reproduction is permitted which does not comply with these terms.

frontiers in Neuroscience

ORIGINAL RESEARCH
published: 22 July 2016
doi: 10.3389/fnins.2016.00348

Noninvasive Focused Ultrasound Stimulation Can Modulate Phase-Amplitude Coupling between Neuronal Oscillations in the Rat Hippocampus

Yi Yuan[1†], *Jiaqing Yan*[2†], *Zhitao Ma*[1] *and Xiaoli Li*[3,4*]

[1] *Institute of Electrical Engineering, Yanshan University, Qinhuangdao, China,* [2] *School of Electrical and Control Engineering, North China University of Technology, Beijing, China,* [3] *State Key Laboratory of Cognitive Neuroscience and Learning and IDG/McGovern Institute for Brain Research, Beijing Normal University, Beijing, China,* [4] *Center for Collaboration and Innovation in Brain and Learning Sciences, Beijing Normal University, Beijing, China*

OPEN ACCESS

Edited by:
Mikhail Lebedev,
Duke University, USA

Reviewed by:
José M. Delgado-García,
Pablo de Olavide University, Spain
James M. Hyman,
University of Nevada, USA

***Correspondence:**
Xiaoli Li
xiaoli@bnu.edu.cn

[†]*These authors have contributed equally to this work.*

Specialty section:
This article was submitted to Neural Technology, a section of the journal Frontiers in Neuroscience

Received: *30 May 2016*
Accepted: *11 July 2016*
Published: *22 July 2016*

Citation:
Yuan Y, Yan J, Ma Z and Li X (2016) Noninvasive Focused Ultrasound Stimulation Can Modulate Phase-Amplitude Coupling between Neuronal Oscillations in the Rat Hippocampus. Front. Neurosci. 10:348. doi: 10.3389/fnins.2016.00348

Noninvasive focused ultrasound stimulation (FUS) can be used to modulate neural activity with high spatial resolution. Phase-amplitude coupling (PAC) between neuronal oscillations is tightly associated with cognitive processes, including learning, attention, and memory. In this study, we investigated the effect of FUS on PAC between neuronal oscillations and established the relationship between the PAC index and ultrasonic intensity. The rat hippocampus was stimulated using focused ultrasound at different spatial-average pulse-average ultrasonic intensities (3.9, 9.6, and 19.2 W/cm^2). The local field potentials (LFPs) in the rat hippocampus were recorded before and after FUS. Then, we analyzed PAC between neuronal oscillations using a PAC calculation algorithm. Our results showed that FUS significantly modulated PAC between the theta (4–8 Hz) and gamma (30–80 Hz) bands and between the alpha (9–13 Hz) and ripple (81–200 Hz) bands in the rat hippocampus, and PAC increased with incremental increases in ultrasonic intensity.

Keywords: focused ultrasound stimulation, neuronal oscillation, phase-amplitude coupling, hippocampus, ultrasonic intensity

INTRODUCTION

Neuronal oscillations provide a mechanism for forming cell assemblies and coordinating cell assemblies by linking the activity of multiple neurons (Wiley, 2010). Neuronal oscillations, which are the complex cognitive functions of the brain that occur from the synergistic interaction of multiple neurons, are mainly involved in cognitive processes, including feature binding, selective attention, and memory. In neuronal oscillations, the amplitude of a faster rhythm is coupled to the phase of a slower rhythm; this is termed phase-amplitude coupling (PAC) and reflects the interactions between local micro-scale and systems-level macro-scale neuronal ensembles. Therefore, PAC can be used as an index of cortical excitability and network interactions (Klausberger et al., 2003; Knight, 2007; Haider and McCormick, 2009; Voytek et al., 2010). Recent findings have shown that PAC was a mechanism for working memory capacity and the discrete

nature of perception. PAC also plays an important role during sleep (Penny et al., 2008; Wang et al., 2014). In brief, PAC is a new index that reflects the dynamic interactions between neuronal oscillations.

Noninvasive focused ultrasound stimulation (FUS) of isolated turtle nerve fibers was first performed in 1929 (Newton, 1929). A previous study showed that the mechanism of FUS involves ultrasound-induced cavitation of nanometric bilayer sonophores, which can induce a complex mechanoelectrical interplay that leads to excitation, primarily through the effect of currents induced by membrane capacitance changes of neurons (Plaksin et al., 2014).Changes in neural networks induced by FUS may be caused by changes in the firing rhythm of several neurons. Low-intensity ultrasound can directly modulate neuronal activity in peripheral nerves (Mihran et al., 1990; Tyler, 2011), elicit action potentials in hippocampal slices (Tyler et al., 2008), synchronous oscillations in the intact hippocampus (Tufail et al., 2010) and stimulate the retina (Menz et al., 2013). Furthermore, it can noninvasively stimulate the intact mouse motor cortex (Tufail et al., 2010). Recently, low-intensity focused ultrasound was used to modulate visuomotor behavior in monkeys (Deffieux et al., 2013). Focused ultrasound was also applied to modulate the activity of the primary somatosensory cortex in humans (Legon et al., 2014). Tufail and Yoo et al used pulses of low-frequency (250–700 kHz) ultrasound to modulate brain function (Tufail et al., 2010; Yoo et al., 2011). Mehiæ et al. used a higher frequency (2 MHz), pulsed and focused ultrasound to stimulate the brain of lightly anesthetized mice (Mehiæ et al., 2014). Compared with transcranial direct current stimulation (tDCS) and repetitive transcranial magnetic stimulation (rTMS), FUS has a higher spatial resolution (<2 mm; Tufail et al., 2010; Bystritsky et al., 2011; Yoo et al., 2011). To date, there have been no reports on the effect of low-intensity ultrasound on PAC between neuronal oscillations. In this study, we focused exclusively on the effect of FUS on PAC between neuronal oscillations derived from the hippocampus. A thorough study of the relationship between PAC and ultrasonic intensity is necessary to evaluate the effects of FUS on neuromodulation and to provide a reference for choosing ultrasonic intensities when applying FUS. Our study investigated PAC between neuronal oscillations in the rat hippocampus induced by different ultrasonic intensities of FUS. Local field potentials (LFPs) were recorded from the rat hippocampus before and after FUS. The effects of FUS on PAC between the theta (4–8 Hz) and gamma (30–80 Hz) bands and between the alpha (9–13 Hz) and ripple (81–200 Hz) bands were analyzed using the phase-amplitude coupling index (PACI).

MATERIALS AND METHODS

Experimental Setup for FUS and Data Acquisition

The schematic of the experimental setup is shown in **Figure 1**. The pulse signals were generated by an ultrasonic transmitter and receiver card (USB-UT350T, Ultratek, USA) that drove the focused ultrasound transducer. In our study, the ultrasound transducer, with a bandwidth of 50% and focal length of 30 mm, was driven at a high frequency (2.5 MHz). The active volume of the ultrasound probe was ∼625.36 mm^3 and the diameter of the ultrasound intensity focus field was ∼4.5 mm. A single stimulation consisted of 4 cycle (1.6 μs) ultrasound pulses with a pulse repetition frequency of 500 Hz and a duration of 160 ms (80 repetitions). An ultrasonic sound power measuring instrument with a diameter of 9.5 mm was used to measure the average intensity of the ultrasound (YP0511F, Hangzhou, China). The spatial-average pulse-average intensities of the ultrasound were 3.9, 9.6, and 19.2 W/cm^2.

LFP signals from the hippocampus were recorded using a 16-channel microelectrode (GBMA-S16, Blackrock Microsystems,

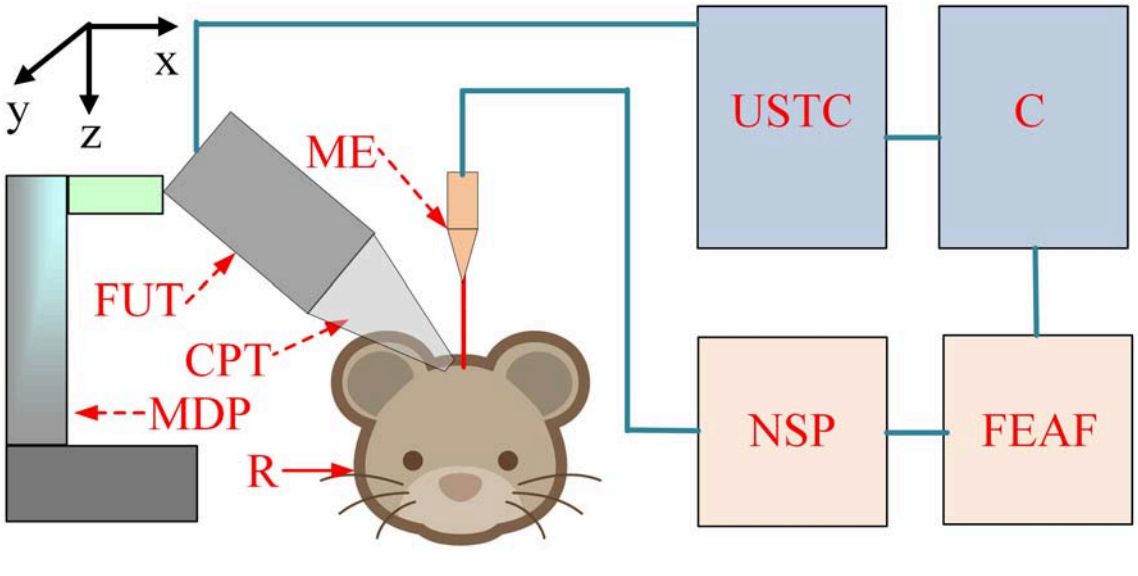


FIGURE 1 | The schematic of the experiment setup. C, computer; USTC, ultrasonic transmitter card; ME, microelectrode; FUT, focused ultrasound transducer; CPT, conic plastic tube; R, rat; MDP, manual displacement platform; NSP, neural signal processor; FEAF, front-end amplifier.

USA) and amplified using a 128-channel front-end amplifier (Cerebus, 128 channels, Blackrock Microsystems, USA). The analog signals were converted into digital signals using a 128-channel neural signal processor (Cerebus128 channels, Cyberknetics, USA), which was then transmitted to a computer for data storage and processing. The data were digitized at a sample rate of 30 kHz, and a low-pass filter with a 250 Hz cutoff frequency for the LFPs was set in the Cerebus system. A heating blanket was used to maintain normal body temperature in the rats. A cold-light source and microscope were used for surgery and a shielding net was used to prevent outside electrical interference.

Animal Surgery and Anesthesia

A total of six Sprague-Dawley rats (3-month-old males, body weights ∼270 g) were used in the experiment. All procedures were carried out in accordance with the Animal Ethics and Administrative Council of Yanshan University and Hebei Province, China. Surgical anesthesia was induced with sodium pentobarbital (3%, 5 mg/100 g, i.p.). The anesthetized rats were fixed on the stereotaxic apparatus (ST-5ND-C, Stoelting Co., USA) with ear bars and a clamping device. The fur covering the rat's skull was shaved, and the skin was cleaned with a 0.9% sodium chloride physiological solution. The scalp was cut along the midline of the skull, and the subcutaneous tissue and periosteum were removed. The location of the hippocampus was determined using an atlas. A section of the skull was removed to expose the brain tissue in an area of ∼0.5 × 0.5 cm. After completion of the surgical procedure, a 16-channel metal microelectrode (GBMA-S16, Blackrock Microsystems, USA) was inserted into the hippocampus. The anteroposterior (AP), mediolateral (ML), and dorsoventral (DL) coordinates of the center of the recording electrode were -5.3, 3.4, and 3 mm, respectively.

Experimental Procedure

In the ultrasound stimulation experiment, the anesthetized rats were fixed on the stereotaxic apparatus (ST-5ND-C, Stoelting Co., USA) with ear bars and a clamping device. The focused transducer was aimed at the rat hippocampus by adjusting a three-axis manual displacement platform (Zolix, China). A 27 mm plastic cone was filled with degassed ultrasound gel and used to couple the ultrasound transducer to the cortex over the hippocampus. The ultrasound transducer then transmitted an ultrasonic wave. The focused ultrasonic wave passed through the ultrasonic coupling medium and stimulated the brain tissue to induce noninvasive brain neuromodulation. The angle between the ultrasound and the recording microelectrode was ∼60°.

PAC Analyses

PAC is the coupling degree index between the low-frequency phase and the high-frequency amplitude. In this study, we

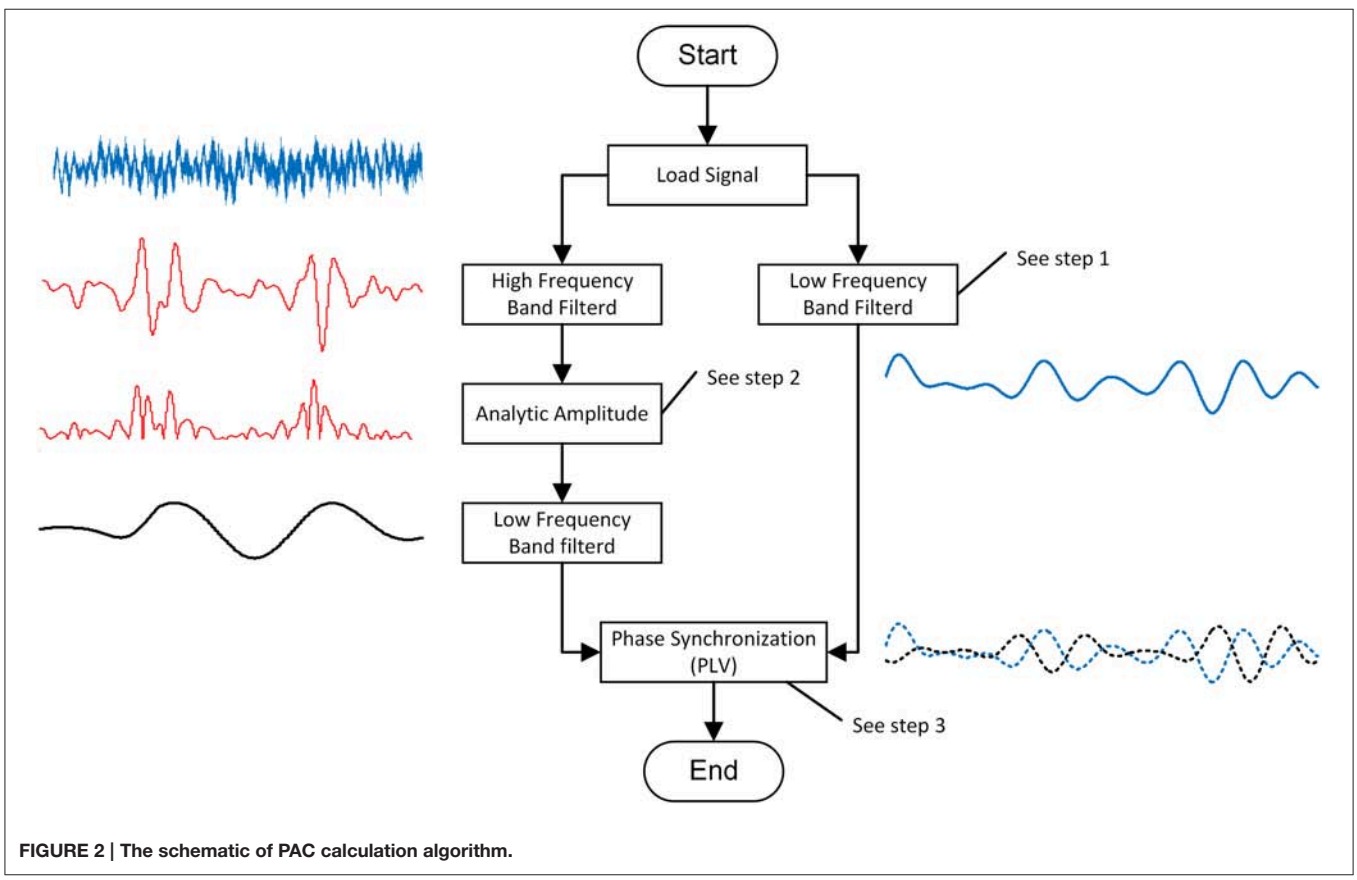


FIGURE 2 | The schematic of PAC calculation algorithm.

modified Voytek's method to calculate the PACI between the low and high frequencies (Voytek et al., 2013). The process (shown in **Figure 2**) of this calculation method included three steps.

Step 1: band-pass filter

A harmonic wavelet was used to provide an unbiased and consistent estimation of the EEG power spectrum (Kapiris et al., 2005). The harmonic wavelet was chosen instead of the more commonly used Morlet wavelet because it is orthogonal and its expression is simple. The wavelet transform passes a filter $\psi(\bullet)$over a time series $x(t)$ to obtain a finite number of filtered signals.

$$W_x(a,\tau) = \frac{1}{\sqrt{|a|}} \int x(t)\,\psi\left(\frac{t-\tau}{a}\right) dt, \tag{1}$$

where $\psi(\bullet)$ is the basic or mother wavelet function and a and τ denote the scale factor and the translation of the origin, respectively. The variable $1/a$ gives the frequency scale, and τ gives the temporal location of an event. $W_x(a,\tau)$ can be interpreted as the "energy" of x of scale a at $t = \tau$. Moreover, the harmonic wavelet function is defined as

$$\psi_{m,n}(t) = \frac{e^{jn2\pi t} - e^{jm2\pi t}}{j(n-m)2\pi t}, \tag{2}$$

where m and n are the real scale parameters but not necessarily integers. For the discrete time series $t = \tau$, the wavelet transform is expressed as

$$W_S(n) = \sum_{n=0}^{N-1} x_n \psi_0^*\left(\frac{n-N}{S}\right), \tag{3}$$

where * indicates the complex conjugate. By varying the wavelet scale s and translating along the localized time index k, one can construct a picture that shows both the amplitude of any feature

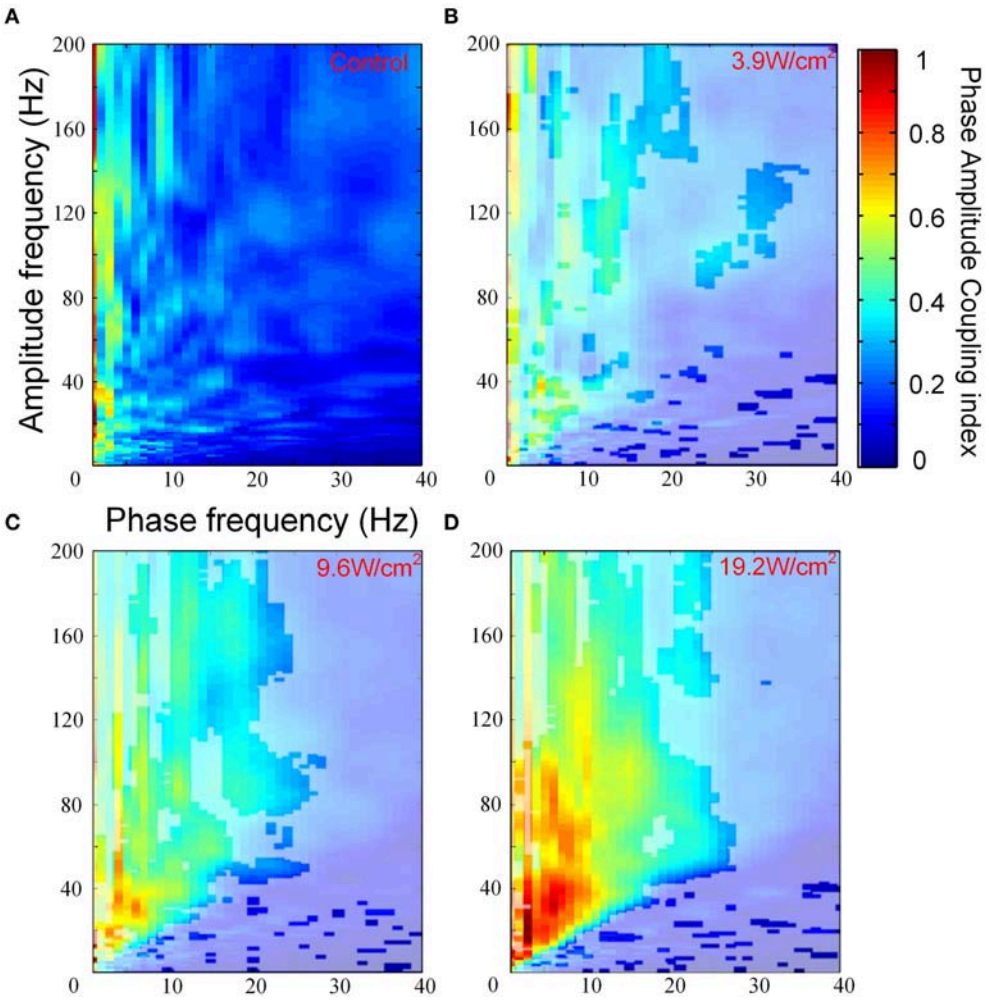


FIGURE 3 | (A) The images of the PACI as a function of the analytic phase (1–40 Hz) and the analytic amplitude (1–200 Hz) for the control ($n = 6$). **(B–D)** The images of the PACI as a function of the analytic phase (1–40 Hz) and the analytic amplitude (1–200 Hz) for the FUS with different ultrasonic intensities: **(B)** 3.9 W/cm^2, **(C)** 9.6 W/cm^2, **(D)** 19.2 W/cm^2 ($n = 6$).

vs. the scale and how this amplitude varies with time. The band pass filtered discrete sequence x_n is defined as

$$x_{filt}(f) = 2 \times real\left(W\left(f\right)\right). \quad (4)$$

Step 2: analytic amplitude

For the filtered signal x_{filt_s}, we used the absolute value to reflect the power of the signal. The power of the discrete sequencex_{filt_s} is defined as

$$P\left(s\right) = \left|x_{filt_s}\right|, \quad (5)$$

where |•| indicates the absolute value.

Step 3: phase synchronization

Phase synchronization describes the phase relationship of the two signals. In this study, we applied the Hilbert transform to estimate the phases (ϕ_l, ϕ_h) for the two signals: (i) the low-frequency oscillation and (ii) the low-frequency band-pass filtered high–frequency oscillation amplitude.

Then, the PACI between the two signals was defined by the following equation

$$PACI = \left|\frac{1}{K}\sum_{k=1}^{K-1}\exp\left(i\left(\phi_l\left[k\right] - \phi_h\left[k\right]\right)\right)\right|, \quad (6)$$

where *PACI* is the phase-locking value between the ongoing phase ϕ_l and ϕ_k, and k is the time index. PAC differences between the control and FUS at the different ultrasonic intensities were analyzed for all subjects using Kruskal-Wallis with Tukey-Kramer *post-hoc* test that is a non-parametric statistical test method.

RESULTS

We investigated PAC that was induced by FUS at different ultrasonic intensities. **Figures 3A–D** show the images of the PACI as a function of the analytic phase (1–40 Hz) and analytic amplitude (1–200 Hz) for the control and FUS at the different intensities. In **Figures 3B–D**, the area not covered by white shadows indicated that they are mean ranks significantly different from the control group (Kruskal-Wallis with Tukey-Kramer *post-hoc* test). When the ultrasonic intensity was 3.9 W/cm^2, the PACI showed that there was a significant difference between FUS and the control in a small frequency range (**Figures 3A,B**). These changes were mainly reflected in the theta, alpha and gamma frequency bands. Compared to the ultrasonic intensity (3.9 W/cm^2), the PACI in the large frequency range was significantly enhanced with an ultrasonic intensity of 9.6 W/cm^2 (**Figure 3C**). This enhancement was obvious in the theta and gamma frequency bands, the alpha and gamma frequency bands, and the ripple frequency bands. When the ultrasonic intensity was 19.2 W/cm^2 (**Figure 3D**), the PACI was further increased compared to the ultrasonic intensity of 9.6 W/cm^2. However, it is worth noting that there were no significant changes in the frequency bands. Based the comparison of the PACI between the three ultrasonic intensities and the control, we found that the change in PAC was obvious in the theta and gamma frequency bands and the alpha and ripple frequency bands. Therefore, to further analyze the effects of ultrasonic intensity on the PACI, we separately calculated the mean PACI in the theta and gamma frequency bands and the alpha and ripple frequency bands.

Furthermore, in **Figures 3A–D**, we quantitatively computed the mean PACI, which is equal to the total PACI divided by the total points. As is shown in **Figure 4A**, the mean PACI between

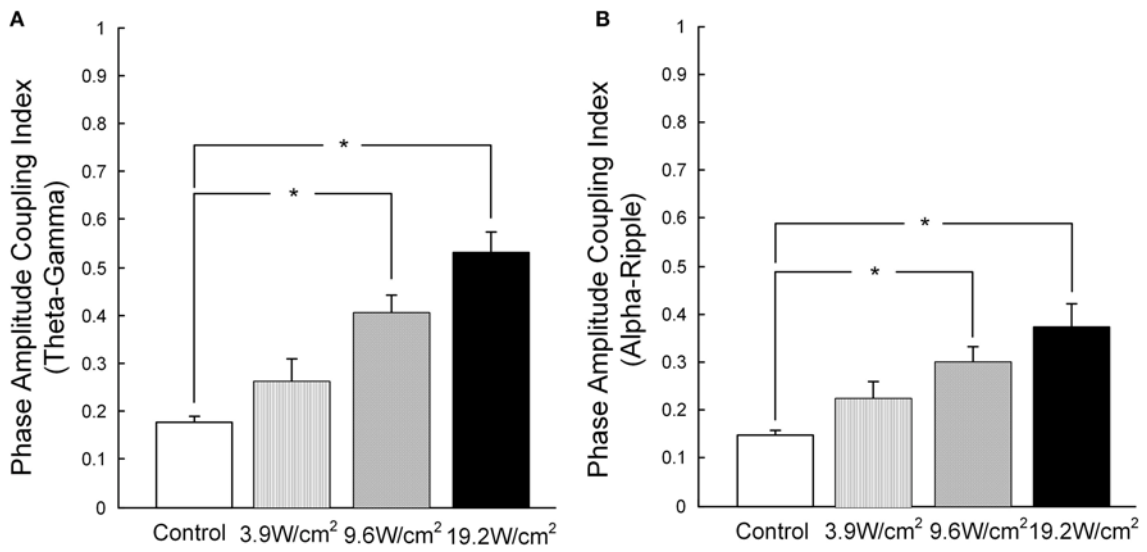


FIGURE 4 | (A) The mean PACI of theta (4–8 Hz) and gamma coupling (30–80 Hz) in the control and with ultrasonic intensities of 3.9, 9.6, and 19.2 W/cm^2 [mean ± SEM, $n = 6$, Chi-Sq (3, 20) = 16.49, $^*p = 0.0009$: mean ranks mean ranks significantly different, Kruskal-Wallis with Tukey-Kramer *post-hoc* test]. **(B)** The mean PACI of alpha (9–13 Hz) and ripple coupling (81–200 Hz) in the control and with ultrasonic intensities of 3.9, 9.6, 19.2 W/cm^2 [mean ± SEM, $n = 6$, Chi-Sq (3, 20) =14.25, $^*p = 0.0026$: mean ranks significantly different, Kruskal-Wallis with Tukey-Kramer *post-hoc* test].

the theta (4–8 Hz) and gamma (30–80 Hz) bands for the control and the different ultrasonic intensities (3.9, 9.6, and 19.2 W/cm^2) was 0.17 ± 0.01, 0.26 ± 0.04, 0.41 ± 0.03, and 0.53 ± 0.04, respectively [mean ± SEM, $n = 6$, Chi-Sq (3, 20) = 16.49, $^*p = 0.0009$: mean ranks significantly different, Kruskal-Wallis with Tukey-Kramer *post-hoc* test). Compared with the control, the mean PACI between the theta and gamma band increased by 1.53-, 2.41-, and 3.12-fold for the ultrasonic intensities of 3.9, 9.6, and 19.2 W/cm^2, respectively. Therefore, the mean PACI between the theta and gamma band significantly increased as the ultrasonic intensity increased. A similar result was found for the alpha (9–13 Hz)-ripple (81–200 Hz) coupling (**Figure 4B**). The mean PACI between the alpha (9–13 Hz) and ripple (81–200 Hz) bands for the control and the different ultrasonic intensities (3.9, 9.6, and 19.2 W/cm^2) was 0.15 ± 0.01, 0.22 ± 0.03, 0.30 ± 0.03, and 0.37 ± 0.05, respectively [mean ± SEM, $n = 6$, Chi-Sq (3, 20) = 14.25, $^*p = 0.0026$: mean ranks significantly different, Kruskal-Wallis with Tukey-Kramer *post-hoc* test]. Compared with the control, the mean PACI between the alpha and ripple band increased by 1.46−, 2.01−, and 2.46−fold for the ultrasonic intensities of 3.9, 9.6, and 19.2 W/cm^2, respectively. These results show that the FUS can significantly enhance the PAC index between the theta and gamma band and between the alpha and ripple band as the ultrasonic intensity increases.

DISCUSSION

In our previous work (Yuan et al., 2015), we used focused ultrasound with different parameters to stimulate the rat hippocampus. We recorded LFPs evoked by FUS in the rat hippocampus. The mean absolute power of the LFPs was calculated using the Welch algorithm at the delta, theta, alpha, beta and gamma frequency bands. The experimental results demonstrate that the mean absolute power of the LFPs at the different frequency bands increases as the ultrasound power increases. However, we did not pay particular attention to the effect of the ultrasonic parameters on PAC of LFP signals. Subsequently, we found that ultrasonic power can influence PAC of the LFP between the low and high-frequency bands, specifically, in the theta and gamma frequency bands and the alpha and ripple frequency bands.

Previous studies have shown that PAC is associated with brain functions. For example, human memory strength can be predicted by theta-frequency phase-locking of singles (Rutishauser et al., 2010). Therefore, investigating the relationship between PAC and FUS is important. We calculated the mean PACI between the alpha and ripple band and between the theta and gamma band at different ultrasonic intensities (3.9, 9.6, and 19.2 W/cm^2). Our results indicated that the PACI between the theta and gamma band and between the alpha and ripple band were closely connected with the ultrasonic intensity. We can alter the amplitude characteristics of the high-frequency LFPs by modulating the phase characteristics of the low-frequency LFPs by adjusting the ultrasonic intensity. Cognitive abilities (such as memory storage, retrieval, etc.) are closely related to PAC (Mann and Mody, 2010); therefore, we can modulate cognitive abilities by altering ultrasonic intensity. PAC can also optimize ultrasonic intensity by modulating brain oscillations during the application of FUS to treat neurological diseases.

In our study, we analyzed PAC in the rat hippocampus using three ultrasonic intensities (3.9, 9.6, and 19.2 W/cm^2). To obtain a more accurate understanding of the functional relationship between PAC and different ultrasonic intensities, we plan to stimulate the rat hippocampus with additional ultrasound intensities in future studies. The range of acoustic parameters can affect neural activity. A previous study showed that the success of ultrasound stimulation increases as a function of both the acoustic intensity and acoustic duration (King et al., 2013). Perhaps other ultrasonic parameters, including the center frequency, stimulus frequency, duration and number of cycles, can also affect PAC in the hippocampus. In this study, we only quantitatively analyzed the effect of different ultrasonic intensities of FUS on PAC in the rat hippocampus. In future studies, we will evaluate the effect of the other ultrasonic parameters mentioned above on PAC in the hippocampus.

Because ultrasound at high intensities or during long exposures can burn and damage tissues, it is very important to control the ultrasonic intensity when FUS is applied to modulate brain activity. In this study, the maximum ultrasonic intensity was 19.2 W/cm^2, which was not only below the maximum recommended limit for diagnostic imaging applications (190 W/cm^2) but was also below the 23.87 W/cm^2 that was used to modulate the activity in the primary somatosensory cortex in humans (Nyborg, 2001). Therefore, the ultrasonic dose in our experiment is safe. Studies have shown that neuromodulation using TMS is based on the motor threshold (Awiszus, 2003). However, TMS cannot modulate brain activity due to the weak intensity of the magnetic field. This study demonstrates that PAC between neuronal oscillations in the rat hippocampus can be altered using different ultrasonic intensities, which may support the use of PAC between neuronal oscillations to select the appropriate ultrasound intensity for FUS.

In summary, PAC between neuronal oscillations in the rat hippocampus can be altered by FUS, and the PACI increased as the ultrasonic intensity increased. To our knowledge, this is the first study of its kind to demonstrate the effect of FUS with different ultrasonic intensities on PAC between neuronal oscillations.

AUTHOR CONTRIBUTIONS

YY and XL designed and coordinated the study, YY, JY, and ZM carried out experiment and data process, and drafted the manuscript. All authors gave final approval for publication.

ACKNOWLEDGMENTS

This research was supported by National Natural Science Foundation of China (61503321, 61273063), Natural science foundation of Hebei Province (F2014203161).

REFERENCES

Awiszus, F. (2003). TMS and threshold hunting. *Suppl. Clin. Neurophysiol.* 56, 13–23. doi: 10.1016/S1567-424X(09)70205-3

Bystritsky, A., Korb, A. S., Douglas, P. K., Cohen, M. S., Melega, W. P., Mulgaonkar, A. P., et al. (2011). A review of low-intensity focused ultrasound pulsation. *Brain Stimul.* 4, 125–136. doi: 10.1016/j.brs.2011.03.007

Deffieux, T., Younan, Y., Wattiez, N., Tanter, M., Pouget, P., and Aubry, J.-F. (2013). Low-intensity focused ultrasound modulates monkey visuomotor behavior. *Curr. Biol.* 23, 2430–2433. doi: 10.1016/j.cub.2013.10.029

Kapiris, P. G., Polygiannakis, J., Li, X. L., Yao, X., and Eftaxias, K. A. (2005). Similarities in precursory features in seismic shocks and epileptic seizures. *Europhys. Lett.* 69, 657–663. doi: 10.1209/epl/i2004-10383-2

Klausberger, T., Magill, P., Márton, L. F., Roberts, J. D., Cobden, P. M., Buzsáki, G., et al. (2003). Brainstate- and cell-type-specific firing of hippocampal interneurons *in vivo*. *Nature* 421, 844–848. doi: 10.1038/nature01374

King, R. L., Brown, J., Newsome, W. T., and Pauly, K. B. (2013). Effective parameters for ultrasound-induced *in vivo* neurostimulation. *Ultrasound Med. Biol.* 393, 312–331. doi: 10.1016/j.ultrasmedbio.2012.09.009

Knight, R. T. (2007). Neural networks debunk phrenology. *Science* 316, 1578–1579. doi: 10.1126/science.1144677

Haider, B., and McCormick, D. (2009). Rapid neocortical dynamics: cellular and network mechanisms. *Neuron* 62, 171–189. doi: 10.1016/j.neuron.2009.04.008

Legon, W., Sato, T. F., Opitz, A., Mueller, J., Barbour, A., Williams, A., et al. (2014). Transcranial focused ultrasound modulates the activity of primary somatosensory cortex in humans. *Nat. Neurosci.* 17, 322–329. doi: 10.1038/nn.3620

Mann, E. O., and Mody, I. (2010). Control of hippocampal gamma oscillation frequency by tonic inhibition and excitation of interneurons. *Nat. Neurosci.* 13, 205–213. doi: 10.1038/nn.2464

Mehiæ, E., Xu, J. M., Caler, C. J., Coulson, N. K., Moritz, C. T., and Mourad, P. D. (2014). Increased anatomical specificity of neuromodulation via modulated focused ultrasound. *PLoS ONE* 9:e86939. doi: 10.1371/journal.pone.0086939

Menz, M. D., Oralkan, Ö., Khuri-Yakub, P. T., and Baccus, S. A. (2013). Precise neural stimulation in the retina using focused ultrasound. *J. Neurosci.* 33, 4550–4560. doi: 10.1523/jneurosci.3521-12.2013

Mihran, R. T., Barnes, F. S., and Wachtel, H. (1990). Temporally-specific modification of myelinated axon excitability *in vitro* following a single ultrasound pulse. *Ultrasound Med. Biol.* 16, 297–309. doi: 10.1016/0301-5629(90)90008-Z

Newton, H. E. (1929). The effect of high frequency sound waves on heart muscle and other irritable tissues. *Am. J. Physiol.* 9, 1284–1290.

Nyborg, W. L. (2001). Biological effects of ultrasound: development of safety guidelines. Part II: general review. *Ultrasound Med. Biol.* 27, 301–333. doi: 10.1016/S0301-5629(00)00333-1

Penny, W. D., Duzel, E., Miller, K. J., and Ojemann, J. G. (2008). Testing for nested oscillation. *J. Neurosci. Methods* 174, 50–61. doi: 10.1016/j.jneumeth.2008.06.035

Plaksin, M., Shoham, S., and Kimmel, E. (2014). Intramembrane cavitation as a predictive bio-piezoelectric mechanism for ultrasonic brain stimulation. *Phys. Rev. X* 4:011004. doi: 10.1103/PhysRevX.4.011004

Rutishauser, U., Ross, I. B., Mamelak, A. N., and Schuman, E. M. (2010). Human memory strength is predicted by theta-frequency phase-locking of single neurons. *Nature* 464, 903–907. doi: 10.1038/nature08860

Tufail, Y., Matyushov, A., Baldwin, N., Tauchmann, M. L., Georges, J., Yoshihiro, A., et al. (2010). Transcranial pulsed ultrasound stimulates intact brain circuits. *Neuron* 66, 681–694. doi: 10.1016/j.neuron.2010.05.008

Tyler, W. J. (2011). Noninvasive neuromodulation with ultrasound? A continuum mechanics hypothesis. *Neuroscientist* 17, 25–36. doi: 10.1177/1073858409348066

Tyler, W. J., Tufail, Y., Finsterwald, M., Tauchmann, M. L., Olson, E. J., and Majestic, C. (2008). Remote excitation of neuronal circuits using low intensity, low-frequency ultrasound. *PLoS ONE* 3:3511. doi: 10.1371/journal.pone.0003511

Voytek, B., Canolty, R. T., Shestyuk, A., Crone, N. E., Parvizi, J., and Knight, R. T. (2010). Shifts in gamma phase-amplitude coupling frequency from theta to alpha over posterior cortex during visual tasks. *Front. Hum. Neurosci.* 4:191. doi: 10.3389/fnhum.2010.00191

Voytek, B., D'Esposito, M., Crone, N., and Knight, R. T. (2013). A method for event-related phase/amplitude coupling. *Neuroimage* 64, 416–424. doi: 10.1016/j.neuroimage.2012.09.023

Wang, J., Gao, D. Q., Li, D., Desroches, A. S., Liu, L., and Li, X. L. (2014). Theta-gamma coupling reflects the interaction of bottom-up and top-down processes in speech perception in children. *Neuroimage* 102, 637–645. doi: 10.1016/j.neuroimage.2014.08.030

Wiley, B. G. (2010). Neural syntax: cell assemblies, synapsembles, and readers. *Neuron* 68, 362–385. doi: 10.1016/j.neuron.2010.09.023

Yoo, S.-S., Bystritsky, A., Lee, J.-H., Zhang, Y. Z., Fischer, K., Min, Y.-K., et al. (2011). Focused ultrasound modulates region-specific brain activity. *Neuroimage* 56, 1267–1275. doi: 10.1016/j.neuroimage.2011.02.058

Yuan, Y., Lu, C. B., and Li, X. L. (2015). Effect of focused ultrasound stimulation at different ultrasonic power levels on the local field potential power spectrum. *Chin. Phys. B* 24:088704. doi: 10.1088/1674-1056/24/8/088704

Conflict of Interest Statement: The authors declare that the research was conducted in the absence of any commercial or financial relationships that could be construed as a potential conflict of interest.

Copyright © 2016 Yuan, Yan, Ma and Li. This is an open-access article distributed under the terms of the Creative Commons Attribution License (CC BY). The use, distribution or reproduction in other forums is permitted, provided the original author(s) or licensor are credited and that the original publication in this journal is cited, in accordance with accepted academic practice. No use, distribution or reproduction is permitted which does not comply with these terms.

frontiers in Cellular Neuroscience

ORIGINAL RESEARCH
published: 10 January 2017
doi: 10.3389/fncel.2016.00300

Histamine Increases Neuronal Excitability and Sensitivity of the Lateral Vestibular Nucleus and Promotes Motor Behaviors via HCN Channel Coupled to H2 Receptor

Bin Li[1†], Xiao-Yang Zhang[1†], Ai-Hong Yang[1,2], Xiao-Chun Peng[1], Zhang-Peng Chen[1], Jia-Yuan Zhou[1], Ying-Shing Chan[3], Jian-Jun Wang[1] and Jing-Ning Zhu[1*]*

[1]State Key Laboratory of Pharmaceutical Biotechnology and Department of Biological Science and Technology, School of Life Sciences, Nanjing University, Nanjing, China, [2]Department of Medicine, Huaibei Vocational and Technical College, Huaibei, China, [3]Department of Physiology, LKS Faculty of Medicine, The University of Hong Kong, Hong Kong, Hong Kong

Histamine and histamine receptors in the central nervous system actively participate in the modulation of motor control. In clinic, histamine-related agents have traditionally been used to treat vestibular disorders. Immunohistochemical studies have revealed a distribution of histaminergic afferents in the brainstem vestibular nuclei, including the lateral vestibular nucleus (LVN), which is critical for adjustment of muscle tone and vestibular reflexes. However, the mechanisms underlying the effect of histamine on LVN neurons and the role of histamine and histaminergic afferents in the LVN in motor control are still largely unknown. Here, we show that histamine, in cellular and molecular levels, elicits the LVN neurons of rats an excitatory response, which is co-mediated by the hyperpolarization-activated cyclic nucleotide-gated (HCN) channels and K^+ channels linked to H2 receptors. Blockage of HCN channels coupled to H2 receptors decreases LVN neuronal sensitivity and changes their dynamic properties. Furthermore, in behavioral level, microinjection of histamine into bilateral LVNs significantly promotes motor performances of rats on both accelerating rota-rod and balance beam. This promotion is mimicked by selective H2 receptor agonist dimaprit, and blocked by selective H2 receptor antagonist ranitidine. More importantly, blockage of HCN channels to suppress endogenous histaminergic inputs in the LVN considerably attenuates motor balance and coordination, indicating a promotion role of hypothalamo-vestibular histaminergic circuit in motor control. All these results demonstrate that histamine H2 receptors and their coupled HCN channels mediate the histamine-induced increase in excitability and sensitivity of LVN neurons and contribute to the histaminergic improvement of the LVN-related motor behaviors. The findings suggest that histamine and the histaminergic afferents may directly modulate LVN neurons and play a critical role in the central vestibular-mediated motor reflexes and behaviors.

Keywords: histamine, histamine H2 receptor, HCN channel, lateral vestibular nucleus, motor control

OPEN ACCESS

Edited by:
Brian R. Noga,
University of Miami, USA

Reviewed by:
Nicola Berretta,
Fondazione Santa Lucia (IRCCS), Italy
De-Lai Qiu,
Yanbian University, China

***Correspondence:**
Jian-Jun Wang
jjwang@nju.edu.cn
Jing-Ning Zhu
jnzhu@nju.edu.cn

[†]These authors have contributed equally to this work.

***Received:** 24 September 2016*
***Accepted:** 19 December 2016*
***Published:** 10 January 2017*

Citation:
Li B, Zhang X-Y, Yang A-H, Peng X-C, Chen Z-P, Zhou J-Y, Chan Y-S, Wang J-J and Zhu J-N (2017) Histamine Increases Neuronal Excitability and Sensitivity of the Lateral Vestibular Nucleus and Promotes Motor Behaviors via HCN Channel Coupled to H2 Receptor. Front. Cell. Neurosci. 10:300. doi: 10.3389/fncel.2016.00300

INTRODUCTION

Histamine, restrictedly synthesized in the tuberomammillary nucleus neurons in the hypothalamus, plays important roles in many brain functions, including feeding, sleep/wakefulness and cardiovascular control (Passani et al., 2007; Haas et al., 2008; Panula and Nuutinen, 2013). Recently, role of histamine in somatic motor control has attracted an increasing attention (Li et al., 2014). Patients with motor disease, such as Parkinson's disease and vestibular disorders, show significant alternation in the central histaminergic system (Lacour, 2013; Shan et al., 2015). And histamine-related agents have been widely used to treat vestibular disorders in clinic (Haas et al., 2008; Tiligada et al., 2011), although the underlying mechanisms are still not entirely clear.

The role of central histaminergic system on motor behaviors is complex. The histidine decarboxylase (the histamine synthesizing enzyme) knockout mice exhibit a reduced locomotor and exploratory activity (Dere et al., 2004), whereas intracerebroventricular injection of histamine induces a transient increase followed by a decrease in locomotor activity in rats (Onodera et al., 1994). These complex effects of histamine on motor activity are mediated by different histamine receptors in various central motor structures. H1R-deficient mice display altered ambulatory activity and reduced exploratory behavior in a new environment (Inoue et al., 1996). The reduced locomotion is also observed in H3R-deficient mice (Toyota et al., 2002). Moreover, by means of pharmacological manipulation combining behavioral tests, our previous studies have demonstrated that histamine remarkably promotes motor balance and coordination on accelerating rota-rod and balance beam via activation of H2 receptors in the rat cerebellar fastigial and interposed nuclei (Song et al., 2006; He et al., 2012; Zhang et al., 2016).

The vestibular nuclei in the brainstem are important motor structures in the central nervous system and responsible for control of muscle tone, posture and body balance. In the vestibular nuclei, the lateral vestibular nucleus (LVN), one of the targets of cerebellar outputs, is implicated in the regulation of muscle tone and postural control during ongoing movements (Wilson and Peterson, 1978; Molina-Negro et al., 1980). Interestingly, neuroanatomical and immunostaining studies have showed a moderately dense histaminergic afferents in the central vestibular nuclei in various mammals, including guinea pig, rat and cat (Schwartz et al., 1991; Steinbusch, 1991; Tighilet and Lacour, 1996). Molecular, autoradiographic and pharmacological studies have also demonstrated that the LVN is endowed with H2 and/or H3 receptors in guinea pigs (Yabe et al., 1993; Vizuete et al., 1997). Our previous electrophysiological study have further reported that histamine post-synaptically depolarizes the LVN neurons via activating H2 receptors in rats (Zhang et al., 2008). However, the role of histamine H2 receptor and its mediated histaminergic modulation in the LVN-mediated motor control remains largely unknown.

Therefore, in this study, by whole-cell patch clamp recordings in brainstem slices and behavioral tests *in vivo*, we examined the ionic mechanisms underlying the histamine H2 receptor-mediated excitatory effect of histamine on LVN neurons, and particularly, the role of histamine and histaminergic afferent inputs in the LVN-mediated motor control. The results demonstrate that the histamine-elicited excitation on the LVN neurons is mediated by histamine H2 receptor and its downstream hyperpolarization-activated cyclic nucleotide-gated (HCN) channels as well as K^+ channels. The activation of HCN channels coupled to H2 receptors increase excitability and sensitivity of LVN neurons, and improves the LVN-mediated motor behaviors.

MATERIALS AND METHODS

Animals

Sprague-Dawley rats were individually housed under controlled environment conditions (22 ± 2°C; 60 ± 5% humidity; and 12-h light/dark cycle with lights on at 8:00 a.m. daily). The animals had free access to standard laboratory chow and water. All animal experiments, approved by the Experimental Animal Care and Use Committee of Nanjing University, were conducted in accordance with U.S. National Institutes of Health Guide for the Care and Use of Laboratory Animals (NIH Publication 85–23, revised 2011) and were reported in accordance with the ARRIVE guidelines (Kilkenny et al., 2010). All efforts were made to minimize the number of animals used.

Whole-Cell Patch-Clamp Recordings on Brain Slices

Under sodium pentobarbital (40 mg/kg) anesthesia, 51 Sprague-Dawley rats of either sex aged 10–16 days were used for these experiments, since the central histaminergic system in rats usually reach adult level by 2 weeks after birth (Haas et al., 2008). Coronal slices (300 μm thick) of brainstem containing the LVN were prepared with a vibroslicer (VT 1200 S, Leica Microsystems, Wetzlar, Germany), according to the rat brain atlas of Paxinos and Watson (2007). The slices were then incubated in oxygenated (95% O_2/5% CO_2) artificial cerebrospinal fluid (ACSF: 124 mM NaCl, 2.5 mM KCl, 1.25 mM NaH_2PO_4, 1.3 mM $MgSO_4$, 26 mM $NaHCO_3$, 2 mM $CaCl_2$ and 10 mM D-glucose) at 35 ± 0.5°C for at least 1 h and then maintained at room temperature. During recording sessions, the slices were transferred to a submerged chamber and continuously perfused with oxygenated ACSF at a rate of 2 mL/min at room temperature.

Whole-cell patch-clamp recordings were performed as our previous report (Zhang et al., 2008, 2011, 2013, 2016; Yu et al., 2016). Briefly, recording pipettes (3–5 MΩ) were filled with an internal solution (140 mM K-methylsulfate, 7 mM KCl, 2 mM $MgCl_2$, 10 mM HEPES, 0.1 mM EGTA, 4 mM Na_2ATP, 0.4 mM GTP-Tris, adjusted to pH 7.25 with 1 M KOH). Patch-clamp recordings were acquired with an Axopatch-200B amplifier (Axon Instruments, Foster City, CA, USA) and the signals were fed into a computer through a Digidata-1550 interface (Axon Instruments) for data capture and analysis (pClamp 10.4, Axon Instruments). Under voltage-clamp mode,

the membrane potential of recorded neurons was held at −60 mV. In slow-ramp test, a voltage command ranged from −60 to −120 mV with dV/dt = −10 mV/s was employed (Zhang et al., 2011, 2013; Yu et al., 2016). Furthermore, under current-clamp mode, depolarizing voltage sag, the hallmark of HCN channel activation, was triggered by hyperpolarizing current steps (70–150 pA, 1 s) and evaluated by subtracting the peak voltage amplitude from the steady-state voltage. Moreover, in current-clamp recording, a depolarizing ramp-like current, consisting a 600 ms ramp (from −150 pA to 150 pA, slope of 0.5 nA/s) followed by a long plateau of current (150 pA, 4400 ms), was injected to evaluate the sensitivity and dynamic properties of LVN neurons (Ris et al., 2001; Uno et al., 2003; Zhang et al., 2011).

Immunofluorescence

The experimental procedures for immunostaining followed our previous reports (Zhang et al., 2011, 2013, 2016; Li et al., 2016). Rat (weighing 230–250 g) were deeply anesthetized with sodium pentobarbital and perfused transcardially with 100 ml of normal saline, followed by 450–500 ml of 4% paraformaldehyde in 0.1 M phosphate buffer. Subsequently, the brain was removed, trimmed and postfixed in the same fixative for 12 h at 4°C, and then cryoprotected in 30% sucrose for 48 h. Coronal brainstem sections (25 μm thick) containing the LVN were prepared with a freezing microtome (CM 3050S, Leica Microsystems). The sections were rinsed with PBS containing 0.1% Triton X-100 (PBST), and then incubated in 10% normal bovine serum in PBST for 30 min. Sections were incubated with a goat anti-H2 receptor polyclonal antibody (1:200; Everest Biotech, Oxfordshire, UK) overnight at 4°C. After wash in PBS, the sections were incubated with the Alexa 488-conjugated donkey anti-goat (1:2000; Invitrogen, Carlsbad, CA, USA) for 2 h at room temperature in the dark. The slides were washed and mounted in Fluoromount-G mounting medium (Southern Biotech, Birmingham, AL, USA). Negative controls were treated with incubations replacing the primary anti-serum with control immunoglobulins and/or omitting the primary antiserum. Images were acquired with a confocal laser scanning microscope (FV1000; Olympus) and recorded with FV10-ASW 3.1 Viewer Software (Olympus).

Stereotactic Implantation of Microinjection Cannulae

Male rats (230–250 g) were anesthetized with sodium pentobarbital (40 mg/kg) intraperitoneally, and then mounted on a stereotaxic frame (1404, David Kopf Instruments, Tujunga, CA, USA) for stereotactic brain surgery under aseptic conditions. A heating pad was used to maintain rectal temperature at 36–38°C. Briefly, two stainless-steel guide tubes (length 8 mm, o.d. 0.8 mm, i.d. 0.5 mm) for the microinjection cannulae were implanted into bilateral LVNs of each rat. The lower ends of the guide tubes were positioned 2.0 mm above the LVN (A −10.5 to 10.8, L 2.2 and H 6.5). After surgery, animals were caged individually and allowed to recover for at least 3 days.

Microinjection in the LVN

For microinjection in the LVNs, two injection cannulae (length 10 mm, o.d. 0.5 mm, i.d. 0.3 mm) were inserted to protrude 2 mm beyond the tip of the guide tube. The lower ends of the injection cannulae were just above bilateral LVNs to minimize lesioning the nuclei. Histamine (5 mM; Tocris, Bristol, UK), dimaprit (10 mM), ranitidine (10 mM; Tocris), ZD7288 (1 mM, 3 mM and 10 mM; Tocris) and saline (0.9% NaCl) were microinjected with Hamilton syringes (1 μl each side, lasting 2 min). The effective extent of the drug diffusion in the present study was restricted in the LVNs according to the estimate by extracellular electrophysiological recording units 0.5–2.0 mm away from the injection site in our previous reports (Song et al., 2006; Zhang et al., 2011).

Behavioral Tests

Animals used in behavioral tests were divided into eight groups: (1) microinjected with saline; (2) microinjected with 5 mM histamine; (3) microinjected with 10 mM dimaprit; (4) microinjected with 10 mM ranitidine; (5) microinjected with 1 mM ZD7288; (6) microinjected with 3 mM ZD7288; (7) microinjected with 10 mM ZD7288; and (8) microinjected with 10 mM dimaprit and 3 mM ZD7288. In order to achieve a stable motor performance, each animal was trained daily for at least 10 trials for 3–5 consecutive days. All training/tests started at 10:00 a.m. each day, and motor performances on accelerating rota-rod and balance beam of each animal were tested before, 0 h, 4 h and 24 h after microinjections.

We used accelerating rota-rod test to assess vestibular-related motor balance and coordination (Song et al., 2006; Zhang et al., 2011, 2014; He et al., 2012). Animals were placed on the rota-rod (Ugo Basile, Varese, Italy) and habituated to low rotation (4 rpm) for 30 s first. Then the rod was evenly accelerated up to 40 rpm during 360 s, and the latency for each rat to fall from the rotating rod was recorded. In the test, each rat was subjected three trials, with a resting interval of 3 min to reduce fatigue and stress.

We also employed balance beam test to evaluate vestibular motor function (Song et al., 2006; Zhang et al., 2011, 2014; He et al., 2012). The balance beam (2.5 cm in diameter) was 190 cm in length. A bright plastic platform (7 cm × 4 cm) was placed at one end of the rod as the start, and a darkened box (15 cm × 15 cm × 8 cm) was set at the opposite end as a goal nest for motivating rat to traverse the beam. The beam was suspended 90 cm above a cushion, which protected the fallen animals from injury, and 50 cm from a wall. The time that each rat spent to cross the beam was recorded. The test consisted of five consecutive trials with a 90 s resting interval.

Histological Identification

To verify the position of microinjection, each rat for behavioral tests was anesthetized with an overdose of sodium pentobarbital at the end of tests. Two insulated stainless steel wires (o.d. 0.4 mm) with 0.2 mm exposed tip were inserted (10 mm) into the brainstem under guidance of guide tubes for depositing iron at the injection site by DC current (10 μA, 20 s). The brain was

then removed and fixed with 4% paraformaldehyde containing 1% potassium ferrocyanide. A week later, frozen serial coronal sections (80 μm thick) were prepared, and the dark blue dots indicating injection sites were identified according to the rat brain atlas (Paxinos and Watson, 2007). Data from rats in which the injection sites were deviated from the LVN were excluded from further analysis.

Statistical Analysis

All data were analyzed with Origin 7.5 (MicroCal Software) and presented as mean ± S.E.M. The Student's *t* test, one-way and repeated measures two-way analysis of variance (ANOVA) was performed for statistical analysis. Newman-Keuls *post hoc* testing was employed to further determine the differences between group means. The values of $P < 0.05$ were considered as statistically significant.

RESULTS

Histamine Excites LVN Neurons via the Activation of H2 Receptors

In the present study, we recorded a total of 67 LVN neurons with the input resistance higher than 150 MΩ. Of the 67 LVN neurons recorded, 42 showed spontaneous firing (mean firing rate = 6.9 ± 0.4 spikes/s) and the remaining 25 were silent at rest. The result was in agreement with the previous reports that 30–50% LVN neurons are silent (Lai and Chan, 2001; Sun et al., 2002; Uno et al., 2003; Zhang et al., 2008, 2011). All the neurons we patched have a diameter >35 μm, indicating they were giant LVN Deiters' (projection) neurons. In addition, there was no morphological difference between the spontaneous firing and silent LVN neurons (**Figures 1A1,B1**). In voltage clamp recordings, brief bath application (1 min) of 30 μm histamine increased the discharge rate of five spontaneous firing neurons in the LVN (**Figure 1A2**) from 5.8 ± 0.9 spikes/s to 7.6 ± 1.7 spikes/s ($P < 0.01$). On the other hand, 30 μM histamine evoked a strong depolarization on five silent LVN neurons, which was even sufficient to bring up the neurons firing (**Figure 1B2**). The results indicate that histamine elicits a significant excitatory response on both types of LVN neurons (**Figures 1A2,B2**).

Postsynaptic H2 receptors have been reported in our previous study to mediate the histamine-induced excitation on LVN neurons (Zhang et al., 2008). Here, we used ranitidine, a selective antagonist for histamine H2 receptor, to examine whether the receptor mechanisms on these two types of LVN neurons are the same. As shown in **Figures 1A2,B2**, bath application of ranitidine (3 μM) totally blocked the histamine-elicited excitation on both spontaneous firing and silent LVN neurons. In addition, dimaprit (30, 100, 300 μM), a highly selective agonist for histamine H2 receptors, induced an inward current (21.5 ± 2.6, 40.6 ± 4.5, 48.3 ± 5.2 pA, respectively) on LVN neurons in a concentration-dependent manner ($n = 6$, **Figures 1C,D**). Fitting the concentration-response curve from six LVN neurons yielded an EC_{50} value for dimaprit (10–300 μM) of 48.5 μM (**Figure 1D**). Notably, the inward current induced by dimaprit (10–300 μM) was totally blocked by 3 μM ranitidine (**Figures 1C,D**). Moreover, ranitidine (0.3–3 μM) concentration-dependently blocked the 100 μM dimaprit-induced inward current on LVN neurons (**Figure 1E**). The inward current elicited by dimaprit decreased remarkably from 44.3 ± 5.6 pA to 31.5 ± 2.3 ($n = 5$, $P < 0.05$), 14.5 ± 1.0 ($n = 5$, $P < 0.001$) and 2.7 ± 0.3 pA ($n = 5$, $P < 0.001$) by application of 0.3, 1 and 3 μM ranitidine (**Figure 1F**), respectively. Furthermore, the immunostaining result revealed that histamine H2 receptors were distributed in the LVN neurons in rats (**Figures 1G1–G4**), confirming our electrophysiological data. All these results demonstrate that histamine depolarizes and excites both types of LVN neurons by activation of H2 receptors.

Activation of Histamine H2 Receptor in the LVN Significantly Promotes Motor Behaviors

Since the LVN holds a key position in the vestibulospinal reflexes and posture control, we microinjected saline, histamine (5 mM), dimaprit (10 mM) and ranitidine (10 mM) into bilateral LVNs to determine the effect of activation of histamine H2 receptor on motor behaviors. The average score of 40 rats of all tested groups for the accelerating rota-rod tests was 152.78 ± 4.32 s, and no significant difference was found among the groups before microinjections ($F_{(3,36)} = 0.03$, $P = 0.992$; **Figure 2A**). A two-way ANOVA with repeated measures showed a significant effect of time ($F_{(3,108)} = 136.95$, $P < 0.01$), treatment ($F_{(3,36)} = 1.615$, $P = 0.203$) and time × treatment interaction ($F_{(9,108)} = 22.927$, $P < 0.01$) among these groups. Furthermore, Newman-Keuls *post hoc* test revealed that the endurance time of the histamine group ($n = 10$) on the rota-rod at 0 h after microinjection significantly increased compared with that of the saline group ($n = 10$; $P < 0.01$, **Figure 2A**), and such effect recovered hours later (**Figure 2A**). Activation of histamine H2 receptors in LVN by microinjection of dimaprit ($n = 10$) mimicked the histamine-induced improvement in motor performances at 0 h after injection ($P < 0.05$, **Figure 2A**). And blockage of histamine H2 receptors in the LVNs by ranitidine ($n = 10$) remarkably shortened the endurance time of rats on the rotating rod at 4 h ($P < 0.05$, **Figure 2A**) and 24 h ($P < 0.05$, **Figure 2A**) after injection.

In the balance beam test, the mean score of 40 rats of all groups on the beam was 4.46 ± 0.06 s, and there was no significant difference among the groups before injections ($F_{(3,36)} = 0.142$, $P = 0.934$; **Figure 2B**). A two-way ANOVA with repeated measures revealed a significant effect of time ($F_{(3,108)} = 151.091$, $P < 0.01$), treatment ($F_{(3,36)} = 7.626$, $P < 0.01$) and time × treatment interaction ($F_{(9,108)} = 36.534$, $P < 0.01$) among these groups. Furthermore, Newman-Keuls *post hoc* test indicated that microinjection of histamine ($n = 10$) into the LVNs significantly shortened the time that traversing the balance beam at 0 h after injection compared with the saline group ($n = 10$; $P < 0.01$, **Figure 2B**), and such effect recovered hours later (**Figure 2B**). Notably, at 0 h after injection, the spending time of the dimaprit group ($n = 10$) was significantly shorter than that of the saline group ($P < 0.01$, **Figure 2B**), whereas the time

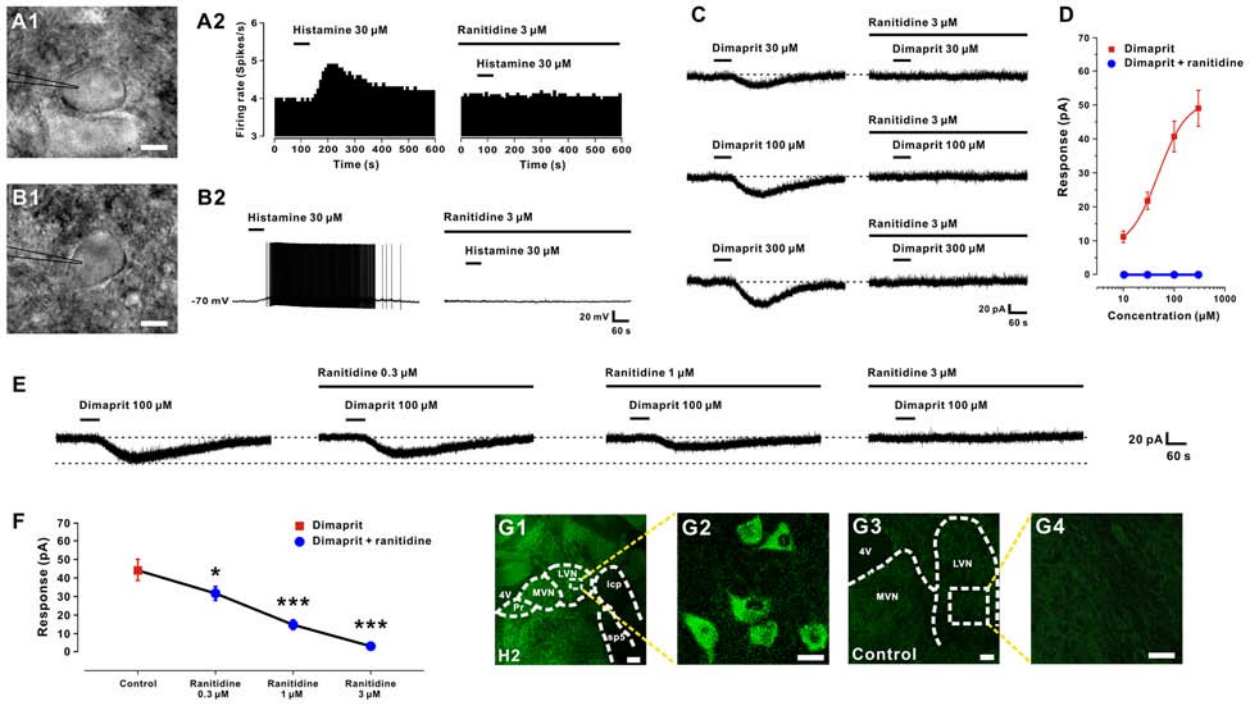


FIGURE 1 | Histamine excites LVN neurons by activation of H2 receptors. (A1,B1) Infrared differential interference contrast images of spontaneous firing and silent LVN neurons captured before whole-cell patch clamp recordings. **(A2,B2)** Histamine elicited a significant excitatory response on both spontaneous firing and silent LVN neurons. Bath application of ranitidine, a selective H2 receptor antagonist, totally blocked the histamine-elicited excitation on both types of recorded LVN neurons. **(C)** Dimaprit, a highly selective agonist for histamine H2 receptors, induced an inward current on a recorded LVN neuron in a concentration-dependent manner. And ranitidine totally blocked the inward current induced by dimaprit of all tested concentrations. **(D)** Concentration-response curves for dimaprit on recorded LVN neurons in the absence and presence of dimaprit. **(E)** Ranitidine (0.3–3 μm) concentration-dependently blocked the 100 μm dimaprit-induced inward current on a LVN neuron. **(F)** Group data of five tested LVN neurons. **(G1–G4)** Immunostaining result showed that histamine H2 receptors are present in the rat LVN neurons. Scale bars: **(A1,B1)**, 20 μm; **(G1)**, 250 μm; **(G2)**, 25 μm; **(G3)**, 150 μm; **(G4)**, 25 μm. Data shown are means ± SEM; $^*P < 0.05$, $^{***}P < 0.001$. 4V, 4th ventricle; MVN, medial vestibular nucleus; LVN, lateral vestibular nucleus; Pr, prepositus nucleus; icp, inferior cerebellar peduncle; sp5, spinal trigeminal tract.

traversing the beam of the ranitidine group (n = 10) markedly prolonged at 4 h, even 24 h after injection compared with that of the saline group ($P < 0.01$, **Figure 2B**). These results indicate that activation of histamine H2 receptors in the LVNs promotes animal's motor balance and coordination.

HCN Channels and K$^+$ Channels Are Involved in the Histamine-Induced Excitation on LVN Neurons

To clarify the ionic mechanisms underlying the excitation of LVN neurons elicited by H2 receptor activation, a slow-ramp command test was employed to assess the dynamic features of dimaprit-induced current. As shown in **Figures 3A1,A2**, two types of the I-V curves induced by dimaprit were observed, indicating that more than one ionic mechanism may be underlying the depolarization induced by the activation of H2 receptors on LVN neurons. Notably, the I-V curves of 18.2% (2/11) recorded LVN neurons intersected at −110 mV (**Figure 3A2**), which means the dimaprit-elicited inward current reverses near the calculated E_k of −108 mV, suggesting an involvement of K$^+$ channels. Moreover, Ba^{2+}, a blocker of K$^+$ channels (McCormick and Williamson, 1991), was applied to examine the dynamic properties of the dimaprit-induced current excluding the component of potassium. As shown in **Figure 3B**, only one change in the I-V curves was observed after blocking K$^+$ current. Subtracting the control from the current recorded during dimaprit application yielded a difference current representing the dimaprit-induced current excluding the K$^+$ component (the insert panel in **Figure 3B**). The difference current showed a significant feature of hyperpolarization activation, which is in line with the characteristics of the current of HCN channels. Since depolarizing voltage sag induced by hyperpolarizing current steps was one of the hallmarks of HCN channel activation (Pape, 1996), we further observed the effect of dimaprit on voltage sag on LVN neurons and found that the sag was remarkably increased by dimaprit (from 11.8 ± 1.6 mV to 14.6 ± 1.9 mV, $n = 6$, $P < 0.01$; **Figures 3C,D**). Furthermore, after blockage of HCN channels with ZD7288 (10 μM), a selective blocker for HCN channels, the HCN channel activation-induced sag vanished and the increase of voltage sag elicited by dimaprit was totally blocked (**Figures 3C,D**). The results, together with the dynamic properties of hyperpolarization activation observed in slow-ramp command test after excluding the component of K$^+$, strongly suggests that HCN channels participate in the mediation of excitation of LVN neurons induced by the activation of

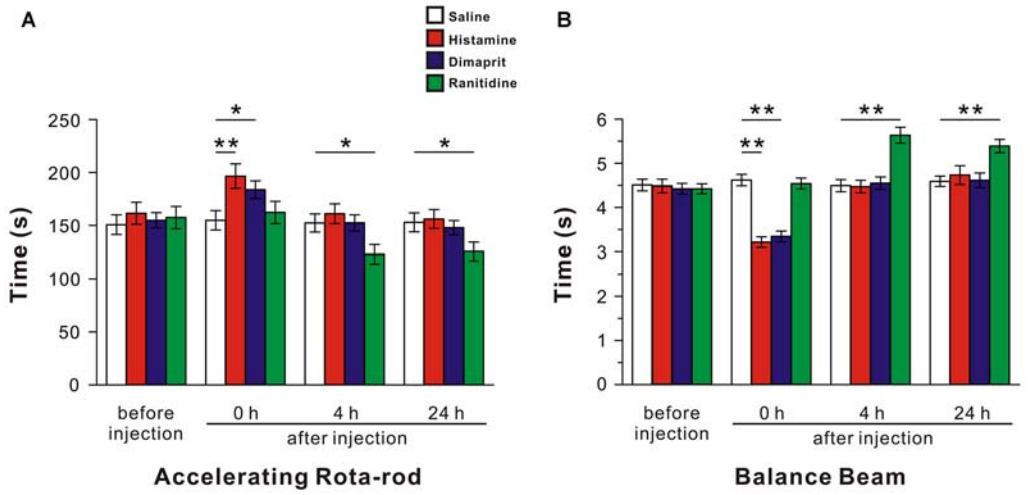


FIGURE 2 | Activation of histamine H2 receptors in the LVN promotes rat motor balance and coordination. The endurance time on an accelerating rota-rod **(A)** and the duration of passage through the balance beam **(B)** of rats treated by bilateral microinjection of saline, histamine, dimaprit, ranitidine. Data shown are means ± SEM; $^{*}P < 0.05$, $^{**}P < 0.01$.

H2 receptors. On the other hand, the dimaprit induced I-V curve changes were also detected in the presence of ZD7288 in the slow-ramp command test (**Figure 3E**). As shown in the insert panel of **Figure 3E**, the dimaprit-induced current excluding the component of HCN channel current reverted near the calculated E_k. Although the residual K^+ current was quite small, the data indicate a co-mediation of K^+ and HCN channels in the dimaprit-induced excitation on LVN neurons. In addition, we found that separate application of $BaCl_2$ or ZD7288 partially inhibited the dimaprit-elicited inward current (50.2 ± 5.8 pA, $n = 11$) to 31.3 ± 5.7 pA ($n = 6$, $P < 0.05$, **Figures 3F,H**) and 16.1 ± 4.7 pA ($n = 5$, $P < 0.01$, **Figures 3G,H**), respectively, whereas combined application of $BaCl_2$ and ZD7288 totally blocked the current induced by dimaprit ($n = 10$, $P < 0.001$, **Figures 3F–H**). Similarly, as shown in **Figures 3I–K**, the histamine-induced inward current (67.4 ± 8.2 pA, $n = 11$) on LVN neurons was also partly blocked by separate application of $BaCl_2$ or ZD7288 to 46.0 ± 9.3 pA ($n = 6$, $P < 0.05$) or 18.8 ± 3.6 pA ($n = 5$, $P < 0.001$), respectively, and totally blocked by combined application of $BaCl_2$ and ZD7288 ($n = 9$, $P < 0.001$). All these results strongly suggest that a dual ionic mechanism, involving both the activation of HCN channels and the closure of K^+ channels, may mediate the excitatory effect of activation of H2 receptors on LVN neurons.

Activation of HCN Channels Coupled to H2 Receptors Increases Sensitivities of LVN Neurons and Changes their Dynamic Properties

Intriguingly, besides increasing the excitability, the activation of H2 receptors also enhanced the sensitivity of the LVN neurons to the stimulation of a depolarizing ramp-like current (**Figures 4A1,A2**), which consists of a 600 ms ramp (from −150 pA to 150 pA, slope of 0.5 nA/s) followed by a long plateau of current (150 pA, 4400 ms; Ris et al., 2001; Uno et al., 2003; Zhang et al., 2011). On five LVN neurons, dimaprit (100 μM) significantly increased the rate of increase in the instantaneous neuronal firing rate (from 100.0 ± 5.1% to 135.2 ± 6.9%, $n = 5$, $P < 0.001$; **Figure 4B**). However, in the presence of ZD7288 (1, 3 and 10 μM), as illustrated in **Figure 4B**, the enhancement in the rate of increase in the instantaneous firing rate induced by dimaprit (100 μM) was blocked in a concentration dependent manner. The normalized enhancement in the rate of increase in the instantaneous firing rate was decreased significantly from 35.2 ± 6.9% to 21.4 ± 4.2% ($n = 5$, $P < 0.05$), 10.0 ± 5.4% ($n = 5$, $P < 0.05$) and 2.6 ± 8.9% ($n = 5$, $P < 0.001$), respectively (**Figure 4B**). The results indicate that the increment in sensitivity of LVN neurons induced by the activation of histamine H2 receptors is mediated by HCN channels.

We also measured the difference between the instantaneous firing rate reached at the end of the ramp and the stable discharge rate at the end of the plateau, i.e., the overshoot (**Figure 4A2**). This parameter reflects the nonlinear, dynamic properties of neurons. We found that dimaprit (100 μM) effectively increased the overshoot of the LVN neurons from 100.0 ± 8.1% to 179.6 ± 12.5% ($n = 5$, $P < 0.001$; **Figure 4C**), and ZD7288 (1, 3 and 10 μM) concentration-dependently blocked the dimaprit-induced increment in overshoot from 79.6 ± 12.5% to 48.6 ± 13.2% ($n = 5$, $P < 0.05$), 20.5 ± 16.1% ($n = 5$, $P < 0.05$) and 8.9 ± 14.8% ($n = 5$, $P < 0.001$), respectively (**Figure 4C**). Therefore, the activation of HCN channels coupled to H2 receptors not only increases sensitivity of LVN neurons, but also changes their dynamic properties.

Besides activation of HCN channels, closure of K^+ channels is the other ionic mechanism underlying the activation of H2 receptors on LVN neurons. Thus, the dimaprit-induced

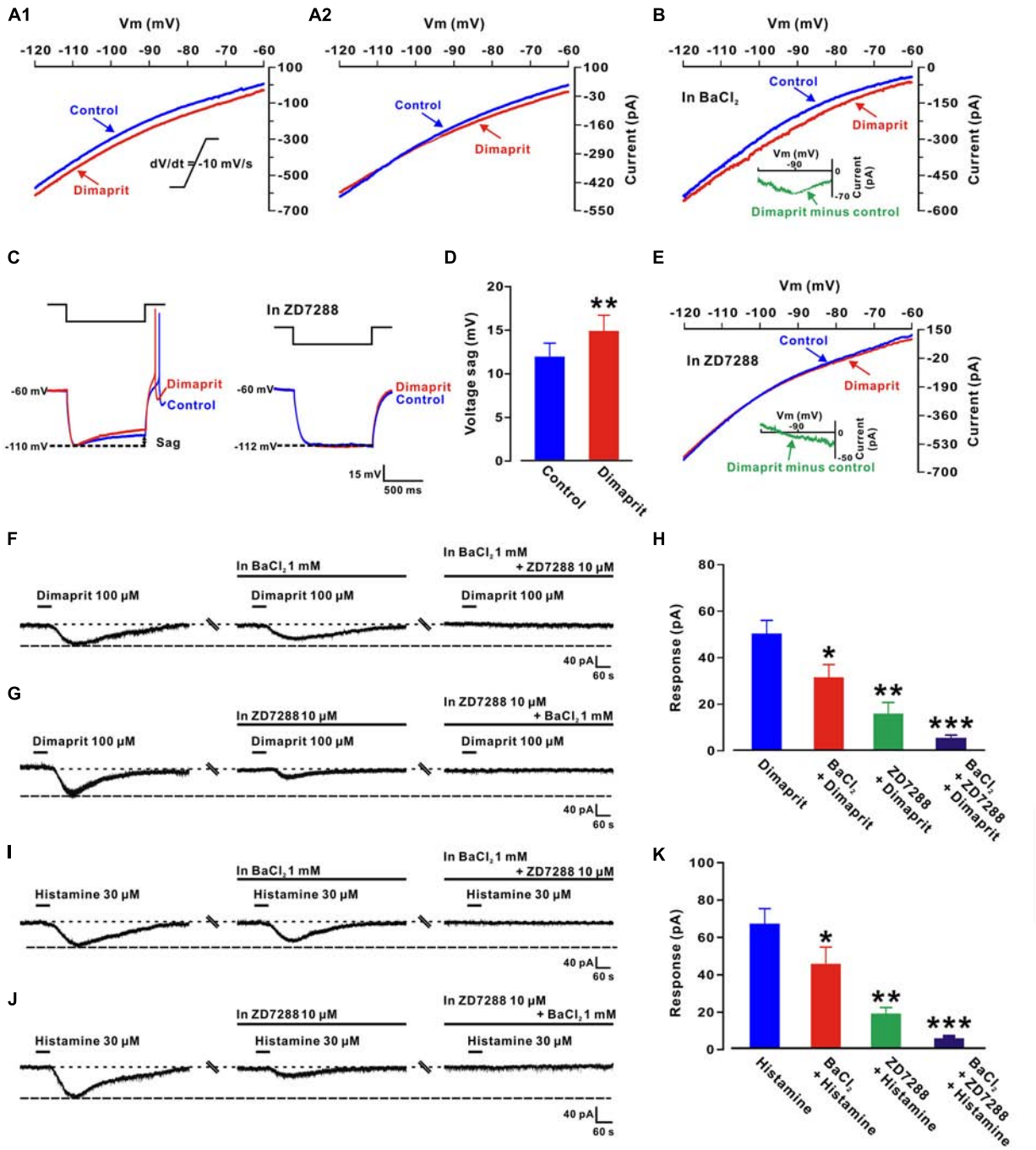


FIGURE 3 | Hyperpolarization-activated cyclic nucleotide-gated (HCN) channels and K^+ channels co-mediate the excitation induced by activation of H2 receptors on LVN neurons. (A1,A2) Two types of dimaprit-induced changes of I-V curves on LVN neurons (n = 9 and 2, respectively) responding to a slow-ramp command (dV/dt = −10 mV/s). The diversity of the dimaprit-induced changes in I-V relationships suggests that more than one ionic basis is involved in histamine H2 receptor-mediated inward current on LVN neurons. The intersection of I-V curves at calculated E_K of −108 mV **(A2)** on 18.2% (2/11) of neurons indicates an involvement of K^+ channels in the H2 receptor-mediated LVN neuronal excitation. **(B)** In the ACSF containing Ba^{2+}, a blocker of K^+ channels, the dimaprit-induced changes of I-V curves and the current excluding K^+ component in slow-ramp command tests. Note that in the presence of Ba^{2+}, the dimaprit-induced current (the inset) showed a significant feature of hyperpolarization activation, which is consistent with the characteristics of current of HCN channels. **(C)** Inward rectification (sag) triggered by hyperpolarizing current steps on an LVN neuron was increased by dimaprit (the left panel). ZD7288, a highly selective HCN channel antagonist, totally blocked the increase in the sag induced by dimaprit (the right panel). **(D)** Group data of the tested LVN neurons. **(E)** In the slow-ramp command test, in the presence of ZD7288 to exclude the component of HCN channel current, the dimaprit-induced residual current (the inset) was very small and reverted near the calculated E_K. **(F)** $BaCl_2$ partly blocked the dimaprit-elicited inward current, and combined application of $BaCl_2$ and ZD7288 totally blocked the current.

(*Continued*)

FIGURE 3 | Continued
(G) The dimaprit-induced inward current was also partly blocked by ZD7288, and totally blocked by combined application of ZD7288 and $BaCl_2$. **(H)** Group data of the tested LVN neurons. **(I,J)** Histamine-induced inward current was partly/totally blocked by separate/combined application of ZD7288 and $BaCl_2$. **(K)** Group data of the tested LVN neurons. Data shown are means ± SEM; $^*P < 0.05$, $^{**}P < 0.01$, $^{***}P < 0.001$.

changes in sensitivities of LVN neurons and their dynamic properties were also measured in the presence of $BaCl_2$. However, we found that $BaCl_2$ (1 mM) blocked neither the dimaprit-induced enhancement in the rate of increase in the instantaneous firing rate (from 30.4 ± 6.3% to 32.6 ± 5.5%, $n = 5$, $P = 0.64$, **Figure 4D**), nor the increment in overshoot (from 66.9 ± 20.2% to 60.1 ± 23.1%, $n = 5$, $P = 0.48$, **Figure 4E**). Therefore, it is HCN channels, but not K^+ channels coupled to H2 receptors, that contribute to the modulation on sensitivity and dynamic properties of LVN neurons by the activation of H2 receptors. We speculate that HCN channels may actively participate in the LVN-mediated motor behaviors.

Blockage of HCN Channels Coupled to H2 Receptors in the LVN Attenuates Motor Balance and Coordination

Given that the effects of HCN channels' activation on both sensitivity and dynamic properties of LVN neurons *in vitro*, ZD7288 (1 mM, 3 mM and 10 mM), or dimaprit together with ZD7288, was microinjected into bilateral LVNs to examine the role of HCN channels in the histamine H2 receptor-mediated promotion in motor behaviors on accelerating rota-rod and balance beam. For the accelerating rota-rod test, no significant difference among the groups before injections was observed ($F_{(3,36)} = 0.19$, $P = 0.904$; **Figure 5A**). A significant effect of time ($F_{(3,108)} = 90.146$, $P < 0.01$), treatment ($F_{(3,36)} = 8.291$, $P < 0.01$) and time × treatment interaction ($F_{(9,108)} = 34.988$, $P < 0.01$) among these groups was revealed by two-way ANOVA with repeated measures. Furthermore, *post hoc* test showed that microinjection of 3 or 10 mM ZD7288 ($n = 10$) into the LVNs remarkably decreased the endurance time of rats on the rotating rod at 0 h and 4 h after injection compared with the rats microinjected with saline ($n = 10$; $P < 0.01$, $P < 0.05$, **Figure 5A**), and such effect recovered hours later (**Figure 5A**). For the balance beam test, no significant difference was found among the groups before injections ($F_{(3,36)} = 0.497$, $P = 0.687$; **Figure 5B**). And a significant effect of time ($F_{(3,108)} = 92.131$, $P < 0.01$), treatment ($F_{(3,36)} = 45.458$, $P < 0.01$) and time × treatment interaction ($F_{(9,108)} = 42.286$, $P < 0.01$) among these groups was determined. Furthermore, *post hoc* test revealed that microinjection of 3 or 10 mM ZD7288 ($n = 10$) into the LVNs concentration-dependently lengthened the spent traversing time of rats on the beam at 0 h and 4 h after injection compared with the saline group ($n = 10$; **Figure 5B**), and such effect recovered hours later (**Figure 5B**). These results indicate that blockage of HCN channels coupled to histamine H2 receptors attenuates motor balance and coordination on the rota-rod and balance beam.

Moreover, the decrement of motor performance in both accelerating rota-rod (**Figure 5C**) and balance beam (**Figure 5D**) tests increased with the increase of the concentration of ZD7288. Also, it is noteworthy that the improvement of motor performances on rota-rod and balance beam induced by activation of H2 receptors by dimaprit was remarkably blocked by ZD7288 ($P < 0.01$, respectively; **Figures 5E,F**). All these results strongly suggest that HCN channels coupled to H2 receptors mediate improvement in motor balance and coordination of histaminergic inputs.

DISCUSSION

Although the central histaminergic system solely originates from the tuberomammillary nucleus of the hypothalamus, it participates in the regulation of various basic physiological functions (Haas et al., 2008). Brain histamine depletion or knockout of histamine receptor reduced animals' locomotor activity and exploratory behavior (Onodera et al., 1994; Inoue et al., 1996; Toyota et al., 2002), indicating the central histaminergic system may also hold a critical position in somatic motor functions. Yet, the functional role of histaminergic system in various motor structures and the underlying mechanism is still little known. Here, in the present study, we report that histamine H2 receptor and its coupled HCN channel mediate the histamine-induced enhancement of LVN neuronal excitability and sensitivity. Via activation of histamine H2 receptors and the downstream HCN channels, histaminergic inputs promote the LVN-mediated motor behaviors.

Electrophysiological and Behavioral Effects of Histamine in the LVN

Immunohistochemical studies have demonstrated that the histaminergic neurons in the tuberomammillary nucleus of the hypothalamus project directly to the vestibular nuclei in brainstem (Schwartz et al., 1991; Steinbusch, 1991; Tighilet and Lacour, 1996). As an essential part of the central histaminergic system, these histaminergic innervations on the vestibular nuclear complex, especially their physiological functions, have received increasing attention. Intriguingly, histamine exerts a uniformly excitatory effect on all four vestibular sub-nuclei (Wang and Dutia, 1995; Zhang et al., 2008, 2013; Peng et al., 2013; Zhuang et al., 2013; Yu et al., 2016). However, the receptor mechanisms underlying the histamine-induced excitation on these sub-nuclei are various (Wang and Dutia, 1995; Zhang et al., 2008, 2013; Peng et al., 2013; Zhuang et al., 2013; Yu et al., 2016). Histamine H1 and H2 receptors co-mediate the excitatory effect of histamine on neurons in the superior and inferior vestibular nuclei (Peng et al., 2013; Zhuang et al., 2013; Yu et al., 2016), whereas histamine H1, H2 and H3 receptors are all involved in the complex modulation of histamine on medial vestibular nucleus (MVN) neuron (Wang and Dutia,

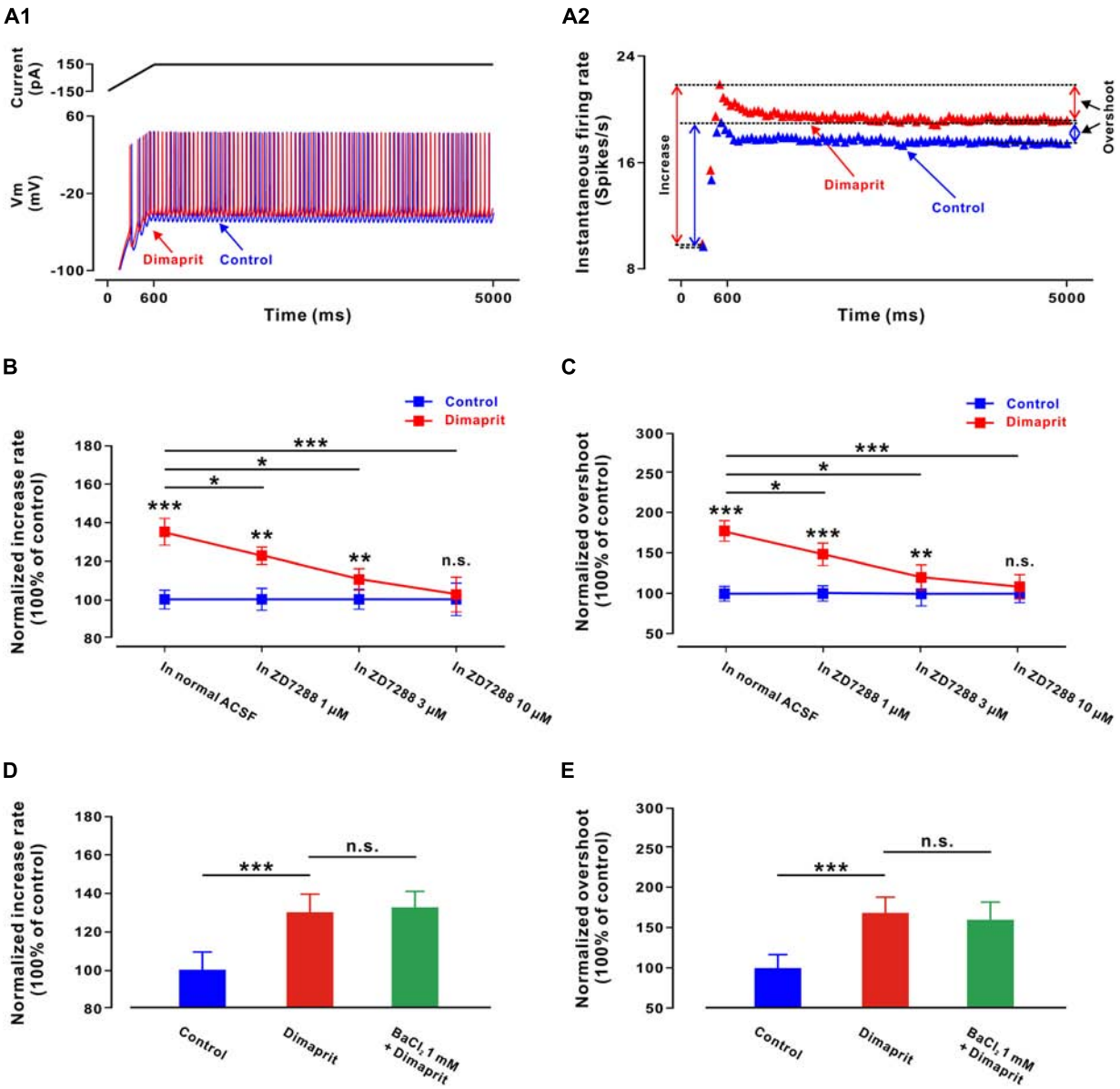


FIGURE 4 | Activation of HCN channels coupled to H2 receptors increases sensitivity of LVN neurons and change their dynamic properties. **(A1)** A ramp-like current was given from a hyperpolarized level of −150 pA for 600 ms to reach +150 pA, with the final steady-state value of +150 pA lasting 4400 ms. Firing response of a LVN neuron to the ramp-like current stimulation in the absence and presence of dimaprit. **(A2)** Instantaneous firing rates of the same LVN neuron to the ramp-like current in the absence and presence of dimaprit showed that H2 receptor activation remarkably raised both the rate of increase of the instantaneous firing rate (spikes/s/nA) and the overshooting response. **(B)** The normalized enhancement in the rate of increase in the instantaneous firing rate was concentration-dependently blocked by ZD7288 (1, 3 and 10 μM), indicating that the dimaprit-induced increment in sensitivity of LVN neurons was mediated by the activation of HCN channels coupled to H2 receptors. **(C)** ZD7288 (1, 3 and 10 μM) concentration-dependently blocked the dimaprit-induced overshoot increment, suggesting that the activation of HCN channels coupled to H2 receptors also contributed to the changes of dynamic properties of LVN neurons. **(D,E)** $BaCl_2$ (1 mM) did not block the dimaprit-induced enhancement in the rate of increase in the instantaneous firing rate and increment in overshoot on five LVN neurons. Data shown are means ± SEM; $^{*}P < 0.05$, $^{**}P < 0.01$ and $^{***}P < 0.001$ and n.s. indicates non-significant.

1995; Bergquist and Dutia, 2006; Zhang et al., 2013). In this study, we found that histamine elicited a significant excitatory response on LVN neurons both having spontaneous firing and being silent. These histamine-elicited excitations were totally blocked by ranitidine (selective histamine H2 receptor antagonist) and mimicked by dimaprit (highly selective agonist for histamine H2 receptors), suggesting that only histamine H2 receptors mediate the excitatory effect of histamine on LVN neurons.

Among the four vestibular sub-nuclei, the LVN receives inputs from the semicircular canals and the utricle, and projects into the lateral vestibulo-spinal tract to ipsilaterally innervate

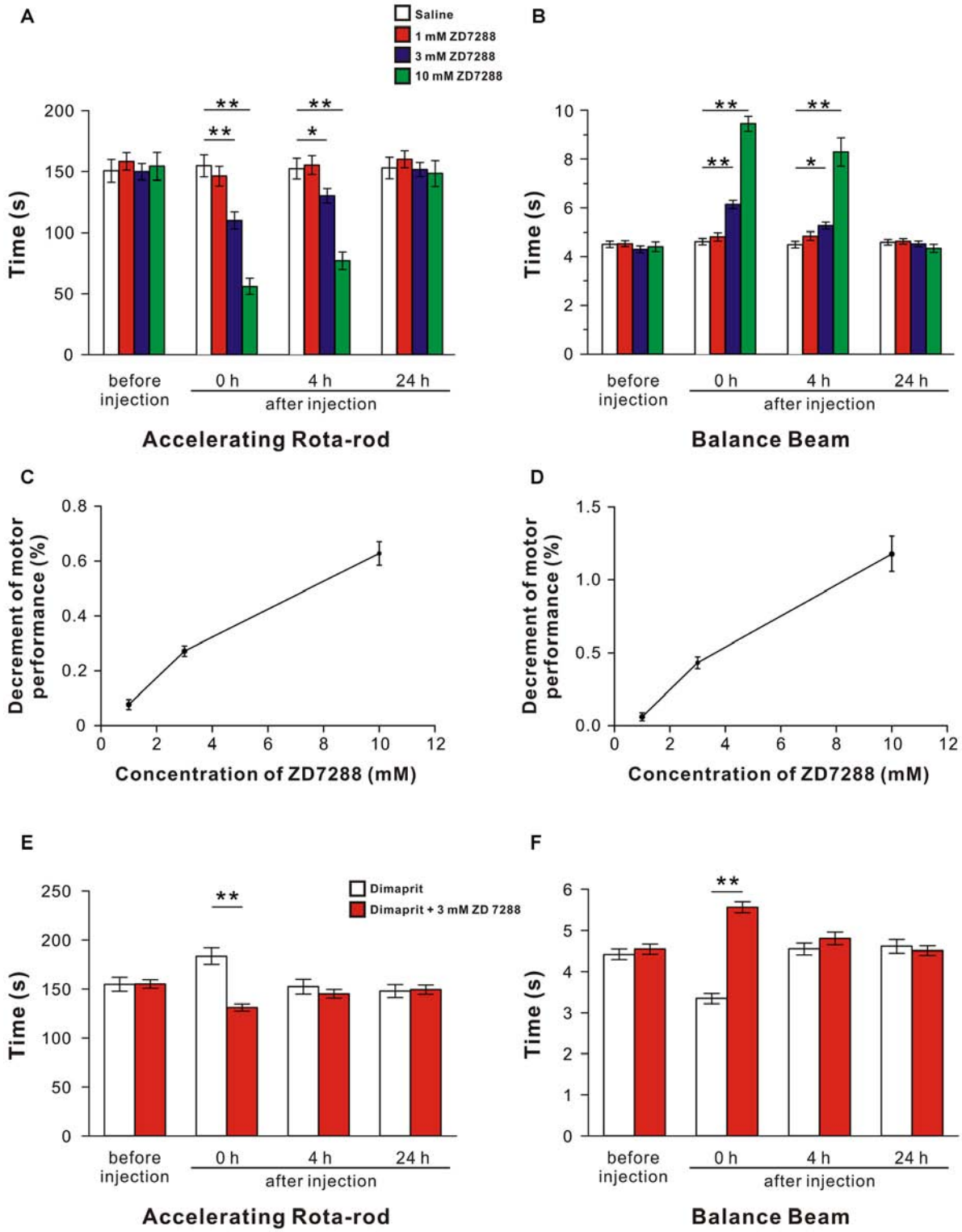


FIGURE 5 | Blockage of HCN channels coupled to H2 receptors in the LVN attenuates spontaneous and the dimaprit-induced promotion on motor balance and coordination. (A,B) The endurance time on an accelerating rota-rod and the duration of passage through the balance beam of rats treated by bilateral microinjection of saline, 1 mM ZD7288, 3 mM ZD7288 or 10 mM ZD7288. **(C,D)** The decrement of motor performance in accelerating rota-rod and balance beam tests increased with the increase of the concentration of ZD7288. **(E,F)** The endurance time on an accelerating rota-rod and the duration of passage through the balance beam of rats treated by bilateral microinjection of dimaprit or dimaprit together with 3 mM ZD7288. Data shown are means ± SEM; $^{*}P < 0.05$, $^{**}P < 0.01$.

the ventral horn of the spinal cord (Carleton and Carpenter, 1983; Sarkisian, 2000). Through facilitating the activity of spinal motoneurons innervating gravity-opposing muscles of the limb, the LVN is actively involved in the vestibule-spinal reflex and postural control. Thus, it is naturally speculated that the excitatory modulation of histamine on LVN neurons via H2 receptors may enhance the output of LVN, excite the neurons of their targets, and influence motor behaviors. In the present study, our results demonstrate that microinjection of histamine into the LVN significantly promotes motor performances on accelerating rota-rod and balance beam. Activation of histamine H2 receptors mimics the histamine-induced promotion in motor performances, whereas blockage of H2 receptors to block endogenous histaminergic inputs into the LVN attenuates motor behaviors. These results suggest that histamine H2 receptors contribute to the improvement of histaminergic inputs in the LVN-mediated motor behaviors. Interestingly, our previous studies found that histamine promoted motor balance and coordination via the activation of H2 receptors in the fastigial nucleus (He et al., 2012) and interpositus nucleus (Song et al., 2006) of the cerebellum. Therefore, histamine H2 receptors may hold a critical position in central histaminergic modulation on motor control.

Ionic Mechanisms Coupled to Histamine H2 Receptor in the LVN

Several types of ionic channels/exchangers have been reported to be linked to histamine receptors and modulate the excitability of central vestibular nuclear neurons (Ris et al., 2001; Zhang et al., 2013, 2016; Yu et al., 2016). Here, we find that both the HCN channels and K^+ channels are involved in the excitation of LVN neurons induced by the activation of histamine H2 receptors. In these dual ionic mechanisms, HCN channels seem to play a major contribution, whereas K^+ component may account for only a small one. Since HCN channels are critical "pacemaker channels" of neurons (Pape, 1996) and K^+ channels are responsible for setting membrane potential, histamine released from the hypothalamus will help to accelerate membrane depolarization and the generation of LVN neuronal activity via opening of HCN channels and closure of K^+ channels. Notably, in this study, we find that HCN channels, but not K^+ channels coupled to H2 receptors, are responsible for the histamine-induced enhancement of sensitivities of LVN neurons and modulation of their dynamic properties. This may be owing to the fact that HCN channels play an essential role in not only governing neuronal excitability but also controlling the way that neurons respond to input. Thus, by activation of HCN channels coupled to H2 receptors, histaminergic inputs may enhance the sensitivity and responsiveness of LVN neuronal circuitry to periphery vestibular inputs and consequently modulate LVN-mediated motor behaviors.

Dysfunction of HCN channels is usually associated with pathological conditions, such as epilepsy, age-related working memory decline and neuropathic pain (Lewis and Chetkovich, 2011; He et al., 2014). In the present study, by means of pharmacological manipulation to block HCN channels in the LVN, we find that rat motor performances on the rota-rod and balance beam remarkably decline (**Figures 5A–D**) and the improvement of motor performances induced by activation of histamine H2 receptors is significantly abolished (**Figures 5E,F**). These results, together with our previous findings that blockage of HCN channels in the cerebellar nuclei attenuates motor performances (Zhang et al., 2016), suggest that HCN channels coupled to histamine H2 receptors may mediate the modulation of the central histaminergic system on motor behaviors and play an important role in somatic motor control.

Functional Significance of Histaminergic Innervation on the LVN

Besides histaminergic innervation, the LVN also receives excitatory orexinergic inputs from the hypothalamus (Zhang et al., 2011). Unlike the critical role of orexinergic modulation in motor challenge (Zhang et al., 2011), excitatory histaminergic inputs on the LVN may be responsible for routine execution of normal function of the central vestibular nuclear circuitry. The functional difference in aspect of LVN's motor control between the histaminergic and orexinergic systems may depend on different functional roles of the origins of these two systems. In conclusion, the present study shows that the histamine-elicited excitation on the LVN neurons is mediated by postsynaptic histamine H2 receptor and its downstream HCN channels and K^+ channels. The activation of HCN channels coupled to H2 receptors increases sensitivity of LVN neurons, and improves the LVN-mediated motor behaviors. Based on these results, we suggest that via histamine H2 receptors and the downstream HCN channels, the excitatory histaminergic inputs may modulate both excitability and sensitivity of the LVN neurons and are actively involved in the central vestibular postural and motor control.

AUTHOR CONTRIBUTIONS

BL and X-YZ performed experiments, analyzed data, and prepared figures and drafts. A-HY, X-CP, Z-PC and J-YZ performed some experiments. Y-SC discussed the research. J-NZ and J-JW designed research and wrote the article.

FUNDING

This work was supported by the National Natural Science Foundation of China (grants 31330033, 91332124, 31471112, 31500848, 81671107, 31600834, J1210026 and NSFC/RGC Joint Research Scheme 31461163001); the Ministry of Education, China (SRFDP/RGC ERG grant 20130091140003, and Fundamental Research Fund for the Central Universities 20620140542 and 020814380048); the Natural Science Foundation of Jiangsu Province, China (grant BK20140599); and the China Postdoctoral Sciences Foundation (grant 2013T60520).

REFERENCES

Bergquist, F., and Dutia, M. B. (2006). Central histaminergic modulation of vestibular function–a review. *Sheng Li Xue Bao* 58, 293–304.

Carleton, S. C., and Carpenter, M. B. (1983). Afferent and efferent connections of the medial, inferior and lateral vestibular nuclei in the cat and monkey. *Brain Res.* 278, 29–51. doi: 10.1016/0006-8993(83)90223-8

Dere, E., De Souza-Silva, M. A., Spieler, R. E., Lin, J. S., Ohtsu, H., Haas, H. L., et al. (2004). Changes in motoric, exploratory and emotional behaviours and neuronal acetylcholine content and 5-HT turnover in histidine decarboxylase-KO mice. *Eur. J. Neurosci.* 20, 1051–1058. doi: 10.1111/j.1460-9568.2004.03546.x

Haas, H. L., Sergeeva, O. A., and Selbach, O. (2008). Histamine in the nervous system. *Physiol. Rev.* 88, 1183–1241. doi: 10.1152/physrev.00043.2007

He, C., Chen, F., Li, B., and Hu, Z. (2014). Neurophysiology of HCN channels: from cellular functions to multiple regulations. *Prog. Neurobiol.* 112, 1–23. doi: 10.1016/j.pneurobio.2013.10.001

He, Y. C., Wu, G. Y., Li, D., Tang, B., Li, B., Ding, Y., et al. (2012). Histamine promotes rat motor performances by activation of H_2 receptors in the cerebellar fastigial nucleus. *Behav. Brain Res.* 228, 44–52. doi: 10.1016/j.bbr.2011.11.029

Inoue, I., Yanai, K., Kitamura, D., Taniuchi, I., Kobayashi, T., Niimura, K., et al. (1996). Impaired locomotor activity and exploratory behavior in mice lacking histamine H1 receptors. *Proc. Natl. Acad. Sci. U S A* 93, 13316–13320. doi: 10.1073/pnas.93.23.13316

Kilkenny, C., Browne, W. J., Cuthill, I. C., Emerson, M., and Altman, D. G. (2010). Improving bioscience research reporting: the ARRIVE guidelines for reporting animal research. *PLoS Biol.* 8:e1000412. doi: 10.1371/journal.pbio.1000412

Lacour, M. (2013). Betahistine treatment in managing vertigo and improving vestibular compensation: clarification. *J. Vestib. Res.* 23, 139–151. doi: 10.3233/VES-130496

Lai, C. H., and Chan, Y. S. (2001). Spontaneous discharge and response characteristics of central otolith neurons of rats during postnatal development. *Neuroscience* 103, 275–288. doi: 10.1016/s0306-4522(00)00539-x

Lewis, A. S., and Chetkovich, D. M. (2011). HCN channels in behavior and neurological disease: too hyper or not active enough? *Mol. Cell. Neurosci.* 46, 357–367. doi: 10.1016/j.mcn.2010.11.007

Li, B., Zhu, J. N., and Wang, J. J. (2014). Histaminergic afferent system in the cerebellum: structure and function. *Cerebellum Ataxias* 1:5. doi: 10.1186/2053-8871-1-5

Li, B., Zhuang, Q. X., Gao, H. R., Wang, J. J., and Zhu, J. N. (2016). Medial cerebellar nucleus projects to feeding-related neurons in the ventromedial hypothalamic nucleus in rats. *Brain Struct. Funct.* doi: 10.1007/s00429-016-1257-2 [Epub ahead of print].

McCormick, D. A., and Williamson, A. (1991). Modulation of neuronal firing mode in cat and guinea-pig lgnd by histamine: possible cellular mechanisms of histaminergic control of Arousal. *J. Neurosci.* 11, 3188–3199.

Molina-Negro, P., Bertrand, R. A., Martin, E., and Gioani, Y. (1980). The role of the vestibular system in relation to muscle tone and postural reflexes in man. *Acta Otolaryngol.* 89, 524–533. doi: 10.3109/00016488009127170

Onodera, K., Yamatodani, A., Watanabe, T., and Wada, H. (1994). Neuropharmacology of the histaminergic neuron system in the brain and its relationship with behavioral-disorders. *Prog. Neurobiol.* 42, 685–702. doi: 10.1016/0301-0082(94)90017-5

Panula, P., and Nuutinen, S. (2013). The histaminergic network in the brain: basic organization and role in disease. *Nat. Rev. Neurosci.* 14, 472–487. doi: 10.1038/nrn3526

Pape, H. C. (1996). Queer current and pacemaker: the hyperpolarization-activated cation current in neurons. *Annu. Rev. Physiol.* 58, 299–327. doi: 10.1146/annurev.physiol.58.1.299

Passani, M. B., Giannoni, P., Bucherelli, C., Baldi, E., and Blandina, P. (2007). Histamine in the brain: beyond sleep and memory. *Biochem. Pharmacol.* 73, 1113–1122. doi: 10.1016/j.bcp.2006.12.002

Paxinos, G., and Watson, C. (2007). *The Rat Brain in Stereotaxic Coordinates.* San Diego, CA: Academic Press.

Peng, S. Y., Zhuang, Q. X., He, Y. C., Zhu, J. N., and Wang, J. J. (2013). Histamine excites neurons of the inferior vestibular nucleus in rats by activation of H1 and H2 receptors. *Neurosci. Lett.* 541, 87–92. doi: 10.1016/j.neulet.2013.02.040

Ris, L., Capron, B., Vibert, N., Vidal, P. P., and Godaux, E. (2001). Modification of the pacemaker activity of vestibular neurons in brainstem slices during vestibular compensation in the guinea pig. *Eur. J. Neurosci.* 13, 2234–2240. doi: 10.1046/j.0953-816x.2001.01603.x

Sarkisian, V. H. (2000). Input-output relations of Deiters, lateral vestibulospinal neurons with different structures of the brain. *Arch. Ital. Biol.* 138, 295–353.

Schwartz, J. C., Arrang, J. M., Garbarg, M., Pollard, H., and Ruat, M. (1991). Histaminergic transmission in the mammalian brain. *Physiol. Rev.* 71, 1–51.

Shan, L., Dauvilliers, Y., and Siegel, J. M. (2015). Interactions of the histamine and hypocretin systems in CNS disorders. *Nat. Rev. Neurol.* 11, 401–413. doi: 10.1038/nrneurol.2015.99

Song, Y. N., Li, H. Z., Zhu, J. N., Guo, C. L., and Wang, J. J. (2006). Histamine improves rat rota-rod and balance beam performances through H_2 receptors in the cerebellar interpositus nucleus. *Neuroscience* 140, 33–43. doi: 10.1016/j.neuroscience.2006.01.045

Steinbusch, H. W. M. (1991). Distribution of histaminergic neurons and fibers in rat brain. Comparison with noradrenergic and serotonergic innervation of the vestibular system. *Acta Otolaryngol. Suppl.* 479, 12–23. doi: 10.3109/00016489109121144

Sun, Y. Z., Waller, H. J., Godfrey, D. A., and Rubin, A. M. (2002). Spontaneous activity in rat vestibular nuclei in brain slices and effects of acetylcholine agonists and antagonists. *Brain Res.* 934, 58–68. doi: 10.1016/s0006-8993(02)02361-2

Tighilet, B., and Lacour, M. (1996). Distribution of histaminergic axonal fibres in the vestibular nuclei of the cat. *Neuroreport* 7, 873–878. doi: 10.1097/00001756-199603220-00008

Tiligada, E., Kyriakidis, K., Chazot, P. L., and Passani, M. B. (2011). Histamine pharmacology and new CNS drug targets. *CNS Neurosci. Ther.* 17, 620–628. doi: 10.1111/j.1755-5949.2010.00212.x

Toyota, H., Dugovic, C., Koehl, M., Laposky, A. D., Weber, C., Ngo, K., et al. (2002). Behavioral characterization of mice lacking histamine H_3 receptors. *Mol. Pharmacol.* 62, 389–397. doi: 10.1124/mol.62.2.389

Uno, A., Idoux, E., Beraneck, M., Vidal, P. P., Moore, L. E., Wilson, V. J., et al. (2003). Static and dynamic membrane properties of lateral vestibular nucleus neurons in guinea pig brain stem slices. *J. Neurophysiol.* 90, 1689–1703. doi: 10.1152/jn.00201.2003

Vizuete, M. L., Traiffort, E., Bouthenet, M. L., Ruat, M., Souil, E., Tardivel-Lacombe, J., et al. (1997). Detailed mapping of the histamine H_2 receptor and its gene transcripts in guinea-pig brain. *Neuroscience* 80, 321–343. doi: 10.1016/s0306-4522(97)00010-9

Wang, J. J., and Dutia, M. B. (1995). Effects of histamine and betahistine on rat medial vestibular nucleus neurones: possible mechanism of action of anti-histaminergic drugs in vertigo and motion sickness. *Exp. Brain Res.* 105, 18–24. doi: 10.1007/bf00242178

Wilson, V. J., and Peterson, B. W. (1978). Peripheral and central substrates of vestibulospinal reflexes. *Physiol. Rev.* 58, 80–105.

Yabe, T., de Waele, C., Serafin, M., Vibert, N., Arrang, J. M., Muhlethaler, M., et al. (1993). Medial vestibular nucleus in the guinea-pig: histaminergic receptors. II. An *in vivo* study. *Exp. Brain Res.* 93, 249–258. doi: 10.1007/bf00228391

Yu, L., Zhang, X. Y., Cao, S. L., Peng, S. Y., Ji, D. Y., Zhu, J. N., et al. (2016). Na^+–Ca^{2+} exchanger, leak K^+ channel and hyperpolarization-activated cyclic nucleotide-gated channel comediate the histamine-induced excitation on rat inferior vestibular nucleus neurons. *CNS Neurosci. Ther.* 22, 184–193. doi: 10.1111/cns.12451

Zhang, J., Han, X.-H., Li, H.-Z., Zhu, J.-N., and Wang, J.-J. (2008). Histamine excites rat lateral vestibular nuclear neurons through activation of post-synaptic H2 receptors. *Neurosci. Lett.* 448, 15–19. doi: 10.1016/j.neulet.2008.10.027

Zhang, J., Li, B., Yu, L., He, Y. C., Li, H. Z., Zhu, J. N., et al. (2011). A role for orexin in central vestibular motor control. *Neuron* 69, 793–804. doi: 10.1016/j.neuron.2011.01.026

Zhang, X. Y., Yu, L., Zhuang, Q. X., Peng, S. Y., Zhu, J. N., and Wang, J. J. (2013). Postsynaptic mechanisms underlying the excitatory action of histamine on medial vestibular nucleus neurons in rats. *Br. J. Pharmacol.* 170, 156–169. doi: 10.1111/bph.12256

Zhang, C.-Z., Zhuang, Q.-X., He, Y.-C., Li, G.-Y., Zhu, J.-N., and Wang, J.-J. (2014). 5-HT_{2A} receptor-mediated excitation on cerebellar fastigial nucleus neurons and promotion of motor behaviors in rats. *Pflugers Arch.-Eur. J. Physiol.* 466, 1259–1271. doi: 10.1007/s00424-013-1378-x

Zhang, J., Zhuang, Q. X., Li, B., Wu, G. Y., Yung, W. H., Zhu, J. N., et al. (2016). Selective modulation of histaminergic inputs on projection neurons of cerebellum rapidly promotes motor coordination via HCN channels. *Mol. Neurobiol.* 53, 1386–1401. doi: 10.1007/s12035-015-9096-3

Zhuang, Q.-X., Wu, Y.-H., Wu, G.-Y., Zhu, J.-N., and Wang, J.-J. (2013). Histamine excites rat superior vestibular nuclear neurons via postsynaptic H_1 and H_2 receptors *in vitro*. *Neurosignals* 21, 174–183. doi: 10.1159/000341980

Conflict of Interest Statement: The authors declare that the research was conducted in the absence of any commercial or financial relationships that could be construed as a potential conflict of interest.

Copyright © 2017 Li, Zhang, Yang, Peng, Chen, Zhou, Chan, Wang and Zhu. This is an open-access article distributed under the terms of the Creative Commons Attribution License (CC BY). The use, distribution and reproduction in other forums is permitted, provided the original author(s) or licensor are credited and that the original publication in this journal is cited, in accordance with accepted academic practice. No use, distribution or reproduction is permitted which does not comply with these terms.

frontiers in Neural Circuits

ORIGINAL RESEARCH
published: 21 February 2017
doi: 10.3389/fncir.2017.00007

Neuronal Correlates of Functional Coupling between Reach- and Grasp-Related Components of Muscle Activity

Shashwati Geed[1,2]†, Martha L. McCurdy[1] and Peter L. E. van Kan[1]*

[1] *Motor Systems Physiology Laboratory, Department of Kinesiology, University of Wisconsin–Madison, Madison, WI, USA,*
[2] *Department of Rehabilitation Medicine, Georgetown University Medical Center, Washington, DC, USA*

Coordinated reach-to-grasp movements require precise spatiotemporal synchrony between proximal forelimb muscles (shoulder, elbow) that transport the hand toward a target during reach, and distal muscles (wrist, digit) that simultaneously preshape and orient the hand for grasp. The precise mechanisms through which the redundant neuromuscular circuitry coordinates reach with grasp, however, remain unclear. Recently, Geed and Van Kan (2016) demonstrated, using exploratory factor analysis (EFA), that limited numbers of global, template-like transport/preshape- and grasp-related muscle components underlie the complexity and variability of intramuscular electromyograms (EMGs) of up to 21 distal and proximal muscles recorded while monkeys performed reach-to-grasp tasks. Importantly, transport/preshape- and grasp-related muscle components showed invariant spatiotemporal coupling, which provides a potential mechanism for coordinating forelimb muscles during reach-to-grasp movements. In the present study, we tested whether ensemble discharges of forelimb neurons in the cerebellar nucleus interpositus (NI) and its target, the magnocellular red nucleus (RNm), a source of rubrospinal fibers, function as neuronal correlates of the transport/preshape- and grasp-related muscle components we identified. EFA applied to single-unit discharges of populations of NI and RNm neurons recorded while the same monkeys that were used previously performed the same reach-to-grasp tasks, revealed neuronal components in the ensemble discharges of both NI and RNm neuronal populations with characteristics broadly similar to muscle components. Subsets of NI and RNm neuronal components were strongly and significantly cross-correlated with subsets of muscle components, suggesting that similar functional units of reach-to-grasp behavior are expressed by NI and RNm neuronal populations and forelimb muscles. Importantly, like transport/preshape- and grasp-related muscle components, their NI and RNm neuronal correlates showed invariant spatiotemporal coupling. Clinical and lesion studies have reported disruption of coupling between reach and grasp following cerebellar damage; the present results expand on those studies by identifying a neuronal mechanism that may underlie cerebellar contributions to spatiotemporal coordination of distal and proximal limb muscles during reaching to

OPEN ACCESS

Edited by:
Ioan Opris,
University of Miami School of Medicine, USA

Reviewed by:
Erik Svensson,
Uppsala University, Sweden
Annalisa Bosco,
University of Bologna, Italy

****Correspondence:***
Shashwati Geed
sg1075@georgetown.edu

†Present address:
Shashwati Geed,
Neuroscience Research Center, MedStar National Rehabilitation Hospital, Washington, DC, USA

Received: *06 December 2016*
Accepted: *23 January 2017*
Published: *21 February 2017*

Citation:
Geed S, McCurdy ML and Van Kan PLE (2017) Neuronal Correlates of Functional Coupling between Reach- and Grasp-Related Components of Muscle Activity. Front. Neural Circuits 11:7. doi: 10.3389/fncir.2017.00007

grasp. We conclude that finding similar functional units of behavior expressed at multiple levels of information processing along interposito-rubrospinal pathways and forelimb muscles supports the hypothesis that functionally related populations of NI and RNm neurons act synergistically in the control of complex coordinated motor behaviors.

Keywords: reach to grasp, cerebellum, magnocellular red nucleus, coordination, nucleus interpositus

INTRODUCTION

Reach-to-grasp movements require precisely coordinated activation of shoulder, elbow, wrist, and digit muscles such that while shoulder and elbow muscles transport the hand toward a target during reach, wrist and digit muscles preshape and orient the hand for grasp. Psychophysical studies of reach-to-grasp movements have demonstrated functional coupling between reach and grasp such that the wrist follows a largely bell-shaped velocity profile during reach and attains peak velocity at approximately 70% of the transport trajectory (Jeannerod, 1984). Peak wrist velocity during the transport phase coincides in time with attainment of maximal grip aperture (i.e., distance between the thumb and index finger), which characterizes hand opening prior to closing the hand in anticipation of grasp (Jeannerod, 1981, 1984). Furthermore, perturbation of target location, which directly impacts the reach, also influences grasp (Paulignan et al., 1991b; Roy et al., 2006), and perturbation of target size or orientation (Paulignan et al., 1991a, 1997; Roy et al., 2006), which directly impacts grasp, also influences the reach. Recently, Geed and Van Kan (2016) demonstrated, using exploratory factor analysis (EFA), invariant spatiotemporal coupling between transport/preshape- and grasp-related components of forelimb muscle activity in monkeys performing reach-to-grasp tasks, consistent with the observed functional coupling between reach and grasp movements.

Reaching to grasp critically depends on cerebellar function. Cerebellar damage causes a specific breakdown in coupling of reach and grasp movement components (Bastian and Thach, 1995; Bastian et al., 1996, 2000; Mason et al., 1998; Lang and Bastian, 1999; Cooper et al., 2000; Rand et al., 2000; Zackowski et al., 2002). Although cerebellar output targets many, if not all, neural structures involved in movement production, its most direct influences are exerted via the pathway from nucleus interpositus (NI), the sole output of intermediate cerebellum, to the magnocellular red nucleus (RNm). RNm receives its dominant input from NI (Humphrey and Rietz, 1976; Kennedy et al., 1986; Houk et al., 1988), and RNm neurons terminate as rubrospinal fibers on spinal interneurons, or directly on motoneurons that innervate digit muscles (Kuypers et al., 1962; Lawrence and Kuypers, 1968a,b; Kuypers, 1982; McCurdy et al., 1987; Holstege et al., 1988; Ralston et al., 1988; McCurdy et al., 1992). In keeping with influences on distal limb muscles, rubrospinal fibers show promise for prehensile recovery following stroke (Carmel et al., 2013; Takenobu et al., 2014), and following experimental lesions of the pyramidal tract in monkeys (Belhaj-Saif and Cheney, 2000). Therefore, studying the role of interposito-rubrospinal (NI-RNm) circuitry in the control of coordinated reach-to-grasp movements is not only important for understanding cerebellar function in general but is also important for potential neuromodulation and rehabilitation post-stroke, which is in line with recent investigations in other subcortical pathways (Baker, 2011; Bradnam et al., 2013; Cunningham et al., 2015).

Although a mechanistic understanding of how NI-RNm circuits contribute to control of spatiotemporal coordination of reach and grasp movement components has remained elusive, several lines of evidence indicate that NI-RNm circuitry is important to this process. First, forelimb NI and RNm neurons discharge consistently and at high rates when monkeys reach to grasp objects (NI: Gibson et al., 1994; Van Kan et al., 1994; Van Kan and McCurdy, 2001, 2002a,b), RNm: (Gibson et al., 1994; Van Kan et al., 1994; Van Kan and McCurdy, 2001, 2002a,b), and the high discharge rates of NI and RNm neurons are associated with coordinating the hand in the context of whole-limb reaching movements (Miller et al., 1993; Van Kan et al., 1994; Van Kan and McCurdy, 2001). Second, behavioral studies indicate that lesioning or inactivating NI or RNm (NI: Mason et al., 1998; Cooper et al., 2000); RNm: (Sybirska and Gorska, 1980; Gibson et al., 1994) profoundly and specifically affect coordination of reach and grasp movement components. Third, anatomical investigations have demonstrated that NI-RNm circuitry projects (through rubrospinal pathways) to interneuronal and motoneuronal pools that innervate forelimb muscles crucial for coordinated reach-to-grasp movements (Kuypers et al., 1962; Lawrence and Kuypers, 1968a,b; Kuypers, 1982; McCurdy et al., 1987; Holstege et al., 1988; Ralston et al., 1988; McCurdy et al., 1992). The combined results of electrophysiological, behavioral, and anatomic studies support strongly the hypothesis that NI-RNm circuitry serves as a potential neuronal correlate of reaching to grasp.

The primary objective of the current study was to test whether EFA, applied to ensembles of single-unit discharges of populations of NI and RNm neurons recorded while the same monkeys that were used previously (Geed and Van Kan, 2016) performed the same reach-to-grasp tasks, would reveal neuronal components with characteristics broadly similar to the muscle components identified. Our results demonstrate that EFA did indeed reveal 5–7 NI or RNm neuronal components in each monkey, which, while explaining a large proportion of the variance in the ensemble discharges of the NI and RNm neurons recorded, showed significant correlations with the transport/preshape- or grasp-related muscle components identified. Importantly, in both NI and RNm populations, invariant spatiotemporal coupling between transport/preshape-

and grasp-related neuronal components closely resembled the coupling observed between transport/preshape- and grasp-related muscle components. The results of the present study significantly strengthen our hypothesis that the combined output from NI-RNm circuitry reflects a neuronal correlate of the functional coupling between reach and grasp movement components.

MATERIALS AND METHODS

Two rhesus macaques (Macaca mulatta, male, 7–10 kg) were trained to perform reach-to-grasp movements. Animal care and experimental procedures complied with the United States Public Health Service Policy on Humane Care and Use of Laboratory Animals, conformed to the National Institutes of Health, "Guide for the Care and Use of Laboratory Animals," and were approved by the Institutional Animal Care and Use Committee of the University of Wisconsin – Madison. A more detailed description of behavioral paradigms, surgical implantation of EMG electrodes, and data collection procedures has been provided in earlier publications (Van Kan and McCurdy, 2001, 2002a). Brief reports of these results have appeared in abstract form (Geed et al., 2011, 2013).

Experimental Protocol

The two monkeys (*W*, *B*) performed reach-to-grasp tasks with their right forelimb while seated upright in a primate chair with their backs and feet supported. A neck collar and waist plate loosely restrained the animals while seated. The reaching forelimb and head were unrestrained. The animals were trained to reach and grasp a cereal reward (Kellogg's® *Froot Loops*® Cereal, thickness: ∼6 mm; diameter: ∼19 mm) using either a precision or whole-hand grasp from a target assembly located in the parasagittal plane through the shoulder of the animal's reaching limb, 56° above the horizontal plane through the shoulder. The cereal reward was dispensed in a horizontally oriented narrow slot (height: 6 mm, width: 25 mm, depth: 25 mm), which necessitated apposition of the index finger and thumb in a precision grasp, or a 50-ml glass beaker (clear, diameter: 32 mm, tilted at a 45° angle toward the animal), which required concerted use of all digits in a whole-hand grasp.

A typical reach-to-grasp trial began with the animal holding a handle at the waist for a variable inter-trial interval of 3-5 *s,* which minimized anticipatory muscle activity prior to movement onset. During the inter-trial interval, the animal received water reward for holding the handle steady at the waist. To initiate a reaching movement, a computer-controlled air cylinder dispensed the cereal reward into either the beaker or narrow slot, and a light-emitting diode (LED) next to the receptacle with the cereal reward lit up cueing the animal to initiate its reach-to-grasp movement as well as instructing whether to reach to the beaker (for whole-hand grasp) or slot (for precision grasp). Upon illumination of the LED, the monkey released the handle at the start location, reached toward the target assembly, retrieved the cereal reward from the beaker or slot as instructed, returned its hand to the mouth to eat the cereal reward, and finally, moved its hand back to the starting position to grasp the handle. The next trial was initiated following the variable inter-trial interval. The cereal reward was presented in the narrow slot or beaker in a pseudorandom fashion, controlled by custom software running in LabVIEW (National Instruments, LabVIEW 7.1).

Data Recording and Preprocessing

Behavioral event time data, intramuscular EMGs, and single-unit discharges from RNm and NI neurons were recorded in both monkeys. EMG recording sessions were carried out separately from the single-unit recording sessions although EMGs and neuronal data were recorded from the same two monkeys performing the same reach-to-grasp tasks.

Behavioral Event Markers

Behavioral event times were recorded with contact sensors on the handle at the starting location, on the slot, and on the beaker's rim at the target locations. Reach onset and offset were defined as the times of breaking contact with the handle and making contact with the slot or beaker, respectively. Grasp onset and offset were defined as the times of making and breaking contact with the slot or beaker, respectively. Behavioral event times were used to normalize the durations of transport and grasp intervals over trials and to align trials.

Intramuscular Electromyograms (EMGs)

The complete sets of muscles implanted in both monkeys, as well as the frequency of recording sessions in a given muscle is shown in **Table 1**. We recorded activity from 14 (monkey *W*) and 20 (monkey *B*) forelimb muscles in sets of 9 muscles/recording session on different days in close succession while the monkeys performed precision and whole-hand reach-to-grasp tasks. EMG signals were rectified, integrated (time constant: 10 ms), band-pass filtered (30 Hz – 3 kHz), and digitized at 167 Hz by A/D computer inputs (CED 1401 *plus*, Cambridge Electrical Design). Rectified, integrated, and band-pass filtered EMG signals were low-pass filtered using a fourth-order zero-lag Butterworth filter with a cut-off frequency of 15 Hz.

Neural Recordings

Discharges of forelimb RNm and NI neurons were recorded with epoxylite-coated tungsten microelectrodes (exposed tip of microelectrodes: 15–25 μm) as monkeys performed the precision or whole-hand reach-to-grasp tasks. We recorded from 33 and 34 forelimb RNm neurons in monkey *W* and monkey *B*, respectively; and from 30 and 48 forelimb NI neurons in monkey *W* and monkey *B*, respectively. Microelectrodes were inserted through the dura mater with a microdrive (Narishige MO-97*)*, modified to include a stainless-steel guide tube assembly, which allowed the microelectrode tip to traverse the dura without being damaged. The microdrive was covered by a lightweight cylinder (diameter: 100 mm), which prevented the animal access to the microdrive. Single-unit discharges were monitored visually on an oscilloscope, filtered (half-amplitude band-pass at 100 Hz and 10 kHz ± 3dB), and fed into a window discriminator circuit that produced a standard pulse for each action potential.

TABLE 1 | Forelimb muscles recorded in each monkey.

	Muscle	Abbreviation	Recording frequency	
			Monkey *W*	Monkey *B*
Digits	Extensor digitorum communis	EDC	7/7	3/5
	Extensor digitorum two and three	ED23		3/5
	Extensor digitorum four and five	ED45	2/7*	1/5
	Flexor digitorum superficialis	FDS	6/7	1/5
	Flexor digitorum profundus	FDP	3/7	2/5
	Extensor pollicis longus	EPL		1/5
	Abductor pollicis longus	APL	7/7	2/5
	Palmaris longus	PL	3/7	3/5
Wrist	Extensor carpii radialis	ECR	6/7	3/5
	Extensor carpii ulnaris	ECU		3/5
	Flexor carpii radialis	FCR	6/7	3/5
	Flexor carpii ulnaris	FCU	2/7	4/5
Elbow	Brachioradialis	BR		2/5
	Biceps	BIC	2/7	2/5
	Triceps	TRI	4/7	2/5
Shoulder	Acromion deltoid	AcDLT	5/7	2/5
	Spino deltoid	SpDLT	4/7	2/5
	Cleido deltoid	ClDLT		2/5
	Pectoralis	PEC	4/7	2/5
	Teres major	TM		2/5
	Latissimus dorsii	LAT	2/7	

*EMGs were recorded in 12 sessions (1 session/day) over a 2–3-week period. Seven sessions were conducted in monkey W, 5 in monkey B. In a given session, EMGs of combinations of 9 muscles were recorded simultaneously. Numerical entries indicate recording frequency, i.e., (number of sessions in which EMGs of a given muscle were recorded) / (total number of sessions). *EMGs of ED45 in monkey W were not included in the analyses because of technical difficulties. EMGs, intramuscular electromyograms.*

Discriminated pulses were used as computer clock triggers to collect interspike intervals with 100-μs precision. **Figure 1B** shows representative spike trains recorded from an individual RNm neuron over 12 reach-to-grasp trials of the precision task in monkey *W*.

Data Preprocessing

Each neuron's discharge frequency was computed from the interspike interval record by averaging the neuron's discharge rate over consecutive 6-ms periods taking into account fractional interspike intervals. Task-related modulations in discharge rate during individual trials were quantified by calculating the average discharge rate over a 100-ms window that was moved, 6 ms at a time, between the times of reach onset and grasp offset. This created a record of the neuron's discharge frequency throughout the reach-to-grasp trial. **Figure 1A** shows records of discharge frequency computed from neural spikes recorded from a single RNm neuron recorded over 12 reach-to-grasp trials. Additional time intervals of 500 ms preceding reach onset, and 250 ms following grasp offset were also included to account for neural activity before reach onset and during the early part of the hand's return to the mouth.

Outlier Removal

Trials with outlier durations of the transport or grasp phase were removed using Rosner's Many Outliers Procedure (Rosner, 1983). A trial was removed if the duration of either the transport or grasp phase was determined to be an outlier. Most outlier trials had unusually long durations. The number of reach-to-grasp trials removed from EMGs ranged from 0/40 (0%) to 6/44 (13.6%) in monkey *B*, and from 1/87 (1.1%) to 6/84 (7.1%) in monkey *W*. The number of reach-to-grasp trials removed from RNm data ranged from 8/223 (3.6%) in monkey *B* to 21/187 (11.2%) in monkey *W*. The number of outlier trials removed in NI data ranged from 40/741 (5.4%) in monkey *B* to 21/209 (10%) in monkey *W*.

Trial Alignment

The transport and the grasp phase of each trial was time normalized to the mean duration of transport or grasp phase in a given monkey. Time-normalized trials were aligned on reach onset and averaged across trials. Thus, all precision reach-to-grasp data from different EMG recording sessions were averaged across trials to give a single dataset with time-normalized, trial-averaged values of the activation amplitudes of 14 muscles in monkey *W* (or 20 muscles in monkey *B*). Similarly, there was a single dataset with time-normalized, trial-averaged values of the 33 RNm neurons, and 30 NI neurons in monkey *W* (or 34 RNm neurons, and 48 NI neurons in monkey *B*). Each of the EMG, RNm, and NI datasets were standardized to have zero mean and unit standard deviation as required for subsequent factor analysis. **Figure 1C** shows the time-normalized, trial-averaged, standardized activity of a representative set of RNm neurons.

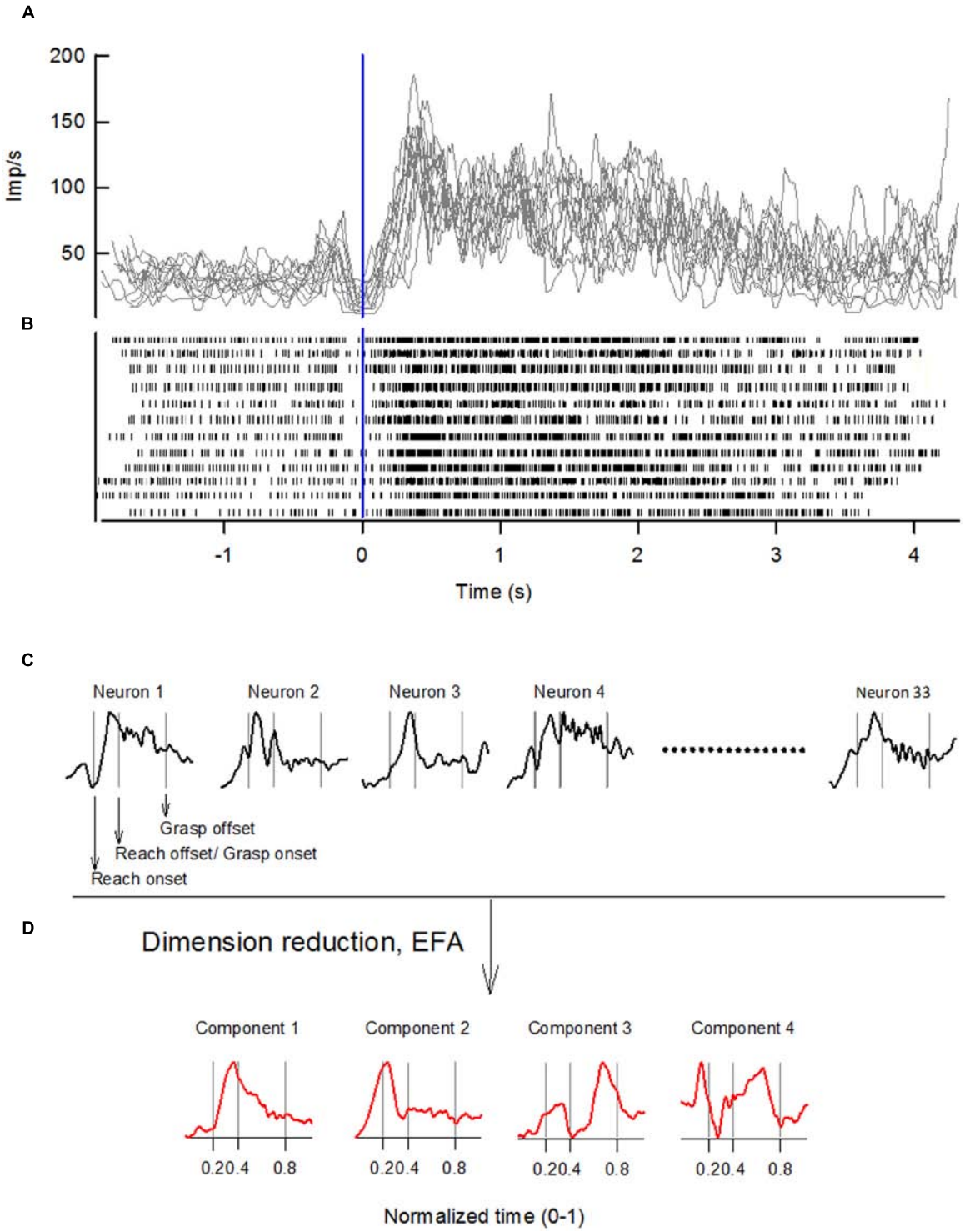


FIGURE 1 | Sequence of steps for extracting neuronal components by applying EFA to ensembles of single-unit discharges of NI and RNm neurons. **(A)** Records of discharge frequency of a single RNm neuron, computed from interspike intervals, are overplotted for 12 representative reach-to-grasp trials of the precision task in monkey *W*. Records are aligned on reach onset (Time 0, vertical line). **(B)** Spike-raster of neural discharge showing the same 12 reach-to-grasp trials as in **(A)**. **(C)** Records of discharge frequency of each neuron were time normalized, standardized, and trial-averaged to yield a dataset of the population of neurons with $n = 1, 2, \ldots$ n (here $n = 33$). EFA with *varimax* factor rotation was applied to the correlation matrix of this neuronal dataset to derive a low-dimensional representation of the data. **(D)** A limited number of neuronal components was retained following EFA. Behavioral event times are indicated by vertical lines in **(C,D)**: reach onset, reach offset/grasp onset, grasp offset respectively.

Data Analysis

Exploratory Factor Analysis on Muscle and Neuronal Data

Exploratory factor analysis with varimax factor rotation was applied to the correlation matrices of time-normalized, trial-averaged, standardized EMGs, RNm, and NI data separately to derive a low-dimensional representation of the data. The low-dimensional representation retained the variance of muscle or neuronal data while allowing for computationally simpler comparisons between groups of 14 or 20 muscles, and the combined output of 33 or 34 RNm neurons, and 30 or 48 NI neurons in monkey W and monkey B, respectively.

The goal of applying EFA is to represent "D" number of muscles (or neurons in case of neuronal components) as a linear combination of N components with N < D such that:

$$m(t) = \sum_{i=1}^{N} c_i(t) w_i$$

Here *m(t)* is a D-dimensional vector that specifies the activation of each muscle (or neuron) at time t. $c_i(t)$, referred to as the component's temporal scaling coefficient is a time-varying scaling coefficient for the *i*-th component. w_i (D × N matrix) represents the weighting coefficients of the i-th component, the relative strength of activation of the muscle (or neuron) in a given component. The weighting coefficients range between +1 and −1, with strong increased activation of a muscle (or neuron) in the component represented by a value close to +1 and strong decreased activation represented by a value close to −1. $c_i(t)$, which is a (N × t) matrix, represents the time-varying temporal scaling coefficient of the i-th component throughout the reach-to-grasp movement. **Figure 1D** shows the temporal scaling coefficients from a representative set of RNm neuronal components.

The number of muscle or neuronal components to retain following EFA was based on *(1)* Kaiser criteria (Kaiser, 1974), and *(2)* Scree plot of the extracted components and amounts of variance explained (Cattell, 1966). The combined criteria ensured that the components retained in the factor analysis contributed to meaningful interpretation of muscle and neuronal activity in the context of reaching to grasp, and captured a sizable amount of variance in the data whereas components that accounted for relatively small contributions to the variance of the collected sample were excluded. EFA was carried out using SPSS version 20 (SPSS IBM, New York).

Characterizing the Functional Contributions of Muscle Components

Detailed criteria for characterizing a muscle component as predominantly transport/preshape- or grasp-related have been described previously (Geed and Van Kan, 2016). Briefly, a muscle component was characterized as either transport/preshape- or grasp-related based on the combination of two criteria: *(1)* combinations of muscles showing weighting coefficient values greater than 0.4 ($w_i > 0.4$), and *(2)* timing of maximal contribution of the temporal scaling coefficient during the reach-to-grasp trial. Cross-referencing the temporal scaling coefficients with weighting coefficients is critical to determine the functional contribution of a given muscle component because the weighting coefficients reflect the relative ratios of activation of a combination of muscles in the component, and the temporal scaling coefficients reflect the activation profile of the combination of muscles in a component over time. Taken together, the weighting and temporal scaling coefficients indicate a component's functional contribution during reach-to-grasp movements. Based on these criteria, cross-referencing showed that muscle components 1 and 2 contributed predominantly during the transport/preshape phase in both monkeys. Muscle components 3 and 4 (4 only in monkey *W*) contributed predominantly during grasp in both monkeys.

Comparison of Neuronal and Muscle Components

The cross-correlation function was used to compare temporal scaling coefficients of muscle components with RNm and NI neuronal components. We hypothesized that if NI and RNm discharges represent neuronal correlates of coordinated reach-to-grasp muscle activity, we would find broad similarities between the temporal scaling coefficients of muscle, RNm, and NI components. Pair-wise cross-correlation magnitudes between each of the muscle-RNm, and muscle-NI component pairs were computed using Matlab® (MathWorks). The highest cross-correlation magnitude within a predefined −50 to +30 normalized time-bin window defined the best-matching muscle-neuronal component pair. The next highest cross-correlation defined the next best-matching muscle-neuronal component pair and so on, until there were no more unpaired components left in either the neuronal or muscle datasets.

Negative cross-correlation lags signify that a neuronal component occurs earlier than the muscle component on the normalized time scale, whereas positive lags signify that a neuronal component lags the muscle component on the normalized time scale. The loss of the absolute durations of individual trials was a drawback of time normalizing each trial for further analysis to compare the forelimb muscle activity and neuronal activities in low-dimensional space; however, we predefined a relative duration of −50 to +30 bins as the relevant time-window for meaningful neuronal-muscle signal interaction. This duration was chosen in accordance with Miller et al. (1993), who have reported that relatively analogous time lag windows (−150 to 200 ms) capture approximately 85% of the significant cross-correlation peaks between activity of single RNm neurons and EMGs recorded during free-form forelimb movements in monkeys. Before time normalization, each bin represented 6-ms worth of EMG or neuronal data, and so our predefined time window of −50 to +30 bins of normalized time captures the majority of the neuronal-muscle interactions of interest. We considered relatively short positive lags as meaningful too because small positive lags may signify parallel descending inputs to muscle components, to which NI-RNm components contribute only partially or at particular times during the entire duration of the reach-to-grasp movement.

Significance tests for cross-correlations are not well defined. Therefore, Monte Carlo simulations were used to determine the probability that the cross-correlation peak at a given time

lag would occur by chance. The muscle component signal was randomly shuffled, and cross-correlations were computed between this randomly shuffled muscle component signal and the neuronal component signal. This process was repeated 10,000 times for each muscle-neuronal component pair to generate a distribution of peak cross-correlation values between the 10,000 randomly shuffled muscle components and the neuronal component. The 0.5th and 99.5th percentiles for this distribution served as the upper and lower bounds of significance for the cross-correlation (i.e., $p \leq 0.01$). If peak cross-correlations between muscle and neuronal components occurred due to chance, values would fall between the upper and lower bounds; however, statistically significant cross-correlation values would be outside the confidence interval allowing us to reject the null hypothesis that muscle and neuronal components were uncorrelated. Significance testing of the cross-correlations using Monte Carlo simulations was performed offline using custom programs in MATLAB® (MathWorks).

Temporal Coupling between Transport/Preshape- and Grasp-Related Neuronal Correlates

Transport/preshape- and grasp-related muscle components show invariant spatiotemporal coupling during reach-to-grasp movements irrespective of the type of grasp or the target location in the workspace (Geed and Van Kan, 2016). The time of peak activation of the transport/preshape-related muscle component occurs simultaneously with the time of peak slope of activation of the grasp-related muscle component. In the present study, we tested the hypothesis that NI and RNm components represent the neuronal correlates of the invariant spatiotemporal coupling between transport/preshape- and grasp-related muscle components. Slope (M) of the grasp-related component was computed using the following equation,

$$M = \frac{(y_2 - y_1)}{(x_2 - x_1)}$$

where (x_1, y_1), and (x_2, y_2) are points on the grasp-related component of interest. A paired-samples t-test was used to determine if the NI and RNm neuronal correlates of the transport/preshape- and grasp-related muscle components showed similar functional coupling as reported for muscle components.

RESULTS

Two monkeys performed reach-to-grasp tasks that required either a precision or whole-hand grasp to retrieve cereal reward. This report is based on single-unit discharges of task-related forelimb NI and magnocellular red nucleus (RNm) neurons (NI: $n = 30$ and $n = 48$, RNm: $n = 33$ and $n = 34$, in monkey W and monkey B, respectively), and intramuscular EMGs of forelimb muscles ($n = 14$ and $n = 20$ in monkey W and monkey B, respectively, **Table 1**). Data from the RNm neurons have been included in previous reports (Van Kan and McCurdy, 2001, 2002a,b). EMGs included in the present report are a subset of those included in Geed and Van Kan (2016). EMGs were recorded during reach-to-grasp movements to only one target location ("up") of the four locations included in the previous report.

For each task condition, EFA was used to determine whether a limited number of components is able to explain a large amount of variance in the ensemble discharges of the NI and RNm neurons of our sample. Scree plots (**Figure 2**, left ordinates, black) show the progressive decrease in eigenvalues of extracted factors as the number of factors selected increases. The first 7 factors (NI, **Figure 2A**) or 5 factors (RNm, **Figure 2B**) extracted had eigenvalues > 1, which fulfills the Kaiser criteria for retaining factors as components (see Materials and Methods). Plots of percent variance accounted for (% VAF) as a function of the number of factors (**Figure 2**, right ordinates, red) demonstrate that the first 7 components (NI, **Figure 2A**) or 5 components (RNm, **Figure 2B**) accounted for >85% of the variance in the ensemble discharges of NI and RNm neurons for both precision (solid lines) and whole-hand tasks (dotted lines). **Table 2** summarizes % VAF by NI and RNm neuronal components, and muscle components. Percent VAF by muscle components was taken from Geed and Van Kan (2016). Supplementary Table 1 shows cumulative variances accounted for by each of the neuronal and muscle components in the two monkeys during precision and whole-hand tasks. In summary, EFA revealed that 7-5 NI and RNm neuronal components accounted for >85% of the variance in ensemble discharges of the NI and RNm neurons of our sample, and 4–6 muscle components accounted for >85% of the variance in EMGs of the forelimb muscles we sampled.

Neuronal Correlates of Muscle Components

In a recent study, Geed and Van Kan (2016) reported that muscle components extracted using EFA were functionally aligned with transport/preshape- or grasp-related aspects of reach-to-grasp movements. In the following sections, we demonstrate similarities in characteristics of the NI, RNm, and muscle components we identified. Pairwise cross-correlations quantified similarities between temporal scaling coefficients $c_i(t)$ of the best-matching NI and RNm neuronal components and those of their corresponding transport/preshape- or grasp-related muscle components. Of note, each muscle component contributed throughout the reach-to-grasp movement; however, components were characterized as mainly transport/preshape- or grasp-related in order to simplify the expression of muscle activity of up to 21 forelimb muscles, and to evaluate relations between muscle components and neuronal components extracted from ensemble discharges of NI and RNm neurons.

Neuronal Correlates of Transport/Preshape-Related Muscle Components

Figure 3 shows correlations between the best-matching NI and RNm neuronal components and transport/preshape-related muscle component 1. Muscle component 1 increased activity at or prior to reach onset, attained peak amplitude during the transport/preshape phase prior to (**Figure 3B**, monkey W) or at the time the hand made contact with the target (**Figure 3F**, monkey B), and sharply decreased activity during the latter half of the transport/preshape phase (**Figure 3B**) or early in the grasp

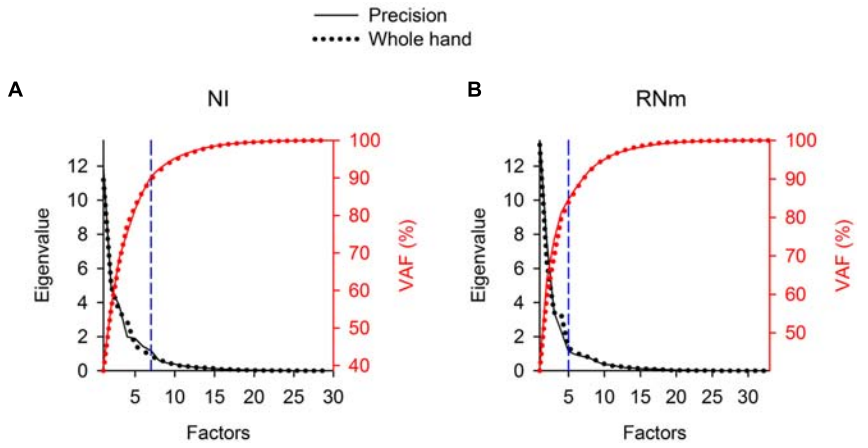


FIGURE 2 | Eigenvalues and percent variance accounted for (%VAF) of NI (A) and RNm **(B)** neuronal components in Monkey *W*. Scree plots (left ordinates, black) illustrate the progressive decrease in eigenvalues of extracted neuronal components as the number of components selected increases. The first 7 (in NI) or 5 (in RNm) components had eigenvalues > 1, which fulfills the Kaiser criteria for retaining factors as components. The "elbow" in the Scree plots (dashed, vertical blue lines) marks the cut off for retaining the first 7 (NI) or 5 (RNm) factors as neuronal components. Plots of %VAF (right ordinates, red) as a function of the number of factors demonstrate that the first 7 (or 5 in RNm) accounted for >85% of the variance in NI or RNm data. Solid lines show data for the precision task, dotted lines show data for the whole-hand task.

TABLE 2 | Variance accounted for by NI, RNm, and muscle components.

	Monkey *W*		Monkey *B*	
	Whole-hand	**Precision**	**Whole-hand**	**Precision**
NI	89.7 (7)	90.4 (7)	92.9 (6)	93.4 (7)
RNm	87.0 (6)	85.0 (5)	91.9 (6)	89.9 (5)
Muscle	90.1 (4)	86.9 (4)	93.0 (6)	91.8 (5)

Values represent percent variance accounted for (% VAF) by the number of components (n) in parentheses.

phase (**Figure 3F**). Component 1 was characterized by strong contributions from proximal muscles with coactivation of wrist and digit muscles (**Figure 3A**, monkey *W*; **Figure 3E**, monkey *B*).

The best-matching NI components (NI component 1 in monkey *W*; NI component 3 in monkey *B*) were strongly correlated with transport/preshape-related muscle component 1 in both animals (**Figure 3C**, $r = 0.62$, precision task in monkey *W*; **Figure 3G**, $r = 0.78$, whole-hand task in monkey *B*). The best-matching NI components explained 23.2 and 19.9% of the variance in the ensemble discharges of the 30 and 48 forelimb NI neurons in monkey *W* and monkey *B*, respectively. The best matching RNm components (component 2 in monkey *W*, precision task; and component 1 in monkey *B*, whole-hand task) were strongly correlated with transport/preshape-related muscle component 1 (**Figure 3D**, $r = 0.83$, precision task in monkey *W*; **Figure 3H**, $r = 0.83$, whole-hand task in monkey *B*). RNm component 2 explained 24.3% and component 1 explained 26.8% of the variance in the ensemble discharges of the 33 and 34 forelimb RNm neurons in monkey *W* and monkey *B*, respectively.

Figure 4 shows correlations between the best-matching NI and RNm neuronal components and transport/preshape-related muscle component 2. Muscle component 2 (**Figure 4B**, monkey *W*; **Figure 4G**, monkey *B*) attained peak activation amplitude during the transport/preshape phase and sharply decreased activity around grasp onset. A second, relatively smaller peak of activation was attained in the latter third of the grasp phase or early during the return phase when the hand moved back to the mouth to ingest the food reward. Muscle component 2 showed combined activity of shoulder, wrist, and digit muscles (**Figure 4A**, monkey *W*; **Figure 4F**, monkey *B*).

The best matching NI neuronal components (NI component 4 in monkey *W*; NI component 1 in monkey *B*) were strongly correlated with transport/preshape-related muscle component 2 (**Figure 4C**, $r = 0.73$, precision task in monkey *W*; **Figure 4H**, $r = 0.76$, whole-hand task in monkey *B*). The best-matching NI components explained 11.3%, and 29.2% of the variance in the ensemble discharges of the 30 and 48 forelimb NI neurons recorded in monkey *W* and monkey *B*, respectively. The best matching RNm components (RNm components 3 and 4 in monkey *W*; RNm component 5 in monkey *B*) were moderately correlated with transport/preshape-related muscle component 2 (**Figure 4D**, $r = 0.52$; **Figure 4E**, $r = 0.41$). The RNm neuronal components explained 12.4% and 8.7% of the variance in the ensemble discharges of the 33 RNm neurons in monkey *W*. RNm component 5 in monkey *B* was moderately correlated with transport/preshape-related muscle component 2 (**Figure 4I**, $r = 0.51$, whole-hand task) and explained 11.1% of the variance in the ensemble discharges of the 34 RNm neurons in monkey *B*.

In summary, a considerable amount of variance in the ensemble discharges within both the NI and RNm populations was directed toward transport/preshape-related aspects of reach-to-grasp movements in both animals during performance of both tasks. In addition, the transport/preshape-related NI and RNm neuronal components showed strong to moderate correlations with the transport/preshape-related muscle components.

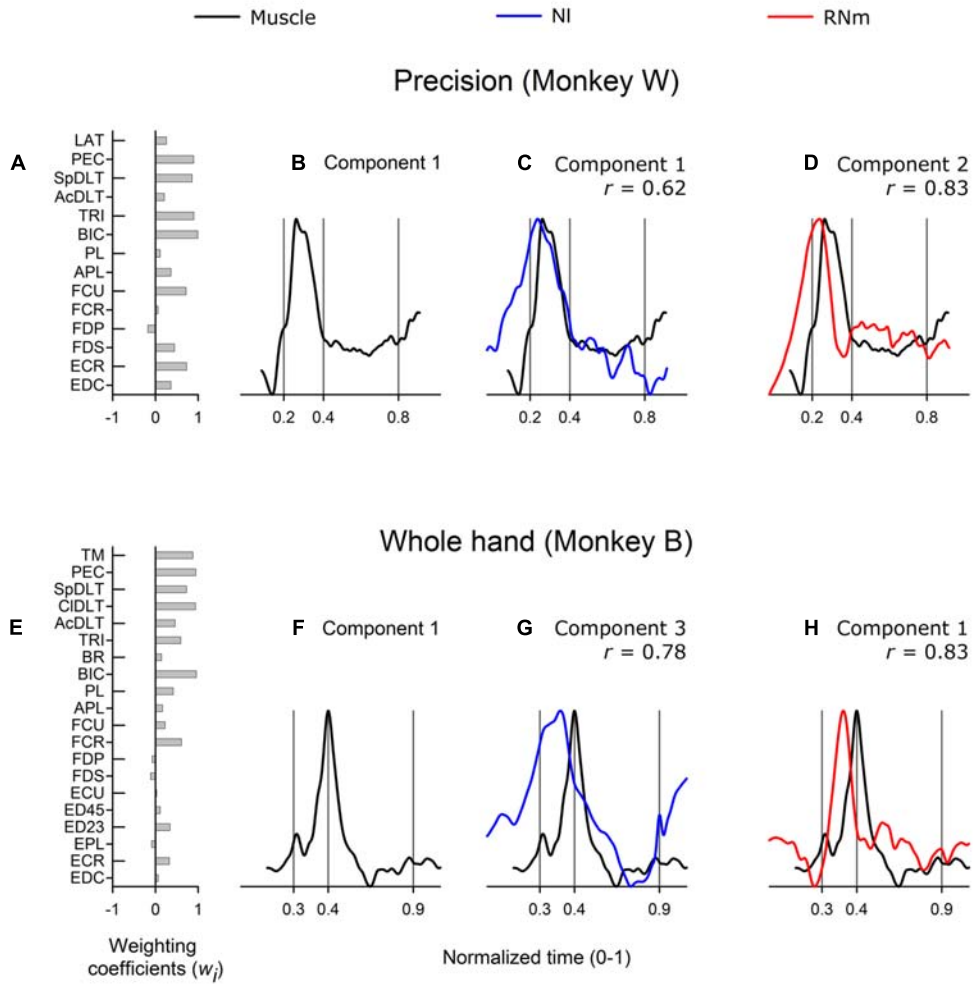


FIGURE 3 | Best-matching NI and RNm neuronal correlates of transport/preshape-related muscle component 1. (A,E) Weighting coefficients of transport/preshape-related muscle component 1 in precision **(A)** and whole-hand **(E)** task in monkey *W* and monkey *B,* respectively. **(B,F)** Temporal scaling coefficients of transport/preshape-related muscle component 1. Temporal scaling coefficients shown in **(B,F)** specify activation of all muscles included in the muscle component according to their corresponding weighting coefficients shown in **(A,E)**, respectively. **(C,G)** Temporal scaling coefficients of the NI components that best matched with transport/preshape-related muscle component 1 shown in **(B,F)**, respectively. **(D,H)** Temporal scaling coefficients of the RNm components that best matched with transport/preshape-related muscle component 1 shown in **(B,F)** respectively. Cross-correlation magnitude between NI or RNm and muscle components is indicated by *r*. Behavioral event times are indicated by vertical lines: reach onset, reach offset/grasp onset, grasp offset respectively. Ordinate scales are arbitrary but uniform throughout. Time scale is normalized (0–1) across neuronal and EMG reach-to-grasp data to allow neuronal-muscle comparisons.

Neuronal Correlates of Grasp-Related Muscle Components

Figure 5 shows correlations between the best-matching RNm and NI neuronal components and grasp-related muscle component 3. Grasp-related muscle component 3 attained peak amplitude early in the grasp phase, near the time the hand contacted the target, and remained active at a relatively high amplitude throughout the first two-thirds (**Figure 5B**, precision task in monkey *W*) or first half (**Figure 5F**, whole-hand task in monkey *B*) of the grasp phase. Grasp-related muscle component 3 included combinations of proximal and distal muscles: EDC, FDP, AcDLT, and SpDLT in monkey *W* (**Figure 5A**, precision task) and various wrist and digit flexor and extensor muscles in combination with BR in monkey *B* (**Figure 5E**, whole-hand task).

The best matching NI neuronal components (NI component 2 in both monkeys) were strongly correlated with grasp-related muscle component 3 in both monkeys (**Figure 5C**, $r = 0.79$, precision task in monkey *W*; **Figure 5G**, $r = 0.76$, whole-hand task in monkey *B*). The best matching NI neuronal components accounted for 19.6 and 20.3% of the variance in the ensemble discharges of the 30 and 48 NI neurons in monkey *W* and monkey *B*, respectively. The best matching RNm neuronal component in monkey *W* (RNm component 1) was strongly correlated with grasp-related muscle component

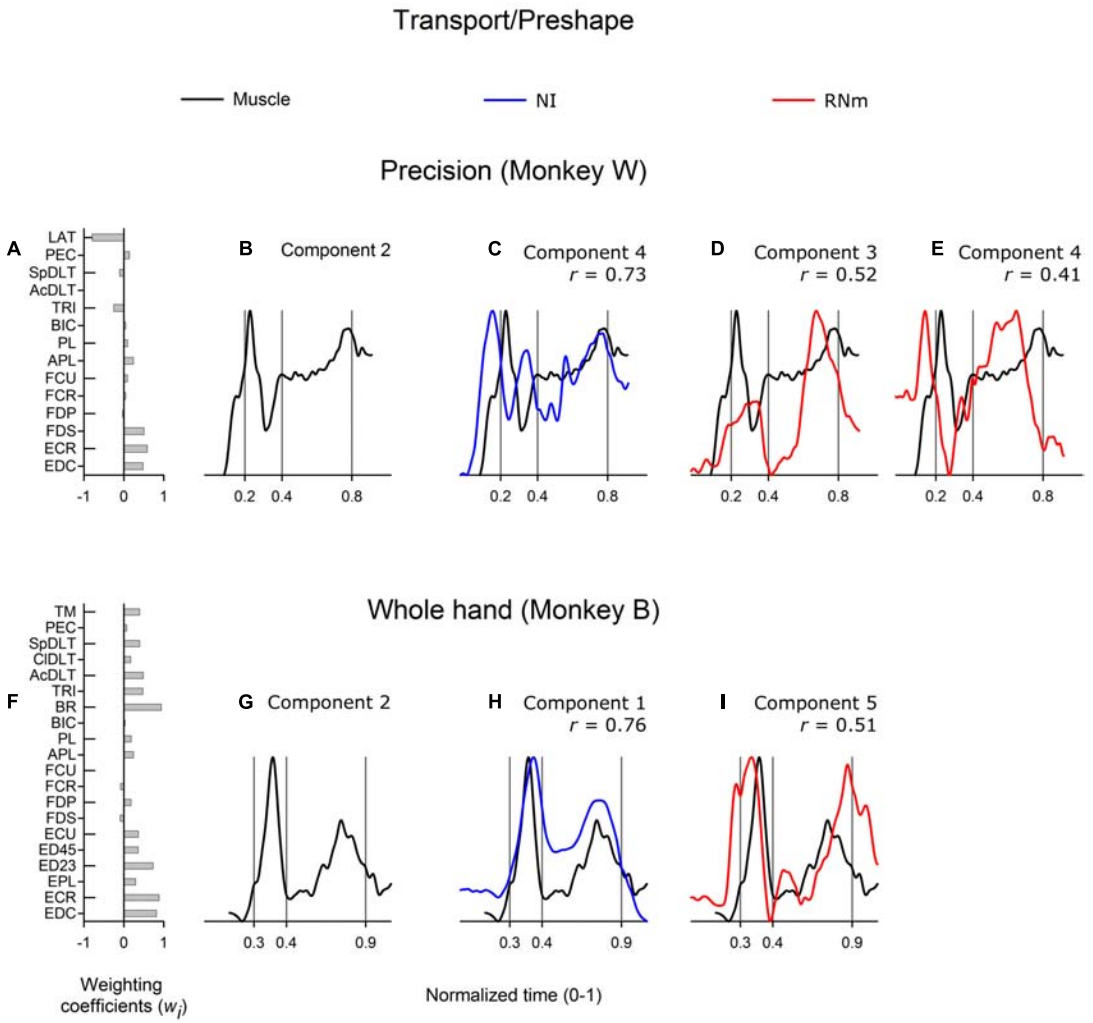


FIGURE 4 | Best-matching NI and RNm neuronal correlates of transport/preshape-related muscle component 2. (A,F) Weighting coefficients of transport/preshape-related muscle component 2 in precision **(A)** and whole-hand **(F)** task in monkey *W* and monkey *B*, respectively. **(B,G)** Temporal scaling coefficients of transport/preshape-related muscle component 2. Temporal scaling coefficients shown in **(B,G)** specify activation of all muscles included in the muscle component according to their corresponding weighting coefficients shown in **(A,F)**, respectively. **(C,H)** Temporal scaling coefficients of the NI components that best matched with transport/preshape-related muscle component 2 shown in **(B,G)**, respectively. **(D,E,I)** Temporal scaling coefficients of the RNm components that best matched with transport/preshape-related muscle component 2 shown in **(B,G)** respectively. Format as in **Figure 3**.

3 (**Figure 5D**, $r = 0.87$), whereas correlations were moderate in monkey *B* (**Figure 5H**, $r = 0.52$). The best matching RNm components accounted for 32.8 and 12.8% of the variance in the ensemble discharges of the 33 and 34 forelimb RNm neurons in monkey *W* and monkey *B*, respectively. Thus, grasp-related components of NI and RNm neuronal populations showed strong to moderate correlations with grasp-related muscle component 3 in both monkeys but explained relatively variable amounts of the variance in the ensemble discharges of RNm versus NI neurons.

Higher-Order Muscle Components

Figure 6 illustrates correlations between best matching neuronal components and higher-order muscle components. Grasp-related muscle component 4 was identified in both precision and whole-hand tasks in monkey W and included wrist and digit flexors (**Figure 6A**). The temporal scaling coefficient (**Figure 6B**) was characterized by a sharp and brief peak in the pre-movement phase when the monkey grasped the device handle prior to reach onset. A second, smaller peak occurred at grasp onset, and a third rapid increase in amplitude occurred during the return phase when the monkey, having grasped the cereal reward, started to move the hand toward the mouth in order to ingest the cereal reward. The best-matching NI component was moderately correlated (**Figure 6C**, $r = 0.46$) and accounted for 2.5% of the variance in ensemble discharges of the 30 forelimb NI neurons in monkey *W*. No best-matching RNm neuronal correlate of grasp-related muscle component 4 was identified.

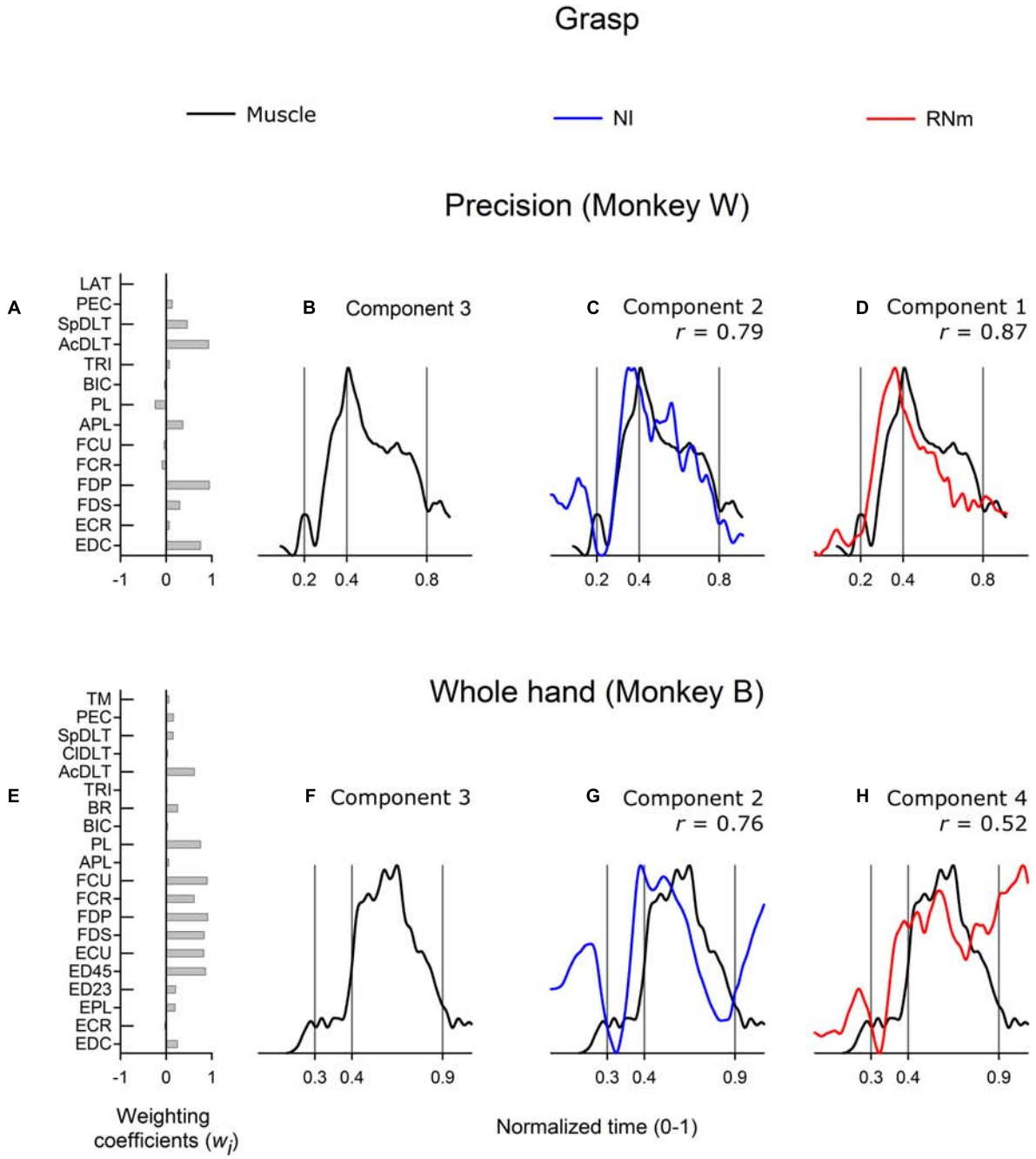


FIGURE 5 | Best-matching NI and RNm neuronal correlates of grasp-related muscle component 3. (A,E) Weighting coefficients of grasp-related muscle component 3 in precision **(A)** and whole-hand **(E)** task in monkey *W* and monkey *B* respectively. **(B,F)** Temporal scaling coefficients of grasp-related muscle component 3. Temporal scaling coefficients shown in **(B,F)** specify activation of all muscles included in the muscle component according to their corresponding weighting coefficients shown in **(A,E)**, respectively. **(C,G)** Temporal scaling coefficient of the NI components that best matched with grasp-related muscle component 3 shown in **(B,F)**, respectively. **(D, H)** Temporal scaling coefficient of the RNm components that best matched with grasp-related muscle component 3 shown in **(B,F)**, respectively. Format as in **Figure 3**.

Muscle components 4 and 5 in monkey *B* were not formally classified as transport/preshape- or grasp-related given our predefined criteria for selection of a factor as a muscle component (eigenvalue > 1, scree-plot criteria; Geed and Van Kan, 2016). Nevertheless, these components were compared with neuronal components extracted from the ensemble discharges of NI or RNm neurons because previous studies have reported that higher-order muscle components carry

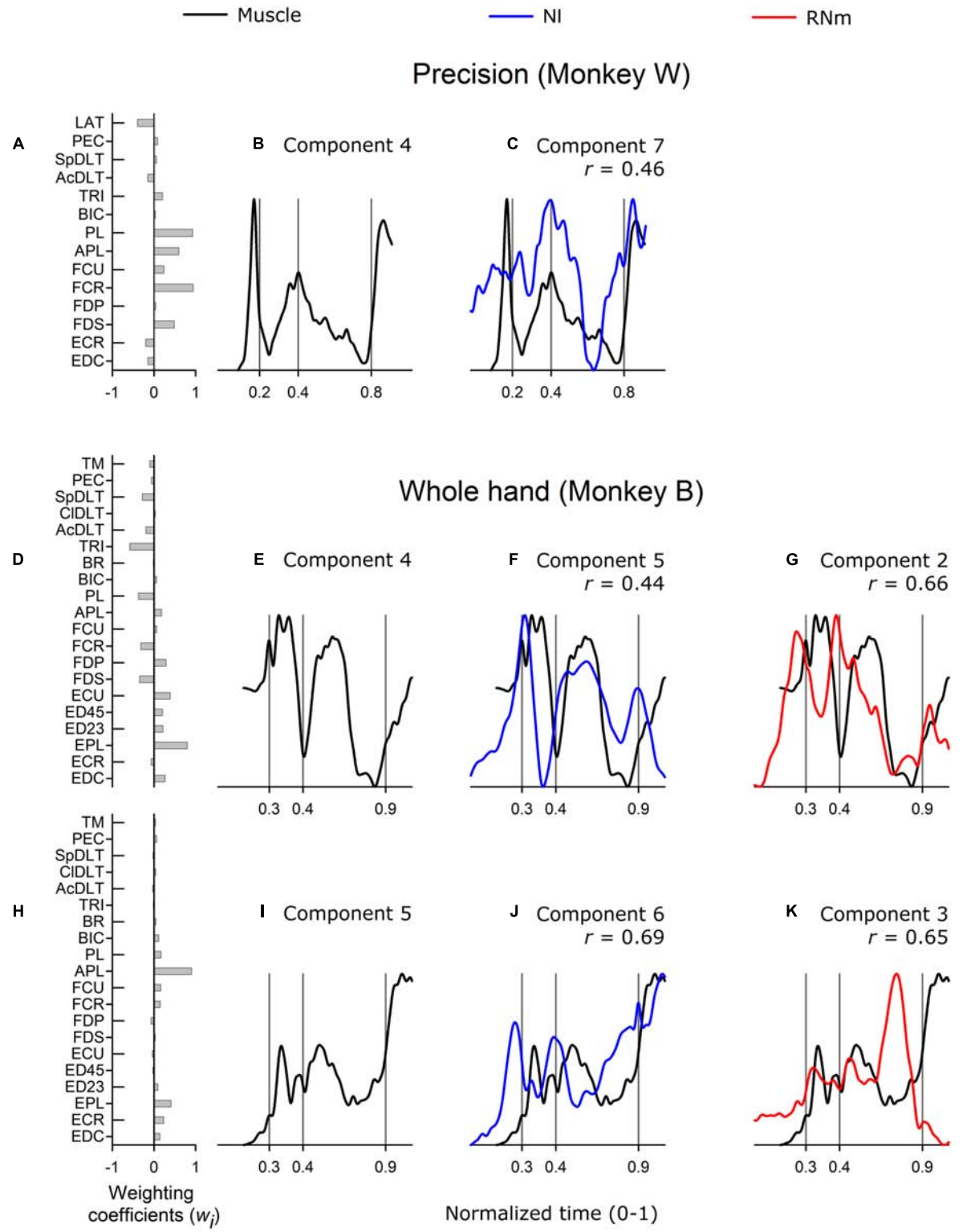


FIGURE 6 | Best-matching NI and RNm neuronal correlates of higher-order muscle components. (A) Weighting coefficients of grasp-related muscle component 4 in precision task in monkey *W.* **(B)** Temporal scaling coefficient of muscle component 4 specifies activation all muscles included in the muscle component according to their corresponding weighting coefficients shown in **(A)**. **(C)** Temporal scaling coefficient of the NI component that best matched with grasp-related muscle component 4 shown in **(A,B)**. **(D,E)** and **(H,I)** Show weighting coefficients and temporal scaling coefficients of muscle components in whole-hand task in monkey *B.* **(F,G)** and **(J,K)** Temporal scaling coefficient of best-matching NI and RNm neuronal components in the whole-hand task in monkey *B*. Format as in **Figure 3**.

meaningful control information (Brochier et al., 2004). Muscle component 4 and 5 were characterized by strong contribution of EPL (**Figure 6D**) or APL (**Figure 6H**) and small contributions from many other forelimb muscles. Muscle components 4 and 5 accounted for relatively small amounts of variance in EMGs (9.6 and 5.8% for components 4 and 5, respectively). The best-matching NI component to muscle component 4 (**Figure 6F**) was moderately correlated ($r = 0.44$) and accounted for 7.8% of the variance in the ensemble discharges of the 48 NI neurons in monkey *B*. The best matching RNm component to muscle component 4 (**Figure 6G**) was strongly correlated ($r = 0.66$) and accounted for 17.4% of the variance in the ensemble discharges of the 34 RNm neurons in monkey *B*. The best matching neuronal correlates to muscle component 5 showed strong correlations (NI, **Figure 6J**, $r = 0.69$; RNm, **Figure 6K**, $r = 0.65$), and accounted for 7.2 and 17.4% of the variance in the ensemble discharges of the 48 NI and 34 RNm neurons in monkey *B*, respectively. Thus, NI and RNm neuronal correlates were identified even for higher-ordered muscle components, which explained relatively small amounts of variance in EMGs.

In summary, a considerable amount of variance in the ensemble discharges within both the NI and RNm populations sampled is directed toward both transport/preshape-related and grasp-related aspects of reach-to-grasp movements in both animals during performance of both tasks. The results of cross-correlating NI and RNm neuronal components and muscle components support the view that the ensemble discharges of populations of NI and RNm neurons are part of the neural substrate underlying coordinated reach-to-grasp behaviors.

Temporal Coupling between Transport/Preshape- and Grasp-Related Neuronal and Muscle Components

Geed and Van Kan (2016) recently demonstrated that transport/preshape- and grasp-related muscle components are spatiotemporally coupled such that peak activation of the transport/preshape-related component is precisely synchronized in time with the peak slope of activation of its corresponding grasp-related component. **Figures 7A,B** (precision task) and **Figures 7G,H** (whole-hand task) illustrate the temporal synchrony between transport/preshape-related muscle component 1 (**Figures 7A,G**, black) and grasp-related muscle component 3 (**Figures 7B,H**) in monkey *B*. Records of the slope of activation amplitudes of grasp-related muscle components as a function of time were calculated (Methods) and are overplotted (**Figures 7A,G**, green) on activation amplitudes of the corresponding transport/preshape-related muscle component (**Figures 7A,G**, black). Analogous to the invariant temporal coupling between transport/preshape- and corresponding grasp-related muscle components, **Figures 7C,D** (precision task) and **Figures 7I,J** (whole-hand task) show similar spatiotemporal coupling between NI neuronal correlates of transport/preshape-related and corresponding grasp-related muscle components. **Figures 7E,F** (precision task) and **Figures 7K,L** (whole-hand task) show similar spatiotemporal coupling between RNm neuronal correlates of transport/preshape-related and corresponding grasp-related muscle components.

Table 3 summarizes the times of peak amplitude of transport/preshape-related components and the times of peak slope of activation of the corresponding grasp-related components in NI, RNm, and muscle domains for precision and whole-hand tasks in both monkeys. Consistent with our hypothesis, the neuronal correlates of transport/preshape- and grasp-related muscle components are temporally coupled such that times of peak activation of transport/preshape-related NI and RNm neuronal correlates are precisely synchronized with times of peak slope of activation of the corresponding grasp-related NI and RNm neural correlates. A paired-samples *t*-test showed no significant difference [$t(11) = -0.64$, $p = 0.54$] between the times of peak activation of the transport/preshape-related components and the times of peak slope of activation of the corresponding grasp-related components in NI, RNm, and muscle domains.

In summary, the results presented in this section provide evidence for invariant spatiotemporal coupling between NI and RNm neuronal correlates of transport/preshape- and grasp-related muscle components that is qualitatively and quantitatively similar to the invariant spatiotemporal coupling observed between corresponding muscle components.

DISCUSSION

Our results demonstrate that neuronal components, extracted from the ensemble of single-unit discharges of populations of NI and RNm neurons recorded while monkeys performed reach-to-grasp tasks, are strongly, consistently, and systematically correlated with transport/preshape- and grasp-related muscle components. Importantly, as was found for transport/preshape- and grasp-related muscle components (Geed and Van Kan, 2016), both NI and RNm neuronal correlates show invariant spatiotemporal coupling, suggesting that during reach-to-grasp movements, ensembles of neurons within NI and RNm distribute their variances along the functional dimensions of transport/preshape or grasp such that the timing of activation of transport/preshape is invariantly coupled with the timing of activation of grasp. These results add mechanistic insight to data from clinical and lesion studies that have reported decoupling between reach and grasp following cerebellar lesions. Overall, the results provide strong support for the hypothesis that interposito-rubrospinal (NI-RNm) circuitry underlies spatiotemporal coordination of complex reach-to-grasp behaviors.

Similar Units of Behavior Are Expressed in Neural and Muscle Signals

Our result of finding similar functional units of behavior at three successive levels (NI, RNm, and EMGs) of information

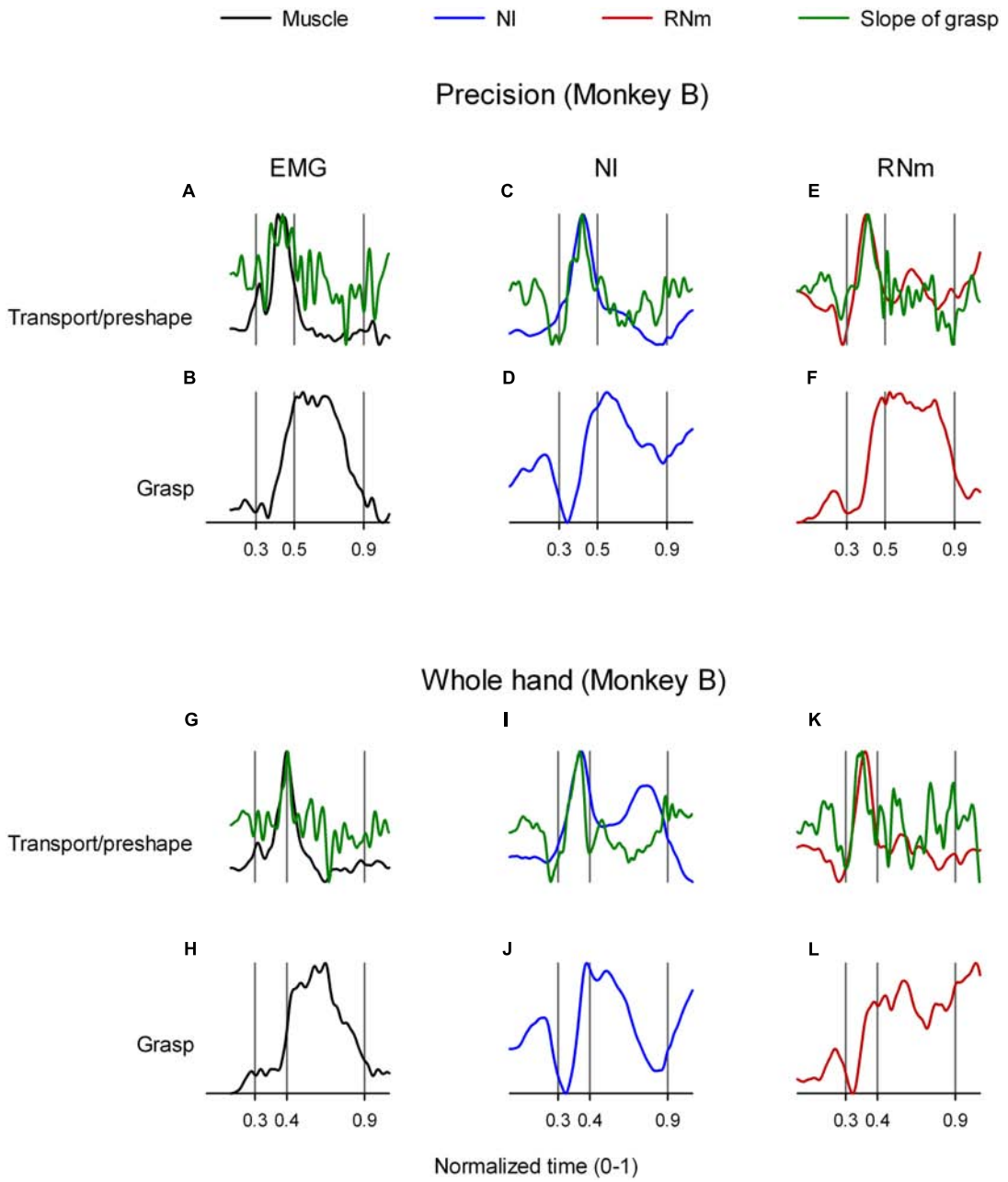


FIGURE 7 | Temporal coupling between transport/preshape- and grasp-related muscle and neuronal components. (A,C,E) and **(G,I,K)** show temporal scaling coefficients of transport/preshape-related muscle (black), NI (blue), and RNm (red) components in monkey *B* during precision **(A,C,E)** and whole-hand **(G,I,K)** tasks. **(B,D,F)** and **(H,J,L)** show temporal scaling coefficients of the grasp-related components that correspond to the transport/preshape-related components shown in **(A,C,E)** and **(G,I K)** respectively. Slope of grasp-related components (green) is overplotted on the temporal scaling coefficient of the corresponding transport/preshape-related components to highlight synchronicity between peak activation of transport/preshape-related components and peak slope of corresponding grasp-related components. For example, **(C,D)** illustrate temporal coupling between transport/preshape- and grasp-related NI neuronal components in monkey *B* during performance of the precision task. Temporal scaling coefficients of the transport/preshape- and the corresponding grasp-related component are plotted (blue) in **(C,D)**, respectively. The slope of the grasp-related component was calculated (see Materials and Methods) and is overplotted (green) on the temporal scaling coefficients of the preshape/transport-related component in *C*.

processing in the NI-RNm circuitry supports the view that intermediate cerebellar output engages synergistic groups of neurons and muscles to coordinate reach-to-grasp movements. The neuronal components we identified provide a weighting of each neuron's contribution to the ensemble average based on the neuron's correlation pattern with all other neurons in the dataset. Each neuron contributes portions of its variance to each of the neuronal components in a neuron-specific, weighted fashion,

TABLE 3 | Temporal coupling between transport/preshape- and grasp-related NI, RNm, and muscle components.

	Whole-hand		Precision	
	$T_{transport}$	T_{grasp}	$T_{transport}$	T_{grasp}
Monkey *W*				
NI	0.29	0.28	0.31	0.32
RNm	0.31	0.32	0.25	0.27
Muscle	0.29	0.28	0.28	0.29
Monkey *B*				
NI	0.39	0.39	0.40	0.40
RNm	0.38	0.35	0.38	0.39
Muscle	0.44	0.44	0.39	0.42

Values represent normalized time (0–1). $T_{transport}$, time of peak activation of transport/preshape-related component. T_{grasp}, time of peak slope of activation of corresponding grasp-related component.

and linear combinations of these neural weights, scaled by the neuronal component's temporal scaling coefficients, account for a large proportion of the variance in the ensemble discharges of the neuronal population. Neuronal components thus distill motor control information distributed across a population of neurons into limited numbers of discrete motor command signals.

The EFA-based neuronal components we identified are comparable with previous reports on information processing in M1 and RNm. For instance, Miller et al. (1993) proposed that groups of mutually correlated RNm neurons may contribute control signals in muscle space that are summed in the spinal cord, in line with the neuronal component framework where linear combinations of a few neuronal components may specify the activation parameters of synergistic groups of muscles. M1 and RNm neurons have been shown to process information in muscle-based "functional linkage vectors (FLVs)" (Miller et al., 1993; Holdefer and Miller, 2002). Krouchev and Drew (2013) demonstrated that a limited number of sparse muscle synergies explained substantial proportions of the variance in cat forelimb EMGs, and they proposed, based on their previously recorded data in cat motor cortex during the same behaviors (Drew, 1993; Drew et al., 1996, 2008), that multiple populations of pyramidal tract neurons (PTNs) may be involved in regulating each of the specific sparse muscle synergies.

Neuronal components, FLVs, and sparse synergies share the conceptual premise that populations of neurons contribute to activity of functionally-related muscle groups; however, the different algorithms underlying cluster and factor analyses result in small differences. FLVs involve correlated activity between individual neurons and groups of muscles, which are then clustered to identify the sub-populations of neurons that share relatively similar correlation patterns with groups of muscles. In contrast, EFA-based neuronal components provide a weighting of each neuron's contribution to the population average according to its pattern of correlation with all other neurons in the sample. Our approach of identifying a neural basis of muscle components thus adopts a relatively direct population-based view of interrelationships within the neuronal ensemble in order to identify how groups of neurons may specify activation parameters to control groups of muscles as synergistic units. Further, clustering of FLVs leads to a model in which each neuron contributes exclusively to a given muscle "synergy" because clustering algorithms group variables (neurons) so that the variance within a cluster is minimized while the variance between clusters is maximized. In our EFA-based approach, each neuron contributes portions of its variance toward each of the components in the model in a weighted fashion. The same set of neurons may thus apportion their variances differently across each of the components to give rise to a flexible and diverse range of motor behaviors. This mechanism is consistent with recent findings from ICMS-evoked cortical "synergies" where each unit (neuron) appeared to also encode synergies other than the "most evoked synergy" (Overduin et al., 2014, 2015).

Our finding of limited numbers of neuronal components underlying the ensemble activity of forelimb NI and RNm neurons is significant because it demonstrates for the first time that NI-RNm circuitry may specify motor commands in the same low-dimensional space as found for muscle components underlying naturally-occurring reach-to-grasp behaviors in monkeys. In particular, finding neuronal correlates of higher-order muscle components (shown in **Figure 6**) indicates that similar functional units of reach-to-grasp behaviors are isolated from ensemble discharges of neurons and EMGs even if the muscle components account for relatively small amounts of variance in the EMGs. Thus, higher-order components of reach-to-grasp muscle activity may transmit meaningful information with respect to behavior, which is consistent with the findings of Brochier et al. (2004) that higher-order muscle components were able to discriminate between grasp types in their reach-to-grasp task. Evidence consistent with our findings has also come from transcranial magnetic stimulation (TMS) (Gentner and Classen, 2006) and intracortical microstimulation (ICMS) (Overduin et al., 2012, 2014, 2015) of various motor cortical sites in human and non-human primates, respectively. TMS- or ICMS-evoked digit movements demonstrate similar muscle synergies as identified during naturally-occurring digit movements, such as grasping either imagined (Gentner and Classen, 2006) or differently shaped objects (Overduin et al., 2012). Whereas the TMS- or ICMS-based studies support the hypothesis of building blocks underlying voluntary motor control in the motor cortex, our framework of neuronal components in NI-RNm circuitry supports and expands previous findings by proposing a mechanism and additional substrates by which neuromotor circuitry may organize functional building blocks of behavior.

Cerebello-Rubrospinal Circuitry and Spatiotemporal Coupling of Reach and Grasp

Transport/preshape- and grasp-related muscle components show invariant temporal coupling with each other such that the time at which the temporal scaling coefficient of a given transport/preshape-related muscle component attains

peak activity during transport coincides exactly with the time of peak slope of activation of the corresponding grasp-related muscle component (Geed and Van Kan, 2016). This relationship was preserved in monkeys preforming reach-to-grasp movements irrespective of the type of grasp or target location in the workspace, indicating that the temporal coupling may reflect a central mechanism to coordinate transport/preshape-related muscle activity with grasp-related muscle activity. The findings in the present study support and extend this hypothesis. NI and RNm neuronal correlates of transport/preshape- and grasp-related muscle components were temporally coupled such that the times of peak activation of transport/preshape-related neuronal correlates coincided with the times of peak slope of activation of corresponding grasp-related neuronal correlates. The invariant spatiotemporal coupling was not a function of the orthogonal relationship between components as a result of the varimax rotation in our factor analysis algorithm because non-orthogonal rotation of extracted factors (promax rotation) yielded similar temporal scaling coefficients and coupling, suggesting that the spatiotemporal coupling did not depend on specific rotation of extracted factors.

Muscle components reflect synchronous activation of functionally-related groups of muscles as synergistic units. Muscles included in a given component are activated in precise ratios with respect to each other as defined by the component weighting coefficients w_i. The temporal scaling coefficients specify the activation amplitude of a muscle component throughout the movement. Thus, a muscle component gives rise to precise spatiotemporal coupling between muscles included in the component. Temporal coupling between muscle components thus enforces a higher-level of structure on how combinations of muscles included in the respective components are activated. Temporal coupling between activation waveform of transport, and slope of activation waveform of grasp, implies that neuromotor circuitry activates transport/preshape-related muscle components in direct relation to corresponding grasp-related muscle components.

Significantly, strong to moderate correlation between neuronal and muscle components suggests that populations of NI and RNm neurons process information about synergistic groups of forelimb muscles. This view is supported by findings that mossy fiber *inputs* to intermediate cerebellum show high joint specificity (Van Kan et al., 1993a,b) whereas even at the hierarchical level of single NI neurons, which represents the sole *output* of intermediate cerebellum, information processing pertains to combinations of multiple forelimb joints (Van Kan et al., 1993b). The transformation of highly joint-specific cerebellar afferent input through mossy fibers into broad whole-limb based neuromotor information in cerebellar output through NI is consistent with our results that the ensemble output from NI reflects control signals for coordinating groups of transport/preshape- and grasp-related muscles synergistically.

Further, NI projects to two extra-cerebellar targets: indirectly, via ventrolateral (VL) thalamus, to primary motor cortex (Rispal-Padel and Latreille, 1974; Jorntell and Ekerot, 1999) and directly to contralateral RNm neurons (Flumerfelt et al., 1973; Asanuma et al., 1983a,b). RNm neurons give rise to descending projections which, via the rubrospinal tract (Shinoda et al., 1977; Shinoda et al., 1982; Holstege et al., 1988; Shinoda et al., 1988; Pong et al., 2002), target interneurons and motoneurons of forelimb muscles (McCurdy et al., 1987; Holstege et al., 1988; Ralston et al., 1988). Converging evidence from behavioral neurophysiology in NI and RNm (Van Kan et al., 1994; Gibson et al., 1996; Van Kan and McCurdy, 2001, 2002a,b), lesion studies in NI (Mason et al., 1998; Cooper et al., 2000; Martin et al., 2000; Johnson et al., 2001), and clinical data from patients with cerebellar lesions (Bastian and Thach, 1995; Bastian, 1997, 2002; Bastian et al., 2000; Zackowski et al., 2002; Morton and Bastian, 2004, 2007) support the view that NI-RNm circuitry plays an important role in the coordination of proximal and distal forelimb muscles during whole-limb multi-joint movements. Thus, physiologically, NI-RNm circuitry is well placed to specify coordination between synergistic groups of proximal and distal forelimb muscles, consistent with the invariant spatiotemporal coupling identified between the functional domains of transport/preshape and grasp.

CONCLUSION

The results provide evidence for the hypothesis that ensemble discharges of forelimb neurons in NI and RNm function as neuronal correlates of synergistic, functionally-related groups of proximal and distal forelimb muscles in monkeys performing natural reach-to-grasp movements. The NI and RNm neuronal correlates of transport/preshape- and grasp-related muscle components show precise and invariant spatiotemporal coupling, which is essential for coordinated activation of forelimb muscles during reach-to-grasp behaviors.

AUTHOR CONTRIBUTIONS

SG, MM, and PvK contributed to design, acquisition, analysis, and interpretation of data for this work. SG wrote the draft for the manuscript and prepared all figures. SG, MM, and PvK revised and edited the manuscript. SG, MM, and PvK approved the final draft of the manuscript, and agree to be accountable for all aspects of the work.

FUNDING

Research reported in this publication was supported by National Institutes of Neurological Disorders and Stroke Grant NS43317 (PI: PvK), by the Graduate School of the University of Wisconsin-Madison (PvK and SG), by National institutes of Neurological Disorders and Stroke Grant 1U10NS086513-01 (NIH StrokeNet awarded to SG; PI: Alexander W. Dromerick, and Amie Hsia, MedStar National Rehabilitation Hospital), by the National Institute on Disability, Independent Living, and Rehabilitation Research (NIDILRR) Advanced Rehabilitation Research Training

(ARRT) Grant H133P100015 (awarded to SG, PI: Barbara S. Bregman, MedStar National Rehabilitation Hospital and Georgetown University), and the National Center For Advancing Translational Sciences of the National Institutes of Health under Award Number TL1TR001431 (NIH-TL1, awarded to SG). The content is solely the responsibility of the authors and does not necessarily represent the official views of the National Institutes of Health.

ACKNOWLEDGMENTS

We thank Robert P. Scobey for design and construction of experimental equipment and Janet L. Ruhland for assistance in data collection. We thank Barbara S. Bregman, Michelle L. Harris-Love, Peter S. Lum, Sahana Kukke, and Susan Ryerson for valuable discussions and feedback on the manuscript. This research was conducted in the Motor Systems Physiology Laboratory at the University of Wisconsin-Madison in partial fulfillment of SG Ph.D. degree.

SUPPLEMENTARY MATERIAL

The Supplementary Material for this article can be found online at: http://journal.frontiersin.org/article/10.3389/fncir.2017.00007/full#supplementary-material

REFERENCES

Asanuma, C., Thach, W. T., and Jones, E. G. (1983a). Brainstem and spinal projections of the deep cerebellar nuclei in the monkey, with observations on the brainstem projections of the dorsal column nuclei. *Brain Res. Rev.* 5, 299–322. doi: 10.1016/0165-0173(83)90017-6

Asanuma, C., Thach, W. T., and Jones, E. G. (1983b). Distribution of cerebellar terminations and their relation to other afferent terminations in the ventral lateral thalamic region of the monkey. *Brain Res.* 286, 237–265. doi: 10.1016/0165-0173(83)90015-2

Baker, S. N. (2011). The primate reticulospinal tract, hand function and functional recovery. *J. Physiol.* 589, 5603–5612. doi: 10.1113/jphysiol.2011.215160

Bastian, A. J. (1997). Mechanisms of ataxia. *Phys. Ther.* 77, 672–675.

Bastian, A. J. (2002). Cerebellar limb ataxia: abnormal control of self-generated and external forces. *Ann. N. Y. Acad. Sci.* 978, 16–27. doi: 10.1111/j.1749-6632.2002.tb07552.x

Bastian, A. J., Martin, T. A., Keating, J. G., and Thach, W. T. (1996). Cerebellar ataxia: abnormal control of interaction torques across multiple joints. *J. Neurophysiol.* 76, 492–509.

Bastian, A. J., and Thach, W. T. (1995). Cerebellar outflow lesions: a comparison of movement deficits resulting from lesions at the levels of the cerebellum and thalamus. *Ann. Neurol.* 38, 881–892. doi: 10.1002/ana.410380608

Bastian, A. J., Zackowski, K. M., and Thach, W. T. (2000). Cerebellar ataxia: torque deficiency or torque mismatch between joints? *J. Neurophysiol.* 83, 3019–3030.

Belhaj-Saif, A., and Cheney, P. D. (2000). Plasticity in the distribution of the red nucleus output to forearm muscles after unilateral lesions of the pyramidal tract. *J. Neurophysiol.* 83, 3147–3153.

Bradnam, L. V., Stinear, C. M., and Byblow, W. D. (2013). Ipsilateral motor pathways after stroke: implications for non-invasive brain stimulation. *Front. Hum. Neurosci.* 7:184. doi: 10.3389/fnhum.2013.00184

Brochier, T., Spinks, R. L., Umilta, M. A., and Lemon, R. N. (2004). Patterns of muscle activity underlying object-specific grasp by the macaque monkey. *J. Neurophysiol.* 92, 1770–1782. doi: 10.1152/jn.00976.2003

Carmel, J. B., Kimura, H., Berrol, L. J., and Martin, J. H. (2013). Motor cortex electrical stimulation promotes axon outgrowth to brain stem and spinal targets that control the forelimb impaired by unilateral corticospinal injury. *Eur. J. Neurosci.* 37, 1090–1102. doi: 10.1111/ejn.12119

Cattell, R. B. (1966). The scree test for the number of factors. *Multivariate Behav. Res.* 1, 245–276. doi: 10.1207/s15327906mbr0102_10

Cooper, S. E., Martin, J. H., and Ghez, C. (2000). Effects of inactivation of the anterior interpositus nucleus on the kinematic and dynamic control of multijoint movement. *J. Neurophysiol.* 84, 1988–2000.

Cunningham, D. A., Potter-Baker, K. A., Knutson, J. S., Sankarasubramanian, V., Machado, A. G., and Plow, E. B. (2015). Tailoring brain stimulation to the nature of rehabilitative therapies in stroke: a conceptual framework based on their unique mechanisms of recovery. *Phys. Med. Rehabil. Clin. N. Am.* 26, 759–774. doi: 10.1016/j.pmr.2015.07.001

Drew, T. (1993). Motor cortical activity during voluntary gait modifications in the cat. I. Cells related to the forelimbs. *J. Neurophysiol.* 70, 179–199.

Drew, T., Jiang, W., Kably, B., and Lavoie, S. (1996). Role of the motor cortex in the control of visually triggered gait modifications. *Can. J. Physiol. Pharmacol.* 74, 426–442. doi: 10.1139/cjpp-74-4-426

Drew, T., Kalaska, J., and Krouchev, N. (2008). Muscle synergies during locomotion in the cat: a model for motor cortex control. *J. Physiol.* 586, 1239–1245. doi: 10.1113/jphysiol.2007.146605

Flumerfelt, B. A., Otabe, S., and Courville, J. (1973). Distinct projections to the red nucleus from the dentate and interposed nuclei in the monkey. *Brain Res.* 50, 408–414. doi: 10.1016/0006-8993(73)90742-7

Geed, S., Mccurdy, M. L., and Van Kan, P. L. E. (2011). Primate magnocellular red nucleus (RNm) encodes muscle synergies during reaching to grasp. *Soc. Neurosci. Abstr.* 37.

Geed, S., Mccurdy, M. L., and Van Kan, P. L. E. (2013). Contribution of interposito-rubrospinal pathway to muscle synergies underlying reaching to grasp. *Soc. Neurosci. Abstr.* 39.

Geed, S., and Van Kan, P. L. E. (2016). Grasp-Based Functional Coupling Between Reach- and Grasp-Related Components of Forelimb Muscle Activity. *J. Mot. Behav.* 48, 1–17. doi: 10.1080/00222895.2016.1204265

Gentner, R., and Classen, J. (2006). Modular organization of finger movements by the human central nervous system. *Neuron* 52, 731–742. doi: 10.1016/j.neuron.2006.09.038

Gibson, A. R., Horn, K. M., Stein, J. F., and Van Kan, P. L. E. (1996). Activity of interpositus neurons during a visually guided reach. *Can. J. Physiol. Pharmacol.* 74, 499–512. doi: 10.1139/y96-039

Gibson, A. R., Horn, K. M., and Van Kan, P. L. E. (1994). "Chapter 5 Grasping Cerebellar Function," in *Advances in Psychology*, eds M. B. B. Keree and C. Umberto (Cambridge, MA: Academic Press), 85–108.

Holdefer, R. N., and Miller, L. E. (2002). Primary motor cortical neurons encode functional muscle synergies. *Exp. Brain Res.* 146, 233–243. doi: 10.1007/s00221-002-1166-x

Holstege, G., Blok, B. F., and Ralston, D. D. (1988). Anatomical evidence for red nucleus projections to motoneuronal cell groups in the spinal cord of the monkey. *Neurosci. Lett.* 95, 97–101. doi: 10.1016/0304-3940(88)90639-8

Houk, J. C., Gibson, A. R., Harvey, C. F., Kennedy, P. R., and Van Kan, P. L. E. (1988). Activity of primate magnocellular red nucleus related to hand and finger movements. *Behav. Brain Res.* 28, 201–206. doi: 10.1016/0166-4328(88)90097-6

Humphrey, D. R., and Rietz, R. R. (1976). Cells of origin of corticorubral projections from the arm area of primate motor cortex and their synaptic actions in the red nucleus. *Brain Res.* 110, 162–169. doi: 10.1016/0006-8993(76)90217-1

Jeannerod, M. (1981). "Intersegmental coordination during reaching at natural visual objects," in *Attention and Performance IX*, eds J. Long and A. Baddeley (Hillsdale, NJ: Erlbaum), 153–169.

Jeannerod, M. (1984). The timing of natural prehension movements. *J. Mot. Behav.* 16, 235–254. doi: 10.1080/00222895.1984.10735319

Johnson, M. T. V., Mason, C. R., and Ebner, T. J. (2001). Central processes for the multiparametric control of arm movements in primates. *Curr. Opin. Neurobiol.* 11, 684–688. doi: 10.1016/S0959-4388(01)00269-0

Jorntell, H., and Ekerot, C. F. (1999). Topographical organization of projections to cat motor cortex from nucleus interpositus anterior and forelimb skin. *J. Physiol.* 514(Pt 2), 551–566. doi: 10.1111/j.1469-7793.1999.551ae.x

Kaiser, H. (1974). An index of factorial simplicity. *Psychometrika* 39, 31–36. doi: 10.1007/BF02291575

Kennedy, P. R., Gibson, A. R., and Houk, J. C. (1986). Functional and anatomic differentiation between parvicellular and magnocellular regions of red nucleus in the monkey. *Brain Res.* 364, 124–136. doi: 10.1016/0006-8993(86)90993-5

Krouchev, N., and Drew, T. (2013). Motor cortical regulation of sparse synergies provides a framework for the flexible control of precision walking. *Front. Comput. Neurosci.* 7:83. doi: 10.3389/fncom.2013.00083

Kuypers, H. G., Fleming, W. R., and Farinholt, J. W. (1962). Subcorticospinal projections in the rhesus monkey. *J. Comp. Neurol.* 118, 107–137. doi: 10.1002/cne.901180109

Kuypers, H. G. J. M. (1982). "A new look at the organization of the motor system," in *Progress in Brain Research*, eds H. G. J. M. Kuypers and G. F. Martin (Amsterdam: Elsevier), 381–403.

Lang, C. E., and Bastian, A. J. (1999). Cerebellar subjects show impaired adaptation of anticipatory EMG during catching. *J. Neurophysiol.* 82, 2108–2119.

Lawrence, D. G., and Kuypers, H. G. (1968a). The functional organization of the motor system in the monkey. I. The effects of bilateral pyramidal lesions. *Brain* 91, 1–14.

Lawrence, D. G., and Kuypers, H. G. (1968b). The functional organization of the motor system in the monkey. II. The effects of lesions of the descending brain-stem pathways. *Brain* 91, 15–36.

Martin, J. H., Cooper, S. E., Hacking, A., and Ghez, C. (2000). Differential effects of deep cerebellar nuclei inactivation on reaching and adaptive control. *J. Neurophysiol.* 83, 1886–1899.

Mason, C. R., Miller, L. E., Baker, J. F., and Houk, J. C. (1998). Organization of reaching and grasping movements in the primate cerebellar nuclei as revealed by focal muscimol inactivations. *J. Neurophysiol.* 79, 537–554.

McCurdy, M. L., Gibson, A. R., and Houk, J. C. (1992). Spatial overlap of rubrospinal and corticospinal terminals with input to the inferior olive. *Neuroimage* 1, 23–41. doi: 10.1016/1053-8119(92)90005-8

McCurdy, M. L., Hansma, D. I., Houk, J. C., and Gibson, A. R. (1987). Selective projections from the cat red nucleus to digit motor neurons. *J. Comp. Neurol.* 265, 367–379. doi: 10.1002/cne.902650306

Miller, L. E., Van Kan, P. L. E., Sinkjaer, T., Andersen, T., Harris, G. D., and Houk, J. C. (1993). Correlation of primate red nucleus discharge with muscle activity during free-form arm movements. *J. Physiol.* 469, 213–243. doi: 10.1113/jphysiol.1993.sp019812

Morton, S. M., and Bastian, A. J. (2004). Cerebellar control of balance and locomotion. *Neuroscientist* 10, 247–259. doi: 10.1177/1073858404263517

Morton, S. M., and Bastian, A. J. (2007). Mechanisms of cerebellar gait ataxia. *Cerebellum* 6, 79–86. doi: 10.1080/14734220601187741

Overduin, S. A., D'avella, A., Carmena, J. M., and Bizzi, E. (2012). Microstimulation activates a handful of muscle synergies. *Neuron* 76, 1071–1077. doi: 10.1016/j.neuron.2012.10.018

Overduin, S. A., D'avella, A., Carmena, J. M., and Bizzi, E. (2014). Muscle synergies evoked by microstimulation are preferentially encoded during behavior. *Front. Comput. Neurosci.* 8:20. doi: 10.3389/fncom.2014.00020

Overduin, S. A., D'avella, A., Roh, J., Carmena, J. M., and Bizzi, E. (2015). Representation of muscle synergies in the primate brain. *J. Neurosci.* 35, 12615–12624. doi: 10.1523/JNEUROSCI.4302-14.2015

Paulignan, Y., Frak, V. G., Toni, I., and Jeannerod, M. (1997). Influence of object position and size on human prehension movements. *Exp. Brain Res.* 114, 226–234. doi: 10.1007/PL00005631

Paulignan, Y., Jeannerod, M., Mackenzie, C., and Marteniuk, R. (1991a). Selective perturbation of visual input during prehension movements. 2. The effects of changing object size. *Exp. Brain Res.* 87, 407–420.

Paulignan, Y., Mackenzie, C., Marteniuk, R., and Jeannerod, M. (1991b). Selective perturbation of visual input during prehension movements. 1. The effects of changing object position. *Exp. Brain Res.* 83, 502–512.

Pong, M., Horn, K. M., and Gibson, A. R. (2002). Spinal projections of the cat parvicellular red nucleus. *J. Neurophysiol.* 87, 453–468.

Ralston, D. D., Milroy, A. M., and Holstege, G. (1988). Ultrastructural evidence for direct monosynaptic rubrospinal connections to motoneurons in *Macaca mulatta*. *Neurosci. Lett.* 95, 102–106. doi: 10.1016/0304-3940(88)90640-4

Rand, M. K., Shimansky, Y., Stelmach, G. E., Bracha, V., and Bloedel, J. R. (2000). Effects of accuracy constraints on reach-to-grasp movements in cerebellar patients. *Exp. Brain Res.* 135, 179–188. doi: 10.1007/s002210000528

Rispal-Padel, L., and Latreille, J. (1974). The organization of projections from the cerebellar nuclei to the contralateral motor cortex in the cat. *Exp. Brain Res.* 19, 36–60. doi: 10.1007/BF00233394

Rosner, B. (1983). Percentage points for a generalized ESD many-outlier procedure. *Technometrics* 25, 165–172. doi: 10.1080/00401706.1983.10487848

Roy, A. C., Paulignan, Y., Meunier, M., and Boussaoud, D. (2006). Prehension movements in the macaque monkey: effects of perturbation of object size and location. *Exp. Brain Res.* 169, 182–193. doi: 10.1007/s00221-005-0133-8

Shinoda, Y., Futami, T., Mitoma, H., and Yokota, J. (1988). Morphology of single neurones in the cerebello-rubrospinal system. *Behav. Brain Res.* 28, 59–64. doi: 10.1016/0166-4328(88)90076-9

Shinoda, Y., Ghez, C., and Arnold, A. (1977). Spinal branching of rubrospinal axons in the cat. *Exp. Brain Res.* 30, 203–218.

Shinoda, Y., Yokota, J.-I., and Futami, T. (1982). Morphology of physiologically identified rubrospinal axons in the spinal cord of the cat. *Brain Res.* 242, 321–325. doi: 10.1016/0006-8993(82)90316-X

Sybirska, E., and Gorska, T. (1980). Effects of red nucleus lesions on forelimb movements in the cat. *Acta Neurobiol. Exp. (Wars)* 40, 821–841.

Takenobu, Y., Hayashi, T., Moriwaki, H., Nagatsuka, K., Naritomi, H., and Fukuyama, H. (2014). Motor recovery and microstructural change in rubrospinal tract in subcortical stroke. *Neuroimage* 4, 201–208. doi: 10.1016/j.nicl.2013.12.003

Van Kan, P. L. E., Gibson, A. R., and Houk, J. C. (1993a). Movement-related inputs to intermediate cerebellum of the monkey. *J. Neurophysiol.* 69, 74–94.

Van Kan, P. L. E., Houk, J. C., and Gibson, A. R. (1993b). Output organization of intermediate cerebellum of the monkey. *J. Neurophysiol.* 69, 57–73.

Van Kan, P. L. E., Horn, K. M., and Gibson, A. R. (1994). The importance of hand use to discharge of interpositus neurones of the monkey. *J. Physiol.* 480(Pt 1), 171–190. doi: 10.1113/jphysiol.1994.sp020351

Van Kan, P. L. E., and McCurdy, M. L. (2001). Role of primate magnocellular red nucleus neurons in controlling hand preshaping during reaching to grasp. *J. Neurophysiol.* 85, 1461–1478.

Van Kan, P. L. E., and McCurdy, M. L. (2002a). Contribution of primate magnocellular red nucleus to timing of hand preshaping during reaching to grasp. *J. Neurophysiol.* 87, 1473–1487.

Van Kan, P. L. E., and McCurdy, M. L. (2002b). Discharge of primate magnocellular red nucleus neurons during reaching to grasp in different spatial locations. *Exp. Brain Res.* 142, 151–157. doi: 10.1007/s00221-001-0924-5

Zackowski, K. M., Thach, W. T. Jr., and Bastian, A. J. (2002). Cerebellar subjects show impaired coupling of reach and grasp movements. *Exp. Brain Res.* 146, 511–522. doi: 10.1007/s00221-002-1191-9

Conflict of Interest Statement: The authors declare that the research was conducted in the absence of any commercial or financial relationships that could be construed as a potential conflict of interest.

Copyright © 2017 Geed, McCurdy and Van Kan. This is an open-access article distributed under the terms of the Creative Commons Attribution License (CC BY). The use, distribution or reproduction in other forums is permitted, provided the original author(s) or licensor are credited and that the original publication in this journal is cited, in accordance with accepted academic practice. No use, distribution or reproduction is permitted which does not comply with these terms.

frontiers in Neural Circuits

ORIGINAL RESEARCH
published: 01 March 2017
doi: 10.3389/fncir.2017.00009

Mapping and Analysis of the Connectome of Sympathetic Premotor Neurons in the Rostral Ventrolateral Medulla of the Rat Using a Volumetric Brain Atlas

*Bowen Dempsey[1], Sheng Le[1], Anita Turner[1], Phil Bokiniec[1], Radhika Ramadas[1], Jan G. Bjaalie[2], Clement Menuet[3], Rachael Neve[4], Andrew M. Allen[3], Ann K. Goodchild[1] and Simon McMullan[1]**

[1] Faculty of Medicine and Health Sciences, Neurobiology of Vital Systems, Macquarie University, Sydney, NSW, Australia, [2] Department of Anatomy, Institute of Basic Medical Sciences, University of Oslo, Oslo, Norway, [3] Department of Physiology, University of Melbourne, Melbourne, VIC, Australia, [4] Viral Core Facility, McGovern Institute for Brain Research, Massachusetts Institute of Technology, Cambridge, MA, USA

Spinally projecting neurons in the rostral ventrolateral medulla (RVLM) play a critical role in the generation of vasomotor sympathetic tone and are thought to receive convergent input from neurons at every level of the neuraxis; the factors that determine their ongoing activity remain unresolved. In this study we use a genetically restricted viral tracing strategy to definitively map their spatially diffuse connectome. We infected bulbospinal RVLM neurons with a recombinant rabies variant that drives reporter expression in monosynaptically connected input neurons and mapped their distribution using an MRI-based volumetric atlas and a novel image alignment and visualization tool that efficiently translates the positions of neurons captured in conventional photomicrographs to Cartesian coordinates. We identified prominent inputs from well-established neurohumoral and viscero-sympathetic sensory actuators, medullary autonomic and respiratory subnuclei, and supramedullary autonomic nuclei. The majority of inputs lay within the brainstem (88–94%), and included putative respiratory neurons in the pre-Bötzinger Complex and post-inspiratory complex that are therefore likely to underlie respiratory-sympathetic coupling. We also discovered a substantial and previously unrecognized input from the region immediately ventral to nucleus prepositus hypoglossi. In contrast, RVLM sympathetic premotor neurons were only sparsely innervated by suprapontine structures including the paraventricular nucleus, lateral hypothalamus, periaqueductal gray, and superior colliculus, and we found almost no evidence of direct inputs from the cortex or amygdala. Our approach can be used to quantify, standardize and share complete neuroanatomical datasets, and therefore provides researchers with a platform for presentation, analysis and independent reanalysis of connectomic data.

Keywords: connectome, RVLM, sympathetic, rabies, volumetric, segmentation, respiratory-sympathetic, mesoscale

OPEN ACCESS

Edited by:
Gordon S. Mitchell, University of Florida, USA

Reviewed by:
Larry M. Jordan, University of Manitoba, Canada
Erik Svensson, Uppsala University, Sweden

****Correspondence:***
Simon McMullan
simon.mcmullan@mq.edu.au

Received: *25 October 2016*
Accepted: *06 February 2017*
Published: *01 March 2017*

Citation:
Dempsey B, Le S, Turner A, Bokiniec P, Ramadas R, Bjaalie JG, Menuet C, Neve R, Allen AM, Goodchild AK and McMullan S (2017) Mapping and Analysis of the Connectome of Sympathetic Premotor Neurons in the Rostral Ventrolateral Medulla of the Rat Using a Volumetric Brain Atlas. Front. Neural Circuits 11:9. doi: 10.3389/fncir.2017.00009

INTRODUCTION

The nascent field of *connectomics* applies rapidly developing ultrastructural, trans-synaptic tracing, and whole brain imaging technologies to identify neural circuits at micro-, meso-, and macroscopic resolutions. The central tenet of the connectomic approach is that insights regarding both the functional properties of specific neural circuits and general brain organizational principles may be gained by definitively resolving network architecture (Carandini, 2012; Denk et al., 2012; Mitra, 2014).

Ultrastructural approaches such as serial block-face electron microscopy can comprehensively identify local synaptic connectivity, but are limited by the enormous time and costs associated with data acquisition and analysis, and are therefore best suited to the examination of small regions of brain in high detail (discussed by Lichtman and Denk, 2011; Wanner et al., 2015). Investigators interested in mapping more diffuse circuits have instead monitored the trans-synaptic spread of replication-competent neurotropic viruses such as rabies (Ugolini, 1995; Kelly and Strick, 2000; Dum et al., 2016) and alpha herpes variants (Strack et al., 1989; Rinaman and Schwartz, 2004; McGovern et al., 2012; reviewed by Nassi et al., 2015; Wojaczynski et al., 2015).

In recent years glycoprotein-deleted EnvA-pseudotyped rabies [SADΔG(EnvA)] has emerged as a flagship tool for tracing connectomes in experimental animals (Wickersham et al., 2007b; Callaway and Luo, 2015). The key insights made by Callaway and colleagues in developing this system are that the ability of SADΔG(EnvA) to enter populations of target neurons and retrogradely spread to monosynaptically connected partners can be controlled by selective expression of the EnvA receptor, TVA, and the rabies glycoprotein respectively. Here we apply this approach to resolve the afferent connectome of putative sympathetic premotor neurons in the rostral ventrolateral medulla (RVLM) of the Sprague Dawley rat.

This population, approximately half of which are adrenergic C1 neurons (Stornetta, 2009), is a major source of the glutamatergic drive that maintains sympathetic vasomotor tone and therefore determines arterial blood pressure (Guyenet, 2006). The factors that determine the ongoing activity of these neurons have for several decades remained an unresolved core issue in the field of autonomic neuroscience (Coote, 2007; Guyenet et al., 2013): electrophysiological recordings from anesthetized animals suggest that RVLM sympathetic premotor neurons are a point of convergence for inputs from visceral and somatic reflex pathways (Brown and Guyenet, 1984; McMullan et al., 2008), from the central respiratory pattern generator (McAllen, 1987; Miyawaki et al., 1995; Verberne et al., 1999; Moraes et al., 2013), hypothalamus (Yang and Coote, 1998; Allen, 2002; Horiuchi et al., 2004; Korim et al., 2014), and higher centers including the prefrontal cortex and amygdala (Gelsema et al., 1989; Verberne, 1996), and that ongoing synaptic drive supports their activity (Lipski et al., 1996). However, the relative contributions of inputs from these regions, and in particular the level of input derived from local medullary neurons, has remained elusive.

Our strategy was first to use a recombinant herpes vector with a retrograde transduction profile, HSV-hCMV-YTB, to drive the expression of TVA, rabies glycoprotein, and a fluorescent reporter (YFP) in neurons that project to the interomediolateral cell column of the spinal cord (IML), a major site of termination of sympathetic premotor neurons. We then focally microinjected SADΔG(EnvA)-mCherry into the RVLM, selectively restricting its access to TVA-expressing bulbospinal neurons. This enabled us to map brain-wide sources of synaptic input to bulbospinal RVLM neurons using an image alignment tool based on the Waxholm volumetric atlas of the rat brain (Papp et al., 2014; Kjonigsen et al., 2015).

MATERIALS AND METHODS

Experiments were approved by Macquarie University Animal Ethics Committee and conformed to the Australian Code of Practice for the Care and Use of Animals for Scientific Purposes.

Vector Preparation

SADΔG Production

Rabies glycoprotein-transcomplemented SADΔG-mCherry (Wickersham et al., 2007a) and SADΔG(EnvA)-mCherry was produced and titrated as described by Osakada and Callaway (2013); the titers used for injections were 2×10^9 and 6.8×10^7 IU/ml respectively. SADΔG(EnvA)-mCherry purity was determined by infection of naïve HEK cells and determined to contain approximately 5.3×10^3 unpseudotyped virions per ml. Injection of SADΔG(EnvA)-mCherry in the absence of YTB expression resulted in no labeling in two control experiments.

Retrograde HSV Vectors

A recombinant herpes simplex type1 (HSV) vector with a retrograde tropism was used to drive expression of rabies glycoprotein, TVA, and YFP (HSV-hCMV-YTB). The gene cassette was derived from the pCAG-YTB plasmid (Addgene 26721) and cloned into recombinant HSV amplicons under the control of the human cytomegalovirus promoter. HSV-hCMV-YTB was supplied at 3×10^8 IU/ml and diluted 1:4 with 0.9% saline containing blue fluorescent polystyrene spheres immediately prior to injection to mark the injection site (1:10,000, Thermo Scientific, Australia, 09980508). Control vectors that drive the expression of reporter proteins (HSV-hCMV-GFP, HSV-hCMV-mCherry) were used in initial experiments to determine the time course of protein translation and segment the anatomical boundary of the RVLM. Control vectors were used undiluted and animals sacrificed after 4–5 days.

Vector Injections

Spinal Cord Injections of Retrograde Herpes Vectors

Adult male Sprague Dawley rats (165–500 g) were anesthetized with intraperitoneal ketamine (75 mg/kg; Parnell Laboratories, Australia) mixed with medetomidine (0.75 mg/kg; Pfizer Animal Health, Australia) and treated with prophylactic antibiotics (100 mg/kg Cephazolin sodium, i.m.; Mayne Pharma, Australia) and analgesia (2.5–10 mg/kg Carprofen, s.c.; Norbrook Pharmaceuticals, Australia). Two 500 nl injections of HSV-hCMV-YTB were made over 5–10 min at coordinates

corresponding to the left T2 IML as previously described (Turner et al., 2013). Injections were separated by 1 mm rostrocaudally and the pipette was left in position after injections for approximately 5 min before its slow retraction. At the end of surgery anesthesia was reversed with atipamazole (1 mg/kg s.c., Pfizer Animal Health, Australia) and rats were observed until ambulatory and then returned to their home cages. Rats were monitored closely for the remainder of the experiment with additional analgesia as required. For experiments in which HSV-hCMV-GFP/mCherry control vectors were used the same general surgical approach was employed, but vector injections were made bilaterally at the T2 and/or T10 spinal cord.

Brainstem Microinjections

One to five days after injection of HSV-hCMV-YTB rats were prepared for surgery as described above and positioned in a stereotaxic frame in the skull flat position. The left facial nucleus, an anatomical landmark directly rostral to the RVLM, was mapped using a micropipette containing SADΔG(EnvA)-mCherry by recording antidromic field potentials evoked by stimulation of the facial nerve (Turner et al., 2013). Fifty to seventy five nl of SADΔG(EnvA)-mCherry was microinjected 100–300 μm caudal to the facial nucleus at a depth equivalent to the ventral surface of the facial nucleus. The pipette was left in position for ∼5 min prior to its withdrawal. Rats were treated as described above and allowed to recover for up to 7 days.

In initial experiments we observed histological signs of injury in HSV-hCMV-YTB-transduced neurons that were independent of rabies infection. Neurons developed a blebby appearance with retracted dendrites and spheroidal somata about 7 days after spinal injections, suggesting latent toxicity of the HSV vector. This effect was largely mitigated by dilution of HSV-hCMV-YTB.

We also found that longer intervals between HSV and rabies injections were associated with more off-target infection of bulbospinal (TVA-expressing) neurons outside of the RVLM (especially the paraventricular nucleus, midline raphe, rostral ventromedial medulla and C3 regions). Such neurons were easily identified by their dual expression of mCherry and YFP: contaminated experiments were excluded from analysis. Optimal results were obtained when SADΔG(EnvA)-mCherry was injected 24 h after HSV-hCMV-YTB and animals kept for a further 6 days.

Histology

Animals were euthanized with sodium pentobarbital (>150 mg/kg, Lethabarb, Virbac, Australia) and immediately transcardially perfused with 300 ml ice cold heparinized saline followed by 300 ml 4% paraformaldehyde. The brain and thoracic spinal cord were then removed and post-fixed overnight. With the assistance of a brain matrix, brains were cut coronally 2 mm caudal to the olfactory bulb and mounted frontal pole down on a vibratome plate so that the ventral surface of the brain was approximately perpendicular to the plate. The entire brain was sectioned at 50 μm in the coronal plane using a Leica VT1200S vibrating microtome and collected in 4 bins in 0.01 M Tris-phosphate buffered saline (TPBS). Pot 1 was mounted directly onto glass slides to maintain section order. Brainstem sections from a second pot were processed for YFP and TH immunoreactivity so that starter neurons could be identified. The other pots were transferred to cryoprotectant solution (500 μM polyvinylpyrrolidone, 76.7 mM Na_2HPO_4, 26.6 mM NaH_2PO_4, 876 mM sucrose, 5 mM ethylene glycol) for storage at − 20°C.

Immunohistochemistry and *In situ* Hybridization

Sections were permeabilized in TPBS containing 0.2% Triton-100 for 3 × 15 min and blocked for nonspecific binding in TPBS containing 2% bovine serum albumin and 0.2% Triton-100 for 1 h at room temperature. Primary antibodies (see **Table 1**) were added to the blocking buffer and sections were incubated for 48 h at 4°C. Sections were washed in TPBS 3 × 30 min and incubated in secondary antibodies for 12 h at 4°C. Processed sections were washed again in TPBS 3 × 30 min before being mounted on glass slides with Dako fluorescence mounting medium and cover slipped. ISH was conducted to examine double labeling of rabies-infected input neurons with GAD67 mRNA, a marker of GABAergic neurons, and GLYT2 mRNA, a marker of glycinergic neurons. ISH probes and processing were identical to those described by Bowman et al. (2013) and Le et al. (2016) respectively.

Imaging

For whole-brain mapping of rabies-infected neurons every 4th histological section lying between the cervical spinal cord and the most rostral section containing labeled neurons was imaged under epifluorescence (Zeiss AxioImager Z2 microscope, 10x/0.30 NA M27 objective lens running ZEN 2011). Images were obtained from sections that were immediately mounted during cutting, preserving order, except for sections from the RVLM region; these data were obtained from alternative sections that were processed for YFP and TH immunoreactivity. Neurons that contained both YFP and mCherry were classified as starter neurons and were further sub-classified as TH-immunoreactive (C1) or TH-negative (non-C1). Input neurons and C1/non-C1 starter neurons were manually annotated on each image using Zen software; the pixel coordinates of annotated neurons were then extracted from file metadata using the ImageJ/FIJI package (NIH, Bethesda, Maryland, USA) and tabulated.

Epifluorescence imaging at 10x permitted efficient imaging of whole-brain datasets at the expense of sensitivity, biasing against lightly labeled or small neurons. This was particularly problematic for detection of lightly-labeled TH-immunoreactive starter neurons; confocal reimaging (20x objective, Leica TCS SP5X) of three sections containing starter neurons previously imaged and analyzed as described above indicated that approximately a third of the C1 starter neurons detected under confocal had been identified as non-C1 under epifluorescence (19/27 vs. 13/27). This problem did not apply to detection of rabies-infected neurons, which were unambiguously labeled.

Image Alignment and Anchoring

Image alignment and anchoring was achieved using a beta version of the AligNII tool embedded in Navigator-3 (N3), a web-based data management system currently under development of the University of Oslo Neuroinformatics group (see Figure 5

TABLE 1 | Antibody Table.

Type	Antigen	Species	Tag	Conc.	Clonality	Manufacturer	Cat No./RRID
1°	TH	Mouse	N/A	1:1000	Mono	Sigma	T1299/AB_477560
1°	NK1R	Rabbit	N/A	1:1000	Poly	Sigma	S8305/AB_261562
1°	Vasopressin	Rabbit	N/A	1:1000	Poly	Millipore	AB1565/AB_11212336
1°	Choline Acetyltransferase (ChAT)	Goat	n/a	1:800	Poly	Chemicon, Millipore	AB144P/AB_2079751
1°	GFP	Rabbit	N/A	1:500	Poly	Life Technologies	A6455/AB_2313717
2°	Rabbit IgG (H+L chain)	Donkey	Alexa Fluor® 488	1:500	Poly	Life Technologies	A21206/AB_141708
2°	Rabbit IgG (H+L chain)	Donkey	Alexa Fluor® 647	1:500	Poly	Life Technologies	A31573/AB_10561706
2°	Mouse IgG (H+L chain)	Donkey	Alexa Fluor® 647	1:500	Poly	Life Technologies	A31571/AB_162542
2°	Sheep IgG (H+L chain)	Donkey	Alexa Fluor® 647	1:500	Poly	Jackson Immunoresearch	713-605-003/AB_2340750

in Papp et al., 2016). An overview of the image alignment workflow is provided in **Figure 1**: microscope images were contrast-optimized for differentiation of gray and white matter and uploaded to N3 where the section images were overlaid onto virtual sections of the Waxholm atlas template, a whole brain MRI dataset obtained from a male Sprague Dawley rat (Papp et al., 2014). The cut angle of the MRI dataset was manually adjusted to match the histological section, allowing the user to align histological sections cut at any plane to the reference dataset and therefore compensating for deviations from standard cutting planes or tissue distortion. Once each image was optimally aligned to its MRI equivalent the image was considered "anchored"; geometric vectors corresponding to the rostrocaudal level of the image origin, deviation from the vertical and horizontal planes, scaling and rotation were calculated by the anchoring tool in the N3 platform and exported as metadata. With this information the position of any point in a histological image could be converted to 3-dimensional Waxholm coordinates in Microsoft Excel. Waxholm coordinates are by convention presented in the xyz format (lateral, rostrocaudal, dorsoventral) with a voxel resolution of 39 μm. The interested reader is directed toward CutNii, a freely downloadable explorer and custom-angle slicer for the Waxholm dataset (Csucs and Bjaalie, 2015), which is similar to the N3 tool used for image alignment (although it does not allow overlay or anchoring of histological images).

Volumetric Brain Modeling

The raw MRI data and corresponding segmentation model of the Waxholm Sprague Dawley rat were downloaded from the International Neuroinformatics Coordinating Facility Software Center (Papp et al., 2015) and imported into Imaris volumetric imaging software (Version 8.1, Bitplane AG, Switzerland) following conversion to the Biorad format in ImageJ. Each segmented area was individually rendered using the Imaris "contour surface" function, resulting in a surface-rendered model that incorporates regions demarcated in Waxholm space. Tabulated Waxholm coordinates of Input, non-C1 starter, and C1 starter neurons were then imported using a Python script ("*CreateSpotsFromFile,*" http://open.bitplane.com/tabid/235/Default.aspx?id=70), resulting in a 3d model of the Waxholm brain populated with points corresponding to identified neurons. Another script was then used to automatically quantify the number of input neurons that lay within each segmented region ("*Spots split into surface objects,*" http://open.bitplane.com/tabid/235/Default.aspx?id=19). The Imaris-rendered Waxholm brain (containing the RVLM connectomic dataset) is available as a supplementary download and can be used freely by other researchers (http://datadryad.org/resource/doi:10.5061/dryad.q5t5s). The dataset can also be viewed with the free Imaris SceneViewer program (www.bitplane.com). The voxel coordinates of starter and input neurons are included in tabulated format in **Data Sheet 1**.

Segmentation of the Facial Nucleus, RVLM, Bötzinger and Pre-Bötzinger Complex in Waxholm Space

The Waxholm segmentation model does not differentiate brainstem subnuclei, so we used the locations of bulbospinal TH-immunoreactive RVLM neurons as the basis for segmentation of the RVLM. Data were obtained from six rats in which neurons projecting to the T2 and/or T10 spinal segments were retrogradely labeled by HSV-hCMV-GFP or -mCherry control vectors. Vector injections and histology were conducted as described above and 273 TH-positive bulbospinal RVLM neurons were annotated and anchored in Waxholm space. The lateral coordinates of all neurons were represented as being on *both* sides of the brainstem for segmentation; two-dimensional contour maps indicating the density of labeling were then generated for each dorsoventral level using the Plotly visualization tool (https://plot.ly, 10 voxel resolution). Contours enclosing pixels that contained >2 neurons/10 pixel radius in the horizontal plane were converted to an image stack, imported into the virtual Waxholm rat brain using Imaris, and surface rendered to define the boundaries of the RVLM (**Video 1**).

The extent of the facial nucleus was annotated directly from the Waxholm MRI dataset in Imaris; the Bötzinger and pre-Bötzinger Complex were defined as longitudinal cylinders, 500 μm in diameter that ran center-aligned and immediately ventral to nucleus ambiguus. The Bötzinger region was defined as starting at the caudal pole of the facial nucleus and running 600 μm caudal; the pre-Bötzinger Complex was defined as

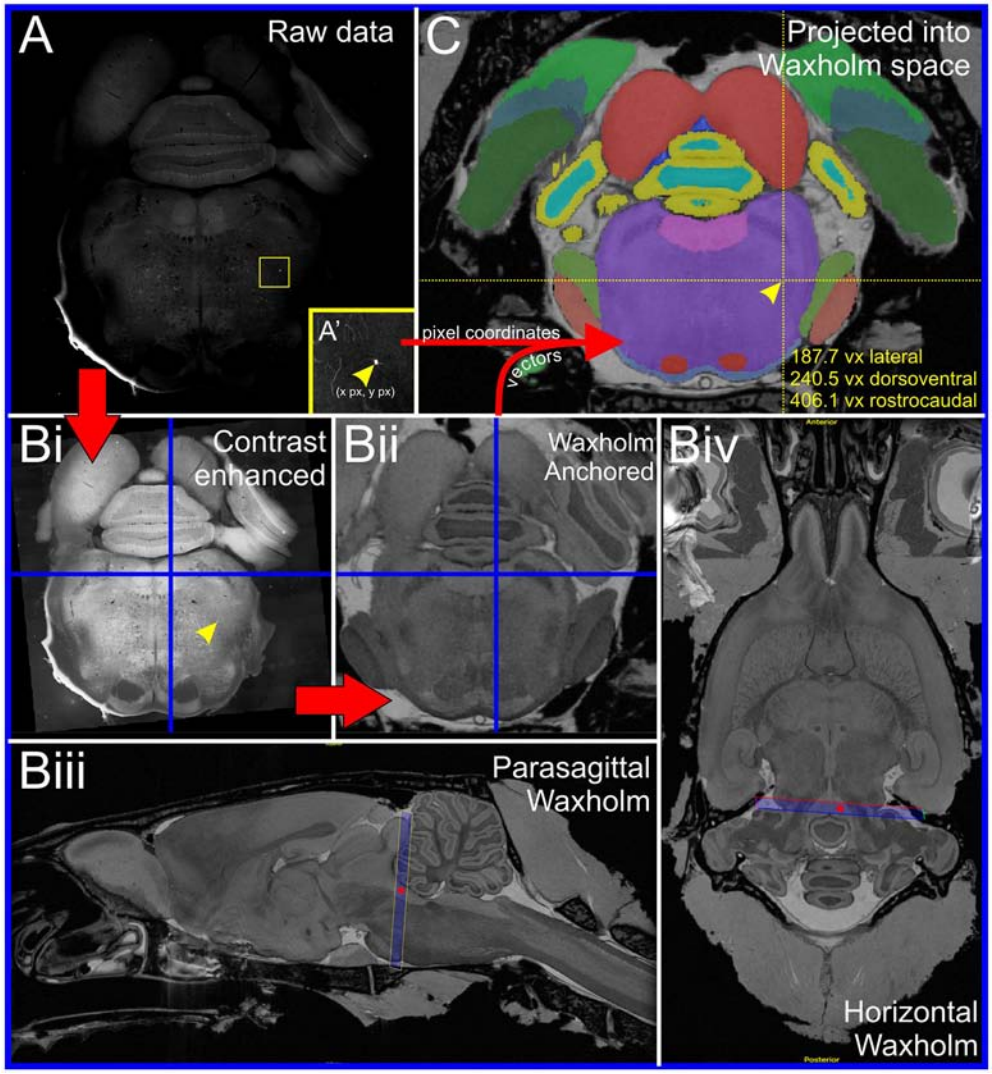


FIGURE 1 | Anchoring workflow. (A) Original coronal epifluorescence image showing the location of a single rabies-labeled input neuron (yellow box, inset in **A'**). Following manual annotation, the pixel coordinates of the neuron were exported to a spreadsheet and the image contrast adjusted for optimal visualization of anatomical landmarks **(Bi)**. The image was then aligned to a corresponding section plane through the Waxholm atlas template **(Bii)** using a beta version of an image alignment/anchoring tool embedded in the Navigator-3 system. The anchoring tool allowed accurate positioning of the image plane in the MRI-derived atlas template. The orientation of the plane of the image is close to coronal, as shown in the blue frames in **(Biii)** and **(Biv)**. The parasagittal plane through the atlas template shown in **(Biii)** corresponds to the vertical blue line in **(Bi)** and **(Bii)**, whereas the horizontal plane in **(Biv)** corresponds to the horizontal blue lines in **(Bi)** and **(Bii)**. The red dots in **(Biii)** and **(Biv)** represent the intersections with the horizontal and parasagittal planes, respectively. Anchoring vectors generated by Navigator-3 were then used to translate the pixel co-ordinates of annotated neurons into xyz Waxholm coordinates and integrated into the Waxholm segmentation model **(C)**.

running between 700 and 1200 μm caudal to the facial nucleus (Le et al., 2016).

Cluster Analysis

K-means analysis was used to partition groups of input neurons based on their 3d distribution. The algorithm determines clusters by assigning data points to a closest mean (centroid), assigned initially at random and iteratively refined as data points are sequentially accumulated within a cluster. Analysis was performed and density plots generated in "R project" (R Foundation for Statistical Computing, Vienna, Austria, 2005, http://www.r-project.org). The voxel coordinates of input neurons segregated by cluster are provided in **Data Sheet 2**.

RESULTS

Retrograde Transduction of Spinally Projecting Neurons and Segmentation of the RVLM in Waxholm-Space

Microinjection of HSV vectors at the thoracic spinal cord drove reporter expression in bulbospinal neurons within

12 h, with maximal expression apparent by 2–4 days. Reporter-labeled neurons spanned the RVLM, rostral ventromedial medulla (RVMM), and midline raphe region, and were identified in other sympathetic premotor nuclei such as the C3, paraventricular, A5, and locus coeruleus (**Supplementary Image 1**).

The distribution of TH-immunoreactive neurons labeled by HSV control vectors was plotted in Waxholm co-ordinates (**Figure 1**) and was used to define the anatomical boundaries of the RVLM (**Supplementary Image 1**). The geometric epicenter was located at Waxholm coordinates 198 lateral, 313 rostrocaudal, 182 dorsoventral (**Supplementary Images 1D–F**), corresponding to a position 1.78 mm lateral to the midline, 117 μm rostral to the caudal pole of the facial nucleus, and 339 μm dorsal to the ventral surface of the medulla immediately beneath the epicenter. The segmentation defined a dorsoventrally flattened ovoid (**Supplementary Images 1G–I**) in which the long axis runs medial in more rostral sections and spans Waxholm coordinates 176–218 lateral (2.6–1 mm lateral to midline), 287–327 rostrocaudal (900 μm caudal to 663 μm rostral to caudal pole of the facial nucleus) and 174–198 dorsoventral (within 897 μm from the ventral surface of the brainstem). This region contained 86% of TH-positive bulbospinal neurons used to generate the segmentation ($n = 236$) and corresponds well with the pressor region that encompasses the rostral RVLM and perifacial zone (Goodchild and Moon, 2009).

Monosynaptic Tracing Was Predominantly Restricted to Putative RVLM Sympathetic Premotor Neurons

Data from 4 animals were selected for detailed connectomic analysis. As illustrated in **Supplementary Image 2**, unilateral injection of HSV-hCMV-YTB directed at the second thoracic (T2) IML resulted in retrograde transduction of bulbospinal neurons in the ventrolateral medulla, the majority of which were ipsilateral to the injection site (82% (71–88) [mean (range), $n =$ 4 rats]). Subsequent injection of SADΔG(EnvA)-mCherry in the RVLM resulted in the primary infection of bulbospinal RVLM neurons. As shown in **Figure 2**, bulbospinal "starter" neurons were identified by their co-expression of YFP and mCherry and many were immunoreactive for TH (**Figure 2B'**).

Neurons were counted on every fourth section: on average 38 starter neurons were identified per animal (range: 19–67), of which 40% (30–45) were confirmed as TH-positive C1 neurons under epifluorescence (which underrepresents the proportion of C1 starter neurons by up to 50%: see Methods–Imaging). Seventy eight percent (74–87%) of starter neurons lay within the Waxholm RVLM boundary defined above (**Figure 2C**). Ectopic starter neurons that fell outside the RVLM were observed around the lateral and dorsal perimeter of the facial nucleus and adjacent sympathetic premotor nuclei which included the rostral ventromedial medulla (RVMM), caudal raphe and contralateral RVLM. **Video 1** shows the Waxholm MRI dataset overlaid with the distribution of C1 and non-C1 starter neurons from 4 rats subjected to detailed analysis, along with the boundary of the RVLM region.

Inputs to Putative RVLM Sympathetic Premotor Neurons Predominantly Arise from Medullary Nuclei

Monosynaptic input neurons were identified throughout the brain as mCherry, non-YFP neurons. 1298 input neurons were identified in total [325 (220–561) per animal], corresponding to an input: starter ratio of 9.8 (4.4–13.4). The overall distribution of input neurons is shown in **Figures 3A,B**: although the absolute number of input neurons and efficiency of trans-synaptic spread was variable, the overall pattern of inputs was consistent between animals: input neurons were encountered from the most caudal point quantified, the cervical medullary junction, to the hypothalamus at the level of the optic chiasm, with a pronounced [77% (75–80)] ipsilateral bias. Nodal edge-length analysis (the shortest distance between each neuron and the epicenter of the RVLM) indicates that most input neurons lie in close proximity to the RVLM, with 50% of inputs residing within 2.5 mm (2.3–2.7) with a progressively diminishing proportion of inputs identified at increasing distances: only 10% of monosynaptic input neurons lie more than 5 mm from the RVLM (**Figure 3C**). Input neurons were also distributed throughout the thoracic and cervical spinal cord, although these data were not quantified.

A script that automatically counts the number of neurons within each region of the Waxholm atlas was used to quantify the regional distribution of input neurons. These data are graphically represented in **Figure 4** and tabulated in **Table S1**: the overwhelming majority of inputs resided within the Waxholm-defined boundary of the brainstem 92% (88–94), with inputs arising from the forebrain and midbrain accounting for 3% each and the remainder originating in the cervical spinal cord and cerebellum. Sub-nuclei of the brainstem are not well represented in the current iteration of the Waxholm atlas; of those regions thus far defined the highest source of input was the RVLM itself, which contained 14% of input neurons.

K-means analysis was used to objectively group input neurons based on their spatial distribution. We empirically determined that 12 was an appropriate number of clusters (k) by which to partition the dataset by plotting the percentage of variance explained by clusters generated for k-values 1–20 and identifying a point at which the increase in explained variance was marginal for further increases in k, denoted by an "elbow" in the curve (**Figure 3Dii**, inset). The 12 clusters identified accounted for 89.3% of variance in the dataset (**Figure 3**); a detailed overview of identified clusters and their correspondence to the literature is presented in **Table S2**. Eight of 12 input clusters were located within the medulla, the largest of which (Cluster 2) encompassed the ipsilateral RVLM (including occasional trans-synaptically labeled C1 neurons: **Figure 2B**), Bötzinger region (**Figure 5D**), nucleus ambiguus (**Figure 5G**), and choline acetyltransferase (ChAT)-immunoreactive cells in a region of the ventral lateral tegmental field (**Figure 6A**) that may represent the rat analog of the post-inspiratory complex (PiCo: Anderson et al., 2016). In a sample of 21 input neurons identified as lying within the Bötzinger region using previously published criteria (Le et al., 2016), none contained glycine

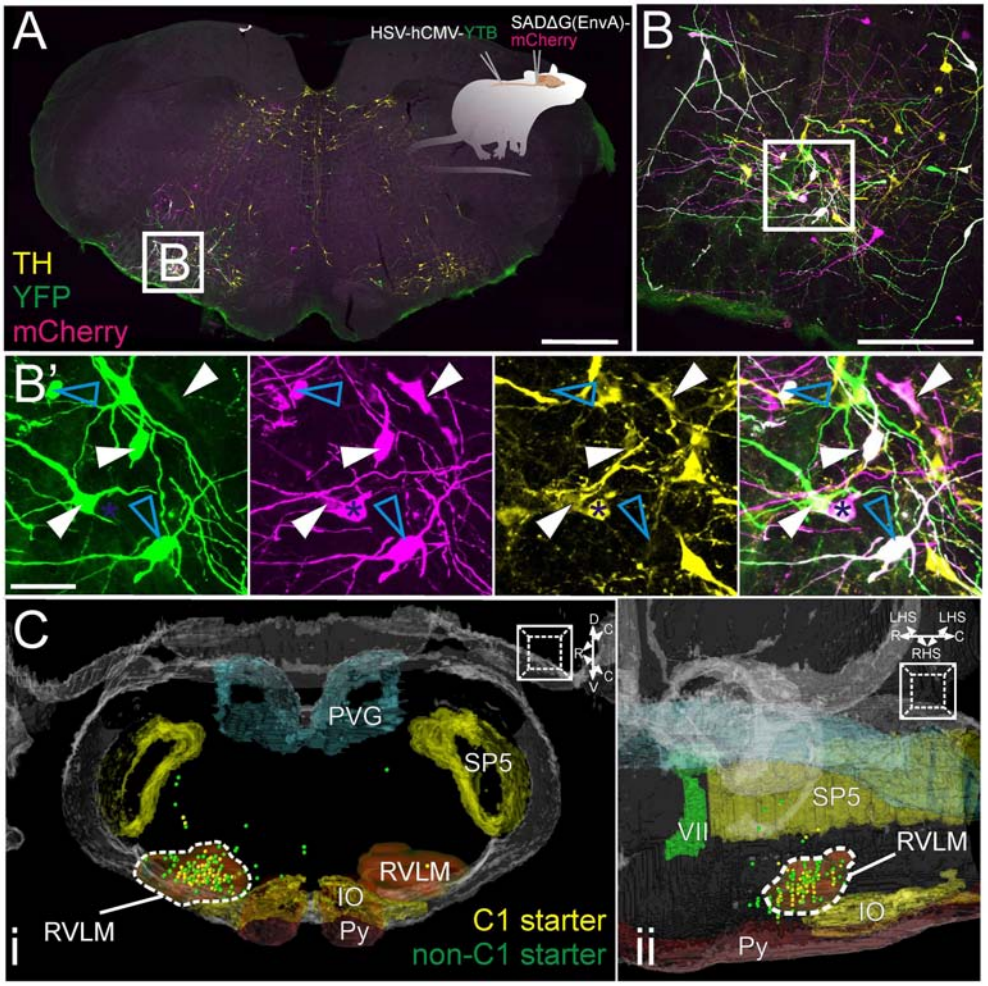


FIGURE 2 | Experimental strategy (inset in A): HSV-hCMV-YTB was injected at the T2 IML, retrogradely driving the expression of TVA, rabies glycoprotein, and YFP in spinally projecting neurons. SADΔG(EnvA)-mCherry was subsequently injected into the RVLM, exclusively infecting neurons that express TVA, and seeding trans-synaptic infection of monosynaptically connected input neurons. **(A)** Coronal brainstem section at the level of the rostral ventrolateral medulla (RVLM) processed for immunoreactivity to TH and YFP; starter neurons are defined by the expression of both YFP and mCherry. **(B)** Confocal detail with magnified **(B')** examples of C1 (solid arrowheads) and non-C1 (cyan arrowheads) starter neurons (individual channels and merged image). Blue asterisk indicates a C1 input neuron. **(C)** Distribution of C1 (yellow) and non-C1 (green) starter neurons from four experiments plotted in Waxholm space, shown from coronal **(Ci)** and parasagittal **(Cii)** perspectives. Anatomical landmarks are Waxholm-segmented boundaries of the inferior olive (IO), spinal trigeminal nucleus (SP5), RVLM, pyramidal tract (Py), facial nerve (VII), and periventricular gray (PVG). Scale bars 1000 μm **(A)**, 250 μm **(B)**, and 100 μm **(B')**.

transporter 2 mRNA, a marker for respiratory function in this region (**Figure 6B**, Schreihofer et al., 1999). Adjacent clusters enveloped the dorsal LTF (Cluster 3) and pre-Bötzinger Complex (Cluster 4, **Figure 5E**), including neurokinin-1 receptor (NK1R) immunoreactive neurons (**Figure 6C**), a putative marker for respiratory function in this region (Gray et al., 2001). Cluster 4 also spanned the rostral ventral respiratory group and caudal ventrolateral medulla (CVLM: **Figure 5A**), including confirmed GABAergic CVLM neurons (**Figure 6D**). Input clusters also included the rostral ventromedial medulla and caudal Raphe nuclei (Cluster 7) and a distinct input from the region immediately ventral to the nucleus prepositus hypoglossi (Cluster 9, **Figure 5B**). Other brainstem clusters spanned the intermediate and commissural nucleus of the solitary tract (NTS: **Figure 5C**, Cluster 6), the caudal pressor area and caudal ventral respiratory group (Cluster 10), and the ventral aspect of the contralateral medulla (Cluster 5). A flythrough of the entire dataset, projected onto the MRI Waxholm dataset and segregated by color into its component clusters, is presented in **Video 2**.

Supramedullary Nuclei Constitute a Minor Source of Input to RVLM Sympathetic Premotor Neurons

Supramedullary inputs included diffuse pontine clusters that encompassed the ipsilateral (Cluster 1) and contralateral (Cluster 11) A5 adrenergic cell group, subcoeruleus, Kölliker-Fuse, and medial and lateral parabrachial nuclei. The single midbrain

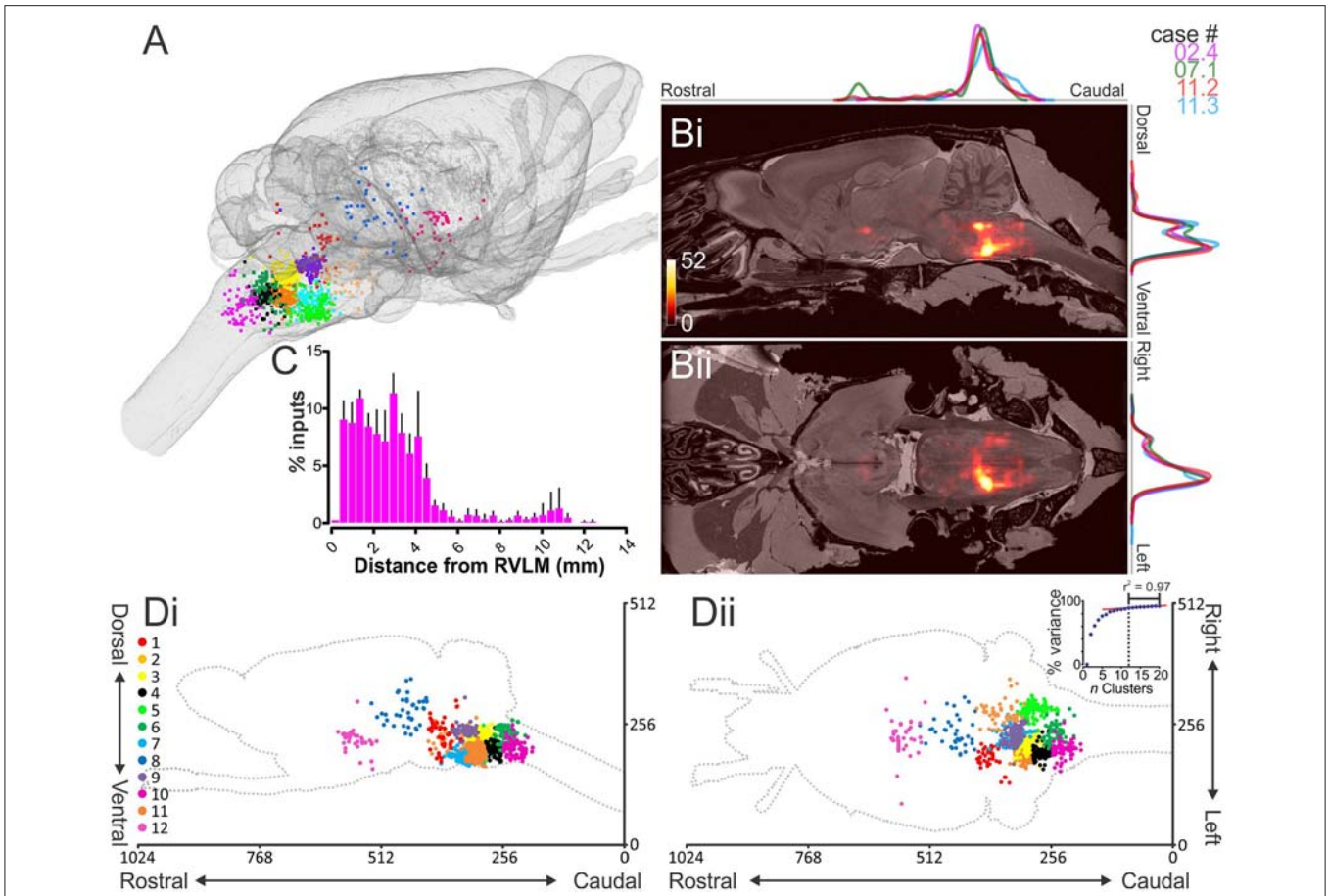


FIGURE 3 | Distribution of monosynaptic input neurons. (A) Input neurons to putative sympathetic premotor neurons in the rostral ventrolateral medulla (RVLM) segregated into 12 distinct clusters and plotted in the Waxholm volumetric rat atlas. **(B)** Heat maps showing input neuron density overlaid on the Waxholm MRI dataset in the parasagittal **(i)** and horizontal **(ii)** planes. Scale indicates number of neurons per 10 voxels. Normalized plots of input densities for individual experiments are plotted alongside heat maps. **(C)** Absolute distance of input neurons from RVLM epicenter ($n = 4$ rats). **(D)** Cluster plots presented in the sagittal **(i)** and horizontal **(ii)** planes. Inset in **(Dii)** shows the proportion of total variance accounted for by incremental increases in cluster number; the turning point of the curve, after which slope becomes linear, occurs at 12 clusters.

cluster (Cluster 8) incorporated the lateral and ventrolateral periaqueductal gray (PAG) and colliculi, and a hypothalamic cluster (Cluster 12) composed from neurons residing within the paraventricular hypothalamic nucleus, including confirmed vasopressinergic neurons (**Figures 5F**, **6E**) and neurons in the lateral and perifornical hypothalamic areas.

DISCUSSION

The objective of the current study was to definitively and quantitatively map the afferent connectome of putative RVLM sympathetic premotor neurons, a regulatory axis through which convergent sensory and limbic inputs are thought to summate to produce baseline sympathetic nerve activity. We identified prominent inputs from well-established neurohumoral and viscero-sympathetic actuators such as the area postrema and NTS, and inputs that spanned medullary autonomic (A5, RVLM, ventromedial medulla, CVLM, LTF) and respiratory nuclei (Bötzinger, pre-Bötzinger Complex, PiCo, rostral ventral respiratory group), as well as supramedullary autonomic nuclei (paraventricular nucleus, ventrolateral PAG, lateral hypothalamus) (Dampney, 1994b; Guyenet, 2006; Card et al., 2011; Stornetta et al., 2016). However, the most striking feature of the connectome is its diffuse distribution, which contrasts with the nodal ball-and-stick schemes sometimes used to conceptualize it (Dampney, 1994a; Pilowsky and Goodchild, 2002; Guyenet, 2006), and its strong weighting toward local inputs, with around 14% of input neurons residing within the RVLM region and 30% of inputs lying within 1 mm of the RVLM epicenter. In contrast, the dataset includes a relatively low number of inputs from the forebrain (3%) and midbrain (3%), and a virtual absence of inputs from locus coeruleus, the amygdala, cortex and subfornical organ and median preoptic nucleus, despite compelling prior evidence for both functional and neuroanatomical connectivity (Dampney et al., 1987; Cassell and Gray, 1989; Gelsema et al., 1989; Verberne, 1996; Saha, 2005; Card et al., 2011; Bou Farah

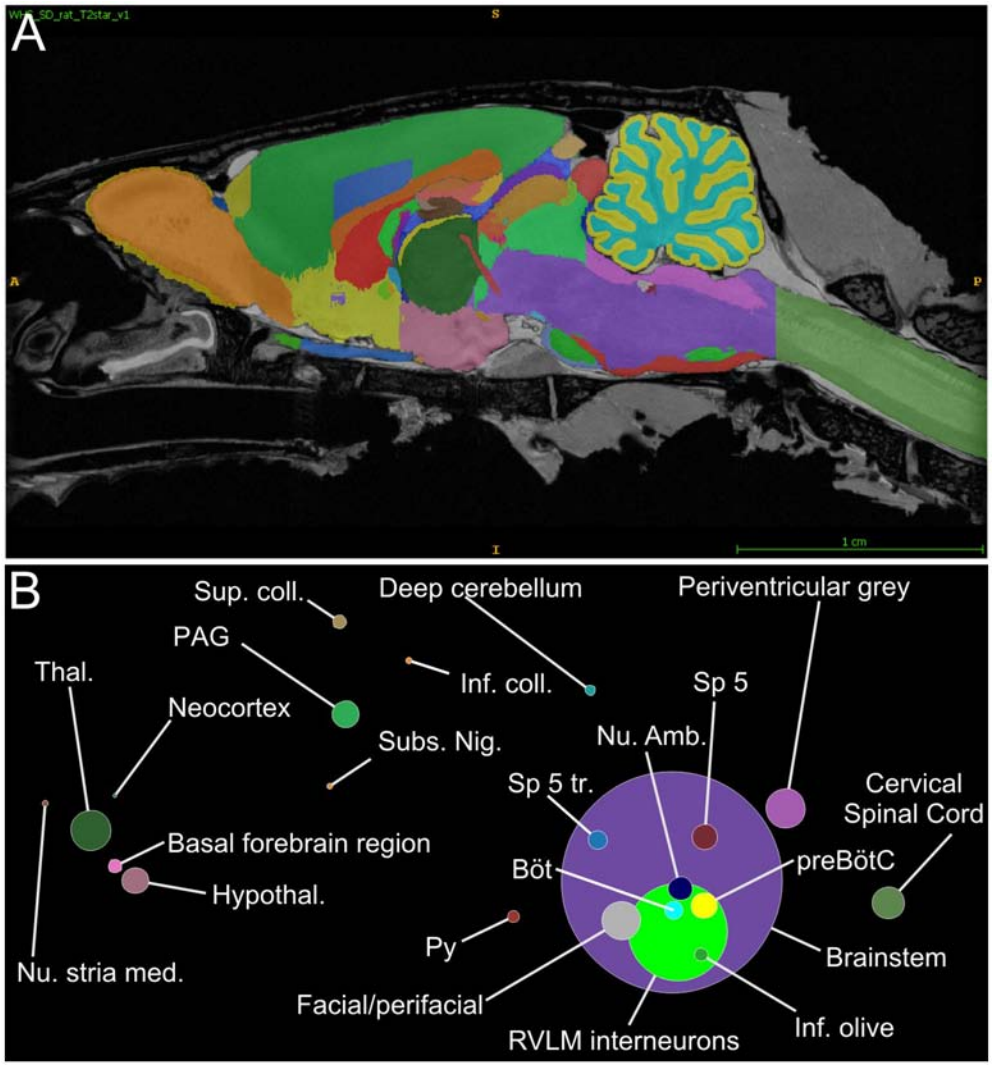


FIGURE 4 | RVLM input neurons organized by Waxholm segment. (A) Parasagittal view through the Waxholm volumetric atlas for reference; different colors indicate different brain segments. **(B)** Proportions of input neurons per Waxholm segment (summed from 4 experiments) colored and positioned according to their corresponding Waxholm regions. The diameter of each circle corresponds to the number of inputs therein. See **Table S2** for source data and abbreviations.

et al., 2016). This pattern of connectivity is consistent with qualitative data from in a similar study that targeted TH-synthesizing RVLM neurons in the mouse (Stornetta et al., 2016) and supports the argument that RVLM sympathetic premotor neurons play little, if any, role in the generation of sympathoexcitatory responses to acute psychological stress or conditioned fear (Dayas et al., 2001; Carrive and Gorissen, 2008; Furlong et al., 2014; Dampney, 2015), although it does not rule out the possibility that input from cortical and limbic structures could be indirect, perhaps involving disynaptic relays through the abundant monosynaptically connected RVLM interneurons identified in this study. Alternatively, as the current study focused exclusively on inputs received by sympathetic premotor neurons that project to the T2 thoracic spinal cord, it could be that higher centers provide a more (numerically) significant input to RVLM neurons that project to other spinal segments.

The minor input received from supramedullary centers is unlikely to represent a limitation of SADΔG(EnvA), as distance is not thought to impair its labeling efficiency (Callaway and Luo, 2015; Schwarz et al., 2015). Furthermore, inputs from the amygdala and cortex were observed in control experiments using rabies glycoprotein-transcomplemented SADΔG-mCherry and retrograde herpes vectors, and have been reported in studies that used classical chemical tracers (Bowman et al., 2013; Bou Farah et al., 2016), confirming that these structures innervate the RVLM region; apparently just not those neurons targeted in the current study. Taken at face value, these data suggest that inputs from numerous local brainstem structures predominate in their capacity to influence sympathetic nerve activity compared

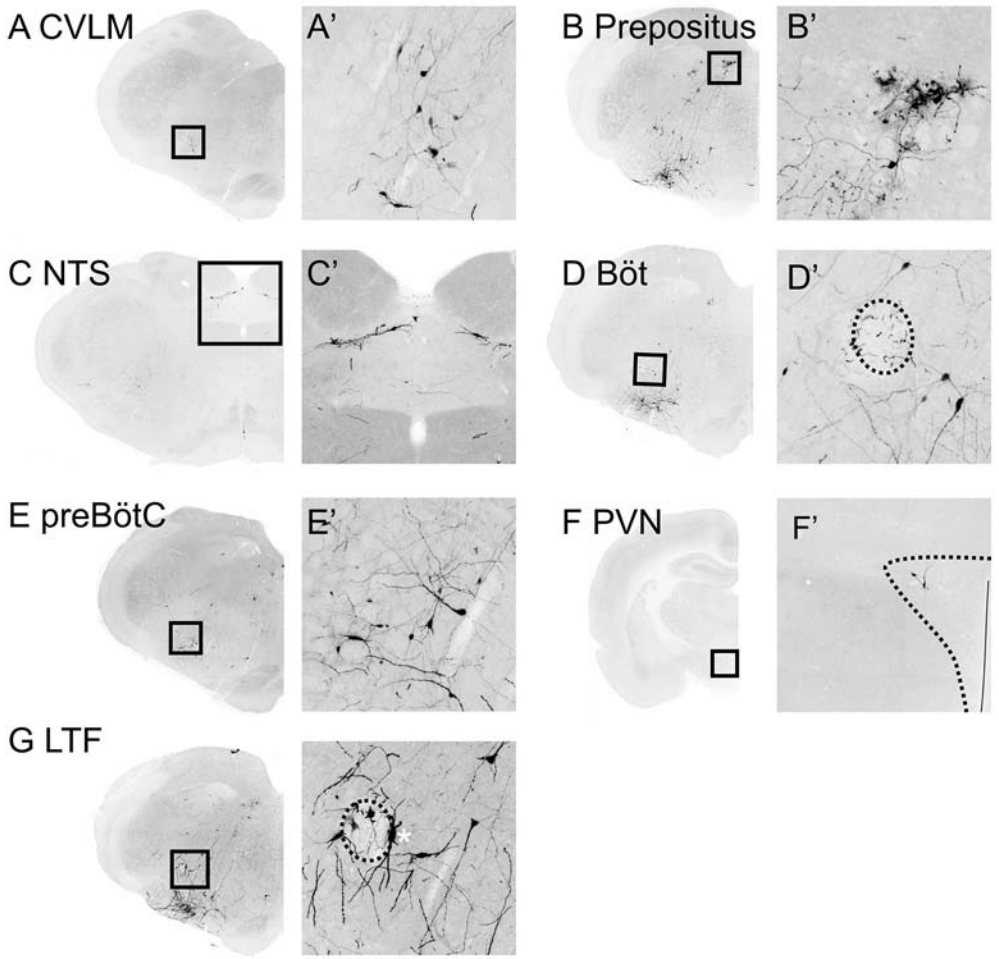


FIGURE 5 | Medullary inputs to RVLM sympathetic premotor neurons. Inverted epifluorescence micrographs with high power insets **(A'–F')** of boxed regions illustrating monosynaptic inputs from the caudal ventrolateral medulla (CVLM: **A**), nucleus prepositus **(B)**, nucleus of the solitary tract (NTS: **C**), Bötzinger (Böt: **D**), pre-Bötzinger Complex (preBötC: **E**), paraventricular nucleus of the hypothalamus (PVN: **F**) and lateral tegmental field (LTF: **G**). Nucleus ambiguus is indicated by the hatched ovals in **(D,G)**. *in Panel **(G)** indicates a TH-positive starter neuron.

to more distant regions, with the caveat that identification of monosynaptically connected neurons does not necessarily denote activity of those inputs: rabies spread is a function of synaptic strength, not synaptic activity (Ugolini, 1995; Brennand et al., 2011).

RVLM sympathetic premotor neurons include both C1 and non-C1 neurons, which differ in their functional and neurochemical phenotypes (Schreihofer and Guyenet, 1997; Stornetta et al., 2001) and may play differing roles in the generation of baseline sympathetic nerve activity and the elaboration of sympathetic reflexes (Schreihofer and Guyenet, 2000; Schreihofer et al., 2000; Madden et al., 2006; Burke et al., 2011). We used a herpes vector with a retrograde tropism to transduce putative sympathetic premotor neurons based on their axonal trajectory, allowing us to target both C1 and non-C1 bulbospinal neurons. One potential limitation of this approach is that SADΔG(EnvA)-mCherry injected into the RVLM could have theoretically infected TVA-expressing spinally-projecting neurons from other brain regions, either as a result of trans-synaptic spread (to spinally projecting neurons that provide collateral input to RVLM sympathetic premotor neurons) or by direct infection of axons that traverse the RVLM. Evidence of such "ectopic" starter neurons was apparent in pilot experiments, but was largely eliminated by limiting the interval between herpes and rabies injections to 24 h and by diluting the herpes vector. We speculate that TVA is differentially expressed on the somata but not the axons of herpes-transduced neurons at 24 h, accounting for the selective accessibility of RVLM neurons at this time-point, and conclude that bulbospinal RVLM neurons do not receive collateral input from other spinally projecting neurons because we did not see any evidence of ectopically infected spinally projecting neurons in other brain regions.

A notable deviation from the standard autonomic circuit model is the discovery of a conspicuous input from the region of the prepositus hypoglossi, a brainstem nucleus conventionally

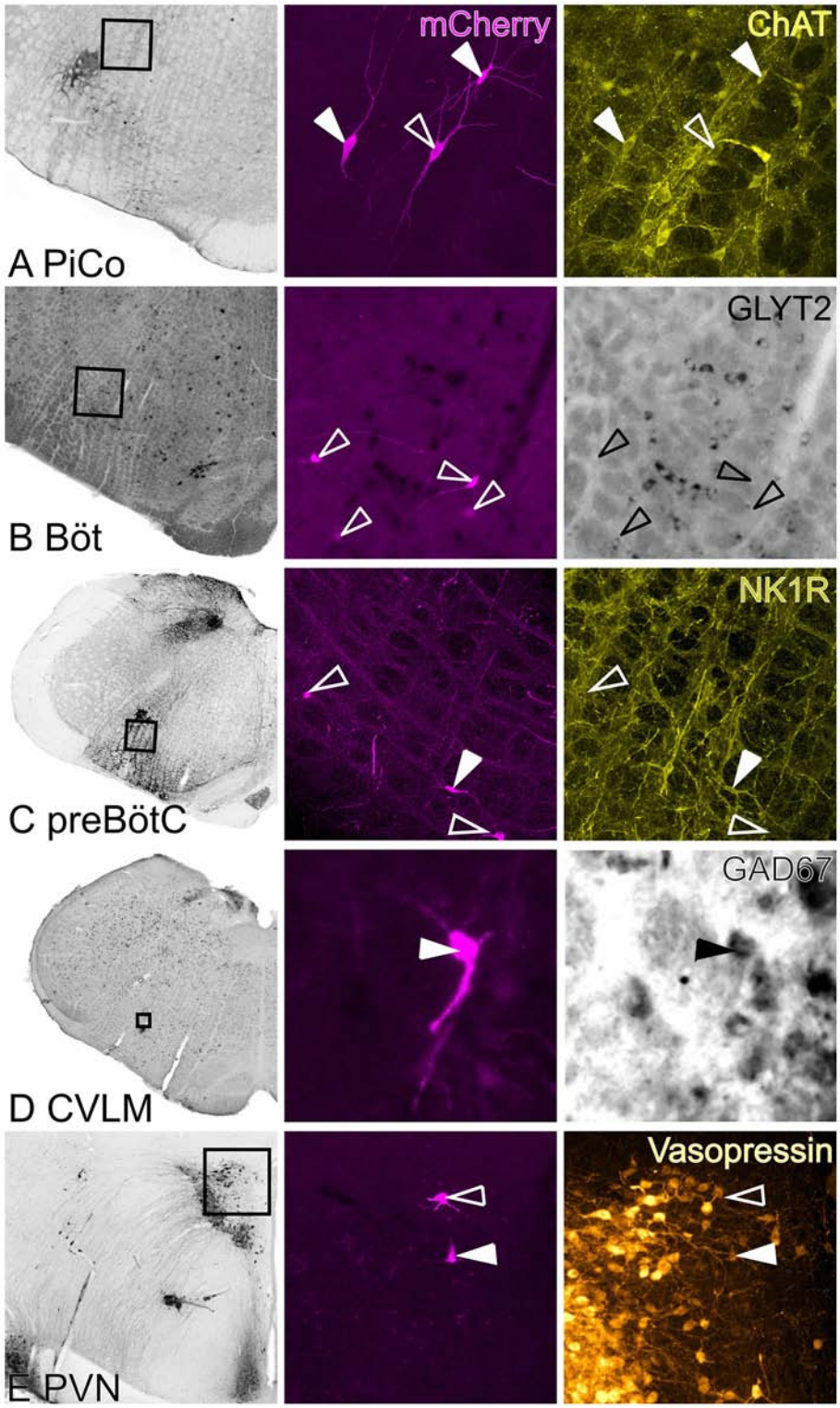


FIGURE 6 | Neurochemical phenotypes of input neurons. Left hand panels are low power images of *in situ* hybridization/immunohistochemistry indicating region shown in high power images. Middle panel shows rabies-labeled input neurons, right panels show *in situ* hybridization/immunofluorescence. Closed arrowheads indicate double-labeled neurons; open arrowheads indicate the positions of rabies labeled input neurons. **(A)** ChAT-immunoreactive input neurons in the region of the lateral reticular formation that corresponds to the mouse PiCo. **(B)** Bötzinger input neurons were abundant but none were identified as GlyT2-positive. **(C)** NK1R-positive and -negative pre-Bötzinger Complex inputs. **(D)** GAD67-positive input neurons in the CVLM. **(E)** Vasopressin-positive and -negative PVN inputs. PiCo: post-inspiratory complex, Böt: Bötzinger, preBötC: pre-Bötzinger Complex, CVLM: caudal ventrolateral medulla, PVN: paraventricular nucleus.

associated with vestibulo-occulomotor integration (McCrea, 1988) but also previously shown to drive pressor responses to glutamate microinjection (Talman and Robertson, 1991). Rabies-labeled prepositus neurons reside along the axonal trajectory of RVLM bulbospinal neurons (Lipski et al., 1995; Stornetta et al., 2016) but are not labeled by traditional retrograde tracers injected at the RVLM pressor region (Dampney, 1994b) (or retrograde rabies/herpes vectors—data not shown): we speculate that trans-synaptic infection of this population may have been via axoaxonic contacts or via the distal dendrites of starter neurons. Future functional studies will be required to elucidate the functional significance of this input.

Our dataset provides unequivocal evidence of monosynaptic inputs from respiratory subnuclei, providing clues to the neuroanatomical substrate responsible for respiratory-sympathetic coupling, the entrainment of sympathetic nerve activity to the phasic bursting of the central respiratory rhythm generator. Although direct interaction between respiratory and cardiovascular neurons in the brainstem has long been suspected (reviewed by Pilowsky et al., 1996; Taylor et al., 1999; Zoccal et al., 2014), technical difficulties have until now precluded unambiguous examination of this hypothesis. We found no evidence that input neurons in the Bötzinger region were glycinergic, (a functional marker of Bötzinger respiratory neurons: Schreihofer et al., 1999; Ezure et al., 2003), undermining the hypothesis that Bötzinger neurons are a source of inhibitory input to sympathetic premotor neurons (Sun et al., 1997). This is consistent with the observation that blockade of RVLM glycinergic transmission does not alter respiratory-sympathetic coupling (Guyenet et al., 1990), and suggests that the close appositions identified by Sun et al. (1997) may not represent functional synapses, an acknowledged limitation of light microscopy for reliable identification of synaptic contacts (Murphy et al., 1995; Descarries and Mechawar, 2000).

On the other hand, we identified pre-Bötzinger Complex input neurons that were immunoreactive for NK1R, a putative marker of glutamatergic inspiratory neurons in this region (Gray et al., 2001; Guyenet and Wang, 2001; Stornetta et al., 2003), providing a plausible structural basis for the inspiratory-locked sympathoexcitation evident in some sympathetic outflows (reviewed by Häbler et al., 1994; Pilowsky et al., 1996) and RVLM sympathetic premotor neurons (McAllen, 1987; Moraes et al., 2013). We also identified inputs from ChAT-immunoreactive neurons in the region of the LTF that may correspond to the PiCo, a group of glutamatergic cholinergic neurons recently reported to underlie the generation of postinspiratory activity in the mouse (Anderson et al., 2016). Although functional studies of the PiCo are yet to be replicated in the rat, we tentatively hypothesize that excitatory input from its analog could underlie the prominent post-inspiratory activity seen in rat lumbar and splanchnic sympathetic nerve activities (Haselton and Guyenet, 1989; Burke et al., 2010; Korim et al., 2012).

Few input neurons were found in the medullary retrotrapezoid/parafacial region that lies close to the ventral brainstem surface immediately adjacent to the RVLM. As this population is not thought to directly contribute to respiratory-sympathetic coupling (Moraes et al., 2012) their neurochemical phenotype was not studied in detail: such inputs that were identified did not conform to the small fusiform morphology or reticular distribution typical of RTN CO_2-sensing neurons (Stornetta et al., 2006).

Like other mesoscale connectomes, the RVLM connectome is diffuse and highly non-uniform in its distribution. This level of complexity makes it difficult to conceptualize as a whole, and makes identification of its major subdivisions susceptible to operator bias. Principle component analysis (cluster analysis) provides a simple and unbiased way to do this but suffers some potential drawbacks. First, selection of the appropriate number of clusters (the value of k) is inexact; it can be estimated by examining the degree of variance accounted for by iterative increases in k and identifying the "elbow" after which the relationship between k and variance becomes linear (Thorndike, 1953: in the current study $k = 12$). However, as this value is a function of the variance of the dataset, one would expect k to increase if more experimental data were added—in other words, if one analyzed 10,000 input neurons instead of 1,000, the sensitivity of the analysis would be higher and it would resolve clusters not currently detectable. Second, cluster analysis was performed on the pooled connectomic dataset, rather than on each individual experiment. Although the overall normalized distribution of inputs was reproducible between experiments, this means that experiments in which a large number of input neurons were detected influence cluster detection more than those in which fewer inputs were detected. Taken together, cluster analysis of connectomic datasets should be seen as a useful platform for breaking complicated datasets down into a readily digestible overview, rather than a definitive structural analysis tool.

Overall, the spatial distribution of the RVLM connectome adheres to two key organizational principles evident when examining interregional connectivity profiles [i.e., at the macroscopic resolution: reviewed by Bullmore and Sporns (2012)]. The first is reciprocity, that is, regions innervated by the collateral branches of putative sympathetic premotor neurons such as the NTS, RVLM, CVLM/A1, raphe and PAG (Card et al., 2006; McMullan and Pilowsky, 2012; Stornetta et al., 2016) all in turn provide afferent input to RVLM sympathetic premotor neurons. The second is spatial embedding: RVLM sympathetic premotor neurons are more likely to receive input from nearby neurons than distant ones. The spatial embedding evident in the rat RVLM connectome is in striking accordance with the nodal edge-length distribution of the mouse mesoscale connectome, the most detailed whole brain connectivity atlas currently available (Oh et al., 2014), and in particular the spatial distribution of reciprocally connected nodes (Henriksen et al., 2016) (see **Supplementary Image 3** for direct comparison). This supports the proposition, reviewed by Bullmore and Sporns (2012), that highly conserved general principles likely govern circuit topography irrespective of species, brain region, cell type or scale, and provides for the first time cell-type specific connectomic data that can be used to test general brain connectivity models.

Cell-specific connectome tracing provides unique insights into the organization of circuits that control populations of neurons selected based on their genetic, functional, or projection profiles (Yonehara et al., 2013; Pollak Dorocic et al., 2014; Pollock et al., 2014; Wertz et al., 2015). However, one of the challenges to this approach lies in the analysis and presentation of the data. A common strategy is to align histological images with corresponding plates from a stereotaxic atlas, count the number of neurons that reside within each segmented region, and then tabulate the output (Pollak Dorocic et al., 2014; Schwarz et al., 2015). Although superficially straightforward, we found that the reliability of this approach depends greatly on the expertise of the operator and can be compromised by even small misalignments in cutting plane. We calculate that each degree in deviation in the lateral plane results in an offset of ∼280 μm rostrocaudal at the widest point of the rat brain, (which is further exaggerated by any deviation in the dorsoventral plane). Perfect histological cutting planes are virtually impossible to achieve, and so data presented in this way are intrinsically error-prone. The longevity of data presented as #cells/region are further undermined by the evolving taxonomy of the brain, variation in segmentation and nomenclature used by different reference atlases, and the ongoing discovery of new cell groups. An alternative approach is to present imaging data in its entirety, either as an online repository of still (Pollak Dorocic et al., 2014) or video images (Stanek et al., 2014). This allows other investigators to access the raw data, but independent analysis is hampered by the enormous volume of imaging data and the time commitment required to reanalyze it.

Our approach sidesteps both of these limitations: alignment of a 3d reference atlas to the histological image (rather than the other way around) eliminates potential errors caused by imperfect cutting angle or tissue distortion. Second, the compact size (current study <100 kb) and standardization of the positional metadata make it amenable to sharing and independent reanalysis, and eliminates the need for other investigators to directly interact with cumbersome raw imaging data (current study >300 Gb). Routine publication of such metadata would enable researchers to present complex neuroanatomical datasets in a standardized and transparent format that improves utility and reproducibility.

The promise of the connectomic approach is reflected by its widespread adoption and the continued refinement of connectome-tracing viral vectors (Osakada et al., 2011; McGovern et al., 2015; Kim et al., 2016; Reardon et al., 2016; Zingg et al., 2017), but tools that compile and quantify connectomic datasets remain primitive. The approach described here allows the quantification, standardization, and sharing of complete neuroanatomical datasets, and therefore provides a platform by which researchers may independently visualize, analyze, and compare each other's data. Bioinformatics at a single-cell resolution may allow researchers to move beyond the ball-and-stick diagrams often used to conceptualize the organization of spatially diffuse real-world neuronal networks (Rockland, 2015) and realize the full potential of novel connectomic technologies.

AUTHOR CONTRIBUTIONS

Conceptualization: SM, AG, and AA; Methodology: BD, RN, and SM; Software: JB; Formal analysis: SL, BD, AT, and SM; Investigation: BD, AT, SL, CM, and SM; Resources: RR, PB, RN, and JB; Data curation: SL, BD, and SM; Writing—Original Draft: BD, AG, and SM; Writing—Review and Editing: All authors; Visualization: BD and SM; Supervision: SM; Project Administration: SM; Funding Acquisition: SM, AA, and AG.

ACKNOWLEDGMENTS

The authors thank Sid Henriksen, Mark Wronkiewicz, and Rich Pang for their assistance in the preparation of the manuscript, Elsa Mardones for providing laboratory access and equipment, and Gergely Csucs, Dmitri Darine, and Maja Puchades for providing technical assistance and advice on the use of the tool for image anchoring. pSADΔG-mCherry genome plasmid (Addgene 32636), pcDNA-SADB19N (Addgene 32630), pcDNA-SADB19P (Addgene 32631), pcDNA-SADB19L (Addgene 32632), and pcDNA-SADB19G (Addgene 32633) plasmids and B7GG, EnvA-BHK and TVA-HEK cell lines were kindly provided by Professor Ed Callaway. This work was supported by grants from the Australian Research Council Discovery Scheme (DP120100920), the Australian National Health & Medical Research Council (APP1030301), The Human Brain Project through the European Union Seventh Framework Program (604102), the Norwegian Node of the International Neuroinformatics Coordinating Facility (INCF) and Macquarie University. BD thanks the Adam J Berry Memorial Fund, Australian Academy of Sciences, and NIH for their support.

SUPPLEMENTARY MATERIAL

The Supplementary Material for this article can be found online at: http://journal.frontiersin.org/article/10.3389/fncir.2017.00009/full#supplementary-material

Supplementary Image 1 | Segmentation of the RVLM in Waxholm space. **(A)** Experimental strategy: HSV vectors encoding GFP or mCherry were microinjected into the T2 or T10 spinal cord and **(B)** retrogradely transduced RVLM neurons (boxed area) were classified as C1 or non-C1; **(C)** shows examples of C1 neurons labeled from the T10 segment (open cyan arrowhead) and from both the T2 and T10 segments (closed white arrowhead). **(D)** Waxholm coordinates of 273 bulbospinal C1 neurons were plotted as 2d heat maps at each horizontal plane (detail in **D'**): the epicenter is indicated by crosshairs in the corresponding horizontal **(D)**, coronal **(E)**, and parasagittal **(F)** sections through the Waxholm MRI dataset. **(G–I)** Coordinates of individual bulbospinal C1 neurons (green spheres) and segmentation that enclosed 86% of neurons (green surface) plotted in 3d model of the Waxholm brain. Regional landmarks are the facial nerve (VII: red) and inferior olive (IO: orange).

Supplementary Image 2 | Retrograde transduction of spinally projecting neurons by HSV-hCMV-YTB. Coronal section at the level of the RVLM showing YFP expression in spinally projecting neurons 7 days after vector injection. Reporter expression was predominantly ipsilateral to the injection side; most transduced neurons were found in the RVLM, RVMM, and ventral raphe nuclei.

Supplementary Image 3 | Spatial distribution of rat rostral ventrolateral medulla (RVLM) input neurons identified in the current study (magenta,

plotted as distance from RVLM epicenter) compared to normalized nodal edge length distributions of reciprocal (blue) and non-reciprocal (black) nodes contained within the Allen Mouse Brain Connectivity Atlas. Mouse connectivity data adapted with permission from Henriksen et al. (2016).

Video 1 | Positions of C1 (yellow) and non-C1 (green) starter neurons in Waxholm space. Data shown first plotted on the Waxholm MRI volume, then in the Waxholm segmentation model, and finally (with monosynaptically connected input neurons, magenta), in the whole brain model.

Video 2 | Virtual flythrough showing the positions of monosynaptically connected input neurons colored according to cluster and projected onto the Waxholm MRI dataset. The video starts at the caudal end of the Waxholm MRI dataset, presented in the coronal plane, and flies in the rostral direction. The audio channel denotes the number of input neurons per section.

Table S1 | RVLM input neurons sorted according to Waxholm-defined region.

Table S2 | Key to cluster analysis and relevant literature. Abbreviations: A1, A1 noradrenergic group; BötC, Bötzinger Complex; C3, C3 adrenergic group; CPA, caudal pressor area; KF, Kolliker-Fuse; LHA, lateral hypothalamic area; MCPA, medullocervical pressor area; MPB/LPB, medial & lateral parabrachial nucleus; mRaphe, midline Raphe; NTS, nucleus of the solitary tract; Pe, perifornical hypothalamus; PiCo, postinspiratory complex; Pr, nucleus prepositus; preBötC, pre-Bötzinger Complex; PVN, paraventricular nucleus; Ramb, nucleus retroambiguus; RVLM, rostral ventrolateral medulla; RVMM, rostral ventromedial medulla; rVRG/cVRG, rostral & caudal ventral respiratory group; SC, superior colliculus; SubLC, sub-coeruleus; VL/LPAG, ventrolateral & lateral periaqueductal gray; vLTF/dLTF, ventral & dorsal lateral tegmental field; ZI, zona incerta.

Data Sheet 1 | Waxholm co-ordinates of entire dataset, segregated by experiment number and cell type (C1 or non-C1 starter neurons and input neurons).

Data Sheet 2 | Waxholm co-ordinates and Kmeans analysis of input neurons, segregated by cluster number.

REFERENCES

Allen, A. M. (2002). Inhibition of the hypothalamic paraventricular nucleus in spontaneously hypertensive rats dramatically reduces sympathetic vasomotor tone. *Hypertension* 39, 275–280. doi: 10.1161/hy0202.104272

Anderson, T. M., Garcia, A. J., Baertsch, N. A., Pollak, J., Bloom, J. C., Wei, A. D., et al. (2016). A novel excitatory network for the control of breathing. *Nature* 536, 76–80. doi: 10.1038/nature18944

Bou Farah, L., Bowman, B. R., Bokiniec, P., Karim, S., Le, S., Goodchild, A. K., et al. (2016). Somatostatin in the rat rostral ventrolateral medulla: origins and mechanism of action. *J. Comp. Neurol.* 524, 323–342. doi: 10.1002/cne.23846

Bowman, B. R., Kumar, N. N., Hassan, S. F., McMullan, S., and Goodchild, A. K. (2013). Brain sources of inhibitory input to the rat rostral ventrolateral medulla. *J. Comp. Neurol.* 521, 213–232. doi: 10.1002/cne.23175

Brennand, K. J., Simone, A., Jou, J., Gelboin-Burkhart, C., Tran, N., Sangar, S., et al. (2011). Modelling schizophrenia using human induced pluripotent stem cells. *Nature* 473, 221–225. doi: 10.1038/nature09915

Brown, D. L., and Guyenet, P. G. (1984). Cardiovascular neurons of brain stem with projections to spinal cord. *Am. J. Physiol.* 247, R1009–R1016.

Bullmore, E., and Sporns, O. (2012). The economy of brain network organization. *Nat. Rev. Neurosci.* 13, 336–349. doi: 10.1038/nrn3214

Burke, P. G., Abbott, S. B., McMullan, S., Goodchild, A. K., and Pilowsky, P. M. (2010). Somatostatin selectively ablates post-inspiratory activity after injection into the Botzinger complex. *Neuroscience* 167, 528–539. doi: 10.1016/j.neuroscience.2010.01.065

Burke, P. G., Neale, J., Korim, W. S., McMullan, S., and Goodchild, A. K. (2011). Patterning of somatosympathetic reflexes reveals nonuniform organization of presympathetic drive from C1 and non-C1 RVLM neurons. *Am. J. Physiol. Regul. Integr. Comp. Physiol.* 301:R1112. doi: 10.1152/ajpregu.00131.2011

Callaway, E. M., and Luo, L. (2015). Monosynaptic circuit tracing with glycoprotein-deleted rabies viruses. *J. Neurosci.* 35, 8979–8985. doi: 10.1523/JNEUROSCI.0409-15.2015

Carandini, M. (2012). From circuits to behavior: a bridge too far? *Nat. Neurosci.* 15, 507–509. doi: 10.1038/nn.3043

Card, J. P., Kobiler, O., McCambridge, J., Ebdlahad, S., Shan, Z., Raizada, M. K., et al. (2011). Microdissection of neural networks by conditional reporter expression from a Brainbow herpesvirus. *Proc. Natl. Acad. Sci. U.S.A.* 108, 3377–3382. doi: 10.1073/pnas.1015033108

Card, J. P., Sved, J. C., Craig, B., Raizada, M., Vazquez, J., and Sved, A. F. (2006). Efferent projections of rat rostroventrolateral medulla C1 catecholamine neurons: implications for the central control of cardiovascular regulation. *J. Comp. Neurol.* 499, 840–859. doi: 10.1002/cne.21140

Carrive, P., and Gorissen, M. (2008). Premotor sympathetic neurons of conditioned fear in the rat. *Eur. J. Neurosci.* 28, 428–446. doi: 10.1111/j.1460-9568.2008.06351.x

Cassell, M. D., and Gray, T. S. (1989). The amygdala directly innervates adrenergic (C1) neurons in the ventrolateral medulla in the rat. *Neurosci. Lett.* 97, 163–168. doi: 10.1016/0304-3940(89)90157-2

Coote, J. H. (2007). Landmarks in understanding the central nervous control of the cardiovascular system. *Exp. Physiol.* 92, 3–18. doi: 10.1113/expphysiol.2006.035378

Csucs, G., and Bjaalie, J. G. (2015). *CutNII for Waxholm Space Atlas of the Sprague Dawley Rat Brain*. INCF Software Center. Available online at: https://www.nitrc.org/frs/shownotes.php?release_id=3396

Dampney, R. A. (1994a). Functional organization of central pathways regulating the cardiovascular system. *Physiol. Rev.* 74, 323–364.

Dampney, R. A. (1994b). The subretrofacial vasomotor nucleus: anatomical, chemical and pharmacological properties and role in cardiovascular regulation. *Prog. Neurobiol.* 42, 197–227. doi: 10.1016/0301-0082(94)90064-7

Dampney, R. A. (2015). Central mechanisms regulating coordinated cardiovascular and respiratory function during stress and arousal. *Am. J. Physiol. Regul. Integr. Comp. Physiol.* 309, R429–R443. doi: 10.1152/ajpregu.00051.2015

Dampney, R. A., Czachurski, J., Dembowsky, K., Goodchild, A. K., and Seller, H. (1987). Afferent connections and spinal projections of the pressor region in the rostral ventrolateral medulla of the cat. *J. Auton. Nerv. Syst.* 20, 73–86. doi: 10.1016/0165-1838(87)90083-X

Dayas, C. V., Buller, K. M., Crane, J. W., Xu, Y., and Day, T. A. (2001). Stressor categorization: acute physical and psychological stressors elicit distinctive recruitment patterns in the amygdala and in medullary noradrenergic cell groups. *Eur. J. Neurosci.* 14, 1143–1152. doi: 10.1046/j.0953-816x.2001.01733.x

Denk, W., Briggman, K. L., and Helmstaedter, M. (2012). Structural neurobiology: missing link to a mechanistic understanding of neural computation. *Nat. Rev. Neurosci.* 13, 351–358. doi: 10.1038/nrn3169

Descarries, L., and Mechawar, N. (2000). Ultrastructural evidence for diffuse transmission by monoamine and acetylcholine neurons of the central nervous system. *Prog. Brain Res.* 125, 27–47. doi: 10.1016/S0079-6123(00)25005-X

Dum, R. P., Levinthal, D. J., and Strick, P. L. (2016). Motor, cognitive, and affective areas of the cerebral cortex influence the adrenal medulla. *Proc. Natl. Acad. Sci. U.S.A.* 113, 9922–9927. doi: 10.1073/pnas.1605044113

Ezure, K., Tanaka, I., and Kondo, M. (2003). Glycine is used as a transmitter by decrementing expiratory neurons of the ventrolateral medulla in the rat. *J. Neurosci.* 23, 8941–8948.

Furlong, T. M., McDowall, L. M., Horiuchi, J., Polson, J. W., and Dampney, R. A. (2014). The effect of air puff stress on c-Fos expression in rat hypothalamus and brainstem: central circuitry mediating sympathoexcitation and baroreflex resetting. *Eur. J. Neurosci.* 39, 1429–1438. doi: 10.1111/ejn.12521

Gelsema, A. J., Agarwal, S. K., and Calaresu, F. R. (1989). Cardiovascular responses and changes in neural activity in the rostral ventrolateral medulla elicited by electrical stimulation of the amygdala of the rat. *J. Auton. Nerv. Syst.* 27, 91–100. doi: 10.1016/0165-1838(89)90091-X

Goodchild, A. K., and Moon, E. A. (2009). Maps of cardiovascular and respiratory regions of rat ventral medulla: focus on the caudal medulla. *J. Chem. Neuroanat.* 38, 209–221. doi: 10.1016/j.jchemneu.2009.06.002

Gray, P. A., Janczewski, W. A., Mellen, N., McCrimmon, D. R., and Feldman, J. L. (2001). Normal breathing requires preBotzinger complex neurokinin-1 receptor-expressing neurons. *Nat. Neurosci.* 4, 927–930. doi: 10.1038/nn0901-927

Guyenet, P. G. (2006). The sympathetic control of blood pressure. *Nat. Rev. Neurosci.* 7, 335–346. doi: 10.1038/nrn1902

Guyenet, P. G., Darnall, R. A., and Riley, T. A. (1990). Rostral ventrolateral medulla and sympathorespiratory integration in rats. *Am. J. Physiol.* 259, R1063–R1074.

Guyenet, P. G., Stornetta, R. L., Bochorishvili, G., Depuy, S. D., Burke, P. G., and Abbott, S. B. (2013). C1 neurons: the body's EMTs. *Am. J. Physiol. Regul. Integr. Comp. Physiol.* 305, R187–R204. doi: 10.1152/ajpregu.00054.2013

Guyenet, P. G., and Wang, H. (2001). Pre-Botzinger neurons with preinspiratory discharges "*in vivo*" express NK1 receptors in the rat. *J. Neurophysiol.* 86, 438–446.

Häbler, H. J., Janig, W., and Michaelis, M. (1994). Respiratory modulation in the activity of sympathetic neurones. *Prog. Neurobiol.* 43, 567–606. doi: 10.1016/0301-0082(94)90053-1

Haselton, J. R., and Guyenet, P. G. (1989). Central respiratory modulation of medullary sympathoexcitatory neurons in rat. *Am. J. Physiol.* 256, R739–R750.

Henriksen, S., Pang, R., and Wronkiewicz, M. (2016). A simple generative model of the mouse mesoscale connectome. *eLife* 5:e12366. doi: 10.7554/eLife.12366

Horiuchi, J., McAllen, R. M., Allen, A. M., Killinger, S., Fontes, M. A., and Dampney, R. A. (2004). Descending vasomotor pathways from the dorsomedial hypothalamic nucleus: role of medullary raphe and RVLM. *Am. J. Physiol. Regul. Integr. Comp. Physiol.* 287, R824–R832. doi: 10.1152/ajpregu.00221.2004

Kelly, R. M., and Strick, P. L. (2000). Rabies as a transneuronal tracer of circuits in the central nervous system. *J. Neurosci. Methods* 103, 63–71. doi: 10.1016/S0165-0270(00)00296-X

Kim, E. J., Jacobs, M. W., Ito-Cole, T., and Callaway, E. M. (2016). Improved monosynaptic neural circuit tracing using engineered rabies virus glycoproteins. *Cell Rep.* 15, 692–699. doi: 10.1016/j.celrep.2016.03.067

Kjonigsen, L. J., Lillehaug, S., Bjaalie, J. G., Witter, M. P., and Leergaard, T. B. (2015). Waxholm Space atlas of the rat brain hippocampal region: three-dimensional delineations based on magnetic resonance and diffusion tensor imaging. *Neuroimage* 108, 441–449. doi: 10.1016/j.neuroimage.2014.12.080

Korim, W. S., Bou Farah, L., McMullan, S., and Verberne, A. J. (2014). Orexinergic activation of medullary premotor neurons modulates the adrenal sympathoexcitation to hypothalamic glucoprivation. *Diabetes* 63, 1895–1906. doi: 10.2337/db13-1073

Korim, W. S., Egwuenu, E., Fong, A. Y., McMullan, S., Cravo, S. L., and Pilowsky, P. M. (2012). Noxious somatic stimuli diminish respiratory-sympathetic coupling by selective resetting of the respiratory rhythm in anaesthetized rats. *Exp. Physiol.* 97, 1093–1104. doi: 10.1113/expphysiol.2012.066365

Le, S., Turner, A. J., Parker, L. M., Burke, P. G., Kumar, N. N., Goodchild, A. K., et al. (2016). Somatostatin 2a receptors are not expressed on functionally identified respiratory neurons in the ventral respiratory column of the rat. *J. Comp. Neurol.* 524, 1384–1398. doi: 10.1002/cne.23912

Lichtman, J. W., and Denk, W. (2011). The big and the small: challenges of imaging the brain's circuits. *Science* 334, 618–623. doi: 10.1126/science.1209168

Lipski, J., Kanjhan, R., Kruszewska, B., and Rong, W. (1996). Properties of presympathetic neurones in the rostral ventrolateral medulla in the rat: an intracellular study "*in vivo*". *J. Physiol.* 490, 729–744. doi: 10.1113/jphysiol.1996.sp021181

Lipski, J., Kanjhan, R., Kruszewska, B., and Smith, M. (1995). Barosensitive neurons in the rostral ventrolateral medulla of the rat *in vivo*: morphological properties and relationship to C1 adrenergic neurons. *Neuroscience* 69, 601–618. doi: 10.1016/0306-4522(95)92652-Z

Madden, C. J., Stocker, S. D., and Sved, A. F. (2006). Attenuation of homeostatic responses to hypotension and glucoprivation after destruction of catecholaminergic rostral ventrolateral medulla (RVLM) neurons. *Am. J. Physiol. Regul. Integr. Comp. Physiol.* 291, R751–R759. doi: 10.1152/ajpregu.00800.2005

McAllen, R. M. (1987). Central respiratory modulation of subretrofacial bulbospinal neurones in the cat. *J. Physiol.* 388, 533–545. doi: 10.1113/jphysiol.1987.sp016630

McCrea, R. A. (1988). Neuroanatomy of the oculomotor system. The nucleus prepositus. *Rev. Oculomot. Res.* 2, 203–223.

McGovern, A. E., Davis-Poynter, N., Rakoczy, J., Phipps, S., Simmons, D. G., and Mazzone, S. B. (2012). Anterograde neuronal circuit tracing using a genetically modified herpes simplex virus expressing EGFP. *J. Neurosci. Methods* 209, 158–167. doi: 10.1016/j.jneumeth.2012.05.035

McGovern, A. E., Driessen, A. K., Simmons, D. G., Powell, J., Davis-Poynter, N., Farrell, M. J., et al. (2015). Distinct brainstem and forebrain circuits receiving tracheal sensory neuron inputs revealed using a novel conditional anterograde transsynaptic viral tracing system. *J. Neurosci.* 35, 7041–7055. doi: 10.1523/JNEUROSCI.5128-14.2015

McMullan, S., Pathmanandavel, K., Pilowsky, P. M., and Goodchild, A. K. (2008). Somatic nerve stimulation evokes qualitatively different somatosympathetic responses in the cervical and splanchnic sympathetic nerves in the rat. *Brain Res.* 1217, 139–147. doi: 10.1016/j.brainres.2008.04.034

McMullan, S., and Pilowsky, P. M. (2012). Sympathetic premotor neurones project to and are influenced by neurones in the contralateral rostral ventrolateral medulla of the rat *in vivo*. *Brain Res.* 1439, 34–43. doi: 10.1016/j.brainres.2011.12.058

Mitra, P. P. (2014). The circuit architecture of whole brains at the mesoscopic scale. *Neuron* 83, 1273–1283. doi: 10.1016/j.neuron.2014.08.055

Miyawaki, T., Pilowsky, P., Sun, Q. J., Minson, J., Suzuki, S., Arnolda, L., et al. (1995). Central inspiration increases barosensitivity of neurons in rat rostral ventrolateral medulla. *Am. J. Physiol.* 268, R909–R918.

Moraes, D. J. A., Dias, M. B., Cavalcanti-Kwiatkoski, R., Machado, B. H., and Zoccal, D. B. (2012). Contribution of the retrotrapezoid nucleus/parafacial respiratory region to the expiratory-sympathetic coupling in response to peripheral chemoreflex in rats. *J. Neurophysiol.* 108, 882–890. doi: 10.1152/jn.00193.2012

Moraes, D. J., Da Silva, M. P., Bonagamba, L. G., Mecawi, A. S., Zoccal, D. B., Antunes-Rodrigues, J., et al. (2013). Electrophysiological properties of rostral ventrolateral medulla presympathetic neurons modulated by the respiratory network in rats. *J. Neurosci.* 33, 19223–19237. doi: 10.1523/JNEUROSCI.3041-13.2013

Murphy, S. M., Pilowsky, P. M., Sun, Q. J., and Llewellyn-Smith, I. J. (1995). Thyrotropin-releasing hormone-immunoreactive varicosities synapse on rat phrenic motoneurons. *J. Comp. Neurol.* 359, 310–322. doi: 10.1002/cne.903590209

Nassi, J. J., Cepko, C. L., Born, R. T., and Beier, K. T. (2015). Neuroanatomy goes viral! *Front. Neuroanat.* 9:80. doi: 10.3389/fnana.2015.00080

Oh, S. W., Harris, J. A., Ng, L., Winslow, B., Cain, N., Mihalas, S., et al. (2014). A mesoscale connectome of the mouse brain. *Nature* 508, 207–214. doi: 10.1038/nature13186

Osakada, F., and Callaway, E. M. (2013). Design and generation of recombinant rabies virus vectors. *Nat. Protoc.* 8, 1583–1601. doi: 10.1038/nprot.2013.094

Osakada, F., Mori, T., Cetin, A. H., Marshel, J. H., Virgen, B., and Callaway, E. M. (2011). New rabies virus variants for monitoring and manipulating activity and gene expression in defined neural circuits. *Neuron* 71, 617–631. doi: 10.1016/j.neuron.2011.07.005

Papp, E. A., Csucs, G., and Bjaalie, J. G. (2015). "Sprague Dawley Atlas v2 bundle", in *Waxholm Space Atlas of the Sprague Dawley Rat Brain* (INCF Software Center: The International Neuroinformatics Coordinating Facility). Available online at: https://www.nitrc.org/projects/whs-sd-atlas/

Papp, E. A., Leergaard, T. B., Calabrese, E., Johnson, G. A., and Bjaalie, J. G. (2014). Waxholm Space atlas of the Sprague Dawley rat brain. *Neuroimage* 97, 374–386. doi: 10.1016/j.neuroimage.2014.04.001

Papp, E. A., Leergaard, T. B., Csucs, G., and Bjaalie, J. G. (2016). Brain-wide mapping of axonal connections: workflow for automated detection and spatial analysis of labeling in microscopic sections. *Front. Neuroinform.* 10:11. doi: 10.3389/fninf.2016.00011

Pilowsky, P., Arnolda, L., Chalmers, J., Llewellyn-Smith, I., Minson, J., Miyawaki, T., et al. (1996). Respiratory inputs to central cardiovascular neurons. *Ann. N.Y. Acad. Sci.* 783, 64–70. doi: 10.1111/j.1749-6632.1996.tb26707.x

Pilowsky, P. M., and Goodchild, A. K. (2002). Baroreceptor reflex pathways and neurotransmitters: 10 years on. *J. Hypertens.* 20, 1675–1688. doi: 10.1097/00004872-200209000-00002

Pollak Dorocic, I., Fürth, D., Xuan, Y., Johansson, Y., Pozzi, L., Silberberg, G., et al. (2014). A whole-brain atlas of inputs to serotonergic neurons of the dorsal and median raphe nuclei. *Neuron* 83, 663–678. doi: 10.1016/j.neuron.2014.07.002

Pollock, J. D., Wu, D. Y., and Satterlee, J. S. (2014). Molecular neuroanatomy: a generation of progress. *Trends Neurosci.* 37, 106–123. doi: 10.1016/j.tins.2013.11.001

Reardon, T. R., Murray, A. J., Turi, G. F., Wirblich, C., Croce, K. R., Schnell, M. J., et al. (2016). Rabies virus CVS-N2c(ΔG) strain enhances retrograde synaptic transfer and neuronal viability. *Neuron* 89, 711–724. doi: 10.1016/j.neuron.2016.01.004

Rinaman, L., and Schwartz, G. (2004). Anterograde transneuronal viral tracing of central viscerosensory pathways in rats. *J. Neurosci.* 24, 2782–2786. doi: 10.1523/JNEUROSCI.5329-03.2004

Rockland, K. S. (2015). About connections. *Front. Neuroanat.* 9:61. doi: 10.3389/fnana.2015.00061

Saha, S. (2005). Role of the central nucleus of the amygdala in the control of blood pressure: descending pathways to medullary cardiovascular nuclei. *Clin. Exp. Pharmacol. Physiol.* 32, 450–456. doi: 10.1111/j.1440-1681.2005.04210.x

Schreihofer, A. M., and Guyenet, P. G. (1997). Identification of C1 presympathetic neurons in rat rostral ventrolateral medulla by juxtacellular labeling *in vivo*. *J. Comp. Neurol.* 387, 524–536. doi: 10.1002/(SICI)1096-9861(19971103)387:4<524::AID-CNE4>3.0.CO;2-4

Schreihofer, A. M., and Guyenet, P. G. (2000). Sympathetic reflexes after depletion of bulbospinal catecholaminergic neurons with anti-DbetaH-saporin. *Am. J. Physiol. Regul. Integr. Comp. Physiol.* 279, R729–R742.

Schreihofer, A. M., Stornetta, R. L., and Guyenet, P. G. (1999). Evidence for glycinergic respiratory neurons: botzinger neurons express mRNA for glycinergic transporter 2. *J. Comp. Neurol.* 407, 583–597. doi: 10.1002/(SICI)1096-9861(19990517)407:4<583::AID-CNE8>3.0.CO;2-E

Schreihofer, A. M., Stornetta, R. L., and Guyenet, P. G. (2000). Regulation of sympathetic tone and arterial pressure by rostral ventrolateral medulla after depletion of C1 cells in rat. *J. Physiol.* 529(Pt 1), 221–236. doi: 10.1111/j.1469-7793.2000.00221.x

Schwarz, L. A., Miyamichi, K., Gao, X. J., Beier, K. T., Weissbourd, B., Deloach, K. E., et al. (2015). Viral-genetic tracing of the input-output organization of a central noradrenaline circuit. *Nature* 524, 88–92. doi: 10.1038/nature14600

Stanek, E., IV, Cheng, S., Takatoh, J., Han, B.-X., and Wang, F. (2014). Monosynaptic premotor circuit tracing reveals neural substrates for oro-motor coordination. *Elife.* 3:e02511 doi: 10.7554/elife.02511

Stornetta, R. L. (2009). Neurochemistry of bulbospinal presympathetic neurons of the medulla oblongata. *J. Chem. Neuroanat.* 38, 222–230. doi: 10.1016/j.jchemneu.2009.07.005

Stornetta, R. L., Inglis, M. A., Viar, K. E., and Guyenet, P. G. (2016). Afferent and efferent connections of C1 cells with spinal cord or hypothalamic projections in mice. *Brain Struct. Funct.* 221, 4027–4044. doi: 10.1007/s00429-015-1143-3

Stornetta, R. L., Moreira, T. S., Takakura, A. C., Kang, B. J., Chang, D. A., West, G. H., et al. (2006). Expression of Phox2b by brainstem neurons involved in chemosensory integration in the adult rat. *J. Neurosci.* 26, 10305–10314. doi: 10.1523/JNEUROSCI.2917-06.2006

Stornetta, R. L., Rosin, D. L., Wang, H., Sevigny, C. P., Weston, M. C., and Guyenet, P. G. (2003). A group of glutamatergic interneurons expressing high levels of both neurokinin-1 receptors and somatostatin identifies the region of the pre-Botzinger complex. *J. Comp. Neurol.* 455, 499–512. doi: 10.1002/cne.10504

Stornetta, R. L., Schreihofer, A. M., Pelaez, N. M., Sevigny, C. P., and Guyenet, P. G. (2001). Preproenkephalin mRNA is expressed by C1 and non-C1 barosensitive bulbospinal neurons in the rostral ventrolateral medulla of the rat. *J. Comp. Neurol.* 435, 111–126. doi: 10.1002/cne.1196

Strack, A. M., Sawyer, W. B., Platt, K. B., and Loewy, A. D. (1989). CNS cell groups regulating the sympathetic outflow to adrenal gland as revealed by transneuronal cell body labeling with pseudorabies virus. *Brain Res.* 491, 274–296. doi: 10.1016/0006-8993(89)90063-2

Sun, Q. J., Minson, J., Llewellyn-Smith, I. J., Arnolda, L., Chalmers, J., and Pilowsky, P. (1997). Botzinger neurons project towards bulbospinal neurons in the rostral ventrolateral medulla of the rat. *J. Comp. Neurol.* 388, 23–31. doi: 10.1002/(SICI)1096-9861(19971110)388:1<23::AID-CNE2>3.0.CO;2-Q

Talman, W. T., and Robertson, S. C. (1991). Nucleus prepositus hypoglossi. A medullary pressor region. *Hypertension* 17, 1173–1176. doi: 10.1161/01.HYP.17.6.1173

Taylor, E. W., Jordan, D., and Coote, J. H. (1999). Central control of the cardiovascular and respiratory systems and their interactions in vertebrates. *Physiol. Rev.* 79, 855–916.

Thorndike, R. L. (1953). Who belongs in the family? *Psychometrika* 18, 267–276. doi: 10.1007/BF02289263

Turner, A., Kumar, N., Farnham, M., Lung, M., Pilowsky, P., and McMullan, S. (2013). Rostroventrolateral medulla neurons with commissural projections provide input to sympathetic premotor neurons: anatomical and functional evidence. *Eur. J. Neurosci.* 38, 2504–2515. doi: 10.1111/ejn.12232

Ugolini, G. (1995). Specificity of rabies virus as a transneuronal tracer of motor networks: transfer from hypoglossal motoneurons to connected second-order and higher order central nervous system cell groups. *J. Comp. Neurol.* 356, 457–480. doi: 10.1002/cne.903560312

Verberne, A. J. (1996). Medullary sympathoexcitatory neurons are inhibited by activation of the medial prefrontal cortex in the rat. *Am. J. Physiol.* 270, R713–R719.

Verberne, A. J., Stornetta, R. L., and Guyenet, P. G. (1999). Properties of C1 and other ventrolateral medullary neurones with hypothalamic projections in the rat. *J. Physiol.* 517(Pt 2), 477–494. doi: 10.1111/j.1469-7793.1999.0477t.x

Wanner, A. A., Kirschmann, M. A., and Genoud, C. (2015). Challenges of microtome-based serial block-face scanning electron microscopy in neuroscience. *J. Microsc.* 259, 137–142. doi: 10.1111/jmi.12244

Wertz, A., Trenholm, S., Yonehara, K., Hillier, D., Raics, Z., Leinweber, M., et al. (2015). PRESYNAPTIC NETWORKS. Single-cell-initiated monosynaptic tracing reveals layer-specific cortical network modules. *Science* 349, 70–74. doi: 10.1126/science.aab1687

Wickersham, I. R., Finke, S., Conzelmann, K. K., and Callaway, E. M. (2007a). Retrograde neuronal tracing with a deletion-mutant rabies virus. *Nat. Methods* 4, 47–49. doi: 10.1038/nmeth999

Wickersham, I. R., Lyon, D. C., Barnard, R. J., Mori, T., Finke, S., Conzelmann, K. K., et al. (2007b). Monosynaptic restriction of transsynaptic tracing from single, genetically targeted neurons. *Neuron* 53, 639–647. doi: 10.1016/j.neuron.2007.01.033

Wojaczynski, G. J., Engel, E. A., Steren, K. E., Enquist, L. W., and Patrick Card, J. (2015). The neuroinvasive profiles of H129 (herpes simplex virus type 1) recombinants with putative anterograde-only transneuronal spread properties. *Brain Struct. Funct.* 220, 1395–1420. doi: 10.1007/s00429-014-0733-9

Yang, Z., and Coote, J. H. (1998). Influence of the hypothalamic paraventricular nucleus on cardiovascular neurones in the rostral ventrolateral medulla of the rat. *J. Physiol.* 513(Pt 2), 521–530. doi: 10.1111/j.1469-7793.1998.521bb.x

Yonehara, K., Farrow, K., Ghanem, A., Hillier, D., Balint, K., Teixeira, M., et al. (2013). The first stage of cardinal direction selectivity is localized to the dendrites of retinal ganglion cells. *Neuron* 79, 1078–1085. doi: 10.1016/j.neuron.2013.08.005

Zingg, B., Chou, X.-l., Zhang, Z.-g., Mesik, L., Liang, F., Tao, H. W., et al. (2017). AAV-mediated anterograde transsynaptic tagging: mapping corticocollicular input-defined neural pathways for defense behaviors. *Neuron* 93, 33–47. doi: 10.1016/j.neuron.2016.11.045

Zoccal, D. B., Furuya, W. I., Bassi, M., Colombari, D. S. A., and Colombari, E. (2014). The nucleus of the solitary tract and the coordination of respiratory and sympathetic activities. *Front. Physiol.* 5:238. doi: 10.3389/fphys.2014.00238

Conflict of Interest Statement: The authors declare that the research was conducted in the absence of any commercial or financial relationships that could be construed as a potential conflict of interest.

Copyright © 2017 Dempsey, Le, Turner, Bokiniec, Ramadas, Bjaalie, Menuet, Neve, Allen, Goodchild and McMullan. This is an open-access article distributed under the terms of the Creative Commons Attribution License (CC BY). The use, distribution or reproduction in other forums is permitted, provided the original author(s) or licensor are credited and that the original publication in this journal is cited, in accordance with accepted academic practice. No use, distribution or reproduction is permitted which does not comply with these terms.

frontiers in Neuroscience

ORIGINAL RESEARCH
published: 07 March 2017
doi: 10.3389/fnins.2017.00088

Evaluation of the Cortical Silent Period of the Laryngeal Motor Cortex in Healthy Individuals

*Mo Chen[1], Rebekah L. S. Summers[1], George S. Goding[2], Sharyl Samargia[3], Christy L. Ludlow[4], Cecília N. Prudente[1] and Teresa J. Kimberley[1]**

[1] Divisions of Physical Therapy and Rehabilitation Science, Department of Rehabilitation Medicine, School of Medicine, University of Minnesota, Minneapolis, MN, USA, [2] Department of Otolaryngology-Head and Neck Surgery, University of Minnesota, Minneapolis, MN, USA, [3] Department of Communication Sciences and Disorders, University of Wisconsin River Falls Campus, River Falls, WI, USA, [4] Department of Communication Sciences and Disorders, James Madison University, Harrisonburg, VA, USA

Objective: This work aimed to evaluate the cortical silent period (cSP) of the laryngeal motor cortex (LMC) using the bilateral thyroarytenoid (TA) muscles with transcranial magnetic stimulation (TMS).

Methods: In 11 healthy participants, fine-wire electromyography (EMG) was used to record bilateral TA muscle responses to single pulse TMS delivered to the LMC in both hemispheres. Peripheral responses to stimulation over the mastoid, where the vagus nerve exits the skull, were collected to verify the central origin of the cortical stimulation responses by comparing the latencies.

Results: The cSP duration ranged from 41.7 to 66.4 ms. The peripherally evoked motor-evoked potential (MEP) peak occurred 5–9 ms earlier than the cortical responses (for both sides of TAs: $p < 0.0001$) with no silent period. The right TA MEP latencies were earlier than the left TA responses for both peripheral and cortical measures ($p \leq 0.0001$).

Conclusion: These findings demonstrate the feasibility of measuring cSP of LMC based on intrinsic laryngeal muscles responses during vocalization in healthy volunteers.

Significance: The technique could be used to study the pathophysiology of neurological disorders that affect TA muscles, such as spasmodic dysphonia. Further, the methodology has application to other muscles of the head and neck not accessible using surface electrodes.

Keywords: Transcranial magnetic stimulation, TMS, larynx, motor cortex excitability, fine wire electrode, cortical silent period, cSP

OPEN ACCESS

Edited by:
Mikhail Lebedev, Duke University, USA

Reviewed by:
Sean Kevin Meehan, University of Michigan, USA
Jason L. Neva, University of British Columbia, Canada

****Correspondence:***
Teresa J. Kimberley
tjk@umn.edu

Specialty section:
This article was submitted to Neural Technology, a section of the journal Frontiers in Neuroscience

Received: *31 October 2016*
Accepted: *10 February 2017*
Published: *07 March 2017*

Citation:
Chen M, Summers RLS, Goding GS, Samargia S, Ludlow CL, Prudente CN and Kimberley TJ (2017) Evaluation of the Cortical Silent Period of the Laryngeal Motor Cortex in Healthy Individuals. Front. Neurosci. 11:88. doi: 10.3389/fnins.2017.00088

INTRODUCTION

The laryngeal motor cortex (LMC) plays a significant role in human voice and speech production (Henriquez et al., 2007; Simonyan et al., 2009; Ludlow, 2015). However, its functional organization and interactions with other brain regions in both healthy humans and patients with neurological voice and speech disorders warrants further investigation (Simonyan and Horwitz, 2011). Specifically, for example, it is unknown how neurotransmitters, such as dopamine and gamma-aminobutyric acid (GABA) influence and modulate the human LMC network during voice and

speech production and how these neurotransmitters are altered in people with neurological voice and speech disorders. This information is crucial in identifying the target brain regions for the development of new neuropharmacological options to modulate the LMC activity in patients with neurological voice problems, such as spasmodic dysphonia (Ludlow et al., 2008).

Transcranial magnetic stimulation (TMS) provides an important non-invasive way to evaluate the corticospinal excitability in a wide range of healthy and disease populations (for review: Eldaief et al., 2013). If the TMS stimulus is delivered to the motor cortex, a response in the peripheral muscles can be measured using electromyography (EMG). The response is defined as a motor-evoked potential (MEP). By assessing the MEPs induced by single or paired pulse techniques, TMS can be used to evaluate different aspects of cortical excitability, e.g., motor threshold, MEP latency and amplitude, and the cortical silent period (cSP) (Hallett, 2007).

Among these excitability measures, cSP is a widely adopted and highly reliable way to evaluate motor cortex excitability and its responses to neuromodulation (Wolters et al., 2008; Chen et al., 2015). Since the first reported cSP evoked by TMS (Calancie et al., 1987), cSP has been studied extensively in physiological and pathological conditions. Currently, it is thought that the cSP reflects intracortical inhibitory process mediated by $GABA_A$ (Paulus et al., 2008) and $GABA_B$ receptors (Wolters et al., 2008). This unique feature makes the cSP a powerful tool to non-invasively probe the GABA receptor mediated intracortical inhibitory process, especially in people with pathological conditions, such as dystonia (Siebner et al., 1998). Significantly shorter cSP has been reported in hand muscles in people with focal hand dystonia (Tinazzi et al., 2005; Kimberley et al., 2009), facial muscles in people with cranial dystonia (Currà et al., 2000) and hand muscles in people with spasmodic dysphonia (Samargia et al., 2014). Thus, cSP has the potential to reveal the abnormal inhibition in neurological disorders and may serve as a biomarker to help with diagnosis and early intervention.

Testing of the cSP can be performed by applying a single suprathreshold TMS pulse to the motor cortical representation of a tonically preactivated target muscle, producing a period of EMG silence in contralateral target muscles (Wolters et al., 2008). The hand region of the motor cortex has been the primary location of cSP testing due to the ease of accessing the corresponding muscles, such as first dorsal interosseous (FDI) or abductor pollicis brevis. The EMG signal from these peripheral muscles is large in amplitude with sufficient latency from the TMS pulse to make it easily identifiable and unaffected by TMS artifact. Furthermore, these muscles are easily accessible with surface electrodes which summate MEPs from a large number of motor units, making the EMG signal less sensitive to noise or the firing of individual motor unit. However, in order to evaluate the cSP from the deep muscles (i.e., the intrinsic laryngeal muscles in people with spasmodic dysphonia), intramuscular electrodes, i.e., fine-wire or needle electrodes, must be used. Signals from intramuscular electrodes are more difficult to assess than surface electrodes (Konrad, 2005). Reasons for the difficulties are as follows: (1) Electrode placement is technically difficult. (2) The position of the two fine-wire electrodes cannot be altered once inserted. If the initial insertion is not accurate another insertion is required; and (3) Fine-wire or needle electrodes summate evoked potentials from fewer motor units than surface electrodes, reducing the MEP amplitude and making it difficult to differentiate the MEP from spontaneous firing of intrinsic motor units. A challenge specific to measurements from the LMC is that the EMG electrode location is close to the stimulation site, which results in a large stimulus artifact. When the stimulation artifact is lengthened due to amplifier saturation, it is difficult to identify MEPs with early latencies. Finally, the LMC brain representation is relatively small compared to regions, such as the hand and, therefore, stimulation location may be challenging to locate.

Overcoming these difficulties, several groups have studied the MEP responses to TMS over the LMC. MEP latency and amplitude values from the cricopharyngeal sphincter muscles during cortical stimulation have been reported (Ertekin et al., 2001); single pulse responses from the cricothyroid muscles were also reported (Espadaler et al., 2012; Rogić Vidaković et al., 2015). Another laryngeal intrinsic muscle, the thyroarytenoid (TA), which directly controls the vocal folds by modulating vocal-fold tension when opposed by other intrinsic muscles, is highly relevant for the pathophysiology of speech related neurological disorders, i.e., spasmodic dysphonia and voice tremor (Ludlow, 2005; Simonyan et al., 2009; Simonyan and Horwitz, 2011). However, the TA muscle has only been used to evaluate the latency of MEPs during cortical stimulation to LMC (Khedr and Aref, 2002; Rödel et al., 2004). These latencies were relatively early ($\leq$10 ms) and some were close to TA latencies found with peripheral stimulation over the mastoid (Sims et al., 1996). Moreover, the excitability of the LMC as measured by cSP in TA muscles has not been investigated. Considering that investigation of the excitability of corticobulbar projections to the TA would be relevant for understanding the neural controls of voice production in both healthy and pathological conditions, the purpose of the current study was to assess the excitability of the LMC by measuring the cSP in the TA muscles. The use of TMS with fine-wire electrodes to measure the cSP of the LMC will provide a tool to evaluate the GABA receptor mediated inhibition process. This will further lead to a better understanding of the pathophysiology of disorders of the larynx i.e., spasmodic dysphonia and voice tremor.

METHODS

Participants

Data from eleven healthy participants (mean age, 54 $\pm$ 7.4 years; 3 females) were collected. Participants gave written, informed consent prior to participation according to the Declaration of Helsinki (World Medical Association, 2013). The study was approved by the Clinical and Translational Science Institute and the Institutional Review Board of the University of Minnesota.

Devices

Transcranial magnetic stimulation (TMS) pulses were delivered using a 70 mm figure-of-eight coil connected to the Bistim^2 and 200^2 stimulator set (The Magstim Company Ltd, UK). Two pairs

of fine-wire electrodes were connected to two bi-polar active pre-amps (Y03-002, Motion Lab Systems, Inc., Baton Rouge, LA) powered by two 9-volt batteries. EMG signals were amplified with a gain of x300, passed through a band-pass filter (15–2000 Hz), and digitized by a 24-bit analog-to-digital converter (NI9234, National Instruments Co., Austin, TX) in AC coupling mode (0.5 Hz) with the sampling rate of 6.4 k Hz. All data were collected and stored using a custom data acquisition program written with LabVIEW (V2012, National Instruments, Austin, TX) on a laptop computer (Latitude, Dell Co., Ltd, Round Rock, TX) which was also used to monitor real-time EMG activity.

Experiment Procedures

Participants were seated comfortably in a reclined armchair with the subject tracker band of a frameless stereotactic neuronavigation system (BrainSight, Rogue Research Inc., Canada) attached to their forehead. The hand region was assessed prior to the laryngeal area.

Hand Region Assessment

Hand region excitability was evaluated by using surface electrodes (6030-TP, Nicolet, CA, USA) attached to right hand FDI muscle. The experiment procedure was the same as previously published protocols (Chen et al., 2015; Rossini et al., 2015). Briefly, the resting motor threshold was determined as the lowest intensity that generated MEPs with the peak-to-peak amplitude $>50\ \mu V$ in 5 out of 10 consecutive trials. The hotspot was the location of the coil where the resting motor threshold was determined. The 1-mV threshold was determined by using a similar protocol with the MEP amplitude response ≥ 1 mV. The 1-mV threshold intensity was used as the initial stimulation intensity for the LMC assessment.

Laryngeal Region Assessment

Skin preparation

Skin around the area of the laryngeal prominence was cleaned using alcohol wipes. A topical anesthetic cream (LMX 4% Lidocaine, Ferndale Laboratories, Inc., Ferndale, MI) was applied to the cleaned area. After approximately 15 min, a numbing agent (Xylocaine, 2% lidocaine HCL and epinephrine, 1:100,000, Professional Veterinary Laboratories, NB, Canada) was injected into the skin of the numbed region.

Electrodes placement

A 30 mm, 27 gauge needle loaded with a pair of fine-wire hooked electrodes (#019-772800, Nicolet Co., Middleton, WI) was inserted into left and right TA muscle by an experienced otolaryngologist following standard procedures for laryngeal EMG (Hirano and Ohala, 1969). Using a percutaneous approach, the needle was passed through the cricothyroid membrane at an angle off midline but medial to the ipsilateral inferior tubercle, to directly enter the TA muscle while avoiding the airway. During insertion, the electrodes were connected to an audio monitor (Grass AM10, Natus Medical Incorporated Co., San Carlos, CA) to allow monitoring of muscle activity in real-time. After the location was confirmed, the needle was removed leaving the fine-wires in the TA muscles (**Figure 1A**). A silver-silver chloride strap with a Velcro fastener (TD-431, Discount Disposables, St. Albans, VT) was attached to the participant's forehead serving as a ground (**Figure 1B**).

Peripheral stimulation

Peripheral stimulation was delivered over the mastoid to: (1) confirm electrode placement in the TA muscles, (2) determine peripheral stimulation response latency, and (3) contrast with the cortical stimulation responses to ensure that there was not stimulus spread to the vagus nerve during cortical stimulation. Ten peripheral stimulation trials were collected; 5 at rest and 5 during a production of sustained /i/. The TMS coil was placed over the mastoid bone to activate the vagus nerve. Placement was tangential to the tip of mastoid bone in a posterior-anterior direction (**Figure 2B**). The center of the coil was located above the mastoid (the exit of vagus nerve from the skull through the jugular foramen) behind the ear. This placement is consistent with previous studies (Sims et al., 1996; Khedr and Aref, 2002). The stimulation intensity was set to 40% of maximum TMS output. Preliminary work determined that 40% was the lowest intensity that consistently generated peripheral evoked potentials in all participants with very little variation. Higher stimulation intensities induced facial muscle contractions during the experiment and caused the magnetic field spread to the electrode area, resulting in amplifier saturation.

Cortical stimulation

An anatomical T1 magnetic resonance image (MRI) with high-resolution ($1 \times 1 \times 1\ mm^3$) was acquired on a separate day prior to the TMS experiment visit. The image was imported into the neuronavigation system to guide the localization of the LMC in the primary motor cortex (M1). The location of the LMC, as determined by Simonyan et al. (2009), was used to help direct neuronavigation of initial coil placement on each participant's skull. This location is reported as approximately 0.5–1 cm anterior and 2–4 cm lateral to the hotspot determined in the afore-determined hand region assessment (Simonyan et al., 2009). This LMC location is similar to the 2 cm anterior and 4–8 cm lateral to the Cz EEG electrode position in the 10–20 system reported by Ertekin et al. (2001). The coil was held tangential to the skull over the targeted area in a posterior-anterior direction parallel to the midline (**Figure 2A**) and was systematically moved in an approximate 1 cm grid. The procedure was monitored by the neuronavigation system in real time. Initially, the intensity used for single TMS pulses was the 1-mV threshold for the FDI muscle as determined in the aforementioned hand region assessment; however, in most cases, the intensity was increased to induce an MEP in TA muscles. Conventional motor threshold determination protocol was attempted with the observation that the MEP amplitude was not modulated with TMS intensity within participant's acceptable/comfortable range (80% of the maximum stimulator output). However, a silent period was clearly observed following the superimposed MEP when a given TMS intensity was reached. Thus, cSP threshold was defined as the lowest TMS intensity that elicits a cSP in 5 out of 10 consecutive trials. The location that corresponded to the lowest

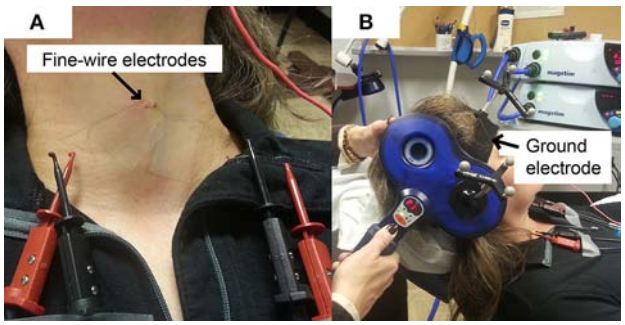


FIGURE 1 | Experimental Set up. (A) Fine-wire electrodes. There were two channels (pairs of fine-wires) inserted into bilateral thyroarytenoid muscles; **(B)** Ground electrode. The strap ground electrode was placed under the BrainSight subject tracker band.

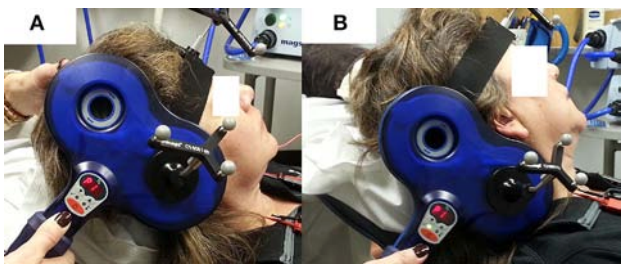


FIGURE 2 | TMS coil placement for laryngeal motor cortex (LMC) and peripheral stimulation. (A) Coil position and angle for LMC stimulation (cSP test); **(B)** coil position and angle for peripheral stimulation.

stimulation intensity (cSP threshold) was used as the LMC "hotspot" in the following experiment procedures. The hotspot coordinates were recorded by the neuronavigation system in MNI standard space using template ICBM152 with 1 mm^3 resolution (Mazziotta et al., 2001).

Outcome measure

cSP was the outcome measure for LMC excitability. The cSP threshold was used as the stimulation intensity. Single pulse cortical stimulations were performed during vocalization of sustained /i/. Participants were instructed to produce a comfortable pitch and volume of vocalization that was kept similar throughout the trials. The single pulse was applied approximately 1 s after initiation of the sustained vocalization. Participants were instructed to relax approximately 2 s after the pulse was delivered. In all participants, cSP threshold and cSP responses were first collected in the left hemisphere followed by the right hemisphere. Fifty trials of bilateral cSP responses in left and right TA muscles were collected in response to stimulation in both hemispheres. Given the low signal-to-noise ratio (SNR) with the fine wire responses, 50 trials were collected and traces were averaged to cancel out noise and increase the SNR. Average MEP amplitude was also calculated.

Data Processing

The cSP data were first averaged and rectified. Then, a 10-ms moving standard deviation (SD) window was applied to generate an SD curve of the signal. The average value of the SD curve during baseline (100–5 ms before stimulus) was calculated as the baseline contraction level. This value was used to define the offset of the cSP when the signal returned to pre-stimulus level. The onset of the cSP was defined as the time point of the stimulus. cSP duration was calculated by subtracting the onset from the offset of the cSP (Wolters et al., 2008; Chen et al., 2015). The MEP peak latency for both cortical and peripheral stimulation was defined as the duration between the stimulation artifact and the first peak of the MEP. The latency of the MEP to peripheral stimulation was calculated from each trial of stimulation; the latency of the MEP from cortical stimulation was identified from the average of 50 trials. The advantage of using the average of 50 trials was that it overcame any obscured response secondary to the active contraction of the TA muscle. MEP amplitude was calculated by the following procedures: in the averaged cSP trace, MEP was first identified within the range of 10–30 ms after the stimulus artifact. Then the peak-to-peak amplitude was extracted to represent the corresponding participant's MEP amplitude.

Data Analysis

Motor-evoked potential (MEP) latencies for peripheral stimulation under both active and resting conditions, and cortical stimulation for each hemisphere were compared. All data were normally distributed as determined by the Shapiro-Wilk W test. Multi-factor ANOVAs were used to examine the following three hypotheses to confirm the cortical nature of the evoked responses. (1) Cortical latencies are longer than peripheral latencies for the TA muscle on the same side. (2) MEP latencies from the left TA are longer than the right TA within the same type of stimulation (due to the longer length of the left recurrent laryngeal nerve Atkins, 1973). (3) There are no differences in latency for TA muscle on the same side when tested under different conditions. This hypothesis was tested with two sub-hypotheses: (3a) There are no differences in TA latency between resting and active with peripheral stimulation; (3b) there are no differences in TA latency between the cortical stimulation on the left and right hemispheres. These three hypotheses have to be tested separately because the cortical and peripheral data are not balanced. That is, all cortical data were collected during active contraction and peripheral data were collected under active and resting. Therefore, a three-step approach was used: for hypotheses 1 and 2 (cortical comparison), cortical and active peripheral data were tested by a two-way ANOVA with "stimulation type" (cortical vs. peripheral) and "TA side" (left vs. right) as interaction factors. For hypotheses 2 (peripheral comparison) and 3a, peripheral data were tested by a two-way ANOVA with "TA state" (rest vs. active) and "TA side" (left vs. right) as interaction factors. For hypothesis 3b, cortical data were tested by a two-way ANOVA with "stimulation side" (left vs. right) and "TA side" (left vs. right) as interaction factors. The significance level was set as $p < 0.05$ for all tests.

TABLE 1 | Participant information.

Participant	Sex	Age (years)	Stimulation intensity (% MSO)	
			L-cortical	R-cortical
1	F	42	60	60
2	F	56	63	63
3	F	49	63	63
4	M	62	57	61
5	M	58	64	65
6	M	67	52	52
7	M	60	67	58
8	M	56	55	52
9	M	47	60	60
10	M	49	60	60
11	M	46	50	52

MSO, maximum stimulator output; L, left hemisphere cortical stimulation; R, right hemisphere cortical stimulation.

RESULTS

No serious or unexpected adverse effects were reported. All participants tolerated the procedures with expected adverse events including skin soreness ($n = 4$), bruising ($n = 1$), and a tender throat ($n = 2$). Cortical stimulation intensities (percentage of the maximum stimulator output) are listed in **Table 1**. Average coordinates (MNI standard space) of the LMC hotspot were $x = -56$, $y = -3$, $z = 36$ in the left hemisphere and $x = 56$, $y = 3$, $z = 37$ in the right hemisphere. Individual coordinates are listed in Supplementary Table 1.

Peripheral stimulation induced unilateral (ipsilateral) responses of shorter latencies both during rest (left TA: 9.1 ± 2.2 ms; right TA: 6.9 ± 1.4 ms) and active contraction (left TA: 9.3 ± 2.2 ms; right TA: 6.8 ± 1.3 ms). Individual responses are listed in Supplementary Table 2. Importantly, no silent period was observed after active peripheral stimulation. Cortical stimulation evoked bilateral responses with silent periods. Average MEP latencies for left hemisphere cortical stimulation were 15.6 ± 2.3 ms in the left TA and 13.1 ± 2.0 ms in the right TA; average MEP latencies for right hemisphere cortical stimulation were 15.5 ± 2.8 ms in the left TA and 13.1 ± 2.3 ms in the right TA. The cSP duration and MEP peak latency values are listed in **Table 2**. Average cSP duration from left hemisphere cortical stimulation was 53.7 ± 7.8 ms in the left TA and 52.8 ± 7.3 ms in the right TA; average cSP duration from right hemisphere cortical stimulation was 53.4 ± 7.8 ms in the left TA and 54.5 ± 5.9 ms in the right TA. The average MEP amplitude from the left hemisphere cortical stimulation was 89.2 ± 80.0 μV in the left TA and 142.1 ± 142.5 μV in the right TA; the average MEP amplitude from the right hemisphere cortical stimulation was 110.6 ± 106.4 μV in the left TA and 196.3 ± 194.0 μV in the right TA. Individual MEP amplitude details are listed in **Table 2**. Samples of MEP responses are shown in **Figure 3** and cSP responses during right cortical stimulation are shown in **Figure 4**.

The two-way ANOVA tested cortical and active peripheral data with "stimulation type" and "TA side" as interaction factors with significant effects in "stimulation type" [$F_{(1, 59)} = 113.4894$, $p < 0.0001$] and "TA side" [$F_{(1, 59)} = 18.0334$, $p < 0.0001$] factors. No significant effect was found in the interaction of the two factors [$F_{(1, 59)} = 0.0140$, $p = 0.9062$]. This indicates that the cortical MEP latencies were longer than the peripheral MEP latencies regardless of TA side; and the left TA MEP latencies were longer than the right TA MEP latencies regardless of stimulation type. These results support hypotheses 1 and 2 (cortical comparison).

The two-way ANOVA test on peripheral data showed a significant effect with "TA side" [$F_{(1, 38)} = 18.2670$, $p = 0.0001$] as a significant factor. No significant effects were found in either "TA state" [$F_{(1, 38)} = 0.0011$, $p = 0.9734$] or the interaction of the two factors [$F_{(1, 38)} = 0.0213$, $p = 0.8849$]. This indicates that the left TA peripheral MEP latencies were longer than the right TA peripheral MEP latencies regardless of the "TA state" (rest vs. active) and that there was no difference in peripheral MEP latencies between the two TA states (rest and active). These findings support hypotheses 2 (peripheral comparison) and 3a.

The final two-way ANOVA test on cortical data with "stimulation side" and "TA side" as interaction factors showed significant effects in "TA side" [$F_{(1, 38)} = 10.5621$, $p = 0.0024$]. No significant effects were observed in either "stimulation side" [$F_{(1, 38)} = 0.0027$, $p = 0.9592$] or the interaction between the two factors [$F_{(1, 38)} = 0.0048$, $p = 0.9450$]. This indicates that in cortical stimulation, left TA latencies were longer than right TA latencies regardless of stimulation side (hemispheres) and that there was no difference between cortical MEP latencies evoked by stimulation to different hemispheres. These results support hypothesis 3b (**Figure 5**).

DISCUSSION

In this work we evaluated the feasibility and validity of testing cortical excitability of LMC with the cSP measurement using fine-wire electrodes inserted into TA muscles. TMS evoked MEP responses were confirmed as cortical in origin by observation of bilateral responses secondary to cortical stimulation, the occurrence of a silent period, and contrasting the MEP peak latencies of peripheral and cortical responses. These results suggest that the cSP may be used as a measure of cortical excitability for the LMC. To our knowledge, these cSP findings were the first report of cSP as a measure of the cortical excitability of the LMC.

Cortical vs. Peripheral Responses

The significant difference in MEP latencies between the peripheral and cortical stimulation confirmed that the cSP and MEP were generated cortically. No early response in the cortical data was observed at a similar latency as the peripheral stimulation, confirming that there was no current spread to the peripheral vagus nerve during cortical stimulation.

TABLE 2 | Cortical stimulation MEP latency, MEP amplitude and CSP duration.

Participant	MEP latency (ms)				MEP amplitude (μV)				CSP duration (ms)			
	Left hemisphere		Right hemisphere		Left hemisphere		Right hemisphere		Left hemisphere		Right hemisphere	
	L-TA	R-TA	L-TA	R-TA	L-TA	R-TA	L-TA	R-TA	L-TA	R-TA	L-TA	R-TA
1	12.3	8.9	11.9	8.6	32.7	296.2	33.5	34.1	51.4	44.8	50.3	46.4
2	12.5	11.4	13.0	11.1	81.0	26.5	95.5	34.3	43.3	44.2	42.5	49.2
3	16.1	13.4	14.2	12.7	26.3	105.1	40.9	100.0	53.6	53.4	53.0	53.0
4	16.3	13.9	15.9	11.6	58.1	23.3	12.6	92.1	50.2	47.7	53.8	55.3
5	16.6	13.6	16.3	12.7	10.0	10.3	7.4	3.9	65.3	62.8	64.7	60.9
6	17.8	13.8	15.2	13.8	26.1	10.7	71.2	16.7	48.4	46.1	48.4	49.2
7	13.9	13.0	13.8	11.7	59.1	398.6	128.8	467.3	41.7	46.7	43.9	46.9
8	N/A	15.5	N/A	15.5	N/A	383.1	N/A	322.6	N/A	55.9	N/A	56.4
9	13.4	10.3	15.3	13.9	246.8	101.0	270.3	314.5	60.0	59.2	63.6	63.1
10	19.7	15.5	22.5	17.0	128.0	165.7	344.0	606.2	63.6	66.4	64.4	63.8
11	17.3	14.5	17.0	15.5	224.5	42.4	101.8	167.3	59.5	53.6	53.4	55.6

Values are calculated from averaged trace. MEP amplitude, peak to peak amplitude; MEP, motor evoked potential; cSP, cortical silent period; TA, thyroarytenoid; L-TA, left TA; R-TA, right TA; N/A, no signal was observed from the corresponding channel.

Cortical Silent Period

The cSP duration for the TA muscles reported in this work were much shorter than previously reported values collected from the hand muscles (Chen et al., 2015). Previous studies have reported that the cSP duration is longest in small hand muscles (up to 300 ms), shorter in leg muscles (up to 100 ms), proximal arm muscles (Roick et al., 1993), axial muscles (Ferbert et al., 1992; Lefaucheur and Lofaso, 2002; Lefaucheur, 2005), facial muscles (the triangularis, range 69–169 ms, and orbicularis oculi, range 68–111 ms) (Werhahn et al., 1995; Paradiso et al., 2005) and the tongue (64.2 ± 4.5 ms at 50% maximum stimulator output) (Katayama et al., 2001). Our reported values are in line with other cranial muscles. Of note, as the brain volume decreases with age, the cSP duration gets shorter (Silbert et al., 2006). Considering the age range (54 ± 7.4 years) of participants in this study, this could also be part of the reason for the early cSP offset observed.

The cSP duration values collected from the left and right TA regardless of hemisphere stimulation were similar, the differences were within 2 ms. This symmetry is consistent with previously reported results of the low interhemispheric difference of cSP duration (usually <10 ms) in healthy subjects (Wolters et al., 2008). Although the motor cortical representation of the cSP is lateralized to the contralateral motor cortex for distal limb muscles, for axial muscles the cSP shows a more bilateral distribution (Wolters et al., 2008) which is consistent with our findings here.

Of note, MEP amplitude was not observed to modulate with changes in TMS intensity. This may be due to the small summation area of fine-wire electrodes, in contrast to surface electrodes on larger muscles, which do demonstrate changes in MEP size with different TMS stimulation intensities. This lack of modulation likely has little effect on cSP values (Rossini et al., 1994), but may render paired pulse responses or stimulus response curve measures unreliable. Also, given that the TA muscles are always active during breathing (Kuna et al., 1988), this makes resting measures difficult to reliably execute. Furthermore, it has been reported that the cSP induced by TMS can be elicited at lower stimulation intensities in the absence of a preceding MEP (Davey et al., 1994; Classen and Benecke, 1995). This low stimulation intensity advantage helps with the suppression of the stimulus artifact due to saturation of the amplifier, especially when the two inputs of the differential amplifier are not balanced, which is very likely with fine-wire electrodes, and the ground impedance is not low enough. Altogether, these inherent limitations of the laryngeal measurements suggest that cSP may be the ideal cortical excitability measure.

Latency of Motor Evoked Potential

The MEP latencies for peripheral and cortical stimulation measured in the current study were longer than those previously reported (Thumfart et al., 1992; Khedr and Aref, 2002). In those investigations, the cortical latency was reported as 9.6 ms in the left TA and 11.1 ms in the right TA contralateral to stimulation; and 9.3 and 9.5 ms in the TA ipsilateral to cortical stimulation. They also reported shorter peripheral latencies (between 2.7 and 6 ms), 1–7 ms shorter than the 3.2–13.2 ms range as we report here. These differences may be due to different definitions of the MEP latency. Khedr and Aref (2002) defined MEP latency as the interval between the stimulation artifact and the *onset* of the MEP. In this study, we measured the interval between the stimulation artifact and the first *peak* of the MEP. We chose this definition because the peak is more easily identified and less ambiguous than the MEP onset due to background EMG activity caused by breathing or voice activation. When compared with the studies using the same definition for MEP latency, our results are in agreement with others' reported values (Atkins, 1973; Rödel et al., 2004). Although it has been reported that the age can be a factor to cause a later onset of MEP (Eisen and Shtybel, 1990), in our findings no such a trend was observed.

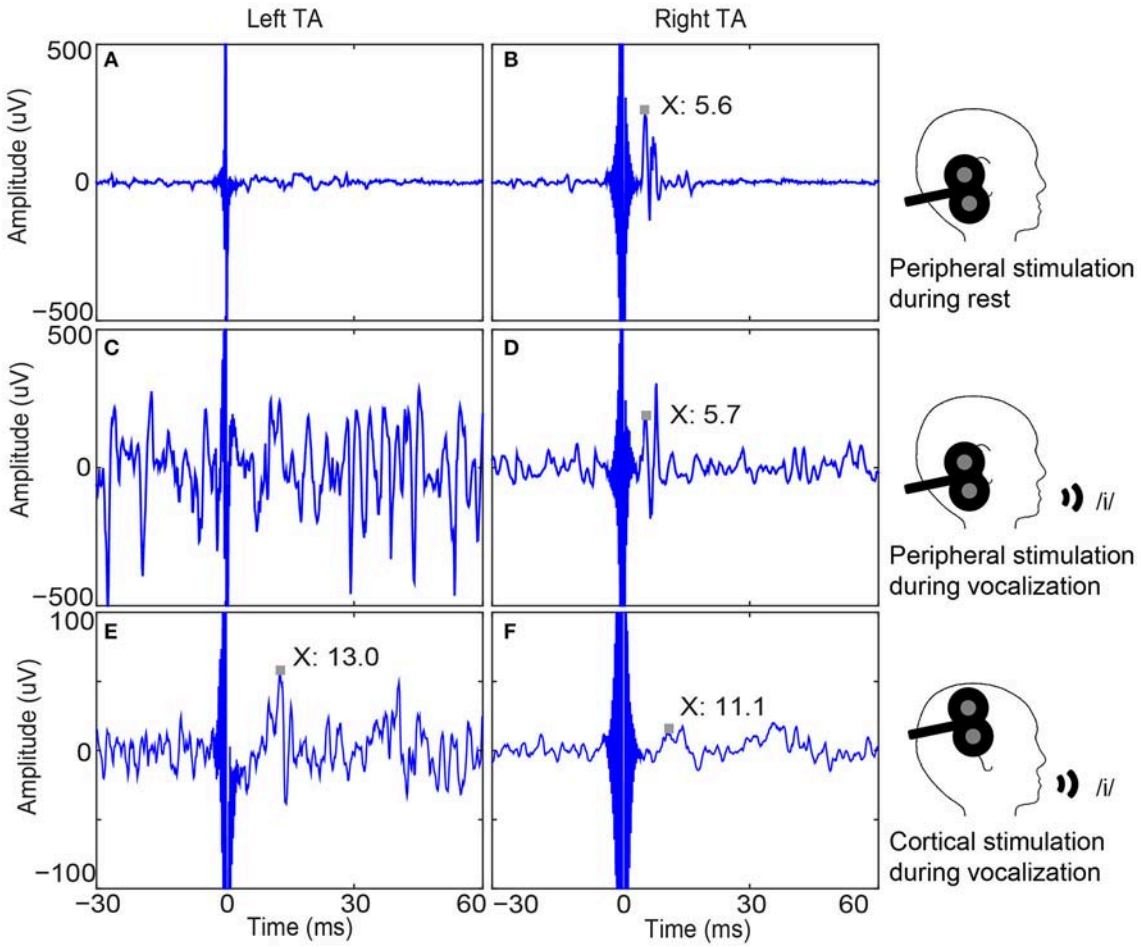


FIGURE 3 | Bilateral thyroarytenoid (TA) muscle responses to right peripheral and cortical stimulation in one participant. (A) Left TA recording without a response to right peripheral stimulation during rest (sample trace); **(B)** Right TA response to right peripheral stimulation during rest (MEP latency is 5.6 ms.); **(C)** Left TA recording without a response to right peripheral stimulation during vocalization (sample trace); **(D)** Right TA response to right peripheral stimulation (MEP peak latency is 5.7 ms.); **(E)** Average of 50 left TA responses to right cortical stimulation (MEP peak latency is 13.0 ms); **(F)** Average of 50 right TA responses to right cortical stimulation (MEP peak latency is 11.1 ms). Note the unilateral (ipsilateral) responses to peripheral stimulation and bilateral responses to cortical stimulation, which demonstrates the validity of cortical responses. MEP: motor evoked potential.

Furthermore, the differences in latency between the left and right TA muscles (2–4 ms) are consistent with the previous reported values (Atkins, 1973; Thumfart et al., 1992; Sims et al., 1996; Khedr and Aref, 2002; Rödel et al., 2004), as are the latency differences between peripheral and cortical responses (4–6 ms) (Thumfart et al., 1992; Khedr and Aref, 2002). The consistency of our results with others supports the validity of this method.

Methodological Considerations

Stimulation Artifact Suppression

Key considerations regarding stimulation artifact suppression were applied for improved signal quality as follows: *First*, a large contact area of the ground electrode suppressed the stimulation artifact, which was essential when the stimulation intensity was high (>80% of the maximum output). We determined that this procedure significantly reduced amplifier saturation as illustrated in **Figure 3**. *Second*, the ground electrode should be located between the stimulation site and the acquisition site and as close to the acquisition site as possible. For the TA or other intrinsic larynx muscles, the forehead or chin were ideal areas to attach the ground electrode. Our testing revealed that participants preferred the head strap due to comfort. Additional ground electrodes can be attached to achieve even greater suppression of the stimulation artifact. *Also*, a relatively low gain (such as x300 or x100) along with a large dynamic range of the amplifier (e.g., using a power supply generated by 9-V batteries or greater) decreased the chances of amplifier saturation. However, the low gain was compensated for by a high quantification resolution analog-to-digital convertor, such as the 24-bit used here. This high quantification resolution helped to improve the signal-noise ratio and increased the quantification accuracy that could have been diminished by the low gain. *Last*, the battery power to the amplifier also had the benefit of reducing

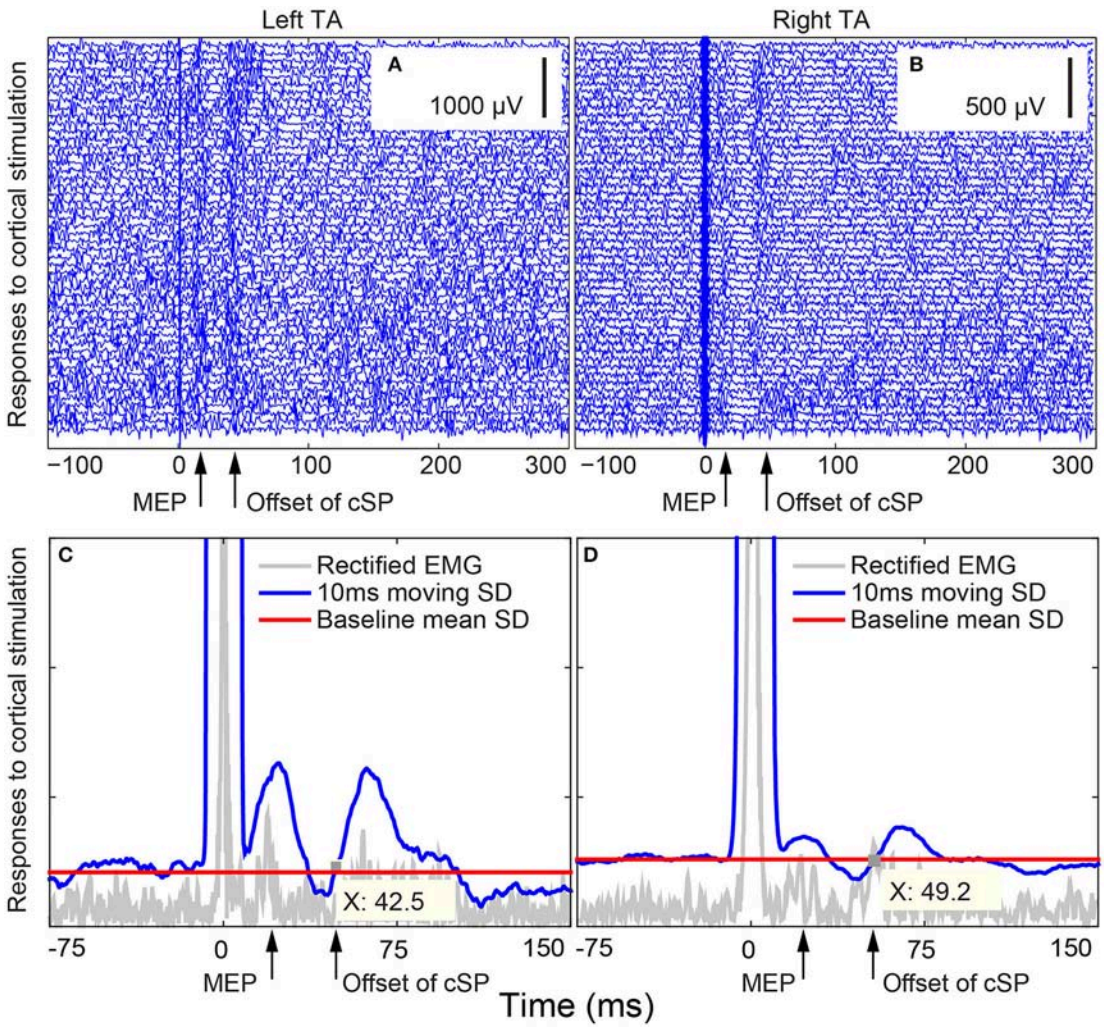


FIGURE 4 | Bilateral thyroarytenoid (TA) motor evoked potential (MEP) responses to right cortical stimulation during voice production in Subject 02. **(A)** 50 individual traces of left TA responses to right cortical stimulation; **(B)** 50 individual traces of right TA responses to right cortical stimulation; **(C)** cSP from the left TA during right cortical stimulation (offset X at 42.5 ms); **(D)** cSP from the right TA during right cortical stimulation (offset X at 49.2 ms). The cSP moving average was calculated based on the average of the 50 trials. The stimuli were delivered at 0 ms. cSP: cortical silent period.

susceptibility to main noise (e.g., 50 or 60 Hz) without requiring a notch filter which should be avoided during EMG/MEP data acquisition because a notch filter would also filter out the informative components of the EMG/MEP within the 50–60 Hz range (Konrad, 2005).

Insertion of Fine-Wire Electrodes

Fine-wire electrodes were chosen instead of needle electrodes because they adapt to the muscle movement. During our experiment, the participants were asked to vocalize "/i/" which contracts the muscles in the vocal folds. Rigid needle electrodes resist muscle contraction causing pain during vocalization and dry swallows. However, insertion accuracy of bi-polar fine-wire pair electrodes is critical to data quality. An experienced otolaryngologist inserted the electrodes in this experiment. In some participants, however, re-insertion was necessary after an insertion did not yield an EMG signal.

In some participants, the two TA muscles had different EMG signal amplitudes, as shown in **Figure 3** (e.g., left > right). This occurred frequently likely due to differences in the insertion angle and depth of the fine-wire electrodes. With different placement in the muscles, the number and size of the motor units between the two poles of the fine-wire electrodes will vary, resulting in differences in the signal amplitude. For this reason, the traditional peak-to-peak motor evoked potentials may not be a valid measure for assessing cortical excitability. The use of cSP, however, diminishes the impact of this issue because the cSP is a temporal/duration measure, not an amplitude measure. Thus, the shape of the MEP has less effect on cSP duration than that of the MEP amplitude. This makes the cSP a useful method for quantifying cortical excitability when using fine-wire electrodes.

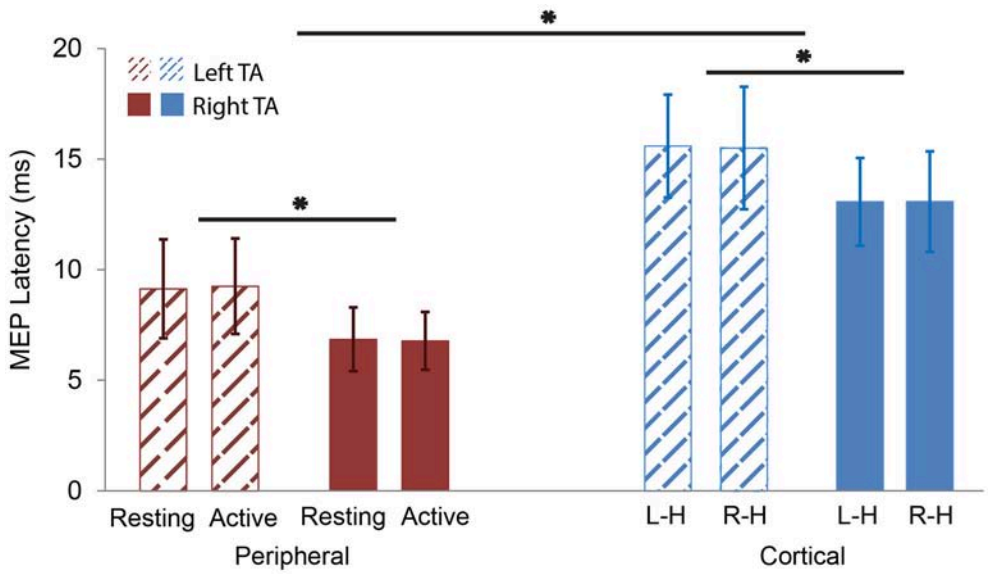


FIGURE 5 | MEP latency comparisons. Red color represents peripheral stimulation responses (left). Blue color represents cortical stimulation responses **(right)**. Thatched represents left TA responses. Solid represents right TA responses. The MEP latencies of left TA were significantly longer than the right TA in both peripheral and cortical stimulation. The MEP latencies of the cortical stimulation were significantly longer than the peripheral one in both left and right TAs. L-H: cortical Left Hemisphere; R-H: cortical Right Hemisphere. *$p < 0.05$.

LIMITATIONS

During data collection, we did not attempt to control TA muscle contraction level as a percent of maximum voluntary contraction (MVC), as is typically performed for hand muscles. The rationale for this decision was that to control the contraction level of TA muscles, both the pitch and the amplitude of vocalization need to be standardized. For the standardization of voice pitch, it is required that the full range of vocal pitch of each participant is measured (similar to the MVC measurement in the conventional TMS test) and, that all participants generate a normalized relative pitch (similar to the 20% of MVC in the conventional hand TMS test) during the experiment. The same procedures apply to the standardization of the amplitude. To control the two factors (pitch and amplitude) synchronously may be difficult for participants to follow, especially when there are fine-wires inserted into their larynx. Thus, in this work we used a compromised but practical method to standardize the TA muscle contraction: participants were instructed to vocalize with their comfortable and natural pitch and volume consistently in each trial. This methodology will allow for future comparisons with populations that have difficulty in controlling their voice, such as people with spasmodic dysphonia. Although the cSP values were likely unaffected by this limitation, as contraction strength of the target muscle does not significantly influence cSP duration (Haug et al., 1992; Inghilleri et al., 1993; Roick et al., 1993; Taylor et al., 1997; Wu et al., 2002; Säisänen et al., 2008). Of note, these previously reported studies were done in large peripheral muscles, i.e., FDI. It is possible that this characteristic is different when measured in intrinsic laryngeal muscles. Thus, it is worth further investigation and may be a useful addition in future experiments.

In the current study, the cSP threshold was used instead of the conventionally adopted 120–130% of resting motor threshold in previous cSP studies (Wolters et al., 2008). This was because that it was difficult to determine a resting motor threshold from the constantly-firing TA muscles. However, it has been reported that the MEP threshold and cSP threshold are usually related (Kimiskidis et al., 2005), suggesting that the stimulation intensity used (cSP threshold) was valid.

Cortical silent period (cSP) threshold and responses were collected first in the left hemisphere followed by the right hemisphere in all participants. Given that the fine-wire electrodes may change position due to swallowing or head rotation during the experiment, we collected data from the hemisphere with higher priority first. The left LMC has been reported to have a more dominant role than the right LMC in vocalization (Simonyan et al., 2009) thus, it was tested first.

Considering the invasive procedure of the fine-wire insertion during the experiment, there was no reliability re-tests attempted in the study design. Although according to previous studies, the intersession variability of cSP is typically <10% (Kukowski and Haug, 1991; Orth and Rothwell, 2004), but this is unknown for laryngeal data.

The MEP amplitudes reported were calculated based on the averaged trace of the 50 cSP trials. Conventionally, the MEP amplitude is calculated based on individual traces and then the average values are reported. However, given the noisy nature of the TA EMG and the relatively low amplitude of the MEP, it is difficult to determine MEP amplitude based on each individual trace. Using the averaged trace provides a clear background to distinguish the MEP from noise or random firing spikes.

CONCLUSION

We assessed the excitability of LMC using the TMS evoked cSP in the TA muscles. The cSP duration was in line with other healthy cranial muscles, such as the tongue (Katayama et al., 2001). The responses were confirmed by contrasting the difference in the MEP peak latencies that were generated by cortical and peripheral stimulation, respectively. Given there are reports of the low intersession variability of the cSP duration in a given subject, typically <10% (Kukowski and Haug, 1991; Orth and Rothwell, 2004), measurement of cSP may be exceptionally suitable for longitudinal studies in patients, or before and after experimental manipulation. We conclude that the TMS evoked cortical excitability cSP measure can be safely tested in intrinsic laryngeal muscles in healthy volunteers. The use of fine-wire electrodes to measure the cSP of the LMC as validated in this work provides a tool to evaluate GABA receptor mediated inhibition process in the LMC. This will enable the direct comparison of inhibitory responses in healthy individuals and people with neurological voice disorders, such as spasmodic dysphonia and voice tremor which in turn will lead to a better understanding of the pathophysiology of these conditions

AUTHOR CONTRIBUTORS

MC, experimental system design, methodology, data collection, data processing, data analysis, data interpretation, drafting the work, final approval of the version to be published; RS, conception of the study, data collection, data interpretation, drafting the work, final approval of the version to be published; GG, conception of the study, methodology, data collection, final approval of the version to be published; SS, methodology assistance, data interpretation, final approval of the version to be published; CL, methodology, data interpretation, final approval of the version to be published; CP, data collection, drafting the work, final approval of the version to be published; TK, conception of the study, methodology, data collection, data analysis, data interpretation, drafting the work, final approval of the version to be published.

FUNDING

This work was partly supported by the National Institute of Communication Disorders and Deafness, National Institutes of Health (grant number R21DC012344), the University of Minnesota's MnDRIVE (Minnesota's Discovery, Research and Innovation Economy) initiative, the National Center for Advancing Translational Sciences of the National Institutes of Health (award number UL1TR000114) and, National Institute of Biomedical Imaging and Bioengineering (grant number P41 EB015894).

ACKNOWLEDGMENTS

This work was partly supported by the University of Minnesota Clinical and Translational Science Institute and Center for Magnetic Resonance Research at University of Minnesota.

SUPPLEMENTARY MATERIAL

The Supplementary Material for this article can be found online at: http://journal.frontiersin.org/article/10.3389/fnins.2017.00088/full#supplementary-material

REFERENCES

Atkins, J. P. (1973). An electromyographic study of recurrent laryngeal nerve conduction and its clinical applications. *Laryngoscope* 83, 796–807. doi: 10.1288/00005537-197305000-00015

Calancie, B., Nordin, M., Wallin, U., and Hagbarth, K. E. (1987). Motor-unit responses in human wrist flexor and extensor muscles to transcranial cortical stimuli. *J. Neurophysiol.* 58, 1168–1185.

Chen, M., Deng, H., Schmidt, R. L., and Kimberley, T. J. (2015). Low-Frequency repetitive transcranial magnetic stimulation targeted to premotor cortex followed by primary motor cortex modulates excitability differently than premotor cortex or primary motor cortex stimulation alone. *Neuromodulation* 18, 678–685. doi: 10.1111/ner.12337

Classen, J., and Benecke, R. (1995). Inhibitory phenomena in individual motor units induced by transcranial magnetic stimulation. *Electroencephalogr. Clin. Neurophysiol.* 97, 264–274. doi: 10.1016/0924-980X(95)00099-2

Currà, A., Romaniello, A., Berardelli, A., Cruccu, G., and Manfredi, M. (2000). Shortened cortical silent period in facial muscles of patients with cranial dystonia. *Neurology* 54, 130–135. doi: 10.1212/WNL.54.1.130

Davey, N. J., Romaiguère, P., Maskill, D. W., and Ellaway, P. H. (1994). Suppression of voluntary motor activity revealed using transcranial magnetic stimulation of the motor cortex in man. *J. Physiol.* 477(Pt 2), 223–235.

Eldaief, M. C., Press, D. Z., and Pascual-Leone, A. (2013). Transcranial magnetic stimulation in neurology: a review of established and prospective applications. *Neurol. Clin. Pract.* 3, 519–526. doi: 10.1212/01.CPJ.0000436213.11132.8e

Ertekin, C., Turman, B., Tarlaci, S., Celik, M., Aydogdu, I., Secil, Y., et al. (2001). Cricopharyngeal sphincter muscle responses to transcranial magnetic stimulation in normal subjects and in patients with dysphagia. *Clin. Neurophysiol.* 112, 86–94. doi: 10.1016/S1388-2457(00)00504-6

Eisen, A. A., and Shtybel, W. (1990). AAEM minimonograph #35: clinical experience with transcranial magnetic stimulation. *Muscle Nerve* 13, 995–1011. doi: 10.1002/mus.880131102

Espadaler, J., Rogić, M., Deletis, V., Leon, A., Quijada, C., and Conesa, G. (2012). Representation of cricothyroid muscles at the primary motor cortex (M1) in healthy subjects, mapped by navigated transcranial magnetic stimulation (nTMS). *Clin. Neurophysiol.* 123, 2205–2211. doi: 10.1016/j.clinph.2012.04.008

Ferbert, A., Caramia, D., Priori, A., Bertolasi, L., and Rothwell, J. C. (1992). Cortical projection to erector spinae muscles in man as assessed by focal transcranial magnetic stimulation. *Electroencephalogr. Clin. Neurophysiol.* 85, 382–387. doi: 10.1016/0168-5597(92)90051-C

Hallett, M. (2007). Transcranial magnetic stimulation: a primer. *Neuron* 55, 187–199. doi: 10.1016/j.neuron.2007.06.026

Haug, B. A., Schönle, P. W., Knobloch, C., and Köhne, M. (1992). Silent period measurement revives as a valuable diagnostic tool with transcranial magnetic stimulation. *Electroencephalogr. Clin. Neurophysiol.* 85, 158–160. doi: 10.1016/0168-5597(92)90081-L

Henriquez, V. M., Schulz, G. M., Bielamowicz, S., and Ludlow, C. L. (2007). Laryngeal reflex responses are not modulated during human voice and respiratory tasks. *J. Physiol.* 585(Pt 3), 779–789. doi: 10.1113/jphysiol.2007.143438

Hirano, M., and Ohala, J. (1969). Use of hooked-wire electrodes for electromyography of the intrinsic laryngeal muscles. *J. Speech Hear. Res.* 12:362. doi: 10.1044/jshr.1202.362

Inghilleri, M., Berardelli, A., Cruccu, G., and Manfredi, M. (1993). Silent period evoked by transcranial stimulation of the human cortex and cervicomedullary junction. *J. Physiol.* 466, 521–534.

Katayama, T., Aizawa, H., Kuroda, K., Suzuki, Y., Kikuchi, K., Kimura, T., et al. (2001). Cortical silent period in the tongue induced by transcranial

magnetic stimulation. *J. Neurol. Sci.* 193, 37–41. doi: 10.1016/S0022-510X(01)00647-5

Khedr, E. M., and Aref, E.-E. M. (2002). Electrophysiological study of vocal-fold mobility disorders using a magnetic stimulator. *Eur. J. Neurol.* 9, 259–267. doi: 10.1046/j.1468-1331.2002.00394.x

Kimberley, T. J., Borich, M. R., Prochaska, K. D., Mundfrom, S. L., Perkins, A. E., and Poepping, J. M. (2009). Establishing the definition and inter-rater reliability of cortical silent period calculation in subjects with focal hand dystonia and healthy controls. *Neurosci. Lett.* 464, 84–87. doi: 10.1016/j.neulet.2009.08.029

Kimiskidis, V. K., Papagiannopoulos, S., Sotirakoglou, K., Kazis, D. A., Kazis, A., and Mills, K. R. (2005). Silent period to transcranial magnetic stimulation: construction and properties of stimulus–response curves in healthy volunteers. *Exp. Brain Res.* 163, 21–31. doi: 10.1007/s00221-004-2134-4

Konrad, P. (2005). *The ABC of EMG: A Practical Introduction to Kinesiological Electromyography*. Scottsdale, AZ: Noraxon INC.

Kukowski, B., and Haug, B. (1991). Quantitative evaluation of the silent period, evoked by transcranial magnetic stimulation during sustained muscle contraction, in normal man and in patients with stroke. *Electromyogr. Clin. Neurophysiol.* 32, 373–378.

Kuna, S. T., Insalaco, G., and Woodson, G. E. (1988). Thyroarytenoid muscle activity during wakefulness and sleep in normal adults. *J. Appl. Physiol.* 65, 1332–1339.

Lefaucheur, J.-P. (2005). Excitability of the motor cortical representation of the external anal sphincter. *Exp. Brain Res.* 160, 268–272. doi: 10.1007/s00221-004-2170-0

Lefaucheur, J.-P., and Lofaso, F. (2002). Diaphragmatic silent period to transcranial magnetic cortical stimulation for assessing cortical motor control of the diaphragm. *Exp. Brain Res.* 146, 404–409. doi: 10.1007/s00221-002-1197-3

Ludlow, C. L. (2005). Central nervous system control of the laryngeal muscles in humans. *Respir. Physiol. Neurobiol.* 147, 205–222. doi: 10.1016/j.resp.2005.04.015

Ludlow, C. L. (2015). Central nervous system control of voice and swallowing. *J. Clin. Neurophysiol.* 32, 294–303. doi: 10.1097/WNP.0000000000000186

Ludlow, C. L., Adler, C. H., Berke, G. S., Bielamowicz, S. A., Blitzer, A., Bressman, S. B., et al. (2008). Research priorities in spasmodic dysphonia. *Otolaryngol. Head Neck Surg.* 139, 495–505. doi: 10.1016/j.otohns.2008.05.624

Mazziotta, J., Toga, A., Evans, A., Fox, P., Lancaster, J., Zilles, K., et al. (2001). A four-dimensional probabilistic atlas of the human brain. *J. Am. Med. Inform. Assoc.* 8, 401–430. doi: 10.1136/jamia.2001.0080401

Orth, M., and Rothwell, J. (2004). The cortical silent period: intrinsic variability and relation to the waveform of the transcranial magnetic stimulation pulse. *Clin. Neurophysiol.* 115, 1076–1082. doi: 10.1016/j.clinph.2003.12.025

Paradiso, G. O., Cunic, D. I., Gunraj, C. A., and Chen, R. (2005). Representation of facial muscles in human motor cortex. *J. Physiol.* 567, 323–336. doi: 10.1113/jphysiol.2005.088542

Paulus, W., Classen, J., Cohen, L. G., Large, C. H., Di Lazzaro, V., Nitsche, M., et al. (2008). State of the art: pharmacologic effects on cortical excitability measures tested by transcranial magnetic stimulation. *Brain Stimul.* 1, 151–163. doi: 10.1016/j.brs.2008.06.002

Rödel, R. M. W., Olthoff, A., Tergau, F., Simonyan, K., Kraemer, D., Markus, H., et al. (2004). Human cortical motor representation of the larynx as assessed by Transcranial Magnetic Stimulation (TMS). *Laryngoscope* 114, 918–922. doi: 10.1097/00005537-200405000-00026

Rogić Vidaković, M., Schönwald, M. Z., Rotim, K., Jurić, T., Vulević, Z., Tafra, R., et al. (2015). Excitability of contralateral and ipsilateral projections of corticobulbar pathways recorded as corticobulbar motor evoked potentials of the cricothyroid muscles. *Clin. Neurophysiol.* 126, 1570–1577. doi: 10.1016/j.clinph.2014.11.001

Roick, H., von Giesen, H. J., and Benecke, R. (1993). On the origin of the postexcitatory inhibition seen after transcranial magnetic brain stimulation in awake human subjects. *Exp. Brain Res.* 94, 489–498. doi: 10.1007/BF00230207

Rossini, P. M., Barker, A. T., Berardelli, A., Caramia, M. D., Caruso, G., Cracco, R. Q., et al. (1994). Non-invasive electrical and magnetic stimulation of the brain, spinal cord and roots: basic principles and procedures for routine clinical application. Report of an IFCN committee. *Electroencephalogr. Clin. Neurophysiol.* 91, 79–92. doi: 10.1016/0013-4694(94)90029-9

Rossini, P. M., Burke, D., Chen, R., Cohen, L. G., Daskalakis, Z., Di Iorio, R., et al. (2015). Non-invasive electrical and magnetic stimulation of the brain, spinal cord, roots and peripheral nerves: basic principles and procedures for routine clinical and research application. An updated report from an I.F.C.N. Committee. *Clin. Neurophysiol.* 126, 1071–1107. doi: 10.1016/j.clinph.2015.02.001

Säisänen, L., Pirinen, E., Teitti, S., Könönen, M., Julkunen, P., Määttä, S., et al. (2008). Factors influencing cortical silent period: optimized stimulus location, intensity and muscle contraction. *J. Neurosci. Methods* 169, 231–238. doi: 10.1016/j.jneumeth.2007.12.005

Samargia, S., Schmidt, R., and Kimberley, T. J. (2014). Shortened cortical silent period in adductor spasmodic dysphonia: evidence for widespread cortical excitability. *Neurosci. Lett.* 560, 12–15. doi: 10.1016/j.neulet.2013.12.007

Siebner, H. R., Dressnandt, J., Auer, C., and Conrad, B. (1998). Continuous intrathecal baclofen infusions induced a marked increase of the transcranially evoked silent period in a patient with generalized dystonia. *Muscle Nerve* 21, 1209–1212. doi: 10.1002/(SICI)1097-4598(199809)21:9<1209::AID-MUS15>3.0.CO;2-M

Silbert, L. C., Nelson, C., Holman, S., Eaton, R., Oken, B. S., Lou, J. S., et al. (2006). Cortical excitability and age-related volumetric MRI changes. *Clin. Neurophysiol.* 117, 1029–1036. doi: 10.1016/j.clinph.2006.02.003

Simonyan, K., and Horwitz, B. (2011). Laryngeal motor cortex and control of speech in humans. *Neuroscientist* 17, 197–208. doi: 10.1177/1073858410386727

Simonyan, K., Ostuni, J., Ludlow, C. L., and Horwitz, B. (2009). Functional but not structural networks of the human laryngeal motor cortex show left hemispheric lateralization during syllable but not breathing production. *J. Neurosci.* 29, 14912–14923. doi: 10.1523/JNEUROSCI.4897-09.2009

Sims, H. S., Yamashita, T., Rhew, K., and Ludlow, C. L. (1996). Assessing the clinical utility of the magnetic stimulator for measuring response latencies in the laryngeal muscles. *Otolaryngol. Head Neck Surg.* 114, 761–767. doi: 10.1016/S0194-5998(96)70099-2

Taylor, J. L., Allen, G. M., Butler, J. E., and Gandevia, S. C. (1997). Effect of contraction strength on responses in biceps brachii and adductor pollicis to transcranial magnetic stimulation. *Exp. Brain Res.* 117, 472–478. doi: 10.1007/s002210050243

Thumfart, W. F., Zorowka, P., Pototschnig, C., and Eckel, H. E. (1992). Electrophysiologic investigation of lower cranial nerve diseases by means of magnetically stimulated neuromyography of the larynx. *Ann. Otol. Rhinol. Laryngol.* 101, 629–634. doi: 10.1177/000348949210100801

Tinazzi, M., Farina, S., Edwards, M., Moretto, G., Restivo, D., Fiaschi, A., et al. (2005). Task-specific impairment of motor cortical excitation and inhibition in patients with writer's cramp. *Neurosci. Lett.* 378, 55–58. doi: 10.1016/j.neulet.2004.12.015

Werhahn, K. J., Classen, J., and Benecke, R. (1995). The silent period induced by transcranial magnetic stimulation in muscles supplied by cranial nerves: normal data and changes in patients. *J. Neurol. Neurosurg. Psychiatr.* 59, 586–596. doi: 10.1136/JNNP.59.6.586

Wolters, A., Ziemann, U., and Benecke, R. (2008). "The cortical silent period," in *Oxford Handbook of Transcranial Stimulation*, eds C. M. Epstein, E. M. Wassermann, and U. Ziemann (New York, NY: Oxford University Press), 1–23.

World Medical Association (2013). World Medical Association Declaration of Helsinki: ethical principles for medical research involving human subjects. *JAMA*. 310, 2191–2194. doi: 10.1001/jama.2013.281053

Wu, L., Goto, Y., Taniwaki, T., Kinukawa, N., and Tobimatsu, S. (2002). Different patterns of excitation and inhibition of the small hand and forearm muscles from magnetic brain stimulation in humans. *Clin. Neurophysiol.* 113, 1286–1294. doi: 10.1016/S1388-2457(02)00160-8

Conflict of Interest Statement: The authors declare that the research was conducted in the absence of any commercial or financial relationships that could be construed as a potential conflict of interest.

Copyright © 2017 Chen, Summers, Goding, Samargia, Ludlow, Prudente and Kimberley. This is an open-access article distributed under the terms of the Creative Commons Attribution License (CC BY). The use, distribution or reproduction in other forums is permitted, provided the original author(s) or licensor are credited and that the original publication in this journal is cited, in accordance with accepted academic practice. No use, distribution or reproduction is permitted which does not comply with these terms.

frontiers in Human Neuroscience

CASE REPORT
published: 06 April 2017
doi: 10.3389/fnhum.2017.00177

Deep Brain Stimulation Improves the Symptoms and Sensory Signs of Persistent Central Neuropathic Pain from Spinal Cord Injury: A Case Report

*Walter J. Jermakowicz[1,2], Ian D. Hentall[1,2,3], Jonathan R. Jagid[1,3], Corneliu C. Luca[3,4], James Adcock[1,3], Alberto Martinez-Arizala[1,2,3,4] and Eva Widerström-Noga[1,2,3]**

[1]The Miami Project to Cure Paralysis, Miller School of Medicine, University of Miami, Miami, FL, USA, [2]Department of Neurological Surgery, Miller School of Medicine, University of Miami, Miami, FL, USA, [3]Research Service, Bruce W. Carter Department of Veterans Affairs Medical Center, Miami, FL, USA, [4]Department of Neurology, Miller School of Medicine, University of Miami, Miami, FL, USA

Central neuropathic pain (CNP) is a significant problem after spinal cord injury (SCI). Pharmacological and non-pharmacological approaches may reduce the severity, but relief is rarely substantial. While deep brain stimulation (DBS) has been used to treat various chronic pain types, the technique has rarely been used to attenuate CNP after SCI. Here we present the case of a 54-year-old female with incomplete paraplegia who had severe CNP in the lower limbs and buttock areas since her injury 30 years prior. She was treated with bilateral DBS of the midbrain periaqueductal gray (PAG). The effects of this stimulation on CNP characteristics, severity and pain-related sensory function were evaluated using the International SCI Pain Basic Data Set (ISCIPBDS), Neuropathic Pain Symptom Inventory (NPSI), Multidimensional Pain Inventory and Quantitative Sensory Testing before and periodically after initiation of DBS. After starting DBS treatment, weekly CNP severity ratings rapidly decreased from severe to minimal, paralleled by a substantial reduction in size of the painful area, reduced pain impact and reversal of pain-related neurological abnormalities, i.e., dynamic-mechanical and cold allodynia. She discontinued pain medication on study week 24. The improvement has been consistent. The present study expands on previous findings by providing in-depth assessments of symptoms and signs associated with CNP. The results of this study suggest that activation of endogenous pain inhibitory systems linked to the PAG can eliminate CNP in some people with SCI. More research is needed to better-select appropriate candidates for this type of therapy. We discuss the implications of these findings for understanding the brainstem's control of chronic pain and for future progress in using analgesic DBS in the central gray.

Keywords: neuromodulation, low-frequency stimulation, periaqueductal gray, pain severity, evoked pain, chronic pain

OPEN ACCESS

Edited by:
Mikhail Lebedev, Duke University, USA

Reviewed by:
Lorys Castelli, University of Turin, Italy
Filippo Brighina, University of Palermo, Italy

****Correspondence:***
Eva Widerström-Noga
ewiderstrom-noga@med.miami.edu

Received: *29 December 2016*
Accepted: *27 March 2017*
Published: *06 April 2017*

Citation:
Jermakowicz WJ, Hentall ID, Jagid JR, Luca CC, Adcock J, Martinez-Arizala A and Widerström-Noga E (2017) Deep Brain Stimulation Improves the Symptoms and Sensory Signs of Persistent Central Neuropathic Pain from Spinal Cord Injury: A Case Report. Front. Hum. Neurosci. 11:177. doi: 10.3389/fnhum.2017.00177

INTRODUCTION

Persistent neuropathic pain is a common and serious consequence of spinal cord injury (SCI) that is especially refractory to both pharmacological and non-pharmacological treatments (Siddall et al., 2003; Vranken, 2009; Finnerup et al., 2014). Electrical stimulation of specific brain structures with the purpose of relieving chronic pain has been used for a long time but the reported efficacy for central neuropathic pain (CNP) is relatively low and difficult to predict. For certain patients, effects of stimulation on CNP may be tremendous (Boccard et al., 2013; Pereira and Aziz, 2014). Nevertheless, because deep brain stimulation (DBS) is an invasive procedure, its use for SCI pain is rare and currently restricted to severe cases refractory to non-invasive therapies. In order to be accepted as a therapy for chronic pain, success rates need to improve. This will require, *inter alia*, a better understanding of CNP mechanisms along with improved patient selection.

The present article describes an almost complete reversal of CNP (which had been present since injury 30 years ago) and associated sensory dysfunction paralleled by a reduction in psychosocial impact in a 54-year-old female with SCI-related CNP who underwent DBS of the periaqueductal gray (PAG). The optimization of stimulation parameters and the time-course of daily changes in general pain intensity over a 42-week period were previously reported for this subject and one other with SCI-related chronic pain (Hentall et al., 2016). Here we provide a more detailed analysis specifically focusing on the CNP below the level of injury evaluating a broader set of pain characteristics, somatosensory function and psychosocial impact conducted at intervals over a 52-week period. We also conducted an exit interview to obtain her personal perspectives on her pain and treatments. The "Discussion" Section contains a brief review of possible mechanisms underlying successful amelioration of CNP by DBS and the prospects for improving treatment efficacy.

BACKGROUND

Clinical History

The subject was a 54-year-old female veteran with an incomplete SCI (T11 level) due to electrocution 30 years ago. Examination according to the International Standards for Neurological Classification of SCI classified her injury as AIS-B (sensory but no motor function preserved).

The patient's worst pain problem was chronic below-level CNP in both lower extremities, with onset shortly after her initial injury. The average weekly pain level for this specific pain preceding the baseline measurement was 8 of 10 on a numerical rating scale (NRS). CNP was daily and constant, and most intense during the night and therefore significantly interfering with sleep. She reported severe "electric" and moderate "stabbing" pain, moderate to severe evoked pain in response to brushing, severe evoked pain to cold stimuli and moderate tingling and pins and needles in the painful area. She was taking a daily dose of 75 mg pregabalin for the pain but had previously tried a wide range of pharmacological options (including opiates and higher doses of pregabalin) and she said: "Medication? I don't like medication. I don't like the way it makes me feel. I don't like the side effects. It . . . They all leave me feeling stupid and foggy and disoriented and . . . So, that's why I wouldn't take them until I absolutely just couldn't . . ."

Pain and Sensory Assessments

Pain was evaluated with respect to location, classification, intensity, temporal pattern and pain interference using the International SCI Pain Basic Dataset (ISCIPBDS; Widerström-Noga et al., 2014). Neuropathic pain symptom severity was evaluated with the Neuropathic Pain Symptom Inventory (NPSI; Bouhassira et al., 2004), and psychosocial impact with the Multidimensional Pain Inventory-SCI version (Widerström-Noga et al., 2006). Sensory function was assessed below the level of injury in the neuropathic pain area with the TSA-II Neurosensory Analyzer (Medoc Ltd., Ramat Yishai, Israel), either via a thermode or a vibratory pin applied to the painful area below the level of injury. Thresholds for cool detection, warm detection, cold pain, hot pain and vibration detection were determined using the method of limits (reaction-time inclusive). We also evaluated thermal allodynia using thermorollers (Somedic, Sweden), and mechanical allodynia using a soft brush and Semmes-Weinstein monofilaments (10 g, #5.07). Further details regarding all QST procedures can be found in a previous publication (Widerström-Noga et al., 2016). Baseline pain testing was performed twice in the subject (1 and 5 weeks before the first surgery) and baseline results were averaged. For a study timeline see **Figure 1**.

DBS Surgery

The work was performed under an Investigative Device Exemption of the U.S. Food and Drug Administration (IDE G120202), and Clinical Trials.gov (NCT02006433).

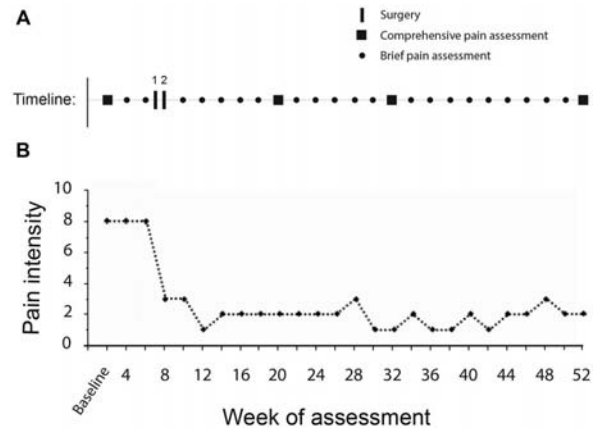


FIGURE 1 | (A) Timeline of study. The subject underwent a comprehensive pain assessment (entire battery of pain tests) on week 2, prior to the two surgical procedures performed on weeks 6 and 7. This was followed by biweekly brief pain assessments (average pain intensity ratings past 7 days by patient in clinic) and periodic repeat comprehensive assessments postoperatively (weeks 20, 32 and 52). **(B)** Average pain intensity ratings past 7 days through duration of the study. Immediately following activation of the device the subject noticed a profound reduction of her central neuropathic pain (CNP).

All study procedures were approved by the University of Miami Institutional Review Board (IRB) with written consent from the subject in accordance with the Declaration of Helsinki.

Two surgeries were performed 1 week apart: (1) bilateral implantation of electrode leads (Medtronic3387S-40) in the anterolateral PAG with the subject awake; and (2) connection of both leads to extension cables under general anesthesia and tunneling to a generator (Activa PC Neurostimulator 37601, Medtronic). Stimulation was briefly tested during the first surgery, eliciting an emotional response in the subject due to near-complete relief of her long-standing symptoms. For more details see Hentall et al. (2016).

RESULTS

The subject reported a rapid and profound improvement in her CNP, from severe to minimal intensity, when the DBS device was activated on the day after the second surgery. Her DBS stimulation settings were adjusted in periodic office visits (monthly, later every 2 months). In addition, the stimulator was programmed with several blinded choices of parameters (frequency or voltage) for selection at home (Hentall et al., 2016). Among salient findings reported previously, she preferred a very low mean pulse rate (0.67 Hz) and the pain level took several days to shift to a new steady state when the blinded stimulation setting was changed. The blinded choice of settings (ineffective 0.1 V vs. effective 4.5 V) also allowed exclusion of potentially powerful placebo effects.

Figure 1B shows a time-line of the subject's average weekly CNP intensity following her DBS procedure. Whereas she typically reported a pain intensity of 7–8 at baseline, following the procedure her median reported CNP intensity was 2 and remained so the length of the study. The subject also noted a significant decrease in the size of the painful area (**Figure 2**). Pain medication was discontinued by the 17th postoperative week.

The rapid reduction in overall neuropathic pain symptom severity after initiation of DBS was maintained over the course of the study (**Figure 3A**). Evoked pain was reduced to a minimal level. Paresthesia/dysesthesia (pins and needles and tingling) in the painful area also decreased to a significantly lower level.

Before surgery, the subject exhibited both dynamic mechanical allodynia evoked by very weak vibratory stimuli and static mechanical allodynia in the painful area in response to punctuate stimuli applied with the von Frey filament (100 g). Cold allodynia was evoked within a normally non-noxious range, between 22.9°C and 25.2°C. After onset of DBS treatment, however, there were no signs of allodynia in the painful area, consistent with the reduction in pain symptoms. Vibratory stimuli at the threshold level for perception and the punctuate stimulus applied with the large von Frey filament (300 g; 6.65) did not evoke pain after DBS was initiated. Cool and warm detection thresholds were in the normal range (**Figure 3B**). Although she initially perceived pain at the maximal temperature (50°C), both cold and hot stimuli within the default minimum/maximum temperatures of 0°C and 50°C did not evoke a pain sensation at follow-up.

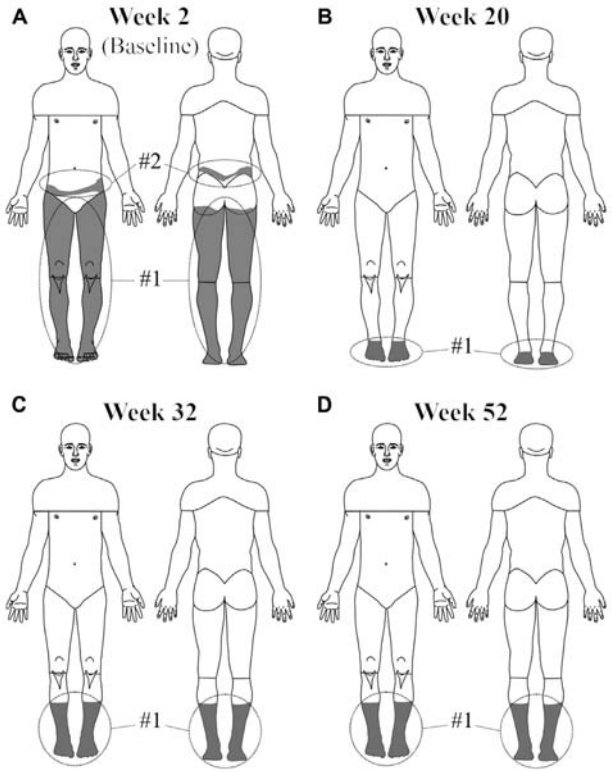


FIGURE 2 | The area of neuropathic pain was greatly reduced in the subject with activation of the device. Whereas before surgery **(A)** her pain was located at the anterior and posterior aspects of both legs and the superior buttocks, by the 20th week after surgery **(B)** pain was only perceived below the ankles. By the 32nd postoperative week **(C)** the pain extended back up to her mid-calf region of both legs and remained unchanged the remainder of the study **(D)**.

Though formal neurocognitive evaluation was not performed, the Beck depression inventory (BDI), MPI-SCI subscales, perceived life control and affective distress did not indicate any negative effects of the DBS (**Supplementary Figure S1**). The BDI scores are not shown because the subject never scored above "1" (including the baseline assessments). Indeed, placement of the PAG DBS device had a tremendous positive impact on the quality of life of the subject. During a qualitative interview after the surgery she stated "It's a whole new world. I'm learning my body all over again. It's life-changing. It still brings tears to my eyes". The DBS device has remained activated with consistent efficacy reported by the patient since implantation over 2 years ago.

DISCUSSION

Electrical stimulation of the PAG significantly reduced the intensity and distribution of CNP-related symptoms and associated abnormal sensory signs (i.e., mechanical and thermal allodynia) in our subject and, consequently, had a profound effect on her quality of life. The consistent beneficial effects on multiple aspects of CNP over the entire study period and the blinded choice of settings controlling for potential placebo

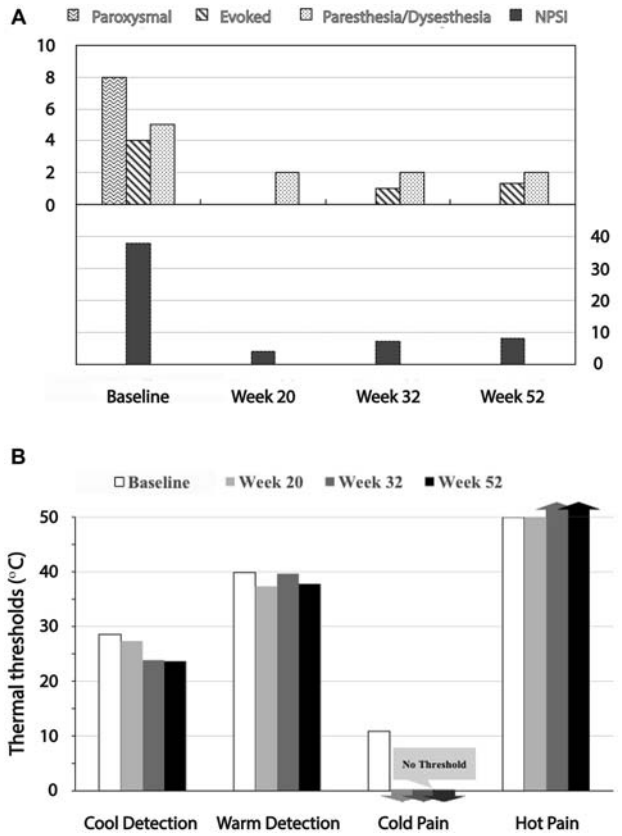


FIGURE 3 | Reduction of Neuropathic Pain Symptom Inventory (NPSI) and QST test scores with device activation. (A) The top graph shows paroxysmal, evoked and paresthesia/dysesthesia scores, all of which were reduced to minimal levels with stimulation. The bottom graph shows the reduction in the NPSI sum score. **(B)** Effects on QST measures. Whereas the subject had significant allodynia before surgery in response to cold and warm, these stimuli within the default minimum/maximum temperatures (0°C and 50°C, respectively) did not evoke pain sensations in follow-up.

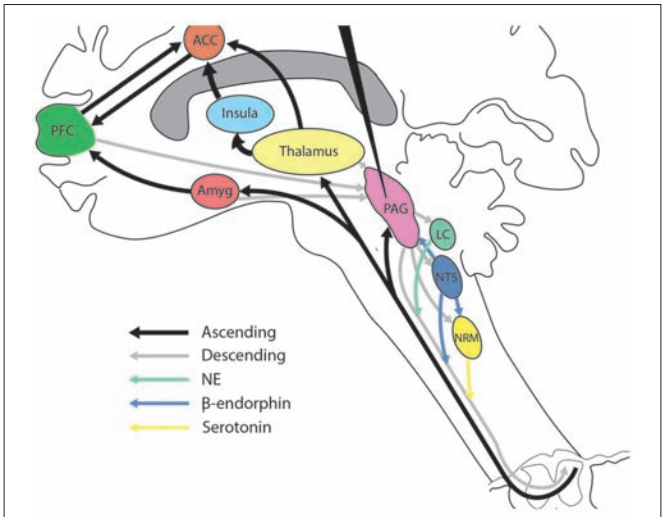


FIGURE 4 | Illustration showing the central role of the periaqueductal gray (PAG) in the modulation of various descending pain systems. Various neurotransmitter systems have been implicated in the treatment of central pain. The PAG has strong ascending and descending connections with each of these systems and is thus in a strong position to modulate CNP. Conventions for the arrows are shown at the bottom left of the figure. ACC, anterior cingulate cortex; Amyg, amygdala; PFC, prefrontal cortex; LC, locus coeruleus; NRM, nucleus raphe magnus; NTS, nucleus tractus solitarius.

effects (Hentall et al., 2016) supports the validity of this case report. Despite 30 years of limited pain relief with various pharmacological treatments she had near-complete relief of her CNP with activation of the DBS device. Such profound and long-lasting improvements in people with CNP pain are rarely reported with conservative measures or other surgical options (Vranken, 2009; Cardenas et al., 2013; Gao et al., 2016).

DBS for Neuropathic Pain

DBS has been used for the treatment of various types of pain since the 1970s, following advances in implantable stimulation devices and the influence of Melzack and Wall's (1965) gate theory. Most evidence available supports the PAG as a useful stimulation target (Pereira and Aziz, 2014). In addition to ascending somatosensory projections, the PAG receives significant inputs from the prefrontal cortex (PFC) and amygdala and then projects to nucleus raphe magnus (NRM) and locus coeruleus (LC) in the midbrain and dorsal horn neurons in the spinal cord (Van Bockstaele et al., 1991; Li et al., 2016). Recent case series on DBS for chronic neuropathic pain, which have utilized superior targeting methods compared to earlier studies and multi-day trials with an externalized electrode prior to final implantation, suggest clinically-relevant improvements of pain symptoms in 67%–83% of patients with heterogeneous types of pain (Boccard et al., 2013). Gray et al. (2014) showed that beyond improving pain symptoms, DBS may also improve mood, anxiety and quality of life. However, very few studies have examined the pain reducing ability of DBS in people with CNP. The acceptance of this therapy in the U.S. has been hindered by the variability of outcomes. Even in cases where patients respond favorably to a several day trial with an externalized stimulator prior to permanent implantation, roughly a quarter of those patients do not experience benefit 1 year after surgery (Boccard et al., 2013).

The recent renewal of interest in DBS for chronic pain has arisen from various factors: (1) improved safety of DBS in general; (2) success with other indications for DBS; (3) advances in imaging and targeting methods; and (4) renewed recognition by the public and health administrators of the detrimental effects of prolonged opioid medication (Schofferman et al., 2014). For patients with CNP of whose etiological or pathological classification is known to make it particularly refractory to typical treatment interventions, particularly if they have failed to respond to conservative measures over many years, DBS may offer benefits. The challenge is to determine which pain phenotypes and patients are most likely to respond. This is an especially hard problem in populations with CNP stemming from CNS injuries, in which multiple pain mechanisms are likely to operate simultaneously (Carlton et al., 2009; Hari et al., 2009; Zeilig et al., 2012; Finnerup et al., 2014).

Possible Mechanisms of DBS for CNP

Spontaneous and evoked excitability within the somatosensory system is normally well-controlled by ascending and descending pain pathways (Basbaum and Fields, 1984; Vranken, 2009). CNP after spinal injury may arise as a consequence of the amplification of signals in residual sensory neurons by spinal and supraspinal processes, such as astrocytic and microglial activation, ultimately influencing various neurotransmitter systems, local connectivity and cytokines (Scholz and Woolf, 2007; Zeilig et al., 2012; Finnerup et al., 2014; Robinson et al., 2016).

The raphe nuclei and their associated modulatory neurotransmitter, serotonin, have long been implicated as important factors influencing pain. However, although selective serotonin reuptake inhibitors are among the most prescribed medications for CNP, little efficacy has been shown in clinical pain trials (Vranken, 2009; Urtikova et al., 2012). While initial behavioral experiments suggested an anti-nociceptive role for serotonin, the link between the neurotransmitter and pain is now viewed as more complex and serotonin may have both pro- and anti-nociceptive properties, depending on the location and mechanism of release (central from raphe vs. peripheral from mast cells) and the serotonergic receptors involved (Urtikova et al., 2012; Bobinski et al., 2015).

The NRM is the largest CNS source of spinal cord serotonin and the PAG is its major input (Van Bockstaele et al., 1991). Serotonergic neurons in the raphe are responsive to inflammatory molecules and markers of CNS injury (Vanegas and Schaible, 2004; Bobinski et al., 2015). It was shown that stimulation of the NRM acutely increases levels of spinal cord PKA, cAMP and CREB, signaling molecules with important roles in development, repair and long-term potentiation. Interestingly, these beneficial effects were elicited at quite low stimulation frequencies (4–8 Hz), not the high frequencies (typically 50–150 Hz) used for nearly all other indications of DBS (Hentall et al., 2006; Carballosa-Gonzalez et al., 2014). This is relevant because while high-frequency DBS is thought to functionally inhibit its target, low-frequency stimulation is considered stimulatory and, in the present case, should lead to activation of PAG and NRM and the release of modulatory neurotransmitters in the spinal cord (Hentall and Gonzalez, 2012).

Norepinephrine (NE) has also been implicated in the modulation of pain (Hickey et al., 2014; Li et al., 2016). NE reuptake inhibitors or combinations of NE and 5-HT reuptake inhibitors are common therapies for CNP and are recommended first-line treatments for patients with SCI (Guy et al., 2016). Also, the α2 receptor agonist clonidine is used to treat the withdrawal effects of opioids (Siddall et al., 2000). Recent optogenetic studies have shown that focal activation of the LC, whose major inputs are from the PFC, amygdala, PAG and dorsal noradrenergic bundle, may be either pro- or anti-nociceptive, suggestive of different neuron subgroups within the LC (Hickey et al., 2014). Consistent with this, recently Li et al. (2016), used a canine adenoviral vector expressing channelrhodopsin2 to target ponto-spinal NE neurons, and found a subset of ventral LC neurons with spinal projections that is likely involved in the regulation of nociception. Interestingly, this subgroup of LC neurons had lower average firing rate than other noradrenergic neurons of the LC.

DBS of the PAG could also relieve pain via neurons that secrete β-endorphin (Siddall et al., 2000; Schofferman et al., 2014). β-endorphin is derived from the prohormone pro-opiomelanocortin (POMC). Cerritelli et al. (2016) recently identified a subset of 100–200 POMC neurons in the nucleus tractus solitarius (NTS) that, when optogenetically stimulated, led to significant analgesic effects, that were blocked by administration of naloxone, an opioid receptor antagonist. Thus several highly interconnected pathways may be involved in modulating ascending pain information and are accessible by DBS in the PAG. For a schematic overview see **Figure 4.**

Prospects for Improved Rates of Success

DBS of brainstem targets can be considered for ameliorating severe CNP that is refractory to pharmacological treatment. The best evidence for any pharmacological treatment of CNP after SCI is for the anticonvulsant pregabalin (Guy et al., 2016). However, the treatment responses to pregabalin for CNP are not consistent. Indeed, a large recent randomized trial showed the numbers needed to treat for >30% pain reduction was about 7 (Cardenas et al., 2013). Long-term opioid therapy has already proven to be a poor long-term option (Schofferman et al., 2014). When available, non-invasive brain stimulation methods, such as repetitive transcranial magnetic stimulation, are preferrable over DBS. However, their efficacy is yet to be proven in heterogeneous pain conditions and they are currently not recommended treatment approaches for patients with CNP related to SCI (Gao et al., 2016; Guy et al., 2016).

If DBS is to become an accepted therapy for CNP, its efficacy and consistency need to be improved. Anecdotally patients may experience outstanding results, but many are left to a greater or lesser extent with the original debilitating pain (Coffey, 2001; Boccard et al., 2013; Pereira and Aziz, 2014). It is thus important to identify predictors of long-term efficacy and understand mechanisms of tolerance. Comprehensive evaluation of neuropathic pain symptoms including severity, location and temporal pattern, and quantitative pain assessments, such as used in this study, may help in this task, along with novel brain imaging techniques. Thus, better defined pain phenotypes based on comprehensive pain assessment protocols may lead to more reliable selection of patients amenable to this therapy. Better knowledge of responsive pain phenotypes in this notoriously difficult patient population is also important for comparing treatments, especially because novel therapies continue to emerge, such as minimally invasive ablative techniques (Tiwari et al., 2014).

AUTHOR CONTRIBUTIONS

WJJ performed the majority of work on preparing the manuscript, figures and integrating other authors' comments.

JA conducted pain assessments and helped prepare the pain data and figures. IDH prepared the application for the clinical trial and helped prepare the manuscript. JRJ, AM-A and CCL performed the surgical and neurological procedures and revised the final versions of the manuscript. EW-N helped prepare the manuscript and oversee and summarize all pain assessments.

FUNDING

Funding for this project was provided by the U.S. Department of Defense—Spinal Cord Injury Program (W81XWH-12-1 -0559).

REFERENCES

Basbaum, A. I., and Fields, H. L. (1984). Endogenous pain control systems: brainstem spinal pathways and endorphin circuitry. *Annu. Rev. Neurosci.* 7, 309–338. doi: 10.1146/annurev.neuro.7.1.309

Bobinski, F., Ferreira, T. A., Córdova, M. M., Dombrowski, P. A., da Cunha, C., Santo, C. C., et al. (2015). Role of brainstem serotonin in analgesia produced by low-intensity exercise on neuropathic pain after sciatic nerve injury in mice. *Pain* 156, 2595–2606. doi: 10.1097/j.pain.0000000000000372

Boccard, S. G., Pereira, E. A., Moir, L., Aziz, T. Z., and Green, A. L. (2013). Long-term outcomes of deep brain stimulation for neuropathic pain. *Neurosurgery* 72, 221–230; discussion 231. doi: 10.1227/NEU.0b013e31827 b97d6

Bouhassira, D., Attal, N., Fermanian, J., Alchaar, H., Gautron, M., Masquelier, E., et al. (2004). Development and validation of the neuropathic pain symptom inventory. *Pain* 108, 248–257. doi: 10.1016/j.pain.2003. 12.024

Carballosa-Gonzalez, M. M., Vitores, A., and Hentall, I. D. (2014). Hindbrain raphe stimulation boosts cyclic adenosine monophosphate and signaling proteins in the injured spinal cord. *Brain Res.* 1543, 165–172. doi: 10.1016/j. brainres.2013.11.013

Cardenas, D. D., Nieshoff, E. C., Suda, K., Goto, S., Sanin, L., and Knapp, L. E. (2013). A randomized trial of pregabalin in patients with neuropathic pain due to spinal cord injury. *Neurology* 80, 533–539. doi: 10.1212/WNL. 0b013e318281546b

Carlton, S. M., Du, J., Tan, H. Y., Nesic, O., Hargett, G. L., Bopp, A. C., et al. (2009). Peripheral and central sensitization in remote spinal cord regions contribute to central neuropathic pain after spinal cord injury. *Pain* 147, 265–276. doi: 10.1016/j.pain.2009.09.030

Cerritelli, S., Hirschberg, S., Hill, R., Balthasar, N., and Pickering, A. E. (2016). Activation of brainstem pro-opiomelanocortin neurons produces opioidergic analgesia, bradycardia and bradypnoea. *PLoS One* 11:e0153187. doi: 10.1371/journal.pone.0153187

Coffey, R. J. (2001). Deep brain stimulation for chronic pain: results of two multicenter trials and a structured review. *Pain Med.* 2, 183–192. doi: 10.1046/j. 1526-4637.2001.01029.x

Finnerup, N. B., Norrbrink, C., Trok, K., Piehl, F., Johannesen, I. L., Sørensen, J. C., et al. (2014). Phenotypes and predictors of pain following traumatic spinal cord injury: a prospective study. *J. Pain* 15, 40–48. doi: 10.1016/j.jpain.2013. 09.008

Gao, F., Chu, H., Li, L., Yang, M., Du, L., Chen, L., et al. (2016). Repetitive transcranial magnetic stimulation for pain after spinal cord injury: a systematic review and meta-analysis. *J. Neurosurg. Sci.* [Epub ahead of print].

Gray, A. M., Pounds-Cornish, E., Eccles, F. J., Aziz, T. Z., Green, A. L., and Scott, R. B. (2014). Deep brain stimulation as a treatment for neuropathic pain: a longitudinal study addressing neuropsychological outcomes. *J. Pain* 15, 283–292. doi: 10.1016/j.jpain.2013.11.003

Guy, S. D., Mehta, S., Casalino, A., Côté, I., Kras-Dupuis, A., Moulin, D. E., et al. (2016). The CanPain SCI clinical practice guidelines for rehabilitation management of neuropathic pain after spinal cord: recommendations for treatment. *Spinal Cord* 54, S14–S23. doi: 10.1038/sc.2016.90

SUPPLEMENTARY MATERIAL

The Supplementary Material for this article can be found online at: http://journal.frontiersin.org/article/10.3389/fnhum.2017.00177/full#supplementary-material

FIGURE S1 | Assessment of psychosocial impact and subjective distress experienced by the patient before and after surgery. Comparison of MPI—spinal cord injury (SCI) subscales, Life Control and Affective Distress, suggest the patient did not develop new cognitive or affective impairments following the surgery. Each assessment was performed by the same assessor. More details about the MPI-SCI may be found at Widerström-Noga et al. (2006).

Hari, A. R., Wydenkeller, S., Dokladal, P., and Halder, P. (2009). Enhanced recovery of human spinothalamic function is associated with central neuropathic pain after SCI. *Exp. Neurol.* 216, 428–430. doi: 10.1016/j. expneurol.2008.12.018

Hentall, I. D., and Gonzalez, M. M. C. (2012). Promotion of recovery from thoracic spinal cord contusion in rats by stimulation of medullary raphe or its midbrain input. *Neurorehabil. Neural Repair* 26, 374–384. doi: 10.1177/1545968311425178

Hentall, I. D., Luca, C. C., Widerstrom-Noga, E., Vitores, A., Fisher, L. D., Martinez-Arizala, A., et al. (2016). The midbrain central gray best suppresses chronic pain with electrical stimulation at very low pulse rates in two human cases. *Brain Res.* 1632, 119–126. doi: 10.1016/j.brainres.2015. 12.021

Hentall, I. D., Pinzon, A., and Noga, B. R. (2006). Spatial and temporal patterns of serotonin release in the rat's lumbar spinal cord following electrical stimulation of the nucleus raphe magnus. *Neuroscience* 142, 893–903. doi: 10.1016/j. neuroscience.2006.06.038

Hickey, L., Li, Y., Fyson, S. J., Watson, T. C., Perrins, R., Hewinson, J., et al. (2014). Optoactivation of locus ceruleus neurons evokes bidirectional changes in thermal nociception in rats. *J. Neurosci.* 34, 4148–4160. doi: 10.1523/JNEUROSCI.4835-13.2014

Li, Y., Hickey, L., Perrins, R., Werlen, E., Patel, A. A., Hirschberg, S., et al. (2016). Retrograde optogenetic characterization of the pontospinal module of the locus coeruleus with a canine adenoviral vector. *Brain Res.* 1641, 274–290. doi: 10.1016/j.brainres.2016.02.023

Melzack, R., and Wall, P. D. (1965). Pain mechanisms: a new theory. *Science* 150, 971–979. doi: 10.1126/science.150.3699.971

Pereira, E. A., and Aziz, T. Z. (2014). Neuropathic pain and deep brain stimulation. *Neurotherapeutics* 11, 496–507. doi: 10.1007/s13311-014-0278-x

Robinson, C., Apgar, C., and Shapiro, L. A. (2016). Astrocyte hypertrophy contributes to aberrant neurogenesis after traumatic brain injury. *Neural Plast.* 2016:1347987. doi: 10.1155/2016/1347987

Schofferman, J., Fishman, S. M., Harden, R. N., and Kirschner, K. L. (2014). Did we reach too far? The opioid epidemic and chronic pain. *PM R* 6, 78–84. doi: 10.1016/j.pmrj.2013.12.003

Scholz, J., and Woolf, C. J. (2007). The neuropathic pain triad: neurons, immune cells and glia. *Nat. Neurosci.* 10, 1361–1368. doi: 10.1038/nn1992

Siddall, P. J., McClelland, J. M., Rutkowski, S. B., and Cousins, M. J. (2003). A longitudinal study of the prevalence and characteristics of pain in the first 5 years following spinal cord injury. *Pain* 103, 249–257. doi: 10.1016/s0304-3959(02)00452-9

Siddall, P. J., Molloy, A. R., Walker, S., Mather, L. E., Rutkowski, S. B., and Cousins, M. J. (2000). The efficacy of intrathecal morphine and clonidine in the treatment of pain after spinal cord injury. *Anesth. Analg.* 91, 1493–1498. doi: 10.1097/00000539-200012000-00037

Tiwari, P., Danish, S., and Madabhushi, A. (2014). Identifying MRI markers to evaluate early treatment related changes post laser ablation for cancer pain management. *Proc. SPIE Int. Soc. Opt. Eng.* 9036:90362L. doi: 10.1117/12.2043729

Urtikova, N., Berson, N., Van Steenwinckel, J., Doly, S., Truchetto, J., Maroteaux, L., et al. (2012). Antinociceptive effect of peripheral serotonin

5-HT_{2B} receptor activation on neuropathic pain. *Pain* 153, 1320–1331. doi: 10.1016/j.pain.2012.03.024

Van Bockstaele, E. J., Aston-Jones, G., Pieribone, V. A., Ennis, M., and Shipley, M. T. (1991). Subregions of the periaqueductal gray topographically innervate the rostral ventral medulla in the rat. *J. Comp. Neurol.* 309, 305–327. doi: 10.1002/cne.903090303

Vanegas, H., and Schaible, H. G. (2004). Descending control of persistent pain: inhibitory or facilitory? *Brain Res. Rev.* 46, 295–309. doi: 10.1016/j.brainresrev.2004.07.004

Vranken, J. H. (2009). Mechanisms and treatment of neuropathic pain. *Cent. Nerv. Syst. Agents Med. Chem.* 9, 71–78. doi: 10.2174/187152409787601932

Widerström-Noga, E., Biering-Sørensen, F., Bryce, T. N., Cardenas, D. D., Finnerup, N. B., Jensen, M. P., et al. (2014). The international spinal cord injury pain basic data set (version 2.0). *Spinal Cord* 52, 282–286. doi: 10.1038/sc.2014.4

Widerström-Noga, E. G., Cruz-Almeida, Y., Martinez-Arizala, A., and Turk, D. C. (2006). Internal consistency, stability and validity of the spinal cord injury version of the multidimensional pain inventory. *Arch. Phys. Med. Rehabil.* 87, 516–523. doi: 10.1016/j.apmr.2005.12.036

Widerström-Noga, E., Felix, E. R., Adcock, J. P., Escalona, M., and Tibbett, J. (2016). Multidimensional neuropathic pain phenotypes after spinal cord injury. *J. Neurotrauma* 33, 482–492. doi: 10.1089/neu.2015.4040

Zeilig, G., Enosh, S., Rubin-Asher, D., Lehr, B., and Defrin, R. (2012). The nature and course of sensory changes following spinal cord injury: predictive properties and implications on the mechanism of central pain. *Brain* 135, 418–430. doi: 10.1093/brain/awr270

Conflict of Interest Statement: The authors declare that the research was conducted in the absence of any commercial or financial relationships that could be construed as a potential conflict of interest.

Copyright © 2017 Jermakowicz, Hentall, Jagid, Luca, Adcock, Martinez-Arizala and Widerström-Noga. This is an open-access article distributed under the terms of the Creative Commons Attribution License (CC BY). The use, distribution or reproduction in other forums is permitted, provided the original author(s) or licensor are credited and that the original publication in this journal is cited, in accordance with accepted academic practice. No use, distribution or reproduction is permitted which does not comply with these terms.

frontiers in Neural Circuits

ORIGINAL RESEARCH
published: 19 May 2017
doi: 10.3389/fncir.2017.00034

LFP Oscillations in the Mesencephalic Locomotor Region during Voluntary Locomotion

Brian R. Noga[1], Francisco J. Sanchez[1], Luz M. Villamil[1], Christopher O'Toole[1], Stefan Kasicki[2], Maciej Olszewski[2], Anna M. Cabaj[2], Henryk Majczyński[2], Urszula Sławińska[2] and Larry M. Jordan[3]*

[1]*The Miami Project to Cure Paralysis, Department of Neurological Surgery, University of Miami Miller School of Medicine, Miami, FL, United States,* [2]*Department of Neurophysiology, Nencki Institute of Experimental Biology, Warsaw, Poland,* [3]*Department of Physiology, Spinal Cord Research Centre, University of Manitoba, Winnipeg, MB, Canada*

Oscillatory rhythms in local field potentials (LFPs) are thought to coherently bind cooperating neuronal ensembles to produce behaviors, including locomotion. LFPs recorded from sites that trigger locomotion have been used as a basis for identification of appropriate targets for deep brain stimulation (DBS) to enhance locomotor recovery in patients with gait disorders. Theta band activity (6–12 Hz) is associated with locomotor activity in locomotion-inducing sites in the hypothalamus and in the hippocampus, but the LFPs that occur in the functionally defined mesencephalic locomotor region (MLR) during locomotion have not been determined. Here we record the oscillatory activity during treadmill locomotion in MLR sites effective for inducing locomotion with electrical stimulation in rats. The results show the presence of oscillatory theta rhythms in the LFPs recorded from the most effective MLR stimulus sites (at threshold $\leq$60 μA). Theta activity increased at the onset of locomotion, and its power was correlated with the speed of locomotion. In animals with higher thresholds (>60 μA), the correlation between locomotor speed and theta LFP oscillations was less robust. Changes in the gamma band (previously recorded *in vitro* in the pedunculopontine nucleus (PPN), thought to be a part of the MLR) were relatively small. Controlled locomotion was best achieved at 10–20 Hz frequencies of MLR stimulation. Our results indicate that theta and not delta or gamma band oscillation is a suitable biomarker for identifying the functional MLR sites.

Keywords: deep brain stimulation, mesencephalic locomotor region, local field potentials, locomotion, spinal cord injury

OPEN ACCESS

Edited by:
Deborah Baro, Georgia State University, United States

Reviewed by:
James Joseph Chrobak, University of Connecticut, United States
Tatiana Korotkova, Leibniz Institute for Molecular Pharmacology (FMP), Germany

****Correspondence:***
Brian R. Noga
bnoga@miami.edu

Received: *24 October 2016*
Accepted: *28 April 2017*
Published: *19 May 2017*

Citation:
Noga BR, Sanchez FJ, Villamil LM, O'Toole C, Kasicki S, Olszewski M, Cabaj AM, Majczyński H, Sławińska U and Jordan LM (2017) LFP Oscillations in the Mesencephalic Locomotor Region during Voluntary Locomotion. Front. Neural Circuits 11:34. doi: 10.3389/fncir.2017.00034

INTRODUCTION

Several areas of the brain have been shown to elicit locomotion when stimulated, including areas of the diencephalon and mesencephalon (Grillner et al., 1997; Jordan and Sławińska, 2014; Kiehn, 2016; Takakusaki et al., 2016). Deep brain stimulation (DBS) of the mesencephalic locomotor region (MLR), a coordination center for activation and control of spinal locomotor generator neurons, is increasingly under consideration as a potential treatment strategy for improving locomotion in Parkinson's disease (PD; freezing of gait, or FOG) and following spinal cord injury (SCI). The MLR was originally described in the cat by Shik et al. (1966), and was considered to be co-extensive with the cuneiform nucleus (CnF). This conclusion has been confirmed by many researchers in subsequent years, and this evidence has been extensively reviewed

(Mori et al., 1989, 1992; Whelan, 1996; Grillner et al., 1997; Jordan, 1998; Ryczko and Dubuc, 2013; Jordan and Sławińska, 2014). The pedunculopontine nucleus (PPN) is considered a component of the MLR, a suggestion advanced by Garcia-Rill et al. (1986, 1987, 2011). They pointed out that the PPN is defined by the presence of cholinergic neurons, and gait defects, especially in PD, have been proposed to be due to pathological changes in the cholinergic neurons in the PPN. As a result, attempts to localize the areas suitable for DBS for improving locomotion by stimulating the MLR area have focused on the PPN, but increasingly it has been recognized that the CnF and associated structures may be more appropriate targets (Mazzone et al., 2005; Stefani et al., 2007; Piallat et al., 2009; Shimamoto et al., 2010; Alam et al., 2011; Hamani et al., 2011; Thevathasan et al., 2012).

Local field potentials (LFPs) can serve as biomarkers for movement disorders and for improved electrode targeting for DBS (Thompson et al., 2014), and the increasing emphasis on MLR DBS for restoring gait in human subjects necessitates the demonstration of LFPs recorded from effective MLR sites. Surprisingly, no study has been carried out on LFPs recorded in the functionally defined MLR under controlled conditions in an animal model. Locomotor activity was initially associated with theta oscillations (6–12 Hz) in hippocampal LFP (Kramis et al., 1975), and this rhythm was subsequently shown to be prominent in hypothalamic locomotor regions that were functionally identified as locomotion-inducing sites (Sławińska and Kasicki, 1995, 1998). Similar LFP activity might be expected of other locomotor areas of the brain, because theta oscillatory rhythms in LFPs are thought to coherently bind cooperating neuronal ensembles to produce behaviors, including locomotion (Bland and Oddie, 2001). However, LFPs have never been recorded during spontaneous locomotion from MLR sites functionally defined by stimulation to evoke locomotion in the same animal, although these sites are clearly a component of the ensemble of brain areas controlling locomotion.

Gamma band activity has been proposed to be a characteristic feature of the PPN (Garcia-Rill et al., 2015), and the intrinsic properties of PPN neurons recorded *in vitro* (Simon et al., 2010; Garcia-Rill et al., 2011, 2015) have led to the suggestion that their discharge in the gamma range of frequencies "...explains the requirement to stimulate this region at 40–60 Hz to optimally induce locomotion" (Garcia-Rill et al., 2015). However, clinical studies using DBS have indicated that lower frequencies of stimulation are more effective (Ferraye et al., 2010; Nosko et al., 2015). Optogenetic activation of the MLR at frequencies lower than 40 Hz has recently been shown to reliably induce locomotion in mice (Lee et al., 2014). Moreover, Ferraye et al. (2010) concluded that "The best effects were seen in the patients with active contacts located slightly posterior to the pedunculopontine nucleus, in the cuneiform and subcuneiform nuclei..." Microelectrode recordings have suggested that neurons that modulate firing in response to imagined gait actually tend to be located in the subcuneiform region dorsal to the PPN (Piallat et al., 2009). Thevathasan et al. (2012) showed in patients with Parkinsonism that alpha power (frequency range equivalent to our theta in rats) was maximal in the caudal PPN region, and they demonstrated a correlation between alpha oscillations and improved gait performance. This caudal "pedunculopontine region" corresponds to the cuneiform and subcuneiform nuclei in humans (Ferraye et al., 2010; Alam et al., 2011). Thus there is increasing evidence that the emphasis on the PPN as the most effective site for DBS to improve locomotion may not be warranted (Alam et al., 2011), and there is increasing evidence for the CnF involvement in human studies instead. We undertook a study focusing on the CnF area of the MLR in the rat model to determine the LFP signature of this area in recordings from confirmed DBS sites for eliciting locomotion.

Takakusaki et al. (2005, 2016) and Takakusaki (2008, 2013) have demonstrated that the CnF is effective for eliciting locomotion in decerebrate cats, while the PPN controls muscle tone and stimulation in this region may actually suppress locomotion. Other workers have challenged the importance of the PPN as a component of the MLR since PPN lesions do not alter locomotor capability (Winn, 2006; Hernández-Chan et al., 2011; MacLaren et al., 2014; Gut and Winn, 2015, 2016). Moreover, neurons activated during locomotion (indicated by the presence of the activity-dependent marker Fos) are found in the CnF and other nearby areas, including the deep mesencephalic nucleus (DpMe; Jordan, 1998; Vianna et al., 2003; Heise and Mitrofanis, 2006), but not in the PPN. PPN cholinergic neurons of the MLR have been implicated in the initiation of locomotion (reviewed in Ryczko and Dubuc, 2013). However, activation of the cholinergic component of the PPN using a chemogenetic approach induced only subtle effects on locomotion in freely moving, control rats (Pienaar et al., 2015). Takakusaki et al. (2016) have shown that the effective MLR sites are not co-extensive with the cholinergic PPN neurons in cats. A recent optogenetic study in the mouse has also cast doubt on the importance of cholinergic neurons within the PPN for the initiation of locomotion from a standstill (Roseberry et al., 2016). Rather, they have demonstrated that cholinergic neurons may play a role in the modulation of ongoing locomotion. Furthermore, they found that within the MLR the glutamatergic subpopulation encodes locomotor state and speed and is necessary and sufficient for locomotion. Taken together, these studies increase the importance of determining the LFP signature of effective MLR sites, especially those in the CnF region.

In this study, we specifically targeted the CnF region to provide the first analysis of LFPs recorded from this portion of the functionally defined MLR in intact, freely moving rats and to determine the LFP signature and the most effective stimulus parameters of these effective MLR sites. We then used recordings from these sites to test the hypothesis that the theta rhythm that is a characteristic of locomotion in other structures such as the hippocampus and the hypothalamic locomotor areas (Sławińska and Kasicki, 1995, 1998) is also prominent in the MLR during voluntary locomotion in these animals, consistent with the suggestion that the theta rhythm might bind cooperating neuronal ensembles to produce locomotion. Here we focus primarily on the theta LFP oscillations, but we also subject

other frequency bands to similar analysis. We also show that the same LFP features that are prominent in intact animals persist after incomplete SCI, and suggest that they might be used as a biomarker of effective sites for electrode placements for DBS.

MATERIALS AND METHODS

Experiments were performed on 28 adult female Sprague-Dawley rats (240–350 g) following their acclimation to housing, handling and treadmill locomotor assessment. Rats were housed separately. Animals were exposed to a 12-h light/dark cycle and had free access to food and water. The number of animals used, and their pain and distress were minimized. Experimental procedures were approved by the University of Miami IACUC committee in accordance with NIH guidelines (National Institutes of Health Publications, No. 80-23; revised 1996). Experiments in Poland were carried out with the approval of the First Ethics Committee for Animal Experimentation according to the principles of experimental conditions and laboratory animal care of the European Union and the Polish Law on Protection of Animals Used for Experiments.

MLR-DBS and EMG Electrode Implantation

Parylene-insulated, tungsten microelectrodes, (A-M Systems Inc., Carlsborg, WA, USA; 127 μm diameter, 12 degree tip taper, adjusted to 0.07–0.4 MΩ) were stereotaxically implanted into the region of the MLR under isoflurane anesthesia (Milner and Mogenson, 1988). After exposing the cranium with a short skin incision, a small ∼1 mm diameter hole was drilled through the left side of the skull above the stereotaxic target (∼0.7–1.2 mm anterior to the interaural line, 2.0 mm lateral to the midline). Small, stainless steel, self-tapping screws served to anchor the electrode base to the skull. A titanium screw was inserted into the parietal bone immediately opposite the electrode insertion point to serve as an attachment for the return lead (anode). The microelectrode assembly was lowered using a micromanipulator aiming for a site ∼6.2 mm DV (Paxinos and Watson, 1998). The base of the microelectrode assembly was then rigidly fixed to the skull and to the screws using dental cement (Stoelting, Wood Dale, IL, USA). The wound was closed by sutures around the implant. Pin connectors projecting vertically from the electrode assembly allowed electrical connection to the voltage and/or current stimulators and to preamplifiers for recording of LFPs (see below).

For the electromyography (EMG) recordings, bipolar electrodes were implanted bilaterally in the soleus (Sol) muscle (extensor, active during the stance phase of the step cycle) and the tibialis anterior (TA) muscle (flexor, active during the swing phase of the step cycle). The electrodes were made of Teflon-coated stainless steel wire (0.24 mm in diameter; AS633, CoonerWire Co., Chatsworth, CA, USA). The tips of the electrodes with 1–1.5 mm of the insulation removed were pulled through a cutaneous incision on the back of the animal, and each of the hook electrode was inserted into the appropriate muscle and secured by a suture (Sławińska et al., 2000). The distance between the electrode tips was 1–2 mm. The connector with the other ends of the wires fixed to it, covered with dental cement (Spofa Dental, Prague, Czech Republic) and silicone (3140 RTV, Dow Corning, Midland, MI, USA), was secured to the back of the animal.

Locomotor Threshold Determination

The current or voltage threshold for locomotor induction (minimum strength to elicit locomotor activity) was determined for all animals by stimulating awake rats in an open field. The MLR was stimulated (cathodal stimulation) during behavioral testing after recovery from surgery (∼1 week) and several weeks after that in some animals to determine stability and effect of long-term implantation. Thresholds were also tested in animals subject to SCIs. Thresholds for locomotor induction were carefully tested over the stimulation range: frequency 10–70 Hz (10, 20, 50 and 70 Hz), and pulse duration 0.2, 0.5, 1.0 and 2.0 ms (Milner and Mogenson, 1988; Coles et al., 1989). During any session, a stimulation frequency was chosen and threshold strengths determined for each pulse width. Thresholds were determined in current mode (1–350 μA), but voltage assessments (typically less than 7 V) were made in some animals. Thresholds were determined by gradually increasing the strength of stimulation until locomotor movements ensued. Locomotor responses to sudden stimulation at strengths above threshold were also examined in most animals. Locomotor responses were visually classified by three experienced independent observers (FJS, CO and BRN). *Slow speed* (walk) or *Fast speed* (trot or gallop; Gillis and Biewener, 2001) was determined based on two (or more) identical observer ratings. Then, in random order, another stimulation frequency was chosen and the process was repeated. Between each pulse width test, animals were allowed to rest for approximately 30–60 s.

LFP Recording

For the chronic LFP recordings in freely moving rats the same electrodes as for MLR-DBS stimulation were used. MLR field potential recordings were made at 2000× gain, 1–300 Hz band pass filtering, with typically a 60 Hz notch filter and sampled at 1–2 kHz for later analysis. Connection to the pre-amplifier was made via wires 60–90 cm in length attached to the pin connectors on the electrode assembly with the indifferent wire connected to the titanium screw placed in the parietal bone. Animals were placed on an adjustable speed treadmill belt enclosed by a transparent plexiglass box, with automated ventilation (Treadmill Simplex II, Columbus Instruments, Columbus, OH, USA). Animals were previously trained to voluntarily walk on the treadmill and did not receive any electrical shocks for motivation. Video of each session was recorded using a 60 Hz frame rate (3-D PeakMotus Motion Measurement System). Field potentials were recorded for 30 s periods at rest and at each treadmill speed (10, 15, 20 m/min). The order varied depending on how cooperative the animals were during the different recording sessions. In most cases,

animals started from rest and the belt speed was increased incrementally to each designated speed and then the belt was turned off. In other cases, recordings commenced once stable locomotion at higher speeds was attained and then the belt speed was decreased to other speeds and then stopped. Field potentials were also recorded following SCI in some animals (up to 17 weeks). For voluntary locomotion on a treadmill in these animals, speeds were dependent upon the severity of the injury.

Spinal Cord Injuries

Mid-thoracic contusion injuries were made using the New York University Impactor device (Gruner, 1992) under isoflurane anesthesia (2% in O_2) and sterile technique. A dorsal laminectomy was performed on the T8 vertebra to expose the dura over the T9 spinal segment. The adjacent vertebrae were clamped to stabilize and support the column during impact. Mild, moderate and severe contusion injuries were made by dropping a 10-g rod onto the exposed spinal cord from a height of 6.25, 12.5 or 25 mm, respectively. The impact height and velocity errors were below 6%, within acceptable parameters to ensure consistency. Average compression distances of 1.283 ± 0.182, 1.653 ± 0.201 and 2.01 ± 0.187 mm for mild, moderate and severe injuries, respectively, were also in close agreement with previously published data (Basso et al., 1996). The muscles were sutured in layers and the skin was closed with stainless-steel surgical clips. Rats were allowed to recover in a temperature controlled environment and were provided with accessible water and food. Gentamicin (2–3 mg/kg; APP Pharmaceuticals, Lake Zurich, IL, USA) and buprenorphine (0.1 mg/kg; Buprenex Inj.; Reckitt Benckiser Pharmaceuticals Inc., Richmond, VA, USA) were administered after surgery for 7 and 3 days, respectively. Lactated Ringers solution was administered BID SC for 7 days (5 ml/injection). The bladder was expressed twice daily until each animal regained continence. Animals were monitored daily for skin and weight changes. Animals were removed from the study if any post-operative complications could not be successfully treated (e.g., excessive weight loss, infections and pain behaviors including self-mutilation such as autonomy or excessive grooming leading to ulceration).

Immunohistochemistry

Under anesthesia, an electrolytic lesion was made at each stimulation site by passing a small (1 mA), brief (2–5 s) DC current through the DBS electrode. Animals were perfused intracardially with paraformaldehyde and their brains removed for histological reconstruction. The tissue surrounding the stimulation site was processed for paraffin and cut into 15 μm coronal sections. Sections were de-paraffinized and the immunohistochemical procedures optimized using a primary antibody dilution series. For the pre-adsorption control, tissue sections were incubated only with normal donkey serum (NDS: 10%; in 0.1 M phosphate buffered saline or PBS) then in 0.3% Triton X-100 in 0.1 M PBS after blocking endogenous peroxidase with 3% H_2O_2 at room temperature. Immunoreactivity was totally absent after omission of the primary antibodies. To examine glial scar formation around the stimulation electrode and to aid in the identification of the electrode tip within the tissue, sections were stained with an antibody to glial fibrillary acidic protein (GFAP). Sections were incubated in 1:500 rabbit polyclonal anti-GFAP (Millipore AB5804) overnight (0.1 M PBS with 0.3% Triton X-100 + 5% NDS), washed in 0.1 M PBS 0.3% Triton X-100 and then incubated in secondary donkey anti-rabbit Alexa 594 (1:200; A21207, Molecular Probes) in 0.1 M PBS with 0.3% Triton X-100 + 5% NDS. Selected sections (each in a series of 10) were then counterstained and coverslipped with either Vectashield Hard-set dry mounting media (H-1500) with 4′,6′-diamidino-2-phenylindole dilactate (DAPI) a fluorescent DNA counterstain or with Cresyl Violet to confirm anatomical localization of the electrode position and anatomical regions of the brain according to Paxinos and Watson (1998). Digital epi-fluorescent images were captured on a Zeiss 200M Axiovert microscope at 5× magnification.

Data Analysis and Statistics

For statistical analysis of LFP activity, 15 of the tested animals were selected on the basis of a consistent and complete sequence of behavior and the absence of noise/movement artifact. The data files (digitized at 2 kHz, band-pass filtered between 1 Hz and 300 Hz) were converted to Spike2 (CED, UK) format. The spectrograms and power spectra were analyzed using built-in functions of Spike2. Movement artifacts in the LFP channels were manually removed before analysis, under visual inspection. For spectrograms a window of 2048 points was used; the calibration of the y axis was adjusted to the dynamics of the data and is shown on the plots. Power spectra were calculated using an FFT algorithm (Hanning window, bins/channel 2048, width of bin 0.488 Hz). The total power for the delta (0–4 Hz), low (4–6 Hz) and high (6–12 Hz) theta, beta (12–28 Hz), low (28–55 Hz) and high (65–100 Hz) gamma frequency bands and the power and frequency for the peak in the power spectra of delta and theta bands related to various locomotor speeds or resting conditions for each trial were imported to Prism 6 (GraphPad Software, Inc., La Jolla, CA, USA). The D'Agostino test was performed before statistical tests to verify that the data followed a Gaussian distribution (normality test). We chose to separate the theta band into low and high components because the theta band recorded in the hippocampus (Kramis et al., 1975) was separated into Type 1 (corresponding to our high theta and linked to locomotion) and Type II (corresponding to our low theta and associated with sleeping and immobility). Comparison of thresholds effective for inducing locomotion was performed with unpaired t-test. Other analyses were performed with two-way Repeated Measures ANOVA (RM ANOVA). The Holm-Sidak's test was used for multiple comparisons. The minimum significance was set at $p = 0.05$. Linear regression analysis was performed using Prism 6 (GraphPad Software, Inc.). The speed was taken as an independent x-variable, while the parameters describing power and frequencies were

taken as *y*-variable (see "Results" Section). The regression coefficient and the significance of slope were calculated for each analysis.

RESULTS

Evoked Locomotion in Freely-Moving Animals

The efficacy of MLR stimulation was examined in freely moving animals within 1 week of implantation. **Figure 1A** shows an example of EMG recordings during electrically induced locomotor behavior of a rat in an open field. A stimulus applied in the MLR at a strength just above threshold (28 μA) induced increased attention indicated by an orienting reaction, looking around and then forward quadrupedal locomotion commencing around 3.5 s after the onset of the stimulation, leading to regular locomotion. This pattern of activity is similar to that observed in freely moving cats with the stimulating electrode implanted in the cuneiform nucleus (Mori et al., 1989).

Figure 1B presents EMGs and LFPs from the same effective site within the MLR during voluntary locomotion of the same rat along a runway. The animal's movement was detected with photocells positioned at intervals along the runway. MLR LFPs recorded prior to, during and after voluntary locomotor activity on a runway showed dramatic changes during the transition from rest to walking. During recording from the effective MLR site we observed irregular LFP activity during resting. Transition to the locomotor activity detected with EMG was associated with clearly enhanced theta rhythm (6–12 Hz; **Figures 1B**, **4B**). This change in LFPs was observed in all animals where the recording site was within an effective MLR stimulus site (**Figures 3A–C**). In **Figure 1B** we also present examples of activity in other filtered bands (delta, low and high theta, beta, low and high gamma). Changes related to locomotor activity were also observed in delta and low theta bands, but they did not persist throughout the locomotor trial, and the delta band activity could also be observed at rest. See below for more detailed analysis.

Stimulation Parameters for Evoked Locomotion in an Open Field

Stimulation of the MLR evoked locomotor responses ranging from slow walking to fast locomotor behavior and jumping depending upon the stimulus parameters. Stimulation strength was slowly increased during testing for locomotor threshold values. At each of the tested stimulation parameters (frequency or pulse width), when strength of stimulation approached threshold value, animals would typically orient themselves and lean forward slightly before initiating locomotion. This response could last many seconds, becoming shorter with an increase in the rate at which the stimulation strength was increased. The delay to the onset of the locomotor response was much shorter (and could be within a second) when stimulation strengths at the onset of stimulation were above threshold and the locomotor response could be abrupt (galloping with or without jumping), often resembling escape behavior.

Locomotor threshold tests over a range of frequencies (10–70 Hz) and pulse widths (0.2–2 ms) were conducted in 21 uninjured animals at ∼1 week of implantation (**Figure 2**). Walking could be most readily produced at 10 or 20 Hz. Stimulation at and above threshold strength at these frequencies produced well-graded locomotor responses evolving from slow walking to galloping. Transition from slow to fast locomotion typically occurred over a range of stimulus strengths (10–20 μA), thus demonstrating good controllability. At 50 or 70 Hz stimulation frequencies the first locomotor response produced at threshold strength was predominantly fast locomotion. Increasing the strength of stimulation above threshold could induce galloping and jumping responses and typically with only slight changes in strength of stimulation (2–5 μA). Tests in SCI animals (n = 3) showed a similar frequency dependence of the locomotor response as uninjured animals at threshold stimulation strengths (**Figure 2B**). Thus, a "controlled" rate of locomotion was difficult to establish at the highest tested frequencies, in contrast to 20 Hz, which produced the best controllable, graded locomotor response.

High vs. Low Locomotor Threshold Sites

Since the most consistent controllable locomotion was obtained at a frequency of 20 Hz with pulse width of 0.5–1 ms (**Figure 2B**), we determined the threshold strengths at approximately 1 week after implantation using 1 ms pulses at 20 Hz and grouped the animals into those with either high or low threshold responses. We defined low threshold (LowTh) sites as those producing locomotion with currents of ≤60 μA and those above 60 μA were defined as high threshold (HighTh).

Locations of all electrode stimulation sites (n = 28) were plotted on three coronal planes centered on Bregma −8.00, −7.04 and −6.30 mm (interaural 1.00–2.70 mm; taken from the atlas of Paxinos and Watson, 1998). High and low current locomotor threshold groups differed in location within the midbrain (**Figures 3A–C**). Low threshold sites were found in the CnF and the DpMe more anteriorly. High threshold sites were observed surrounding these areas dorsally, medially and ventrally.

GFAP staining was observed along each electrode tract and especially at the tip. This is illustrated in **Figure 3D** taken from an animal with a 5 month implant. GFAP staining typically did not extend into surrounding tissue for more than 50 or 60 μm even after prolonged implantation. To determine whether prolonged implantation of the electrode and increased glial scar formation (He and Bellamkonda, 2008) would affect locomotor thresholds (at 20 Hz, 1 ms pulse duration), we re-tested thresholds in 19 animals at various times (9–116 days) following the initial threshold assessment. Using current controlled stimulation, eight animals showed increased current thresholds, while nine showed decreased thresholds and two were unchanged. Overall, current thresholds were not significantly different (p = 0.342; paired samples t-test) with time from implantation, indicating that the small deposition of GFAP around the electrode tip did not interfere with electrode stimulation efficacy.

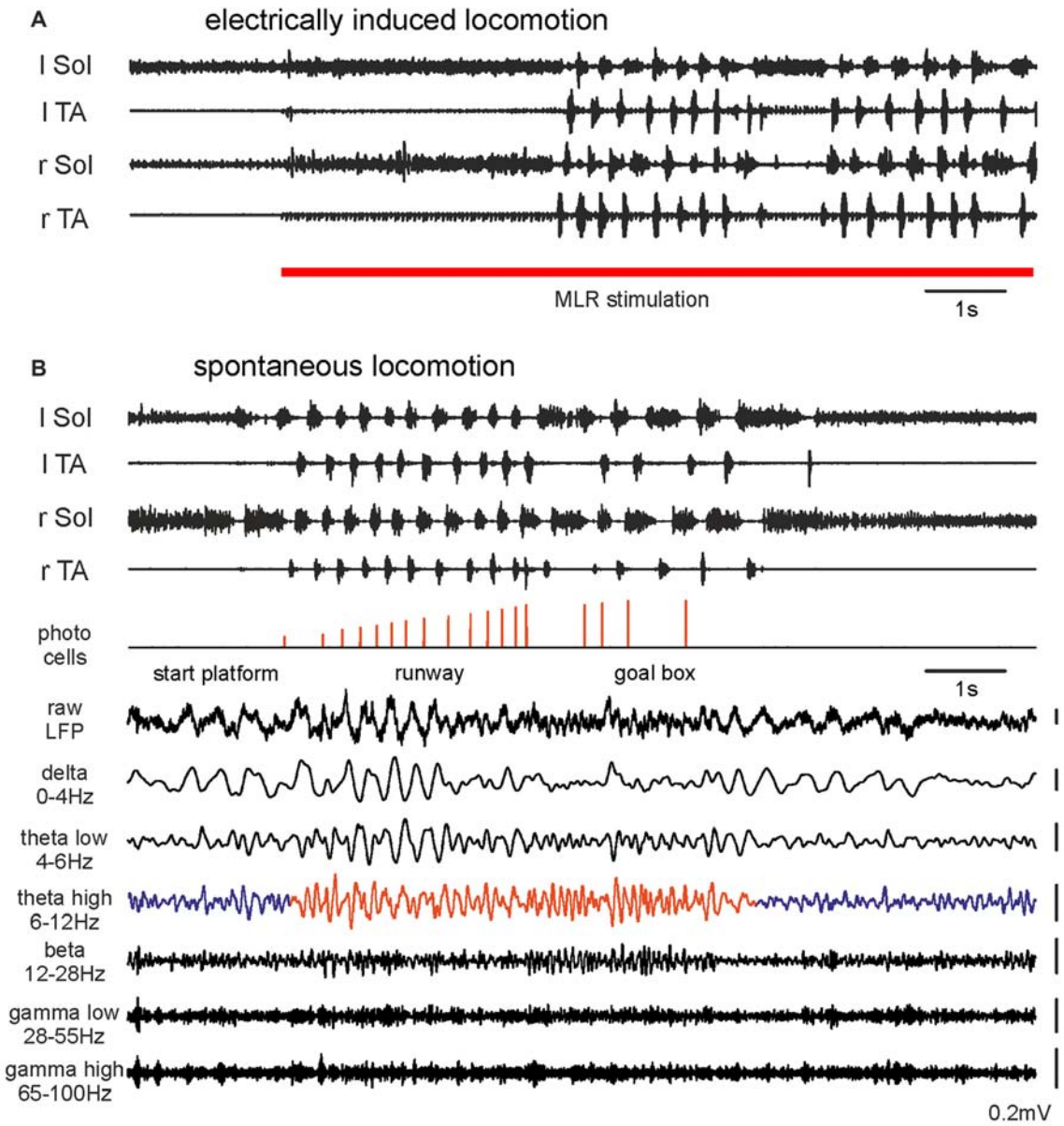


FIGURE 1 | Hindlimb muscle electromyography (EMG) and mesencephalic locomotor region (MLR) LFP activity during transition from resting to walking: (A) A rat with motor activity induced by right MLR electrical stimulation (28 μA, 20 Hz, 0.5 ms pulse duration). **(B)** The same rat walking spontaneously along a 2 m runway. Photocells events with increasing pulse amplitudes show progression along the runway. The bottom traces show simultaneously occurring raw LFP recorded from the right MLR and successive activity in filtered frequency bands. Abbreviations: Sol, Soleus muscle; TA, Tibialis Anterior muscle; r, right; l, left; LFP, local field potential.

LFP Recorded from MLR-DBS Sites during Treadmill Locomotion

The chronic LFP recordings in freely moving rats were obtained using electrodes that were implanted for DBS. Analysis of LFPs was done for periods before and during forced locomotion at various speeds (10, 15 and 20 m/min) of the treadmill belt. Examples of the LFPs (filtered within the theta range, 6–12 Hz) recorded from a HighTh and a LowTh site in rats during transition from resting to walking are shown in **Figures 4A1,B1** (bottom). In contrast to rats of the HighTh group, in all rats of the LowTh group, a regular theta rhythm was present from the start to the end of locomotion. Before locomotion started, short lasting episodes of regular activity in the LFP with a peak frequency of about 6–7 Hz were recorded (spectrogram in **Figure 4B2**—left). Interrupting these were short episodes of rhythmic LFP activity with a peak frequency below 7 Hz that were usually related to exploratory behavior of the rat in the treadmill cage. When the rat started to walk a clear peak of rhythmic theta activity (7–9 Hz)

appeared in the spectrogram. A comparison of the power spectra calculated for the LFP recorded during resting and locomotion shows that the different experimental conditions differ in both frequency and amplitude of the peak in the power spectra of the theta band (see example in **Figures 4A2,B2**). There was also a change in the peak in the power spectra of the delta band (0–4 Hz; see analysis below and **Figure 7**). The data presented on the logarithmic scale show no peak in LFP power in the higher frequency bands (**Figures 4A3,B3**).

We performed an analysis comparing the frequency of the peak of theta rhythm and its power between the LowTh and HighTh groups. We selected eight LowTh and seven HighTh cases for statistical analysis based on the fact that they were all subjected to the protocol for LFP recordings at rest and at all defined treadmill speeds (10, 15 and 20 m/min). Average threshold currents for these LowTh and HighTh sites were 32.8 ± 3.2 and 151.5 ± 38.3 μA and were significantly different (*t*-test, $p \leq 0.001$). Statistical analysis (two-way RM ANOVA) showed a significant increase in frequency of the peak of theta rhythm over the resting condition at all speeds of locomotion in both groups of animals ($F_{(3,39)} = 16.34, p < 0.0001$; **Figure 5A**). Interestingly, within each experimental condition (rest or locomotion) the differences of the frequency of the theta oscillations between the LowTh and HighTh groups were not significant.

Analysis of the peak power of the theta rhythm (**Figure 5B**) showed significant differences between resting and locomotion at 15 m/min and 20 m/min, and between 10 m/min and 20 m/min in the LowTh group only ($F_{(3,39)} = 5.075$, $p < 0.005$). In the HighTh group we found no significant differences between any of the experimental conditions. Thus, it is clear that the theta rhythm was present both during rest and locomotion and the frequency of the theta rhythm was not different, but the peak power of the theta rhythm differentiated the LowTh and HighTh groups. It is noteworthy that the peak power of the theta oscillations was significantly different (Sidak's test, $p = 0.0066$) when comparing LowTh and HighTh rats during locomotion at the highest speed (20 m/min; **Figure 5B**). In summary, our results show that both the frequency and peak power of the theta rhythm change depending on the locomotor speed of animals in the LowTh group, while in the HighTh group only the frequency of the peak of the theta rhythm changes.

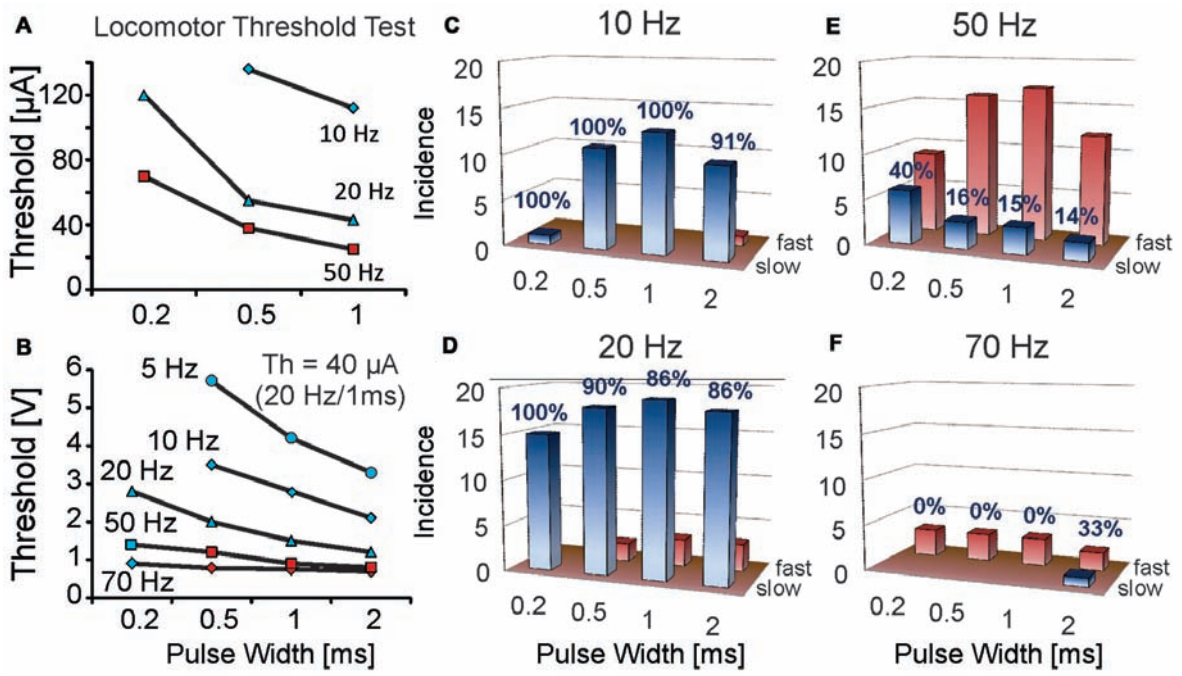


FIGURE 2 | Rate of locomotion at threshold strengths for initiating locomotion varies with different stimulation frequencies and pulse widths. Locomotor threshold parameter tests for single MLR stimulation sites were conducted at various stimulus frequencies and pulse widths. **(A,B)** Thresholds plotted relative to pulse width and frequency for two animals; one intact **(A)** and one with mid-thoracic moderate contusion injury **(B)**. Current threshold (Th) for the spinal cord injury (SCI) animal at 20 Hz, 1 ms duration was 40 μA. Note that greater strengths of stimulation were required with lower frequencies and shorter pulse widths. Initial locomotor responses vary according to frequency and pulse width of stimulation: stimulation frequencies of 20 Hz typically produce slow locomotion at threshold (blue symbols) in contrast to higher stimulation frequencies which typically initiate fast locomotion at threshold (red symbols). **(C–F)** Incidence of slow or fast locomotion at threshold strengths for initiating locomotion for different stimulation frequencies and pulse widths in uninjured animals 1 week after electrode implant. Note higher incidence of slow locomotion (percentage indicated) at low stimulation frequencies (10 and 20 Hz) vs. high frequencies (50 and 70 Hz). The number of trials is indicated on the ordinate (1 trial per animal). Red bars indicate the incidence of fast locomotion, while the blue bars indicate the incidence of slow locomotion. Only one data point per animal is included for each frequency and pulse width test combination. A similar response was observed during threshold tests in the SCI animal **(B)**.

This shows that theta oscillations are associated with sites that are most effective for eliciting locomotion. In line with this result is a conclusion presented by Thevathasan et al. (2012) who found that in PD patients the best outcome of DBS was achieved at the level of maximal alpha activity in the caudal PPN region.

Next, we analyzed the differences in power of delta, theta, beta and gamma bands between the LowTh and HighTh groups for the different experimental conditions (**Figure 6**). For the theta band we analyzed two sub-bands: low (4–6 Hz) and high (6–12 Hz) theta; for gamma we analyzed low (28–55 Hz) and high (65–100 Hz) sub-bands.

For the LowTh group a two-way RM ANOVA did not show significant differences between experimental conditions for the delta band ($F_{(3,39)} = 2.739$, $p = 0.056$). *Post hoc* Sidak's multiple comparison tests showed that power was significantly different between resting and locomotion at 15 m/min and between 10 m/min and 20 m/min locomotion (**Figure 6A**). There were no significant differences between the different behavioral states in the HighTh group. Moreover, the difference between LowTh

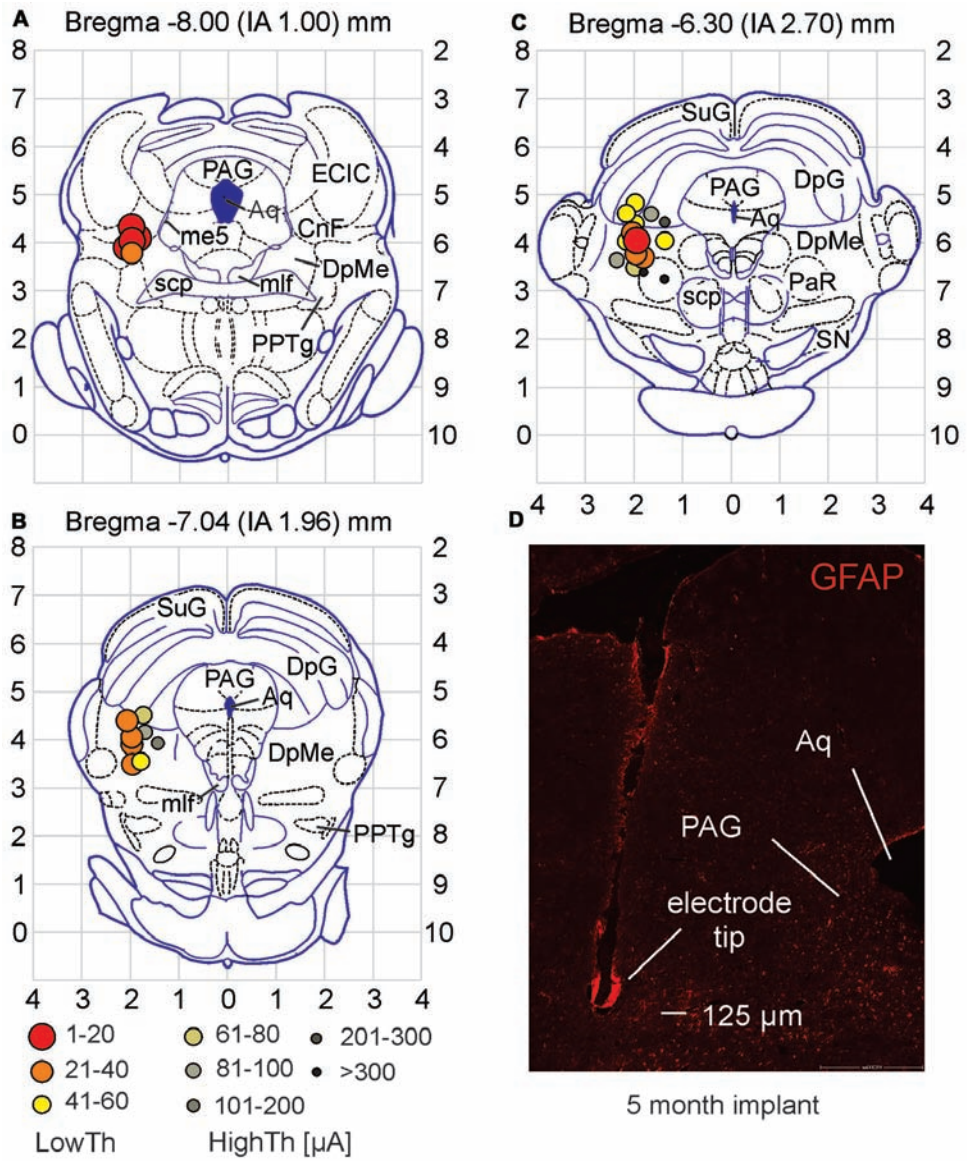


FIGURE 3 | Stimulation sites for high and low current locomotor threshold groups differ in location. (A–C) Low threshold sites were found in the CnF and DpMe of midbrain. High threshold sites were observed surrounding these areas. Current thresholds for each site are defined by symbols in **(B)**. **(D)** Example of electrode tip site in the brain tissue (coronal section). Note the minor tissue response to the electrode as observed with GFAP staining. Abbreviations as per Paxinos and Watson (1998). Aq, aqueduct; CnF, cuneiform n.; DpG, deep gray layer of superior colliculus; DpMe, deep mesencephalic n.; ECIC, external cortex of inferior colliculus; me5, mesencephalic n. of 5th nerve; mlf, medial longitudinal fasciculus; PAG, periaqueductal gray; PaR, pararubral n.; PPTg, pedunculopontine tegmental n.; scp, superior cerebellar peduncle; SN, substantia nigra; SuG, superficial gray layer of superior colliculus.

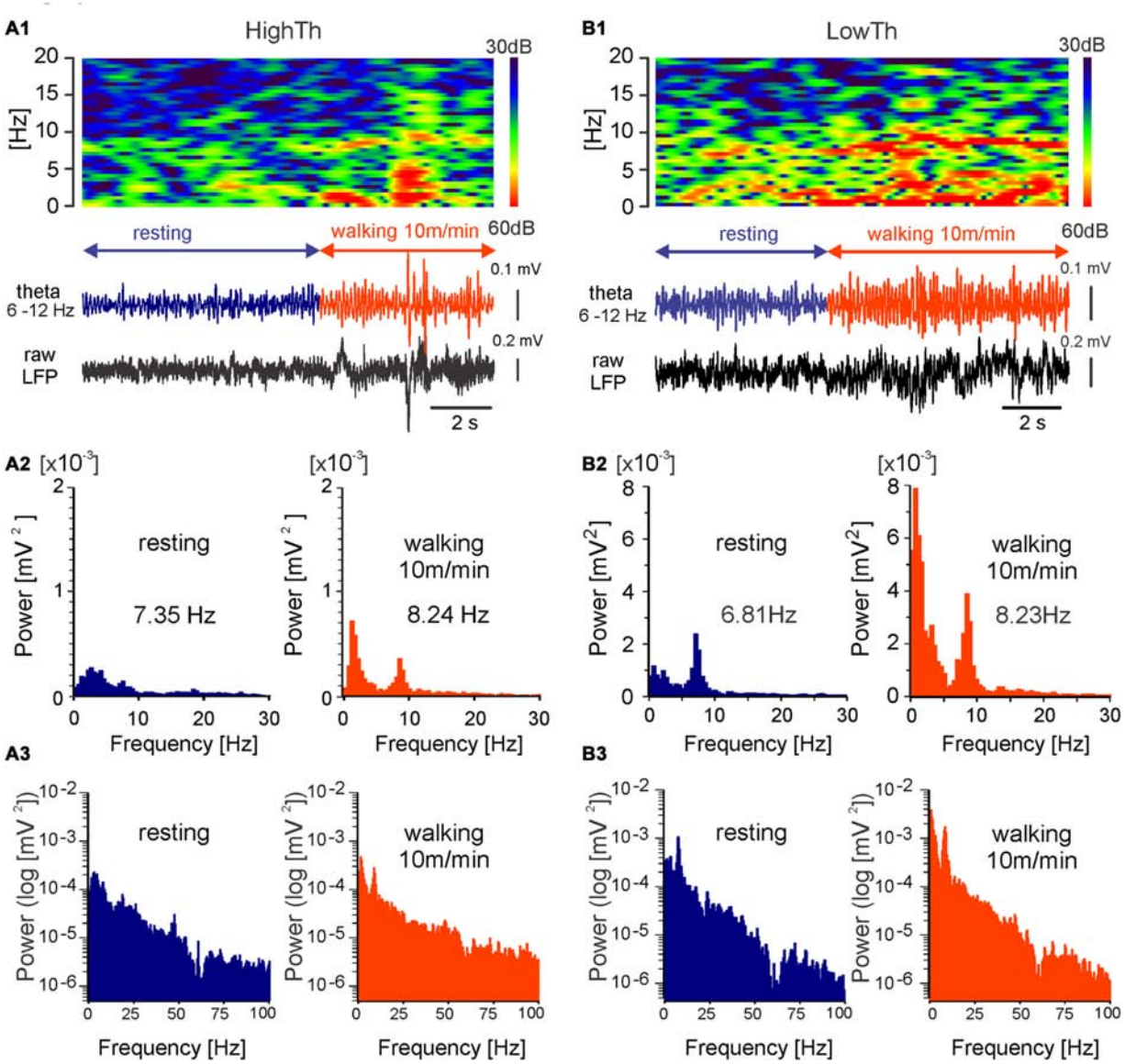


FIGURE 4 | MLR LFP activity during transition from resting to walking in freely moving rat. LFPs recorded during locomotion from LowTh sites show a larger increase in the power of delta and theta bands in comparison to the HighTh sites. Top in **(A1)** frequency spectrogram (frequencies between 0 Hz and 20 Hz) plotted vs. time of LFP recorded from a HighTh site; bottom in **(A1)** LFP, filtered 6–12 Hz and raw, recorded from a HighTh site; **(A2)** histograms of power spectra in linear scale for corresponding data segments; **(A3)** histograms of power spectra in logarithmic scale for corresponding data segments; Top in **(B1)** frequency spectrogram (frequencies between 0 Hz and 20 Hz) plotted vs. time; bottom in **(B1)** LFP, filtered 6–12 Hz and raw, recorded from LowTh site; **(B2)** histograms of power spectra for corresponding data segments. **(B3)** histograms of power spectra in logarithmic scale for corresponding data segments.

and HighTh groups for locomotion at 20 m/min was significant (**Figure 6A**).

For the LowTh group a two-way RM ANOVA showed significant differences between experimental conditions for the low theta band ($F_{(3,39)}$ = 6.642, p = 0.001) and for the high theta band ($F_{(3,39)}$ = 3.790, p = 0.0177). *Post hoc* Sidak's multiple comparison tests showed that power was significantly different between resting and locomotion for both bands of theta at speeds of 15 m/min and 20 m/min, and between 10 m/min and 20 m/min (**Figures 6B,C**). There were no significant differences between the different behavioral states in the HighTh group. Moreover, the difference between LowTh and HighTh groups for locomotion at 20 m/min was significant (**Figure 6C**).

For the power of the beta band, the differences between various behavioral states (i.e., resting and locomotion at different speeds) were significant ($F_{(3,39)}$ = 3.071, p = 0.0389) only in the LowTh group (**Figure 6D**). The power observed at rest was significantly different from that observed during locomotion at 20 m/min (Sidak's test, p = 0.0026).

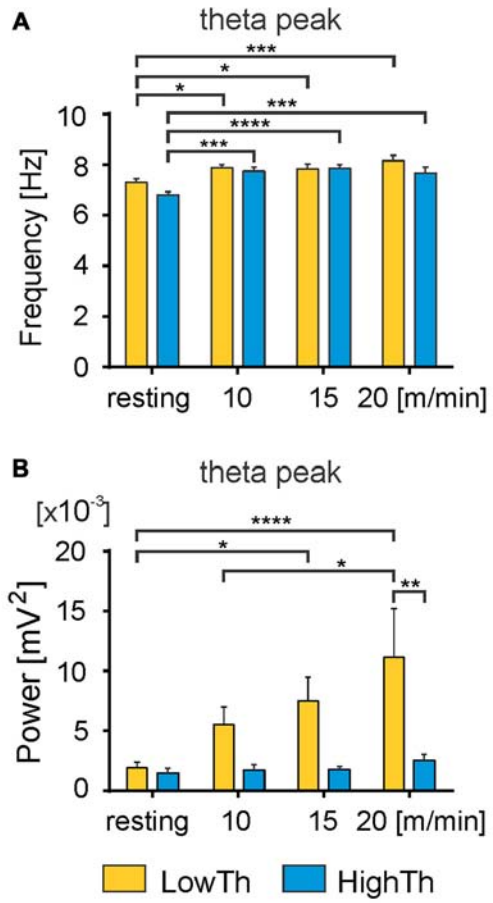


FIGURE 5 | Changes in frequency and power of the theta peak with the transition from resting state to locomotion. A significant increase in the frequency of theta peak was observed with the transition from resting to locomotion in both LowTh and HighTh animals **(A)**. Note significant increase in power of the theta peak in the LowTh group between resting and locomotion at 15 m/min and 20 m/min, and between 10 m/min and 20 m/min **(B)**. The power of the theta peak was significantly different when comparing LowTh and HighTh rats during locomotion at the highest speed (20 m/min). $^{*}P < 0.05$, $^{**}P < 0.01$, $^{***}P < 0.001$, $^{****}P < 0.0001$.

For the low gamma band we found significant differences between various behavioral states ($F_{(3,39)} = 4.189$, $p = 0.0116$). *Post hoc* analysis showed differences between resting and locomotion at 20 m/min, and locomotion at speeds of 10 m/min and 20 m/min (**Figure 6E**) only in the LowTh group. The same results were obtained for the high gamma band ($F_{(3,39)} = 4.203$, $p = 0.0114$; **Figure 6F**). These results show that there are progressive changes for all frequency bands as locomotion increases in speed.

Results shown in **Figure 6** suggested the possibility of a relationship between the power of frequency bands and the speed. Thus, we performed linear regression analysis which showed that changes in power of delta, theta, beta and gamma bands are related to the speed changes (data not shown). As the relation between speed and the power of delta and theta bands were much stronger (for delta $R^2 = 0.96$, $p = 0.016$; for theta high $R^2 = 0.97$, $p = 0.015$) than for the other bands and as in both bands there is characteristic peak of frequency visible, we decided to analyze their parameters further, i.e., the frequency and power of the peak frequency in relation to the speed of locomotion. **Figure 7** shows the regression lines for LowTh and HighTh groups. For the peak of the power spectra of the theta band the changes of both the frequency (**Figure 7A**) and power (**Figure 7C**) were positively related to the speed in the LowTh group (slopes of both regression lines were significantly different from zero ($p < 0.05$ and $p < 0.02$, respectively). For the peak of the delta band such a relationship was significant only for the power (slope significantly different from zero at $p < 0.05$) but not for the frequency of the delta peak (**Figures 7B,D**). This suggests that the theta rhythm represents a more meaningful biomarker for effective MLR sites.

Because the LFP frequency is a potential means of localizing the most effective sites for DBS for therapeutic purposes, we also determined whether the theta rhythm in LFPs persists after SCI. As **Figure 8** illustrates, in rats after chronic SCI the theta oscillations can be observed in MLR LFP spectrograms and power spectra during locomotion, similar to those we have described for intact rats. These characteristics of LFP that we describe here can therefore be considered reliable indices of the location of potentially effective MLR stimulus sites in injured animals. These LFP characteristics were observed in all of the rats with SCI with low threshold MLR sites ($n = 8$) included in this article. In each of these animals, DBS improved locomotor activity. A full analysis of the effect of MLR stimulation on locomotor activity observed following contusive SCI will be presented elsewhere.

DISCUSSION

LFPs in Functionally Defined MLR in Intact Rats Display a Characteristic Theta Rhythm during Voluntary Locomotor Activity

This is the first observation of LFP activity recorded in freely moving rats from functionally identified locomotion-inducing MLR sites. We found that the onset of voluntary locomotor activity was invariably accompanied by a transition from disorganized activity to a prominent theta rhythm. This is in accordance with previous studies on hypothalamic locomotor sites that were functionally identified (Sławińska and Kasicki, 1995, 1998). This is also the typical LFP frequency band observed in hippocampal CA1 at bipolar recording sites during locomotion (Kramis et al., 1975; Bland, 1986). Our data confirm our hypothesis that the theta rhythm is a characteristic of LFP activity in the MLR during voluntary locomotion, and are consistent with the suggestion that the theta rhythm serves to link different cell groups together in functional ensembles (Tort et al., 2008; Colgin, 2016).

The transition from resting to locomotion was associated with increases in the power spectra. For two bands, delta and theta, the increase was clear. Moreover, in both bands clear

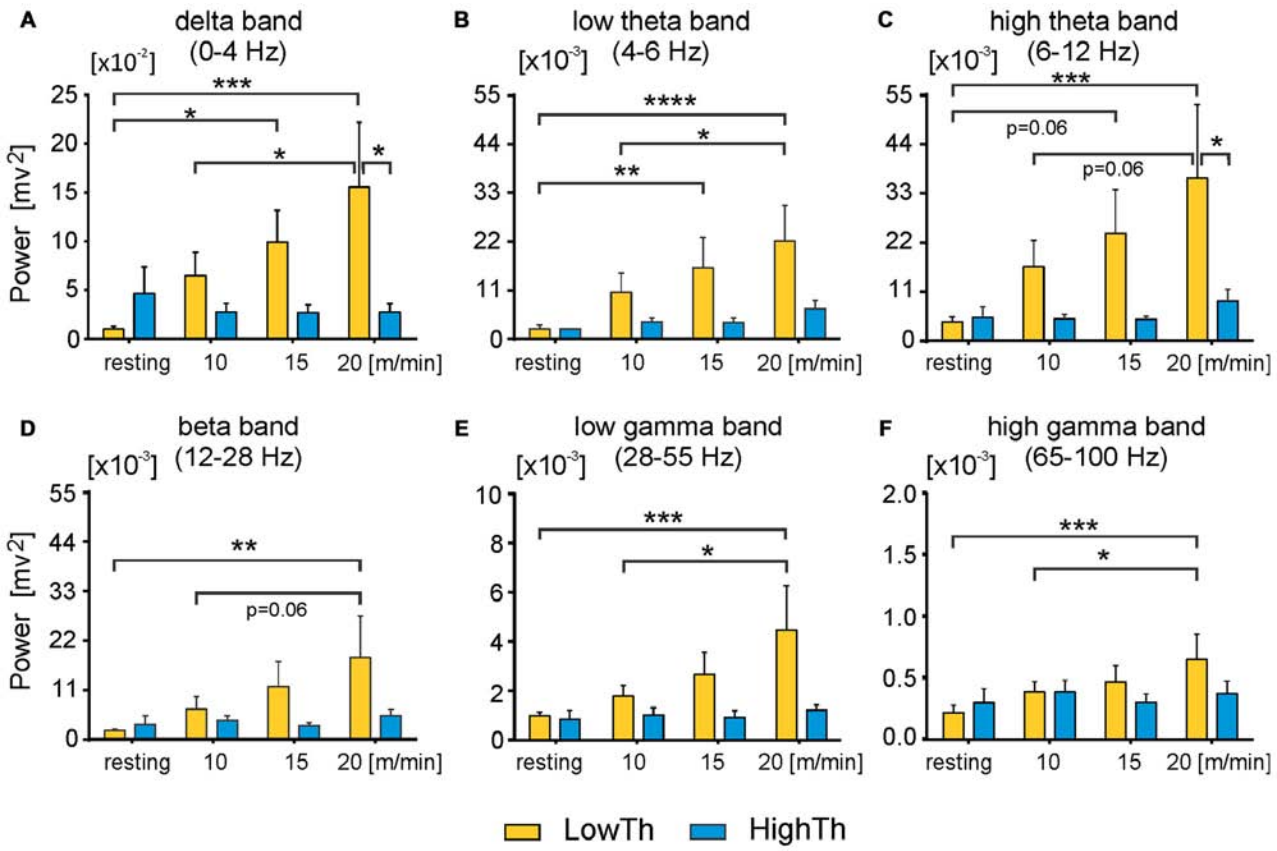


FIGURE 6 | Power of all analyzed frequency bands in LFPs significantly increases in low threshold MLR sites but not high threshold sites as locomotor speed increases. Power of delta **(A)** low and high theta band (**B,C** respectively) and beta band **(D)** significantly increases in LowTh sites, but not HighTh sites as voluntary locomotor speed increases. **(E,F)** Power of low and high gamma band in LowTh sites also shows significant increases as locomotor speed increases. Note, difference in scaling between individual plots for power of different bands. Power of any band is the integral of the power in the specific frequency ranges: delta: 0–4 Hz; theta low: 4–6 Hz; theta high: 6–12 Hz; beta: 12–28 Hz; gamma low: 28–55 Hz; gamma high: 65–100 Hz (n = 8 LowTh; n = 7 HighTh). $^{*}P < 0.05$, $^{**}P < 0.01$, $^{***}P < 0.001$, $^{****}P < 0.0001$).

peaks were visible. Thus, we did a more thorough analysis for those bands. Namely, we analyzed the frequency and power of the peak frequency in both bands. For the delta band, we found that the frequency of the peak was not related to the speed for either the LowTh or the HighTh group. The power of the delta peak frequency was related to the speed for the LowTh group only. Thus, we can conclude that the changes in delta band parameters are not locomotion related. We also analyzed the relationship of the theta rhythm to the speed of locomotion. There are several differences between theta band parameters when comparing the LowTh vs. HighTh groups. The power of the theta band was significantly greater (by up to 5-fold) in the LowTh animals than in the HighTh groups. Furthermore, the power and the frequency of the peak theta frequency was related to the speed of locomotion in the LowTh group of animals, but not in the HighTh group, analogous to our previous finding, where we showed theta recorded from the hippocampus was related to the speed of locomotion (Sławińska and Kasicki, 1998). We consider these facts as further support for the suggestion that locomotion is associated with theta rhythm in structures implicated in the control of locomotion, including the MLR.

Our finding that the peak in the power spectrum is highly correlated with the speed of locomotion in the LowTh cases suggests that the theta oscillations may be a reliable biomarker for electrode placement in an effective MLR site for inducing locomotion. We are aware of the potential for signal contamination due to the use of monopolar recording, but we think this is an unlikely confound. The fact that the power of the theta peak is significantly larger in the LowTh cases than in the HighTh cases that are spatially more remote from the most effective site clearly demonstrates that the LFPs recorded in these cases are generated locally and not due to volume conductance. The placement of our reference electrode also argues against volume conduction from the hippocampus, because it was substantially caudal to the region of the hippocampus, and the hippocampus was not between the reference and the LFP electrodes.

The relationship of our theta LFPs (the peak frequency and power) to speed of locomotion is noteworthy, because

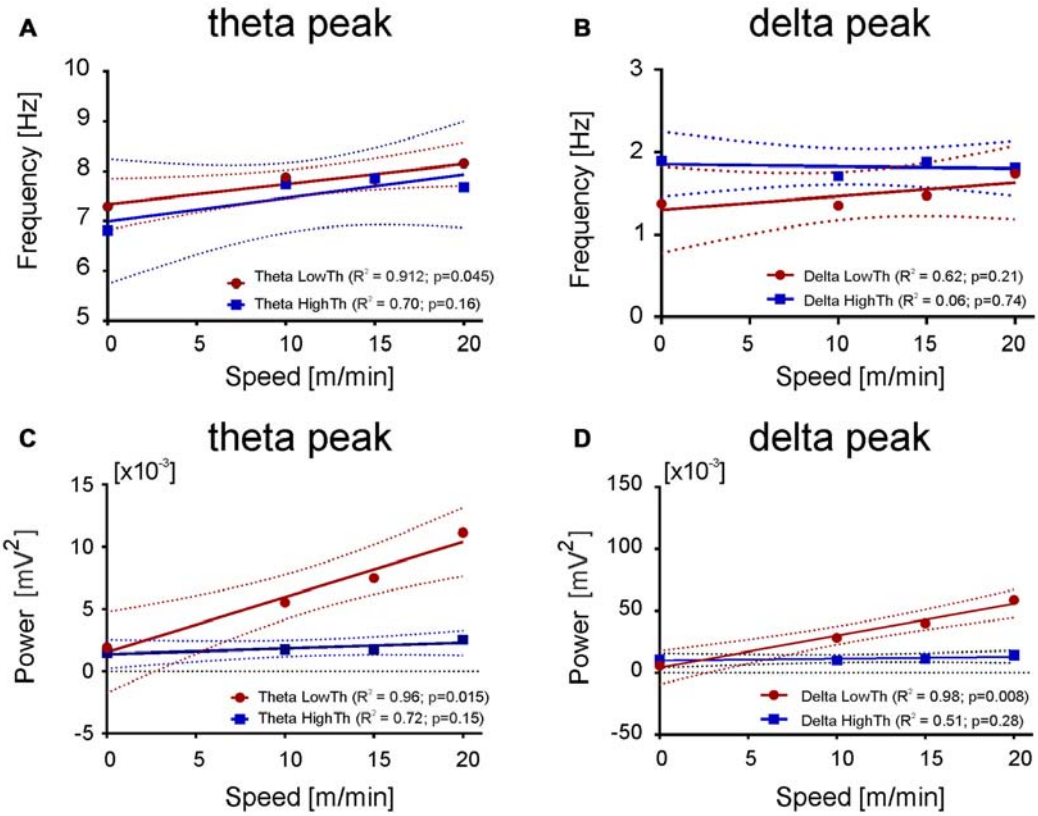


FIGURE 7 | Relationship between the frequency and power of maximum in the delta and theta band and the speed. (A,C) Both frequency and power of theta peak increase with the speed of an animal for LFPs recorded from the LowTh sites, while for the HighTh sites the relationship was not significant. **(B,D)** Opposite to that the frequency of delta peak was not related with the speed of rat both for LowTh and HighTh sites. Note that in contrast to the theta peak, in the delta peak only the power was related to the speed of locomotion of the animals of LowTh group only.

this is typical of other areas in the brain implicated in locomotor control, including the hypothalamus and the hippocampus. Theta oscillations in the hippocampus depend on the activity of the medial septal neurons, and the speed of locomotion is conveyed to the hippocampus via glutamatergic septohippocampal projections (King et al., 1998; Fuhrmann et al., 2015). Optogenetic stimulation at theta frequencies of axons of medial septal GABAergic cells in the hippocampus via an optic fiber implanted above the CA1 area induced theta oscillations but did not initiate locomotion in immobile mice (Bender et al., 2015), while optogenetic activation of the medial septal glutamatergic input to the hippocampus induced locomotion and hippocampal theta rhythm (Fuhrmann et al., 2015). However, both articles described that theta oscillations were correlated with the speed of locomotion. The means whereby the hippocampal activity can modulate or initiate locomotion is not known, but either the hypothalamic or mesencephalic locomotor regions may be involved. This is an issue that needs clarification. It is of particular interest because hippocampal theta oscillations are thought to be involved in encoding the animal's position during spatial navigation (Bender et al., 2015). The presence of a locomotor speed-related theta rhythm in the MLR is consistent with the hypothesis that these areas are coherently bound together during locomotion. Perhaps the purpose of such binding might be to preserve position and speed information throughout the locomotor system.

The presence of similar theta rhythms in multiple sites related to locomotion (MLR, hypothalamic locomotor regions and hippocampus) is consistent with functional coupling of these structures. Although Bland and Vanderwolf (1972) showed electrical stimulation of the hippocampus does not induce locomotion, recent experiments showed chemogenetic or optogenetic activation of hippocampal cells (including CA1 neurons) resulted in enhanced locomotor behavior (Alexander et al., 2009; Fuhrmann et al., 2015). In the chemogenetic study, Alexander et al. (2009) expressed HA-hM3Dq driven by the CaMKIIa promoter in mice and found that the otherwise inert ligand for hM3Dq, clozapine-N-oxide (CNO), markedly increased locomotor activity. These findings are consistent with the well-known coupling between the limbic and motor systems (Mogenson and Nielsen, 1984), and with functional coupling of locomotor regions through a common LFP frequency as previously proposed (Sławińska and Kasicki, 1995).

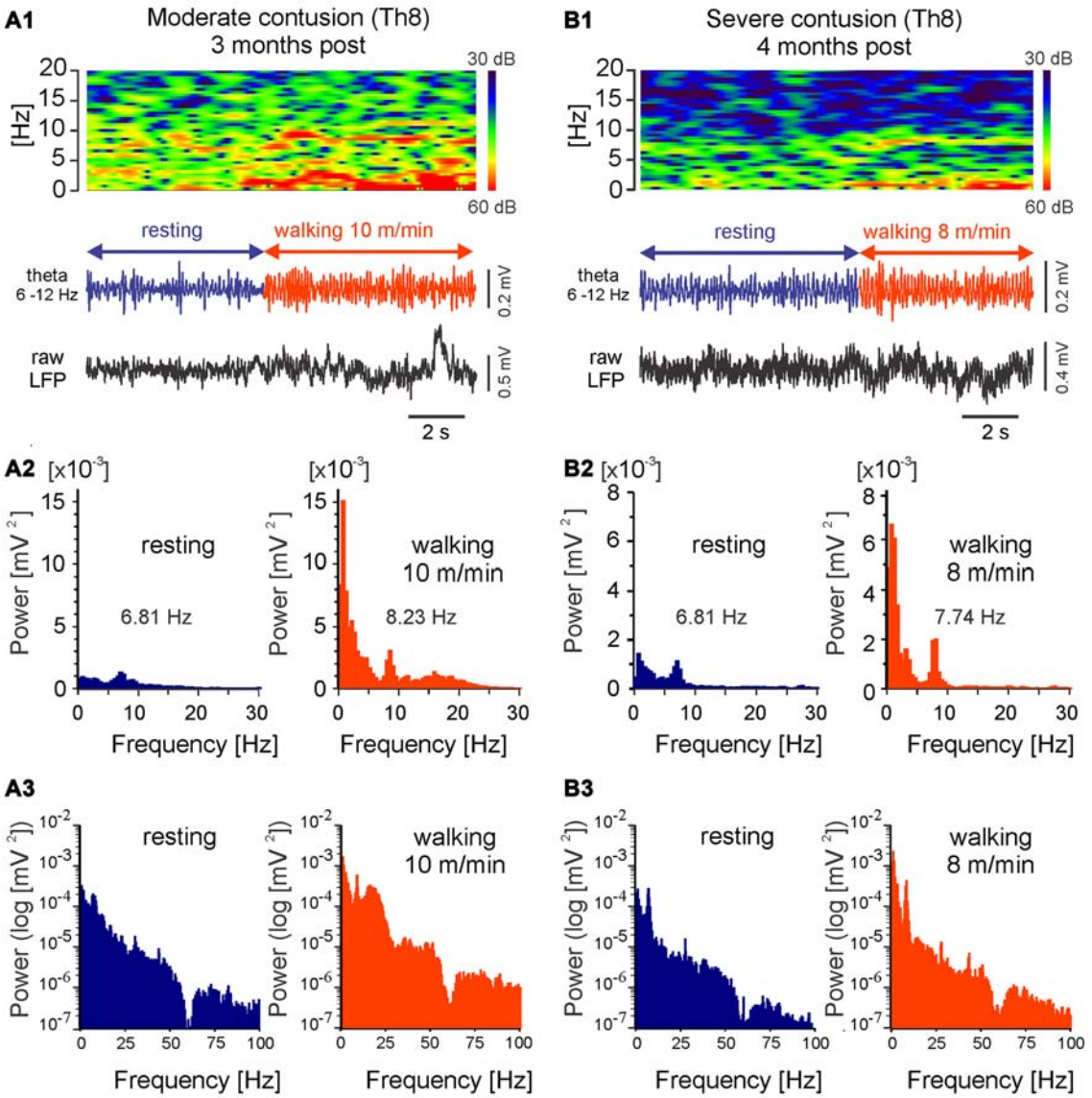


FIGURE 8 | LFPs recorded from LowTh sites in rats with moderate or severe mid-thoracic contusion SCI show similar correlation to locomotor speed as intact animals. Top in **(A1,B1)**: frequency spectrogram plot vs. time; bottom in **(A1,B1)**: LFP, filtered 6–12 Hz and raw; **(A2,B2)**: histograms of power spectra in linear scale; **(A3,B3)**: histograms of power spectra in logarithmic scale. Note increased power within the theta band (<12 Hz) and shift in the dominating theta frequency with the transition to walking.

The persistence of this characteristic theta oscillation at sites that promote locomotor recovery after SCI suggests that it can be used as a biomarker in clinically relevant circumstances, and can guide that placement of DBS electrodes for effective restoration of locomotion in injured subjects. Further studies are needed to determine the impact, if any, of damage or degeneration in cases such as partial SCI on the MLR locomotor system. There is evidence of plasticity in multiple descending pathways after SCI (Ballermann and Fouad, 2006; Filli et al., 2014; Leszczyńska et al., 2015; Fink and Cafferty, 2016; Hansen et al., 2016), and changes in brainstem locomotor circuits are possible. However, our results so far provide a clear indication that the factors producing theta oscillations in the MLR during even impaired locomotion after partial SCI persist to the degree that the potential biomarker role for theta oscillations is maintained.

A predominance of gamma band activity in the MLR might be expected based on the activity of single PPN neurons *in vitro* (Garcia-Rill et al., 2015). However, in contrast to those results, no other peak in higher frequency bands (including gamma) was visible in the power spectra in the rats included in our study. This is consistent with the observation that the firing of single PPN neurons during actual locomotion was less than 6 Hz in normal rats (Geng et al., 2016).These same authors reported LFP results from PPN during locomotion consistent with our

findings from effective MLR sites, with the highest percentage of relative LFP power observed in the 0.7–12 Hz range. Their PPN sites were not confirmed to be effective locomotion-inducing sites, however. And their PPN recording sites were anatomically distinct from our MLR sites (more ventral). The much lower power of beta and gamma bands also varied for different experimental conditions (treadmill speed) in the LowTh group but no such variations occurred in the HighTh animals. The frequency of the theta rhythm increased significantly as the animal started to walk. This is consistent with the association of the theta rhythm at these sites with the processes underlying locomotion. These findings have the potential to aid in the identification of brainstem sites that should be the most effective for DBS facilitation of locomotion, providing for the first time a theta rhythm signature for the MLR. Emerging clinical data is consistent with this. According to Tattersall et al. (2014), LFP recordings from the supposed PPN area of the MLR have shown oscillations in both the alpha (6–12 Hz) and beta (12–30 Hz) frequency bands (Weinberger et al., 2008; Shimamoto et al., 2010; Tsang et al., 2010; Thevathasan et al., 2012; Tattersall et al., 2014). Active gait was also accompanied by increased LFP alpha power in this area (Thevathasan et al., 2012; Tattersall et al., 2014). Recordings from DBS electrodes implanted in the PPN area (PD patients) showed an increase of the power in the range 7–11 Hz (the alpha range in human, which overlaps with the high theta; 6–12 Hz in our article) after symptom improvement with levodopa administration (Androulidakis et al., 2008). It was also shown in PD patients after levodopa that LFPs recorded from the PPN area showed "an increase in PPNa alpha (5–12 Hz) oscillatory activity and a decrease in beta (13–35 Hz) and gamma (65–90 Hz) bands activity" (Fraix et al., 2013).

Like most areas of the brain, the MLR region receives input in a range of frequencies. The arrangement of MLR neurons, the orientation of their dendritic fields, and the organization of the synaptic input could create more synchronous LFPs or they could cancel out others in the MLR area. Thus neurons in MLR may be receiving significant gamma frequency input, for example, but because of the microanatomy of local circuits, synchronized extracellular current flow may be minimal in the gamma range. However, we were unable to find evidence for an endogenous rhythm in the gamma range, as suggested for the PPN (Simon et al., 2010; Garcia-Rill et al., 2011).

Effective Stimulus Sites and Parameters for Inducing Locomotion in Freely-Moving Rats

Low threshold MLR sites (below 60 μA, mean 32.8 μA) were found in the CnF and the more rostral DpMe. This is consistent with recent findings from human studies using DBS for treatment of FOG, where it has been suggested that the most effective targets are within the CnF and subcuneiform regions instead of the PPN (Piallat et al., 2009; Alam et al., 2011). This conclusion is in agreement with many previous animal studies (Shik et al., 1966; Ross and Sinnamon, 1984; Steeves and Jordan, 1984; Milner and Mogenson, 1988; Coles et al., 1989; Mori et al., 1989; Jordan, 1998; Takakusaki et al., 2016). A recent trans-synaptic tracing study also implicates the CnF (Xiang et al., 2013). Although there are a number of studies implicating the PPN as the effective site for DBS in humans (reviewed in Collomb-Clerc and Welter, 2015; Hamacher et al., 2015; Nonnekes et al., 2015; Udupa and Chen, 2015), it is widely recognized that the effective sites are difficult to clearly identify (Alam et al., 2011). fMRI of the brainstem in human subjects shows the CnF is activated during imaginary gait (Karachi et al., 2012). Nevertheless, it is common in the clinical literature to equate the PPN with the MLR, and the suggestion has been made that the term MLR can now be "retired" (Garcia-Rill et al., 2015). But Hernández-Chan et al. (2011) and Winn and co-workers (Winn, 2006; Gut and Winn, 2015, 2016) have pointed out weaknesses in the argument that the PPN is an essential component of the MLR, and these arguments along with our data support the notion that a functional definition of the MLR is still valid. Takakusaki et al. (2005, 2016) and Takakusaki (2008, 2013) have directly compared the effects of CnF and PPN stimulation, and they found that the CnF is effective for eliciting locomotion in decerebrate cats, while the PPN controls muscle tone, and stimulation in this region may actually suppress locomotion. Also, they showed the effective MLR sites are not co-extensive with cholinergic neurons that define the location of PPN. Moreover, neurons activated during locomotion (indicated by the presence of the activity-dependent marker Fos) are found in the CnF and other nearby areas, including the DpMe (Jordan, 1998; Vianna et al., 2003; Heise and Mitrofanis, 2006), but not in the PPN. Stimulation in the DpMe area also induces locomotion in the rat (Melnikova, 1975; Milner and Mogenson, 1988; Coles et al., 1989; Cabaj et al., 2017) and does not harbor cholinergic neurons.

PPN cholinergic neurons have been considered essential for MLR initiation of locomotion (Garcia-Rill and Skinner, 1987) in mammals and lamprey (reviewed in Ryczko and Dubuc, 2013). However, recent data does not support a critical role for a cholinergic component of the MLR in the initiation of locomotion. Activation of the cholinergic component of the PPN using a chemogenetic approach induced only subtle effects on locomotion in freely moving, control rats (Pienaar et al., 2015), and optogenetic stimulation of cholinergic neurons in the PPN did not elicit locomotion in stationary mice (Roseberry et al., 2016). Glutamatergic rather than cholinergic neurons of the MLR have been shown to be effective for eliciting locomotion with optogenetic stimulation (Lee et al., 2014; Roseberry et al., 2016). Furthermore, cholinergic antagonists do not impair the initiation of locomotion due to electrical stimulation of the MLR (Jordan et al., 2014). Taken together these data increase the likelihood that components of the MLR other than the PPN should be the target for DBS to restore locomotion.

In clinical DBS studies, the electrode size and methods of detecting electrode placement do not provide sufficient resolution to rule out the possibility that the stimulus activates structures outside of the anatomically defined PPN. As a result the term PPNa, for the area of the brainstem surrounding the PPN, including CnF and precuneiformis, has been introduced (Fraix et al., 2013; Welter et al., 2015). Further research in animal models is required using modern methods of activating and

silencing genetically defined putative MLR constituents to clarify this issue, but the continued use of the term PPN instead of MLR to describe effective sites for locomotion induction is misleading.

We determined the most effective stimulation parameters for inducing controllable locomotion (pulses of 1.0 ms duration at 20 Hz). These are relevant to the selection of stimulation parameters for the treatment of gait defects using DBS, but are in contrast to the previous claim, based upon results from PPN stimulation in decerebrate rats and recordings from PPN neurons *in vitro*, that stimuli in the 40–60 Hz range should be required (Garcia-Rill et al., 2015). Our results show that the effective frequency for electrical stimulation is not predicted by the peak frequency of LFP recorded during locomotion in the same area, but must be determined empirically. We contend that the definition of "optimal stimulation frequency" should necessarily take into consideration the ability to induce controllable locomotion, i.e., to "dial-in" locomotor speed and maintain it. According to this definition and in these targeted sites, stimulation frequencies lower than gamma are optimal. In keeping with this, DBS experience for gait improvement in PD has led to the conclusion that the effective frequency of stimulation is often in the range of 10–25 Hz instead of higher frequencies (Androulidakis et al., 2008; Ferraye et al., 2010, 2011; Nosko et al., 2015). Others have also shown that stimulation in the MLR at the lower frequency ranges (5–30 Hz) was suitable for inducing locomotion in adult rats (Melnikova, 1975; MacDonell et al., 2015) and cats (Douglas et al., 1993; Guertin et al., 1995; Noga et al., 2003).

Concluding Remarks

Our results are consistent with earlier observations that the onset of locomotion is characterized by theta frequency oscillations of the LFPs in hippocampus and in locomotion-inducing sites in the subthalamic locomotor region and posterior hypothalamus (Sławińska and Kasicki, 1995, 1998). We suggest that theta oscillatory LFPs may coherently bind cooperating neuronal ensembles during locomotor activity in order to encode the animal's position during spatial navigation. It is clear from our results that after injury the theta rhythm can also be used as a signature for effective sites for DBS, especially as DBS in the MLR dramatically improved locomotion in animals with a SCI.

AUTHOR CONTRIBUTIONS

LMJ, US and BRN: conceptualization; BRN, LMJ, US and SK: methodology; BRN, FJS, CO, LMV, US, MO, AMC and HM: investigation; BRN, US and SK: formal analysis; BRN and US: visualization; BRN, LMJ, US and SK: writing—original draft; BRN, LMJ, US and SK: writing—review and editing; BRN and US: supervision; BRN, US, SK and LMJ: funding acquisition.

ACKNOWLEDGMENTS

This study was supported by The Christopher and Dana Reeve Foundation (Grant no. NA1-1001-2), the Craig H. Neilsen Foundation (Grant no. 190550) and National Institute of Neurological Disorders and Stroke (NINDS) Grant 2 R56NS-46404-061A to BRN, the Nencki Institute to US and SK and Canadian Institutes of Health Research (CIHR; FRN 115147) to LMJ. We would like to thank Sławomir Stasieńko for his contribution to LFP analysis and Ioan Opris for his constructive recommendations on the manuscript and figures.

REFERENCES

Alam, M., Schwabe, K., and Krauss, J. K. (2011). The pedunculopontine nucleus area: critical evaluation of interspecies differences relevant for its use as a target for deep brain stimulation. *Brain* 134, 11–23. doi: 10.1093/brain/awq322

Alexander, G. M., Rogan, S. C., Abbas, A. I., Armbruster, B. N., Pei, Y., Allen, J. A., et al. (2009). Remote control of neuronal activity in transgenic mice expressing evolved G protein-coupled receptors. *Neuron* 63, 27–39. doi: 10.1016/j.neuron.2009.06.014

Androulidakis, A. G., Mazzone, P., Litvak, V., Penny, W., Dileone, M., Gaynor, L. M., et al. (2008). Oscillatory activity in the pedunculopontine area of patients with Parkinson's disease. *Exp. Neurol.* 211, 59–66. doi: 10.1016/j.expneurol.2008.01.002

Ballermann, M., and Fouad, K. (2006). Spontaneous locomotor recovery in spinal cord injured rats is accompanied by anatomical plasticity of reticulospinal fibers. *Eur. J. Neurosci.* 23, 1988–1996. doi: 10.1111/j.1460-9568.2006.04726.x

Basso, D. M., Beattie, M. S., and Bresnahan, J. C. (1996). Graded histological and locomotor outcomes after spinal cord contusion using the NYU weight-drop device versus transection. *Exp. Neurol.* 139, 244–256. doi: 10.1006/exnr.1996.0098

Bender, F., Gorbati, M., Cadavieco, M. C., Denisova, N., Gao, X., Holman, C., et al. (2015). Theta oscillations regulate the speed of locomotion via a hippocampus to lateral septum pathway. *Nat. Commun.* 6:8521. doi: 10.1038/ncomms9521

Bland, B. H. (1986). The physiology and pharmacology of hippocampal formation theta rhythms. *Prog. Neurobiol.* 26, 1–54. doi: 10.1016/0301-0082(86)90019-5

Bland, B. H., and Oddie, S. D. (2001). Theta band oscillation and synchrony in the hippocampal formation and associated structures: the case for its role in sensorimotor integration. *Behav. Brain Res.* 127, 119–136. doi: 10.1016/s0166-4328(01)00358-8

Bland, B. H., and Vanderwolf, C. H. (1972). Electrical stimulation of the hippocampal formation: behavioral and bioelectrical effects. *Brain Res.* 43, 89–106. doi: 10.1016/0006-8993(72)90276-4

Cabaj, A. M., Majczyński, H., Couto, E., Gardiner, P. F., Stecina, K., Sławińska, U., et al. (2017). Serotonin controls initiation of locomotion and afferent modulation of coordination via 5-HT_7 receptors in adult rats. *J. Physiol.* 595, 301–320. doi: 10.1113/JP272271

Coles, S. K., Iles, J. F., and Nicolopoulos-Stournaras, S. (1989). The mesencephalic centre controlling locomotion in the rat. *Neuroscience* 28, 149–157. doi: 10.1016/0306-4522(89)90239-x

Colgin, L. L. (2016). Rhythms of the hippocampal network. *Nat. Rev. Neurosci.* 17, 239–249. doi: 10.1038/nrn.2016.21

Collomb-Clerc, A., and Welter, M. L. (2015). Effects of deep brain stimulation on balance and gait in patients with Parkinson's disease: a systematic neurophysiological review. *Neurophysiol. Clin.* 45, 371–388. doi: 10.1016/j.neucli.2015.07.001

Douglas, J. R., Noga, B. R., Dai, X., and Jordan, L. M. (1993). The effects of intrathecal administration of excitatory amino acid agonists and antagonists on the initiation of locomotion in the adult cat. *J. Neurosci.* 13, 990–1000.

Ferraye, M. U., Debû, B., Fraix, V., Goetz, L., Ardouin, C., Yelnik, J., et al. (2010). Effects of pedunculopontine nucleus area stimulation on gait disorders in Parkinson's disease. *Brain* 133, 205–214. doi: 10.1093/brain/awp229

Ferraye, M. U., Debû, B., Fraix, V., Krack, P., Charbardès, S., Seigneuret, E., et al. (2011). Subthalamic nucleus versus pedunculopontine nucleus stimulation in Parkinson disease: synergy or antagonism? *J. Neural Transm. (Vienna)* 118, 1469–1475. doi: 10.1007/s00702-011-0673-y

Filli, L., Engmann, A. K., Zörner, B., Weinmann, O., Moraitis, T., Gullo, M., et al. (2014). Bridging the gap: a reticulo-propriospinal detour bypassing an incomplete spinal cord injury. *J. Neurosci.* 34, 13399–13410. doi: 10.1523/JNEUROSCI.0701-14.2014

Fink, K. L., and Cafferty, W. B. (2016). Reorganization of intact descending motor circuits to replace lost connections after injury. *Neurotherapeutics* 13, 370–381. doi: 10.1007/s13311-016-0422-x

Fraix, V., Bastin, J., David, O., Goetz, L., Ferraye, M., Benabid, A. L., et al. (2013). Pedunculopontine nucleus area oscillations during stance, stepping and freezing in Parkinson's disease. *PLoS One* 8:e83919. doi: 10.1371/journal.pone.0083919

Fuhrmann, F., Justus, D., Sosulina, L., Kaneko, H., Beutel, T., Friedrichs, D., et al. (2015). Locomotion, theta oscillations, and the speed-correlated firing of hippocampal neurons are controlled by a medial septal glutamatergic circuit. *Neuron* 86, 1253–1264. doi: 10.1016/j.neuron.2015.05.001

Garcia-Rill, E., Houser, C. R., Skinner, R. D., Smith, W., and Woodward, D. J. (1987). Locomotion-inducing sites in the vicinity of the pedunculopontine nucleus. *Brain Res. Bull.* 18, 731–738. doi: 10.1016/0361-9230(87)90208-5

Garcia-Rill, E., Hyde, J., Kezunovic, N., Urbano, F. J., and Petersen, E. (2015). The physiology of the pedunculopontine nucleus: implications for deep brain stimulation. *J. Neural Transm. (Vienna)* 122, 225–235. doi: 10.1007/s00702-014-1243-x

Garcia-Rill, E., Simon, C., Smith, K., Kezunovic, N., and Hyde, J. (2011). The pedunculopontine tegmental nucleus: from basic neuroscience to neurosurgical applications: arousal from slices to humans: implications for DBS. *J. Neural Transm. (Vienna)* 118, 1397–1407. doi: 10.1007/s00702-010-0500-x

Garcia-Rill, E., and Skinner, R. D. (1987). The mesencephalic locomotor region. I. Activation of a medullary projection site. *Brain Res.* 411, 1–12. doi: 10.1016/0006-8993(87)90675-5

Garcia-Rill, E., Skinner, R. D., Conrad, C., Mosley, D., and Campbell, C. (1986). Projections of the mesencephalic locomotor region in the rat. *Brain Res. Bull.* 17, 33–40. doi: 10.1016/0361-9230(86)90158-9

Geng, X., Xie, J., Wang, X., Wang, X., Zhang, X., Hou, Y., et al. (2016). Altered neuronal activity in the pedunculopontine nucleus: an electrophysiological study in a rat model of Parkinson's disease. *Behav. Brain Res.* 305, 57–64. doi: 10.1016/j.bbr.2016.02.026

Gillis, G. B., and Biewener, A. A. (2001). Hindlimb muscle function in relation to speed and gait: *in vivo* patterns of strain and activation in a hip and knee extensor of the rat (*Rattus norvegicus*). *J. Exp. Biol.* 204, 2717–2731.

Grillner, S., Georgopoulos, A. P., and Jordan, L. M. (1997). "Selection and initiation of motor behavior," in *Neurons, Network and Motor Behavior*, eds P. S. G. Stein, A. I. Selverston and D. G. Stuart (Cambridge, MA: MIT Press), 3–19.

Gruner, J. A. (1992). A monitored contusion model of spinal cord injury in the rat. *J. Neurotrauma* 9, 123–126; discussion 126–128. doi: 10.1089/neu.1992.9.123

Guertin, P., Angel, M. J., Perreault, M. C., and McCrea, D. A. (1995). Ankle extensor group I afferents excite extensors throughout the hindlimb during fictive locomotion in the cat. *J. Physiol.* 487, 197–209. doi: 10.1113/jphysiol.1995.sp020871

Gut, N. K., and Winn, P. (2015). Deep brain stimulation of different pedunculopontine targets in a novel rodent model of parkinsonism. *J. Neurosci.* 35, 4792–4803. doi: 10.1523/JNEUROSCI.3646-14.2015

Gut, N. K., and Winn, P. (2016). The pedunculopontine tegmental nucleus-A functional hypothesis from the comparative literature. *Mov. Disord.* 31, 615–624. doi: 10.1002/mds.26556

Hamacher, D., Herold, F., Wiegel, P., Hamacher, D., and Schega, L. (2015). Brain activity during walking: a systematic review. *Neurosci. Biobehav. Rev.* 57, 310–327. doi: 10.1016/j.neubiorev.2015.08.002

Hamani, C., Moro, E., and Lozano, A. M. (2011). The pedunculopontine nucleus as a target for deep brain stimulation. *J. Neural Transm. (Vienna)* 118, 1461–1468. doi: 10.1007/s00702-010-0547-8

Hansen, C. N., Faw, T. D., White, S., Buford, J. A., Grau, J. W., and Basso, D. M. (2016). Sparing of descending axons rescues interneuron plasticity in the lumbar cord to allow adaptive learning after thoracic spinal cord injury. *Front. Neural Circuits* 10:11. doi: 10.3389/fncir.2016.00011

He, W., and Bellamkonda, R. V. (2008). "A molecular perspective on understanding and modulating the performance of chronic central nervous system (CNS) recording electrodes," in *Indwelling Neural Implants: Strategies for Contending with the in vivo Environment*, ed. W. M. Reichert (Boca Raton, FL: CRC Press), 151–175.

Heise, C. E., and Mitrofanis, J. (2006). Fos immunoreactivity in some locomotor neural centres of 6OHDA-lesioned rats. *Anat. Embryol. (Berl)* 211, 659–671. doi: 10.1007/s00429-006-0130-0

Hernández-Chan, N. G., Góngora-Alfaro, J. L., Álvarez-Cervera, F. J., Solís-Rodríguez, F. A., Heredia-López, F. J., and Arankowsky-Sandoval, G. (2011). Quinolinic acid lesions of the pedunculopontine nucleus impair sleep architecture, but not locomotion, exploration, emotionality or working memory in the rat. *Behav. Brain Res.* 225, 482–490. doi: 10.1016/j.bbr.2011.08.007

Jordan, L. M. (1998). Initiation of locomotion in mammals. *Ann. N Y Acad. Sci.* 860, 83–93. doi: 10.1111/j.1749-6632.1998.tb09040.x

Jordan, L. M., McVagh, J. R., Noga, B. R., Cabaj, A. M., Majczyński, H., Slawińska, U., et al. (2014). Cholinergic mechanisms in spinal locomotion-potential target for rehabilitation approaches. *Front. Neural Circuits* 8:132. doi: 10.3389/fncir.2014.00132

Jordan, L. M. J., and Sławińska, U. (2014). "The brain and spinal cord networks controlling locomotion," in *Neuronal Networks in Brain Function, CNS Disorders and Therapeutics*, eds C. L. Faingold and H. Blumenfeld (Amsterdam: Academic Press), 215–233.

Karachi, C., André, A., Bertasi, E., Bardinet, E., Lehéricy, S., and Bernard, F. A. (2012). Functional parcellation of the lateral mesencephalus. *J. Neurosci.* 32, 9396–9401. doi: 10.1523/JNEUROSCI.0509-12.2012

Kiehn, O. (2016). Decoding the organization of spinal circuits that control locomotion. *Nat. Rev. Neurosci.* 17, 224–238. doi: 10.1038/nrn.2016.9

King, C., Recce, M., and O'Keefe, J. (1998). The rhythmicity of cells of the medial septum/diagonal band of Broca in the awake freely moving rat: relationships with behaviour and hippocampal theta. *Eur. J. Neurosci.* 10, 464–477. doi: 10.1046/j.1460-9568.1998.00026.x

Kramis, R., Vanderwolf, C. H., and Bland, B. H. (1975). Two types of hippocampal rhythmical slow activity in both the rabbit and the rat: relations to behavior and effects of atropine, diethyl ether, urethane, and pentobarbital. *Exp. Neurol.* 49, 58–85. doi: 10.1016/0014-4886(75)90195-8

Lee, A. M., Hoy, J. L., Bonci, A., Wilbrecht, L., Stryker, M. P., and Niell, C. M. (2014). Identification of a brainstem circuit regulating visual cortical state in parallel with locomotion. *Neuron* 83, 455–466. doi: 10.1016/j.neuron.2014.06.031

Leszczyńska, A. N., Majczynski, H., Wilczynski, G. M., Sławińska, U., and Cabaj, A. M. (2015). Thoracic hemisection in rats results in initial recovery followed by a late decrement in locomotor movements, with changes in coordination correlated with serotonergic innervation of the ventral horn. *PLoS One* 10:e0143602. doi: 10.1371/journal.pone.0143602

MacDonell, C. W., Power, K. E., Chopek, J. W., Gardiner, K. R., and Gardiner, P. F. (2015). Extensor motoneurone properties are altered immediately before and during fictive locomotion in the adult decerebrate rat. *J. Physiol.* 593, 2327–2342. doi: 10.1113/JP270239

MacLaren, D. A., Santini, J. A., Russell, A. L., Markovic, T., and Clark, S. D. (2014). Deficits in motor performance after pedunculopontine lesions in rats—impairment depends on demands of task. *Eur. J. Neurosci.* 40, 3224–3236. doi: 10.1111/ejn.12666

Mazzone, P., Lozano, A., Stanzione, P., Galati, S., Scarnati, E., Peppe, A., et al. (2005). Implantation of human pedunculopontine nucleus: a safe and clinically relevant target in Parkinson's disease. *Neuroreport* 16, 1877–1881. doi: 10.1097/01.wnr.0000187629.38010.12

Melnikova, Z. L. (1975). The locomotion of the rat evoked by stimulation of the midbrain. *Vestn. Moscow. Univ.* 2, 45–51.

Milner, K. L., and Mogenson, G. J. (1988). Electrical and chemical activation of the mesencephalic and subthalamic locomotor regions in freely moving rats. *Brain Res.* 452, 273–285. doi: 10.1016/0006-8993(88)90031-5

Mogenson, G. J., and Nielsen, M. (1984). A study of the contribution of hippocampal-accumbens-subpallidal projections to locomotor activity. *Behav. Neural Biol.* 42, 38–51. doi: 10.1016/s0163-1047(84)90412-6

Mori, S., Matsuyama, K., Kohyama, J., Kobayashi, Y., and Takakusaki, K. (1992). Neuronal constituents of postural and locomotor control systems and their interactions in cats. *Brain Dev.* 14, S109–S120.

Mori, S., Sakamoto, T., Ohta, Y., Takakusaki, K., and Matsuyama, K. (1989). Site-specific postural and locomotor changes evoked in awake, freely moving intact cats by stimulating the brainstem. *Brain Res.* 505, 66–74. doi: 10.1016/0006-8993(89)90116-9

Noga, B. R., Kriellaars, D. J., Brownstone, R. M., and Jordan, L. M. (2003). Mechanism for activation of locomotor centers in the spinal cord by stimulation of the mesencephalic locomotor region. *J. Neurophysiol.* 90, 1464–1478. doi: 10.1152/jn.00034.2003

Nonnekes, J., Snijders, A. H., Nutt, J. G., Deuschl, G., Giladi, N., and Bloem, B. R. (2015). Freezing of gait: a practical approach to management. *Lancet Neurol.* 14, 768–778. doi: 10.1016/S1474-4422(15)00041-1

Nosko, D., Ferraye, M. U., Fraix, V., Goetz, L., Chabardes, S., Pollak, P., et al. (2015). Low-frequency versus high-frequency stimulation of the pedunculopontine nucleus area in Parkinson's disease: a randomised controlled trial. *J. Neurol. Neurosurg. Psychiatry* 86, 674–679. doi: 10.1136/jnnp-2013-307511

Paxinos, G., and Watson, C. (1998). *The Rat Brain in Stereotaxic Coordinates.* New York, NY: Academic Press.

Piallat, B., Chabardès, S., Torres, N., Fraix, V., Goetz, L., Seigneuret, E., et al. (2009). Gait is associated with an increase in tonic firing of the sub-cuneiform nucleus neurons. *Neuroscience* 158, 1201–1205. doi: 10.1016/j.neuroscience.2008.10.046

Pienaar, I. S., Gartside, S. E., Sharma, P., De Paola, V., Gretenkord, S., Withers, D., et al. (2015). Pharmacogenetic stimulation of cholinergic pedunculopontine neurons reverses motor deficits in a rat model of Parkinson's disease. *Mol. Neurodegener.* 10:47. doi: 10.1186/s13024-015-0044-5

Roseberry, T. K., Lee, A. M., Lalive, A. L., Wilbrecht, L., Bonci, A., and Kreitzer, A. C. (2016). Cell-type-specific control of brainstem locomotor circuits by Basal Ganglia. *Cell* 164, 526–537. doi: 10.1016/j.cell.2015.12.037

Ross, G. S., and Sinnamon, H. M. (1984). Forelimb and hindlimb stepping by the anesthetized rat elicited by electrical stimulation of the pons and medulla. *Physiol. Behav.* 33, 201–208. doi: 10.1016/0031-9384(84)90100-8

Ryczko, D., and Dubuc, R. (2013). The multifunctional mesencephalic locomotor region. *Curr. Pharm. Des.* 19, 4448–4470. doi: 10.2174/1381612811319240011

Shik, M. L., Severin, F. V., and Orlovskii, G. N. (1966). Control of walking and running by means of electric stimulation of the midbrain. *Biofizika* 11, 659–666.

Shimamoto, S. A., Larson, P. S., Ostrem, J. L., Glass, G. A., Turner, R. S., and Starr, P. A. (2010). Physiological identification of the human pedunculopontine nucleus. *J. Neurol. Neurosurg. Psychiatry* 81, 80–86. doi: 10.1136/jnnp.2009.179069

Simon, C., Kezunovic, N., Ye, M., Hyde, J., Hayar, A., Williams, D. K., et al. (2010). Gamma band unit activity and population responses in the pedunculopontine nucleus. *J. Neurophysiol.* 104, 463–474. doi: 10.1152/jn.00242.2010

Sławińska, U., and Kasicki, S. (1995).Theta-like rhythm in depth EEG activity of hypothalamic areas during spontaneous or electrically induced locomotion in the rat. *Brain Res.* 678, 117–126. doi: 10.1016/0006-8993(95)00174-o

Sławińska, U., and Kasicki, S. (1998). The frequency of rat's hippocampal theta rhythm is related to the speed of locomotion. *Brain Res.* 796, 327–331. doi: 10.1016/s0006-8993(98)00390-4

Sławińska, U., Majczyński, H., and Djavadian, R. (2000). Recovery of hindlimb notor functions after spinal cord transection is enhanced by grafts of the embryonic raphe nuclei. *Exp. Brain Res.* 132, 27–38. doi: 10.1007/s002219900323

Steeves, J. D., and Jordan, L. M. (1984). Autoradiographic demonstration of the projections from the mesencephalic locomotor region. *Brain Res.* 307, 263–276. doi: 10.1016/0006-8993(84)90480-3

Stefani, A., Lozano, A. M., Peppe, A., Stanzione, P., Galati, S., Tropepi, D., et al. (2007). Bilateral deep brain stimulation of the pedunculopontine and subthalamic nuclei in severe Parkinson's disease. *Brain* 130, 1596–1607. doi: 10.1093/brain/awl346

Takakusaki, K. (2008). Forebrain control of locomotor behaviors. *Brain Res. Rev.* 57, 192–198. doi: 10.1016/j.brainresrev.2007.06.024

Takakusaki, K. (2013). Neurophysiology of gait: from the spinal cord to the frontal lobe. *Mov. Disord.* 28, 1483–1491. doi: 10.1002/mds.25669

Takakusaki, K., Chiba, R., Nozu, T., and Okumura, T. (2016). Brainstem control of locomotion and muscle tone with special reference to the role of the mesopontine tegmentum and medullary reticulospinal systems. *J. Neural Transm. (Vienna)* 123, 695–729. doi: 10.1007/s00702-015-1475-4

Takakusaki, K., Takahashi, K., Saitoh, K., Harada, H., Okumura, T., Kayama, Y., et al. (2005). Orexinergic projections to the cat midbrain mediate alternation of emotional behavioural states from locomotion to cataplexy. *J. Physiol.* 568, 1003–1020. doi: 10.1113/jphysiol.2005.085829

Tattersall, T. L., Stratton, P. G., Coyne, T. J., Cook, R., Silberstein, P., Silburn, P. A., et al. (2014). Imagined gait modulates neuronal network dynamics in the human pedunculopontine nucleus. *Nat. Neurosci.* 17, 449–454. doi: 10.1038/nn.3642

Thevathasan, W., Pogosyan, A., Hyam, J. A., Jenkinson, N., Foltynie, T., Limousin, P., et al. (2012). Alpha oscillations in the pedunculopontine nucleus correlate with gait performance in parkinsonism. *Brain* 135, 148–160. doi: 10.1093/brain/awr315

Thompson, J. A., Lanctin, D., Ince, N. F., and Abosch, A. (2014). Clinical implications of local field potentials for understanding and treating movement disorders. *Stereotact. Funct. Neurosurg.* 92, 251–263. doi: 10.1159/000364913

Tort, A. B., Kramer, M. A., Thorn, C., Gibson, D. J., Kubota, Y., Graybiel, A. M., et al. (2008). Dynamic cross-frequency couplings of local field potential oscillations in rat striatum and hippocampus during performance of a T-maze task. *Proc. Natl. Acad. Sci. U S A* 105, 20517–20522. doi: 10.1073/pnas.0810524105

Tsang, E. W., Hamani, C., Moro, E., Mazzella, F., Poon, Y. Y., Lozano, A. M., et al. (2010). Involvement of the human pedunculopontine nucleus region in voluntary movements. *Neurology* 75, 950–959. doi: 10.1212/wnl.0b013e3181f25b35

Udupa, K., and Chen, R. (2015). The mechanisms of action of deep brain stimulation and ideas for the future development. *Prog. Neurobiol.* 133, 27–49. doi: 10.1016/j.pneurobio.2015.08.001

Vianna, D. M., Borelli, K. G., Ferreira-Netto, C., Macedo, C. E., and Brandao, M. L. (2003). Fos-like immunoreactive neurons following electrical stimulation of the dorsal periaqueductal gray at freezing and escape thresholds. *Brain Res. Bull.* 62, 179–189. doi: 10.1016/j.brainresbull.2003.09.010

Weinberger, M., Hamani, C., Hutchison, W. D., Moro, E., Lozano, A. M., and Dostrovsky, J. O. (2008). Pedunculopontine nucleus microelectrode recordings in movement disorder patients. *Exp. Brain Res.* 188, 165–174. doi: 10.1007/s00221-008-1349-1

Welter, M. L., Demain, A., Ewenczyk, C., Czernecki, V., Lau, B., El Helou, A., et al. (2015). PPNa-DBS for gait and balance disorders in Parkinson's disease: a double-blind, randomised study. *J. Neurol.* 262, 1515–1525. doi: 10.1007/s00415-015-7744-1

Whelan, P. J. (1996). Control of locomotion in the decerebrate cat. *Prog. Neurobiol.* 49, 481–515. doi: 10.1016/0301-0082(96)00028-7

Winn, P. (2006). How best to consider the structure and function of the pedunculopontine tegmental nucleus: evidence from animal studies. *J. Neurol. Sci.* 248, 234–250. doi: 10.1016/j.jns.2006.05.036

Xiang, H. B., Zhu, W. Z., Guan, X. H., and Ye, D. W. (2013). The cuneiform nucleus may be involved in the regulation of skeletal muscle tone by motor pathway: a virally mediated trans-synaptic tracing study in surgically sympathectomized mice. *Brain* 136:e251. doi: 10.1093/brain/awt123

Conflict of Interest Statement: The authors declare that the research was conducted in the absence of any commercial or financial relationships that could be construed as a potential conflict of interest.

Copyright © 2017 Noga, Sanchez, Villamil, O'Toole, Kasicki, Olszewski, Cabaj, Majczyński, Sławińska and Jordan. This is an open-access article distributed under the terms of the Creative Commons Attribution License (CC BY). The use, distribution or reproduction in other forums is permitted, provided the original author(s) or licensor are credited and that the original publication in this journal is cited, in accordance with accepted academic practice. No use, distribution or reproduction is permitted which does not comply with these terms.

frontiers in Neuroscience

MINI REVIEW
published: 26 May 2017
doi: 10.3389/fnins.2017.00295

Dopamine and the Brainstem Locomotor Networks: From Lamprey to Human

Dimitri Ryczko[1†] *and Réjean Dubuc*[1,2*]

[1] *Groupe de Recherche sur le Système Nerveux Central, Département de Neurosciences, Université de Montréal, Montréal, QC, Canada,* [2] *Groupe de Recherche en Activité Physique Adaptée, Département des Sciences de l'Activité Physique, Université du Québec à Montréal, Montréal, QC, Canada*

In vertebrates, dopamine neurons are classically known to modulate locomotion via their ascending projections to the basal ganglia that project to brainstem locomotor networks. An increased dopaminergic tone is associated with increase in locomotor activity. In pathological conditions where dopamine cells are lost, such as in Parkinson's disease, locomotor deficits are traditionally associated with the reduced ascending dopaminergic input to the basal ganglia. However, a descending dopaminergic pathway originating from the *substantia nigra pars compacta* was recently discovered. It innervates the mesencephalic locomotor region (MLR) from basal vertebrates to mammals. This pathway was shown to increase locomotor output in lampreys, and could very well play an important role in mammals. Here, we provide a detailed account on the newly found dopaminergic pathway in lamprey, salamander, rat, monkey, and human. In lampreys and salamanders, dopamine release in the MLR is associated with the activation of reticulospinal neurons that carry the locomotor command to the spinal cord. Dopamine release in the MLR potentiates locomotor movements through a D1-receptor mechanism in lampreys. In rats, stimulation of the *substantia nigra pars compacta* elicited dopamine release in the pedunculopontine nucleus, a known part of the MLR. In a monkey model of Parkinson's disease, a reduced dopaminergic innervation of the brainstem locomotor networks was reported. Dopaminergic fibers are also present in human pedunculopontine nucleus. We discuss the conserved locomotor role of this pathway from lamprey to mammals, and the hypothesis that this pathway could play a role in the locomotor deficits reported in Parkinson's disease.

Keywords: locomotion, brainstem, dopamine, mesencephalic locomotor region, *substantia nigra pars compacta*, pedunculopontine nucleus, conservation, Parkinson's disease

OPEN ACCESS

Edited by:
Brian R. Noga,
University of Miami, United States

Reviewed by:
Abdel El Manira,
Karolinska Institutet, Sweden
Pascal Darbon,
University of Strasbourg, France

***Correspondence:**
Réjean Dubuc
rejean.dubuc@gmail.com

†*Present Address:*
Dimitri Ryczko, Département de Pharmacologie-Physiologie, Université de Sherbrooke, Sherbrooke, QC, Canada

Specialty section:
This article was submitted to Neural Technology, a section of the journal Frontiers in Neuroscience

Received: *08 March 2017*
Accepted: *11 May 2017*
Published: *26 May 2017*

Citation:
Ryczko D and Dubuc R (2017) Dopamine and the Brainstem Locomotor Networks: From Lamprey to Human. Front. Neurosci. 11:295. doi: 10.3389/fnins.2017.00295

ASCENDING DOPAMINERGIC PATHWAY AND LOCOMOTION

Dopaminergic neurons degenerate in patients with Parkinson's disease (PD), resulting in serious motor dysfunctions including locomotor deficits (falls, gait freezing, dysfunctional turning), which constitute major problems in advanced forms of the disease (Stack and Ashburn, 2008, for review see Bloem et al., 2004). These locomotor deficits are traditionally associated with a loss of the ascending dopaminergic projections from the *substantia nigra pars compacta* (SNc) to the basal

ganglia (Carlsson et al., 1958; Carlsson, 1959; Sano et al., 1959; Poirier and Sourkes, 1965; Sourkes and Poirier, 1965; Albin et al., 1989; Ehringer and Hornykiewicz, 1998; Kravitz et al., 2010; Roseberry et al., 2016, for review see Fahn, 2015). In turn, the basal ganglia project down to the Mesencephalic Locomotor Region (MLR), a brainstem region that controls locomotion in vertebrates (Shik et al., 1966; for review see Ryczko and Dubuc, 2013, **Figure 1**). The MLR was initially found in cats to initiate locomotion and control its frequency and intensity (Shik et al., 1966). It was later identified in lamprey (Sirota et al., 2000), salamander (Cabelguen et al., 2003), stingray (Bernau et al., 1991), bird (Sholomenko et al., 1991), rat (Garcia-Rill et al., 1987), mouse (Lee et al., 2014; Roseberry et al., 2016), rabbit (Musienko et al., 2008), guinea-pig (Marlinsky and Voitenko, 1991), and monkey (Eidelberg et al., 1981; Karachi et al., 2010; Goetz et al., 2016a). In basal vertebrates, the MLR comprises the laterodorsal tegmental nucleus and the pedunculopontine nucleus (PPN). In mammals, it comprises the PPN, but also the cuneiform nucleus (CnF). In humans, damage to the MLR is associated with locomotor deficits (Masdeu et al., 1994; Kuo et al., 2008; Demain et al., 2014). The MLR is explored as a target for deep brain stimulation to improve locomotor function in Parkinsonian patients (Plaha and Gill, 2005; for review see Hamani et al., 2016a,b).

The ascending dopaminergic projections mostly target the striatum, a major entry of the basal ganglia. These projections favor locomotion initiation by increasing the excitability of D_1-expressing striatal neurons of the direct pathway, and this reduces the tonic inhibition sent by the output stations of the basal ganglia to the MLR. In parallel, dopamine decreases the excitability of D_2-expressing striatal neurons of the indirect pathway. This also contributes to disinhibit the MLR, and initiate movement (Albin

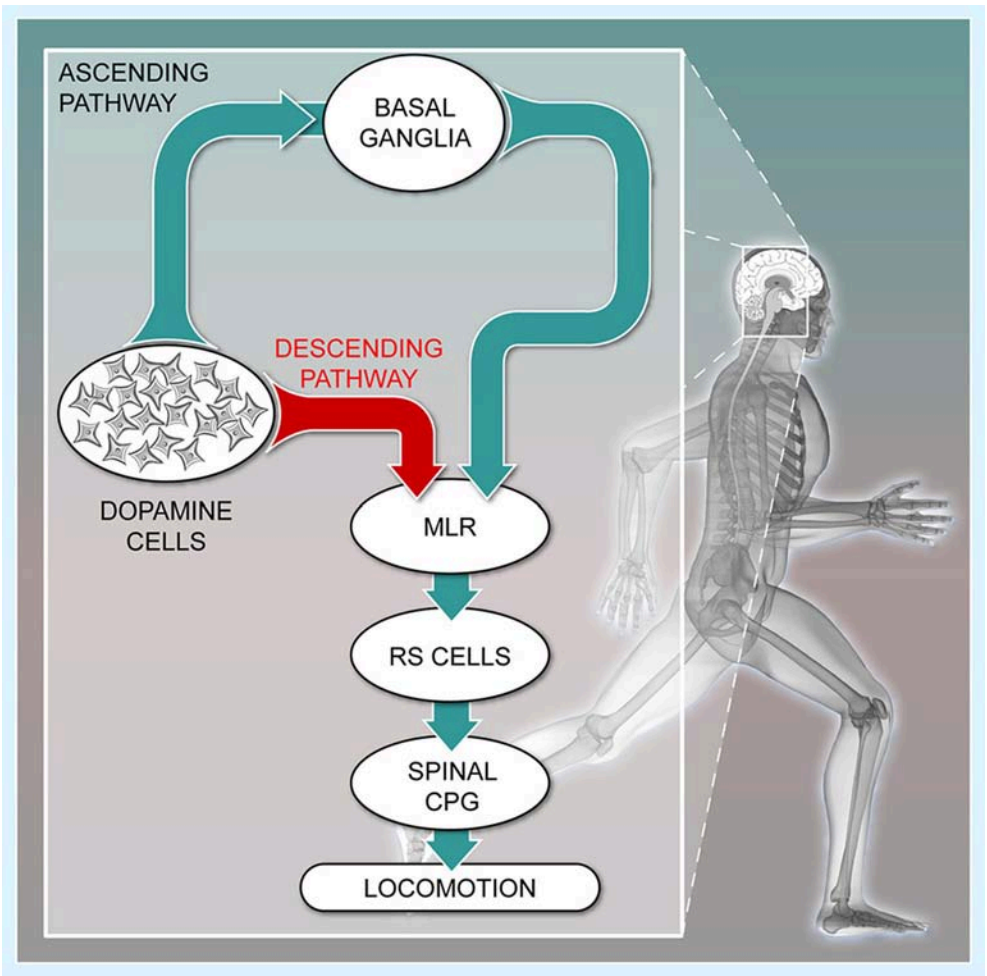


FIGURE 1 | The descending dopaminergic pathway recently uncovered in vertebrates. Schematic representation of the connectivity between the meso-diencephalic dopamine cells, the basal ganglia, the Mesencephalic Locomotor Region (MLR), the reticulospinal cells (RS), and the Central Pattern Generator (CPG) for locomotion. The meso-diencephalic dopamine cells refer to the posterior tuberculum in basal vertebrates and to the *substantia nigra pars compacta* in mammals. For convenience, the well-established direct and indirect pathways within the basal ganglia are not illustrated. (Adapted from (Le Ray et al., 2011). No permission is required for this reproduction).

et al., 1989; Kravitz et al., 2010; Freeze et al., 2013; Roseberry et al., 2016). Such organization is conserved within the basal ganglia from lamprey to mammals (see Grillner and Robertson, 2016). Once disinhibited, the MLR initiates locomotion by sending descending excitatory inputs to reticulospinal neurons, which activate the central pattern generator for locomotion (**Figure 1**, cat: Orlovskii, 1970; Steeves and Jordan, 1980; Garcia-Rill and Skinner, 1987a,b; Noga et al., 1988, 1991; rat: Bachmann et al., 2013; bird: Sholomenko et al., 1991; lamprey: Buchanan and Grillner, 1987; Brodin et al., 1988; Ohta and Grillner, 1989; Brocard and Dubuc, 2003; Le Ray et al., 2003; mouse: Bretzner and Brownstone, 2013; salamander: Ryczko et al., 2016b). MLR glutamatergic neurons are of primary importance to activate reticulospinal neurons and elicit locomotion (lamprey: Brocard and Dubuc, 2003, salamander: Ryczko et al., 2016b, mouse: Lee et al., 2014; Roseberry et al., 2016). MLR cholinergic neurons provide additional excitation to reticulospinal cells (lamprey: Le Ray et al., 2003; Smetana et al., 2010; mouse: Roseberry et al., 2016). The functional significance of this circuitry was elegantly summed in a mouse study, in which it was shown that ascending dopaminergic pathways to the basal ganglia indirectly control MLR glutamatergic cells and locomotion (Roseberry et al., 2016). The loss of the ascending dopaminergic pathway is thus considered the main cause of locomotor deficits in PD.

A NEW DESCENDING DOPAMINERGIC PATHWAY HAS BEEN UNRAVELED

There was some indication in the literature that in addition to their ascending projections, dopaminergic cells also sent direct descending projections to brainstem locomotor networks. In rat, dopamine was detected using radiometric assays or microdialysis in the CnF (Versteeg et al., 1976; Saavedra et al., 1979) and PPN (Steiniger and Kretschmer, 2003) that are both part of the MLR in mammals (see Ryczko and Dubuc, 2013). Moreover, dopaminergic fibers were detected in rat brainstem using immunohistochemistry (Kitahama et al., 2000). In monkey, dopaminergic terminals were found in proximity with cholinergic cells of the PPN and CnF (Rolland et al., 2009). The origin of this dopaminergic projection remained unknown, but tracing studies mentioned a descending projection from the SNc to the PPN in rat (Beckstead et al., 1979; Semba and Fibiger, 1992; Steininger et al., 1992; Ichinohe et al., 2000) and in cat (Edley and Graybiel, 1983). The presence of such descending input was also supported by recordings of short latency antidromic activation of SNc neurons following PPN stimulation in rat (Scarnati et al., 1984, 1987).

We investigated the origin of the dopaminergic innervation of the MLR in vertebrates. In lamprey (Ryczko et al., 2013) and salamander (Ryczko et al., 2016a), dopaminergic fibers were found around MLR cholinergic cells, a conserved landmark of the MLR (see Ryczko and Dubuc, 2013). We identified the origin of this dopaminergic innervation in lamprey (**Figure 2G**, Ryczko et al., 2013; see also Perez-Fernandez et al., 2014) and in salamander (**Figure 2H**, Ryczko et al., 2016a) as a diencephalic dopaminergic region called the posterior tuberculum. This region sends ascending projection to the striatum, and is considered homologous to the mammalian SNc and/or ventral tegmental area (Marin et al., 1997; Pombal et al., 1997; Puelles and Verney, 1998; Smeets et al., 2000; Rink and Wullimann, 2001; Blin et al., 2008; for review see Yamamoto and Vernier, 2011; Wullimann, 2014). We then found that such "new pathway" (**Figure 1**) is conserved in higher vertebrates. In rat, PPN cholinergic cells were innervated by dopaminergic fibers (Ryczko et al., 2016a). Using virogenetic tracing, we found that the dopaminergic innervation of the rat MLR originates from the SNc and to a lesser extent the retrorubral field (**Figure 2I**, Ryczko et al., 2016a). This was confirmed using conventional tracers coupled with immunofluorescence experiments (Ryczko et al., 2016a). While only a few dopamine neurons sent both an ascending projection to the striatum and a descending one to the MLR in lampreys and salamanders, numerous SNc dopamine neurons sent both ascending and descending projections in rats. The proportion of the ascending dopaminergic projection may have increased during evolution due to the expansion of the basal ganglia (see Grillner and Robertson, 2016). We then found in the human brain that PPN cholinergic cells are surrounded by dopaminergic fibers (**Figures 2J–L**, Ryczko et al., 2016a), indicating that the innervation of the MLR is conserved in vertebrates.

The descending dopaminergic pathway was shown to release dopamine in the MLR with fast-scan voltammetry (Ryczko et al., 2016a). Stimulation of the dopaminergic region evoked dopamine release in the MLR *in vitro* in lamprey (**Figures 2A,D**, Ryczko et al., 2013) and in salamander (**Figures 2B,E**, Ryczko et al., 2016a). In rat, SNc stimulation evoked dopamine release in the PPN *in vivo* (**Figures 2C,F**) that was potentiated by intraperitoneal amphetamine injection (Ryczko et al., 2016a). Altogether, these results established that the descending dopaminergic pathway is conserved and functional from basal vertebrates (lampreys, salamanders) to mammals (rats).

The role of the descending dopaminergic pathway in modulating locomotor activity was examined in two basal vertebrates. In lampreys and salamanders, stimulation of the dopamine region evoked dopamine release in the MLR, associated with activation of reticulospinal cells, which carry the locomotor command to the spinal cord (Ryczko et al., 2013, 2016a). There was a precise correlation in time linking MLR dopamine release and the activation of reticulospinal cells. The behavioral role of dopamine release in the MLR was examined in a lamprey semi-intact preparation (Ryczko et al., 2013), where the brain is exposed while the body swims as reported in many studies from our group (Sirota et al., 2000; Viana Di Prisco et al., 2000; Le Ray et al., 2003; Brocard et al., 2005, 2010; Gravel et al., 2007; Menard et al., 2007; Derjean et al., 2010; Smetana et al., 2010; Gariepy et al., 2012; Juvin et al., 2016). Stimulation of the dopaminergic region elicited reticulospinal activity together with locomotion, and microinjections of a D_1 antagonist in the MLR decreased the number of locomotor cycles, the frequency of locomotor movements, and the duration of the locomotor bout (Ryczko et al., 2013). Conversely, microinjection of dopamine in the MLR had an opposite effect (Ryczko et al., 2013). In mammals, whether MLR dopamine release is associated with

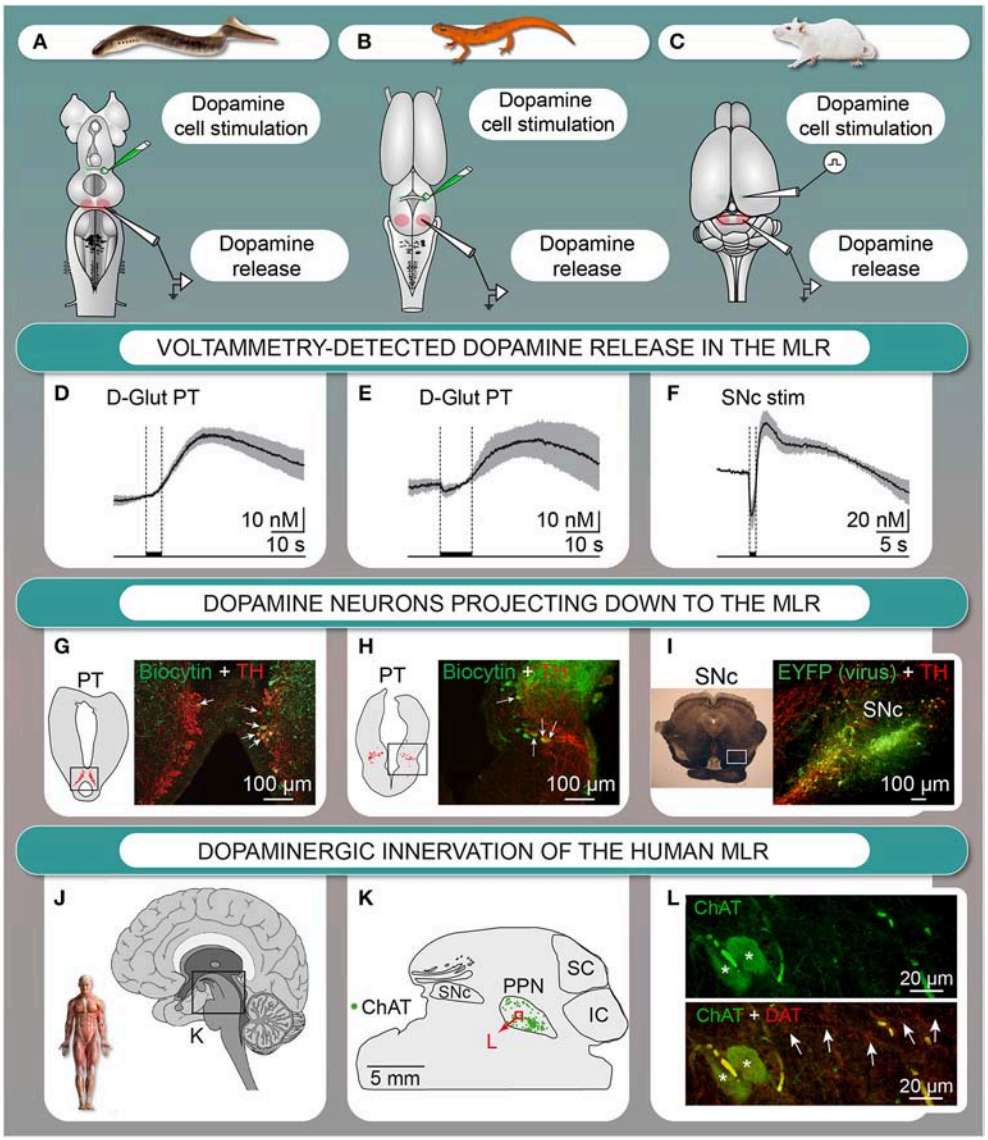


FIGURE 2 | The descending dopaminergic (DA) pathway is conserved from basal vertebrates to mammals. (A–F) Dopamine is released in the MLR after chemical stimulation of DA cells in the posterior tuberculum (PT) of lampreys **(A,D)** or salamanders (*in vitro* isolated brain) **(B,E)**, or after electrical stimulation of the *substantia nigra pars compacta* (SNc) in rats (anesthetized) **(C,F)**. **(D–F)** mean ± sem is illustrated. **(G)** Lamprey tyrosine hydroxylase (TH)-containing cells (red) in the PT and cells projecting to the MLR (green) with arrows indicating double labeled cells. **(H)** Salamander TH-containing cells (red) in the PT and cells projecting to the MLR (green) with arrows indicating double labeled cells. **(I)** DA cells in the SNc retrogradely labeled by an injection of a Cre-dependent adeno-associated virus encoding for the enhanced yellow fluorescent protein (EYFP, green) in the MLR of transgenic rats expressing the Cre-recombinase in TH neurons as shown by immunostaining against TH (red). **(J–L)** DA innervation of the human MLR. **(J–L)** The location of cholinergic cells (choline acetyltransferase-positive, ChAT) of the pedunculopontine nucleus (PPN), part of the MLR, is indicated. **(L)** Fibers containing the dopamine active transporter (DAT, red, highlighted by arrows) in proximity with cholinergic cells (ChAT, green) in the PPN. IC, inferior colliculus; SC, superior colliculus. (Panels **A,D,G** adapted from D. Ryczko, S. Gratsch, F. Auclair, C. Dube, S. Bergeron, M.H. Alpert, J.J. Cone, M.F. Roitman, S. Alford, and R. Dubuc, Forebrain dopamine neurons project down to a brainstem region controlling locomotion. Proceedings of the National Academy of Sciences of the United States of America 110 (2013) E3235–E3242. No permission is required for this reproduction; panels **B,C,E,F,H,I,J–L** adapted from D. Ryczko, J.J. Cone, M.H. Alpert, L. Goetz, F. Auclair, C. Dube, M. Parent, M.F. Roitman, S. Alford, and R. Dubuc, A descending dopamine pathway conserved from basal vertebrates to mammals. Proceedings of the National Academy of Sciences of the United States of America 113 (2016) E2440–E2449. No permission is required for this reproduction).

activation of the locomotor system remains to be addressed. The observation that amphetamine increases dopamine release in the rat MLR (Ryczko et al., 2016a) suggests an involvement of the descending dopaminergic pathway in the well-characterized increase in locomotor activity elicited by dopaminergic drugs (e.g., psychostimulants, L-DOPA).

The mechanisms through which dopamine potentiates MLR cell activity remain to be determined. It is possible that

MLR dopamine enhances locomotor output by potentiating glutamatergic inputs to the MLR. In support of this, stimulation of the dopaminergic region evokes fast excitatory synaptic inputs in MLR cells in lampreys (Gariepy et al., 2012; Ryczko et al., 2013). This fast input could be glutamatergic and monosynaptic according to anatomical and electrophysiological data (Derjean et al., 2010). Future research should determine whether the two transmitters cooperate pre- and/or post-synaptically, and establish the role of dopaminergic inputs on intrinsic properties of MLR cells.

POSSIBLE ROLE OF THE DESCENDING DOPAMINERGIC PATHWAY IN PD

There is accumulating evidence indicating that the MLR plays a similar role in humans as described in animal models. Moreover, it appears that some of the locomotor deficits observed in PD can be attributed to changes in the brainstem locomotor circuitry including the MLR. The PPN and CnF, both parts of the MLR, are activated in healthy individuals when they are asked to imagine that they are walking (Jahn et al., 2008; Snijders et al., 2011; Karachi et al., 2012; Peterson et al., 2014; Tattersall et al., 2014). In Parkinsonian subjects, similar observations were reported (Piallat et al., 2009; Lau et al., 2015; for review see Bohnen and Jahn, 2013). PPN activity increases during walking, and is modulated by L-DOPA with increase in alpha band (5–12 Hz) and decrease in beta (13–35) and gamma (65–90 Hz) bands (Fraix et al., 2013). Gait freezing is associated with a decreased alpha band activity in the PPN (Thevathasan et al., 2012). Motor arrests are associated with decreased blood oxygen levels in the MLR (Shine et al., 2013). Neuronal losses were reported in the PPN of patients with PD or progressive supranuclear palsy (Hirsch et al., 1987; Zweig et al., 1987, 1989; Jellinger, 1988). In PD this includes degeneration of cholinergic (Rinne et al., 2008; Karachi et al., 2010; Pienaar et al., 2013), GABAergic and glycinergic cells (Pienaar et al., 2013). Neuroimaging indicates that locomotor deficits in PD patients are associated with additional MLR abnormalities (notably in the PPN), including altered connectivity between the MLR, thalamus, and motor cortical regions (Fling et al., 2013, 2014), abnormal microstructure (Vercruysse et al., 2015; Youn et al., 2015; Wang et al., 2016), atrophy of the MLR gray matter (Snijders et al., 2011; Fioravanti et al., 2015) and abnormal metabolic activity following a walking task (Tard et al., 2015). Additionally, anatomopathological studies revealed the presence in the MLR of alpha-synuclein immuno-reactive Lewy Bodies (e.g., Seidel et al., 2015), and mitochondrial abnormalities (Pienaar et al., 2013) in PD. The severity of the locomotor deficits increases with the amplitude of PPN damage as captured by neuroimaging (Canu et al., 2015). These data are consistent with those showing that non-Parkinsonian individuals with MLR lesion display locomotor deficits (Masdeu et al., 1994; Kuo et al., 2008; Yeo et al., 2012), and that elderly with high level gait and balance disorders display midbrain gray matter atrophy including in the MLR (Demain et al., 2014). Finally, more and more studies point to the involvement of the PPN in the locomotor improvements related to deep brain stimulation of the subthalamic nucleus (human: Holiga et al., 2015; Knight et al., 2015; Weiss et al., 2015), which sends excitatory glutamatergic input to the PPN (e.g., Breit et al., 2001; Neagu et al., 2013; see Ryczko and Dubuc, 2013).

The benefits of MLR deep brain stimulation on locomotor function in PD (Plaha and Gill, 2005) are variable, from promising to modest (for recent studies, see Schrader et al., 2013; Mazzone et al., 2014; Holiga et al., 2015; Liu et al., 2015; Nosko et al., 2015; Welter et al., 2015) or unsustained benefits over the years (Mestre et al., 2016). This variability could be attributed to degeneration of MLR cells and to the variability of the brainstem anatomy from patient to patient (Mazzone et al., 2013). Reviewing the fast-growing body of literature on this neurosurgical approach is beyond the scope of the present review (for recent reviews, see Collomb-Clerc and Welter, 2015; DeLong and Wichmann, 2015; Fasano et al., 2015; Golestanirad et al., 2016; Rowe et al., 2016; Snijders et al., 2016). Several authors pointed out that adequate control trials and more standardization are needed before concluding on the efficacy of MLR deep brain stimulation (Windels et al., 2015; for review, see Hamani et al., 2016a,b).

The dopaminergic innervation of the PPN and CnF dramatically degenerates in a monkey model of PD (Rolland et al., 2009). The degeneration elicited by MPTP was even more marked in aged monkeys, maybe underlining the increasing fragility of this innervation over lifetime. The loss of dopaminergic innervation in the MLR could contribute to the pathophysiology of PD in several ways. If the role of the descending dopaminergic pathway to the MLR is conserved in higher vertebrates, locomotor deficits in PD may result, at least in part, from the loss of excitatory dopaminergic inputs to the MLR. This would lead to a reduced amplification of descending locomotor commands. Conversely, the descending dopaminergic pathway may improve locomotor function evoked by L-DOPA in people with PD (e.g., Moore et al., 2008; Chastan et al., 2009; Bryant et al., 2011a,b) by increasing the excitability of MLR cells. Importantly, locomotor deficits that are unresponsive to L-DOPA are associated with MLR degeneration (Chastan et al., 2009; Karachi et al., 2010; Snijders et al., 2011). It is thus possible that the beneficial effects of increasing dopamine release in the MLR with L-DOPA, or of stimulating MLR cells with dopaminergic agonists could improve locomotor function before MLR cells are lost in large number.

It is also possible that the loss of dopaminergic inputs to the MLR may disrupt the excitability of MLR cells, causing them to eventually degenerate. Such *transneuronal degeneration* can occur anterogradely or retrogradely and is characterized by a "structural deterioration of areas remote from the initial insult" (Fornito et al., 2015). This phenomenon was shown in the visual (e.g., Hubel and Wiesel, 1970; Herbin et al., 1999) and olfactory systems (e.g., Pinching and Powell, 1971). Transneuronal degeneration was also shown to damage dopaminergic neurons following striatal lesion (Macaya et al., 1994; Marti et al., 1997; El-Khodor and Burke, 2002; Canudas et al., 2005) and was proposed to contribute to PD (Pedersen and Schmidt, 2000). It was also proposed to occur in other neurodegenerative diseases

including Alzheimer's disease and amyotrophic lateral sclerosis (see Fornito et al., 2015). The multiple alterations in the MLR in PD are compatible with such phenomenon (see Fornito et al., 2015). The reciprocal projections between the SNc and the PPN (McGeer and McGeer, 1984; Lavoie and Parent, 1994; Ryczko et al., 2013, 2016a; Perez-Fernandez et al., 2014) could also contribute to potentiate the transneuronal degeneration process. Nigral dopamine cell degeneration would cause a loss of the dopaminergic input to the MLR, causing MLR cells to degenerate. In turn, degeneration of PPN cholinergic and glutamatergic cells projecting to the nigral dopamine neurons would contribute to nigral dopamine cell loss. Studies in rat and monkey indicate that destruction of dopamine cells causes degeneration of MLR cholinergic cells (Pienaar et al., 2015b; Bensaid et al., 2016). Conversely, lesion of PPN cholinergic neurons induces a loss of dopaminergic nigral neurons (Bensaid et al., 2016). Finally, lesion of nigral dopaminergic neurons followed by lesion of PPN cholinergic cells induces a more dramatic degeneration of PPN cholinergic cells (Bensaid et al., 2016), suggesting that the two lesions interact to create a transneuronal degeneration loop. Stabilization of the reciprocal interactions between dopamine and cholinergic neurons could be a promising avenue to alleviate degeneration of the two systems. Interestingly, activation of PPN cholinergic cells with designer receptors exclusively activated by designer drugs (DREADDs) improves locomotor function in a rat model of PD (Pienaar et al., 2015a). It would be interesting to determine whether this approach would decrease degeneration of cholinergic and dopaminergic cells.

The descending dopaminergic projections to the PPN could also regulate other important functions such as cognition, sleep (Stefani et al., 2013; Karachi and Francois, 2017), modulation of visual inputs during locomotion (Lee et al., 2014), arousal state (Garcia-Rill et al., 2015a,b; Goetz et al., 2016b), motivation, and reward (Xiao et al., 2016; Yoo et al., 2017). How the descending dopaminergic input to the PPN influences these functions should be the subject of future research. Interestingly, the multifunctional aspects of the MLR, well established in lampreys (i.e., regulation of locomotion, respiration, control of sensory inputs, see Ryczko and Dubuc, 2013), are mirrored by the multifunctionality of the PPN in mammals.

In conclusion, studies carried out in two basal vertebrates (lampreys and salamanders) allowed us to discover a direct dopaminergic projection from the SNc down to the MLR. Several lines of evidence indicate that this new dopaminergic pathway is functional in rats, and could also be present in humans. Future research should address whether the descending dopaminergic pathway potentiates locomotion in mammals as in basal vertebrates, whether it contributes to other PPN functions, and whether this dopaminergic innervation degenerates in PD patients.

AUTHOR CONTRIBUTORS

DR and RD wrote the article.

FUNDING

This work was supported by the Canadian Institutes of Health Research Grant 15129 (to RD); the Natural Sciences and Engineering Research Council of Canada Grant 217435 (to RD); the Great Lakes Fishery Commission Grants 54011, 54021 and 54035 (to RD); the Parkinson Society Canada Grant 2011-11 (to RD); the Fonds de Recherche du Québec—Santé (FRQS: Groupe de Recherche sur le Système Nerveux Central, GRSNC, 5249). DR received fellowships from FRQS and the GRSNC Jasper fellowship.

ACKNOWLEDGMENTS

We thank Danielle Veilleux for her technical assistance and Frédéric Bernard for his help with the graphics.

REFERENCES

Albin, R. L., Young, A. B., and Penney, J. B. (1989). The functional anatomy of basal ganglia disorders. *Trends Neurosci.* 12, 366–375. doi: 10.1016/0166-2236(89)90074-X

Bachmann, L. C., Matis, A., Lindau, N. T., Felder, P., Gullo, M., and Schwab, M. E. (2013). Deep brain stimulation of the midbrain locomotor region improves paretic hindlimb function after spinal cord injury in rats. *Sci. Transl. Med.* 5:208ra146. doi: 10.1126/scitranslmed.3005972

Beckstead, R. M., Domesick, V. B., and Nauta, W. J. (1979). Efferent connections of the substantia nigra and ventral tegmental area in the rat. *Brain Res.* 175, 191–217. doi: 10.1016/0006-8993(79)91001-1

Bensaid, M., Michel, P. P., Clark, S. D., Hirsch, E. C., and Francois, C. (2016). Role of pedunculopontine cholinergic neurons in the vulnerability of nigral dopaminergic neurons in Parkinson's disease. *Exp. Neurol.* 275(Pt 1), 209–219. doi: 10.1016/j.expneurol.2015.11.004

Bernau, N. A., Puzdrowski, R. L., and Leonard, R. B. (1991). Identification of the midbrain locomotor region and its relation to descending locomotor pathways in the Atlantic stingray, Dasyatis sabina. *Brain Res.* 557, 83–94. doi: 10.1016/0006-8993(91)90119-G

Blin, M., Norton, W., Bally-Cuif, L., and Vernier, P. (2008). NR4A2 controls the differentiation of selective dopaminergic nuclei in the zebrafish brain. *Mol. Cell. Neurosci.* 39, 592–604. doi: 10.1016/j.mcn.2008.08.006

Bloem, B. R., Hausdorff, J. M., Visser, J. E., and Giladi, N. (2004). Falls and freezing of gait in Parkinson's disease: a review of two interconnected, episodic phenomena. *Mov. Disord.* 19, 871–884. doi: 10.1002/mds.20115

Bohnen, N. I., and Jahn, K. (2013). Imaging: what can it tell us about parkinsonian gait? *Mov. Disord.* 28, 1492–1500. doi: 10.1002/mds.25534

Breit, S., Bouali-Benazzouz, R., Benabid, A. L., and Benazzouz, A. (2001). Unilateral lesion of the nigrostriatal pathway induces an increase of neuronal activity of the pedunculopontine nucleus, which is reversed by the lesion of the subthalamic nucleus in the rat. *Eur. J. Neurosci.* 14, 1833–1842. doi: 10.1046/j.0953-816x.2001.01800.x

Bretzner, F., and Brownstone, R. M. (2013). Lhx3-Chx10 reticulospinal neurons in locomotor circuits. *J. Neurosci.* 33, 14681–14692. doi: 10.1523/JNEUROSCI.5231-12.2013

Brocard, F., Bardy, C., and Dubuc, R. (2005). Modulatory effect of substance P to the brain stem locomotor command in lampreys. *J. Neurophysiol.* 93, 2127–2141. doi: 10.1152/jn.00401.2004

Brocard, F., and Dubuc, R. (2003). Differential contribution of reticulospinal cells to the control of locomotion induced by the mesencephalic locomotor region. *J. Neurophysiol.* 90, 1714–1727. doi: 10.1152/jn.00202.2003

Brocard, F., Ryczko, D., Fenelon, K., Hatem, R., Gonzales, D., Auclair, F., et al. (2010). The transformation of a unilateral locomotor command into a symmetrical bilateral activation in the brainstem. *J. Neurosci.* 30, 523–533. doi: 10.1523/JNEUROSCI.3433-09.2010

Brodin, L., Tossman, U., Ohta, Y., Ungerstedt, U., and Grillner, S. (1988). The effect of an uptake inhibitor (dihydrokainate) on endogenous excitatory amino acids in the lamprey spinal cord as revealed by microdialysis. *Brain Res.* 458, 166–169. doi: 10.1016/0006-8993(88)90511-2

Bryant, M. S., Rintala, D. H., Hou, J. G., Charness, A. L., Fernandez, A. L., Collins, R. L., et al. (2011a). Gait variability in Parkinson's disease: influence of walking speed and dopaminergic treatment. *Neurol. Res.* 33, 959–964. doi: 10.1179/1743132811Y.0000000044

Bryant, M. S., Rintala, D. H., Hou, J. G., Lai, E. C., and Protas, E. J. (2011b). Effects of levodopa on forward and backward gait patterns in persons with Parkinson's disease. *NeuroRehabilitation* 29, 247–252. doi: 10.3233/NRE-2011-0700

Buchanan, J. T., and Grillner, S. (1987). Newly identified "glutamate interneurons" and their role in locomotion in the lamprey spinal cord. *Science* 236, 312–314. doi: 10.1126/science.3563512

Cabelguen, J. M., Bourcier-Lucas, C., and Dubuc, R. (2003). Bimodal locomotion elicited by electrical stimulation of the midbrain in the salamander *Notophthalmus viridescens*. *J. Neurosci.* 23, 2434–2439.

Canu, E., Agosta, F., Sarasso, E., Volonte, M. A., Basaia, S., Stojkovic, T., et al. (2015). Brain structural and functional connectivity in Parkinson's disease with freezing of gait. *Hum. Brain Mapp.* 36, 5064–5078. doi: 10.1002/hbm.22994

Canudas, A. M., Pezzi, S., Canals, J. M., Pallas, M., and Alberch, J. (2005). Endogenous brain-derived neurotrophic factor protects dopaminergic nigral neurons against transneuronal degeneration induced by striatal excitotoxic injury. *Brain Res. Mol. Brain Res.* 134, 147–154. doi: 10.1016/j.molbrainres.2004.11.012

Carlsson, A. (1959). The occurrence, distribution and physiological role of catecholamines in the nervous system. *Pharmacol. Rev.* 11, 490–493.

Carlsson, A., Lindqvist, M., Magnusson, T., and Waldeck, B. (1958). On the presence of 3-hydroxytyramine in brain. *Science* 127:471. doi: 10.1126/science.127.3296.471

Chastan, N., Do, M. C., Bonneville, F., Torny, F., Bloch, F., Westby, G. W., et al. (2009). Gait and balance disorders in Parkinson's disease: impaired active braking of the fall of centre of gravity. *Mov. Disord.* 24, 188–195. doi: 10.1002/mds.22269

Collomb-Clerc, A., and Welter, M. L. (2015). Effects of deep brain stimulation on balance and gait in patients with Parkinson's disease: a systematic neurophysiological review. *Neurophysiol. Clin.* 45, 371–388. doi: 10.1016/j.neucli.2015.07.001

DeLong, M. R., and Wichmann, T. (2015). Basal ganglia circuits as targets for neuromodulation in Parkinson disease. *JAMA Neurol.* 72, 1354–1360. doi: 10.1001/jamaneurol.2015.2397

Demain, A., Westby, G. W., Fernandez-Vidal, S., Karachi, C., Bonneville, F., Do, M. C., et al. (2014). High-level gait and balance disorders in the elderly: a midbrain disease? *J. Neurol.* 261, 196–206. doi: 10.1007/s00415-013-7174-x

Derjean, D., Moussaddy, A., Atallah, E., St-Pierre, M., Auclair, F., Chang, S., et al. (2010). A novel neural substrate for the transformation of olfactory inputs into motor output. *PLoS Biol.* 8:e1000567. doi: 10.1371/journal.pbio.1000567

Di Prisco, G. V., Pearlstein, E., Le Ray, D., Robitaille, R., and Dubuc, R. (2000). A cellular mechanism for the transformation of a sensory input into a motor command. *J. Neurosci.* 20, 8169–8176.

Edley, S. M., and Graybiel, A. M. (1983). The afferent and efferent connections of the feline nucleus tegmenti pedunculopontinus, pars compacta. *J. Comp. Neurol.* 217, 187–215. doi: 10.1002/cne.902170207

Ehringer, H., and Hornykiewicz, O. (1998). Distribution of noradrenaline and dopamine (3-hydroxytyramine) in the human brain and their behavior in diseases of the extrapyramidal system. *Parkinsonism Relat. Disord.* 4, 53–57. doi: 10.1016/S1353-8020(98)00012-1

Eidelberg, E., Walden, J. G., and Nguyen, L. H. (1981). Locomotor control in macaque monkeys. *Brain* 104, 647–663. doi: 10.1093/brain/104.4.647-a

El-Khodor, B. F., and Burke, R. E. (2002). Medial forebrain bundle axotomy during development induces apoptosis in dopamine neurons of the substantia nigra and activation of caspases in their degenerating axons. *J. Comp. Neurol.* 452, 65–79. doi: 10.1002/cne.10367

Fahn, S. (2015). The medical treatment of Parkinson disease from James Parkinson to George Cotzias. *Mov. Disord.* 30, 4–18. doi: 10.1002/mds.26102

Fasano, A., Aquino, C. C., Krauss, J. K., Honey, C. R., and Bloem, B. R. (2015). Axial disability and deep brain stimulation in patients with Parkinson disease. *Nat. Rev. Neurol.* 11, 98–110. doi: 10.1038/nrneurol.2014.252

Fioravanti, V., Benuzzi, F., Codeluppi, L., Contardi, S., Cavallieri, F., Nichelli, P., et al. (2015). MRI correlates of Parkinson's disease progression: a voxel based morphometry study. *Parkinson's Dis.* 2015:378032. doi: 10.1155/2015/378032

Fling, B. W., Cohen, R. G., Mancini, M., Carpenter, S. D., Fair, D. A., Nutt, J. G., et al. (2014). Functional reorganization of the locomotor network in Parkinson patients with freezing of gait. *PLoS ONE* 9:e100291. doi: 10.1371/journal.pone.0100291

Fling, B. W., Cohen, R. G., Mancini, M., Nutt, J. G., Fair, D. A., and Horak, F. B. (2013). Asymmetric pedunculopontine network connectivity in parkinsonian patients with freezing of gait. *Brain* 136, 2405–2418. doi: 10.1093/brain/awt172

Fornito, A., Zalesky, A., and Breakspear, M. (2015). The connectomics of brain disorders. *Nat. Rev. Neurosci.* 16, 159–172. doi: 10.1038/nrn3901

Fraix, V., Bastin, J., David, O., Goetz, L., Ferraye, M., Benabid, A. L., et al. (2013). Pedunculopontine nucleus area oscillations during stance, stepping and freezing in Parkinson's disease. *PLoS ONE* 8:e83919. doi: 10.1371/journal.pone.0083919

Freeze, B. S., Kravitz, A. V., Hammack, N., Berke, J. D., and Kreitzer, A. C. (2013). Control of basal ganglia output by direct and indirect pathway projection neurons. *J. Neurosci.* 33, 18531–18539. doi: 10.1523/JNEUROSCI.1278-13.2013

Garcia-Rill, E., Houser, C. R., Skinner, R. D., Smith, W., and Woodward, D. J. (1987). Locomotion-inducing sites in the vicinity of the pedunculopontine nucleus. *Brain Res. Bull.* 18, 731–738. doi: 10.1016/0361-9230(87)90208-5

Garcia-Rill, E., Luster, B., D'Onofrio, S., and Mahaffey, S. (2015a). Arousal, motor control, and parkinson's disease. *Transl. Neurosci.* 6, 198–207. doi: 10.1515/tnsci-2015-0021

Garcia-Rill, E., Luster, B., D'Onofrio, S., Mahaffey, S., Bisagno, V., and Urbano, F. J. (2015b). Pedunculopontine arousal system physiology - Deep brain stimulation (DBS). *Sleep Sci.* 8, 153–161. doi: 10.1016/j.slsci.2015.09.001

Garcia-Rill, E., and Skinner, R. D. (1987a). The mesencephalic locomotor region. I. Activation of a medullary projection site. *Brain Res.* 411, 1–12. doi: 10.1016/0006-8993(87)90675-5

Garcia-Rill, E., and Skinner, R. D. (1987b). The mesencephalic locomotor region. II. Projections to reticulospinal neurons. *Brain Res.* 411, 13–20. doi: 10.1016/0006-8993(87)90676-7

Gariepy, J. F., Missaghi, K., Chevallier, S., Chartre, S., Robert, M., Auclair, F., et al. (2012). Specific neural substrate linking respiration to locomotion. *Proc. Natl. Acad. Sci. U.S.A.* 109, E84–E92. doi: 10.1073/pnas.1113002109

Goetz, L., Piallat, B., Bhattacharjee, M., Mathieu, H., David, O., and Chabardes, S. (2016a). On the role of the pedunculopontine nucleus and mesencephalic reticular formation in locomotion in nonhuman primates. *J. Neurosci.* 36, 4917–4929. doi: 10.1523/JNEUROSCI.2514-15.2016

Goetz, L., Piallat, B., Bhattacharjee, M., Mathieu, H., David, O., and Chabardes, S. (2016b). The primate pedunculopontine nucleus region: towards a dual role in locomotion and waking state. *J. Neural Transm.* 123, 667–678. doi: 10.1007/s00702-016-1577-7

Golestanirad, L., Elahi, B., Graham, S. J., Das, S., and Wald, L. L. (2016). Efficacy and safety of pedunculopontine nuclei (PPN) deep brain stimulation in the treatment of gait disorders: a meta-analysis of clinical studies. *Can. J. Neurol. Sci.* 43, 120–126. doi: 10.1017/cjn.2015.318

Gravel, J., Brocard, F., Gariepy, J. F., Lund, J. P., and Dubuc, R. (2007). Modulation of respiratory activity by locomotion in lampreys. *Neuroscience* 144, 1120–1132. doi: 10.1016/j.neuroscience.2006.10.019

Grillner, S., and Robertson, B. (2016). The basal ganglia over 500 million years. *Curr. Biol.* 26, R1088–R1100. doi: 10.1016/j.cub.2016.06.041

Hamani, C., Aziz, T., Bloem, B. R., Brown, P., Chabardes, S., Coyne, T., et al. (2016a). Pedunculopontine nucleus region deep brain stimulation in Parkinson disease: surgical anatomy and terminology. *Stereotact. Funct. Neurosurg.* 94, 298–306. doi: 10.1159/000449010

Hamani, C., Lozano, A. M., Mazzone, P. A., Moro, E., Hutchison, W., Silburn, P. A., et al. (2016b). Pedunculopontine nucleus region deep brain stimulation in

Parkinson disease: surgical techniques, side effects, and postoperative imaging. *Stereotact. Funct. Neurosurg.* 94, 307–319. doi: 10.1159/000449011

Herbin, M., Boire, D., Theoret, H., and Ptito, M. (1999). Transneuronal degeneration of retinal ganglion cells in early hemispherectomized monkeys. *Neuroreport* 10, 1447–1452. doi: 10.1097/00001756-199905140-00011

Hirsch, E. C., Graybiel, A. M., Duyckaerts, C., and Javoy-Agid, F. (1987). Neuronal loss in the pedunculopontine tegmental nucleus in Parkinson disease and in progressive supranuclear palsy. *Proc. Natl. Acad. Sci. U.S.A.* 84, 5976–5980. doi: 10.1073/pnas.84.16.5976

Holiga, S., Mueller, K., Moller, H. E., Urgosik, D., Ruzicka, E., Schroeter, M. L., et al. (2015). Resting-state functional magnetic resonance imaging of the subthalamic microlesion and stimulation effects in Parkinson's disease: indications of a principal role of the brainstem. *NeuroImage Clin.* 9, 264–274. doi: 10.1016/j.nicl.2015.08.008

Hubel, D. H., and Wiesel, T. N. (1970). The period of susceptibility to the physiological effects of unilateral eye closure in kittens. *J. Physiol.* 206, 419–436. doi: 10.1113/jphysiol.1970.sp009022

Ichinohe, N., Teng, B., and Kitai, S. T. (2000). Morphological study of the tegmental pedunculopontine nucleus, substantia nigra and subthalamic nucleus, and their interconnections in rat organotypic culture. *Anat. Embryol.* 201, 435–453. doi: 10.1007/s004290050331

Jahn, K., Deutschlander, A., Stephan, T., Kalla, R., Wiesmann, M., Strupp, M., et al. (2008). Imaging human supraspinal locomotor centers in brainstem and cerebellum. *Neuroimage* 39, 786–792. doi: 10.1016/j.neuroimage.2007.09.047

Jellinger, K. (1988). The pedunculopontine nucleus in Parkinson's disease, progressive supranuclear palsy and Alzheimer's disease. *J. Neurol. Neurosurg. Psychiatry* 51, 540–543. doi: 10.1136/jnnp.51.4.540

Juvin, L., Gratsch, S., Trillaud-Doppia, E., Gariepy, J. F., Buschges, A., and Dubuc, R. (2016). A specific population of reticulospinal neurons controls the termination of locomotion. *Cell Rep.* 15, 2377–2386. doi: 10.1016/j.celrep.2016.05.029

Karachi, C., Andre, A., Bertasi, E., Bardinet, E., Lehericy, S., and Bernard, F. A. (2012). Functional parcellation of the lateral mesencephalus. *J. Neurosci.* 32, 9396–9401. doi: 10.1523/JNEUROSCI.0509-12.2012

Karachi, C., and Francois, C. (2017). Role of the pedunculopontine nucleus in controlling gait and sleep in normal and parkinsonian monkeys. *J. Neural Transm*. doi: 10.1007/s00702-017-1678-y. [Epub ahead of print].

Karachi, C., Grabli, D., Bernard, F. A., Tande, D., Wattiez, N., Belaid, H., et al. (2010). Cholinergic mesencephalic neurons are involved in gait and postural disorders in Parkinson disease. *J. Clin. Invest.* 120, 2745–2754. doi: 10.1172/JCI42642

Kitahama, K., Nagatsu, I., Geffard, M., and Maeda, T. (2000). Distribution of dopamine-immunoreactive fibers in the rat brainstem. *J. Chem. Neuroanat.* 18, 1–9. doi: 10.1016/S0891-0618(99)00047-2

Knight, E. J., Testini, P., Min, H. K., Gibson, W. S., Gorny, K. R., Favazza, C. P., et al. (2015). Motor and nonmotor circuitry activation induced by subthalamic nucleus deep brain stimulation in patients with parkinson disease: intraoperative functional magnetic resonance imaging for deep brain stimulation. *Mayo Clin. Proc.* 90, 773–785. doi: 10.1016/j.mayocp.2015.03.022

Kravitz, A. V., Freeze, B. S., Parker, P. R., Kay, K., Thwin, M. T., Deisseroth, K., et al. (2010). Regulation of parkinsonian motor behaviours by optogenetic control of basal ganglia circuitry. *Nature* 466, 622–626. doi: 10.1038/nature09159

Kuo, S. H., Kenney, C., and Jankovic, J. (2008). Bilateral pedunculopontine nuclei strokes presenting as freezing of gait. *Mov. Disord.* 23, 616–619. doi: 10.1002/mds.21917

Lau, B., Welter, M. L., Belaid, H., Fernandez Vidal, S., Bardinet, E., Grabli, D., et al. (2015). The integrative role of the pedunculopontine nucleus in human gait. *Brain* 138, 1284–1296. doi: 10.1093/brain/awv047

Lavoie, B., and Parent, A. (1994). Pedunculopontine nucleus in the squirrel monkey: cholinergic and glutamatergic projections to the substantia nigra. *J. Comp. Neurol.* 344, 232–241. doi: 10.1002/cne.903440205

Lee, A. M., Hoy, J. L., Bonci, A., Wilbrecht, L., Stryker, M. P., and Niell, C. M. (2014). Identification of a brainstem circuit regulating visual cortical state in parallel with locomotion. *Neuron* 83, 455–466. doi: 10.1016/j.neuron.2014.06.031

Le Ray, D., Brocard, F., Bourcier-Lucas, C., Auclair, F., Lafaille, P., and Dubuc, R. (2003). Nicotinic activation of reticulospinal cells involved in the control of swimming in lampreys. *Eur. J. Neurosci.* 17, 137–148. doi: 10.1046/j.1460-9568.2003.02417.x

Le Ray, D., Juvin, L., Ryczko, D., and Dubuc, R. (2011). Chapter 4–supraspinal control of locomotion: the mesencephalic locomotor region. *Prog. Brain Res.* 188, 51–70. doi: 10.1016/B978-0-444-53825-3.00009-7

Liu, H. G., Zhang, K., Yang, A. C., and Zhang, J. G. (2015). Deep brain stimulation of the subthalamic and pedunculopontine nucleus in a patient with Parkinson's disease. *J. Korean Neurosurg. Soc.* 57, 303–306. doi: 10.3340/jkns.2015.57.4.303

Macaya, A., Munell, F., Gubits, R. M., and Burke, R. E. (1994). Apoptosis in substantia nigra following developmental striatal excitotoxic injury. *Proc. Natl. Acad. Sci. U.S.A.* 91, 8117–8121. doi: 10.1073/pnas.91.17.8117

Marin, O., Smeets, W. J., and Gonzalez, A. (1997). Basal ganglia organization in amphibians: catecholaminergic innervation of the striatum and the nucleus accumbens. *J. Comp. Neurol.* 378, 50–69.

Marlinsky, V. V., and Voitenko, L. P. (1991). The effect of procaine injection into the medullary reticular formation on forelimb muscle activity evoked by mesencephalic locomotor region and vestibular stimulation in the decerebrated guinea-pig. *Neuroscience* 45, 753–759. doi: 10.1016/0306-4522(91)90287-X

Marti, M. J., James, C. J., Oo, T. F., Kelly, W. J., and Burke, R. E. (1997). Early developmental destruction of terminals in the striatal target induces apoptosis in dopamine neurons of the substantia nigra. *J. Neurosci.* 17, 2030–2039.

Masdeu, J. C., Alampur, U., Cavaliere, R., and Tavoulareas, G. (1994). Astasia and gait failure with damage of the pontomesencephalic locomotor region. *Ann. Neurol.* 35, 619–621. doi: 10.1002/ana.410350517

Mazzone, P., Paoloni, M., Mangone, M., Santilli, V., Insola, A., Fini, M., et al. (2014). Unilateral deep brain stimulation of the pedunculopontine tegmental nucleus in idiopathic Parkinson's disease: effects on gait initiation and performance. *Gait Posture* 40, 357–362. doi: 10.1016/j.gaitpost.2014.05.002

Mazzone, P., Sposato, S., Insola, A., and Scarnati, E. (2013). The clinical effects of deep brain stimulation of the pedunculopontine tegmental nucleus in movement disorders may not be related to the anatomical target, leads location, and setup of electrical stimulation. *Neurosurgery* 73, 894–906; discussion 905–906. doi: 10.1227/neu.0000000000000108

McGeer, E. G., and McGeer, P. L. (1984). Substantia nigra cell death from kainic acid or folic acid injections into the pontine tegmentum. *Brain Res.* 298, 339–342. doi: 10.1016/0006-8993(84)91433-1

Menard, A., Auclair, F., Bourcier-Lucas, C., Grillner, S., and Dubuc, R. (2007). Descending GABAergic projections to the mesencephalic locomotor region in the lamprey Petromyzon marinus. *J. Comp. Neurol.* 501, 260–273. doi: 10.1002/cne.21258

Mestre, T. A., Sidiropoulos, C., Hamani, C., Poon, Y. Y., Lozano, A. M., Lang, A. E., et al. (2016). Long-term double-blinded unilateral pedunculopontine area stimulation in Parkinson's disease. *Mov. Disord.* 31, 1570–1574. doi: 10.1002/mds.26710

Moore, S. T., MacDougall, H. G., Gracies, J. M., and Ondo, W. G. (2008). Locomotor response to levodopa in fluctuating Parkinson's disease. *Exp. Brain Res.* 184, 469–478. doi: 10.1007/s00221-007-1113-y

Musienko, P. E., Zelenin, P. V., Lyalka, V. F., Orlovsky, G. N., and Deliagina, T. G. (2008). Postural performance in decerebrated rabbit. *Behav. Brain Res.* 190, 124–134. doi: 10.1016/j.bbr.2008.02.011

Neagu, B., Tsang, E., Mazzella, F., Hamani, C., Moro, E., Hodaie, M., et al. (2013). Pedunculopontine nucleus evoked potentials from subthalamic nucleus stimulation in Parkinson's disease. *Exp. Neurol.* 250, 221–227. doi: 10.1016/j.expneurol.2013.09.018

Noga, B. R., Kettler, J., and Jordan, L. M. (1988). Locomotion produced in mesencephalic cats by injections of putative transmitter substances and antagonists into the medial reticular formation and the pontomedullary locomotor strip. *J. Neurosci.* 8, 2074–2086.

Noga, B. R., Kriellaars, D. J., and Jordan, L. M. (1991). The effect of selective brainstem or spinal cord lesions on treadmill locomotion evoked by stimulation of the mesencephalic or pontomedullary locomotor regions. *J. Neurosci.* 11, 1691–1700.

Nosko, D., Ferraye, M. U., Fraix, V., Goetz, L., Chabardes, S., Pollak, P., et al. (2015). Low-frequency versus high-frequency stimulation of the pedunculopontine nucleus area in Parkinson's disease: a randomised controlled trial. *J. Neurol. Neurosurg. Psychiatry* 86, 674–679. doi: 10.1136/jnnp-2013-307511

Ohta, Y., and Grillner, S. (1989). Monosynaptic excitatory amino acid transmission from the posterior rhombencephalic reticular nucleus to spinal neurons involved in the control of locomotion in lamprey. *J. Neurophysiol.* 62, 1079–1089.

Orlovskii, G. N. (1970). [Work of reticulo-spinal neurons during locomotion]. *Biofizika* 15, 728–737.

Pedersen, V., and Schmidt, W. J. (2000). The neuroprotectant properties of glutamate antagonists and antiglutamatergic drugs. *Neurotox. Res.* 2, 179–204. doi: 10.1007/BF03033793

Perez-Fernandez, J., Stephenson-Jones, M., Suryanarayana, S. M., Robertson, B., and Grillner, S. (2014). Evolutionarily conserved organization of the dopaminergic system in lamprey: SNc/VTA afferent and efferent connectivity and D2 receptor expression. *J. Comp. Neurol.* 522, 3775–3794. doi: 10.1002/cne.23639

Peterson, D. S., Pickett, K. A., Duncan, R., Perlmutter, J., and Earhart, G. M. (2014). Gait-related brain activity in people with Parkinson disease with freezing of gait. *PLoS ONE* 9:e90634. doi: 10.1371/journal.pone.0090634

Piallat, B., Chabardes, S., Torres, N., Fraix, V., Goetz, L., Seigneuret, E., et al. (2009). Gait is associated with an increase in tonic firing of the sub-cuneiform nucleus neurons. *Neuroscience* 158, 1201–1205. doi: 10.1016/j.neuroscience.2008.10.046

Pienaar, I. S., Elson, J. L., Racca, C., Nelson, G., Turnbull, D. M., and Morris, C. M. (2013). Mitochondrial abnormality associates with type-specific neuronal loss and cell morphology changes in the pedunculopontine nucleus in Parkinson disease. *Am. J. Pathol.* 183, 1826–1840. doi: 10.1016/j.ajpath.2013.09.002

Pienaar, I. S., Gartside, S. E., Sharma, P., De Paola, V., Gretenkord, S., Withers, D., et al. (2015a). Pharmacogenetic stimulation of cholinergic pedunculopontine neurons reverses motor deficits in a rat model of Parkinson's disease. *Mol. Neurodegener.* 10:47. doi: 10.1186/s13024-015-0044-5

Pienaar, I. S., Harrison, I. F., Elson, J. L., Bury, A., Woll, P., Simon, A. K., et al. (2015b). An animal model mimicking pedunculopontine nucleus cholinergic degeneration in Parkinson's disease. *Brain Struct. Funct.* 220, 479–500. doi: 10.1007/s00429-013-0669-5

Pinching, A. J., and Powell, T. P. (1971). Ultrastructural features of transneuronal cell degeneration in the olfactory system. *J. Cell Sci.* 8, 253–287.

Plaha, P., and Gill, S. S. (2005). Bilateral deep brain stimulation of the pedunculopontine nucleus for Parkinson's disease. *Neuroreport* 16, 1883–1887. doi: 10.1097/01.wnr.0000187637.20771.a0

Poirier, L., and Sourkes, T. L. (1965). Influence of the substantia nigra on the catecholamine content of the striatum. *Brain* 88, 181–192. doi: 10.1093/brain/88.1.181

Pombal, M. A., El Manira, A., and Grillner, S. (1997). Afferents of the lamprey striatum with special reference to the dopaminergic system: a combined tracing and immunohistochemical study. *J. Comp. Neurol.* 386, 71–91.

Puelles, L., and Verney, C. (1998). Early neuromeric distribution of tyrosine-hydroxylase-immunoreactive neurons in human embryos. *J. Comp. Neurol.* 394, 283–308.

Rink, E., and Wullimann, M. F. (2001). The teleostean (zebrafish) dopaminergic system ascending to the subpallium (striatum) is located in the basal diencephalon (posterior tuberculum). *Brain Res.* 889, 316–330. doi: 10.1016/S0006-8993(00)03174-7

Rinne, J. O., Ma, S. Y., Lee, M. S., Collan, Y., and Roytta, M. (2008). Loss of cholinergic neurons in the pedunculopontine nucleus in Parkinson's disease is related to disability of the patients. *Parkinsonism Relat. Disord.* 14, 553–557. doi: 10.1016/j.parkreldis.2008.01.006

Rolland, A. S., Tande, D., Herrero, M. T., Luquin, M. R., Vazquez-Claverie, M., Karachi, C., et al. (2009). Evidence for a dopaminergic innervation of the pedunculopontine nucleus in monkeys, and its drastic reduction after MPTP intoxication. *J. Neurochem.* 110, 1321–1329. doi: 10.1111/j.1471-4159.2009.06220.x

Roseberry, T. K., Lee, A. M., Lalive, A. L., Wilbrecht, L., Bonci, A., and Kreitzer, A. C. (2016). Cell-type-specific control of brainstem locomotor circuits by basal ganglia. *Cell* 164, 526–537. doi: 10.1016/j.cell.2015.12.037

Rowe, J., Khan, A., Romanowski, C., Isaac, C., Khan, S., Mair, R., et al. (2016). Clinical experience with pedunculopontine nucleus stimulation in conditions with nigrostriatal disconnection. *World Neurosurg.* 89, 9–18. doi: 10.1016/j.wneu.2015.11.054

Ryczko, D., Auclair, F., Cabelguen, J. M., and Dubuc, R. (2016b). The mesencephalic locomotor region sends a bilateral glutamatergic drive to hindbrain reticulospinal neurons in a tetrapod. *J. Comp. Neurol.* 524, 1361–1383. doi: 10.1002/cne.23911

Ryczko, D., Cone, J. J., Alpert, M. H., Goetz, L., Auclair, F., Dube, C., et al. (2016a). A descending dopamine pathway conserved from basal vertebrates to mammals. *Proc. Natl. Acad. Sci. U.S.A.* 113, E2440–E2449. doi: 10.1073/pnas.1600684113

Ryczko, D., and Dubuc, R. (2013). The multifunctional mesencephalic locomotor region. *Curr. Pharm. Des.* 19, 4448–4470. doi: 10.2174/1381612811319240011

Ryczko, D., Gratsch, S., Auclair, F., Dube, C., Bergeron, S., Alpert, M. H., et al. (2013). Forebrain dopamine neurons project down to a brainstem region controlling locomotion. *Proc. Natl. Acad. Sci. U.S.A.* 110, E3235–E3242. doi: 10.1073/pnas.1301125110

Saavedra, J. M., Kvetnansky, R., and Kopin, I. J. (1979). Adrenaline, noradrenaline and dopamine levels in specific brain stem areas of acutely immobilized rats. *Brain Res.* 160, 271–280. doi: 10.1016/0006-8993(79)90424-4

Sano, I., Gamo, T., Kakimoto, Y., Taniguchi, K., Takesada, M., and Nishinuma, K. (1959). Distribution of catechol compounds in human brain. *Biochim. Biophys. Acta* 32, 586–587. doi: 10.1016/0006-3002(59)90652-3

Scarnati, E., Campana, E., and Pacitti, C. (1984). Pedunculopontine-evoked excitation of substantia nigra neurons in the rat. *Brain Res.* 304, 351–361. doi: 10.1016/0006-8993(84)90339-1

Scarnati, E., Proia, A., Di Loreto, S., and Pacitti, C. (1987). The reciprocal electrophysiological influence between the nucleus tegmenti pedunculopontinus and the substantia nigra in normal and decorticated rats. *Brain Res.* 423, 116–124. doi: 10.1016/0006-8993(87)90831-6

Schrader, C., Seehaus, F., Capelle, H. H., Windhagen, A., Windhagen, H., and Krauss, J. K. (2013). Effects of pedunculopontine area and pallidal DBS on gait ignition in Parkinson's disease. *Brain Stimul.* 6, 856–859. doi: 10.1016/j.brs.2013.05.005

Seidel, K., Mahlke, J., Siswanto, S., Kruger, R., Heinsen, H., Auburger, G., et al. (2015). The brainstem pathologies of Parkinson's disease and dementia with Lewy bodies. *Brain Pathol.* 25, 121–135. doi: 10.1111/bpa.12168

Semba, K., and Fibiger, H. C. (1992). Afferent connections of the laterodorsal and the pedunculopontine tegmental nuclei in the rat: a retro- and antero-grade transport and immunohistochemical study. *J. Comp. Neurol.* 323, 387–410. doi: 10.1002/cne.903230307

Shik, M. L., Severin, F. V., and Orlovskii, G. N. (1966). [Control of walking and running by means of electric stimulation of the midbrain]. *Biofizika* 11, 659–666.

Shine, J. M., Matar, E., Ward, P. B., Bolitho, S. J., Gilat, M., Pearson, M., et al. (2013). Exploring the cortical and subcortical functional magnetic resonance imaging changes associated with freezing in Parkinson's disease. *Brain* 136, 1204–1215. doi: 10.1093/brain/awt049

Sholomenko, G. N., Funk, G. D., and Steeves, J. D. (1991). Avian locomotion activated by brainstem infusion of neurotransmitter agonists and antagonists. II. gamma-Aminobutyric acid. *Exp. Brain Res.* 85, 674–681. doi: 10.1007/BF00231753

Sirota, M. G., Di Prisco, G. V., and Dubuc, R. (2000). Stimulation of the mesencephalic locomotor region elicits controlled swimming in semi-intact lampreys. *Eur. J. Neurosci.* 12, 4081–4092. doi: 10.1046/j.1460-9568.2000.00301.x

Smeets, W. J., Marin, O., and Gonzalez, A. (2000). Evolution of the basal ganglia: new perspectives through a comparative approach. *J. Anat.* 196(Pt 4), 501–517. doi: 10.1046/j.1469-7580.2000.19640501.x

Smetana, R., Juvin, L., Dubuc, R., and Alford, S. (2010). A parallel cholinergic brainstem pathway for enhancing locomotor drive. *Nat. Neurosci.* 13, 731–738. doi: 10.1038/nn.2548

Snijders, A. H., Leunissen, I., Bakker, M., Overeem, S., Helmich, R. C., Bloem, B. R., et al. (2011). Gait-related cerebral alterations in patients with Parkinson's disease with freezing of gait. *Brain* 134, 59–72. doi: 10.1093/brain/awq324

Snijders, A. H., Takakusaki, K., Debu, B., Lozano, A. M., Krishna, V., Fasano, A., et al. (2016). Physiology of freezing of gait. *Ann. Neurol.* 80, 644–659. doi: 10.1002/ana.24778

Sourkes, T. L., and Poirier, L. (1965). Influence of the substantia nigra on the concentration of 5-hydroxytryptamine and dopamine of the striatum. *Nature* 207, 202–203. doi: 10.1038/207202a0

Stack, E., and Ashburn, A. (2008). Dysfunctional turning in Parkinson's disease. *Disabil. Rehabil.* 30, 1222–1229. doi: 10.1080/09638280701829938

Steeves, J. D., and Jordan, L. M. (1980). Localization of a descending pathway in the spinal cord which is necessary for controlled treadmill locomotion. *Neurosci. Lett.* 20, 283–288. doi: 10.1016/0304-3940(80)90161-5

Stefani, A., Peppe, A., Galati, S., Bassi, M. S., D'Angelo, V., and Pierantozzi, M. (2013). The serendipity case of the pedunculopontine nucleus low-frequency brain stimulation: chasing a gait response, finding sleep, and cognition improvement. *Front. Neurol.* 4:68. doi: 10.3389/fneur.2013.00068

Steiniger, B., and Kretschmer, B. D. (2003). Glutamate and GABA modulate dopamine in the pedunculopontine tegmental nucleus. *Exp. Brain Res.* 149, 422–430. doi: 10.1007/s00221-003-1382-z

Steininger, T. L., Rye, D. B., and Wainer, B. H. (1992). Afferent projections to the cholinergic pedunculopontine tegmental nucleus and adjacent midbrain extrapyramidal area in the albino rat. I. Retrograde tracing studies. *J. Comp. Neurol.* 321, 515–543. doi: 10.1002/cne.903210403

Tard, C., Delval, A., Devos, D., Lopes, R., Lenfant, P., Dujardin, K., et al. (2015). Brain metabolic abnormalities during gait with freezing in Parkinson's disease. *Neuroscience* 307, 281–301. doi: 10.1016/j.neuroscience.2015.08.063

Tattersall, T. L., Stratton, P. G., Coyne, T. J., Cook, R., Silberstein, P., Silburn, P. A., et al. (2014). Imagined gait modulates neuronal network dynamics in the human pedunculopontine nucleus. *Nat. Neurosci.* 17, 449–454. doi: 10.1038/nn.3642

Thevathasan, W., Pogosyan, A., Hyam, J. A., Jenkinson, N., Foltynie, T., Limousin, P., et al. (2012). Alpha oscillations in the pedunculopontine nucleus correlate with gait performance in parkinsonism. *Brain* 135, 148–160. doi: 10.1093/brain/awr315

Vercruysse, S., Leunissen, I., Vervoort, G., Vandenberghe, W., Swinnen, S., and Nieuwboer, A. (2015). Microstructural changes in white matter associated with freezing of gait in Parkinson's disease. *Mov. Disord.* 30, 567–576. doi: 10.1002/mds.26130

Versteeg, D. H., Van Der Gugten, J., De Jong, W., and Palkovits, M. (1976). Regional concentrations of noradrenaline and dopamine in rat brain. *Brain Res.* 113, 563–574. doi: 10.1016/0006-8993(76)90057-3

Wang, M., Jiang, S., Yuan, Y., Zhang, L., Ding, J., Wang, J., et al. (2016). Alterations of functional and structural connectivity of freezing of gait in Parkinson's disease. *J. Neurol.* 263, 1583–1592. doi: 10.1007/s00415-016-8174-4

Weiss, P. H., Herzog, J., Potter-Nerger, M., Falk, D., Herzog, H., Deuschl, G., et al. (2015). Subthalamic nucleus stimulation improves Parkinsonian gait via brainstem locomotor centers. *Mov. Disord.* 30, 1121–1125. doi: 10.1002/mds.26229

Welter, M. L., Demain, A., Ewenczyk, C., Czernecki, V., Lau, B., El Helou, A., et al. (2015). PPNa-DBS for gait and balance disorders in Parkinson's disease: a double-blind, randomised study. *J. Neurol.* 262, 1515–1525. doi: 10.1007/s00415-015-7744-1

Windels, F., Thevathasan, W., Silburn, P., and Sah, P. (2015). Where and what is the PPN and what is its role in locomotion? *Brain* 138, 1133–1134. doi: 10.1093/brain/awv059

Wullimann, M. F. (2014). Ancestry of basal ganglia circuits: new evidence in teleosts. *J. Comp. Neurol.* 522, 2013–2018. doi: 10.1002/cne.23525

Xiao, C., Cho, J. R., Zhou, C., Treweek, J. B., Chan, K., McKinney, S. L., et al. (2016). Cholinergic mesopontine signals govern locomotion and reward through dissociable midbrain pathways. *Neuron* 90, 333–347. doi: 10.1016/j.neuron.2016.03.028

Yamamoto, K., and Vernier, P. (2011). The evolution of dopamine systems in chordates. *Front. Neuroanat.* 5:21. doi: 10.3389/fnana.2011.00021

Yeo, S. S., Lee, D. G., Choi, B. Y., Chang, C. H., Jung, Y. J., Kim, S. H., et al. (2012). Neural connectivity of the pedunculopontine nucleus in relation to walking ability in chronic patients with intracerebral hemorrhage. *Eur. Neurol.* 67, 226–231. doi: 10.1159/000335248

Yoo, J. H., Zell, V., Wu, J., Punta, C., Ramajayam, N., Shen, X., et al. (2017). Activation of pedunculopontine glutamate neurons is reinforcing. *J. Neurosci.* 37, 38–46. doi: 10.1523/JNEUROSCI.3082-16.2017

Youn, J., Lee, J. M., Kwon, H., Kim, J. S., Son, T. O., and Cho, J. W. (2015). Alterations of mean diffusivity of pedunculopontine nucleus pathway in Parkinson's disease patients with freezing of gait. *Parkinsonism Relat. Disord.* 21, 12–17. doi: 10.1016/j.parkreldis.2014.10.003

Zweig, R. M., Jankel, W. R., Hedreen, J. C., Mayeux, R., and Price, D. L. (1989). The pedunculopontine nucleus in Parkinson's disease. *Ann. Neurol.* 26, 41–46. doi: 10.1002/ana.410260106

Zweig, R. M., Whitehouse, P. J., Casanova, M. F., Walker, L. C., Jankel, W. R., and Price, D. L. (1987). Loss of pedunculopontine neurons in progressive supranuclear palsy. *Ann. Neurol.* 22, 18–25. doi: 10.1002/ana.410220107

Conflict of Interest Statement: The authors declare that the research was conducted in the absence of any commercial or financial relationships that could be construed as a potential conflict of interest.

Copyright © 2017 Ryczko and Dubuc. This is an open-access article distributed under the terms of the Creative Commons Attribution License (CC BY). The use, distribution or reproduction in other forums is permitted, provided the original author(s) or licensor are credited and that the original publication in this journal is cited, in accordance with accepted academic practice. No use, distribution or reproduction is permitted which does not comply with these terms.

frontiers in Behavioral Neuroscience

ORIGINAL RESEARCH
published: 13 June 2017
doi: 10.3389/fnbeh.2017.00115

Parameter Optimization Analysis of Prolonged Analgesia Effect of tDCS on Neuropathic Pain Rats

*Hui-Zhong Wen[1], Shi-Hao Gao[1], Yan-Dong Zhao[1], Wen-Juan He[2], Xue-Long Tian[3] and Huai-Zhen Ruan[1]**

[1]*Department of Neurobiology, College of Basic Medical Science, Chongqing Key Laboratory of Neurobiology, Third Military Medical University, Chongqing, China,* [2]*Department of Pathophysiology and High Altitudepathology, College of High Altitude Military Medicine, Third Military Medical University, Chongqing, China,* [3]*Bioengineering College, Chongqing University, Chongqing, China*

Background: Transcranial direct current stimulation (tDCS) is widely used to treat human nerve disorders and neuropathic pain by modulating the excitability of cortex. The effectiveness of tDCS is influenced by its stimulation parameters, but there have been no systematic studies to help guide the selection of different parameters.

Objective: This study aims to assess the effects of tDCS of primary motor cortex (M1) on chronic neuropathic pain in rats and to test for the optimal parameter combinations for analgesia.

Methods: Using the chronic neuropathic pain models of chronic constriction injury (CCI), we measured pain thresholds before and after anodal-tDCS (A-tDCS) using different parameter conditions, including stimulation intensity, stimulation time, intervention time and electrode located (ipsilateral or contralateral M1 of the ligated paw on male/female CCI models).

Results: Following the application of A-tDCS over M1, we observed that the antinociceptive effects were depended on different parameters. First, we found that repetitive A-tDCS had a longer analgesic effect than single stimulus, and both ipsilateral-tDCS (ip-tDCS) and contralateral-tDCS (con-tDCS) produce a long-lasting analgesic effect on neuropathic pain. Second, the antinociceptive effects were intensity-dependent and time-dependent, high intensities worked better than low intensities and long stimulus durations worked better than short stimulus durations. Third, timing of the intervention after injury affected the stimulation outcome, early use of tDCS was an effective method to prevent the development of pain, and more frequent intervention induced more analgesia in CCI rats, finally, similar antinociceptive effects of con- and ip-tDCS were observed in both sexes of CCI rats.

Conclusion: Optimized protocols of tDCS for treating antinociceptive effects were developed. These findings should be taken into consideration when using tDCS to produce analgesic effects in clinical applications.

Keywords: transcranial direct current stimulation, tDCS, chronic constriction injury, neuropathic pain, intervention time, parameter optimization

OPEN ACCESS

Edited by:
Mikhail Lebedev,
Duke University, United States

Reviewed by:
Satoru Otani,
Ryotokuji University, Japan
Gordon Alfred Barr,
Children's Hospital of Philadelphia, United States

****Correspondence:***
Huai-Zhen Ruan
hzruan163@163.com

Received: *23 January 2017*
Accepted: *26 May 2017*
Published: *13 June 2017*

Citation:
Wen H-Z, Gao S-H, Zhao Y-D, He W-J, Tian X-L and Ruan H-Z (2017) Parameter Optimization Analysis of Prolonged Analgesia Effect of tDCS on Neuropathic Pain Rats.
Front. Behav. Neurosci. 11:115.
doi: 10.3389/fnbeh.2017.00115

INTRODUCTION

Chronic neuropathic pain is a common and severely disabling state that typically develops when peripheral nerves are damaged due to surgery, bone compression in cancer, diabetes or infection (Dworkin et al., 2013). Recent studies indicate increased activation of descending modulatory circuits (both descending facilitation and inhibition) in chronic neuropathic pain syndrome, and these circuit changes reflect long-lasting changes in synaptic efficacy (Zhuo, 2008, 2013). An increasing number of investigators hold the view that non-invasive brain stimulation techniques can be used to treat chronic neuropathic pain (O'Connell et al., 2011; Volz et al., 2012). The aim of brain stimulation in managing of pain is to reduce pain symptoms by altering activity in brain areas that are involved in processing painful stimuli (Nguyen et al., 2011; Mylius et al., 2012; Woods et al., 2016).

Repetitive transcranial magnetic stimulation (rTMS) and transcranial direct current stimulation (tDCS) are two typical and common techniques of non-invasive brain stimulation techniques (Woods et al., 2016). Relative to invasive stimulation, non-invasive stimulation requires no surgical procedure and is therefore easier and safer to administer. However, there are several advantages of tDCS over rTMS, such as lower cost, increased portability, and more convincing sham conditions (Zaghi et al., 2009). TDCS is considered as a neuromodulatory intervention for the brain (Nitsche et al., 2008) which modulates the membrane potential dependently by type of electrode's application. Anode-tDCS (A-tDCS) is able to facilitate the depolarization of neurons and increase the cortical excitability. However, cathode-tDCS (C-tDCS) hyperpolarizes the resting membrane potential and reduces the cortical excitability (Nitsche et al., 2008; Mylius et al., 2012). Numerous clinical studies have concluded that A-tDCS is an effective method for pain modulations, which is helpful at reducing both fibromyalgia and spinal cord injury related-pain (Fregni et al., 2006; Roizenblatt et al., 2007; Soler et al., 2010). There are also studies showing effects of A-tDCS in inflammatory and neuropathic pain in animals (Laste et al., 2012; Spezia Adachi et al., 2012; Cioato et al., 2016; Filho et al., 2016).

Sensory-motor cortex has been reported to decrease pain sensation and to increase pain threshold (Xie et al., 2009; Ossipov et al., 2010). As a result, the primary motor cortex (M1) is regarded as the location for stimulation electrode placement in the vast majority of trials in patients (Ferrucci et al., 2015; Woods et al., 2016), but there was little research testing the location of the stimulation electrode in animal research, the stimulation electrodes of those studies were placed on the middle of the scalp of rat rather than on a particular location (Ferrucci et al., 2015; Woods et al., 2016). There are three location modes for electrodes as related to the region of pain: contralateral M1, bilateral M1 and ipsilateral M1 to the injured region. A-tDCS delivered to contralateral M1 and bilateral M1 have been reported to have an antinociceptive effect in a number of patients with chronic pain (Ngernyam, 2014; O'Neill et al., 2015; Woods et al., 2016), whereas few studies of tDCS of ipsilateral M1 have been reported.

Beside the location of the stimulation electrode, physical parameters and practical applications of tDCS are important factors in treating neuropathic pain in animal and clinical experiments (Nitsche et al., 2008; Nitsche and Paulus, 2011; Stagg and Nitsche, 2011). Therefore, tDCS protocols should state current intensity, electrode size, stimulation duration and other parameters to aid in assessing comparability among studies (Nitsche et al., 2008). Originally, tDCS was believed to follow simple rules: the more electric charge flowing through the electrode, the stronger the analgesic effect would be (Nitsche et al., 2008; Nitsche and Paulus, 2011). However, the safety and side effects of tDCS on participants should be precisely calculated, because high current density can cause tissue damage (Nitsche et al., 2008; Liebetanz et al., 2009). Another important parameter of tDCS is the intervention time, which involves the time when stimulation is administered in relation to the course of pain processing and how many times tDCS is delivered. According to previous findings, repetitive stimulation has been proven to enhance efficacy and prolong after-effects of tDCS during specific time intervals (Nitsche et al., 2008). In addition, because the course of neuropathic pain is fairly long and easy to be targeted repeatedly (Dworkin et al., 2013), it will be significant if the patient can be treated when the pain is onset with negligible side effects.

Therefore, a combination of tDCS stimulation parameters including current intensity as well as stimulation time, interval and position need to be studied systematically in clinical and animal experiments. However, due to the limitation of choosing suitable parameters in clinical studies, optimal protocol characteristics have not been explored systematically (Ngernyam, 2014). In this article, we conducted studies to explore the optimal physical parameters and practical applications of A-tDCS in treating chronic neuropathic pain in both male and female rats.

MATERIALS AND METHODS

Experimental Animals

Experiments were carried out on adult Sprague–Dawley rats (8–10 weeks old weighing 220–250 g), which were purchased from the Center of Laboratory Animal, Third Military Medical University, Chongqing, China. The SD rats were housed in plastic cages with soft bedding under controlled temperature settings (24 ± 1°C), humidity (60 ± 5%) and a 12-h light/dark cycle. The study, animal care and handling procedures were in strict accordance with the recommendations of International Association for the Study of Pain's ethical guidelines (Zimmermann, 1983), and the protocol was also approved by the Ethical Committee for Animal Research of Third Military Medical University.

Animal Model of Neuropathic Pain

A typical neuropathic pain model was established through chronic constriction injury (CCI) of the sciatic nerve (Bennett and Xie, 1988).The right sciatic nerve of rats was tied with four 4-0 chromic gut ligatures 1 mm apart under 4% chloral hydrate-anesthesia (10 ml/kg, i.p.). The sutures were not tied so tight

that blood flow was affected. The overlying muscle was sutured and the skin wound was sealed with topical antibiotics. Rats with right sciatic nerve exposed without chromic gut ligature served as sham CCI controls.

Transcranial Direct Current Stimulation

We improved the previously implanted electrode protocol by optimizing the internal structural stability and by decreasing the contact impedance of the electrode (Liebetanz et al., 2006; Yu et al., 2015). Three days before CCI or sham CCI surgery, a saline soaked sponge was placed at the end of a plastic tube (inner diameter: 2 mm; length: 1 cm; **Figures 1A,B**). A copper wire was inserted into the sponge and held in place inside the tube with polyacrylate adhesive. Next, the tube was fixed with glass ionomer cement onto the cranium over M1 as a stimulation electrode using a stereotaxic apparatus; ipsilateral tDCS (ip-tDCS) refers to a stimulation electrode being fixed overlying the ipsilateral M1 to the ligated hind paw, and contralateral tDCS (con-tDCS) refers to stimulation electrode fixed overlying the contralateral M1 to the ligated hind paw (**Figure 1A**). A far larger conventional sponge electrode (10 cm^2) was placed on the ventral thorax with a corset and served as a reference electrode (**Figure 1B**).

As described below, constant current was applied via the stimulation electrode as A-tDCS at the schedule times (1st, 7th or 14th days after CCI; **Figure 1C**). For sham tDCS, the stimulation electrode was placed in the same positions as for real stimulation, but stimulation duration of 10 s was used as described above (Yu et al., 2015). Meanwhile, at the beginning and end of tDCS, current was ramped up and down for 10 s to prevent damage to the brain tissues by suddenly changing current (Bindman et al., 1964; Yu et al., 2015). Saline was injected continuously into the sponge through the hole that we left on the top of the tube during the DC stimulation in order to reduce contact impedance when stimulating (Yu et al., 2015). Notably, animals were not anesthetized during tDCS or sham tDCS.

Experimental Protocols

The experiment was composed by seven series (**Figure 1C**, Supplementary Table S1):

- **Series 1**: changes of pain thresholds after CCI. Thirty-three male rats were randomly divided into three groups: control (CT), sham CCI (SC) and CCI. Pain thresholds were tested 1 day before the CCI surgery and at days 1, 3, 7, 10, 14, 21 and 28 after CCI surgery.
- **Series 2**: changes of pain thresholds after single A-tDCS on CCI rats. On day 14 after CCI surgery, contralateral or ipsilateral A-tDCS was delivered in a single session of 20 min with stimulation current intensity of 100/200 μA. Male rats were divided into 12 groups: SC, sham CCI + sham 200 μA ip-tDCS (SCSIT), sham CCI + 200 μA sham con-tDCS (SCSCT), sham CCI + 200 μA ip-tDCS (SCIT), sham CCI + 200 μA con-tDCS (SCCT), CCI, CCI + sham 200 μA ip-tDCS (CSIT), CCI + sham 200 μA con-tDCS (CSCT), CCI + 100 μA ip-tDCS (CIT100), CCI + 200 μA ip-tDCS (CIT200), CCI + 100 μA con-tDCS (CCT100) and CCI + 200 μA con-tDCS (CCT200; n = 11 per group, of which were observed before, and 30 min, 2 h and 24 h after A-tDCS or sham A-tDCS).
- **Series 3**: changes of pain thresholds after processed with repetitive ip-tDCS and con-tDCS on CCI rats. Daily A-tDCS (20 min/200 μA) was applied over five sessions over the contralateral or ipsilateral M1 from the 7th day after CCI. In this series, male rats were divided into four groups: SC, CCI, CIT and CCT.
- **Series 4**: observation of pain thresholds changes after repetitive contralateral A-tDCS with different intensities. Five times daily A-tDCS with different intensities was applied for 20 min on the contralateral M1 from the 7th day after CCI. In this series, male rats were divided into six groups: SC, CCI, CCI + 15 μA con-tDCS (CCT15), CCI + 50 μA con-tDCS (CCT50), CCI + 100 μA con-tDCS (CCT100), and CCI + 200 μA con-tDCS (CCT200).
- **Series 5**: observation of pain thresholds changes after repetitive contralateral A-tDCS with different times. Daily 200 μA A-tDCS was applied on five sessions over the contralateral M1 from the 7th day after CCI. In this series, male rats were divided into six groups: SC, CCI, CCI + 5 min con-tDCS (CCT200-5), CCI + 10 min con-tDCS (CCT200-10), CCI + 20 min con-tDCS (CCT200-20), and CCI + 30 min con-tDCS (CCT200-30).
- **Series 6**: changes in the pain thresholds after A-tDCS on CCI model with different intervention time and sessions. In this series, CCI rats were given with five sessions of repetitive contralateral A-tDCS (20 min/200 μA) on the 1st day (5CCI-1), 7th day (5CCI-7) and 14th day (5CCI-14) after CCI surgery. Other rats were given 10 sessions of repetitive tDCS (20 min/200 μA) starting on the 1st day (10CCT-1) after CCI surgery. Male rats were divided into six groups: SC, CCI, 5CCT-1, 5CCT-7, 5CCT-14, and 10CCT-1.
- **Series 7**: changes in the pain thresholds after repetitive A-tDCS on female rats of the CCI model. Fifty-five female rats were divided into five groups: CT, SC, CCI, CCT and CIT, and daily A-tDCS (20 min/200 μA) was applied on five sessions over the contralateral or ipsilateral M1 from the 7th day after CCI.
- **Series 2–7**: pain thresholds were tested 1 day before CCI surgery and on days 1, 3, 7, 10, 14, 21 and 28 after CCI surgery (n = 11, per group).

Radiant Heat Test

The radiant heat test was carried out to estimate the thermal withdrawal latency (TWL; Hargreaves et al., 1988). After an adaptation period of 30 min, the rats were placed into the test cage with a glass plate under which a light was located; 52 ± 0.2°C radiant heat was applied to the plantar surface of the right hind-paw. The latency period was recorded in response to the thermal hyperalgesia by lifting hind-paw licking, flicking or commences jumping. To avoid tissue injury, the cut-off limit was set at 60 s (Hargreaves et al., 1988). Each hind-paw was measured for three times alternately at a 5 min interval. The mean was recorded as TWL.

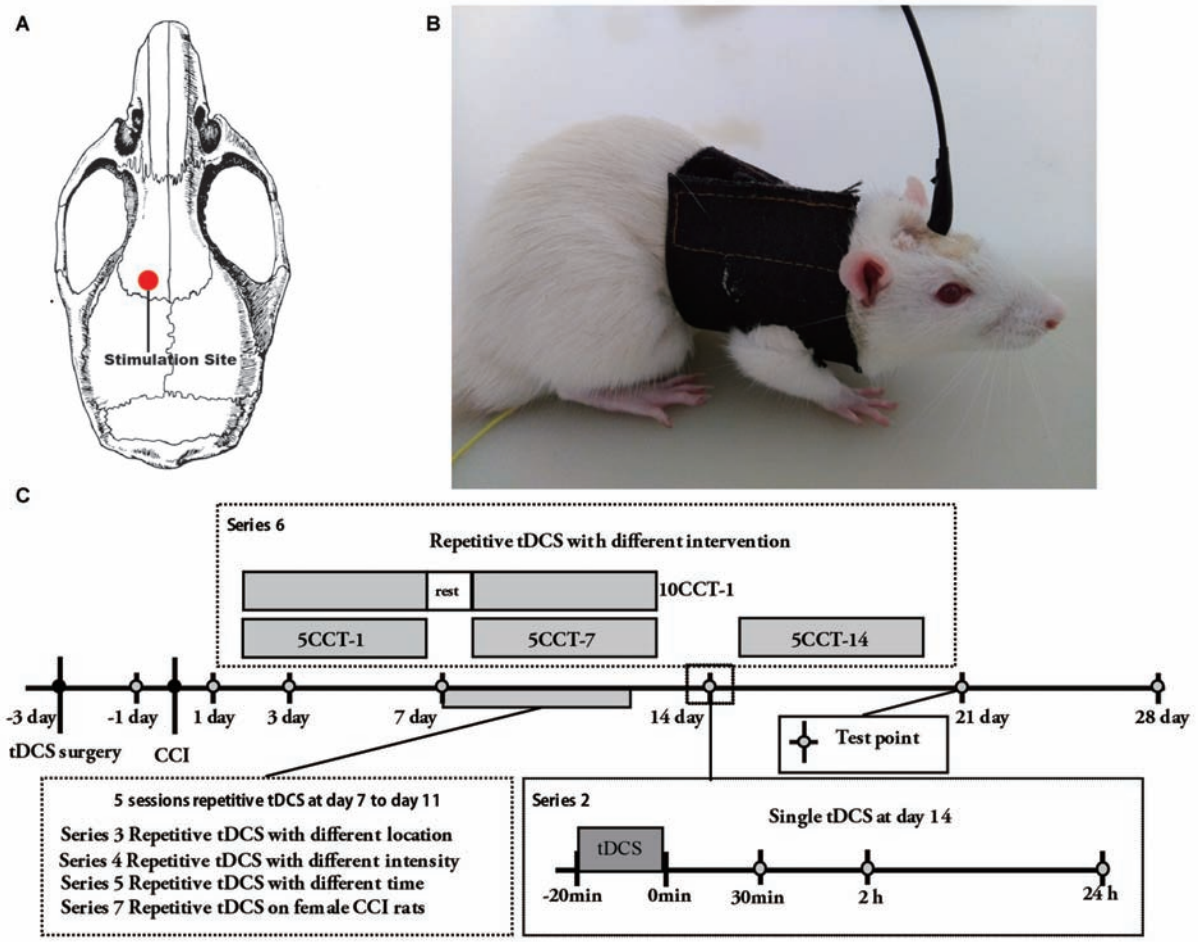


FIGURE 1 | (A) Schematic diagram displaying the location of the stimulation electrode in the rat brain model. **(B)** Electrode configurations in rat. Two electrodes were applied during transcranial direct current stimulation (tDCS). The stimulation electrode was fixed onto the skull and a reference electrode was attached onto the thorax. **(C)** Schematic diagram of the experiment protocol schedule. 5CCT-1/5CCT-7/5CCT-14 means five times daily contralateral-tDCS (con-tDCS) started on day 1, 7, or 14 following chronic constriction injury (CCI), respectively; 10CCT-1 means 10 times con-tDCS at 2 weeks. Test point was the day to test the mechanical allodynia and thermal hyperalgesia on the hind paw of CCI.

Von Frey Filaments Test

The von Frey filaments test using an up-down method was performed to estimate the 50% system mechanical withdrawal threshold (MWT) with bending forces at a range of 0.3–20.3 g von Frey hairs (vFh; Chaplan et al., 1994). Each rat was placed inside a transparent acrylic cage (18 cm × 12 cm × 12 cm) with wire mesh floor with 60 min of acclimatization. The test was initiated with 4.10 g vFh. The filament was applied to the ventral surface of each right hind-paw for 4–6 s, hind paw withdrawal was considered as a positive response. When a positive result was noted, then the filament was decremented by one step size. If a negative result occurs, the filament was increased. The test continues until four measurements have been made after the first change in direction.

Statistical Analysis

Analyses were done with the SPSS software package (version 19). All data are expressed as the mean ± SD. The pain thresholds were evaluated by one way (**Figure 2**) or two-way (except **Figure 2**) repeated measure analysis of variance (ANOVA), when significant differences were observed, a *post hoc* test was made via Tukey's test. In all cases, $p < 0.05$ was considered to be statistically significant.

RESULTS

Changes of Pain Thresholds in CCI Rats

Significant mechanical allodynia and thermal hyperalgesia were elicited in surgical hind paw CCI rats (**Figure 2**). Two-way repeated measures ANOVA showed a significant main effect of group on the MWT (main effect of group $F_{(2,30)} = 663.718$, $p = 0.000$) and TWL ($F_{(2,30)} = 828.857$, $p = 0.000$). The values of MWT and TWL were decreased starting 1 day after CCI surgery, and the most severe stage appeared around day 14 (MWT: 1.03 ± 0.21 g, TWL: 8.61 ± 0.44 s) and then began

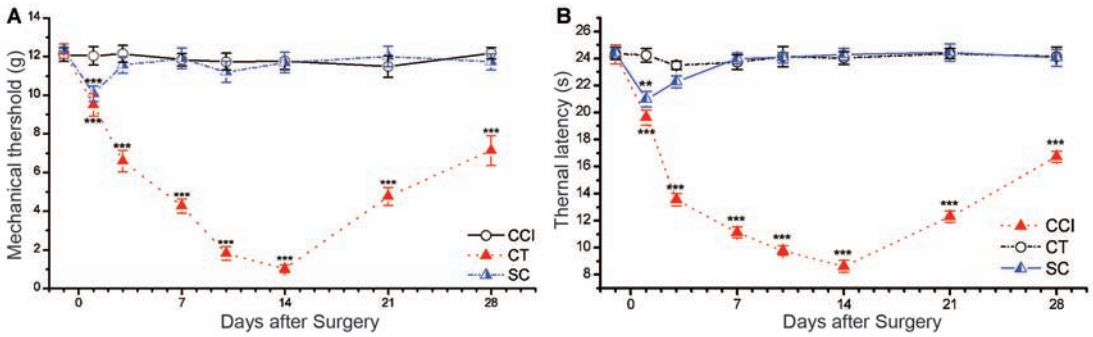


FIGURE 2 | CCI induced significant mechanical allodynia and thermal hyperalgesia in rat. **(A)** Mechanical withdrawal threshold (MWT). **(B)** Thermal withdrawal latency (TWL). Control (CT); sham CCI (SC). All behavior tests were examined 1 day before the CCI surgery and on days 1, 3, 7, 10, 14, 21 and 28 after CCI surgery. Statistical significance was analyzed by two-way analysis of variance (ANOVA) followed by Tukey's *post hoc* test. The data are shown as mean ± SEM; $^{**}p < 0.01$, $^{***}p < 0.001$ vs. CT group.

to recover on the following day (**Figure 2**). This trend was in line with our previous studies (Xiao et al., 2010; Ou et al., 2011; He et al., 2012). There was no significant difference in the thermal latency and mechanical threshold between control and sham CCI groups (p = 0.259 of TWL, p = 0.128 of MWT).

Effects of Single tDCS Treatment Disappeared within 24 h after Stimulation

We chose the 14th day after CCI to test the duration of antinociceptive effects after one time tDCS.

No difference was found in TWL and MWT among SC, SCSIT, SCSCT, SCIT and SCCT groups at all test points (one-way ANOVA, all $p > 0.05$). Sham tDCS (both SCSCT and SCSIT) had no impact on behaviors of Sham CCI rats, and the tDCS (both SCIT and SCCT) also did not have impact on behaviors of sham CCI rats (one-way ANOVA, all $p > 0.05$; **Figure 3**).

Compared with CCI, single con-tDCS (both CCT100 and CCT200) sharply increased TWL and MWT after one session of A-tDCS that ended 30 min before behavioral tests (one-way ANOVA, all p = 0.000). The effects were gradually diminished in the following 2 h (one-way ANOVA, TWL: p = 0.000 for CCT100, p = 0.000 for CCT200; MWT: p = 0.001 for CCT100, p = 0.000 for CCT200 vs. CCI). After 24 h, the antinociceptive effects were almost completely gone and there were no differences compared with the CCI group (one-way ANOVA, all $p > 0.05$). Moreover, we also observed a better recovery of pain in CCT200 than CCT100 (one-way ANOVA, TWL: p = 0.044 for 30 min, p = 0.004 for 2 h, p = 0.490 for 24 h; MWT: p = 0.037 for 30 min, p = 0.009 for 2 h, p = 0.523 for 24 h).

Similarly, single ip-tDCS (CIT100 and CIT200) also showed analgesia effects on CCI rats (one-way ANOVA, 30 min: all p = 0.000 vs. CCI). However, compared to the effects observed with con-tDCS, the antinociceptive effects decreased in the following 2 h (one-way ANOVA, TWL: p = 0.005 for CIT100 and p = 0.000 for CIT200; MWT: p = 0.010 for CIT100 and p = 0.000 for CIT200) and disappeared after 24 h with ip-tDCS (one-way ANOVA, all $p > 0.05$; **Figure 3**). We also observed increased pain recovery in the CIT200 group compared to the CIT100 group (one-way ANOVA, TWL: p = 0.000 for 30 min, p = 0.006 for 2 h, p = 1.000 for 24 h; MWT: p = 0.001 for 30 min, p = 0.028 for 2 h, p = 0.582 for 24 h; **Figure 3**).

However, we did not observed changes in pain thresholds of sham tDCS (both CSIT and CSCT) in CCI rats (one-way ANOVA, all $p > 0.05$; **Figure 3**).

Both ip- and con-Repetitive tDCS Had Long-Term Antinociceptive Effects in CCI Rats

Repetitive A-tDCS had long-term antinociceptive effects, significant increases in TWL and MWT were observed not only during the stimulation process, but also 1 or more weeks following A-tDCS (**Figures 4A,C**). Five sessions of repetitive A-tDCS had similar antinociceptive effects in both CIT and CCT groups; similar effects were observed in surgical hind paw of CCI rats (two-way repeated measures ANOVA: TWL: $F_{(3,40)}$ = 480.888, p = 0.000; MWT: $F_{(3,40)}$ = 150.201, p = 0.000. Tukey's test of groups: all p = 0.000 vs. CCI). Moreover, the values of TWL and MWT in the CCT group were slightly higher than those in the CIT group at every test point, but the differences did not reach statistical significance (Tukey: TWL: p = 0.226, MWT: p = 0.051).

We also normalized the values of TWL and MWT (% of control) and observed the significant analgesia effect during and after tDCS in CIT and CCT groups (**Figures 4B,D**).

Intensity-Dependent Antinociceptive Effects of Repetitive tDCS in CCI Rats

After confirming the location of stimulation electrode in the above studies, we chose different stimulation intensities and simulation times to determine the most effective stimulation current.

Increasing stimulation current intensity resulted in an intensity-dependent increase in TWL of the ipsilateral

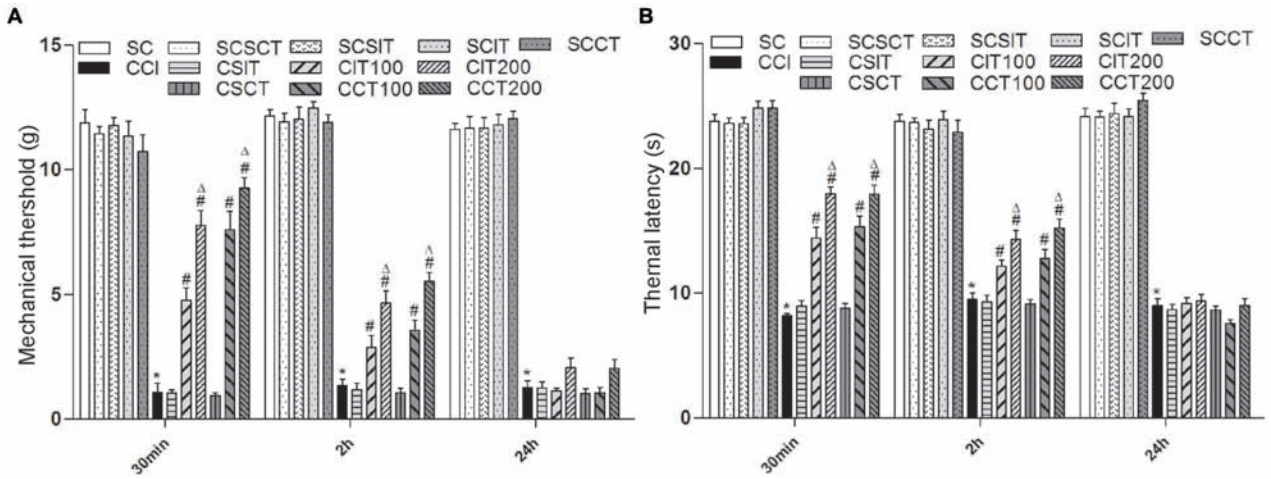


FIGURE 3 | Effects of single tDCS on mechanical allodynia and thermal hyperalgesia. All behavior tests were examined before, and then 30 min, 2 h and 24 h after tDCS. Administration of tDCS started on day 14 after CCI surgery. Experimental groups include, sham CCI (SC); CCI; sham CCI + sham 200 μA ip-tDCS (SCSIT); sham CCI + sham 200 μA con-tDCS (SCSCT); sham CCI + 200 μA ip-tDCS (SCIT); sham CCI + 200 μA con-tDCS (SCCT); CCI + sham 200 μA ip-tDCS (CSIT); CCI + sham 200 μA con-tDCS (CSCT); CCI + 100 μA ip-tDCS (CIT100); CCI + 200 μA ip-tDCS (CIT200); CCI + 100 μA con-tDCS (CCT100); CCI + 200 μA con-tDCS (CCT200). **(A)** MWT. **(B)** TWL. Group analysis was performed by one-way ANOVA followed by Tukey's test. In all three test phases, there were no difference between SC and SCSIT, SCSCT, SCIT, SCCT groups, and there was also no difference between CCI and CSCT, CSIT groups. However, there were significant differences between SC, SCSIT, SCSCT, SCIT, SCCT and CCI groups (all $^{*}p < 0.05$ vs. CCI group). 30 min: the CIT and CCT groups (both 100 μA and 200 μA) differ from the CCI, CSIT and CSCT groups; 2 h: the CIT and CCT groups (both 100 μA and 200 μA) differ from the CCI, CSIT and CSCT groups; 24 h: there is no significant difference from CCI, CSIT, CSST, CIT and CCT groups ($^{\#}p < 0.05$ compared with CCI group, and $^{\Delta}p < 0.05$ compared with CIT100 or CCT100 group).

hind paw after five repetitive A-tDCS (two-way repeated measures ANOVA: TWL: $F_{(5,60)} = 336.733$, $p = 0.000$; MWT: $F_{(5,60)} = 172.656$, $p = 0.000$; **Figure 5**). Compared to the CCI group, the CCT50, CCT100 and CCT200 induced significant increases in TWL and MWT during and after stimulation (Tukey's test of groups: TWL and MWT: all $p = 0.000$), but the CCT15 did not induced analgesia effect (TWL: CCT15 $p = 0.320$; MWT: $p = 0.833$), The analgesic effects were higher in high intensity groups as compared to low intensity groups (Tukey's test of groups: TWL: CCT50 vs. CCT15 $p = 0.009$, CCT100 vs. CCT50 $p = 0.000$, CCT200 vs. CCT100 $p = 0.009$; MWT: CCT50 vs. CCT15 $p = 0.018$, CCT100 vs. CCT50 $p = 0.000$, CCT200 vs. CCT100 $p = 0.589$; **Figure 5**).

Time-Dependent Antinociceptive Effects of Repetitive tDCS in CCI Rats

We observed time-dependent increases in pain thresholds in the ligated hind paw after five daily 200 μA con-tDCS, time points used were 5 min, 10 min, 20 min and 30 min (two-way repeated measures ANOVA: TWL: $F_{(5,60)} = 347.503$, $p = 0.000$; MWT: $F_{(5,60)} = 132.278$, $p = 0.000$; **Figure 6**). The CCT200-5, CCT200-10, CCT200-20 and CCT200-30 groups increased the pain values sharply during the test periods (Tukey's test of groups: TWL and MWT: all $p = 0.000$). We also observed time-dependent increases in pain thresholds (Tukey's test of groups: TWL: CCT200-5 vs. CCT200-10 $p = 0.000$, CCT200-10 vs. CCT200-20 $p = 0.000$, CCT200-20 vs. CCT200-30 $p = 0.681$; MWT: CCT200-5 vs. CCT200-10 $p = 0.000$, CCT200-10 vs. CCT200-20 $p = 0.030$, CCT200-20 vs. CCT200-30 $p = 0.967$).

Proper Intervention Time Enhanced the Long-Term Antinociceptive Effects of Repetitive tDCS in CCI Rats

Intervention time also played a role in the antinociceptive effects following repetitive tDCS, the after-effects were different depending on the time of intervention of tDCS (two-way repeated measures ANOVA: TWL: $F_{(5,60)} = 258.796$, $p = 0.000$; MWT: $F_{(5,60)} = 160.171$, $p = 0.000$; **Figures 7A,C**).

When intervention was performed at 1 day after CCI (5CCT-1), repetitive A-tDCS maintained pain thresholds of the MWT and the TWL in the days following tDCS (Tukey's test of groups: all: $p = 0.000$ vs. CCI). Given tDCS 7 days after CCI (5CCT-7) reversed the development of pain thresholds which gradually approached normal (Tukey's test of groups: all: $p = 0.000$ vs. CCI). Pain thresholds were began to recover 14 days after CCI, and giving A-tDCS at this time point (5CCT-14) greatly reduced the recovery time and increased pain thresholds (Tukey's test of groups: TWL: $p = 0.000$, MWT: $p = 0.639$ vs. CCI). We also observed using twice the number of stimulation sessions (10CCT-1) was helpful in reducing mechanical allodynia and thermal hyperalgesia (Tukey's test of groups: all: $p = 0.000$ vs. CCI). The antinociceptive effects of 10CCT-1 was greater than those observed in the 5CCT-7 group following thermal hyperalgesia (TWL: $p = 0.000$: MWT: $p = 0.379$ vs. 5CCT-7; **Figures 7A,C**). Moreover, we found that inter-quartile range in the 10CCT-1 group was more centralized than that for other groups on 14th day following CCI, which reflected the spread of the threshold data (one-way measures ANOVA: TWL: $F_{(4,50)} = 122.89$, $p = 0.000$; MWT: $F_{(4,50)} = 75.96$, $p = 0.000$; **Figures 7B,D**).

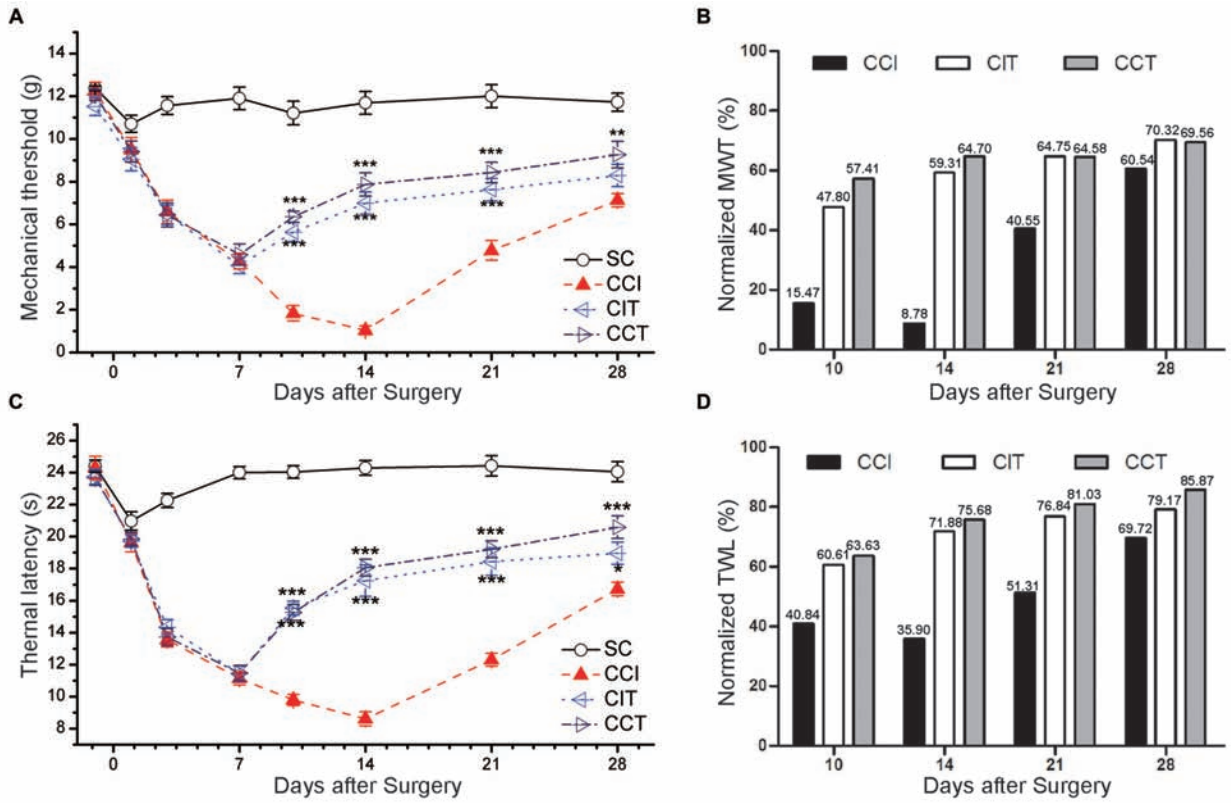


FIGURE 4 | Effects of repetitive tDCS on mechanical allodynia and thermal hyperalgesia with different electrode locations. **(A)** MWT. **(B)** Normalized of MWT. **(C)** TWL. **(D)** Normalized of TWL. Five sessions daily of tDCS (200 μA, 20 min) were administered starting on day 7 after CCI surgery. SC (sham CCI); CCI + ip-tDCS (CIT); CCI + con-tDCS (CCT). CIT and CCT treatments significantly increased the values of TWL and MWT. All behavior tests were tested 1 day before the CCI surgery and on days 1, 3, 7, 10, 14, 21 and 28 after CCI surgery. Statistical significance was analyzed by two-way ANOVA followed by Tukey's *post hoc* test. $^{*}p < 0.05$, $^{**}p < 0.01$, $^{***}p < 0.001$ vs. CCI group.

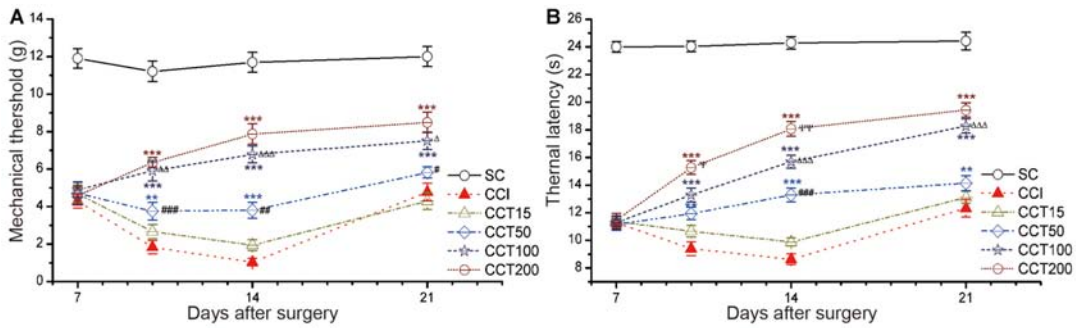


FIGURE 5 | Effects of repetitive tDCS on mechanical allodynia and thermal hyperalgesia with different stimulation intensities. **(A)** MWT. **(B)** TWL. Five sessions daily of con-tDCS (20 min) with different intensity administrations started on day 7 after CCI surgery. Sham CCI (SC); CCI + 15 μA con-tDCS treatment (CCT15); CCI + 50 μA con-tDCS treatmen (CCT50); CCI + 100 μA con-tDCS treatment (CCT100); CCI + 200 μA con-tDCS treatment (CCT200). All behavior tests were examined at days 7, 10, 14, and 21 after CCI surgery. Statistical significance was analyzed by two-way ANOVA followed by Tukey's *post hoc* test. $^{**}p < 0.01$, $^{***}p < 0.001$ vs. CCI group; $^{\#}p < 0.05$, $^{\#\#}p < 0.01$, $^{\#\#\#}p < 0.001$ vs. CCT15 group; $^{\Delta}p < 0.05$, $^{\Delta\Delta}p < 0.01$, $^{\Delta\Delta\Delta}p < 0.001$ vs. CCT50 group; $^{\Psi}p < 0.05$, $^{\Psi\Psi}p < 0.01$ vs. CCT100 group.

Antinociceptive Effects in Female Rats after Repetitive tDCS

A similar pain tend was observed in female rats compared to male rats following CCI, the TWL and MWT were significantly decreased in CCI rats compared to CT rats (Tukey's test of groups: TWL and MWT: all $p = 0.000$; **Figure 8**). Consecutive sessions of tDCS (both CIT and CCT) induced antinociceptive effects which lasted for at least 1 week after stimulation in

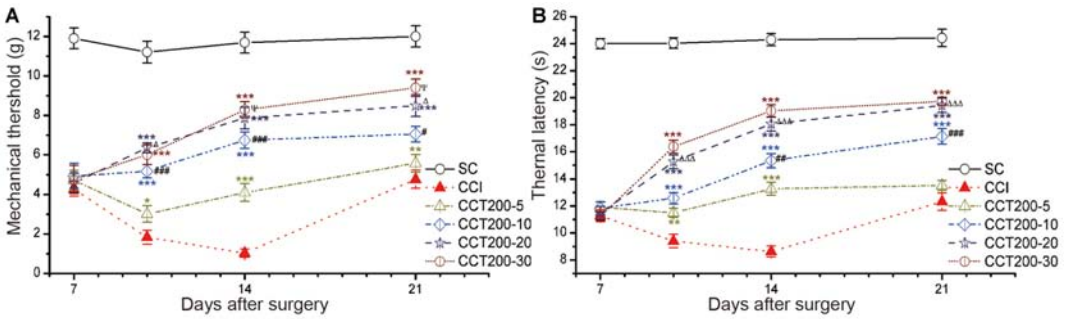


FIGURE 6 | Effects of repetitive tDCS on mechanical allodynia and thermal hyperalgesia with different stimulation times. **(A)** MWT. **(B)** TWL. Five sessions daily of con-tDCS (200 μA) with different time administrations started on day 7 after CCI surgery. Sham CCI (SC); CCI + 5 min con-tDCS treatment (CCT200-5); CCI + 10 min con-tDCS treatment (CCT200-10); CCI + 20 min con-tDCS treatment (CCT200-20); CCI + 30 min con-tDCS treatment (CCT200-30). All behavior tests were examined at days 7, 10, 14 and 21 after CCI surgery. Statistical significance was analyzed by two-way ANOVA followed by Tukey's *post hoc* test. $^{**}p < 0.01$, $^{***}p < 0.001$ vs. CCI group; $^{\#}p < 0.05$, $^{\#\#}p < 0.01$, $^{\#\#\#}p < 0.001$ vs. CCT200-5 group; $^{\Delta}p < 0.05$, $^{\Delta\Delta\Delta}p < 0.001$ vs. CCT200-10 group; $^{\Psi}p < 0.05$ vs. CCT200-20 group.

female CCI rats (two-way repeated measures ANOVA: TWL: $F_{(4,50)} = 248.424$, $p = 0.000$; MWT: $F_{(4,50)} = 136.015$, $p = 0.000$). Compared to the CCI group, A-tDCS significantly increased the pain values to a high level in both CIT group (Tukey's test of groups: TWL and MWT: all $p = 0.000$) and CCT group (Tukey's test of groups: TWL and MWT: all $p = 0.000$). We also observed that the mechanical allodynia and thermal hyperalgesia of the CCT group were mildly increased compared to the CIT group, but the differences did not reach statistical significance (Tukey's test of groups: TWL: $p = 0.074$; MWT: $p = 0.093$; **Figure 8**). We also normalized the values of TWL and MWT (% of control) and observed the significant analgesia effect during and after tDCS (**Figures 8B,D**).

DISCUSSION

Clinical treatment of neuropathic pain is still a major challenge because of its long duration and difficulty in managing (Brunoni et al., 2012). As a non-invasive electrical stimulation treatment, tDCS technology has been used for many years in clinical settings (Gandiga et al., 2006; Brunoni et al., 2012). Radiological and clinical practice have proven that tDCS can play a role in the plasticity of CNS regulation and serve as a treatment for neuronal abnormalities (Borckardt et al., 2012; Brunoni et al., 2012; DosSantos et al., 2014; Woods et al., 2016). However, as systematical basic research is lacking, clinical effects are inconsistent and critical stimulus parameters are uncertain (Lee et al., 2015; Dedoncker et al., 2016). In this article, we choose a rat CCI model as the neuropathic pain model, which is the most common pain model that could finely simulate the clinical chronic neuropathic pain as reported by previous studies (Xiao et al., 2010; Ou et al., 2011; He et al., 2012). The pain threshold of MWT and TWL were evaluated at the different times after CCI.

Previous clinical studies chose the M1 cerebral cortex as the stimulus location because of its roles in the modulation of chronic pain, as it receives pain-related information from the thalamus and the somatosensory cortex (Nguyen et al., 2011; Mylius et al., 2012). Earlier findings indicated that the neural activity of contralateral M1 to an injured paw was increased after CCI (Ooi et al., 2006), and contralateral M1 stimulation has been used as a clinical treatment of chronic pain with the use of transdural motor cortex stimulation (MCS) and rTMS (Lefaucheur, 2006; Fontaine et al., 2009; Young et al., 2014). However, previous work has also reported that M1 stimulation with MCS or rTMS ipsilateral to injury could also significantly suppress pain-related responses in rats and human (Nahmias et al., 2009; Lucas et al., 2011; Viisanen et al., 2012), but there have been no extensive experimental study testing tDCS. In our study, the anode stimulation electrode was mounted contralateral or ipsilateral to the injured paw to measure the antinociceptive effect of tDCS, and our results demonstrated that both locations of A-tDCS led to significant decreases in pain. Our study supplements previous experiments in which the location of the electrode was not taken into consideration (Cioato et al., 2016; Filho et al., 2016). A possible mechanism of these results is supra-spinal antinociceptive activities via multiple parallel pathways (Pertovaara and Wei, 2003). Recent studies had found that M1 stimulation can also active the adjacent regions, including the periaqueductal gray, anterior cingulate cortex and amygdale (Nguyen et al., 2011). Further experiments have shown that rTMS enhances the corticospinal inhibitory system which might in turn mediate M1 stimulation-induced spinal antinociception (Rojas-Piloni et al., 2010; Dall Agnol et al., 2014). The transduction mechanism of antinociception release needs further study in the future.

We observed that the effects of A-tDCS on reducing hyperalgesia and allodynia depended on stimulus intensity and time. Stronger intensities or longer duration correlates with more charged input to the cortex (Nitsche and Paulus, 2011), and a better after-effect on relieving pain (Nitsche et al., 2008). In Series 2, we found the analgesic effect of single tDCS was diminished following 2 h, but repetitive tDCS prolongs the duration of analgesic effect (Series 3). We found that greater charge inputs given 1 week after original stimulation maintained high pain thresholds when

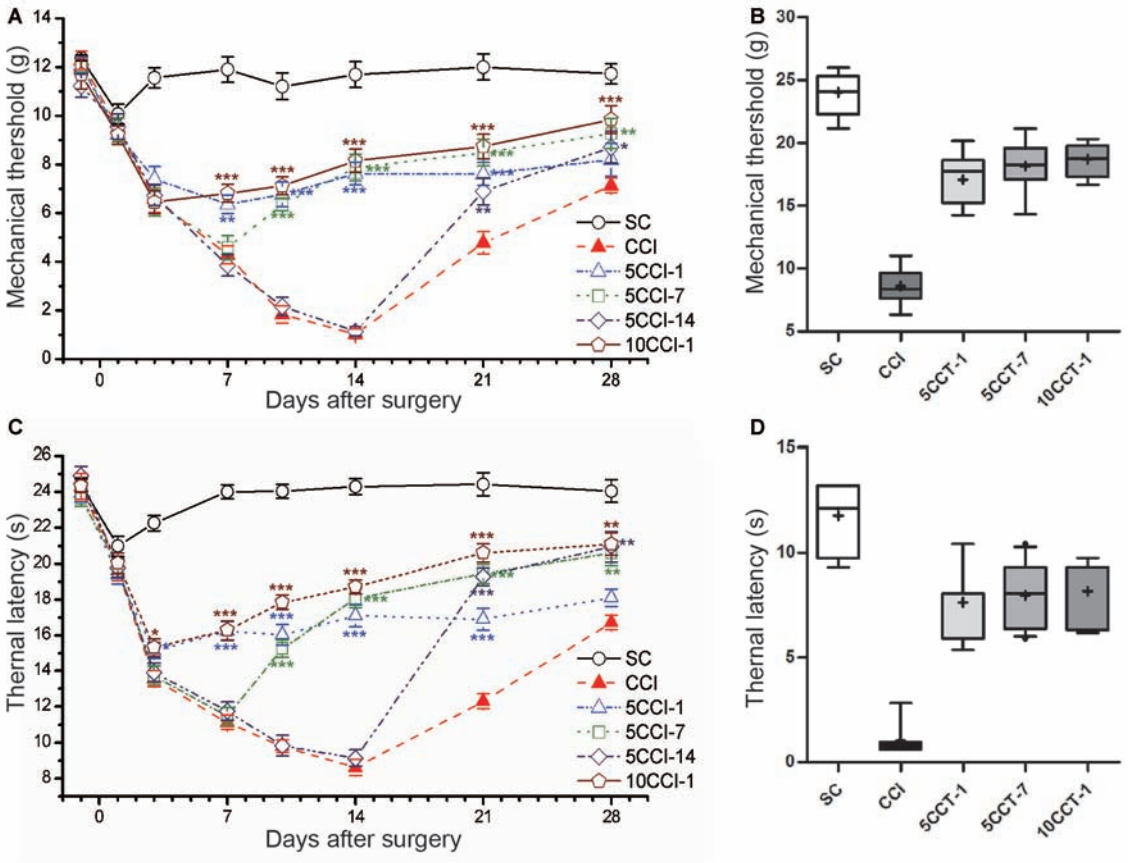


FIGURE 7 | Effects of repetitive tDCS on mechanical allodynia and thermal hyperalgesia with different intervention times. **(A)** MWT. **(B)** Boxplot graph of MWT at day 14 after CCI. **(C)** TWL. **(D)** Boxplot graph of TWL at day 14 after CCI. Five or 10 sessions repetitive tDCS (20 min and 200 μA) with different intervention times were administered started on days 1, 7 and 14 following CCI surgery, respectively. Sham CCI (SC); CCI plus five sessions daily con-tDCS from day 1 after CCI (5CCT-1); CCI plus five sessions daily con-tDCS from day 7 after CCI (5CCT-7); CCI plus five sessions daily con-tDCS from day 14 after CCI (5CCT-14); CCI plus 10 sessions con-tDCS from day 1 after CCI (10CCT-1). All behavior tests were tested 1 day before the CCI surgery and at days 1, 3, 7, 10, 14, 21 and 28 after CCI surgery. Statistical significance was analyzed by two-way ANOVA followed by Tukey's *post hoc* test. $^{*}p < 0.05$, $^{**}p < 0.01$, $^{***}p < 0.001$ vs. CCI group.

re-assessed on days 21 and 28 following CCI. Therefore, to create more effective and long-lasting after-effects, we should increase the stimulation duration and the current intensity. In the last few decades, there has been consensus that increasing stimulation duration prolongs the occurrence and duration of after-effects in humans and animals (Nitsche et al., 2008), which we verified in our study. However, increasing of duration and intensity has limitations. Considering the safety of tDCS, we choose 200 μA as the highest intensity because in our preliminary experiments we observed transient tremors if the intensity was over 220 μA. On the other hand, we found that there were no statistical differences in pain thresholds between CCT200-30 and CCT200-20 groups (**Figure 6**), suggesting that the antinociceptive effects of tDCS may be saturated after 20 min of tDCS at 200 μA. As such, it is necessary to determine the best intervention time if the stimulation intensity and duration cannot be further increased to continue prolonging the after-effects of tDCS.

CCI was first reported by Bennett and Xie (1988) and was regarded as a typical model in neuropathic pain research. The duration of neuropathic pain was divided into two parts (**Figure 2**). Part one was described as the "progression period" and referred to days 1 through 14 following CCI, peaking between days 10 and 14; part two was described as "recovery period" and referred to the period following day 14 in which the sensitivity to pain decreased daily. We chose two time points (1 and 7 days after surgery) in the progression period and one point in the recovery period (14 days after surgery) for delivering tDCS. There were substantial signs of recovery in each treatment group compared to the CCI group: (1) repetitive A-tDCS reversed the decreased thresholds observed in CCI rats at every time point; (2) early intervention prevented the sharp decrease in the pain threshold, but did not restore the threshold to its normal level; (3) as chronic pain worsened, the degree of antinociception following tDCS decreased and the after-effect were not well maintained; (4) antinociceptive effects were present when tDCS was delivered throughout the progressed

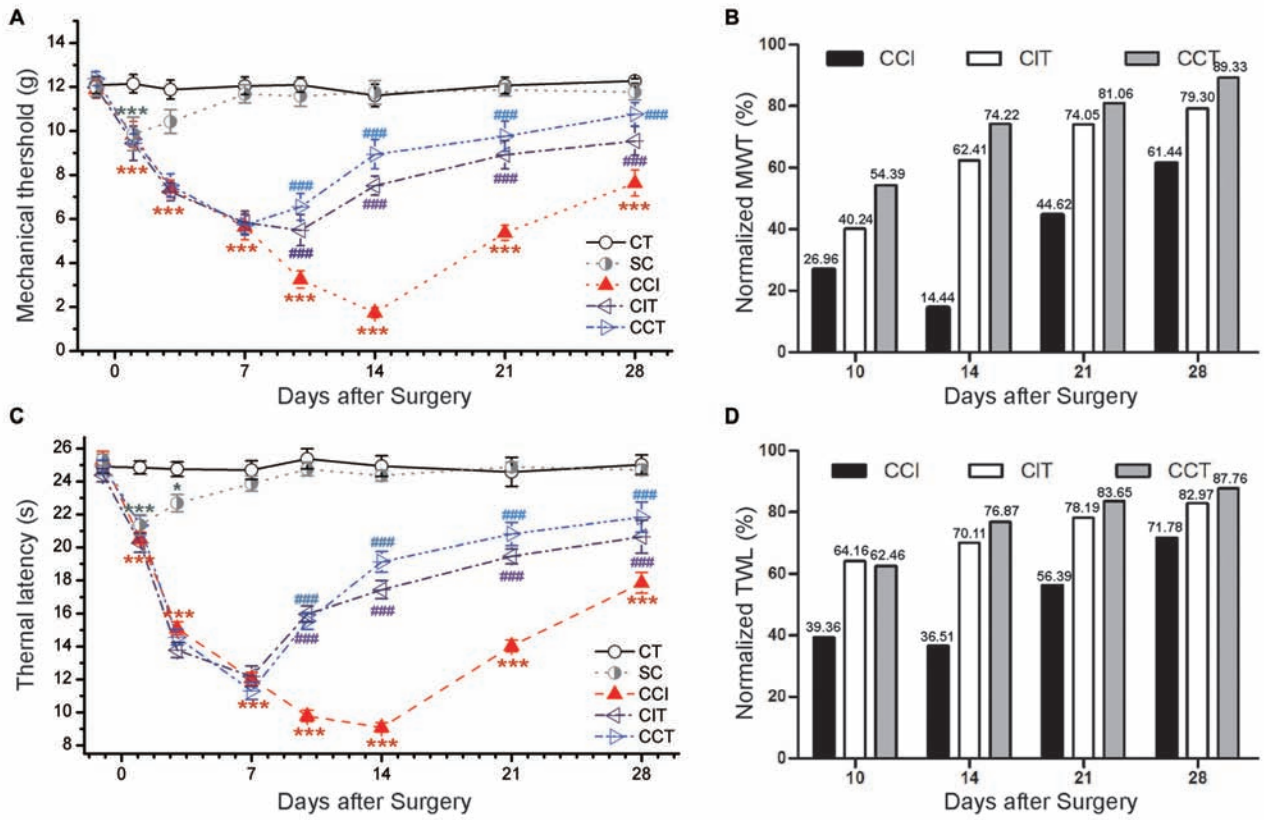


FIGURE 8 | Effects of repetitive tDCS on mechanical allodynia and thermal hyperalgesia with different locations in female rats. **(A)** MWT. **(B)** Normalized of MWT. **(C)** TWL. **(D)** Normalized of TWL. Five sessions daily of tDCS (200 μA, 20 min) were administration started on day 7 following CCI surgery. CT (control); SC (sham CCI); CIT (CCI + ip-tDCS treatment); CCT (CCI + con-tDCS treatment). CIT and CCT treatments significantly increased the values of TWL and MWT. All behavior tests were tested 1 day before the CCI surgery and on days 1, 3, 7, 10, 14, 21 and 28 after CCI surgery. Statistical significance was analyzed by two-way ANOVA followed by Tukey's *post hoc* test. $^{*}p < 0.05$, $^{***}p < 0.001$ vs. CT group, $^{\#\#\#}p < 0.001$ vs. CCI group.

period; and (5) pain thresholds significantly improved when tDCS were given at the beginning of the recovery period (**Figure 7**).

To the best of our knowledge, we are the first to discover that intervention time is another key factor that influences the efficacy of stimulation. With the same intensity and duration, the efficacy of analgesia was prolonged and consolidated by choosing the right time points when stimulation is participated in the pain processing and extending the original session of tDCS.

Clinically, A-tDCS is widely used in chronic pain treatment, an intensity of 2 mA and duration of 20 min with five or seven daily repetitions are usually chosen, parameters that have proven effects (Mori et al., 2010; Ngernyam, 2014). However, other researchers have also been obtained in which A-tDCS was ineffective in the treatment of chronic pain using the same conditions (Ihle et al., 2014; Nardone et al., 2014) The patient described in this study had stable chronic pain for at least 6 months with a high VAS scores before the stimulation, however, intervention time was not considered during therapy. A proper intervention time, the number of session and the length of stimulus duration should be considered and may be dependent on different states and causes of illness (Ihle et al., 2014). Our results suggest that clinicians should consider personalized treatment in patients with chronic neuropathic pain, pay attention to specific stimulus parameters and disease characteristics.

Furthermore, brain lesions were reported when the current density was greater than 142.9 A/m^2 in rat experiments. Our studies used a maximum current density of 63.69 A/m^2 (200 μA/3.14 mm^2) which is not associated with any tissue injure after tDCS (Liebetanz et al., 2009).

Futhermore, we examined the effect of tDCS in female rats. Previous work found gender-related differences in utilitarian behavior after tDCS with greater effects in females as compared to males (Chaieb et al., 2008). For CCI rats, the chronic nociceptive processing was similar in both sexes, but male rats responded more quickly than females to a thermal nociceptive stimulus, and the stimulus elicited less robust thermal hyperalgesic symptoms in males than in females (Tall et al., 2001). In our study, we also found hyperalgesia and allodynia in female CCI rats. Both ip- and con-tDCS had the similar antinociceptive effects in female CCI rats. However, the hormonal fluctuate could be interfere in the nociceptive response

(Tall et al., 2001) and the mechanism of gender difference needs further study in the future.

There is increasing evidence that the after-effects of tDCS are not only driven by the regulation of inhibition and excitation, but also by the modification of synapses (Nguyen et al., 2011; Stagg and Nitsche, 2011). Another view is that tDCS does not only elicit that rapid depolarization required to produce action potentials in neurons, but also may produces long-lasting changes in cortical excitability and activity (Mylius et al., 2012). Consistent with this, another key hypothesis holds that chronic pain is likely to employ highly selective synaptic connections and molecular signaling pathways within pain-related cortical areas (Zhuo, 2008, 2013), resulting in cortical plasticity in both the descending and ascending systems. In the rat with peripheral injured, bilateral M1 receives pain-related information from the thalamus and the somatosensory cortex that maps to the injured paw (Xie et al., 2009; Ossipov et al., 2010). Stimulation of M1 might induce plasticity changes and reorganizations in the expression of neurotransmitter receptors (Lefaucheur et al., 2010; Stagg and Nitsche, 2011) which might include tonic activation of NMDA receptors (Pertovaara and Wei, 2003; Nguyen et al., 2011) and an enhanced anti-hypersensitivity effect in dopamine receptors (Viisanen et al., 2012). We observed increased NMDA receptors in bilateral M1 regions in CCI rats after repetitive tDCS (unpublished results). Therefore, the changes in NMDA receptors after tDCS might decrease the function of brain areas related to pain management through long-term potentiation (LTP) synaptic efficacy, thereby inducing cortical reorganization and CNS network processing. These affects are likely to reintroduce an optimal excitation/inhibition balance that allows for optimal homeostatic plasticity (Nitsche and Paulus, 2011; Stagg and Nitsche, 2011; Krause et al., 2013; Ngernyam, 2014).

The present study demonstrates the antinociceptive effect of tDCS in the male and female CCI rats. Both ip-DCS and con-tDCS produce a long-lasting analgesic effect on neuropathic pain, and the optimal stimulation parameters of tDCS are future studied. These dates may be helpful for the clinical applications of tDCS in pain control. More investigations on the synaptic mechanisms of tDCS should be conducted in the future.

AUTHOR CONTRIBUTIONS

H-ZR and H-ZW conceived and designed the study. H-ZW wrote the manuscript. S-HG, Y-DZ and W-JH carried out the animals' experiments. H-ZW and X-LT participated in the treatment of tDCS. H-ZW and S-HG participated in data analyses and arranged the figures. All authors have read and approved the final manuscript.

ACKNOWLEDGMENTS

This work was supported by the National Natural Science Foundation of China (Grant number 31171069, 2011).

SUPPLEMENTARY MATERIAL

The Supplementary Material for this article can be found online at: http://journal.frontiersin.org/article/10.3389/fnbeh.2017.00115/full#supplementary-material

REFERENCES

Bennett, G. J., and Xie, Y. K. (1988). A peripheral mononeuropathy in rat that produces disorders of pain sensation like those seen in man. *Pain* 33, 87–107. doi: 10.1016/0304-3959(88)90209-6

Bindman, L. J., Lippold, O. C. J., and Redfearn, J. W. (1964). The action of brief polarizing currents on the cerebral cortex of the rat (1) during current flow and (2) in the production of long-lasting after-effects. *J. Physiol.* 172, 369–382. doi: 10.1113/jphysiol.1964.sp007425

Borckardt, J. J., Bikson, M., Frohman, H., Reeves, S. T., Datta, A., Bansal, V., et al. (2012). A pilot study of the tolerability and effects of high-definition transcranial direct current stimulation (HD-tDCS) on pain perception. *J. Pain* 13, 112–120. doi: 10.1016/j.jpain.2011.07.001

Brunoni, A. R., Nitsche, M. A., Bolognini, N., Bikson, M., Wagner, T., Merabet, L., et al. (2012). Clinical research with transcranial direct current stimulation (tDCS): challenges and future directions. *Brain Stimul.* 5, 175–195. doi: 10.1016/j.brs.2011.03.002

Chaieb, L., Antal, A., and Paulus, W. (2008). Gender-specific modulation of short-term neuroplasticity in the visual cortex induced by transcranial direct current stimulation. *Vis. Neurosci.* 25, 77–81. doi: 10.1017/s0952523808080097

Chaplan, S. R., Bach, F. W., Pogrel, J. W., Chung, J. M., and Yaksh, T. L. (1994). Quantitative assessment of tactile allodynia in the rat paw. *J. Neurosci. Methods* 53, 55–63. doi: 10.1016/0165-0270(94)90144-9

Cioato, S. G., Medeiros, L. F., Marques Filho, P. R., Vercelino, R., de Souza, A., Scarabelot, V. L., et al. (2016). Long-lasting effect of transcranial direct current stimulation in the reversal of hyperalgesia and cytokine alterations induced by the neuropathic pain model. *Brain Stimul.* 9, 209–217. doi: 10.1016/j.brs.2015.12.001

Dall Agnol, L., Medeiros, L. F., Torres, I. L. S., Deitos, A., Brietzke, A., Laste, G., et al. (2014). Repetitive transcranial magnetic stimulation increases the corticospinal inhibition and the brain-derived neurotrophic factor in chronic myofascial pain syndrome: an explanatory double-blinded, randomized, sham-controlled trial. *J. Pain* 15, 845–855. a doi: 10.1016/j.jpain.2014.05.001

Dedoncker, J., Brunoni, A. R., Baeken, C., and Vanderhasselt, M. (2016). A Systematic review and meta-analysis of the effects of transcranial direct current stimulation (tDCS) over the dorsolateral prefrontal cortex in healthy and neuropsychiatric samples: influence of stimulation parameters. *Brain Stimul.* 9, 501–517. doi: 10.1016/j.brs.2016.04.006

DosSantos, M. F., Martikainen, I. K., Nascimento, T. D., Love, T. M., DeBoer, M. D., Schambra, H. M., et al. (2014). Building up analgesia in humans via the endogenous mu-opioid system by combining placebo and active tDCS: a preliminary report. *PLoS One* 9:e102350. doi: 10.1371/journal.pone.0102350

Dworkin, R. H., O'Connor, A. B., Kent, J., Mackey, S. C., Raja, S. N., Stacey, B. R., et al. (2013). Interventional management of neuropathic pain: NeuPSIG recommendations. *Pain* 154, 2249–2261. doi: 10.1016/j.pain.2013.06.004

Ferrucci, R., Cortese, F., and Priori, A. (2015). Cerebellar tDCS: how to do it. *Cerebellum* 14, 27–30. doi: 10.1007/s12311-014-0599-7

Filho, P. R. M., Vercelino, R., Cioato, S. G., Medeiros, L. F., de Oliveira, C., Scarabelot, V. L., et al. (2016). Transcranial direct current stimulation (tDCS) reverts behavioral alterations and brainstem BDNF level increase induced by neuropathic pain model: long-lasting effect. *Prog. Neuropsychopharmacol. Biol. Psychiatry* 64, 44–51. doi: 10.1016/j.pnpbp.2015.06.016

Fontaine, D., Hamani, C., and Lozano, A. (2009). Efficacy and safety of motor cortex stimulation for chronic neuropathic pain: critical review of the literature. *J. Neurosurg.* 110, 251–256. doi: 10.3171/2008.6.17602

Fregni, F., Boggio, P. S., Lima, M. C., Ferreira, M. J. L., Wagner, T., Rigonatti, S. P., et al. (2006). A sham-controlled, phase II trial of transcranial direct current stimulation for the treatment of central pain in traumatic spinal cord injury. *Pain* 122, 197–209. doi: 10.1016/j.pain.2006.02.023

Gandiga, P. C., Hummel, F. C., and Cohen, L. G. (2006). Transcranial DC stimulation (tDCS): a tool for double-blind sham-controlled clinical studies in brain stimulation. *Clin. Neurophysiol.* 117, 845–850. doi: 10.1016/j.clinph.2005.12.003

Hargreaves, K., Dubner, R., Brown, F., Flores, C., and Joris, J. (1988). A new and sensitive method for measuring thermal nociception in cutaneous hyperalgesia. *Pain* 32, 77–88. doi: 10.1016/0304-3959(88)90026-7

He, W., Cui, J., Du, L., Zhao, Y., Burnstock, G., Zhou, H., et al. (2012). Spinal P2X7 receptor mediates microglia activation-induced neuropathic pain in the sciatic nerve injury rat model. *Behav. Brain Res.* 226, 163–170. doi: 10.1016/j.bbr.2011.09.015

Ihle, K., Rodriguez-Raecke, R., Luedtke, K., and May, A. (2014). tDCS modulates cortical nociceptive processing but has little to no impact on pain perception. *Pain* 155, 2080–2087. doi: 10.1016/j.pain.2014.07.018

Krause, B., Márquez-Ruiz, J., and Cohen Kadosh, R. C. (2013). The effect of transcranial direct current stimulation: a role for cortical excitation/inhibition balance? *Front. Hum. Neurosci.* 7:602. doi: 10.3389/fnhum.2013.00602

Laste, G., Caumo, W., Adachi, L. N. S., Rozisky, J. R., de Macedo, I. C., Filho, P. R. M., et al. (2012). After-effects of consecutive sessions of transcranial direct current stimulation (tDCS) in a rat model of chronic inflammation. *Exp. Brain Res.* 221, 75–83. doi: 10.1007/s00221-012-3149-x

Lee, M., Kim, Y. H., Im, C. H., Kim, J. H., Park, C. H., Chang, W. H., et al. (2015). What is the optimal anodal electrode position for inducing corticomotor excitability changes in transcranial direct current stimulation? *Neurosci. Lett.* 584, 347–350. doi: 10.1016/j.neulet.2014.10.052

Lefaucheur, J., Holsheimer, J., Goujon, C., Keravel, Y., and Nguyen, J. (2010). Descending volleys generated by efficacious epidural motor cortex stimulation in patients with chronic neuropathic pain. *Exp. Neurol.* 223, 609–614. doi: 10.1016/j.expneurol.2010.02.008

Lefaucheur, J. P. (2006). The use of repetitive transcranial magnetic stimulation (rTMS) in chronic neuropathic pain. *Neurophysiol. Clin.* 36, 117–124. doi: 10.1016/j.neucli.2006.08.002

Liebetanz, D., Fregni, F., Monte-Silva, K. K., Oliveira, M. B., Amâncio-dos-Santos, A., Nitsche, M. A., et al. (2006). After-effects of transcranial direct current stimulation (tDCS) on cortical spreading depression. *Neurosci. Lett.* 398, 85–90. doi: 10.1016/j.neulet.2005.12.058

Liebetanz, D., Koch, R., Mayenfels, S., König, F., Paulus, W., and Nitsche, M. A. (2009). Safety limits of cathodal transcranial direct current stimulation in rats. *Clin. Neurophysiol.* 120, 1161–1167. doi: 10.1016/j.clinph.2009.01.022

Lucas, J. M., Ji, Y., and Masri, R. (2011). Motor cortex stimulation reduces hyperalgesia in an animal model of central pain. *Pain* 152, 1398–1407. doi: 10.1016/j.pain.2011.02.025

Mori, F., Codecà, C., Kusayanagi, H., Monteleone, F., Buttari, F., Fiore, S., et al. (2010). Effects of anodal transcranial direct current stimulation on chronic neuropathic pain in patients with multiple sclerosis. *J. Pain* 11, 436–442. doi: 10.1016/j.jpain.2009.08.011

Mylius, V., Borckardt, J. J., and Lefaucheur, J. (2012). Noninvasive cortical modulation of experimental pain. *Pain* 153, 1350–1363. doi: 10.1016/j.pain.2012.04.009

Nahmias, F., Debes, C., de Andrade, D. C., Mhalla, A., and Bouhassira, D. (2009). Diffuse analgesic effects of unilateral repetitive transcranial magnetic stimulation (rTMS) in healthy volunteers. *Pain* 147, 224–232. doi: 10.1016/j.pain.2009.09.016

Nardone, R., Höller, Y., Leis, S., Höller, P., Thon, N., Thomschewski, A., et al. (2014). Invasive and non-invasive brain stimulation for treatment of neuropathic pain in patients with spinal cord injury: a review. *J. Spinal Cord Med.* 37, 19–31. doi: 10.1179/2045772313Y.0000000140

Ngernyam, N. (2014). Transcranial direct current stimulation in neuropathic pain. *J. Pain Relief* s3:1. doi: 10.4172/2167-0846.1000s3-001

Nguyen, J. P., Nizard, J., Keravel, Y., and Lefaucheur, J. P. (2011). Invasive brain stimulation for the treatment of neuropathic pain. *Nat. Rev. Neurol.* 7, 699–709. doi: 10.1038/nrneurol.2011.138

Nitsche, M. A., Cohen, L. G., Wassermann, E. M., Priori, A., Lang, N., Antal, A., et al. (2008). Transcranial direct current stimulation: state of the art 2008. *Brain Stimul.* 1, 206–223. doi: 10.1016/j.brs.2008.06.004

Nitsche, M. A., and Paulus, W. (2011). Transcranial direct current stimulation—update 2011. *Restor. Neurol. Neurosci.* 29, 463–492. doi: 10.3233/RNN-2011-0618

O'Connell, N. E., Wand, B. M., Marston, L., Spencer, S., and Desouza, L. H. (2011). Non-invasive brain stimulation techniques for chronic pain. A report of a Cochrane systematic review and meta-analysis. *Eur. J. Phys. Rehabil. Med.* 47, 309–326.

O'Neill, F., Sacco, P., and Nurmikko, T. (2015). Evaluation of a home-based transcranial direct current stimulation (tDCS) treatment device for chronic pain: study protocol for a randomised controlled trial. *Trials* 16:186. doi: 10.1186/s13063-015-0710-5

Ooi, Y., Satomura, Y., Seki, J., Yanagida, T., and Seiyama, A. (2006). Optical coherence tomography reveals *in vivo* cortical plasticity of adult mice in response to peripheral neuropathic pain. *Neurosci. Lett.* 397, 35–39. doi: 10.1016/j.neulet.2005.12.010

Ossipov, M. H., Dussor, G. O., and Porreca, F. (2010). Central modulation of pain. *J. Clin. Invest.* 120, 3779–3787. doi: 10.1172/JCI43766

Ou, S., Zhao, Y., Xiao, Z., Wen, H., Cui, J., and Ruan, H. (2011). Effect of lappaconitine on neuropathic pain mediated by P2X3 receptor in rat dorsal root ganglion. *Neurochem. Int.* 58, 564–573. doi: 10.1016/j.neuint.2011.01.016

Pertovaara, A., and Wei, H. (2003). A dissociative change in the efficacy of supraspinal versus spinal morphine in the neuropathic rat. *Pain* 101, 237–250. doi: 10.1016/s0304-3959(02)00320-2

Roizenblatt, S., Fregni, F., Gimenez, R., Wetzel, T., Rigonatti, S. P., Tufik, S., et al. (2007). Site-specific effects of transcranial direct current stimulation on sleep and pain in fibromyalgia: a randomized, sham-controlled study. *Pain Pract.* 7, 297–306. doi: 10.1111/j.1533-2500.2007.00152.x

Rojas-Piloni, G., Martínez-Lorenzana, G., Condés-Lara, M., and Rodríguez-Jiménez, J. (2010). Direct sensorimotor corticospinal modulation of dorsal horn neuronal C-fiber responses in the rat. *Brain Res.* 1351, 104–114. doi: 10.1016/j.brainres.2010.06.010

Soler, M. D., Kumru, H., Pelayo, R., Vidal, J., Tormos, J. M., Fregni, F., et al. (2010). Effectiveness of transcranial direct current stimulation and visual illusion on neuropathic pain in spinal cord injury. *Brain* 133, 2565–2577. doi: 10.1093/brain/awq184

Spezia Adachi, L. N., Caumo, W., Laste, G., Fernandes Medeiros, L., Ripoll Rozisky, J., de Souza, A., et al. (2012). Reversal of chronic stress-induced pain by transcranial direct current stimulation (tDCS) in an animal model. *Brain Res.* 1489, 17–26. doi: 10.1016/j.brainres.2012.10.009

Stagg, C. J., and Nitsche, M. A. (2011). Physiological basis of transcranial direct current stimulation. *Neuroscientist* 17, 37–53. doi: 10.1177/1073858410386614

Tall, J. M., Stuesse, S. L., Cruce, W. L. R., and Crisp, T. (2001). Gender and the behavioral manifestations of neuropathic pain. *Pharmacol. Biochem. Behav.* 68, 99–104. doi: 10.1016/s0091-3057(00)00461-5

Viisanen, H., Ansah, O. B., and Pertovaara, A. (2012). The role of the dopamine D2 receptor in descending control of pain induced by motor cortex stimulation in the neuropathic rat. *Brain Res. Bull.* 89, 133–143. doi: 10.1016/j.brainresbull.2012.08.002

Volz, M. S., Volz, T. S., Brunoni, A. R., de Oliveira, J. P. V. T., and Fregni, F. (2012). Analgesic effects of noninvasive brain stimulation in rodent animal models: a systematic review of translational findings. *Neuromodulation* 15, 283–295. doi: 10.1111/j.1525-1403.2012.00478.x

Woods, A. J., Antal, A., Bikson, M., Boggio, P. S., Brunoni, A. R., Celnik, P., et al. (2016). A technical guide to tDCS, and related non-invasive brain stimulation tools. *Clin. Neurophysiol.* 127, 1031–1048. doi: 10.1016/j.clinph.2015.11.012

Xiao, Z., Ou, S., He, W., Zhao, Y., Liu, X., and Ruan, H. (2010). Role of midbrain periaqueductal gray P2X3 receptors in electroacupuncture-mediated endogenous pain modulatory systems. *Brain Res.* 1330, 31–44. doi: 10.1016/j.brainres.2010.03.030

Xie, Y.-F., Huo, F.-Q., and Tang, J.-S. (2009). Cerebral cortex modulation of pain. *Acta Pharmacol. Sin.* 30, 31–41. doi: 10.1038/aps.2008.14

Young, N. A., Sharma, M., and Deogaonkar, M. (2014). Transcranial magnetic stimulation for chronic pain. *Neurosurg. Clin. N. Am.* 25, 819–832. doi: 10.1016/j.nec.2014.07.007

Yu, X., Li, Y., Wen, H., Zhang, Y., and Tian, X. (2015). Intensity-dependent effects of repetitive anodal transcranial direct current stimulation on learning and memory in a rat model of Alzheimer's disease. *Neurobiol. Learn. Mem.* 123, 168–178. doi: 10.1016/j.nlm.2015.06.003

Zaghi, S., Heine, N., and Fregni, F. (2009). Brain stimulation for the treatment of pain: a review of costs, clinical effects, and mechanisms of treatment for three different central neuromodulatory approaches. *J. Pain Manag.* 2, 339–352.

Zhuo, M. (2008). Cortical excitation and chronic pain. *Trends Neurosci.* 31, 199–207. doi: 10.1016/j.tins.2008.01.003

Zhuo, M. (2013). Long-term potentiation in the anterior cingulate cortex and chronic pain. *Philos. Trans. R. Soc. Lond. B Biol. Sci.* 369:20130146. doi: 10.1098/rstb.2013.0146

Zimmermann, M. (1983). Ethical guidelines for investigations of experimental pain in conscious animals. *Pain* 16, 109–110. doi: 10.1016/0304-3959(83)90201-4

Conflict of Interest Statement: The authors declare that the research was conducted in the absence of any commercial or financial relationships that could be construed as a potential conflict of interest.

Copyright © 2017 Wen, Gao, Zhao, He, Tian and Ruan. This is an open-access article distributed under the terms of the Creative Commons Attribution License (CC BY). The use, distribution or reproduction in other forums is permitted, provided the original author(s) or licensor are credited and that the original publication in this journal is cited, in accordance with accepted academic practice. No use, distribution or reproduction is permitted which does not comply with these terms.

frontiers in Neuroscience

ORIGINAL RESEARCH
published: 19 June 2017
doi: 10.3389/fnins.2017.00346

Hypotensive Response to Angiotensin II Type 2 Receptor Stimulation in the Rostral Ventrolateral Medulla Requires Functional GABA-A Receptors

Laura Légat[1,2,3]*, *Sofie Brouwers*[1,2,3], *Ilse J. Smolders*[1] and *Alain G. Dupont*[1,2,3]

[1] Laboratory of Pharmaceutical Chemistry, Drug Analysis and Drug Information (FASC), Research Group Experimental Pharmacology (EFAR), Center for Neurosciences (C4N), Vrije Universiteit Brussel, Brussels, Belgium, [2] Cardiovascular Center, Universitair Ziekenhuis Brussel, Brussels, Belgium, [3] Department of Clinical Pharmacology and Clinical Pharmacy, Universitair Ziekenhuis Brussel, Brussels, Belgium

Objectives: Angiotensin II, glutamate and gamma-aminobutyric acid (GABA) interact within the rostral ventrolateral medulla (RVLM) and the paraventricular nucleus (PVN) modulating the central regulation of blood pressure and sympathetic tone. Our aim was to assess the effects of local angiotensin II type 2 receptor stimulation within the RVLM and the PVN on neurotransmitter concentrations and mean arterial pressure (MAP).

Methods: *In vivo* microdialysis was used for measurement of extracellular glutamate and GABA levels and for local infusion of the angiotensin II type 2 receptor agonist Compound 21 in the RVLM and the PVN of conscious normotensive Wistar rats. The MAP response to local Compound 21 was monitored with a pressure transducer under anaesthesia. Angiotensin II type 2 receptor selectivity was assessed using the angiotensin II type 2 receptor antagonist PD123319; the GABA-A receptor antagonist bicuculline was used to assess the involvement of GABA-A receptors.

Results: Infusion of Compound 21 (0.05 μg/μl/h) in the RVLM significantly increased GABA levels and lowered blood pressure. These effects were abolished by co-infusion with PD123319. No changes in neurotransmitter levels or effects on blood pressure were seen with PD123319 infusion alone. Co-infusion of bicuculline abolished the Compound 21 evoked decrease in MAP. Infusion of Compound 21 within the PVN did not change extracellular neurotransmitter levels nor MAP.

Conclusion: Selective stimulation of angiotensin II type 2 receptor within the RVLM by local Compound 21 infusion reduces blood pressure and increases local GABA levels in normotensive rats. This hypotensive response requires functional GABA-A receptors, suggesting that GABAergic neurons are involved in the sympatho-inhibitory action underlying this hypotensive response.

Keywords: renin-angiotensin-system, angiotensin II type 2 receptor, compound 21, mean arterial pressure, gamma-aminobutyric acid, rostral ventrolateral medulla

OPEN ACCESS

Edited by:
Brian R. Noga,
University of Miami, United States

Reviewed by:
Enrico Sanna,
Università degli studi di Cagliari, Italy
Petra Scholze,
Medical University of Vienna, Austria

***Correspondence:**
Laura Légat
laura.legat@vub.be

Specialty section:
This article was submitted to Neuropharmacology, a section of the journal Frontiers in Neuroscience

Received: *28 October 2016*
Accepted: *02 June 2017*
Published: *19 June 2017*

Citation:
Légat L, Brouwers S, Smolders IJ and Dupont AG (2017) Hypotensive Response to Angiotensin II Type 2 Receptor Stimulation in the Rostral Ventrolateral Medulla Requires Functional GABA-A Receptors. Front. Neurosci. 11:346. doi: 10.3389/fnins.2017.00346

INTRODUCTION

Angiotensin II (Ang II) is the most important effector within the renin-angiotensin-aldosterone system (RAAS), mediating its actions through the angiotensin II type 1 receptors (AT1R), and angiotensin II type 2 receptors (AT2R). Activation of the AT1R mediates most known effects of Ang II, such as vasoconstriction, renal sodium retention, promotion of inflammatory responses, vascular smooth muscle cell proliferation and hypertrophy. The AT2R counteracts these AT1R effects and mediates vasodilation, apoptosis, natriuresis and anti-inflammatory, anti-proliferative and anti-fibrotic responses (de Gasparo et al., 2000; Padia and Carey, 2013). It has been demonstrated that activation of the AT2R, part of the "protective arm" of the RAAS, leads to therapeutic protective effects against myocardial and brain injury (Namsolleck et al., 2014). Despite the fact that AT2R stimulation causes vasodilation *ex* and *in vivo,* due to the dominating AT1R mediated vasoconstrictor tone, peripheral AT2R stimulation *in vivo* does not cause lowering in blood pressure (Steckelings et al., 2012).

The brain RAAS plays a major role in the regulation of blood pressure and sympathetic tone and that brain Ang II induces tonic sympatho-excitatory effects resulting in blood pressure increases through stimulation of central AT1R (Guyenet, 2006; Dupont and Brouwers, 2010). However, the possible role of the central AT2R herein are incompletely understood although recent data support the involvement of central AT2Rs in the regulation of blood pressure and sympathetic tone (Gao and Zucker, 2011; Li et al., 2012). Intracerebroventricular (icv) injection of Ang II in AT2R-knockout mice was reported to result in a larger increase in blood pressure compared to wild type mice, suggesting a counter-regulatory protective role of brain AT2R in the regulation of blood pressure (Siragy et al., 1999; Li et al., 2003).

The development of the first orally active, selective, non-peptide agonist of the AT2R, Compound 21 (C21) offers the possibility to selectively and specifically investigate AT2R mediated effects (Wan et al., 2004; Steckelings et al., 2011). C21 was reported to induce cardio-, cerebro-, and nephroprotective as well as anti-inflammatory effects in different animal models. Although we, as others, could not demonstrate a putative hypotensive response after peripheral administration of a range of different doses of C21, with or without concomitant AT1R blockade (Yang et al., 2011; Brouwers et al., 2013, 2015), we did observe significant blood pressure decreases after chronic icv infusion of C21 (Yang et al., 2011; Brouwers et al., 2015). Specific and selective stimulation of brain AT2R with C21 evoked a sustained hypotensive response not only in normotensive but also in spontaneously hypertensive rats *in vivo*. In addition, we observed that this hypotensive response was associated with sympatho-inhibition and increased spontaneous baroreflex sensitivity (Steckelings et al., 2012; Brouwers et al., 2015).

The central regulation of blood pressure involves different parts of the brain. However, the most important site within the brainstem, involved in the short- and longterm central regulation of the blood pressure is the rostral ventrolateral medulla (RVLM) region, the so-called "pressor area," which is responsible for the sympathetic drive. The RVLM receives inputs from multiple integrative areas in the hypothalamus and the medulla and is the main region from which the sympathetic outflow from the brain originates (Guyenet, 2006; Dupont and Brouwers, 2010). The neurons in the paraventricular nucleus (PVN) of the hypothalamus have projections to the RVLM and are also known to significantly affect sympathetic output indirectly through modulation of the neurons within the RVLM region (Guyenet, 2006; Dupont and Brouwers, 2010). Therefore, the RVLM and the PVN are generally considered the two most appropriate sites to study the central regulation of sympathetic activity. Neuronal excitability in the RVLM and the PVN are mainly modulated by the "classical" excitatory and inhibitory neurotransmitters, glutamate and gamma-aminobutyric acid (GABA), respectively (Miyawaki et al., 1996; Butcher and Cechetto, 1998; Tasker et al., 1998; Li et al., 2006; Hatam and Ganjkhani, 2012).

Brain Ang II, acting through AT1R, increases the sympathetic outflow through stimulation of glutamatergic neurons in the RVLM (Dupont and Brouwers, 2010). The presence of AT2R in the RVLM opposing the effect of neuronal stimulation through the AT1R has also been demonstrated (Gao et al., 2008a). Current evidence suggests that AT2R in the RVLM may mediate a sympatho-inhibitory effect (Gao et al., 2008a,b). Brain angiotensin peptides, glutamate and GABA appear to interact within the RVLM and the PVN to regulate sympathetic tone and blood pressure (Li et al., 2006; Dupont and Brouwers, 2010).

In the present study we aimed to further investigate the possible role of AT2R located within the RVLM-PVN axis and their interaction with glutamate and GABA in the central regulation of blood pressure. We therefore assessed blood pressure changes and possible effects on local glutamate and GABA concentrations in response to local unilateral administration of C21 within the RVLM and the PVN through microdialysis.

MATERIALS AND METHODS

Animals

All experiments were carried out on normotensive male albino Wistar rats (Charles River Laboratories, France) weighing between 250 and 300 g. Animals were kept in the animal house of the Vrije Universiteit Brussel minimum 1 week before surgery at constant temperature (24°C) and relative humidity (50%) with 12 h light-dark cycle and had *ad libitum* food and water. All protocols used and described for animal experiments on rats ($n = 4$–9 per experimental group) were carried out according to the National and European guidelines for animal experimental research and were approved by the Ethical Committee for Animal Experiments of the Faculty of Medicine and Pharmacy of the VUB. All possible steps were taken to avoid animals' suffering at each stage of the experiment.

Drugs

S-(+)-1-[(4-(Dimethylamino)-3-methylphenyl)methyl]-5-(diphenylacetyl)-4,5,6,7-tetrahydro-1H-imidazo[4,5-c]pyridine-6-carboxylic acid di(trifluoroacetate) salt hydrate (PD123319) and bicuculline were purchased form Sigma-Aldrich Co. (St.

Louis, USA). Compound 21 (C21) was provided by Vicore Pharma AB (Göteborg, Sweden). Doses of C21, PD133319 and bicuculline were selected based on previous studies (Smolders et al., 1995a; Brouwers et al., 2015).

Experimental Protocol

Normotensive Wistar rats were first subjected to brain surgery, as described in "*surgical procedures*" for implantation of a guide cannula. The following day, samples were collected through *in vivo* microdialysis on freely moving rats allowing us to measure neurotransmitters at many time points in each animal. All dialysis samples were analyzed by high performance liquid chromatography for measurement of glutamate and GABA levels. On day three, the same rats as used for microdialysis experiments were anaesthetized in order to cannulate the right carotid artery for continuous monitoring of mean arterial pressure (MAP) with a pressure transducer and the pharmacological experiments were repeated.

Post-mortem evaluation was done after each experiment in order to exclude animals with inaccurately implanted probes.

Surgical Procedures

Animals were anaesthetized prior to surgery with a ketamine/diazepam mixture (90/4.5 mg/kg) intraperitoneally and received ketoprofen (4 mg/kg) subcutaneously. A stainless steel cannula (CMA12, Solna, Sweden) was stereotaxically implanted into the left RVLM (AP: −2.2, L: −12.3, V: 7) or left PVN (AP: −0.5, L: −1.8, V: 7), according to the atlas of Paxinos and Watson (1998) and fixed with dental cement.

In vivo Microdialysis

After overnight recovery, rats were single housed in experimental cages and the microdialysis probe (CMA12/1 mm membrane length, Solna, Zweden) was inserted into the guide-cannula. For collection of basal brain dialysates, the microdialysis probe was continuously perfused at a flow rate of 2 μl/min with modified Ringer's solution (147 mM NaCl, 2.3 mM $CaCl_2$, 4 mM KCl). Samples were collected with a temporal resolution of 20 min and split into two aliquots of 15 μl. The experiment proceeded through perfusion with modified Ringer's solution for 120 min. Consecutively, one of the treatments at a rate of 2 μl/min: [C21 (0.05 μg/μl/h), PD123319 (0.05 μg/μl/h) or C21 (0.05 μg/μl/h) + PD123319 (0.05 μg/μl/h)] were dissolved in modified Ringer's solution and perfused through the microdialysis probe for 120 min and finally modified Ringer's solution for 120 min. Samples were stored at −20°C and thawed prior to analysis.

Determination of Glutamate and GABA Dialysate Levels via Liquid Chromatography

Two distinct chromatographic systems were used in the present study to determine glutamate and GABA dialysate levels following there derivatization with o-phtalaldehyde and β-mercapto-ethanol or tert-butylthiol respectively. Glutamate concentrations were determined using reversed-phase narrowbore liquid chromatography with gradient elution and fluorescence detection as described previously (Smolders et al., 1995b), while GABA was analyzed by reversed-phase microbore liquid chromatography with isocratic elution and electrochemical detection as described in detail in Van Hemelrijck et al. (2005).

Mean Arterial Pressure (MAP) Measurements

Animals were anaesthetized prior to surgery by 4% sevoflurane gas, and during surgery anaesthesia was maintained by 2.5% sevoflurane administration. The right jugular vein was catheterized for fluid maintenance (saline 0.9%), and the right carotid artery was cannulated for continuous monitoring of MAP with a pressure transducer (HP Hewlett Packard, Boebingen, Germany). The experimental protocol started after a 30 min equilibration period following surgery in order to record baseline values before the administration of the pharmacological compounds. The experiment proceeded through perfusion of modified Ringer's solution for 30 min. Consecutively, one of the treatments at a rate of 2 μl/min: [C21 (0.05 μg/μl/h), PD123319 (0.05 μg/μl/h), bicuculline (100 μM), C21 (0.05 μg/μl/h) + PD123319 (0.05 μg/μl/h) or C21 (0.05 μg/μl/h) + bicuculline (100 μM)] were dissolved in modified Ringer's solution and perfused through the microdialysis probe for 120 min, and finally modified Ringer's solution for 30 min.

Post-mortem Evaluation

At the end of every experiment, rats were killed by an overdose of Nembutal. In order to fix the brain, perfusing was performed by 4% paraformaldehyde solution and removed brains were preserved on formol. After slicing brain tissue, probe localization and tissue damage were histologically verified and evaluated post-mortem by a neutral red staining in order to exclude animals with inaccurately implanted probes.

Statistical Analysis

Data are expressed as mean ± standard error of the mean (SEM), all calculations and graphs were obtained using Graphpad Prism 4.03 (Graphpad Software Inc., San Diego, CA, USA). The mean values of the basal microdialysis samples obtained before drug administration were considered as the 100% baseline value for each animal. All neurotransmitter (glutamate and GABA) results were expressed as percentages of this baseline value ± SEM. All MAP measurements are shown as the MAP by SEM. For determination of intragroup differences of the treatment an one-way ANOVA for repeated measures followed by *post-hoc* Dunnett's multiple comparison test was used. Subsequently, for the microdialysis results, an area under the curve (AUC) analysis was performed to determine if there was an overall difference in neurotransmitter (glutamate and GABA) concentrations between different compounds. AUC values, expressed in arbitrary units, were compared by a Kruskal Wallis test with Dunn's multiple comparison *post-hoc* test. A value of $p < 0.05$ was considered to be statistically significant.

RESULTS

AT2R-Mediated Changes in Neurotransmitter Concentrations in the RVLM

The baseline values for glutamate and GABA in the microdialysis samples of the RVLM were 432 ± 219 nM for glutamate and 10 ± 5 nM for GABA in the group receiving 0.01 μg/μl/h C21 (data not shown), and 44±12 nM for glutamate (**Figure 1A**) ($n = 4$) and 3 ± 1 nM for GABA (**Figure 1B**) ($n = 6$) in the group receiving 0.05 μg/μl/h C21. No changes from baseline levels were seen for glutamate or GABA levels during infusion of C21 (0.01 μg/μl/h) within the RVLM (data not shown). Infusion of the higher dose of C21 (0.05 μg/μl/h) within RVLM significantly increased GABA levels ($p < 0.05$; **Figure 1B**) but tended to decrease glutamate levels (**Figure 1A**), with a subsequent return to baseline levels for both transmitters after switching the infusion again to Ringer's solution alone.

In the group receiving 0.05 μg/μl/h PD123319 alone, average baseline dialysate concentrations of the RVLM were 354 ± 9 nM for glutamate and 8 ± 6 nM for GABA (data not shown). These values were not significantly different from the mean baseline levels during infusion with the AT2R antagonist.

In the group receiving 0.05 μg/μl/h C21 with PD123319, baseline concentrations were 113 ± 17 nM for glutamate (**Figure 1A**) ($n = 4$) and 14 ± 1 nM for GABA (**Figure 1B**) ($n = 5$). Neurotransmitter concentrations during co-infusion of C21 + PD123319 were not significantly different from the mean baseline levels. Co- infusion of the AT2R antagonist, PD123319 (0.05 μg/μl/h) with C21 (0.05 μg/μl/h) thus abolished the C21-evoked increase in GABA concentrations (**Figure 1B**).

Figure 2 shows the AUC values of glutamate and GABA dialysate levels under C21 infusion compared to vehicle infusion. AUC of glutamate levels (**Figure 2A**) ($n = 4$) did not significantly change under C21 (0.05 μg/μl/h) infusion or under C21 + PD123319 (0.05 μg/μl/h) infusion (**Figure 2C**) ($n = 4$). However, GABA levels (**Figure 2B**) ($n = 6$) significantly ($p < 0.05$) increased under C21 (0.05 μg/μl/h) infusion compared to baseline values. This increase in GABA levels mediated by C21 infusion was abolished by co-infusion with PD123319 (**Figure 2D**) ($n = 5$).

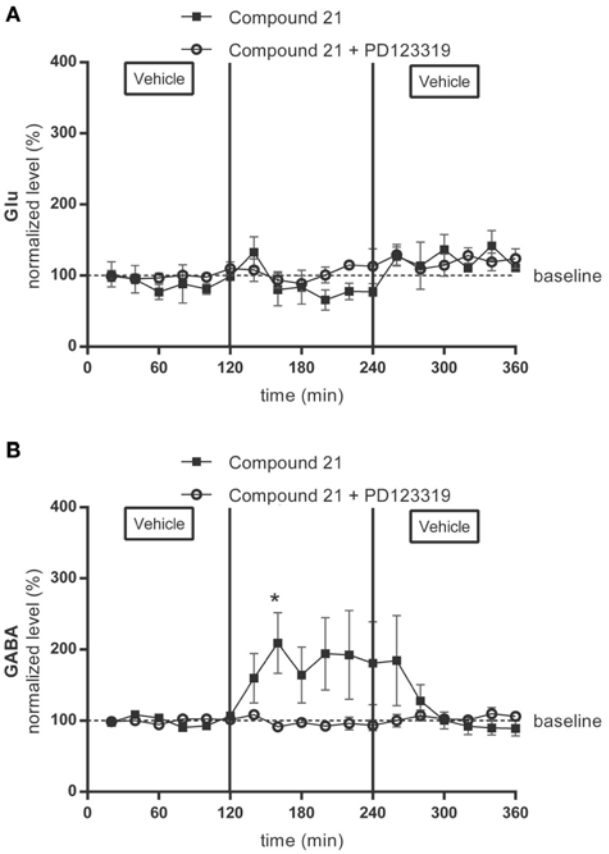


FIGURE 1 | Microdialysis experiment: effect of AT2R stimulation and infusion of the AT2R agonist C21 alone (0.05 μg/μl/h) on the extracellular glutamate (Glu) **(A)** ($n = 4$) and GABA **(B)** ($n = 6$) concentrations and of co-infusion of C21 with the AT2R antagonist PD123319 (0.05 μg/μl/h) on the extracellular glutamate (Glu) **(A)** ($n = 4$) and GABA **(B)** ($n = 5$) concentrations in the RVLM in normotensive freely moving Wistar rats. Dialysates were collected every 20 min. C21 and C21 + PD123319 were dissolved in modified Ringer's solution and administered through the dialysis probe from time 120 to 240 min. Data are presented as the mean percentage of the baseline values (vehicle) ± SEM. Statistical analysis for intragroup differences of the treatment is performed using one-way ANOVA for repeated measures and the Dunnett's multiple comparison test; significant data compared to basal levels are indicated by asterisks (*$p < 0.05$).

Lack of AT2R-Mediated Changes on Neurotransmitter Concentrations in the PVN

Average baseline extracellular concentrations in the microdialysis samples of the PVN were 198 ± 107 nM for glutamate (**Figure 3A**) ($n = 4$) and 5 ± 4 nM for GABA (**Figure 3B**) ($n = 4$). Glutamate and GABA levels were not significantly altered by local infusion of C21 (0.05 μg/μl/h) (**Figures 3A**,**B**).

AT2R-Mediated MAP Response to C21 Infusion into the RVLM

Baseline MAP in Wistar rats were 96 ± 10 mmHg for the group receiving 0.01 μg/μl/h C21 (data not shown), and 103 ± 8 mmHg for the group receiving 0.05 μg/μl/h C21 (**Figure 4A**) ($n = 6$). Infusion of low dose C21 (0.01 μg/μl/h) within the RVLM did not change MAP (data not shown). Infusion of C21 into the RVLM for 120 min at a dose of 0.05 μg/μl/h significantly lowered MAP (-7 mmHg compared to baseline after 20 min of C21 infusion, $p < 0.01$; −6 mmHg after 40 min, $p < 0.05$) (**Figure 4A**).

Local infusion of PD123319 alone (0.05 μg/μl/h) did not modify the baseline MAP (94 ± 15 mmHg; **Figure 4A**) ($n = 9$).

Baseline MAP in the group of rats receiving co-infusion of C21 with PD123319 were 107 ± 7 mmHg (**Figure 4A**) ($n = 4$). Co-infusion of the AT2R antagonist PD123319 with C21 (0.05 μg/μl/h) abolished the C21 evoked decrease in MAP (**Figure 4A**).

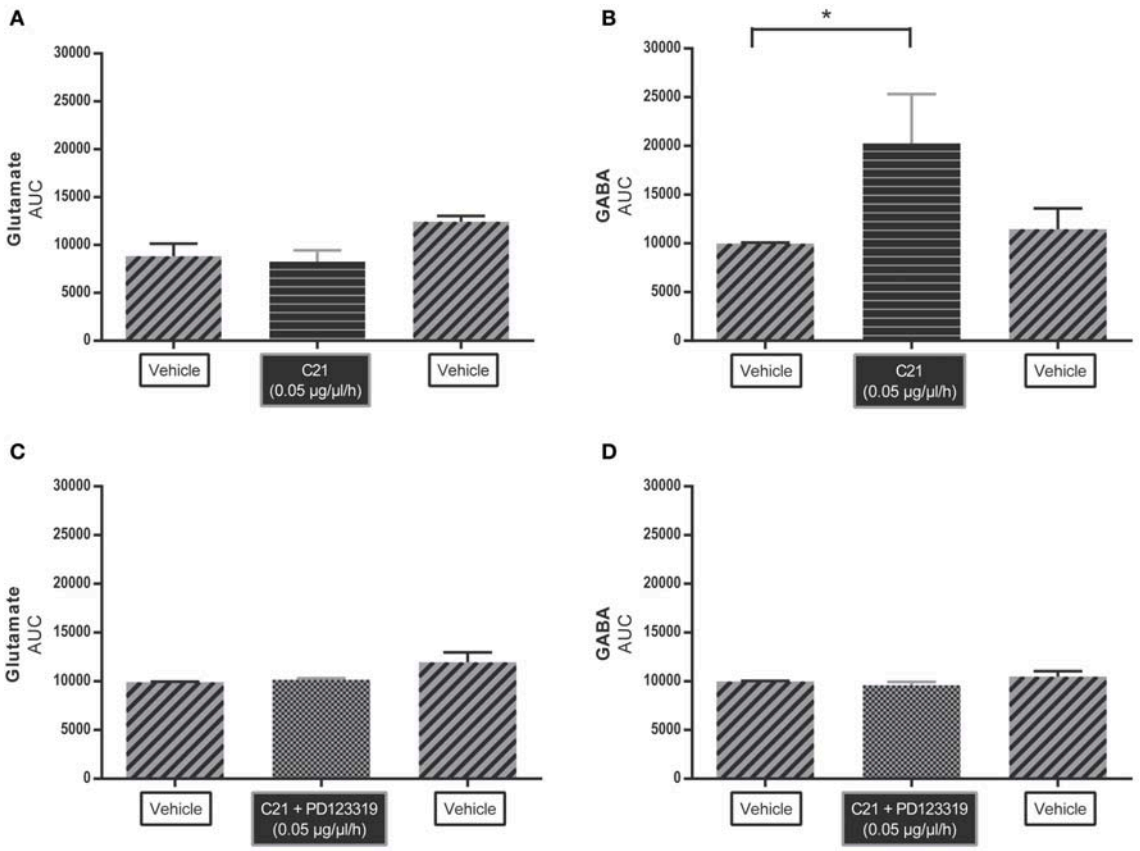


FIGURE 2 | Microdialysis experiment: area under the curve (AUC) values of C21 alone **(A)** ($n = 4$) and **(B)** ($n = 6$) and in co-infusion with PD123319 **(C)** ($n = 4$) and **(D)** ($n = 5$) applied by microdialysis into the RVLM in normotensive freely moving Wistar rats on extracellular levels of glutamate **(A,C)** and GABA **(B,D)**. Data are represented as the mean AUC ± SEM. Statistical analysis for overall differences in neurotransmitter (glutamate and GABA) concentrations between different compounds is performed using Kruskal Wallis test with Dunn's multiple comparison test; significant data are indicated by asterisks (*$p < 0.05$).

Baseline MAP in the group of rats receiving co-infusion of C21 (0.05 µg/µl/h) with bicuculline were 89 ± 9 mmHg (**Figure 4B**) ($n = 7$). Co-infusion of the GABA-A antagonist bicuculline with C21 (0.05 µg/µl/h) abolished the C21 evoked decrease in MAP (**Figure 4B**).

Lack of Blood Pressure Response to C21 Infusion into the PVN

Local infusion of C21 (0.05 µg/µl/h) into the PVN did not change baseline MAP (96 ± 8 mmHg; **Figure 5**; $n = 5$).

DISCUSSION

Although there is increasing evidence for a neuro- and cardioprotective role of the AT2R, several studies have indicated that stimulation of peripheral AT2R does not result in consistent blood pressure lowering effects (Yang et al., 2011; Steckelings et al., 2012; Brouwers et al., 2013; Matavelli and Siragy, 2015; Sumners et al., 2015). However, we recently demonstrated that icv infusion of the selective AT2R agonist C21 evoked a sustained hypotensive response in both normotensive and hypertensive rats, and that this central AT2R mediated hypotensive response is associated with sympatho-inhibition and increased baroreflex sensitivity (Brouwers et al., 2015), confirming and extending earlier results with icv administration of C21 in conscious normotensive Sprague-Dawley rats (Gao et al., 2011). Similar infusions in rats with heart failure also suppress sympathetic outflow by improving baroreflex sensitivity (Gao et al., 2014).

The major novel finding of the present study in male normotensive rats is that the hypotensive response to central administration of the selective non-peptide AT2R agonist C21 appears to be mediated at least in part by stimulation of AT2R located in the RVLM, whereas putative AT2R stimulation in the PVN does not seem to be involved. Indeed, local administration of C21 via microdialysis into the PVN did not alter local extracellular fluid neurotransmitter concentrations and did not reduce blood pressure. However, microdialysis administration of C21 into the RVLM resulted in a consistent blood pressure lowering effect and a significant increase in local GABA concentrations, and tended to decrease local glutamate concentrations. Moreover, these responses to local administration of C21 into the RVLM were abolished by local co-infusion with the selective AT2R antagonist PD123319

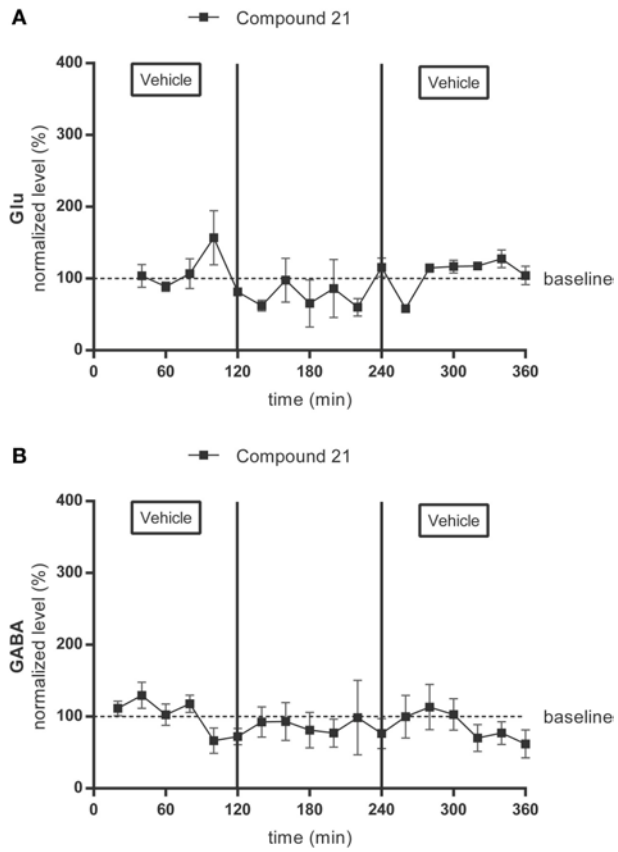


FIGURE 3 | Microdialysis experiment: effect of infusion with the AT2R agonist C21 (0.05 μg/μl/h) on the extracellular glutamate (Glu) **(A)** ($n = 4$) and GABA **(B)** ($n = 4$) concentrations in the PVN in normotensive freely moving Wistar rats. Dialysates were collected every 20 min. C21 was dissolved in modified Ringer's solution and administered through the dialysis probe from time 120 to 240 min. Data are presented as the mean percentage of the baseline values (vehicle) ± SEM. Statistical analysis for intragroup differences of the treatment is performed using one-way ANOVA for repeated measures and the Dunnett's multiple comparison test.

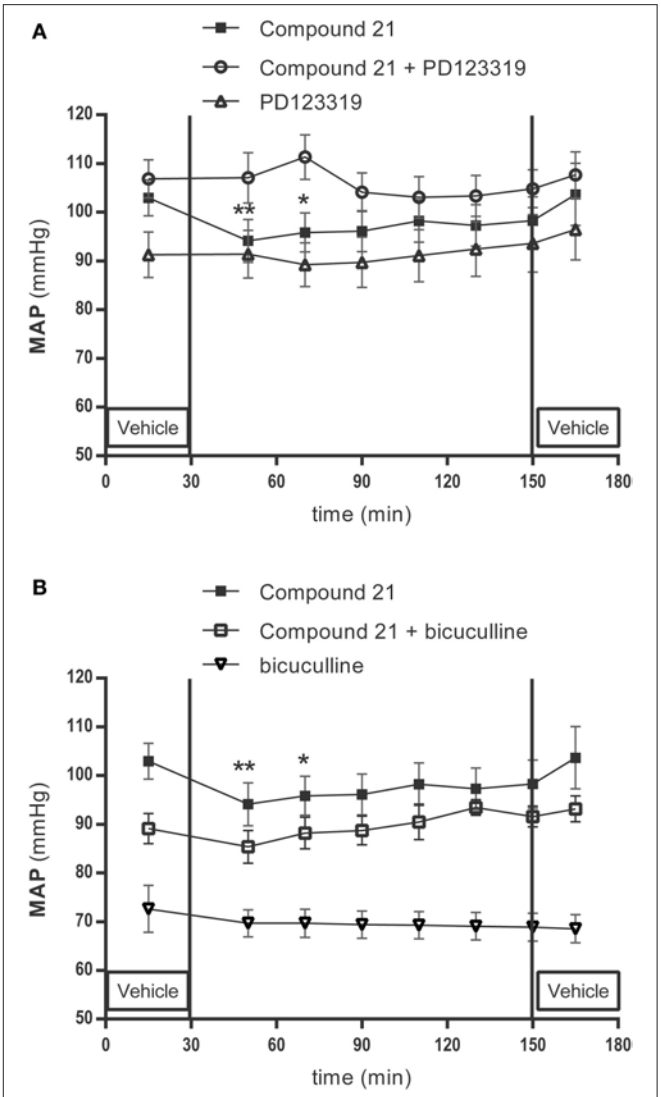


FIGURE 4 | Mean arterial pressure (MAP) measurement experiment: effect of infusion in the RVLM with the AT2R agonist C21 (0.05 μg/μl/h) ($n = 6$), co-infusion of C21 with the AT2R antagonist PD123319 (0.05 μg/μl/h) ($n = 4$) and infusion of PD123319 (0.05 μg/μl/h) alone ($n = 9$) **(A)**; C21 (0.05 μg/μl/h) infusion alone, co-infusion of C21 (0.05 μg/μl/h) with the GABA-A R antagonist bicuculline (100μM) ($n = 7$), or infusion of bicuculline alone ($n = 4$) **(B)** on MAP in normotensive anesthetized Wistar rats. MAP was recorded every 2 s. C21, PD123319 and bicuculline were dissolved in modified Ringer's solution and administered through the dialysis probe from time 30 to 150 min. Data are shown as mean ± SEM. Statistical analysis for intragroup differences of the treatment is performed using one-way ANOVA for repeated measures and the Dunnett's multiple comparison test; significant data compared to the mean of baseline values are indicated by asterisks (*$p < 0.05$; **$p < 0.01$).

confirming that these responses are AT2R-mediated. There was some variation in baseline mean blood pressure between different groups of rats, which is not unusual in anesthetized rats from different batches. However, the reduction in mean blood pressure was very consistent and occurred in all animals at the same moment after starting the infusion of C21, with a return to baseline blood pressure levels after stopping the infusion. The absence of this effect of C21 in animals co-infused with either PD123319 or bicuculline was also consistent in all animals.

It is of interest to note that, whereas the effects of local administration of C21 were abolished by PD123319, indicating that exogenous stimulation of AT2R in the RVLM in normotensive rats results in a hypotensive response, local administration of PD123319 alone had no effect on blood pressure nor on neurotransmitter levels, suggesting that endogenous activation of AT2R in the RVLM is not involved in the regulation of blood pressure under basal conditions. This in line with our previously reported observations after icv infusion of C21 (Brouwers et al., 2015), and with those of Dai et al. (2015, 2016) who also reported that icv infusion of the AT2R antagonist had no effect on basal blood pressure. These authors further suggested that endogenous AT2R activation in the brain protects against the development of DOCA/salt induced hypertension in female, but not in male rats (Dai et al., 2015, 2016).

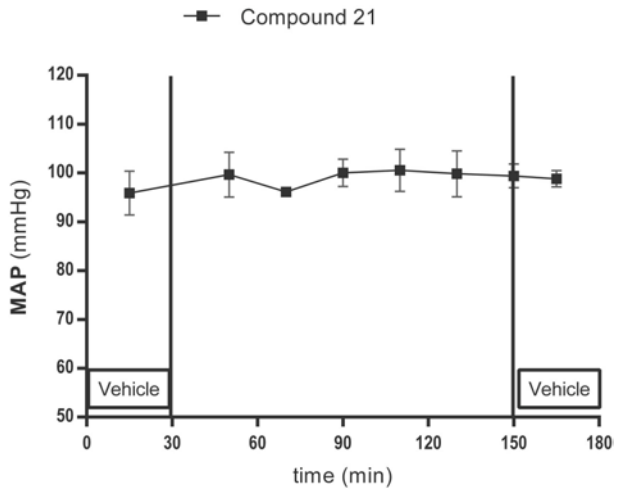


FIGURE 5 | Mean arterial pressure (MAP) measurement experiment: lack of effect of AT2R stimulation and infusion with the AT2R agonist C21(0.05 μg/μl/h) in the PVN on MAP in normotensive anesthetized Wistar rats ($n = 5$). MAP was recorded every 2 s. C21 was dissolved in modified Ringer's solution and administered through the dialysis probe from time 30 to 150 min. Data are shown as mean ± SEM. Statistical analysis for intragroup differences of the treatment is performed using one-way ANOVA for repeated measures and the Dunnett's multiple comparison test.

Most studies on central regulation of blood pressure target the RVLM, the PVN of the hypothalamus and the nucleus tractus solitarii (NTS) (Dampney et al., 2003; Guyenet, 2006; Dupont and Brouwers, 2010). The RVLM receives mainly tonic excitatory signal projections from neurons in the PVN. The RVLM presympathetic neurons, the major source of sympatho-excitatory outflow from the brain, project to sympathetic preganglionic neurons in the spinal cord (Sun et al., 1988; Pan, 2004; Kantzides and Badoer, 2005; Dupont and Brouwers, 2010). The excitatory drive from the RVLM originates from glutamatergic neurons (Ross et al., 1984; Guyenet et al., 2004; Dupont and Brouwers, 2010), which are tonically active under resting conditions but can be modulated by both excitatory and inhibitory synaptic inputs (Dampney et al., 2003). The neuronal activity of the RVLM region is modulated indirectly by input from the NTS, where baroreceptor afferents terminate, by the PVN, and by the caudal ventrolateral medulla (CVLM), which has an inhibitory influence on RVLM neurons (Schreihofer and Guyenet, 2002; Dupont and Brouwers, 2010). Therefore, the RVLM region is considered the most important site in the central regulation of sympathetic tone and blood pressure (Pointer, 2005; Guyenet, 2006; Dupont and Brouwers, 2010).

Several studies have indicated that the hypertensive response and the increased sympathetic tone evoked by central Ang II administration involves the activation of AT1R on spinally projecting glutamatergic vasomotor neurons located in the RVLM, which then further directly or indirectly elevate the sympathetic outflow (Hu et al., 1985; Dupont and Brouwers, 2010).

Although initial studies using receptor binding techniques and autoradiography studies suggested that central nervous system (CNS) cardiovascular control areas in the brainstem such as the RVLM are devoid of or only express low levels of AT2R (Millan et al., 1991; Lenkei et al., 1997; Hu et al., 1985), observations made in earlier functional studies did support a role for AT2R within the RVLM. Gao et al suggested that AT2R in the RVLM exhibit an inhibitory effect on sympathetic outflow and suggested down-regulation of AT2R in the RVLM as a contributory factor in the sympatho-excitation in congestive heart failure (Gao et al., 2008b). The same group further reported that overexpression of AT2R within the RVLM in normotensive rats reduced blood pressure, probably by sympatho-inhibition (Gao et al., 2008a). Further, Tedesco and Ally reported that the pressor and tachycardic responses to static muscle contraction were enhanced by selective blockade of AT2R in the RVLM in anaesthetized rats (Tedesco and Ally, 2009). In addition, electrophysiological studies in AT1Ra knockout mice suggest that AT2R play an antagonistic role against AT1R mediated actions of Ang II through AT2R mediated hyperpolarization and decrease in firing rate in bulbospinal RVLM neurons (Matsuura et al., 2005). The results of the present study in male normotensive rats validate and extend the results of these earlier studies and support the hypothesis that functional AT2R are present within the RVLM of normotensive rats and that their selective stimulation mediates a blood pressure lowering response probably mediated by sympatho-inhibition.

The results are also in line with those of a recent study that used a reporter mouse strain to provide an in-depth analysis of cellular and regional localization of AT2R in the mouse brain (de Kloet et al., 2016b). These investigations showed that AT2R are present in or near different brain sites involved in blood pressure regulation. These authors did not observe AT2R positive neurons within the PVN, which is in line with our observation that local administration of C21 within the PVN had no effect on blood pressure and neurotransmitter levels, confirming the absence of functional AT2R within the PVN. However, they found indications that AT2R are localized on efferents terminating in the PVN and within GABAergic neurons surrounding this nucleus (de Kloet et al., 2016b). They further reported that patch-clamp electrophysiological experiments revealed that selective activation of AT2R not within the PVN but in the peri-PVN area using C21 facilitates inhibitory (i.e., GABAergic) neurotransmission and leads to reduced activity of arginine vasopressin neurons within the PVN (de Kloet et al., 2016a,b).

Although not many AT2R were observed on neuronal cell bodies within the RVLM, de Kloet et al reported that the RVLM (and also the CLVM) are densely populated with AT2R positive nerve terminals/fibers (de Kloet et al., 2016b). It is therefore possible that presynaptic AT2R are expressed on nerve terminals within the RVLM and that their activation may influence neurotransmitter release from these terminals.

Of particular interest is also the observation by de Kloet et al. that AT2R containing neurons in the hindbrain are primarily GABAergic (de Kloet et al., 2016b). This may be important as GABA is known to have potent inhibitory actions within the RVLM (Menezes and Fontes, 2007). Projections of

inhibitory GABAergic neurons to the RVLM region decrease its output to the sympathetic preganglionic regions. The CVLM which receives input from the NTS that is stimulated following blood pressure elevation, is one of the important sources of GABA (Blessing and Li, 1989; Dampney et al., 2003; Dupont and Brouwers, 2010). It was previously shown that the tonic excitatory AT1R mediated effect of Ang II on RVLM sympatho-excitatory neurons in normotensive animals is unmasked when tonic inhibitory GABAergic output is blocked (Tagawa et al., 2000). These and other observations suggest that the overall AT1R mediated effect on sympathetic tone of brain Ang II may depend on a balance between the activation of excitatory glutamatergic neurons and the inhibitory GABAergic neurons, which are both known to express AT1R (Dupont and Brouwers, 2010). Pharmacological blockade of GABA-A receptors in the sympathoexcitatory region of the RVLM has previously been shown to almost entirely eliminate the action of caudal inhibitory vasomotor neurons resulting in increased sympathetic tone and blood pressure (Blessing and Li, 1989; Tagawa et al., 2000), whereas GABA-A receptor stimulation in the RVLM lowered blood pressure (Menezes and Fontes, 2007) indicating a functional sympatho-inhibitory role for GABA-A receptors within the RVLM, in contrast to GABA-B receptors, the stimulation of which does not reduce blood pressure (Menezes and Fontes, 2007).

It is therefore tempting to speculate that the hypotensive response to local administration of C21 within the RVLM observed in the present study might be mediated by stimulation of presynaptic AT2R located on inhibitory GABAergic nerve terminals resulting in increased GABA release and subsequent GABA-A receptor-mediated reduction in sympathetic tone. Our observations of a significant increase in local GABA concentration after C21 administration, which was also abolished by co-infusion of the AT2R antagonist, and that the hypotensive response was equally abolished by local administration of the GABA-A receptor antagonist bicuculline, are in line with this hypothesis.

In addition, nitric oxide may also be involved in the observed increase in GABA within the RVLM. Nitric oxide is indeed also an important mediator within the RVLM acting on presynaptic terminals to increase GABA release (Kishi et al., 2001; Shinohara et al., 2012) and impacts on central AT2R mediated modulation of baroreflex regulation (Abdulla and Johns, 2014). This is also in line with our previous observation that the hypotensive and sympatho-inhibitory response to chronic selective stimulation of central AT2R through chronic icv infusion of C21, required a functioning central nitric-oxide pathway (Brouwers et al., 2015).

As mentioned above, we and others found no evidence that endogenous activation of AT2R in the RVLM contributes significantly to the control of blood pressure under basal conditions. This could be due to the dominant Ang II dependent AT1R mediated balance between glutamatergic and GABAergic activity, and may be different in pathologic conditions associated with sympatho-excitation.

Nevertheless, if confirmed by further studies, the presence of AT2R on GABAergic sympatho-inhibitory nerve terminals within the RVLM could open the possibility to develop selective AT2R agonists as a possible new therapy for conditions characterized by increased sympathetic activity. C21 barely crosses the blood-brain-barrier (Shraim et al., 2011), therefore the development of more lipophilic AT2R agonists would be needed to target AT2R within the RVLM as a possible new antihypertensive strategy.

The present study has some limitations. The study was done in normotensive male rats only and some studies have indicated that the role of AT2R in regulating blood pressure may be sex specific (Hilliard et al., 2012; Dai et al., 2015, 2016). Moreover, different or more pronounced responses may be observed in future similar studies in rat models of hypertension.

We observed differences in baseline glutamate and GABA levels between different groups of rats. Such variations in baseline neurotransmitter values, are not unusual and also not a problem, taken into account that the conclusions we drew from our experiments are based on relative changes in transmitter levels in response to the interventions. Our group as well as others previously reported substantial intrastrain differences in for example hippocampal extracellular levels of noradrenalin, dopamine, serotonin, glutamate and GABA (Miller et al., 1968; Portelli et al., 2009). Therefore, we believe that observing intrastrain differences between different batches, even coming from the same vendor, in basal glutamate and GABA levels within the PVN and the RVLM is not unexpected. In addition all rats were outbred, and as described by Yilmazer-Hanke (2008), outbred strains are genetically heterogeneous populations with a high intrastrain variation. Another important factor that needs to be taken into account related to observed variations in our baseline measurements is the yield of a microdialysis probe. Microdialysis does not reflect the absolute values present in the extracellular environment. Indeed, due to the kinetic process of dialysis the yield is not 100%, which is not unusual. However, microdialysis is an excellent tool to measure relative changes in concentrations in function of time after an intervention. There may be variation in probe yields between different experiments, but for each animal the effect (relative increase in GABA) occurred always at the same time (shortly after the start of the C21 administration), and the levels returned again to baseline after withdrawal of the C21 infusion. This relative change from baseline in GABA levels in response to C21 was consistently observed during the same time period in each rat. Moreover, in each rat, GABA levels remained stable when co-infusion with the AT2R antagonist. Further, the results were confirmed when expressed as AUC of GABA values before-during- and after C21 infusion (**Figure 2**).

The fact that we did not observe an increase in blood pressure after bicuculline alone does not exclude a tonic inhibitory GABA output as previously suggested by Smith and Barron (1990). These authors reported an increase in blood pressure after bilateral microinjections of bicuculline. In the present study, we administered bicuculline unilaterally into the left-sided RVLM only, hence leaving the GABA receptors in the RVLM at the other side unaffected. We assume that a blood pressure increase resulting from interruption of a putative tonic inhibitory GABAergic tone can only be detected after bilateral GABA receptor blockade within the RVLM.

It would also be of interest to further explore the effect of local administration of C21 into the NTS which is also known to contain AT2R (de Kloet et al., 2016b).

In conclusion, the results of the present study provide evidence that acute stimulation of AT2R within the RVLM by the non-peptide AT2R agonist C21 lowers blood pressure and increases local GABA release in normotensive rats, and that this hypotensive response requires functional GABA-A receptors.

AUTHOR CONTRIBUTIONS

LL, First author, performed the research and wrote the research paper; SB, Co-promoter and supervisor of practical work and design of the reseach study; IJS, Co-promotor and design of the research study and critical insights in the research paper (Head of Center for Neurosciences, VUB); AD, Promotor Design of the research study and critical insights in the research paper (Head of the department of Clinical Pharmacology and Clinical Pharmacy, UZ Brussel).

FUNDING

This study was supported by Research Council of the Vrije Universiteit Brussel and the department of Pharmaceutical Chemistry, Drug Analysis and Drug Information and the department of Clinical Pharmacology and Clinical Pharmacy, respectively provided to Prof. Dr. Apr. I. J. Smolders and Prof. Dr. A. G. Dupont.

ACKNOWLEDGMENTS

The authors acknowledge the excellent technical assistance of Mrs. R. Berckmans and Mr. G. De Smet.

REFERENCES

Abdulla, M. H., and Johns, E. J. (2014). Nitric oxide impacts on angiotensin AT2 receptor modulation of high-pressure baroreflex control of renal sympathetic nerve activity in anaesthetized rats. *Acta Physiol.* 210, 832–844. doi: 10.1111/apha.12207

Blessing, W. W., and Li, Y. W. (1989). Inhibitory vasomotor neurons in the caudal ventrolateral region of the medulla oblongata. *Prog. Brain Res.* 81, 83–97. doi: 10.1016/S0079-6123(08)62000-2

Brouwers, S., Smolders, I., Massie, A., and Dupont, A. G. (2013). Angiotensin II type 2 receptor-mediated and nitric oxide-dependent renal vasodilator response to compound 21 unmasked by angiotensin-converting enzyme inhibition in spontaneously hypertensive rats *in vivo*. *Hypertension* 62, 920–926. doi: 10.1161/HYPERTENSIONAHA.112.00762

Brouwers, S., Smolders, I., Wainford, R. D., and Dupont, A. G. (2015). Hypotensive and sympathoinhibitory responses to selective central AT2 receptor stimulation in spontaneously hypertensive rats. *Clin. Sci.* 129, 81–92. doi: 10.1042/CS20140776

Butcher, K. S., and Cechetto, D. F. (1998). Receptors in lateral hypothalamic area involved in insular cortex sympathetic responses. *Am. J. Physiol.* 275(2 Pt 2), H689–H696.

Dai, S. Y., Peng, W., Zhang, Y. P., Li, J. D., Shen, Y., and Sun, X. F. (2015). Brain endogenous angiotensin II receptor type 2 (AT2-R) protects against DOCA/salt-induced hypertension in female rats. *J. Neuroinflammation* 12:47. doi: 10.1186/s12974-015-0261-47

Dai, S. Y., Zhang, Y. P., Peng, W., Shen, Y., and He, J. J. (2016). Central infusion of Angiotensin II Type 2 receptor agonist compound 21 attenuates DOCA/NaCl-induced hypertension in female rats. *Oxid. Med. Cell. Longev.* 2016:3981790. doi: 10.1155/2016/3981790

Dampney, R. A., Horiuchi, J., Tagawa, T., Fontes, M. A., Potts, P. D., and Polson, J. W. (2003). Medullary and supramedullary mechanisms regulating sympathetic vasomotor tone. *Acta Physiol. Scand.* 177, 209–218. doi: 10.1046/j.1365-201X.2003.01070.x

de Gasparo, M., Catt, K. J., Inagami, T., Wright, J. W., and Unger, T. (2000). International union of pharmacology. XXIII. The angiotensin II receptors. *Pharmacol. Rev.* 52, 415–472.

de Kloet, A. D., Pitra, S., Wang, L., Hiller, H., Pioquinto, D. J., Smith, J. A., et al. (2016a). Angiotensin Type-2 receptors influence the activity of vasopressin neurons in the paraventricular nucleus of the hypothalamus in male mice. *Endocrinology* 157, 3167–3180. doi: 10.1210/en.2016-1131

de Kloet, A. D., Wang, L., Ludin, J. A., Smith, J. A., Pioquinto, D. J., Hiller, H., et al. (2016b). Reporter mouse strain provides a novel look at angiotensin type-2 receptor distribution in the central nervous system. *Brain Struct. Funct.* 221, 891–912. doi: 10.1007/s00429-014-0943-1

Dupont, A. G., and Brouwers, S. (2010). Brain angiotensin peptides regulate sympathetic tone and blood pressure. *J. Hypertens.* 28, 1599–1610. doi: 10.1097/HJH.0b013e32833af3b2

Gao, J., Zhang, H., Le, K. D., Chao, J., and Gao, L. (2011). Activation of central angiotensin type 2 receptors suppresses norepinephrine excretion and blood pressure in conscious rats. *Am. J. Hypertens.* 24, 724–730. doi: 10.1038/ajh.2011.33

Gao, J., Zucker, I. H., and Gao, L. (2014). Activation of central angiotensin type 2 receptors by compound 21 improves arterial baroreflex sensitivity in rats with heart failure. *Am. J. Hypertens.* 27, 1248–1256. doi: 10.1093/ajh/hpu044

Gao, L., Wang, W., Li, H., Sumners, C., and Zucker, I. H. (2008a). Effects of angiotensin type 2 receptor overexpression in the rostral ventrolateral medulla on blood pressure and urine excretion in normal rats. *Hypertension* 51, 521–527. doi: 10.1161/HYPERTENSIONAHA.107.101717

Gao, L., Wang, W. Z., Wang, W., and Zucker, I. H. (2008b). Imbalance of angiotensin type 1 receptor and angiotensin II type 2 receptor in the rostral ventrolateral medulla: potential mechanism for sympathetic overactivity in heart failure. *Hypertension* 52, 708–714. doi: 10.1161/HYPERTENSIONAHA.108.116228

Gao, L., and Zucker, I. H. (2011). AT2 receptor signaling and sympathetic regulation. *Curr. Opin. Pharmacol.* 11, 124–130. doi: 10.1016/j.coph.2010.11.004

Guyenet, P. G. (2006). The sympathetic control of blood pressure. *Nat. Rev. Neurosci.* 7, 335–346. doi: 10.1038/nrn1902

Guyenet, P. G., Stornetta, R. L., Weston, M. C., McQuiston, T., and Simmons, J. R. (2004). Detection of amino acid and peptide transmitters in physiologically identified brainstem cardiorespiratory neurons. *Auton. Neurosci.* 114, 1–10. doi: 10.1016/j.autneu.2004.06.003

Hatam, M., and Ganjkhani, M. (2012). Effect of GABA(A) receptors in the rostral ventrolateral medulla on cardiovascular response to the activation of the bed nucleus of the stria terminalis in female ovariectomized rats. *Iran J. Med. Sci.* 37, 242–252.

Hilliard, L. M., Jones, E. S., Steckelings, U. M., Unger, T., Widdop, R. E., and Denton, K. M. (2012). Sex-specific influence of angiotensin type 2 receptor stimulation on renal function: a novel therapeutic target for hypertension. *Hypertension* 59, 409–414. doi: 10.1161/HYPERTENSIONAHA.111.184986

Hu, L., Zhu, D. N., Yu, Z., Wang, J. Q., Sun, Z. J., and Yao, T. (1985). Expression of angiotensin II type 1 (AT(1)) receptor in the rostral ventrolateral medulla in rats. *J. Appl. Physiol.* 92, 2153–2161.

Kantzides, A., and Badoer, E. (2005). nNOS-containing neurons in the hypothalamus and medulla project to the RVLM. *Brain Res.* 1037, 25–34. doi: 10.1016/j.brainres.2004.11.032

Kishi, T., Hirooka, Y., Sakai, K., Shigematsu, H., Shimokawa, H., and Takeshita, A. (2001). Overexpression of eNOS in the RVLM causes hypotension and bradycardia via GABA release. *Hypertension* 38, 896–901.

Lenkei, Z., Palkovits, M., Corvol, P., and Llorens-Cortès, C. (1997). Expression of angiotensin type-1 (AT1) and type-2 (AT2) receptor mRNAs in the adult rat brain: a functional neuroanatomical review. *Front. Neuroendocrinol.* 18, 383–439. doi: 10.1006/frne.1997.0155

Li, Y. F., Jackson, K. L., Stern, J. E., Rabeler, B., and Patel, K. P. (2006). Interaction between glutamate and GABA systems in the integration of sympathetic outflow by the paraventricular nucleus of the hypothalamus. *Am. J. Physiol. Heart Circ Physiol.* 291, H2847–H2856. doi: 10.1152/ajpheart.00625.2005

Li, Y., Li, X. H., and Yuan, H. (2012). Angiotensin II type-2 receptor-specific effects on the cardiovascular system. *Cardiovasc. Diagn. Ther.* 2, 56–62. doi: 10.3978/j.issn.2223-3652.2012.02.02

Li, Z., Iwai, M., Wu, L., Shiuchi, T., Jinno, T., Cui, T. X., et al. (2003). Role of AT2 receptor in the brain in regulation of blood pressure and water intake. *Am. J. Physiol. Heart Circ. Physiol.* 284, H116–H121. doi: 10.1152/ajpheart.00515.2002

Matavelli, L. C., and Siragy, H. M. (2015). AT2 receptor activities and pathophysiological implications. *J. Cardiovasc. Pharmacol.* 65, 226–232. doi: 10.1097/FJC.0000000000000208

Matsuura, T., Kumagai, H., Onimaru, H., Kawai, A., Iigaya, K., Onami, T., et al. (2005). Electrophysiological properties of rostral ventrolateral medulla neurons in angiotensin II 1a receptor knockout mice. *Hypertension* 46, 349–354. doi: 10.1161/01.HYP.0000173421.97463.ac

Menezes, R. C., and Fontes, M. A. (2007). Cardiovascular effects produced by activation of GABA receptors in the rostral ventrolateral medulla of conscious rats. *Neuroscience* 144, 336–343. doi: 10.1016/j.neuroscience.2006.08.062

Millan, M. A., Jacobowitz, D. M., Aguilera, G., and Catt, K. J. (1991). Differential distribution of AT1 and AT2 angiotensin II receptor subtypes in the rat brain during development. *Proc. Natl. Acad. Sci. U.S.A.* 88, 11440–11444. doi: 10.1073/pnas.88.24.11440

Miller, F. P., Cox, R. H., and Maickel, R. P. (1968). Intrastrain difference in serotonin and norepinephrine in discrete areas of rat brain. *Science* 162, 463–464. doi: 10.1126/science.162.3852.463

Miyawaki, T., Minson, J., Arnolda, L., Chalmers, J., Llewellyn-Smith, I., and Pilowsky, P. (1996). Role of excitatory amino acid receptors in cardiorespiratory coupling in ventrolateral medulla. *Am. J. Physiol.* 271(5 Pt 2), R1221–R1230.

Namsolleck, P., Recarti, C., Foulquier, S., Steckelings, U. M., and Unger, T. (2014). AT(2) receptor and tissue injury: therapeutic implications. *Curr. Hypertens. Rep.* 16:416. doi: 10.1007/s11906-013-0416-6

Padia, S. H., and Carey, R. M. (2013). AT2 receptors: beneficial counter-regulatory role in cardiovascular and renal function. *Pflugers Arch.* 465, 99–110. doi: 10.1007/s00424-012-1146-3

Pan, H. L. (2004). Brain angiotensin II and synaptic transmission. *Neuroscientist* 10, 422–431. doi: 10.1177/1073858404264678

Paxinos, G., and Watson, S. (1998). *The Rat Brain in Stereotaxic Coordinates*, 2*nd Edn.* San Diego, CA: Academic Press.

Pointer, M. A. (2005). Is central nitric oxide essential in hypertension? *J. Hypertens.* 23, 1637–1638. doi: 10.1097/01.hjh.0000180352.99042.f3

Portelli, J., Aourz, N., De Bundel, D., Meurs, A., Smolders, I., Michotte, Y., et al. (2009). Intrastrain differences in seizure susceptibility, pharmacological response and basal neurochemistry of Wistar rats. *Epilepsy Res.* 87, 234–246. doi: 10.1016/j.eplepsyres.2009.09.009

Ross, C. A., Ruggiero, D. A., Park, D. H., Joh, T. H., Sved, A. F., Fernandez-Pardal, J., et al. (1984). Tonic vasomotor control by the rostral ventrolateral medulla: effect of electrical or chemical stimulation of the area containing C1 adrenaline neurons on arterial pressure, heart rate, and plasma catecholamines and vasopressin. *J. Neurosci.* 4, 474–494.

Schreihofer, A. M., and Guyenet, P. G. (2002). The baroreflex and beyond: control of sympathetic vasomotor tone by GABAergic neurons in the ventrolateral medulla. *Clin. Exp. Pharmacol. Physiol.* 29, 514–521. doi: 10.1046/j.1440-1681.2002.03665.x

Shinohara, K., Hirooka, Y., Kishi, T., and Sunagawa, K. (2012). Reduction of nitric oxide-mediated gamma-amino butyric acid release in rostral ventrolateral medulla is involved in superoxide-induced sympathoexcitation of hypertensive rats. *Circ. J.* 76, 2814–2821. doi: 10.1253/circj.CJ-12-0399

Shraim, N., Mertens, B., Clinckers, R., Sarre, S., Michotte, Y., and Van Eeckhaut, A. (2011). Microbore liquid chromatography with UV detection to study the *in vivo* passage of compound 21, a non-peptidergic AT_2, receptor agonist, to the striatum in rats. *J. Neurosci. Methods* 202, 137–142. doi: 10.1016/j.jneumeth.2011.06.009

Siragy, H. M., Inagami, T., Ichiki, T., and Carey, R. M. (1999). Sustained hypersensitivity to angiotensin II and its mechanism in mice lacking the subtype-2 (AT2) angiotensin receptor. *Proc. Natl. Acad. Sci. U.S.A.* 96, 6506–6510. doi: 10.1073/pnas.96.11.6506

Smith, J. K., and Barron, K. W. (1990). GABAergic responses in ventrolateral medulla in spontaneously hypertensive rats. *Am. J. Physiol.* 258(2 Pt 2), R450–R456.

Smolders, I., De Klippel, N., Sarre, S., Ebinger, G., and Michotte, Y. (1995a). Tonic GABA-ergic modulation of striatal dopamine release studied by *in vivo* microdialysis in the freely moving rat. *Eur. J. Pharmacol.* 284, 83–91. doi: 10.1016/0014-2999(95)00369-V

Smolders, I., Sarre, S., Michotte, Y., and Ebinger, G. (1995b). The analysis of excitatory, inhibitory and other amino acids in rat brain microdialysates using microbore liquid chromatography. *J. Neurosci. Methods* 57, 47–53. doi: 10.1016/0165-0270(94)00124-Y

Steckelings, U. M., Larhed, M., Hallberg, A., Widdop, R. E., Jones, E. S., Wallinder, C., et al. (2011). Non-peptide AT2-receptor agonists. *Curr. Opin. Pharmacol.* 11, 187–192. doi: 10.1016/j.coph.2010.11.002

Steckelings, U. M., Paulis, L., Namsolleck, P., and Unger, T. (2012). AT2 receptor agonists: hypertension and beyond. *Curr. Opin. Nephrol. Hypertens.* 21, 142–146. doi: 10.1097/MNH.0b013e328350261b

Sumners, C., de Kloet, A. D., Krause, E. G., Unger, T., and Steckelings, U. M. (2015). Angiotensin type 2 receptors: blood pressure regulation and end organ damage. *Curr. Opin. Pharmacol.* 21, 115–121. doi: 10.1016/j.coph.2015.01.004

Sun, M. K., Hackett, J. T., and Guyenet, P. G. (1988). Sympathoexcitatory neurons of rostral ventrolateral medulla exhibit pacemaker properties in the presence of a glutamate-receptor antagonist. *Brain Res.* 438, 23–40. doi: 10.1016/0006-8993(88)91320-0

Tagawa, T., Fontes, M. A., Potts, P. D., Allen, A. M., and Dampney, R. A. (2000). The physiological role of AT1 receptors in the ventrolateral medulla. *Braz. J. Med. Biol. Res.* 33, 643–652. doi: 10.1590/S0100-879X2000000600005

Tasker, J. G., Boudaba, C., and Schrader, L. A. (1998). Local glutamatergic and GABAergic synaptic circuits and metabotropic glutamate receptors in the hypothalamic paraventricular and supraoptic nuclei. *Adv. Exp. Med. Biol.* 449, 117–121. doi: 10.1007/978-1-4615-4871-3_11

Tedesco, A., and Ally, A. (2009). Angiotensin II type-2 (AT2) receptor antagonism alters cardiovascular responses to static exercise and simultaneously changes glutamate/GABA levels within the ventrolateral medulla. *Neurosci. Res.* 64, 372–379. doi: 10.1016/j.neures.2009.04.008

Van Hemelrijck, A., Sarre, S., Smolders, I., and Michotte, Y. (2005). Determination of amino acids associated with cerebral ischaemia in rat brain microdialysates using narrowbore liquid chromatography and fluorescence detection. *J. Neurosci. Methods* 144, 63–71. doi: 10.1016/j.jneumeth.2004.10.013

Wan, Y., Wallinder, C., Plouffe, B., Beaudry, H., Mahalingam, A. K., Wu, X., et al. (2004). Design, synthesis, and biological evaluation of the first selective nonpeptide AT2 receptor agonist. *J. Med. Chem.* 47, 5995–6008. doi: 10.1021/jm049715t

Yang, R., Smolders, I., Vanderheyden, P., Demaegdt, H., Van Eeckhaut, A., Vauquelin, G., et al. (2011). Pressor and renal hemodynamic effects of the novel angiotensin A peptide are angiotensin II type 1A receptor dependent. *Hypertension* 57, 956–964. doi: 10.1161/HYPERTENSIONAHA.110.161836

Yilmazer-Hanke, D. M. (2008). Morphological correlates of emotional and cognitive behaviour: insights from studies on inbred and outbred rodent strains and their crosses. *Behav. Pharmacol.* 19, 403–434. doi: 10.1097/FBP.0b013e32830dc0de

Conflict of Interest Statement: The authors declare that the research was conducted in the absence of any commercial or financial relationships that could be construed as a potential conflict of interest.

Copyright © 2017 Légat, Brouwers, Smolders and Dupont. This is an open-access article distributed under the terms of the Creative Commons Attribution License (CC BY). The use, distribution or reproduction in other forums is permitted, provided the original author(s) or licensor are credited and that the original publication in this journal is cited, in accordance with accepted academic practice. No use, distribution or reproduction is permitted which does not comply with these terms.

frontiers in Human Neuroscience

CLINICAL TRIAL
published: 28 June 2017
doi: 10.3389/fnhum.2017.00338

Rapid Alleviation of Parkinson's Disease Symptoms via Electrostimulation of Intrinsic Auricular Muscle Zones

Yusuf O. Cakmak[1], Hülya Apaydin[2], Güneş Kiziltan[2], Ayşegül Gündüz[2], Burak Ozsoy[3], Selim Olcer[4], Hakan Urey[4], Ozgur O. Cakmak[5], Yasemin G. Ozdemir[5] and Sibel Ertan[2]*

[1] Department of Anatomy, School of Medical Sciences, Otago University, Dunedin, New Zealand, [2] Department of Neurology, Cerrahpasa School of Medicine, Istanbul University, Istanbul, Turkey, [3] Global Dynamic Systems (GDS) ARGE, Teknopark Istanbul, Istanbul, Turkey, [4] Department of Electrical Engineering, College of Engineering, Koç University, Istanbul, Turkey, [5] Department of Neurology, School of Medicine, Koç University, Istanbul, Turkey

Background: Deep brain stimulation of the subthalamic nucleus (STN-DBS) and the pedunculopontine nucleus (PPN) significantly improve cardinal motor symptoms and postural instability and gait difficulty, respectively, in Parkinson's disease (PD).

Objective and Hypothesis: Intrinsic auricular muscle zones (IAMZs) allow the potential to simultaneously stimulate the C2 spinal nerve, the trigeminal nerve, the facial nerve, and sympathetic and parasympathetic nerves in addition to providing muscle feedback and control areas including the STN, the PPN and mesencephalic locomotor regions. Our aim was to observe the clinical responses to IAMZ stimulation in PD patients.

Method: Unilateral stimulation of an IAMZ, which includes muscle fibers for proprioception, the facial nerve, and C2, trigeminal and autonomic nerve fibers, at 130 Hz was performed in a placebo- and sham-controlled, double-blinded, within design, two-armed study of 24 PD patients.

Results: The results of the first arm (10 patients) of the present study demonstrated a substantial improvement in Unified Parkinson's Disease Ratings Scale (UPDRS) motor scores due to 10 min of IAMZ electrostimulation ($p = 0.0003$, power: 0.99) compared to the placebo control ($p = 0.130$). A moderate to large clinical difference in the improvement in UPDRS motor scores was observed in the IAMZ electrostimulation group. The results of the second arm (14 patients) demonstrated significant improvements with dry needling ($p = 0.011$) and electrostimulation of the IAMZ ($p < 0.001$) but not with sham electrostimulation ($p = 0.748$). In addition, there was a significantly greater improvement in UPDRS motor scores in the IAMZ electrostimulation group compared to the IAMZ dry needling group ($p < 0.001$) and the sham electrostimulation ($p < 0.001$) groups. The improvement in UPDRS motor scores of the IAMZ electrostimulation group (ΔUPDRS = 5.29) reached moderate to high clinical significance, which was not the case for the dry needling group (ΔUPDRS = 1.54). In addition, both arms of the study demonstrated bilateral improvements in motor symptoms in response to unilateral IAMZ electrostimulation.

OPEN ACCESS

Edited by:
Ioan Opris,
Leonard M. Miller School of Medicine, United States

Reviewed by:
Filippo Brighina,
University of Palermo, Italy
Didem Gokcay,
Middle East Technical University, Turkey

***Correspondence:**
Yusuf O. Cakmak
yusuf.cakmak@otago.ac.nz

Received: *27 October 2016*
Accepted: *12 June 2017*
Published: *28 June 2017*

Citation:
Cakmak YO, Apaydin H, Kiziltan G, Gündüz A, Ozsoy B, Olcer S, Urey H, Cakmak OO, Ozdemir YG and Ertan S (2017) Rapid Alleviation of Parkinson's Disease Symptoms via Electrostimulation of Intrinsic Auricular Muscle Zones. Front. Hum. Neurosci. 11:338. doi: 10.3389/fnhum.2017.00338

Conclusion: The present study is the first demonstration of a potential role of IAMZ electrical stimulation in improving the clinical motor symptoms of PD patients in the short term.

Keywords: Parkinson's disease, electrostimulation, auricular muscles, PPN, STN, mesencephalon, locomotor, neuromodulation

INTRODUCTION

Bilateral high-frequency stimulation of the subthalamic nucleus (STN), commonly known as deep brain stimulation of the STN (STN-DBS), provides a significant improvement in cardinal motor symptoms and in the control of drug-induced complications of Parkinson's disease (PD). To be clinically effective, stimulation of the STN must be applied at frequencies greater than 100 Hz (Limousin et al., 1995; Limousin et al., 1997), and electrostimulation is usually delivered at 130 Hz (Little and Brown, 2012). Effective stimulation was shown to be associated with a significant decrease in the activity of the ipsilateral primary sensorimotor cortex at rest and a significant increase in premotor, anterior cingulate, pre-supplementary motor areas (pre-SMAs) and dorsolateral prefrontal cortices during movement (Payoux et al., 2004). On the other hand, axial symptoms, such postural instability and gait difficulty (PIGD), freezing of gait, and impaired speech, have been reported to be resistant to STN-DBS and levodopa treatments (Hamani et al., 2007; Tattersall et al., 2014). Recent clinical results have indicated the potential effectiveness of deep brain stimulation of the pedunculopontine nucleus (PPN-DBS) on PGID (Hamani et al., 2007; Tattersall et al., 2014). It has been demonstrated that lesions of the PPN induce gait deficits (Karachi et al., 2010; Tattersall et al., 2014). Moreover, cholinergic cell loss in the caudal PPN is accompanied by PIGD (Hirsch et al., 1987; Zweig et al., 1989; Karachi et al., 2010; Tattersall et al., 2014). Therefore, PIGD is thought to be related to the mesencephalic locomotor region rather than dopaminergic motor centers such as the STN (Garcia-Rill, 1991). The major components of the mesencephalic locomotor region are the PPN and the cuneiform nucleus (Garcia-Rill, 1991). In the context of different outcomes of STN-DBS and PPN-DBS, PPN dysfunction likely contributes to PIGD in PD (Tykocki et al., 2011). The PPN receives direct inputs from the pre-SMA and the basal ganglion to modulate muscle tone by directly exciting pontine reticular formation (Burn, 2013). Central pattern generators in the spinal cord can also be modulated directly and indirectly by the PPN (**Figure 1B**). Notably, sensory proprioceptive afferents have also been demonstrated to modify these patterns (Jankowska et al., 1983; Takakusaki et al., 2008; Burn, 2013).

Although altered proprioception is not a prominent symptom of PD, proprioception deficits have been reported in PD patients (Lee et al., 2013), and improvements in proprioception have been reported with STN stimulation (Lee et al., 2013). Selective muscle afferent nerve stimulation has been reported to cause significant activation in motor-related areas compared with cutaneous stimuli (Wardman et al., 2014). Muscle afferent stimulation evokes more widespread cortical, subcortical, and cerebellar activations than cutaneous afferents (Wardman et al., 2014). Separate precentral and post-central excitation foci were observed with muscle afferent stimulation, emphasizing the importance of muscle afferent nerve stimulation in the modulation of cortical motor areas (Wardman et al., 2014). Therefore, peripheral nerve stimulation may also hold the potential as an alternative and minimally invasive approach to modulate the activity in the premotor, anterior cingulate, pre-SMA and dorsolateral prefrontal cortices and basal ganglia such as the STN and the PPN and should be investigated in PD. Median nerve stimulation has been shown to result in the activation of STN neurons, which form a motor homunculus (Nambu et al., 1996, 1997, 2000; Hanajima et al., 2004). In theory, stimulation of other peripheral motor nerves may also activate motor homunculus of the STN.

Upper facial muscles around the orbital region are controlled bilaterally by the motor cortex through the facial nerve (Mima et al., 1999). In addition, unilateral STN-DBS has been demonstrated to induce strictly contralateral motor-evoked potentials in the trapezius, deltoid, biceps, and thenar muscles; however, the same stimulus reportedly always induces bilateral motor-evoked potentials in the orbicularis oculi, orbicularis oris, masseter, and sternocleidomastoid in Parkinson's patients (Costa et al., 2007). The intrinsic auricular muscles of the tragicus and antitragicus muscles have also been shown to simultaneously contract with the orbicularis oculi muscles (Matsuo and Hirose, 1987). The latter demonstration is also indirect proof of bilateral cortical connections of intrinsic auricular muscles, such as in the orbicularis oculi.

In the context of these anatomical relationships, unilateral stimulation of the intrinsic auricular muscle zones (IAMZs) may hold potential for bilateral feedback stimulation of muscle feedback and motor driver cortical areas. In addition to the possible proprioceptive outcomes of IAMZ stimulation, contributions of the facial nerve branches stimulating the intrinsic auricular muscles (Fujita, 1934; Matsuo and Hirose, 1987), the vagus nerve via the Arnold branch as a parasympathetic contribution (Alvord and Farmer, 1997; Peuker and Filler, 2002), the trigeminal nerve via the auriculotemporal nerve branch (Alvord and Farmer, 1997; Peuker and Filler, 2002) and the C2 spinal nerve within the great auricular nerve (Alvord and Farmer, 1997; Peuker and Filler, 2002) to IAMZ have been demonstrated in the literature (**Figure 1A**). In addition, cervical sympathetic nerves are distributed to the auricula within the ear arteries (Daniel and Paton, 1975; Lambru et al., 2013) (**Figure 1A**). Therefore, stimulation of the IAMZ has the potential for synchronous stimulation of the C2 spinal nerve, the trigeminal nerve, and sympathetic and parasympathetic nerves (**Figure 1A**), each of which may contribute to motor regulation.

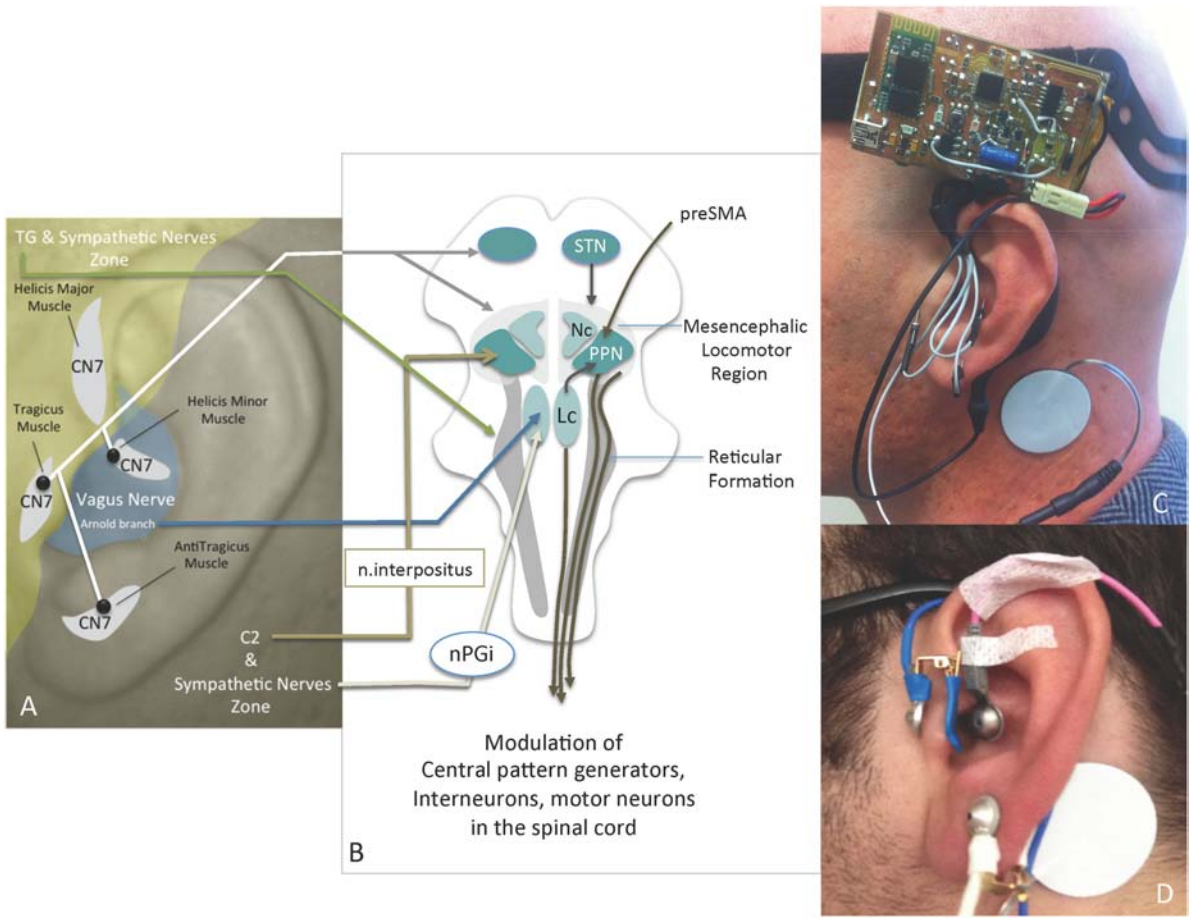


FIGURE 1 | (A) Innervation of the ear, the IAMZs and IAMZ electrode locations (black dots); **(B)** relevant anatomical pathways of IAMZs via auricular nerves for motion regulation and mesencephalic locomotor regions (modified from Burn, 2013); **(C)** active stimulation with needle electrodes of the IAMZ and with TENS electrode of the SCM; **(D)** placebo group TENS electrode placements in the IAMZ and SCM; CN7, facial nerve; C2, C2 spinal nerve; TG, trigeminal nerve; Nc, nucleus cuneatus; Lc, locus coerulei; nPGi, nucleus paragigantocellularis; STN, subthalamic nucleus; PPN, pedunculopontine nucleus. *Yellow zone*: trigeminal nerve + sympathetic nerve zone; *Gray zone*: C2 + sympathetic nerve zone; *White areas*: intrinsic auricular muscles zones. *Blue area*: Arnold branch of the vagus nerve, C2, CN7, and sympathetic nerves overlapping zone.

It has been demonstrated that the C2 spinal nerve forms anatomical connections with the deep cerebellar nucleus of the interpositus (represented by the nucleus globosus and the emboliformis in humans) in animals (Matsushita and Xiong, 2001). The interpositus has projections to the PPN and from the PPN to the STN (Schell and Strick, 1984; Hazrati and Parent, 1992; Lavoie and Parent, 1994; Harting, 1997; McFarland and Haber, 2000; Muthusamy et al., 2007). In addition, the C2-interpositus nucleus-PPN-reticulospinal axis may play a cardinal role in motion and position regulation: a substantial body of evidence suggests that the reticulospinal system is essential and plays a fundamental role in the integration of commands for whole-body movement and postural adjustment rather than the movement of a single limb (Magni and Willis, 1964; Keizer and Kuypers, 1984, 1989; Drew and Rossignol, 1990; Luccarini et al., 1990; Drew, 1991; Massion, 1992; Mori et al., 1992; Kably and Drew, 1998; Schepens and Drew, 2003) (**Figure 1B**). Of note, the reticulospinal system is also directly excited by the PPN and mediates DBS-PPN to modulate muscle tone in PD patients (Burn, 2013) (**Figure 1B**). In addition to the potential effects of the C2 spinal nerve on the reticulospinal system via the interpositus nucleus-PPN axis, the mesencephalic trigeminal nucleus as the principal nucleus of the facial muscles' proprioceptive center, projects to the reticular formation and to the spinal cord via propriospinal neurons (Lawrence and Kuypers, 1968; Gorska and Sybirska, 1980; Alstermark et al., 1981, 1989; Hobbs et al., 1992; Usunoff et al., 1997; Whishaw et al., 1998; Sasaki, 2004; Jankowska and Edgley, 2006) (**Figures 1A,B**). This connection also underlines the potential role of intrinsic auricular muscle proprioception feedback on reticular formation and the possible influences on movement and posture, in addition to C2-related pathways, on reticular formation and propriospinal neurons. The C2 spinal nerve projects to the lower ear lobe and the corresponding skin that overlays the intrinsic muscles of the antitragicus muscle by the greater auricular nerve and the trigeminal nerve; its auriculotemporal branch innervates the skin

areas over the tragicus and helicis major muscles (Matsuo and Hirose, 1987; Alvord and Farmer, 1997; Peuker and Filler, 2002; Lambru et al., 2013; Drake et al., 2015) (**Figure 1A**).

In addition to the possible indirect autonomic effects of IAMZ stimulation via the C2 nerve, autonomic fibers of the auricula also directly contribute to these zones. While the sympathetic nerves overlay the IAMZ within the arterial walls, the Arnold branch of the vagus nerve is distributed only over the helicis minor muscle zone (Matsuo and Hirose, 1987; Alvord and Farmer, 1997; Peuker and Filler, 2002; Lambru et al., 2013; Drake et al., 2015) (**Figure 1A**). Thus far, no neuromodulation studies of the Arnold branch or neurotraces of the efferent connections of the Arnold branch have considered the existence of the helicis minor muscle in the concha area where the Arnold branch is distributed.

The earliest accumulation of α-synuclein and Lewy bodies have been shown to occur in the dorsal motor nucleus of the vagus nerve in PD (Braak et al., 2003). A recent study also showed that chronic impairment of vagus nerve function leads to inhibition of dopamine and that low frequency stimulation of the vagus nerve significantly inhibited the dopamine system in rat brain structures (Ziomber et al., 2012). It is worth noting that low- and high-frequency electrostimulation induce opposite outcomes on the autonomic nerve system and neurotransmitters (Cakmak et al., 2008, 2016; Zhao, 2008), so that high frequency of stimulation may result with the stimulation of the dopaminergic system.

In the context of the demonstrated structural and functional anatomical connections of the IAMZ and the underlined mechanisms of deep brain stimulation studies in PD, the IAMZ is the only potential auricular zone to synchronously stimulate the C2 spinal nerve, the trigeminal nerve, autonomic nerve fibers and proprioceptive centers to modulate motor modulatory centers including mesencephalic locomotor region. We hypothesized that the stimulation of IAMZ would be beneficial to alleviate the PD motor symptoms. A clinical trial is designed to investigate the potential clinical outcomes (motor symptoms) of the IAMZ stimulation in PD patients. We stimulated the IAMZ (which includes the helicis minor, tragicus, and antitragicus muscles) unilaterally (ipsilateral to the dominant PD symptoms) at a high frequency and analyzed the efficacy of this technique on 24 PD patients via a double-blind, placebo- and sham controlled within-subject design, two-armed study.

MATERIALS AND METHODS

All subjects provided written informed consent to undergo the procedure. The study was approved by the Ethics Committee of the Koç University, Turkey, and it was carried out in accordance with the Ethical Principles for Medical Research Involving Human (Declaration of Helsinki).

Koç University Clinical Trials Ethics Committee Approval Number: 2015.091.IRB1.018,
ClinicalTrials.gov Identifier: NCT02722824,
Turkey Ministry of Health: Follow up number - 133235.

Research Participants

Ten volunteer patients with idiopathic PD who had been followed in our movement disorders outpatient clinic were enrolled for the first arm of the study. Another 14 volunteer patients with idiopathic PD with the same criteria were enrolled for the second arm of the study. PD diagnoses were made by a neurologist who was an expert in movement disorders using the UK Parkinson's Disease Society Brain Bank clinical diagnostic criteria (Hughes et al., 1992).

All patients underwent a detailed neurological examination, and parkinsonian features were rated according to the Unified Parkinson's Disease Rating Scale (UPDRS) Part III. Patients with a disease duration longer than 2 years and Hoehn and Yahr stage $\geq$ 2 were included. Patients with cognitive impairment that might prevent cooperation during tests and patients with any other neurological or systemic disease in which electrostimulation was contraindicated were excluded.

Electrostimulation and Analysis of Symptoms

Arm 1 [*10 patients – 10 min of electrostimulation of the IAMZ with needle electrodes and 10 min of placebo using transcutaneous electrodes (TENS) for IAMZ*]*:* two movement disorder specialists blind to the nature of stimulation rated all patients twice according to the motor section of the UPDRS just before the stimulation (baseline evaluation) and 10 min after the onset of stimulation or placebo application. The patients and two movement disorder specialists were informed that there would be two modes of stimulation, sub-threshold stimulation with TENS of the IAMZ (placebo group, **Figure 1D**) and above the sensory threshold with needle electrodes of the IAMZ (active group, **Figure 1C**). In the placebo-control application in which there was no stimulation and the device was in off-mode, the patients and two movement disorder specialists were informed that a new device would be placed on the ear to improve their motor symptoms and that they would not sense the stimulation of the device because of the sub-threshold stimulation of the IAMZ via the TENS. In the active group, the patients and two movement disorder specialists were informed that the stimulation would be above the sensory threshold and applied via the needle electrodes to the IAMZ. In both groups, there was a TENS electrode on the sternocleidomastoid muscle (SCM) (**Figures 1C,D**). The consort flow chart (**Figure 2**) demonstrates the study design in the first arm.

Arm 2 [*14 patients – 20 min of stimulation in three sessions: electrostimulation of the IAMZ with needles, needling of the IAMZ without electrostimulation (dry needling) and sham region electrostimulation with needles*]: the main aims of the second arm of the study were to assess the following:

- a potential effect of dry needling on the IAMZ without electrostimulation (dry needling of the IAMZ zones without electrostimulation but keeping the needle electrodes connected with to the electrostimulator),
- the potential effect of stimulation of only the C2/sympathetic nerve by ensuring no or minimal

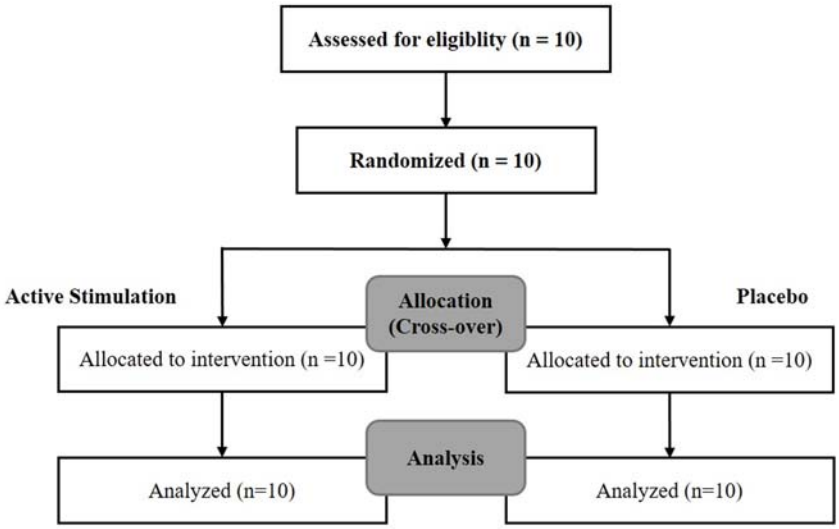


FIGURE 2 | The consort flow chart of the first arm of the study.

stimulation of the SCM, the vagus facial nerve and the trigeminal nerve (sham stimulation),
- the specificity of the IAMZ zone electrostimulation (active group-IAMZ electrostimulation),
- the sole specificity of 130 Hz stimulation (sham stimulation zone),
- a potential long-term effect of the stimulation (50th-minute).

In the second arm of the study, the stimulation duration proceeded to the 20th-minute, and patients were assessed at the 50th-minute (30 min after the termination of 20-min stimulation). The two movement disorder specialists who participated in the first arm and who were blind to the nature of stimulation rated all ($n = 24$) patients twice according to the motor section of the UPDRS.

The two movement disorder specialists were blinded to the type of stimulation by covering the entire auricula with cotton pads, including the needle electrodes (**Figure 3A**). Patients were also informed that there would be three modes of stimulation: sub-threshold stimulation with needles (dry needling of the IAMZ without electrostimulation but with the needles connected to stimulator as in the needle electrostimulation group, **Figure 1C**) and electrostimulation with needle electrodes above the sensory threshold at two different auricular zones (electrostimulation with needle electrodes on the IAMZ **Figure 1C** and a sham region **Figure 3B**). These groups ensured that the patients were blind to the active stimulation group. A part of the upper helix that is innervated by C2/sympathetic nerves but free or with minimal contributions of the SCM, vagal, facial, and trigeminal nerves was selected as the sham electrostimulation region (**Figure 3B**). The consort flow chart in **Figure 4** demonstrates the study flow in the second arm.

Stimulation Procedure

All examinations and electrostimulations were performed during "off" periods of the patients (when the effect of the dopaminergic drug was minimal). We designed and built an electrical signal generator with a changeable voltage output (0–5 V), frequency (2–300 Hz) and pulse length (50–200 μs) with external electrodes able to be connected to press needles (KINGLI, China) placed on the three intrinsic auricular muscles (tragicus, antitragicus, and helicis minor muscles). While the needle electrodes were placed on the IAMZ (**Figure 1C**) in the active stimulation and dry needling groups and over the upper helix in the sham stimulation group (**Figure 3B**), the transcutaneous electrode was placed on the SCM 1–2 cm to its mastoid origin (**Figure 1C**) near the electrical stimulation circuit. In the sham group, the transcutaneous electrode was placed but remained inactive to keep the electrical field of stimulation in the selected helix region for C2/sympathetic nerve stimulation. It was also placed and kept inactive in the dry needling group to maintain observer blindness.

The SCM was chosen for surface electrode placement for three reasons:

(1) STN contribution: bilateral SCM activation has been reported during unilateral STN stimulation, which underlines the bilateral STN connections to each SCM (Costa et al., 2007).
(2) Nucleus cuneatus contribution: the mesencephalic locomotor region has two major components: the PPN and the nucleus cuneatus. SCM proprioception projects to the nucleus cuneatus as the neck muscle proprioception center [6] and as a mesencephalic locomotor component (Garcia-Rill, 1991) (**Figure 1B**).
(3) C2 spinal nerve contribution: the skin over the SCM (1–2 cm to its mastoid origin) is also innervated by the C2 spinal nerve (Matsuo and Hirose, 1987; Alvord and Farmer, 1997;

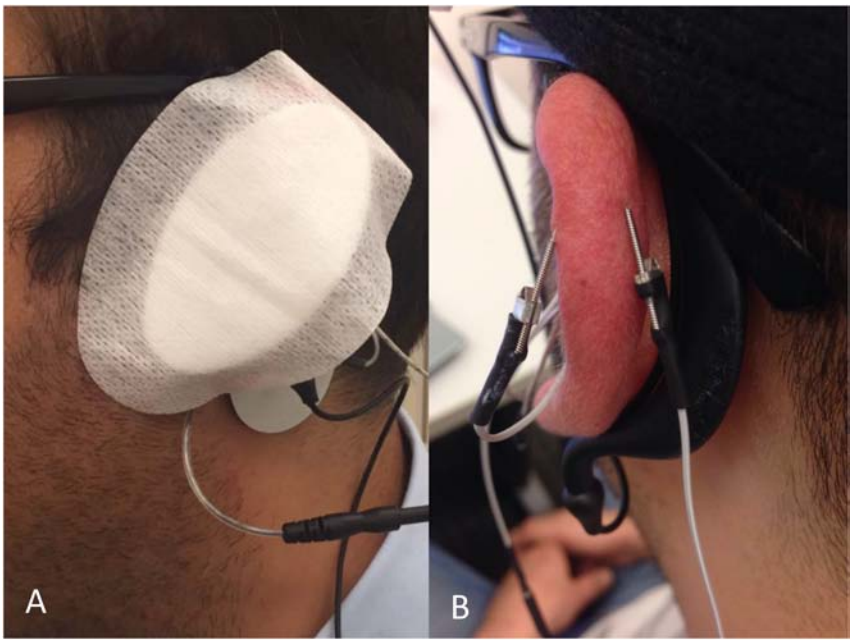


FIGURE 3 | (A) A pad covered the ear to ensure observer blindness in the groups of the second arm of the study. **(B)** Sham stimulation zone needle electrode placement.

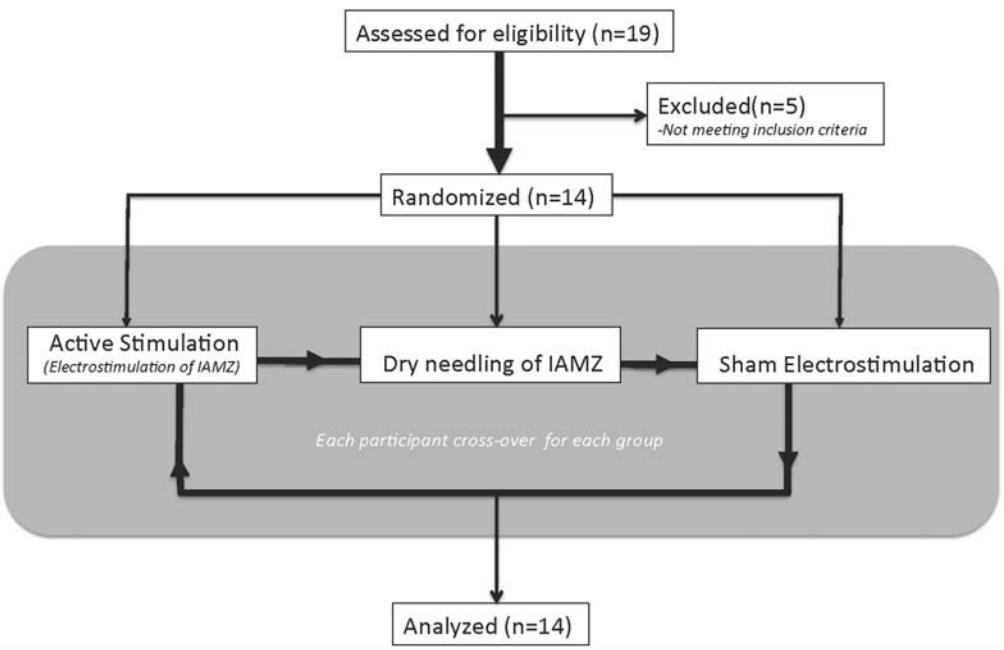


FIGURE 4 | The consort flow chart of the second arm of the study.

Peuker and Filler, 2002; Lambru et al., 2013; Drake et al., 2015) (**Figure 1A**).

In the present study, we used a biphasic wave-form and a stimulation style that alternated the anode and cathode for each stimulus during the stimulation period such that the needle electrodes on the intrinsic auricular muscles and the surface electrode on the SCM served as both the anode and cathode in an alternating manner. Given the much larger contact surface of the transcutaneous electrode compared with the needle electrodes and taking into account the difference in the skin conductance between the needle electrode and the transcutaneous electrode

in addition to the low power of the stimulus, the transcutaneous electrode on the SCM would have a minimal impact on the stimulation-related outcomes.

Auricular electrical stimulation was applied with the following STN-DBS parameters: 130 Hz with a wavelength of 100 μs and an intensity just under the pain threshold (1–4 V). The stimulation was administered unilaterally (ipsilateral to the side of prominent symptoms). We did not set a power (V) for the stimulation because such an approach does not eliminate the probability of current differences due to skin conductance differences in different subjects or within subjects during different sessions. To overcome this possible problem, the electrostimulator contained a built-in current-control feature so that the current was stabilized in the range of 100–130 μÅ during the stimulation period by modulating the power and ensuring that the tingling sensation was under the pain threshold. This approach overcomes the interindividual and intraindividual (in active and control sessions) differences in skin conductance.

In addition to the traditional approach of taking into account the dominant symptom side scores of lateralized subitems (items 20–26) for the UPDRS Part-III motor scale scoring, the scores of lateralized subitems on both sides (ipsilateral and contralateral to the dominant symptoms and to the stimulator) were also documented to reveal any potential effects of unilateral stimulation over the bilateral motor symptoms. Moreover, subscores of the UPDRS Part-III were also classified and analyzed as Tremor (items 20–21), Rigidity (item 22), Bradykinesia (items 23–26,31), Gait and Postural Stability (items 27–30) and Bulbar Anomalies (items 18–19), as in previous studies (Postuma et al., 2008). All statistical analyses were performed using Student's paired *t*-tests (Prism 7 demo version, GraphPad Software, Inc., La Jolla, CA, United States, 2016). In addition, the Bonferroni correction was also applied as a conservative approach for the subscore group analysis [$n = 2$ (active and placebo), $p < 0.025$ in Arm 1, and $n = 3$ (active, dry needling, and sham), $p < 0.016$ in Arm 2]. The second arm of the study, which included three groups, also analyzed via analysis of variance (ANOVA) for group comparisons.

RESULTS

Arm 1

The mean age of the patients was 55.7 ±SD 7.8 years, and only one patient was female. The mean disease duration was 8.3 ±SD 4.4 years. Detailed clinical features of the patients are presented in **Table 1**.

There were no statistically significant differences between the baseline UPDRS motor scores of the patients in the active and placebo groups ($p = 0.735$). The UPDRS motor scores showed a statistically significant improvement 10 min after auricular stimulation compared with baseline UPDRS scores ($p = 0.0003$, power: 0.99). The placebo group did not show statistically significant differences in UPDRS motor scores compared with baseline ($p = 0.130$). At the 10th-minute, the mean improvement rates were 35% (ΔUPDRS = 5.9) in the active group [mean UPDRS motor scores: 17.0 at baseline, 11.1

TABLE 1 | Detailed clinical features of the patients in the first arm of the study.

	Patient 1	Patient 2	Patient 3	Patient 4	Patient 5	Patient 6	Patient 7	Patient 8	Patient 9	Patient 10
Age (years)	61	46	55	48	54	48	61	71	52	61
Gender	F	M	M	M	M	M	M	M	M	M
Dominant hand	R	R	R	R	R	R	R	R	R	R
Affected side at onset	Right	Left	Right	Right	Right	Left	Left	Right	Right	Right
Symptoms at onset	UE BK, R > Tr	UE BK, R	UE BK > Tr	UE and LE BK	UE BK, R > Tr	LE BK	UE and LE Tr	UE Tr	UE BK	UE Tr
PD type	Akinetic rigidity	Akinetic rigidity	Akinetic rigidity	Akinetic rigidity	Akinetic rigidity	Akinetic rigidity	Tremor dominant	Tremor dominant	Akinetic rigidity	Tremor dominant
PD duration (years)	12	4	8	12	6	8	6	17	2	8
Wearing off	+	+	+	+	+	+	+	+	–	+
Dyskinesia	+	+	+	+	–	+	–	+	–	+
Medication	LDED: 1100 mg/day, Amantadine	LDED: 500 mg/day, Amantadine	LDED: 700 mg/day, Amantadine	LDED: 600 mg/day, Amantadine	LDED: 650 mg/day, Amantadine, Rasagiline	LDED: 800 mg/day, Rasagiline	LDED: 1025 mg/day	LDED: 950 mg/day, Amantadine	LDED: 450 mg/day, Rasagiline	LDED: 1100 mg/day, Amantadine
H&Y stage	3	3	2	2	2	2	2	2	2	3

F, female; M, male; R, right; L, left; UE, upper extremity; LE, lower extremity; BK, bradykinesia; R, rigidity; Tr, tremor; PD, Parkinson's disease; LDED, levodopa equivalent dose; H&Y, Hoehn and Yahr.

at the 10th-minute, standard deviation (SD): 3.6 at baseline and 4.6 at the 10th-minute, ΔUPDRS range = 1.5–12] and 5% (ΔUPDRS = 1) in the placebo-control group (mean UPDRS motor scores: 17.4 at baseline, 16.4 at the 10th-minute, *SD*: 4.6 at baseline and 4.5 at the 10th-minute, ΔUPDRS range = −1.5–4.5).

Figure 5 shows the UPDRS Part-III scores and the group comparison for each case and an overall summary of the first arm. **Figure 6** summarizes the classified UPDRS subscore differences for the group comparisons with *t*-tests, **Figure 7** gives these differences for the group comparisons after the Bonferroni correction. **Table 2** summarizes the *p*-values for the *t*-tests and after the Bonferroni correction of the classified UPDRS subscores for the 10th-minute compared with baseline.

The bilateral assessments of the symptomatic improvements of PD patients before and after electrical stimulation revealed that unilateral stimulation of the intrinsic auricular muscles can relieve PD symptoms on both sides at the 10th-minute. The 10th-minute mean improvements in the lateralized (UPDRS Part III subscore 20–26) UPDRS motor subscores were 3.0 on the contralateral side and 3.2 on the ipsilateral side in the active

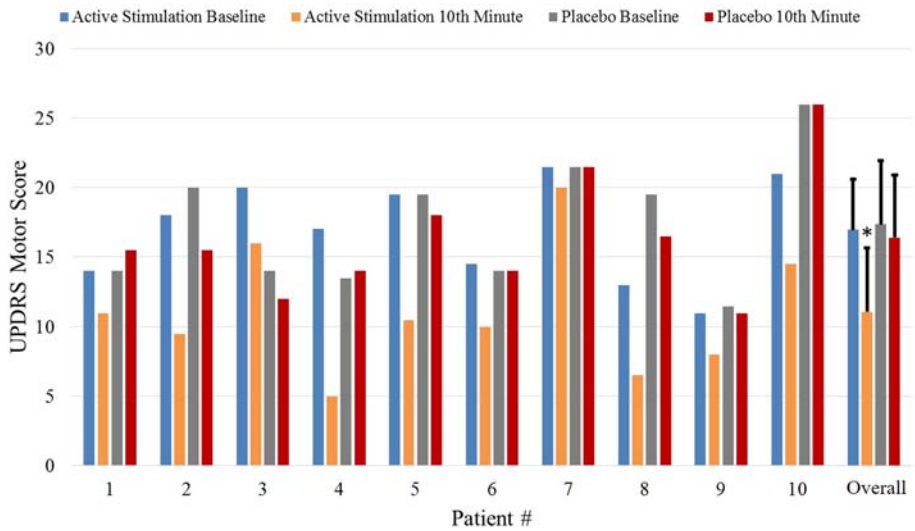


FIGURE 5 | The UPDRS part III scores at baseline and at the 10th-minute for the placebo and active groups and overall comparisons of the first arm. *Statistically significant.

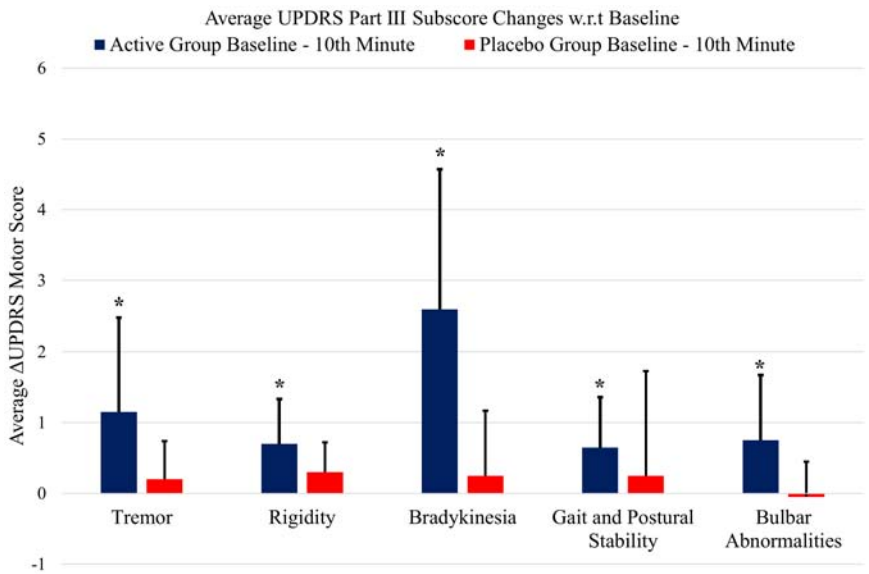


FIGURE 6 | The classified UPDRS subscore differences for group comparisons of the first arm ($p < 0.05$, *t*-test). *Statistically significant.

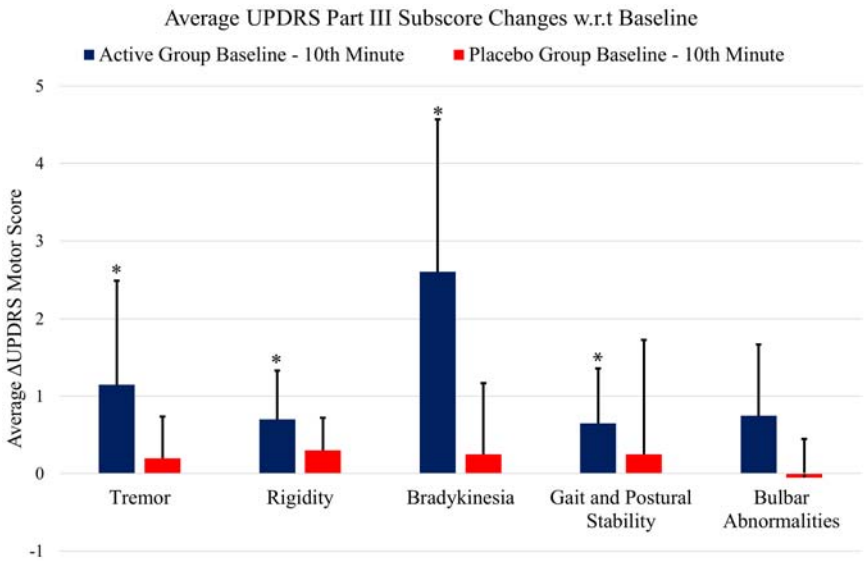


FIGURE 7 | The classified UPDRS subscore differences for group comparisons with Bonferroni correction. *Statistically significant.

TABLE 2 | The *p*-values after Bonferroni correction of the classified UPDRS subscores for the 10th-minute compared with baseline of the first arm study groups.

Subgroup	*p*-Value active group	*p*-Value placebo group
Tremor	***0.023***	0.398
Rigidity	***0.007***	0.051
Bradykinesia	***0.002***	0.413
Gait and postural instability	***0.018***	0.605
Bulbar abnormalities	*0.030*	0.758

t-test; p < 0.05, Bonferroni correction p < 0.025, Italic: significant in t-test, bold: significant after Bonferroni correction, bold and italic: significant in t-test and Bonferroni.

group. The 10th-minute difference in the lateralized UPDRS motor subscores in the placebo-control group were 0.5 on the contralateral side and 0.8 on the ipsilateral side.

Arm 2

The mean age of the patients was 58.1 ±SD 9.8 years, and 6 of the patients were female. The mean disease duration was 7.9 ±SD 3.7 years. Detailed clinical features of the patients are presented in **Table 3**. Baseline UPDRS motor scores of the three groups were compared via one-way repeated measures ANOVA. There were no statistically significant differences between the baseline UPDRS motor scores of the patients in the active (IAMZ electrostimulation), IAMZ dry needling and sham electrostimulation groups prior to the interventions (pairwise comparison *p*-values: active vs. dry needling: 0.286, active vs. sham: 0.052, sham vs. dry needling: 1.0).

In the active group, the UPDRS motor scores were significantly improved at the 50th-minute after the initiation of IAMZ electrostimulation (i.e., 30 min after the termination of the 20-min stimulation) compared with baseline UPDRS scores ($p < 0.001$, power: 0.99). The IAMZ dry needling group also showed statistically significant differences in UPDRS motor scores after the dry needling procedure compared with baseline ($p = 0.011$). However, the improvement in UPDRS motor scores of dry needling stimulation of the IAMZ (ΔUPDRS = 1.54) did not reach clinical significance (Shulman et al., 2010) as electrostimulation of the IAMZ (ΔUPDRS = 5.29). The improvement in the UPDRS score observed in the active group (electrostimulation of the IAMZ) was in the range of moderate to high clinical significance (Shulman et al., 2010). There was no significant difference in UPDRS motor scores in the sham electrostimulation group ($p = 0.748$).

The mean improvement rates at the 50th-minute were 31% (ΔUPDRS = 5.29) in the active group (mean UPDRS motor scores: 17.71 at baseline, 12.42 at the 50th-minute, *SD*: 4.27 at baseline and 4.61 at the 50th-minute, ΔUPDRS range = 0.50–9.50), 9% (ΔUPDRS = 1.54) in the dry needling group (mean UPDRS motor scores: 16.04 at baseline, 14.50 at the 50th-minute, *SD*: 3.1 at baseline and 3.3 at the 50th-minute, ΔUPDRS range = 0.50–7.0) and 0% (ΔUPDRS = 0.20) in the sham stimulation group (mean UPDRS motor scores: 15.25 at baseline, 15.05 at the 50th-minute, *SD*: 5.09 at baseline and 5.15 at the 50th-minute, ΔUPDRS range = −3.5 to 4.0).

One-way repeated measures ANOVA was also performed for the difference in each group's baseline and post-stimulation UPDRS scores (ΔUPDRS comparison). The ΔUPDRS comparison for the active vs. dry needling groups and the active vs. sham groups were significant ($p < 0.001$ for both comparisons); however, the comparison of ΔUPDRS for the sham vs. dry needling groups was not statistically significant ($p = 0.319$).

Figure 8 gives the UPDRS Part-III scores and the group comparison for each case and the overall summary of the second arm. **Figure 9** summarizes the classified UPDRS subscore

TABLE 3 | Detailed clinical features of the patients in the second arm of the study.

	Patient 1	Patient 2	Patient 3	Patient 4	Patient 5	Patient 6	Patient 7	Patient 8	Patient 9	Patient 10	Patient 11	Patient 12	Patient 13	Patient 14
Age (years)	56	47	63	58	54	70	64	45	71	45	63	72	45	60
Gender	M	F	M	F	M	F	M	F	M	F	F	M	M	M
Dominant hand	R	R	R	R	R	R	R	R	R	R	R	R	L	R
Affected side at onset	Right	Right	Right	Right	Right	Right	Left	Left	Right	Left	Right	Left	Right	Right
Symptoms at onset	UE BK	UE TR > BK	UE TR	UE TR > BK	UE TR	UE BK	UE BK	UE TR	UE BK	LE TR	LE TR	BK	TR	BK
PD type	Akinetic rigidity	Akinetic rigidity	Akinetic rigidity	Tremor dominant	Akinetic rigidity	Akinetic rigidity	Akinetic rigidity	Tremor dominant	Akinetic rigidity	Tremor dominant	Tremor dominant	Akinetic rigidity	Akinetic rigidity	Akinetic rigidity
PD duration (years)	7	10	8	15	9	8	1	4	5	8	4	13	8	10
Wearing off	+	+	−	+	+	+	−	−	−	−	−	−	+	−
Dyskinesia	−	+	+	−	+	+	−	−	−	−	+	+	−	+
Medication	LDED: 950 mg/day, Amantadine	LDED: 1200 mg/day, Amantadine	LDED: 300 mg/day, Amantadine	LDED: 1400 mg/day, Amantadine, Rasagiline	LDED: 1316.2 mg/day	LDED: 1000 mg/day	LDED: 500 mg/day	LDED: 940 mg/day, Rasagline	LDED: 660 mg/day	LDED: 840 mg/day	LDED: 800 mg/day	LDED: 850 mg/day, Amantadine	LDED:600 mg/day, Rasagline	LDED: 1162.5 mg/day
H&Y stage	2	2	2	2	3	3	2	2	2	2	2	2	2	2

F, female; M, male; R, right; L, left; UE, upper extremity; LE, lower extremity; BK, bradykinesia; R, rigidity; Tr, tremor; PD, Parkinson's disease; LDED, levodopa equivalent dose; H&Y, Hoehn and Yahr.

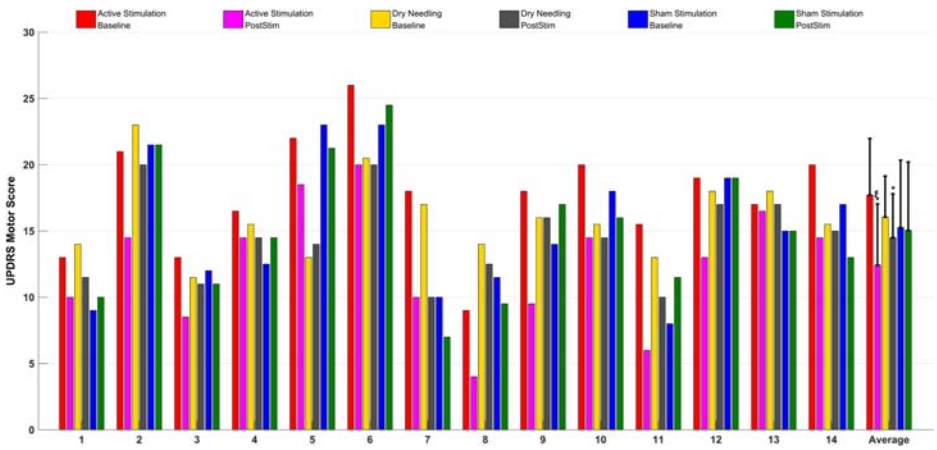


FIGURE 8 | The UPDRS part III scores at baseline and at the 50th-minute for the active group (electrostimulation of the IAMZ), IAMZ dry needling group, and sham stimulation group and overall comparisons of the second arm. *Statistically significant, ξstatistically and clinically significant.

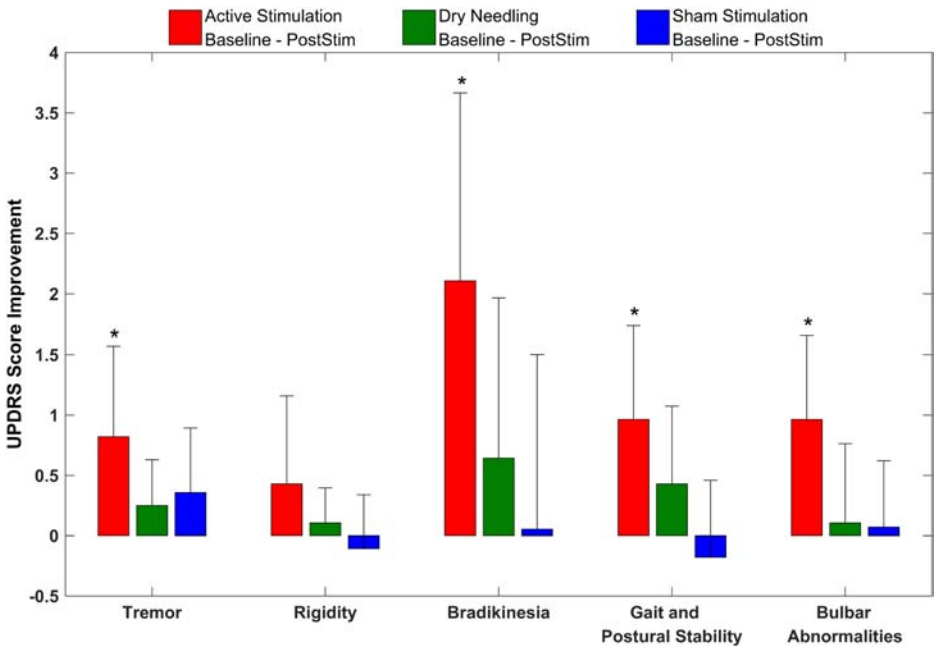


FIGURE 9 | The classified UPDRS subscore differences for group comparisons with Bonferroni correction of the second arm of the study. *Statistically significant.

differences in the group comparisons with Bonferroni correction. **Table 4** summarizes the *p*-values for *t*-tests and after Bonferroni correction of the classified UPDRS subscores for the 50th-minute compared with baseline.

Bilateral assessments of the symptomatic improvements of PD patients before and after electrical stimulation of the IAMZ revealed that unilateral stimulation of the intrinsic auricular muscles can relieve PD symptoms on both sides at the 50th-minute. The 50th-minute mean improvements in the lateralized (UPDRS Part III subscore 20–26) UPDRS motor subscores were 2.39 on the contralateral side and 1.89 on the ipsilateral side in the active group. The 50th-minute differences in the contralateral and ipsilateral UPDRS motor subscores were 0.79 and 0.61 in the dry needling group and 0.48 and 0.0 in the sham group, respectively.

DISCUSSION

The results of the present study demonstrated a substantial improvement in UPDRS motor scores after electrostimulation of the IAMZ but not after placebo or sham stimulation. The UPDRS score improvements in the electrostimulation of IAMZ groups were statistically and clinically significant. Comparison of the ΔUPDRS (5.9 in the first arm and 5.29 in the second arm) of

TABLE 4 | The *p*-values after Bonferroni correction of the classified UPDRS subscores for the 50th-minute compared with baseline of the second arm study groups.

	***p*-Values - Baseline vs. Post-stim**		
Subgroup	**Active**	**Dry needling**	**Sham**
Tremor	***0.001***	*0.029*	*0.027*
Rigidity	*0.047*	0.189	0.385
Bradykinesia	***<0.001***	0.092	0.892
Gait and postural instability	***<0.001***	*0.028*	0.315
Bulbar abnormalities	***<0.001***	0.551	0.635

t-test; p < 0.05, Bonferroni correction p < 0.016. Italic: significant in t-test, bold: significant after Bonferroni correction, bold and italic: significant in t-test and Bonferroni.

the active groups considering the clinically important difference (CID) values described by Shulman et al. (ΔUPDRS 2.5, 5.2, and 10.8 for minimal, moderate, and large CIDs, respectively) indicated that the improvement in UPDRS scores obtained with electrostimulation of the IAMZ in the present study falls between a moderate and large CID (Shulman et al., 2010). In addition, dry needling of IAMZ group reached to a statistically significant improvement (but not a CID) in UPDRS scores which was not the case for the sham or placebo groups. The dry needling group results also underlined the significance of the IAMZ. Invasive deep brain stimulation modalities of neuromodulation utilize bilateral approaches to document UPDRS improvement rates. It must be noted that the results of the present study were obtained using only unilateral stimulation, and bilateral stimulation needs to be investigated.

In addition to UPDRS score improvements, the classified UPDRS subitem paired *t*-test analysis also demonstrated that symptomatic suppression for all subitem groups in both arms of the study, including tremor, rigidity, bradykinesia, gait and postural stability and bulbar abnormalities, were statistically significant for only the electrostimulation of IAMZ group. All of the other study groups were not statistically significant after *t*-test analysis for all of the subitem analysis.

The Bonferroni correction is a conservative approach that has advantages and disadvantages, especially for pilot studies. To clarify the outcomes of the conservative Bonferroni correction, we also performed analyses of the subscore groups. The suppression of tremor, rigidity, gait and postural stability and bradykinesia symptoms were still statistically significant after Bonferroni correction in the first arm of the study, and all subgroups (except rigidity) exhibited statistically significant reductions after bonferroni correction in the second arm of the study. In addition, although the improvements in bulbar abnormalities of the first arm and rigidity in the second arm were not statistically significant after the Bonferroni correction, there was a trend toward significance in both groups (p-crit: 0.025, *p*: 0.030 for bulbar abnormalities in arm 1; and p-crit: 0.016, *p*: 0.047 for rigidity in arm 2). Axial symptoms, including speech, have also been reported to worsen with DBS-STN (Tornqvist et al., 2005; Hammer et al., 2010; Moreau et al., 2011; Sidiropoulos et al., 2013). None of the subitems worsened in the active stimulation group in the present study, in contrast to other DBS-STN applications (Tornqvist et al., 2005; Hammer et al., 2010; Moreau et al., 2011; Sidiropoulos et al., 2013). On the other hand, DBS-PPN has been reported to induce greater improvements in PIGD (Hamani et al., 2007; Tykocki et al., 2011). In the context of the different outcomes of DBS-STN and DBS-PPN on motor symptoms and the outcomes in the present study, we suggest that the underlying mechanism of IAMZ stimulation may be related to PPN-associated pathways rather than STN-associated pathways or that both the STN and the PPN may be responsible for the observed effect; however, a sole contribution of the STN is not suggested.

The results of the bilateral assessments of the symptomatic improvements of PD patients before and after electrical stimulation of the IAMZ revealed that unilateral stimulation (ipsilateral to dominant, lateralized motor symptoms) of the IAMZ relieved PD symptoms on both sides of patients in both arms of this study. These improved contralateral motor symptoms may suggest a bihemispheric contribution of the intrinsic auricular muscles. Whether the stimulation of facial nerve branches over the intrinsic auricular muscles is solely responsible for all of the bilateral symptomatic improvements observed in this study or whether other nerves in the IAMZ also contribute remains unclear. The C2 spinal nerve may also play a role in bilateral symptomatic improvement. Although the C2-related role of the propriospinal tracts is more active on the ipsilateral side, animal studies demonstrated that C2 spinal nerves have ipsilateral and contralateral connections with the interpositus nucleus of the cerebellum (Matsushita and Xiong, 2001). As such, C2 spinal nerve stimulation may act on the bilateral PPN through bilateral cerebellar nuclei, and bilateral PPN stimulation may act on the bilateral reticulospinal tract to modulate bilateral motor symptoms. However, C2 zone stimulation in the sham group of the second arm was ineffective.

Autonomic nerve modulation may also contribute to the bilateral symptomatic relief observed in the present study. Low-frequency vagal nerve stimulation leads to impaired vagus nerve function and inhibition of the dopamine system in brain structures (Ziomber et al., 2012). Considering that low- and high-frequency electrostimulation have different outcomes on the autonomic nerve system and on neurotransmitters (Cakmak et al., 2008, 2016; Zhao, 2008), high-frequency stimulation of the Arnold branch of the vagus nerve may in fact have the opposite effect. The present study used 130 Hz stimulation, which is very high compared with the frequency (0.5 Hz) that inhibits the dopaminergic system via vagus nerve stimulation (Ziomber et al., 2012). Therefore, the beneficial bilateral effects obtained in the present study may also be derived from improved dopamine levels. Although there was not a formal feedback survey, the patients in the active group also reported that they felt like they had their levodopa pills. The underlying neurotransmitter related mechanism of action will be the focus of animal studies in addition to levodopa integrated clinical trials for the IAMZ stimulation.

A recent study reported bilateral c-fos activation in the nucleus tractus solitarius (NTS) and the locus coerulei (LC) after stimulation of the left cavum concha area, which is located in the bed of the Arnold branch of the vagus nerve

in rats (Ay et al., 2015) (**Figures 1A,B**). On the other hand, transganglionic neurotracing studies with horseradish peroxidase (HRP) injections to the central cut end of the Arnold branch did not result in LC labeling (Nomura and Mizuno, 1984). Interestingly, the same study investigated left cavum concha stimulation and reported c-fos activation in the facial nerve nucleus in one of the experimental animals. The cavum concha is located next to the helicis minor muscle, and facial nerve fibers to the helicis minor may also be distributed in this area. Therefore, it is always possible that some facial nerve fibers will be stimulated along with the Arnold branch of the vagus nerve within the cavum concha. The authors attributed the c-fos labeling in the bilateral LC to projections from the NTS and as a result of stimulation of the Arnold branch of the vagus nerve. The Arnold branch of the vagus-NTS-LC axis may not be the only option for bilateral LC c-fos labeling after cavum concha stimulation, as sympathetic nerves also contribute to the cavum concha area within the arterial walls, and the cervical sympathetic ganglia were not investigated for possible labeling in that particular study. A major input to the LC originates from the nucleus paragigantocellularis (nPGi) in the reticular formation (Ennis and Aston-Jones, 1988; Kessel et al., 2008) (**Figure 1B**). The nPGi directly innervates sympathetic neurons and receives inputs (Ennis and Aston-Jones, 1988; Aston-Jones et al., 1996; Berntson et al., 1998) (**Figures 1A,B**). This pathway is involved in transmitting information of sympathetic control and state between the nPGi and the LC (Garcia-Rill, 1991; Limousin et al., 1997) (**Figures 1A,B**). In addition, the nPGi has been shown to be antidromically activated by electrostimulation of the LC, which may also be the case for sympathetic afferents. The major efferent pathways of the LC, the major wakefulness-promoting nucleus, project to the PPN (Samuels and Szabadi, 2008) (**Figure 1B**). Therefore, the possible role of the auricular sympathetic nerves in LC activation and, as a consequence, their possible effects on motor regulation via the LC-PPN axis, cannot be excluded. In contrast, the sham stimulation zone, which included the C2 and sympathetic nerves in the second arm of the study, did not affect the UPDRS motor scores, which may suggest that the sympathetic nerves had a minimal role in the UPDRS improvements observed in the present study. On the other hand, the distribution of the sympathetic nerves may have less contribution to sham zone stimulation area in comparison to the IAMZ electrostimulation zones so that sympathetic nerves may still have a potential role in the observed clinical improvement.

Although there are different possible anatomical pathways from the IAMZ to the LC-PPN axis that need to be investigated, the demonstration of bilateral LC activation through unilateral stimulation of the cavum concha area (Ay et al., 2015) may also explain the bilateral motor improvements observed in our study.

Proprioception nerve fibers of the intrinsic auricular muscles may project to the mesencephalic trigeminal nucleus, to the cuneate nucleus, or both. The mesencephalic trigeminal nucleus projects to the reticular formation and to the spinal cord (Usunoff et al., 1997) (**Figures 1A,B**). This connection indicates the presence of potential intrinsic auricular muscle proprioception feedback over reticular formation, which is the PPN's gateway for influencing movement and posture. On the other hand, imaging studies have revealed that the cortical representation of the ear is distributed not as a single zone over the cortical face-head representation area but as numerous different zones over the face, head and neck representation areas (Nihashi et al., 2001). If this unique auricular sensory representation finding is extrapolated to intrinsic auricular muscle representations, then the proprioceptive feedback of the intrinsic auricular muscles may also contribute to the neck proprioceptive center, the nucleus cuneatus. A recent study also supported such a connection: in an fMRI study, stimulation of the antitragicus muscle zone as a control demonstrated activation of the nucleus cuneatus, whereas there was no activation in the nucleus cuneatus when a non-muscular area of the ear was stimulated (Frangos et al., 2015) (**Figures 1A,B**). The nucleus cuneatus and the PPN are the two major components of the mesencephalic locomotor region that modulates PGID (Garcia-Rill, 1991). The SCM, where the transcutaneous electrode was placed, may also play a role in nucleus cuneatus modulation because of the alternating anode-cathode stimulation method that we used in the present study. On the other hand, the effect would be relatively small compared with the effect that occurs by IAMZ stimulation because of the transcutaneous electrode usage and the very low power of the stimulus. We did not observe any contractions of the SCM during stimulation. In addition, the patients also reported a distinct tingling sensation over the IAMZ but not of the SCM where the transcutaneous electrode was placed. The different surface size of the needle electrodes placed on the IAMZ compared with the transcutaneous electrodes on the SCM may be the reason behind this difference, in addition to the skin conductance factor between the needle electrodes and the transcutaneous electrodes. In conclusion, the contribution of the SCM electrode to the symptomatic improvements observed in the present study, if any, would be minimal. The sham region in the present study is selected to eliminate the potential effect of stimulation of only the C2/sympathetic nerve by ensuring no or minimal stimulation of the SCM, the vagus facial nerve and the trigeminal nerve, on the other hand the character of the sham design has limitations for surface SCM stimulation contributions (if any). Different sham group designs are needed to eliminate the SCM only stimulation effects.

The upper face muscles, such as the orbicularis oculi and frontalis muscles, have similar bilateral hemispheric connections; however, reports of the muscle spindle content of the orbicularis oculi highlight the lack of muscle spindles in this muscle group (Urban et al., 2004). In addition, these muscles are actively used to as mimics and as sphincters, and the contraction of these muscles with external electrostimulation may induce visible contractions that counteract their functions. In conclusion, these muscles are not the ideal targets, not only because they lack muscle spindles but also because they are actively used in daily life, and therefore, the contraction of these muscles may be annoying to patients. Subthreshold stimulation that does not induce visible contractions of these muscles may be another option for an alternative non-invasive electrostimulation modality for modulating similar networks related to IAMZ, but the lack of muscle spindles is still a major concern. On the other hand, intrinsic auricular muscles have active roles in shaping

the external ear surface features during the prenatal period and become functionally regressed but anatomically intact in adult humans, such that stimulation of intrinsic muscles does not induce the visible contractions observed in the frontalis and orbicularis oculi (Zerin et al., 1982; Yotsuyanagi et al., 1999). Finally, although no studies on the muscle spindle content of human intrinsic auricular muscles have been published thus far, muscle spindles have been examined in peri-auricular muscles in non-human primates, including, rhesus monkeys (Lovell et al., 1977). The statistically significant (but clinically not significant) effect that was observed in the IAMZ dry needling group in the second arm of the study also underlines the significance of the IAMZ zone during minimal stimulation. In addition, it is worth noting that electrostimulation with the same parameters of a muscle-free area of the auricula in the sham group had no effect on UPDRS scores.

The current study was a pilot study performed on a small group of patients that investigated the immediate effects of IAMZ stimulation on PD motor symptoms. Although the study includes numerous groups including sham, placebo, dry needling and active, the SCM contribution (if any), and the potential perception differences of the sham and real IAMZ stimulations were the limitations. The results require further validation in subsequent studies with more participants. Further investigations of bilateral stimulation applications and different stimulation frequencies are also needed to clarify the efficacy of the technique, as in DBS, for patient-specific frequency effects on tremor. In addition, although postural tremor and tremor at rest significantly improved after active stimulation, we observed that tremor developed more erratically and was modulated by the emotional states of patients. In addition, the patients also well-tolerated the device without any side effect or discomfort with short term (20 min) stimulation. The usability of the device for longer terms will be the focus of future trials. Responsiveness regarding the stage of the disease, different stimulation frequencies and long-term effects should also be investigated. Moreover, we only observed the short-term effects of stimulation, and the second arm of the study indicates that the effect may persist up to the 30th-minute after termination of stimulation, which corresponded to the 50th-minute after the initiation of the stimulation. Prolonged efficacy will also be the focus of the next phase of clinical trials. Responsiveness regarding the stage of the disease must also be investigated in future studies.

CONCLUSION

We provide the first demonstration of a potential role of IAMZ electrical stimulation in improving (moderate to large clinical improvement) the clinical motor symptoms of PD patients in the short term. The underlying neuronal pathways and mechanisms need to be investigated in future studies.

AUTHOR CONTRIBUTIONS

Developed the concept: YC; experiment design: YC, YO, SE; performed stimulation experiments: YC, BO; performed patient enrollments and/or clinical assessments: HA, GK, SE, AG, OC; development of hardware: HU, SO, YC; development of software and code writing: HU, SO, BO, YC; development of analytical tools: HU, SO, BO, YC; data collection: BO, YC, OC, SO; analyzed data: YC, SE, AG, BO, YO, SE; wrote the draft: YC; wrote the main paper: YC, HA, GK, SE, AG, BO, OC, YO, HU, BO.

FUNDING

This project was supported by Koç University, School of Medicine.

REFERENCES

Alstermark, B., Isa, T., Lundberg, A., Pettersson, L. G., and Tantisira, B. (1989). The effect of low pyramidal lesions on forelimb movements in the cat. *Neurosci. Res.* 7, 71–75. doi: 10.1016/0168-0102(89)90038-2

Alstermark, B., Lundberg, A., Norrsell, U., and Sybirska, E. (1981). Integration in descending motor pathways controlling the forelimb in the cat. 9. Differential behavioural defects after spinal cord lesions interrupting defined pathways from higher centres to motoneurones. *Exp. Brain Res.* 42, 299–318. doi: 10.1007/BF00237496

Alvord, L. S., and Farmer, L. B. (1997). Anatomy and orientation of the human external ear. *J. Am. Acad. Audiol.* 8, 383–390.

Aston-Jones, G., Rajkowski, J., Kubiak, P., Valentino, R. J., and Shipley, M. T. (1996). Role of the locus coeruleus in emotional activation. *Prog. Brain Res.* 107, 379–402. doi: 10.1016/S0079-6123(08)61877-4

Ay, I., Napadow, V., and Ay, H. (2015). Electrical stimulation of the vagus nerve dermatome in the external ear is protective in rat cerebral ischemia. *Brain Stimul.* 8, 7–12. doi: 10.1016/j.brs.2014.09.009

Berntson, G. G., Sarter, M., and Cacioppo, J. T. (1998). Anxiety and cardiovascular reactivity: the basal forebrain cholinergic link. *Behav. Brain Res.* 94, 225–248. doi: 10.1016/S0166-4328(98)00041-2

Braak, H., del Tredici, K., Rub, U., de Vos, R. A., Jansen Steur, E. N., and Braak, E. (2003). Staging of brain pathology related to sporadic Parkinson's disease. *Neurobiol. Aging* 24, 197–211. doi: 10.1016/S0197-4580(02)00065-9

Burn, D. (2013). *Oxford Textbook of Movement Disorders*. Oxford: Oxford University Press, 16–22. doi: 10.1093/med/9780199609536.001.0001

Cakmak, Y. O., Akpinar, I. N., Ekinci, G., and Bekiroglu, N. (2008). Point- and frequency–specific response of the testicular artery to abdominal electroacupuncture in humans. *Fertil. Steril.* 90, 1732–1738. doi: 10.1016/j.fertnstert.2007.08.013

Cakmak, Y. O., Akpinar, I. N., and Yoldemir, T. (2016). Decreasing the uterine blood flow with electroacupuncture: bidermatomal and monodermatomal applications. *Gynecol. Obstet. Invest.* 82, 151–156. doi: 10.1159/000446947

Costa, J., Valls-Sole, J., Valldeoriola, F., Rumia, J., and Tolosa, E. (2007). Motor responses of muscles supplied by cranial nerves to subthalamic nucleus deep brain stimuli. *Brain* 130, 245–255. doi: 10.1093/brain/awl336

Daniel, E. E., and Paton, D. M. (1975). *Methods in Pharmacology, Smooth Muscle,* Vol. 3. New York, NY: Plenum Press, 442. doi: 10.1007/978-1-4684-2751-6

Drake, R. L., Vogl, W., and Mitchell, A. W. M. (2015). *Gray's Anatomy for Students*. Philadelphia, PA: Churchill Livingstone, 954.

Drew, T. (1991). Functional organization within the medullary reticular formation of the intact unanesthetized cat. III. Microstimulation during locomotion. *J. Neurophysiol.* 66, 919–938.

Drew, T., and Rossignol, S. (1990). Functional organization within the medullary reticular formation of intact unanesthetized cat. I. movements evoked by microstimulation. *J. Neurophysiol.* 64, 767–781.

Ennis, M., and Aston-Jones, G. (1988). Activation of locus coeruleus from nucleus paragigantocellularis: a new excitatory amino acid pathway in brain. *J. Neurosci.* 8, 3644–3657.

Frangos, E., Ellrich, J., and Komisaruk, B. R. (2015). Non-invasive access to the vagus nerve central projections via electrostimulation of the external ear: fMRI evidence in humans. *Brain Stimul.* 8, 624–636. doi: 10.1016/j.brs.2014.11.018

Fujita, T. (1934). Die motorische innervation der genuinen aurikularmuskeln beim menschen, nebst bemerkungen zu ihrer phylogenetischen herkunft. *Anat. Anz.* 78, 321.

Garcia-Rill, E. (1991). The pedunculopontine nucleus. *Prog. Neurobiol.* 36, 363–389. doi: 10.1016/0301-0082(91)90016-T

Gorska, T., and Sybirska, E. (1980). Effects of pyramidal lesions on forelimb movements in the cat. *Acta Neurobiol. Exp.* 40, 843–859.

Hamani, C., Stone, S., Laxton, A., and Lozano, A. M. (2007). The pedunculopontine nucleus and movement disorders: anatomy and the role for deep brain stimulation. *Parkinsonism Relat. Disord.* 13, S276–S280. doi: 10.1016/S1353-8020(08)70016-6

Hammer, M. J., Barlow, S. M., Lyons, K. E., and Pahwa, R. (2010). Subthalamic nucleus deep brain stimulation changes speech respiratory and laryngeal control in Parkinson's disease. *J. Neurol.* 257, 1692–1702. doi: 10.1007/s00415-010-5605-5

Hanajima, R., Chen, R., Ashby, P., Lozano, A. M., Hutchison, W. D., Davis, K. D., et al. (2004). Very fast oscillations evoked by median nerve stimulation in the human thalamus and subthalamic nucleus. *J. Neurophysiol.* 92, 3171–3182. doi: 10.1152/jn.00363.2004

Harting, J. K. (1997). *The Global Cerebellum '97*. Ph.D. thesis, University of Wisconsin Medical School, Madison, WI.

Hazrati, L. N., and Parent, A. (1992). Projection from the deep cerebellar nuclei to the pedunculopontine nucleus in the squirrel monkey. *Brain Res.* 585, 267–271. doi: 10.1016/0006-8993(92)91216-2

Hirsch, E. C., Graybiel, A. M., Duyckaerts, C., and Javoy-Agid, F. (1987). Neuronal loss in the pedunculopontine tegmental nucleus in Parkinson's disease and in progressive supranuclear palsy. *Proc. Natl. Acad. Sci. U.S.A.* 84, 5976–5980. doi: 10.1073/pnas.84.16.5976

Hobbs, S. F., Oh, U. T., Chandler, M. J., Fu, Q. G., Bolser, D. C., and Foreman, R. D. (1992). Evidence that C1 and C2 propriospinal neurons mediate the inhibitory effects of viscerosomatic spinal afferent input on primate spinothalamic tract neurons. *J. Neurophysiol.* 67, 852–860.

Hughes, A. J., Daniel, S. E., Kilford, L., and Lees, A. J. (1992). Accuracy of clinical diagnosis of idiopathic Parkinson's disease: a clinico–pathological study of 100 cases. *J. Neurol. Neurosurg. Psychiatry* 55, 181–184. doi: 10.1136/jnnp.55.3.181

Jankowska, E., and Edgley, S. A. (2006). How can corticospinal tract neurons contribute to ipsilateral movements? A question with implications for recovery of motor functions. *Neuroscientist* 12, 67–79. doi: 10.1177/107385840528 3392

Jankowska, E., Lundberg, A., and Stuart, D. (1983). Propriospinal control of interneurons in spinal reflex pathways from tendon organs in the cat. *Brain Res.* 261, 317–320. doi: 10.1016/0006-8993(83)90636-4

Kably, B., and Drew, T. (1998). Corticoreticular pathways in the cat. I. Projection patterns and collaterization. *J. Neurophysiol.* 80, 389–405.

Karachi, C., Grabli, D., Bernard, F. A., Tande, D., Wattiez, N., Belaid, H., et al. (2010). Cholinergic mesencephalic neurons are involved in gait and postural disorders in Parkinson's disease. *J. Clin. Invest.* 120, 2745–2754. doi: 10.1172/JCI42642

Keizer, K., and Kuypers, H. G. (1984). Distribution of corticospinal neurons with collaterals to lower brain stem reticular formation in cat. *Exp. Brain Res.* 54, 107–120. doi: 10.1007/BF00235823

Keizer, K., and Kuypers, H. G. (1989). Distribution of corticospinal neurons with collaterals to the lower brain stem reticular formation in monkey (*Macaca fascicularis*). *Exp. Brain Res.* 74, 311–318. doi: 10.1007/BF00248864

Kessel, F., Rosenfield, P., and Anderson, N. (2008). *Expanding the Boundaries of Health and Social Science: Case Studies in Interdisciplinary Innovation*. New York, NY: Oxford University Press, 27.

Lambru, G., Miller, S., and Matharu, M. S. (2013). The red ear syndrome. *J. Headache Pain* 2:83. doi: 10.1186/1129-2377-14-83

Lavoie, B., and Parent, A. (1994). Pedunculopontine nucleus in the squirrel monkey: projections to the basal ganglia as revealed by anterograde tract-tracing methods. *J. Comp. Neurol.* 344, 210–231. doi: 10.1002/cne.903440204

Lawrence, D. G., and Kuypers, H. G. (1968). The functional organization of the motor system in the monkey: I. The effects of bilateral pyramidal lesions. *Brain* 91, 1–14. doi: 10.1093/brain/91.1.1

Lee, D., Henriques, D. Y., Snider, J., Song, D., and Poizner, H. (2013). Reaching to proprioceptively defined targets in Parkinson's disease: effects of deep brain stimulation therapy. *Neuroscience* 244, 99–112. doi: 10.1016/j.neuroscience.2013.04.009

Limousin, P., Greene, J., Pollak, P., Rothwell, J., Benabid, A. L., and Frackowiak, R. (1997). Changes in cerebral activity pattern due to subthalamic nucleus or internal pallidum stimulation in Parkinson's disease. *Ann. Neurol.* 42, 283–291. doi: 10.1002/ana.410420303

Limousin, P., Pollak, P., Benazzouz, A., Hoffmann, D., Le Bas, J. F., Broussolle, E., et al. (1995). Effect of parkinsonian signs and symptoms of bilateral subthalamic nucleus stimulation. *Lancet* 345, 91–95. doi: 10.1016/S0140-6736(95)90062-4

Little, S., and Brown, P. (2012). What brain signals are suitable for feedback control of deep brain stimulation in Parkinson's disease? *Ann. N. Y. Acad. Sci.* 1265, 9–24. doi: 10.1111/j.1749-6632.2012.06650.x

Lovell, M., Sutton, D., and Lindeman, R. C. (1977). Muscle spindles in nonhuman primate extrinsic auricular muscles. *Anat. Rec.* 189, 519–523. doi: 10.1002/ar.1091890310

Luccarini, P., Gahery, Y., and Pompeiano, O. (1990). Cholinoceptive pontine reticular structures modify the postural adjustments during the limb movements induced by cortical stimulation. *Arch. Ital. Biol.* 128, 19–45.

Magni, F., and Willis, W. D. (1964). Cortical control of brain stem reticular neurons. *Arch. Ital. Biol.* 102, 418–433.

Massion, J. (1992). Movement, posture and equilibrium: interaction and coordination. *Prog. Neurobiol.* 38, 35–56. doi: 10.1016/0301-0082(92)90034-C

Matsuo, K., and Hirose, T. (1987). Tragicus and antitragicus muscles as constrictors of the external auditory meatus. *Eur. J. Plastic Surg.* 10, 82–83. doi: 10.1007/BF00578381

Matsushita, M., and Xiong, G. (2001). Uncrossed and crossed projections from the upper cervical spinal cord to the cerebellar nuclei in the rat, studied by anterograde axonal tracing. *J. Comp. Neurol.* 432, 101–118. doi: 10.1002/cne.1091

McFarland, N. R., and Haber, S. N. (2000). Convergent inputs from thalamic motor nuclei and frontal cortical areas to the dorsal striatum in the primate. *J. Neurosci.* 20, 3798–3813.

Mima, T., Sadato, N., Yazawa, S., Hanakawa, T., Fukuyama, H., Yonekura, Y., et al. (1999). Brain structures related to active and passive finger movements in man. *Brain* 122, 1989–1997. doi: 10.1093/brain/122.10.1989

Moreau, C., Pennel-Ployart, O., Pinto, S., Plachez, A., Annic, A., Viallet, F., et al. (2011). Modulation of dysarthropneumophonia by low–frequency STN DBS in advanced Parkinson's disease. *Mov. Disord.* 26, 659–663. doi: 10.1002/mds.23538

Mori, S., Matsuyama, K., Kohyama, J., Kobayashi, Y., and Takakusaki, K. (1992). Neuronal constituents of postural and locomotor control systems and their interactions in cats. *Brain Dev.* 14, S109–S120.

Muthusamy, K. A., Aravamuthan, B. R., Kringelbach, M. L., Jenkinson, N., Voets, N. L., Johansen-Berg, H., et al. (2007). Connectivity of the human pedunculopontine nucleus region and diffusion tensor imaging in surgical targeting. *J. Neurosurg.* 107, 814–820. doi: 10.3171/JNS-07/10/0814

Nambu, A., Takada, M., Inase, M., and Tokuno, H. (1996). Dual somatotopical representations in the primate subthalamic nucleus: evidence for ordered but reversed body-map transformations from the primary motor cortex and the supplementary motor area. *J. Neurosci.* 16, 2671–2683.

Nambu, A., Tokuno, H., Hamada, I., Kita, H., Imanishi, M., Akazawa, T., et al. (2000). Excitatory cortical inputs to pallidal neurons via the subthalamic nucleus in the monkey. *J. Neurophysiol.* 84, 289–300.

Nambu, A., Tokuno, H., Inase, M., and Takada, M. (1997). Corticosubthalamic input zones from forelimb representations of the dorsal and ventral divisions of the premotor cortex in the macaque monkey: comparison with the input zones from the primary motor cortex and the supplementary motor area. *Neurosci. Lett.* 239, 13–16. doi: 10.1016/S0304-3940(97)00877-X

Nihashi, T., Kakigi, R., Kawakami, O., Hoshiyama, M., Itomi, K., Nakanishi, H., et al. (2001). Representation of the ear in human primary somatosensory cortex. *Neuroimage* 13, 295–304. doi: 10.1006/nimg.2000.0695

Nomura, S., and Mizuno, N. (1984). Central distribution of primary afferent fibers in the Arnold's nerve (the auricular branch of the vagus nerve): a

transganglionic HRP study in the cat. *Brain Res.* 292, 199–205. doi: 10.1016/0006-8993(84)90756-X

Payoux, P., Remy, P., Damier, P., Miloudi, M., Loubinoux, I., Pidoux, B., et al. (2004). Subthalamic nucleus stimulation reduces abnormal motor cortical overactivity in Parkinson disease. *Arch. Neurol.* 61, 1307–1313. doi: 10.1001/archneur.61.8.1307

Peuker, T. E., and Filler, T. J. (2002). The nerve supply of the human auricle. *Clin. Anat.* 15, 35–37. doi: 10.1002/ca.1089

Postuma, R. B., Gagnon, J. F., Vendette, M., Charland, K., and Montplaisir, J. (2008). Research paper REM sleep behaviour disorder in Parkinson's disease is associated with specific motor features. *J. Neurol. Neurosurg. Psychiatry* 79, 1117–1121. doi: 10.1136/jnnp.2008.149195

Samuels, E. R., and Szabadi, E. (2008). Functional neuroanatomy of the noradrenergic locus coeruleus: its roles in the regulation of arousal and autonomic function part I: principles of functional organisation. *Curr. Neuropharmacol.* 6, 235–253. doi: 10.2174/15701590878577 7229

Sasaki, S. (2004). Dexterous finger movements in primate without monosynaptic corticomotoneuronal excitation. *J. Neurophysiol.* 92, 3142–3147. doi: 10.1152/jn.00342.2004

Schell, G. R., and Strick, P. L. (1984). The origin of thalamic inputs to the arcuate premotor and supplementary motor areas. *J. Neurosci.* 4, 539–560.

Schepens, B., and Drew, T. (2003). Strategies for the integration of posture and movement during reaching in the cat. *J. Neurophysiol.* 90, 3066–3086. doi: 10.1152/jn.00339.2003

Shulman, L. M., Gruber-Baldini, A. L., Anderson, K. E., Fishman, P. S., Reich, S. G., and Weiner, W. J. (2010). The clinically important difference on the unified Parkinson's disease rating scale. *Arch. Neurol.* 67, 64–70. doi: 10.1001/archneurol.2009.295

Sidiropoulos, C., Walsh, R., Meaney, C., Poon, Y. Y., Fallis, M., and Moro, E. (2013). Low–frequency subthalamic nucleus deep brain stimulation for axial symptoms in advanced Parkinson's disease. *J. Neurol.* 260, 2306–2311. doi: 10.1007/s00415-013-6983-2

Takakusaki, K., Tomita, N., and Yano, M. (2008). Substrates for normal gait and pathophysiology of gait disturbances with respect to the basal ganglia dysfunction. *J. Neurol.* 255, 19–29. doi: 10.1007/s00415-008-4004-7

Tattersall, T. L., Stratton, P. G., Coyne, T. J., Cook, R., Silberstein, P., Silburn, P. A., et al. (2014). Imagined gait modulates neuronal network dynamics in the human pedunculopontine nucleus. *Nat. Neurosci.* 17, 449–454. doi: 10.1038/nn.3642

Tornqvist, A. L., Schalen, L., and Rehncrona, S. (2005). Effects of different electrical parameter settings on the intelligibility of speech in patients with Parkinson's disease treated with subthalamic deep brain stimulation. *Mov. Disord.* 20, 416–423. doi: 10.1002/mds.20348

Tykocki, T., Mandat, T., and Nauman, P. (2011). Pedunculopontine nucleus deep brain stimulation in Parkinson's disease. *Arch. Med. Sci.* 7, 555–564. doi: 10.5114/aoms.2011.24119

Urban, P., Bohl, J., Abrao, L., and Stofft, E. (2004). Absence of muscle spindles in human facial muscles. *Klin. Neurophysiol.* 35, 297.

Usunoff, K. G., Marani, E., and Schoen, J. H. R. (1997). *The Trigeminal System in Man: Advances in Anatomy, Embryology and Cell Biology*, Vol. 136. Berlin: Springer, 1–126. doi: 10.1007/978-3-642-60779-0

Wardman, D. L., Gandevia, S. C., and Colebatch, J. G. (2014). Cerebral, subcortical, and cerebellar activation evoked by selective stimulation of muscle and cutaneous afferents: an fMRI study. *Physiol. Rep.* 2:e00270. doi: 10.1002/phy2.270

Whishaw, I. Q., Gorny, B., and Sarna, J. (1998). Paw and limb use in skilled and spontaneous reaching after pyramidal tract, red nucleus and combined lesions in the rat: behavioral and anatomical dissociations. *Behav. Brain Res.* 93, 167–183. doi: 10.1016/S0166-4328(97)00152-6

Yotsuyanagi, T., Nihei, Y., Shinmyo, Y., and Sawada, Y. (1999). Stahl's ear caused by an abnormal intrinsic auricular muscle. *Plast. Reconstr. Surg.* 103, 171–174. doi: 10.1097/00006534-199901000-00027

Zerin, M., Van Allen, M. I., and Smith, D. W. (1982). Intrinsic auricular muscles and auricular form. *Pediatrics* 69, 91–93.

Zhao, Z. Q. (2008). Neural mechanism underlying acupuncture analgesia. *Prog. Neurobiol.* 85, 355–375. doi: 10.1016/j.pneurobio.2008.05.004

Ziomber, A., Thor, P., Krygowska-Wajs, A., Zalecki, T., Moskala, M., Romanska, I., et al. (2012). Chronic impairment of the vagus nerve function leads to inhibition of dopamine but not serotonin neurons in rat brain structures. *Pharmacol. Rep.* 64, 1359–1367. doi: 10.1016/S1734-1140(12)70933-7

Zweig, R. M., Jankel, W. R., Hedreen, J. C., Mayeux, R., and Price, D. L. (1989). The pedunculopontine nucleus in Parkinson's disease. *Ann. Neurol.* 26, 41–46. doi: 10.1002/ana.410260106

Conflict of Interest Statement: YC, HU, SO, and BO have a related pending patent application.

The other authors declare that the research was conducted in the absence of any commercial or financial relationships that could be construed as a potential conflict of interest.

Copyright © 2017 Cakmak, Apaydin, Kiziltan, Gündüz, Ozsoy, Olcer, Urey, Cakmak, Ozdemir and Ertan. This is an open-access article distributed under the terms of the Creative Commons Attribution License (CC BY). The use, distribution or reproduction in other forums is permitted, provided the original author(s) or licensor are credited and that the original publication in this journal is cited, in accordance with accepted academic practice. No use, distribution or reproduction is permitted which does not comply with these terms.

frontiers in Pharmacology

ORIGINAL RESEARCH
published: 28 June 2017
doi: 10.3389/fphar.2017.00401

Astrocyte Activation in Locus Coeruleus Is Involved in Neuropathic Pain Exacerbation Mediated by Maternal Separation and Social Isolation Stress

*Kazuo Nakamoto[1], Fuka Aizawa[1], Megumi Kinoshita[1], Yutaka Koyama[2] and Shogo Tokuyama[1]**

[1] Department of Clinical Pharmacy, School of Pharmaceutical Sciences, Kobe Gakuin University, Kobe, Japan, [2] Laboratory of Pharmacology, Faculty of Pharmacy, Osaka Ohtani University, Osaka, Japan

OPEN ACCESS

Edited by:
Mikhail Lebedev, Duke University, United States

Reviewed by:
Min-Yu Sun, Washington University in St. Louis, United States
Ernest Jennings, James Cook University Townsville, Australia
Bruno Pierre Guiard, University of Toulouse, France

***Correspondence:**
Shogo Tokuyama
stoku@pharm.kobegakuin.ac.jp

Specialty section:
This article was submitted to Neuropharmacology, a section of the journal Frontiers in Pharmacology

Received: *29 March 2017*
Accepted: *07 June 2017*
Published: *28 June 2017*

Citation:
Nakamoto K, Aizawa F, Kinoshita M, Koyama Y and Tokuyama S (2017) Astrocyte Activation in Locus Coeruleus Is Involved in Neuropathic Pain Exacerbation Mediated by Maternal Separation and Social Isolation Stress. Front. Pharmacol. 8:401. doi: 10.3389/fphar.2017.00401

Our previous studies demonstrated that emotional dysfunction associated with early life stress exacerbated nerve injury-induced mechanical allodynia. Sex differences were observed in several anxiety tests, but not in mechanical allodynia. To elucidate the mechanism underlying these findings, we have now investigated the involvement of astrocytes in emotional dysfunction and enhancement of nerve injury-induced mechanical allodynia in mice subjected to maternal separation combined with social isolation (MSSI) as an early life stress. We measured expression of glial fibrillary acidic protein (GFAP), an astrocyte maker, in each brain area by immunohistochemistry. GFAP expression in the locus coeruleus (LC) of female, but not of male mice, significantly increased after MSSI, corresponding to the behavioral changes at 7 and 12 weeks of age. Lipopolysaccharide (LPS)-treated astrocyte-derived supernatant was administered to local brain regions, including LC. Intra-LC injection of conditioned medium from cultured astrocytes treated with LPS increased GFAP expression, anxiety-like behavior and mechanical allodynia in both male and female mice. Furthermore, increases in anxiety-like behavior correlated with increased mechanical allodynia. These findings demonstrate that emotional dysfunction and enhanced nerve injury-induced mechanical allodynia after exposure to MSSI are mediated, at least in part, by astrocyte activation in the LC. Male but not female mice may show resistance to MSSI stress during growth.

Keywords: early life stress, astrocyte, glia, locus coeruleus, maternal separation and social isolation stress

INTRODUCTION

Pain is a complex experience that involves purely sensory aspects, such as nociceptive stimuli, as well as emotional effects and feelings of unease (Bushnell et al., 2013). While pain serves as a warning against noxious stimuli (Woolf, 2010), chronic pain severely decreases quality of life. Also, emotional states heavily influence pain (Villemure and Bushnell, 2009). The severity of psychopathology in patients with major depressive disorder was positively associated with the prevalence of pain (Kishi et al., 2015). Thus, pain is modulated by both sensory and emotional factors. We previously demonstrated that emotional states altered mechanical

allodynia and behavioral responses in mice (Nishinaka et al., 2015b). Another report showed that exposure to restraint stress before induction of neuropathic pain significantly increased mechanical allodynia (Norman et al., 2010). To obviate hyperalgesic effects associated directly with a physical stressor, we chose to use the maternal separation and social interaction (MSSI) stress model, a purely psychological form of stress. The MSSI model shows long-lasting behavioral and pathophysiological impairments (Niwa et al., 2011). We previously indicated that MSSI exacerbated mechanical allodynia. Interestingly, mice showed sex differences in several anxiety tests following MSSI, while pain was observed in both sexes after MSSI (Nishinaka et al., 2015b). These findings suggested that differences in sex may influence the relationship between pain control and emotional states.

Accumulating evidence indicates that astrocytes play a crucial role in the regulation of neural function in the central nervous system (CNS). Astrocytes are the most numerous type of glial cell. (Sofroniew and Vinters, 2010) and are important regulators of neural activity. For example, they contribute to neurotransmitter uptake and the CNS vascular response to neural activity (Sattler and Rothstein, 2006; Gordon et al., 2007). Moreover, astrocytes alter neural excitability via direct release of neuromodulator molecules (Halassa et al., 2009). In fact, astrocytes can release gliotransmitters (e.g., glutamate, GABA, D-serine, ATP) in response to neuronal activity including increase in the intracellular Ca^{2+} concentration (Araque et al., 2014; Gundersen et al., 2015). Exocytotic release of gliotransmitters or channel-mediated release via Ca^{2+}-dependent Cl^{-} channel and volume-regulated anion channel (Kimelberg et al., 2006; Park et al., 2013) were induced by increase in the cytosolic Ca^{2+} concentration. Furthermore, gliotransmitters can also be released through Ca^{2+}-independent opening of P2X purinergic receptors (Duan et al., 2003) or connexin/pannexin such as Cx43 hemichannels (Montero and Orellana, 2015). These factors can act on receptors on the presynaptic nerve terminal, or on post-synaptic dendrites when gliotransmitters are released from astrocytes. Astrocytes also contribute to the clinical and pathological mechanisms of disease processes. In a chronic pain study, reactive transformation of astrocytes following neuropathic pain contributed to the enhancement of neuropathic pain by releasing growth factors and inflammatory mediators (Zhang et al., 2013). Further, an astrocyte specific intermediate filament is up-regulated after nerve injury (Wei et al., 2008) and matrix metalloproteinase (MMP)-2-cleaved interleukin (IL)-1β induced astrocyte activation in the later phase of neuropathic pain (Kawasaki et al., 2008). More recently, glucocorticoid regulation of ATP release from spinal astrocytes underlies diurnal exacerbation of neuropathic mechanical allodynia (Koyanagi et al., 2016). Based on these reports, it is thought that astrocytes may play a role in modulation of pain.

On the other hand, astrocytes may influence neural networks that underlie specific behaviors, including aberrant behaviors associated with stress. For example, Cui et al. (2014), showed that glial dysfunction causes depressive-like behaviors and sleep disturbance. Chronic restraint stress causes dysfunction of astrocytes (Imbe et al., 2013). Zhang et al. (2015), showed that Chronic corticosterone exposure reduces hippocampal astrocyte structural plasticity in mice. A postmortem study reported that levels of glial fibrillary acidic protein (GFAP), a marker of reactive astrocytes, decreased in multiple brain regions in mood disorder patients (Miguel-Hidalgo et al., 2000; Bowley et al., 2002; Banasr and Duman, 2008; Chocyk et al., 2011; Gittins and Harrison, 2011). Although the mechanisms underlying emotional dysfunction mediated by astrocytes are unclear, these findings suggest that astrocytic abnormalities are associated with stress. In addition, astrocytes are regulated by sex hormones (Schwarz and Bilbo, 2012), indicating that there are sex differences in astrocytic function. We hypothesized that astrocytes are involved in sex-dependent emotional dysfunction induced by MSSI.

To examine our hypothesis, we investigated the influence of MSSI on GFAP expression levels and associated nociception and emotion in neuropathic pain states. Furthermore, to evaluate the involvement of local astrocytic activation, we developed a local activation model involving microinjection of supernatant from lipopolysaccharide (LPS)-treated astrocytes.

MATERIALS AND METHODS

Animals

Pregnant ddY mice at gestational day 14 and timed-pregnant Wister rats (day 16 or 17) and were obtained from Japan SLC, Inc. (Hamamatsu, Japan). The pregnant mice and rat were housed individually under standard conditions (23–24°C, 12 h light/dark cycle with lights on from 8 a.m. to 8 p.m.) with food and water available ad libitum. The present study was conducted in accordance with the Guiding Principles for the Care and Use of Laboratory Animals adopted by the Japanese Pharmacological Society. The Ethical Committee for Animal Experimentation of Kobe Gakuin University approved all experiments (approval number A15-33; Kobe, Japan).

Maternal Separation Combined with Social Isolation Stress Paradigm

Maternal separation combined with social isolation was performed as previously described (Nishinaka et al., 2015b). Pups both MSSI and control groups were housed with dams until postnatal day 14. On postnatal day 15, the pups in the MSSI group were placed in individual isolation cages (25 cm × 15 cm × 13 cm) for 6 h/day. The isolation cage was surrounded by the black paper to shut out visualization of other. After maternal separation for 7 days, pups were kept in isolation cages until 12 weeks of age. Dams and pups assigned to the control group were reared in standard conditions without maternal separation until weaning. After weaning, the control pups were separated by sex and housed 2–4 per cage.

Elevated Plus-Maze Test

The elevated plus-maze (EPM) test was performed as previously described (Nishinaka et al., 2015b). Mice were placed on the EPM

consisted of two open arms and two enclosed arms (both 25 cm length × 8 cm width) which elevated 50 cm above the floor. The illumination levels of the open and enclosed arms were similar (approximately 360 lx). The behavior was tracked for 5 min by using a web camera. The number of entries to the open arms was expressed as a percentage of enties to all arms. The time spent in the open arms was expressed as a percentage of times in the open arms. A decreased the number of entry and the time spent to the open arms indicaeted anixis-behavior (Nishinaka et al., 2015b).

Partial Sciatic Nerve Ligation (PSL)

Mice were deeply anesthetized with sodium pentobarbital (65 mg/kg), and then surgery was performed as previously described at 9 weeks of age (Seltzer et al., 1990). In brief, the sciatic nerve of the right hind limb was exposed through a small incision. Half or two-thirds of the nerve thickness was tightly ligated with a silk suture. In sham-operated mice, the sciatic nerve was exposed without ligation.

von Frey Test

Mechanical allodynia after nerve injury was measured using the von Frey test as previously described (Nishinaka et al., 2015b). Mice were placed on a 5 mm × 5 mm wire mesh grid floor for 2–3 h prior to testing. The middle of the plantar surface of each hind paw was probed with 0.4 g von Frey filaments (Neuroscience, Inc., Tokyo, Japan). The withdrawal response to probing of the hind paw was measured 10 times. The intertrial interval was >10 s. An increase in the number of withdrawals indicates the degree of pain associated with mechanical stimulation (Nishinaka et al., 2015b).

Immunoflurorescence

Immunofluorescence staining was performed as previously described (Nakamoto et al., 2015) with some modifications. Mice were deeply anesthetized with diethyl ether and perfused transcardially with phosphate-buffered saline (PBS, pH 7.4) followed by 4% paraformaldehyde in 0.1 M PBS, pH 7.4. After perfusion, brain sections were incubated in 10% sucrose at 4°C for 3 h, and were kept 20% sucrose at 4°C overnight. Sections were cut at 20 μm on a cryostat (CM1850, Leica, Microsystems GmbH, Wetzlar, Germany). The brain sections were incubated with blocking buffer (3% BSA in PBST) for 1 h at room temperature, and then incubated overnight at 4°C with a mouse monoclonal anti-GFAP antibody (MAB3402, Merck Millipore KGaA, Darmstadt, Germany; 1:1000) and chicken polyclonal anti- tyrosine hydroxylase (TH) (Abcam, Tokyo, Japan; 1:200). The slices were incubated at room temperature for 2 h in secondary antibody (goat polyclonal anti-mouse IgG conjugated with AlexaFluor 488 or 594, goat polyclonal anti-chicken IgG conjugated with AlexaFluor 594; Life Technologies, Inc., Carlsbad, CA, United States; 1:200). The positive cells were detected with a confocal fluorescence microscope (FV1000, Olympus Corporation, Tokyo, Japan) or BZ-X710 microscope (Keyence, Itasca, IL, United States). Reactive astrocytes are characterized by cellular hypertrophy, hyperplasia, immunoreactivity of increased GFAP on tissue slides. The immunoreactivity of GFAP-positive astrocytic cells were quantified with the Image J cell counter analysis tool (ImageJ; NIH, Bethesda, MD, United States) in defined area of interest on the locus coeruleus (LC). The score was blinded to sampling times and animal treatments.

Preparation of Primary Cultured Astrocytes from Rat Brain

Astrocytes were prepared from the cerebra of 1- to 2-day-old Wistar rats as described (Koyama et al., 2004). The isolated cells were seeded at 1×10^4 cells/cm^2 in 75 cm^2 culture flasks and grown in minimal essential medium supplemented with 10% fetal bovine serum. To remove small process-bearing cells (mainly oligodendrocyte progenitors and microglia from the protoplasmic cell layer), the culture flasks were shaken at 250 rpm overnight 10–14 days after seeding. The monolayer cells were trypsinized and seeded on six-well culture plates or on 15 mm glass cover slips in 24-well culture plates. At this stage, approximately 95% of the cells showed immunoreactivity for GFAP.

Lipopolysaccharide (LPS) Stimulation of Rat Astrocytes

Before treatment, astrocytes in six well-culture plates were incubated in serum-free medium for 48 h. LPS was minimally diluted using serum-free medium before treatment. After incubation in serum-free medium, the cells were treated with 1,000 ng/mL LPS for 24 h.

Microinjection of Astrocyte Supernatant

Microinjection of astrocyte culture supernatant into the LC was performed as previously described (Nakamoto et al., 2015), with some modifications. Briefly, mice were anesthetized with pentobarbital (65 mg/kg) and immobilized on a stereotaxic frame (SR-5M; NARISHIGE, Co., Ltd, Tokyo, Japan). A microsyringe with a 30-gauge stainless steel needle was inserted unilaterally into the LC (5.4 mm posterior to bregma, 0.9 mm lateral from the midline, and 4.0 mm deep) and astrocyte supernatant (0.2 μL) injected incrementally over 1 min (**Figure 3A**). The injection site in LC was confirmed using 0.5% Trypan blue in saline.

Statistical Analyses

All data are expressed as the mean ± the standard error of the mean (SEM). Significant differences were determined by a one-way analysis of variance (ANOVA) followed by Scheffe's multiple comparison tests (for comparisons between more than three groups) or Student's *t*-test (for comparisons between two groups). A P-value < 0.05 was considered significant.

RESULTS

MSSI Stress Induced an Increase in GFAP Protein Expression in the LC Area of Female But Not Male Mice

Immunoreactivity for GFAP was observed surrounding TH positive cells in the LC. In males, MSSI stress did not affect GFAP

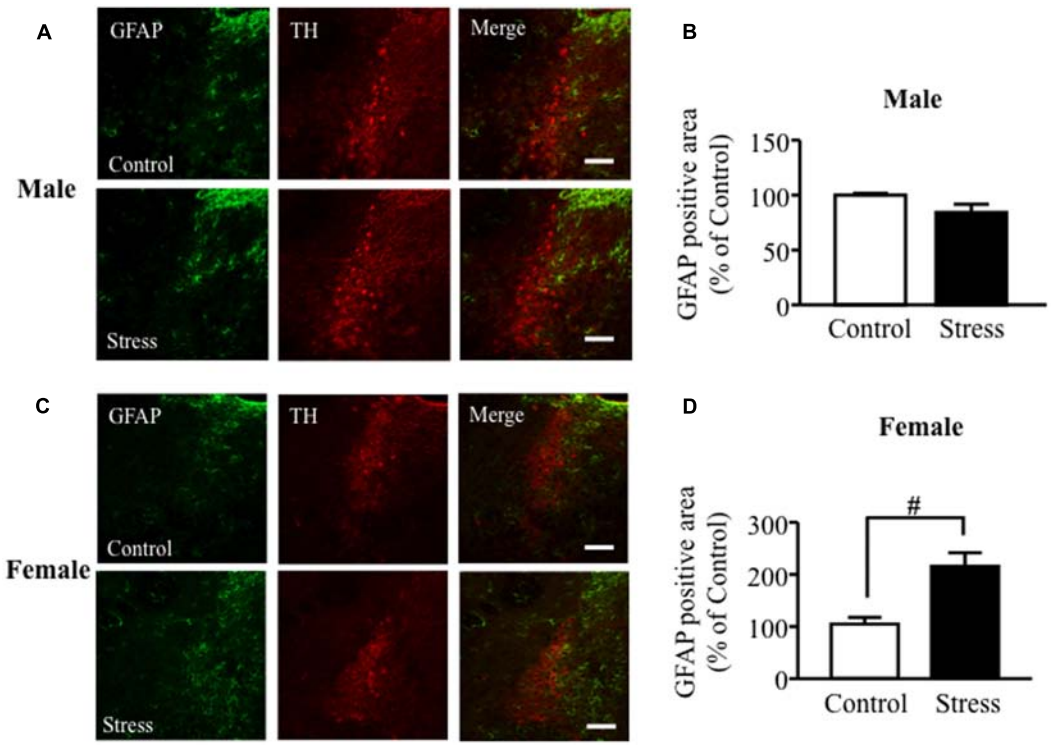


FIGURE 1 | Maternal separation combined with social isolation (MSSI) stress induced an increase in GFAP protein expression in the LC area of female but not male mice. Representative images showing immunofluorescence labeling of GFAP (green) and TH (Red) in the LC of MSSI stressed mice at 7 weeks of age, before PSL. Percentage of the GFAP positive area over the total area including LC after MSSI in **(A,B)** male mice and **(C,D)** female mice. Panel shows representative images of the GFAP positive area. Results expressed as percent of Control (mean ± SEM) from $n = 3$ male mice and $n = 3$ female mice. $^{\#}P < 0.05$, vs. Control, Student's *t*-test. Scale bar = 100 mm. LC, locus coeruleus.

expression in the LC at 7 weeks of age, before PSL (**Figures 1A,B**). In contrast, MSSI stress induced a significant increase in GFAP expression in the LC of female mice, compared to control female mice, at 7 weeks of age (**Figures 1C,D**).

The MSSI-Induced Increase in LC GFAP Expression Was Suppressed by PSL in Female Mice

At 12 weeks of age, the increased GFAP protein expression was observed in brain regions including the LC of MSSI-stressed female mice, compared to control female mice. This MSSI-induced increase in LC GFAP expression was suppressed by PSL (**Figures 2A,B**). In other region of the brain, GFAP protein expression did not change in male and female mice (Supplementary Figure 1).

LPS-Treated Astrocyte-Conditioned Medium Microinjection into the LC Induced Increased GFAP Expression in Male and Female Mice

In male and female mice, microinjection of LPS-treated astrocyte-derived supernatant into the brainstem area, including the LC, significantly increased local GFAP expression compared to non-treated control medium (**Figures 3B–E**). GFAP positive cells were observed surrounding TH positive cells in the LC (**Figure 3F**).

LPS-Treated Astrocyte-Conditioned Medium Microinjection into the LC Induced Anxiety-Like Behavior and PSL-Induced Mechanical Allodynia in Male Mice

In male mice, microinjection of LPS-treated astrocyte-derived supernatant into the brainstem area, including the LC, significantly decreased the number of open arm crossings and time spent in the open arms compared to vehicle-treated male mice (**Figures 4A,B**). In contrast, there was no difference in the number of center zone crossings between vehicle- and LPS-treated groups (**Figure 4C**). The entries into open arms (%) or the time spent in open arms (%) correlated negatively with the response time to mechanical stimuli after PSL in vehicle- or LPS-treated male mice (**Figure 4D**). At 1 week after PSL, the vehicle- and LPS-treated astrocyte-derived supernatant treated mice showed an increased number of responses to mechanical stimuli compared to vehicle- and LPS-treated injected sham injured male mice. Mice injected with LPS-treated astrocyte-derived supernatant showed a tendency toward an

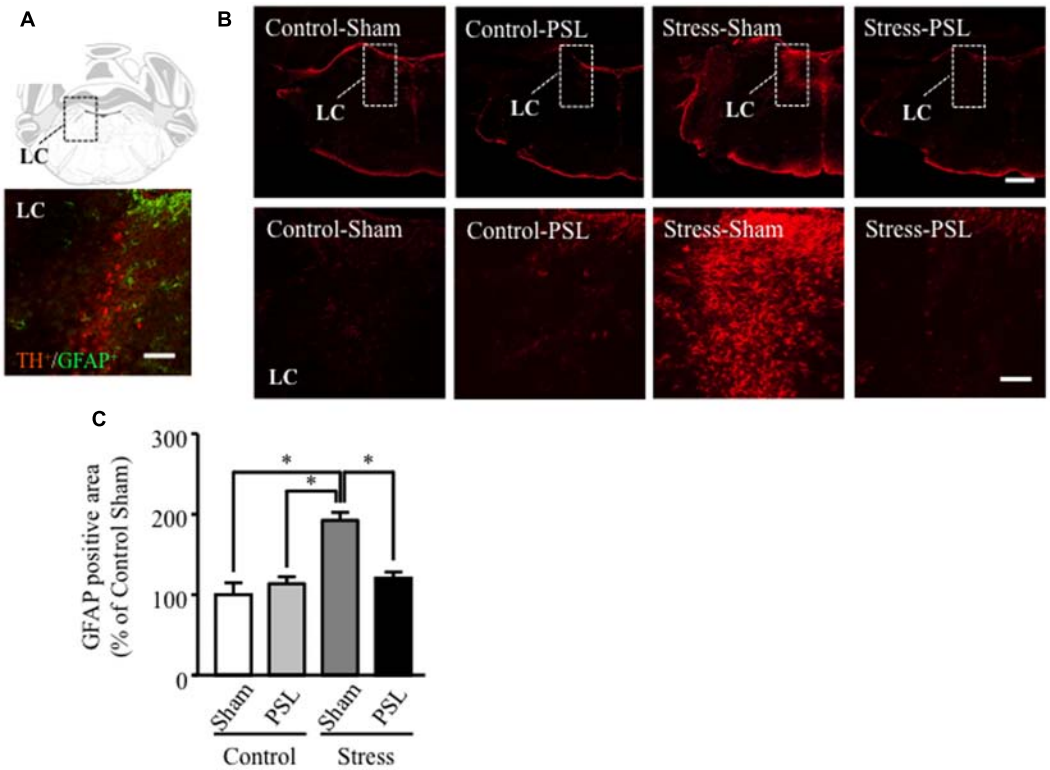


FIGURE 2 | The MSSI-induced increase in LC GFAP expression was suppressed by PSL in female mice. Representative images showing immunofluorescence labeling of GFAP (green) and TH (Red) in the LC of mice **(A)**. Percentage of the GFAP positive area over the total area including LC of MSSI stressed mice at 12 weeks of age, after PSL after PSL **(B)**. Panel shows representative images of the GFAP positive area. Results expressed as percent of Control (mean ± SEM in female mice: $n = 3$) **(C)**. $^*P < 0.01$ vs. Control-Sham, vs. Control-PSL, vs. Stress-PSL, Scheffe's test. Scale bar = 100 mm. LC, locus coeruleus.

increase in the number of responses to mechanical stimuli compared to vehicle-treated injected PSL male mice. However, the number of responses against mechanical stimuli did not change between the vehicle treated group and the LPS-treated astrocyte-derived supernatant group prior to PSL (**Figure 4E**).

LPS-Treated Astrocyte-Derived Supernatant Microinjection into the LC Caused Anxiety-Like Behavior and PSL-Induced Mechanical Allodynia in Female Mice

Similar results were obtained in female mice. Female mice microinjected with LPS-treated astrocyte-derived supernatant showed a decreased number of open arm crossings and time spent in the open arms compared to vehicle-treated female mice (**Figures 5A,B**). The number of crossings in the center zone was comparable to that in vehicle-treated female mice (**Figure 5C**). The entries into open arms (%) or the time spent in open arms (%) correlated negatively with the response time to mechanical stimuli after PSL in vehicle- or LPS-treated female mice (**Figure 5D**). At 1 week after PSL, vehicle- and LPS-treated astrocyte-derived supernatant female mice showed an increased number of responses to mechanical stimuli compared to vehicle- and LPS-treated supernatant- injected female mice. Furthermore, the number of responses to mechanical stimuli showed a significant increase in LPS-treated PSL female mice compared to vehicle-treated PSL female mice. In contrast, the number of responses to mechanical stimuli before PSL was similar in both vehicle- and LPS-treated supernatant-injected female mice (**Figure 5E**).

DISCUSSION

Both the LC in the pons and the rostral ventromedial medulla (RVM) contribute to the regulation of pain and emotion (Aston-Jones et al., 1999; Yoshimura and Furue, 2006). Noradrenergic and serotonergic neurons are localized to the LC and RVM, respectively, and project to multiple higher brain areas as well as to the spinal cord. The descending pathways regulate nociceptive signaling in the spinal cord. It has been reported that chronic stress activates or suppress neuronal activity in the LC, and neuropathic pain suppress neuronal activity in the LC, which is associated with the development of anxiety-like behaviors in mice (Borges et al., 2015). Selective depletion of noradrenaline in the LC causes anxiety- and depression-like behaviors (Itoi et al., 2011). Physiological changes in glial cells of the medulla oblongata are associated with disease states and altered neuronal activity (Alvarez-Maubecin et al., 2000;

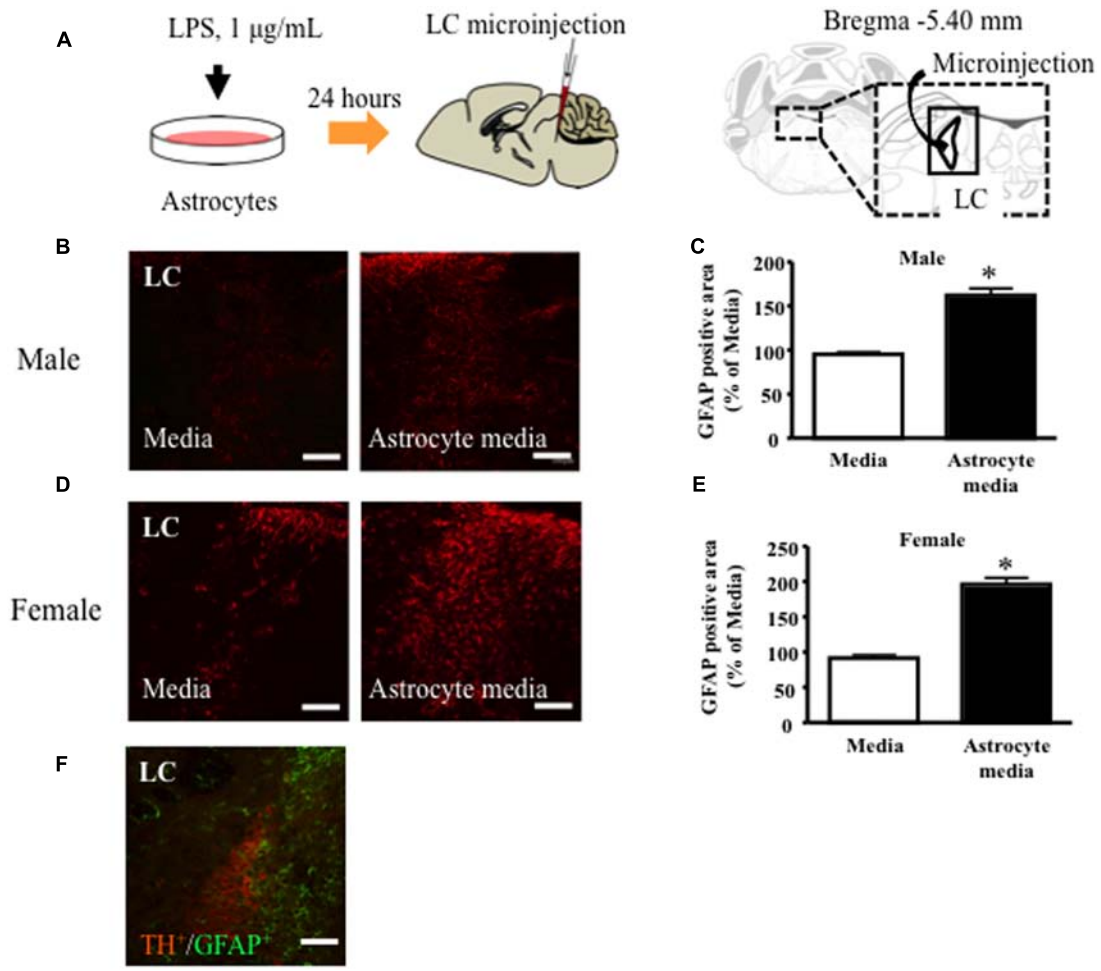


FIGURE 3 | Lipopolysaccharide (LPS)-treated astrocyte-conditioned medium microinjection into the LC increased GFAP expression in male and female mice. **(A)** Schematic diagram of the experimental protocol for microinjection into the LC. LC, locus coeruleus. Representative images showing immunofluorescence labeling of GFAP (red) in the LC of mice. **(A)** Percentage of the GFAP positive area over the total area including LC after microinjection in male **(B,C)** and female **(D,E)** mice. GFAP (Red) $*P < 0.05$, vs. Media, Student's *t*-test. Representative images showing immunofluorescence labeling of GFAP (green) and TH (Red) in the LC of mice **(F)**. Representative images of astrocytes in LC after microinjection. GFAP (Green), TH (Red). Scale bar = 100 mm.

O'Donnell et al., 2012). For example, downregulation of astrocytic gene expression was observed in the postmortem LC of major depressive disorder patients (Chandley et al., 2013). Chronic restraint stress decreased the expression of GFAP and S100β calcium-binding protein in the cytoplasm of astrocytes (Gerlai et al., 1995) in the RVM (Imbe et al., 2013), while inflammation-induced reactive astrocytes enhanced the activity of the serotonergic descending pain facilitation system, which increased nociceptive signaling in the spinal cord via the RVM (Cunha and Dias, 2009; Roberts et al., 2009). In this study, we examined the influence of MSSI on astrocytes in the LC to determine whether astrocytes were involved in the exacerbation of neuropathic pain by emotional dysfunction. We found that MSSI significantly increased GFAP expression in the LC of female but not male mice. Furthermore, we found that GFAP expression in the medulla oblongata of MSSI stressed female mice shows tendency of increase at 12 weeks age, but not male mice (Supplementary Figures 1, 2). It is well-known that up-regulation of GFAP levels is associated with functional changes in astrocytes that in turn affect neuronal function, due to changes in astrocyte-neuron signaling (Gómez-Galán et al., 2013). Therefore, these findings suggest that MSSI-induced dysfunctional astrocytes in the LC are involved in the development of abnormal emotional states and alterations of the pain modulatory system.

Our previous results demonstrated that MSSI increased anxiety-like behaviors in female but not male mice (Nishinaka et al., 2015b) and MSSI did not influence GFAP expression in the LC of male mice. However, Niwa et al. (2011) previously found that MSSI increased EPM anxiety-like behavior in both male and female C57BL/6J mice. In mice, anxiety and depression-like behaviors differ according to strain or sex (Millstein and Holmes, 2007; McDermott et al., 2015). Generally, females have increased stress sensitivity, likely due to differences in sex hormones,

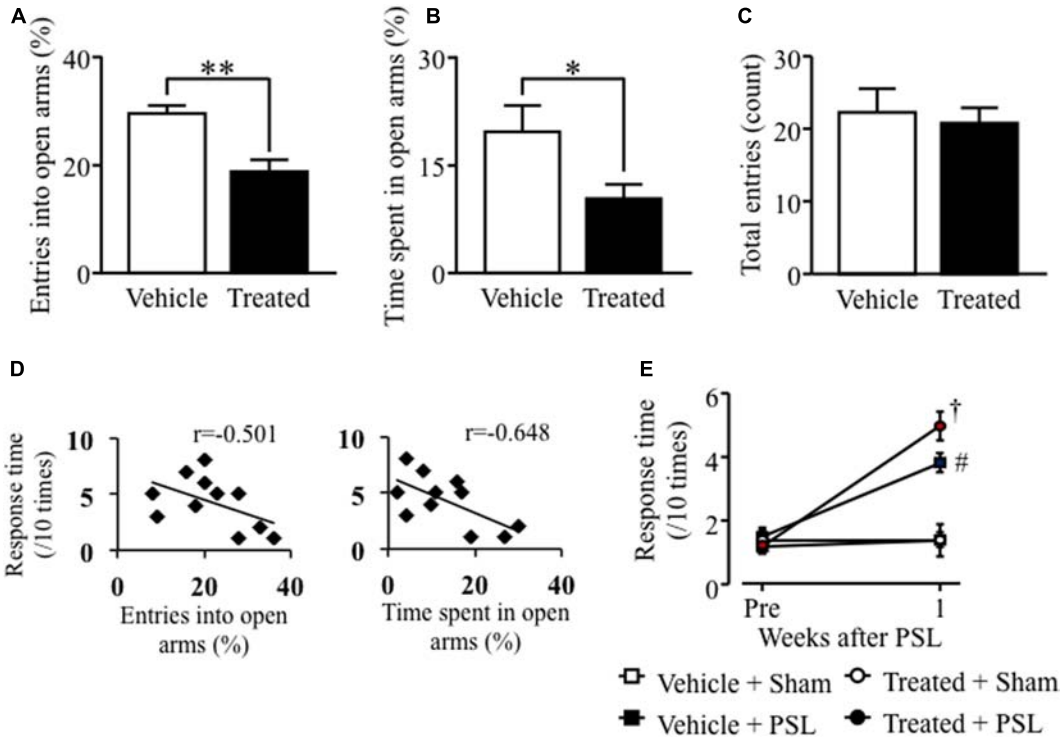


FIGURE 4 | Lipopolysaccharide-treated astrocyte-conditioned medium microinjection into the LC induced anxiety-like behavior and PSL-induced mechanical allodynia in male mice. **(A)** The number of entries into open arms (%). **(B)** Time spent in the open arms (%). **(C)** The total number of entries into the four arms. Vehicle group: $n = 8$, Treated group: $n = 9$. **(D)** Correlation between the entries into open arms (%) or the time spent in open arms (%) and mechanical stimuli after PSL in vehicle- or LPS-treated male mice. **(E)** 0.4 g filament. Vehicle-Sham group: $n = 5$, Vehicle-PSL group: $n = 6$, Treated-Sham group: $n = 5$, Treated-PSL group: $n = 11$. Data expressed as the mean ± SEM. $^{*}P < 0.05$, $^{**}P < 0.01$ vs. Vehicle, Student's *t*-test. $^{\#}P < 0.05$ vs. Vehicle + Sham, $^{\dagger}P < 0.05$ vs. Treated + Sham, Scheffe's test.

although the detailed mechanisms are not clear (Maeng and Milad, 2015). As show in **Figures 1**, **2**, at 7 or 12 weeks age, the GFAP expression in the LC of MSSI stressed mice with or without PSL treated was different between male and female. These results indicate that MSSI-mediated emotional dysfunction and neuropathic pain exacerbation might be more sensitively induced or worked astrocyte activation in female stressed mice, but not male stressed mice. Therefore, our findings suggest that sex differences in LC astrocytic activation induced by MSSI are responsible, at least in part, for the sex differences in anxiety-like behavior and are mediated through the damaging effects of reactive astrocytes on female LC neurons.

Furthermore, to investigate the effect of acute and region-selective activation of LC astrocytes on anxiety-like or nociceptive behaviors, we microinjected the supernatant of LPS-treated astrocytes into the LC region. We found that LC astrocytes up-regulated GFAP expression and showed morphological changes, indicating that astrocytes were activated by the supernatant injection. LPS binds to toll like receptor (TLR) 4, which is expressed in astrocytes. It is thought that these signaling-induced inflammatory responses, which are mediated by the NF-κB pathway, may result in activation of astrocytes (Gorina et al., 2011; Li et al., 2016). Activated astrocytes show up-regulated GFAP protein levels and morphological changes, such as cellular hypertrophy and outgrowth of astrocytic foot processes (von Boyen et al., 2004; Pekny and Pekna, 2014). In this study, we used the LPS-treated astrocytes from rat cell culture. As shown in previous reports, co-culture systems have been used which combined rat astrocytes with mouse neurons. And also, it is reported that rat astrocytes provided optimum conditions for synaptic functioning of mouse neurons (Goudriaan et al., 2014). Further, it is reported that there was no cross-reactivity toward mouse-derived embryonic stem cells injected into rat retina (Gregory-Evans et al., 2009). In this study, microinjection of supernatant from vehicle-treated astrocytes was not affected GFAP expression in the LC area. Based on these reports, we believe that cross-reactivity which may be induced by the microinjection of supernatant from rat astrocytes into mice may have a negligible effect on GFAP protein expression.

The important point is that LC administration of supernatant derived from LPS-treated astrocytes increased anxiety-like behavior and GFAP expression in both male and female mice. These results indicate that activation of astrocytes in the LC might result in emotional dysfunction and exacerbated mechanical allodynia. However, the GFAP expression in the LC of MSSI mice with PSL was different between males and females. We previously showed that MSSI sex-dependently induced emotional dysfunction after nerve injury, which was associated with sex

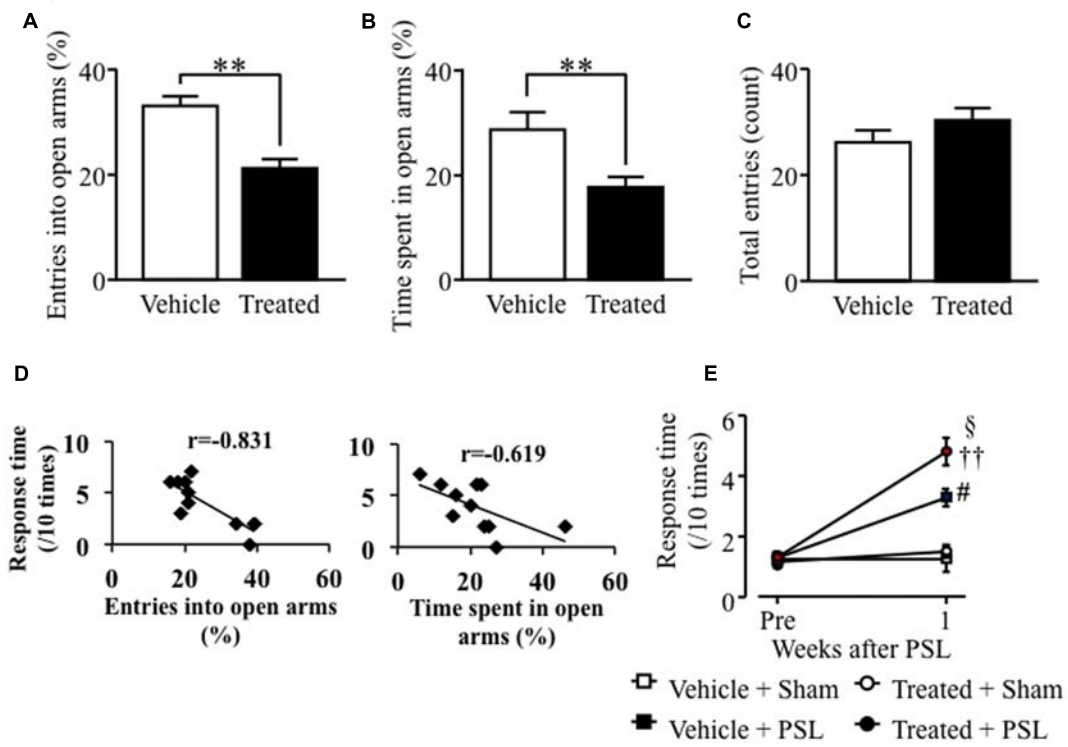


FIGURE 5 | Lipopolysaccharide-treated astrocyte-derived supernatant microinjection into the LC caused anxiety-like behavior and PSL-induced mechanical allodynia in female mice. **(A)** The number of entries into open arms (%). **(B)** Time spent in the open arms (%). **(C)** The total number of entries into the four arms. Vehicle group: $n = 8$, Treated group: $n = 11$. **(D)** Correlation between the entries into open arms (%) or the time spent in open arms (%) and mechanical stimuli after PSL in vehicle- or LPS-treated female mice. **(E)** 0.4 g filament. Vehicle-Sham group: $n = 4$, Vehicle-PSL group: $n = 7$, Treated-Sham group: $n = 6$, Treated-PSL group: $n = 10$. Data expressed as mean ± SEM. $^{**}P < 0.01$ vs. Vehicle, Student's *t*-test. $^{\#}P < 0.05$ vs. Vehicle + Sham, $^{\dagger\dagger}P < 0.01$ vs. Treated + Sham, $^{\S}P < 0.05$ vs. Treated + PSL, Scheffe's test.

differences in the stress-induced regulation of BDNF expression (Nishinaka et al., 2015a). It is thought that neuronal function in the brain of male mice is protected from early life stresses, such as MSSI, by altered expression of several stress-responsive factors, including BDNF upregulation, such that MSSI male mice might acquire resistance to stress. Our findings suggest that activation of astrocytes in the LC, caused by MSSI, might be involved in the induction of emotional dysfunction.

We also found that LC astrocytic dysfunction caused by MSSI contributes to the exacerbation of mechanical allodynia after PSL. Despite downregulation of MSSI-induced LC GFAP overexpression by PSL, MSSI enhanced nerve injury-induced mechanical allodynia. Many studies on the relationship between pain and astrocytic function have demonstrated that inflammation or nerve injury activates astrocytes in the spinal cord and supraspinal area, and that these activated cells contribute to the development and maintenance of persistent pain (Ji et al., 2013). Previous studies have also shown that anti-inflammatory drugs, such as steroids, suppress activated astrocytes (Kuypers et al., 2013; Evans et al., 2014). The MSSI-induced increase in GFAP expression was reversed to control levels by PSL, which would appear to be an improvement in the MSSI effect. From our results, it is unclear whether PSL-induced downregulation of LC GFAP expression in MSSI-stressed mice is associated with the exacerbation of nerve injury-induced mechanical allodynia. We suggest that the MSSI-induced increase in LC GFAP expression in the absence of nerve injury may induce a reduction in mechanical threshold in the presence of nerve injury. The activated astrocytes produce various neurotrophic factors, cytokines, chemokines, and free radicals, with both neuroprotective and neurotoxic effects. The balance between these factors is important for preservation of neuronal function and may act to trigger a compensatory condition against MSSI. Nerve injury may shift this balance and thereby enhance mechanical allodynia.

Furthermore, as shown in **Figures 4**, **5**, we found that activation of astrocytes which induced by microinjection of astrocyte conditioned medium with LPS caused emotional dysfunction and exacerbated mechanical allodynia. On the other hand, there is no increased GFAP expression following MSSI in male mice although MSSI-mediated neuropathic pain exacerbation observed in male mice (Nishinaka et al., 2015a). This discrepancy between male and female indicates that other factors which inhibit astrocyte activation may be produced in MSSI stressed male mice, but not female stressed mice.

Further studies will be needed to clarify sex difference between astrocyte activation and pain.

CONCLUSION

We found that MSSI sex-dependently activated astrocytes in the LC, as indicated by increased GFAP expression, with increases in anxiety-like behavior. These MSSI-induced activated astrocytes in the LC may contribute to the exacerbation of neuropathic pain. Furthermore, male mice, but not female mice, might acquire resistance to MSSI-induced stress during growth. We have thus identified one possible and unexpected mechanism linking emotional state with changes in the pain control system, i.e., astroglial activation in the LC.

AUTHOR CONTRIBUTIONS

Study conception and design: KN and ST; acquisition of data: KN, MK, YK; analysis and interpretation: KN, MK and ST; drafting of the manuscript: KN and ST; critical revision of the manuscript for important intellectual content; ST, statistical analysis; KN, MK; obtained funding; KN, ST, administrative, technical, or material support; KN, MK, YK, study supervision; KN, ST. All authors read and approved the final manuscript.

ACKNOWLEDGMENTS

Part of this work was supported by Grants-in-Aid and Special Coordination Funds from the Kobe Gakuin University Joint Research (B). We thank Dr. Takashi Nishinaka for technical help in performing animal study. The authors would like to thank Enago (www.enago.jp) for the English language review.

SUPPLEMENTARY MATERIAL

The Supplementary Material for this article can be found online at: http://journal.frontiersin.org/article/10.3389/fphar.2017.00401/full#supplementary-material

REFERENCES

Alvarez-Maubecin, V., Garcia-Hernandez, F., Williams, J. T., and Van Bockstaele, E. J. (2000). Functional coupling between neurons and glia. *J. Neurosci.* 20, 4091–4098.

Araque, A., Carmignoto, G., Haydon, P. G., Oliet, S. H., Robitaille, R., and Volterra, A. (2014). Gliotransmitters travel in time and space. *Neuron* 81, 728–739. doi: 10.1016/j.neuron.2014.02.007

Aston-Jones, G., Rajkowski, J., and Cohen, J. (1999). Role of locus coeruleus in attention and behavioral flexibility. *Biol. Psychiatry* 46, 1309–1320. doi: 10.1016/S0006-3223(99)00140-7

Banasr, M., and Duman, R. S. (2008). Glial loss in the prefrontal cortex is sufficient to induce depressive-like behaviors. *Biol. Psychiatry* 64, 863–870. doi: 10.1016/j.biopsych.2008.06.008

Borges, G., Berrocoso, E., Mico, J. A., and Neto, F. (2015). ERK1/2: Function, signaling and implication in pain and pain-related anxio-depressive disorders. *Prog. Neuropsychopharmacol. Biol. Psychiatry* 60, 77–92. doi: 10.1016/j.pnpbp.2015.02.010

Bowley, M. P., Drevets, W. C., Ongür, D., and Price, J. L. (2002). Low glial numbers in the amygdala in major depressive disorder. *Biol. Psychiatry* 52, 404–412. doi: 10.1016/S0006-3223(02)01404-X

Bushnell, M. C., Ceko, M., and Low, L. A. (2013). Cognitive and emotional control of pain and its disruption in chronic pain. *Nat. Rev. Neurosci.* 14, 502–511. doi: 10.1038/nrn3516

Chandley, M. J., Szebeni, K., Szebeni, A., Crawford, J., Stockmeier, C. A., Turecki, G., et al. (2013). Gene expression deficits in pontine locus coeruleus astrocytes in men with major depressive disorder. *J. Psychiatry Neurosci.* 38, 276–284. doi: 10.1503/jpn.120110

Chocyk, A., Dudys, D., Przyborowska, A., Majcher, I., Maćkowiak, M., and Wędzony, K. (2011). Maternal separation affects the number, proliferation and apoptosis of glia cells in the substantia nigra and ventral tegmental area of juvenile rats. *Neuroscience* 173, 1–18. doi: 10.1016/j.neuroscience.2010.11.037

Cui, W., Mizukami, H., Yanagisawa, M., Aida, T., Nomura, M., Isomura, Y., et al. (2014). Glial dysfunction in the mouse habenula causes depressive-like behaviors and sleep disturbance. *J. Neurosci.* 34, 16273–16285. doi: 10.1523/JNEUROSCI.1465-14.2014

Cunha, T. M., and Dias, Q. M. (2009). Glial modulation of pain: a step beyond. *J. Neurosci.* 29, 3340–3342. doi: 10.1523/JNEUROSCI.5938-08.2009

Duan, S., Anderson, C. M., Keung, E. C., Chen, Y., Chen, Y., and Swanson, R. A. (2003). P2X7 receptor-mediated release of excitatory amino acids from astrocytes. *J. Neurosci.* 23, 1320–1328.

Evans, M. C., Gaillard, P. J., de Boer, M., Appeldoorn, C., Dorland, R., Sibson, N. R., et al. (2014). CNS-targeted glucocorticoid reduces pathology in mouse model of amyotrophic lateral sclerosis. *Acta Neuropathol. Commun.* 2:66. doi: 10.1186/2051-5960-2-66

Gerlai, R., Wojtowicz, J. M., Marks, A., and Roder, J. (1995). Overexpression of a calcium-binding protein, S100 beta, in astrocytes alters synaptic plasticity and impairs spatial learning in transgenic mice. *Learn. Mem.* 2, 26–39. doi: 10.1101/lm.2.1.26

Gittins, R. A., and Harrison, P. J. (2011). A morphometric study of glia and neurons in the anterior cingulate cortex in mood disorder. *J. Affect. Disord.* 133, 328–332. doi: 10.1016/j.jad.2011.03.042

Gómez-Galán, M., De Bundel, D., Van Eeckhaut, A., Smolders, I., and Lindskog, M. (2013). Dysfunctional astrocytic regulation of glutamate transmission in a rat model of depression. *Mol. Psychiatry* 18, 582–594. doi: 10.1038/mp.2012.10

Gordon, G. R. J., Mulligan, S. J., and MacVicar, B. A. (2007). Astrocyte control of the cerebrovasculature. *Glia* 55, 1214–1221. doi: 10.1002/glia.20543

Gorina, R., Font-Nieves, M., Márquez-Kisinousky, L., Santalucia, T., and Planas, A. M. (2011). Astrocyte TLR4 activation induces a proinflammatory environment through the interplay between MyD88-dependent NFκB signaling, MAPK, and Jak1/Stat1 pathways. *Glia* 59, 242–255. doi: 10.1002/glia.21094

Goudriaan, A., Camargo, N., Carney, K. E., Oliet, S. H., Smit, A. B., and Verheijen, M. H. (2014). Novel cell separation method for molecular analysis of neuron-astrocyte co-cultures. *Front. Cell Neurosci.* 8:12. doi: 10.3389/fncel.2014.00012

Gregory-Evans, K., Chang, F., Hodges, M. D., and Gregory-Evans, C. Y. (2009). Ex vivo gene therapy using intravitreal injection of GDNF-secreting mouse embryonic stem cells in a rat model of retinal degeneration. *Mol. Vis.* 15, 962–973.

Gundersen, V., Storm-Mathisen, J., and Bergersen, L. H. (2015). Neuroglial transmission. *Physiol. Rev.* 95, 695–726. doi: 10.1152/physrev.00024.2014

Halassa, M. M., Fellin, T., and Haydon, P. G. (2009). Tripartite synapses: roles for astrocytic purines in the control of synaptic physiology and behavior. *Neuropharmacology* 57, 343–346. doi: 10.1016/j.neuropharm.2009.06.031

Imbe, H., Kimura, A., Donishi, T., and Kaneoke, Y. (2013). Effects of restraint stress on glial activity in the rostral ventromedial medulla. *Neuroscience* 241, 10–21. doi: 10.1016/j.neuroscience.2013.03.008

Itoi, K., Sugimoto, N., Suzuki, S., Sawada, K., Das, G., Uchida, K., et al. (2011). Targeting of locus ceruleus noradrenergic neurons expressing human interleukin-2 receptor α-subunit in transgenic mice by a recombinant immunotoxin anti-Tac(Fv)-PE38: a study for exploring noradrenergic influence

upon anxiety-like and depression-like beha. *J. Neurosci.* 31, 6132–6139. doi: 10.1523/JNEUROSCI.5188-10.2011

Ji, R. R., Berta, T., and Nedergaard, M. (2013). Glia and pain: is chronic pain a gliopathy? *Pain* 154(Suppl.), S10–S28. doi: 10.1016/j.pain.2013.06.022

Kawasaki, Y., Xu, Z. Z., Wang, X., Park, J. Y., Zhuang, Z. Y., Tan, P. H., et al. (2008). Distinct roles of matrix metalloproteases in the early- and late-phase development of neuropathic pain. *Nat. Med.* 14, 331–336. doi: 10.1038/nm1723

Kimelberg, H. K., MacVicar, B. A., and Sontheimer, H. (2006). Anion channels in astrocytes: biophysics, pharmacology, and function. *Glia* 54, 747–757. doi: 10.1002/glia.20423

Kishi, T., Matsuda, Y., Mukai, T., Matsunaga, S., Yasue, I., Fujita, K., et al. (2015). A cross-sectional survey to investigate the prevalence of pain in Japanese patients with major depressive disorder and schizophrenia. *Compr. Psychiatry* 59, 91–97. doi: 10.1016/j.comppsych.2015.02.004

Koyama, Y., Yoshioka, Y., Shinde, M., Matsuda, T., and Baba, A. (2004). Focal adhesion kinase mediates endothelin-induced cyclin D3 expression in rat cultured astrocytes. *J. Neurochem.* 90, 904–912. doi: 10.1111/j.1471-4159.2004.02546.x

Koyanagi, S., Kusunose, N., Taniguchi, M., Akamine, T., Kanado, Y., Ozono, Y., et al. (2016). Glucocorticoid regulation of ATP release from spinal astrocytes underlies diurnal exacerbation of neuropathic mechanical allodynia. *Nat. Commun.* 7:13102. doi: 10.1038/ncomms13102

Kuypers, E., Jellema, R. K., Ophelders, D. R. M. G., Dudink, J., Nikiforou, M., Wolfs, T. G. A. M., et al. (2013). Effects of intra-amniotic lipopolysaccharide and maternal betamethasone on brain inflammation in fetal sheep. *PLoS ONE* 8:e81644. doi: 10.1371/journal.pone.0081644

Li, N., Zhang, X., Dong, H., Zhang, S., Sun, J., and Qian, Y. (2016). Lithium ameliorates LPS-induced astrocytes activation partly via inhibition of toll-like receptor 4 expression. *Cell Physiol. Biochem.* 38, 714–725. doi: 10.1159/000443028

Maeng, L. Y., and Milad, M. R. (2015). Sex differences in anxiety disorders: interactions between fear, stress, and gonadal hormones. *Horm. Behav.* 76, 106–117. doi: 10.1016/j.yhbeh.2015.04.002

McDermott, C. M., Liu, D., Ade, C., and Schrader, L. A. (2015). Estradiol replacement enhances fear memory formation, impairs extinction and reduces COMT expression levels in the hippocampus of ovariectomized female mice. *Neurobiol. Learn. Mem.* 118, 167–177. doi: 10.1016/j.nlm.2014.12.009

Miguel-Hidalgo, J. J., Baucom, C., Dilley, G., Overholser, J. C., Meltzer, H. Y., Stockmeier, C. A., et al. (2000). Glial fibrillary acidic protein immunoreactivity in the prefrontal cortex distinguishes younger from older adults in major depressive disorder. *Biol. Psychiatry* 48, 861–873. doi: 10.1016/S0006-3223(00)00999-9

Millstein, R. A., and Holmes, A. (2007). Effects of repeated maternal separation on anxiety- and depression-related phenotypes in different mouse strains. *Neurosci. Biobehav. Rev.* 31, 3–17. doi: 10.1016/j.neubiorev.2006.05.003

Montero, T. D., and Orellana, J. A. (2015). Hemichannels: new pathways for gliotransmitter release. *Neuroscience* 286, 45–59. doi: 10.1016/j.neuroscience.2014.11.048

Nakamoto, K., Nishinaka, T., Sato, N., Aizawa, F., Yamashita, T., Mankura, M., et al. (2015). The activation of supraspinal GPR40/FFA1 receptor signalling regulates the descending pain control system. *Br. J. Pharmacol.* 172, 1250–1262. doi: 10.1111/bph.13003

Nishinaka, T., Kinoshita, M., Nakamoto, K., and Tokuyama, S. (2015a). Sex differences in depression-like behavior after nerve injury are associated with differential changes in brain-derived neurotrophic factor levels in mice subjected to early life stress. *Neurosci. Lett.* 592, 32–36. doi: 10.1016/j.neulet.2015.02.053

Nishinaka, T., Nakamoto, K., and Tokuyama, S. (2015b). Enhancement of nerve-injury-induced thermal and mechanical hypersensitivity in adult male and female mice following early life stress. *Life Sci.* 121, 28–34. doi: 10.1016/j.lfs.2014.11.012

Niwa, M., Matsumoto, Y., Mouri, A., Ozaki, N., and Nabeshima, T. (2011). Vulnerability in early life to changes in the rearing environment plays a crucial role in the aetiopathology of psychiatric disorders. *Int. J. Neuropsychopharmacol.* 14, 459–477. doi: 10.1017/S1461145710001239

Norman, G. J., Karelina, K., Zhang, N., Walton, J. C., Morris, J. S., and Devries, A. C. (2010). Stress and IL-1beta contribute to the development of depressive-like behavior following peripheral nerve injury. *Mol. Psychiatry* 15, 404–414. doi: 10.1038/mp.2009.91

O'Donnell, J., Zeppenfeld, D., McConnell, E., Pena, S., and Nedergaard, M. (2012). Norepinephrine: a neuromodulator that boosts the function of multiple cell types to optimize CNS performance. *Neurochem. Res.* 37, 2496–2512. doi: 10.1007/s11064-012-0818-x

Park, H., Han, K. S., Oh, S. J., Jo, S., Woo, J., Yoon, B. E., et al. (2013). High glutamate permeability and distal localization of Best1 channel in CA1 hippocampal astrocyte. *Mol. Brain* 6:54. doi: 10.1186/1756-6606-6-54

Pekny, M., and Pekna, M. (2014). Astrocyte reactivity and reactive astrogliosis: costs and benefits. *Physiol. Rev.* 94, 1077–1098. doi: 10.1152/physrev.00041.2013

Roberts, J., Ossipov, M. H., and Porreca, F. (2009). Glial activation in the rostroventromedial medulla promotes descending facilitation to mediate inflammatory hypersensitivity. *Eur. J. Neurosci.* 30, 229–241. doi: 10.1111/j.1460-9568.2009.06813.x

Sattler, R., and Rothstein, J. D. (2006). Regulation and dysregulation of glutamate transporters. *Handb. Exp. Pharmacol.* 175, 277–303. doi: 10.1007/3-540-29784-7_14

Schwarz, J. M., and Bilbo, S. D. (2012). Sex, glia, and development: interactions in health and disease. *Horm. Behav.* 62, 243–253. doi: 10.1016/j.yhbeh.2012.02.018

Seltzer, Z., Dubner, R., and Shir, Y. (1990). A novel behavioral model of neuropathic pain disorders produced in rats by partial sciatic nerve injury. *Pain* 43, 205–218. doi: 10.1016/0304-3959(90)91074-S

Sofroniew, M. V., and Vinters, H. V. (2010). Astrocytes: biology and pathology. *Acta Neuropathol.* 119, 7–35. doi: 10.1007/s00401-009-0619-8

Villemure, C., and Bushnell, M. C. (2009). Mood influences supraspinal pain processing separately from attention. *J. Neurosci.* 29, 705–715. doi: 10.1523/JNEUROSCI.3822-08.2009

von Boyen, G. B., Steinkamp, M., Reinshagen, M., Schäfer, K. H., Adler, G., and Kirsch, J. (2004). Proinflammatory cytokines increase glial fibrillary acidic protein expression in enteric glia. *Gut* 53, 222–228. doi: 10.1136/gut.2003.012625

Wei, F., Guo, W., Zou, S., Ren, K., and Dubner, R. (2008). Supraspinal glial-neuronal interactions contribute to descending pain facilitation. *J. Neurosci.* 28, 10482–10495. doi: 10.1523/JNEUROSCI.3593-08.2008

Woolf, C. J. (2010). What is this thing called pain? *J. Clin. Invest.* 120, 3742–3744. doi: 10.1172/JCI45178

Yoshimura, M., and Furue, H. (2006). Mechanisms for the anti-nociceptive actions of the descending noradrenergic and serotonergic systems in the spinal cord. *J. Pharmacol. Sci.* 101, 107–117. doi: 10.1254/jphs.CRJ06008X

Zhang, H., Zhao, Y., and Wang, Z. (2015). Chronic corticosterone exposure reduces hippocampal astrocyte structural plasticity and induces hippocampal atrophy in mice. *Neurosci. Lett.* 592, 76–81. doi: 10.1016/j.neulet.2015.03.006

Zhang, Z. J., Cao, D. L., Zhang, X., Ji, R. R., and Gao, Y. J. (2013). Chemokine contribution to neuropathic pain: respective induction of CXCL1 and CXCR2 in spinal cord astrocytes and neurons. *Pain* 154, 2185–2197. doi: 10.1016/j.pain.2013.07.002

Conflict of Interest Statement: The authors declare that the research was conducted in the absence of any commercial or financial relationships that could be construed as a potential conflict of interest.

Copyright © 2017 Nakamoto, Aizawa, Kinoshita, Koyama and Tokuyama. This is an open-access article distributed under the terms of the Creative Commons Attribution License (CC BY). The use, distribution or reproduction in other forums is permitted, provided the original author(s) or licensor are credited and that the original publication in this journal is cited, in accordance with accepted academic practice. No use, distribution or reproduction is permitted which does not comply with these terms.

frontiers in Cellular Neuroscience

ORIGINAL RESEARCH
published: 28 June 2017
doi: 10.3389/fncel.2017.00177

Frontal Connectivity in EEG Gamma (30–45 Hz) Respond to Spinal Cord Stimulation in Minimally Conscious State Patients

Yang Bai[1], Xiaoyu Xia[2], Zhenhu Liang[1], Yong Wang[1], Yi Yang[2], Jianghong He[2] and Xiaoli Li[3,4]**

[1] Institute of Electrical Engineering, Yanshan University, Qinhuangdao, China, [2] Department of Neurosurgery, PLA General Hospital, Beijing, China, [3] State Key Laboratory of Cognitive Neuroscience and Learning, Beijing Normal University, Beijing, China, [4] IDG/McGovern Institute for Brain Research, Beijing Normal University, Beijing, China

Spinal cord stimulation (SCS) has become a valuable brain-intervention technique used to rehabilitate patients with disorders of consciousness (DOC). To explore how the SCS affects the cerebral cortex and what possible electrophysiological mechanism of SCS effects on the cortex, the present study investigated the functional connectivity and network properties during SCS in minimally conscious state (MCS) patients. MCS patients received both SCS and sham sessions. Functional connectivity of the phase lock value (PLV) in the gamma band (30–45 Hz) was investigated at the pre-, on- and post-SCS stages. In addition, to evaluate global network properties, complex network parameters, including average path length, cluster coefficient and small-world, were measured. When SCS was turned on, significantly decreased connectivity was noted in the local scale of the frontal-frontal region and in the large scales of the frontal-parietal and frontal-occipital regions. The global network showed fewer small-world properties, average path lengths increased and cluster coefficients decreased. When SCS was turned off, the large-scale connectivity and global network returned to its pre-SCS level, but the local scale of frontal-frontal connectivity remained significantly lower than its pre-SCS level. Sham sessions produced no significant changes in either functional connectivity or network. The findings directly showed that SCS could effectively intervene cortical gamma activity, and the intervention included immediate global effects (large scale connectivity and network alteration only occurred in stimulation period) and long-lasting local effects (local scale connectivity alteration persist beyond stimulation period). Moreover, considering the mechanism and propagation of gamma activity, it indicates that the frontal cortex plays a crucial role in the SCS effects on the cerebral cortex.

Keywords: spinal cord stimulation, EEG, minimally conscious state, gamma, functional connectivity

OPEN ACCESS

Edited by:
Mikhail Lebedev,
Duke University, United States

Reviewed by:
Christoph Guger,
g.tec, Austria and Neurotechnology USA Inc., United States
Thierry Ralph Nieus,
Luigi Sacco Hospital, Italy
Fengyu Cong,
Dalian University of Technology, China

***Correspondence:**
Jianghong He
he_jianghong@sina.cn
Xiaoli Li
xiaoli@bnu.edu.cn

Received: *31 March 2017*
Accepted: *12 June 2017*
Published: *28 June 2017*

Citation:
Bai Y, Xia X, Liang Z, Wang Y, Yang Y, He J and Li X (2017) Frontal Connectivity in EEG Gamma (30–45 Hz) Respond to Spinal Cord Stimulation in Minimally Conscious State Patients. Front. Cell. Neurosci. 11:177. doi: 10.3389/fncel.2017.00177

INTRODUCTION

Despite considerable research, there is currently no effective standardized treatment for patients with disorders of consciousness (DOC). However, in recent years, spinal cord stimulation (SCS) has become a valuable brain-intervention technique for rehabilitating DOC patients because it is a less-invasive, simpler surgical procedure than deep-brain stimulation (Georgiopoulos et al., 2010;

Mattogno et al., 2017). Studies have shown its efficacy in modulating the brains of DOC patients (Yamamoto et al., 2012, 2013, 2017), but the underlying mechanism of its effects on the cerebral cortex is still unclear.

Electrophysiological studies investigating the effects of SCS on DOC patients are limited. Studies using pain-related P250 amplitude have shown that SCS may indirectly stimulate the frontal cortex, which is part of the awareness and attention network (Yampolsky et al., 2012; Yamamoto et al., 2013). In a previous study, we reported that SCS modulated frontal delta and gamma activity in patients in a minimally conscious state (MCS) (Bai et al., 2017), showing that SCS modulated the brain functions of MCS patients and providing EEG evidence supporting the potential mechanism for doing so: stimulating the reticular formation and further affecting the frontal cortical region through the formation-thalamus-cortex network. However, further research is needed to provide detailed evidence about the pathway by which SCS affects the cerebral cortices of DOC patients.

Gamma oscillatory activity is thought to be a fundamental mechanism that integrates neural networks within and across brain structures, facilitates coherent sensory registration and mediates cognitive functions (Kaiser and Lutzenberger, 2005; Herrmann et al., 2010; Roye et al., 2010). This activity may represent a coding operator for brain functions and inter-area communications (Basar, 2013). Gamma connectivity has been implicated relevant in subjective consciousness (Llinas et al., 1998; Singer, 1998), and gamma coherence has been shown to be a fundamental prerequisite in the aware process and the potential to participate cognitive processes (Naro et al., 2016). In addition, gamma connectivity has been identified as an important awareness-level marker in DOC patients (Cavinato et al., 2015; Naro et al., 2016). In MCS and vegetative state (VS) patients, significant differences have been demonstrated in the responses of short-range parietal and long-range fronto-parietal gamma coherences to simple sensory stimulus modalities (Cavinato et al., 2015). Our previous study found that SCS, particularly at 70 Hz, significantly changed gamma activity, increasing its relative power and decreasing both coherence and global synchronization. Therefore, considering gamma activity's critical role in cognitive and brain function, gamma activity alteration induced by SCS may increase understanding of the possible physiological basis for the effects of SCS.

Functional connectivity and corresponding network parameters have been identified as valuable characteristic to assess the brain states of DOC patients (Kotchoubey et al., 2013; Chennu et al., 2014; Monti et al., 2015). Functional connectivity measures the relationships among the activities measured in various regions of interest in the brain. Analysing complex networks based on graph theory has enabled the application of new methods useful to investigating both local and global properties of functional connectivity in the brain (Bullmore and Sporns, 2009). Combination of functional connectivity and network properties play a prominent role in analysing, describing and understanding human brain function (Stam and Reijneveld, 2007). Therefore, the present study focused on assessing the functional connectivity and network characteristics of gamma activity. Given that SCS at a frequency of 70 Hz proved to significantly change gamma activity, 70 Hz was chosen as the frequency parameter of stimulation during sessions that included EEG recording at the pre-, on- and post-SCS stages. We hypothesized that the relationships among various brain regions would identify the pathway responsible for the SCS effects.

EXPERIMENTAL PROCEDURES

Patients

As reported in our previous study, 16 MCS patients, aged 19–65, who had received SCS implants were enrolled in a multiple-session stimulation study. All participants were at least 3 weeks post-surgery and had stable clinical states. During the study, 5 participants dropped out due to infection and other clinical factors. **Table 1** shows the clinical features of the 11 participants who completed the entire study. The consciousness state of each patient was assessed using the JFK Coma Recovery Scale-Revised (JFK CRS-R) (Giacino et al., 2004). Any treatment or drugs that could modify cortical excitability were excluded. Written informed consent to participate in the study was obtained from the patient's caregivers, and the study was approved by the ethics committee of PLA Army General Hospital.

Stimulation Protocol

The participants received both sessions that included real stimulation and sham stimulations, with at least 2 days' washout between sessions. Stimulation was delivered by a pulse generator (Prime Advanced, Medtronic Inc., Minneapolis, MN, USA) that delivered electric pulses with a 3-V amplitude and a 210-μs pulse width. The pulse generator was implanted under the anterior chest wall. And the pulse generator was connected to stimulation electrodes through Touhy needle. The needle was implanted into the midline epidural space at the cervical-thoracic junction. And the stimulation electrodes were inserted into the epidural space of the cervical vertebrae, and placed at the C2–C4 levels. The stimulation was caused by periodic occurrence of voltage

TABLE 1 | Participants' demographic characteristics.

Patient	Etiology	Post-injury (months)	CRS-R
Patient 1	Hemorrhage	18	8
Patient 2	Hemorrhage	12	10
Patient 3	Hemorrhage	11	7
Patient 4	Hemorrhage	11	7
Patient 5	Anoxia	4	10
Patient 6	Hemorrhage	3	9
Patient 7	Hemorrhage	4	7
Patient 8	Anoxia	3	7
Patient 9	Infarction	4	7
Patient 10	Anoxia	8	7
Patient 11	Anoxia	28	9

CRS-R, Coma recovery scale-revised.

difference between two electrodes. The stimulation parameters could be setup by a wireless controller *in vitro*. In this study, the stimulation frequency parameter was set at 70 Hz and delivered for 20 min consecutively. Sham stimulations were conducted with the stimulator turned off.

EEG Recordings and Pre-processing

Resting state EEG was recorded for 10 min before stimulation, for 20 min during the real or sham stimulation and for 10 min immediately after the stimulation. EEGs were recorded using 32 channels (BrainAmp 64 MRplus, Brain Products, Germany) and Ag/AgCl pin electrodes having a sampling rate of 1 kHz. The skin/electrode impedance was maintained below 5 kΩ. During the experiments, participants were behaviorally awake (eyes open, EO), and if they showed signs of sleepiness (prolonged eye closure, EC), either the JFK CRS-R arousal-facilitation protocol was applied or the experiment was suspended.

EEG pre-processing was conducted using EEGLAB software version 12.0.2.5b, running on a MATLAB environment (Version 2013b, MathWorks Inc.; Natick, MA, USA). The 50-Hz power signal was removed by a notch filter. The EEG signal was band filtered between 1 and 45 Hz. The Independent Component Analysis (ICA) was used to identify and remove artifact-relevant components, including eye movements and muscle activation. The EEG data were divided into epochs of 10 s with overlaps of 50%. The selected artifact-free epochs were average referenced.

EEG Analysis

Phase Locking Value (PLV)

Connectivity between pairwise channels in the gamma band (30–45 Hz) was computed using phase synchronization, which is briefly described as follows. For each epoch EEG signal, the instantaneous phases $\varphi_x(t)$ and $\varphi_y(t)$ of the pairwise channel were evaluated based on the Hilbert transform. Then, the phase difference was defined by

$$\Delta\phi_{xy}(t) = \varphi_x(t) - \varphi_y(t). \tag{1}$$

Several indices based on the phase difference within a short term can be used to indicate the phase synchronization between two series (Rosenblum et al., 2001). The present study applied PLV based on the circular variance of the phase difference, yielding

$$PLV_{xy} = \frac{1}{N}\left|\sum_{t=1}^{N} e^{j\Delta\varphi_{xy}(t)}\right|. \tag{2}$$

This measure of PLV varied between 0 and 1, and the computation involved no parameter choices. Therefore, the synchrony can be described by a phase-synchronization matrix C with each element of PLV_{xy}.

Graph Theoretical Analysis

Graph theoretical analysis was performed on the phase synchronization matrices. The nodes in the graph were defined as the electrodes and the links as the measure of the phase synchronization between the nodes. Weighted graphs were created using synchronization matrix C with each element of PLV_{xy}.

Graphs can be characterized using various measures, two of the most fundamental of which are the clustering coefficient, which denotes the likelihood that neighbors of a vertex will also be connected to each other, and the average path length, which indicates the average number of edges of the shortest path between pairs of vertices. Stam et al. (2009) provided full definitions for calculating the clustering index (C_w) and the path length (L_w) to analyse weighted networks. To calculate the clustering index from weighted networks, the weights between the node i and the other nodes j should be symmetrical ($\omega_{ij} = \omega_{ji}$), and $0 \leq \omega_{ij} \leq 1$, as proposed by Onnela et al. (2005). Indeed, both conditions are readily fulfilled when using PLV values as the weight definition. Then, the weighted clustering index of vertex i is defined as

$$C_i = \frac{\sum_{k\neq i}\sum_{l\neq i,l\neq k}\omega_{ik}\omega_{il}\omega_{kl}}{\sum_{k\neq i}\sum_{l\neq i,l\neq k}\omega_{ik}\omega_{il}}. \tag{3}$$

Note that all sums terms with $k = i$, $l = i$ or $k = l$ are skipped. The mean clustering of the total network is defined as

$$C_w = \frac{1}{N}\sum_{i=1}^{N} C_i \tag{4}$$

Then, the length of a weighted path between two vertices is defined as the sum of the lengths of the edges of this path. The shortest path L_{ij} between two vertices i and j is the path between i and j with the shortest length. The averaged path length of the entire network is computed as

$$L_w = \frac{1}{(1/N(N-1))\sum_{i=1}^{N}\sum_{j\neq i}^{N}(1/L_{ij})} \tag{5}$$

In this formula, the harmonic mean is used to handle disconnected edges resulting in infinite path lengths (i.e., $1/\infty \rightarrow 0$) (Newman, 2003). Then, the small-world parameter can be calculated as $S = \frac{C_w}{L_w}$.

To obtain measures that are independent of network size, the mean edge weight and the mean path length were compared to the mean of 50 random networks. The C_w^s and L_w^s denote weighted clustering coefficient and path length, respectively, averaged over an ensemble of 50 random, surrogate networks that were derived from the original network by randomly reshuffling the edge weights. Then, the final index was obtained from $\widehat{C}_w = C_w/C_w^s$ and $\hat{L}_w = L_w/L_w^s$. Finally, the small-world parameter was denoted as $S = \frac{\widehat{C}_w}{\hat{L}_w}$.

RESULTS

Functional connectivity was measured using the PLV between each set of pairwise EEG channels. Then, interest regions were defined as follows: frontal (Fp1, Fp2, Fz, F3, and F4), central (Cz, C3, and C4), parietal (Pz, P3, and P4) and occipital (Oz, O3, and O4). **Figure 1** shows the functional connectivity of electrodes in the regions of interest and the overall brain in gamma band. Comparison of on-SCS and pre-SCS shows a

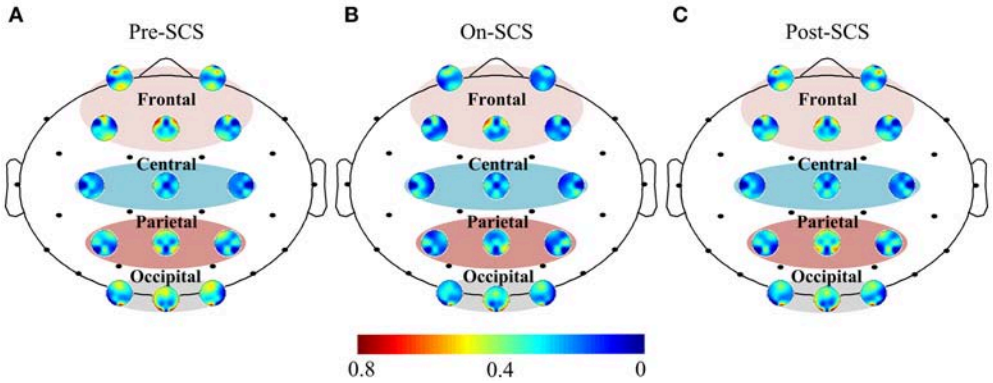


FIGURE 1 | Functional connectivity of electrodes in regions of interest and overall brain in gamma band. **(A)** Average functional connectivity of the electrodes with overall brain pre-SCS. **(B)** Average functional connectivity of the electrodes with overall brain on-SCS. **(C)** Average functional connectivity of the electrodes with others post-SCS. Each colored circle shows the connectivity between the identified electrode and other electrodes. The regions of interest are the frontal, central, parietal and occipital. Colors indicate the average strength of connectivity.

distinct decrease of connectivity among the frontal, frontal-parietal and frontal-occipital regions. After the SCS was turned off, connectivity of frontal-frontal, frontal-parietal and frontal-occipital were markedly returned.

SCS induced connectivity changes were found in frontal-frontal, frontal-parietal, and frontal-occipital (**Figure 2A**). To investigate the changes at different stages, we compared the average connectivity between pairwise stages using paired *t*-tests: On-SCS vs. Pre-SCS, Post-SCS vs. On-SCS and Post-SCS vs. Pre-SCS (**Figure 2B**). Bonferroni correction was performed after multiple comparisons. When SCS was turned on (On-SCS vs. Pre-SCS), significant decreases of connectivity were found in frontal-frontal ($p < 0.001$), frontal-parietal ($p < 0.001$) and frontal-occipital ($p = 0.011$). When SCS was turned off, all the connectivity rebounded but only with significance in the frontal-parietal ($p < 0.001$). But when post-SCS compared with pre-SCS, significance was only found within frontal-frontal connectivity ($p < 0.001$). As **Table 2** shows, in sham sessions, in all three stages, the average connectivity showed no significant changes.

Then, pairwise comparisons of each connectivity were performed using paired *t*-tests, and correction of the false discovery rate was performed after multiple comparisons (*q*-value = 0.05). Top panel of **Figure 2C** shows the significantly altered connecitities in comparison of pairwise stages. Then, we defined the electrodes which were included in at least three significantly changed connectivities as critical electrodes (bottom panel of **Figure 2C**). The location of the significantly altered connectivity and critical eletrodes was generally consistent with the average connectivity findings. When SCS was turned on or turned off, the significantly altered connectivity and critical electrodes were both located mostly in the frontal and parietal regions. And after SCS stimulation, the locations of the significantly decreased connectivity and the critical electrodes were found in frontal regions.

In order to explore the effects of SCS on the global cerebral cortex, graph theoretical based network parameters were calculated using the connectivity matrix in the gamma band at three stages: path length, cluster coefficient and small-world. Comparisons between pairwise stages were performed using paired *t*-tests with Bonferroni corrections. **Figure 3** shows the boxplot of the parameters at each stage. Significant increases of average path length ($p = 0.004$) and decreases of cluster coefficient ($p = 0.040$) were found during SCS stimulation period. The global network showed less small-world property. And the network perturbation company with the stimulation. When SCS was turned off, the network parameters rebound to the baseline level. In sham sessions, the various stages produced no significant alterations of the network parameters.

DISCUSSION

SCS has been demonstrated as a valuable brain-intervention technique for rehabilitating DOC patients (Georgiopoulos et al., 2010; Mattogno et al., 2017; Yamamoto et al., 2017). But there was still few studies investigating the potential mechanism. In a previous study (Bai et al., 2017), we reported that SCS at a frequency of 70 Hz could effectively modulate MCS patients' frontal gamma activities by increasing the relative power and decreasing the coherence and global synchronization. In order to further explore the effects of SCS with 70 Hz on interventing gamma activity, the present study measured functional connectivity and network properties in the gamma band at different SCS stages. By this way, we aim to investigate how the SCS effects on the cortex and what the potential pathway participate SCS modulation on the cerebral. Comparing with pre-SCS, SCS turning on induced significant decreases in functional connectivity in local scale of frontal-frontal and large scale of frontal-parietal and frontal-occipital regions. When SCS was turned off, the large scale connectivity and global network features returned to the pre-SCS level. But the local scale of frontal-frontal connectivity stays lower than pre-SCS. The findings directly show that, SCS turning on effectively modulate the gamma activity. The interventaion includes immediate global

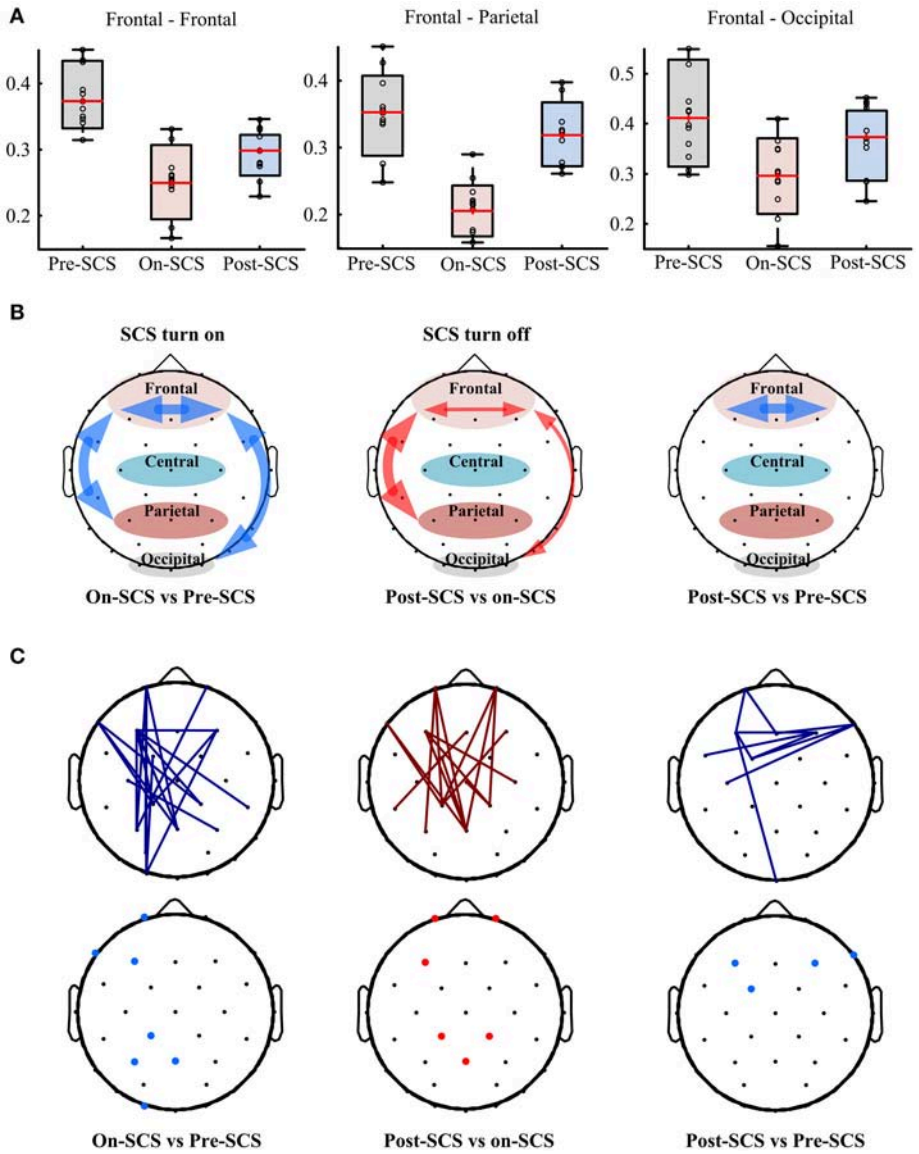


FIGURE 2 | (A) Functional connectivity in patients' gamma bands at pre-, on- and post-SCS. **(B)** Compasions of patients' average frontal-frontal, frontal-parietal and frontal-occipital connectivity using paired *t*-test. Heavy red arrows mean significant increases, thin red arrows mean increase without significance, and blue arrows mean significant decreases. **(C)** Top panel shows significantly altered connectivities and bottom panel shows critical electrodes compared between pairwise stages. Red lines mean significantly increased connectivity, and blue lines mean significant decreased connectivity. Red dots mean critical electrodes included in significantly increased connectivities, and blue dots mean critical electrodes included in significantly decreased connectivities.

TABLE 2 | Gamma band functional connectivity and network parameters (mean ± standard deviation) pre-SCS, on-SCS and post-SCS in sham sessions.

	Pre-SCS	On-SCS	Post-SCS
Frontal-Frontal	0.374 ± 0.047	0.380 ± 0.042	0.357 ± 0.031
Frontal-Parietal	0.341 ± 0.052	0.358 ± 0.070	0.332 ± 0.060
Frontal-Occipital	0.399 ± 0.076	0.389 ± 0.076	0.386 ± 0.073
Average path length	0.189 ± 0.020	0.186 ± 0.018	0.190 ± 0.013
Cluster coefficient	5.664 ± 0.396	5.584 ± 0.458	5.627 ± 0.048
Small-World	31.26 ± 5.448	31.24 ± 6.784	31.29 ± 3.806

effects (large scale connectivity and network property), and local effects (local scale connectivity) which last beyond period of the stimulation. The global and local effects imply that regions of frontal, parietal and occipital were the direct targets of SCS. But, potential after-effects of local or global effects of SCS on consciousness rehabilitation should be further explored in long-term clinical assessment.

These results provide further evidence supporting the critical role of the frontal cortex in the SCS effects. All significantly altered connectivity was relevant to the frontal region, no matter whether it was in global or local effects. When SCS was turned off,

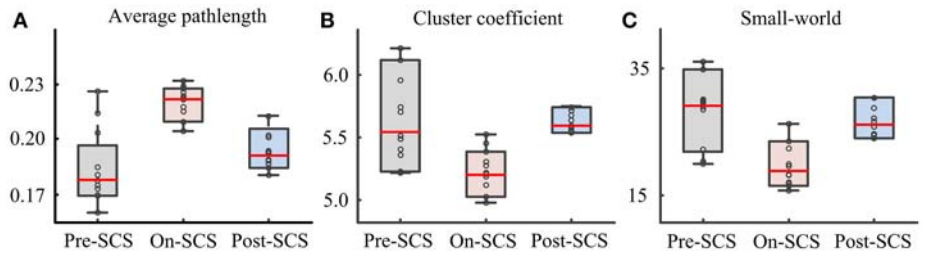


FIGURE 3 | Network parameters in gamma bands at pre-SCS, on-SCS and post-SCS. **(A)** Average path length. **(B)** Cluster coefficients. **(C)** Small-world.

connectivity of the frontal-parietal and frontal-occipital returned to pre-SCS levels, but frontal-frontal connectivity in post-SCS remained lower than pre-SCS. These decreases in the frontal regions were consistent with the coherence results from our previous study (Bai et al., 2017). Evidence demonstrating the role of the frontal cortex in SCS has also been provided by other studies using pain-related P250 amplitude. These studies demonstrated the capability of SCS to directly affect the frontal cortex (Yampolsky et al., 2012; Yamamoto et al., 2013). Therefore, the intervention global effects occurring in the parietal and occipital cortices may be induced by their interaction with frontal cortex, and the interaction could be represented in gamma connectivity.

Considering the crucial role of gamma activity in brain function, the gamma alteration induced by SCS stimulation may imply brain modulation in DOC patients. Gamma activity can be measured in a wide range of cortical and subcortical structures (Basar and Bullock, 1992). One important potential mechanism considered existing a subcortical pacemaker (thalamus) that drove the cortex at a frequency in the gamma band (Llinas et al., 1998). Then, the gamma activity measured in the cortex was propagated by thalamo-cortical connections (Steriade et al., 1996; Llinas et al., 2005), meaning that the intra-laminar thalamic nuclei might drive large areas of the cortex using gamma oscillations (Llinas and Ribary, 1993). Therefore, these global changes in connectivity and network in the gamma activity suggest the capability of SCS to modulate the gamma pacemaker: thalamus. The altered thalamus interrupts the established model of gamma "command" activity in the cortex, thus causing fewer small-world network features, including increasing average path length and decreasing cluster coefficient, in the cortex. When combined with the results of our previous research, those of the present study suggest that gamma activity detected in the cortex, especially the frontal cortex, may be a significant biomarker for evaluating the effects of SCS.

The results of the present study provide EEG evidence demonstrating the anatomical pathway by which SCS modulates the brain: the thalamus-cortex connection. This is consistent with the indications that the SCS mechanism may be that it enhances the specific firing of the cerebral cortex by exerting a direct effect on the reticular formation-thalamus pathway. In addition, the crucial role of the frontal region in altering connectivity along with SCS stimulation prompts us to propose the frontal cortex as a relay station in the SCS modulation pathway. SCS affects the cerebral cortex by first modulating the frontal cortex and then propagating to other regions via frontal cortex connectivity. Coincidentally, this pathway has been included in a meso-circuit model that attempts to explain DOC after brain injuries (Schiff, 2010). In this explanation, the connections between the thalamus, frontal cortex and parietal/occipital/temporal cortices are crucial to maintaining the consciousness-related network (Giacino et al., 2014). The significant changes in connectivity in the gamma that are induced by SCS being turned on and off are closely related to the three important nodes (thalamus, frontal cortex and parietal/occipital cortices) in this circuit-level pathway. Therefore, we propose that the effects of SCS on consciousness may benefit from interfering with the circuit-level network.

CONCLUSIONS

The present study investigated connectivity and network characteristics in the gamma band at pre-, on- and post-SCS using an SCS frequency of 70 Hz. Significantly frontal related connectivity alterations and network parameters changes were found in gamma band. The findings indicated that SCS could effectively affect the cerebral cortex and the intervention includes immediate global effects (large scale connectivity of frontal-parietal and frontal-occipital, and network alteration) and long-lasting local effects (local connectivity of frontal-frontal). Considering the mechanism of gamma generation and propagation, we suggest that the frontal cortex plays the crucial role in pathway of the stimulation: the SCS alters the frontal cortex by using the thalamus-cortex connection, and then the global brain are modulated via connectivity with the frontal cortex. In addition, the pathway may be the anatomical basis by which the SCS modulates the brain. Since the thalamus, frontal cortex and parietal/occipital cortex play crucial roles in the consciousness-related network, the effects of SCS on consciousness may benefit from interfering with the circuit-level network.

ETHICS STATEMENT

This study was carried out in accordance with the recommendations of the ethics committee of PLA Army

General Hospital with written informed consent from all subjects. All subjects gave written informed consent in accordance with the Declaration of Helsinki. The protocol was approved by the ethics committee of PLA Army General Hospital.

AUTHOR CONTRIBUTIONS

YB had full access to all the data in the study and takes responsibility for the integrity of the data and the accuracy of the data analysis. Study concept and design: YB and XX. Acquisition, analysis, or interpretation of data: YB and XX. Drafting of the manuscript: YB. Critical revision of the manuscript for important intellectual content: All authors. Statistical analysis: YB. Obtained funding: JH and XL. Administrative, technical, or material support: YW. Study supervision: JH and XL.

FUNDING

This work was supported by the National Natural Science Foundation of China (grant numbers 61273063, 81230023); the Beijing Municipal Science and Technology Commission (grant number Z141107002514111); the Innovation Cultivation Fund of the PLA Army General Hospital (grant number 2015-LC-09); The commercialization of research fund supported by Beijing Municipal Commission of Education.

ACKNOWLEDGMENTS

The authors are grateful for the assistance of all persons and volunteers whose participation was essential for the successful completion of this study.

REFERENCES

Bai, Y., Xia, X., Li, X., Wang, Y., Yang, Y., Liu, Y., et al. (2017). Spinal cord stimulation modulates frontal delta and gamma in patients of minimally consciousness state. *Neuroscience* 346, 247–254. doi: 10.1016/j.neuroscience.2017.01.036

Basar, E. (2013). A review of gamma oscillations in healthy subjects and in cognitive impairment. *Int. J. Psychophysiol.* 90, 99–117. doi: 10.1016/j.ijpsycho.2013.07.005

Basar, E., and Bullock, T. H. (1992). *Induced Rhythms in the Brain*. Boston, MA: Springer. doi: 10.1007/978-1-4757-1281-0

Bullmore, E., and Sporns, O. (2009). Complex brain networks: graph theoretical analysis of structural and functional systems. *Nat. Rev. Neurosci.* 10, 186–198. doi: 10.1038/nrn2575

Cavinato, M., Genna, C., Manganotti, P., Formaggio, E., Storti, S. F., Campostrini, S., et al. (2015). Coherence and consciousness: study of fronto-parietal gamma synchrony in patients with disorders of consciousness. *Brain Topogr.* 28, 570–579. doi: 10.1007/s10548-014-0383-5

Chennu, S., Finoia, P., Kamau, E., Allanson, J., Williams, G. B., Monti, M. M., et al. (2014). Spectral signatures of reorganised brain networks in disorders of consciousness. *PLoS Comput. Biol.* 10:e1003887. doi: 10.1371/journal.pcbi.1003887

Georgiopoulos, M., Katsakiori, P., Kefalopoulou, Z., Ellul, J., Chroni, E., and Constantoyannis, C. (2010). Vegetative state and minimally conscious state: a review of the therapeutic interventions. *Stereotact. Funct. Neurosurg.* 88, 199–207. doi: 10.1159/000314354

Giacino, J. T., Fins, J. J., Laureys, S., and Schiff, N. D. (2014). Disorders of consciousness after acquired brain injury: the state of the science. *Nat. Rev. Neurol.* 10, 99–114. doi: 10.1038/nrneurol.2013.279

Giacino, J. T., Kalmar, K., and Whyte, J. (2004). The JFK Coma Recovery Scale-Revised: measurement characteristics and diagnostic utility. *Arch. Phys. Med. Rehabil.* 85, 2020–2029. doi: 10.1016/j.apmr.2004.02.033

Herrmann, C. S., Frund, I., and Lenz, D. (2010). Human gamma-band activity: a review on cognitive and behavioral correlates and network models. *Neurosci. Biobehav. Rev.* 34, 981–992. doi: 10.1016/j.neubiorev.2009.09.001

Kaiser, J., and Lutzenberger, W. (2005). Cortical oscillatory activity and the dynamics of auditory memory processing. *Rev. Neurosci.* 16, 239–254. doi: 10.1515/REVNEURO.2005.16.3.239

Kotchoubey, B., Merz, S., Lang, S., Markl, A., Muller, F., Yu, T., et al. (2013). Global functional connectivity reveals highly significant differences between the vegetative and the minimally conscious state. *J. Neurol.* 260, 975–983. doi: 10.1007/s00415-012-6734-9

Llinas, R., and Ribary, U. (1993). Coherent 40-Hz oscillation characterizes dream state in humans. *Proc. Natl. Acad. Sci. U.S.A.* 90, 2078–2081. doi: 10.1073/pnas.90.5.2078

Llinas, R., Ribary, U., Contreras, D., and Pedroarena, C. (1998). The neuronal basis for consciousness. *Philos. Trans. R. Soc. Lond. B Biol. Sci.* 353, 1841–1849. doi: 10.1098/rstb.1998.0336

Llinas, R., Urbano, F. J., Leznik, E., Ramirez, R. R., and van Marle, H. J. (2005). Rhythmic and dysrhythmic thalamocortical dynamics: GABA systems and the edge effect. *Trends Neurosci.* 28, 325–333. doi: 10.1016/j.tins.2005.04.006

Mattogno, P. P., Barbagallo, G., Iacopino, G., Pappalardo, G., LA Rocca, G., Signorelli, F., et al. (2017). Recovery from chronic diseases of consciousness: state of the art in neuromodulation for persistent vegetative state and minimally conscious state. *Acta Neurochir. Suppl.* 124, 19–25. doi: 10.1007/978-3-319-39546-3_4

Monti, M. M., Rosenberg, M., Finoia, P., Kamau, E., Pickard, J. D., and Owen, A. M. (2015). Thalamo-frontal connectivity mediates top-down cognitive functions in disorders of consciousness. *Neurology* 84, 167–173. doi: 10.1212/WNL.0000000000001123

Naro, A., Russo, M., Leo, A., Cannavo, A., Manuli, A., Bramanti, A., et al. (2016). Cortical connectivity modulation induced by cerebellar oscillatory transcranial direct current stimulation in patients with chronic disorders of consciousness: a marker of covert cognition? *Clin. Neurophysiol.* 127, 1845–1854. doi: 10.1016/j.clinph.2015.12.010

Newman, M. E. (2003). Properties of highly clustered networks. *Phys. Rev. E Stat. Nonlin. Soft Matter Phys.* 68(2 Pt 2):026121. doi: 10.1103/PhysRevE.68.026121

Onnela, J. P., Saramaki, J., Kertesz, J., and Kaski, K. (2005). Intensity and coherence of motifs in weighted complex networks. *Phys. Rev. E Stat. Nonlin. Soft Matter Phys.* 71(6 Pt 2):065103. doi: 10.1103/PhysRevE.71.065103

Rosenblum, M., Pikovsky, A., Kurths, J., Schäfer, C., and Tass, P. A. (2001). Phase synchronization: from theory to data analysis. *Handb. Biol. Phys.* 4, 279–321. doi: 10.1016/S1383-8121(01)80012-9

Roye, A., Schroger, E., Jacobsen, T., and Gruber, T. (2010). Is my mobile ringing? Evidence for rapid processing of a personally significant sound in humans. *J. Neurosci.* 30, 7310–7313. doi: 10.1523/JNEUROSCI.1113-10.2010

Schiff, N. D. (2010). Recovery of consciousness after brain injury: a mesocircuit hypothesis. *Trends Neurosci.* 33, 1–9. doi: 10.1016/j.tins.2009.11.002

Singer, W. (1998). Consciousness and the structure of neuronal representations. *Philos. Trans. R. Soc. Lond. B Biol. Sci.* 353, 1829–1840. doi: 10.1098/rstb.1998.0335

Stam, C. J., de Haan, W., Daffertshofer, A., Jones, B. F., Manshanden, I., van Cappellen van Walsum, A. M., et al. (2009). Graph theoretical analysis of magnetoencephalographic functional connectivity in Alzheimer's disease. *Brain* 132(Pt 1), 213–224. doi: 10.1093/brain/awn262

Stam, C. J., and Reijneveld, J. C. (2007). Graph theoretical analysis of complex networks in the brain. *Nonlin. Biomed. Phys.* 1:3. doi: 10.1186/1753-4631-1-3

Steriade, M., Contreras, D., Amzica, F., and Timofeev, I. (1996). Synchronization of fast (30–40 Hz) spontaneous oscillations in intrathalamic and thalamocortical networks. *J. Neurosci.* 16, 2788–2808.

Yamamoto, T., Katayama, Y., Obuchi, T., Kobayashi, K., Oshima, H., and Fukaya, C. (2012). Spinal cord stimulation for treatment of patients in the minimally conscious state. *Neurol. Med. Chir.* 52, 475–481. doi: 10.2176/nmc.52.475

Yamamoto, T., Katayama, Y., Obuchi, T., Kobayashi, K., Oshima, H., and Fukaya, C. (2013). Deep brain stimulation and spinal cord stimulation for vegetative state and minimally conscious state. *Neurosurgery* 80, S30 e31–39. doi: 10.1016/j.wneu.2012.04.010

Yamamoto, T., Watanabe, M., Obuchi, T., Kobayashi, K., Oshima, H., Fukaya, C., et al. (2017). Spinal cord stimulation for vegetative state and minimally conscious state: changes in consciousness level and motor function. *Acta Neurochir. Suppl.* 124, 37–42. doi: 10.1007/978-3-319-39546-3_6

Yampolsky, C., Hem, S., and Bendersky, D. (2012). Dorsal column stimulator applications. *Surg. Neurol. Int.* 3, S275–S289. doi: 10.4103/2152-7806.103019

Conflict of Interest Statement: The authors declare that the research was conducted in the absence of any commercial or financial relationships that could be construed as a potential conflict of interest.

Copyright © 2017 Bai, Xia, Liang, Wang, Yang, He and Li. This is an open-access article distributed under the terms of the Creative Commons Attribution License (CC BY). The use, distribution or reproduction in other forums is permitted, provided the original author(s) or licensor are credited and that the original publication in this journal is cited, in accordance with accepted academic practice. No use, distribution or reproduction is permitted which does not comply with these terms.

frontiers in Cellular Neuroscience

CORRECTION
published: 18 August 2017
doi: 10.3389/fncel.2017.00251

Corrigendum: Frontal Connectivity in EEG Gamma (30–45 Hz) Respond to Spinal Cord Stimulation in Minimally Conscious State Patients

Yang Bai[1], *Xiaoyu Xia*[2], *Zhenhu Liang*[1], *Yong Wang*[1], *Yi Yang*[2], *Jianghong He*[2]* and *Xiaoli Li*[3,4]*

[1] Institute of Electrical Engineering, Yanshan University, Qinhuangdao, China, [2] Department of Neurosurgery, PLA Army General Hospital, Beijing, China, [3] State Key Laboratory of Cognitive Neuroscience and Learning, Beijing Normal University, Beijing, China, [4] IDG/McGovern Institute for Brain Research, Beijing Normal University, Beijing, China

Keywords: spinal cord stimulation, EEG, minimally conscious state, gamma, functional connectivity

OPEN ACCESS

Edited and reviewed by:
Mikhail Lebedev,
Duke University, United States

***Correspondence:**
Jianghong He
he_jianghong@sina.cn
Xiaoli Li
xiaoli@bnu.edu.cn

Received: *23 July 2017*
Accepted: *07 August 2017*
Published: *18 August 2017*

Citation:
Bai Y, Xia X, Liang Z, Wang Y, Yang Y, He J and Li X (2017) Corrigendum: Frontal Connectivity in EEG Gamma (30–45 Hz) Respond to Spinal Cord Stimulation in Minimally Conscious State Patients. Front. Cell. Neurosci. 11:251. doi: 10.3389/fncel.2017.00251

A corrigendum on

Frontal Connectivity in EEG Gamma (30–45 Hz) Respond to Spinal Cord Stimulation in Minimally Conscious State Patients

by Bai, Y., Xia, X., Liang, Z., Wang, Y., Yang, Y., He, J., et al. (2017). Front. Cell. Neurosci. 11:177. doi: 10.3389/fncel.2017.00177

In the published article, there was an error in the Affiliation 2. Instead of "Department of Neurosurgery, PLA General Hospital, Beijing, China," it should be "Department of Neurosurgery, PLA Army General Hospital, Beijing, China." The authors apologize for this error and state that this does not change the scientific conclusions of the article in any way.

Conflict of Interest Statement: The authors declare that the research was conducted in the absence of any commercial or financial relationships that could be construed as a potential conflict of interest.

Copyright © 2017 Bai, Xia, Liang, Wang, Yang, He and Li. This is an open-access article distributed under the terms of the Creative Commons Attribution License (CC BY). The use, distribution or reproduction in other forums is permitted, provided the original author(s) or licensor are credited and that the original publication in this journal is cited, in accordance with accepted academic practice. No use, distribution or reproduction is permitted which does not comply with these terms.

frontiers in Physiology

ORIGINAL RESEARCH
published: 22 September 2017
doi: 10.3389/fphys.2017.00676

Inappropriate Timing of Swallow in the Respiratory Cycle Causes Breathing–Swallowing Discoordination

Naomi Yagi[1,2,3], *Yoshitaka Oku*[1,4*], *Shinsuke Nagami*[2,3,4], *Yoshie Yamagata*[5], *Jun Kayashita*[5], *Akira Ishikawa*[6], *Kazuhisa Domen*[7] and *Ryosuke Takahashi*[2]

[1] Department of Swallowing Physiology, Hyogo College of Medicine, Nishinomiya, Japan, [2] Department of Neurology, Graduate School of Medicine, Kyoto University, Kyoto, Japan, [3] Clinical Research Center for Medical Equipment Development, Kyoto University Hospital, Kyoto, Japan, [4] Department of Physiology, Hyogo College of Medicine, Nishinomiya, Japan, [5] Department of Health Sciences, Prefectural University of Hiroshima, Hiroshima, Japan, [6] Graduate School of Health Sciences, Kobe University, Kobe, Japan, [7] Department of Physical Medicine & Rehabilitation, Hyogo College of Medicine, Nishinomiya, Japan

Rationale: Swallowing during inspiration and swallowing immediately followed by inspiration increase the chances of aspiration and may cause disease exacerbation. However, the mechanisms by which such breathing–swallowing discoordination occurs are not well-understood.

Objectives: We hypothesized that breathing–swallowing discoordination occurs when the timing of the swallow in the respiratory cycle is inappropriate. To test this hypothesis, we monitored respiration and swallowing activity in healthy subjects and in patients with dysphagia using a non-invasive swallowing monitoring system.

Measurements and Main Results: The parameters measured included the timing of swallow in the respiratory cycle, swallowing latency (interval between the onset of respiratory pause and the onset of swallow), pause duration (duration of respiratory pause for swallowing), and the breathing–swallowing coordination pattern. We classified swallows that closely follow inspiration (I) as I-SW, whereas those that precede I as SW-I pattern. Patients with dysphagia had prolonged swallowing latency and pause duration, and tended to have I-SW or SW-I patterns reflecting breathing–swallows discoordination.

Conclusions: We conclude that swallows at inappropriate timing in the respiratory cycle cause breathing–swallowing discoordination, and the prolongation of swallowing latency leads to delayed timing of the swallow, and results in an increase in the SW-I pattern in patients with dysphagia.

Keywords: aspiration, coordination between breathing and swallowing, phase resetting, dysphagia, deglutition disorders

OPEN ACCESS

Edited by:
Brian R. Noga,
University of Miami, United States

Reviewed by:
Donald C. Bolser,
University of Florida, United States
Thomas E. Dick,
Case Western Reserve University, United States

****Correspondence:***
Yoshitaka Oku
yoku@hyo-med.ac.jp

Specialty section:
This article was submitted to Respiratory Physiology, a section of the journal Frontiers in Physiology

Received: *03 March 2017*
Accepted: *24 August 2017*
Published: *22 September 2017*

Citation:
Yagi N, Oku Y, Nagami S, Yamagata Y, Kayashita J, Ishikawa A, Domen K and Takahashi R (2017) Inappropriate Timing of Swallow in the Respiratory Cycle Causes Breathing–Swallowing Discoordination. Front. Physiol. 8:676. doi: 10.3389/fphys.2017.00676

INTRODUCTION

Breathing–swallowing coordination is one of the most important airway defense mechanisms (Nishino, 2012). Swallowing normally occurs during expiration, and the subsequent respiration reinitiates with expiration (Shaker et al., 1992; Martin et al., 1994; Martin-Harris et al., 2005). This expiration-swallow-expiration (E-SW-E) pattern prevents the pharyngeal contents from invading

the lower airway. However, other swallowing patterns are observed even in healthy subjects, although the occasion is rare (Martin-Harris et al., 2005). Namely, swallowing occurs during inspiration (I-SW pattern) and inspiration occurs immediately after a swallow (SW-I pattern). The frequency of I-SW and SW-I patterns increases with age, in patients with stroke (Leslie et al., 2002), head-neck cancer after treatment (Gillespie et al., 2005), Parkinson's disease (Gross et al., 2008), and chronic obstructive pulmonary disease (COPD) (Gross et al., 2009). An increase in the discoordination between breathing and swallowing may predispose patients to aspiration pneumonia and exacerbation of COPD. Indeed, an increase in I-SW pattern is associated with a risk of aspiration in Parkinson's disease (Troche et al., 2011). Recently, we reported that frequent I-SW and/or SW-I patterns (high I-SW/SW-I rate) exacerbated COPD (Nagami et al., 2017). Therefore, the identification of such subjects with a high I-SW/SW-I rate and treating them to reduce the I-SW/SW-I rate may prevent exacerbations of these diseases.

The present study was aimed to gain insight into the mechanisms underlying I-SW and/or SW-I patterns, and to determine a possible means to reduce the I-SW/SW-I rate via various types of interventions. We hypothesized that breathing–swallowing discoordination occurs when the timing of the swallow in the respiratory cycle is inappropriate. The concept in which swallowing is considered as a perturbation to the respiratory cycle was originally proposed by Paydarfar et al. (1995). Although, they reported that the period of expiration is the shortest when swallows are initiated near the expiratory-to-inspiratory transition, they did not describe whether the swallowing is followed by inspiration or expiration. In addition, it is not clear whether the increase in the I-SW/SW-I rate in patients with dysphagia is accompanied by shifts in the timing of swallowing in the respiratory cycle, and most importantly, why such shifts in timing occur. To clarify these issues, we monitored the parameters associated with breathing–swallowing coordination in healthy subjects and in patients with dysphagia, using a non-invasive swallowing measurement system (Yagi et al., 2016).

MATERIALS AND METHODS

The study protocol has been approved by local ethical committees of Hyogo College of Medicine (No. 1580) and Kyoto University (No. C819). All subjects gave written informed consent in accordance with the Declaration of Helsinki. We recruited 250 volunteer subjects from Daito City Cohort, who regularly participate in community-operated exercise program for care prevention, and 43 volunteer subjects who visited a health promotion festival at Ashiya Municipal Hospital. Subjects who have a history of aspiration pneumonia, manifest clinically evident cerebrovascular or respiratory disease, or have medication with dopaminergic drugs were excluded. We also recruited 30 patients with dysphagia (stable subacute–chronic phase of illness) who were hospitalized for swallowing rehabilitation. Characteristics of these patients are shown in **Table 1**. Underlying diseases included stroke, intracranial hemorrhage, tuberculous spondylitis, pneumonia, myocardial infarction, and unknown etiology (possible frail condition or sarcopenia). Dysphagia in stroke patients was classified as upper motor neuron lesions in all cases, however, a detailed evaluation with regard to the location of stroke (e.g., whether it included swallow-related cortical areas) was not undertaken, because stroke location is not typically related to the risk of aspiration (Steinhagen et al., 2009; Daniels et al., 2017).

TABLE 1 | Characteristics of 30 subjects with dysphagia.

No.	Underlying diseases	Gender	Age	BMI
1	Aortic dissection, post-operative state, suspect of left recurrent nerve palsy	F	56	20.8
2	Brainstem infarction (left ventral pons)	M	77	22.0
3	Cerebral hemorrhage (right putamen)	F	79	18.6
4	Cerebral hemorrhage (right thalamus)	M	81	19.0
5	Cerebral infarction	F	76	28.5
6	Cerebral infarction (left temporal lobe)	M	63	23.9
7	Cervical spondylotic myelopathy	F	71	24.9
8	Encephalitis	M	55	25.3
9	Myocardial infarction	M	77	24.0
10	Old cerebral infarction	M	81	21.8
11	Organizing pneumonia	M	78	22.3
12	Right femoral trochanter fracture	F	70	17.4
13	Subcortical infarction	F	67	24.2
14	Tracheostomized state	M	58	18.8
15	Tuberculous spondylitis	M	72	19.9
16	Unknown etiology	F	84	29.9
17	Unknown etiology	F	82	22.3
18	Right carotid endarterectomy, post-operative state	M	89	22.3
19	Parkinson's disease	M	74	18.7
20	Cerebral infarction (left corona radiata, right frontal lobe), dementia with Lewy body, diabetes mellitus	F	87	19.1
21	Brain contusion (left frontal lobe)	F	76	16.0
22	Multiple brain infarction	M	55	18.5
23	Multiple brain infarction	F	69	18.1
24	Left subarachnoid hemorrhage	F	70	20.8
25	Cardiogenic brain embolism	M	65	19.4
26	Cerebral hemorrhage (right thalamus)	M	62	16.9
27	Cerebral infarction (right corona radiata)	M	73	19.0
28	Brain tumor	F	88	16.5
29	Cerebral hemorrhage (left putamen)	F	85	21.5
30	Cerebral hemorrhage	F	80	17.9
		M:15 F:15	73.3 ± 9.9 (range: 55–89)	20.9 ± 3.4 (range: 16.0–29.9)

Evaluation of Swallowing Function

Dysphagia was diagnosed if any of the following four criteria was met:

1. Food intake level scale (FILS) (Kunieda et al., 2013) less than Level 10. This scale categorizes the severity of dysphagia primarily based on methods of feeding. Subjects who receive nutrition via non-oral pathways are categorized as Levels 1–3,

subjects who receive nutrition by both oral dysphagia diet and alternative nutrition are categorized as Levels 4–6, subjects who receive nutrition by various degrees of dysphagia diet are categorized as Levels 7–9, and normative subjects are categorized as Level 10.

2. Repetitive Saliva-Swallowing Test (RSST) (Hori et al., 2016), a count of swallows over a 30-s period, <3. In this test, subjects are instructed to swallow saliva as many times as possible within 30 s. An RSST count of less than three times in 30 s suggests suspected dysphagia, and the sensitivity and specificity of RSST to predict aspiration in videofluorographic examination are reported to be 0.98 and 0.66, respectively (Oguchi et al., 2000).
3. Water swallowing test (WST) >1. In this test, subjects are instructed to drink 30 ml of water from a cup, and the condition of swallowing is scored. Score 1 indicates a normative swallowing function (ability to swallow 30 ml water at once in 5 s), whereas Score 5 indicates the worst swallowing function (frequent cough or inability to swallow) (Zhang et al., 2016; **Table 2**).
4. Modified water swallowing test (MWST) score <5. In this test, subjects are instructed to swallow 3 ml of water, which is injected into the subject's oral cavity with a syringe, and the condition of swallowing is scored. If the subject is unable to swallow, or experienced dyspnea, coughing, or wet-hoarse dysphonia after swallowing, a score of 1–3 is recorded and the test is discontinued. If the subject is able to swallow the water, the subject is asked to perform two dry (saliva) swallows. If the patient is able to complete the water and both dry swallows, a score of 5 is recorded, otherwise, a score of 4 is recorded (Tohara et al., 2003; Murakami et al., 2015; **Table 3**). The sensitivity and specificity of MWST to differentiate between aspirators and non-aspirators with a cutoff level of 3 are 70 and 88%, respectively (Tohara et al., 2003).

FILS was recorded for all patients, and all subjects scored <10 (7.3 ± 2.8). Since the severity of dysphagia in these patients was mild, each subject additionally underwent at least one of three swallowing screening tests to confirm the functional impairment (RSST: 2.2 ± 1.3, $n = 28$; MWST: 4.4 ± 0.5, $n = 14$; WST: 1.9 ± 0.3, $n = 10$).

For those who were recruited from the Daito City Cohort and at the health promotion festival, the Japanese version of the 10-item eating assessment tool (EAT-10) was performed to facilitate clear differentiation of healthy subjects within the elderly population. EAT-10 score of 3 or higher was considered as possible dysphagia (Belafsky et al., 2008). According to this criterion, 269 subjects belonged to the healthy group, and 24 subjects belonged to the possible dysphagic group. The mean ages of the healthy, possible dysphagic group and of the dysphagic group were not statistically different (healthy: 75.0 ± 6.1 years old, range 56–92 years old, 21 males and 248 females, possible dysphagia: 75.9 ± 6.6 years old, range 66–96 years old, 3 males and 21 females, dysphagia: 73.3 ± 9.9 years old, range 55–89 years old, 15 males and 15 females, $p = 0.324$).

Monitoring of Swallowing

To evaluate breathing–swallowing coordination, we developed a unique swallow monitoring device with minimal instrumentation, which enabled even ambulant monitoring of the swallowing function (Yagi et al., 2016). The device consists of a nasal cannula-type flow sensor connected to a differential pressure transducer, a film-type piezoelectric sensor attached on the surface of the thyroid cartilage, and a logging system that stores signals in a microSD card. The piezoelectric sensor has a wide dynamic range (0–4 kHz) so that both the laryngeal motion and sound are captured. Swallowing periods are extracted semi-automatically with an algorithm using the respiratory flow, the swallowing sound, and the laryngeal motion.

We analyzed the following parameters associated with breathing–swallowing coordination, as shown in **Figure 1**, using custom-made programs, written in MATLAB R2014b (Mathworks, Natick, MA, USA). A total of 2,648 swallows were analyzed.

1. Old phase
   The timing of swallow in the respiratory cycle, which is expressed as the time from the preceding inspiration normalized by the mean length of the respiratory cycle being 1 (Paydarfar et al., 1995).
2. Co-phase
   The time from the swallowing onset to the immediately following inspiration normalized by the mean length of the respiratory cycle being 1 (Paydarfar et al., 1995).
3. Pause duration
   The duration of respiratory pause associated with swallowing. The respiratory pause for voluntary swallow is highly variable (Palmer and Hiiemae, 2003; Matsuo et al., 2008), and thus we avoid using the term "deglutition apnea," which is regulated by interactions between the central pattern generators of breathing and swallowing in the brainstem (Oku et al., 1994).
4. Swallowing latency
   The time from the onset of respiratory pause to the onset of the swallowing reflex, defined as the time point when the speed

TABLE 2 | Thirty milliliter Water swallow test (WST).

Score	Performance
1	Swallow water at once in 5 s without cough
2	Swallow more than twice, without cough
3	Swallow water at once, but with cough
4	Swallow more than twice, but with cough
5	Cough frequently, or inability to swallow water

TABLE 3 | Three milliliter Modified water swallow test (MWST).

Score	Performance
1	Inability to swallow with choking and/or breathing changes
2	Swallow occurred, but with breathing changes
3	Swallow occurred, but with choking and/or wet hoarseness
4	Swallow successfully
5	Swallow successfully with ability of additional dry swallowing twice in 30 s

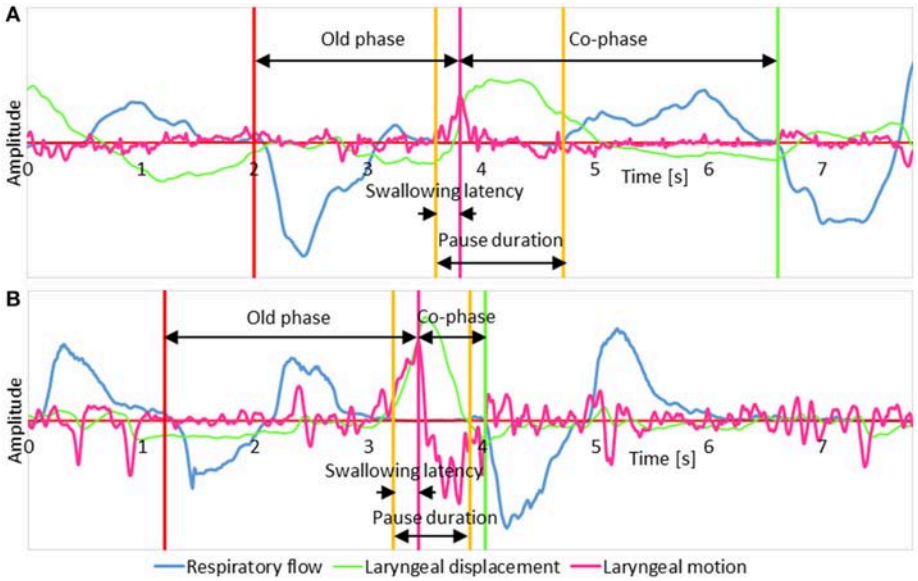


FIGURE 1 | The schema illustrates parameters measured on signal traces. **(A)** A representative case of a swallow with the expiration-swallow-expiration pattern; **(B)** A representative case of a swallow with the expiration-swallow-inspiration pattern. In both traces, respiratory flow, laryngeal motion, and laryngeal displacement signals are shown in blue, magenta, and green, respectively. A positive shift in the respiratory flow signal represents expiration, and a negative shift represents inspiration. The laryngeal displacement signal was derived by integrating the laryngeal motion signal.

of the laryngeal elevation reaches the maximum (Yagi et al., 2016).

5. The time from the onset of swallow to the next inspiration.
6. Breathing–swallowing coordination pattern
   We categorized the breathing–swallowing pattern using two types of parameters: (1) B-SW type, a parameter describing the combination of swallow and the preceding respiratory phase, either E-SW (expiration-swallow) or I-SW (inspiration-swallow), and (2) SW-B type, a parameter describing the combination of swallow and the following respiratory phase, either SW-E (swallow-expiration) or SW-I (swallow-inspiration).

Test Foods

We used soft jelly and water for test foods. The properties of the soft jelly, i.e., hardness, adhesiveness, and cohesiveness are strictly controlled to meet the criteria of Level 0 dysphagia diet according to the Japanese Society of Dysphagia Rehabilitation (JSDR) specification described in IDDSI (International Dysphagia Diet Standardization Initiative) report (Cichero et al., 2016). Subjects were in an upright position sitting on a chair, and swallowed voluntarily about 3 g of Level 0 test food from a teaspoon and 3 ml of water from a 5-ml syringe, two to five times for each. Subjects were instructed to swallow the Level 0 jelly without chewing.

Statistical Analysis

The correlations between parameters were evaluated using Pearson's product-moment correlation analysis. Comparisons of the parameters between different breathing–swallowing coordination types were performed using single-measurement, simple-factorial analysis of variance (ANOVA), followed by *post hoc* analyses with Tukey-Kramer test. Differences in the frequency of breathing–swallowing coordination patterns between three different timings of swallow in the respiratory cycle, and differences in timings of swallow in the respiratory cycle between healthy, possible dysphagic, and dysphagic groups were compared using the chi-squared test followed by Haberman's residual analysis. All data are presented as mean ± standard deviation. *P*-values were two-sided, and $P < 0.05$ was considered as statistically significant.

RESULTS

Correlations between Breathing–Swallowing Coordination Parameters

For analyses in this subsection, we utilized all data from the healthy, possible dysphagic, and dysphagic groups. We found a strong correlation between swallowing latency and pause duration ($r = 0.867$, $p < 0.0001$; **Table 4**), and weak correlations between old phase and swallowing latency ($r = 0.316$, $p < 0.0001$), between old phase and pause duration ($r = 0.216$, $p < 0.0001$), and between old phase and I-SW frequency ($r = -0.259$, $p < 0.0001$). The swallowing latency was variable, which resulted in scattered phase resetting characteristics shown as a co-phase plot (**Figure 2**). To gain insight into the variability of swallowing latency and pause duration, we quantified the variability of swallowing latency and pause duration (deglutition apnea) for those who had more than eight swallow records. Neither swallowing latency nor variability [coefficient of variation; (*SD*/mean) * 100] of swallowing latency was correlated with age (**Figure 3**). Further, neither pause duration nor variability of pause duration was correlated with age.

Swallows with E-SW-I pattern had a significantly larger old phase, smaller co-phase, and shorter time to the following

TABLE 4 | Correlations between parameters associated with breathing–swallowing coordination.

	Old phase	Co-phase	Swallow latency	Pause duration	I-SW frequency	SW-I frequency
Old phase	1.000	0.041	0.316##	0.216##	−0.259##	0.202#
Co-phase	0.041	1.000	−0.033	0.039	0.173**	−0.388##
Swallow latency	0.316##	−0.033	1.000	0.867##	0.189#	0.029
Pause duration	0.216##	0.039	0.867##	1.000	0.203#	0.056
I-SW frequency	−0.259##	0.173**	0.189#	0.203#	1.000	−0.026
SW-I frequency	0.202#	−0.388##	0.029	0.056	−0.026	1.000

$^{**}p < 0.01$, #$p < 0.001$, ##$p < 0.0001$.

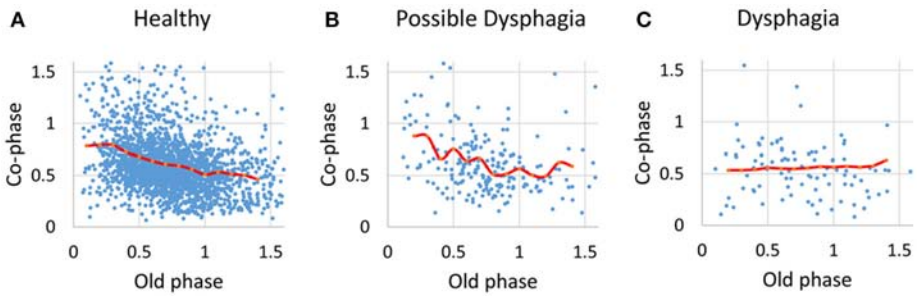


FIGURE 2 | The relationships between old phase and co-phase are plotted for healthy subjects **(A)**, possible dysphagic subjects **(B)**, and dysphagic subjects **(C)**. Red lines indicate the phase-response curves for each subject group calculated by averaging the co-phase within a bin (bin width = 0.1).

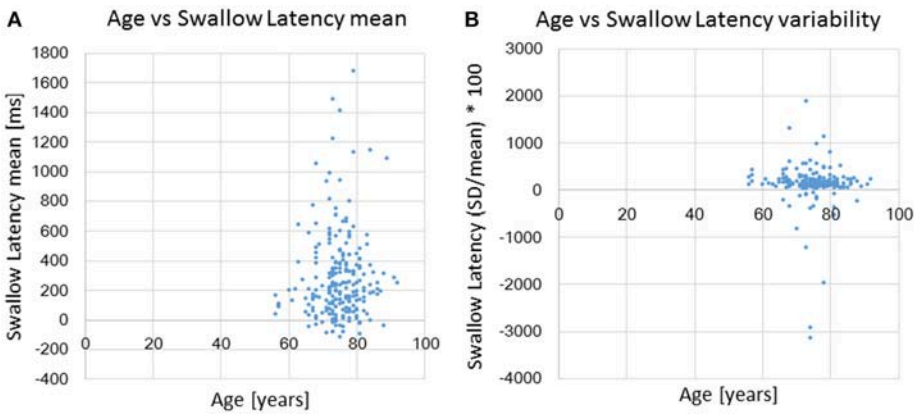


FIGURE 3 | The relationships between age and swallowing latency **(A)** and age and coefficient of variation [(*SD*/mean) * 100] of swallowing latency **(B)**.

inspiration as compared to those with E-SW-E pattern, whereas swallows with I-SW-E pattern had a significantly smaller old phase, larger co-phase, and longer time to the following inspiration (**Table 5**). To further elucidate the relationship between old phase and breathing–swallowing discoordination, we divided the old phase into three groups, early (old phase <0.4), intermediate (old phase between 0.4 and 1.0), and late (old phase >1.0). Swallows with an early old phase had a greater chance of I-SW pattern as compared to those with intermediate and late old phases, whereas swallows with a late old phase had a greater chance of SW-I pattern as compared to those with early and intermediate old phases (**Table 6**). This relationship between old phase and breathing–swallowing discoordination was common in both healthy subjects and patients with dysphagia, suggesting that the characteristic does not depend on a specific etiology of dysphagia.

Comparison of Parameters between Healthy Subjects, Patients with Dysphagia, and Possible Dysphagic Subjects

Parameters associated with breathing–swallowing coordination in healthy, dysphagic, and possible dysphagic groups are listed in **Table 7**. When we put together all swallows from Level

TABLE 5 | Comparisons of parameter values between different breathing-swallowing coordination patterns.

	E-SW-E	E-SW-I	I-SW-E	I-SW-I
N	2,197	199	242	10
Old phase	0.790 ± 0.377	1.019 ± 0.576##	0.483 ± 0.308##	0.229 ± 0.133##
Co-phase	0.617 ± 0.298	0.232 ± 0.080##	0.836 ± 0.320##	0.251 ± 0.083#
Swallow latency (ms)	244 ± 466	281 ± 693	624 ± 787 # #	162 ± 288
Pause duration (s)	0.911 ± 0.578	0.992 ± 0.749	1.252 ± 0.873##	0.941 ± 0.407
Time to the next inspiration (s)	2.385 ± 1.672	0.777 ± 0.242##	3.268 ± 1.546##	0.844 ± 0.267*

*Tukey-Kramer test P-value to E-SW-E (*p < 0.05, #p < 0.001, ##p < 0.0001).*

TABLE 6 | Frequency distributions of different breathing-swallowing coordination patterns in three timings of swallow.

Old phase type	E-SW-E	E-SW-I	I-SW-E	I-SW-I
Early	53.5 (154)##	2.1 (6)**	41.3 (119)##	3.1 (9)##
Intermediate	82.0 (1602)	14.5 (115)	3.5 (104)	0.0 (1)
Late	87.9 (441)#	6.3 (78)##	5.7 (19)*	0.1 (0)

*Frequencies are indicated as percent. Values in parentheses indicate numbers of swallow. Haberman test P-value to Intermediate (*p < 0.05, **p < 0.01, #p < 0.001, ##p < 0.0001).*

TABLE 7 | Comparisons of parameter values and frequencies of breathing-swallowing coordination patterns between healthy, possible dysphagic, and dysphagic groups.

		Healthy	Possible dysphagia	Dysphagia
N		2,327	216	105
Old phase		0.770 ± 0.376	0.776 ± 0.381	0.946 ± 0.837##
Pause duration (s)		0.931 ± 0.597	1.059 ± 0.803*	1.099 ± 0.886*
Swallow latency (ms)		271 ± 506	332 ± 674	413 ± 750*
Swallow type (%) (*N*)	E-SW-E	83.8 (1950)	79.2 (171)	72.4 (76)**
	E-SW-I	7.0 (163)	9.3 (20)	15.2 (16)**
	I-SW-E	8.9 (208)	11.6 (25)	8.6 (9)
	I-SW-I	0.3 (6)	0.0 (0)	3.8 (4)##

**p < 0.05, **p < 0.01, ##p < 0.0001.*
Tukey-Kramer test P-value to Healthy in Old phase, Pause duration, and Swallow latency.
Haberman test P-value to Healthy in Swallow type.

0 and water swallows, the old phase, pause duration, and swallowing latency were significantly larger in dysphagic group, however in possible dysphagic group, only pause duration was significantly larger as compared to healthy group. Further, the frequencies of E-SW-I and I-SW-I patterns were significantly higher in dysphagic group, but not in possible dysphagic group, as compared to healthy group. Timings of swallow in patients with dysphagia were shifted to either early or late timings (**Figure 4**, **Table 8**). The difference in the timings of swallow and the I-SW frequency between healthy and dysphagic groups was more marked in water swallows.

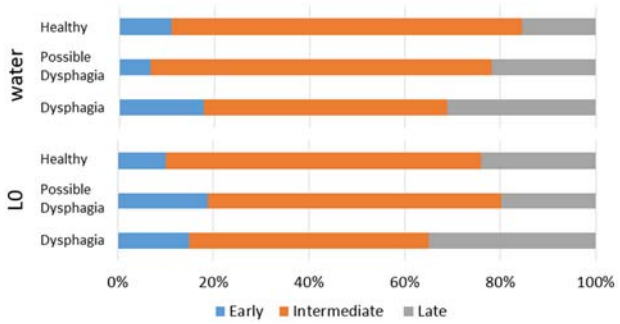


FIGURE 4 | Distributions of timings of swallow in the respiratory cycle in healthy, possible dysphagic, and dysphagic subjects. Upper panel: water swallows; Lower panel: Level 0 dysphagia diet (L0) swallows.

Correlation between Breathing–Swallowing Discoordination and Severity of Dysphagia

We evaluated correlations between parameters associated with breathing–swallowing coordination and those associated with severity of dysphagia to determine whether breathing–swallowing discoordination is deteriorated in proportion to the severity of dysphagia (**Table 9**). A significant negative correlation was found between MWST and SW-I frequency. MWST of subjects in the present study was either 4 or 5 points, thus the result implies that patients who could swallow twice additionally within 30 s after 3 ml water swallow (5 points) had fewer SW-I patterned swallows. Significant negative correlations were also found between WST and I-SW or SW-I frequency. WST of subjects in the present study was either 1 or 2 points, thus the result implies that patients who could swallow water at once in 5 s had, ironically, a higher chance of I-SW or SW-I swallow patterns as compared to those who needed to swallow more than twice. FILS, RSST, and EAT-10 were not correlated with I-SW frequency or SW-I frequency, indicating that these dysphagia screening tools could not detect breathing–swallowing discoordination.

Logistic Analysis to Discriminate Healthy Subjects and Patients with Dysphagia

We performed univariate and multivariate logistic regression analyses in an attempt to discriminate healthy subjects and patients with dysphagia using parameters associated with

TABLE 8 | Comparisons of timings of swallow and frequencies of breathing-swallowing coordination for different types of test foods.

Test type		Old phase type	Early	Intermediate	Late
L0	frequency (%) (*N*)	Healthy	10.1 (119)	66.0 (778)	23.9 (281)
		Possible dysphasia	18.9 (21)**	61.3 (68)	19.8 (22)
		Dysphagia	15.0 (9)	50.0 (30)*	35.0 (21)*
Water	frequency (%) (*N*)	Healthy	10.8 (124)	73.8 (848)	15.4 (177)
		Possible dysphasia	6.7 (7)	71.4 (75)	21.9 (23)
		Dysphagia	17.8 (8)	51.1 (23)#	31.1 (14) **

Test Type		Healthy	Possible Dysphasia	Dysphagia
L0	*N*	266	24	29
	I-SW frequency (%)	10.5 ± 18.2	16.0 ± 17.5	5.2 ± 20.5
	SW-I frequency (%)	6.3 ± 17.8	8.1 ± 15.0	12.9 ± 24.7
Water	*N*	265	24	20
	I-SW frequency (%)	7.7 ± 16.4	6.3 ± 12.4	19.8 ± 28.8**
	SW-I frequency (%)	9.4 ± 19.3	11.0 ± 21.7	18.5 ± 29.1

*Haberman test P-value to Healthy (*p < 0.05, **p < 0.01, #p < 0.001); L0: Level 0 dysphagia diet (Matsuo et al., 2008).*

TABLE 9 | Correlations between severity of dysphagia and parameter values associated with breathing-swallowing coordination.

	EAT-10	FILS	RSST	MWST	WST
N	298	30	28	14	10
Old phase	0.138*	−0.065	−0.190	−0.333	0.432
Co-phase	−0.038	−0.178	−0.248	0.671**	0.343
Swallow latency	0.032	−0.358	−0.327	−0.325	0.072
Pause duration	0.046	−0.286	−0.325	−0.119	−0.023
Time to the next inspiration	−0.025	−0.300	−0.447*	0.515	0.434
I-SW frequency	−0.027	0.163	0.081	−0.198	−0.890#
SW-I frequency	0.105	0.073	0.195	−0.628*	−0.646*

*(*p < 0.05, **p < 0.01, #p < 0.001).*

TABLE 10 | Univariate and multivariate regression analyses to differentiate between healthy and dysphagic subjects.

	Univariate logistic regression *P*-value	Multivariate logistic regression *P*-value	AUC
SW-I frequency	0.052	0.024	0.730
Old phase out of range	0.023	0.008	
Pause duration	0.002	0.002	

breathing–swallowing coordination. For the logistic analysis, we introduced a new variable, the frequency of "old phase out of range," which was defined as the old phase either within the range of early old phase (<0.4) or late old phase (>1.0). We calculated the area under the curve (AUC) of the receiver operating characteristic (ROC) curve to evaluate the model performance for different combinations of parameters. The model parameters were selected from those having a small *p*-value in univariate regression analysis (**Table 10**). We found that the combination of SW-I frequency, the frequency of old phase out of range, and pause duration showed the best performance (AUC = 0.730) in multivariate logistic regression analyses.

DISCUSSION

The new findings of the present study are the following: (1) swallows with either early or late old phase are likely to be an uncoordinated breathing–swallowing pattern in both healthy and patient groups, (2) the old phase of patients with dysphagia is delayed as compared to that of healthy subjects, and (3) respiratory pause duration, highly coupled with swallowing latency, is prolonged in patients with dysphagia. These results suggest that the breathing–swallowing discoordination tends to occur when the timing of swallow in the respiratory cycle is either advanced or delayed, and the prolongation of swallowing latency would cause the delay in timing of swallow in the respiratory cycle, and consequently result in an increase in SW-I pattern in patients with dysphagia. Therefore, interventions to shorten the swallowing latency may be a target of treatment.

Relationship between Breathing–Swallowing Coordination and Timing of Swallows Relative to Respiratory Phases

When an intrinsic oscillator is perturbed by external stimuli, the timing at which a specific phase initiates is shifted (either advanced or delayed). The amount of phase shift depends on the timing and strength of the stimulus; the relationship between timing and amount of shift is termed phase resetting characteristic, which characterizes the oscillator (Glass and

Mackey, 1988; Oku and Dick, 1992). Swallows are one of natural perturbations of the respiratory cycle. Paydarfar et al. (1995) investigated the relationship between timing of swallows and phase shift of the respiratory timing, and found that swallows strongly reset the respiratory rhythm (type-0 resetting, Glass and Mackey, 1988), and swallows at the expiratory-to-inspiratory phase transition have the smallest co-phase (i.e., the shortest time to the next inspiration), and swallows at early expiration have the longest co-phase (i.e., the longest time to the next inspiration). Although they did not discuss the frequency of SW-I pattern, the shortest time to the next inspiration for swallows at the expiratory-to-inspiratory phase transition implies an increase in chance of SW-I pattern, which is consistent with the results of the present study.

The major difference between phase resetting by involuntary swallowing and that by voluntary swallowing in the present study is the variability of swallowing latency in voluntary swallowing. It has been reported that the onset of respiratory pause for swallowing is approximately coincident with the bolus propulsion of liquid into the pharynx (Martin-Harris et al., 2005), however, the pause duration is highly variable when eating solid foods (Palmer and Hiiemae, 2003; Matsuo et al., 2008). Even with water swallows, we observed a considerable variability in swallowing latency. The pause in breathing often began substantially before the swallow, and the old phase sometimes exceeded the whole respiratory cycle length. We think that this is because voluntary swallowing is controlled by the cortex, while the occurrence of involuntary swallow in the respiratory cycle is regulated by the interaction between the central pattern generators of breathing and swallowing within the brainstem. We assume that the variability of cortically-controlled swallowing latency causes the scattering of the co-phase plot and breathing–swallowing discoordination.

Neuronal Mechanisms of Respiratory Phase Resetting

By using transgenic mice in which Channelrhdopsin-2 (ChR2) or Archaerhodopsin (Arch) is specifically expressed in glycinergic neurons, it has been recently shown that activation of glycinergic neurons in the pre-Bötzinger complex (preBötC) leads to interruption of respiratory activity, whereas silencing of glycinergic neurons in the preBötC induces inspiration (Sherman et al., 2015). Simulation using a neural mass model consisting of five types of respiratory neurons in the Bötzinger Complex (BötC), the pre-BötC, and the rostral ventrolateral respiratory group (rVRG) could reproduce the experimental results (Oku and Hulsmann, 2017). On the other hand, the nucleus tractus solitarii (NTS) is the primary relay nucleus which receives afferent signals from pharyngeal mechanoreceptors and chemoreceptors primarily via the superior laryngeal nerve (SLN) (Jean, 2001; Miller, 2008). What we still do not know is the relay pathway from the solitary nucleus to respiratory neurons in the BötC and preBötC, and the types of glycinergic respiratory neurons that are activated or inhibited by the afferent signals. Neurons orthodromically activated by electrical stimulation of the SLN, which exhibited burst firing at the onset of swallowing, project to NTS, the nucleus ambiguus, the hypoglossal nucleus, the medullary reticular formation, and the dorsal motor nucleus of the vagus (Ezure et al., 1993; Sugiyama et al., 2011). These neurons may be involved in the phase resetting associated with swallowing.

Relationship between Pause Duration and Swallowing Latency

We found a strong correlation between the duration of respiratory pause for swallowing and the swallowing latency. This relationship holds true regardless of the type of food, and regardless of whether the subjects are in healthy, dysphagic, or possible dysphagic groups. We do not know the neural mechanisms of this tight coupling, or mechanisms by which the duration of respiratory pause is regulated. One of the reasons for the strong correlation might be the fact that, as the respiratory pause lengthens, the swallowing latency occupies the majority of the respiratory pause.

As we discussed in the previous subsection, a swallow perturbs the respiratory cycle, and shifts the timing of the following inspiration depending on the timing in the respiratory cycle that the swallow occurred, however, this phase resetting theory does not consider factors associated with swallowing latency and pause duration. Paydarfar et al. (1995) reported that the duration of respiratory pause does not depend on the timing of swallow within the respiratory cycle. However, we found that both swallowing latency and pause duration are weakly correlated with the old phase, the timing of swallow in the respiratory cycle. Our analysis indicates that the swallowing latency and pause duration lengthen as the old phase becomes greater, however, interestingly, swallows with I-SW-E pattern, i.e., with early old phase, also had a longer swallowing latency and longer pause duration. This issue is further discussed below.

Comparison between Healthy Subjects and Patients with Dysphagia

We found that the timing of swallows is delayed in patients. Considering that a swallow with a delayed timing tends to be SW-I pattern, we suggest that the increase in SW-I pattern in patients is the consequence of the delayed timing of swallows in the respiratory cycle.

We found that the duration of respiratory pause for swallowing is prolonged in patients with dysphagia. This is consistent with the study of Wang et al. (2015). We also found that the swallowing latency is prolonged in patients, and the pause duration was closely correlated with swallowing latency both in healthy subjects and in patients with dysphagia. It is known that the onset of swallowing reflex relative to a bolus invasion into the pyriform recess is delayed in patients with dysphagia (Miyaji et al., 2012). In addition, the time for food to be propelled into the pharynx may also be delayed in patients with dysphagia. We therefore suggest that the prolongation of the pause duration is a consequence of the delayed onset of swallowing reflex (relative to the respiratory phase) in patients with dysphagia.

Interestingly, we found that the swallowing latency as well as the pause duration are lengthened in swallows with I-SW-E pattern as compared to E-SW-E swallows. Therefore, I-SW-E swallows may be an adaptive behavior to compensate for the delayed onset of swallowing reflex. In contrast, I-SW-I pattern seen in patients with dysphagia would be unsafe swallows, since the time to the next inspiration is much shorter than that in swallows of E-SW-E pattern.

Breathing–Swallowing Discoordination and Severity of Dysphagia

Currently, EAT-10, RSST, and WST are widely used for screening dysphagia. The FILS is generally used to describe the severity of dysphagia in Japan (Kunieda et al., 2013). It is noteworthy in that none of these tests are correlated with either I-SW frequency or SW-I frequency. This might be because patients we recruited had relatively mild dysphagia. Further studies are needed to elucidate whether breathing–swallowing discoordination correlates with the severity of dysphagia. Nevertheless, it should be noted that for patients with mild dysphagia, breathing–swallowing discoordination cannot be predicted by screening tools such as EAT-10, RSST, or WST.

Differentiation between Healthy Subjects and Patients with Dysphagia

We found that the combination of SW-I frequency, the frequency of old phase out of range, and pause duration was the best logit model to differentiate between healthy and dysphagic subjects. However, AUC of this model was only 0.730, suggesting that there is considerable overlap between healthy and dysphagic groups. Indeed there were a number of healthy subjects who showed a high frequency of I-SW/SW-I patterns. We do not know whether these subjects will manifest symptoms of dysphagia as they become older. Discoordination between breathing and swallowing may be a personal trait, which is modified by age and disease (e.g., stroke, Parkinson's disease, and COPD), and could be corrected by rehabilitation (Martin-Harris et al., 2015).

Limitations and Future Perspectives

Although we focused on the discoordination between breathing and swallowing, multiple factors affect the vulnerability of aspiration during swallowing. These include anatomical abnormalities and physiological impairments associated with the triggering of the pharyngeal stage, pharyngeal motor response, and the esophageal stage of swallowing (Lundy et al., 1999). Troche et al. (2010) showed that increasing expiratory muscle strength attenuates aspiration without changing the timing of swallow, presumably due to improved hyolaryngeal complex movement. Therefore, comprehensive measures should be taken to ameliorate the vulnerability for aspiration.

Coughing is another, and probably the most important airway defensive mechanism. The coordination of breathing, swallowing, and coughing has been recently studied by a group of the University of Florida (Pitts et al., 2012, 2013; Bolser et al., 2013). Although we did not record coughs, these studies are a natural extension exploring the mechanisms of airway protective reflexes, and should be further extended to human studies.

We tested only 30 patients with dysphagia. In addition, these patients had diverse etiologies, and were poorly characterized, which might have obscured the unique manifestations of swallowing-breathing coordination in patients with specific diseases or etiologies. Therefore, a future direction of study would be to test a sufficient number of patients with a uniform etiological background.

CONCLUSION

In summary, breathing–swallowing discoordination occurs when the timing of swallow in the respiratory cycle is inappropriate. In patients with dysphagia, the swallowing latency is prolonged, the timing of swallow in the respiratory cycle is delayed, and consequently, the SW-I pattern is increased.

AUTHOR CONTRIBUTIONS

Substantial contributions to the conception or design of the work: YO, KD, and RT. Substantial contributions to the acquisition of data for the work: NY, SN, YY, JK, and AI. Substantial contributions to the analysis, or interpretation of data for the work: NY, YO, and SN. Drafting the work or revising it critically for important intellectual content: NY and YO. Final approval of the version to be published: NY, YO, SN, YY, JK, AI, KD, and RT. Agreement to be accountable for all aspects of the work in ensuring that questions related to the accuracy or integrity of any part of the work are appropriately investigated and resolved: NY, YO, SN, YY, JK, AI, KD, and RT.

ACKNOWLEDGMENTS

This work was supported by Grant-in-Aid for Scientific Research (C) 16K01546. We thank Tohru Yabe and Kenji Tanaka of Murata Manufacturing Co., Ltd. for providing film-type piezoelectric sensors, Hiroshi Ueno of J Craft Co., Ltd., Hiroyuki Takeda of Foodcare/CareIdo Co., Ltd., and Hideo Matsumoto of Murata Manufacturing Co., Ltd. for managing the industry-academia collaboration, Nobuko Osaka of Daito City Hall, Takahisa Imai of Ashiya Municipal Hospital, Masataka Itoda of Wakakusa-Tatsuma Rehabilitation Hospital, Hiroyuki Suganuma of Sapporo-Higashi Tokushukai Hospital, Kazutoshi Yokogushi, Yuji Mitani, and Takayuki Sakurai of Keijinkai Sapporo Nishi-Maruyama Hospital, Hajime Takahashi, Seiichi Mishima, and Ryoko Asai of Takahashi Hospital, Yutaro Oki of Kobe University, Takatsugu Okamoto and Mitsuko Watanabe of Nishi-Hiroshima Rehabilitation Hospital, for helping to obtain data from healthy volunteers and patients.

REFERENCES

Belafsky, P. C., Mouadeb, D. A., Rees, C. J., Pryor, J. C., Postma, G. N., Allen, J., et al. (2008). Validity and reliability of the Eating Assessment Tool (EAT-10). *Ann. Otol. Rhinol. Laryngol.* 117, 919–924. doi: 10.1177/000348940811701210

Bolser, D. C., Gestreau, C., Morris, K. F., Davenport, P. W., and Pitts, T. E. (2013). Central neural circuits for coordination of swallowing, breathing, and coughing: predictions from computational modeling and simulation. *Otolaryngol. Clin. North Am.* 46, 957–964. doi: 10.1016/j.otc.2013.09.013

Cichero, J. A., Lam, P., Steele, C. M., Hanson, B., Chen, J., Dantas, R. O., et al. (2016). Development of international terminology and definitions for texture-modified foods and thickened fluids used in dysphagia management: the IDDSI framework. *Dysphagia* 32, 293–314. doi: 10.1007/s00455-016-9758-y

Daniels, S. K., Pathak, S., Mukhi, S. V., Stach, C. B., Morgan, R. O., and Anderson, J. A. (2017). The relationship between lesion localization and dysphagia in acute stroke. *Dysphagia*. doi: 10.1007/s00455-017-9824-0. [Epub ahead of print].

Ezure, K., Oku, Y., and Tanaka, I. (1993). Location and axonal projection of one type of swallowing interneurons in cat medulla. *Brain Res.* 632, 216–224. doi: 10.1016/0006-8993(93)91156-M

Gillespie, M. B., Brodsky, M. B., Day, T. A., Sharma, A. K., Lee, F. S., and Martin-Harris, B. (2005). Laryngeal penetration and aspiration during swallowing after the treatment of advanced oropharyngeal cancer. *Arch. Otolaryngol. Head Neck Surg.* 131, 615–619. doi: 10.1001/archotol.131.7.615

Glass, L., and Mackey, M. C. (1988). *From Clocks to Chaos*. Princeton, NJ: Princeton University Press.

Gross, R. D., Atwood, C. W. Jr., Ross, S. B., Eichhorn, K. A., Olszewski, J. W., and Doyle, P. J. (2008). The coordination of breathing and swallowing in Parkinson's disease. *Dysphagia* 23, 136–145. doi: 10.1007/s00455-007-9113-4

Gross, R. D., Atwood, C. W. Jr., Ross, S. B., Olszewski, J. W., and Eichhorn, K. A. (2009). The coordination of breathing and swallowing in chronic obstructive pulmonary disease. *Am. J. Respir. Crit. Care Med.* 179, 559–565. doi: 10.1164/rccm.200807-1139OC

Hori, R., Isaka, M., Oonishi, K., Yabe, T., and Oku, Y. (2016). Coordination between respiration and swallowing during non-invasive positive pressure ventilation. *Respirology* 21, 1062–1067. doi: 10.1111/resp.12790

Jean, A. (2001). Brain stem control of swallowing: Neuronal network and cellular mechanisms. *Physiol. Rev.* 81, 929–969.

Kunieda, K., Ohno, T., Fujishima, I., Hojo, K., and Morita, T. (2013). Reliability and validity of a tool to measure the severity of dysphagia: the Food Intake LEVEL Scale. *J. Pain Symptom Manag.* 46, 201–206. doi: 10.1016/j.jpainsymman.2012.07.020

Leslie, P., Drinnan, M. J., Ford, G. A., and Wilson, J. A. (2002). Swallow respiration patterns in dysphagic patients following acute stroke. *Dysphagia* 17, 202–207. doi: 10.1007/s00455-002-0053-8

Lundy, D. S., Smith, C., Colangelo, L., Sullivan, P. A., Logemann, J. A., Lazarus, C. L., et al. (1999). Aspiration: cause and implications. *Otolaryngol. Head Neck Surg.* 120, 474–478. doi: 10.1053/hn.1999.v120.a91765

Martin, B. J., Logemann, J. A., Shaker, R., and Dodds, W. J. (1994). Coordination between respiration and swallowing: respiratory phase relationships and temporal integration. *J. Appl. Physiol. (1985)* 76, 714–723.

Martin-Harris, B., Brodsky, M. B., Michel, Y., Ford, C. L., Walters, B., and Heffner, J. (2005). Breathing and swallowing dynamics across the adult lifespan. *Arch. Otolaryngol. Head Neck Surg.* 131, 762–770. doi: 10.1001/archotol.131.9.762

Martin-Harris, B., McFarland, D., Hill, E. G., Strange, C. B., Focht, K. L., Wan, Z., et al. (2015). Respiratory-swallow training in patients with head and neck cancer. *Arch. Phys. Med. Rehabil.* 96, 885–893. doi: 10.1016/j.apmr.2014.11.022

Matsuo, K., Hiiemae, K. M., Gonzalez-Fernandez, M., and Palmer, J. B. (2008). Respiration during feeding on solid food: alterations in breathing during mastication, pharyngeal bolus aggregation, and swallowing. *J. Appl. Physiol. (1985)* 104, 674–681. doi: 10.1152/japplphysiol.00527.2007

Miller, A. J. (2008). The neurobiology of swallowing and dysphagia. *Dev. Disabil. Res. Rev.* 14, 77–86. doi: 10.1002/ddrr.12

Miyaji, H., Umezaki, T., Adachi, K., Sawatsubashi, M., Kiyohara, H., Inoguchi, T., et al. (2012). Videofluoroscopic assessment of pharyngeal stage delay reflects pathophysiology after brain infarction. *Laryngoscope* 122, 2793–2799. doi: 10.1002/lary.23588

Murakami, K., Hirano, H., Watanabe, Y., Edahiro, A., Ohara, Y., Yoshida, H., et al. (2015). Relationship between swallowing function and the skeletal muscle mass of older adults requiring long-term care. *Geriatr. Gerontol. Int.* 15, 1185–1192. doi: 10.1111/ggi.12572

Nagami, S., Oku, Y., Yagi, N., Sato, S., Uozumi, R., Morita, S., et al. (2017). Breathing–swallowing discoordination is associated with frequent exacerbations of COPD. *BMJ Open Respir. Res.* 4:e000202. doi: 10.1136/bmjresp-2017-000202

Nishino, T. (2012). The swallowing reflex and its significance as an airway defensive reflex. *Front. Physiol.* 3:489. doi: 10.3389/fphys.2012.00489

Oguchi, K., Saito, E., Mizuno, M., Kusudo, S., Tanaka, T., and Onogi, K. (2000). The repetitive saliva swallowing test (RSST) as a screening test of functional dysphagia (2) Validity of RSST. *Jpn. J. Rehabil. Med.* 37, 383–388. doi: 10.2490/jjrm1963.37.383

Oku, Y., and Dick, T. E. (1992). Phase resetting of the respiratory cycle before and after unilateral pontine lesion in cat. *J. Appl. Physiol. (1985)* 72, 721–730.

Oku, Y., and Hulsmann, S. (2017). A computational model of the respiratory network challenged and optimized by data from optogenetic manipulation of glycinergic neurons. *Neuroscience* 347, 111–122. doi: 10.1016/j.neuroscience.2017.01.041

Oku, Y., Tanaka, I., and Ezure, K. (1994). Activity of bulbar respiratory neurons during fictive coughing and swallowing in the decerebrate cat. *J. Physiol. Lond.* 480, 309–324. doi: 10.1113/jphysiol.1994.sp020361

Palmer, J. B., and Hiiemae, K. M. (2003). Eating and breathing: interactions between respiration and feeding on solid food. *Dysphagia* 18, 169–178. doi: 10.1007/s00455-002-0097-9

Paydarfar, D., Gilbert, R. J., Poppel, C. S., and Nassab, P. F. (1995). Respiratory phase resetting and airflow changes induced by swallowing in humans. *J. Physiol.* 483(Pt 1), 273–288. doi: 10.1113/jphysiol.1995.sp020584

Pitts, T., Morris, K., Lindsey, B., Davenport, P., Poliacek, I., and Bolser, D. (2012). Co-ordination of cough and swallow *in vivo* and *in silico*. *Exp. Physiol.* 97, 469–473. doi: 10.1113/expphysiol.2011.063362

Pitts, T., Rose, M. J., Mortensen, A. N., Poliacek, I., Sapienza, C. M., Lindsey, B. G., et al. (2013). Coordination of cough and swallow: a meta-behavioral response to aspiration. *Respir. Physiol. Neurobiol.* 189, 543–551. doi: 10.1016/j.resp.2013.08.009

Shaker, R., Li, Q., Ren, J., Townsend, W. F., Dodds, W. J., Martin, B. J., et al. (1992). Coordination of deglutition and phases of respiration: effect of aging, tachypnea, bolus volume, and chronic obstructive pulmonary disease. *Am. J. Physiol.* 263(5 Pt 1), G750–G755.

Sherman, D., Worrell, J. W., Cui, Y., and Feldman, J. L. (2015). Optogenetic perturbation of preBotzinger complex inhibitory neurons modulates respiratory pattern. *Nat. Neurosci.* 18, 408–414. doi: 10.1038/nn.3938

Steinhagen, V., Grossmann, A., Benecke, R., and Walter, U. (2009). Swallowing disturbance pattern relates to brain lesion location in acute stroke patients. *Stroke* 40, 1903–1906. doi: 10.1161/STROKEAHA.108.535468

Sugiyama, Y., Shiba, K., Nakazawa, K., Suzuki, T., Umezaki, T., Ezure, K., et al. (2011). Axonal projections of medullary swallowing neurons in guinea pigs. *J. Comp. Neurol.* 519, 2193–2211. doi: 10.1002/cne.22624

Tohara, H., Saitoh, E., Mays, K. A., Kuhlemeier, K., and Palmer, J. B. (2003). Three tests for predicting aspiration without videofluorography. *Dysphagia* 18, 126–134. doi: 10.1007/s00455-002-0095-y

Troche, M. S., Huebner, I., Rosenbek, J. C., Okun, M. S., and Sapienza, C. M. (2011). Respiratory-swallowing coordination and swallowing safety in patients with Parkinson's disease. *Dysphagia* 26, 218–224. doi: 10.1007/s00455-010-9289-x

Troche, M. S., Okun, M. S., Rosenbek, J. C., Musson, N., Fernandez, H. H., Rodriguez, R., et al. (2010). Aspiration and swallowing in Parkinson disease

and rehabilitation with EMST: a randomized trial. *Neurology* 75, 1912–1919. doi: 10.1212/WNL.0b013e3181fef115

Wang, C. M., Shieh, W. Y., Chen, J. Y., and Wu, Y. R. (2015). Integrated non-invasive measurements reveal swallowing and respiration coordination recovery after unilateral stroke. *Neurogastroenterol. Motil.* 27, 1398–1408. doi: 10.1111/nmo.12634

Yagi, N., Nagami, S., Lin, M. K., Yabe, T., Itoda, M., Imai, T., et al. (2016). A noninvasive swallowing measurement system using a combination of respiratory flow, swallowing sound, and laryngeal motion. *Med. Biol. Eng. Comput*. 55, 1001–1017. doi: 10.1007/s11517-016-1561-2

Zhang, M., Tao, T., Zhang, Z. B., Zhu, X., Fan, W. G., Pu, L. J., et al. (2016). Effectiveness of neuromuscular electrical stimulation on patients with dysphagia with medullary infarction. *Arch. Phys. Med. Rehabil.* 97, 355–362. doi: 10.1016/j.apmr.2015.10.104

Conflict of Interest Statement: The authors declare that this study received funding from CareIdo Co., Ltd. and J Craft Co., Ltd. The funders were not involved in the study design or collection, analysis, or interpretation of the data. This study was conducted under industry-academia collaboration contracts among Hyogo College of Medicine, Kyoto University, Kobe University, Hiroshima Prefectural University, Foodcare Co., Ltd., CareIdo Co., Ltd., J Craft Co., Ltd., Murata Manufacturing Co., Ltd., and EuSense Medical Co., Ltd.

Copyright © 2017 Yagi, Oku, Nagami, Yamagata, Kayashita, Ishikawa, Domen and Takahashi. This is an open-access article distributed under the terms of the Creative Commons Attribution License (CC BY). The use, distribution or reproduction in other forums is permitted, provided the original author(s) or licensor are credited and that the original publication in this journal is cited, in accordance with accepted academic practice. No use, distribution or reproduction is permitted which does not comply with these terms.

frontiers in Neuroscience

REVIEW
published: 18 October 2017
doi: 10.3389/fnins.2017.00581

Integration of Descending Command Systems for the Generation of Context-Specific Locomotor Behaviors

Linda H. Kim[1,2†], *Sandeep Sharma*[1,3†], *Simon A. Sharples*[1,2], *Kyle A. Mayr*[1,2], *Charlie H. T. Kwok*[1,3] *and Patrick J. Whelan*[1,2,3*]

[1] Hotchkiss Brain Institute, University of Calgary, Calgary, AB, Canada, [2] Department of Neuroscience, University of Calgary, Calgary, AB, Canada, [3] Department of Comparative Biology and Experimental Medicine, University of Calgary, Calgary, AB, Canada

Over the past decade there has been a renaissance in our understanding of spinal cord circuits; new technologies are beginning to provide key insights into descending circuits which project onto spinal cord central pattern generators. By integrating work from both the locomotor and animal behavioral fields, we can now examine context-specific control of locomotion, with an emphasis on descending modulation arising from various regions of the brainstem. Here we examine approach and avoidance behaviors and the circuits that lead to the production and arrest of locomotion.

Keywords: locomotor behavior, supraspinal, descending, goal-directed, approach, aversion

OPEN ACCESS

Edited by:
Brian R. Noga,
University of Miami, United States

Reviewed by:
Noriko Hiroi,
Keio University, Japan
Urszula Slawinska,
Nencki Institute of Experimental Biology, Poland

***Correspondence:**
Patrick J. Whelan
whelan@ucalgary.ca

[†] These authors have contributed equally to this work.

Specialty section:
This article was submitted to Systems Biology, a section of the journal Frontiers in Neuroscience

Received: *08 May 2017*
Accepted: *04 October 2017*
Published: *18 October 2017*

Citation:
Kim LH, Sharma S, Sharples SA, Mayr KA, Kwok CHT and Whelan PJ (2017) Integration of Descending Command Systems for the Generation of Context-Specific Locomotor Behaviors. Front. Neurosci. 11:581. doi: 10.3389/fnins.2017.00581

INTRODUCTION

Animals produce a wide array of locomotor behaviors in response to internal and external cues. Normally, animals survey the environment in search of appropriate olfaction, audition, visual, or tactile sensory inputs. Internally motivated cues may be due to appetitive drive such as food and reproduction, and other physiological needs like safety, shelter, or adaptation to a new environment. These cues inform ongoing movement sequences by converging onto locomotor

Abbreviations: A10, Dopaminergic cell group A10; A11, Dopaminergic cell group A11; A13, Dopaminergic cell group A13; ABA, Accessory basal amygdala; AMG, Amygdala; BG, Basal ganglia; BLA, Basolateral amygdala complex; CeA, Central nucleus of the amygdala; CeM, Medial central nucleus of the amygdala; ChR2, Channelrhodopsin 2; Chx10, Transcription factor Chx10; CnF, Cuneiform nucleus; D1, Dopamine receptor subtype 1; D2, Dopamine receptor subtype 2; DDS, Diencephalospinal dopamine system (in zebrafish); dlPAG, Dorsolateral periaqueductal gray; DLR, Diencephalic locomotor region; dMSNs, Direct pathway medium spiny neurons; dPAG, Dorsal periaqueductal gray; GABA, gamma-Aminobutyric acid; GAD65, glutamic acid decarboxylase; Gi, Gigantocellular reticular nucleus; GiA, Gigantocellular reticular nucleus alpha part; GiV, Gigantocellular reticular nucleus ventral part; GP, Globus pallidus; GPe, Globus pallidus external; GPi, Globus pallidus internal; iMSNs, Indirect pathway medium spiny neurons; LH, Lateral hypothalamus; Lhx3, Transcription factor Lhx3; lPAG, Lateral periaqueductal gray; LPGi, Lateral paragigantocellular nucleus; MdV, Ventral part of medullary reticular formation; MLR, Mesencephalic locomotor region; MRF, Medullary reticular formation; NAc, Nucleus accumbens; PAG, Periaqueductal gray; PMH, Premammillary nucleus of the hypothalamus; PnC, Pontine reticular nucleus caudal; PnO, Pontine reticular nucleus oral; PPN, Pedunculopontine nuclei; PPTg, Pedunculopontine tegmental nucleus; SC, Superior colliculus; SLR, Subthalamic locomotor region; SN, Substantia nigra; SNc, Substantia nigra pars compacta; SNr, Substantia nigra pars reticulata; STh/ STN, Subthalamic nucleus; V1, Primary visual cortex; V1 L5, Layer 5 of the primary visual cortex; Vglut2, Vesicular glutamate 2; vlPAG, Ventrolateral periaqueductal gray; VMH, Ventromedial hypothalamus; VP, Ventral pallidum; VTA, Ventral tegmental area; ZI, Zona incerta.

control centers in the brainstem and spinal cord, thus facilitating the generation of context-appropriate locomotor behaviors.

In the first part of this review, we focus on key supraspinal regions for locomotor control, with emphasis placed on how technological advances are beginning to reveal cell types and the underlying functional connectome. In the second part of this review, we will explore the afferent projections to these locomotor regions and discuss how internal and external triggers can drive appetitive (approach) or aversive (avoidance) locomotor responses.

DESCENDING COMMAND SYSTEMS FOR LOCOMOTION

Over the past 75 years, studies on the descending control of locomotion have been directed toward three regions (Whelan, 1996; Jordan et al., 2008); the Subthalamic Locomotor Region (SLR), the Mesencephalic Locomotor Region (MLR: **Figure 1**), and the Medullary Reticular Formation (MRF: **Figure 1**). These regions were initially identified based on their ability to elicit various forms of locomotor behaviors in response to direct electrical stimulation of these regions. The term "locomotor region" was used since electrical stimulation cannot be confined to anatomically-defined nuclei. These regions are conserved across vertebrate species studied (reviews Rossignol et al., 2006; Fetcho et al., 2008; Grillner et al., 2008; Jordan et al., 2008; Ryczko and Dubuc, 2013) with initial experiments being performed in cats (Shik et al., 1969—English translation of their 1966 publication; reviews Armstrong, 1986; Whelan, 1996), later in rats (Mel'nikova, 1975, 1977 as cited by Ross and Sinnamon, 1984; Sinnamon et al., 1984; Skinner and Garcia-Rill, 1984), and recently in mice (Bouvier et al., 2015; Roseberry et al., 2016).

Investigations into the underlying cellular and system mechanisms for the generation of locomotor behaviors begun in tandem with the identification of locomotor regions. Earlier work was performed in relatively simple organisms (Gillette et al., 1978; Olson and Krasne, 1981; Edwards et al., 1999; Esch and Kristan, 2002) and primitive vertebrates (Grillner et al., 2008). Work on the leech, lamprey and xenopus have provided fascinating similarities between swim behaviors and circuit organization of organisms separated by up to 560 million years of evolution (Mullins et al., 2011). Recent advances in molecular biology and genetic tools have enabled the functional connectivity of locomotor circuit elements in mammalian systems to be explored (Bouvier et al., 2015; Roseberry et al., 2016).

THE MEDULLARY RETICULAR FORMATION: A CENTRE FOR LOCOMOTOR STOP AND GO

The MRF contains groups of diffusely located nuclei that form an important integration center for the control of locomotion, with descending projections onto interneurons and motoneurons of the cervical and lumbar spinal cord (Grillner et al., 1968; Peterson et al., 1979; Bouvier et al., 2015). Shik et al. (1969) were the first to show the existence of a pathway from the MLR to the MRF. Although, activity in the MRF is known to correspond to locomotor activity, recordings from the MRF in freely walking cats showed that activity patterns were complex, as only some units corresponded to the rhythmic electromyographic activity of muscles while others did not (Drew et al., 1986; Perreault et al., 1993). Both electrical and direct drug-based stimulation of the MRF can elicit locomotion (Garcia-Rill and Skinner, 1987a,b; Noga et al., 1988; Jordan, 1998). Similarly, rhythmic patterns or locomotor-like rhythmicity in the isolated *in vitro* brainstem-spinal cord preparation can be evoked (Liu and Jordan, 2005; Hägglund et al., 2010; Kiehn, 2016). Additionally, stimulation of ventrolateral funiculi, containing the reticulospinal projections, can produce bouts of rhythmic motor activity (Magnuson et al., 1995). Acute lesions of this tract eliminate locomotion elicited by stimulation of the MLR in decerebrate cats (Steeves and Jordan, 1980) and result in changes of gait in freely moving animals (Brustein and Rossignol, 1998).

Classically, the MRF has been subdivided into four key nuclei distributed across the medulla and the pons and is also

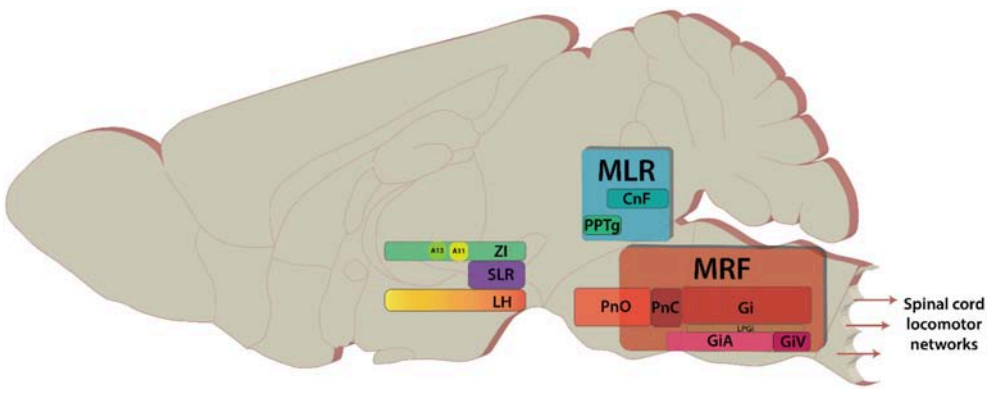


FIGURE 1 | Key areas of the brain discussed in the review. The brain areas are included here have diverse functions in addition to modulating locomotion. Sagittal view of representative locations of locomotor centers.

known as ponto-medullary reticular formation (review Drew et al., 2004). In rodents, these regions correspond with pontine reticular nucleus oral (PnO) and caudal (PnC), gigantocellular reticular nucleus (Gi), and magnocellular nucleus of medulla which encompasses lateral paragigantocellular nucleus (LPGi), gigantocellular reticular nucleus alpha (GiA), and ventral section (GiV), respectively (Paxinos and Franklin, 2008; Esposito et al., 2014). Recent work has focused on the Gi, LPGi, GiA, and GiV. These nuclei form the reticulospinal pathway, and contain cells that descend ipsilaterally via the ventrolateral and ventromedial funiculi (Petras, 1967; Peterson et al., 1979). Contralateral projections also exist (Jankowska et al., 2003; Krutki et al., 2003; Szokol et al., 2011). Recent work using genetic and intersectional viral tracing has revealed that reticulospinal pathways are more diverse than previously thought, and cells can be organized into clusters based on their projections either in the cervical or lumbar spinal cord (Esposito et al., 2014). The ventral part of the MRF (MdV) was highlighted as a region with functional connectivity to forelimb motor neurons suggesting that MRF regions may be organized somatotopically. Interestingly in cat MRF cells were observed to project over long distances to multiple segments (Matsuyama et al., 1999). These differences may represent the different demands of grasping for rodents compared to cats (Whishaw et al., 2008). However, projections to multiple segments have also been observed in the monkey (Kneisley et al., 1978; Coulter et al., 1979).

Most descending MRF cells are glutamatergic and were traditionally thought to form the excitatory command signal for locomotion. Photostimulation of vesicular glutamate 2 (Vglut2)-expressing cells in the brainstem with channelrhodopsin 2 (ChR2) can elicit spinal rhythmicity *in vitro* (Hägglund et al., 2010). Subsequent investigations explored a subpopulation of glutamatergic cells in the brainstem that can be identified by the Chx10 and Lhx3 transcription factors. These cells express c-fos (a marker of neuronal activation) following bouts of locomotor activity, receive input from the MLR, and project to the cervical spinal cord (Bretzner and Brownstone, 2013). Manipulation of activity of these cells *in vivo* did not alter locomotor behavior in mice (Bretzner and Brownstone, 2013), however, activation of these cells in zebrafish is sufficient to drive locomotor activity (Kimura et al., 2013). Surprisingly, recent work on the Chx10 population in mice found that activation of this cell-type at the junction between the rostral medulla (rostral Gi) and caudal pons (PnC) disrupted spinally-generated rhythmicity *in vitro,* and caused the animal to stop when activated *in vivo* (Bouvier et al., 2015). Recruitment of spinally-located premotor inhibitory interneurons by the Chx10 MRF neurons was implicated (Bouvier et al., 2015). Conversely, stop commands in fish (Wannier et al., 1995) and tadpoles (Boothby and Roberts, 1992; Perrins et al., 2002; Li et al., 2003) are reported to be mediated by descending inhibitory cells of the MRF, which project mono-synaptically to motoneurons and are triggered by sensory afferents in the head. This poses an interesting possibility for a parallel stopping mechanism in mammals that remains to be discovered (review Klemm, 2001). Indeed, a GABAergic/glycinergic projection from the MRF to the spinal cord exists in rodents but its function in locomotor control remains unknown (Holstege, 1991).

In addition to the glutamatergic and GABAergic/glycinergic descending pathways within the brainstem are several monoaminergic neuromodulatory pathways that can modulate locomotor activity. The major descending brainstem modulatory pathways are the serotonergic raphespinal pathway and the noradrenergic coeruleospinal pathways. These systems have been reviewed elsewhere (Jordan et al., 2008). Recent work suggests that monoamines (5-HT and noradrenaline) increase in concentration many seconds before locomotion and decrease gradually to baseline once locomotion is terminated. These long timeframes suggest that monoamines are not involved in moment-to-moment modulation of spinal cord circuits and may possibly be released extrasynaptically (Noga B. R. et al., 2017).

THE MESENCEPHALIC LOCOMOTOR REGION: AN INTEGRATIVE HUB FOR LOCOMOTOR SPEED AND GAIT

The MLR is located on the mesopontine border and comprises of the cuneiform (CnF) and the pedunculopontine nuclei (PPN) (**Figure 1**). In basal vertebrates, the MLR comprises the laterodorsal tegmental nucleus and the PPN. In mammals, it comprises the PPN, but also the CnF (Ryczko and Dubuc, 2013, 2017). It can be described as a classical region for locomotor control. Electrical stimulation of the mesopontine border with increasing intensity led to a serial progression from walking to running to galloping (Shik et al., 1969). Initially it was thought that the MLR projects serially to the MRF and acts as a "volume-control" for locomotion, as ablation of the MRF abolished MLR-evoked responses in the spinal cord (Noga et al., 2003). Since the original finding the location of the nuclei comprising the MLR and its projections have been steadily refined.

The PPN, referred to as the pedunculopontine tegmental nucleus (PPTg) in rodents (Paxinos and Franklin, 2008) and sometimes the nucleus tegmenti pedulculopontinus in humans (Schaltenbrand and Wahren, 1977), is located in the ventrolateral portion of the MLR (Olszewski and Baxter, 1954). It is composed of cells with heterogeneous neurotransmitter phenotypes including but not limited to: GABA, glutamate, acetylcholine, and calcium-binding proteins and neuropeptides (Clements and Grant, 1990; Lavoie and Parent, 1994; Fortin and Parent, 1999; Vincent, 2000; Mena-Segovia et al., 2008, 2009). There is no doubt that the use of different terms has led to confusion in the field. In this review we will refer to the PPTg when discussing rodent relevant papers and PPN when referring to cat, monkey, or human work. In terms of projections, the PPN and CnF connect to sensorimotor, associative, and limbic areas of the basal ganglia and the thalamus in monkeys and humans (Sébille et al., 2017). Analysis of these projections suggests that the PPN may integrate sensorimotor, cognitive, and emotional information. The anterior part of the PPN may be related to motor control in the monkey. In contrast, the CnF connectome is more restricted involving predominantly limbic brain regions (Sébille et al., 2017). Some reports have identified

the PPTg as an effective site for evoking locomotion, and direct efferent projections to the lumbar spinal cord have been reported (Skinner et al., 1990). Of the two regions, stimulation of the CnF appears to be more robust in driving locomotion in the cat (Shik and Orlovsky, 1976—original article in Russian: Sirota and Shik, 1973). The CnF lies dorsal to PPTg and borders the inferior colliculi ventrally (Allen Brain Atlas: https://tinyurl.com/k8g98tl). Like the PPTg, the CnF is composed of heterogenous cell types including GABAergic (Ford et al., 1995), glutamatergic (Heise and Mitrofanis, 2006), peptidergic (Sar et al., 1978; Beitz, 1982a,b) cells with some cholinergic neurons (Ford et al., 1995).

Recent work examined MLR cell types for their roles in locomotor behaviors (Roseberry et al., 2016; Kroeger et al., 2017; Mena-Segovia and Bolam, 2017). Activity of the glutamatergic MLR cells correlate with spontaneous locomotor episodes and their activation is sufficient to produce locomotor bouts. Conversely, activity of the GABAergic population is associated with stationary states and their activation stops locomotion, partly through suppression of the local MLR glutamatergic population (Roseberry et al., 2016). This suggests that GABAergic and glutamatergic MLR cells collectively control decelerating and accelerating locomotor behaviors. Work in cats shows that the substantia nigra pars reticulata (SNr) projects to the PPN and suppresses muscle tone while another projection from the lateral SNr to the CnF promotes locomotor activity (Takakusaki et al., 2003). It is thought that the cholinergic MLR population modulates locomotion, but activation of these cells is not sufficient to elicit a locomotor bout. Instead, stimulation of cholinergic MLR cells leads to acceleration of locomotion (Roseberry et al., 2016). However, there are interspecies differences in the density of cholinergic cells. For example, in Parkinsonian patients where the number of cholinergic cells in the PPN are reduced (Hirsch et al., 1987; Jellinger, 1988; Zweig et al., 1989), gait disturbances are often observed (reviews Pahapill and Lozano, 2000; Alam et al., 2011). In addition, basal ganglia afferent connectivity onto the PPN, and from the PPN onto the basal ganglia differ between species. This may help explain the uncertainty in the efficacy of deep brain stimulation stimulation in Parkinson's patients (Alam et al., 2011). Some studies have reported beneficial effects but other studies are less supportive. There is a debate about whether stimulation is targeting the PPN, with the most effective site being slightly posterior to the PPN, in the CnF and the subCnF (Ferraye et al., 2010). Notably the location of the nuclei encompassing the MLR is still a matter of debate, and there appears to be interspecies differences (for details refer to Alam et al., 2011, 2013; Liang et al., 2011, 2012; Thankachan et al., 2012; Ryczko and Dubuc, 2013; Xiang et al., 2013; Sherman et al., 2015). The CnF is an important part of MLR in higher mammals such as cats and monkeys, whereas the precuneiform nucleus (PrCnF) is the mouse analog of CnF. In mice the PrCnF projects directly to the spinal cord (Liang et al., 2011, 2012). This is not the case in the cat where the CnF was found to project to the first cervical segment. Likewise, in monkeys, the CnF projects ipsilaterally within segments of the spinal cord. An additional complexity in interpreting the literature is that the size of the PrCnF in cats (Satoda et al., 2002) and possibly monkeys (Castiglioi et al., 1978) is likely underestimated as the boundaries between the PrCnF and CnF in cats are not as distinct (Liang et al., 2011).

To summarize, the MLR is well-studied, but comparing and contrasting studies, especially between species can be difficult. Generally speaking, in rodents, the data suggest that the PPTg (PPN) is better associated with reward-based motor behaviors, place preference, and sensorimotor gating, than locomotion (Koch et al., 1993; Inglis et al., 1994; Olmstead and Franklin, 1994; Alam et al., 2011). On the other hand, the CnF and PrCnF seem to be better associated with locomotion (Garcia-Rill and Skinner, 1987a; Milner and Mogenson, 1988; Noga B. et al., 2017).

THE DIENCEPHALON: A HUB FOR GOAL-DIRECTED LOCOMOTION

The diencephalon is home to several regions that can elicit locomotion. Although, diencephalic sites have been described in several species, they have been named differently based on the differences in anatomy and effective sites for stimulation. A region of the diencephalon that was pro-locomotory was first described in the cat in the 1930's (Ectors et al., 1938; Masserman, 1938), and electrical stimulation of the subthalamic region was conducted by Waller (1940). Additional work in the 1980s from Orlovsky, Sinnamon, and Mori amongst others provided new insight into areas within the posterior hypothalamus, lateral hypothalamus, and zona incerta that could elicit locomotor activity. While differences were observed, a general finding was in freely moving animals, it was found that an initial scan of the area was performed before exploratory activity was initiated (Mori et al., 1989). These behaviors are often indistinguishable from spontaneous locomotor behavior (Grossen and Kelley, 1972; Leppänen et al., 2006; Lamprea et al., 2008).

Initial reports suggested the site for eliciting locomotion in the cat was the subthalamic nucleus (STN) (abbreviated as STh in rodents); and thus, it was named the subthalamic locomotor region (SLR) (Grossman, 1958; Kaelber and Smith, 1979). Work conducted later in the rat found that the zona incerta (or "zone of uncertainty" dorsal to STh) and medial lateral hypothalamus (LH) had lower thresholds for electrical stimulation (**Figure 1**; Sinnamon and Stopford, 1987; Milner and Mogenson, 1988; Sinnamon, 1993). In the lamprey, this region is known as the diencephalic locomotor region (DLR) (Manira et al., 1997; Ménard and Grillner, 2008), and is located ventral to the thalamus—a region analogous to the lateral hypothalamus in mammals (Ménard and Grillner, 2008). Unfortunately, like the MLR, the terminology used over the years has been confusing. Here we will use the historic SLR term but, where possible, we'll specify the anatomical region.

The SLR is necessary for goal-directed locomotion as bilateral ablation of the SLR abolishes spontaneous locomotion for several weeks following surgery (Shik and Orlovsky, 1976—original article in Russian: Sirota and Shik, 1973). Although, the SLR is connected to the MLR, the MLR is not necessary for SLR-evoked locomotor behavior (Shik et al., 1969). It appears from these findings that the SLR serves as a parallel command system for locomotor control. What remains unclear is if the MRF

is a necessary integration center to spinal cord to produce locomotion. In the lamprey, the DLR, an analog of the SLR in fish, projects to reticulospinal cells (Manira et al., 1997). However, in mammals, direct descending projections from the SLR and DLR to the spinal cord have been reported (Skagerberg and Lindvall, 1985; Sakurai, 2005; Stoyanova et al., 2010; Koblinger et al., 2014). Therefore, it is possible that an MRF-relay may not be necessary for all locomotor behaviors. A more likely scenario is that parallel pathways converge on spinal circuits to coordinate most behaviors.

Local infusion of glutamate agonists and GABA antagonists into the zona incerta (ZI) or the LH are sufficient to drive locomotor behaviors, suggesting that both inhibitory and excitatory afferents regulate SLR output (Di Scala et al., 1984; Milner and Mogenson, 1988; Sinnamon, 1993). The cell types of the ZI and LH have been well-characterized, and like other locomotor command centers are composed of heterogeneous cell types. These include fast-transmitting GABA, glutamatergic cells, and various peptidergic and neuromodulatory subtypes (review Mitrofanis, 2005; Stuber and Wise, 2016). Two modulatory systems that robustly drive locomotion are orexin (Valenstein et al., 1970; Valenstein, 1971; Ida et al., 1999; Thakkar et al., 2001; Sakurai, 2005; Siegel and Boehmer, 2006) and dopamine (Wagner et al., 1995; Kolmac and Mitrofanis, 1999).

The orexin cells in the brain originate mainly in the LH and activity of orexinergic cells is tightly coupled to the regulation of arousal, sleep, appetite, attention, and sensory modulation (Valenstein et al., 1970; Valenstein, 1971; Ida et al., 1999; Thakkar et al., 2001; Sakurai, 2005; Siegel and Boehmer, 2006). These cells have extensive projections throughout the brain including, but not limited to, the SNr, MLR, MRF, and spinal cord (Peyron et al., 1998; Sakurai, 2005; Stoyanova et al., 2010). Mice exhibit enhanced locomotor activity following intracerebroventricular administration of orexin (Hagan et al., 1999; Ida et al., 1999), and blocking orexin-1 receptors attenuates movement (Duxon et al., 2001). A recent study showed presence of orexin receptors on the reticulospinal MLR cells (Sherman et al., 2015). Moreover, focal injection of orexin into the MLR in decerebrate cats either reduced the intensity to evoke locomotion or elicited locomotion without stimulation, whereas an injection of orexin in either PPTg or SNr increased the intensity required to induce muscle atonia (Takakusaki et al., 2005). Recent work has reported that orexin cells may drive locomotor activity by increasing the activity of glutamic acid decarboxylase (GAD65)—expressing inhibitory neurons located in the LH. This population of inhibitory cells was found to be able to drive locomotor behavior when activated, and suppress locomotion when inhibited. These GAD65-expressing cells send projections to ZI, raphe magnus as well as superior colliculus and periaqueductal gray (Kosse et al., 2017; see section Interactions between Appetitive, Defensive, and Exploratory Behavior); however, the underlying circuitry responsible for orexinergic locomotor control requires further characterization.

The A13 and A11 dopaminergic nuclei are in the ZI and the rostral portion of the posterior hypothalamus, respectively. The contribution of the A11 to locomotor control is well characterized in zebrafish and is known as the diencephalospinal dopamine system (DDS; Tay et al., 2011; Lambert et al., 2012). The most recent work on the DDS demonstrates that these cells are rhythmically active during swimming and are both sufficient and necessary for swimming episodes (Jay et al., 2015). Currently, little is known about the locomotor functions of the A13 and A11 in mammals. However, the A11 projects to the spinal cord (Commissiong and Sedgwick, 1975; Skagerberg and Lindvall, 1985; Holstege et al., 1996; Koblinger et al., 2014; review Sharples et al., 2014) and has known roles in pain modulation (Charbit et al., 2009) and motor control (Ondo et al., 2000; Clemens et al., 2006; Qu et al., 2007). It has also been shown that dopamine modulates mammalian spinal CPG networks (Barrière et al., 2004; Humphreys and Whelan, 2012; Sharples et al., 2015; Picton et al., 2017; Sharples, 2017; Sharples and Whelan, 2017). These data support a possibility for a descending dopamine system in mammalian locomotor control. Nonetheless, the role of A11 and A13 cell populations in locomotor behaviors remains to be tested.

FACTORS MEDIATING DECISION MAKING AND MOTOR SELECTION TO APPROACH OR TO AVOID

So far, we have discussed locomotor regions by illustrating the nuclei and cell types involved in each pathway. These regions must interact with other brain areas to produce behaviorally relevant locomotion. Broadly speaking, there are two basic forms of locomotor responses observed in vertebrate species—approach or avoid—and a balance between these is necessary for survival (Glickman and Schiff, 1967). Here we will describe how internal (affective state, cognitive, reward, motivation, homeostatic, etc.) and external (sensory) cues are integrated to decide on approach or aversion (**Figure 2A**). We will describe the functional role of different types of locomotion based on their behavioral correlates, with emphasis on: (1) the role of the superior colliculus (SC) in deciding the appropriate locomotor response based on external sensory cues; (2) key limbic structures mediating locomotor responses based on internal cognitive and affective information; and (3) subsequent motor selection via the basal ganglia circuitry.

EXTERNAL SENSORY CUES CAN FACILITATE APPROPRIATE MOTOR SELECTION

External sensory cues are broadly classified as olfactory, visual, auditory, and tactile stimuli. When animals encounter such cues they must react appropriately to meet survival needs (**Figure 2B**).

The SC is an integral player in triggering appropriate locomotor responses based on novel visual stimuli in the environment. The superficial layers of the SC make use of retinotopic information relayed via the lateral geniculate nucleus of the thalamus (Nagata and Hayashi, 1984; Born and Schmidt, 2008) and primary visual cortex to orient the eyes, head, and body movement toward objects of interest (reviews Sparks, 1986; Grillner et al., 2008; Gandhi and Katnani, 2011). This permits the SC to trigger approach or avoidance responses based on visuospatial input. The location of visual information

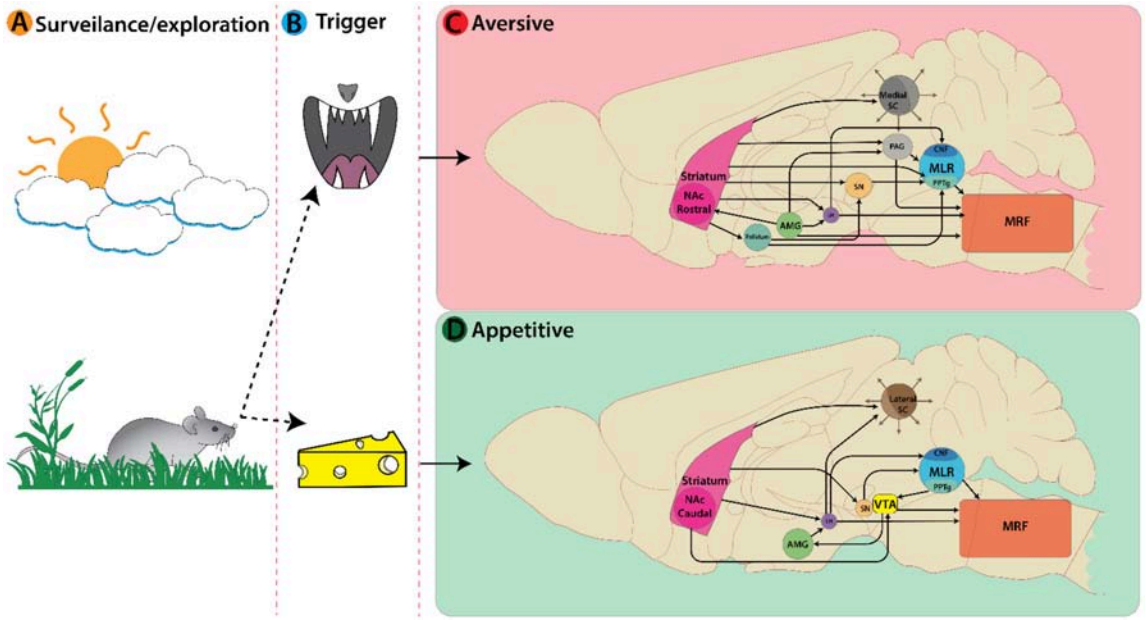


FIGURE 2 | Active nuclei in the mouse brain following a decision or trigger from a surveillance state. **(A)** Representation of an animal's decision process during a surveillance state. In this example a mouse encounters an aversive trigger (**B** top, predatory threat) activating nuclei associated with avoidance behaviors **(C)**. Main nuclei active here are: Striatum, Amygdala, Superior colliculi, etc. On the bottom **(B)** the mouse encounters an appetitive trigger of food/cheese activating nuclei associated with approach behaviors **(D)**.

within the visual field is key for identifying visual cues as food or a threat. Presenting an approaching visual stimulus in the upper visual field can evoke defensive responses such as escape and freezing in mice (Yilmaz and Meister, 2013). In rodents, predatory visual input is in the upper visual field and mapped in the medial SC **(Figure 2C)**, whereas appetitive stimuli are detected in the lower visual field and mapped in the lateral SC (Comoli et al., 2012; **Figure 2D**). This functional organization is reflected by increased c-Fos protein expression (sign of recent neural activity) in the lateral SC following a hunting session for roaches on the floor (Favaro et al., 2011). In addition, unilateral electrical stimulation of lateral SC elicits contralateral orienting and approach-like responses, while stimulation of medial SC induces ipsilateral cringe-like defensive movement that develops into locomotion, running, and jumping with increasing stimulation intensity (Sahibzada et al., 1986). Such orienting responses involve contralateral MRF pathways, whereas movement away from the stimulus is mediated exclusively by an ipsilateral MRF pathways originating from the ventral and lateral SC (Sparks, 1986).

The SC projects ipsilaterally to the CnF and contralaterally to PPTg (Dean et al., 1989) with a major projection onto GABAergic MLR cells (Roseberry et al., 2016). The progression of locomotion elicited by stimulation of the medial SC is like that observed following stimulation at the MLR (Shik et al., 1969; Roseberry et al., 2016). One possibility is that this projection is inhibitory in nature, allowing for locomotion to occur via disinhibition of the MLR. Alternatively, if this circuit is glutamatergic, activation of GABAergic MLR neurons could suppress glutamatergic MLR output, producing motor arrest (see section Reflexive Startle Response Driven by Sudden External Sensory Stimuli).

DECISIONS TO APPROACH OR AVOID ARE GUIDED BY INTERNALIZED CONTEXTUAL INFORMATION

Generally, animals approach rewarding stimuli and avoid aversive stimuli. Aside from the positive and negative values associated with external stimuli, the coordination of approach- or aversive-like behaviors depend on the animal's internal affective and motivational states (Loewenstein et al., 2015). In early studies, Denny-Brown (1962) showed that bilateral lesions of the striatum caused animals to follow anything that moved. Since then the limbic system is understood to contribute to context-specific locomotion that drive decisions to approach or avoid.

Within the limbic system, the nucleus accumbens (NAc) of ventral striatum is an important limbic-motor interface underlying reward and motivation states (Mogenson et al., 1980; Roitman et al., 2005; Carlezon and Thomas, 2009; Levita et al., 2009; Humphries and Prescott, 2010; Richard and Berridge, 2011; McCutcheon et al., 2012; Salgado and Kaplitt, 2015). For example, amphetamine injected in the NAc results in hyper-locomotion demonstrating the key role of dopamine in both locomotion and reward. The NAc is divided into two subregions:

the shell and the core. Traditionally, the shell of the NAc orchestrates the response to unconditioned, innate reward and indeed lesions of the shell produce hypolocomotion (Ito et al., 2004; Aragona et al., 2008; Ito and Hayen, 2011). On the other hand, the core mediates approach behaviors associated with Pavlovian reward-associated cues (Parkinson et al., 2000; Ito et al., 2004; Stefanik et al., 2013, 2016; Hamel et al., 2017). The NAc has diverse outputs that enable recruitment of locomotor circuits. The NAc recruits locomotor circuitry via projections to: globus pallidus (GP), substantia nigra pars compacta (SNc), SNr, LH, ventral tegmental area (VTA), periaqueductal gray (PAG), PPTg, and ventral pallidum (VP) (Mogenson et al., 1983; review Nicola, 2007). It may be noted here that in some of these experiments PPTg also included overlapping brain regions including the CnF. Together these outputs explain the strong locomotory effect of stimulation of the NAc [sections Locomotor Response in Anticipation of Reward and Defensive Locomotor Responses (Escape and Freeze) Associated with Aversive Cues].

The amygdala is implicated in decisions regarding approach and avoidance locomotor behaviors (Petrovich, 2011). Learned food cues are relayed to the LH from the basolateral amygdala complex (BLA) to facilitate feeding, and aversive cues can suppress feeding by direct and indirect projections from the central nucleus of the amygdala (CeA) to LH (Petrovich et al., 1996; Petrovich, 2011). Differential modulation by the CeA and BLA onto striatal projection neurons is known and thus can bias approach and avoid behavior selection (Wall et al., 2013). Discrete nuclei within the amygdala have direct and indirect projections to the PAG, which are involved in defensive locomotion (Gross and Canteras, 2012). Although, the amygdala is involved in both approach and avoidance, its role in driving the corresponding locomotor response to associated triggers requires interactions with various brain regions. The role of the amygdala in both appetitive and aversive locomotor behavior will be revisited separately in the following sections (sections from Motivation to Approach: Execution of Forward Locomotion and Reflexive Startle Response Driven by Sudden External Sensory Stimuli).

MOTOR SELECTION DERIVED FROM THE DECISION TO APPROACH OR AVOID

Both external and internal cues interact with basal ganglia (BG) circuits for precise execution and selection of appropriate locomotor behavior. One widely accepted hypothesis is that the direct dopamine pathway facilitates reward-oriented motor behavior (reviews Everitt and Robbins, 2013; Kim and Hikosaka, 2015; Grillner and Robertson, 2016; Averbeck and Costa, 2017) while the indirect pathway suppresses unrewarded movements. Hence, these two pathways may regulate most associative learning and reward-oriented motor actions (Frank, 2006; Kravitz et al., 2010; Hong and Hikosaka, 2011). The two pathways originate from GABAergic striatal projection neurons that are known as the direct and indirect pathway medium spiny neurons, dMSNs, and iMSNs, respectively (review Utter and Basso, 2008). The dMSNs which express dopamine D1 receptors are excited by dopamine and project directly to the output nuclei of the basal ganglia, the SNr and GPi. Tonically active GABAergic projection neurons comprise these output nuclei and are responsible for tonic inhibition of the thalamus, SC, and PPTg. Thus, inhibition of GPi/SNr neurons by GABAergic dMSNs leads to disinhibition of brainstem motor centers and allow movement initiation. In contrast, iMSNs express dopamine D2 receptors and are inhibited by dopamine. These send GABAergic projections to the globus pallidus external (GPe) which in turn projects inhibitory output to the GPi. Sequentially, the GPe sends inhibitory output to excitatory STh that targets the SNr. Therefore, the net effect of the indirect pathway is an enhancement of inhibitory input from GPi and SNr to the descending motor centers. The GPi/SNr projects to the PPTg providing tonic inhibition affecting locomotor behavior. The anatomical tracing studies provide evidence for SNc projections to the PPN in rat (Beckstead et al., 1979; Semba and Fibiger, 1992; Steininger et al., 1992; Ichinohe et al., 2000) and in cat (Edley and Graybiel, 1983). The presence of such descending input was also supported by recordings of short latency antidromic activation of SNc neurons following PPN stimulation in rat (Scarnati et al., 1984, 1987). This is important as it suggests that dopamine has exclusive projections to brainstem nuclei distinct from the BG circuitry (Ryczko and Dubuc, 2013; Ryczko et al., 2016), which adds an extra degree of monoaminergic control over movement initiation.

PRIMARY APPETITIVE LOCOMOTOR SYSTEM: APPROACH-LIKE RESPONSES TO REWARDING & APPETITIVE CUES

Internalized contextual information such as reward and motivation combine to form approach-like behaviors across species. For example, place preference and self-stimulation paradigms often require association with rewarding cues, such as food to facilitate subsequent approach responses toward stimuli. Here we will examine work focused on how locomotion toward a rewarding stimulus is achieved. We will describe the functional connectivity between the limbic circuitry and descending locomotor centers, relevant for mediating forward locomotion in the context of appetitive behaviors (**Figure 3**).

FROM MOTIVATION TO APPROACH: EXECUTION OF FORWARD LOCOMOTION

The motivation to approach a stimulus in the environment stems from associations between the stimulus and its value as a physiological need or reward. Limbic structures such as the amygdala are key in mediating an approach locomotor response toward a rewarding stimulus such as food. As mentioned in section Decisions to Approach or Avoid are Guided by Internalized Contextual Information, the amygdala (BLA) directly projects to the LH which is a key hub for appetitive behaviors. The LH is an

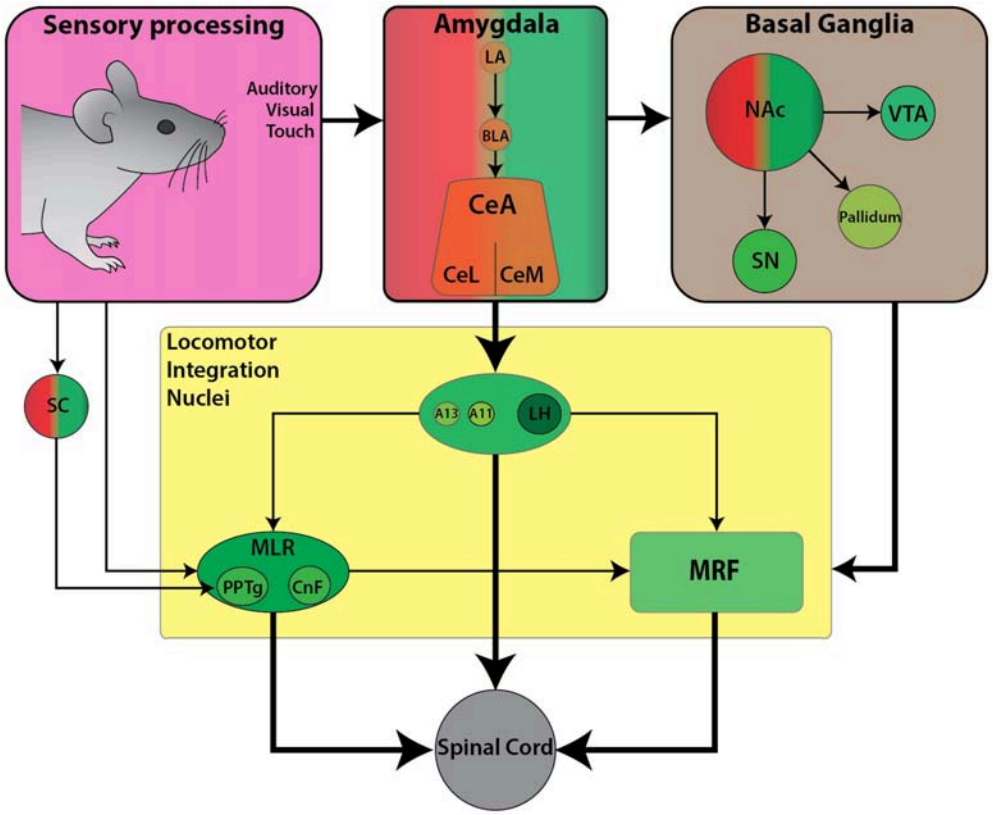


FIGURE 3 | Schematic diagram of the currently known descending connectivity of appetitive (approach) locomotor control. (Complementary to **Figure 2D**. Some connections omitted for lack of data or complexity of connectivity). Weighted arrows represent complex connectivity between regions described in further detail in text. Ascending connectivity has been omitted for clarity.

excellent candidate for investigating how reward-related information integrates with descending locomotor centers to facilitate forward locomotion toward reward-associated stimuli.

The LH is a large structure and has multiple functions. In the locomotor field, the initial descriptions of the LH were studied in the context of appetitive locomotor control (Sinnamon, 1993). However, most recent work has been directed toward the role of the LH in modulating homeostatic demands. Electrical stimulation of the LH elicits diverse responses beyond locomotion, such as feeding, drinking, gnawing and predatory attack that often vary from animal to animal but are linked to the current external stimuli (Coons et al., 1965; Roberts and Carey, 1965; Mogenson and Stevenson, 1967; review Stuber and Wise, 2016). Several LH cell populations have been shown to play a key role in feeding and appetite regulation including orexin, GABAergic, and glutamatergic cells. Projections onto the LH are predictably diverse and include olfactory and pyriform cortex, NAc, dorsal striatum, GP, ZI, perifornical region, most hypothalamic areas including magnocellular and medial preoptic, supraoptic, paraventricular and periventricular nuclei, posterior hypothalamus, arcuate and mammillary nuclei, bed nucleus of stria terminalis, ventral thalamic nuclei, VTA, SN, MRF, PAG, locus coeruleus, and parabrachial region (Barone et al., 1981).

The LH orexinergic transmission plays a key role in mediating locomotor responses via SN and brainstem locomotor regions (section The Diencephalon: A Hub for Goal-Directed Locomotion) and are active during feeding behavior (de Lecea et al., 1998; Sakurai et al., 1998), reward and arousal (Peyron et al., 1998; Baldo et al., 2003; Harris et al., 2005; Swanson et al., 2005; Aston-Jones et al., 2010). Indeed, the orexinergic neuronal population shows the highest level of spiking activity when animals are moving toward a food source. Orexinergic neurons are not the only LH neurons involved in locomotion; recently GABAergic LH cells have been reported to contribute to modulate locomotor activity. Chemogenetic silencing of LH GABAergic cells depresses voluntary locomotion, while stimulation leads to hyper-locomotion (Kosse et al., 2017). Anterograde tracing of these GABAergic cells uncovered substantial projections onto the ZI. The downstream projections are unknown. These ZI cells could also be modulated by orexin since photostimulation of orexinergic cells rapidly recruits GABAergic LH cells, and spiking of these GABAergic LH cells precedes spontaneous running bouts (Kosse et al., 2017).

LOCOMOTOR RESPONSE IN ANTICIPATION OF REWARD

While motivation contributes to an animal's approach behavior toward rewarding stimuli (Mogenson et al., 1980), anticipation of reward can also drive forward locomotion. Such anticipatory reward signals are integrated to locomotor centers via corticolimbic structures including the cortex, striatum and pallidum, which have descending projections to the locomotor regions (Swanson, 2000).

As well as participating in motor selection (section Motor Selection Derived from the Decision to Approach or Avoid), dopamine circuits including mesolimbic, mesocortical, and nigrostriatal pathways govern reward-related behaviors. Dopamine release within the NAc is an important determinant of reward processing. Furthermore, NAc is known to have reciprocal projections to dopaminergic neurons in VTA and the SN which projects to the dorsal striatum (Haber et al., 2000; Ikemoto, 2007). The dorsal striatum and its dopaminergic inputs serve key roles in the regulation of locomotor control (Faure et al., 2005; Belin and Everitt, 2008; Palmiter, 2008). Striatal pathway projections are differentially modulated by dopamine, and are either excitatory via the direct pathway (D1 receptor) or inhibitory via the indirect pathway (D2 receptor) (Surmeier et al., 2007). The locomotor modulation observed within BG circuitry could occur via glutamatergic and cholinergic MLR neurons that mediate initiation and acceleration of locomotion while GABAergic populations could facilitate deceleration, respectively (Roseberry et al., 2016). Dopaminergic fibers have been reported around cholinergic cells in MLR of lamprey (Ryczko et al., 2013), salamander (Ryczko et al., 2016), rat (Ryczko et al., 2016), monkeys (Rolland et al., 2009), and human (Ryczko et al., 2016) indicating that the innervation of the MLR is conserved in vertebrates (Ryczko and Dubuc, 2017). In lamprey and salamander, the origin of this dopaminergic innervation to cholinergic cells in MLR was found to be a diencephalic dopaminergic region termed as posterior tuberculum which sends ascending projections to the striatum and is considered homologous to mammalian SNc and/or VTA (Yamamoto and Vernier, 2011; Wullimann, 2014; Ryczko et al., 2016; Ryczko and Dubuc, 2017). While only a few dopamine neurons sent collaterals to the striatum and the MLR in lampreys and salamanders, numerous SNc dopamine neurons have both ascending and descending collaterals in rats (Ryczko et al., 2016). The number of ascending dopaminergic collaterals may be related to evolutionary expansion of the basal ganglia (Grillner and Robertson, 2016; Ryczko and Dubuc, 2017). These findings suggest that the role of dopaminergic activity in reward-related behavior is bidirectional and could occur in anticipation of obtaining a reward.

Following a similar theme, neurons within the PPTg are important for modulating speed and gait during locomotion (section The Mesencephalic Locomotor Region: An Integrative Hub for Locomotor Speed and Gait), but also respond in anticipation of reward signals. PPTg neurons respond phasically to auditory and visual sensory stimuli that predict reward with a shorter latency (5–10 ms) than dopaminergic VTA/SNc cells (Pan and Hyland, 2005). Furthermore, Norton et al. (2011) examined PPTg neural activity as rats solved a spatial working memory task that involved retrieving rewards of different magnitudes from known locations. Interestingly, they reported separate populations of PPTg neurons independently code for reward or movement. Thus, the reward anticipatory response within PPTg is part of a feedforward mechanism to trigger a fast locomotor response triggered by a reward-associated cue. In support of this idea, photoactivation of cholinergic PPTg terminals at SNc has been shown to increase locomotion (Xiao et al., 2016). Electrical stimulation of PPTg induces a burst firing of midbrain dopaminergic neurons (Lokwan et al., 1999; Floresco et al., 2003) with concomitant release of dopamine in striatum (Chapman et al., 1996; Miller and Blaha, 2004). This suggests that the PPTg may facilitate feedforward and feedback loops with SNc via reciprocal projections. Calcium transients within dopaminergic terminals in dorsal striatum precede (100–150 ms) bouts of locomotion independent of reward expectation (Howe and Dombeck, 2016). Photoactivation of these dopaminergic axons leads to initiation of locomotion bouts. Thus, rapid sub-second phasic signaling contributes to locomotion bout initiation associated with ongoing accelerations. Since glutamatergic MLR cells can facilitate acceleration (Roseberry et al., 2016), the role of these populations in potentiating locomotion in anticipation of reward is of interest.

PRIMARY DEFENSIVE LOCOMOTOR SYSTEM: AVOIDANCE RESPONSES TO AVERSIVE ASSOCIATED CUES

Locomotion is a critical element in the primary defensive system since it serves to increase the distance away from threatening or painful stimuli (Sinnamon, 1993). In general, aversive behaviors are characterized by three types of responses: (1) a reflexive startle response, (2) escape behavior to flee from an aversive stimulus, and (3) a freezing response. Of these three defensive responses, the circuitry for startle response has been best described. On the other hand, escape and freezing responses have often been used as behavioral outcomes in pain and fear related studies, but the associated locomotor components have received less attention (reviews Klemm, 2001; Roseberry and Kreitzer, 2017; **Figure 4**).

REFLEXIVE STARTLE RESPONSE DRIVEN BY SUDDEN EXTERNAL SENSORY STIMULI

The mammalian startle response is characterized by fast twitch of facial and body muscles as well as an arrest of ongoing movement in response to a sudden and intense sensory stimulus (Koch, 1999). It protects the animal from predation by preparing for a flight or fight response, or by freezing so the animal can't be easily seen (Landis and Hunt, 1939). A startle response can be elicited by different sensory modalities which act via separate pathways. These include: (1) trigeminal for sudden tactile stimuli, (2) auditory

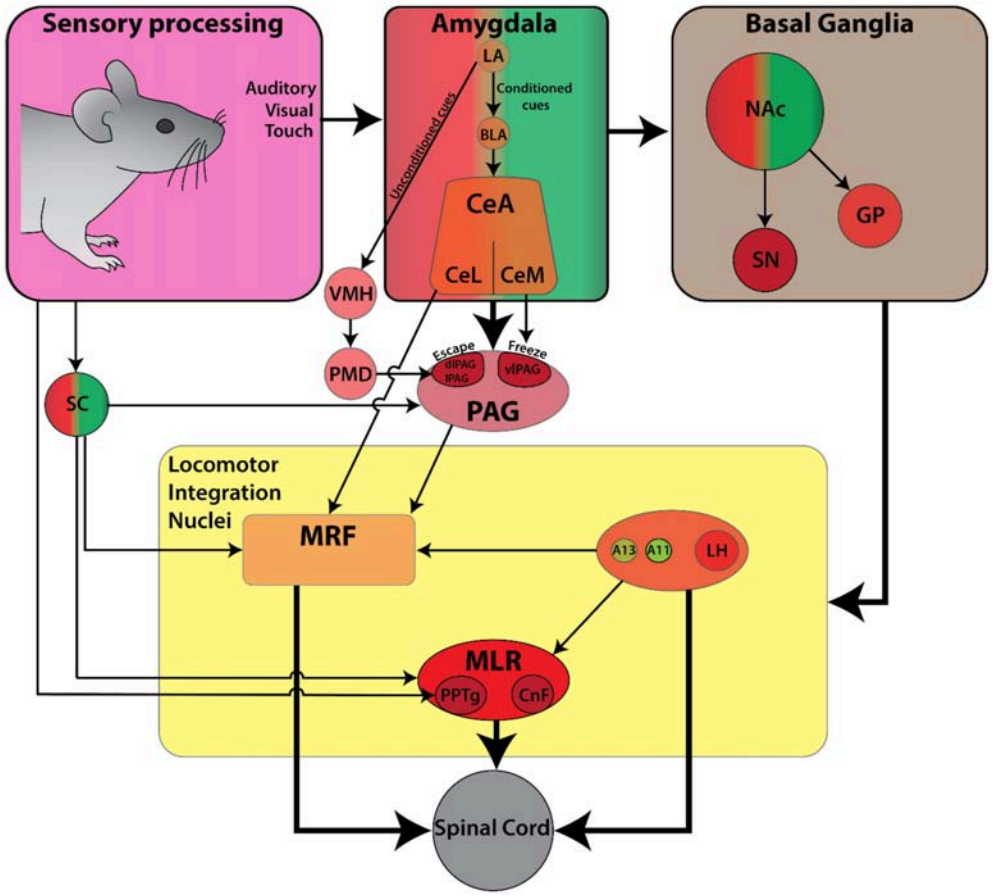


FIGURE 4 | Schematic diagram of the currently known descending connectivity of defensive (avoidance) locomotor control. (Complementary to **Figure 2C**. Some connections omitted for lack of data or complexity of connectivity). Ascending connectivity has been omitted for clarity.

for sudden acoustic stimuli, and (3) vestibular for sudden head movements. Though these startle pathways originate from different second-order afferents (nucleus V for tactile, cochlear root nucleus for auditory, and vestibular nucleus for balance), they converge onto giant neurons in the PnC projecting directly to motoneurons and interneurons of the spinal cord (reviews Koch, 1999; Yeomans et al., 2002). Less well understood is the light-induced startle response characterized by temporary locomotor arrest following brief flashes of light (Liang et al., 2015). This phenomenon can be partly driven by input to the SC from layer 5 of the primary visual cortex (V1 L5). Photoactivation of V1 L5 neurons projecting to SC directly triggers locomotor arrest in running mice (Liang et al., 2015). Inactivating the SC with muscimol reduces the arrest behavior by 76%, whereas silencing V1 by optical activation of parvalbumin-positive inhibitory neurons reduces arrest by 33% (Liang et al., 2015). Overall, these startle pathways are fine-tuned to detect specific triggers from the environment during the default exploration state of the animal, allowing an animal to quickly transition into a defensive state (Yeomans and Frankland, 1995).

DEFENSIVE LOCOMOTOR RESPONSES (ESCAPE AND FREEZE) ASSOCIATED WITH AVERSIVE CUES

In comparison to the startle response, which is reflexive in nature, the choice between escaping a stimulus and freezing is highly dependent on contextual cues. Behavioral outcomes that measure fear and pain such as conditioned place preference/aversion and dynamic weight bearing analysis rely on quantification of locomotor behavior. The descending control of locomotor circuits in response to aversive stimuli has not been fully explored. Nonetheless, aversive responses rely heavily on locomotor circuit interactions between the amygdala and PAG (LeDoux, 2012; Koutsikou et al., 2015, 2017).

Aversive stimuli can be thought of as either unconditioned and innate, or learned and associated with pain and fear. The association between the unconditioned stimulus and the conditioned stimulus required may involve memory processing related to fear. This is mediated in part by both the CeA and BLA of the amygdala (LeDoux, 2000; Medina et al., 2002; Wilensky et al., 2006; Ciocchi et al., 2010; Duvarci et al., 2011;

Li et al., 2013; Han et al., 2015; Sato et al., 2015). The CeA is an important neural substrate for the expression of the freeze response (Davis and Whalen, 2001; Phelps and LeDoux, 2005). It projects to the hypothalamus, dorsal and ventral striatum, PAG, and MRF, and could also modulate cognition in a broader sense, via its outputs to ascending monoaminergic and cholinergic systems such as: noradrenergic LC, dopaminergic SNc and VTA, serotonergic raphe, and the cholinergic nucleus basalis (Davis and Whalen, 2001; Sara, 2009). Recent cell-type-specific viral tracing studies have also revealed a strong projection from the CeA to glutamatergic MLR neurons, which can initiate locomotion from rest when activated (Roseberry et al., 2016). Similarly, chemical or electrical stimulation of CeA can elicit freezing or fleeing behavior (Brandão et al., 1999, 2015; Vianna et al., 2001; Muthuraju et al., 2016). Thus, the CeA is important for orchestrating defensive freeze and escape responses (Sah et al., 2003; Oka et al., 2008).

The PAG also plays a central role in regulating defensive locomotor behaviors. Bandler was the first to show the PAG's direct role in defensive reactions in cats by pharmacological activation with microinjections of glutamate (Bandler, 1982) and excitatory amino acids (Bandler and Carrive, 1988). Subsequent studies identified five subregions that can be differentiated based on anatomy, physiology, and behavioral outcomes when activated (Carrive, 1993). The dorsolateral/lateral (dl/l) and ventrolateral (vl) columns of the PAG appear to be the most relevant in the context of defensive locomotor behaviors. Activation of the lPAG can elicit a variety of responses such as: strong hindlimb movements for flight reaction, reactive immobility accompanied by heightened responsiveness to surrounding stimuli, backward locomotion, and forward escape locomotion with occasional jumps (Bandler and Depaulis, 1988; Depaulis et al., 1989, 1992; Carrive, 1993). Meanwhile, activation of the vlPAG can induce hyporeactive immobility characterized by reduced spontaneous activity and/or responsiveness to surrounding stimuli (Bandler and Depaulis, 1988; Depaulis et al., 1992; Carrive, 1993). In line with this, electrolytic lesions of vlPAG in rats decrease freezing induced by unconditioned and conditioned stimuli, whereas lesions of dlPAG enhanced freezing (Fanselow et al., 1995; De Oca et al., 1998). Photoactivation of glutamatergic cells of the dorsal PAG (dPAG) can evoke both freeze and escape behavior in a gradual manner via firing rate and temporal coding mechanism (Chen et al., 2015). Increasing either frequency or intensity of photoactivation progressed defensive phenotype from freeze to escape and then to jump. Given the lack of a clear boundary between observed phenotypes, it is possible that these cells may perform this function through differing neurotransmitter release and/or its afferent and efferent connections.

Sensory cues that trigger aversive behaviors are either unconditioned or conditioned, and are processed through different pathways. Unconditioned odor cues are conveyed via the medial amygdala, whereas auditory and visual cues are conveyed via the accessory basal amygdala. These signals are further processed through the circuitry of the ventromedial hypothalamus (VMH)-premammillary nucleus of the hypothalamus (PMH) and the dPAG. On the other hand, conditioned cues are processed via the LA and intra-amygdala connections onto CeA, and then project onto vlPAG from medial CeA (CeM) (Motta et al., 2009). The CeA also projects directly onto PnC (Davis and Whalen, 2001) where Chx10 stop neurons could be found (Bouvier et al., 2015) and glutamatergic MLR neurons which are associated with acceleration of ongoing movement (Roseberry et al., 2016). Therefore, defensive responses may be mediated through these projections as well. Furthermore, glutamatergic cells within PAG innervate the GiA, GiV, and LPGi (Tovote et al., 2016). Most work has focused primarily on fear induced freezing; however, the neural circuitry of PAG-mediated defensive locomotor control remains undefined. Considering this, Tovote et al. (2016) selectively manipulated inhibitory projections from the CeA to local inhibitory interneurons within the vlPAG. Glutamatergic neurons of the vlPAG are under local inhibition, and upon disinhibition by the CeA, they induce freezing via GiA, GiV, and LPGi targets. In contrast to activation of glutamatergic vlPAG neurons, photostimulation of glutamatergic dl/lPAG neurons evoke bouts of escape locomotor behavior intermingled with short freezing periods (Tovote et al., 2016). It seems that the PAG could play an important role in translating locomotor behaviors related to freezing or escape and may interact with locomotor command centers. A few studies suggest that an interaction between PAG and locomotor command centers (e.g., CnF) may be relevant for locomotor behaviors in freezing and/or escape (Ferreira-Netto et al., 2007). Connectivity between PAG and Chx10 neurons within caudal PnC and rostral Gi which can evoke stop has not yet been explored. With these multiple possible points of integration between the pain, limbic, and motor systems that have been found through tracing techniques, we can begin to create testable models of functional circuitry within specific contexts that modulate locomotion.

INTERACTIONS BETWEEN APPETITIVE, DEFENSIVE, AND EXPLORATORY BEHAVIOR

Appetitive, defensive and exploratory locomotor behavior are all necessary for survival. This is reflected at the neural systems level, where processes for these behaviors are closely intertwined along with circuits involved in maintenance of food and resources, defense, fluid balance, thermoregulation, and reproduction (Saper, 2006). Eating must often co-exist with the threat of predation for many species. The risks need to be weighed with the rewards and clearly, they are weighed differently in satiated compared to hungry animals. In the above sections, we have provided examples of nuclei that contribute to this complex predation calculus such as SC, NAc, and amygdala.

Since the locomotor responses are driven by the animal's interaction with the environment, there are multiple overlapping cognitive or associative and emotional processing structures modulating locomotor responses. Nevertheless, differential signaling processes for various contexts can facilitate approach while suppressing avoidance responses and vice versa. For

example, GABA cells in the LH are excited by orexin and activity of these cells drives locomotion (section The Diencephalon: A Hub for Goal-Directed Locomotion). These inhibitory cells project to the SC and the PAG; both of which drive aversive locomotor behaviors. These inhibitory circuits are strong candidates for the suppression of aversive locomotor behaviors in situations where motivation to seek food is high.

In summary, innervation onto NAc could disinhibit the MLR via VP and the SNr to initiate, modulate or terminate locomotion. In addition, BLA and CeA send efferents to dMSNs preferentially (Roseberry et al., 2016) and the LH area (Petrovich et al., 1996; Petrovich, 2011), which could facilitate approach locomotion for cues associated with food and reward, or mediate suppression of appetitive behavior during defensive response and unrewarded movement, respectively. For example, in a behavioral conflict between aversion and reward, cholinergic and glutamatergic PPTg projections onto the dopaminergic VTA neurons may mediate a bias toward reward-oriented locomotion. Furthermore, PPTg projections to dopaminergic SNc neurons may facilitate suppression of unrewarded movements via the indirect pathway, or reinforce reward oriented motor action via direct pathway (Frank, 2006; Kravitz et al., 2010; Hong and Hikosaka, 2011). In addition, A11 and A13 (DLR) could provide a parallel dopaminergic modulation to mediate a balance between approach and avoidance behaviors.

FUTURE DIRECTIONS

This review has examined how locomotion is integrated into contextual demands. Recent advances in functional connectomics will enable us to decipher the circuits that underlie different approach and avoid motor behaviors. Specifically, optogenetics and chemogenetics coupled with viral-vector based approaches provide the tool kits necessary to advance our understanding. These methods can overcome limitations of electrical stimulation, and lesion approaches. That said direct comparisons with electrical stimulation remain useful since translational approaches using deep brain stimulation rely on this technology. In some cases, electrical stimulation may be advantageous since it's lack of selectivity may be required to adequately activate a network. Electrical stimulation will recruit more neurons due to failures in transfection. While optogenetics and chemogenetics are an excellent choice for understanding the connectome we need to carefully evaluate if these are the tool of choice for clinical use.

It is sobering to consider that establishing the connectome from an anatomical point of view is only half the story; the dynamic recruitment of multiple parallel pathways also needs to be considered. No matter which nuclei one focuses on there are multiple projections to other members within the overall circuit. We need to consider sampling key areas of the circuit simultaneously when designing studies so that we can begin to understand the dynamic recruitment of several centers during approach and avoidance tasks. These centers will include the PPTg, CnF, and MRF since they form key integrative centers in the brain. Depending on the type of study recordings need to be captured from the striatum, hypothalamic nuclei, and the LC.

CHALLENGES FACED IN DRIVING CONTEXTUAL BEHAVIORAL RESPONSE

Meanwhile, as more sophisticated technologies and experimental tools became readily available, thus enabling the study of underlying mechanisms and circuitries associated with motor functions with much higher precision, there are several caveats. It is important to consider that the study of motor behaviors using experimental animal models generally require extensive training or conditioning, which rely on memory and learning processes. The impact of this training on the motor behavior being tested needs to be understood.

Learning and memory formation were initially thought to be driven by dynamic changes in synaptic strengths, which can be experimentally induced by high frequency stimulation (Bliss and Lomo, 1973). A few key regions of the brain were implicated, including the hippocampus, the neocortex, cerebellar, and brainstem nuclei (Medina et al., 2002). This is known as the synaptic plasticity and memory hypothesis, within this there are assumptions that synaptic inputs converge, or there are specific "relay centres" for information processing. This hypothesis has been reappraised because the mechanisms underlying the initial encoding and subsequent learning are likely to be different (Medina et al., 2002). This can be demonstrated by the observations that: (1) habituation occurs over relatively short periods of time for certain behaviors (e.g., forced swim, open field induced anxiety); and (2) neuronal plasticity often persists even when the conditioned behavior has fully extinguished (Hansel et al., 2001). The key point here is that whilst neuronal plasticity in specific regions contributes to the initiation of behavior, the maintenance may involve activity of other neuronal populations or pathways.

Similarly, the extinction of behaviors (e.g., fear extinction), indicate that learning is a state-dependent process. It was established that the amygdala, a brain region important for the regulation of emotion, receives input from the hippocampus and provides "context" (i.e., based on the animal's affective states) during conditioning (Phelps and LeDoux, 2005). In line with this review, modulation of locomotor behaviors is also context-dependent and are driven by the animal's need and/or adaptation to the ever-changing environments. At present, many studies investigating changes in cellular mechanisms or functional circuitry associated with motor behaviors are relatively short-term compared to behavior studies from other fields, such as sensory and cognitive neuroscience. Future studies must consider appropriate experiment paradigms to account for the changes in behaviors over time, and that there may be multiple changes at both cellular and systems levels in context-driven motor learning.

CONCLUSION

To navigate through the environment, animals need to make on-the-fly adjustments to gait. Consider a baseball player running

to catch a ball. The person will need to be motivated to run quickly to catch the ball, and this motivation may be higher at the World Series compared to a regular training day. Catching the ball requires visual input which is integrated through the dorsal stream to the motor cortex, which is then relayed back to diencephalic circuits including the BG and hypothalamic circuits. Modifications to gait need to be accomplished to execute accelerations, jumps, and slides. This is presumably integrated at the level of the MRF and MLR and integrated into ongoing activity within rhythm centers of the spinal cord. We are at a critical juncture in our understanding of how emotional and contextual cues affect locomotor performance. Many tools exist to tease apart circuit function in awake behaving animals and show how they affect downstream brainstem and spinal cord function. This of course dramatically increases the complexity of experiments directed at understanding motor control, but it will serve to highlight the interplay between regions of the brain involved in movement decisions that evolved to maximize survival of the organism.

AUTHOR CONTRIBUTIONS

All authors (LK, SS, SAS, KM, CC, and PW) contributed to the conception, drafting, and critical revision of the review.

FUNDING

We would like to acknowledge funding awarded to PW from the Canadian Institute for Health Research (CIHR MOP-130528; PJT-148682), Natural Sciences and Engineering Research Council of Canada (NSERC RGPIN/356153-2013), Wings for Life (WFL-CA011/15), the Hotchkiss Brain Institute (HBI) and Faculty for Veterinary Medicine. LK was supported by the Alberta Parkinson's Society and the Cumming School of Medicine, KM was supported by the Branch Out Foundation and HBI and SAS supported by Alberta Innovates and HBI.

ACKNOWLEDGMENTS

We would like to acknowledge support from members of the Whelan Lab.

REFERENCES

Alam, M., Schwabe, K., and Krauss, J. K. (2011). The pedunculopontine nucleus area: critical evaluation of interspecies differences relevant for its use as a target for deep brain stimulation. *Brain* 134, 11–23. doi: 10.1093/brain/awq322

Alam, M., Schwabe, K., and Krauss, J. (2013). Reply: the cuneiform nucleus may be involved in the regulation of skeletal muscle tone by motor pathway: a virally mediated trans-synaptic tracing study in surgically sympathectomized mice. *Brain* 136, e252. doi: 10.1093/brain/awt125

Aragona, B. J., Cleaveland, N. A., Stuber, G. D., Day, J. J., Carelli, R. M., Wightman, R. M. (2008). Preferential enhancement of dopamine transmission within the nucleus accumbens shell by cocaine is attributable to a direct increase in phasic dopamine release events. *J. Neurosci.* 28, 8821–8831. doi: 10.1523/JNEUROSCI.2225-08.2008

Armstrong, D. M. (1986). Supraspinal contributions to the initiation and control of locomotion in the cat. *Prog. Neurobiol.* 26, 273–361. doi: 10.1016/0301-0082(86)90021-3

Aston-Jones, G., Smith, R., Sartor, G., Moorman, D., Massi, L., Tahsili-Fahadan, P., et al. (2010). Lateral hypothalamic orexin/hypocretin neurons: a role in reward-seeking and addiction. *Brain Res.* 1314, 74–90. doi: 10.1016/j.brainres.2009.09.106

Averbeck, B. B., and Costa, V. D. (2017). Motivational neural circuits underlying reinforcement learning. *Nat. Neurosci.* 20, 505–512. doi: 10.1038/nn.4506

Baldo, B. A., Daniel, R. A., Berridge, C. W., and Kelley, A. E. (2003). Overlapping distributions of orexin/hypocretin- and dopamine-β-hydroxylase immunoreactive fibers in rat brain regions mediating arousal, motivation, and stress. *J. Comp. Neurol.* 464, 220–237. doi: 10.1002/cne.10783

Bandler, R. (1982). Induction of "page" following microinjections of glutamate into midbrain but not hypothalamus of cats. *Neurosci. Lett.* 30, 183–188. doi: 10.1016/0304-3940(82)90294-4

Bandler, R., and Carrive, P. (1988). Integrated defence reaction elicited by excitatory amino acid microinjection in the midbrain periaqueductal grey region of the unrestrained cat. *Brain Res.* 439, 95–106. doi: 10.1016/0006-8993(88)91465-5

Bandler, R., and Depaulis, A. (1988). Elicitation of intraspecific defence reactions in the rat from midbrain periaqueductal grey by microinjection of kainic acid, without neurotoxic effects. *Neurosci. Lett.* 88, 291–296. doi: 10.1016/0304-3940(88)90226-1

Barone, F. C., Wayner, M. J., Scharoun, S. L., Guevara-Aguilar, R., and Aguilar-Baturoni, H. U. (1981). Afferent connections to the lateral hypothalamus: a horseradish peroxidase study in the rat. *Brain Res. Bull.* 7, 75–88. doi: 10.1016/0361-9230(81)90101-5

Barrière, G., Mellen, N., and Cazalets, J. (2004). Neuromodulation of the locomotor network by dopamine in the isolated spinal cord of newborn rat. *Eur. J. Neurosci.* 19, 1325–1335. doi: 10.1111/j.1460-9568.2004.03210.x

Beckstead, R. M., Domesick, V. B., and Nauta, W. J. (1979). Efferent connections of the substantia nigra and ventral tegmental area in the rat. *Brain Res.* 175, 191–217. doi: 10.1016/0006-8993(79)91001-1

Beitz, A. J. (1982a). The sites of origin brain stem neurotensin and serotonin projections to the rodent nucleus raphe magnus. *J. Neurosc.* 2, 829–842.

Beitz, A. J. (1982b). The nuclei of origin of brain stem enkephalin and substance pprojections to the rodent nucleus raphe magnus. *Neuroscience* 7, 2753–2768. doi: 10.1016/0306-4522(82)90098-7

Belin, D., and Everitt, B. (2008). Cocaine seeking habits depend upon dopamine-dependent serial connectivity linking the ventral with the dorsal Striatum. *Neuron* 57, 432–441. doi: 10.1016/j.neuron.2007.12.019

Bliss, T. V., and Lomo, T. (1973). Long-lasting potentiation of synaptic transmission in the dentate area of the anaesthetized rabbit following stimulation of the perforant path. *J. Physiol.* 232, 331–356. doi: 10.1113/jphysiol.1973.sp010273

Boothby, K. M., and Roberts, A. (1992). The stopping response of *Xenopus laevis* embryos: behaviour, development and physiology. *J. Comp. Physiol. A* 170, 171–180. doi: 10.1007/BF00196899

Born, G., and Schmidt, M. (2008). A reciprocal connection between the ventral lateral geniculate nucleus and the pretectal nuclear complex and the superior colliculus: an *in vitro* characterization in the rat. *Vis. Neurosci.* 25, 39–51. doi: 10.1017/S0952523808080048

Bouvier, J., Caggiano, V., Leiras, R., Caldeira, V., Bellardita, C., Balueva, K., et al. (2015). Descending command neurons in the brainstem that halt locomotion. *Cell* 163, 1191–1203. doi: 10.1016/j.cell.2015.10.074

Brandão, M. L., Anseloni, V. Z., Pandóssio, J. E., Araújo, J. E., and Castilho, V. M. (1999). Neurochemical mechanisms of the defensive behavior in the dorsal midbrain. *Neurosci. Biobehav. Rev.* 23, 863–875. doi: 10.1016/S0149-7634(99)00038-X

Brandão, M., de Oliveira, A., Muthuraju, S., Colombo, A., Saito, V., and Talbot, T. (2015). Dual role of dopamine D_2-like receptors in the mediation of conditioned and unconditioned fear. *FEBS Lett.* 589, 3433–3437. doi: 10.1016/j.febslet.2015.02.036

Bretzner, F., and Brownstone, R. (2013). Lhx3-Chx10 reticulospinal neurons in locomotor circuits. *J. Neurosci.* 33, 14681–14692. doi: 10.1523/JNEUROSCI.5231-12.2013

Brustein, E., and Rossignol, S. (1998). Recovery of locomotion after ventral and ventrolateral spinal lesions in the cat. I. Deficits and adaptive mechanisms. *J. Neurophysiol.* 80, 1245–1267.

Carlezon, W. A., and Thomas, M. J. (2009). Biological substrates of reward and aversion: a nucleus accumbens activity hypothesis. *Neuropharmacology* 56, 122–132. doi: 10.1016/j.neuropharm.2008.06.075

Carrive, P. (1993). The periaqueductal gray and defensive behavior: functional representation and neuronal organization. *Behav. Brain Res.* 58, 27–47. doi: 10.1016/0166-4328(93)90088-8

Castiglioni, A. J., Gallaway, M. C., and Coulter, J. D. (1978). Spinal projections from the midbrain in monkey. *J. Comp. Neurol.* 178, 329–345. doi: 10.1002/cne.901780208

Chapman, C., Yeomans, J., Blaha, C., and Blackburn, J. (1996). Increased striatal dopamine efflux follows scopolamine administered systemically or to the tegmental pedunculopontine nucleus. *Neuroscience* 76, 177–186. doi: 10.1016/S0306-4522(96)00358-2

Charbit, A. R., Akerman, S., Holland, P. R., and Goadsby, P. J. (2009). Neurons of the dopaminergic/calcitonin gene-related peptide A11 cell group modulate neuronal firing in the trigeminocervical complex: an electrophysiological and immunohistochemical study. *J. Neurosci.* 29, 12532–12541. doi: 10.1523/JNEUROSCI.2887-09.2009

Chen, S., Zhou, H., Guo, S., Zhang, J., Qu, Y., Feng, Z., et al. (2015). Optogenetics based rat–robot control: optical stimulation encodes "stop" and "escape" commands. *Ann. Biomed. Eng.* 43, 1851–1864. doi: 10.1007/s10439-014-1235-x

Ciocchi, S., Herry, C., Grenier, F., Wolff, S. B., Letzkus, J., Vlachos, I., Ehrlich, I., et al. (2010). Encoding of conditioned fear in central amygdala inhibitory circuits. *Nature* 468, 277–282. doi: 10.1038/nature09559

Clemens, S., Rye, D., and Hochman, S. (2006). Restless legs syndrome: revisiting the dopamine hypothesis from the spinal cord perspective. *Neurology* 67, 125–130. doi: 10.1212/01.wnl.0000223316.53428.c9

Clements, J. R., and Grant, S. (1990). Glutamate-like immunoreactivity in neurons of the laterodorsal tegmental and pedunculopontine nuclei in the rat. *Neurosci. Lett.* 120, 70–73. doi: 10.1016/0304-3940(90)90170-E

Commissiong, J. W., and Sedgwick, E. M. (1975). Letter: dopamine and noradrenaline in human spinal cord. *Lancet* 1, 347. doi: 10.1016/S0140-6736(75)91269-6

Comoli, E., Favaro, P., Vautrelle, N., Leriche, M., Overton, P. G., and Redgrave, P. (2012). Segregated anatomical input to sub-regions of the rodent superior colliculus associated with approach and defense. *Front. Neuroanat.* 6:9. doi: 10.3389/fnana.2012.00009

Coons, E. E., Levak, M., and Miller, N. E. (1965). Lateral hypothalamus: learning of food-seeking response motivated by electrical stimulation. *Science* 150, 1320–1321. doi: 10.1126/science.150.3701.1320

Coulter, J. D., Bowker, R. M., Wise, S. P., Murray, E. A., Castiglioni, A. J., and Westlund, K. N. (1979). Cortical, tectal and medullary descending pathways to the cervical spinal cord. *Prog. Brain Res.* 50, 263–274. doi: 10.1016/S0079-6123(08)60827-4

Davis, M., and Whalen, P. (2001). The amygdala: vigilance and emotion. *Mol. Psychiatry* 6, 13–34. doi: 10.1038/sj.mp.4000812

de Lecea, L., Kilduff, T. S., Peyron, C., Gao, X.-B., Foye, P. E., Danielson, P. E., et al. (1998). The hypocretins: hypothalamus-specific peptides with neuroexcitatory activity. *Proc. Natl. Acad. Sci. U.S.A.* 95, 322–327. doi: 10.1073/pnas.95.1.322

De Oca, B. M., DeCola, J. P., Maren, S., and Fanselow, M. S. (1998). Distinct regions of the periaqueductal gray are involved in the acquisition and expression of defensive responses. *J. Neurosci.* 18, 3426–3432.

Dean, P., Redgrave, P., and Westby, G. W. M. (1989). Event or emergency? Two response systems in the mammalian superior colliculus. *Trends Neurosci.* 12, 137–147. doi: 10.1016/0166-2236(89)90052-0

Denny-Brown, D. (1962). *The Basal Ganglia and Their Relation to Disorder of Movement*. New York, NY: Oxford University Press Inc.

Depaulis, A., Bandler, R., and Vergnes, M. (1989). Characterization of pretentorial periaqueductal gray matter neurons mediating intraspecific defensive behaviors in the rat by microinjections of kainic acid. *Brain Res.* 486, 121–132. doi: 10.1016/0006-8993(89)91284-5

Depaulis, A., Keay, K. A., and Bandler, R. (1992). Longitudinal neuronal organization of defensive reactions in the midbrain periaqueductal gray region of the rat. *Exp. Brain Res.* 90, 307–318. doi: 10.1007/BF00227243

Di Scala, G., Schmitt, P., and Karli, P. (1984). Flight induced by infusion of bicuculline methiodide into periventricular structures. *Brain Res.* 309, 205–209. doi: 10.1016/0006-8993(84)90585-7

Drew, T., Dubuc, R., and Rossignol, S. (1986). Discharge patterns of reticulospinal and other reticular neurons in chronic, unrestrained cats walking on a treadmill. *J. Neurophysiol.* 55, 375–401.

Drew, T., Prentice, S., and Schepens, B. (2004). Cortical and brainstem control of locomotion. *Prog. Brain Res.* 143, 251–261. doi: 10.1016/S0079-6123(03)43025-2

Duvarci, S., Popa, D., and Paré, D. (2011). Central amygdala activity during fear conditioning. *J. Neurosci.* 31, 289–294. doi: 10.1523/JNEUROSCI.4985-10.2011

Duxon, M., Stretton, J., Starr, K., Jones, D., Holland, V., Riley, G., et al. (2001). Evidence that orexin-A-evoked grooming in the rat is mediated by orexin-1 (OX_1) receptors, with downstream 5-HT_{2C} receptor involvement. *Psychopharmacology* 153, 203–209. doi: 10.1007/s002130000550

Ectors, L., Brookens, N. L., and Gerard, R. W. (1938). Autonomic and motor localization in the hypothalamus. *Arch. Neurol. Psychiatry* 39, 789–798. doi: 10.1001/archneurpsyc.1938.02270040145009

Edley, S. M., and Graybiel, A. M. (1983). The afferent and efferent connections of the feline nucleus tegmenti pedunculopontinus, pars compacta. *J. Comp. Neurol.* 217, 187–215. doi: 10.1002/cne.902170207

Edwards, D. H., Heitler, W. J., and Krasne, F. B. (1999). Fifty years of a command neuron: the neurobiology of escape behavior in the crayfish. *Trends Neurosci.* 22, 153–161. doi: 10.1016/S0166-2236(98)01340-X

Esch, T., and Kristan, W. (2002). Decision-making in the leech nervous system. *Integr. Comp. Biol.* 42, 716–724. doi: 10.1093/icb/42.4.716

Esposito, M. S., Capelli, P., and Arber, S. (2014). Brainstem nucleus MdV mediates skilled forelimb motor tasks. *Nature* 508, 351–356. doi: 10.1038/nature13023

Everitt, B. J., and Robbins, T. W. (2013). From the ventral to the dorsal striatum: devolving views of their roles in drug addiction. *Neurosci. Biobehav. Rev.* 37, 1946–1954. doi: 10.1016/j.neubiorev.2013.02.010

Fanselow, M., Decola, J., Oca, B., and Landeira-Fernandez, J. (1995). Ventral and dorsolateral regions of the midbrain periaqueductal gray (PAG) control different stages of defensive behavior: dorsolateral PAG lesions enhance the defensive freezing produced by massed and immediate shock. *Aggress. Behav.* 21, 63–77. doi: 10.1002/1098-2337(1995)21:1<63::AID-AB2480210109>3.0.CO;2-F

Faure, A., Haberland, U., Condé, F., and Massioui, N. (2005). Lesion to the nigrostriatal dopamine system disrupts stimulus-response habit formation. *J. Neurosci.* 25, 2771–2780. doi: 10.1523/JNEUROSCI.3894-04.2005

Favaro, P. D. N., Gouvêa, T. S., de Oliveira, S. R., Vautrelle, N., Redgrave, P., and Comoli, E. (2011). The influence of vibrissal somatosensory processing in rat superior colliculus on prey capture. *Neuroscience* 176, 318–327. doi: 10.1016/j.neuroscience.2010.12.009

Ferraye, M. U., Debû, B., Fraix, V., Goetz, L., Ardouin, C., Yelnik, J., et al. (2010). Effects of pedunculopontine nucleus area stimulation on gait disorders in Parkinson's disease. *Brain* 133, 205–214. doi: 10.1093/brain/awp229

Ferreira-Netto, C., Borelli, K. G., and Brandão, M. L. (2007). Distinct Fos expression in the brain following freezing behavior elicited by stimulation with NMDA of the ventral or dorsal inferior colliculus. *Exp. Neurol.* 204, 693–704. doi: 10.1016/j.expneurol.2006.12.023

Fetcho, J. R., Higashijima, S., and McLean, D. L. (2008). Zebrafish and motor control over the last decade. *Brain Res. Rev.* 57, 86–93. doi: 10.1016/j.brainresrev.2007.06.018

Floresco, S. B., West, A. R., Ash, B., Moore, H., and Grace, A. A. (2003). Afferent modulation of dopamine neuron firing differentially regulates tonic and phasic dopamine transmission. *Nat. Neurosci.* 6, 968–973. doi: 10.1038/nn1103

Ford, B., Holmes, C. J., Mainville, L., and Jones, B. E. (1995). GABAergic neurons in the rat pontomesencephalic tegmentum: codistribution with cholinergic and other tegmental neurons projecting to the posterior lateral hypothalamus. *J. Comp. Neurol.* 363, 177–196. doi: 10.1002/cne.903630203

Fortin, M., and Parent, A. (1999). Calretinin-immunoreactive neurons in primate pedunculopontine and laterodorsal tegmental nuclei. *Neuroscience* 88, 535–547. doi: 10.1016/S0306-4522(98)00214-0

Frank, M., J. (2006). Dynamic dopamine modulation in the basal ganglia: a neurocomputational account of cognitive deficits in medicated and nonmedicated Parkinsonism. *J. Cogn. Neurosci.* 17, 51–72. doi: 10.1162/0898929052880093

Gandhi, N. J., and Katnani, H. A. (2011). Motor functions of the superior colliculus. *Annu. Rev. Neurosci.* 34, 205–231. doi: 10.1146/annurev-neuro-061010-113728

Garcia-Rill, E., and Skinner, R. D. (1987a). The mesencephalic locomotor region. I. Activation of a medullary projection site. *Brain Res.* 411, 1–12. doi: 10.1016/0006-8993(87)90675-5

Garcia-Rill, E., and Skinner, R. D. (1987b). The mesencephalic locomotor region. II. Projections to reticulospinal neurons. *Brain Res.* 411, 13–20. doi: 10.1016/0006-8993(87)90676-7

Gillette, R., Kovac, M. P., and Davis, W. J. (1978). Command neurons in Pleurobranchaea receive synaptic feedback from the motor network they excite. *Science* 199, 798–801. doi: 10.1126/science.622571

Glickman, S. E., and Schiff, B. B. (1967). A biological theory of reinforcement. *Psychol. Rev.* 74, 81–109. doi: 10.1037/h0024290

Grillner, S., and Robertson, B. (2016). The basal ganglia over 500 million years. *Curr. Biol.* 26, R1088–R1100. doi: 10.1016/j.cub.2016.06.041

Grillner, S., Hongo, T., and Lund, S. (1968). The origin of descending fibres monosynaptically activating spinoreticular neurones. *Brain Res.* 10, 259–262. doi: 10.1016/0006-8993(68)90130-3

Grillner, S., Wallén, P., Saitoh, K., Kozlov, A., and Robertson, B. (2008). Neural bases of goal-directed locomotion in vertebrates—An overview. *Brain Res. Rev.* 57, 2–12. doi: 10.1016/j.brainresrev.2007.06.027

Gross, C. T., and Canteras, N. S. (2012). The many paths to fear. *Nat. Rev. Neurosci.* 13, 651–658. doi: 10.1038/nrn3301

Grossen, N. E., and Kelley, M. J. (1972). Species-specific behavior and acquisition of avoidance behavior in rats. *J. Comp. Physiol. Psychol.* 81, 307. doi: 10.1037/h0033536

Grossman, R. (1958). Effects of stimulation of non-specific thalamic system on locomotor movements in cat. *J. Neurophysiol.* 21, 85–93.

Haber, S. N., Fudge, J. L., and McFarland, N. R. (2000). Striatonigrostriatal pathways in primates form an ascending spiral from the shell to the dorsolateral striatum. *J. Neurosci.* 20, 2369–2382. Available online at: http://www.jneurosci.org/content/20/6/2369

Hagan, J. J., Leslie, R. A., and Patel, S. (1999). Orexin A activates locus coeruleus cell firing and increases arousal in the rat. *Proc. Natl. Acad. Sci. U.S.A.* 96, 10911–10916. doi: 10.1073/pnas.96.19.10911

Hägglund, M., Borgius, L., Dougherty, K. J., and Kiehn, O. (2010). Activation of groups of excitatory neurons in the mammalian spinal cord or hindbrain evokes locomotion. *Nat. Neurosci.* 13, 246–252. doi: 10.1038/nn.2482

Hamel, L., Thangarasa, T., Samadi, O., and Ito, R. (2017). Caudal nucleus accumbens core is critical in the regulation of cue-elicited approach-avoidance decisions. *eNeuro* 4:ENEURO.0330-16.2017. doi: 10.1523/ENEURO.0330-16.2017

Han, S., Soleiman, M. T., Soden, M. E., Zweifel, L. S., and Palmiter, R. D. (2015). Elucidating an affective pain circuit that creates a threat memory. *Cell* 162, 363–374. doi: 10.1016/j.cell.2015.05.057

Hansel, C. E., Linden, D. J., and D'Angelo, E. (2001). Beyond parallel fiber LTD: the diversity of synaptic and non-synaptic plasticity in the cerebellum. *Nat. Neurosci.* 4, 467–475. doi: 10.1038/87419

Harris, G., Wimmer, M., and Aston-Jones, G. (2005). A role for lateral hypothalamic orexin neurons in reward seeking. *Nature* 437, 556–559. doi: 10.1038/nature04071

Heise, C., and Mitrofanis, J. (2006). Fos immunoreactivity in some locomotor neural centres of 6OHDA-lesioned rats. *Anat. Embryol.* 211, 659–671. doi: 10.1007/s00429-006-0130-0

Hirsch, E. C., Graybiel, A. M., Duyckaerts, C., and Javoy-Agid, F. (1987). Neuronal loss in the pedunculopontine tegmental nucleus in Parkinson disease and in progressive supranuclear palsy. *Proc. Natl. Acad. Sci. U.S.A.* 84, 5976–5980. doi: 10.1073/pnas.84.16.5976

Holstege, J. C. (1991). Ultrastructural evidence for GABAergic brain stem projections to spinal motoneurons in the rat. *J. Neurosci.* 11, 159–167.

Holstege, J. C., Van Dijken, H., Buijs, R. M., Goedknegt, H., Gosens, T., and Bongers, C. M. (1996). Distribution of dopamine immunoreactivity in the rat, cat, and monkey spinal cord. *J. Comp. Neurol.* 376, 631–652. doi: 10.1002/(SICI)1096-9861(19961223)376:4<631::AID-CNE10>3.0.CO;2-P

Hong, S., and Hikosaka, O. (2011). Dopamine-mediated learning and switching in cortico-striatal circuit explain behavioral changes in reinforcement learning. *Front. Behav. Neurosci.* 5:15. doi: 10.3389/fnbeh.2011.00015

Howe, M. W., and Dombeck, D. A. (2016). Rapid signalling in distinct dopaminergic axons during locomotion and reward. *Nature* 535, 505–510. doi: 10.1038/nature18942

Humphreys, J. M., and Whelan, P. J. (2012). Dopamine exerts activation-dependent modulation of spinal locomotor circuits in the neonatal mouse. *J. Neurophysiol.* 108, 3370–3381. doi: 10.1152/jn.00482.2012

Humphries, M. D., and Prescott, T. J. (2010). The ventral basal ganglia, a selection mechanism at the crossroads of space, strategy, and reward. *Prog. Neurobiol.* 90, 385–417. doi: 10.1016/j.pneurobio.2009.11.003

Ichinohe, N., Teng, B., and Kitai, S. T. (2000). Morphological study of the tegmental pedunculopontine nucleus, substantia nigra and subthalamic nucleus, and their interconnections in rat organotypic culture. *Anat. Embryol.* 201, 435–453. doi: 10.1007/s004290050331

Ida, T., Nakahara, K., Katayama, T., and Murakami, N. (1999). Effect of lateral cerebroventricular injection of the appetite-stimulating neuropeptide, orexin and neuropeptide Y, on the various behavioral activities of rats. *Brain Res.* 821, 526–529. doi: 10.1016/S0006-8993(99)01131-2

Ikemoto, S. (2007). Dopamine reward circuitry: two projection systems from the ventral midbrain to the nucleus accumbens–olfactory tubercle complex. *Brain Res. Rev.* 56, 27–78. doi: 10.1016/j.brainresrev.2007.05.004

Inglis, W. L., Dunbar, J. S., and Winn, P. (1994). Outflow from the nucleus accumbens to the pedunculopontine tegmental nucleus: a dissociation between locomotor activity and the acquisition of responding for conditioned reinforcement stimulated by d-amphetamine. *Neuroscience* 62, 51–64. doi: 10.1016/0306-4522(94)90314-X

Ito, R., and Hayen, A. (2011). Opposing roles of nucleus accumbens core and shell dopamine in the modulation of limbic information processing. *J. Neurosci.* 31, 6001–6007. doi: 10.1523/JNEUROSCI.6588-10.2011

Ito, R., Robbins, T. W., and Everitt, B. (2004). Differential control over cocaine-seeking behavior by nucleus accumbens core and shell. *Nat. Neurosci.* 7, 389–397. doi: 10.1038/nn1217

Jankowska, E., Hammar, I., Slawinska, U., Maleszak, K., and Edgley, S. A. (2003). Neuronal basis of crossed actions from the reticular formation on feline hindlimb motoneurons. *J. Neurosci.* 23, 1867–1878. Available online at: http://www.jneurosci.org/content/23/5/1867.long

Jay, M., De Faveri, F., and McDearmid, J. (2015). Firing dynamics and modulatory actions of supraspinal dopaminergic neurons during zebrafish locomotor behavior. *Curr. Biol.* 25, 435–444. doi: 10.1016/j.cub.2014.12.033

Jellinger, K. (1988). The pedunculopontine nucleus in Parkinson's disease, progressive supranuclear palsy and Alzheimer's disease. *J. Neurol. Neurosurg. Psychiatry* 51, 540–543. doi: 10.1136/jnnp.51.4.540

Jordan, L. M. (1998). Initiation of locomotion in mammals. *Ann. N.Y. Acad. Sci.* 860, 83–93. doi: 10.1111/j.1749-6632.1998.tb09040.x

Jordan, L. M., Liu, J., Hedlund, P. B., Akay, T., and Pearson, K. G. (2008). Descending command systems for the initiation of locomotion in mammals. *Brain Res. Rev.* 57, 183–191. doi: 10.1016/j.brainresrev.2007.07.019

Kaelber, W. W., and Smith, T. B. (1979). Projections of the zona incerta in the cat, with stimulation controls. *Exp. Neurol.* 63, 177–200. doi: 10.1016/0014-4886(79)90192-4

Kiehn, O. (2016). Decoding the organization of spinal circuits that control locomotion. *Nat. Rev. Neurosci.* 17, 224–238. doi: 10.1038/nrn.2016.9

Kim, H. F., and Hikosaka, O. (2015). Parallel basal ganglia circuits for voluntary and automatic behaviour to reach rewards. *Brain* 138, 1776–1800. doi: 10.1093/brain/awv134

Kimura, Y., Satou, C., Fujioka, S., Shoji, W., Umeda, K., Ishizuka, T., et al. (2013). Hindbrain V2a neurons in the excitation of spinal locomotor circuits during zebrafish swimming. *Curr. Biol.* 23, 843–849. doi: 10.1016/j.cub.2013.03.066

Klemm, W. R. (2001). Behavioral arrest: in search of the neural control system. *Prog. Neurobiol.* 65, 453–471. doi: 10.1016/S0301-0082(01)00016-8

Kneisley, L. W., Biber, M. P., and LaVail, J. H. (1978). A study of the origin of brainstem projections to monkey spinal cord using the retrograde transport method. *Exp. Neurol.* 60, 116–139. doi: 10.1016/0014-4886(78)90172-3

Koblinger, K., Füzesi, T., Ejdrygiewicz, J., Krajacic, A., Bains, J., and Whelan, P. (2014). Characterization of A11 neurons projecting to the spinal cord of mice. *PLoS ONE* 9:e109636. doi: 10.1371/journal.pone.0109636

Koch, M. (1999). The neurobiology of startle. *Prog. Neurobiol.* 59, 107–128. doi: 10.1016/S0301-0082(98)00098-7

Koch, M., Kungel, M., and Herbert, H. (1993). Cholinergic neurons in the pedunculopontine tegmental nucleus are involved in the mediation of prepulse inhibition of the acoustic startle response in the rat. *Exp. Brain Res.* 97, 71–82. doi: 10.1007/BF00228818

Kolmac, C., and Mitrofanis, J. (1999). Distribution of various neurochemicals within the zona incerta: an immunocytochemical and histochemical study. *Anat. Embryol.* 199, 265–280. doi: 10.1007/s004290050227

Kosse, C., Schöne, C., Bracey, E., and Burdakov, D. (2017). Orexin-driven GAD65 network of the lateral hypothalamus sets physical activity in mice. *Proc. Natl. Acad. Sci. U.S.A.* 114, 4525–4530. doi: 10.1073/pnas.1619700114

Koutsikou, S., Apps, R., and Lumb, B. (2017). Top down control of spinal sensorimotor circuits essential for survival. *J. Physiol.* 595, 4151–4158. doi: 10.1113/JP273360

Koutsikou, S., Watson, T. C., Crook, J. J., Leith, J. L., Lawrenson, C. L., Apps, R., et al. (2015). The periaqueductal gray orchestrates sensory and motor circuits at multiple levels of the neuraxis. *J. Neurosci.* 35, 14132–14147. doi: 10.1523/JNEUROSCI.0261-15.2015

Kravitz, A., Freeze, B., Parker, P., Kay, K., Thwin, M., Deisseroth, K., et al. (2010). Regulation of parkinsonian motor behaviours by optogenetic control of basal ganglia circuitry. *Nature* 466, 622–626. doi: 10.1038/nature09159

Kroeger, D., Ferrari, L., Petit, G., Mahoney, C., Fuller, P., Arrigoni, E., et al. (2017). Cholinergic, glutamatergic, and GABAergic neurons of the pedunculopontine tegmental nucleus have distinct effects on sleep/wake behavior in mice. *J. Neurosci.* 37, 1352–1366. doi: 10.1523/JNEUROSCI.1405-16.2016

Krutki, P., Jankowska, E., and Edgley, S. A. (2003). Are crossed actions of reticulospinal and vestibulospinal neurons on feline motoneurons mediated by the same or separate commissural neurons? *J. Neurosci.* 23, 8041–8050.

Lambert, A. M., Bonkowsky, J. L., Masino, M. A. (2012). The conserved dopaminergic diencephalospinal tract mediates vertebrate locomotor development in zebrafish larvae. *J. Neuroscience.* 32, 13488–13500. doi: 10.1523/JNEUROSCI.1638-12.2012

Lamprea, M. R., Cardenas, F. P., Setem, J., and Morato, S. (2008). Thigmotactic responses in an open-field. *Braz. J. Med. Biol. Res.* 41, 135–140. doi: 10.1590/S0100-879X2008000200010

Landis, C., and Hunt, W. (1939). *The Startle Pattern*. Oxford: Farrar & Rinehart.

Lavoie, B., and Parent, A. (1994). Pedunculopontine nucleus in the squirrel monkey: cholinergic and glutamatergic projections to the substantia nigra. *J. Comp. Neurol.* 344, 232–241. doi: 10.1002/cne.903440205

LeDoux, J. (2000). Emotion circuits in the brain. *Annu. Rev. Neurosci.* 23, 155–184. doi: 10.1146/annurev.neuro.23.1.155

LeDoux, J. (2012). Rethinking the emotional brain. *Neuron* 73, 653–676. doi: 10.1016/j.neuron.2012.02.004

Leppänen, P., Ravaja, N., and Ewalds-Kvist, S. B. M. (2006). Twenty-three generations of mice bidirectionally selected for open-field thigmotaxis: selection response and repeated exposure to the open field. *Behav. Process.* 72, 23–31. doi: 10.1016/j.beproc.2005.11.010

Levita, L., Hare, T. A., Voss, H., Glover, G., Ballon, D. J., and Casey, B. J. (2009). The bivalent side of the nucleus accumbens. *Neuroimage* 44, 1178–1187. doi: 10.1016/j.neuroimage.2008.09.039

Li, H., Penzo, M. A., Taniguchi, H., Kopec, C. D., Huang, Z. J., and Li, B. (2013). Experience-dependent modification of a central amygdala fear circuit. *Nat. Neurosci.* 16, 332–339. doi: 10.1038/nn.3322

Li, W.-C. C., Perrins, R., Walford, A., and Roberts, A. (2003). The neuronal targets for GABAergic reticulospinal inhibition that stops swimming in hatchling frog tadpoles. *J. Comp. Physiol. A* 189, 29–37. doi: 10.1007/s00359-002-0372-0

Liang, F., Xiong, X., Zingg, B., Ji, X., Zhang, L., and Tao, H. (2015). Sensory cortical control of a visually induced arrest behavior via corticotectal projections. *Neuron* 86, 755–767. doi: 10.1016/j.neuron.2015.03.048

Liang, H., Paxinos, G., and Watson, C. (2011). Projections from the brain to the spinal cord in the mouse. *Brain Struct. Funct.* 215, 159–186. doi: 10.1007/s00429-010-0281-x

Liang, H., Paxinos, G., and Watson, C. (2012). Spinal projections from the presumptive midbrain locomotor region in the mouse. *Brain Struct. Funct.* 217, 211–219. doi: 10.1007/s00429-011-0337-6

Liu, J., and Jordan, L. M. (2005). Stimulation of the parapyramidal region of the neonatal rat brain stem produces locomotor-like activity involving spinal 5-HT7 and 5-HT2A receptors. *J. Neurophysiol.* 94, 1392–1404. doi: 10.1152/jn.00136.2005

Loewenstein, G., O'donoghue, T., and Bhatia, S. (2015). Modeling the interplay between affect and deliberation. *Decision* 2, 55–81. doi: 10.1037/dec0000029

Lokwan, S. J., Overton, P. G., Berry, M. S., and Clark, D. (1999). Stimulation of the pedunculopontine tegmental nucleus in the rat produces burst firing in A9 dopaminergic neurons. *Neuroscience* 92, 245–254. doi: 10.1016/S0306-4522(98)00748-9

Magnuson, D., Schramm, M., and MacLean, J. (1995). Long-duration, frequency-dependent motor responses evoked by ventrolateral funiculus stimulation in the neonatal rat spinal cord. *Neurosci. Lett.* 192, 97–100. doi: 10.1016/0304-3940(95)99208-M

Manira, E., Pombal, M. A., and Grillner, S. (1997). Diencephalic projection to reticulospinal neurons involved in the initiation of locomotion in adult lampreys *Lampetra fluviatilis*. *J. Comp. Neurol.* 389, 603–616. doi: 10.1002/(SICI)1096-9861(19971229)389:4<603::AID-CNE5>3.0.CO;2-4

Masserman, J. H. (1938). Destruction of the hypothalamus in cats: effects of activity of the central nervous system and its reaction to sodium amytal. *Arch. Neurol. Psychiatry* 39, 1250–1271. doi: 10.1001/archneurpsyc.1938.02270060140007

Matsuyama, K., Mori, F., Kuze, B., and Mori, S. (1999). Morphology of single pontine reticulospinal axons in the lumbar enlargement of the cat: a study using the anterograde tracer PHA-L. *J. Comp. Neurol.* 410, 413–430. doi: 10.1002/(SICI)1096-9861(19990802)410:3<413::AID-CNE5>3.0.CO;2-Q

McCutcheon, J., Ebner, S., Loriaux, A., and Roitman, M. (2012). Encoding of aversion by dopamine and the nucleus accumbens. *Front. Neurosci.* 6:137. doi: 10.3389/fnins.2012.00137

Medina, J., Repa, C., Mauk, M., and LeDoux, J. (2002). Parallels between cerebellum- and amygdala-dependent conditioning. *Nat. Rev. Neurosci.* 3, 122–131. doi: 10.1038/nrn728

Mel'nikova, Z. L. (1975). Locomotion of rats induced by stimulation of the mesencephalon. *Bull. Moscow Univ.* 30, 45–51.

Mel'nikova, Z. L. (1977). Study of the relationships between the "locomotor regions" of the subthalamus and midbrain in rats. *Neiřofiziol. Neurophysiol.* 9, 275–280.

Ménard, A., and Grillner, S. (2008). Diencephalic locomotor region in the lamprey—Afferents and efferent control. *J. Neurophysiol.* 100, 1343–1353. doi: 10.1152/jn.01128.2007

Mena-Segovia, J., and Bolam, J. P. (2017). Rethinking the pedunculopontine nucleus: from cellular organization to function. *Neuron* 94, 7–18. doi: 10.1016/j.neuron.2017.02.027

Mena-Segovia, J., Micklem, B. R., Nair-Roberts, R. G., Ungless, M. A., and Bolam, J. P. (2009). GABAergic neuron distribution in the pedunculopontine nucleus defines functional subterritories. *J. Comp. Neurol.* 515, 397–408. doi: 10.1002/cne.22065

Mena-Segovia, J., Sims, H. M., Magill, P. J., and Bolam, J. P. (2008). Cholinergic brainstem neurons modulate cortical gamma activity during slow oscillations. *J. Physiol.* 586, 2947–2960. doi: 10.1113/jphysiol.2008.153874

Miller, A., and Blaha, C. (2004). Nigrostriatal dopamine release modulated by mesopontine muscarinic receptors. *Neuroreport* 15:1805. doi: 10.1097/01.wnr.0000135692.81613.85

Milner, K., and Mogenson, G. (1988). Electrical and chemical activation of the mesencephalic and subthalamic locomotor regions in freely moving rats. *Brain Res.* 452, 273–285. doi: 10.1016/0006-8993(88)90031-5

Mitrofanis, J. (2005). Some certainty for the "zone of uncertainty"? Exploring the function of the zona incerta. *Neuroscience* 130, 1–15. doi: 10.1016/j.neuroscience.2004.08.017

Mogenson, G. J., and Stevenson, J. A. F. (1967). Drinking induced by electrical stimulation of the lateral hypothalamus. *Exp. Neurol.* 17, 119–127. doi: 10.1016/0014-4886(67)90139-2

Mogenson, G. J., Jones, D., and Yim, C. (1980). From motivation to action: functional interface between the limbic system and the motor system. *Prog. Neurobiol.* 14, 69–97. doi: 10.1016/0301-0082(80)90018-0

Mogenson, G. J., Swanson, L. W., and Wu, M. (1983). Neural projections from nucleus accumbens to globus pallidus, substantia innominata, and lateral preoptic-lateral hypothalamic area: an anatomical and electrophysiological investigation in the rat. *J. Neurosci.* 3, 189–202.

Mori, S., Sakamoto, T., Ohta, Y., Takakusaki, K., and Matsuyama, K. (1989). Site-specific postural and locomotor changes evoked in awake, freely moving intact cats by stimulating the brainstem. *Brain Res.* 505, 66–74. doi: 10.1016/0006-8993(89)90116-9

Motta, S., Goto, M., Gouveia, F., Baldo, M., Canteras, N., and Swanson, L. (2009). Dissecting the brain's fear system reveals the hypothalamus is critical for responding in subordinate conspecific intruders. *Proc. Natl. Acad. Sci. U.S.A.* 106, 4870–4875. doi: 10.1073/pnas.0900939106

Mullins, O., Hackett, J., Buchanan, J., and Friesen, O. (2011). Neuronal control of swimming behavior: comparison of vertebrate and invertebrate model systems. *Prog. Neurobiol.* 93, 244–269. doi: 10.1016/j.pneurobio.2010.11.001

Muthuraju, S., Talbot, T., and Brandão, M. (2016). Dopamine D_2 receptors regulate unconditioned fear in deep layers of the superior colliculus and dorsal periaqueductal gray. *Behav. Brain Res.* 297, 116–123. doi: 10.1016/j.bbr.2015.10.005

Nagata, T., and Hayashi, Y. (1984). The visual field representation of the rat ventral lateral geniculate nucleus. *J. Comp. Neurol.* 227, 582–588. doi: 10.1002/cne.902270409

Nicola, S. (2007). The nucleus accumbens as part of a basal ganglia action selection circuit. *Psychopharmacology* 191, 521–550. doi: 10.1007/s00213-006-0510-4

Noga, B. R., Kettler, J., and Jordan, L. M. (1988). Locomotion produced in mesencephalic cats by injections of putative transmitter substances and antagonists into the medial reticular formation and the pontomedullary locomotor strip. *J. Neurosci.* 8, 2074–2086.

Noga, B. R., Kriellaars, D. J., Brownstone, R. M., and Jordan, L. M. (2003). Mechanism for activation of locomotor centers in the spinal cord by stimulation of the mesencephalic locomotor region. *J. Neurophysiol.* 90, 1464–1478. doi: 10.1152/jn.00034.2003

Noga, B., Sanchez, F., Villamil, L., O'Toole, C., Kasicki, S., Olszewski, M., et al. (2017). LFP oscillations in the mesencephalic locomotor region during voluntary locomotion. *Front. Neural Circuit* 11:34. doi: 10.3389/fncir.2017.00034

Noga, B. R., Turkson, R. P., Xie, S., Taberner, A., Pinzon, A., and Hentall, I. D. (2017). Monoamine release in the cat lumbar spinal cord during fictive locomotion evoked by the mesencephalic locomotor region. *Front. Neural Circuits* 11:59. doi: 10.3389/fncir.2017.00059

Norton, A., Jo, Y., Clark, E., Taylor, C., and Mizumori, S. (2011). Independent neural coding of reward and movement by pedunculopontine tegmental nucleus neurons in freely navigating rats. *Eur. J. Neurosci.* 33, 1885–1896. doi: 10.1111/j.1460-9568.2011.07649.x

Oka, T., Tsumori, T., Yokota, S., and Yasui, Y. (2008). Neuroanatomical and neurochemical organization of projections from the central amygdaloid nucleus to the nucleus retroambiguus via the periaqueductal gray in the rat. *Neurosci. Res.* 62, 286–298. doi: 10.1016/j.neures.2008.10.004

Olmstead, M. C., and Franklin, K. B. (1994). Lesions of the pedunculopontine tegmental nucleus abolish catalepsy and locomotor depression induced by morphine. *Brain Res.* 662, 134–140. doi: 10.1016/0006-8993(94)90805-2

Olson, G., and Krasne, F. (1981). The crayfish lateral giants as command neurons for escape behavior. *Brain Res.* 214, 89–100. doi: 10.1016/0006-8993(81)90440-6

Olszewski, J., and Baxter, D. (1954). *Cytoarchitecture of the Human Brain Stem*. New York, NY: Basle: S. Karger.

Ondo, W. G., He, Y., Rajasekaran, S., and Le, W. D. (2000). Clinical correlates of 6-hydroxydopamine injections into A11 dopaminergic neurons in rats: a possible model for restless legs syndrome. *Mov. Disord.* 15, 154–158. doi: 10.1002/1531-8257(200001)15:1<154::AID-MDS1025>3.0.CO;2-Q

Pahapill, P., and Lozano, A. (2000). The pedunculopontine nucleus and Parkinson's disease. *Brain* 123, 1767–1783. doi: 10.1093/brain/123.9.1767

Palmiter, R. (2008). Dopamine signaling in the dorsal striatum is essential for motivated behaviors. *Ann. N.Y. Acad. Sci.* 1129, 35–46. doi: 10.1196/annals.1417.003

Pan, W.-X., and Hyland, B. (2005). Pedunculopontine tegmental nucleus controls conditioned responses of midbrain dopamine neurons in behaving rats. *J. Neurosci.* 25, 4725–4732. doi: 10.1523/JNEUROSCI.0277-05.2005

Parkinson, J. A., Cardinal, R. N., and Everitt, B. J. (2000). Limbic cortical-ventral striatal systems underlying appetitive conditioning. *Prog. Brain Res.* 126, 263–285. doi: 10.1016/S0079-6123(00)26019-6

Paxinos, G., and Franklin, K. B. (2008). *The Mouse Brain in Stereotaxic Coordinates, Compact, Third Edition: The Coronal Plates and Diagrams, 3rd Edn*. New York, NY: Elsevier Publishing.

Perreault, M. C., Drew, T., and Rossignol, S. (1993). Activity of medullary reticulospinal neurons during fictive locomotion. *J. Neurophysiol.* 69, 2232–2247.

Perrins, R., Walford, A., and Roberts, A. (2002). Sensory activation and role of inhibitory reticulospinal neurons that stop swimming in hatchling frog tadpoles. *J. Neurosci.* 22, 4229–4240.

Peterson, B. W., Pitts, N. G., and Fukushima (1979). Reticulospinal connections with limb and axial motoneurons. *Exp. Brain Res.* 36, 1–20. doi: 10.1007/BF00238464

Petras, J. M. (1967). Cortical, tectal and tegmental fiber connections in the spinal cord of the cat. *Brain Res.* 6, 275–324. doi: 10.1016/0006-8993(67)90196-5

Petrovich, G. D. (2011). Learning and the motivation to eat: forebrain circuitry. *Physiol. Behav.* 104, 582–589. doi: 10.1016/j.physbeh.2011.04.059

Petrovich, G. D., Risold, P. Y., and Swanson, L. W. (1996). Organization of projections from the basomedial nucleus of the amygdala: a PHAL study in the rat. *J. Comp. Neurol.* 374, 387–420. doi: 10.1002/(SICI)1096-9861(19961021)374:3<387::AID-CNE6>3.0.CO;2-Y

Peyron, C., Tighe, D. K., van den Pol, A. N., de Lecea, L., Heller, H. C., Sutcliffe, J. C., et al. (1998). Neurons containing hypocretin (orexin) project to multiple neuronal systems. *J. Neurosci.* 18, 9996–10015.

Phelps, E., and LeDoux, J. (2005). Contributions of the amygdala to emotion processing: from animal models to human behavior. *Neuron* 48, 175–187. doi: 10.1016/j.neuron.2005.09.025

Picton, L., Nascimento, F., Broadhead, M., Sillar, K., and Miles, G. (2017). Sodium pumps mediate activity-dependent changes in mammalian motor networks. *J. Neurosci.* 37, 906–921. doi: 10.1523/JNEUROSCI.2005-16.2016

Qu, S., Le, W., Zhang, X., Xie, W., Zhang, A., and Ondo, W. (2007). Locomotion is increased in a11-lesioned mice with iron deprivation: a possible animal model for restless legs syndrome. *J. Neuropathol. Exp. Neurol.* 66, 383–388. doi: 10.1097/nen.0b013e3180517b5f

Richard, J., and Berridge, K. (2011). Nucleus accumbens dopamine/glutamate interaction switches modes to generate desire versus dread: D1 alone for appetitive eating but D1 and D2 together for fear. *J. Neurosci.* 31, 12866–12879. doi: 10.1523/JNEUROSCI.1339-11.2011

Roberts, W. W., and Carey, R. J. (1965). Rewarding effect of performance of gnawing aroused by hypothalamic stimulation in the rat. *J. Comp. Physiol. Psychol.* 59, 317–324. doi: 10.1037/h0022030

Roitman, M., Wheeler, R., and Carelli, R. (2005). Nucleus accumbens neurons are innately tuned for rewarding and aversive taste stimuli, encode their predictors, and are linked to motor output. *Neuron* 45, 587–597. doi: 10.1016/j.neuron.2004.12.055

Rolland, A.-S. S., Tandé, D., Herrero, M.-T. T., Luquin, M.-R. R., Vazquez-Claverie, M., Karachi, C., et al. (2009). Evidence for a dopaminergic innervation of the pedunculopontine nucleus in monkeys, and its drastic reduction after MPTP intoxication. *J. Neurochem.* 110, 1321–1329. doi: 10.1111/j.1471-4159.2009.06220.x

Roseberry, T. K., Lee, A. M., Lalive, A. L., Wilbrecht, L., Bonci, A., and Kreitzer, A. C. (2016). Cell-type-specific control of brainstem locomotor circuits by basal ganglia. *Cell* 164, 526–537. doi: 10.1016/j.cell.2015.12.037

Roseberry, T., and Kreitzer, A. (2017). Neural circuitry for behavioural arrest. *Philos. Trans. R. Soc. B* 372:20160197. doi: 10.1098/rstb.2016.0197

Ross, G. S., and Sinnamon, H. M. (1984). Forelimb and hindlimb stepping by the anesthetized rat elicited by electrical stimulation of the pons and medulla. *Physiol. Behav.* 33, 201–208. doi: 10.1016/0031-9384(84)90100-8

Rossignol, S., Dubuc, R., and Gossard, J.-P. (2006). Dynamic sensorimotor interactions in locomotion. *Physiol. Rev.* 86, 89–154. doi: 10.1152/physrev.00028.2005

Ryczko, D., Cone, J., Alpert, M., Goetz, L., Auclair, F., Dubé, C., et al. (2016). A descending dopamine pathway conserved from basal vertebrates to mammals. *Proc. Natl. Acad. Sci. U.S.A.* 113, E2440–E2449. doi: 10.1073/pnas.1600684113

Ryczko, D., and Dubuc, R. (2013). The multifunctional mesencephalic locomotor region. *Curr. Pharm. Des.* 19, 4448–4470. doi: 10.2174/1381612811319240011

Ryczko, D., and Dubuc, R. (2017). Dopamine and the brainstem locomotor networks: from lamprey to human. *Front. Neurosci.* 11:295. doi: 10.3389/fnins.2017.00295

Ryczko, D., Grätsch, S., Auclair, F., Dubé, C., Bergeron, S., Alpert, M. H., et al. (2013). Forebrain dopamine neurons project down to a brainstem region controlling locomotion. *Proc. Natl. Acad. Sci. U.S.A.* 110, E3235–E3242. doi: 10.1073/pnas.1301125110

Sah, P., Faber, E., Armentia, L. M., and Power, J. (2003). The amygdaloid complex: anatomy and physiology. *Physiol. Rev.* 83, 803–834. doi: 10.1152/physrev.00002.2003

Sahibzada, N., Dean, P., and Redgrave, P. (1986). Movements resembling orientation or avoidance elicited by electrical stimulation of the superior colliculus in rats. *J. Neurosci.* 6, 723–733.

Sakurai, T. (2005). *The Orexin/Hypocretin System*. Totowa, NJ: Humana Press.

Sakurai, T., Amemiya, A., Ishii, M., Matsuzaki, I., Chemelli, R. M., Tanaka, H., et al. (1998). Orexins and orexin receptors: a family of hypothalamic neuropeptides and G protein-coupled receptors that regulate feeding behavior. *Cell* 92, 573–585. doi: 10.1016/S0092-8674(00)80949-6

Salgado, S., and Kaplitt, M. G. (2015). The nucleus accumbens: a comprehensive review. *Stereot. Funct. Neuros* 93, 75–93. doi: 10.1159/000368279

Saper, C. B. (2006). Staying awake for dinner: hypothalamic integration of sleep, feeding, and circadian rhythms. *Prog. Brain Res.* 153, 243–252. doi: 10.1016/S0079-6123(06)53014-6

Sar, M., Stumpf, W., Miller, R., Chang, K., and Cuatrecasas, P. (1978). Immunohistochemical localization of enkephalin in rat brain and spinal cord. *J. Comp. Neurol.* 182, 17–37. doi: 10.1002/cne.901820103

Sara, S. (2009). The locus coeruleus and noradrenergic modulation of cognition. *Nat. Rev. Neurosci.* 10, 211–223. doi: 10.1038/nrn2573

Sato, M., Ito, M., Nagase, M., Sugimura, Y., Takahashi, Y., Watabe, A., et al. (2015). The lateral parabrachial nucleus is actively involved in the acquisition of fear memory in mice. *Mol. Brain* 8, 1–15. doi: 10.1186/s13041-015-0108-z

Satoda, T., Matsumoto, H., Zhou, L., Rose, P. K., and Richmond, F. J. (2002). Mesencephalic projections to the first cervical segment in the cat. *Exp. Brain Res.* 144, 397–413. doi: 10.1007/s00221-002-1047-3

Scarnati, E., Campana, E., and Pacitti, C. (1984). Pedunculopontine-evoked excitation of substantia nigra neurons in the rat. *Brain Res.* 304, 351–361. doi: 10.1016/0006-8993(84)90339-1

Scarnati, E., Proia, A., Di Loreto, S., and Pacitti, C. (1987). The reciprocal electrophysiological influence between the nucleus tegmenti pedunculopontinus and the substantia nigra in normal and decorticated rats. *Brain Res.* 423, 116–124. doi: 10.1016/0006-8993(87)90831-6

Schaltenbrand, G., and Wahren, W. (1977). *Atlas for Stereotaxy of the Human Brain*. Stuttgart; New York, NY: Thieme.

Sébille, S. B., Belaid, H., Philippe, A.-C. C., André, A., Lau, B., François, C., et al. (2017). Anatomical evidence for functional diversity in the mesencephalic locomotor region of primates. *Neuroimage* 147, 66–78. doi: 10.1016/j.neuroimage.2016.12.011

Semba, K., and Fibiger, H. C. (1992). Afferent connections of the laterodorsal and the pedunculopontine tegmental nuclei in the rat: a retro- and antero-grade transport and immunohistochemical study. *J. Comp. Neurol.* 323, 387–410. doi: 10.1002/cne.903230307

Sharples, S. A. (2017). Dopamine pumping up spinal locomotor network function. *J. Neurosci.* 37, 3103–3105. doi: 10.1523/JNEUROSCI.0019-17.2017

Sharples, S. A., and Whelan, P. J. (2017). Modulation of rhythmic activity in mammalian spinal networks is dependent on excitability state. *eNeuro* 4:ENEURO.0368-16.2017. doi: 10.1523/ENEURO.0368-16.2017

Sharples, S. A., Humphreys, J. M., Jensen, A. M., Dhoopar, S., Delaloye, N., Clemens, S., et al. (2015). Dopaminergic modulation of locomotor network activity in the neonatal mouse spinal cord. *J. Neurophysiol.* 113, 2500–2010. doi: 10.1152/jn.00849.2014

Sharples, S. A., Koblinger, K., Humphreys, J. M., and Whelan, P. J. (2014). Dopamine: a parallel pathway for the modulation of spinal locomotor networks. *Front. Neural Circuits* 8:55. doi: 10.3389/fncir.2014.00055

Sherman, D., Fuller, P., Marcus, J., Yu, J., Zhang, P., Chamberlin, N., et al. (2015). Anatomical location of the mesencephalic locomotor region and its possible role in locomotion, posture, cataplexy, and parkinsonism. *Front. Neurol.* 6:140. doi: 10.3389/fneur.2015.00140

Shik, M. L., and Orlovsky, G. N. (1976). Neurophysiology of locomotor automatism. *Physiol. Rev.* 56, 465–501.

Shik, M. L., Severin, F. V., and Orlovsky, G. N. (1969). Control of walking and running by means of electrical stimulation of the mesencephalon. *Electr. Clin. Neurol.* 26:549.

Siegel, J., and Boehmer, L. (2006). Narcolepsy and the hypocretin system—where motion meets emotion. *Nat. Clin. Pract. Neurol.* 2, 548–556. doi: 10.1038/ncpneuro0300

Sinnamon, H. (1993). Preoptic and hypothalamic neurons and the initiation of locomotion in the anesthetized rat. *Prog. Neurobiol.* 41, 323–344. doi: 10.1016/0301-0082(93)90003-B

Sinnamon, H. M., Lee, S. H., Adams, D. B., and Stopford, C. K. (1984). Locomotor stepping elicited by electrical stimulation of the lateral hypothalamus requires an ipsilateral descending pathway. *Physiol. Behav.* 33, 209–215. doi: 10.1016/0031-9384(84)90101-X

Sinnamon, H., and Stopford, K. (1987). Locomotion elicited by lateral hypothalamic stimulation in the anesthetized rat does not require the dorsal midbrain. *Brain Res.* 402, 78–86. doi: 10.1016/0006-8993(87)91049-3

Sirota, M. G., and Shik, M. L. (1973). Locomotion of the cat on stimulation of the mesencephalon. *Fiziol. Zhurnal Sssr Imeni M Sechenova* 59, 1314–1321.

Skagerberg, G., and Lindvall, O. (1985). Organization of diencephalic dopamine neurones projecting to the spinal cord in the rat. *Brain Res.* 342, 340–351. doi: 10.1016/0006-8993(85)91134-5

Skinner, R. D., and Garcia-Rill, E. (1984). The mesencephalic locomotor region (MLR) in the rat. *Brain Res.* 323, 385–389.

Skinner, R. D., Kinjo, N., Henderson, V., and Garcia-Rill, E. (1990). Locomotor projections from the pedunculopontine nucleus to the spinai cord. *Neuroreport* 1, 183–186. doi: 10.1097/00001756-199011000-00001

Sparks, D. L. (1986). Translation of sensory signals into commands for control of saccadic eye movements: role of primate superior colliculus. *Physiol. Rev.* 66, 118–171.

Steeves, J., and Jordan, L. (1980). Localization of a descending pathway in the spinal cord which is necessary for controlled treadmill locomotion. *Neurosci. Lett.* 20, 283–288. doi: 10.1016/0304-3940(80)90161-5

Stefanik, M., Kupchik, Y., and Kalivas, P. (2016). Optogenetic inhibition of cortical afferents in the nucleus accumbens simultaneously prevents cue-induced transient synaptic potentiation and cocaine-seeking behavior. *Brain Struct. Funct.* 221, 1681–1689. doi: 10.1007/s00429-015-0997-8

Stefanik, M., Kupchik, Y., Brown, R., and Kalivas, P. (2013). Optogenetic evidence that pallidal projections, not nigral projections, from the nucleus accumbens core are necessary for reinstating cocaine seeking. *J. Neurosci.* 33, 13654–13662. doi: 10.1523/JNEUROSCI.1570-13.2013

Steininger, T. L., Rye, D. B., and Wainer, B. H. (1992). Afferent projections to the cholinergic pedunculopontine tegmental nucleus and adjacent midbrain extrapyramidal area in the albino rat. I. Retrograde tracing studies. *J. Comp. Neurol.* 321, 515–543. doi: 10.1002/cne.903210403

Stoyanova, I. I., Rutten, W. L., and le Feber, J. (2010). Orexin-A and orexin-B during the postnatal development of the rat brain. *Cell. Mol. Neurobiol.* 30, 81–89. doi: 10.1007/s10571-009-9433-z

Stuber, G. D., and Wise, R. A. (2016). Lateral hypothalamic circuits for feeding and reward. *Nat. Neurosci.* 19, 198–205. doi: 10.1038/nn.4220

Surmeier, J., Ding, J., Day, M., Wang, Z., and Shen, W. (2007). D1 and D2 dopamine-receptor modulation of striatal glutamatergic signaling in striatal medium spiny neurons. *Trends Neurosci.* 30, 228–235. doi: 10.1016/j.tins.2007.03.008

Swanson, L. W. (2000). Cerebral hemisphere regulation of motivated behavior. *Brain Res.* 886, 113–164. doi: 10.1016/S0006-8993(00)02905-X

Swanson, L., Sanchez-Watts, G., and Watts, A. (2005). Comparison of melanin-concentrating hormone and hypocretin/orexin mRNA expression patterns in a new parceling scheme of the lateral hypothalamic zone. *Neurosci. Lett.* 387, 80–84. doi: 10.1016/j.neulet.2005.06.066

Szokol, K., Glover, J., and Perreault, M.-C. (2011). Organization of functional synaptic connections between medullary reticulospinal neurons and lumbar descending commissural interneurons in the neonatal mouse. *J. Neurosci.* 31, 4731–4742. doi: 10.1523/JNEUROSCI.5486-10.2011

Takakusaki, K., Habaguchi, T., Ohtinata-Sugimoto, J., Saitoh, K., and Sakamoto, T. (2003). Basal ganglia efferents to the brainstem centers controlling postural muscle tone and locomotion: a new concept for understanding

motor disorders in basal ganglia dysfunction. *Neuroscience* 119, 293–308. doi: 10.1016/S0306-4522(03)00095-2

Takakusaki, K., Takahashi, K., Saitoh, K., Harada, H., Okumura, T., Kayama, Y., et al. (2005). Orexinergic projections to the cat midbrain mediate alternation of emotional behavioural states from locomotion to cataplexy. *J. Physiol.* 568, 1003–1020. doi: 10.1113/jphysiol.2005.085829

Tay, T., Ronneberger, O., Ryu, S., Nitschke, R., and Driever, W. (2011). Comprehensive catecholaminergic projectome analysis reveals single-neuron integration of zebrafish ascending and descending dopaminergic systems. *Nat. Commun.* 2:171. doi: 10.1038/ncomms1171

Thakkar, M. M., Ramesh, V., Strecker, R. E., and McCarley, R. W. (2001). Microdialysis perfusion of orexin-A in the basal forebrain increases wakefulness in freely behaving rats. *Arch. Ital. Biol.* 139, 313–328. doi: 10.4449/aib.v139i3.506

Thankachan, S., Fuller, P. M., and Lu, J. (2012). Movement- and behavioral state-dependent activity of pontine reticulospinal neurons. *Neuroscience* 221, 125–139. doi: 10.1016/j.neuroscience.2012.06.069

Tovote, P., Esposito, M., Botta, P., Chaudun, F., Fadok, J., Markovic, M., et al. (2016). Midbrain circuits for defensive behaviour. *Nature* 534, 206–212. doi: 10.1038/nature17996

Utter, A., and Basso, M. (2008). The basal ganglia: an overview of circuits and function. *Neurosci. Biobehav. Rev.* 32, 333–342. doi: 10.1016/j.neubiorev.2006.11.003

Valenstein, E. (1971). Channeling of responses elicited by hypothalamic stimulation. *J. Psychiatr. Res.* 8, 335–344. doi: 10.1016/0022-3956(71)90029-X

Valenstein, E., Cox, V., and Kakolewski, J. (1970). Reexamination of the role of the hypothalamus in motivation. *Psychol. Rev.* 77:16. doi: 10.1037/h0028581

Vianna, D. M. L., Landeira-Fernandez, J., and Brandão, M. L. (2001). Dorsolateral and ventral regions of the periaqueductal gray matter are involved in distinct types of fear. *Neurosci. Biobehav. Rev.* 25, 711–719. doi: 10.1016/S0149-7634(01)00052-5

Vincent, S. R. (2000). The ascending reticular activating system–from aminergic neurons to nitric oxide. *J. Chem. Neuroanat.* 18, 23–30. doi: 10.1016/S0891-0618(99)00048-4

Wagner, C. K., Eaton, M. J., Moore, K. E., and Lookingland, K. J. (1995). Efferent projections from the region of the medial zona incerta containing A13 dopaminergic neurons: a PHA-L anterograde tract-tracing study in the rat. *Brain Res.* 677, 229–237. doi: 10.1016/0006-8993(95)00128-D

Wall, N., De La Parra, M., Callaway, E., and Kreitzer, A. (2013). Differential innervation of direct- and indirect-pathway striatal projection neurons. *Neuron* 79, 347–360. doi: 10.1016/j.neuron.2013.05.014

Waller, W. H. (1940). Progression movements elicited by subthalamic stimulation. *J. Neurophysiol.* 3, 300–307.

Wannier, T., Orlovsky, G., and Grillner, S. (1995). Reticulospinal neurones provide monosynaptic glycinergic inhibition of spinal neurones in lamprey. *Neuroreport* 6, 1597. doi: 10.1097/00001756-199508000-00003

Whelan, P. J. (1996). Control of locomotion in the decerebrate cat. *Prog. Neurobiol.* 49, 481–515. doi: 10.1016/0301-0082(96)00028-7

Whishaw, I., Alaverdashvili, M., and Kolb, B. (2008). The problem of relating plasticity and skilled reaching after motor cortex stroke in the rat. *Behav. Brain Res.* 192, 124–136. doi: 10.1016/j.bbr.2007.12.026

Wilensky, A., Schafe, G., Kristensen, M., and LeDoux, J. (2006). Rethinking the fear circuit: the central nucleus of the amygdala is required for the acquisition, consolidation, and expression of pavlovian fear conditioning. *J. Neurosci.* 26, 12387–12396. doi: 10.1523/JNEUROSCI.4316-06.2006

Wullimann, M. F. (2014). Ancestry of basal ganglia circuits: new evidence in teleosts. *J. Comp. Neurol.* 522, 2013–2018. doi: 10.1002/cne.23525

Xiang, H.-B. B., Zhu, W.-Z. Z., Guan, X.-H. H., and Ye, D.-W. W. (2013). The cuneiform nucleus may be involved in the regulation of skeletal muscle tone by motor pathway: a virally mediated trans-synaptic tracing study in surgically sympathectomized mice. *Brain* 136:e251. doi: 10.1093/brain/awt123

Xiao, C., Cho, J., Zhou, C., Treweek, J., Chan, K., McKinney, S., et al. (2016). Cholinergic mesopontine signals govern locomotion and reward through dissociable midbrain pathways. *Neuron* 90, 333–347. doi: 10.1016/j.neuron.2016.03.028

Yamamoto, K., and Vernier, P. (2011). The evolution of dopamine systems in chordates. *Front. Neuroanat.* 5:21. doi: 10.3389/fnana.2011.00021

Yeomans, J. S., and Frankland, P. W. (1995). The acoustic startle reflex: neurons and connections. *Brain Res. Rev.* 21, 301–314. doi: 10.1016/0165-0173(96)00004-5

Yeomans, J., Li, L., Scott, B., and Frankland, P. (2002). Tactile, acoustic and vestibular systems sum to elicit the startle reflex. *Neurosci. Biobehav. Rev.* 26, 1–11. doi: 10.1016/S0149-7634(01)00057-4

Yilmaz, M., and Meister, M. (2013). Rapid innate defensive responses of mice to looming visual stimuli. *Curr. Biol.* 23, 2011–2015. doi: 10.1016/j.cub.2013.08.015

Zweig, R., Jankel, W., Hedreen, J., Mayeux, R., and Price, D. (1989). The pedunculopontine nucleus in Parkinson's disease. *Ann. Neurol.* 26, 41–46. doi: 10.1002/ana.410260106

Conflict of Interest Statement: The authors declare that the research was conducted in the absence of any commercial or financial relationships that could be construed as a potential conflict of interest.

Copyright © 2017 Kim, Sharma, Sharples, Mayr, Kwok and Whelan. This is an open-access article distributed under the terms of the Creative Commons Attribution License (CC BY). The use, distribution or reproduction in other forums is permitted, provided the original author(s) or licensor are credited and that the original publication in this journal is cited, in accordance with accepted academic practice. No use, distribution or reproduction is permitted which does not comply with these terms.

frontiers in Physiology

ORIGINAL RESEARCH
published: 10 November 2017
doi: 10.3389/fphys.2017.00900

Modulation of Neurogenesis through the Promotion of Energy Production Activity Is behind the Antidepressant-Like Effect of Colonial Green Alga, *Botryococcus braunii*

Kazunori Sasaki[1,2], *Mahmoud B. Othman*[3], *Mikihide Demura*[4], *Makoto Watanabe*[4,5] *and Hiroko Isoda*[3,5]*

[1] Interdisciplinary Research Center for Catalytic Chemistry, National Institute of Advanced Industrial Science and Technology, Tsukuba, Japan, [2] Faculty of Pure and Applied Sciences, University of Tsukuba, Tsukuba, Japan, [3] Alliance for Research on North Africa, University of Tsukuba, Tsukuba, Japan, [4] Algal Biomass and Energy System R&D Center, University of Tsukuba, Tsukuba, Japan, [5] Faculty of Life and Environmental Sciences, University of Tsukuba, Tsukuba, Japan

OPEN ACCESS

Edited by:
Geoffrey A. Head,
Baker Heart and Diabetes Institute, Australia

Reviewed by:
Jie Liu,
Tangdu Hospital, Fourth Military Medical University, China
Antonio Longo,
Università degli Studi di Catania, Italy

***Correspondence:**
Hiroko Isoda
isoda.hiroko.ga@u.tsukuba.ac.jp

Specialty section:
This article was submitted to Integrative Physiology, a section of the journal Frontiers in Physiology

Received: 28 April 2017
Accepted: 24 October 2017
Published: 10 November 2017

Citation:
Sasaki K, Othman MB, Demura M, Watanabe M and Isoda H (2017) Modulation of Neurogenesis through the Promotion of Energy Production Activity Is behind the Antidepressant-Like Effect of Colonial Green Alga, Botryococcus braunii. Front. Physiol. 8:900. doi: 10.3389/fphys.2017.00900

Algae have been recognized as important resources providing functional components due to their capacity to exert beneficial effects on health. Therefore, there is increasing interest in investigating the biological activity of algae. In this study, we evaluated the antidepressant-like effect of the administration of 100 mg/kg/day of the ethanol extract of colonial green alga *Botryococcus braunii* (EEB) for 14 consecutive days in the forced swimming test (FST)-induced depression in imprinting control region (ICR) mice. Imipramine, a commercial antidepressant drug, was used as a positive control. In addition, we investigated the molecular mechanisms underlying the effect of EEB by measuring ATP production and by assessing any change in gene expression at the end of the treatment using real-time polymerase chain reaction (PCR) and microarray assays. We showed that the immobility time in the water-administered control (FST stress) group gradually increased from day 1 to day 14. However, treatment with EEB caused a significant decrease of immobility time in the FST compared with that in the FST stress group. Microarray and real-time PCR results revealed that EEB treatment induced variation in the expression of several genes associated with neurogenesis, energy metabolism, and dopamine synthesis. Interestingly, we revealed that only EEB treatment enhanced the promotion of energy production, while treatment with imipramine was ineffective. Our study provides the first evidence that *B. braunii* enhances energy production, which may contribute to the modulation of neurogenesis and to the enhancement of dopaminergic function, in turn potentially underlying the antistress- and antidepressant-like effects that we observed.

Keywords: microalgae, *Botryococcus braunii*, depression, forced swimming test, dopamine synthesis, energy promotion activity, neurogenesis

INTRODUCTION

Stress is a part of everyday life and particularly prevalent in modern societies. There are various sources of stress in people's lives, and excessive or prolonged exposure to such stress factors has a significant impact on our wellbeing, ultimately leading to emotional and behavioral changes, together with reduced cognitive function and physical illness. Therefore, it is not surprising that stress remains a top health concern, particularly in developed countries. The damaging effect of stress on cells is well-documented; in particular, stress affects neuronal cells and may lead to the induction of neurodegenerative disorders, such as Alzheimer's disease, Parkinson's disease, and major depression. Depression is a psychiatric disorder commonly characterized by a sense of prostration; in its most severe forms, it can be life-threatening. This disorder has a worldwide prevalence of ∼17% (Liu et al., 2013). Depression, which is the most common type of affective disorders, is caused by a combination of biological, psychological, social, and other factors. Depressive syndrome is characterized by significant and lasting low mood (Lu et al., 2015). In clinical practice, drug classes used for the treatment of depression include monoamine oxidase inhibitors, selective serotonin noradrenaline reuptake inhibitors (SNRIs), selective serotonin reuptake inhibitors, and tricyclic antidepressants (Bouvier et al., 2003; Fava, 2003; Shen and Liang, 2007). However, these drugs can cause a variety of adverse effects, including nausea, headaches, and nerve pain. Therefore, new and safer antidepressants, which are derived from natural products and lack side effects, need to be developed.

Algae are photosynthetic organisms that mainly inhabit the hydrosphere. They form a large and diverse group within which over 40,000 species have been described so far. However, the total number of algal species is estimated to exceed 10 million, including those that remain undiscovered and undescribed (Norton et al., 1996). Some algae and particularly microalgae have served as important sources of functional materials, such as n-3 polyunsaturated fatty acids (PUFA), vitamins, minerals, polysaccharides, and bioactive compounds (Shahidi and Janak Kamil, 2001). Moreover, microalgae are known to exhibit various biological and physiological activities, including antioxidant, anticoagulant, antiviral, and antitumoral effects (Pangestuti and Kim, 2011). Therefore, we speculated that microalgae have the potential to be a valuable natural resource of novel bioactive compounds and focused on the colonial green alga *Botryococcus braunii* Kützing (Trebouxiophyceae, Chlorophyta), which is found worldwide in freshwater and brackish lakes, reservoirs, and ponds. *B. braunii* produces large amounts of hydrocarbons, which are excreted from cells and accumulate in its colonies. Therefore, it is considered to have great potential as a renewable source of chemical products and is useful for searching for new antidepressant drugs. Moreover, to the best of our knowledge, few reports on studies exploring the physiological effects of *B. braunii* have been published.

The objectives of this study were to evaluate the antidepressant-like effect of ethanol extract of *B. braunii* (EEB), using the forced swimming test (FST) to obtain a rodent model of depression by inducing stress in imprinting control region (ICR) mice, and to understand the molecular mechanism behind the antidepressant-like effect of EEB. We also focused our attention on changes in expression levels for genes associated with neurogenesis, energy promotion activity, and dopamine synthesis. In addition, we analyzed the neuroprotective effect of EEB using rat pheochromocytoma PC12 cells.

MATERIALS AND METHODS

Preparation of Ethanol Extract of *B. braunii* (EEB)

A dried sample of *B. braunii* was provided by ABES, the University of Tsukuba, Japan. The dried sample was extracted using 99.5% ethanol, in the dark, and at room temperature for 2 weeks, with shaking of the mixture occurring at least once a day. At the end of the procedure, the liquid fraction (EEB) was collected, filtered through a 0.22-μm filter (Merck Millipore, Billerica, MA, USA), and used in the *in vitro* assays. For animal dosing in the *in vivo* assay, EEB was concentrated using SpeedVac (Thermo Fisher Scientific, Waltham, MA, USA) and the dried EEB was dissolved in MilliQ water.

Animals

Male ICR mice (Charles River Laboratories Japan Inc., Yokohama, Kanagawa, Japan), 5 weeks old, weighing 35–40 g, were used for *in vivo* experiments. The animals were kept individually in cages and maintained with free access to water and food *ad libitum*, under a 12/12-h light/dark cycle. All of the experiments were carried out between 09:00 and 16:00, and the animals had been acclimatized for 7 days to the laboratory conditions ahead of the experiment. This animal experiment was approved by the Ethics Animal Care and Use Committee of the University of Tsukuba.

Administration of Ethanol Extract of *B. braunii* (EEB) to ICR Mice

After 1 week of acclimatization to the laboratory conditions, mice were assigned to three groups: a control group (n = 8), a group administered 20 mg/kg imipramine daily ($n = 8$), and a group administered 100 mg/kg EEB daily (n = 8). EEB dissolved in drinking water was administered orally using a tube and a syringe for 14 consecutive days. The control group was administered an equivalent volume of tap water.

Imipramine, an SNRI antidepressant drug that selectively increases dopamine and noradrenaline levels in the synaptic cleft, was used as a positive control. Imipramine was freshly dissolved in distilled water and orally administered to mice at a dose of 20 mg/kg, as reported in our previous study (Ben Othman et al., 2013).

Forced Swimming Test

The FST was conducted as previously described by Ben Othman et al. (2013) To carry out the FST, we used a cylindrical jar (14 cm in diameter × 25 cm in height) filled from the bottom with 19 cm of water at 25 ± 1°C. The FST was performed at 1, 2, 6, 10, and 14 d during the period of the oral administration of EEB. Each mouse was placed gently into the water and allowed

to swim freely for 5 min. The mouse was considered immobile when it showed disparity and became motionless in the water. Periods of immobility were defined as when mice only made those movements that were necessary to keep their head above the water. The duration of immobility was recorded and analyzed off-line over the last 4 min of the test.

RNA Isolation from Mouse Brain

Following the last FST at day 14, all mice were sacrificed by dislocation of the cervical spine and their brains were isolated. A small amount (0.1 mg) of cerebral tissue was removed and washed with ice-cold phosphate-buffered solution (PBS). The total RNA was extracted from it using the ISOGEN kit (Nippon Gene Co. Ltd., Toyama, Japan), as we reported previously (Sasaki et al., 2013). Total RNA was quantified and assessed for its quality with the NanoDrop 2000 spectrophotometer (Thermo Scientific, Wilmington, DE, USA).

DNA Microarray Analysis

DNA microarray analysis was conducted on isolated RNA samples from brains treated with EEB. DNA microarray analysis was performed as reported previously (Isoda et al., 2012; Samet et al., 2015). Double-stranded cDNA was synthesized from 100 ng of total RNA with the GeneAtlas 3′ IVT Express Kit (Affymetrix Inc., Santa Clara, CA, USA). Biotin-labeled amplified RNA (aRNA) was synthesized by *in vitro* transcription using the GeneChip 3′ IVT Express Kit (Affymetrix Inc., Santa Clara, CA, USA). A total of 9.4 mg of purified aRNA was fragmented using the GeneAtlas 3′ IVT Express Kit and was hybridized for 16 h at 45°C using GeneChip MG-430 PM microarray (Affymetrix Inc., Santa Clara, CA, USA). The chip was washed and stained in the Gene Atlas Fluidics Station 400 (Affymetrix Inc., Santa Clara, CA, USA) and then the resulting image was scanned using the GeneAtlas Imaging Station (Affymetrix Inc., Santa Clara, CA, USA). Data analysis was performed using the Partek Express software (Partek Inc., St. Louis, MO, USA) provided by Affymetrix as part of their GeneAtlas system. Compared with the control (water-treated group), fold change in expression in the imipramine- or EEB-treated group was calculated and converted to log 2 data.

Taqman Quantitative RT-PCR Analysis of Gene Expression in Mouse Brain

Based on the microarray analysis, reverse transcription reactions were carried out with the SuperScript III Reverse Transcriptase (RT) kit (Invitrogen, Carlsbad, CA, USA). In accordance with the manufacturer's instructions, 1 μg of total RNA and 1 μl of oligo$(dT)_{12–18}$ primers were denatured at 65°C for 5 min and subsequently chilled at 4°C. After the addition of SuperScript III RT (200 U), the reaction mix was incubated at 42°C for 60 min, followed by another 10 min at 70°C. All primer sets and TaqMan probes for experimental genes were from Applied Biosystems (Foster City, CA, USA): mouse tyrosine hydroxylase (TH) (Mm00447557_m1), mouse pyruvate carboxylase (PC) (Mm00500992_m1), mouse brain-derived neurotrophic factor (BDNF) (Mm04230607_s1), and mouse GAPDH (Mm99999915_g1). For the quantification of mRNA, TaqMan Real Time-PCR amplification reactions were carried out using an AB 7500 Fast Real-Time PCR system (Applied Biosystems). Amplifications were performed in a final volume of 20 μl, using 10 μl of TaqMan Universal PCR Master Mix UNG (Applied Biosystems), 1 μl of the corresponding primer/probe mix, and 9 μl of template cDNA (final concentration 100 ng/20 μl). Cycling conditions were as follows: 2 min at 50°C, 10 min at 95°C, and 40 cycles at 95°C for 15 s followed by 60°C for 1 min.

Measurement of Brain ATP Content

ATP levels in the bupropion tissues were measured with firefly bioluminescence using a luminescence luciferase assay kit (TOYO Ink, Tokyo, Japan). A small amount (0.1 mg) of cerebral tissue was homogenized with 10 mL of ice-cold homogenate buffer (0.25 M sucrose, 10 mM HEPES-NaOH, pH 7.4). After centrifugation, the supernatant was collected and 100 μL of it was transferred to a 96-well plate. After adding 100 μL of luciferin-luciferase solution (TOYO Ink, Tokyo, Japan), 150 μL of the mixed solution was transferred to another 96-well plate and incubated for 10 min. After 10 min of incubation, light emission was recorded using a luminometer (Powerscan HT; Dainippon Pharmaceutical, Osaka, Japan).

Cell Culture

PC12 cell culture and MTT assay were performed in accordance with our previous work (Sasaki et al., 2013). PC12 cells (RIKEN, Tsukuba, Japan) were cultured in 75 cm^2 flasks (BD Biosciences, San Jose, CA, USA) and maintained in Dulbecco's Modified Eagle's Medium (DMEM) (Sigma-Aldrich, St. Louis, MO, USA) containing 10% heat-inactivated horse serum (Gibco, Yokohama, Japan), 5% fetal bovine serum (Sigma-Aldrich), and supplemented with 100 $U{\cdot}ml^{-1}$ penicillin and 100 $\mu g{\cdot}ml^{-1}$ streptomycin (ICN Biomedicals, Tokyo, Japan), in a water-saturated 5% CO_2 atmosphere at 37°C. For the experiments in this study, cells were used between passage 3 and passage 8.

MTT Assay for Neuroprotection

Cell viability was measured using the 3-(4,5-dimethylthiazol-2-yl)-2,5-diphenyltetrazolium bromide (MTT) assay. PC12 cells (1×10^5 $cells{\cdot}ml^{-1}$) cultured in a 96-well plate (BD Biosciences) were pretreated with 1/1,000 dilution of EEB for 10 min, followed by the addition of 200 μM corticosterone (Sigma-Aldrich, St. Louis, MO, USA) for 48 h. After sample treatment, 100 μl of culture medium and 10 μl of MTT (5 $mg{\cdot}ml^{-1}$) were added and the cells were incubated for 6 h. The MTT formazan formed was dissolved in 100 μl of 10% SDS (w/v) and the absorbance was measured using a microtiter plate reader (Powerscan HT; Dainippon Sumitomo Pharma Co. Ltd., Osaka, Japan).

Statistical Analysis

Results are expressed as mean ± standard error of the mean (SEM). Statistical analysis of the results obtained in the FST was carried out using two-way ANOVA with Ryan-einot-gabriel-welsch multiple range test. One-way ANOVA followed by Ryan-einot-gabriel-welsch multiple range test was also used. The statistical evaluation was performed using the Student's *t*-test

between control and corticosterone-treatment group in *in vitro* experiment. A $P < 0.05$ was considered statistically significant.

RESULTS

EEB Reversal of Depression-Like Behavior Induced by FST

FST is a behavioral animal model that has been widely adopted for investigating depression. To determine whether EEB has antidepressant-like activity, its effect on FST-induced stress in mice was investigated. The administration of 100 mg/kg EEB for 14 consecutive days caused no mortality or significant body weight change in any animal. As shown in **Figure 1**, the immobility time in the water-administered control (FST stress) group gradually increased from day 1 to day 14 (D = day; D1, 46.5 ± 13.2 s; D2, 55.4 ± 12.0 s; D6, 68.4 ± 11.5 s; D10, 71.5 ± 7.14 s; D14, 80.3 ± 6.40 s; $P < 0.05$). However, this trend was not observed in the imipramine- and EEB-administered groups.

At day 14, the average immobility time for the EEB-administered group (33.3 ± 7.0 s) was similar to that in the imipramine-administered group (26.3 ± 10.7 s), which represented our positive control (**Figure 1**). In mice treated with imipramine, EEB induced a three-fold reduction of the average immobility time compared with that in the water-administered control mice (80.3 ± 6.40 s; $P < 0.01$).

EEB-Induced Variation of Energy Metabolism-, Dopamine Production-, and Neurogenesis-Related Gene Expression

To evaluate the molecular mechanism behind the antidepressant-like effect of EEB, we performed microarray analysis of ICR mouse cerebrum to investigate changes in gene expression. We found that the expression of eight genes was altered in the ICR mice administered EEB compared with their levels in the control group (**Table 1**). These included the short stature homeobox 2 (Shox2), paired-like homeodomain transcription factor 2 (Pitx2), teashirt zinc finger family member 1 (Tshz1), and LIM homeobox protein 9 (Lhx9) genes associated with neurogenesis ($P < 0.05$; compared with the control group). Moreover, the expression of the polyribonucleotide nucleotidyltransferase 1 (Pnpt1) gene associated with energy metabolism was upregulated, while that of the arrestin domain containing 4 (Arrdc4) gene involved in the regulation of ATP production was downregulated ($P < 0.05$; compared with the control group). In addition, the expression of two genes associated with dopamine synthesis was modulated: the arginine/serine-rich coiled-coil 1 (Rsrc1) gene was upregulated, while the protein phosphatase 1, regulatory (inhibitor) subunit 1B (Ppp1r1b) gene was downregulated ($P < 0.05$; compared with the control group). A similar pattern of alterations of expression for the genes involved in neurogenesis and dopamine synthesis was observed in the imipramine-administered group. In summary, our results show that the administration of EEB induced variation in the expression of energy metabolism-, dopamine production-, and neurogenesis-related genes.

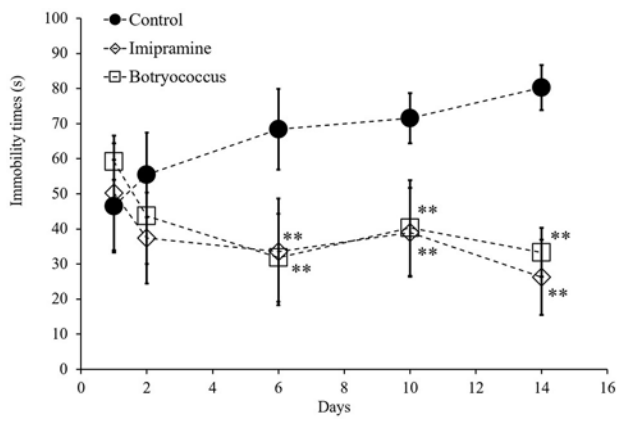


FIGURE 1 | Effects of administration of ethanol extract of *Botryococcus braunii* (EEB) on the immobility time in the forced swimming test (FST). Mice were orally administered water (control), imipramine (20 mg/kg), and EEB (100 mg/kg) daily for 14 consecutive days. FST was carried out on days 1, 2, 6, 10, and 14. The immobility time during the final 4 min of a 5-min total session was measured. FST immobility time measured for each group. Each data point expressed as the means ± SEM ($n = 8$) and were analyzed by two-way ANOVA followed by Ryan-einot-gabriel-welsch multiple range test, $^{**}P < 0.01$ vs. control group.

EEB-Induced Upregulation of BDNF, TH, and PC Gene Expression in ICR Mouse Cerebrum

Based on the results obtained from the microarray analysis, we investigated the mRNA expression levels of TH, PC, and BDNF in the ICR mouse cerebrum from the four experimental groups. Real-time (RT) PCR results (**Figure 2**) showed that the mRNA expression levels of TH were significantly upregulated in the EEB-administered groups (168.6 ± 21.0%, compared with the control group; $P < 0.01$; **Figure 2A**). The mRNA expression levels of PC and BDNF were also upregulated in the EEB-administered groups (PC: 142 ± 14.6% compared with the control group, $P < 0.01$; BDNF: 151.1 ± 22.4% compared with the control group, $P < 0.01$; **Figures 2B,C**). The administration of imipramine induced the overexpression of TH and BDNF, while it did not affect the mRNA level of PC (**Figure 2**).

EEB-Induced Production of ATP in ICR Mouse Cerebrum

The results obtained from the microarray analysis and RT-PCR showed that the upregulation of PC expression occurred in the EEB-administered groups, but not in the imipramine-administered mice. This indicates that EEB may increase the energy level of mice. Therefore, we determined the ATP content in the brains of the mice administered EEB. ATP is a multifunctional nucleotide referred to as the "molecular unit of currency" of intracellular energy transfer. It is also widely used as a marker of cell proliferation as it transports the chemical energy necessary for metabolic activity into the cells. The levels of ATP production in the EEB-administered mice were measured using a luciferase method. Mice administered EEB had significantly

TABLE 1 | Classification of the modulated genes and their fold change in expression in imipramine- and EEB-administered imprinting control region mice in comparison to the control, as identified by DNA microarray analysis.

Gene symbol	Gene name	Fold change (Control vs. imipramine)	Fold change (Control vs. EEB)	Molecular function	Associated phenotype
Shox2	Short stature homeobox 2	2.41**	3.09**	Plays an important role during the cerebellar neurogenesis, by maintaining the bone morphogenetic protein expression levels (Rosin et al., 2015)	Neurogenesis
Pitx2	Paired-like homeodomain transcription factor 2	1.84*	2.37*	Necessary for the normal development of the subthalamic nucleus	
Tshz1	Teashirt zinc finger family member 1	2.24**	2.02**	Maintain the expression of the prokineticin receptor 2, a G protein–coupled receptor essential for OB development and related to prokineticin signaling (Ragancokova et al., 2014)	
Lhx9	LIM homeobox protein 9	1.69**	1.39*	The typical marker genes of neurogenesis at the stage of immature neuronal cells (Ng et al., 2005).	
Pnpt1	Polyribonucleotide nucleotidyltransferase 1	1.06	2.05**	Gene encoding for PNPase, associate with Mitochondrial importation of nucleus-encoded RNAs (Kamenski et al., 2007; Tarassov et al., 2007; Duchene et al., 2009; Smirnov et al., 2011).	Energy Promotion
Arrdc4	Arrestin domain containing 4	−1.08	−1.33**	Negative regulator of glucose uptake (Patwari et al., 2009)	
Rsrc1	Arginine/serine-rich coiled-coil 1	1.63**	1.49**	Function in dopamine, glutamate, and fibroblast growth factor receptor signaling (Potkin et al., 2009)	Dopamine synthesis
Ppp1r1b	Protein phosphatase 1, regulatory (inhibitor) subunit 1B	−3.83**	−5.54**	Involved in the regulation of dopaminergic and glutaminergic signaling (Albert et al., 2002; Svenningsson et al., 2002)	

*Table values are expressed as mean ± SEM for three mice in each group. *P < 0.05, **P < 0.01 in comparison to control mice.*

upregulated levels of luminescence (152.8 ± 25.9%) compared with the control group ($P < 0.05$; **Figure 3**). In contrast, ATP levels of imipramine-administered mice were not significantly altered (**Figure 3**).

EEB-Mediated Protection against Corticosterone-Induced Cell Death

We next performed the MTT assay to investigate the viability of PC12 cells after treatment with corticosterone. Application of 200 μM corticosterone significantly decreased cell viability to 42.4 ± 4.3% compared with that of untreated cells ($P < 0.01$; **Figure 4**). However, pretreatment with a 1/1,000 dilution of EEB for 10 min reversed this corticosterone-induced cell death, resulting in a significant increase of cell viability by 34.3 ± 3.2% compared with that in the corticosterone-treated group" and revise ($P < 0.01$; **Figure 4**).

DISCUSSION

The present study was conducted to investigate the potential antidepressant-like effect of the microalga *B. braunii* and to elucidate the mechanism behind this effect. It is estimated that about 72,500 algal species have been characterized globally (Guiry, 2012). Algae produce bioactive secondary metabolites that include polyphenolic compounds, polysaccharides, steroids, fatty acids, carotenoids, mycosporine-like amino acids, halogenated compounds, polyketides, lectins, peptides, and their derivatives (Faulkner, 2001; Cardozo et al., 2007). Among the large number of biological functionalities of marine algal natural products, antioxidant, anti-inflammatory, anticancer, immunomodulatory, antidiabetic, antimicrobial, anticoagulant, tyrosinase inhibitory, and UV-protective effects have been highlighted, based on extensive studies (Blunt et al., 2015). However, there have been no reports on the antidepressant-like effect of *B. braunii*. Therefore, the discovery of novel antidepressants from these microalgae could provide new insight in the fields of biomedical and pharmaceutical research.

The FST is a standard animal model for behavioral measurement of depression. In this test, the degree to which the animal ceases to struggle and becomes relatively passively immobile is used to assess the depressive behavior. Immobility displayed in this behavioral model has been hypothesized to reflect behavioral despair, which may mimic depressive disorders in humans. Moreover, there is a significant correlation between the clinical potency of antidepressants and the potency of the same drugs in this model. Therefore, FST is usually adopted to screen or evaluate antidepressant drugs (Porsolt et al., 1978). The current study showed that the duration of immobility in

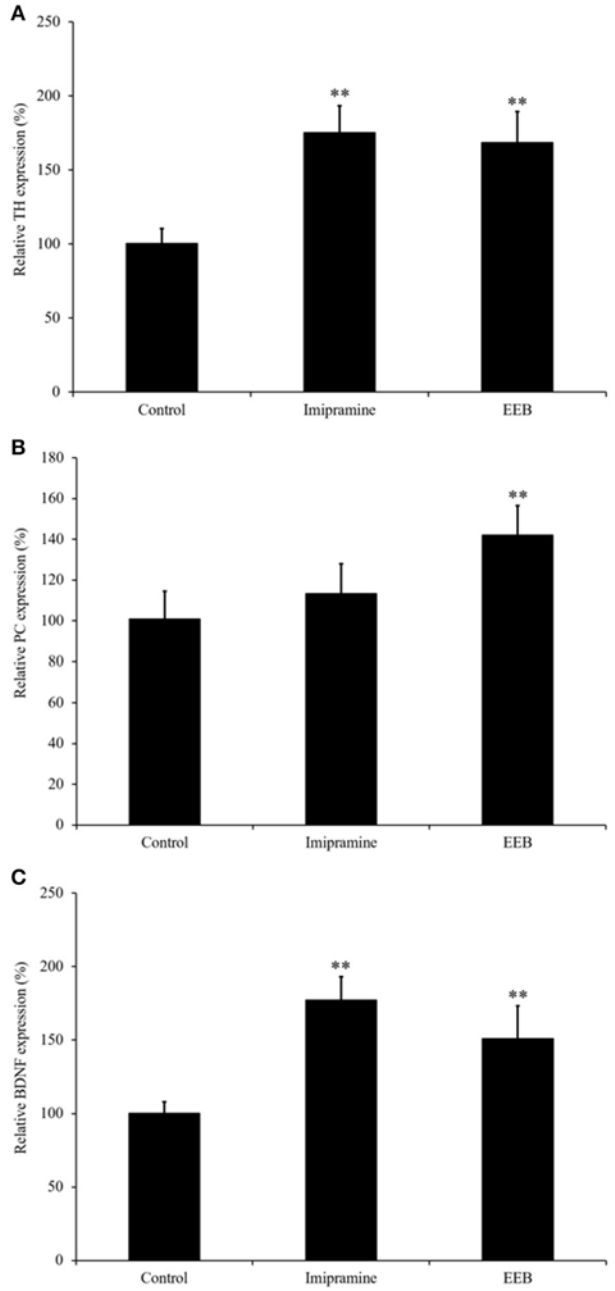


FIGURE 2 | Effect of the administration of ethanol extract of *Botryococcus braunii* (EEB) on mRNA expression of pyruvate carboxylase (PC), brain-derived neurotrophic factor (BDNF), and tyrosine hydroxylase (TH) in imprinting control region mouse cerebrum. Mice were orally administered water (control), imipramine (20 mg/kg), and EEB (100 mg/kg) daily for 14 consecutive days. Gene expression levels of TH **(A)**, PC **(B)**, and BDNF **(C)** were normalized to the GAPDH level and were expressed as the ratio of that in the control group. Values are expressed as the means ± SEM ($n = 3$ independent experiments) and were analyzed by one-way ANOVA followed by Ry8an-einot-gabriel-welsch multiple range test, $^{**}P < 0.01$ vs. control group.

the FST was significantly decreased after the administration of 100 mg/kg EEB, indicating that *B. braunii* has antidepressant effects. Furthermore, the oral administration of *B. braunii* showed a comparable effect to that of imipramine, a commercial antidepressant drug.

Microarray studies have been utilized as a useful tool to characterize depression-related biomarkers in patients as well as to further our understanding of the mechanisms underlying depression in rodent models of this disease. In this study, we identified eight genes that may be related to the pathophysiology of depressive-like behavior induced by FST-related stress. Three biological pathways (I: dopamine synthesis; II: energy metabolism; III: neurogenesis) were identified to be significantly altered in EEB-administered groups compared with their levels in the control group.

As proposed by Li et al. (2015), the monoamine hypothesis suggests that major depression might result from the dysregulation of monoaminergic neurotransmitters such as dopamine, serotonin, and norepinephrine in the central nervous system. Dopamine is the most abundant monoamine neurotransmitter in the brain, and plays a critical role in the regulation of emotions, motivation, cognition, reward circuits, and reinforcement behavior (Nieoullon and Coquerel, 2003; Wise, 2004; Perkins et al., 2008). In this study, microarray results showed that EEB induced downregulation of the Ppp1r1b gene, which encodes the dopamine- and cAMP-regulated neuronal phosphoprotein (DARPP-32). DARPP-32 is involved in the regulation of dopaminergic and glutaminergic signaling, and it has been implicated in various neurological and psychiatric disorders including schizophrenia (Albert et al., 2002) and depression (Svenningsson et al., 2002). In addition, EEB also induced overexpression of the Rsc1 gene, which functions in dopamine, glutamate, and fibroblast growth factor receptor signaling (Potkin et al., 2009). Moreover, we determined the mRNA expression of tyrosine hydroxylase (or tyrosine 3-monooxygenase, TH), the rate-limiting enzyme in the biosynthesis of the catecholamine neurotransmitters dopamine (DA) and norepinephrine (NE), and of adrenaline in neurons. The regulated activity of TH is thought to play a critical role in modulating the functional activity of the dopaminergic neuronal systems in the brain (Fu et al., 2006). Catecholamines, such as DA and NE, are known to play an important role in several behavioral and neurodegenerative diseases such as depression and Parkinson's disease. In our study, we demonstrated that EEB treatments increased the level of TH by 168.6 ± 21.0%, in comparison to that in vehicle-treated animals. Therefore, our results demonstrate that *B. braunii* may act as an antidepressant by enhancing catecholamine synthesis in the brain.

Energy metabolic pathways [including glycolysis/gluconeogenesis, the tricarboxylic acid (TCA) cycle, and oxidative phosphorylation] have been studied extensively in major depression disorder (Reininghaus et al., 2013). In our study, we reported the variation in the expression of Pnpt1 and Arrdc4 genes, which are involved in energy production. The Pnpt1 gene product is a polynucleotide phosphorylase (PNPase), an enzyme associated with the import of nucleus-encoded RNAs such as transfer RNA (tRNA), 5S ribosomal RNA (5S rRNA), ribonuclease P RNA (RNase P RNA), and MRP (mitochondrial RNA processing) RNAse into mitochondria. These nucleus-encoded RNAs are essential for mitochondrial DNA replication,

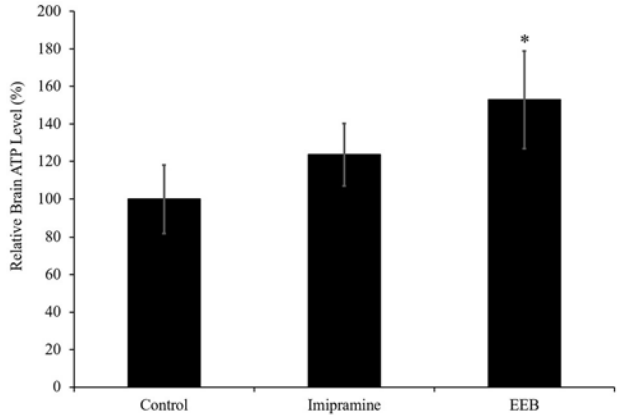


FIGURE 3 | Effects of the administration of ethanol extract of *B. braunii* (EEB) on the ATP levels in imprinting control region mouse cerebrum. Mice were orally administered water (control), imipramine (20 mg/kg), and EEB (100 mg/kg) daily for 14 consecutive days. Values are expressed as the means ± SEM ($n = 4$ independent experiments) and were analyzed by one-way ANOVA followed by Ryan-einot-gabriel-welsch multiple range test, $^{*}P < 0.05$ vs. control group.

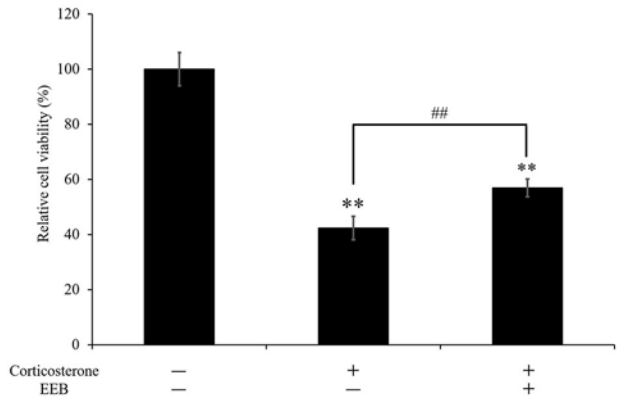


FIGURE 4 | Effect of ethanol extract of *B. braunii* (EEB) on the corticosterone-induced changes in PC12 cell viability. Values are expressed as the means ± SEM ($n = 5$ independent experiments) and were analyzed by one-way ANOVA followed by Ryan-einot-gabriel-welsch multiple range test, $^{**}P < 0.01$ vs. control cells, $^{\#\#}P < 0.01$ vs. corticosterone-treated cells.

transcription, and translation (Kamenski et al., 2007; Tarassov et al., 2007; Duchene et al., 2009; Smirnov et al., 2011). It is reported that deficiency of PNPase leads to cellular changes secondary to mitochondrial dysfunction, which include lactate accumulation, reduction in steady-state ATP levels, and reduced cell proliferation (Chen et al., 2006). The expression of Arrdc4, a negative regulator of glucose uptake (Patwari et al., 2009), was also downregulated in the cerebrum of EEB-administered ICR mice. Glucose is a fundamental nutrient, providing ATP for energy as well as carbon for biosynthesis (Vander Heiden et al., 2009). In addition, from the microarray results, we determined the gene expression of pyruvate carboxylase (PC), the rate-limiting enzyme catalyzing the ATP-dependent carboxylation of pyruvate to oxaloacetate. Our findings demonstrate that EEB may have an antidepressant-like effect by enhancing the level of energy availability. Interestingly, we demonstrated that only EEB treatments increased PC expression and ATP level in mouse cerebrum, while treatment with imipramine was ineffective on both of these parameters.

It is reported that ATP can induce an increase of BDNF expression (Klein et al., 2012). In our study, we demonstrated that EEB significantly increased BDNF gene expression in mouse brain. BDNF is essential for neurogenesis and for the rearrangement of axonal arbors in the brain (Jeanneteau et al., 2010). Furthermore, it has been shown that the exogenous application of BDNF to hippocampal neurons alleviates the neurotoxic insult induced by corticosterone (Nitta et al., 1999). In our *in vitro* experiment, we confirmed that 200 μM corticosterone induced a significant decrease in the viability of PC12 cells. However, EEB attenuated the cell death induced by corticosterone. This result indicates a close functional relationship between BDNF and glucocorticoids, and may explain the important role of BDNF in the modulation of major depressive disorder. In addition to our findings, previous publications demonstrated that the promotion of neurogenesis in mouse hippocampus could be the mechanism underlying the antidepressant-like effect of some drugs (Ito et al., 2008). Moreover, it was shown that compounds with an antidepressant-like effect in animal models of chronic unpredicted stress restored the levels of BDNF expression in hippocampal neurons and astrocytes (Jin et al., 2013).

Our results from the microarray analysis also revealed that EEB treatment induced the overexpression of a few genes related to the process of neurogenesis (Shox2, Pitx2, Tshz1, and Lhx9). Shox2 plays an important role during cerebellar neurogenesis, by maintaining the proper balance of morphogen sonic hedgehog and bone morphogenetic protein (BMP) expression levels (Rosin et al., 2015). The Pitx2 gene product is necessary for the normal development of the subthalamic nucleus and its projections to the tegmentum, as well as for the development of the projections arising in the midbrain. Pitx2 protein is expressed in postmitotic neurons of the midgestation central nervous system, including GABAergic neurons of the future thalamus and midbrain, and neurons of the subthalamic nucleus (Martin et al., 2002). Moreover, Pitx2 is required to establish functional connectivity of these terminally differentiated neurons (Martin et al., 2004). Tshz1 is expressed in the developing olfactory bulb (OB) and the dorsolateral ganglionic eminence (Caubit et al., 2005). It is reported that the major function of Tshz1 in the OB is to maintain the expression of prokineticin receptor 2, a G protein-coupled receptor essential for OB development and related to prokineticin signaling (Ragancokova et al., 2014). Prokineticin signaling is involved in several biological processes, including nociception, circadian rhythm, and neurogenesis (Ng et al., 2005; Hu et al., 2006; Li et al., 2012). Lhx9 was isolated by degenerate RT-PCR followed by mouse embryonic library screening. Lhx9 is one of the typical marker genes of neurogenesis at the stage of immature neuronal cells (Peukert et al., 2011). These results suggest that EEB treatment induced the enhancement of neurogenesis through the promotion of energy production.

The results from our study showed that *B. braunii* has an antidepressant-like effect in ICR mice with FST-induced

depression. This microalga may contain proteins, carbohydrates, lipids, or bioactive molecules such as n-3 PUFA and carotenoids that exert an antidepressant-like effect. And, *B. braunii* produces carotenoids including β-carotene, lutein, violaxanthin, canthaxanthin, astaxanthin, and zeaxanthin (Ranga Rao et al., 2006, 2010). A number of reports have been published on studies in which attempts were made to elucidate the antidepressant effect of these active substances. For example, astaxanthin was shown to improve the impaired behavior in an animal model of autism, presumably by its antioxidant activity (Al-Amin et al., 2015). Additionally, n-3 PUFAs are under investigation for their possible use in the treatment and prevention of depression. An early study in rodents demonstrated that a reduction of dietary n-3 PUFA intake induced a decrease in the levels of nerve growth factor (NGF) in the hippocampus, and that NGF levels in different brain regions were affected differently by dietary n-3 PUFA deficiency and restoration (Ikemoto et al., 2000). Interestingly, meta-analysis of clinical trials using a combination of different types of n-3 PUFA, such as EPA and DHA, supplementation in patients with affective disorders and depression showed the therapeutic benefit of this combination for the amelioration of symptoms in patients affected by major depressive disorder (Grosso et al., 2014). Therefore, *B. braunii*, which is rich in n-3 PUFA and carotenoids, may be useful as a new therapeutic agent for depression. Further studies on the chemical composition of *B. braunii* will be necessary.

CONCLUSION

In summary, we report here for the first time evidence showing that *B. braunii* exerts an antidepressant-like effect in an animal model of depression. This appears to be mediated by the enhancement of energy promotion, neurogenesis, and dopamine synthesis in the brain. The observed effects of this alga showed in terms of significant differences compared with imipramine, a commercial antidepressant drug that was used as a positive control in this study, indicating a difference in the molecular mechanism underlying their antidepressant effects. These molecular mechanisms are currently not understood and will be the focus of our future research.

AUTHOR CONTRIBUTIONS

KS, MO, and HI conceived and designed the experiments; KS and MO performed the experiments; KS prepared the figures and tables; KS analyzed and interpreted the results, and wrote the paper; MD and MW provided *B. braunii*; and HI edited and revised the manuscript.

FUNDING

This study was supported by the Fukushima Algae Project.

ACKNOWLEDGMENTS

We wish to thank Hiroshi Kobayashi (ABES) for purification of the botryococcene.

We also wish to thank Shinji Kayano (Sobio Technologies Inc.), Hidenori Michikawa (Sobio Technologies Inc.), and Yuki Sakai (Sobio Technologies Inc.) for the cultivation of *B. braunii*.

REFERENCES

Al-Amin, M. M., Rahman, M. M., Khan, F. R., Zaman, F., and Mahmud Reza, H. (2015). Astaxanthin improves behavioral disorder and oxidative stress in prenatal valproic acid-induced mice model of autism. *Behav. Brain Res.* 286, 112–121. doi: 10.1016/j.bbr.2015.02.041

Albert, K. A., Hemmings, H. C. Jr., Adamo, A. I. B., Potkin, S. G., Akbarian, S., Sandman, C. A., et al. (2002). Evidence for decreased DARPP-32 in the prefrontal cortex of patients with schizophrenia. *Arch. Gen. Psychiatry* 59, 705–712. doi: 10.1001/archpsyc.59.8.705

Ben Othman, M., Han, J., El Omri, A., Ksouri, R., Neffati, M., and Isoda, H. (2013). Antistress effects of the ethanolic extract from *Cymbopogon schoenanthus* growing wild in Tunisia. *Evid. Based Complement. Alternat. Med.* 2013:737401. doi: 10.1155/2013/737401

Blunt, J. W., Copp, B. R., Keyzers, R. A., Munro, M. H. G., and Prinsep, M. R. (2015). Marine natural products. *Nat. Prod. Rep.* 32, 116–211. doi: 10.1039/C4NP00144C

Bouvier, N., Trenque, T., and Millart, H. (2003). Development of antidepressant drugs. experience and prospects. *Presse Med.* 32, 519–522.

Cardozo, K. H. M., Guaratini, T., Barros, M. P., Falcão, V. R., Tonon, A. P., Lopes, N. P., et al. (2007). Metabolites from algae with economical impact. *Comp. Biochem. Physiol. C Pharmacol. Toxicol.* 146, 60–78. doi: 10.1016/j.cbpc.2006.05.007

Caubit, X., Tiveron, M. C., Cremer, H., and Fasano, L. (2005). Expression patterns of the three teashirt-related genes define specific boundaries in the developing and postnatal mouse forebrain. *J. Comp. Neurol.* 486, 76–88. doi: 10.1002/cne.20500

Chen, H. W., Rainey, R. N., Balatoni, C. E., Dawson, D. W., Troke, J. J., Wasiak, S., et al. (2006). Mammalian polynucleotide phosphorylase is an intermembrane space RNase that maintains mitochondrial homeostasis. *Mol. Cell Biol.* 26, 8475–8487. doi: 10.1128/MCB.01002-06

Duchene, A. M., Pujol, C., and Marechal-Drouard, L. (2009). Import of tRNAs and aminoacyl-tRNA synthetases into mitochondria. *Curr. Genet.* 55, 1–18. doi: 10.1007/s00294-008-0223-9

Faulkner, D. J. (2001). Marine natural products. *Nat. Prod. Rep.* 18, 1–49. doi: 10.1039/B006897G

Fava, M. (2003). Diagnosis and definition of treatment-resistant depression. *Biol. Psychiatry* 53, 649–659. doi: 10.1016/S0006-3223(03)00231-2

Fu, A. L., Wu, S. P., Dong, Z. H., and Sun, M. J. (2006). A novel therapeutic approach to depression via supplement with tyrosine hydroxylase. *Biochem. Biophys. Res. Commun.* 351, 140–145. doi: 10.1016/j.bbrc.2006.10.013

Grosso, G., Pajak, A., Marventano, S., Castellano, S., Galvano, F., Bucolo, C., et al. (2014). Role of omega-3 fatty acids in the treatment of depressive disorders, a comprehensive meta-analysis of randomized clinical trials. *PLoS ONE* 9:e96905. doi: 10.1371/journal.pone.0096905

Guiry, M. D. (2012). How many species of algae are there? *J. Phycol.* 48, 1057–1063. doi: 10.1111/j.1529-8817.2012.01222.x

Hu, W. P., Zhang, C., Li, J. D., Luo, Z. D., Amadesi, S., Bunnett, N., et al. (2006). Impaired pain sensation in mice lacking prokineticin 2. *Mol. Pain.* 2:35. doi: 10.1186/1744-8069-2-35

Ikemoto, A., Nitta, A., Furukawa, S., Ohishi, M., Nakamura, A., Fujii, Y., et al. (2000). Dietary n-3 fatty acid deficiency decreases nerve growth factor content in rat hippocampus. *Neurosci. Lett.* 285, 99–102. doi: 10.1016/S0304-3940(00)01035-1

Isoda, H., Motojima, H., Margout, D., Neves, M., Han, J., Nakajima, M., et al. (2012). Antiallergic effect of picholine olive oil-in-water emulsions

through β-hexosaminidase release inhibition and characterization of their physicochemical properties. *J. Agric. Food Chem.* 60, 7851–7858. doi: 10.1021/jf3016078

Ito, N., Yabe, T., Gamo, Y., Nagai, T., Oikawa, T., Yamada, H., et al. (2008). Rosmarinic acid from Perillae herba produces an antidepressant-like effect in mice through cell proliferation in the hippocampus. *Biol. Pharm. Bull.* 31, 1376–1380. doi: 10.1248/bpb.31.1376

Jeanneteau, F., Deinhardt, K., Miyoshi, G., Bennett, A. M., and Chao, M. V. (2010). The MAP kinase phosphatase MKP-1 regulates BDNF-induced axon branching. *Nat. Neurosci.* 13, 1373–1379. doi: 10.1038/nn.2655

Jin, X., Liu, P., Yang, F., Zhang, Y. H., and Miao, D. (2013). Rosmarinic acid ameliorates depressive-like behaviors in a rat model of CUS and Up-regulates BDNF levels in the hippocampus and hippocampal-derived astrocytes. *Neurochem. Res.* 38, 1828–1837. doi: 10.1007/s11064-013-1088-y

Kamenski, P., Kolesnikova, O., Jubenot, V., Entelis, N., Krasheninnikov, I. A., Martin, R. P., et al. (2007). Evidence for an adaptation mechanism of mitochondrial translation via tRNA import from the cytosol. *Mol. Cell.* 26, 625–637. doi: 10.1016/j.molcel.2007.04.019

Klein, K., Aeschlimann, A., Jordan, S., Gay, R., Gay, S., and Sprott, H. (2012). ATP induced brain-derived neurotrophic factor expression and release from osteoarthritis synovial fibroblasts is mediated by purinergic receptor P2X4. *PLoS ONE.* 7:e36693. doi: 10.1371/journal.pone.0036693

Li, J. D., Hu, W. P., and Zhou, Q. Y. (2012). The circadian output signals from the suprachiasmatic nuclei. *Prog. Brain Res.* 199, 119–127. doi: 10.1016/B978-0-444-59427-3.00028-9

Li, Z., He, Y., Tang, J., Zong, X., Hu, M., and Chen, X. (2015). Molecular imaging of striatal dopamine transporters in major depression - a meta-analysis. *J. Affect. Disord.* 174, 137–143. doi: 10.1016/j.jad.2014.11.045

Liu, W., Sheng, H., Xu, Y., Liu, Y., Lu, J., and Ni, X. (2013). Swimming exercise ameliorates depression-like behavior in chronically stressed rats, relevant to proinflammatory cytokines and IDO activation. *Behav. Brain Res.* 242, 110–116. doi: 10.1016/j.bbr.2012.12.041

Lu, S. H., Guo, J., Cai, C., Liang, X. B., Guan, J. H., Peng, X., et al. (2015). Effects of kaixin powder on expression of 5-HT receptor in hippocampus of depressed rats induced by CUMS. *Chin. Herb. Med.* 7, 150–154. doi: 10.1016/S1674-6384(15)60031-4

Martin, D. M., Skidmore, J. M., Fox, S. E., Gage, P. J., and Camper, S. A. (2002). Pitx2 distinguishes subtypes of terminally differentiated neurons in the developing mouse neuroepithelium. *Dev. Biol.* 252, 84–99. doi: 10.1006/dbio.2002.0835

Martin, D. M., Skidmore, J. M., Philips, S. T., Vieira, C., Gage, P. J., Condie, B. G., et al. (2004). PITX2 is required for normal development of neurons in the mouse subthalamic nucleus and midbrain. *Dev. Biol.* 267, 93–108. doi: 10.1016/j.ydbio.2003.10.035

Ng, K. L., Li, J. D., Cheng, M. Y., Leslie, F. M., Lee, A. G., and Zhou, Q. Y. (2005). Dependence of olfactory bulb neurogenesis on prokineticin 2 signaling. *Science* 308, 1923–1927. doi: 10.1126/science.1112103

Nieoullon, A., and Coquerel, A. (2003). Dopamine: a key regulator to adapt action, emotion, motivation and cognition. *Curr. Opin. Neurol.* 16(Suppl. 2), S3–S9. doi: 10.1097/00019052-200312002-00002

Nitta, A., Ohmiya, M., Sometani, A., Itoh, M., Nomoto, H., Furukawa, Y., et al. (1999). Brain-derived neurotrophic factor prevents neuronal cell death induced by corticosterone. *J. Neurosci. Res.* 57, 227–235. doi: 10.1002/(SICI)1097-4547(19990715)57:2<227::AID-JNR8>3.0.CO;2-E

Norton, T. A., Melkonian, M., and Andersen, R. A. (1996). Algal biodiversity. *Phycologia* 35, 308–326. doi: 10.2216/i0031-8884-35-4-308.1

Pangestuti, R., and Kim, S. K. (2011). Biological activities and health benefit effects of natural pigments derived from marine algae. *J. Funct. Foods* 3, 255–266. doi: 10.1016/j.jff.2011.07.001

Patwari, P., Chutkow, W. A., Cummings, K., Verstraeten, V. L. R. M., Lammerding, J., Schreiter, E. R., et al. (2009). Thioredoxin-independent regulation of metabolism by the α-arrestin proteins. *J. Biol. Chem.* 284, 24996–25003. doi: 10.1074/jbc.M109.018093

Perkins, K. A., Lerman, C., Grottenthaler, A., Ciccocioppo, M. M., Milanak, M. E., Conklin, C. A., et al. (2008). Dopamine and opioid gene variants are associated with increased smoking reward and reinforcement owing to negative mood. *Behav. Pharmacol.* 19, 641–649. doi: 10.1097/FBP.0b013e32830c367c

Peukert, D., Weber, S., Lumsden, A., and Scholpp, S. (2011). Lhx2 and Lhx9 determine neuronal differentiation and compartition in the caudal forebrain by regulating Wnt signaling. *PLoS Biol.* 9:e1001218. doi: 10.1371/journal.pbio.1001218

Porsolt, R. D., Bertin, A., and Jalfre, M. (1978). "Behavioral despair" in rats and mice, strain differences and the effects of imipramine. *Eur. J. Pharmacol.* 51, 291–294. doi: 10.1016/0014-2999(78)90414-4

Potkin, S. G., Turner, J. A., Fallon, J. A., Lakatos, A., Keator, D. B., Guffanti, G., et al. (2009). Gene discovery through imaging genetics, identification of two novel genes associated with schizophrenia. *Mol. Psychiatry* 14, 416–428. doi: 10.1038/mp.2008.127

Ragancokova, D., Rocca, E., Oonk, A. M., Schulz, H., Rohde, E., et al. (2014). TSHZ1-dependent gene regulation is essential for olfactory bulb development and olfaction. *J. Clin. Invest.* 124, 1214–1227. doi: 10.1172/JCI72466

Ranga Rao, A., Sarada, R., Baskaran, V., and Ravishankar, G. A. (2006). Antioxidant activity of *Botryococcus braunii* extract elucidated *in vitro* models. *J. Agric. Food Chem.* 54, 4593–4599. doi: 10.1021/jf060799j

Ranga Rao, A., Sarada, R., and Ravishankar, G. A. (2010). Enhancement of carotenoids in green alga-*Botryococcus braunii* in various autotrophic media under stress conditions. *Int. J. Pharm. Bio Sci.* 4, 87–92.

Reininghaus, E. Z., Reininghaus, B., Ille, R., Fitz, W., Lassnig, R. M., Ebner, C., et al. (2013). Clinical effects of electroconvulsive therapy in severe depression and concomitant changes in cerebral glucose metabolism-an exploratory study. *J. Affect. Disord.* 146, 290–294. doi: 10.1016/j.jad.2012.07.034

Rosin, J. M., McAllister, B. B., Dyck, R. H., Percival, C. J., Kurrasch, D. M., and Cobb, J. (2015). Mice lacking the transcription factor SHOX2 display impaired cerebellar development and deficits in motor coordination. *Dev. Biol.* 399, 54–67. doi: 10.1016/j.ydbio.2014.12.013

Samet, I., Villareal, M. O., Motojima, H., Han, J., Sayadi, S., and Isoda, H. (2015). Olive leaf components apigenin 7-glucoside and luteolin 7-glucoside direct human hematopoietic stem cell differentiation towards erythroid lineage. *Differentiation* 89, 146–155. doi: 10.1016/j.diff.2015.07.001

Sasaki, K., El Omri, A., Kondo, S., Han, J., and Isoda, H. (2013). *Rosmarinus officinalis* polyphenols produce anti-depressant like effect through monoaminergic and cholinergic functions modulation. *Behav. Brain Res.* 238, 86–94. doi: 10.1016/j.bbr.2012.10.010

Shahidi, F., and Janak Kamil, Y. V. A. (2001). Enzymes from fish and aquatic invertebrates and their application in the food industry. *Trends Food Sci. Technol.* 12, 435–464. doi: 10.1016/S0924-2244(02)00021-3

Shen, J. W., and Liang, Z. J. (2007). Advances in research on biological etiology of depression and the antidepressants. *Pharm Care Res.* 7, 94–99.

Smirnov, A., Entelis, N., Martin, R. P., and Tarassov, I. (2011). Biological significance of 5S rRNA import into human mitochondria, role of ribosomal protein MRP-L18. *Genes Dev.* 25, 1289–1305. doi: 10.1101/gad.624711

Svenningsson, P., Tzavara, E. T., Witkin, J. M., Fienberg, A. A., Nomikos, G. G., and Greengard, P. (2002). Involvement of striatal and extrastriatal DARPP-32 in biochemical and behavioral effects of fluoxetine (Prozac). *Proc. Natl. Acad. Sci. U.S.A.* 99, 3182–3187. doi: 10.1073/pnas.052712799

Tarassov, I., Kamenski, P., Kolesnikova, O., Karicheva, O., Martin, R. P., Krasheninnikov, I. A., et al. (2007). Import of nuclear DNA- encoded RNAs into mitochondria and mitochondrial translation. *Cell Cycle* 6, 2473–2477. doi: 10.4161/cc.6.20.4783

Vander Heiden, M. G., Cantley, L. C., and Thompson, C. B. (2009). Understanding the Warburg effect, the metabolic requirements of cell proliferation. *Science* 324, 1029–1033. doi: 10.1126/science.1160809

Wise, R. A. (2004). Dopamine, learning and motivation. *Nat. Rev. Neurosci.* 5, 483–494. doi: 10.1038/nrn1406

Conflict of Interest Statement: The authors declare that the research was conducted in the absence of any commercial or financial relationships that could be construed as a potential conflict of interest.

Copyright © 2017 Sasaki, Othman, Demura, Watanabe and Isoda. This is an open-access article distributed under the terms of the Creative Commons Attribution License (CC BY). The use, distribution or reproduction in other forums is permitted, provided the original author(s) or licensor are credited and that the original publication in this journal is cited, in accordance with accepted academic practice. No use, distribution or reproduction is permitted which does not comply with these terms.

frontiers in Neurology

SYSTEMATIC REVIEW
published: 22 December 2017
doi: 10.3389/fneur.2017.00702

A Meta-Analysis of Adenosine A2A Receptor Antagonists on Levodopa-Induced Dyskinesia *In Vivo*

Wen-Wen Wang[1†], Man-Man Zhang[2†], Xing-Ru Zhang[2], Zeng-Rui Zhang[2], Jie Chen[2], Liang Feng[2] and Cheng-Long Xie[2*]*

[1] The Center of Traditional Chinese Medicine, The Second Affiliated Hospital, Yuying Children's Hospital of Wenzhou Medical University, Wenzhou, China, [2] Department of Neurology, The First Affiliated Hospital of Wenzhou Medical University, Wenzhou, China

Background: Long-term use of levodopa (L-dopa) is inevitably complicated with highly disabling fluctuations and drug-induced dyskinesias, which pose major challenges to the existing drug therapy of Parkinson's disease.

Methods: In this study, we conducted a systematic review and meta-analysis to assess the efficacy of A2A receptor antagonists on reducing L-dopa-induced dyskinesias (LID).

Results: Nine studies with a total of 152 animals were included in this meta-analysis. Total abnormal involuntary movements (AIM) score, locomotor activity, and motor disability were reported as outcome measures in 5, 5, and 3 studies, respectively. Combined standardized mean difference (SMD) estimates were calculated using a random-effects model. We pooled the whole data and found that, when compared to L-dopa alone, A2A receptor antagonists plus L-dopa treatment showed no effect on locomotor activity (SMD −0.00, 95% confidence interval (CI): −2.52 to 2.52, $p = 1.0$), superiority in improvement of motor disability (SMD −5.06, 95% CI: −9.25 to −0.87, $p = 0.02$) and more effective in control of AIM (SMD −1.82, 95% CI: −3.38 to −0.25, $p = 0.02$).

Conclusion: To sum up, these results demonstrated that A2A receptor antagonists appear to have efficacy in animal models of LID. However, large randomized clinical trials testing the effects of A2A receptor antagonists in LID patients are always warranted.

Keywords: adenosine, A2A receptor antagonists, levodopa-induced dyskinesia, Parkinson's disease, meta-analysis

OPEN ACCESS

Edited by:
Mikhail Lebedev, Duke University, United States

Reviewed by:
Luigi Bubacco, Università degli Studi di Padova, Italy
Emma Louise Lane, Cardiff University, United Kingdom

***Correspondence:**
Liang Feng
fengliangyw@126.com;
Cheng-Long Xie
cl_xie1987@sohu.com

[†]These authors have contributed equally to this work.

Specialty section:
This article was submitted to Neurodegeneration, a section of the journal Frontiers in Neurology

Received: *08 December 2016*
Accepted: *06 December 2017*
Published: *22 December 2017*

Citation:
Wang W-W, Zhang M-M, Zhang X-R, Zhang Z-R, Chen J, Feng L and Xie C-L (2017) A Meta-Analysis of Adenosine A2A Receptor Antagonists on Levodopa-Induced Dyskinesia In Vivo. Front. Neurol. 8:702. doi: 10.3389/fneur.2017.00702

INTRODUCTION

Parkinson's disease (PD) is defined by a set of motor signs and symptoms that are caused by selective degeneration of the dopamine (DA) neurons, which originate in the substantia nigra pars compacta and project into the striatum (1). The most efficacious treatment for PD is the DA precursor levodopa (L-dopa), which not only improves all typical parkinsonian motor symptoms but also increases patients' life expectancy (2). However, the long-term use of L-dopa produces motor complications which include highly disabling fluctuations and L-dopa-induced dyskinesias (LID), representing the major challenges to the existing drug therapy of PD (3, 4). The management of LID includes switching to a controlled-release L-dopa or adding a COMT inhibitor/monoamineoxidase B inhibitor/a

longer acting DA agonist (5). However, once LID is established, the increase in dopaminergic load resulted from these strategies can only lead to an aggravation of the condition, not only in the severity but also the duration (6). Moreover, recent researches have revealed that a wide series of non-dopaminergic neurotransmitter systems (glutamatergic, serotoninergic, adrenergic, and cholinergic, etc.) are involved in pre- and postsynaptic changes and thereby contributing to the pathophysiology of LID (5). Based on such therapies, many drugs are available in the market to treat disabling LID, but potential side effects have limited their clinical use (7).

The general pathophysiological interpretation and various hypotheses have been discussed for the genesis and development of LID. However, the exact mechanisms and the molecular targets are still poorly understood (8). Adenosine is believed to play a neuroprotective role in central neurodegenerative disorders and its actions are mediated by different receptors such as A1, A2A, A2B, and A3 (9). It has been suggested that A2A receptors are highly localized to the basal ganglia nuclei of the indirect output pathway, where they are co-localized with DA D2 receptors, and may be capable of influencing motor activity by acting at different levels (10). It is hypothesized that the effects of adenosine A2A receptor antagonists on motor function is attributed to their inhibitory function on neurons of the indirect pathway that expressing both A2A and D2 receptors (10). Moreover, inactivation A2A receptors on striatopallidal neurons of the indirect pathway can produce a parallel behavioral activation by means of mimicking the motor stimulant actions of co-localized D2 receptors on these neurons (11). Preclinical behavioral investigations reported that pharmacological antagonism or genetic knockdown of A2A receptors may be of interest to the management of LID (12). Furthermore, results from clinical studies had also shown that A2A receptor antagonists' significantly reduced off-time as an adjunctive therapy to L-dopa in advanced PD patients with motor fluctuations, also suggesting a possible reduced risk of L-dopa-induced motor complications (13). However, to date, few clinical trials have tested the benefits of A2A antagonists in LID patients. Limited clinical data demonstrate the possibility that in PD patients with established dyskinesia, we might be able to maintain the anti-parkinsonian response and reduce dyskinesia by adding an A2A antagonist and lowering the L-dopa dose, though this remains to be proven (14).

Systematic reviews and meta-analyses of preclinical animal data could facilitate the planning of further investigations and improve the likelihood of success of future clinical trials, also identify where there is a need for further experiment research, preclude unnecessary study replication, and contribute to both reduction and refinement in animal experimentation (15). Therefore, we report a systematic review and meta-analysis of adenosine A2A receptor antagonists in experimental models of PD with LID.

MATERIALS AND METHODS

The whole process and methods of this meta-analysis were performed according to our previous published paper (16) and based on the modified Preferred Reporting Items for Systematic Reviews and Meta-Analyses (PRISMA) Statement.

Search Strategy

We electronically searched three databases (PubMed, Google scholar, and EMBASE database) up to January 2016 for all publications written in English. All searches were limited to studies on animals. Reference lists from the included literature were scrutinized to identify further relevant publications. The search strategy as follows:

1. adenosine
2. adenocard
3. adenoscan
4. or/1–3
5. dyskinesia
6. abnormal
7. involuntary movements
8. hemiballismus
9. or/5–8
10. 4 and 9

Inclusion and Exclusion Criteria

Inclusion criteria:

(1) Test the effects of adenosine A2A receptor antagonists on LID in animal models of PD. Adenosine A2A receptor antagonists are defined as a drug with reported agonism on at least one class of A2A receptor irrespective of actions at other receptor classes.
(2) Use abnormal involuntary movements (AIM) or neurobehavioral score as the outcome measure comparing LID animals receiving combined treatment (both adenosine A2A receptor antagonists and L-dopa) and L-dopa/benserazide or L-dopa/carbidopa alone. AIM ratings were performed as we previously described (17). Briefly, 0 = absent, 1 = present less than 50% of the observation period, 2 = present more than 50% of the observation time, 3 = present all the times but suppressible by external stimuli, and 4 = present all the times and not interfering by external stimuli.
(3) Original data being independent of other studies.

Pre-specified exclusion criteria were: (1) case reports, abstracts, comments, reviews, editorials, and clinical trials; (2) dyskinesia was not developed by long-term L-dopa; (3) not testing the efficacy of adenosine receptor antagonists on LID; and (4) AIM or neurobehavioral score was not the outcome measure.

Data Extraction

From included studies, data listed out as follows were extracted using a comprehensive approach: (1) the first author's name and publication year, experimental models [1-methyl-4-phenyl-1, 2,3,6-tetrahydropyridine (MPTP) models or 6-Hydroxydopamine (6-OHDA) models, etc.]; (2) individual data for each animal including number, species, sex, weight, and anesthetic used; (3) information on treatment including route of administration and

dosage; and (4) outcome measures and time of assessment of outcomes. If outcomes were presented at different time points, we extracted data from the last one reported. If the data for meta-analysis were missing or only expressed graphically, we tried to contact the authors for further information, or calculate by ourselves using digital ruler software, or excluded the study which we could not get enough information. For each comparison, we extracted data of mean value and standard deviation from treatment and control group, respectively, of each study.

Quality Assessment

Study quality was evaluated based on a six-item modified scale (18): peer-reviewed publication, random allocation to groups, blinded assessment of outcome, sample size calculation, compliance with animal welfare regulations, and a statement of a potential conflict of interest. For the calculation of an aggregate quality score, each item of the six-item modified scale was attributed one point. Two authors (Cheng-Long Xie and Jie Chen) independently extracted data and assessed study quality. Disagreements were solved after discussion on the details of the studies.

Statistical Analysis

We utilized a random-effects model because it took into account the fact that the true treatment effects had likely varied among the included trials. We conceived the main outcome measures as continuous data, and were given an estimate of the combined overall effect sizes using standardized mean difference (SMD) and its standard error, with 95% confidence interval (CI). To pool different scales, we used the SMD as the summary statistic in our meta-analysis as it reveals the effect size of the treatment relative to the variability observed in the same study (19). For the assessment of heterogeneity, the I^2 statistic was used. To assess the stability of the results, a sensitivity analysis was performed by removing each individual study in turn from the total and reanalyzing the remainder. Meanwhile, we performed a stratified meta-analysis with experiments grouped according to different kinds of adenosine A2A receptor antagonists. All the analyses were done with Revman software 5.0. Probability value $p < 0.05$ was considered significant.

RESULTS

Results of the Search

From the electronic search, 621 publications were initially identified, from which we excluded 456 due to repetition. After screening the titles and abstracts, 108 were further excluded because they failed to meet the inclusion criteria. By reading the full text of the remaining 57 articles, 40 studies were excluded as a result of not testing the efficacy of adenosine A2A receptor antagonists on LID ($n = 21$), inappropriate outcome indicators ($n = 14$), and the problem of duplicate data ($n = 7$). Another eight studies were excluded as the dyskinesia presented was not developed by long-term L-dopa. Ultimately, nine eligible studies were identified (12, 20–27) (**Figure 1**).

Study Characteristics

These studies involved 152 animals (A2A receptor antagonists 83, control 69) from three species: Mice ($n = 53$), Sprague-Dawley rats ($n = 67$), and Marmosets ($n = 32$), respectively. The studies varied in size, ranging from 8 to 36 animals. Three out of nine (3/9, 33.3%) studies were MPTP models, while the remaining utilized the 6-OHDA models (6/9, 66.7%). The studies were published between 2000 and 2014. These studies included animals of both sexes ($n = 4$), [22,23,24,25] male only ($n = 3$), [18,19,23] female only ($n = 1$), [21] and gender not reported ($n = 1$) (12). To induce LID in PD model, animals were treated, once parkinsonism was stable, with twice-daily administration of L-dopa (2–25 mg/kg, i.p.) plus benserazide/carbidopa (2.5–15 mg/kg, i.p.) for several weeks, ranging from 16 days to 8 weeks. KW-6002 as the A2A receptor antagonist was reported in four studies (12, 20, 21, 27), ST1535 (22, 23) in two, Caffeine (24, 25) in two, and SCH 412348 (26) in one study. Meanwhile, total AIM score, locomotor activity, and motor disability were reported as a outcome measure in 5, 5, and 3 studies, respectively. The basic characteristics of the nine selected studies are summarized in **Table 1**.

Risk of Bias

Of whom, one study got 6 points (1/9, 11.1%), four studies got 5 (4/9, 44.4%), three studies got 4 (3/9, 33.3%), and one study got 3 (1/9, 11.1%). Only one study described a sample size calculation. Random allocation to a treatment group and blinded assessment of outcome were described in seven studies. Eight studies mentioned the statement of potential conflict of interests. All studies reported compliance with animal welfare regulations (**Table 2**). Generally, all of the included studies were deemed to have a low risk of bias.

Meta-Analyses

All the data for meta-analysis were expressed graphically. We used digital ruler software to calculate the mean and standard error. In the present paper, five studies reported the locomotor activity as the outcome measure with 67 animals were included in the final meta-analyses. We pooled the whole data and found no significant difference between A2A receptor antagonists plus L-dopa treatment and L-dopa alone (SMD −0.00, 95% CI: −2.52 to 2.52, $p = 1.0$, **Figure 2A**). Meanwhile, there was obvious heterogeneity for the analysis of locomotor activity between studies ($Tau^2 = 7.16$, $Chi^2 = 42.62$, $p < 0.00001$, $I^2 = 87\%$, **Figure 2A**). After sequentially excluding each study, the results of heterogeneity and locomotor activity were consistent (I^2 range from 80 to 92%; $p = 0.56$ to $1.53 > 0.05$, respectively). Consequently, we should interpret the pool result prudently.

Three studies reported mild significant effects of A2A receptor antagonists plus L-dopa treatment for improving motor disability compared with L-dopa alone (SMD −5.06, 95% CI: −9.25 to −0.87, $p = 0.02$, **Figure 2B**). Nevertheless, there was severe heterogeneity for the analysis of motor disability between studies ($Tau^2 = 10.90$, $Chi^2 = 10.90$, $p = 0.004$, $I^2 = 82\%$, **Figure 2B**). Removal of the outlier studies (22) led to more homogeneous results ($Tau^2 = 0.00$, $Chi^2 = 0.19$, $p = 0.66$, $I^2 = 0\%$), as well as increased the effect size by −2.18, yielding a still significant pooled SMD of −7.24.

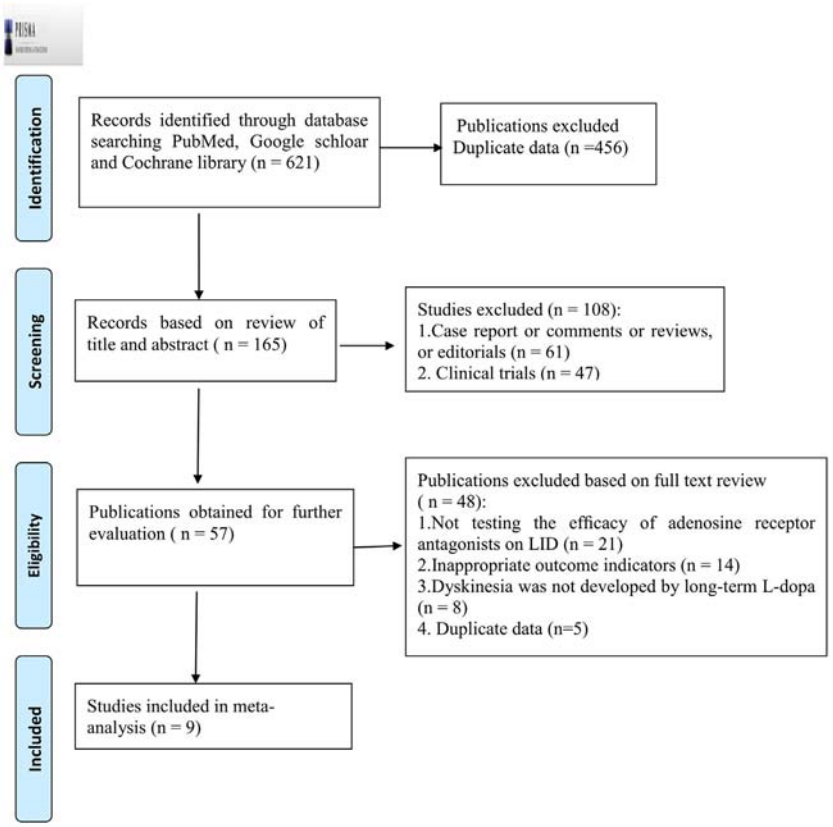


FIGURE 1 | PRISMA 2009 Flow Diagram of trial identification, inclusion, and exclusion. LID, levodopa-induced dyskinesia.

Total AIM was reported by five trials, the result showed a significant difference in the reduction of the score between the A2A receptor antagonists plus L-dopa treatment and L-dopa alone (SMD −1.82, 95% CI: −3.38 to −0.25, $p = 0.02$, **Figure 2C**). Nevertheless, inspection of the data showed that the heterogeneity for the analysis of total AIM between studies was high ($Tau^2 = 2.74$, $Chi^2 = 37.38$, $p < 0.00001$, $I^2 = 89\%$). After sequentially excluding each study, the results of heterogeneity were consistent with the previous result. The remaining four studies (20, 22, 23, 27) failed to enter the pool analysis due to the lack of a Total AIM, one using limb and axial AIM to reflect LID, two using locomotor activity as the outcome measures, and the last one not reporting the criteria to assess the dyskinesia. Funnel plots were not applied to test the publication bias in this paper as the numbers of included studies were small.

Subgroup Analysis

In the subgroup analysis focusing on locomotors activity, the efficacy of KW-6002 was similar with ST1535 (SMD −0.58, 95% CI: −4.85 to 3.69, $p = 0.79$; SMD 0.88, 95% CI: −4.08 to 5.85, $p = 0.73$, respectively, **Figure 3**). Moreover, in terms of total AIM score, efficacy was observed to be higher with the administration of Caffeine than KW-6002 or SCH 412348 (SMD −2.14, 95% CI: −3.86 to −0.41, $p = 0.02 < 0.05$; SMD −2.57, 95% CI: −8.37 to 3.24, $p = 0.39$; SMD −0.55, 95% CI: −1.71 to 0.61, $p = 0.93$, respectively, **Figure 4**).

DISCUSSION

Summary of Main Results

This meta-analysis demonstrated that A2A receptor antagonists substantially reduced total AIM in animal models of LID. Meanwhile, we found A2A receptor antagonists plus L-dopa has similar anti-parkinsonism effects on the locomotors activity and motor disability scores when compared with L-dopa alone. Based on the subgroup analysis, the results showed that effect size of KW-6002 on the locomotors activity in animals was similar with ST1535. Moreover, we found that animals who received Caffeine showed remarkable improvement on the total AIM score compared with KW-6002 or SCH 412348. The improvement in LID behavior without an impact of motor function is highly significant as it differentiates A2A receptor antagonists from the known effects of dopaminergic therapies.

We conducted a preclinical animal meta-analysis for a better understanding and also to facilitate the conversion of experimental evidence to future clinical trials. With such aim, 6-OHDA and MPTP models were chosen as the pathophysiological model as they were closer to human LID. The analysis of A2A receptor

TABLE 1 | Basic characteristics of the included studies.

Reference	Species, weight, anesthetic	Model (Parkinson's disease/L-dopa-induced dyskinesias)	Intervention	Outcome index	*p*-Value
6-0HDA models					
Lundblad et al. (21)	SD rats (female, 9/10), 225 g, NR	Unilateral 6-OHDA (8 μg/3 μl) lesioned; L-dopa (4 mg/kg)/carbidopa (12 mg/kg) for 16 days	KW-6002 (3 and 10 ml/kg, p.o.) for 16 days	1. Rotarod performance 2. Total AIM	1. $p > 0.05$ 2. $p < 0.05$
Danqing (12)	Mice (NR,10/7), NR, avertin	Unilateral 6-OHDA (8 μg/4 μl) lesioned; L-DOPA (2 mg/kg)/benserazide (2 mg/kg) for 21 days	KW-6002 (0.03 mg/kg and 0.3 mg/kg, i.p.) for 21 days	1. Locomotor Activity 2. Total AIM	1. $p > 0.05$ 2. $p < 0.05$
Elisabetta (23)	SD rats (male, 8/8), 275–300 g, chloral hydrate	Unilateral 6-OHDA (8 μg/4 μl) lesioned; L-DOPA (3 mg/kg)/benserazide (6 mg/kg) for 18 days	ST1535 (20 mg/kg, p.o.) for 18 days	1. Locomotor Activity 2. limb and axial AIM	1. $p > 0.05$ 2. $p < 0.05$
Yi-xian (24)	SD rats (male, 10/10), 180–220 g, chloral hydrate	Unilateral 6-OHDA (8 μg/4 μl) lesioned; L-dopa (25 mg/kg)/benserazide (6.25 mg/kg) for 21 days	Caffeine (2.5 mg/kg, i.p.) for 21 days	1. Rotational response 2. Total AIM, limb AIM 3. Orolingual AIM	1. $p > 0.05$ 2. $p < 0.05$ 3. $p < 0.05$
Danqing (25)	Mice (both sex, 24/12), NR, avertin	Unilateral 6-OHDA (10 μg/4 μl) lesioned; L-dopa (2 mg/kg)/benserazide (2 mg/kg) for 21 days	Caffeine (3 and 15 mg/kg, i.p.) for 21 days	1. Total AIM	1. $p < 0.05$
Jones et al. (26)	SD rats (male, 6/6), 350–400 g, NR	Unilateral 6-OHDA (8 μg/4 μl) lesioned; L-dopa (6 mg/kg)/benserazide (15 mg/kg) for 22 days	SCH 412348 (3 mg/kg, i.p.) for 22 days	1. Catalepsy 2. Total AIM	1. $p > 0.05$ 2. $p > 0.05$
MPTP models					
Tomoyuki (20)	Marmosets (both sex, 4/4), 285–420 g, NR	MPTP 2.0 mg/kg sc for 5 days; L-dopa (12.5 mg/kg)/carbidopa (12.5 mg/kg) for 21 days	KW-6002 (10 ml/kg, p.o.) for 21 days	1. Locomotor Activity 2. Motor disability	1. $p > 0.05$ 2. $p < 0.05$
Sarah (22)	Marmosets (both sex, 4/4), 265–437 g, NR	MPTP 2.0 mg/kg sc for 5 days; L-dopa (2.5 mg/kg)/carbidopa (12.5 mg/kg) for 8 weeks	ST1535 (20 mg/kg, p.o.) for 8 weeks	1. Locomotor Activity 2. Motor disability	1. $p > 0.05$ 2. $p < 0.05$
Shin-ichi (27)	Marmosets (both sex, 8/8), 285–420 g, NR	MPTP 2.0 mg/kg sc for 5 days; L-dopa (10 mg/kg)/carbidopa (2.5 mg/kg) for 28 days	KW-6002 (10 mg/kg, p.o.) for 28 days	1. Locomotor Activity 2. Motor disability	1. $p > 0.05$ 2. $p < 0.05$

AIM, abnormal involuntary movements; SD rats, Sprague-Dawley rats; 6-OHDA, 6-hydroxydopamine; NR, no report; MPTP, 1-methyl-4-phenyl-1, 2, 3, 6-tetrahydropyridine; MFB, medial forebrain bundle; L-dopa, levodopa.

TABLE 2 | Risk of bias of included studies.

Reference	Tomoyuki (20)	Lundblad (21)	Danqing (12)	Sarah (22)	Elisabetta (23)	Yi-xian (24)	Danqing (25)	Jones et al. (26)	Shin-ichi (27)
A	Y	Y	Y	Y	Y	Y	Y	Y	Y
B	Y	Y	Y	N	Y	Y	N	Y	Y
C	N	Y	Y	Y	Y	N	Y	Y	Y
D	N	N	Y	N	N	N	N	N	N
E	Y	Y	Y	Y	Y	Y	Y	Y	Y
F	Y	Y	Y	N	Y	Y	Y	Y	Y
Total	4	5	6	3	5	4	4	5	5

Studies fulfilling the criteria of: A: peer-reviewed publication; B: random allocation to group; C: blinded assessment of outcome; D: a sample size calculation; E: compliance with animal welfare regulations; and F: a statement of a potential conflict of interest. Y, yes; N, no.

antagonists in LID could be of great interest for future studies. However, these findings have to be interpreted with caution, because only a few different A2A receptor antagonists' studies were tested in this paper. Nevertheless, the present results reinforced the neuroprotective role of A2A receptor antagonists in experimental LID models, but we did not sure whether it reliably informed human studies. Undoubtedly, further evidence was required to confirm this efficacy in human.

To date, alternative to modification of L-dopa therapy to avoid LID may resort to non-dopaminergic strategies of the indirect pathway of the basal ganglia. One possible strategy is to inactivate the A2A receptors (28). It has been displayed that the expression of adenosine A2A receptors was increased following L-dopa treatment and the appearance of AIM or LID as shown by biochemical, post-mortem, and imaging investigations, suggesting that inhibitation of A2A receptors is helpful for LID. Moreover, numerous preclinical studies have reported that A2A receptor antagonists might hinder the development of LID, which are consistent with this review (29). Moreover, clinical trials have showed that oral administration A2A antagonists increase functional on-time duration in PD patients suffering from wearing-off phenomenon (less effective than DBS or L-dopa continuous infusion), although they may increase dyskinesia in patients with advanced PD (14). Thus, critical aspects of the potential function of A2A antagonists on LID patients are yet to be evaluated.

Interpretation of the Results

The interaction between adenosine A2A and D2 DA receptors has recently attracted much attention as a possible therapeutic target in LID (30). In addition, an increase in adenosine A2A receptor was observed in the striatum of dyskinetic primate's models (31). A2A receptors were reported to adjust the activity of the indirect

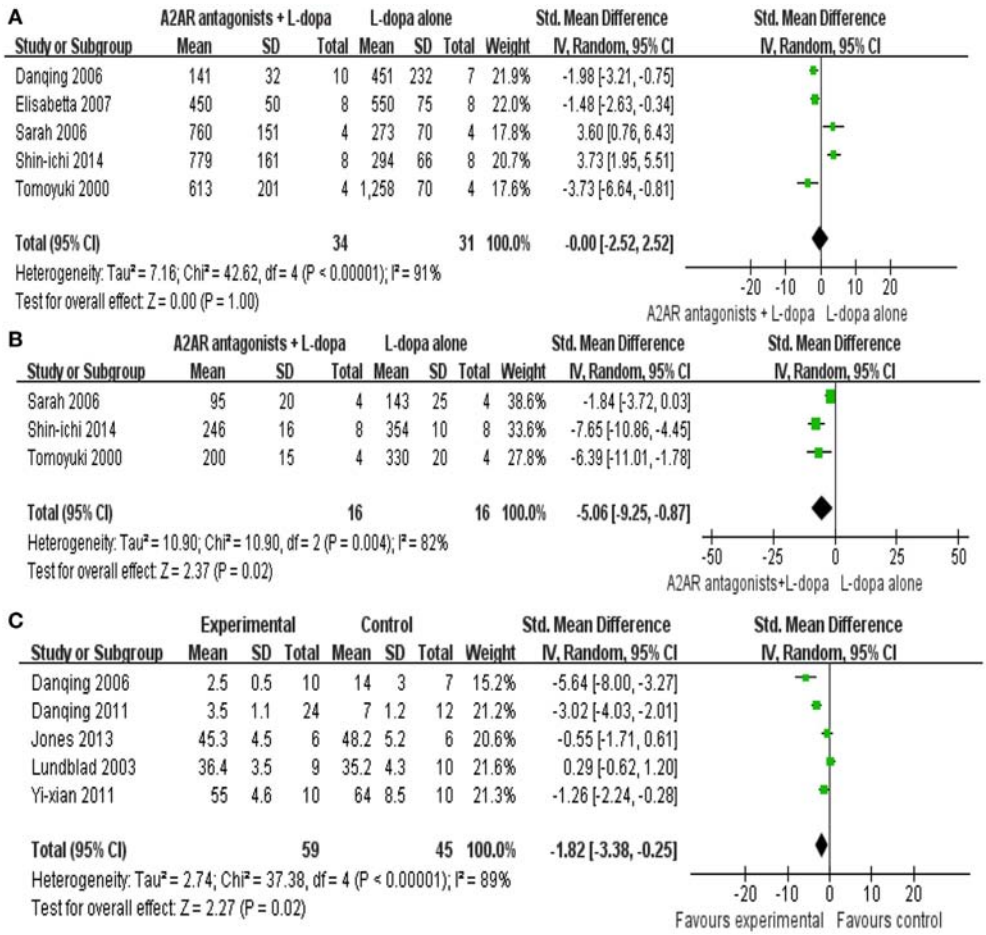


FIGURE 2 | Total effect size of A2A receptor antagonists on locomotor activity score **(A)** reduction including 65 animals in five comparisons, motor disability score outcome **(B)** improvement (32 animals in three comparisons) and total abnormal involuntary movements (AIM) score **(C)** comprising 104 animals in five comparisons.

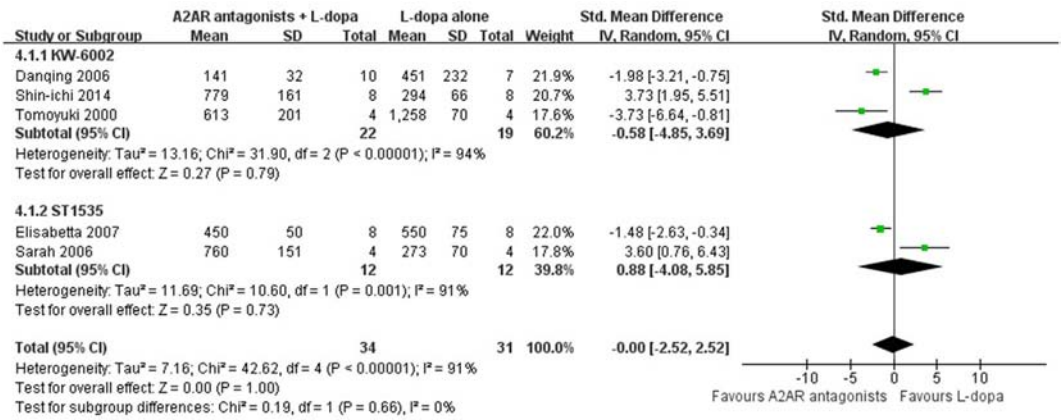


FIGURE 3 | Subgroup analysis: the impact of different classes of A2A receptor antagonists (KW-6002 and ST1535) on the estimate of improvement in locomotor activity score outcome.

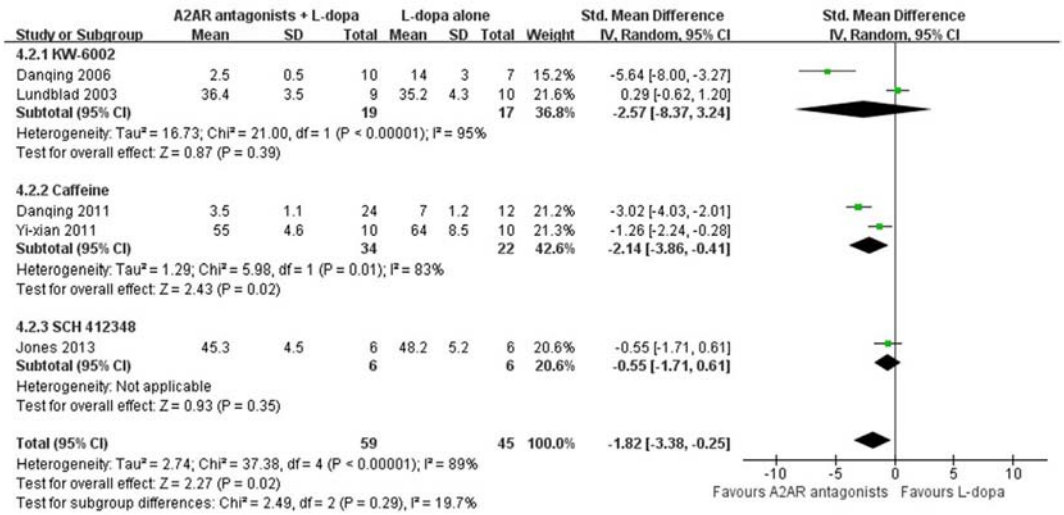


FIGURE 4 | Subgroup analysis: the impact of different classes of A2A receptor antagonists (KW-6002, caffeine and SCH 412348) on the estimate of decrement in total abnormal involuntary movements (AIM) score outcome.

pathway and modulate acetylcholine and glutamate release in the striatum, where they form functional heteromeric complexes with D2 receptors (10). Namely, agonists of A2A receptors inhibit the binding of DA to D2 receptors and have been shown to inhibit D2-mediated neurotransmitter release. On the other hand, evidence shows that A2A receptors antagonists mimic the effects of D2 agonists (29). Interestingly, recent evidence demonstrates that A2A receptors co-localize postsynaptically not only with D2 receptors, but also with the cholinergic interneurons, the cannabinoid receptor and the glutamate receptor, suggesting the existence of important multifunctional interactions between A2A and these receptors (32). In summary, these data strongly indicate that A2A receptors can target a couple of cellular mechanisms involved in the underlying neurodegenerative process, and likely to play a functional role in the modulation of motor behavior in LID.

In our study, caffeine showed more remarkable improvement on the total AIM score when compared with other A2A antagonists. The underlying mechanism by which caffeine attenuates LID remains largely unclear. One previous study reported that chronic administration of L-dopa increased the striatal A2A expression significantly. Nevertheless, co-administration of L-dopa with caffeine not only attenuated the AIM induced by L-dopa, but also lower the level of striatal A2A expression (24). Moreover, Xiao et al. suggested that blocking both A1 and A2A receptors simultaneously, as occurred with caffeine use, might also confer a disease-modifying benefit of reduced risk of disabling LID, suggesting A1 may also play a pivotal role in the function of caffeine (25). On the other hand, SCH 412348 was given concurrently with L-dopa over the course of 19 days of treatment. This treatment paradigm did not reduce the severity of AIM score compared with treatment with L-dopa alone ($p = 0.35$). With regard to KW-6002, our data showed that KW-6002 could not prevent the development of AIM score even when the combined treatment is administered *de novo* ($p = 0.39$).

Limitations

Several limitations of this meta-analysis should be considered. First, there is a chance of overestimation of the efficacy because our paper can only include available data which have been published in some forms, and hence negative studies that are less likely to be published will be missed. Therefore, the inclusion of unpublished studies and the use of trial registries become reasonable means to avoid publication bias (33). Second, a notable feature of the present review is the marked heterogeneity between studies due to the variation in study quality and experimental designs, implying that the overall estimate of efficacy should be interpreted with some caution. Meanwhile, this meta-analysis included a limited number of small studies ($n = 9$) and type-II errors due to chance cannot be entirely excluded as an alternative explanation for our main finding (34), making these findings less robust. Although there is no fixed minimum number of studies required for a meta-analysis, too small a number could lead to an unstable effect size. Therefore, further studies, particularly those of large sample, were warranted to support the drugs' superiority to placebo. Third, our meta-analysis is based on observational research rather than experimental, and thus we are only able to obtain associations rather than causation. Moreover, no study in this meta-analysis using animals with co-morbidities, which is the typical situation in human PD and LID. Finally, as the studies only involved a few classes of A2A receptor antagonists, the majority being KW-6002 ($n = 4$), the results cannot be extrapolated to other A2A receptor antagonist's classes.

Implications for Further Studies

When included in systematic reviews, high-quality studies with lower variance will show larger effects, and improvement in the quality of reporting studies will also help to reduce bias. Therefore, well-designed and high-quality studies would be required to test the efficacy of A2A receptor antagonists on

LID. In the present study, no studies investigated A2A receptor antagonists in LID models with concomitant conditions, such as hypertension, diabetes, dyslipidemia, or aged animals. This lack of information should certainly be addressed in future studies. Our meta-analysis suggested that the efficacy was maximal when Caffeine ($n = 2$, $p = 0.02$) was administered but not KW-6002 ($n = 2$, $p = 0.39$) or SCH 412348 ($n = 1$, $p = 0.35$) in terms of reduced the AIM score. However, the results generated from this subgroup analysis should be interpreted with caution due to the limited studies. We have no sufficient evidence to suggest initiating clinical trials based on these data. Consequently, further studies would be demanded to determine which kinds of A2A receptor antagonists were more effective than others. Moreover, there is currently little accordance on which neurobehavioral tests in rats would offer measures that are predictive of a benefit in clinical patients. In terms of PD, after a few years of L-dopa therapy, most patients will be accompanied with AIM (including movements with dystonic, choreiform, ballistic, or stereotypic features) that appear when plasma and brain levels of L-dopa are high, mimicking the peak-dose variant of human LID (35). It was long assumed that the responsiveness to L-dopa merely could be measured with contralateral rotation test but LID movements was unable to be assessed at all, until Cenci and collaborators first introduced the concept of AIM in 1998 (36). Although contralateral rotations have been used as a measure of LID, it has become increasingly recognized that this neurobehavioral not always correlates with the development of LID (37). Therefore, further studies should use AIM score as an indicator to reflect LID behavior.

CONCLUSION

In summary, we have shown that adenosine A2A receptor antagonists are effective in the management of LID in animal models. Although some factors, such as study quality and total sample sizes, may undermine the validity of the positive findings, A2A receptor antagonists still probably have a potential neuroprotective role in LID models. The systematic review and meta-analysis here provides a framework for an evidence-based approach to the development of new treatments for LID and for the design of future preclinical and clinical studies.

AUTHOR CONTRIBUTIONS

M-MZ and LF conceived and participated in its design, searched databases, extracted and assessed studies, and helped to draft the manuscript. X-RZ, JC, and Z-RZ carried out the statistical analysis and interpretation of data. W-WW and C-LX participated in the conceptualization and design of the review, performed the selection of studies, data extraction and analysis, and drafted the review. All authors read and approved the final manuscript.

FUNDING

The study was supported by the Projects of National Science Foundation of China (No. 81600977), National Key Technology Research and Development Program of the Ministry of Science and Technology of China (grant number: 2015BAI13B01), and Wenzhou Municipal Sci-Tech Bureau Program (Y20160002).

REFERENCES

1. Sharma S, Singh S, Sharma V, Singh VP, Deshmukh R. Neurobiology of l-dopa induced dyskinesia and the novel therapeutic strategies. *Biomed Pharmacother* (2015) 70:283–93. doi:10.1016/j.biopha.2015.01.029
2. Francardo V, Cenci MA. Investigating the molecular mechanisms of L-dopa-induced dyskinesia in the mouse. *Parkinsonism Relat Disord* (2014) 20(Suppl 1): S20–2. doi:10.1016/S1353-8020(13)70008-7
3. Obeso JA, Merello M, Rodriguez-Oroz MC, Marin C, Guridi J, Alvarez L. Levodopa-induced dyskinesias in Parkinson's disease. *Handb Clin Neurol* (2007) 84:185–218. doi:10.1016/S0072-9752(07)84040-1
4. Xie CL, Wang WW, Zhang SF, Gan J, Liu ZG. Continuous dopaminergic stimulation (CDS)-based treatment in Parkinson's disease patients with motor complications: a systematic review and meta-analysis. *Sci Rep* (2014) 4:6027. doi:10.1038/srep06027
5. Schaeffer E, Pilotto A, Berg D. Pharmacological strategies for the management of levodopa-induced dyskinesia in patients with Parkinson's disease. *CNS Drugs* (2014) 28:1155–84. doi:10.1007/s40263-014-0205-z
6. Tokunaga N, Choudhury ME, Nishikawa N, Nagai M, Tujii T, Iwaki H, et al. Pramipexole upregulates dopamine receptor D2 and D3 expression in rat striatum. *J Pharmacol Sci* (2012) 120:133–7. doi:10.1254/jphs.12096SC
7. Bezard E, Brotchie JM, Gross CE. Pathophysiology of levodopa-induced dyskinesia: potential for new therapies. *Nat Rev Neurosci* (2001) 2:577–88. doi:10.1038/35086062
8. Calabresi P, Di Filippo M, Ghiglieri V, Tambasco N, Picconi B. Levodopa-induced dyskinesias in patients with Parkinson's disease: filling the bench-to-bedside gap. *Lancet Neurol* (2010) 9:1106–17. doi:10.1016/S1474-4422(10)70218-0
9. Rivera-Oliver M, Diaz-Rios M. Using caffeine and other adenosine receptor antagonists and agonists as therapeutic tools against neurodegenerative diseases: a review. *Life Sci* (2014) 101:1–9. doi:10.1016/j.lfs.2014.01.083
10. Morelli M, Di Paolo T, Wardas J, Calon F, Xiao D, Schwarzschild MA. Role of adenosine A2A receptors in parkinsonian motor impairment and l-dopa-induced motor complications. *Prog Neurobiol* (2007) 83:293–309. doi:10.1016/j.pneurobio.2007.07.001
11. Kulisevsky J, Poyurovsky M. Adenosine A2A-receptor antagonism and pathophysiology of Parkinson's disease and drug-induced movement disorders. *Eur Neurol* (2012) 67:4–11. doi:10.1159/000331768
12. Xiao D, Bastia E, Xu YH, Benn CL, Cha JH, Peterson TS, et al. Forebrain adenosine A2A receptors contribute to L-3,4-dihydroxyphenylalanine-induced dyskinesia in hemiparkinsonian mice. *J Neurosci* (2006) 26:13548–55. doi:10.1523/JNEUROSCI.3554-06.2006
13. Hauser RA, Shulman LM, Trugman JM, Roberts JW, Mori A, Ballerini R, et al. Study of istradefylline in patients with Parkinson's disease on levodopa with motor fluctuations. *Mov Disord* (2008) 23:2177–85. doi:10.1002/mds.22095
14. Kanda T, Uchida S. Clinical/pharmacological aspect of adenosine A2A receptor antagonist for dyskinesia. *Int Rev Neurobiol* (2014) 119:127–50. doi:10.1016/B978-0-12-801022-8.00006-4
15. Wang WW, Xie CL, Lu L, Zheng GQ. A systematic review and meta-analysis of Baihui (GV20)-based scalp acupuncture in experimental ischemic stroke. *Sci Rep* (2014) 4:3981. doi:10.1038/srep03981
16. Xie CL, Pan JL, Zhang SF, Gan J, Liu ZG. Effect of nicotine on L-dopa-induced dyskinesia in animal models of Parkinson's disease: a systematic review and meta-analysis. *Neurol Sci* (2014) 35:653–62. doi:10.1007/s10072-014-1652-5
17. Xie CL, Wang WW, Zhang SF, Yuan ML, Che JY, Gan J, et al. Levodopa/benserazide microsphere (LBM) prevents L-dopa induced dyskinesia by inactivation of the DR1/PKA/P-tau pathway in 6-OHDA-lesioned Parkinson's rats. *Sci Rep* (2014) 4:7506. doi:10.1038/srep07506
18. Macleod MR, O'Collins T, Howells DW, Donnan GA. Pooling of animal experimental data reveals influence of study design and publication bias. *Stroke* (2004) 35:1203–8. doi:10.1161/01.STR.0000125719.25853.20

19. Vesterinen HM, Sena ES, Egan KJ, Hirst TC, Churolov L, Currie GL, et al. Meta-analysis of data from animal studies: a practical guide. *J Neurosci Methods* (2014) 221:92–102. doi:10.1016/j.jneumeth.2013.09.010
20. Kanda T, Jackson MJ, Smith LA, Pearce RK, Nakamura J, Kase H, et al. Combined use of the adenosine A(2A) antagonist KW-6002 with L-dopa or with selective D1 or D2 dopamine agonists increases antiparkinsonian activity but not dyskinesia in MPTP-treated monkeys. *Exp Neurol* (2000) 162:321–7. doi:10.1006/exnr.2000.7350
21. Lundblad M, Vaudano E, Cenci MA. Cellular and behavioural effects of the adenosine A2a receptor antagonist KW-6002 in a rat model of l-dopa-induced dyskinesia. *J Neurochem* (2003) 84:1398–410. doi:10.1046/j.1471-4159.2003.01632.x
22. Rose S, Jackson MJ, Smith LA, Stockwell K, Johnson L, Carminati P, et al. The novel adenosine A2a receptor antagonist ST1535 potentiates the effects of a threshold dose of L-dopa in MPTP treated common marmosets. *Eur J Pharmacol* (2006) 546:82–7. doi:10.1016/j.ejphar.2006.07.017
23. Tronci E, Simola N, Borsini F, Schintu N, Frau L, Carminati P, et al. Characterization of the antiparkinsonian effects of the new adenosine A2A receptor antagonist ST1535: acute and subchronic studies in rats. *Eur J Pharmacol* (2007) 566:94–102. doi:10.1016/j.ejphar.2007.03.021
24. Huang YX, Luo WF, Li D, Hu WD, Liu CF. CSC counteracts l-dopa-induced overactivity of the corticostriatal synaptic ultrastructure and function in 6-OHDA-lesioned rats. *Brain Res* (2011) 1376:113–21. doi:10.1016/j.brainres.2010.12.070
25. Xiao D, Cassin JJ, Healy B, Burdett TC, Chen JF, Fredholm BB, et al. Deletion of adenosine A(1) or A((2)A) receptors reduces L-3,4-dihydroxyphenylalanine-induced dyskinesia in a model of Parkinson's disease. *Brain Res* (2011) 1367:310–8. doi:10.1016/j.brainres.2010.08.099
26. Jones N, Bleickardt C, Mullins D, Parker E, Hodgson R. A2A receptor antagonists do not induce dyskinesias in drug-naive or L-dopa sensitized rats. *Brain Res Bull* (2013) 98:163–9. doi:10.1016/j.brainresbull.2013.07.001
27. Uchida S, Soshiroda K, Okita E, Kawai-Uchida M, Mori A, Jenner P, et al. The adenosine A2A receptor antagonist, istradefylline enhances anti-parkinsonian activity induced by combined treatment with low doses of L-dopa and dopamine agonists in MPTP-treated common marmosets. *Eur J Pharmacol* (2015) 766:25–30. doi:10.1016/j.ejphar.2015.09.028
28. Pinna A, Pontis S, Borsini F, Morelli M. Adenosine A2A receptor antagonists improve deficits in initiation of movement and sensory motor integration in the unilateral 6-hydroxydopamine rat model of Parkinson's disease. *Synapse* (2007) 61:606–14. doi:10.1002/syn.20410
29. Tomiyama M. Adenosine receptors and dyskinesia in pathophysiology. *Int Rev Neurobiol* (2014) 119:117–26. doi:10.1016/B978-0-12-801022-8.00005-2
30. Chen JF, Moratalla R, Impagnatiello F, Grandy DK, Cuellar B, Rubinstein M, et al. The role of the D(2) dopamine receptor (D(2)R) in A(2A) adenosine receptor (A(2A)R)-mediated behavioral and cellular responses as revealed by A(2A) and D(2) receptor knockout mice. *Proc Natl Acad Sci U S A* (2001) 98:1970–5. doi:10.1073/pnas.98.4.1970
31. Calon F, Dridi M, Hornykiewicz O, Bedard PJ, Rajput AH, Di Paolo T. Increased adenosine A2A receptors in the brain of Parkinson's disease patients with dyskinesias. *Brain* (2004) 127:1075–84. doi:10.1093/brain/awh128
32. Blandini F, Armentero MT. New pharmacological avenues for the treatment of L-dopa-induced dyskinesias in Parkinson's disease: targeting glutamate and adenosine receptors. *Expert Opin Investig Drugs* (2012) 21:153–68. doi:10.1517/13543784.2012.651457
33. Furlan AD, Pennick V, Bombardier C, van Tulder M. 2009 updated method guidelines for systematic reviews in the Cochrane back review group. *Spine* (2009) 34:1929–41. doi:10.1097/BRS.0b013e3181b1c99f
34. Skapinakis P, Bakola E, Salanti G, Lewis G, Kyritsis AP, Mavreas V. Efficacy and acceptability of selective serotonin reuptake inhibitors for the treatment of depression in Parkinson's disease: a systematic review and meta-analysis of randomized controlled trials. *BMC Neurol* (2010) 10:49. doi:10.1186/1471-2377-10-49
35. Iderberg H, Francardo V, Pioli EY. Animal models of L-dopa-induced dyskinesia: an update on the current options. *Neuroscience* (2012) 211:13–27. doi:10.1016/j.neuroscience.2012.03.023
36. Cenci MA, Lee CS, Björklund A. L-dopa-induced dyskinesia in the rat is associated with striatal overexpression of prodynorphin- and glutamic acid decarboxylase mRNA. *Eur J Neurosci* (1998) 10:2694–706. doi:10.1046/j.1460-9568.1998.00285.x
37. Henry B, Crossman AR, Brotchie JM. Characterization of enhanced behavioral responses to L-dopa following repeated administration in the 6-hydroxydopamine-lesioned rat model of Parkinson's disease. *Exp Neurol* (1998) 151:334–42. doi:10.1006/exnr.1998.6819

Conflict of Interest Statement: The authors declare that the research was conducted in the absence of any commercial or financial relationships that could be construed as a potential conflict of interest.

Copyright © 2017 Wang, Zhang, Zhang, Zhang, Chen, Feng and Xie. This is an open-access article distributed under the terms of the Creative Commons Attribution License (CC BY). The use, distribution or reproduction in other forums is permitted, provided the original author(s) or licensor are credited and that the original publication in this journal is cited, in accordance with accepted academic practice. No use, distribution or reproduction is permitted which does not comply with these terms.

frontiers in Neuroscience

ORIGINAL RESEARCH
published: 09 February 2018
doi: 10.3389/fnins.2018.00053

Influence of Brain Stem on Axial and Hindlimb Spinal Locomotor Rhythm Generating Circuits of the Neonatal Mouse

Céline Jean-Xavier[†] *and Marie-Claude Perreault*[*]

Department of Physiology, Emory University School of Medicine, Atlanta, GA, United States

The trunk plays a pivotal role in limbed locomotion. Yet, little is known about how the brain stem controls trunk activity during walking. In this study, we assessed the spatiotemporal activity patterns of axial and hindlimb motoneurons (MNs) during drug-induced fictive locomotor-like activity (LLA) in an isolated brain stem-spinal cord preparation of the neonatal mouse. We also evaluated the extent to which these activity patterns are affected by removal of brain stem. Recordings were made in the segments T7, L2, and L5 using calcium imaging from individual axial MNs in the medial motor column (MMC) and hindlimb MNs in lateral motor column (LMC). The MN activities were analyzed during both the rhythmic and the tonic components of LLA, the tonic component being used as a readout of generalized increase in excitability in spinal locomotor networks. The most salient effect of brain stem removal was an increase in locomotor rhythm frequency and a concomitant reduction in burst durations in both MMC and LMC MNs. The lack of effect on the tonic component of LLA indicated specificity of action during the rhythmic component. Cooling-induced silencing of the brain stem reproduced the increase in rhythm frequency and accompanying decrease in burst durations in L2 MMC and LMC, suggesting a dependency on brain stem neuron activity. The work supports the idea that the brain stem locomotor circuits are operational already at birth and further suggests an important role in modulating trunk activity. The brain stem may influence the axial and hindlimb spinal locomotor rhythm generating circuits by extending their range of operation. This may represent a critical step of locomotor development when learning how to walk in different conditions and environments is a major endeavor.

Keywords: motor command, subcortical, reticulospinal, vestibulospinal, CPG, trunk-hindlimb coordination

OPEN ACCESS

Edited by:
Brian R. Noga,
University of Miami, United States

Reviewed by:
Pascal Darbon,
Université de Strasbourg, France
Robert M. Brownstone,
University College London, United Kingdom

****Correspondence:***
Marie-Claude Perreault
m-c.perreault@emory.edu

[†]Present Address:
Céline Jean-Xavier,
Department of Comparative Biology and Experimental Medicine, Faculty of Veterinary Medicine, Hotchkiss Brain Institute, University of Calgary, Calgary, AB, Canada

Specialty section:
This article was submitted to Neural Technology, a section of the journal Frontiers in Neuroscience

Received: *29 October 2017*
Accepted: *23 January 2018*
Published: *09 February 2018*

Citation:
Jean-Xavier C and Perreault M-C (2018) Influence of Brain Stem on Axial and Hindlimb Spinal Locomotor Rhythm Generating Circuits of the Neonatal Mouse. Front. Neurosci. 12:53. doi: 10.3389/fnins.2018.00053

INTRODUCTION

Locomotion in mammals is efficient when both trunk and hindlimbs are appropriately controlled (Carlson et al., 1979; Thorstensson et al., 1982; Gramsbergen, 1998; Jamon, 2006; Schilling, 2011). Evidence indicates that both the brainstem and the spinal cord participate in the control of trunk and hindlimb activity during locomotion (Musienko et al., 2014). However, little is known about the respective contribution of these two control systems.

Our understanding of the circuits controlling locomotor activity in trunk muscles relies heavily on studies in vertebrates that either have no legs or only simple forms of hindlimbs, including

lamprey (Grillner, 2006; Ryczko et al., 2010), xenopus (Combes et al., 2004; Beyeler et al., 2008; Roberts et al., 2012), leech (Kristan et al., 2005), zebrafish (Thorsen, 2004; Bagnall and McLean, 2014; Kishore et al., 2014; Grillner and Manira, 2015), and amphibian tetrapods (Cabelguen et al., 2014; Ryczko et al., 2015). Recent work in rodents suggests that some of the basic mechanisms that underlie control of trunk in limbless vertebrates are retained in limbed mammals (Falgairolle et al., 2013; Beliez et al., 2015; Hinckley et al., 2015). However, the more complex mechanisms that have developed along with the specialization that came with the morphological evolution of the hindlimbs (Beyeler et al., 2008; Le Gal et al., 2016) have yet to be studied.

The present study in a brain stem-spinal cord preparation of the neonatal mouse was designed to examine the contribution of the brain stem to trunk and hindlimb motoneurons (MNs) activities during drug-induced fictive locomotor-like activity (LLA; Kudo and Yamada, 1987; Smith and Feldman, 1987; Jiang et al., 1999; Bonnot et al., 2002). We used calcium imaging to record locomotor activity from individual MNs in T7, L2, or L5 segments and compare recordings from MNs in the medial and lateral motor column (MMC and LMC) before and after removal of the brain stem. This approach enables before/after comparison in the same preparation, making for a more robust interpretation of the results.

The findings suggest an early influence of the brain stem directed to the axial and hindlimb spinal locomotor rhythm generating circuits. This early influence may be critical when animals learn how to walk in different conditions and environment. Preliminary results have been published previously in abstract form (Jean-Xavier and Perreault, 2013).

MATERIALS AND METHODS

Animals

Experiments were performed on neonatal [post-natal day (P) 0–2] ICR/Ha mice ($n = 36$). All animal protocols followed US National Institutes of Health guidelines and were approved by Emory University Institutional Animal Care and Use Committee.

In Vitro Brain Stem-Spinal Cord Preparation

Under deep isoflurane (4%) anesthesia, animals were decerebrated by transecting the brain rostral to the superior colliculus and eviscerated. Preparations were then placed in a dissection chamber filled with ice cold oxygenated (95% O_2/5% CO_2) glycerol-based dissecting solution containing (in mM): glycerol 250, KCl 2, D-glucose 11, $CaCl_2$ 0.15, $MgSO_4$ 2, NaH_2PO_4 1.2, HEPES 5 and $NaHCO_3$ 25 (pH of 7.4). After a craniotomy and a laminectomy, the brain stem-spinal cords, with the dorsal and ventral roots attached, were gently dissected out. Brain stem-spinal cords were then transferred to a Sylgard-coated recording chamber where they were positioned ventral side up. The recording chamber was partitioned into a brain stem and a spinal cord compartments using a plastic wall sealed with petroleum jelly at cervical segment C1-C2. Room temperature (RT; 23°C) oxygenated artificial cerebrospinal fluid (aCSF) containing (in mM): NaCl 128, KCl 3, D-glucose 11, $CaCl_2$ 2.5, $MgSO_4$ 1, NaH_2PO_4 1.2, HEPES 5 and $NaHCO_3$ 25, was pumped into each compartment. The tightness of the seal was verified by adding phenol red to one of the compartment.

Loading of Motoneurons with Fluorescent Calcium Indicator

Spinal segments were identified by counting the ventral roots using as a starting point the C1 ventral root and/or the L5 ventral root which is last large diameter root of the lumbar enlargement. Motoneurons (MNs) in the thoracic segment T7 and lumbar segments L2 and L5 were loaded with Calcium Green 1-conjugated dextran amine (CaGDA; 3000 MW; Molecular Probes, for indicator kinetics (see Zhao et al., 1996; Kreitzer et al., 2000; Putney, 2006) by applying reconstituted CaGDA crystals (Glover, 1995) to the cut end of the corresponding ventral roots. Labeling via retrograde axonal transport continued in the dark at RT for at least 3 h.

Drug-Induced Fictive Locomotor-Like Activity (LLA)

LLA was induced by applying a neurochemical cocktail composed of N-Methyl-D-aspartate (5 μM NMDA), 5-hydroxytryptamine hydrochloride (10 μM 5-HT) and dopamine hydrochloride (50 μM DA) dissolved in aCSF. The locomotor cocktail was applied specifically to the spinal cord compartment (recycling flow rate of 15 ml/min). All neurochemicals were purchased from Sigma Aldrich and kept as frozen (−30°C) stock (10–100 mM).

Removal of the Brain Stem

The brain stem was removed by complete transection of the spinal cord at the level of C1 segment using superfine Vannas scissors (WPI, USA). To avoid transecting during states of high excitability, neurochemicals were washed out for ≥20 min prior to transection. The locomotor cocktail solution was re-applied to the isolated spinal cord only after a post-transection recovery period of ≥20 min.

Reversible Cooling of the Brain Stem

In a subset of experiments, the excitability of the brain stem was reduced using cooling. For these experiments, temperature probes (Yellow Spring Instruments, YSI-402) were placed in each bath compartment. Prior to cooling, the brain stem compartment was set to an initial temperature of 28°C using warm aCSF. The brain stem was then cooled down to 18°C using ice-cold aCSF. After cooling, but before final removal of the brain stem, the brain stem compartment was rewarmed to 28°C. The spinal cord compartment was kept at RT at all times. Isothermal values were reached in 5 min.

Calcium Imaging

Drug-induced LLA is usually monitored using electrical recording from ventral roots which contain mixed axonal populations (axons from axial and limb MNs and sympathetic preganglionic neurons). Here, we used calcium imaging, which enable us to resolve activity in individual MNs identified as axial MNs of the medial motor column (MMC) or limb MNs

of the lateral motor column (LMC) based on their mediolateral locations (Lev-Tov and O'Donovan, 1995; O'Donovan et al., 2008; Szokol and Perreault, 2009; Hinckley et al., 2015). Individual CaGDA-labeled MNs were visualized through the ventral white matter up to about 100 μm under the surface (Szokol and Perreault, 2009) using a 40x water immersion objective (LUMPLFLN 40X, 0.8 NA, Olympus USA) of an epi-fluorescence microscope (BX51, Olympus, USA) equipped with a 100 W halogen lamp driven by a DC power supply (PAN35-20A, Kikusui Electronics Corporation, Japan) and excitation and emission filters (BP 450–490 nm and LP 515 nm, respectively). Fluorescence images were captured using a sCMOS camera (PCO.edge, PCO, Canada) mounted on a video zoom adapter set at 0.5x. Image (16 bit) streams (480 frames) were stored at 4 frames/s (binning 2×2, gain 1) using the acquisition software Metamorph (v7.7, Universal Imaging Corporation, Molecular Devices, USA). All recording sessions (controls and trials) lasted 120 s.

Data Analysis

Using the acquisition and image analysis software Metamorph, circular regions of interest (ROIs) were positioned over the soma of individual MNs so as to cover as much of the field of view as possible. The selection of the MN somata was made according to labeling intensity and availability in the same focus plane. Fluorescence intensity within each ROI averaged over all pixels. These data were converted to text files and exported to pClamp (Clampfit 10.4, Molecular Devices, USA) where they were expressed as waveforms or changes in fluorescence over time for further analysis. Changes in fluorescence were measured and reported as percent changes from an average baseline level F0 [ΔF/F or (F–F0)/F0]. For the recordings that contained the onset of LLA (see "Tonic component" section below), F0 was measured prior to the arrival of the neurochemicals in the bath and thus estimated well the true baseline calcium level ("rest" period in absence of neurochemicals). For the recordings that contained only rhythmic activity (see "Rhythmic component" section below), F0 was measured as the minimum inter-burst fluorescence and thus likely overestimated the true baseline calcium level.

Locomotor-Like Activity (LLA)

Tonic component

An initial, slowly rising, tonic plateau of activity often preceded rhythmic LLA. Its onset was detected using a threshold function (Clampfit 10.4, Molecular Devices, USA) set to average baseline fluorescence + 4SD (horizontal dotted lines in **Figure 1B**) whereas its magnitude was quantified as the average plateau fluorescence (measured once the plateau had stabilized) minus the average baseline fluorescence. The baseline fluorescence and the plateau fluorescence were average over a 5 s-period.

Rhythmic component

Although cyclic changes in fluorescence were often observed within 3 min of neurochemicals application, we only analyzed recordings obtained ≥20 min (stable rhythm).

Frequency of occurrence of double-peak bursts in MMC MNs. Double-peak bursts were defined as bursts with a transient dip in fluorescence (>30% decrease from the highest peak value and duration of at least 1 s) about midway through their crest (**Figure 3A**). The proportion of double-peak bursts was assessed by compiling their numbers during 2 min- recording sessions (2–5 MMC MNs per experiment).

Rhythm frequency and burst durations. The onset and offset of the locomotor bursts in individual MNs were detected using a threshold function (single channel search function in Clampfit 10.4) set at 30% of the peak value (Tazerart et al., 2007). Times between consecutive onsets were used to determine the duration of each locomotor cycle and assess rhythm frequency whereas times between onsets and offsets were used to calculate burst durations.

Temporal relationships and coupling strengths. Temporal relationships and coupling strengths between pairs of MNs were determined for MNs of the same motor column (intra-columnar) and MNs of different motor columns (inter-columnar). For these analyses, we used "Spinalcore," a program for signal processing and analyses in frequency/time domain of stationary and non-stationary time series (Mor and Lev-Tov, 2007). Briefly, the calcium signal from each individual MN was decomposed in the frequency domain over the time course of the recordings using a continuous Morlet wavelet transform (10 octaves per scale). Then, using coherent cross-power wavelet transform (CXWT, spectrograms in **Figure 6A**), we determined if two individual signals had 1) common bands of high-power frequencies and 2) a phase relationship that was consistent over time. The degree of consistency of the phase relationship (coupling strength or coherence) ranged from zero to one for highly coherent signals. The high-power frequencies band of interest in the CXWT was selected (white rectangle in spectrograms of **Figure 6A**) and used to extract rhythm frequency, phase differences and coupling strengths (coherence) between pairs of MNs. Rhythm frequencies and coupling strengths were presented as bar graphs and phase differences as circular plots.

Statistics

Data are reported as mean±SEM, unless indicated otherwise. Tests of significance were performed on the grand averages across preparations and included: the paired *t*-test, unpaired *t*-test and one-way ANOVA followed by Holm-Sidak *post-hoc* multiple comparison. When the assumption of normality was violated, we instead used the Fisher's exact-test, Wilcoxon matched-paired test, Mann-Whitney test and Kruskal-Wallis test followed by Dunn's multiple comparison. These tests were performed using GraphPad Prism 6 (San Diego, CA, USA). To test mean phase differences, we performed Watson–Williams *F*-test using Oriana (Kovach Computing Services, Pentraeth, UK). Significance level was set at $p < 0.05$.

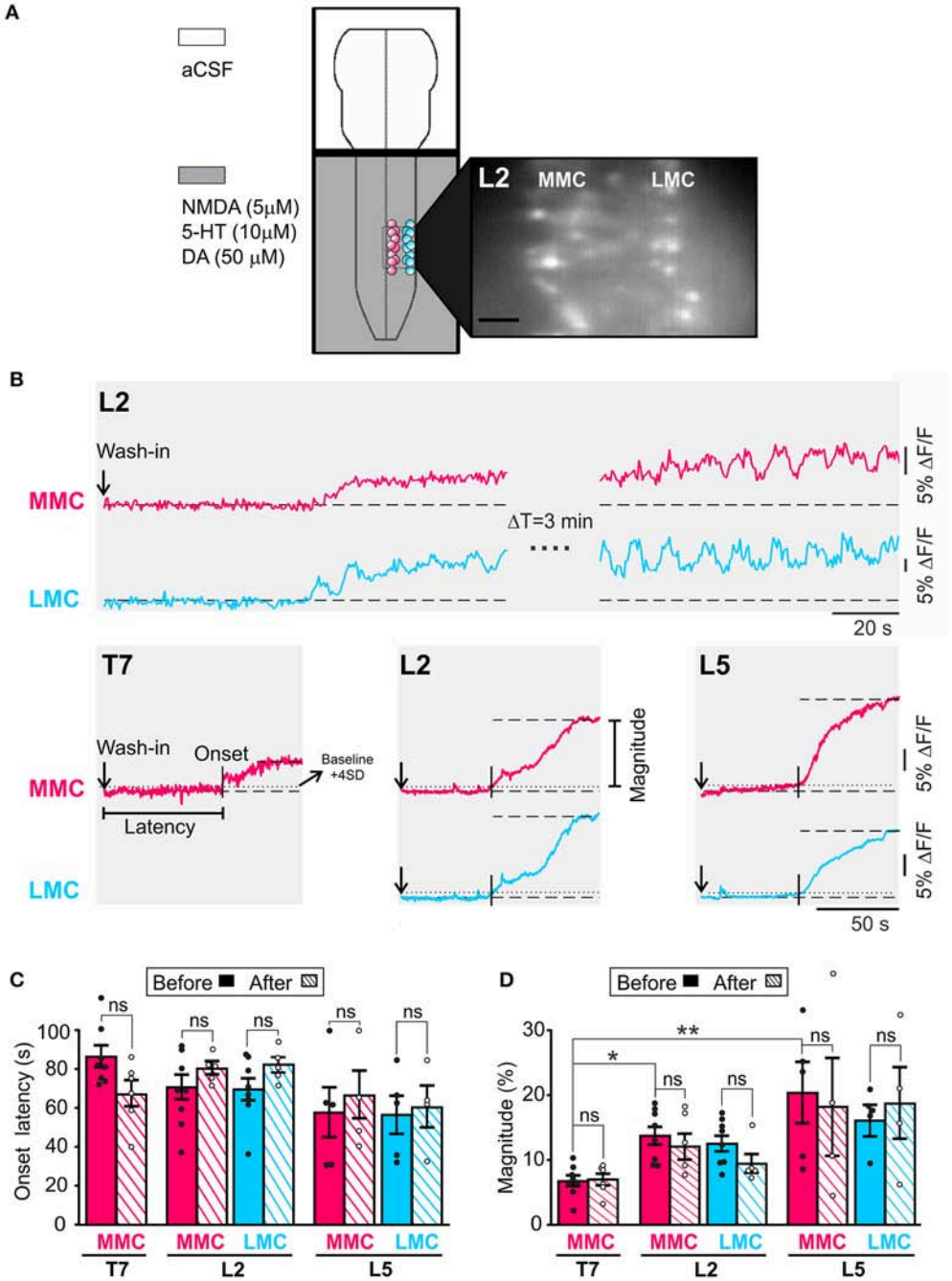


FIGURE 1 | An initial period of tonic activity accompanies rhythmic activity both in MMC and in LMC MNs. **(A)** Schematic representation of the experimental arrangement. The recording chamber was partitioned in two compartments with a plastic bridge sealed with petroleum jelly. The brain stem compartment (top) was superfused with aCSF while the spinal cord compartment (bottom) was superfused with aCSF plus NMDA (5 μM), 5HT (10 μM), and DA (50 μM). The presence of the neurochemicals is indicated by the gray shading. MNs in the MMC (red circles) and LMC (blue circles) were loaded with fluorescent calcium indicator CaGDA (see Methods). Inset: Photomicrograph of CaGDA loaded MMC and LMC MNs in L2. Scale bar is 25 μm. **(B)** Top: Changes in fluorescence following the arrival of the neurochemicals to the spinal cord compartment in a single MMC MN (red waveform) and LMC MN (blue waveform). The recording bouts on the left show the slow building up of the tonic component of LLA in each MNs. The recording bouts on the right, which were acquired 3 min later, show the same tonic component as it reaches maximal magnitude (plateau). Bottom: Population responses (large ROI covering the entirety of the motor columns) showing the tonic component of LLA in MMC MNs of T7, L2, and L5 segments and LMC MNs of L2 and L5 segment. Vertical arrows: Time of application of neurochemicals. Vertical bars: Onset latency. Horizontal dashed line: Mean baseline fluorescence. Horizontal dotted line: Mean baseline fluorescence +4 SD. **(C)** Bar graph showing the mean onset latency of the tonic component in T7, L2, and L5 MNs before (solid bars) and after (hatched bars) removal of the brain stem. Each bar is a grand average across all experiments (individual points). Mean onset latencies of tonic activity were similar before and after removal of the brain stem (Wilcoxon matched-pairs test, T7 MMC^{before} vs.

(Continued)

FIGURE 1 | MMC^{after} p= 0.22; L2 MMC^{before} vs. MMC^{after} p= 0.31; L5 MMC^{before} vs. MMC^{after} p= 0.25; L2 LMC^{before} vs. LMC^{after} p= 0.31; L5 LMC^{before} vs. LMC^{after} $p > 0.99$). **(D)** Bar graph showing the magnitude of the tonic component in T7, L2, and L5 MNs before (solid bars) and after (hatched bars) removal of the brain stem. Each bar is a grand average across all experiments (individual points). The mean magnitudes of tonic component were similar before and after removal of the brain stem (Wilcoxon matched-pairs test, T7 MMC^{before} vs. MMC^{after} p= 0.84; L2 MMC^{before} vs. MMC^{after} p= 0.88; L5 MMC^{before} vs. MMC^{after} $p > 0.99$; L2 LMC^{before} vs. LMC^{after} $p > 0.99$; L5 LMC^{before} vs. LMC^{after} $p > 0.99$). $^{*}p < 0.05$, $^{**}p < 0.01$.

RESULTS

We analyzed optical recordings from more than 4000 individual MNs in the T7, L2, and L5 segments during drug-induced LLA. To achieve single-cell resolution each segment was investigated in different preparations. Below, sample sizes "*n*" refer to the number of animals.

Initial Tonic Activity

An initial period of tonic activity preceding rhythmic activity has been reported during drug-induced LLA in the isolated spinal cord of the neonatal rat (Kjaerulff and Kiehn, 1996; Beliez et al., 2015) and during MLR-evoked fictive locomotion in adult the decerebrate cat and rat (Perreault et al., 1999; MacDonell et al., 2015). However, this tonic activity has not been described in the mouse. Here, we measured tonic activity in individual MNs in T7, L2, and L5 segments (5–10 MNs per motor column) and show that tonic activity develops both in MMC and in LMC MNs (**Figure 1**, $n = 21$). In both MN groups, tonic activity appeared within less than 2 min and increased until it reached a plateau (**Figure 1B**). Few minutes after that, rhythmic activity started. Occasionally, tonic and rhythmic activity would appear concomitantly (LMC trace in **Figure 1B**). On average, the magnitude of the tonic activity in MMC MNs was significantly smaller in T7 than that in L2 and L5 (**Figure 1D**, Kruskal-Wallis test followed by Dunn's multiple comparison, T7 vs. L2, $p = 0.02$; T7 vs. L5, $p = 0.01$), suggesting an inter-segmental difference between thoracic and lumbar segments. However, in the absence of dependable measure for difference in excitability between preparations, this suggestion must remain tentative.

Pairwise comparisons before and after removal of the brain stem ($n = 15$) revealed no significant differences in mean onset latency or magnitude (compare solid and hatched bars in **Figures 1C,D**, see figure legend for *p*-values). Since the presence of the brain stem did not appear to change the inherent capability of the spinal cord to generate tonic activity, we suggest that initial tonic activity during drug-induced LLA is organized largely by neural networks in the spinal cord.

Rhythmic Locomotor-Like Activity

Rhythmic activity was analyzed in T7, L2, and L5 segments ($n =$ 10 animals per segment) before and after removal of the brain stem. Measurements were performed on individual MNs (10 MNs per motor column) and included rhythm frequency, burst durations, phase relationships and strengths of coupling between MNs. Data presented below include the first measurements of rhythmic locomotor activity in MMC MNs of the brain stem-spinal cord of the neonatal mouse.

Rhythm frequency and burst duration

The rhythm frequencies and burst durations were assessed in all three segments and, when eligible, in both MMC and LMC MNs (**Figure 2**). Analyses were performed on both combined (**Figure 2C**) and individual segments/columns (**Figures 2D,E**).

Before removal of the brain stem, the average frequencies ranged between 0.11 and 0.31 Hz without significant difference in average frequencies between the segments (one-way ANOVA test followed by a Holm-Sidak multiple comparison, all $p >$ 0.17). Removal of the brain stem increased the average rhythm frequency (solid circles in **Figure 2C**, paired *t*-test, $p = 0.0008$). When motor columns were analyzed separately, L2 showed that the increase in frequency occurred both in MMC and LMC (**Figure 2D**, solid vs. hatched bars, see figure legend for *p*-values).

We then tested whether the increase in locomotor frequency might have arisen from a reduction in locomotor burst durations. Prior to removal of the brain stem, the average burst durations ranged between 3.3 and 4.5 s without significant difference in average burst duration between segments (One-way ANOVA test followed by a Holm-Sidak multiple comparison, all $p >$ 0.85). When motor columns were analyzed separately, L2 showed significantly longer burst durations in MMC than LMC MNs (paired *t*-test, $p = 0.04$). Removal of the brain stem reduced the average burst duration (solid triangles in **Figure 2C**, paired *t*-test, $p = 0.0007$). Again, when motor columns were analyzed separately, L2 showed that the reduction in burst duration occurred both in MMC and LMC (**Figure 2E**, solid vs. hatched bars, see figure l egend for *p*-values). Thus, it is likely that the increase in rhythm frequency after removal of the brainstem arose from a reduction in locomotor burst durations in both MMC and LMC MNs.

Additionally, removal of the brain stem eliminated the difference in L2 burst duration between MMC and LMC MNs seen in the brain stem-attached preparation (paired *t*-test, $p =$ 0.10). This observation prompted us to look more closely at the shape of the bursts in MMC MNs. We observed that some of the bursts in MMC MNs displayed double-peak, similar to those reported previously in the L3–L5 segments of the isolated spinal cord (O'Donovan et al., 2008). Therefore, we wanted to test whether regulation of double-peak bursts by the brain stem could contribute to the reduction in burst duration in L2 MMC MNs. We compared the proportion of double-peak bursts during 2 min-recording sessions before and after removal of the brain stem ($n = 7$, **Figure 3**). Comparisons were made for L2 and T7 segments. Before removal of the brain stem, we observed double-peak bursts in MMC MNs (asterisks in **Figure 3A**, see also MMC traces in **Figure 2**) in both L2 and T7, albeit at a lower proportion in T7 (54% in L2 vs. 21% in T7, **Figure 3B**, solid bars). After removal of the brain

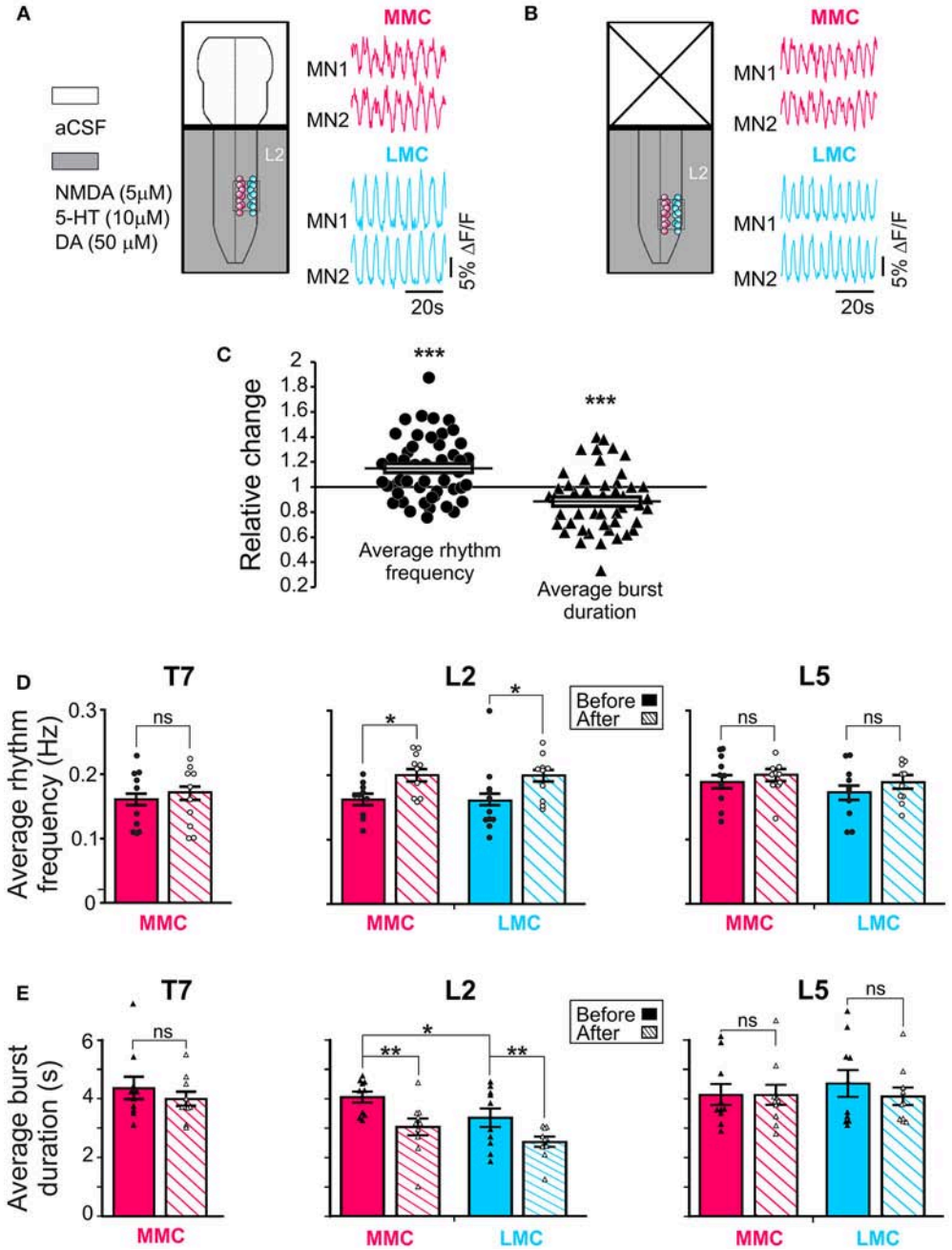


FIGURE 2 | Regulation of the locomotor rhythm frequency and burst durations by the brain stem. Schematic representations of the experimental arrangement before **(A)** and after **(B)** removal of the brain stem shown together with corresponding set of waveforms displaying changes in fluorescence in two L2 MMC MNs (red) and two L2 LMC (blue) MNs (for other details, see **Figure 1A**). The same four MNs are shown in the two panels. **(C)** Pooled data from 50 motor columns (10 motor columns in T7, 20 motor columns in L2 and in L5) showing relative change in average rhythm frequency (solid circles) and burst duration (solid triangles) after removal of the brain stem. **(D,E)** Bar graphs showing the average rhythm frequency and average burst duration in MMC (red) and LMC MNs (blue) in the individual segments before and after removal of the brain stem (solid and hatched bars, respectively). Each bar is a grand average across all experiments. The increase in rhythm frequency after removal of the brainstem was statistically significant in L2 (paired *t*-test, L2 MMC^{before} vs. MMC^{after} $p = 0.003$; L2 LMC^{before} vs. LMC^{after} $p= 0.048$; T7 MMC^{before} vs. MMC^{after} $p=0.79$; L5 MMC^{before} vs. MMC^{after} $p =0.86$; L5 LMC^{before} vs. LMC^{after} $p =0.26$). Removal of the brain stem also significantly reduced the average burst durations in L2 (paired *t*-test, L2 MMC^{before} vs. MMC^{after} $p = 0.003$; L2 LMC^{before} vs. LMC^{after} $p = 0.004$; T7 MMC^{before} vs. MMC^{after} $p = 0.26$; L5 MMC^{before} vs. MMC^{after} $p = 0.97$; L5 LMC^{before} vs. LMC^{after} $p = 0.34$). $^{*}p < 0.05$, $^{**}p < 0.01$, $^{***}p < 0.001$.

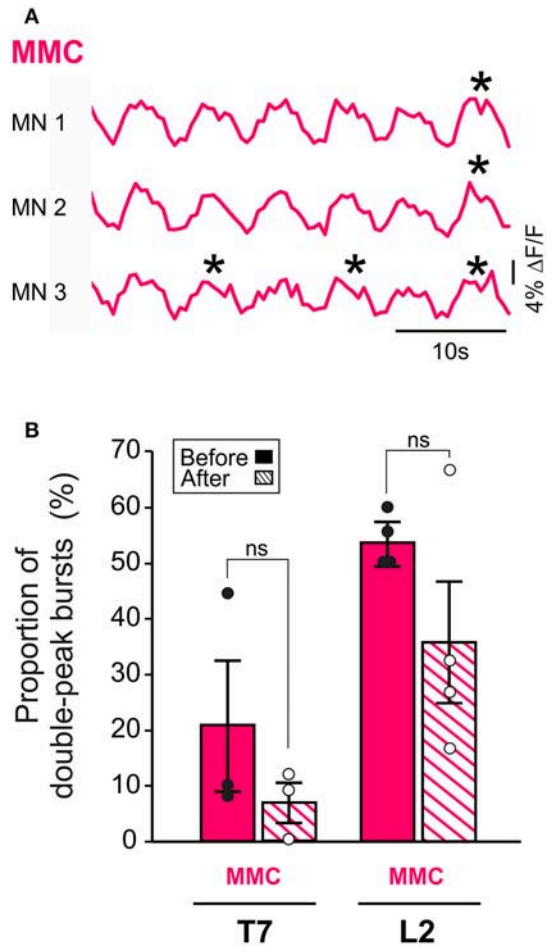


FIGURE 3 | MMC MNs display double-peak bursts during LLA. **(A)** Changes in fluorescence in three individual MNs in the left MMC (top) and right MMC (bottom). *Asterisks* indicate double-peak bursts (see Methods). **(B)** Bar graphs showing the mean frequency of occurrence of double-peak bursts in MMC MNs of T7 and L2 before (solid bars) and after (hatched bars) removal of the brain stem. Each bar is a grand average across all experiments (individual points).

stem (**Figure 3B**, hatched bars), the proportion of double-peak bursts in L2 decreased to 36%. However, the decrease was not statistically significant (Fisher's exact test, $p = 0.07$) nor was it specific to L2 (decrease to 7% in T7, Fisher's exact test, $p = 0.11$).

Altogether, these findings suggest that the brain stem contributes to the regulation of the rhythm frequency and burst duration of both MMC and LMC MNs during drug-induced LLA. When columns were analyzed separately, the threshold for significance was reached in L2 but not in T7 or L5. This is likely because MNs in this segment display tighter temporal relationships (see Supplemental Figure 1 and section below). We also observed a reduced incidence of double-peak bursts in L2 MMC MNs after removal of the brain stem but this does not appear to contribute to the reduction in locomotor burst durations in these MNs.

Phase relationships and coupling strengths between MNs of the same motor column

We then sought to determine the temporal relationships and strengths of coupling between MNs within individual motor columns. Several pair of MNs were analyzed within each motor column. Each pair consisted of a reference MN and another, randomly selected, MN within the motor column. The reference MN was selected based on its rostral most location in the field of view. All intra-columnar phase relationships (mean phase vector) and coupling strengths (mean coherence) analyzed in T7, L2, and L5 are shown in **Figure 4**.

Before removal of the brain stem (**Figure 4A**), all the mean phase vectors were close to 0°, suggesting that MN pairs discharged synchronously. However, the mean vector length "rvec" was lower in T7 MMC compared to L2 or L5 MMC, indicating a more widespread distribution of phase differences. As shown in the circular plot of T7, this widespread distribution was not the result of a uniform distribution of phase differences around the circle (Watson's U^2-test, $p < 0.01$), but rather a clustering of phase differences into two groups separated by 180°; one large cluster of MN pairs discharging synchronously and a smaller cluster of MN pairs discharging out-of-phase. Removal of the brain stem did not significantly alter the mean phase vectors in any of the segment (**Figure 4B**, see figure legend for *p*-values).

The mean coherences between MN pairs ranged between 0.75 and 0.96 and were significantly higher between MNs of L2 motor columns than between MNs of the T7 and L5 motor columns (**Figure 4C**, filled bars, see figure legend for *p*-values). The lower coherence between T7 MMC MNs T7 may be attributable to the presence of less well-correlated MN pairs (dots close to the thick, black outline circle in circular plots). This is consistent with the recent finding of Beliez et al. (2015) who reported a substantial number of non-locomotor-driven MNs in this segment. Removal of the brain stem did not significantly alter the mean coherences (**Figure 4C**, hatched bars; see figure legend for *p*-values).

Altogether, these data indicate that MNs within L2 and L5 motor columns discharge in phase with each other during drug-induced LLA in the brain stem-spinal cord preparation. In T7 motor columns, many MNs discharge in phase while a substantial number discharge out-of-phase. We also found that the temporal relationships between MNs were tightest in L2, a finding that is compatible with a higher potential for rhythmogenesis (see Discussion). Removal of the brain stem, despite its clear effect on the locomotor frequency and burst durations, did not significantly affect intra-columnar phase relationships or coupling strengths between MNs.

Phase relationships and coupling strengths between MNs of different motor columns

We next examined the temporal relationships and strengths of coupling between MNs in different motor columns. Inter-columnar relationships were determined between MNs of the left and right MMCs in L2 and between MNs in the MMC and LMC in both L2 and L5. All inter-columnar phase relationships

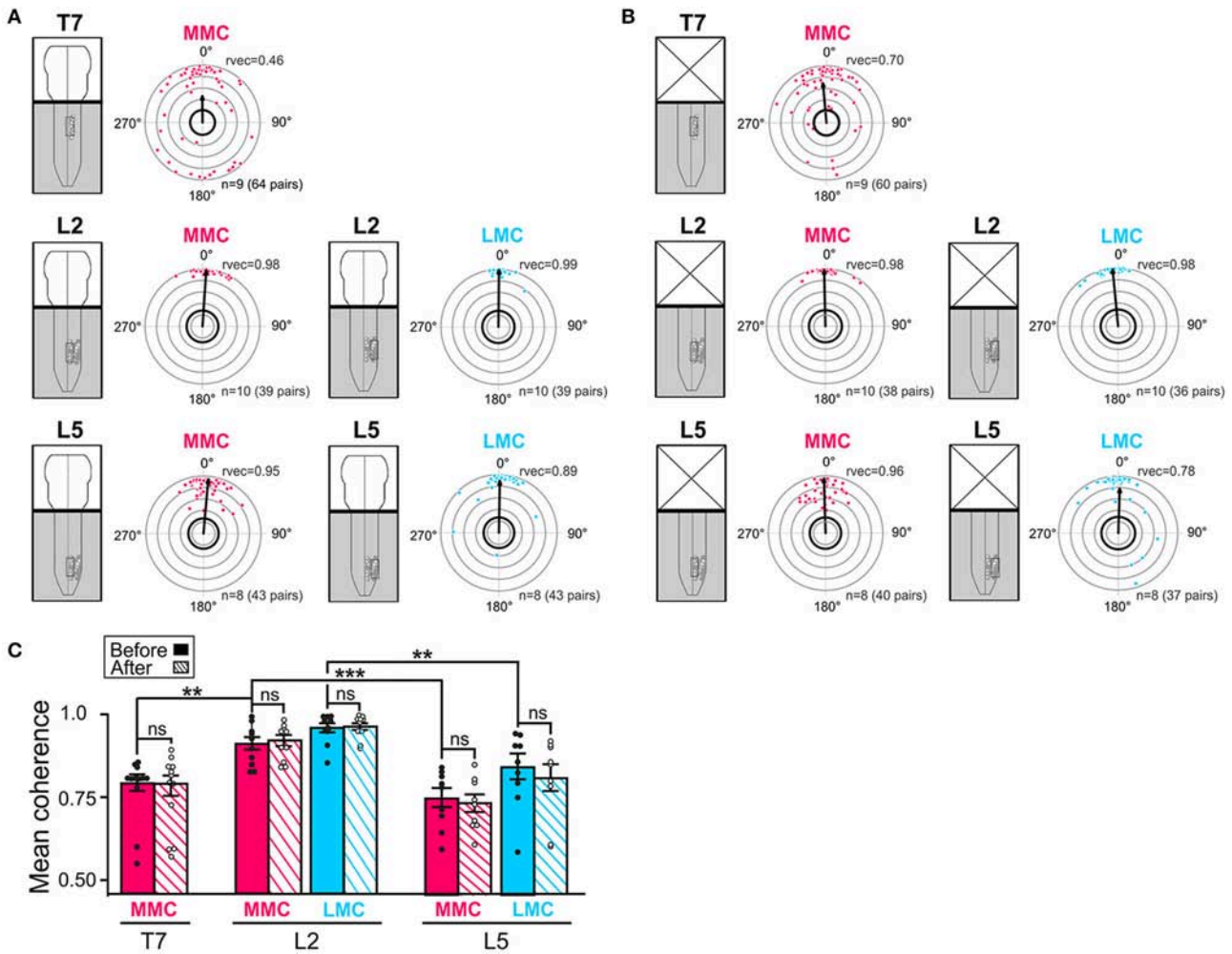


FIGURE 4 | Temporal relationships and coupling strengths (coherence) between MNs of the same motor column before and after removal of the brain stem. **(A,B)** Intra-columnar phase relationships between pairs of MNs in T7 MMC (top), L2 MMC and LMC (middle) and L5 MMC and LMC (bottom) before and after removal of the brain stem, respectively. Phase relationships between MN pairs are shown as phase differences in circular plots. Individual dots represent individual MN pairs (red=>MMC, blue=>LMC). The direction of the vectors (arrows) indicates mean phase difference (0° =>synchronous, 180° difference=>alternating) whereas the length of the vectors (rvec) indicates the extent to which the phase differences are clustered around the mean on a scale from 0.0 (origin) to 1.0 (outermost gray circle). The circle with thick black outline indicates the $p < 0.05$ level of statistical significance as determined by the Rayleigh test. Number of experiments and number MN pairs analyzed indicated at the bottom of each circular plots. The lower average vector length "rvec" in T7 indicates a more widespread distribution of phase differences between MNs in this segment than in L2 or L5. Phase differences were clustered in two groups around 0 and 180°. The changes in mean phase vectors after removal of the brainstem were not statistically significantly (Watson–Williams F-test, T7 MMC^{before} vs. MMC^{after} $F = 0.83$, $p = 0.38$; L2 MMC^{before} vs. MMC^{after} $F = 2.25$, $p = 0.15$; L2 LMC^{before} vs. LMC^{after} $F = 2.53$, $p = 0.13$; L5 MMC^{before} vs. MMC^{after} $F = 1.28$, $p = 0.28$; L5 LMC^{before} vs. LMC^{after} $F = 1.28$, $p = 0.63$). **(C)** Bar graph showing the mean coherence before (solid bars) and after (hatched bars) removal of the brain stem. The coupling between MNs was significantly tighter in L2 than in T7 or L5 both before and after removal of the brain stem (Kruskal-Wallis test followed by a Dunn's multiple comparison, L2 MMC^{before} vs. T7 MMC^{before} $p = 0.007$; L2 MMC^{before} vs. L5 MMC^{before} $p = 0.0004$; L2 LMC^{before} vs. L5 LMC^{before} $p = 0.001$; L5 MMC^{before} vs. T7 MMC^{before} $p > 0.99$; Wilcoxon matched paired test, T7 MMC^{before} vs. MMC^{after} $p = 0.82$; L2 MMC^{before} vs. MMC^{after} $p = 0.56$; L2 LMC^{before} vs. LMC^{after} $p > 0.99$; L5 MMC^{before} vs. MMC^{after} $p = 0.73$; L5 LMC^{before} vs. LMC^{after} $p = 0.57$). $^{**}p < 0.01$, $^{***}p < 0.001$.

(mean phase vector) and coupling strengths (mean coherence) are shown in **Figure 5**.

Before removal of the brain stem (**Figure 5A**), the mean phase vector between left and right L2 MMC MNs was around 180°, indicating left/right alternation between axial MNs. In contrast, the mean phase vector between MMC and LMC MNs on the same side of L2 was close to 0°, indicating synchronous activation. In L5, the mean phase vector between MMC and LMC MNs was close to 90°, differing significantly from the mean phase vector in L2 (Watson–Williams F-test, $F = 9.462$, $p = 0.007$). The mean vector length in L5 was also smaller than in L2, indicating a more widespread distribution of phase differences. However, the distribution was not uniform (Watson's U^2-test, $p < 0.01$) and close inspection of the L5 circular plots revealed a clustering of phase differences into at least two groups; one group where MMC and LMC MNs discharged mostly in-phase (quadrant 0–90°)

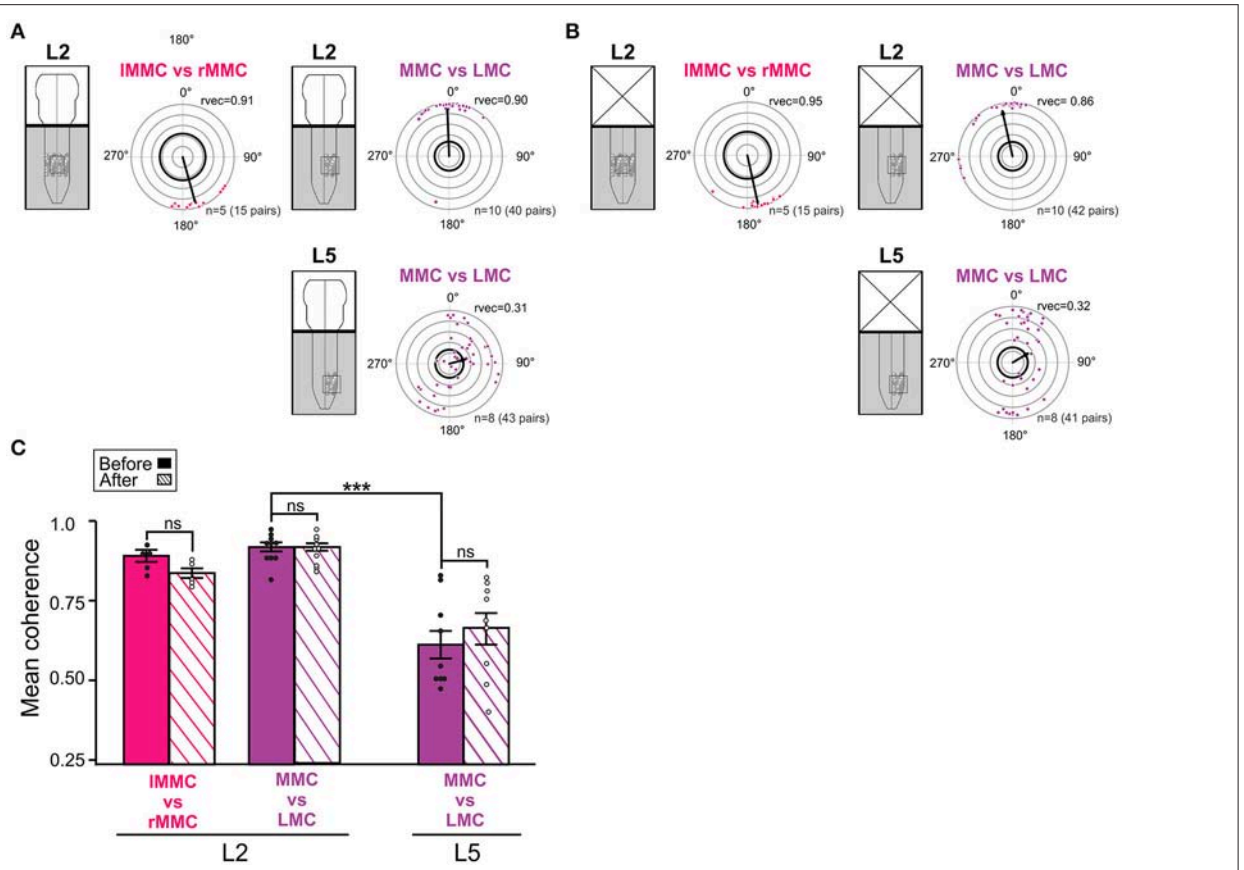


FIGURE 5 | Temporal relationships and coupling strengths between MNs of different motor columns before and after removal of the brain stem. **(A,B)** Inter-columnar phase relationships between pairs of MNs in left and right MMC in L2, MMC and LMC in L2, and MMC and LMC in L5 before and after removal of the brain stem. Phase relationships between MMCs are shown in red and phase relationships between MMC and LMCs are shown in purple. Removal of the brain stem did not significantly change the mean phase differences between MNs (Watson–Williams *F*-test, L2 IMMC/rMMC^{before} vs. IMMC/rMMC^{after} $F = 0.03$, $p = 0.87$; L2 MMC/LMC^{before} vs. MMC/LMC^{after} $F = 0.60$, $p = 0.45$; L5 MMC/LMC^{before} vs. MMC/LMC^{after} $F = 0.21$, $p = 0.65$). **(C)** Bar graph showing mean coherence before (solid bars) and after (hatched bars) removal of the brain stem. The strengths of the coupling between MNs was not significantly affected by removal of the brain stem (Wilcoxon matched-pairs test, L2 IMMC/rMMC^{before} vs. IMMC/rMMC^{after} $p = 0.19$; Kruskal-Wallis test followed by a Dunn's multiple comparison, L2 MMC/LMC^{before} vs. L2 MMC/LMC^{after} $p > 0.99$; L5 MMC/LMC^{before} vs. L5 MMC/LMC^{after} $p > 0.99$). ***$p < 0.001$. For other details, see **Figure 4**.

and another one group where MMC and LMC MNs discharged out-of-phase (around 180°).

In addition, several MMC/LMC pairs were less, or not, correlated (dots close or within the thick black outline circle). Removal of the brain stem did not significantly change the mean phase vectors between left and right L2 MMC MNs or between MMC and LMC MNs in L2 and L5 (**Figure 5B**, see figure legend for *p*-values).

The coherence between MMC and LMC MNs was found to be significantly lower in L5 than in L2 (MMC vs. LMC solid bars in **Figure 5C**, Kruskal-Wallis test followed by a Dunn's multiple comparison, $p = 0.0005$), suggesting a much more labile coupling between MMC and LMC MNs in L5 than in L2. This might be attributable to the presence of some poorly correlated MNs in the MMC (see previous section) rather than in the LMC. Removal of the brain stem did not significantly change the coherence between MMC and LMC MNs either in L2 or L5 (**Figure 5C**, hatched bars see figure legend for *p*-values).

Altogether, these findings demonstrate left/right alternation between L2 MMC MNs, synchrony between L2 MMC and LMC MNs, and combinations of synchrony and alternation between L5 MMC and LMC MNs during drug-induced LLA in the brain stem-spinal cord preparation. As intra-columnar relationships, inter-columnar relationships were not significantly affect by removal of the brain stem, suggesting that during drug-induced LLA these relationships are organized largely by the spinal networks.

Effect of Reversible Cooling of the Brain Stem on L2 Rhythm Frequency

To investigate whether activity in brain stem neurons contributed to the increase in L2 rhythm frequency observed after removal of the brain stem, we cooled down the brain stem to 18°C ($n = 4$). At this temperature, activity in neuronal somata is blocked and transmission along axons is greatly reduced (Brooks, 1983).

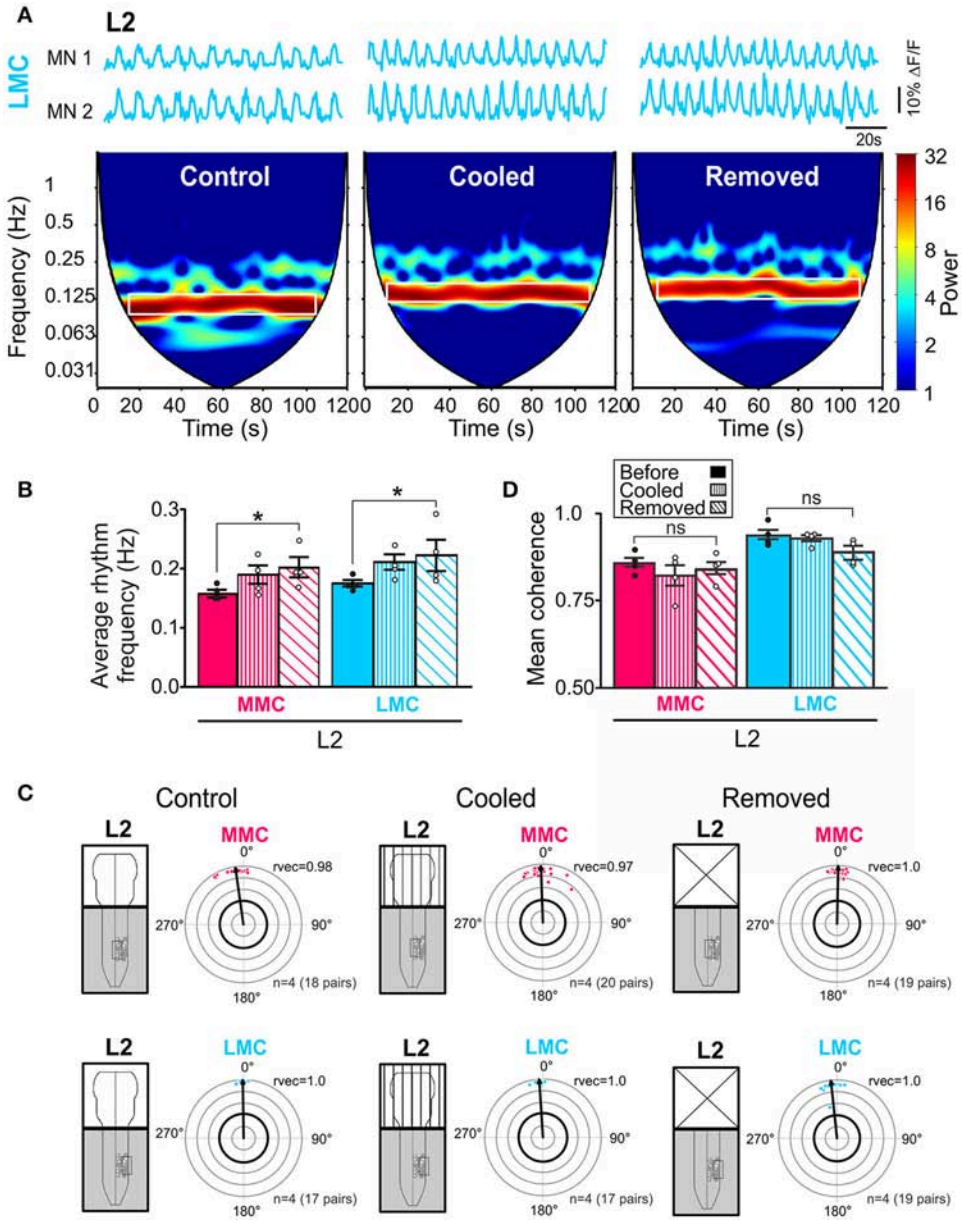


FIGURE 6 | Reduced brain stem activity also increases locomotor rhythm frequency. **(A)** Three sets of waveforms showing changes in fluorescence in two L2 LMC MNs before and during cooling of the brain stem and after removal of the brain stem. Each set of waveforms is shown with corresponding coherent cross-wavelet transform (CXWT) spectrogram (see Methods). The band of high-power (red) frequencies is marked with a white rectangle indicates a significantly coherence between the two signals in the neighborhood of the locomotor rhythm frequency. The two bottom white regions on either side of the V-shaped "cone of influence" indicate spectra regions not analyzed due to edge effects (Mor and Lev-Tov, 2007). **(B)** Bar graphs showing the average rhythm frequency in each motor column before (solid bars) and during cooling (vertically hatched bars) of the brain stem, and after removal of the brain stem (obliquely hatched bars). The increase after cooling was not as large as the increase after complete removal of the brain stem but it was observed in all experiments in both MMC and LMC MNs (Friedman test followed by Dunn's multiple *post-hoc* comparison, $MMC^{control}$ vs. MMC^{cooled} $p = 0.23$ $MMC^{control}$ vs. $MMC^{removed}$ $p = 0.04$; MMC^{cooled} vs. $MMC^{removed}$ $p > 0.99$; $LMC^{control}$ vs. LMC^{cooled} $p = 0.23$; $LMC^{control}$ vs. $LMC^{removed}$ $p = 0.04$; LMC^{cooled} vs. $LMC^{removed}$ $p > 0.99$). **(C)** Circular plots showing the effect of cooling and removing the brain stem on the intra-columnar phase differences (Watson–Williams *F*-test, $MMC^{control}$ vs. MMC^{cooled} $F = 0.69$, $p = 0.46$; $MMC^{control}$ vs. $MMC^{removed}$ $F = 2.23$, $p = 0.19$; MMC^{cooled} vs. $MMC^{removed}$ $F = 0.18$, $p = 0.68$; $LMC^{control}$ vs. LMC^{cooled} $F = 2.28$, $p = 0.18$; $LMC^{control}$ vs. $LMC^{removed}$ $F = 5.56$, $p = 0.06$ LMC^{cooled} vs. $LMC^{removed}$ $F = 1.07$, $p = 0.34$). **(D)** Bar graphs showing the effect of cooling and removal the brain stem on the intra-columnar coupling strengths (Friedman test followed by a Dunn's multiple comparison, $MMC^{control}$ vs. MMC^{cooled} $p = 0.47$; $MMC^{control}$ vs. $MMC^{removed}$ $p > 0.99$; MMC^{cooled} vs. $MMC^{removed}$ $p > 0.99$; $LMC^{control}$ vs. LMC^{cooled} $p > 0.99$; $LMC^{control}$ vs. $LMC^{removed}$ $p = 0.23$; LMC^{cooled} vs. $LMC^{removed}$ $p = 0.47$). $^*p < 0.05$.

Cooling of the brain stem increased the locomotor rhythm frequency (**Figure 6A**), an effect that was reversible. In the spectrograms of **Figure 6A**, the increase is shown as a shift of the high-power frequencies band (white rectangle) toward higher frequencies. The increase was not as large as the increase observed after complete removal of the brain stem but it was observed in all experiments both in MMC and LMC MNs (**Figure 6B**, see figure legend for *p*-values). We also analyzed intra-columnar phase relationships and strengths of coupling during cooling and, as shown in **Figures 6C,D**, the effects of cooling on these parameters were indistinguishable from the effects observed after removal of the brain stem (see figure legend for *p*-values).

These results demonstrate a similar effect of cooling and removal of the brain stem on the locomotor rhythm and support a contribution from brain stem descending neurons.

DISCUSSION

General Findings

In this study, we characterized for the first time the activities of trunk (MMC) and hindlimb (LMC) MNs during drug-induced fictive locomotion in the brain stem-spinal cord preparation of the neonatal mouse. We found that (1) trunk and hindlimb MNs display a preparatory period of tonic activity prior to rhythmic activity, (2) trunk MNs in T7 burst either in-phase or out-of-phase during rhythmic activity whereas trunk MNs in L2 or L5 burst in-phase, and (3) most trunk MNs in L2 burst in-phase with hindlimb MNs whereas in L5, several trunk MNs also burst out-of-phase with hindlimb MNs. Removal of the brain stem significantly increased the locomotor rhythm frequency with concomitant shortening in locomotor bursts. When individual segments were considered separately, the effects of removing the brain stem were significant in L2 but not T7 or L5. One interpretation of this result is that, in neonatal mouse, the brain stem targets its influence specifically on the thoracolumbar segments that have the highest potential for generating rhythmic locomotor activity (Ho and O'Donovan, 1993; Cazalets et al., 1995; Kjaerulff and Kiehn, 1996; Cowley et al., 2009; Hägglund et al., 2013).

Our work adds to a previous study in neonatal decerebrate mice in which an increase in locomotor rhythm frequency after removal of the brainstem was observed in L2 MNs (Gordon and Whelan, 2008). Both the recording method and the method used to induce fictive locomotion in this study differed from the methods used in the present study, suggesting that the increase in L2 locomotor rhythm frequency after removal of the brainstem is a robust phenomenon. In the adult decerebrate mice, spinalization also produces an increase in locomotor frequency (Meehan et al., 2012).

Candidate Subcortical Descending Systems

The increase in locomotor rhythm frequency after brainstem removal may be attributable to the loss of inputs from one or more brainstem descending systems. Prime candidates are the reticulospinal and the vestibulospinal systems (Grillner, 1981; Armstrong, 1988; Jordan, 1991; Zaporozhets et al., 2004; Jordan et al., 2008; Hägglund et al., 2010; Bretzner and Brownstone, 2013; Perreault and Glover, 2013).

Both the reticulospinal system and the lateral vestibulospinal system have the functional connectivity that would allow control over MMC and LMC MNs in the newborn mouse (Szokol et al., 2008; Szokol and Perreault, 2009; Kasumacic et al., 2010; Sivertsen et al., 2014). Although there is currently no available data on the discharge pattern of the reticulo- or vestibulospinal neurons during locomotor activity in the decerebrated mouse, earlier studies in adult decerebrate lampreys, guinea pigs, and cats indicate that the majority of these neurons discharge rhythmically during fictive locomotion (Kasicki et al., 1989; Bussières and Dubuc, 1992; Marlinsky, 1992; Perreault et al., 1993). Electrical or optogenetic stimulation to increase the ongoing locomotor discharge of reticulo- or vestibulospinal neurons in decerebrated preparations can lead to a prolongation of the locomotor cycle (Russell and Zajac, 1979; Vinay and Grillner, 1993; Perreault et al., 1994; Leblond and Gossard, 1997; Bouvier et al., 2015). Hence, loss of reticulo- and/or vestibulo-spinal inputs after spinal cord transection would be consistent with a decrease in locomotor cycle.

Monoaminergic descending systems such as the coerulospinal and raphespinal systems could also participate. The discharge pattern of monoaminergic descending neurons during locomotor activity has not been investigated in decerebrate neonatal mouse but available evidence from experiments in adult cats suggests that a majority of raphespinal neurons are tonically active during locomotion (Veasey et al., 1995; Noga et al., 2017). Serotonin prolongs locomotor cycle and axial MN burst durations in adult decerebrate lampreys (Buchanan, 2011). Conversely, serotoninergic receptor antagonists reduce the locomotor burst and cycle duration in limb MNs in decerebrate rats (Cabaj et al., 2017). Thus, loss of tonic raphespinal input after spinal transection would also be consistent with a decrease in locomotor cycle. However, a more precise assessment of the relative contribution of the different supraspinal neuronal groups must await a future characterization of their locomotor discharge patterns in the mouse.

Tonic Activity, Double-Peak Bursts in Axial MNs and Trunk-Hindlimb Coordination

We report tonic and rhythmic LLA in axial MNs of T7, L2, and L5 segment. The tonic activity in axial MNs have similar spatiotemporal characteristics as the tonic activity in hindlimb MNs, a finding that is consistent with the idea that tonic activity in MNs act as a constant background for rhythmic activity (Kjaerulff and Kiehn, 1996). Tonic activity was not affected by removal of the brain stem, suggesting that it is produced by neuronal networks located in the spinal cord. We speculate that these spinal networks may play an important role in production of the postural responses that accompany locomotor movement by setting the level of

excitability of the spinal neurons that form the locomotor rhythm generator.

We report single locomotor burst and double-peak locomotor bursts in axial MNs. The functional significance of the double-peak bursts is unclear but *double-bursts* in trunk muscles in various adult mammalian species has been associated with a multifunctional role in mobilization and stabilization of the trunk and pelvis, a requirement for movement of the limbs during walking (Carlson et al., 1979; English, 1980; Thorstensson et al., 1982; Zomlefer et al., 1984; Ritter et al., 2001; Wada and Kanda, 2004; Wada et al., 2006; de Sèze et al., 2008; Ceccato et al., 2009; Schilling and Carrier, 2010). Double-peak locomotor bursts tend to be less common after removal of the brainstem. Interestingly, double-bursts in adult trunk muscles are also less frequent after spinal transection unless animals are provided with neurochemicals, training, or sensory afferent input activation (Koehler et al., 1984; Zomlefer et al., 1984; Barbeau and Rossignol, 1987). Future experiments on the development of double-peak bursts are required to determine if more parallels exist between double-peak bursts in neonates and double-bursts in adults, and ultimately inform about the possibility that double-peak bursts lead to the expression of full-fledge double-bursts in adults.

Our findings on the temporal dynamic of the locomotor activities between axial and hindlimb MNs add to previous single-cell resolution work in the isolated lumbar spinal cord and confirm a more complex coupling between axial and hindlimb MNs in the L5 (O'Donovan et al., 2008; Hinckley et al., 2015). Removal of the brain stem does not significantly affect inter-columnar phase relationships either in L2 or in L5, suggesting that trunk-hindlimb coordination in neonates greatly relies on propriospinal mechanisms. These mechanisms may include segmental as well as inter-segmental mechanisms (Falgairolle and Cazalets, 2007). Finally, in addition to their role in trunk-hindlimb coordination, thoracolumbar MNs innervating abdominal and pelvic musculature (Schrøder, 1980; Canon et al., 1991; Giraudin et al., 2008) may also assist respiratory exhalation during rhythmic motor activity (Iscoe, 1998; Hodges et al., 2007). Compatible with such a role, thoracolumbar MNs innervating abdominal muscles have recently been shown to display LLA during drug-induced fictive locomotion both before and after silencing of the brain stem (Le Gal et al., 2016).

CONCLUSION

In the current study, we have assessed the influence of the brain stem on locomotor activity in axial and hindlimb spinal networks in newborn mammals. The study reveals an influence on the timing of the locomotor activity not only in hindlimb but also in axial motor pools. This influence on the axial and hindlimb spinal locomotor rhythm generating circuits may extend the range of frequencies over which these circuits operate. Having this ability early during development may be critical when learning how to walk is a major undertaking.

AUTHOR CONTRIBUTIONS

Funding acquisition: M-CP; Conceptualization: M-CP and CJ-X; Supervision: M-CP; Methodology: CJ-X and M-CP; Experiments: CJ-X; Analyses: CJ-X and M-CP; Interpretation: M-CP and CJ-X; Writing of original draft: M-CP; Editing and approval of final version approval: M-CP and CJ-X.

ACKNOWLEDGMENTS

Ms. Renee Shaw for technical support, Drs Yoav Mor and Aharon Lev-Tov providing the SpinalCore software, and Dr. Morten Raastad for constructive comments on an earlier draft of this manuscript. This research was supported by the International Foundation for Research on Paraplegia (IRP), the Craig H. Neilsen Foundation and the National Institutes of Health (NIH) grant R01 NS085387.

SUPPLEMENTARY MATERIAL

The Supplementary Material for this article can be found online at: https://www.frontiersin.org/articles/10.3389/fnins.2018.00053/full#supplementary-material

REFERENCES

Armstrong, D. M. (1988). The supraspinal control of mammalian locomotion. *J. Physiol.* 405, 1–37. doi: 10.1113/jphysiol.1988.sp017319

Bagnall, M. W., and McLean, D. L. (2014). Modular organization of axial microcircuits in zebrafish. *Science* 343, 197–200. doi: 10.1126/science.1245629

Barbeau, H., and Rossignol, S. (1987). Recovery of locomotion after chronic spinalization in the adult cat. *Brain Res.* 412, 84–95. doi: 10.1016/0006-8993(87)91442-9

Beliez, L., Barrière, G., Bertrand, S. S., and Cazalets, J.-R. (2015). Origin of thoracic spinal network activity during locomotor-like activity in the neonatal rat. *J. Neurosci.* 35, 6117–6130. doi: 10.1523/JNEUROSCI.4145-14.2015

Beyeler, A., Métais, C., Combes, D., Simmers, J., and Le Ray, D. (2008). Metamorphosis-induced changes in the coupling of spinal thoraco-lumbar motor outputs during swimming in *Xenopus laevis*. *J. Neurophysiol.* 100, 1372–1383. doi: 10.1152/jn.00023.2008

Bonnot, A., Whelan, P. J., Mentis, G. Z., and O'Donovan, M. J. (2002). Locomotor-like activity generated by the neonatal mouse spinal cord. *Brain Res. Rev.* 40, 141–151. doi: 10.1016/S0165-0173(02)00197-2

Bouvier, J., Caggiano, V., Leiras, R., Caldeira, V., Bellardita, C., Balueva, K., et al. (2015). Descending command neurons in the brainstem that halt locomotion. *Cell* 163, 1191–1203. doi: 10.1016/j.cell.2015.10.074

Bretzner, F., and Brownstone, R. M. (2013). Lhx3-Chx10 Reticulospinal neurons in locomotor circuits. *J. Neurosci.* 33, 14681–14692. doi: 10.1523/JNEUROSCI.5231-12.2013

Brooks, V. B. (1983). Study of brain function by local, reversible cooling. *Rev. Physiol. Biochem. Pharmacol.* 95, 1–109. doi: 10.1007/BFb0034097

Buchanan, J. T. (2011). Flexibility in the patterning and control of axial locomotor networks in lamprey. *Integr. Comp. Biol.* 51, 869–878. doi: 10.1093/icb/icr077

Bussières, N., and Dubuc, R. (1992). Phasic modulation of vestibulospinal neuron activity during fictive locomotion in lampreys. *Brain Res.* 575, 174–179. doi: 10.1016/0006-8993(92)90441-B

Cabaj, A. M., Majczynski, H., Couto, E., Gardiner, P. F., Stecina, K., Sławinska, U., et al. (2017). Serotonin controls initiation of locomotion and afferent modulation of coordination via 5-HT 7 receptors in adult rats: 5-HT 7 receptors in locomotor control. *J. Physiol.* 595, 301–320. doi: 10.1113/JP272271

Cabelguen, J.-M., Charrier, V., and Mathou, A. (2014). Modular functional organisation of the axial locomotor system in salamanders. *Zoology* 117, 57–63. doi: 10.1016/j.zool.2013.10.002

Canon, E., Reznik, M., and Timmermans, L. M. (1991). Morphometry of sacral neurons innervating the pelvic muscles. Experimental study. *Acta Urol. Belg.* 59, 1–16.

Carlson, H., Halbertsma, J., and Zomlefer, M. (1979). Control of the trunk during walking in the cat. *Acta Physiol. Scand*. 105, 251–253. doi: 10.1111/j.1748-1716.1979.tb06338.x

Cazalets, J.-R., Borde, M., and Clarac, F. (1995). Localization and organization of the central pattern generator for hindlimb locomotion in newborn rat. *J. Neurosci*. 15, 4943–4951.

Ceccato, J.-C., de Sèze, M., Azevedo, C., and Cazalets, J.-R. (2009). Comparison of trunk activity during gait initiation and walking in humans. *PLoS ONE* 4:e8193. doi: 10.1371/journal.pone.0008193

Combes, D., Merrywest, S. D., Simmers, J., and Sillar, K. T. (2004). Developmental segregation of spinal networks driving axial- and hindlimb-based locomotion in metamorphosing *Xenopus laevis*. *J. Physiol.* 559, 17–24. doi: 10.1113/jphysiol.2004.069542

Cowley, K. C., Zaporozhets, E., Joundi, R. A., and Schmidt, B. J. (2009). Contribution of commissural projections to bulbospinal activation of locomotion in the *in vitro* neonatal rat spinal cord. *J. Neurophysiol*. 101, 1171–1178. doi: 10.1152/jn.91212.2008

de Sèze, M., Falgairolle, M., Viel, S., Assaiante, C., and Cazalets, J.-R. (2008). Sequential activation of axial muscles during different forms of rhythmic behavior in man. *Exp. Brain Res*. 185, 237–247. doi: 10.1007/s00221-007-1146-2

English, A. W. (1980). The functions of the lumbar spine during stepping in the cat. *J. Morphol*. 165, 55–66. doi: 10.1002/jmor.1051650106

Falgairolle, M., Ceccato, J.-C., de Seze, M., Herbin, M., and Cazalets, J.-R. (2013). Metachronal propagation of motor activity. *Front. Biosci*. 18, 820–837. doi: 10.2741/4146

Falgairolle, M., and Cazalets, J.-R. (2007). Metachronal coupling between spinal neuronal networks during locomotor activity in newborn rat: synchronization between neuronal networks. *J. Physiol.* 580, 87–102. doi: 10.1113/jphysiol.2006.115709

Giraudin, A., Cabirol-Pol, M.-J., Simmers, J., and Morin, D. (2008). Intercostal and abdominal respiratory motoneurons in the neonatal rat spinal cord: spatiotemporal organization and responses to limb afferent stimulation. *J. Neurophysiol.* 99, 2626–2640. doi: 10.1152/jn.01298.2007

Glover, J. C. (1995). Retrograde and anterograde axonal tracing with fluorescent dextrans in the embryonic nervous system. *Neurosci. Protoc.* 30, 1–13.

Gordon, I. T., and Whelan, P. J. (2008). Brainstem modulation of locomotion in the neonatal mouse spinal cord: descending control of locomotion in the developing mouse. *J. Physiol.* 586, 2487–2497. doi: 10.1113/jphysiol.2007.148320

Gramsbergen, A. (1998). Posture and locomotion in the rat: independent or interdependent development? *Neurosci. Biobehav. Rev*. 22, 547–553. doi: 10.1016/S0149-7634(97)00043-2

Grillner, S. (1981). "Control of locomotion in bipeds, tetrapods, and fish," in *Comprehensive Physiology,* Vol. II, ed R. Terjung (Hoboken, NJ: John Wiley & Sons, Inc.), 1179–1236.

Grillner, S. (2006). Biological pattern generation: the cellular and computational logic of networks in motion. *Neuron* 52, 751–766. doi: 10.1016/j.neuron.2006.11.008

Grillner, S., and Manira, A. E. (2015). The intrinsic operation of the networks that make us locomote. *Curr. Opin. Neurobiol*. 31, 244–249. doi: 10.1016/j.conb.2015.01.003

Hägglund, M., Borgius, L., Dougherty, K. J., and Kiehn, O. (2010). Activation of groups of excitatory neurons in the mammalian spinal cord or hindbrain evokes locomotion. *Nat. Neurosci.* 13, 246–252. doi: 10.1038/nn.2482

Hägglund, M., Dougherty, K. J., Borgius, L., Itohara, S., Iwasato, T., and Kiehn, O. (2013). Optogenetic dissection reveals multiple rhythmogenic modules underlying locomotion. *Proc. Natl. Acad. Sci. U.S.A.* 110, 11589–11594. doi: 10.1073/pnas.1304365110

Hinckley, C. A., Alaynick, W. A., Gallarda, B. W., Hayashi, M., Hilde, K. L., Driscoll, S. P., et al. (2015). Spinal locomotor circuits develop using hierarchical rules based on motorneuron position and identity. *Neuron* 87, 1008–1021. doi: 10.1016/j.neuron.2015.08.005

Ho, S., and O'Donovan, M. J. (1993). Regionalization and intersegmental coordination of rhythm-generating networks in the spinal cord of the chick embryo. *J. Neurosci.* 13, 1354–1371.

Hodges, P. W., Sapsford, R., and Pengel, L. H. M. (2007). Postural and respiratory functions of the pelvic floor muscles. *Neurourol. Urodyn*. 26, 362–371. doi: 10.1002/nau.20232

Iscoe, S. (1998). Control of abdominal muscles. *Prog. Neurobiol*. 56, 433–506. doi: 10.1016/S0301-0082(98)00046-X

Jamon, M. (2006). The early development of motor control in neonate rat. *Comptes Rendus Palevol* 5, 657–666. doi: 10.1016/j.crpv.2005.11.018

Jean-Xavier, C., and Perreault, M.-C. (2013). "Brainstem control of trunk and hindlimb motoneurons during fictive locomotion in the neonatal mouse," in *Neuroscience Meeting Planner, Society for Neuroscience*. Online Program No 560.08 (San Diego, CA).

Jiang, Z., Carlin, K. P., and Brownstone, R. M. (1999). An *in vitro* functionally mature mouse spinal cord preparation for the study of spinal motor networks. *Brain Res*. 816, 493–499. doi: 10.1016/S0006-8993(98)01199-8

Jordan, L. M. (1991). "Brainstem and spinal cord mechanisms for the initiation of locomotion", in *Neurobiological Basis of Human Locomotion*, eds M. Shimamura, S. Grillner, and V. R. Edgerton (Tokyo: Japan Scientific Societies), 3–20.

Jordan, L. M., Liu, J., Hedlund, P. B., Akay, T., and Pearson, K. G. (2008). Descending command systems for the initiation of locomotion in mammals. *Brain Res. Rev*. 57, 183–191. doi: 10.1016/j.brainresrev.2007.07.019

Kasicki, S., Grillner, S., Ohta, Y., Dubuc, R., and Brodin, L. (1989). Phasic modulation of reticulospinal neurones during fictive locomotion and other types of spinal motor activity in lamprey. *Brain Res.* 484, 203–216. doi: 10.1016/0006-8993(89)90363-6

Kasumacic, N., Glover, J. C., and Perreault, M.-C. (2010). Segmental patterns of vestibular-mediated synaptic inputs to axial and limb motoneurons in the neonatal mouse assessed by optical recording: imaging vestibulospinal inputs to spinal motoneurons. *J. Physiol.* 588, 4905–4925. doi: 10.1113/jphysiol.2010.195644

Kishore, S., Bagnall, M. W., and McLean, D. L. (2014). Systematic shifts in the balance of excitation and inhibition coordinate the activity of axial motor pools at different speeds of locomotion. *J. Neurosci*. 34, 14046–14054. doi: 10.1523/JNEUROSCI.0514-14.2014

Kjaerulff, O., and Kiehn, O. (1996). Distribution of networks generating and coordinating locomotor activity in the neonatal rat spinal cord *in vitro*: a lesion study. *J. Neurosci*. 16, 5777–5794.

Koehler, W. J., Schomburg, E. D., and Steffens, H. (1984). Phasic modulation of trunk muscle efferents during fictive spinal locomotion in cats. *J. Physiol.* 353, 187–197. doi: 10.1113/jphysiol.1984.sp015331

Kreitzer, A. C., Gee, K. R., Archer, E. A., and Regehr, W. G. (2000). Monitoring presynaptic calcium dynamics in projection fibers by *in vivo* loading of a novel calcium indicator. *Neuron* 27, 25–32. doi: 10.1016/S0896-6273(00)00006-4

Kristan, W. B., Calabrese, R. L., and Friesen, W. O. (2005). Neuronal control of leech behavior. *Prog. Neurobiol*. 76, 279–327. doi: 10.1016/j.pneurobio.2005.09.004

Kudo, N., and Yamada, T. (1987). N-methyl-D,L-aspartate-induced locomotor activity in a spinal cord-hindlimb muscles preparation of the newborn rat studied *in vitro*. *Neurosci. Lett*. 75, 43–48. doi: 10.1016/0304-3940(87)90072-3

Leblond, H., and Gossard, J.-P. (1997). Supraspinal and segmental signals can be transmitted through separate spinal cord pathways to enhance locomotor activity in extensor muscles in the cat. *Exp. Brain Res.* 114, 188–192. doi: 10.1007/PL00005619

Le Gal, J.-P., Juvin, L., Cardoit, L., and Morin, D. (2016). Bimodal respiratory-locomotor neurons in the neonatal rat spinal cord. *J. Neurosci.* 36, 926–937. doi: 10.1523/JNEUROSCI.1825-15.2016

Lev-Tov, A., and O'Donovan, M. J. (1995). Calcium imaging of motoneuron activity in the en-bloc spinal cord preparation of the neonatal rat. *J. Neurophysiol*. 74, 1324–1334. doi: 10.1152/jn.1995.74.3.1324

MacDonell, C. W., Power, K. E., Chopek, J. W., Gardiner, K. R., and Gardiner, P. F. (2015). Extensor motoneurone properties are altered immediately before and during fictive locomotion in the adult decerebrate rat: motoneurone properties during fictive locomotion. *J. Physiol.* 593, 2327–2342. doi: 10.1113/JP270239

Marlinsky, V. V. (1992). Activity of lateral vestibular nucleus neurons during locomotion in the decerebrate guinea pig. *Exp. Brain Res.* 90, 583–588. doi: 10.1007/BF00230942

Meehan, C. F., Grondahl, L., Nielsen, J. B., and Hultborn, H. (2012). Fictive locomotion in the adult decerebrate and spinal mouse *in vivo*: fictive locomotion in the decerebrate mouse. *J. Physiol.* 590, 289–300. doi: 10.1113/jphysiol.2011.214643

Mor, Y., and Lev-Tov, A. (2007). Analysis of rhythmic patterns produced by spinal neural networks. *J. Neurophysiol.* 98, 2807–2817. doi: 10.1152/jn.00740.2007

Musienko, P. E., Deliagina, T. G., Gerasimenko, Y. P., Orlovsky, G. N., and Zelenin, P. V. (2014). Limb and trunk mechanisms for balance control during locomotion in quadrupeds. *J. Neurosci.* 34, 5704–5716. doi: 10.1523/JNEUROSCI.4663-13.2014

Noga, B. R., Turkson, R. P., Xie, S., Taberner, A., Pinzon, A., and Hentall, I. D. (2017). Monoamine release in the cat lumbar spinal cord during fictive locomotion evoked by the mesencephalic locomotor region. *Front. Neural Circuits* 11:59. doi: 10.3389/fncir.2017.00059

O'Donovan, M. J., Bonnot, A., Mentis, G. Z., Arai, Y., Chub, N., Shneider, N. A., et al. (2008). Imaging the spatiotemporal organization of neural activity in the developing spinal cord. *Dev. Neurobiol.* 68, 788–803. doi: 10.1002/dneu.20620

Perreault, M. C., Drew, T., and Rossignol, S. (1993). Activity of medullary reticulospinal neurons during fictive locomotion. *J. Neurophysiol.* 69, 2232–2247. doi: 10.1152/jn.1993.69.6.2232

Perreault, M.-C., and Glover, J. C. (2013). Glutamatergic reticulospinal neurons in the mouse: developmental origins, axon projections, and functional connectivity: glutamatergic reticulospinal neurons in the mouse. *Ann. N.Y. Acad. Sci.* 1279, 80–89. doi: 10.1111/nyas.12054

Perreault, M. C., Rossignol, S., and Drew, T. (1994). Microstimulation of the medullary reticular formation during fictive locomotion. *J. Neurophysiol.* 71, 229–245. doi: 10.1152/jn.1994.71.1.229

Perreault, M.-C., Shefchyk, S. J., Jimenez, I., and McCrea, D. A. (1999). Depression of muscle and cutaneous afferent-evoked monosynaptic field potentials during fictive locomotion in the cat. *J. Physiol.* 521, 691–703. doi: 10.1111/j.1469-7793.1999.00691.x

Putney, J. W. (ed.). (2006). *Calcium Signaling, 2nd Edn.* Boca Raton, FL: CRC/Taylor & Francis.

Ritter, D. A., Nassar, P. N., Fife, M., and Carrier, D. R. (2001). Epaxial muscle function in trotting dogs. *J. Exp. Biol.* 204, 3053–3064.

Roberts, A., Li, W.-C., and Soffe, S. R. (2012). A functional scaffold of CNS neurons for the vertebrates: the developing *Xenopus laevis* spinal cord. *Dev. Neurobiol.* 72, 575–584. doi: 10.1002/dneu.20889

Russell, D. F., and Zajac, F. E. (1979). Effects of stimulating Deiters' nucleus and medial longitudinal fasciculus on the timing of the fictive locomotor rhythm induced in cats by DOPA. *Brain Res.* 177, 588–592. doi: 10.1016/0006-8993(79)90478-5

Ryczko, D., Dubuc, R., and Cabelguen, J.-M. (2010). Rhythmogenesis in axial locomotor networks: an interspecies comparison. *Prog. Brain Res.* 187, 189–211. doi: 10.1016/B978-0-444-53613-6.00013-7

Ryczko, D., Knüsel, J., Crespi, A., Lamarque, S., Mathou, A., Ijspeert, A. J., et al. (2015). Flexibility of the axial central pattern generator network for locomotion in the salamander. *J. Neurophysiol.* 113, 1921–1940. doi: 10.1152/jn.00894.2014

Schilling, N. (2011). Evolution of the axial system in craniates: morphology and function of the perivertebral musculature. *Front. Zool.* 8:4. doi: 10.1186/1742-9994-8-4

Schilling, N., and Carrier, D. R. (2010). Function of the epaxial muscles in walking, trotting and galloping dogs: implications for the evolution of epaxial muscle function in tetrapods. *J. Exp. Biol.* 213, 1490–1502. doi: 10.1242/jeb.039487

Schrøder, H. D. (1980). Organization of the motoneurons innervating the pelvic muscles of the male rat. *J. Comp. Neurol.* 192, 567–587. doi: 10.1002/cne.901920313

Sivertsen, M. S., Glover, J. C., and Perreault, M.-C. (2014). Organization of pontine reticulospinal inputs to motoneurons controlling axial and limb muscles in the neonatal mouse. *J. Neurophysiol.* 112, 1628–1643. doi: 10.1152/jn.00820.2013

Smith, J. C., and Feldman, J. L. (1987). *In vitro* brainstem-spinal cord preparations for study of motor systems for mammalian respiration and locomotion. *J. Neurosci. Methods* 21, 321–333. doi: 10.1016/0165-0270(87)90126-9

Szokol, K., Glover, J. C., and Perreault, M.-C. (2008). Differential origin of reticulospinal drive to motoneurons innervating trunk and hindlimb muscles in the mouse revealed by optical recording: imaging reticulospinal inputs to lumbar spinal cord. *J. Physiol.* 586, 5259–5276. doi: 10.1113/jphysiol.2008.158105

Szokol, K., and Perreault, M.-C. (2009). Imaging synaptically mediated responses produced by brainstem inputs onto identified spinal neurons in the neonatal mouse. *J. Neurosci. Methods* 180, 1–8. doi: 10.1016/j.jneumeth.2009.01.018

Tazerart, S., Viemari, J.-C., Darbon, P., Vinay, L., and Brocard, F. (2007). Contribution of persistent sodium current to locomotor pattern generation in neonatal rats. *J. Neurophysiol.* 98, 613–628. doi: 10.1152/jn.00316.2007

Thorsen, D. H. (2004). Swimming of larval zebrafish: fin-axis coordination and implications for function and neural control. *J. Exp. Biol.* 207, 4175–4183. doi: 10.1242/jeb.01285

Thorstensson, A., Carlson, H., Zomlefer, M. R., and Nilsson, J. (1982). Lumbar back muscle activity in relation to trunk movements during locomotion in man. *Acta Physiol. Scand.* 116, 13–20. doi: 10.1111/j.1748-1716.1982.tb10593.x

Veasey, S. C., Fornal, C. A., Metzler, C. W., and Jacobs, B. L. (1995). Response of serotonergic caudal raphe neurons in relation to specific motor activities in freely moving cats. *J. Neurosci.* 15, 5346–5359.

Vinay, L., and Grillner, S. (1993). The spino-reticulo-spinal loop can slow down the NMDA-activated spinal locomotor network in lamprey. *Neuroreport* 4, 609–612. doi: 10.1097/00001756-199306000-00001

Wada, N., Akatani, J., Miyajima, N., Shimojo, K., and Kanda, K. (2006). The role of vertebral column muscles in level versus upslope treadmill walking—an electromyographic and kinematic study. *Brain Res.* 1090, 99–109. doi: 10.1016/j.brainres.2006.01.132

Wada, N., and Kanda, K. (2004). Trunk movements and EMG activity in the cat: level versus upslope walking. *Prog. Brain Res.* 143, 175–181. doi: 10.1016/S0079-6123(03)43017-3

Zaporozhets, E., Cowley, K. C., and Schmidt, B. J. (2004). A reliable technique for the induction of locomotor-like activity in the *in vitro* neonatal rat spinal cord using brainstem electrical stimulation. *J. Neurosci. Methods* 139, 33–41. doi: 10.1016/j.jneumeth.2004.04.009

Zhao, M., Hollingworth, S., and Baylor, S. M. (1996). Properties of tri- and tetracarboxylate Ca2+ indicators in frog skeletal muscle fibers. *Biophys. J.* 70, 896–916. doi: 10.1016/S0006-3495(96)79633-9

Zomlefer, M. R., Provencher, J., Blanchette, G., and Rossignol, S. (1984). Electromyographic study of lumbar back muscles during locomotion in acute high decerebrate and in low spinal cats. *Brain Res.* 290, 249–260. doi: 10.1016/0006-8993(84)90942-9

Conflict of Interest Statement: The authors declare that the research was conducted in the absence of any commercial or financial relationships that could be construed as a potential conflict of interest.

Copyright © 2018 Jean-Xavier and Perreault. This is an open-access article distributed under the terms of the Creative Commons Attribution License (CC BY). The use, distribution or reproduction in other forums is permitted, provided the original author(s) and the copyright owner are credited and that the original publication in this journal is cited, in accordance with accepted academic practice. No use, distribution or reproduction is permitted which does not comply with these terms.

frontiers in Neuroscience

ORIGINAL RESEARCH
published: 27 February 2018
doi: 10.3389/fnins.2018.00117

Age-Related Changes in Neuromodulatory Control of Bladder Micturition Contractions Originating in the Skin

Harumi Hotta, Harue Suzuki, Kaori Iimura and Nobuhiro Watanabe*

Department of Autonomic Neuroscience, Tokyo Metropolitan Institute of Gerontology, Tokyo, Japan

The brainstem is essential for producing micturition contractions of the urinary bladder. Afferent input from perineal skin evoked by gentle mechanical stimulation inhibits micturition contractions by decreasing both ascending and descending transmissions between the brainstem and spinal cord. Dysfunction of this inhibitory mechanism may be one cause of the increase in the prevalence of overactive bladder in old age. The aim of this study was to examine effect of aging on function of skin afferent fibers that inhibit bladder micturition contractions in rats. We used anesthetized male rats in three different age groups: young adult (4–5 months old), middle aged (6–9 months old), and aged (27–30 months old). The bladder was expanded to produce isovolumetric rhythmic micturition contractions. Skin afferent fibers were activated for 1 min either by electrical stimulation (0.5 ms, 0.2–10 V, 0.1–10 Hz) of the cutaneous branch of the pudendal nerve (CBPN) or by gentle mechanical skin stimulation with an elastomer roller. When skin afferent nerves were activated electrically, micturition contractions were inhibited in a similar manner in all age groups, with long latency inhibition induced by excitation of Aβ fibers and short latency inhibition by additional Aδ and C fiber excitation (at 1–10 Hz). On the contrary, when skin afferent nerves were activated mechanically by rolling, latency of inhibition following rolling stimulation was prolonged in aged rats. Single unitary afferent nerve activity of low-threshold mechanoreceptors (LTMs) from the cutaneous nerve was recorded. The discharge rate during rolling was not significantly reduced in Aβ units but was much lower in Aδ and C units in aged rats (0.4 and 0.5 Hz, respectively) than in young adult rats (3 and 7 Hz). These results suggest that the neural mechanism that inhibits bladder micturition contractions by skin afferent input is well maintained in old age, but the early inhibition by gentle skin stimulation is decreased because of reduced responses of Aδ- and C-LTMs.

Keywords: electrical stimulation, myelinated nerve fibers, unmyelinated nerve fibers, reflexes, urinary bladder, skin, mechanoreceptors, perineum

OPEN ACCESS

Edited by:
Brian R. Noga,
University of Miami, United States

Reviewed by:
Linda F. Hayward,
University of Florida, United States
Changfeng Tai,
University of Pittsburgh, United States

****Correspondence:***
Harumi Hotta
hhotta@tmig.or.jp

Specialty section:
This article was submitted to Neural Technology, a section of the journal Frontiers in Neuroscience

Received: *19 September 2017*
Accepted: *14 February 2018*
Published: *27 February 2018*

Citation:
Hotta H, Suzuki H, Iimura K and Watanabe N (2018) Age-Related Changes in Neuromodulatory Control of Bladder Micturition Contractions Originating in the Skin. Front. Neurosci. 12:117. doi: 10.3389/fnins.2018.00117

INTRODUCTION

The prevalence of lower urinary tract symptoms such as nocturia, urinary incontinence, and overactive bladder increases with older age (Homma et al., 2006; Irwin et al., 2006; Bosch and Weiss, 2010). Various age-related changes in bladder activity have been reported in humans and other animals. For example, a combination of detrusor overactivity with impaired contraction is seen in bladders in the elderly. In human bladder tissue, cholinergic bladder contractions decrease, while purinergic contractions increase with age (Yoshida et al., 2001). In rats, an increase in bladder volume, a reduced sensitivity of pelvic nerve afferents to bladder volume, and a reduced ability to raise bladder pressure in response to pelvic nerve efferent stimulation are associated with aging (Hotta et al., 1995). Pelvic nerve unmyelinated fibers with smaller diameters decrease in number in aged rats (Nakayama et al., 1998), and pelvic arterial insufficiency has been suggested to play an important role in the development of bladder dysfunctions in humans and other animals (Andersson et al., 2017). However, in addition to such peripheral factors, age-related changes in complex neuronal networks, including the spinal cord and brainstem, regulating bladder function might also be important. The micturition reflex is induced by positive feedback between the bladder and the pontine micturition center (PMC) in the brainstem and is facilitated or inhibited by various sensory inputs. Reduction in the inhibitory mechanism of the micturition reflex may contribute to susceptibility to overactive bladder due to aging. However, the age-related changes in the inhibitory mechanism of the micturition reflex remain to be determined.

In anesthetized adult animals, micturition contractions induced by bladder filling are inhibited by exciting somatic afferent nerves, either by electrical stimulation (Sato et al., 1980; Boggs et al., 2006; Tai et al., 2012; Ferroni et al., 2015) or with natural stimuli (Sato et al., 1975, 1977, 1992; Morrison et al., 1995; Budgell et al., 1998; Hotta et al., 2012). This is because the burst discharges of the pelvic nerve inducing bladder contractions are inhibited by somatosensory input (Sato et al., 1977, 1992, 1997; Hotta et al., 2012). We have recently reported the properties of somatic afferent nerves in the cutaneous branch of the pudendal nerve (CBPN) involved in the inhibition of bladder contraction. The excitation of Aβ fibers at 0.1–10 Hz for 1 min causes late inhibition, emerging several minutes after the end of stimulation, excitation of Aδ fibers at 1–10 Hz produced early inhibition, emerging immediately after stimulus onset, and excitation of C fibers at 1–10 Hz promoted both early and late inhibition (Onda et al., 2016). Similarly, gentle mechanical stimulation of the perineal skin surface with a roller that excites Aβ, Aδ, and C low-threshold mechanoreceptor (LTM) units to discharge at a rate of 2–8 Hz strongly inhibits micturition contraction (Hotta et al., 2012). Perineal rolling inhibits bladder contraction induced by electrical stimulation of the PMC or of the descending tract from the PMC and also inhibits afferent (ascending) transmission from the bladder to the PMC. Therefore, perineal rolling was suggested to shut down the positive feedback between the bladder and the PMC, resulting in inhibition of the micturition reflex (Hotta and Watanabe, 2015). It was shown by randomized clinical trial that perineal rolling reduces the nocturia associated with overactive bladder (Iimura et al., 2016). Such light stimulation to the skin may be applied spontaneously in daily life, and if this inhibitory mechanism is attenuated with age, it may be related to the cause of overactive bladder in the elderly.

The purpose of this study was to examine the effect of aging on the bladder micturition contraction inhibiting function of skin afferent nerve fibers. We employed anesthetized rats of three different age groups and compared the effect of perineal skin stimulation (gentle stimulation with a roller) on micturition contraction. We hypothesized that the inhibitory effect of mechanical skin stimulation is attenuated with age. For comparison, the effects of electrical stimulation of Aβ, Aδ, and C afferent nerve fibers in the skin were also examined. In the present study, age-related changes were observed following only mechanical skin stimulation, so we further examined the possibility of reduced responses of single unitary afferent Aβ-, Aδ-, and C-LTM fibers in the skin of the aged rats.

MATERIALS AND METHODS

The experiments were performed on 38 male Wistar or Fischer rats. There were no significant differences in their responses, so we combined all data from different strains. The animals were divided into three groups according to their different ages: (1) young adult (4–5 months old, $n = 15$, body weight 260–380 g), (2) middle aged (6–9 months old, $n = 10$, 360–410 g), and (3) aged (27–30 months old, $n = 13$, 330–435 g). The animals were bred at the Tokyo Metropolitan Institute of Gerontology (TMIG) and kept in a specific pathogen-free environment with free access to a commercial pelleted diet and filtered tap water with 2 ppm of chloride. This study was conducted in accordance with the Guidelines for Proper Conduct of Animal Experiments (established by the Science Council of Japan in 2006) and was approved by the animal care and use committee of TMIG. Basic preparation including anesthesia and artificial respiration, recordings of intravesical pressure of micturition contraction, skin stimulation with a roller, electrical stimulation and recordings of unit activity of cutaneous afferents were essentially the same as in our previous studies (Hotta et al., 2012; Onda et al., 2016).

General Surgery

The animals were anesthetized with urethane, after initial inhalation of 3% halothane or 3–4% isoflurane for 2–3 min. During the surgery, 0.3–1.0% halothane or isoflurane was additionally provided as required. An initial dose of urethane was given at 0.9–1.1 g/kg, subcutaneously (s.c.). Additional doses of 0.1–0.2 g/kg were administered intravenously (i.v.), if necessary, to maintain anesthesia at a relatively constant level as judged by the recorded blood pressure. The animals were artificially ventilated via a tracheal cannula to maintain the end-tidal CO_2 at 3.0–4.0%. Rectal temperature was maintained at 37–38°C by means of an automatically regulated heating pad and lamp (ATB-1100, Nihon Kohden, Tokyo). A jugular vein was catheterized for i.v. administration of supplemental anesthetics and other drugs. A common carotid artery was catheterized to record arterial

blood pressure. Rats were euthanized by injecting an overdose of pentobarbital at the end of each experiment.

Recording of Intravesical Pressure

A laparotomy was performed, and a catheter was inserted into the bladder via the anterior urethra. The catheter was secured to the urethra by a thread, closing the urethral cavity. To measure intravesical pressure, the urethral catheter was connected to a transducer (TP-200T, Nihon Kohden, Tokyo) via a T-shaped connector. The other end of the T-shaped connector was connected to a syringe pump to manipulate bladder volume. The bladder was filled with saline at a speed of 0.1 ml/min by means of a syringe pump (EP-70, EICOM, Kyoto) connected to the bladder cannula. The saline infusion was stopped when micturition contractions (two or three consecutive contractions) were produced. Then, the micturition contractions continued rhythmically because the urethra had been closed to keep the bladder volume at a suitable range for the micturition reflex (Sato et al., 1992). The frequency of contractions was summarized as a time histogram of contractions counted every 2 min and expressed as contractions per min. Each contraction was counted as one contraction only when its amplitude was above one third of the prestimulus control size.

Cutaneous Stimulation

Gentle mechanical stimulation was applied to the skin of the perineum using a roller with a smooth, soft surface made of elastic polymer (Somaplane, Toyoresin Co., Shizuoka; 17 mm in diameter, 15 mm in length, weighing 4 g), as described previously (Hotta et al., 2012). The hair of the skin area to be stimulated was trimmed with a conventional clipper. The stimulus was applied to a skin area of about 3 cm^2 for a period of 1 min with a rolling speed of approximately 3 mm/s and a frequency of 10 strokes/min. Rolling was performed manually with a force (roller weight) of 4 g and was paced with an auditory cue.

Electrical Stimulation of Cutaneous Afferent Nerve

After cutting the skin of the lower back on the left side when in the prone position, the CBPN was separated and cut at greater than 20 mm caudal to the sacral plexus. The cavity was kept open by pulling back the edge of the cut skin with threads, and the cavity was filled with warm paraffin oil. The central cut segments of the nerve were placed on bipolar platinum-iridium wire stimulation electrodes, and repetitive rectangular pulses (0.5 ms) were delivered to the nerve. The evoked compound action potential of the CBPN was recorded 17–25 mm proximal from the stimulating site in some cases. During data collection, gallamine triethiodide (20 mg/kg, i.v.) was administered to avoid interference by skeletal muscle activity.

Recording of Unitary Afferent Nerve Activity from Perineal Skin

Single unitary afferent nerve activity was recorded from CBPN in five young adult rats and four aged rats. The CBPN was separated either in the prone position or the supine position and cut close to the sacral plexus. The peripheral cut segments of the nerve were placed on bipolar platinum-iridium wire recording electrodes. Action potentials of single units were amplified (MEG-2100, Nihon Kohden), audibly monitored through connection to a speaker, visually displayed on an oscilloscope (TS-8500, IWATSU, Tokyo), and digitized (Micro1401, Cambridge Electronic Design, UK) for later processing (Spike 2 software, Cambridge Electronic Design, UK). Receptive fields and mechanical thresholds of each unit were determined using 0.08–4.0 mN von Frey hairs (Touch-test sensory filaments, US Neurologicals). The conduction velocity of each single unit was measured to classify nerve fibers which had conduction velocities >15.6 m/s as Aβ fibers, fibers with conduction velocities between 2 and 15.6 m/s as Aδ fibers, and fibers with conduction velocities <2 m/s as C fibers, as described previously (Hotta et al., 2012).

Data Acquisition and Analysis

All analog signals obtained (including intravesical pressure and neuronal potentials) were digitized (Micro1401, Cambridge Electronic Design, UK) for display on a computer monitor and for on-line and off-line analysis using Spike 2 software (Cambridge Electronic Design). Statistical analysis was performed using Prism6 software (GraphPad Software Inc., La Jolla, CA, USA). Values were expressed as mean ± standard error (S.E.). One-way factorial analysis of variance (ANOVA) followed by the Fisher's least significant difference test was used for comparison of values among the three different age groups. The time course of changes in rhythmic micturition contractions induced by somatic stimulation was assessed using repeated measures two-way ANOVA (time and different age groups), followed by Dunnett's multiple comparison test. The properties of single afferent units in aged rats were compared with corresponding data from young adult rats using Student's *t*-test (unpaired). Statistical significance was set at the 5% level.

RESULTS

Baseline Bladder Conditions

Body weight and the basal state of bladder micturition contractions before application of any somatic stimuli were compared between the young adult, middle aged, and aged rat groups (**Table 1**). Body weight was significantly heavier in middle aged (391 ± 5 g; $p = 0.0002$) and aged (388 ± 11 g, $p = 0.0004$) groups than in the young adult group (332 ± 12 g). However, the bladder volume required to induce micturition contraction was significantly larger in the aged group (1.72 ± 0.30 ml; range 0.6–3.7 ml) than in the young adult (0.96 ± 0.13 ml; range 0.4–1.6 ml, $p = 0.0083$) and middle aged (1.12 ± 0.11 ml; range 0.5–1.6 ml, $p = 0.0342$) groups. Basal pressure, maximum pressure, amplitude, and frequency of micturition contractions did not differ significantly between the three groups. Systolic blood pressure, recorded simultaneously, ranged from 100 to 150 mmHg and did not significantly differ between the three groups.

TABLE 1 | Summary of body weight and baseline conditions of the bladders in young adult, middle-aged, and aged rats.

	Young adult (4–5 months old) $n = 11$	Middle aged (6–9 months old) $n = 10$	Aged (27–30 months old) $n = 9$
Body weight (g)	332 ± 12	391 ± 5**	388 ± 11**
Bladder volume (ml)	0.96 ± 0.13	1.12 ± 0.11	1.72 ± 0.30**,#
Basal pressure (mmH_2O)	116 ± 7	131 ± 14	137 ± 16
Maximum pressure (mmH_2O)	526 ± 47	475 ± 56	476 ± 25
Amplitude of contraction (mmH_2O)	410 ± 45	344 ± 50	339 ± 25
Frequency of contraction (times/min)	1.27 ± 0.18	0.85 ± 0.11	0.83 ± 0.08

*Values are mean ± SE; **$p < 0.01$ vs. young adult, #$p < 0.05$ vs. middle-aged rats, determined by Fisher's least significant difference tests.*

Inhibition of Micturition Contractions by Electrical Stimulation of Skin Afferent Nerves

By recording the strength–response curve of compound action potentials in the CBPN, we confirmed in young adult, middle aged, and aged rats that 0.2 V was suprathreshold for Aβ fibers but subthreshold for Aδ and C fibers, 1.0 V was suprathreshold for Aβ and Aδ fibers but subthreshold for C fibers, and 10 V was suprathreshold for all fibers. Electrical stimulation (pulse duration: 0.5 ms) was applied to the CBPN with these voltages at three different frequencies of 0.1, 1, and 10 Hz for 1 min, and changes in micturition contractions were examined in young adult ($n = 5$), middle aged ($n = 4$), and aged ($n = 5$) rats. The order of nine different stimulus parameters was randomized.

Figure 1 shows sample recordings in rats of different ages after application of 10-Hz electrical stimulation to CBPN afferents for 1 min with 1 V (**Figure 1A**) or 10 V (**Figure 1B**). With 1 V, micturition contractions completely stopped for 6–8 min and then recovered. With 10 V, micturition contractions completely stopped for >15 min. These responses were similar in all age groups. The time course of the effect of electrical stimulation of CBPN at three different voltage intensities (0.2, 1, and 10 V) and three different frequencies (0.1, 1, and 10 Hz) are summarized in **Figure 2**.

In all nine different stimulus parameters, effects of CBPN stimulation on contraction frequency were similar among different age groups (**Figure 2**). Two-way ANOVA revealed that the main effect of age was not statistically significant ($p > 0.19$) for all nine stimulus parameters. Interaction was also not significant ($p > 0.068$). However, there were significant time-dependent effects ($p < 0.019$) for eight of the stimulus parameters but not for stimulation at 0.1 Hz with 10-V intensity. Therefore, *post-hoc* tests were performed for the eight parameters on pooled data in all age groups of rats. With 0.2-V intensity at 0.1–10 Hz, the frequency of micturition contractions significantly decreased 7–11 min after the stimulus onset (late inhibition). With 1-V intensity at 1 Hz, the frequency of micturition contractions significantly decreased at 1–5 min (early inhibition) and throughout 1–11 min at 10 Hz (both early and late inhibition). With 10-V intensity at 1–10 Hz, contractions significantly decreased throughout 1–11 min; especially at 10 Hz, contractions were stopped completely in all except one case. Contractions recommenced 14–47 min later in all rat age groups.

Inhibition of Micturition Contractions by Gentle Mechanical Skin Stimulation

Figure 3 shows sample recordings from three rats in the different age groups, in which gentle mechanical stimulation was applied to the perineal skin with a roller for 1 min. Following stimulation, the frequency of micturition contractions decreased in all age groups. However, there was a difference in the time course of inhibition. The onset of inhibition following rolling stimulation of the skin was gradually delayed with age. In a typical case of a young adult rat (upper part of **Figure 3**), contractions stopped immediately during perineal stimulation and then recovered within 15 min. In a typical case of a middle-aged rat (**Figure 3** middle), the contractions continued for several min after stimulation ended and then stopped. In a typical example of an aged rat, the intercontraction interval was gradually increased after stimulation (lower part of **Figure 3**).

The time course of the effects of rolling stimulation is summarized from six rats for each group in **Figure 4**, as time histograms of contraction. A significant interaction ($p = 0.022$) was observed when the frequency of micturition contractions was compared between the three groups with two-way ANOVA. The main effect of time was also significant ($p < 0.0001$). However, the main effect of age was not significant ($p = 0.90$). Therefore, *post-hoc* multiple comparison tests of the effect of time were performed for each age group. The *post-hoc* analysis revealed that the time course differed in each group; the decrease in micturition contractions was significant from 1 to 7 and 11 min after stimulation in the young adult group and from 7 to 11 min in the middle-aged group but only at 11 min in the aged group (**Figure 4**).

The magnitude of the decrease of micturition contractions at 1 min (early inhibition) and 11 min (late inhibition) was expressed as a percentage of the prestimulus control level and compared among the three age groups (**Figure 5**). The magnitudes of early inhibition were −92% ± 8%, −42% ± 20%, and −8% ± 30% in the young adult, middle-aged, and aged rats, respectively (**Figure 5A**), gradually reducing with age ($p = 0.045$). The value in the aged rats was significantly lower than that in the young adult rats ($p = 0.015$). The value for the middle-aged rats was not significantly different between the other groups. In contrast, late inhibition (−79 ± 13%, −86 ± 9%, and −83 ± 11% in young adult, middle-aged, and aged rats, respectively) was not significantly different ($p = 0.90$) between the three age groups (**Figure 5B**). The responses in the aged

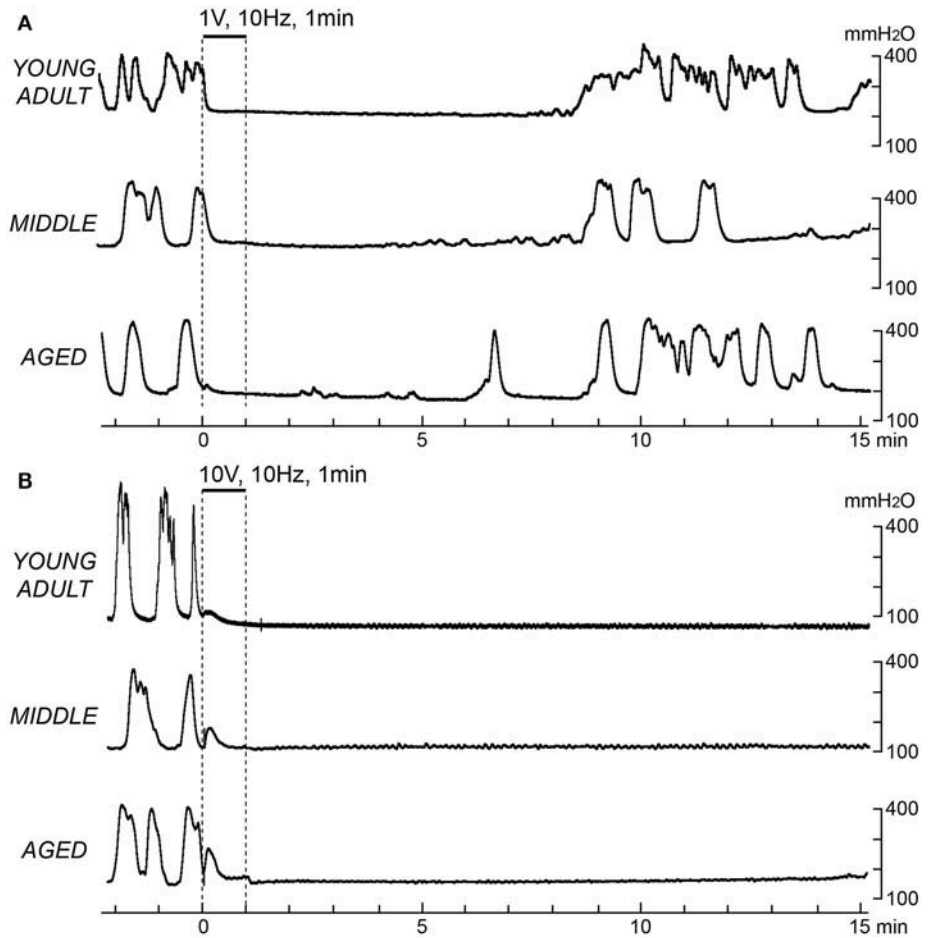


FIGURE 1 | Effects of electrical stimulation of cutaneous branch of the pudendal nerve afferents on rhythmic micturition contractions. Sample recordings in a young adult (upper), a middle-aged (middle), and an aged rat (lower) are shown. Stimulation for 1 min at 10 Hz with 1 V **(A)** and 10 V **(B)** is indicated by the upper horizontal bar and the vertical dashed lines, respectively.

group, in which late inhibition was predominant, were similar to those induced by selective excitation of Aβ afferents with 0.2-V electrical stimulation.

Response of Single Unitary Activity of Skin Afferent LTM Fibers

The above results showed that contraction inhibition by skin stimulation was delayed by aging although inhibition by electrical stimulation of CBPN afferents was well maintained. This suggests that the cause of the age-related changes in response to skin stimulation may be due to changes in the function of skin mechanoreceptors. Therefore, firing activity of skin afferent Aβ-, Aδ-, and C-LTM units in response to perineal rolling stimulation was examined in aged rats and compared with the results of young adult rats.

Figure 6 shows an example recording of single unitary afferent nerve activities of Aβ-, Aδ-, and C-LTM units in aged rats responsive to the perineal rolling stimulus. The conduction velocity of each unit was 16.1, 7.3, and 0.94 m/s, respectively. In each of these units, periodic activities synchronized with the movement of the rollers on the receptive field were observed. The average discharge frequency of Aβ, Aδ, and C fiber action potentials during stimulation for 60 s was 2.4, 1.5, and 0.5 Hz, respectively.

A total of 26 and 23 units were recorded in young adult and aged rats, including 12 and 9 units classified as Aβ fibers, 9 and 9 units classified as Aδ fibers, and 5 and 5 units classified as C fibers, respectively. In young adult and aged rats, the conduction velocities of Aβ fibers were 27.4 ± 1.6 m/s (with a range of 19.0–37.9 m/s) and 23.6 ± 1.6 m/s (16.1–30.0 m/s), Aδ fibers were 9.6 ± 1.1 m/s (5.5–15.3 m/s) and 8.6 ± 0.8 m/s (4.2–12.4 m/s), and C fibers were 0.90 ± 0.12 m/s (0.6–1.3 m/s) and 0.87 ± 0.17 m/s (0.43–1.35 m/s), respectively. All values in aged rats were equivalent to those in young adult rats.

The von Frey thresholds measured in 21 units from aged rats were within the range of 0.08–4 mN, which was the same as those in 24 units from young adult rats. However, in young adult rats, variations of the threshold in Aβ-, Aδ-, and C-LTM units were equal, whereas in the aged group, all C-LTM units responded to the lowest level of 0.08 mN stimulation.

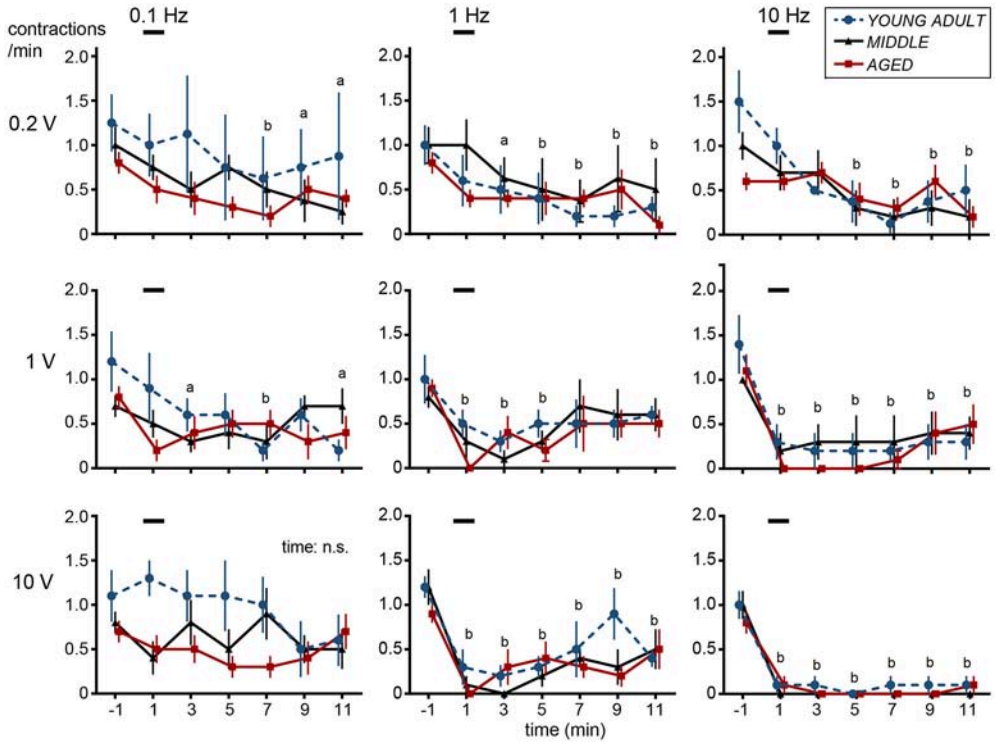


FIGURE 2 | Time histograms of micturition contractions after electrical stimulation of cutaneous branch of the pudendal nerve afferents compiled from five young adult rats (blue circles and dashed lines), four middle-aged rats (triangles and solid lines), and five aged rats (red squares and solid lines). Each rat was subjected to 1–2 trials. Each point represents mean ± SE (4–5 trials from 4–5 rats) for the number of contractions counted every 2 min, expressed as contractions per minute. Onset of stimulation was set as time zero; $^{a}p < 0.05$, $^{b}p < 0.01$, significant differences from prestimulus control values determined by Dunnett's multiple comparison test in pooled data from all three groups.

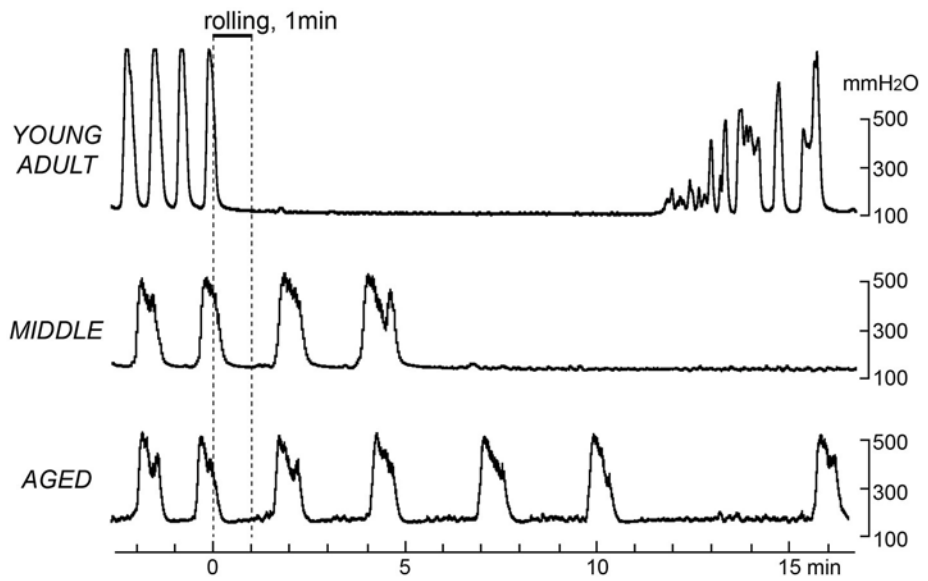


FIGURE 3 | Effects of gentle perineal skin stimulation by a roller on rhythmic micturition contractions. Sample recordings in a young adult **(upper)**, a middle-aged **(middle)**, and an aged **(lower)** rat are shown. Stimulation by perineal rolling for 1 min is indicated by the upper horizontal bar and vertical dashed lines.

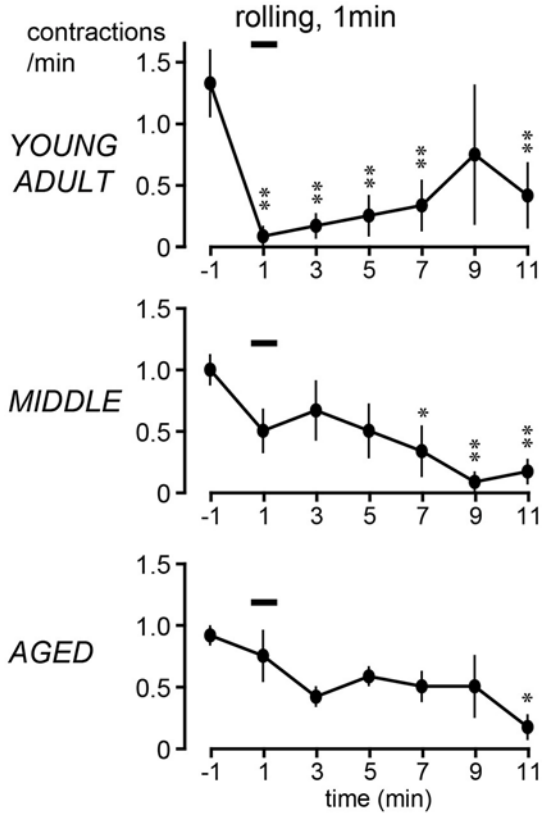


FIGURE 4 | Peristimulus time histograms of micturition contractions after perineal rolling stimulation, compiled from six rats each in young adult (upper), middle-aged (middle), and aged (lower) rats. Details of histogram are same as in **Figure 2**; $^{*}p < 0.05$, $^{**}p < 0.01$, significant differences from prestimulus control values determined by Dunnett's multiple comparison test.

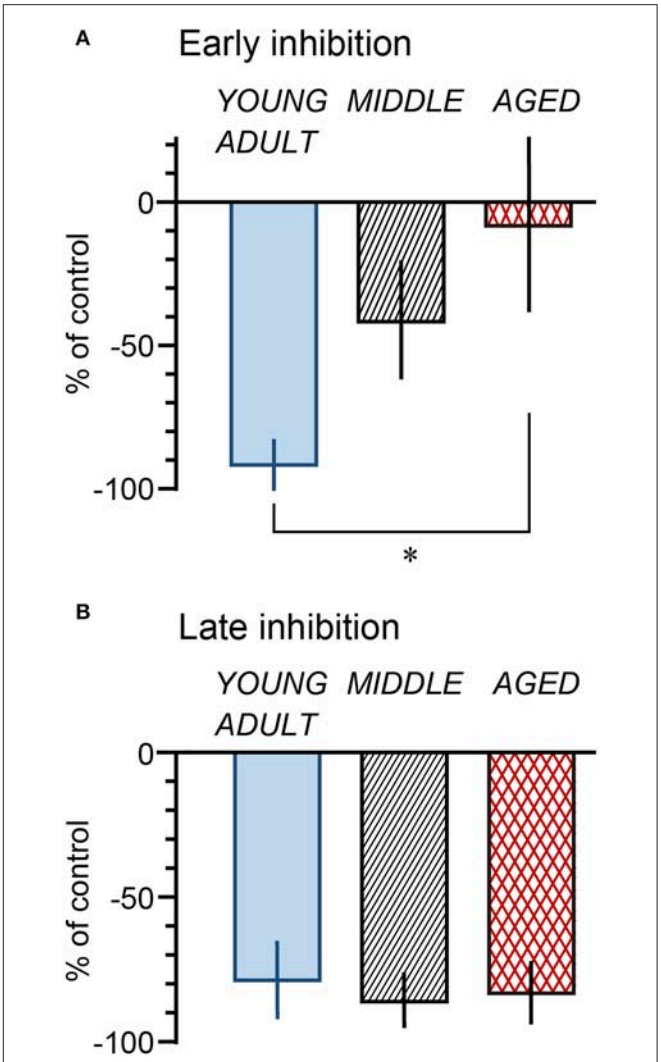


FIGURE 5 | Summary of magnitude of early (**A**: at 1 min) and late (**B**: at 11 min) inhibition by perineal rolling in young adult, middle-aged, and aged rats. Each column and vertical bar indicates the mean ± SE; $^{*}p < 0.05$, significant differences determined by Fisher's least significant difference test.

In the young adult and aged rats, the mean discharge rates during cutaneous stimulation of the Aβ fibers were in the range of 0.03–11.2 (2.4 ± 0.9) Hz and 0.08–2.8 (1.1 ± 0.4) Hz, respectively (**Figure 7**), a slight but not significant ($p = 0.24$) reduction for the aged rats. However, the mean discharge rates during cutaneous stimulation of the Aδ fibers were 0.1–7.3 (2.9 ± 0.8) Hz and 0.02–1.5 (0.4 ± 0.2) Hz in the young adult and aged rats, respectively, showing significant reduction ($p = 0.0078$) in aged rats. Further, the mean discharge rates during cutaneous stimulation of the C fibers were 3.3–11.1 (7.3 ± 1.3) Hz in young adult rats, the highest among three fiber groups, but were much reduced to 0.1–1.1 (0.5 ± 0.2) Hz in aged rats ($p = 0.0007$; **Figure 7**).

DISCUSSION

In the present study, the inhibition of micturition contractions in response to gentle mechanical cutaneous stimulation delayed with age. The weaker bladder inhibition may be due to changes in the peripheral or central nervous system, bladder, or skin mechanoreceptors. However, inhibition in response to electrical stimulation of the skin afferent nerve was well maintained in aged rats and was similar to that in adult rats. Therefore, age-related functional changes in the peripheral or central nervous system or bladder do not appear to be involved in the changes in contraction inhibition. Moreover, the discharge rate of skin Aδ- and C-LTM afferent fibers during gentle mechanical stimulation was markedly reduced in aged rats compared to that in adult rats. These results suggest that age-related functional changes in skin mechanoreceptors, specifically in Aδ and C fibers that trigger early inhibition, are responsible for the delay of contraction inhibition.

Basal Condition of the Aged Bladder

The basal pressure, maximum pressure, amplitude, and frequency of micturition contractions were not significantly different between the young adult, middle-aged, and aged groups.

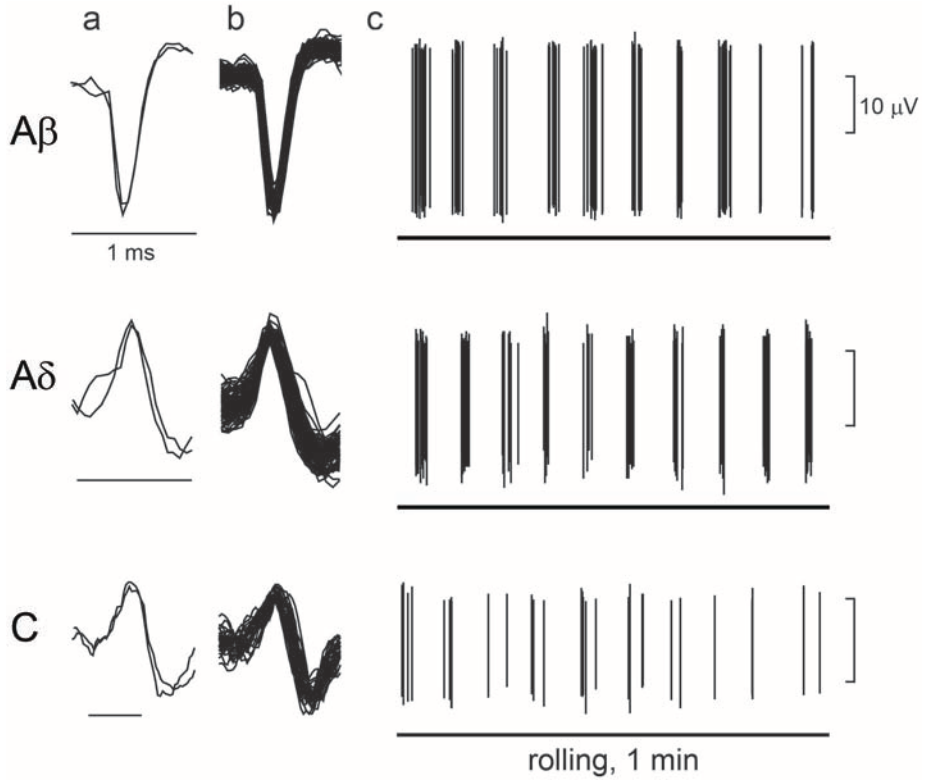


FIGURE 6 | Response of low-threshold mechanoreceptor (LTM) afferent nerve units during rolling. Examples of unitary afferent fiber recordings of Aβ-, Aδ- and C-LTM units in aged rats. **(a)** Action potentials evoked by electrical stimulation of the receptive field. **(b)** Superimposed action potentials recorded during manual rolling stimulation. **(c)** Responses of each unitary afferent fiber to rolling stimulation of the receptive field skin by a roller. A horizontal line indicates the period of rolling stimulation.

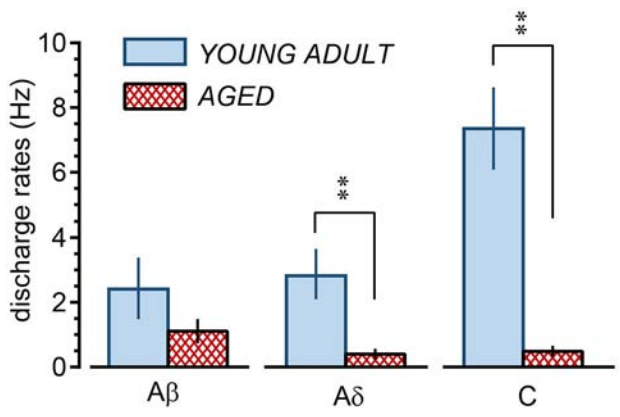


FIGURE 7 | Summary of discharge rates of low-threshold mechanoreceptor afferent nerve fibers during perineal rolling (1 min) in young adult and aged rats. Each column and vertical bar indicates the mean ± SE; $^{**}p < 0.01$, significant differences determined by Student's *t*-test.

However, the bladder volume inducing micturition contractions was about 70% larger in aged (27–30 months old) than in young adult (4–5 months old) and middle-aged (6–9 months old) rats. The results showing the increase in bladder capacity in aged rats are consistent with previous results comparing cystometrograms of young adult rats of 2–3 months old with aged rats of 26–29 months old. In that study, the volume at an intravesical pressure of 200 mmH_2O was 1.75 ± 0.26 ml in aged rats vs. 0.33 ± 0.05 ml in young-adult rats, and the cystometrograms were significantly shifted to the right in the aged rats (Hotta et al., 1995). Zhao et al. also reported that conscious, freely moving, old (28–30 months old) rats had increased bladder capacity, post-void residual volume, baseline, and intermicturition pressure but decreased micturition pressure compared with young (4–6 months old) rats. These changes were associated with decreased muscle mass and increased collagen deposition in the old bladder (Zhao et al., 2010). Recently, age-related increases in the collagen-smooth muscle ratio were also reported in old (85-week-old) mice using *ex vivo* two-photon laser scanning microscopy (Schueth et al., 2016).

Inhibition by Electrical Stimulation of Perineal Skin Afferents

The stimulation intensity and frequency dependence of inhibition of micturition contractions due to electrical stimulation in aged rats was essentially maintained as in younger adult rats. This result suggests that both the peripheral and central neural mechanisms involved in the somato-vesical

inhibitory reflex are maintained in aged rats. Late inhibition was induced by activation of only Aβ fibers over a wide range of 0.1–10 Hz, but excitation of Aδ or C fibers at 1–10 Hz was required to induce early inhibition. These features are in accord with a previous study in adult rats (Onda et al., 2016). Complete inhibition by 10 V, 10-Hz stimulation was shown not to be affected by blocking capsaicin-sensitive C fibers in adult rats (Onda et al., 2016). The present results indicate that the mechanisms for late inhibition by excitation of Aβ fibers, early inhibition by additional excitation of Aδ fibers, and early and late inhibition by further excitation of C fibers, are all well-maintained during aging. Treatment of overactive bladder by electrical stimulation is used clinically, and many of the patients are elderly (Guo et al., 2014). The influence of age on the inhibition of micturition contractions induced by electrical stimulation has not previously been reported. Our results suggest that electrical stimulation therapy may be effective for the elderly, as for younger adults.

Inhibition by Gentle Stimulation of Perineal Skin

In contrast to the well-maintained inhibition of micturition contractions by electrical stimulation, inhibition by gentle mechanical skin stimulation changed with age. Although the inhibitory effect itself was maintained, the latency of inhibition was prolonged with age. The inhibition of micturition contractions following cutaneous rolling in the aged group was similar to that following electrical stimulation of only Aβ fibers. By recording the LTM unitary activity, the response of Aβ-LTM units during rolling was maintained in the aged group, but Aδ- and C-LTM unitary activity during rolling in aged rats was much lower than in adult rats. Mean discharge rates of Aδ- and C-LTM units in young adult rats were 3–7 Hz, whereas those in aged rats were 0.4–0.5 Hz. Therefore, considering that electrical stimulation of Aδ and C fibers at frequencies of 1–10 Hz was necessary for inducing early inhibition, lack of the early inhibition by skin stimulation in aged rats appears to be due to reduced responses of Aδ- and C-LTMs, and the late inhibition observed in aged rats appears to be caused by activity of Aβ-LTMs.

It has been shown in adult rats that rolling of the skin inhibits PMC neuronal activity induced by bladder distension and also inhibits bladder contraction by PMC stimulation (Hotta and Watanabe, 2015). The inhibitory effect on PMC activity may be delayed in aged rats, resulting in a delay of inhibition of micturition contractions. In humans, rolling stimulation, self-applied before bedtime for 1 min, has been shown to alleviate nocturia caused by overactive bladder in the elderly (Iimura et al., 2016). As a clinical effect of the rolling on nocturia, late inhibition rather than early inhibition would be important. However, the lack of rapid inhibition by gentle skin stimulation may be related to urge incontinence, which increases with age.

Age-Related Changes in Skin Mechanoreceptors

Tactile sensations involving Aβ fibers, such as sensing vibration, and the density of Pacinian corpuscles and Meissner bodies connecting to Aβ fibers decreases with age (reviews of Wickremaratchi and Llewelyn, 2006; Decorps et al., 2014). Although only one report has examined the function of single afferent Aβ units, there were no differences in the receptive field sizes and von Frey thresholds in the planter nerve of 6- and 24- to 27-month-old rats (Reinke and Dinse, 1996). Their result on hairless skin is consistent with our result on hairy skin. However, there have been no reports investigating age-related changes in single unitary activities of small diameter LTM fibers from the skin. Our study showed for the first time that the responses of Aδ- and C-LTM units are selectively decreased with age.

Aδ-LTMs and C-LTMs are abundantly present in the hairy skin of humans and animals (Adriaensen et al., 1983; Djouhri, 2016) and suggested to project to the limbic cortices (Olausson et al., 2002; Watanabe et al., 2013) but do not contribute to tactile sensation. This contrasts with Aβ fibers, which project to the neocortical primary somatosensory cortex and contribute to tactile sensation. Inhibition of the somato-cardiac sympathetic C-reflex by gentle touch (Hotta et al., 2010; Watanabe et al., 2012), mainly caused by activity of Aδ- and C-LTMs (Watanabe et al., 2015), was attenuated in aged rats (Watanabe et al., 2011). On the contrary, inhibition of adrenal sympathetic nerve activity by brushing, mainly caused by activity of Aβ- and Aδ-LTMs (Isa et al., 1985), was well maintained in the aged rats (Kurosawa et al., 1987). These different cutaneous effects of aging may be explained by our results showing the attenuated responses of Aδ- and C-LTMs and the well-maintained responses of Aβ-LTMs.

The frequency of discharges to mechanical stimuli and the size of the receptive fields of LTMs, including unmyelinated tactile afferents, generally depend on the strength of the indentation (Wessberg et al., 2003), and if the mechanical threshold is higher, the frequency of discharge in response to the same 4-g roller stimulus would lower. However, it is of note that for Aδ- and C-LTM units in aged rats, the von Frey threshold was not higher, but the response frequency during rolling was much lower than that in younger adult rats. This may be due to receptor-specific changes that evoke afferent volleys in Aδ- and C-LTMs, such as a decrease in the number and/or changes in the properties of fine Zigzag hairs in which Aδ- and C-LTMs are selectively distributed (Abraira and Ginty, 2013). It will be important to clarify the mechanisms of age-related changes in responses of Aδ- and C-LTMs in future studies.

CONCLUSION

In summary, we reported three important age-related results in response to gentle mechanical cutaneous and electrical stimulation: (1) inhibition of micturition contractions induced by gentle mechanical stimulation had a delayed onset, (2) discharge rate of Aδ and C-LTM skin afferent fibers was markedly reduced, and (3) inhibition of micturition contractions induced by electrical stimulation was well maintained during aging. Electrical stimulation can maintain the firing rate of the cutaneous afferent, which is different from mechanical rolling stimulation (**Table 2**). Therefore, we can conclude that the reduced firing rate in skin mechanoreceptors during mechanical stimulation is the cause of weak inhibition observed in aged rats study.

TABLE 2 | Summary of the present results.

Skin afferent fiber type	Electrical stimulation		Gentle mechanical stimulation	
	Afferent activity (Hz)	Effect on bladder	Afferent activity (Hz)	Effect on bladder
(A) YOUNG ADULT				
Aβ fiber	0.1–10	Late inhibition	2	Early and Late inhibition
Aδ fiber	1–10	Early inhibition	3	
C fiber	1–10	Early and Late inhibition	7	
(B) AGED				
Aβ fiber	0.1–10	Late inhibition	1	Late inhibition
Aδ fiber	1–10	Early inhibition	0.4	
C fiber	1–10	Early and Late inhibition	0.5	

The autonomic nerve itself is relatively resistant to aging (Hotta and Uchida, 2010), but the aging processes affecting tactile function begin from an early age (Verrillo, 1980; Giuseppe et al., 1994; Stevens and Patterson, 1995). This study showed for the first time the possibility that age-related changes in skin function may affect brainstem functions regulating visceral activities.

AUTHOR CONTRIBUTIONS

HH contributed to study design, data acquisition, data analysis, data interpretation and manuscript writing. HS contributed to data analysis, data interpretation and manuscript writing. KI contributed to data acquisition, data analysis and manuscript revising. NW contributed to study design, data interpretation and manuscript writing. All authors approved the final version of the manuscript and agreed to be accountable for all aspects of the work in ensuring that questions related to the accuracy or integrity of any part of the work are appropriately investigated and resolved.

FUNDING

The present study was supported by JPSP KAKENHI Grant Number JP17K01550.

REFERENCES

Abraira, V. E., and Ginty, D. D. (2013). The sensory neurons of touch. *Neuron* 79, 618–639. doi: 10.1016/j.neuron.2013.07.051

Adriaensen, H., Gybels, J., Handwerker, H. O., and Van Hees, J. (1983). Response properties of thin myelinated (A-delta) fibers in human skin nerves. *J. Neurophysiol.* 49, 111–122. doi: 10.1152/jn.1983.49.1.111

Andersson, K. E., Boedtkjer, D. B., and Forman, A. (2017). The link between vascular dysfunction, bladder ischemia, and aging bladder dysfunction. *Ther. Adv. Urol.* 9, 11–27. doi: 10.1177/1756287216675778

Boggs, J. W., Wenzel, B. J., Gustafson, K. J., and Grill, W. M. (2006). Frequency-dependent selection of reflexes by pudendal afferents in the cat. *J. Physiol.* 577, 115–126. doi: 10.1113/jphysiol.2006.111815

Bosch, J. L., and Weiss, J. P. (2010). The prevalence and causes of nocturia. *J. Urol.* 184, 440–446. doi: 10.1016/j.juro.2010.04.011

Budgell, B. S., Hotta, H., and Sato, A. (1998). Reflex responses of bladder motility after stimulation of interspinous tissues in the anesthetized rat. *J. Manipulative Physiol. Ther.* 21, 593–599.

Decorps, J., Saumet, J. L., Sommer, P., Sigaudo-Roussel, D., and Fromy, B. (2014). Effect of ageing on tactile transduction processes. *Ageing Res. Rev.* 13, 90–99. doi: 10.1016/j.arr.2013.12.003

Djouhri, L. (2016). Aδ-fiber low threshold mechanoreceptors innervating mammalian hairy skin: a review of their receptive, electrophysiological and cytochemical properties in relation to Aδ-fiber high threshold mechanoreceptors. *Neurosci. Biobehav. Rev.* 61, 225–238. doi: 10.1016/j.neubiorev.2015.12.009

Ferroni, M. C., Slater, R. C., Shen, B., Xiao, Z., Wang, J., Lee, A., et al. (2015). Role of the brain stem in tibial inhibition of the micturition reflex in cats. *Am. J. Physiol. Renal Physiol.* 309, F242–F250. doi: 10.1152/ajprenal.00135.2015

Giuseppe, R., Santo, D. S., Donato, F., Mariano, M., and Luciano, M. (1994). Comparison of tactile sensitivity in a group of elderly and young adults and children using a new instrument called a 'Tangoceptometer'. *Arch. Gerontol. Geriatr.* 18, 207–214. doi: 10.1016/0167-4943(94)90014-0

Guo, Z. F., Liu, Y., Hu, G. H., Liu, H., and Xu, Y. F. (2014). Transcutaneous electrical nerve stimulation in the treatment of patients with poststroke urinary incontinence. *Clin. Interv. Aging* 9, 851–856. doi: 10.2147/CIA.S61084

Homma, Y., Yamaguchi, O., Hayashi, K., and Neurogenic Bladder Society Committee (2006). Epidemiologic survey of lower urinary tract symptoms in Japan. *Urology* 68, 560–564. doi: 10.1016/j.urology.2006.03.035

Hotta, H., Masunaga, K., Miyazaki, S., Watanabe, N., and Kasuya, Y. (2012). A gentle mechanical skin stimulation technique for inhibition of micturition contractions of the urinary bladder. *Auton. Neurosci.* 167, 12–20. doi: 10.1016/j.autneu.2011.11.002

Hotta, H., Morrison, J. F., Sato, A., and Uchida, S. (1995). The effects of aging on the rat bladder and its innervation. *Jpn. J. Physiol.* 45, 823–836. doi: 10.2170/jjphysiol.45.823

Hotta, H., Schmidt, R. F., Uchida, S., and Watanabe, N. (2010). Gentle mechanical skin stimulation inhibits the somatocardiac sympathetic C-reflex elicited by excitation of unmyelinated C-afferent fibers. *Eur. J. Pain* 14, 806–813. doi: 10.1016/j.ejpain.2010.02.009

Hotta, H., and Uchida, S. (2010). Aging of the autonomic nervous system and possible improvements in autonomic activity using somatic afferent stimulation. *Geriatr. Gerontol. Int.* 10(Suppl. 1), S127–S136. doi: 10.1111/j.1447-0594.2010.00592.x

Hotta, H., and Watanabe, N. (2015). Gentle mechanical skin stimulation inhibits micturition contractions via the spinal opioidergic system and by decreasing both ascending and descending transmissions of the micturition reflex in the spinal cord. *PLoS ONE* 10:e0135185. doi: 10.1371/journal.pone.0135185

Iimura, K., Watanabe, N., Masunaga, K., Miyazaki, S., Hotta, H., Kim, H., et al. (2016). Effects of a gentle, self-administered stimulation of perineal skin for nocturia in elderly women: a randomized, placebo-controlled, double-blind crossover trial. *PLoS ONE* 11:e0151726. doi: 10.1371/journal.pone.0151726

Irwin, D. E., Milsom, I., Hunskaar, S., Reilly, K., Kopp, Z., Herschorn, S., et al. (2006). Population-based survey of urinary incontinence, overactive bladder, and other lower urinary tract symptoms in five countries: results of the EPIC study. *Eur. Urol*. 50, 1306–1315. doi: 10.1016/j.eururo.2006.09.019

Isa, T., Kurosawa, M., Sato, A., and Swenson, R. S. (1985). Reflex responses evoked in the adrenal sympathetic nerve to electrical stimulation of somatic afferent nerves in the rat. *Neurosci. Res*. 3, 130–144. doi: 10.1016/0168-0102(85)90026-4

Kurosawa, M., Sato, A., Sato, Y., and Suzuki, H. (1987). Undiminished reflex responses of adrenal sympathetic nerve activity to stimulation of baroreceptors and cutaneous mechanoreceptors in aged rats. *Neurosci. Lett*. 77, 193–198. doi: 10.1016/0304-3940(87)90585-4

Morrison, J. F., Sato, A., Sato, Y., and Yamanishi, T. (1995). The influence of afferent inputs from skin and viscera on the activity of the bladder and the skeletal muscle surrounding the urethra in the rat. *Neurosci. Res*. 23, 195–205. doi: 10.1016/0168-0102(95)00942-M

Nakayama, H., Noda, K., Hotta, H., Ohsawa, H., and Hosoya, Y. (1998). Effects of aging on numbers, sizes and conduction velocities of myelinated and unmyelinated fibers of the pelvic nerve in rats. *J. Auton. Nerv. Syst*. 69, 148–155. doi: 10.1016/S0165-1838(98)00013-7

Olausson, H., Lamarre, Y., Backlund, H., Morin, C., Wallin, B. G., Starck, G., et al. (2002). Unmyelinated tactile afferents signal touch and project to insular cortex. *Nat. Neurosci*. 5, 900–904. doi: 10.1038/nn896

Onda, A., Uchida, S., Suzuki, H., and Hotta, H. (2016). Stimulus frequency-dependent inhibition of micturition contractions of the urinary bladder by electrical stimulation of afferent Aβ, Aδ, and C fibers in cutaneous branches of the pudendal nerve. *J. Physiol. Sci*. 66, 491–496. doi: 10.1007/s12576-016-0468-x

Reinke, H., and Dinse, H. R. (1996). Functional characterization of cutaneous mechanoreceptor properties in aged rats. *Neurosci. Lett*. 216, 171–174. doi: 10.1016/0304-3940(96)13039-1

Sato, A., Sato, Y., and Schmidt, R. F. (1980). Reflex bladder activity induced by electrical stimulation of hind limb somatic afferents in the cat. *J. Auton. Nerv. Syst*. 1, 229–241. doi: 10.1016/0165-1838(80)90019-3

Sato, A., Sato, Y., and Schmidt, R. F. (1997). The impact of somatosensory input on autonomic functions. *Rev. Physiol. Biochem. Pharmacol*. 130, 1–328. doi: 10.1007/BFb0046598

Sato, A., Sato, Y., Shimada, F., and Torigata, Y. (1975). Changes in vesical function produced by cutaneous stimulation in rats. *Brain Res*. 94, 465–474. doi: 10.1016/0006-8993(75)90229-2

Sato, A., Sato, Y., Sugimoto, H., and Terui, N. (1977). Reflex changes in the urinary bladder after mechanical and thermal stimulation of the skin at various segmental levels in cats. *Neuroscience* 2, 111–117. doi: 10.1016/0306-4522(77)90072-0

Sato, A., Sato, Y., and Suzuki, A. (1992). Mechanism of the reflex inhibition of micturition contractions of the urinary bladder elicited by acupuncture-like stimulation in anesthetized rats. *Neurosci. Res*. 15, 189–198. doi: 10.1016/0168-0102(92)90004-V

Schueth,. A., Spronck, B., van Zandvoort, M. A., and van Koeveringe, G. A. (2016). Age-related changes in murine bladder structure and sensory innervation: a multiphoton microscopy quantitative analysis. *Age* 38:17. doi: 10.1007/s11357-016-9878-1

Stevens, J. C., and Patterson, M. Q. (1995). Dimensions of spatial acuity in the touch sense: changes over the life span. *Somatosens. Mot. Res*. 12, 29–47. doi: 10.3109/08990229509063140

Tai, C., Shen, B., Mally, A. D., Zhang, F., Zhao, S., Wang, J., et al. (2012). Inhibition of micturition reflex by activation of somatic afferents in posterior femoral cutaneous nerve. *J. Physiol.* 590, 4945–4955. doi: 10.1113/jphysiol.2012.239475

Verrillo, R. T. (1980). Age related changes in the sensitivity to vibration. *J. Gerontol*. 35, 185–193. doi: 10.1093/geronj/35.2.185

Watanabe, N., Ishii, K., Hotta, H., Oda, K., Sakata, M., Toyohara, J., et al. (2013). Differential human brain activity induced by two perceptually indistinguishable gentle cutaneous stimuli. *Neuroreport* 24, 425–430. doi: 10.1097/WNR.0b013e32836164d4

Watanabe, N., Miyazaki, S., Mukaino, Y., and Hotta, H. (2012). Effect of gentle cutaneous stimulation on heat-induced autonomic response and subjective pain intensity in healthy humans. *J. Physiol. Sci*. 62, 343–350. doi: 10.1007/s12576-012-0210-2

Watanabe, N., Piché, M., and Hotta, H. (2015). Types of skin afferent fibers and spinal opioid receptors that contribute to touch-induced inhibition of heart rate changes evoked by noxious cutaneous heat stimulation. *Mol. Pain* 11:4. doi: 10.1186/s12990-015-0001-x

Watanabe, N., Uchida, S., and Hotta, H. (2011). Age-related change in the effect of gentle mechanical cutaneous stimulation on the somato-cardiac sympathetic C-reflex. *J. Physiol. Sci*. 61, 287–291. doi: 10.1007/s12576-011-0146-y

Wessberg, J., Olausson, H., Fernström, K. W., and Vallbo, Å. B. (2003). Receptive field properties of unmyelinated tactile afferents in the human skin. *J. Neurophysiol*. 89, 1567–1575. doi: 10.1152/jn.00256.2002

Wickremaratchi, M. M., and Llewelyn, J. G. (2006). Effects of ageing on touch. *Postgrad. Med. J*. 82, 301–304. doi: 10.1136/pgmj.2005.039651

Yoshida, M., Homma, Y., Inadome, A., Yono, M., Seshita, H., Miyamoto, Y., et al. (2001). Age-related changes in cholinergic and purinergic neurotransmission in human isolated bladder smooth muscles. *Exp. Gerontol*. 36, 99–109. doi: 10.1016/S0531-5565(00)00175-3

Zhao, W., Aboushwareb, T., Turner, C., Mathis, C., Bennett, C., Sonntag, W. E., et al. (2010). Impaired bladder function in aging male rats. *J. Urol*. 184, 378–385. doi: 10.1016/j.juro.2010.03.004

Conflict of Interest Statement: The authors declare that the research was conducted in the absence of any commercial or financial relationships that could be construed as a potential conflict of interest.

Copyright © 2018 Hotta, Suzuki, Iimura and Watanabe. This is an open-access article distributed under the terms of the Creative Commons Attribution License (CC BY). The use, distribution or reproduction in other forums is permitted, provided the original author(s) and the copyright owner are credited and that the original publication in this journal is cited, in accordance with accepted academic practice. No use, distribution or reproduction is permitted which does not comply with these terms.

frontiers in Neuroscience

ORIGINAL RESEARCH
published: 05 April 2018
doi: 10.3389/fnins.2018.00219

Effect of Different Movement Speed Modes on Human Action Observation: An EEG Study

*Tian-jian Luo, Jitu Lv, Fei Chao and Changle Zhou**

Fujian Provincal Key Lab of Brain-Inspired Computing, Department of Cognitive Science, School of Informatics, Xiamen University, Xiamen, China

Action observation (AO) generates event-related desynchronization (ERD) suppressions in the human brain by activating partial regions of the human mirror neuron system (hMNS). The activation of the hMNS response to AO remains controversial for several reasons. Therefore, this study investigated the activation of the hMNS response to a speed factor of AO by controlling the movement speed modes of a humanoid robot's arm movements. Since hMNS activation is reflected by ERD suppressions, electroencephalography (EEG) with BCI analysis methods for ERD suppressions were used as the recording and analysis modalities. Six healthy individuals were asked to participate in experiments comprising five different conditions. Four incremental-speed AO tasks and a motor imagery (MI) task involving imaging of the same movement were presented to the individuals. Occipital and sensorimotor regions were selected for BCI analyses. The experimental results showed that hMNS activation was higher in the occipital region but more robust in the sensorimotor region. Since the attended information impacts the activations of the hMNS during AO, the pattern of hMNS activations first rises and subsequently falls to a stable level during incremental-speed modes of AO. The discipline curves suggested that a moderate speed within a decent inter-stimulus interval (ISI) range produced the highest hMNS activations. Since a brain computer/machine interface (BCI) builds a path-way between human and computer/mahcine, the discipline curves will help to construct BCIs made by patterns of action observation (AO-BCI). Furthermore, a new method for constructing non-invasive brain machine brain interfaces (BMBIs) with moderate AO-BCI and motor imagery BCI (MI-BCI) was inspired by this paper.

Keywords: action observation, different speed modes, hMNS activations, ERD suppressions, BCI

OPEN ACCESS

Edited by:
Ioan Opris,
University of Miami, United States

Reviewed by:
Liang Li,
Peking University, China
Dan Zhang,
Tsinghua University, China

****Correspondence:***
Changle Zhou
dozero@xmu.edu.cn

Specialty section:
This article was submitted to Neural Technology, a section of the journal Frontiers in Neuroscience

Received: *09 January 2018*
Accepted: *19 March 2018*
Published: *05 April 2018*

Citation:
Luo T, Lv J, Chao F and Zhou C (2018) Effect of Different Movement Speed Modes on Human Action Observation: An EEG Study. Front. Neurosci. 12:219. doi: 10.3389/fnins.2018.00219

1. INTRODUCTION

Human mirror neuron system (hMNS) components activate the sensorimotor, parietal, and occipital cortices when a human performs, observes, or imitates an action (Rizzolatti, 2005; Tanji et al., 2015). Initial studies of the hMNS focused on motor imitation and learning, as well as action understanding and observation (Rizzolatti and Sinigaglia, 2010; Pineda et al., 2013). Furthermore, the hMNS has gradually come to be regarded as crucial for social skills such as understanding the intensions and emotional states of others (Blakemore and Decety, 2001; Schulte-Rüther et al., 2007). Action observation (AO) was considered one of the primary ways of inducing hMNS activations in

early studies (Caspers et al., 2010; Mukamel et al., 2010; Rozzi and Fogassi, 2017). The modulation of hMNS recruitments by AO has positive effects on cognitive psychology and sport rehabilitation for creating scientific recovery strategies (Franceschini et al., 2012). hMNS activations by AO also provide another way to construct a brain computer/machine interface (BCI) for mechanical control and medical auxiliary purposes (Neuper et al., 2009). A BCI constructs an alternative method for communicating between human and computers/machines. In BCIs, the motor related BCI was constructed by the variation patterns in mu (8–12 Hz) and beta (18–25 Hz) bands power extracted by electroencephalography (EEG) when a human image, observer, or execute limb/leg movements. Variations in band power in the two rhythms are referred to as event-related desynchronization (ERD) suppression. Hence, the ERD suppression will be caused by motor imagery (MI) and AO. In fact, the definitions of AO tasks influence the degree of ERD suppression. However, the relationships between action definitions for AO and hMNS activations are still unknown from a scientific view.

In general, in the movements designing of an AO therapy for stroke patients or a BCI system, the parameters and affecting factors will influence the performance of therapy or BCI accuracy. In fact, the affecting factors will be controlled if we explore the disciplines of the relationships between movements for AO and the hMNS activations. Hence, the the research of the affecting factors of movements for action observation will do favor for designing a AO therapy scheme or an AO-BCI system. Most prior studies offer different hypotheses regarding the relationships between movements for AO and the hMNS activations (Iacoboni et al., 2005; Filimon et al., 2007; Newman-Norlund et al., 2007). Since many AO studies are based in cognitive psychology and sports psychology, while few are based in rehabilitation and BCI research, the distribution and degree of hMNS activations remain controversial with respect to several features of AO (Perry et al., 2010; Vogt et al., 2013). The mode of AO movements is the main factor that limits hMNS and motor system activation. Several neurophysiological studies indicate that ongoing movement plays an important role in triggering hMNS responses when activations are induced by AO (Maranesi et al., 2013). Aside from the condition of ongoing movements, other studies hypothesize that the manifestations of actions in AO tasks influence hMNS activations. In a study of action meaning (Agnew et al., 2012), compared with meaningless movements, meaningful movements caused higher hMNS activations. For example, lipreading of speech is one of the meaningful movements. Researches on lipreading showed lipreading will enhance speech perception and speech recognition (Summerfield, 1992; Silsbee and Bovik, 1996). Lipreading enhancement in young deaf children will help auditory speech perception (Geers, 1994). Lipreading and audiovisual speech integration are used in therapy of autism (Smith and Bennetto, 2007). Hence, the researches on action meaning will be useful for the therapy, rehabilitation, and neuroscience. In addition, the degree of movement complexity in an mode of AO movement has also been found to affecting hMNS activations (Biagi et al., 2010; Gatti et al., 2017). Moreover, additional variables that modulate hMNS activation and ERD suppression, such as experience and familiarity, have also been studied (Calvo-Merino et al., 2006; Bello et al., 2014).

Although the factors affecting the relationships between movements for AO and hMNS activation have been explored by the above studies, hMNS specificity and its full significance remain uncertain. The definitions of AO tasks clearly influence the degree of ERD suppression (Orgs et al., 2008). Furthermore, the manifestations of AO tasks and their stimuli affect attentional resources and hMNS activation (Oberman et al., 2007). Since the majority of affecting factors are related to the modes of AO movements, explorations of the relationships between movements for AO and hMNS activation are translated into the relationships between movement modes and the degree of ERD suppressions. Speed, complexity, magnitude, and individual proficiency are well-characterized factors known to affect movement modes, and have been explored in previous studies (Abdi and Williams, 2010; Biagi et al., 2010; Agnew et al., 2012; Maranesi et al., 2013; Bello et al., 2014). However, to the best of our knowledge, the present study is the first to investigate the effect of speed during AO. If the speed affecting factor is well-explored for AO among individuals, the designing for therapy scheme and AO-BCI will be more accurate for individuals. In addition, since the parameters and affecting factors will be well controlled in designing AO-BCI, but not in designing MI-BCI, the performance of AO-BCI will be better than MI-BCI. Furthermore, based on BCI system, the brain computer/machine brain interfaces (BMBIs) are capable of bidirectional communication with the brain. The interfaces consist of efferent and afferent modules. The efferent modules decode motor intentions by the variation patterns in mu and beta bands power, like conventional BCIs. The afferent modules encode feedback about the interactions of the machine through patterns of intracortical microstimulation. In general, the efferent modules are always designed by patterns of motor imagery. Meanwhile, the afferent modules can't be designed by patterns of MI. However, the afferent modules will be designed by patterns of action observation. When the efferent modules by MI drive a machine performing movements, the feedback by observation to activate hMNS will cause ERD suppression to design afferent modules. Today's BMBIs are constructed without considering the affecting factors of movements, so the performance is bad. However, if the speed and other affecting factors are considered for designing BMBIs, the performance will be better.

EEG (Lei et al., 2015; Abbott, 2016) has been widely used to construct BCI systems for exploring hMNS activations due to its high temporal resolution. In our study, the experimental movements were made by a humanoid robot at four different speed modes for AO tasks. A humanoid robot platform provides identical appearance, background and complexity to eliminate other effects. All four speed modes, slow (0.25 Hz), moderate (1.25 Hz), fast (2.75 Hz), and finalistic (4 Hz), were defined by questionnaires administered to 26 participants. Another six subjects were asked to attend AO experiments and an MI experiment for comparison. All eight stimuli (left movement and right movement at four speed modes) were randomly presented to all subjects in AO experiments, and another two stimuli were randomly presented to the same subjects in MI experiments. Both experiments are designed by a BCI form to validate

the relationships between speed mode of AO and the hMNS activations. Due to the high temporal resolution, quantitative EEG (Lei et al., 2015; Abbott, 2016) is used as a convenient and cheap method to explore hMNS activations by measuring ERD suppressions (Oberman et al., 2007; Orgs et al., 2008). The ERD suppressions in EEG data are analyzed using a series of BCI methods and spatio-spectral-temporal characteristics. The following three main points are analyzed and discussed in this study:

(1) The brain regions involved in AO, such as the sensorimotor and occipital regions, are compared since studies on activation regions for AO have paradoxical conclusions (Perry et al., 2010; Frenkel-Toledo et al., 2013).
(2) The patterns of the relationships between AO speed modes and hMNS activations. If the patterns are clearly explored by experiments, individual rehabilitation strategies with specific optimal speeds will be precisely designed for individuals.
(3) Application to brain machine brain interface (BMBI). The average pattern of all individuals will show optimal speed ranges that are best suited to constructing AO-BCIs. Moreover, a well-established non-invasive AO-BCI with a high rate of accuracy and information transfer rate (ITR) will help to build BMBIs.

2. MATERIALS AND METHODS

2.1. Ethics Statement

This study was carried out in accordance with the recommendations of the guideline of EEG experiment, Xiamen University ethics committee with written informed consent from all subjects. All subjects gave written informed consent in accordance with the Declaration of Helsinki. The protocol was approved by the Xiamen University ethics committee.

2.2. Participants

Six right-handed healthy human subjects (five male and one female, mean age: 24.6 years, $SD = 1.46$) were invited to participate in AO and MI experiments with payment. All subjects had no history of neurological disease and either normal or corrected-to-normal vision. Subjects also did not have any professional experience with AO or MI experiments. In accordance with the principles of the Helsinki Declaration, all subjects provided written informed consent approved by the Xiamen University.

2.3. Stimuli Design

As shown in **Figure 1**, stimuli for AO in different speed modes were performed by a humanoid robot. AO stimuli were presented to all subjects in 12 sessions as experiment 1. Afterwards, an MI comparison experiment in which two guidance arrows were presented to the same subjects in three sessions was performed as experiment 2.

2.3.1. Experiment 1:AO Experiments in Different Speed Modes

In previous studies, AO experimental paradigms were designed with sequential video clips of human arm, hand, or finger movements presented to subjects (Frenkel-Toledo et al., 2014; Gatti et al., 2017). However, our experiments were designed to explore speed factor during AO. Because human movements feature unconstant speed, angle, and magnitude across repetitive experiments, the inconsistency of the variables will introduce confounding factors that disturb the analyses of hMNS activations. To eliminate such confounding factors, a fine-tuning parameter-setting paradigm must be incorporated into the design. Based on the anthropomorphic and relevant AO studies (Press, 2011), the hMNS is strongly activated by observations of both human and non-human agents (e.g., humanoid robots). Human or non-human agents do not differ significantly in their ability to activate the hMNS in AO studies involving humans and humanoid robots. Since the robot platform features an operating system for controlling all movement parameters, a humanoid robot platform was used in the design of our AO experimental paradigms.

Based on the "NAO Choregraphe 1.14 platform" (Pot et al., 2009), periodic-swinging movements of the robot's left/right arm

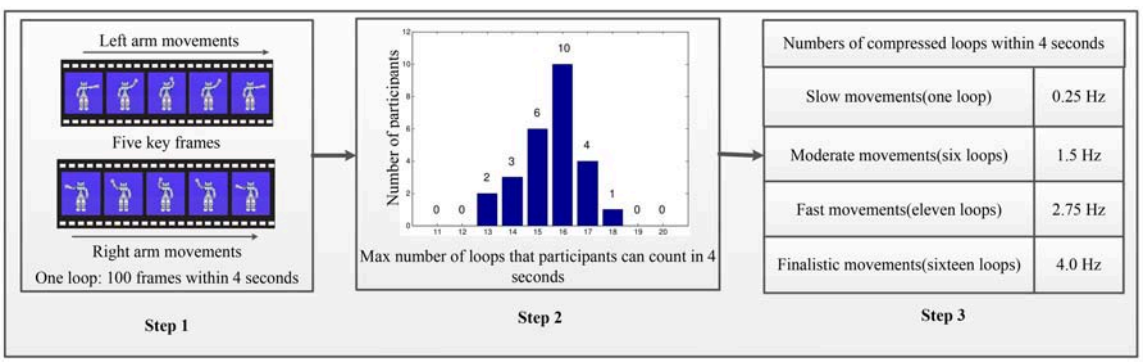


FIGURE 1 | Stimuli design of AO in different speed modes. The Step 1 contains one loop of periodic-swinging arm movement includes 100 frames over four seconds because the platform has a fixed frame rate of 25 fps. The Step 2 summarizes the results of the correct maximum loop number counted by each participant. The Step 3 defines the role of speed modes in the pattern of relationships between AO tasks and hMNS activations. As well as for simplicity and convenience, four different loops with a constant interval were constructed. Step 1: One loop for AO at standard speed. Step 2: Twenty-six participants count loops at higher speed modes to determine the max (16 loops). Step 3: Select four speed modes for experiments by equi-partition.

were utilized as AO tasks in experiment 1. As shown in **Figure 1** (Step 1), one loop of periodic-swinging arm movement includes 100 frames over 4 s because the platform has a fixed frame rate of 25 fps. Five key frames for both the left and right arms show the same procedure of the periodic movements. The robot stretches its arm at the beginning of the loop and waves its arm up to the head during half of the loop. The remainder of the loop consists of the same procedure in the opposite direction. The platform ensures that the robot's left/right-arm movements maintain a constant speed, angle, and magnitude. The entity body of the robot was presented to subjects in order to distinguish left-arm or right-arm movements during AO using EEG-based BCI analysis methods (Bauer and Gharabaghi, 2015). The robot's arms are dynamic, while the other parts of the robot remain static to keep the speed variable clear and unique.

Theoretically, more speed modes will be better for the results. However, due to the limitation of participants and the experimental platform, we only explore the rough pattern of the factor affections for simplicity and convenience. Four different loops with a constant interval were constructed as shown in **Figure 1** (Step 3). For simplicity, the four incremental speed movements are defined as "slow movement," "moderate movement," "fast movement," and "finalistic movement." In **Figure 1** (Step 1), one loop of 100 frames over 4 s is defined as "slow movement." Due to time duration in AO experiments (4 s per trial), we obtain higher movement speed modes by adding number of loops, and compressing multi-loops within 4 s. To identify a robust and suitable number of multi-loops for "finalistic movement," 26 participants were invited to watch 10 different looped (11–20) video clips that were compressed into 4 s. Participants were asked to count the number of loop in each video clip. The results from all participants were then compared with ground truth to identify the maximum loop number for each participant. **Figure 1** (Step 2) summarizes the results of the correct maximum loop number counted by each participant. The results show that 16 loops was the maximum loop number for all of the participants. Therefore, "finalistic movement" was defined as 16 loops compressed into 4 s. "Moderate movement" was set to six loops, and "fast movement" was set to 11 loops, by the principle of equipartition. In all, experiment 1 gives four different speed modes of AO to explore the role of speed. All four speed modes were presented to subjects during AO in experiment 1.

2.3.2. Experiment 2: Relevant MI Experiment

After experiment 1, all six healthy human subjects were asked to attend experiment 2. The MI experiment was compared with the AO experiment. Following the design criteria of MI experimental paradigms (Tangermann et al., 2012), two guidance arrows were defined in experiment 2 to guide the imagined movement direction. In experiment 2, the subjects were asked to imagine his/her-self as performing the same movement as the humanoid robot in experiment 1. Both MI guidance arrows used in experiment 2 were presented to all subjects after experiment 1.

2.4. Experimental Procedures

As shown in **Figure 2**, the experimental procedures for AO in different speed modes and MI were divided into trials and sessions. EEG recordings were set for both AO and MI experiments.

2.4.1. Trial Procedures

Influenced by conventional AO/MI experimental trial setups (Calvo-Merino et al., 2004; Wang et al., 2012), the presentation of a trial is shown in **Figure 2A**. In each trial, initial instructions guided subjects to simply observe the robot's movements (experiment 1) or guidance arrows (experiment 2) on the screen and a manually respond as rapidly as possible whenever the catch trial static robot (experiment 1) or blank (experiment 2) is presented. Subjects were also asked to minimize eye movements and keep their eyes fixed on the monitor when observing the stimuli. Manual responses to the catch trial were input by pressing the "SPACE" button. Each trial started with a fixation cross presented in the middle of a gray screen. The duration of the fixation cross was 2,000 ms. After presentation of the fixation cross, stimuli were presented in the middle of the gray screen for 4,000 ms to investigate participants' ERD suppressions via EEG recordings and were followed by a 2,000-ms pause as a break. If the presentation was an AO stimulus (experiment 1), subjects were asked to focus on the moving arm of the robot; otherwise, when the presentation was an MI stimulus (experiment 2), subjects were asked to imagine him/her-self moving like the robot by following the guidance arrows. Subsequent trials followed the same procedure for both experiment 1 and experiment 2.

2.4.2. Session Procedures

In experiment 1, each subject completed 12 AO sessions within 6 days, whereas in experiment 2, each subject completed three MI sessions within 2 days. Data recordings for one session occurred in the morning, with another session taking place later in the afternoon the same day. As shown in **Figure 2D**, each session comprised two tasks, and each task was divided into 40 trials. A relaxation time to prevent fatigue was determined by subjects between the two tasks. Experiment 1 comprised eight AO stimuli and one catch trial stimulus, which are described in **Figure 2B**. Each of the eight AO stimuli (left and right in four speed modes) was randomly presented four times, and the catch trial stimulus was randomly presented eight times within one session (See **Figure 2D**). Experiment 2 comprised two MI stimulus arrows and one blank catch trial stimulus, which are described in **Figure 2C**. Each of the two MI stimuli (left and right) was randomly presented four times, and the catch trial stimulus was randomly presented eight times within one session (See **Figure 2D**). Response times to the catch trial stimulus were recorded for both experiments 1 and 2 because the response times help confirm attentional states during AO and MI experiments.

2.4.3. EEG Recordings

Each subject was seated individually in a comfortable arm chair in front of a computer monitor in a dimly lit, sound-attenuated room and asked to read the instructions carefully on the screen. AO stimuli (experiment 1) and MI stimuli (experiment 2) were displayed on a DELL P2314H LCD monitor with a refresh rate of 60 frames/s. Displays were controlled by the psychology software tool "E-Prime 2.0." The distances between monitor and the

subjects were set at 100 cm by following the BCI experimental criterion to prevent other confounding factors in the hMNS activation (Onishi et al., 2017). During the entire run of both experiments, a spatially homogeneous gray background with a luminance of 38 cd/m2 was enabled. EEG recordings for all subjects were performed on a "NeuroScan SynAmps2" device with a "Neuroscan QuikCap international 10–20 system." EEG signals were referenced to the nose, grounded at the frontal position (Fpz), and sampled at 250 Hz. After data acquisition, the preprocessing operations on the signals for notch filtering and bandpass filtering were 48–52 and 0.1–100 Hz, respectively. All 64 electrode impedances in QuikCap were kept below 5kω during the experiment. Moreover, the horizontal and vertical EOG signals were recorded. The EOG signals were used to correct for the influence of blinking and eyeball movements.

2.5. Analysis Methods

As shown in **Figure 3**, three main EEG data analyses procedures were utilized in this study. **Figure 3** (Step 1) illustrates the preprocessing procedure. Raw EEGs from six subjects were first corrected for EOG artifacts via blind component separation. Then, a band filter ranging from 0.15 to 30 Hz was adopted

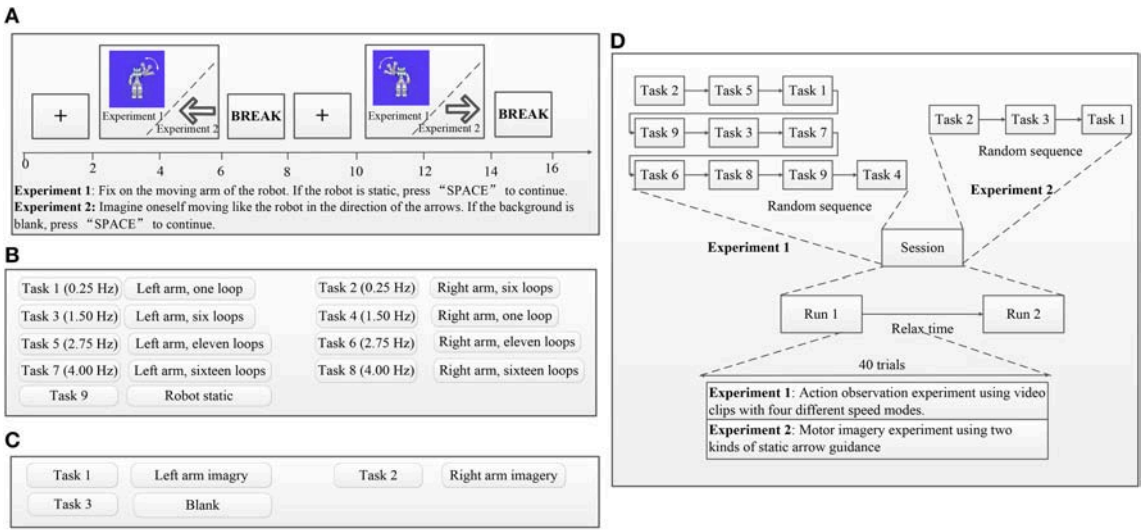


FIGURE 2 | Experimental procedures. In each trial, initial instructions guided subjects to simply observe the robot's movements (experiment 1) or guidance arrows (experiment 2) on the screen and a manually respond as rapidly as possible whenever the catch trial static robot (experiment 1) or blank (experiment 2) is presented. Each trial started with a fixation cross presented in the middle of a gray screen. The duration of the fixation cross was 2,000 ms. After presentation of the fixation cross, stimuli were presented in the middle of the gray screen for 4,000 ms to investigate participants' ERD suppressions via EEG recordings and were followed by a 2,000-ms pause as a break. Each of the eight AO stimuli (left and right in four speed modes) was randomly presented four times, and the catch trial stimulus was randomly presented eight times within one session in Experiment 1. Each of the two MI stimuli (left and right) was randomly presented four times, and the catch trial stimulus was randomly presented eight times within one session in Experiment 2. **(A)** Example trial sequence for experiment 1 and experiment 2. **(B)** Task descriptions for experiment 1. **(C)** Task descriptions for experiment 2. **(D)** Example session sequence for experiment 1 and experiment 2.

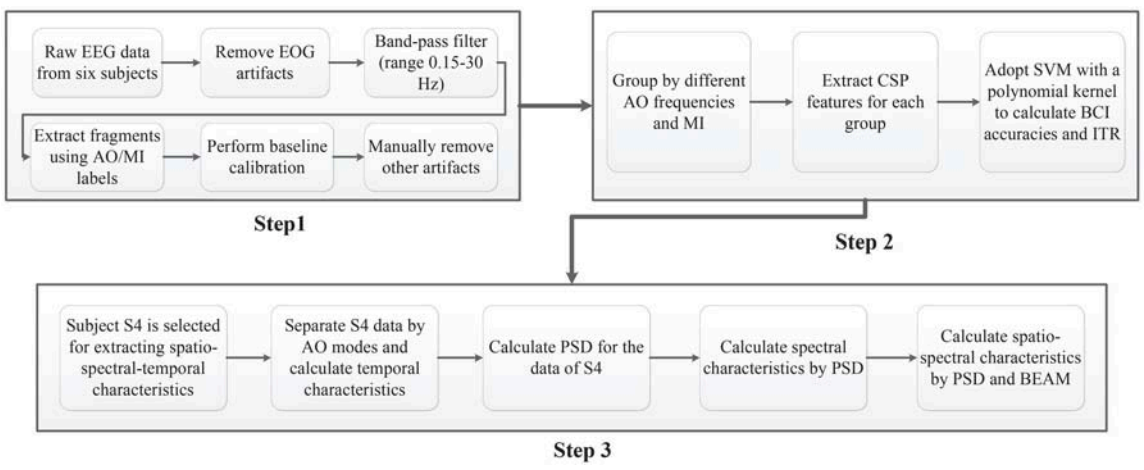


FIGURE 3 | EEG data analysis procedures. Step 1: Pre-processing. Step 2: BCI analyses. Step 3: Extracting spatio-spectral-temporal characteristics.

for EEG data, since the effective parts are above 0.15 Hz and under 30 Hz. By using AO (experiment 1) and MI (experiment 2) labels recorded in "NeuroScan," fragments of each experimental condition were extracted for all subjects. After fragment extraction, a baseline calibration method to prevent deviation and a manual removal method to reducing artifacts were performed on all fragments.

Recent studies first found that hMNS activations initially occurs in the sensorimotor region of the brain during AO (Perry et al., 2010). The ERD suppressions in the sensorimotor region then extend to attentional resources, which cause more intense hMNS activations in the occipital region (Frenkel-Toledo et al., 2013). Likewise, ERD suppressions caused by MI are first found in the sensorimotor region and then extend to global cerebral activity. To explore the affected regions of the brain during AO, the patterns of relationships between AO speed modes and hMNS activations, as well as to compare AO and MI to construct a BMBI, the sensorimotor, occipital and "sensorimotor + occipital" regions were adopted for BCI analyses of both AO and MI experiments. Potentials covering central-parietal regions C3, C1, Cz, C2, C4, P3, P1, Pz, P2, and P4 were chosen for the sensorimotor region, while potentials covering parietal-occipital regions PO5, PO3, POz, PO4, PO6, O1, Oz, and O2 were chosen for the occipital region. The "sensorimotor + occipital" region included both sets of potentials.

As illustrated in **Figure 3** (Step 2), the procedure for BCI analyses comprised four steps. First, left fragments and right fragments were grouped by identical AO speed (experiment 1). Second, all groups of fragments were presented to extract filter bank common spatial pattern (FB-CSP) features (Ang et al., 2012). Since ERD suppressions are modulated by the power variations of the left and right cerebral hemispheres, an FB-CSP algorithm was adopted to extract power variations using a bank of filters and an optimization method. The optimal CSP eigenvectors were set to $S = 4$ based on experience. Third, the principal component analysis (PCA) algorithm of a linear dimensionality reduction technique was adopted to reduce feature dimensions (Abdi and Williams, 2010). Because of the high sampling rate in EEG recordings, FB-CSP features have a high number of dimensions that are hard to classify by machine-learning models. The PCA algorithm looks for the highest variability in FB-CSP features by projecting original features to lower dimensions. The optimal PCA was set to $M = 10$ for the regulation of "99%" of the variability. Finally, the dimension-reduced FB-CSP features were incorporated into the support vector machine (SVM) classifier for BCI classification (Sardouie and Shamsollahi, 2012). The SVM classifier is a common BCI classifier with excellent generalizability by searching for the largest margin of a decision hyperplane that will strictly classify the unseen test data. The reductive features were incorporated into SVM classifiers with a polynomial kernel. A 6*6 cross-validation strategy was applied to train the SVM classifiers for all five groups. Since each group has 392 trials of effective EEG fragments with a random order for left and right, 320 trials were provided as training data, and the remaining 64 trials as evaluation data in one loop of evaluation.

Figure 3 (Step 3) displays the procedure for extracting spatio-spectral-temporal characteristics. Subject 4, who had the best BCI accuracies, was chosen for the analyses of these characteristics. The temporal characteristics were first extracted by calculating mean voltages of EEG fragments among four different speed AO modes (both for left and right). Then, a power spectral density (PSD) (Demandt et al., 2012) algorithm with parameters of specific rhythm ranges was used for each average fragment to obtain spectral characteristics. The spectral characteristics were drawn by the "eeglab 14.1.1" tool as "ERD images" (Delorme and Makeig, 2004). Brain electrical activity maps (BEAMs) (Duffy et al., 1979) were imported to obtain the positions of the potentials, and the spatio-spectral characteristics were drawn by the "eeglab 14.1.1" tool.

In addition, the response times of catch trial stimuli as feedback behavioral data were analyzed by statistical analyses. Mean time values for all 15 sessions (Sessions 1–12 for experiment 1 and sessions 13–15 for experiment 2) were calculated for all subjects to obtain the attentional conditions of all sessions by calculating mean values and standard deviations among all sessions.

3. RESULTS

3.1. Feedback Behavioral Data

Catch trial stimuli appear 16 times in each session, and we have recorded the response times for all catch trial stimuli in each session. **Tables 1**, **2** illustrate the mean response times within one session for experiment 1 and experiment 2, respectively. The mean time and standard deviations among all sessions in both experiments are also presented.

As shown in **Table 1**, the average response times among all sessions of experiment 1 were within 2,000 ms, and the corresponding standard deviations were within 100–200 ms. These results demonstrate that all subjects exhibited focused attention during AO experiments and EEG recordings. Therefore, EEG recordings in experiment 1 were free from attention artifacts. The standard deviations of all subjects were within a similar range, indicating that the responses to stimuli were stable. The response times of Subjects 2 and 3 had lower averages and standard deviations, which may be related to their younger age, as this tends to be related to faster response times. Since our behavioral data conform to experimental principles, the EEG data of experiment 1 were considered objective and appropriate for analyses. Similarly, as illustrated in **Table 2**, the average response time among all sessions of experiment 2 were within 300 ms, and the corresponding standard deviations were within 10 and 20 ms. These results conform with the response times of MI experiments, indicating that the EEG recordings in experiment 2 were objective and appropriate for analyses. Compared with **Tables 1**, **2**, the blank catch trial stimuli was easier to recognize than a static robot, and the individual differences in the response times of younger subjects has less influence on the MI experiments.

3.2. BCI Analyses of AO and MI Experiments

After preprocessing, the EEG fragments (left and right) of four speed AO modes and MI modes were used for BCI analyses. In

FB-CSP feature extraction, the bank of bank filters following a previous study are shown in **Table 3**. **Table 3** illustrates the BCI analysis results for three regions in four AO speed modes and MI mode. The average accuracies and standard deviations of BCI classification and ITR were calculated. To display the comparison of the results, **Figure 4** shows the average accuracies of all modes in all regions.

From the BCI analysis results in **Table 4** and **Figure 4**, we see four findings:

(1) For the accuracies in the occipital region, the results were AO-0.25 Hz (71.44%), AO-1.5 Hz (74.78%), AO-2.75 Hz (58.42%), and AO-4 Hz (59.29%). However, the results were AO-0.25 Hz (61.76%), AO-1.5 Hz (69.27%), AO-2.75 Hz (56.29%), and AO-4 Hz (55.99%) in the sensorimotor region. Similarity, the accuracies of the "sensorimotor+occipital" were AO-0.25 Hz (62.07%), AO-1.5 Hz (68.92%), AO-2.75 Hz (56.81%), and AO-4 Hz (56.33%). Considering the results across all regions, the BCI accuracies from increasing speed modes of AO presented a pattern of initially increasing and then decreasing to a stable level.

(2) Comparing AO-BCI accuracies between occipital and sensorimotor regions, the results were 71.44 and 61.76% at AO-0.25 Hz, 74.78 and 69.27% at AO-1.5 Hz, 58.42 and 56.29% at AO-2.75 Hz, and 59.29 and 55.99% at AO-4 Hz. AO in any speed mode had a more significant BCI accuracy in the occipital region than in the sensorimotor region. However, the accuracies of MI-BCI were 57.72% in the occipital region and 61.35% in the sensorimotor region. MI mode had a more significant BCI accuracy in the sensorimotor region than in the occipital region.

(3) The BCI accuracies in the "sensorimotor+occipital" region were at a similar level to those in the sensorimotor region. The results were 62.07 and 61.76% at AO-0.25 Hz, 68.92 and 69.27% at AO-1.5 Hz, 56.81 and 56.29% at AO-2.75 Hz, and 56.33 and 55.99% at AO-4 Hz. However, a large difference was detected between the "sensorimotor+occipital" and occipital regions. The results were 62.07 and 71.44% at AO-0.25 Hz, 68.92 and 74.78% at AO-1.5 Hz, 56.81 and 58.42% at AO-2.75 Hz, and 56.33 and 55.99% at AO-4 Hz. These results suggested the BCI accuracy was more robust in the sensorimotor region and was resistant the influence of other regions. Moreover, the higher BCI accuracies in the occipital region may be influenced by factors other than hMNS activations.

(4) Because the standard deviations of all experimental modes in all regions were within the range of [0, 10], AO in different speed modes and MI mode have similar robustness. The average standard deviations in all regions between AO modes showed that AO-0.25 Hz (5.69) and AO-1.5 Hz (5.80) have lower robustness than AO-2.75 Hz (2.98) and AO-4 Hz (2.13). Since ITR presents the efficiency of BCI, the average results of ITR in all regions showed that AO-1.5 Hz (2.01) had a significantly higher efficiency than AO-0.25 Hz (1.10), AO-2.75 Hz (0.23), AO-4 Hz (0.24), and MI (0.43). AO in moderate-speed mode was more suitable for the design of BCIs.

(5) The average accuracies have the same pattern of initially increasing and then decreasing to a stable level. In the results between subjects, subjects "S1, S3, S4" correspond to the average pattern, but subjects "S2 and S5" not correspond to the average pattern from AO-0.25 Hz to AO-4 Hz. However, subjects "S2 and S5" have approximate accuracies in AO-0.25

TABLE 1 | Statistical analyses of response times for Experiment 1 (ms).

Sessions	Subject 1	Subject 2	Subject 3	Subject 4	Subject 5	Subject 6
Session 1	1760.53	868.97	868.97	1521.47	1716.25	1007.38
Session 2	1087.91	912.84	696.41	1411.47	1254.91	1706.56
Session 3	1201.75	993.75	621.06	1031.94	1695.63	1436.28
Session 4	1141.13	890.38	642.44	1102.09	1783.66	1093.78
Session 5	1243.38	943.69	518.03	1052.81	1644.91	1306.13
Session 6	1175.63	1047.78	749.00	1625.84	1701.25	1577.13
Session 7	1115.03	853.84	829.81	1306.88	1304.25	1420.00
Session 8	1417.50	818.72	777.56	1367.94	1562.38	1513.63
Session 9	1417.50	699.81	763.16	1655.03	1301.03	1268.88
Session 10	1392.31	660.88	759.81	1509.13	1284.75	1204.16
Session 11	1339.03	557.09	828.41	1509.13	1450.06	1181.03
Session 12	1582.00	656.63	790.31	1348.56	1526.16	1181.09
Average	1310.30	825.37	727.84	1370.19	1518.77	1324.67
Standard	201.81	150.67	92.55	213.45	194.04	208.90

The average accuracies and standard deviations of response times were calculated for experiment 1.

TABLE 2 | Statistical analyses of response times for Experiment 2 (ms).

Sessions	Subject 1	Subject 2	Subject 3	Subject 4	Subject 5	Subject 6
Session 13	234.44	238.09	183.81	298.13	286.75	193.63
Session 14	284.31	282.72	219.16	307.94	317.06	221.09
Session 15	258.03	262.84	204.41	287.88	262.31	237.88
Average	258.93	261.22	202.46	297.98	288.71	217.53
Standard	24.95	22.36	17.76	10.03	27.43	22.34

The average accuracies and standard deviations of response times were calculated for experiment 2.

TABLE 3 | The subbands of band-pass filters in FB-CSP feature extraction.

Subbands	fb_1	fb_2	fb_3	fb_4	fb_5	fb_6	fb_7	fb_8	fb_9	fb_{10}
Frequency(Hz)	[0, 4]	[4, 8]	[8, 12]	[12, 16]	[16, 20]	[20, 24]	[24, 28]	[28, 32]	[32, 36]	[36, 40]

A bank of 10 band-pass filters from 0 to 40 Hz without overlaps are set.

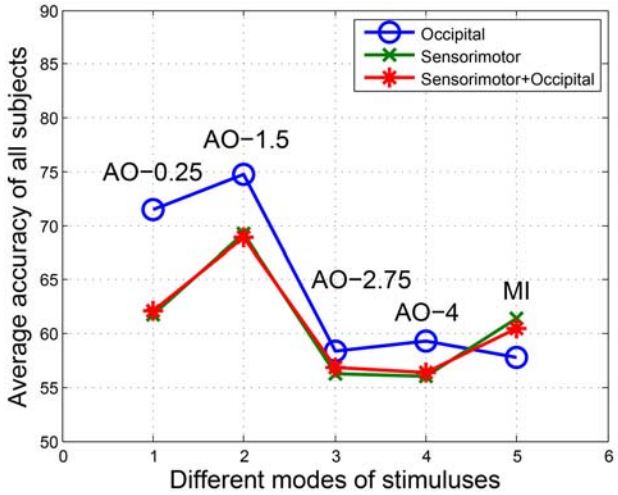


FIGURE 4 | The average accuracies of all modes in all regions. Potentials covering central-parietal regions C3, C1, Cz, C2, C4, P3, P1, Pz, P2, and P4 were chosen for the sensorimotor region, while potentials covering parietal-occipital regions PO5, PO3, POz, PO4, PO6, O1, Oz, and O2 were chosen for the occipital region. The "sensorimotor + occipital" region included both sets of potentials.

Hz and AO-4 Hz. This because different individuals have different patterns of speed modes, and our study was researched on rough speeds due to limitations of device and platform.

These five findings will help us understand affected regions in the brain during AO and the patterns of relationships between AO speed modes and hMNS activations. By selecting the optimal speed mode of AO, we also solved the problem of BMBI. These findings and conclusions are discussed below.

3.3. Spatio-Spectral-Temporal Characteristics of AO Experiments

To further analyse the detailed characteristics, the best-performing data, S4, was chosen to extract the spatio-spectral-temporal characteristics of AO modes.

3.3.1. Temporal Characteristics

The average microvolt of C3 and C4 are drawn on left movements and right movements, respectively. The difference of "C3-C4" in left movements and "C4-C3" in right movements are drawn for temporal characteristics in **Figure 5**. Two key sites, C3 and C4 from the sensorimotor region, were chosen to analyse temporal characteristics.

Three key findings from the results in **Figure 5** are as follows:

(1) Look from the overall, the average microvolt variations of C4 sites are higher than C3 sites on left movements, while the average microvolt variations of C3 sites are higher than C4 sites on right movements. These findings demonstrate the brain's hemisphere lateralization effect during AO.

TABLE 4 | The BCI analysis results for three regions for four AO modes and MI modes.

Subjects	AO-0.25 Hz	AO-1.5 Hz	AO-2.75 Hz	AO-4.0 Hz	MI
OCCIPITAL REGION					
S1	69.27	79.17	54.43	59.38	60.16
S2	77.08	69.79	59.11	59.38	59.90
S3	69.01	76.30	54.95	62.24	57.03
S4	69.27	81.77	68.75	61.46	57.29
S5	67.71	65.36	56.25	54.43	58.85
S6	76.30	76.30	57.03	58.85	53.13
Average	71.44	74.78	58.42	59.29	57.72
Standard	4.12	6.10	5.33	2.73	2.60
ITR (bits/min)	2.06	2.78	0.31	0.38	0.26
SENSORIMOTOR REGION					
S1	69.01	75.52	56.77	56.77	55.47
S2	72.14	68.49	57.03	57.29	57.03
S3	56.77	67.45	58.33	55.47	54.69
S4	54.69	67.19	56.51	52.60	54.69
S5	60.42	70.83	55.21	56.77	67.97
S6	57.55	66.15	53.91	57.03	78.29
Average	61.76	69.27	56.29	55.99	61.35
Standard	7.14	3.45	1.54	1.77	9.72
ITR (bits/min)	0.61	1.65	0.17	0.16	0.56
"OCCIPITAL + SENSORIMOTOR" REGION					
S1	55.21	73.96	56.25	56.25	55.47
S2	71.61	69.53	60.68	58.85	55.21
S3	65.10	59.11	54.43	58.33	56.25
S4	58.33	81.25	56.77	54.17	55.47
S5	62.76	64.32	56.77	55.47	61.72
S6	59.38	65.36	55.99	54.95	78.39
Average 62.07	68.92	56.81	56.33	60.42	
Standard	5.82	7.84	2.08	1.88	9.14
ITR (bits/min)	0.64	1.59	0.20	0.17	0.47

Potentials covering central-parietal regions C3, C1, Cz, C2, C4, P3, P1, Pz, P2, and P4 were chosen for the sensorimotor region, while potentials covering parietal-occipital regions PO5, PO3, POz, PO4, PO6, O1, Oz, and O2 were chosen for the occipital region. The "sensorimotor + occipital" region included both sets of potentials. The average accuracies and standard deviations of BCI classification and ITR were calculated.

(2) Look from the difference average microvolt variations of (C3-C4) in left movements and (C4-C3) in right movements, the differences of AO-0.25 Hz and AO-1.5 Hz are significantly higher than AO-2.75 Hz and AO-4 Hz for both left movements and right movements. These results confirm that variations during AO captured a pattern of increases with slow-speed movements and decreases with fast-speed movements.

(3) In fact, we have calculated the average of difference variations from 1,000 samples for both four different speed modes on left movements and right movements. The results are 0.958 (AO-0.25 Hz), 0.974 (AO-1.5 Hz), 0.048 (AO-2.75 Hz), and 0.112 (AO-4 Hz) on left movements, and 0.907 (AO-0.25

Hz), 0.988 (AO-1.5 Hz), 0.821 (AO-2.75 Hz), and 0.5865 (AO-4 Hz) on right movements. These results suggest some relationships between speed and stimulus direction.

3.3.2. Spectral Characteristics

Figure 6 shows the spectral characteristics of AO in four different speed modes. Four key potentials, C3 and C4 for the

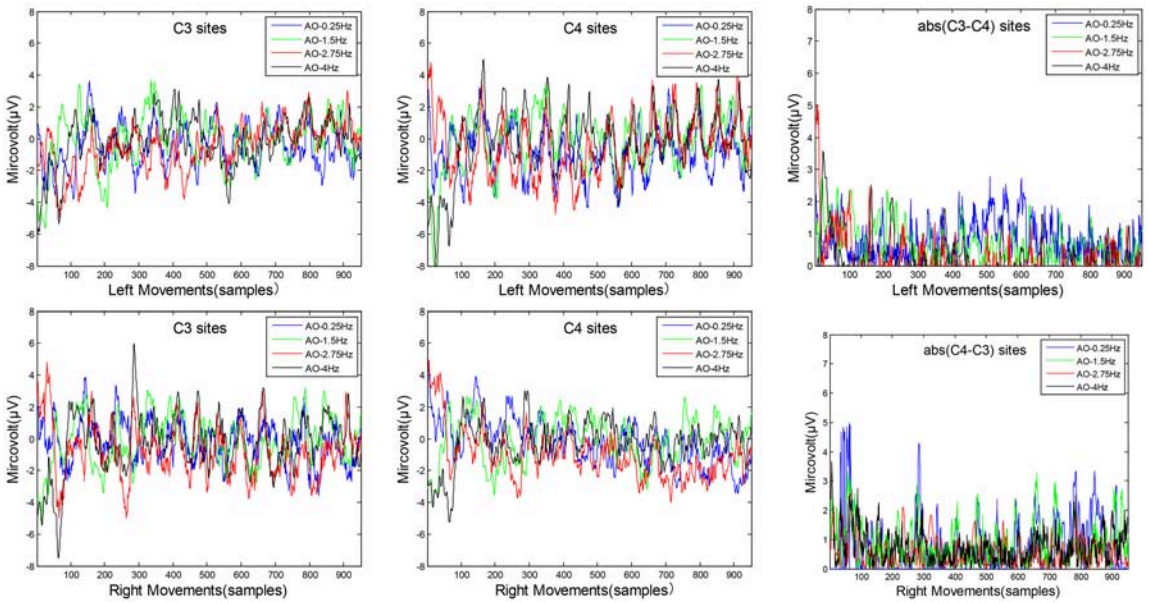


FIGURE 5 | The temporal characteristics of AO in four different speed modes. Two key sites, C3 and C4 from the sensorimotor region, were chosen to analyse temporal characteristics. The average microvolt of C3 and C4 are drawn on left movements and right movements, respectively. The difference of "C3–C4" in left movements and "C4–C3" in right movements are also drawn for temporal characteristics.

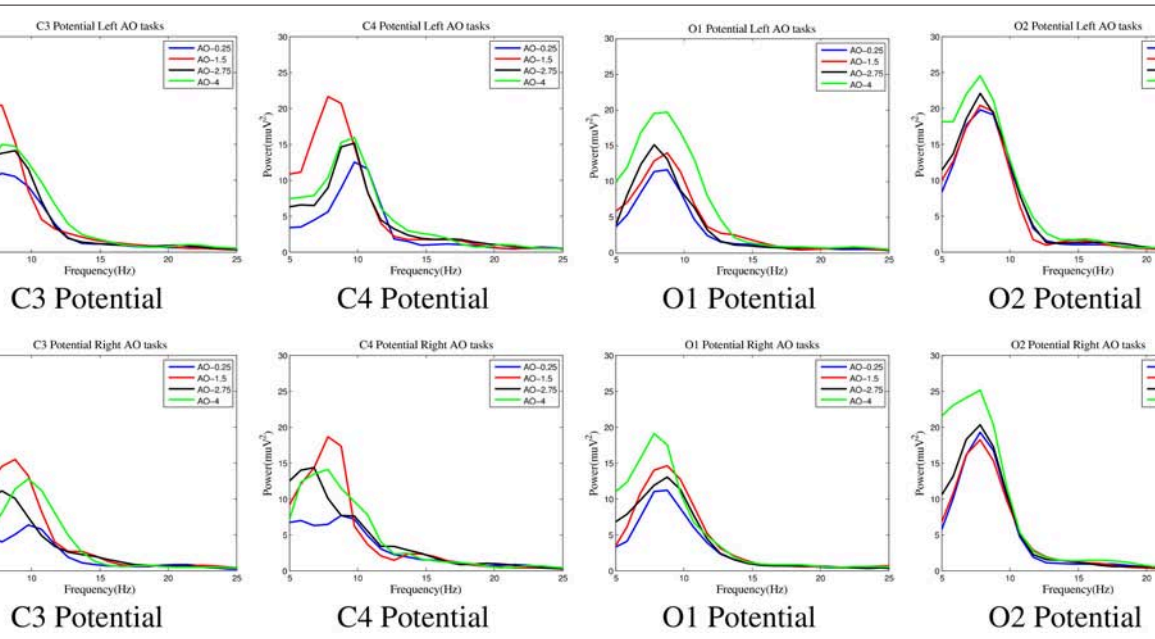


FIGURE 6 | The spectral characteristics of AO in four different speed modes. Four key potentials, C3 and C4 for the sensorimotor region and O1 and O2 for the occipital region, were chosen to analyse the spectral characteristics. The curves for all four AO modes (left movements and right movements) are drawn by "MATLAB R2012a." **(A)** Left movements of AO. **(B)** Right movements of AO.

sensorimotor region and O1 and O2 for the occipital region, were chosen to analyse the spectral characteristics.

Three important findings from **Figure 6** are as follows:

(1) In all of the AO modes, the power varied significantly in the mu range (8–12 Hz) at all C3/C4/O1/O2 potentials, but the variation in the beta range (18–25 Hz) was lower. These results show that the mu range is more sensitive in hMNS during AO.
(2) Regardless of whether left or right movements were examined, the power captured variation in the sensorimotor region (C3/C4) with a pattern where the largest was in AO-1.5 Hz, moderate was in AO-2.75 Hz and AO-4 Hz, and the smallest as in AO-0.25 Hz. However, the power captured variation in the occipital region (O1/O2) had an entirely different pattern in which the largest was in AO-4 Hz and the smallest was AO-1.5 Hz, AO-2.75 Hz, and AO-0.25 Hz with no obvious differences. These results suggest that the sensorimotor region was significantly activated at AO-1.5 Hz, whereas the occipital region was significantly activated at AO-4 Hz.
(3) Regardless of whether left or right movements were examined, the hemisphere effect of the power difference was prominent in the occipital region (O1/O2) but was not obvious in the sensorimotor region (C3/C4). These results demonstrate that the occipital region is more activated than the sensorimotor region.

3.3.3. Spatio-Spectral Characteristics

Figure 7 shows the spatio-spectral characteristics of AO in four different speed modes. The key rhythms, 8, 12, 18, and 25 Hz, were chosen to extract spatio-spectral characteristics from 64 potentials, since the ERD suppressions were induced in the mu (8–12 Hz) and beta (18–25 Hz) ranges.

From the results in **Figure 7**, we find that:

(1) In all eight AO modes, the BEAMs showed that the power in the mu range (8–12 Hz) was higher than that in the beta range (18–25 Hz) in the occipital region. These results demonstrate that the mu range plays a predominant role in hMNS activations.
(2) In contrast to the ERD suppressions during the four different AO speed modes, the ERD suppressions were stronger at AO-0.25 Hz and AO-1.5 Hz than at AO-2.75 Hz and AO-4 Hz in the sensorimotor region. These findings demonstrate that in the sensorimotor region, slow-speed movements cause greater hMNS activation than fast-speed movements during AO.
(3) Comparing left and right movements in one AO mode, the left movements produced more obvious ERD suppressions in the right hemisphere of the brain, whereas the right movements produced more obvious ERD suppressions in the left hemisphere of the brain. These results are due to the mirror effect from the hMNS. However, the movements that subjects observed were also mirror movements. Therefore,

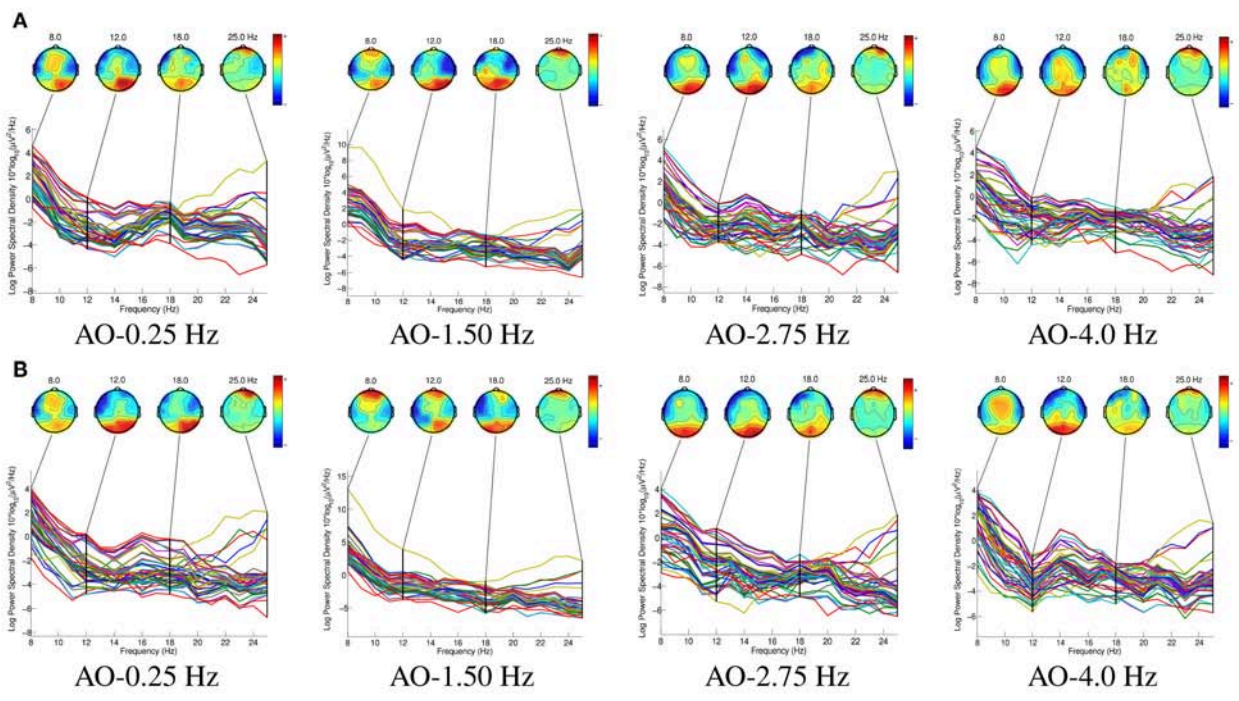


FIGURE 7 | The spatio-spectral characteristics of AO in four different speed modes. The key rhythms, 8, 12, 18, and 25 Hz, were chosen to extract spatio-spectral characteristics from 64 potentials, since the ERD suppressions were induced in the mu (8–12 Hz) and beta (18–25 Hz) ranges. The "BEAM" for all four AO modes(left and right movements) are drawn by "eeglab 14.1.1." **(A)** Left movements of AO. **(B)** Right movements of AO.

the ERD suppressions occurred in the ipsilateral region of the subject's brain relative to the movements of the robot.

4. DISCUSSION

This study further explored the brain regions affected during AO, the patterns of relationships between AO speed modes and hMNS activations, and the comparison of AO and MI for constructing BMBIs. AO experiments with different speed modes (experiment 1) and an MI mode (experiment) were explored at the central nervous system level since hMNS activation caused by AO are reflected by ERD suppressions, which are measured via EEG recording. BCI analyses and spatio-spectral-temporal characteristics were used to explore the variations in ERD suppressions. Based on our results, we were able to draw three major conclusions, which are discussed below:

(1) The occipital region exhibits higher hMNS activation than the sensorimotor region during AO, but the sensorimotor region shows more robust hMNS activations than the occipital region.
(2) hMNS activations initially rise and then fall to a stable level during incremental AO speed modes. A moderate-speed AO produced the best hMNS activations in our results.
(3) The BCI accuracy and ITR of moderate-speed AO-BCI produced the same level of MI-BCI as training experience, suggesting a new method for constructing non-invasive BMBIs in healthy individuals.

4.1. The Affected Regions of the Brain During AO

According to a statistical study (Molenberghs et al., 2012), the support of mirror neurons, the connections across regions, and the strong mirror properties in the hMNS produce mirror properties in the sensorimotor and occipital regions during AO. In fact, the sensorimotor region is related to action imitation and action presentation. Processing of the subjects' action preparation and spatial orientation for a specific action depend on the sensorimotor region. The occipital region is part of the lateral occipitotemporal cortex (LOTC) (Barton et al., 1996; Kable and Chatterjee, 2006). The LOTC is a set of regions that are thought to function in integrating information and determining the purpose of an action. Several previous studies have found that the LOTC region forms direct and indirect connections with hMNS regions (Weiner and Grill-Spector, 2011; Lingnau and Downing, 2015). Therefore, the occipital, sensorimotor, and "sensorimotor+occipital" regions were adopted for BCI analyses and the extraction of spatio-spectral-temporal characteristic from EEG data during AO in this study.

The accuracies of BCI show that the occipital region exhibits higher ERD suppressions than the sensorimotor region (see **Figure 4**). Similar results were also found in the BEAMs (see **Figure 7**). The differences in affected regions during AO found in our study support a previous model of hMNS activation affecting multiple regions (Perry et al., 2010; Frenkel-Toledo et al., 2013). Two main reasons may account for the differences in hMNS activations between the two regions: First, AO paradigms are visually evoked stimuli (Wieser et al., 2016; Park, 2017). Therefore, the visually relevant occipital region first generates power variations (Pegado et al., 2014). After recognition of stimuli, hMNS activations generate power variations in the sensorimotor region (Oberman et al., 2005, 2008). Since the occipital region undergoes rapid and prolonged activation in response to visual stimuli, the degree of activation in the occipital region must be higher than that in the sensorimotor region. Second, the arm movements of the robot turn into attended information during the presentation of AO stimuli (Hwang et al., 2018). Recent studies suggest that attended information increases the activation of mu rhythms (8–12 Hz) in the occipital region during the presentation of visually evoked stimuli (Gray et al., 2015; Sprague et al., 2015). However, distracting information will suppress the activation of the alpha rhythm in the occipital region (Händel et al., 2011; Klimesch, 2012; Zumer et al., 2014). In addition, spectral characteristics and spatio-spatial characteristics suggest that the mu range plays a prominent role in hMNS activations (See **Figures 5**, **6**). Therefore, the attended information provided by the left/right-arm movements of the robot cause more intense power differences in the occipital region than in the sensorimotor region.

Comparing the accuracies of BCI in the three explored regions, the results reflect the robustness of hMNS activation in these regions. The accuracies of BCI in the "sensorimotor+occipital" region remained the same as the sensorimotor region but were significantly different in the occipital region (See **Figure 4**). Since the activation of the sensorimotor region is caused by ERD suppressions, whereas the activation of the occipital region is caused by both ERD suppressions and attended information, ERD suppressions play a dominant role in the activation of the "sensorimotor+occipital" region. In fact, a large number of sessions must be presented over several days. Therefore, the attended information will change during all sessions. As time passes, the activation of the mu range caused by attended information will gradually reduce due to visual fatigue (Lambooij et al., 2009). However, ERD suppressions remain steady during the presentation of stimuli without influence from visual fatigue (Nam et al., 2011). Therefore, the sensorimotor region is more robust for hMNS activations than the occipital region during AO. The findings in our study of hMNS activations conform to the affected regions and formation principles during AO and support further studies on the hMNS.

4.2. The Patterns of hMNS Activations Affected by AO Speed Modes

We found that the patterns of hMNS activations first rise and then fall to a stable level during incremental-speed modes of AO (See **Figure 4**). Relationships between speed modes and left/right movements were also found in spatio-spatial characteristics (See **Figure 7**). The patterns were appropriate for both the sensorimotor region and the occipital region. The reasons why the curves reveal these patterns are as follows. Since AO stimuli in different speed modes were presented in a periodic way in experiment 1, the refractory period of visual

stimuli must be considered during the presentation (Huettel and McCarthy, 2000). Previous studies suggest that the inter-stimulus intervals (ISIs) in the refractory period are within 360–2,000 ms for auditory and visual senses (Coch et al., 2005; Brisson and Jolicœur, 2007). Other studies demonstrate that the ISIs of repetitive contents are within 500 ms (Davis et al., 1972; Johannsen and Röder, 2014). In fact, the ISIs in our experiments were 4,000 ms (slow movement), 666.7 ms (moderate movement), 363.6 ms (fast movement), and 250 ms (finalistic movement). Comparing the ISIs of the four speed modes, the fast and finalistic movements exceeded the repetitive content limits of ISI. Therefore, a visual refractory period will appear during the presentation of fast- and finalistic-movement AO tasks. Since the ERD suppressions are also affected by the visual refractory period during AO (Luck et al., 2000; Caravaglios et al., 2015), the hemisphere effects of ERD suppressions will be reduced by the visual refractory period. In other words, increased speed modes of AO within the limits of ISI will promote hMNS activations that benefit from the absence of a visual refractory period.

The patterns suggested that different speed modes of AO define the extent and distribution of hMNS activations. The purpose of our study was to explore the patterns of relationships between AO speed modes and hMNS activations, since the AO speed modes affect action imitation and action presentation during AO. Meanwhile, the speed modes of AO also play important roles in action information integration and the purpose of action in previous studies (Rizzolatti, 2005; Hobson and Bishop, 2016). Therefore, the speed factor must be considered in relevant studies and applications related to action, such as cognitive psychology, rehabilitation treatment, and BCI. The patterns in our study suggest that periodic actions performed at a moderate speed within decent ISI ranges as visual stimuli for observation will contribute to optimized rehabilitation treatment setups for healthy or unhealthy individuals. AO stimuli of moderate speed within decent ISI will also improve the performance of AO-BCI.

Recently, neurological diseases have been remedied by AO strategies, which are good at ameliorating motor recovery (Buccino et al., 2011). For healthy individuals, AO strategies are good at facilitating motor learning and increasing force (Stefan et al., 2005). Actions performed at a suitable speed mode for observation may enhance action motivation and optimize the recruitment of motor function (Porro et al., 2007). Current treatments for chronic stroke and motor impairment patients construct action execution (AE) strategies based on ecological values (Buccino, 2014), which are valid for improving motor function and ameliorating autonomy, such as grasping cups or cleaning the floor (Ertelt et al., 2007). However, since individual patients with neurological diseases usually have clinical impairments, these patients cannot accomplish such AE assignments in daily treatment without help. The limits for individual patients in AE will be remitted by an optimal AO strategy design. Because the AO assignments are visual stimuli, which need patients to focus their attention, AO assignments are easier to accomplish in daily treatment than AE assignments. In addition, regardless of whether AE or AO assignments are used, the treatment strategies of the medical rehabilitative field must be tailored to satisfy the individual needs of each subject. Treatment strategies should be designed with due consideration of environmental, social, and economic factors, as well as the pathology and characteristics of the subject. Our study suggests that an individually tailored speed within a decent ISI range must be considered when constructing rehabilitation AO treatments for individual subjects.

4.3. The Construction of BMBI Based on AO-BCI and MI-BCI

Our study suggests a new way to construct AO-BCI on a humanoid robot platform. Experimental paradigms are defined by parameters such that confounding factors are eliminated by precise settings. Compared with MI-BCI, AO-BCI offers a number of advantages. Typically, MI-BCI is constructed on the self-imaged spontaneous potential of ERD suppressions. Subjects may imagine self-motion, others-motion, wrist movement, arm movement, or hand movement without specific instruction. In addition, the familiarity factor also affects MI-BCI performance, since MI-BCI performance significantly increases for fully fledged subjects (Schroeder and Chestek, 2016; Subramanian et al., 2016). However, AO-BCI, as a visually evoked stimulus, eliminates the uncertainties of spontaneous MI-BCI. Moreover, familiarity in the BCI is controlled by the stimulus design. In experiments 1 and 2, none of the subjects had previous training experience. However, the BCI results of experiment 1 significantly outperformed those of experiment 2 for slow and moderate movements (See **Figure 4**). A comparison of the results demonstrated that fixed AO modes were less influenced by the subjects' experience, which is another advantage of constructing AO-BCIs.

The performance of AO-BCI and MI-BCI are mismatched in this study since the subjects for MI-BCI lacked MI training. With enough training in MI-BCI, the average accuracy and ITR among subjects can reach 75% and 1.8 bits/min for two classes of MI-BCI (Park et al., 2013). Due to confounding factors, achieving the same level of average accuracy and ITR in AO-BCI has thus far proven difficult. However, by adopting fine-tuned stimuli in AO, as in the present study, the average accuracy and ITR of AO-BCI reached 70% and 1.65 bits/min, which are similar to those of a well-trained MI-BCI (See **Figure 4**). These findings prompted us to construct a BMBI in healthy subjects using the stimulus paradigms of AO and well-trained MI. In recent studies, the majority of BMBIs were based on invasive signal processing technology and used animal carriers (Tessadori et al., 2012). However, BMBIs are rarely based on healthy human brains given the requirement for non-invasive signal processing techniques. As a system of bi-directional transmission, the BMBI must be built on two kinds of stimulators. The accuracy of performance and the ITR of efficiency must achieve the same level for both transmissions. Designing BMBIs that are influenced by variables remains a meaningful but difficult problem. The construction of BMBIs based on AO-BCI and MI-BCI in our study was based on EEG recordings, which will satisfy the requirement for a non-invasive method in healthy individual subjects.

5. CONCLUSION

Our experimental results suggest that the occipital region exhibits higher but less robust hMNS activations than the sensorimotor region. In addition, the patterns of hMNS activations first rise and then fall to a stable level during incremental-speed modes of AO. Moreover, the creation of an AO-BCI provides a novel means of building BMBI systems in healthy individuals with well-trained MI-BCI. However, as time passes, the subjects' refractory period, fatigue and pressure for waiting will lead limit the EEG recordings. Thus, our results provide only rough patterns of the relationships between AO speed modes and hMNS activations. Further studies with larger experimental trials are needed to explore the exact patterns. More modes of AO are also needed to explore confounding factors. Only then can accurate patterns of AO be completed to study the human brain.

AUTHOR CONTRIBUTIONS

CZ, TL, and JL designed the experiments; TL and JL completed the experiments; TL analyzed the EEG data; CZ, FC, and TL wrote the paper.

ACKNOWLEDGMENTS

This work was supported by the National Natural Science Foundation of China (No.61673322 and 61673326), the Major State Basic Research Development Program of China (973 Program) (No. 2013CB329502), the Fundamental Research Funds for the Central Universities (No. 20720160126), and Natural Science Foundation of Fujian Province of China (No. 2017J01128 and 2017J01129).

REFERENCES

Abbott, D. F. (2016). Probing the human brain functional connectome with simultaneous EEG and fMRI. *Front. Neurosci.* 10:302. doi: 10.3389/fnins.2016.00302

Abdi, H., and Williams, L. J. (2010). Principal component analysis. *Wiley Interdisc. Rev. Comput. Stat.* 2, 433–459. doi: 10.1002/wics.101

Agnew, Z. K., Wise, R. J., and Leech, R. (2012). Dissociating object directed and non-object directed action in the human mirror system; implications for theories of motor simulation. *PLoS ONE* 7:e32517. doi: 10.1371/journal.pone.0032517

Ang, K. K., Chin, Z. Y., Wang, C., Guan, C., and Zhang, H. (2012). Filter bank common spatial pattern algorithm on BCI competition IV datasets 2a and 2b. *Front. Neurosci.* 6:39. doi: 10.3389/fnins.2012.00039

Barton, J. J., Simpson, T., Kiriakopoulos, E., Stewart, C., Crawley, A., Guthrie, B., et al. (1996). Functional MRI of lateral occipitotemporal cortex during pursuit and motion perception. *Ann. Neurol.* 40, 387–398.

Bauer, R., and Gharabaghi, A. (2015). Reinforcement learning for adaptive threshold control of restorative brain-computer interfaces: a Bayesian simulation. *Front. Neurosci.* 9:36. doi: 10.3389/fnins.2015.00036

Bello, J. P., Modroño, C., Marcano, F., and González-Mora, J. (2014). The mirror neuron system and motor dexterity: what happens? *Neuroscience* 275, 285–295. doi: 10.1016/j.neuroscience.2014.06.010

Biagi, L., Cioni, G., Fogassi, L., Guzzetta, A., and Tosetti, M. (2010). Anterior intraparietal cortex codes complexity of observed hand movements. *Brain Res. Bull.* 81, 434–440. doi: 10.1016/j.brainresbull.2009.12.002

Blakemore, S.-J., and Decety, J. (2001). From the perception of action to the understanding of intention. *Nat. Rev. Neurosci.* 2, 561–567. doi: 10.1038/35086023

Brisson, B., and Jolicœur, P. (2007). A psychological refractory period in access to visual short-term memory and the deployment of visual–spatial attention: multitasking processing deficits revealed by event-related potentials. *Psychophysiology* 44, 323–333. doi: 10.1111/j.1469-8986.2007.00503.x

Buccino, G. (2014). Action observation treatment: a novel tool in neurorehabilitation. *Philos. Trans. R. Soc. Lond. B Biol. Sci.* 369:20130185. doi: 10.1098/rstb.2013.0185

Buccino, G., Gatti, R., Giusti, M. C., Negrotti, A., Rossi, A., Calzetti, S., et al. (2011). Action observation treatment improves autonomy in daily activities in Parkinson's disease patients: results from a pilot study. *Mov. Disord.* 26, 1963–1964. doi: 10.1002/mds.23745

Calvo-Merino, B., Glaser, D. E., Grèzes, J., Passingham, R. E., and Haggard, P. (2004). Action observation and acquired motor skills: an fMRI study with expert dancers. *Cereb. Cortex* 15, 1243–1249. doi: 10.1093/cercor/bhi007

Calvo-Merino, B., Grèzes, J., Glaser, D. E., Passingham, R. E., and Haggard, P. (2006). Seeing or doing? Influence of visual and motor familiarity in action observation. *Curr. Biol.* 16, 1905–1910. doi: 10.1016/j.cub.2006.07.065

Caravaglios, G., Muscoso, E. G., Di Maria, G., and Costanzo, E. (2015). Patients with mild cognitive impairment have an abnormal upper-alpha event-related desynchronization/synchronization (ERD/ERS) during a task of temporal attention. *J. Neural Transm.* 122, 441–453. doi: 10.1007/s00702-014-1262-7

Caspers, S., Zilles, K., Laird, A. R., and Eickhoff, S. B. (2010). ALE meta-analysis of action observation and imitation in the human brain. *Neuroimage* 50, 1148–1167. doi: 10.1016/j.neuroimage.2009.12.112

Coch, D., Skendzel, W., and Neville, H. J. (2005). Auditory and visual refractory period effects in children and adults: an ERP study. *Clin. Neurophysiol.* 116, 2184–2203. doi: 10.1016/j.clinph.2005.06.005

Davis, H., Osterhammel, P., Wier, C., and Gjerdingen, D. (1972). Slow vertex potentials: interactions among auditory, tactile, electric and visual stimuli. *Electroencephalogr. Clin. Neurophysiol.* 33, 537–545.

Delorme, A., and Makeig, S. (2004). EEGLAB: an open source toolbox for analysis of single-trial EEG dynamics including independent component analysis. *J. Neurosci. Methods* 134, 9–21. doi: 10.1016/j.jneumeth.2003.10.009

Demandt, E., Mehring, C., Vogt, K., Schulze-Bonhage, A., Aertsen, A., and Ball, T. (2012). Reaching movement onset-and end-related characteristics of EEG spectral power modulations. *Front. Neurosci.* 6:65. doi: 10.3389/fnins.2012.00065

Duffy, F. H., Burchfiel, J. L., and Lombroso, C. T. (1979). Brain electrical activity mapping (beam): a method for extending the clinical utility of EEG and evoked potential data. *Ann. Neurol.* 5, 309–321.

Ertelt, D., Small, S., Solodkin, A., Dettmers, C., McNamara, A., Binkofski, F., et al. (2007). Action observation has a positive impact on rehabilitation of motor deficits after stroke. *Neuroimage* 36, T164–T173. doi: 10.1016/j.neuroimage.2007.03.043

Filimon, F., Nelson, J. D., Hagler, D. J., and Sereno, M. I. (2007). Human cortical representations for reaching: mirror neurons for execution, observation, and imagery. *Neuroimage* 37, 1315–1328. doi: 10.1016/j.neuroimage.2007.06.008

Franceschini, M., Ceravolo, M. G., Agosti, M., Cavallini, P., Bonassi, S., Dall'Armi, V., et al. (2012). Clinical relevance of action observation in upper-limb stroke rehabilitation: a possible role in recovery of functional dexterity. a randomized clinical trial. *Neurorehabil. Neural Repair* 26, 456–462. doi: 10.1177/1545968311427406

Frenkel-Toledo, S., Bentin, S., Perry, A., Liebermann, D. G., and Soroker, N. (2013). Dynamics of the EEG power in the frequency and spatial domains during observation and execution of manual movements. *Brain Res.* 1509, 43–57. doi: 10.1016/j.brainres.2013.03.004

Frenkel-Toledo, S., Bentin, S., Perry, A., Liebermann, D. G., and Soroker, N. (2014). Mirror-neuron system recruitment by action observation: effects of focal brain damage on mu suppression. *Neuroimage* 87, 127–137. doi: 10.1016/j.neuroimage.2013.10.019

Gatti, R., Rocca, M. A., Fumagalli, S., Cattrysse, E., Kerckhofs, E., Falini, A., et al. (2017). The effect of action observation/execution on mirror neuron system

recruitment: an fMRI study in healthy individuals. *Brain Imaging Behav.* 11, 565–576. doi: 10.1007/s11682-016-9536-3

Geers, A. (1994). Techniques for assessing auditory speech perception and lipreading enhancement in young deaf children. *Volta Rev.* 96, 85–96.

Gray, M. J., Frey, H.-P., Wilson, T. J., and Foxe, J. J. (2015). Oscillatory recruitment of bilateral visual cortex during spatial attention to competing rhythmic inputs. *J. Neurosci.* 35, 5489–5503. doi: 10.1523/JNEUROSCI.2891-14.2015

Händel, B. F., Haarmeier, T., and Jensen, O. (2011). Alpha oscillations correlate with the successful inhibition of unattended stimuli. *J. Cogn. Neurosci.* 23, 2494–2502. doi: 10.1162/jocn.2010.21557

Hobson, H. M., and Bishop, D. V. (2016). Mu suppression–a good measure of the human mirror neuron system? *Cortex* 82, 290–310. doi: 10.1016/j.cortex.2016.03.019

Huettel, S. A., and McCarthy, G. (2000). Evidence for a refractory period in the hemodynamic response to visual stimuli as measured by MRI. *Neuroimage* 11, 547–553. doi: 10.1006/nimg.2000.0553

Hwang, K., Shine, J. M., and D'Esposito, M. (2018). Frontoparietal activity interacts with task-evoked changes in functional connectivity. *Cereb. Cortex*. doi: 10.1093/cercor/bhy011. [Epub ahead of print].

Iacoboni, M., Molnar-Szakacs, I., Gallese, V., Buccino, G., Mazziotta, J. C., and Rizzolatti, G. (2005). Grasping the intentions of others with one's own mirror neuron system. *PLoS Biol.* 3:e79. doi: 10.1371/journal.pbio.0030079

Johannsen, J., and Röder, B. (2014). Uni-and crossmodal refractory period effects of event-related potentials provide insights into the development of multisensory processing. *Front. Hum. Neurosci.* 8:552. doi: 10.3389/fnhum.2014.00552

Kable, J. W., and Chatterjee, A. (2006). Specificity of action representations in the lateral occipitotemporal cortex. *J. Cogn. Neurosci.* 18, 1498–1517. doi: 10.1162/jocn.2006.18.9.1498

Klimesch, W. (2012). α-band oscillations, attention, and controlled access to stored information. *Trends Cogn. Sci.* 16, 606–617. doi: 10.1016/j.tics.2012.10.007

Lambooij, M., Fortuin, M., Heynderickx, I., and IJsselsteijn, W. (2009). Visual discomfort and visual fatigue of stereoscopic displays: a review. *J. Imaging Sci. Technol.* 53, 1–14. doi: 10.2352/J.ImagingSci.Technol.2009.53.3.030201

Lei, X., Wu, T., and Valdes-Sosa, P. A. (2015). Incorporating priors for EEG source imaging and connectivity analysis. *Front. Neurosci.* 9:284. doi: 10.3389/fnins.2015.00284

Lingnau, A., and Downing, P. E. (2015). The lateral occipitotemporal cortex in action. *Trends Cogn. Sci.* 19, 268–277. doi: 10.1016/j.tics.2015.03.006

Luck, S. J., Woodman, G. F., and Vogel, E. K. (2000). Event-related potential studies of attention. *Trends Cogn. Sci.* 4, 432–440. doi: 10.1016/S1364-6613(00)01545-X

Maranesi, M., Ugolotti Serventi, F., Bruni, S., Bimbi, M., Fogassi, L., and Bonini, L. (2013). Monkey gaze behaviour during action observation and its relationship to mirror neuron activity. *Eur. J. Neurosci.* 38, 3721–3730. doi: 10.1111/ejn.12376

Molenberghs, P., Cunnington, R., and Mattingley, J. B. (2012). Brain regions with mirror properties: a meta-analysis of 125 human fmri studies. *Neurosci. Biobehav. Rev.* 36, 341–349. doi: 10.1016/j.neubiorev.2011.07.004

Mukamel, R., Ekstrom, A. D., Kaplan, J., Iacoboni, M., and Fried, I. (2010). Single-neuron responses in humans during execution and observation of actions. *Curr. Biol.* 20, 750–756. doi: 10.1016/j.cub.2010.02.045

Nam, C. S., Jeon, Y., Kim, Y.-J., Lee, I., and Park, K. (2011). Movement imagery-related lateralization of event-related (de) synchronization (ERD/ERS): Motor-imagery duration effects. *Clin. Neurophysiol.* 122, 567–577. doi: 10.1016/j.clinph.2010.08.002

Neuper, C., Scherer, R., Wriessnegger, S., and Pfurtscheller, G. (2009). Motor imagery and action observation: modulation of sensorimotor brain rhythms during mental control of a brain–computer interface. *Clin. Neurophysiol.* 120, 239–247. doi: 10.1016/j.clinph.2008.11.015

Newman-Norlund, R. D., van Schie, H. T., van Zuijlen, A. M., and Bekkering, H. (2007). The mirror neuron system is more active during complementary compared with imitative action. *Nat. Neurosci.* 10:nn1911. doi: 10.1038/nn1911

Oberman, L. M., Hubbard, E. M., McCleery, J. P., Altschuler, E. L., Ramachandran, V. S., and Pineda, J. A. (2005). EEG evidence for mirror neuron dysfunction in autism spectrum disorders. *Brain Res. Cogn. Brain Res.* 24, 190–198. doi: 10.1016/j.cogbrainres.2005.01.014

Oberman, L. M., Pineda, J. A., and Ramachandran, V. S. (2007). The human mirror neuron system: a link between action observation and social skills. *Soc. Cogn. Affect. Neurosci.* 2, 62–66. doi: 10.1093/scan/nsl022

Oberman, L. M., Ramachandran, V. S., and Pineda, J. A. (2008). Modulation of mu suppression in children with autism spectrum disorders in response to familiar or unfamiliar stimuli: the mirror neuron hypothesis. *Neuropsychologia* 46, 1558–1565. doi: 10.1016/j.neuropsychologia.2008.01.010

Onishi, A., Takano, K., Kawase, T., Ora, H., and Kansaku, K. (2017). Affective stimuli for an auditory p300 brain-computer interface. *Front. Neurosci.* 11:522. doi: 10.3389/fnins.2017.00522

Orgs, G., Dombrowski, J.-H., Heil, M., and Jansen-Osmann, P. (2008). Expertise in dance modulates alpha/beta event-related desynchronization during action observation. *Eur. J. Neurosci.* 27, 3380–3384. doi: 10.1111/j.1460-9568.2008.06271

Park, C., Looney, D., ur Rehman, N., Ahrabian, A., and Mandic, D. P. (2013). Classification of motor imagery BCI using multivariate empirical mode decomposition. *IEEE Trans. Neural Syst. Rehabil. Eng.* 21, 10–22. doi: 10.1109/TNSRE.2012.2229296

Park, J. (2017). A neural basis for the visual sense of number and its development: a steady-state visual evoked potential study in children and adults. *Dev. Cogn. Neurosci.* doi: 10.1016/j.dcn.2017.02.011. [Epub ahead of print].

Pegado, F., Comerlato, E., Ventura, F., Jobert, A., Nakamura, K., Buiatti, M., et al. (2014). Timing the impact of literacy on visual processing. *Proc. Natl. Acad. Sci. U.S.A.* 111, E5233–E5242. doi: 10.1073/pnas.1417347111

Perry, A., Bentin, S., Shalev, I., Israel, S., Uzefovsky, F., Bar-On, D., et al. (2010). Intranasal oxytocin modulates EEG mu/alpha and beta rhythms during perception of biological motion. *Psychoneuroendocrinology* 35, 1446–1453. doi: 10.1016/j.psyneuen.2010.04.011

Pineda, J. A., Grichanik, M., Williams, V., Trieu, M., Chang, H., and Keysers, C. (2013). EEG sensorimotor correlates of translating sounds into actions. *Front. Neurosci.* 7:203. doi: 10.3389/fnins.2013.00203

Porro, C. A., Facchin, P., Fusi, S., Dri, G., and Fadiga, L. (2007). Enhancement of force after action observation: behavioural and neurophysiological studies. *Neuropsychologia* 45, 3114–3121. doi: 10.1016/j.neuropsychologia.2007.06.016

Pot, E., Monceaux, J., Gelin, R., and Maisonnier, B. (2009). "Choregraphe: a graphical tool for humanoid robot programming," in *The 18th IEEE International Symposium on Robot and Human Interactive Communication* (Toyama), 46–51.

Press, C. (2011). Action observation and robotic agents: learning and anthropomorphism. *Neurosci. Biobehav. Rev.* 35, 1410–1418. doi: 10.1016/j.neubiorev.2011.03.004

Rizzolatti, G. (2005). The mirror neuron system and its function in humans. *Anat. Embryol.* 210, 419–421. doi: 10.1007/s00429-005-0039-z

Rizzolatti, G., and Sinigaglia, C. (2010). The functional role of the parieto-frontal mirror circuit: interpretations and misinterpretations. *Nat. Rev. Neurosci.* 11, 264–274. doi: 10.1038/nrn2805

Rozzi, S., and Fogassi, L. (2017). Neural coding for action execution and action observation in the prefrontal cortex and its role in the organization of socially driven behavior. *Front. Neurosci.* 11:492. doi: 10.3389/fnins.2017.00492

Sardouie, S. H., and Shamsollahi, M. B. (2012). Selection of efficient features for discrimination of hand movements from meg using a BCI competition IV data set. *Front. Neurosci.* 6:42. doi: 10.3389/fnins.2012.00042

Schroeder, K. E., and Chestek, C. A. (2016). Intracortical brain-machine interfaces advance sensorimotor neuroscience. *Front. Neurosci.* 10:291. doi: 10.3389/fnins.2016.00291

Schulte-Rüther, M., Markowitsch, H. J., Fink, G. R., and Piefke, M. (2007). Mirror neuron and theory of mind mechanisms involved in face-to-face interactions: a functional magnetic resonance imaging approach to empathy. *J. Cogn. Neurosci.* 19, 1354–1372. doi: 10.1162/jocn.2007.19.8.1354

Silsbee, P. L., and Bovik, A. C. (1996). Computer lipreading for improved accuracy in automatic speech recognition. *IEEE Trans. Speech Audio Process.* 4, 337–351.

Smith, E. G., and Bennetto, L. (2007). Audiovisual speech integration and lipreading in autism. *J. Child Psychol. Psychiatry* 48, 813–821. doi: 10.1111/j.1469-7610.2007.01766.x

Sprague, T. C., Saproo, S., and Serences, J. T. (2015). Visual attention mitigates information loss in small-and large-scale neural codes. *Trends Cogn. Sci.* 19, 215–226. doi: 10.1016/j.tics.2015.02.005

Stefan, K., Cohen, L. G., Duque, J., Mazzocchio, R., Celnik, P., Sawaki, L., et al. (2005). Formation of a motor memory by action observation. *J. Neurosci.* 25, 9339–9346. doi: 10.1523/JNEUROSCI.2282-05.2005

Subramanian, L., Morris, M. B., Brosnan, M., Turner, D. L., Morris, H. R., and Linden, D. E. (2016). Functional magnetic resonance imaging neurofeedback-guided motor imagery training and motor training for Parkinson's disease: randomized trial. *Front. Behav. Neurosci.* 10:111. doi: 10.3389/fnbeh.2016.00111

Summerfield, Q. (1992). Lipreading and audio-visual speech perception. *Philos. Trans. R. Soc. Lond. B Biol. Sci.* 335, 71–78.

Tangermann, M., Müller, K.-R., Aertsen, A., Birbaumer, N., Braun, C., Brunner, C., et al. (2012). Review of the BCI competition IV. *Front. Neurosci.* 6:55. doi: 10.3389/fnins.2012.00055

Tanji, K., Sakurada, K., Funiu, H., Matsuda, K., Kayama, T., Ito, S., et al. (2015). Functional significance of the electrocorticographic auditory responses in the premotor cortex. *Front. Neurosci.* 9:78. doi: 10.3389/fnins.2015.00078

Tessadori, J., Bisio, M., Martinoia, S., and Chiappalone, M. (2012). Modular neuronal assemblies embodied in a closed-loop environment: toward future integration of brains and machines. *Front. Neural Circ.* 6:99. doi: 10.3389/fncir.2012.00099

Vogt, S., Di Rienzo, F., Collet, C., Collins, A., and Guillot, A. (2013). Multiple roles of motor imagery during action observation. *Front. Hum. Neurosci.* 7:807. doi: 10.3389/fnhum.2013.00807

Wang, D., Miao, D., and Blohm, G. (2012). Multi-class motor imagery EEG decoding for brain-computer interfaces. *Front. Neurosci.* 6:151. doi: 10.3389/fnins.2012.00151

Weiner, K. S., and Grill-Spector, K. (2011). Not one extrastriate body area: using anatomical landmarks, hMT+, and visual field maps to parcellate limb-selective activations in human lateral occipitotemporal cortex. *Neuroimage* 56, 2183–2199. doi: 10.1016/j.neuroimage.2011.03.041

Wieser, M. J., Reicherts, P., Juravle, G., and von Leupoldt, A. (2016). Attention mechanisms during predictable and unpredictable threat-a steady-state visual evoked potential approach. *Neuroimage* 139, 167–175. doi: 10.1016/j.neuroimage.2016.06.026

Zumer, J. M., Scheeringa, R., Schoffelen, J.-M., Norris, D. G., and Jensen, O. (2014). Occipital alpha activity during stimulus processing gates the information flow to object-selective cortex. *PLoS Biol.* 12:e1001965. doi: 10.1371/journal.pbio.1001965

Conflict of Interest Statement: The authors declare that the research was conducted in the absence of any commercial or financial relationships that could be construed as a potential conflict of interest.

Copyright © 2018 Luo, Lv, Chao and Zhou. This is an open-access article distributed under the terms of the Creative Commons Attribution License (CC BY). The use, distribution or reproduction in other forums is permitted, provided the original author(s) and the copyright owner are credited and that the original publication in this journal is cited, in accordance with accepted academic practice. No use, distribution or reproduction is permitted which does not comply with these terms.

frontiers in Human Neuroscience

ORIGINAL RESEARCH
published: 09 April 2018
doi: 10.3389/fnhum.2018.00131

Altered Neuromodulatory Drive May Contribute to Exaggerated Tonic Vibration Reflexes in Chronic Hemiparetic Stroke

Jacob G. McPherson[1,2], *Laura M. McPherson*[1,2,3], *Christopher K. Thompson*[4,5], *Michael D. Ellis*[2], *Charles J. Heckman*[2,5] *and Julius P. A. Dewald*[2,6]*

[1] Department of Biomedical Engineering, Florida International University, Miami, FL, United States, [2] Department of Physical Therapy and Human Movement Sciences, Northwestern University Feinberg School of Medicine, Chicago, IL, United States, [3] Department of Physical Therapy, Florida International University, Miami, FL, United States, [4] Department of Physical Therapy, Temple University, Philadelphia, PA, United States, [5] Department of Physiology, Northwestern University Feinberg School of Medicine, Chicago, IL, United States, [6] Department of Biomedical Engineering, Northwestern University, Evanston, IL, United States

Exaggerated stretch-sensitive reflexes are a common finding in elbow flexors of the contralesional arm in chronic hemiparetic stroke, particularly when muscles are not voluntarily activated prior to stretch. Previous investigations have suggested that this exaggeration could arise either from an abnormal tonic ionotropic drive to motoneuron pools innervating the paretic limbs, which could bring additional motor units near firing threshold, or from an increased influence of descending monoaminergic neuromodulatory pathways, which could depolarize motoneurons and amplify their responses to synaptic inputs. However, previous investigations have been unable to differentiate between these explanations, leaving the source(s) of this excitability increase unclear. Here, we used tonic vibration reflexes (TVRs) during voluntary muscle contractions of increasing magnitude to infer the sources of spinal motor excitability in individuals with chronic hemiparetic stroke. We show that when the paretic and non-paretic elbow flexors are preactivated to the same percentage of maximum prior to vibration, TVRs remain significantly elevated in the paretic arm. We also show that the rate of vibration-induced torque development increases as a function of increasing preactivation in the paretic limb, even though the amplitude of vibration-induced torque remains conspicuously unchanged as preactivation increases. It is highly unlikely that these findings could be explained by a source that is either purely ionotropic or purely neuromodulatory, because matching preactivation should control for the effects of a potential ionotropic drive (and lead to comparable tonic vibration reflex responses between limbs), while a purely monoaminergic mechanism would increase reflex magnitude as a function of preactivation. Thus, our results suggest that increased excitability of motor pools innervating the paretic limb post-stroke is likely to arise from both ionotropic and neuromodulatory mechanisms.

Keywords: stroke, motor control, stretch reflex, bulbospinal monoaminergic drive, motoneurons, sensorimotor integration

OPEN ACCESS

Edited by:
Mikhail Lebedev,
Duke University, United States

Reviewed by:
Pavel Lindberg,
INSERM U894 Centre de Psychiatrie et Neurosciences, France
Andrew Joseph Fuglevand,
University of Arizona, United States

***Correspondence:**
Julius P. A. Dewald
j-dewald@northwestern.edu

Received: *04 November 2017*
Accepted: *22 March 2018*
Published: *09 April 2018*

Citation:
McPherson JG, McPherson LM, Thompson CK, Ellis MD, Heckman CJ and Dewald JPA (2018) Altered Neuromodulatory Drive May Contribute to Exaggerated Tonic Vibration Reflexes in Chronic Hemiparetic Stroke. Front. Hum. Neurosci. 12:131. doi: 10.3389/fnhum.2018.00131

INTRODUCTION

Focal ischemic stroke causes changes in descending neural drive that alter spinal motor excitability (Stinear et al., 2007; Heckman et al., 2009; Bradnam et al., 2012; McMorland et al., 2015; McPherson et al., 2017, 2018; Owen et al., 2017). This can occur through direct effects on spinal neurons and/or by facilitating adaptive processes associated with shifts in the overall balance of spinal excitation and inhibition. In the chronic state post-stroke, spinal motor excitability generally increases in regions that control the paretic limbs; in regions innervating the non-paretic limbs, excitability remains at approximately pre-injury levels or is increased to a lesser degree (Lee et al., 1987; Powers et al., 1989; Thilmann et al., 1990, 1991; Ibrahim et al., 1993; McPherson et al., 2011, 2017; Hu et al., 2015). Increased spinal motor excitability could theoretically be related to alterations in ionotropic drive (i.e., signaling via ligand-gated channels that directly elicits excitatory or inhibitory post-synaptic potentials), neuromodulatory drive (i.e., signaling via metabotropic receptors to modify the intrinsic excitability of the cell), or both. However, it is currently unknown which of these options primarily underlies increased spinal motor excitability in paretic motor pools because the results of previous investigations could have plausibly been explained by either phenomenon alone (Powers et al., 1989; McPherson et al., 2008; Mottram et al., 2009, 2010).

Stretch-sensitive reflexes are a useful assay of spinal motor excitability. For example, exaggerated mechanical and electromyographical responses to imposed joint excursions in paretic limbs have proven to be both conspicuous and enduring findings in chronic hemiparetic stroke. These reflex exaggerations are known clinically as spasticity (Lance, 1980). Reflexive contractions developed during maintained muscle or tendon vibration can also be used to assess spinal motor excitability (Eklund and Hagbarth, 1966; Hagbarth and Eklund, 1966; Gillies et al., 1971; Matthews, 1984; McPherson et al., 2008). These contractions are known as tonic vibration reflexes (TVRs). We have previously shown that TVRs are dramatically amplified in resting muscles of the paretic arm compared to homologous muscles of the non-paretic arm, and robust muscle activation persists in the paretic arm long after removal of the vibration (McPherson et al., 2008). The finding of both amplification and prolongation of motor output in paretic muscles is important because it may point to an increased influence of descending monoaminergic neuromodulatory pathways. Indeed, a hallmark of monoaminergic actions on somatic motoneurons is the development of persistent inward currents (PICs) in motoneuron dendrites, which uniquely amplify and prolong motoneuron output in response to excitatory synaptic inputs (Schwindt and Crill, 1977; Powers and Binder, 2001; Heckman et al., 2003, 2009).

However, some signs of an increased neuromodulatory influence appear to diminish when muscles are volitionally preactivated. For example, we and others have demonstrated that stretch reflex amplitude equilibrates between paretic and non-paretic muscles when the muscles are preactivated to the same extent prior to stretch (Lee et al., 1987; Burne et al., 2005; Mottram et al., 2009, 2010; McPherson et al., 2017). Additionally, some estimates of PIC amplitude are indistinguishable between paretic and control muscles during volitional ramp contractions (Mottram et al., 2009, 2010). Although equivocal, these findings are usually taken as evidence that a tonic, low-level ionotropic drive mediates the resting excitability imbalance between arms rather than an increased neuromodulatory drive (Mottram et al., 2009, 2010). In this scenario, the tonic ionotropic drive provides a sub-threshold depolarization to the resting motoneuron pool. The pre-reflex volitional descending drive depolarizes the motoneuron pool above spiking threshold, eclipsing the tonic ionotropic drive and effectively washing out the resting excitability imbalance. As a result, reflex amplitude is comparable in both limbs and increases as a function of pre-reflex muscle activation.

Here, we characterize TVRs in elbow flexors of the paretic and non-paretic arms of individuals with chronic hemiparetic stroke at three levels of preactivation. In particular, we quantify TVR-evoked elbow flexion joint torque amplitude and rise time, metrics that can be used to infer the spinal neuromodulatory state (McPherson et al., 2008; Revill and Fuglevand, 2017). We predicted that TVR-evoked torque would equilibrate between paretic and non-paretic arms when muscles were preactivated to the same degree prior to vibration, based on parallels with torque responses to stretch reflexes elicited by imposed joint excursion. Contrary to our prediction, we found pronounced amplification of TVR responses in the paretic arm despite matching preactivation levels between limbs. Perhaps more conspicuously, however, the magnitude of TVR-evoked torque did not scale with preactivation level in either limb. This finding stands in contrast to the well-documented positive correlation between preactivation level and reflex amplitude in response to imposed joint excursion (Ibrahim et al., 1993; Burne et al., 2005; McPherson et al., 2017). We also found that the rise time of TVR-evoked torque was significantly more rapid with increasing preactivation in the paretic limb compared to the non-paretic limb. Given these surprising results, we then corroborated our findings in a proof-of-principle decerebrate cat preparation that also allowed visualization of individual motor unit firing characteristics. In this model, descending monoaminergic drive is elevated and invariant to synaptic input, and force output is *not* influenced by volition. Thus, force output in this model is due only to three factors: the sustained monoaminergic drive, Ia input (via vibration), and the resulting input-output function of the motoneurons. We interpret these results as evidence that both an ionotropic and monoaminergic neuromodulatory drive are likely to contribute to the apparent increased excitability of motor pools innervating paretic muscles post-stroke.

MATERIALS AND METHODS

Human-Subjects Experiments

Participant Characteristics and Ethics Statement

Ten individuals fulfilled all criteria for involvement in the study and subsequently completed the experimental protocol. The same individuals also participated in our original study of TVR responses post-stroke (McPherson et al., 2008). Each of these

individuals (mean age: 59 ± 10 yrs) sustained a first-ever cortical or subcortical stroke at least 1 year prior to enrollment in the investigation (range: 40–124 months) and had lingering motor deficits on one side of the body. Fugl-Meyer motor assessment (FMA) scores ranged from 13 to 43 of a possible 66, representing severe to moderate impairment, and Ashworth scores (available for 6 of 10 participants) ranged from 2 to 4 (scoring: 0, 1, 2, 3, 4). Participant demographic and clinical data are summarized in **Table 1.**

For inclusion in the study, all participants were required to possess at least 90 degrees passive range of motion in shoulder flexion, shoulder abduction, and elbow flexion/extension. Participants were additionally required to exhibit some volitional control of elbow flexion/extension in order to obtain maximum voluntary torques (MVTs). The absence of inflammatory conditions at the shoulder, elbow, wrist and fingers was verified by overpressure at the end-range of motion. Potential participants were excluded from the study if the demonstrated minimal (50–66 on the FMA) or very severe (0–9 on the FMA) impairment, significant impairment of upper extremity tactile sensation or proprioception (O'Sullivan and Schmitz, 2001), or difficulties sitting for extended periods of time. All participants were required to have discontinued use of antispastic medications at least 6 months prior to enrollment; more recent or ongoing use was grounds for exclusion from the study.

All participants provided informed consent to participate in the investigation, which was approved by the Institutional Review Board of Northwestern University in accordance with the ethical standards stipulated by the 1964 Declaration of Helsinki for research involving human participants.

Experimental Setup

Participants were secured to a Biodex experimental chair (Biodex Medical Systems, Shirley, NY) by shoulder and lap belt restraints. The forearm, wrist and hand of each participant's paretic and non-paretic arms were fitted with custom fiberglass casts. The casted arm was coupled at the level of the wrist to a 6 degree-of-freedom load cell (Model 45E15A; JR3, Woodland, CA), and the limb was positioned such that it retained 75° of shoulder abduction, 40° of shoulder flexion, and 90° of elbow flexion. The test apparatus supported the weight of the limb throughout these experimental protocols.

TABLE 1 | Participant demographic and clinical data.

Participant	Age	Biological sex	Paretic arm	Fugl-meyer motor assessment	Ashworth score
1	68	M	R	18	2
2	40	M	L	40	2
3	53	F	R	13	2
4	59	M	R	14	4
5	61	M	L	43	2
6	50	F	R	21	2
7	65	M	L	18	NA
8	59	M	L	24	NA
9	77	M	R	30	NA
10	51	F	R	26	NA

Fugl-Meyer: 0–66; Ashworth: 0, 1, 2, 3, 4; NA, not available.

Experimental Protocol

While interfaced with the isometric testing setup described above, participants were first required to generate MVTs in elbow flexion and extension. Visual feedback of performance was provided in real time for all trials. To obtain a reliable estimate of the true maximum torque capability in each direction, collection of MVTs continued until 3 trials were obtained within 10% of one another, without the last trial being the greatest.

For the TVR protocol, participants remained interfaced with the isometric setup used for testing MVTs, and a therapeutic massage vibrator (frequency: 112 Hz, model 91, Daito-Thrive, Showa-cho, Japan) was placed over the distal muscle belly of the biceps brachii. TVR trial onset and offset were indicated to the participant and experimentalist by auditory cues. TVR trials began after the experimentalist determined that the participant was fully relaxed (via real-time EMG and torque feedback). Upon trial onset, participants were first instructed to generate and maintain either 5 or 15% of their elbow flexion MVT, guided by visual feedback. Once the requisite torque was achieved, visual feedback was extinguished, and vibration commenced. The vibratory stimulus lasted for 5 s. Following each trial, participants were given at least a 15–30 s rest period to allow the limb to relax before beginning the next trial. First-pass trial acceptability was examined on-line by visual feedback provided to the experimentalist, and trials were excluded from further analysis if postural or unconstrained extremity movements occurred during the trial or if participants closed their eyes and appeared to fall asleep. Approximately 20 TVR response trials were collected at each of the 5 and 15% elbow flexion levels, and the protocol was performed on both the paretic and non-paretic limbs.

Data Analysis

Analyses of TVR-evoked elbow flexion torque were used as outcome measures in this study, computed using custom Matlab software (The MathWorks, Natick, MA). A Jacobian-based algorithm converted forces and moments recorded by the loadcell into elbow flexion/extension torques. The resulting torque curves were filtered with an eighth-order low-pass Butterworth filter with cutoff frequency of 50 Hz. Window averages of individual TVR trials were taken from 3.5 to 5.0 s after trial onset, corresponding to the preactivation phase, and from 9.5 to 10.0 s post-trial onset, corresponding to the last 500 ms of the vibration phase. We did not extract data during the post-vibration period because reflexive torque and EMG responses could not be reliably decoupled from volitional efforts to decrease elbow flexion torque. Preactivation windows and during-vibration windows were then ensemble-averaged for each participant and limb (paretic and non-paretic) for use in subsequent group analyses.

To quantify TVR-evoked torque amplitude, we computed the change in torque from preactivation to during-vibration for each participant's ensemble-averaged torque response. We

computed this difference at each preactivation level (0, 5, 15%), and these values were subsequently used in group statistical analyses. Because of the likely difference in elbow flexion strength between paretic and non-paretic limbs, we calculated the TVR-evoked torque amplitude using both unnormalized torque (Nm) and normalized torque (% MVT). This dual approach ensured that between-limb results would not be inflated by normalization of paretic torque to lower MVT values.

We used two approaches to quantify the temporal profile of the rising phase of the TVR-evoked torque response. First, we computed the slope of a linear fit between each participant's preactivation torque and the time at which TVR-evoked torque reached 85% of the maximum stable response (Equation 1):

$$Rising\ slope\ of\ TVR\ \ evoked\ torque = \frac{(torque_{85\%max} - torque_{preac})}{time_{85\%max} - time_{Vib.ON}}[\%MVT]/sec \quad (1)$$

Second, because TVR-evoked torque generally exhibits a non-linear temporal profile, we used non-linear least squares estimation to determine the optimal fit of each group mean ensemble-averaged torque response (i.e., paretic and non-paretic, each at 5 and 15% preactivation) to a function of the form:

$$Modeled\ TVR\ evoked\ torque = a*(1 - e^{-t/b}) \quad (2)$$

In this equation, term a generally represents the amplitude of the TVR-evoked torque (add preactivation torque to a to approximate the final steady-state torque amplitude in the plots below), term b is the time constant describing the rate of rise of TVR-evoked torque, and t is elapsed time. The model was fit to experimental data from the time of vibration onset to the time of vibration offset; a and b are coefficients fit by the optimization routine and t is elapsed time. The parameters of this model are not intended to reflect specific biophysical features of motoneuron firing.

Statistical Analysis

For TVR-evoked torque amplitude, all statistical analyses were calculated on the normalized torque values. Unnormalized torque values are presented for comparison. A 2 × 3 repeated measures ANOVA was used to determine the main effects of limb (paretic, non-paretic) and preactivation level (0, 5, 15%), as well as the limb-by-preactivation level interaction, on normalized TVR-evoked torque amplitude. To reiterate, all participants included in this investigation were included in our original study of TVR responses post-stroke (McPherson et al., 2008), enabling data to be pooled across experiments to generate the new analyses presented here. Two sets of *post-hoc* t-tests were used. First, t-tests were used to determine differences between limbs at each preactivation level, with Bonferroni correction for multiple comparisons. Second, t-tests within each limb were used to evaluate differences between all combinations of preactivation levels, using Tukey correction for multiple comparisons within each limb.

For the slope of TVR-evoked torque, there were 60 total values (2 limbs × 3 preactivation levels × 10 participants). Several outliers were detected in both paretic and non-paretic values, which were excluded from further analysis. Outliers were defined as values exceeding 3 scaled median absolute deviations from the median. Given that a 2-way repeated measures ANOVA (which is most appropriate for this experimental design) requires no missing cases, the following method was used to account for the missing data and allow for a repeated measures ANOVA. First, if a participant had missing data for more than one preactivation level, all data for that participant was removed. This resulted in removing data from two participants for the non-paretic limb (with $N = 8$ remaining) and data from one participant in the paretic limb (with $N = 9$ remaining). Together, these removals reduced the total number of torque values from 60 to 51. There were two missing cases at one preactivation level for the non-paretic limb (for one participant at 0% and for another participant at 15%). Values for these cases were imputed by taking the average of values from the seven other participants. For the paretic limb, there was one missing case at the 0% condition, and the value was imputed by taking the average of the eight other participants for this condition. As a result, the number of total values that were imputed was 3 out of 51, or 5.9%. This method allowed for an ANOVA with a repeated factor of preactivation; however, because the number of participants for each limb was not the same, the factor of limb could not be repeated. Therefore, a mixed-model 2 × 3 ANOVA was used to determine the main effects of limb (paretic, non-paretic) and preactivation level (repeated measure; 0, 5, 15%) as well as the limb-by-preactivation level interaction on TVR-evoked slope magnitude. Between-limb *post-hoc* t-tests were used to determine differences in slope between paretic and non-paretic limbs at each preactivation level, with Bonferroni correction for multiple comparisons. Within-limb *post-hoc* t-tests were used to evaluate differences between all combinations of preactivation levels, using Tukey correction for multiple comparisons within each limb. Finally, a 2-way non-repeated measures ANOVA was also calculated without accounting for the missing data to ensure that the above analyses were not biased by methods used for accounting for missing data. Results from this ANOVA were virtually identical to those from the 2-way repeated measures ANOVA that is presented in the Results section below, with the same significant ANOVA effects and *post-hoc* test results.

To evaluate the goodness-of-fit of the non-linear model of TVR-evoked torque, we computed the variance accounted for (VAF) and sum-of-squared error (SSE) of the model. The effect of preactivation on the model parameters associated with the TVR-evoked portion of the torque profile was examined qualitatively for each limb.

Results of all analyses were considered significant at the $p < 0.05$ level, and p-values for the t-tests are presented in the results after application of corrections for multiple comparisons. All statistical analyses were performed in Prism (GraphPad software, Inc., version 7.0a).

Animal Experiments

As a first step toward providing additional mechanistic context for our human-subjects findings, we conducted a set of proof-of-principle TVR experiments in a decerebrate cat model. The primary goal of this model was to determine the impact of

increasing preactivation level on the amplitude and rate of rise of TVR-evoked force. We chose the decerebrate cat preparation because it has a well-documented elevation of descending monoaminergic drive that does not scale with motor output (Crone et al., 1988) thus paralleling one potential mechanism underlying our chronic hemiparetic stroke findings. Further, we examined the motor unit firing patterns underlying the TVR-evoked forces to evaluate the effect of preactivation on motor unit rate modulation and recruitment during and after vibration.

Experimental Setting and Ethics Statement

Data were also collected in one adult cat sourced from a designated breeding establishment for scientific research. The animal was housed at Northwestern University's Center for Comparative Medicine, an AAALAC accredited animal research program. All procedures were approved by the Institutional Animal Care and Use Committee at Northwestern University and conform with accepted ethics standards (Grundy, 2015).

Surgical Procedure

Anesthesia was induced with 4% isoflurane and a 1:3 mixture of N_2O and O_2. Anesthetic depth was monitored via blood pressure, heart and respiratory rate, and withdrawal reflexes. Once surgically anesthetized, a tracheostomy was performed and a permanent tracheal tube was implanted. Isoflurane (0.5–2.5%) and gasses were delivered through the tube for the duration of the surgery. The animal was then transferred to a stereotaxic frame and immobilized by a head clamp, spinal clamp on the L2 dorsal vertebral process, and bilateral hip pins at the iliac crest. The left hindlimb was fixed with pins at the knee and clamps at the ankle, and the right hindlimb was secured using a clamp on the lower leg. The left soleus was dissected, isolated, and its distal tendon was attached to a load cell via a calcaneus bone chip in series with a linear variable differential transformer and customized voice coil. A distal, cutaneous branch of the right superficial peroneal nerve was dissected and a cuff electrode was secured around the nerve. The animal was then decerebrated at the precollicular level and anesthesia was discontinued (animals lack sentience after decerebration; Silverman et al., 2005). A thermistor was then placed in the esophagus and core temperature was maintained at 35–37°C. At the end of the experiment, the animal was euthanized using a 2 mM/kg solution of KCl in addition to a bilateral thoracotomy.

Data Collection

Referenced monopolar EMG activity was acquired using a custom 64-channel electrode array that covered the surface of the exposed soleus. The array consisted of 64 individual rigid silver pins, 7.5 mm in length and 0.7 mm in diameter, configured in a 5 × 13 matrix with an interelectrode distance of 2.54 mm. A ground electrode was place on the animal's back and a reference electrode was placed on the upper thigh. EMG data were bandpass filtered (100–900 Hz), amplified (0.5–2 k) and digitized (5,120 Hz) by a 12-bit A/D converter (EMG-USB 2, 256-channel EMG amplifier, OT Bioelettronica, Torino, Italy). Force data from the soleus muscle were simultaneously acquired.

With the animal's hindlimbs fixed, the soleus was activated by stimulating the contralateral superficial peroneal nerve through a cuff electrode (voltage-controlled stimulation; 50 Hz; 1 ms pulse width). This elicits the crossed-extension reflex and a maintained contraction. The magnitude of contraction is generally proportional to the applied voltage, and here, we used voltages ranging from 3.5 to 5 V. This evoked sub-maximal contractions up to ∼25% of maximum force output, as confirmed by the appearance of force saturation with voltages at or above 6 V in this animal. After at least 2 s of stimulation (to acquire a stable baseline preactivation), 3–5 s of vibration of the soleus tendon commenced (∼130 Hz; ∼80 μm). This elicited a TVR. Electrical stimulation of the contralateral peroneal nerve continued for the duration of vibration, and we varied the applied voltage between trials to explore the impact of vibration at a range of preactivation levels.

Data and Statistical Analysis

Force data from the soleus was analyzed similarly to the elbow flexion torque data from the human subjects experiments. Preactivation force was calculated as the average of force values generated during the 0.5 s prior to vibration onset. TVR-evoked force amplitude was calculated as the change in force from the preactivation value to the average torque between 1 and 2 s post-vibration onset. The rising slope of the TVR-evoked force was calculated as with Eqn. 1 for the human data. The time to 85% max TVR-evoked force was calculated relative to vibration onset. Separate Pearson correlation calculations were used to determine if increasing preactivation level was associated with changes in TVR-evoked force amplitude, rising slope of the TVR-evoked force, or the time to 85% max TVR-evoked force.

To examine motor unit recruitment and rate modulation patterns underlying the TVR-evoked force due to different levels of preactivation, multi-channel EMG data from each trial were decomposed into individual motor unit spike trains using a blind source separation approach (Holobar et al., 2010, 2014; Negro et al., 2016). The instantaneous firing rate for each motor unit spike train was calculated as the reciprocal of the inter-spike interval.

RESULTS

TVR-Evoked Torque Amplitude

Across participants, maximum voluntary elbow flexion torque for the paretic limb averaged 34.85 Nm, whereas the non-paretic elbow flexion MVT averaged 62.29 Nm. Elicitation of the TVR in the paretic and non-paretic limbs in all cases resulted in an increase in net elbow flexion torque above the target preactivation level (**Figure 1**). Qualitatively, this torque developed rapidly upon vibration onset in the paretic limb and either monotonically increased during vibration or reached a stable plateau following the initial rising phase. The non-paretic limb demonstrated a more gradual increase in torque following vibration onset, which was also characterized by a monotonic rise or an initial increase followed by a plateau.

Table 2 shows the TVR-evoked torque amplitude (unnormalized and normalized; left and middle panels,

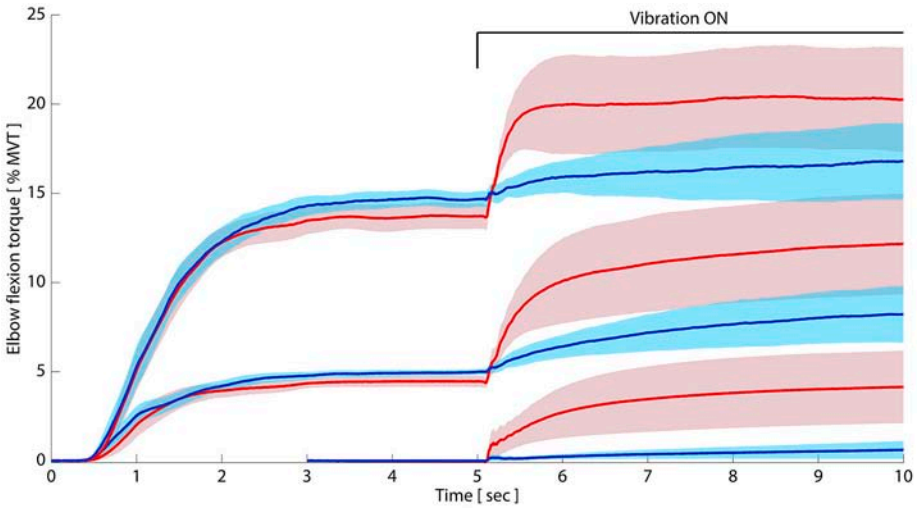


FIGURE 1 | Paretic limb tonic vibration reflexes remain exaggerated despite preactivation. Paretic and non-paretic elbow flexors were preactivated to 5 and 15% of MVT, respectively, before vibration began. Despite matching preactivation levels between limbs, group average ($N = 10$) paretic TVRs (pink) significantly exceeded non-paretic TVRs (blue). Bottom paretic and non-paretic traces are TVR responses in relaxed elbow flexors, with data adapted with permission from McPherson et al. (2018). Shaded region around each TVR curve represents ± 95% confidence interval. *Y-axis:* elbow flexion torque as percent of maximum; *x-axis*: time in seconds. Permission to adapt images from McPherson et al. (2008) is afforded by the American Physiological Society under original author rights.

TABLE 2 | TVR-evoked torque amplitude.

	TVR-evoked torque amplitude (Difference from preactivation to vibration-ON)						**Torque amplitude during vibration (incl. preactivation torque) (% MVT)**		
	Unnormalized Torque (Nm)			**Normalized Torque (%MVT)**					
Preactivation	**0%**	**5%**	**15%**	**0%**	**5%**	**15%**	**0%**	**5%**	**15%**
Paretic	1.20 ± 0.98	2.52 ± 1.32	2.25 ± 1.23%	3.75 ± 3.18%	7.79 ± 5.19%	7.41 ± 5.22%	4.48 ± 3.88%	12.02 ± 5.00%	21.00 ± 4.65%
Non-Paretic	0.35 ± 0.54	1.76 ± 1.27	0.88 ± 1.72	0.64 ± 0.94%	3.23 ± 2.55%	2.15 ± 3.52%	0.72 ± 1.03%	8.15 ± 2.59%	16.79 ± 3.65%

Data presented as mean ± standard deviation.

respectively) for both limbs at the three preactivation levels, as well as the normalized absolute torque values during vibration (i.e., those including preactivation torque; right panel). The data from the 0% MVT level is reproduced with permission from our previous work (McPherson et al., 2008). At the 5% MVT preactivation level in the paretic limb, vibration induced an increase in torque from 4.23% MVT during the preactivation period to 12.02% MVT during vibration (difference: 7.79% MVT, 2.52 Nm). In the non-paretic limb, preactivation to 5% MVT led to a TVR-evoked torque increase from 4.92 to 8.15% MVT (difference: 3.23% MVT, 1.76 Nm; **Table 2**). At the 15% MVT preactivation level, vibration induced an increase in torque from 13.39 to 21.00% MVT in the paretic limb (difference: 7.41% MVT, 2.25 Nm) and an increase in torque from 14.46 to 16.79% MVT in the non-paretic limb (difference: 2.15% MVT, 0.88 Nm).

The 2 × 3 repeated measures ANOVA revealed significant main effects of limb ($p = 0.004$) and preactivation level ($p = 0.0004$) on normalized TVR-evoked torque amplitude, and a non-significant limb-by-preactivation level interaction ($p = 0.16$). Examining the significant main effect of limb, paretic limb values were greater than non-paretic values, averaging 6.32% MVT across pre-activation levels vs. 2.00% MVT. The uniform increase in paretic vs. non-paretic TVR-evoked torque amplitude at all preactivation levels (i.e., significant main effect of limb and non-significant limb-by-preactivation interaction) was contrary to our prediction that the torque response would become similar across limbs with preactivation vs. the relaxed condition.

Results from within-limb *post-hoc t*-tests are summarized in **Table 3**, top panel. Paretic normalized TVR-evoked torque amplitude values from the 0% condition were significantly less than those from the 5 and 15% conditions ($p = 0.009$ and $p = 0.025$, respectively). Notably, however, there was no difference in TVR-evoked torque amplitude in the paretic limb between trials with torque preactivation of 5 and 15% MVT ($p = 0.84$). The same analysis in the non-paretic limb revealed a significant difference between the 0 and 5% conditions only ($p = 0.007$); comparisons of 0 vs. 15% ($p = 0.32$) and 5 vs. 15% ($p = 0.30$) were not statistically significant. Results from between-limb *post-hoc t*-tests are summarized in **Table 3**, bottom panel. As expected from the significant main effect of limb and non-significant

TABLE 3 | *Post-hoc* comparisons of TVR-evoked torque.

	TVR-evoked torque amplitude		Slope of torque rise	
Within-limb	**Paretic**	**Non-paretic**	**Paretic**	**Non-paretic**
0% vs. 5% MVT	**	**	*ns*	*ns*
0% vs. 15% MVT	*	*ns*	****	*ns*
5% vs. 15% MVT	*ns*	*ns*	****	*ns*
Between-limb	**Paretic vs. Non-Paretic**		**Paretic vs. Non-Paretic**	
0% MVT	**		*ns*	
5% MVT	****		*ns*	
15% MVT	****		****	

*Asterisks indicate significant differences at *$p < 0.05$, **$p < 0.01$, or ****$p < 0.0001$. ns indicates $p > 0.05$. Post-hoc comparisons computed from normalized torque.*

limb-by-preactivation interaction, paretic TVR-evoked torque amplitude values were higher than non-paretic values at all preactivation levels.

Slope of TVR-Evoked Torque

Qualitatively, the rate of rise of TVR-evoked torque in the paretic limb appears to increase with increasing preactivation. Further, the rate of rise in the paretic limb appears to be more rapid than that of the non-paretic limb at matched levels of preactivation (**Figure 1**). We evaluated these observations quantitatively by computing the slope of the rising TVR-evoked torque according to Equation (1), including a new analysis of TVR responses previously collected with 0% preactivation (adapted from McPherson et al., 2008; **Figure 2**). The 2 × 3 mixed-model ANOVA revealed significant main effects of limb ($p = 0.002$) and preactivation level ($p < 0.0001$) as well as a significant limb-by-preactivation level interaction ($p = 0.0002$). A 2-way non-repeated measures ANOVA, without imputation, likewise revealed significant main effects of limb ($p = 0.0003$) and preactivation level ($p = 0.0002$) and a significant limb-by-preactivation level interaction ($p = 0.0008$). The nature of the significant interaction can be appreciated from visual inspection of **Figure 2**. Slope values for the paretic limb increased with preactivation level, but slope values for the non-paretic limb remained constant. Paretic group mean slope of TVR-evoked torque averaged 1.0, 3.5, and 12.5% MVT/s (for 0, 5, and 15% MVT preactivation levels, respectively), and 0.2, 1.6, and 1.4% MVT/s in the non-paretic limb. As such, the significant main effect of preactivation level was driven by the paretic limb values.

Post-hoc t-tests comparing between-limb differences in the slope of TVR-evoked torque at each pre-activation level revealed a significant difference at the 15% condition ($p < 0.0001$) and not the 0 or 5% conditions ($p = 0.99$ and $p = 0.95$, respectively) (**Table 3**, bottom panel).

Post-hoc t-tests comparing within-limb differences in the slope of TVR-evoked torque between each combination of the three preactivation levels (**Table 3**, top panel) revealed that in the paretic limb, values for the 0 and 5% conditions were significantly less than those of the 15% condition ($p < 0.0001$ for both comparisons), but there was no significant difference between values for the 0 and 5% conditions ($p = 0.31$). The same analysis in the non-paretic limb revealed no significant differences in the slope of TVR-evoked torque among any preactivation level comparisons (*p*-values ranging from 0.72 to 0.98).

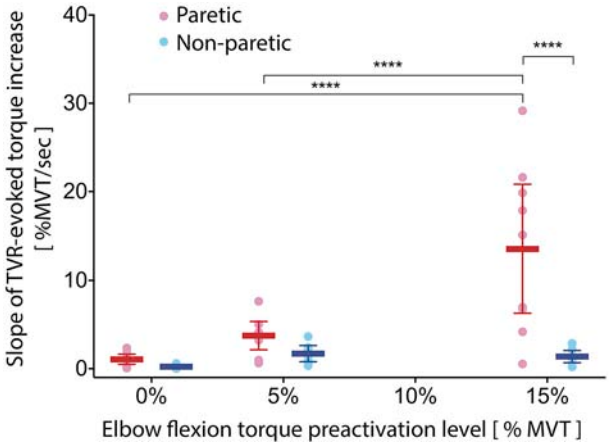


FIGURE 2 | Slope of TVR-evoked torque increases with preactivation only in paretic limb. As preactivation level increases, the slope of TVR-evoked torque increases in the paretic (pink/red) but not the non-paretic (light blue/royal blue) elbow flexors. Differences between limbs emerge at the 15% preactivation level. Individual circles represent single participant values; horizontal lines indicate group means, with error bars corresponding to 95% confidence intervals. *Y-axis*: slope of TVR-evoked torque (%MVT per second); *x-axis*: elbow flexion torque preactivation level expressed as percent of MVT. ****$p < 0.0001$.

Modeled TVR-Evoked Torque Profile

Because the temporal profile of TVR-evoked torque is non-linear, particularly during the first ∼1 s of vibration, we also modeled TVR-evoked torque as an exponential function according to Equation (2). All data were well-fit by this model, as can be appreciated visually in **Figure 3A** (black lines superimposed on data records). In **Table 4,** we present the optimal parameters for each group mean torque response at each preactivation level, as well as the SSE and VAF for each fit.

In **Figure 3B**, we plot parameters *a* and *b* from the model (left and right panels, respectively) for the paretic (pink) and non-paretic (blue) limbs as a function of preactivation level. These two parameters describe the shape of the during-vibration profile. Parameter *a*, most closely associated with the amplitude of TVR-evoked torque, tends to increase as a function of preactivation level for the paretic limb but not the non-paretic limb. Parameter *b,* reflective of the rate-of-rise of the TVR-evoked torque, is lower overall in the paretic limb—indicating more rapid torque development during vibration—and qualitatively appears to decrease as preactivation level increases.

Because parameters of modeled TVR-evoked torque data from the non-paretic limb had relatively less change across preactivation levels than those of the paretic limb, we also computed the VAF when applying the model fit *from* the 5% preactivation data *to* the 15% preactivation data (separately for

the non-paretic and paretic limbs). This manipulation gives an estimate of similarity between TVR-evoked responses at increasing preactivation levels, particularly during the rising phase of the contraction. We found that the optimal parameters for describing the 5% preactivation response in the non-paretic limb also accounted for 98.25% of the variability in the 15% preactivation trials in the same limb (**Figure 4**; purple trace overlaid on raw data). Conversely, for the paretic limb only 75.41% of the variability in the 15% preactivation data could be explained by the optimal fit to the 5% preactivation torque responses (down from 96.33%; **Figure 4**; purple trace overlaid on raw data). This finding, too, is consistent both with the relative invariance of linear slope in the non-paretic limb to preactivation level and the strong dependency of paretic limb linear slope on preactivation.

TVR Responses in Decerebrate Cat Preparation

To examine mechanisms of why the TVR did not vary with preactivation level, we undertook studies of the TVR in a decerebrate cat preparation. We reasoned that if the same pre-activation invariance occurred in this preparation, it would reflect the basic input-output behavior of the motor pool in response to stable, sustained Ia input (in the presence of increased spinal monoamines) instead of some type of compensation by descending inputs.

We found that the pattern of TVR-evoked force in the decerebrate cat was strikingly similar to that of the paretic elbow flexors in individuals with chronic hemiparetic stroke (**Figure 5**). Specifically, we found that increasing preactivation force was *not* associated with a larger TVR-evoked force amplitude, with virtually no correlation between the two variables ($r = -0.10$; $p = 0.8$). In comparison, there was a higher correlation between preactivation force and the rising slope of the TVR-evoked force ($r = 0.48$) and time to 85% max TVR-evoked force ($r = -0.62$); however, neither of these correlations reached significance at the $p < 0.05$ level with the amount of data available ($p = 0.19$ and $p = 0.08$).

To further investigate how the TVR-evoked torque arose, we utilized motor unit spike trains to characterize motor unit recruitment and rate modulation. Motor unit spike trains for two TVR trials with different preactivation levels are represented in **Figure 6** by their instantaneous firing rates. Thirty-six motor units were decomposed from the trial with lower preactivation (left panel) and 39 motor units were decomposed from the trial with higher preactivation (right panel). Qualitatively, motor units followed expected trends of recruitment order and rate modulation during preactivation and vibration: increasing preactivation increased the number of motor units recruited before vibration, and vibration led both to recruitment of additional motor units and an increased firing rate in motor units previously recruited with preactivation (**Figure 6**). However, it can be seen that for both levels of preactivation, recruitment of additional motor units is the dominant contributor to the development of TVR-evoked force, with an increased firing rate of previously recruited motor units contributing to a lesser extent.

The decerebrate cat preparation also allowed us to examine potential post-vibration force production (given the lack of descending voluntary drive as a confounding factor), and, by extension, the ability of a purely spinal mechanism to account for any such effects. When vibration was discontinued, force

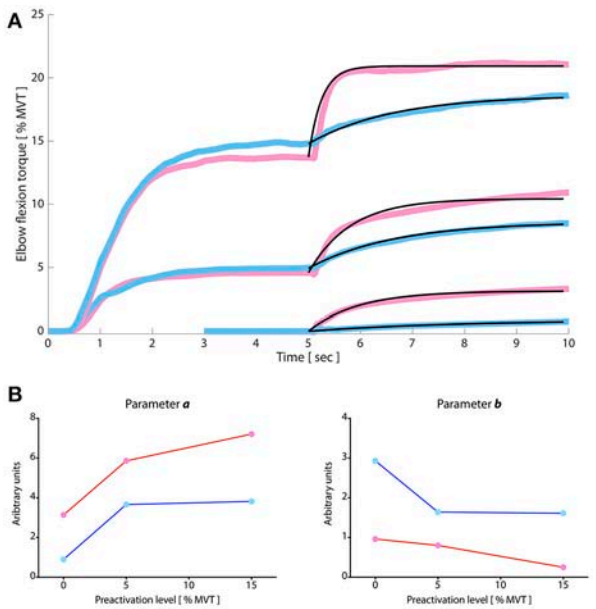


FIGURE 3 | TVR torque responses modeled by a composition of exponential functions. **(A)** Paretic and non-paretic TVR responses were well fit by exponential functions (black lines from 5 to 10 s), with Variances Accounted For of approximately >94% in all cases. Vibration commences at 5 s and continues for the duration of the plot. *Y-axis:* elbow flexion torque, expressed as a percentage of max; *x-axis:* time in seconds. Pink (paretic) and blue (non-paretic) traces are group averaged data ($N = 10$). **(B)**. Optimal parameters of exponential fit expressed as function of preactivation level. Pink/red: paretic limb; blue: non-paretic limb. Qualitatively, parameter *a* is greater in the paretic than the non-paretic limb; it trends toward an increased magnitude with increasing preactivation in the paretic limb but plateaus in the non-paretic limb. Parameter *b* is lower in the paretic limb than the non-paretic limb and decreases as a function of increasing preactivation. Permission to adapt images from McPherson et al. (2008) is afforded by the American Physiological Society under original author rights.

TABLE 4 | Modeled TVR-evoked torque.

	Preactivation level (% MVT)	*a*	*b*	SSE	VAF
Paretic	0%	3.14	0.96	97.3	97.14%
	5%	5.86	0.8	549.37	94.21%
	15%	7.21	0.25	247.17	96.33%
Non-paretic	0%	0.9	2.93	2.98	98.90%
	5%	3.66	1.64	31.84	99.44%
	15%	3.82	1.61	111.9	98.13%

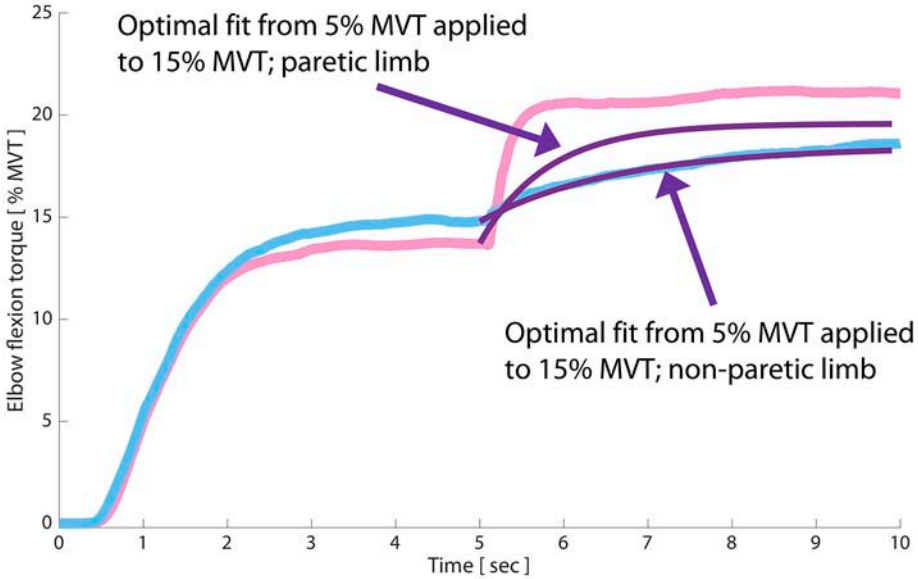


FIGURE 4 | Initial TVR-evoked torque development is invariant to preactivation magnitude in the non-paretic but not the paretic limb. Blue trace: non-paretic limb at 15% MVT preactivation; pink trace: paretic limb; black traces: optimal fits of an exponential composition to paretic and non-paretic data, respectively; purple traces: overlay of optimal fit of each limb's TVR-evoked torque at 5% MVT preactivation onto the 15% MVT preactivation records. In the non-paretic limb, the optimal fit at 5% MVT is able to explain ∼98% of the variance in the torque response at 15% MVT preactivation. Conversely, the 5% MVT fit is only able to explain ∼75% of the variance in torque response at 15% MVT in the paretic limb.

persisted at an elevated level until peroneal nerve stimulation was discontinued (**Figures 5**, **6**; force produced after $t = \sim$3.5–4.5 s). This persistent elevated force was accompanied by sustained firing of the vibration-recruited motor units despite removal of the vibration stimulus. Interestingly, we also observed differences between the two trials in the proportion of vibration-recruited motor units that demonstrated sustained firing. For the trial with lower preactivation, 32 of the 33 vibration-recruited motor units demonstrated sustained firing. For the trial with higher preactivation, however, only 12 of the 24 vibration-recruited motor units demonstrated sustained firing through the end of the trial.

DISCUSSION

We demonstrated that TVR-evoked torque amplitude in the paretic arm of individuals with chronic hemiparetic stroke significantly exceeds that of the non-paretic arm when muscles are preactivated to the same degree. Interestingly, within both the paretic and the non-paretic arm, TVR-evoked torque amplitude did not increase further when preactivation increased from 5 to 15% MVT. The rising *slope* of TVR-evoked torque did, however, increase with increasing preactivation in the paretic arm, whereas non-paretic values were not influenced by preactivation. Likewise, parameters extracted from the nonlinear model of TVR-evoked torque changed as a function of preactivation level only in the paretic arm. These findings contrast with the results of many classical stretch reflex paradigms, which suggest that reflex amplitude should equilibrate between paretic and non-paretic muscles when preactivation is matched (Lee et al., 1987; Burne et al., 2005; McPherson et al., 2017). Below, we discuss potential neural mechanisms that could underlie our findings.

Increased TVR-Evoked Torque Amplitude in the Paretic vs. Non-paretic Limb

One potential explanation for the increased amplitude of TVR-evoked torque in the paretic compared to the non-paretic arm (**Figure 1**) could be an increased monoaminergic drive to spinal motoneurons from the brainstem ponto-medullary reticular formation (PMRF). The PMRF has both a descending motor and a descending neuromodulatory component (Holstege and Kuypers, 1987), and recent evidence suggests that the motor component is progressively recruited post-stroke as volitional force production increases in the paretic arm (McPherson et al., 2018). The neuromodulatory component uses the monoamines serotonin and norepinephrine to regulate spinal excitability (Holstege and Kuypers, 1987; Hochman et al., 2001; Heckman et al., 2003), and is co-activated with the motor component (Veasey et al., 1995; Jacobs et al., 2002; Chan et al., 2006; Schwarz et al., 2008). Monoamines are uniquely excitatory to motoneurons, for example amplifying post-synaptic potentials 3–5-fold via PICs (Schwindt and Crill, 1977; Perrier and Hounsgaard, 2003; Heckman et al., 2009) while depolarizing the resting membrane potential and hyperpolarizing the spike threshold (Fedirchuk and Dai, 2004; Harvey et al., 2006). Thus, an increased descending monoaminergic drive could result in elevated TVR responses in paretic muscles through greater PIC-mediated amplification of motoneurons and/or by additional motor unit recruitment during vibration. It should be noted,

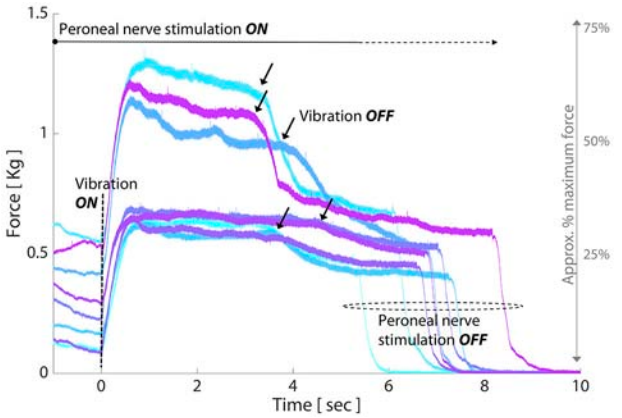


FIGURE 5 | TVR responses in decerebrate cat follow similar trends to paretic elbow flexors post-stroke as preactivation increases. Each colored line represents the force evoked in response to a single TVR trial at a given level of preactivation. Crossed extension reflex is initiated prior to vibration onset ($t = 0$ s) to achieve a stable preactivation force and is maintained throughout the duration of vibration. *Y-axis*: evoked force (Kg); *x-axis*: time (sec); black arrows: vibration offset. TVR-evoked force amplitude exhibits negligible change with increased preactivation, and involuntary force production is maintained after cessation of vibration (black arrows) and until peroneal nerve stimulation is stopped.

however, that previous investigations have yet to find changes in PIC amplitude in paretic muscles relative to non-paretic muscles post-stroke (Mottram et al., 2009, 2010), although methodological differences prevent a direct comparison to the findings presented here. Also, it should be noted for clarification that a *decrease* in monoaminergic drive may contribute to hyperreflexia after spinal cord injury (as opposed to the hypothetical increase described here post-stroke), because a lack of monoamines below the lesion appears to drive adaptive processes that result in constitutive activity of monoaminergic receptors on motoneurons (Murray et al., 2010).

Alternatively, it is possible that a tonic excitatory ionotropic drive to paretic motor pools could have contributed to the increased TVR amplitude we observed in the paretic arm. Such a drive could arise from ionotropic reticulospinal or vestibulospinal pathways following stroke-induced damage to primary motor resources (Mottram et al., 2009, 2010; Miller and Dewald, 2012; Miller D. M. et al., 2014; McMorland et al., 2015; McPherson et al., 2017), and would provide a maintained depolarizing input to motor pools innervating the paretic muscles. This would bring motoneurons closer to firing threshold, enabling vibration to more readily recruit them. It could also depolarize a small portion of the motor pool above firing threshold, leading to spontaneous motoneuron firing (Mottram et al., 2010)—a common finding post-stroke.

Our findings contrast with some aspects of the ionotropic drive hypothesis, particularly as they relate to other studies that cite this mechanism as possible explanation for exaggerated stretch-sensitive reflexes post-stroke. For example, when stretch reflexes are evoked by imposed joint excursions in the paretic and non-paretic arms at matched levels of preactivation, the difference in reflex response between arms is often extinguished (Lee et al., 1987; Burne et al., 2005; McPherson et al., 2017). Results from these studies suggest that the postulated tonic ionotropic drive is low enough that even small amounts of preactivation normalize the difference in resting excitability attributed to the tonic drive. Although a key assumption of the tonic ionotropic drive hypothesis is that preactivation is an effective means of balancing the excitability offset between limbs, it remains unknown if this is indeed the case. Nevertheless, if preactivation *does* abolish the resting excitability imbalance between limbs, then our results cannot be explained solely by a tonic ionotropic drive to motor pools innervating the paretic muscles. If that were the case, then TVR responses in paretic and non-paretic limbs would equilibrate with preactivation.

Changes in spinal circuits post-stroke could have also contributed to the increased TVR amplitude we observed in the paretic arm, although our experimental paradigm and analyses were not able to directly measure or clearly infer the potential contribution of such changes to our results. Nevertheless, there is evidence that the net effect of Group Ib afferent feedback transitions to from a combination of inhibition and excitation (Houk et al., 1970; Conway et al., 1987; Pearson and Collins, 1993; Prochazka et al., 1997) to preferential excitation in motor pools innervating the paretic muscles post-stroke (Delwaide and Oliver, 1988). While tendon vibration provides a strong volley of a Group Ia afferent feedback from muscle spindles, it also provides afferent information from Golgi tendon organs via Group Ib fibers. Given that Golgi tendon organs/Group Ib fibers are progressively activated by vibration as background muscle tension increases (Fallon and Macefield, 2007), a lateralized shift in Ib feedback toward excitation could explain a portion of our elevated paretic limb TVR responses. Further, if descending monoaminergic drive is indeed increased, interneuron responses to Group Ia and Ib feedback could be potentiated (Jankowska et al., 2000). And, while the effects of monoamines on Group II-evoked responses are both complex and incompletely characterized (Jankowska et al., 2000; Grey et al., 2001; Kurtzer et al., 2018), changes in this feedback mechanism would likely alter TVR responses as well. Likewise, a reduction of presynaptic inhibition, which is associated with spasticity following multiple sclerosis, spinal cord injury, and possibly stroke (Faist et al., 1994; Aymard et al., 2000; Morita et al., 2001; Nielsen et al., 2005; Lamy et al., 2009), could differentially alter reflex gain between arms and contribute to elevated TVR responses in the paretic arm.

Invariance of TVR-Evoked Torque Amplitude to Increasing Preactivation

It is unclear why the magnitude of TVR-evoked torque did not increase in either limb when preactivation increased from 5 to 15% MVT. Indeed, it is well accepted that the amplitude of stretch reflexes elicited by imposed joint excursions increases with increasing preactivation in paretic, non-paretic, and control limbs. Further, Henneman's size principle (Binder et al., 1983; Bawa et al., 1984; Henneman, 1985) suggests that, at low force levels, recruitment of progressively larger force motor units

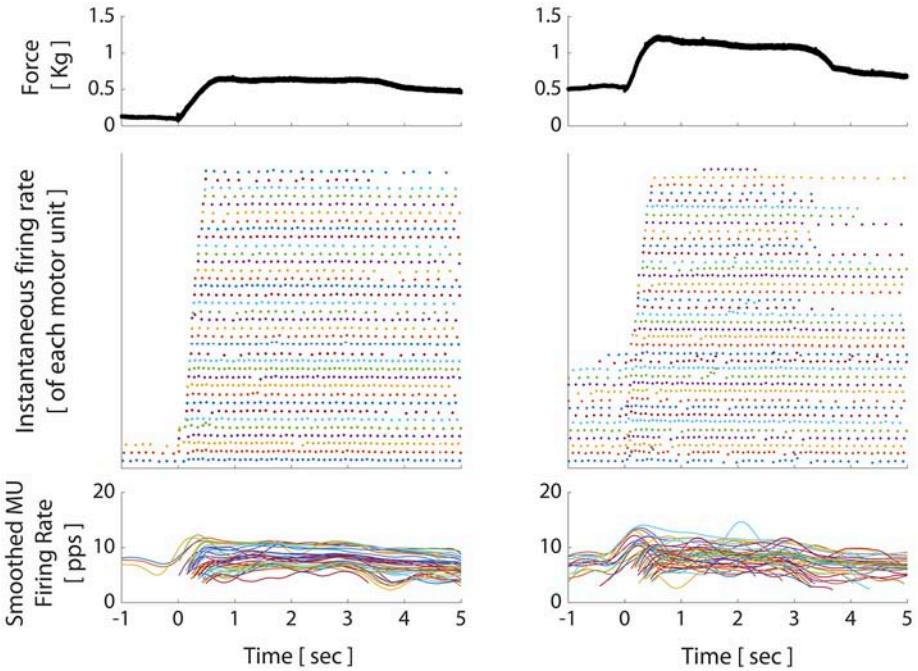


FIGURE 6 | Motor unit firing patterns in decerebrate cat during crossed extension reflex and TVR trials. Top panel: muscle force; middle panel: instantaneous firing rate individual motor units recruited during the corresponding force trace (each color/row represents a separate motor unit); bottom panel: smoothed motor unit firing rates during the corresponding force trace. X-axis for all panels: elapsed time, relative to onset of vibration. Increasing preactivation force (mediated by the crossed extension reflex) led to increasing motor unit recruitment, as seen in left and right middle panels from $t = -1{:}0$ s. Vibration onset was marked primarily by further increases in motor unit recruitment and less so by increases in firing rate of previously recruited units. After vibration stops (at $t = 3.5$ s), persistent motor unit firing is evident, particularly in low-threshold units; a hallmark of motoneuron PICs.

will impart an upwards curvature to the input-output function, regardless of the motoneuron input mixture (Heckman, 1994). This should cause TVR-evoked torque amplitude to increase with pre-activation level in both arms.

Two potential mechanisms could contribute to this unexpected finding. In the first, synaptic inhibition could simultaneously increase and decrease in direct proportion to preactivation level, a phenomenon known as "proportional," or "balanced," inhibition (Powers et al., 2012; Powers and Heckman, 2017). Because monoaminergic actions on motoneurons are exquisitely sensitive to synaptic inhibition (Johnson and Heckman, 2014), even small amounts of additional inhibition during contraction could prevent the predicted increase in TVR response amplitude. In the second scenario, monoaminergic drive to the paretic limb could be elevated yet relatively static post-stroke, contributing approximately the same net amount of excitation across the preactivation levels tested here. Because the non-paretic limb is presumably less reliant on monoaminergic drive for motoneuron activation than the paretic limb (due to an intact corticospinal tract), it is more likely to maintain an appropriate level of baseline inhibition, retain the capacity for presynaptic and reciprocal inhibition, and use a homeostatic "push-pull" method to regulate the excitation/inhibition balance during contraction (Powers et al., 2012; Powers and Heckman, 2017). These characteristics would enable more precise control of synaptic integration, potentially leading to similar levels of motoneuron recruitment during vibration for the relatively low submaximal contractions investigated here.

Corroboration With Animal Model

To further explore our finding that paretic limb TVR-evoked torque amplitude was not different between 5 and 15% preactivation levels post-stroke, we investigated the impact of increasing preactivation level on the amplitude and rate of rise of TVR-evoked force in a decerebrate cat model. This model has a strong descending monoaminergic drive, the magnitude of which is not modified by vibration or crossed-extension reflex inputs (Lee and Heckman, 1996; Hyngstrom et al., 2008). Thus, force output in this model is due only to three factors: the sustained monoaminergic drive, Ia input (via vibration), and the resulting input-output function of the motoneurons. Like our human-subjects findings, the magnitude of TVR-evoked force in the cat did not scale with preactivation level. Also similar to our human-subjects findings, there was a stronger correlation between preactivation level and rate of rising force; however, the correlation was not statistically significant in cat data. Also, because vibration is very selective for Ia inputs in the decerebrate cat model (Hyngstrom et al., 2008), the similarity of our cat and human-subjects results suggests that monosynaptic Ia feedback was the predominant driver of motoneuron activation in the human-subjects torque as well, with less influence from Ib or other sensory inputs.

Importantly, the decerebrate cat model also enabled us to investigate force production *after* vibration was discontinued, which was not possible in our human-subjects experiments. We found maintained, elevated force post-vibration rather than a return to preactivation level or the relaxed state. This behavior is characteristic of PICs in motoneurons (Heckman et al., 2008) and is consistent with post-vibration TVR responses seen in humans when no preactivation is present, as was detailed in our previous study (McPherson et al., 2008). The finding that sustained firing of vibration-recruited motor units accompanied the post-vibration force maintenance is highly consistent with activation of PICs, which characteristically enable a motoneuron to continue firing after removal of the excitatory stimulus that recruited it. Further, our observation that a greater percentage of motor units exhibited sustained firing in the trial with lower preactivation (32 of 33) compared to the trial with higher preactivation (12 of 24) is consistent with the greater impact that PICs have on sustained firing in low vs. higher threshold motor units (Heckman et al., 2008).

Together, these findings corroborate and extend key aspects of our overall unexpected human-subjects findings, and reinforce the notion that monoaminergic mechanisms are a potential component of the observed paretic arm TVR responses. However, it should be noted that in the decerebrate cat there is no natural analog to the non-paretic arm in humans, and it is unknown how the afferent drive provided by peripheral nerve stimulation in the cat compares to volitional preactivation in humans with regard to its inhibitory and excitatory content.

Slope of TVR-Evoked Torque and Modeled Torque Gain

We found that the slope of TVR-evoked torque amplitude and the gain of the modeled torque both increased with increasing preactivation in the paretic limb. These findings are consistent with an increased influence of monoamines in paretic motor pools, which could result in a combination of larger PICs in recruited motoneurons, more motoneurons recruited, and/or a reduced time to PIC activation as preactivation increases.

PIC activation time is proportional to the difference in membrane potential and PIC threshold potential (Heckman and Lee, 2001). Thus, as membrane potential depolarizes toward PIC threshold, the time required to activate the PIC by a given stimulus is reduced. Here, this phenomenon could occur when transitioning from the relaxed case to 5 and 15% MVT preactivation: as preactivation increases, an increasing amount of motoneurons are brought near to or above their PIC threshold. Assuming that monoaminergic drive would be elevated to paretic motoneurons compared to non-paretic motoneurons, PICs will be more rapidly activated in paretic motoneurons when vibration begins. The net effect of an increased PIC activation rate will be a faster rate of force production, and thus a higher TVR slope and gain. By comparison, the lower slope and modeled torque gain in the non-paretic limb could reflect a lack of robust neuromodulatory effects.

Comparison With Stretch Reflex Studies

Finally, an intriguing question raised by these results is why TVR responses continue to be elevated in the paretic limb compared to the non-paretic limb at matched levels of preactivation, yet stretch reflex responses equilibrate under analogous conditions. It is conceivable that this distinction is related to the potency of vibration as an input to motor pools compared to imposed joint excursions. Indeed, it has been suggested that vibration elicits more robust activation of Ia afferents than group Ib or II fibers, which may be activated more strongly by joint excursion (Matthews, 1984). More specifically, if vibration elicits a larger response in spinal motor pools than joint excursion, then lingering imbalances in motor pool excitability that were not well controlled by preactivation could "re-appear" through enhanced motor unit recruitment during vibration. Or, put another way, if joint excursion is a relatively modest stimulus, it may not recruit substantially more motor units over those already recruited via preactivation. This could mask persistent excitability imbalances.

This explanation seems unlikely, however, both because spindle-mediated feedback appears to be unchanged post-stroke (Hagbarth et al., 1973) and because our TVR paradigm actually appears to evoke a relatively small motor output compared to the joint excursions typically used to gauge motor excitability. Indeed, we found that when preactivated to 5% MVT, vibration only increased net elbow flexion torque output to ∼13% MVT in the paretic limb. By comparison, a rapid joint excursion (270°/s) at 5% MVT preactivation can routinely drive reflex responses that exceed 20–25% MVT (McPherson et al., 2017), even though the stretch duration is only ∼300 ms (compared to 5 s for vibration). Further, if our paretic limb TVR responses are compared to previously reported stretch reflex data post-stroke (McPherson et al., 2017), we find that they most closely match an approximately quasi-static imposed joint excursion (6°/s) in terms of rise time and amplitude. Thus, it remains an open question as to why the two stimuli modalities yield such differing responses.

Limitations

Our study has important limitations. First, we reiterate that because our human-subjects experiments used indirect probes of spinal neural excitability, our interpretation of the underlying mechanisms remains inferential. Additionally, we did not conduct TVR analyses in individuals without neurological injury. Although this choice was motivated by an attempt to limit variability, the ipsilesional arm is not truly unaffected post-stroke, and thus, future studies are warranted. We also did not acquire elbow flexion/extension torque after cessation of vibration in the human-subjects portion of the study. While this choice was made to avoid the confound of volitional activity in any persistent muscle activation post-TVR, it prevents our study from assessing the impact of preactivation on persistent motoneuron firing—an important component of PICs. And finally, regarding the decerebrate cat experiments: because the primary purpose of this

preliminary cat model was to provide context for the mechanical response to vibration in a situation with known elevation of monoaminergic drive, we did not design the protocol with the specific goal of acquiring EMG data amenable to studying PICs. As a result, we are not able to make inferences about PICs from these data.

CONCLUSIONS

Our results suggest that a combination of both ionotropic and neuromodulatory mechanisms likely underlie the exaggerated TVR responses we observed in the paretic elbow flexors post-stroke, although the relative impact of each remains unclear. The finding that TVR-evoked torque amplitude did not change with preactivation level could imply a more pronounced role for synaptic inhibition in motor pools innervating the paretic muscles than previously thought. For example, an increase in inhibitory drive as volitional motor output increases (Powers and Heckman, 2017; Revill and Fuglevand, 2017) would reduce PIC-mediated effects on motoneuron firing dynamics, potentially stabilizing TVR-evoked torque output. Advanced yet available technologies such as high-density surface EMG grids and motor unit decomposition algorithms, which can be incorporated into both human experiments and animal preparations (Miller L. C. et al., 2014; McPherson et al., 2016; Johnson et al., 2017), will be essential for more fully characterizing these effects.

AUTHOR CONTRIBUTIONS

All authors contributed to the conception and design of the work; JM, LM, CT, ME contributed to the acquisition of data; JM, LM, CT contributed to analysis of data; all authors contributed to the interpretation of data and drafting, revising and approving the manuscript for publication. All authors are in agreement to be accountable for all aspects of the work.

FUNDING

This work was supported by NIH grants: R01NS054269, R01HD039343, and R01NS047567.

REFERENCES

Aymard, C., Katz, R., Lafitte, C., Lo, E., Penicaud, A., Pradat-Diehl, P., et al. (2000). Presynaptic inhibition and homosynaptic depression: a comparison between lower and upper limbs in normal human subjects and patients with hemiplegia. *Brain* 123 (Pt 8), 1688–1702. doi: 10.1093/brain/123.8.1688

Bawa, P., Binder, M. D., Ruenzel, P., and Henneman, E. (1984). Recruitment order of motoneurons in stretch reflexes is highly correlated with their axonal conduction velocity. *J. Neurophysiol.* 52, 410–420. doi: 10.1152/jn.1984.52.3.410

Binder, M. C., Bawa, P., Ruenzel, P., and Henneman, E. (1983). Does orderly recruitment of motoneurons depend on the existence of different types of motor units? *Neurosci. Lett.* 36, 55–58.

Bradnam, L. V., Stinear, C. M., Barber, P. A., and Byblow, W. D. (2012). Contralesional hemisphere control of the proximal paretic upper limb following stroke. *Cereb. Cortex* 22, 2662–2671. doi: 10.1093/cercor/bhr344

Burne, J. A., Carleton, V. L., and O'dwyer, N. J. (2005). The spasticity paradox: movement disorder or disorder of resting limbs? *J. Neurol. Neurosurg. Psychiatr.* 76, 47–54. doi: 10.1136/jnnp.2003.034785

Chan, E., Steenland, H. W., Liu, H., and Horner, R. L. (2006). Endogenous excitatory drive modulating respiratory muscle activity across sleep-wake states. *Am. J. Respir. Crit. Care Med.* 174, 1264–1273. doi: 10.1164/rccm.200605-597OC

Conway, B. A., Hultborn, H., and Kiehn, O. (1987). Proprioceptive input resets central locomotor rhythm in the spinal cat. *Exp. Brain Res.* 68, 643–656. doi: 10.1007/BF00249807

Crone, C., Hultborn, H., Kiehn, O., Mazieres, L., and Wigstrom, H. (1988). Maintained changes in motoneuronal excitability by short-lasting synaptic inputs in the decerebrate cat. *J. Physiol.* 405, 321–343. doi: 10.1113/jphysiol.1988.sp017335

Delwaide, P. J., and Oliver, E. (1988). Short-latency autogenic inhibition (IB inhibition) in human spasticity. *J. Neurol. Neurosurg. Psychiatr.* 51, 1546–1550. doi: 10.1136/jnnp.51.12.1546

Eklund, G., and Hagbarth, K. E. (1966). Normal variability of tonic vibration reflexes in man. *Exp. Neurol.* 16, 80–92. doi: 10.1016/0014-4886(66)90088-4

Faist, M., Mazevet, D., Dietz, V., and Pierrot-Deseilligny, E. (1994). A quantitative assessment of presynaptic inhibition of Ia afferents in spastics. Differences in hemiplegics and paraplegics. *Brain* 117 (Pt 6), 1449–1455.

Fallon, J. B., and Macefield, V. G. (2007). Vibration sensitivity of human muscle spindles and Golgi tendon organs. *Muscle* Nerve 36, 21–29. doi: 10.1002/mus.20796

Fedirchuk, B., and Dai, Y. (2004). Monoamines increase the excitability of spinal neurones in the neonatal rat by hyperpolarizing the threshold for action potential production. *J. Physiol.* 557, 355–361. doi: 10.1113/jphysiol.2004.064022

Gillies, J. D., Burke, D. J., and Lance, J. W. (1971). Supraspinal control of tonic vibration reflex. *J. Neurophysiol.* 34, 302–309. doi: 10.1152/jn.1971.34.2.302

Grey, M. J., Ladouceur, M., Andersen, J. B., Nielsen, J. B., and Sinkjaer, T. (2001). Group II muscle afferents probably contribute to the medium latency soleus stretch reflex during walking in humans. *J. Physiol.* 534, 925–933. doi: 10.1111/j.1469-7793.2001.00925.x

Grundy, D. (2015). Principles and standards for reporting animal experiments in The Journal of Physiology and Experimental Physiology. *J. Physiol.* 593, 2547–2549. doi: 10.1113/JP270818

Hagbarth, K. E., and Eklund, G. (1966). Tonic vibration reflexes (TVR) in spasticity. *Brain Res.* 2, 201–203. doi: 10.1016/0006-8993(66)90029-1

Hagbarth, K. E., Wallin, G., and Lofstedt, L. (1973). Muscle spindle responses to stretch in normal and spastic subjects. *Scand. J. Rehabil. Med.* 5, 156–159.

Harvey, P. J., Li, X., Li, Y., and Bennett, D. J. (2006). 5-HT2 receptor activation facilitates a persistent sodium current and repetitive firing in spinal motoneurons of rats with and without chronic spinal cord injury. *J. Neurophysiol.* 96, 1158–1170. doi: 10.1152/jn.01088.2005

Heckman, C. J. (1994). Computer simulations of the effects of different synaptic input systems on the steady-state input-output structure of the motoneuron pool. *J. Neurophysiol.* 71, 1727–1739. doi: 10.1152/jn.1994.71.5.1727

Heckman, C. J., Johnson, M., Mottram, C., and Schuster, J. (2008). Persistent inward currents in spinal motoneurons and their influence on human motoneuron firing patterns. *Neuroscientist* 14, 264–275. doi: 10.1177/1073858408314986

Heckman, C. J., and Lee, R. H. (2001). "Advances measuring active dendritic currents in spinal motoneurons *in vivo*," in *Motor Neurobiology of the Spinal Cord,* ed T. C. Cope (Boca Raton, FL: CRC Press), 89–106.

Heckman, C. J., Lee, R. H., and Brownstone, R. M. (2003). Hyperexcitable dendrites in motoneurons and their neuromodulatory control during motor behavior. *Trends Neurosci.* 26, 688–695. doi: 10.1016/j.tins.2003.10.002

Heckman, C. J., Mottram, C., Quinlan, K., Theiss, R., and Schuster, J. (2009). Motoneuron excitability: the importance of neuromodulatory inputs. *Clin. Neurophysiol.* 120, 2040–2054. doi: 10.1016/j.clinph.2009.08.009

Henneman, E. (1985). The size-principle: a deterministic output emerges from a set of probabilistic connections. *J. Exp. Biol.* 115, 105–112.

Hochman, S., Garraway, S., Machacek, D., and Shay, B. (2001). "5-HT receptors and the neuromodulatory control of spinal cord function," in *Motor*

Neurobiology of the Spinal Cord, ed T. C. Cope (Boca Raton, FL: CRC Press), 47–87.

Holobar, A., Minetto, M. A., Botter, A., Negro, F., and Farina, D. (2010). Experimental analysis of accuracy in the identification of motor unit spike trains from high-density surface EMG. *IEEE Trans. Neural Syst. Rehabil. Eng.* 18, 221–229. doi: 10.1109/TNSRE.2010.2041593

Holobar, A., Minetto, M. A., and Farina, D. (2014). Accurate identification of motor unit discharge patterns from high-density surface EMG and validation with a novel signal-based performance metric. *J. Neural Eng.* 11:016008. doi: 10.1088/1741-2560/11/1/016008

Holstege, J. C., and Kuypers, H. G. (1987). Brainstem projections to spinal motoneurons: an update. *Neuroscience* 23, 809–821. doi: 10.1016/0306-4522(87)90160-6

Houk, J. C., Singer, J. J., and Goldman, M. R. (1970). An evaluation of length and force feedback to soleus muscles of decerebrate cats. *J. Neurophysiol.* 33, 784–811. doi: 10.1152/jn.1970.33.6.784

Hu, X., Suresh, N. L., Chardon, M. K., and Rymer, W. Z. (2015). Contributions of motoneuron hyperexcitability to clinical spasticity in hemispheric stroke survivors. *Clin. Neurophysiol.* 126, 1599–1606. doi: 10.1016/j.clinph.2014.11.005

Hyngstrom, A. S., Johnson, M. D., and Heckman, C. J. (2008). Summation of excitatory and inhibitory synaptic inputs by motoneurons with highly active dendrites. *J. Neurophysiol.* 99, 1643–1652. doi: 10.1152/jn.01253.2007

Ibrahim, I. K., Berger, W., Trippel, M., and Dietz, V. (1993). Stretch-induced electromyographic activity and torque in spastic elbow muscles. Differential modulation of reflex activity in passive and active motor tasks. *Brain* 116 (Pt 4), 971–989. doi: 10.1093/brain/116.4.971

Jacobs, B. L., Martin-Cora, F. J., and Fornal, C. A. (2002). Activity of medullary serotonergic neurons in freely moving animals. *Brain Res. Brain Res. Rev.* 40, 45–52. doi: 10.1016/S0165-0173(02)00187-X

Jankowska, E., Hammar, I., Chojnicka, B., and Heden, C. H. (2000). Effects of monoamines on interneurons in four spinal reflex pathways from group I and/or group II muscle afferents. *Eur. J. Neurosci.* 12, 701–714. doi: 10.1046/j.1460-9568.2000.00955.x

Johnson, M. D., and Heckman, C. J. (2014). Gain control mechanisms in spinal motoneurons. *Front. Neural Circuits* 8:81. doi: 10.3389/fncir.2014.00081

Johnson, M. D., Thompson, C. K., Tysseling, V. M., Powers, R. K., and Heckman, C. J. (2017). The potential for understanding the synaptic organization of human motor commands via the firing patterns of motoneurons. *J. Neurophysiol.* 118, 520–531. doi: 10.1152/jn.00018.2017

Kurtzer, I., Bouyer, L. J., Bouffard, J., Jin, A., Christiansen, L., Nielsen, J. B., et al. (2018). Variable impact of tizanidine on the medium latency reflex of upper and lower limbs. *Exp. Brain Res.* 236, 665–677. doi: 10.1007/s00221-017-5162-6

Lamy, J. C., Wargon, I., Mazevet, D., Ghanim, Z., Pradat-Diehl, P., and Katz, R. (2009). Impaired efficacy of spinal presynaptic mechanisms in spastic stroke patients. *Brain* 132, 734–748. doi: 10.1093/brain/awn310

Lance, J. W. (1980). The control of muscle tone, reflexes, and movement: Robert Wartenberg Lecture. *Neurology* 30, 1303–1313. doi: 10.1212/WNL.30.12.1303

Lee, R. H., and Heckman, C. J. (1996). Influence of voltage-sensitive dendritic conductances on bistable firing and effective synaptic current in cat spinal motoneurons *in vivo*. *J. Neurophysiol.* 76, 2107–2110. doi: 10.1152/jn.1996.76.3.2107

Lee, W. A., Boughton, A., and Rymer, W. Z. (1987). Absence of stretch reflex gain enhancement in voluntarily activated spastic muscle. *Exp. Neurol.* 98, 317–335. doi: 10.1016/0014-4886(87)90245-7

Matthews, P. B. (1984). Observations on the time course of the electromyographic response reflexly elicited by muscle vibration in man. *J. Physiol.* 353, 447–461. doi: 10.1113/jphysiol.1984.sp015346

McMorland, A. J., Runnalls, K. D., and Byblow, W. D. (2015). A neuroanatomical framework for upper limb synergies after stroke. *Front. Hum. Neurosci.* 9:82. doi: 10.3389/fnhum.2015.00082

McPherson, J. G., Chen, A., Ellis, M. D., Yao, J., Heckman, C. J., and Dewald, J. P. A. (2018). Progressive recruitment of contralesional cortico-reticulospinal pathways drives motor impairment post stroke. *J. Physiol.* 596, 1211–1225. doi: 10.1113/JP274968

McPherson, J. G., Ellis, M. D., Heckman, C. J., and Dewald, J. P. (2008). Evidence for increased activation of persistent inward currents in individuals with chronic hemiparetic stroke. *J. Neurophysiol.* 100, 3236–3243. doi: 10.1152/jn.90563.2008

McPherson, J. G., Stienen, A. H. A., Drogos, J. M., and Dewald, J. P. A. (2017). Modification of spastic stretch reflexes at the elbow by flexion synergy expression in individuals with chronic hemiparetic stroke. *Arch. Phys. Med. Rehabil.* 99, 491–500. doi: 10.1016/j.apmr.2017.06.01

McPherson, J. G., Stienen, A. H., Drogos, J. M., and Dewald, J. P. (2011). The relationship between the flexion synergy and stretch reflexes in individuals with chronic hemiparetic stroke. *IEEE Int. Conf. Rehabil. Robot.* 2011:5975516. doi: 10.1109/ICORR.2011.5975516

McPherson, L. M., Negro, F., Thompson, C. K., Sanchez, L., Heckman, C. J., Dewald, J., et al. (2016). Properties of the motor unit action potential shape in proximal and distal muscles of the upper limb in healthy and post-stroke individuals. *Conf. Proc. IEEE Eng. Med. Biol. Soc.* 2016, 335–339. doi: 10.1109/EMBC.2016.7590708

Miller, D. M., Klein, C. S., Suresh, N. L., and Rymer, W. Z. (2014). Asymmetries in vestibular evoked myogenic potentials in chronic stroke survivors with spastic hypertonia: evidence for a vestibulospinal role. *Clin. Neurophysiol.* 125, 2070–2078. doi: 10.1016/j.clinph.2014.01.035

Miller, L. C., and Dewald, J. P. (2012). Involuntary paretic wrist/finger flexion forces and EMG increase with shoulder abduction load in individuals with chronic stroke. *Clin. Neurophysiol.* 123, 1216–1225. doi: 10.1016/j.clinph.2012.01.009

Miller, L. C., Thompson, C. K., Negro, F., Heckman, C. J., Farina, D., and Dewald, J. P. (2014). High-density surface EMG decomposition allows for recording of motor unit discharge from proximal and distal flexion synergy muscles simultaneously in individuals with stroke. *Conf. Proc. IEEE Eng. Med. Biol. Soc.* 2014, 5340–5344. doi: 10.1109/EMBC.2014.6944832

Morita, H., Crone, C., Christenhuis, D., Petersen, N. T., and Nielsen, J. B. (2001). Modulation of presynaptic inhibition and disynaptic reciprocal Ia inhibition during voluntary movement in spasticity. *Brain* 124, 826–837. doi: 10.1093/brain/124.4.826

Mottram, C. J., Suresh, N. L., Heckman, C. J., Gorassini, M. A., and Rymer, W. Z. (2009). Origins of abnormal excitability in biceps brachii motoneurons of spastic-paretic stroke survivors. *J. Neurophysiol.* 102, 2026–2038. doi: 10.1152/jn.00151.2009

Mottram, C. J., Wallace, C. L., Chikando, C. N., and Rymer, W. Z. (2010). Origins of spontaneous firing of motor units in the spastic-paretic biceps brachii muscle of stroke survivors. *J. Neurophysiol.* 104, 3168–3179. doi: 10.1152/jn.00463.2010

Murray, K. C., Nakae, A., Stephens, M. J., Rank, M., D'amico, J., Harvey, P. J., et al. (2010). Recovery of motoneuron and locomotor function after spinal cord injury depends on constitutive activity in 5-HT2C receptors. *Nat. Med.* 16, 694–700. doi: 10.1038/nm.2160

Negro, F., Muceli, S., Castronovo, A. M., Holobar, A., and Farina, D. (2016). Multi-channel intramuscular and surface EMG decomposition by convolutive blind source separation. *J. Neural Eng.* 13:026027. doi: 10.1088/1741-2560/13/2/026027

Nielsen, J. B., Petersen, N. T., Crone, C., and Sinkjaer, T. (2005). Stretch reflex regulation in healthy subjects and patients with spasticity. *Neuromodulation* 8, 49–57. doi: 10.1111/j.1094-7159.2005.05220.x

O'Sullivan, S. B., and Schmitz, T. J. (2001). *Physical Rehabilitation.* Philadelphia, PA: F.A. Davis Company.

Owen, M., Ingo, C., and Dewald, J. P. A. (2017). Upper extremity motor impairments and microstructural changes in bulbospinal pathways in chronic hemiparetic stroke. *Front. Neurol.* 8:257. doi: 10.3389/fneur.2017.00257

Pearson, K. G., and Collins, D. F. (1993). Reversal of the influence of group Ib afferents from plantaris on activity in medial gastrocnemius muscle during locomotor activity. *J. Neurophysiol.* 70, 1009–1017. doi: 10.1152/jn.1993.70.3.1009

Perrier, J. F., and Hounsgaard, J. (2003). 5-HT2 receptors promote plateau potentials in turtle spinal motoneurons by facilitating an L-type calcium current. *J. Neurophysiol.* 89, 954–959. doi: 10.1152/jn.00753.2002

Powers, R. K., and Binder, M. D. (2001). Input-output functions of mammalian motoneurons. *Rev. Physiol. Biochem. Pharmacol.* 143, 137–263. doi: 10.1007/BFb0115594

Powers, R. K., Campbell, D. L., and Rymer, W. Z. (1989). Stretch reflex dynamics in spastic elbow flexor muscles. *Ann. Neurol.* 25, 32–42. doi: 10.1002/ana.410250106

Powers, R. K., Elbasiouny, S. M., Rymer, W. Z., and Heckman, C. J. (2012). Contribution of intrinsic properties and synaptic inputs to motoneuron discharge patterns: a simulation study. *J. Neurophysiol.* 107, 808–823. doi: 10.1152/jn.00510.2011

Powers, R. K., and Heckman, C. J. (2017). Synaptic control of the shape of the motoneuron pool input-output function. *J. Neurophysiol.* 117, 1171–1184. doi: 10.1152/jn.00850.2016

Prochazka, A., Gillard, D., and Bennett, D. J. (1997). Implications of positive feedback in the control of movement. *J. Neurophysiol.* 77, 3237–3251. doi: 10.1152/jn.1997.77.6.3237

Revill, A. L., and Fuglevand, A. J. (2017). Inhibition linearizes firing rate responses in human motor units: implications for the role of persistent inward currents. *J. Physiol.* 595, 179–191. doi: 10.1113/JP272823

Schwarz, P. B., Yee, N., Mir, S., and Peever, J. H. (2008). Noradrenaline triggers muscle tone by amplifying glutamate-driven excitation of somatic motoneurones in anaesthetized rats. *J. Physiol.* 586, 5787–5802. doi: 10.1113/jphysiol.2008.159392

Schwindt, P., and Crill, W. E. (1977). A persistent negative resistance in cat lumbar motoneurons. *Brain Res.* 120, 173–178. doi: 10.1016/0006-8993(77)90510-8

Silverman, J., Garnett, N. L., Giszter, S. F., Heckman, C. J. II., Kulpa-Eddy, J. A., Lemay, M. A., et al. (2005). Decerebrate mammalian preparations: unalleviated or fully alleviated pain? A review and opinion. *Contemp. Top. Lab. Anim. Sci.* 44, 34–36.

Stinear, C. M., Barber, P. A., Smale, P. R., Coxon, J. P., Fleming, M. K., and Byblow, W. D. (2007). Functional potential in chronic stroke patients depends on corticospinal tract integrity. *Brain* 130, 170–180. doi: 10.1093/brain/awl333

Thilmann, A. F., Fellows, S. J., and Garms, E. (1990). Pathological stretch reflexes on the "good" side of hemiparetic patients. *J. Neurol. Neurosurg. Psychiatr.* 53, 208–214. doi: 10.1136/jnnp.53.3.208

Thilmann, A. F., Fellows, S. J., and Garms, E. (1991). The mechanism of spastic muscle hypertonus. Variation in reflex gain over the time course of spasticity. *Brain* 114 (Pt 1A), 233–244.

Veasey, S. C., Fornal, C. A., Metzler, C. W., and Jacobs, B. L. (1995). Response of serotonergic caudal raphe neurons in relation to specific motor activities in freely moving cats. *J. Neurosci.* 15, 5346–5359.

Conflict of Interest Statement: The authors declare that the research was conducted in the absence of any commercial or financial relationships that could be construed as a potential conflict of interest.

Copyright © 2018 McPherson, McPherson, Thompson, Ellis, Heckman and Dewald. This is an open-access article distributed under the terms of the Creative Commons Attribution License (CC BY). The use, distribution or reproduction in other forums is permitted, provided the original author(s) and the copyright owner are credited and that the original publication in this journal is cited, in accordance with accepted academic practice. No use, distribution or reproduction is permitted which does not comply with these terms.

frontiers in Neural Circuits

REVIEW
published: 18 April 2018
doi: 10.3389/fncir.2018.00030

Reticulospinal Systems for Tuning Motor Commands

Robert M. Brownstone and Jeremy W. Chopek*

Sobell Department of Motor Neuroscience and Movement Disorders, Institute of Neurology, University College London, London, United Kingdom

The pontomedullary reticular formation (RF) is a key site responsible for integrating descending instructions to execute particular movements. The indiscrete nature of this region has led not only to some inconsistencies in nomenclature, but also to difficulties in understanding its role in the control of movement. In this review article, we first discuss nomenclature of the RF, and then examine the reticulospinal motor command system through evolution. These command neurons have direct monosynaptic connections with spinal interneurons and motoneurons. We next review their roles in postural adjustments, walking and sleep atonia, discussing their roles in movement activation or inhibition. We propose that knowledge of the internal organization of the RF is necessary to understand how the nervous system tunes motor commands, and that this knowledge will underlie strategies for motor functional recovery following neurological injuries or diseases.

Keywords: locomotion, mesencephalic locomotor region, reticular formation, microcircuits, sleep atonia

OPEN ACCESS

Edited by:
Brian R. Noga,
University of Miami, United States

Reviewed by:
Marie-Claude Perreault,
Emory University, United States
Stuart Baker,
Newcastle University,
United Kingdom
Joel C. Glover,
University of Oslo, Norway

****Correspondence:***
Robert M. Brownstone
r.brownstone@ucl.ac.uk

Received: *23 December 2017*
Accepted: *29 March 2018*
Published: *18 April 2018*

Citation:
Brownstone RM and Chopek JW (2018) Reticulospinal Systems for Tuning Motor Commands. Front. Neural Circuits 12:30. doi: 10.3389/fncir.2018.00030

INTRODUCTION

As movement is necessary for the expression of all behavior, much of the vertebrate nervous system is involved in its production. A key site for integration of descending instructions to move is the reticular formation (RF), which is situated in the brain stem and comprised of multiple nuclei. The indiscrete nature of these regions combined with disparate neuronal types within each nucleus has led not only to some inconsistencies in nomenclature, but also to difficulties in understanding RF control of movement.

The RF is comprised of different neural types including monoaminergic, cholinergic, GABA/glycinergic and glutamatergic neurons, with glutamatergic reticulospinal neurons (RSNs) forming the key descending output. Axons of these neurons extend into the spinal cord such that RSN activity can lead to a variety of motor behaviors. Inputs to RSNs descend from diverse brain regions including the telencephalon, diencephalon and cerebellum, and ascend from the spinal cord. Local circuits within RF nuclei may also contribute to their output. RSNs therefore play a role in integrating and processing these diverse inputs in order to produce effective motor behaviors. Recent reviews have addressed the role of the RF in context specific locomotion (Kim et al., 2017) and the interaction of the control of posture and locomotion (Takakusaki et al., 2016). In this review, we will discuss glutamatergic RSN systems with a focus on their organization, connectivity with spinal neurons, control of hind limb movement, and the role of these systems in recovery of

Abbreviations: DTF, dorsal tegmental field; Gi, gigantocellular reticular nucleus; GiA, gigantocellular reticular nucleus, pars alpha; GRN, gigantocellular reticular nucleus; LPGi, lateral paragigantocellular nucleus; MdV, medulla reticular formation-ventral part; medRF, medulla reticular formation; MLR, mesencephalic locomotor region; PnC, pontine reticular formation, caudal part; PnO, pontine reticular formation, oral part; PPN, pedunculopontine nucleus; RF, reticular formation; RSN, reticulospinal neurons; SLDT, sublaterodorsal tegmental; VTF, ventral tegmental field.

function after neurological injury. Additionally, we address the lack of information regarding the internal organization of RF nuclei and why this knowledge is vital for understanding how RS output is refined.

RETICULAR FORMATION NOMENCLATURE

One difficulty in determining specific functions of the RF arises from the non-discrete boundaries between nuclei and the inconsistent nomenclature in the literature. In this review, we will use the terminology as set out by Paxinos and Franklin (2008). As different investigators have used different terms, in this section we have attempted to harmonize the nomenclature through assessment of the available anatomical sections provided in publications focussed on the role of RSNs in movement.

The RF extends through the mesencephalon, pons and medulla and is traditionally divided into three columns—median, medial and lateral. In this review, we will focus on RSNs involved in limb movement, which arise from the medial column in the pons and medulla. Descending neurons from the median column arise from the raphe nuclei and are responsible for serotoninergic neuromodulation (see review: Schmidt and Jordan, 2000). The neurons of the lateral column and those in the mesencephalic RF do not project to the spinal cord.

The medial pontine RF, from rostral to caudal, comprises the nucleus reticularis pontis oralis (PnO), from the decussation of the superior cerebellar peduncles to the trigeminal motor pool, and the nucleus reticularis pontis caudalis (PnC), overlapping with PnO and extending caudally to the facial nucleus. Situated dorsal to these nuclei are the pontine tegmental nuclei, divided into ventral (region referred to as the ventral tegmental field, or VTF), dorsal (region referred to as the dorsal tegmental field, or DTF), and lateral tegmental nuclei, as well as the sublaterodorsal tegmental (SLDT) nucleus. The dorsal tegmental nucleus extends caudally to lie dorsal to the gigantocellular reticular nucleus (GRN, *vide infra*), by which point the ventral and lateral tegmental nuclei merge to form the laterodorsal tegmental nucleus (LDT). In addition, rodents may have a ventral nucleus of the medial pontine RF (PnV, Liang et al., 2011) that contains a small population of RS neurons, although it has been suggested this is part of the rostral medullary GRN (see Sivertsen et al., 2016).

The rostral portion of the medial medullary RF (medRF) begins at the most caudal portion of the PnC, with the GRN lying ventral to PnC and extending from the facial nucleus to the obex. The GRN (sometimes referred to as Gi) is a large nucleus that contains the largest cells in the RF. Ventral to this is the pars alpha of the GRN (GiA), which merges with the Gi pars ventral (GiV) caudally. In the cat literature, the GRN is often referred to as the nucleus reticularis gigantocellularis (NRGc) or gigantocellular tegmental field (FTG), and the GiA/GiV as the nucleus reticularis magnocellularis (NRMc) or magnocellular tegmental field (FTM, see Noga et al., 1988; Takakusaki et al., 2016), with medullary sections 9 mm caudal to the junction of the superior and inferior colliculi (P9) in the cat corresponding approximately to Bregma −7 in the mouse (Paxinos and Franklin, 2008). The dorsal paragigantocellular nucleus (DPGi) is dorsal to the GRN, and the parvocellular reticular nucleus (PCRt) is dorsolateral to the GRN. The intermediate reticular zone (IRt) which contains the nucleus ambiguus, separates the GRN from the PCRt (Paxinos et al., 2012). The lateral paragigantocellular nucleus (LPGi), lies lateral to GiV and ventromedial to nucleus ambiguus. In the caudal medulla which lacks giant GRN neurons, the central nucleus can be subdivided into the medRF ventral part (MdV), and more cellular dorsal part (MdD), separated by the caudal IRt and located in the caudal medulla lateral to the medial longitudinal fasciculus.

It should be noted that the borders between these regions are somewhat indistinct, necessitating a degree of caution when interpreting experimental findings involving either electrical stimulation (Mori et al., 1978; Garcia-Rill and Skinner, 1987; Takakusaki et al., 2016) or local injections (Noga et al., 1988; Takakusaki et al., 2016; Capelli et al., 2017). The comparison of histological sections between studies is helpful, but co-labeling with antibodies against choline acetyltransferase would be helpful in aligning sections based on consistent cholinergic nuclei such as motor pools.

RETICULOSPINAL NEURONS ARE COMMAND NEURONS FOR MOVEMENT

RSNs Are Evolutionary Conserved Command Neurons

The reticulospinal (RS) system is a distributed network of neurons extending from the caudal midbrain through the pons and medulla (Peterson, 1984). RSNs receive inputs from rostral motor centers and have axons that descend through the ventrolateral funiculus of the spinal cord to form synapses with spinal interneurons and motoneurons that participate in movement. As RSNs are located between higher centers that select movement and spinal cord circuits where movement is organized, RSNs may be considered as command neurons.

Command neurons are widespread across invertebrate and vertebrate species. To be classified as a command neuron, a candidate neuron must satisfy the criteria of both sufficiency and necessity for initiating a given behavior (Kupfermann and Weiss, 1978). Command neurons in the brain stem have been identified in a number of vertebrate species in which they have been shown to be involved in motor behaviors such as escape and locomotion.

Dating back more than 500 million years, the early appearing agnathans, lampreys and hagfish, developed RS command neurons called Müller cells, that have axons that cross in the brainstem and descend the length of the spinal cord to evoke swimming (Shapovalov, 1972). Perhaps the prototypical RS command neuron, though, is the Mauthner cell, initially described in teleosts which arose ∼310 million years ago. Given that Mauthner cells were readily identifiable and that they share similar location, morphology, and synaptic connectivity across species, they have been well studied as command neurons (Sillar et al., 2016). Mauthner cells are likely present in lower vertebrates

such as lamprey, but their function has mostly been studied in later-evolving fish as well as amphibians.

Two Mauthner cells, located directly opposite each other near the midline of the medulla can readily be identified in the RF based on their large cell size and location at the level of the 4th rhombomere (Sillar et al., 2016; Hildebrand et al., 2017). The axons of Mauthner cells cross in the brain stem and project through the spinal cord where they form glutamatergic, excitatory connections to large primary motoneurons and premotor excitatory interneurons (Fetcho and Faber, 1988; Faber et al., 1989; Fetcho, 1991). These interneurons have descending projections, are electrotonically coupled to large motoneurons, and form chemical synapses with small motoneurons (Fetcho, 1992). The Mauthner cell axon is also electrotonically coupled to glycinergic commissural interneurons that inhibit the large motoneurons and interneurons on the contralateral side (Yasargil and Sandri, 1990; Fetcho, 1991).

Mauthner cells receive multiple sensory inputs (Sillar et al., 2016). In response to acoustic stimuli (cf. startle response in humans below), Mauthner cells fire a single action potential (Zottoli, 1977). Based on the connectivity described above, this results in excitation of contralateral motoneurons and inhibition of ipsilateral motoneurons. This produces a fast and forceful C-start escape, arising from the initial C-bend, in which the fish moves away from the initial stimulus (Fetcho, 1992). Thus, Mauthner cell activation produces a conserved stereotypical C-start response that mediates escape (Eaton et al., 1988; Faber et al., 1989).

It is now recognized that the C-start escape response is not necessarily stereotypical, and that depending on the stimulus site and intensity, combinations of RSNs, including Mauthner cells, can produce variations of the escape response (Eaton et al., 2001). For example, it was recently demonstrated that Mauthner cells are involved in a second type of escape response, the S-start escape, when bilaterally activated (Liu and Hale, 2017). The selection of the S- vs. C-start was determined by the recruitment of segmental inhibitory neurons in spinal circuits, which would modify the response. The adaptability in behavioral responses mediated by the RS system indicates that responses to command neuron activity are variable and state-dependent.

With further study, it became apparent that the Mauthner cell has multiple smaller homologoues and that they are organized in a segmental plan, similar to the segmented organization seen in invertebrates (Kimmel, 1993). It was also demonstrated that there are additional command neurons in the teleost RS system, which comprises approximately 500 neurons (Prasada Rao et al., 1987). Thus, even in these relatively early appearing teleosts, complex descending systems were present.

As supraspinal systems developed to control limbed movement, the RS system remained a dominant system mediating movement. Across species including frog, turtle, rat, cat and rhesus monkey, RSNs project to and monosynaptically excite limb motoneurons (Shapovalov, 1972). It is noteworthy that, in addition to the RS system, other descending systems such as the vestibulospinal system appeared beginning in amphibians (Shapovalov, 1972). While these other systems evolved further in reptiles, the RS system also expanded and diversified to include, for example, inhibitory RSNs. With further evolution of corticospinal including corticomotoneuronal systems in primates, the RS system persisted, producing responses in spinal motoneurons similar to those seen in fish. Thus, the RS system remains conserved though evolution (Shapovalov, 1972), and plays an important role in vertebrate, including human, movement.

In fact, the RS system was not only conserved but it flourished in evolution. For instance, compared to the 500 RSNs in the fish, there are approximately 50,000 RSNs in the mouse. Of these, approximately 19,000 are located in the GRN alone (Liang et al., 2011). Based on a comparison of EPSPs and IPSPs across species, Shapovalov concluded "the basic similarity between reticulo-motoneuronal projections across all vertebrates investigated may evidently be attributable to the common origin of the reticulospinal system, which undergoes mainly quantitative changes in the course of evolution" (Shapovalov, 1972, p. 353). In other words, as behavior became more complex, so too did the RS system. But the fundamental architecture and role of the RS system persisted across species: RSNs are large cells with dense arborizations and large fast-conducting axons that descend in the spinal cord, forming synapses with interneurons and motoneurons in multiple segments in order to produce movement.

Reticulospinal Neurons Project to Spinal Interneurons and Motoneurons

The influence of the brainstem on posture was documented by Sherrington (1898) who noted that decerebration led to "decerebrate rigidity" or hyperactivity of extensor muscles, suggesting that there is an excitatory influence from sub-cerebral structures to the spinal cord. In the 1940s Rhines and Magoun demonstrated that following decerebration, stimulation of the ventral medulla could result in the complete loss of muscle tone, and cessation of stimulation led to the immediate return of hyperextensor activity, demonstrating that the RS system had both an excitatory and inhibitory influence on postural muscles (Magoun and Rhines, 1946; Rhines and Magoun, 1946). They also demonstrated that the RS system could either facilitate or inhibit spinal reflexes in the cat (Magoun, 1944; Magoun and Rhines, 1946; Rhines and Magoun, 1946), and found that the area responsible for inhibition resided in the ventral rostral medulla (Magoun and Rhines, 1946), whereas the excitatory regions extended through the pons and medulla (Rhines and Magoun, 1946). However, Sprague and Chamber (1954) found that in intact cats, for the most part, micro-stimulation of the RF led to reciprocal (flexion-extension as well as right-left) responses in the limbs rather than generalized facilitation or inhibition. Neurons in the caudal pons and GRN form either excitatory (Grillner and Lund, 1968) or inhibitory (Llinas and Terzuolo, 1964a,b) connections with flexor or extensor hindlimb motoneurons. In addition to the hindlimb responses, RS stimulation can produce direct excitation or inhibition of neck, back, and forelimb motoneurons (Wilson and Yoshida, 1969; Wilson et al., 1970; Peterson et al., 1978). In non-human primates, activation of movement by RS stimulation is achieved by both direct and

indirect connectivity to motoneurons (Riddle et al., 2009). Thus, RSNs produce effects that are heterogeneous and widespread in the spinal cord.

It is important to note that, in contrast to other descending systems such as the lateral vestibulospinal and corticofugal systems, the RS system is not exclusively excitatory. A proportion of RSNs descending in the MLF are inhibitory (Du Beau et al., 2012), and approximately 20% of RS synaptic contacts on propriospinal and spinal commissural interneurons in the lumbar spinal cord are inhibitory (Mitchell et al., 2016). Recently it has been shown that glycinergic neurons located in the GRN descend to the lumbar spinal cord (Valencia Garcia et al., 2018; *vide infra*).

Within the RF, specific regions have been found to be responsible for specific responses (Drew and Rossignol, 1990). Ipsilateral projecting pontine RSNs outnumber contralateral projecting pontine RSNs three to one and are located throughout the pontine RF whereas the contralateral projecting neurons are concentrated in the rostral pontine RF (Sivertsen et al., 2016). In neonatal mice, medial neurons in the medRF predominantly activate lateral motor column (limb-innervating) MNs in the lumbar spinal cord, whereas lateral medRF neurons predominantly activate medial motor column (axial muscle-innervating) MNs (Szokol et al., 2008). In both cases, these actions may be mediated through polysynaptic pathways mediated by ipsilateral and contralateral descending spinal commissural interneurons (Szokol et al., 2011; Perreault and Glover, 2013).

Microstimulation within the RF can result in movement across multiple joints or limbs. For example, stimulation that produced forelimb movement was regularly accompanied by movement of the head or hindlimbs (Drew and Rossignol, 1990). Furthermore, homologous to Mauthner cell responses, motoneuron responses were not restricted to one side: microstimulation could evoke ipsilateral flexion and contralateral extension of the either the fore or hind limbs (Drew and Rossignol, 1990). These evoked movements are consistent with the axonal projections of RSNs, with 85% of axons extending to both the cervical and lumbar enlargements, and, at least in the cervical enlargement, axons projecting bilaterally (Peterson et al., 1975). Thus, RSNs have divergent spinal projections and are involved in multi-joint, multi-limb motor commands. In summary, the RS system in the mammal is functionally organized and acts to coordinate multiple movements including excitation and inhibition across joints and across limbs.

medRF Reticulospinal Neurons and Locomotion

The rhythm and pattern of locomotion are produced by spinal cord circuits in response to descending commands (Graham Brown, 1911; Jankowska et al., 1967). RF locomotor command neurons are activated by an upstream center called the mesencephalic locomotor region (MLR). MLR stimulation produces locomotion in decerebrate cats (Shik et al., 1966), rats (Skinner and Garcia-Rill, 1984), and mice (Roseberry et al., 2016; Stecina, 2017; Caggiano et al., 2018) through a pathway mediated by medRF RSNs (Noga et al., 2003). The medRF has been shown to be crucial for locomotion in a number of other species as well, including lamprey (McClellan and Grillner, 1984), ducks and geese (Steeves et al., 1987) and guinea pigs (Marlinskii and Voitenko, 1992). In the cat, medRF RSNs in the GRN are necessary for MLR-evoked locomotion, and are sufficient to induce locomotor activity through electrical (Jordan et al., 2008) or chemical stimulation (Noga et al., 1988). These "locomotor" medRF RSNs also receive input from the contralateral cerebellar locomotor region (Mori et al., 1998) and from the ipsilateral lateral hypothalamic area, termed the subthalamic locomotor region (Sinnamon and Stopford, 1987). Given the multitude of locomotor-related inputs, Orlovskii (1970) stated that "the invariable mediating link for initiating locomotion is the reticulospinal system."

Locomotor medRF RSNs are fast conducting (Orlovskii, 1970; Degtyarenko et al., 1998; Noga et al., 2003) and glutamatergic (Douglas et al., 1993; Jordan et al., 2008). They are phasically active during spontaneous locomotion in thalamic cats (Shimamura et al., 1982; Shimamura and Kogure, 1983), treadmill locomotion in unrestrained cats (Drew et al., 1986; Matsuyama and Drew, 2000), and spontaneous or MLR-evoked fictive locomotion in the absence of movement related feedback in decerebrate cats (Perreault et al., 1993). Locomotion-inducing RSN axons descend in the ventrolateral funiculus (Steeves and Jordan, 1980), may innervate the ipsi- or contra-lateral spinal cord (Matsuyama et al., 1988, 1999), and are known to innervate commissural interneurons in the lumbar spinal cord (Matsuyama et al., 2004; Jankowska, 2008). That is, RSNs in the medRF GRN provide extensive innervation to bilateral spinal motor regions, and seemingly fulfil the criteria of command neurons for locomotion.

While RSNs thus integrate inputs from multiple higher centers in order to send commands to the spinal cord, there may also be local processing of commands within the RF. Neurons within the RF have heterogeneous characteristics, leading to the suggestion that there may be local circuit processing of reticulospinal commands (Shimamura et al., 1980), but this has not been explored in detail. For example, a subset of neurons in this region in lamprey (Einum and Buchanan, 2004; Buchanan, 2011) and cat (Shimamura et al., 1980, 1982) receive inputs from the spinal cord. In the cat, it has been suggested that the phasic activity of RSNs during fictive locomotion may arise from inputs from the spinal cord (Perreault et al., 1993). This hypothesis is supported by the demonstrated phase-dependent modulation of RSN activity in response to cutaneous stimulation during locomotion (Drew et al., 1996). How these ascending inputs are processed and how they might affect the descending commands is not yet clear.

There is also evidence that some RSNs receive neuromodulatory input (Takakusaki et al., 1993a), indicating that their activity may be state dependent (Takakusaki et al., 2016). While there has been focus on modulation of RSNs by acetylcholine (Takakusaki et al., 1993b; Le Ray et al., 2010), serotonin also may play a role (Takakusaki et al., 1993a). Given the importance of serotoninergic activity in locomotion (Schmidt and Jordan, 2000), it is possible that this modulatory

system is involved in both brain stem and spinal circuits for locomotion.

Pathways for different types of locomotor activity, such as escape vs. exploration, may differ (Sinnamon, 1993; Jordan, 1998). The MLR is comprised primarily of the cuneiform nucleus (Jordan, 1998), but recent evidence in the mouse suggests that while higher speed locomotion is mediated by the cuneiform nucleus, exploratory activity is initiated by a region just ventral to this, the pedunculopontine nucleus (PPN, Caggiano et al., 2018). The PPN has diverse projections to RF nuclei (Gi, GiV, GiA, LPGi, MdV), whereas the cuneiform projections are more restricted (LPGi, GiV, GiA but not the Gi or MdV, Caggiano et al., 2018). While cat studies have pointed towards the medial regions of the medRF as the command for locomotion (Noga et al., 2003), there has been a recent suggestion that in the mouse, LPGi activation is necessary for higher speed locomotion (Capelli et al., 2017). This suggests that there may be species differences in descending commands, a difference in the state of the circuits being studied across experiments, or that locomotor activity is initiated via indirect pathways in some experiments (see Noga et al., 2003). In summary, it is clear across multiple species that the medRF plays a key role in integrating and processing instructions for locomotion from more rostral centers.

In addition to their well-defined role in initiating locomotion, RSNs have recently been implicated in stopping locomotion. Optogenetic activation of a subset of glutamatergic neurons defined by expression of the transcription factor Chx10 located in the PnC and GRN regions can lead to cessation of locomotor activity in the mouse (Bouvier et al., 2015) and lamprey (Juvin et al., 2016). Three activity patterns in RSNs were seen in this region during swimming in lamprey: those that fired exclusively at the onset of swimming ("start" RSNs), those that fired throughout the swimming bout ("start and maintain" RSNs), and those that fired prior to the termination of locomotion ("stop" RSNs; Juvin et al., 2016). This indicates that there is a diversity of neuronal function within the RSN. In the mouse and possibly lamprey, the behavioral response from the stop RSNs is likely mediated by spinal inhibitory neurons targeted by these descending glutamatergic RSNs (Bouvier et al., 2015; Juvin et al., 2016).

The ability of RSNs in the medRF/GRN to act as command neurons for a variety of behaviors in addition to starting and stopping locomotion is highlighted by its involvement in a multitude of tasks ranging from, for example, maintaining posture during walking to atonia during sleep (*vide infra*).

Interaction of Reticulospinal Systems for Locomotion and Posture

In the late 1970s, it was shown that postural adjustments associated with locomotion originated in the caudal portion of the pontine RF (see Mori, 1987). Stimulation of the dorsal area of the caudal pontine tegmental field (DTF) resulted in the relaxation of extensor muscles, whereas stimulation of the ventral area of the caudal pontine tegmental field (VTF) resulted in activation or an increase in extensor muscle tone. More recently, it has been shown that injections of cholinergic and serotonergic agonists into the PnO resulted in atonia and hypertonia respectively. These effects were mediated through medRF RSNs, with atonia-related RSNs located in the dorsomedial part of the medRF and hypertonus-related RSNs located in the ventromedial part of the medRF (Takakusaki et al., 2016). Thus it is clear that RSNs, through excitation and inhibition of spinal circuits, regulate muscle tone (for review see Takakusaki et al., 2016).

Extensor muscle tone is necessary for locomotion as there must be adequate force production to support the body and propel limbs forward (Mori et al., 1978, 1982). The interplay of posture and locomotion was demonstrated during MLR evoked locomotion, when stimulation of the DTF halted locomotion and stimulation of the VTF resulted in enhanced locomotor activity or a change in gait pattern (Mori et al., 1978). In freely moving cats with electrodes implanted in the DTF or VTF and the MLR, DTF stimulation during walking (naturally or MLR induced) led to sequential postural reduction to a sitting then prone position, and VTF stimulation when lying led to a rise to stance followed by locomotion (Mori et al., 1986).

The co-expression of postural tone and locomotion is likely due to shared neural pathways. For example, in addition to projecting to locomotor neurons in the GRN, the MLR also projects to postural areas (DTF and VTF). About 70% of DTF neurons are activated by MLR stimulation, with most being tonically active but some demonstrating rhythmic activity (Kawahara et al., 1985). Thus the MLR through two DTF pathways may participate in both tonic regulation of posture for locomotion and phasic regulation contributing to step cycle timing.

Reticulospinal Neurons and Reaching

RSNs are involved in movements other than posture and locomotion. For example, some RSNs in the cat are active during the preparatory phase in anticipation of reaching, while others are active during the actual reaching task (Schepens, 2004). Anatomical evidence using viral tracing has demonstrated glutamatergic RSNs in the MdV that form synapses exclusively with forelimb and not hindlimb MNs, unlike other neurons, including those in the GRN, which form synapses with both forelimbs and hindlimb MNs (Esposito et al., 2014). Furthermore, these synapses are motor pool specific, appearing on biceps but not triceps motoneurons. Inhibition of these RSNs resulted in decreased ability of the mice to accurately reach and grasp during a food pellet challenge. Because these RSNs are not involved in hindlimb movement, we will not consider them further here.

Reticulospinal Neurons and Sleep Atonia

While descending commands can stop locomotion (*vide supra*), the prototypical "stop" command is that which produces sleep atonia, in which limb muscle tone is curtailed to prevent movement during REM sleep (Saper et al., 2010). This atonic command originates in the SLDT nucleus, which contains glutamatergic neurons that project both to GRN and to the spinal cord (Sastre et al., 1981; Chase et al., 1986; Saper et al., 2010). Both of these targets contribute to sleep atonia, but whether

the direct descending command from the GRN is inhibitory and/or whether its inhibitory effects are mediated by spinal interneurons is not clear (Fuller et al., 2007; Arrigoni et al., 2016). Recent evidence, however, suggests that there is descending inhibitory input that produces sleep atonia (Valencia Garcia et al., 2018).

In cats, lesions to the subcoeruleus region (analogous to the SLDT) result in behavior in which the cats appear to act out their dreams during sleep (Mouret et al., 1967; Henley and Morrison, 1974). Similarly, lesions to the SLDT in rodents led to complex motor behaviors during REM sleep (Lu et al., 2006). These behaviors are akin to REM behavior disorder (RBD) in humans (Schenck and Mahowald, 1995). That RBD can be localized to the SLDT has been shown in a case report of a woman with a lesion in this region who suffered from RBD and somnambulism (Limousin et al., 2009). Interestingly, RSNs that are associated with specific movements during waking are also active during REM sleep (Siegel et al., 1981). This suggests that extraneous movements during RBD are produced by the same neurons as during wakefulness. RBD is perhaps an extreme example of pathological RSN circuit selection. Other examples could include other disorders affecting movement selection such as dystonic syndromes.

INTRINSIC ORGANIZATION OF THE RETICULAR FORMATION

Clearly, rostral centers must activate different populations of RSNs in order to produce selected movements. Given that there can be net inhibitory (sleep atonia) and net excitatory (locomotion) effects produced by RSNs, we propose that movement selection circuits activate smaller ensembles or microcircuits of RSNs in order to facilitate specific movements whilst inhibiting other movements. This concept is not unlike that of the direct and indirect pathways of the basal ganglia that cooperate in movement selection (Cui et al., 2013). This example also demonstrates that the control of moving and not moving are intimately intertwined, and that neurological disorders that alter either one or the other of these two classes of microcircuits can lead to significant impairment in quality of life. How these microcircuits interact with each other, however, is yet to be defined.

What determines the tuning of appropriate commands? As RSNs are involved in diverse movements and comprise a subset of RF neurons, it would be prudent to ask whether RSNs simply integrate and relay inputs from higher brain centers to the spinal cord, or whether local microcircuits participate in refining motor commands.

Whilst our knowledge of the functional and topographical organization of RSNs is increasing, little is known about the internal organization of the RF. Some neurons within these nuclei are inhibitory, presumably interneurons (Sivertsen et al., 2016), but there is little information about local connectivity. Several modeling studies have addressed this lack of understanding of the internal circuitry. One proposal is that the RF is a "small-world network" in which dense connectivity within small groups of nodes is responsible for appropriate action selection (Humphries et al., 2006). Individual nodes would comprise small diameter local interneurons, most likely inhibitory, that project medially and laterally and connect with larger projecting cells (likely RSNs) within their own node. Node to node connectivity would be via axon collaterals of the large projecting neurons which would form synapses at relatively short distances, allowing for nearby nodes to activate quickly and concurrently (Humphries et al., 2007).

Experimental data to support this model are in short supply to date. But it is clear that knowledge of the internal organization of the RF is critical to understand how the RF and RSNs are selected to produce a wide array of finely tuned motor commands.

RETICULOSPINAL NEURONS IN HUMANS AND THEIR ROLE IN RECOVERY OF MOTOR FUNCTION

The corticofugal system plays an important role in human movement (Lemon, 2008). Axon collaterals from descending corticospinal neurons have diffuse projections, including to the RF (Kita and Kita, 2012). It is of interest that, although there was a deficit in fractionated finger movements in monkeys following lesions of these tracts below the level of the collaterals to the RF, other movements including climbing and running persisted (Lawrence and Kuypers, 1968a,b). Furthermore, monosynaptic corticomotoneuronal synapses are not necessary for hand movements in non-human primates, which improved over time following pyramidal tract lesions (Sasaki et al., 2004). Similarly, rare reports of sectioning these tracts in humans have demonstrated initial hemiparesis followed by recovery, ultimately leaving patients with a relative lack of movement deficit (Bucy et al., 1964). These data suggest that other systems such as RSNs can play a prominent role in movement in primates, including humans.

RS systems have been studied in humans via the startle reflex. This reflex response is seen across species and been shown to originate in the caudal brainstem—most likely the PnC (Hammond, 1973; Leitner et al., 1980; Davis et al., 1982). The startle reflex is seen in response to a loud acoustic stimulus (cf. Mauthner cells, above), and is stereotypically comprised of activation of the sternocleidomastoid muscle, followed by cranial nerve innervated muscles and rectus abdominus, and finally forelimb and hindlimb muscles (Rothwell, 2006). Evidence for a brainstem origin for this response has come from electrophysiological studies. When the instruction to start voluntary movement was combined with a loud auditory cue, the time to movement onset was significantly reduced (Rothwell, 2006). For example, the onset to volitional arm movement was found to be 150 ms, whereas arm movement initiated by the startle response can occur in 80 ms. This reduced latency has also been associated with an increased rate of force development, as well as increased force output (Anzak et al., 2011). Moreover, in more complex movements involving sequential activation of agonist and antagonist muscles, auditory stimulation sped up the activation of movement without affecting the pattern of muscle

activity (Valls-Solé et al., 1999). Together, these data all point towards a subcortical, and more specifically RS, origin for startle reflexes.

The startle response in humans integrates with voluntary movements and may thus facilitate a potential therapeutic approach for regaining volitional movement post neurological insults to the cortex such as stroke (Rothwell, 2006) or to enhance motor performance in diseases such as Parkinson's disease (Anzak et al., 2016). In stroke patients, when the startle response was combined with voluntary movement, the latency to EMG response was shorter and the response was much larger than when either was performed alone, leading to the suggestion that detail of voluntary movement can be stored in the brainstem and can be accessed to produce movement in the absence of descending inputs from the cerebral cortex (Rothwell, 2006).

Given that RSNs are important in movement, and that many neurological injuries occur above the level of the RF, it is reasonable to ask whether the RS system could be a therapeutic target for therapies aimed at recovery of motor function in neurological diseases and injuries such as stroke (Baker et al., 2015). Data from non-human primates supports this concept (Zaaimi et al., 2012). Presumably, intentional signals from higher centers would still need to reach the RF, but as noted above, there are many supramedullary inputs that converge on RSNs. For example, following unilateral stroke, there are non-crossed cortico-reticular inputs that could possibly harness the unaffected ipsilateral cortex to promote RF plasticity and motor functional recovery (Jankowska and Edgley, 2006). The RS system is well connected to play a key role in recovery from motor deficits, as it projects to all levels of the spinal cord including to key movement circuits.

Such RS-mediated functional recovery need not be limited to axial movement. Although initially proposed to be important for axial and proximal muscles, it is becoming clear from studies in non-human primates that RSNs are also involved in hand function (Riddle et al., 2009), and could thus be a substrate for functional recovery of hand movements following neurological injury (Baker, 2011). In support of this possibility, recent evidence from humans points to the RS system as being involved in gross hand function after spinal cord injury (Baker and Perez, 2017).

To promote RSN-mediated recovery of motor function, however, several challenges exist. It will be necessary to understand the functional organization of motor command circuits in the RF, including how nodes or microcircuits in the RF are engaged to produce movement, whether individual microcircuits participate in more than one motor behavior, how individual microcircuits are recruited by rostral circuits, whether these circuits are under neuromodulatory control, and whether "on" movement and "off" movement microcircuits are simultaneously recruited to refine motor commands. Understanding these concepts could form the foundation for future therapeutic strategies.

Ultimately, it is clear that our focus in understanding the RF should include not only an "integrate and relay" function, but also an understanding of the internal organization and processing that controls RSNs such that a great versatility of movements can be produced. This understanding will lead not only to improved knowledge of how we move, but potentially also to new experimental paradigms to understand motor system changes in injury and disease, and ultimately to the development of new therapeutic strategies aimed at improving motor functional recovery.

AUTHOR CONTRIBUTIONS

RB and JC conceived and wrote the manuscript.

FUNDING

RB was supported by Wellcome Trust (grant no. 110193) and Brain Research UK.

REFERENCES

Anzak, A., Tan, H., Pogosyan, A., and Brown, P. (2011). Doing better than your best: loud auditory stimulation yields improvements in maximal voluntary force. *Exp. Brain Res.* 208, 237–243. doi: 10.1007/s00221-010-2474-1

Anzak, A., Tan, H., Pogosyan, A., Khan, S., Javed, S., Gill, S. S., et al. (2016). Subcortical evoked activity and motor enhancement in Parkinson's disease. *Exp. Neurol.* 277, 19–26. doi: 10.1016/j.expneurol.2015.12.004

Arrigoni, E., Chen, M. C., and Fuller, P. M. (2016). The anatomical, cellular and synaptic basis of motor atonia during rapid eye movement sleep. *J. Physiol.* 594, 5391–5414. doi: 10.1113/JP271324

Baker, S. N. (2011). The primate reticulospinal tract, hand function and functional recovery. *J. Physiol.* 589, 5603–5612. doi: 10.1113/jphysiol.2011.215160

Baker, S. N., and Perez, M. A. (2017). Reticulospinal contributions to gross hand function after human spinal cord injury. *J. Neurosci.* 37, 9778–9784. doi: 10.1523/JNEUROSCI.3368-16.2017

Baker, S. N., Zaaimi, B., Fisher, K. M., Edgley, S. A., and Soteropoulos, D. S. (2015). Pathways mediating functional recovery. *Prog. Brain Res.* 218, 389–412. doi: 10.1016/bs.pbr.2014.12.010

Bouvier, J., Caggiano, V., Leiras, R., Caldeira, V., Bellardita, C., Balueva, K., et al. (2015). Descending command neurons in the brainstem that halt locomotion. *Cell* 163, 1191–1203. doi: 10.1016/j.cell.2015.10.074

Buchanan, J. T. (2011). Spinal locomotor inputs to individually identified reticulospinal neurons in the lamprey. *J. Neurophysiol.* 106, 2346–2357. doi: 10.1152/jn.01100.2010

Bucy, P. C., Keplinger, J. E., and Siqueira, E. B. (1964). Destruction of the 'pyramidal tract' in man. *J. Neurosurg.* 21, 285–298.

Caggiano, V., Leiras, R., Goñi-Erro, H., Masini, D., Bellardita, C., Bouvier, J., et al. (2018). Midbrain circuits that set locomotor speed and gait selection. *Nature* 553, 455–460. doi: 10.1038/nature25448

Capelli, P., Pivetta, C., Soledad Esposito, M., and Arber, S. (2017). Locomotor speed control circuits in the caudal brainstem. *Nature* 551, 373–377. doi: 10.1038/nature24064

Chase, M. H., Morales, F. R., Boxer, P. A., Fung, S. J., and Soja, P. J. (1986). Effect of stimulation of the nucleus reticularis gigantocellularis on the membrane potential of cat lumbar motoneurons during sleep and wakefulness. *Brain Res.* 386, 237–244. doi: 10.1016/0006-8993(86)90160-5

Cui, G., Jun, S. B., Jin, X., Pham, M. D., Vogel, S. S., Lovinger, D. M., et al. (2013). Concurrent activation of striatal direct and indirect pathways during action initiation. *Nature* 494, 238–242. doi: 10.1038/nature11846

Davis, M., Gendelman, D. S., Tischler, M. D., and Gendelman, P. M. (1982). A primary acoustic startle circuit: lesion and stimulation studies. *J. Neurosci.* 2, 791–805.

Degtyarenko, A. M., Simon, E. S., and Burke, R. E. (1998). Locomotor modulation of disynaptic EPSPs from the mesencephalic locomotor region in cat motoneurons. *J. Neurophysiol.* 80, 3284–3296. doi: 10.1152/jn.1998.80.6.3284

Douglas, J. R., Noga, B. R., Dai, X., and Jordan, L. M. (1993). The effects of intrathecal administration of excitatory amino-acid agonists and antagonists on the initiation of locomotion in the adult cat. *J. Neurosci.* 13, 990–1000.

Drew, T., Cabana, T., and Rossignol, S. (1996). Responses of medullary reticulospinal neurones to stimulation of cutaneous limb nerves during locomotion in intact cats. *Exp. Brain Res.* 111, 153–168. doi: 10.1007/bf00227294

Drew, T., Dubuc, R., and Rossignol, S. (1986). Discharge patterns of reticulospinal and other reticular neurons in chronic, unrestrained cats walking on a treadmill. *J. Neurophysiol.* 55, 375–401. doi: 10.1152/jn.1986.55.2.375

Drew, T., and Rossignol, S. (1990). Functional organization within the medullary reticular formation of intact unanesthetized cat. II. Electromyographic activity evoked by microstimulation. *J. Neurophysiol.* 64, 782–795. doi: 10.1152/jn.1990.64.3.782

Du Beau, A., Shakya Shrestha, S., Bannatyne, B. A., Jalicy, S. M., Linnen, S., and Maxwell, D. J. (2012). Neurotransmitter phenotypes of descending systems in the rat lumbar spinal cord. *Neuroscience* 227, 67–79. doi: 10.1016/j.neuroscience.2012.09.037

Eaton, R. C., DiDomenico, R., and Nissanov, J. (1988). Flexible body dynamics of the goldfish C-start: implications for reticulospinal command mechanisms. *J. Neurosci.* 8, 2758–2768.

Eaton, R. C., Lee, R. K. K., and Foreman, M. B. (2001). The Mauthner cell and other identified neurons of the brainstem escape network of fish. *Prog. Neurobiol.* 63, 467–485. doi: 10.1016/s0301-0082(00)00047-2

Einum, J. F., and Buchanan, J. T. (2004). Reticulospinal neurons receive direct spinobulbar inputs during locomotor activity in lamprey. *J. Neurophysiol.* 92, 1384–1390. doi: 10.1152/jn.00625.2003

Esposito, M. S., Capelli, P., and Arber, S. (2014). Brainstem nucleus MdV mediates skilled forelimb motor tasks. *Nature* 508, 351–356. doi: 10.1038/nature13023

Faber, D. S., Fetcho, J. R., and Korn, H. (1989). Neuronal networks underlying the escape response in goldfish. *Ann. N Y Acad. Sci.* 563, 11–33. doi: 10.1111/j.1749-6632.1989.tb42187.x

Fetcho, J. R. (1991). Spinal network of the Mauthner cell. *Brain Behav. Evol.* 37, 298–316. doi: 10.1159/000316094

Fetcho, J. R. (1992). The spinal motor system in early vertebrates and some of its evolutionary changes. *Brain Behav. Evol.* 40, 82–97. doi: 10.1159/000113905

Fetcho, J. R., and Faber, D. S. (1988). Identification of motoneurons and interneurons in the spinal network for escapes initiated by the mauthner cell in goldfish. *J. Neurosci.* 8, 4192–4213.

Fuller, P. M., Saper, C. B., and Lu, J. (2007). The pontine REM switch: past and present. *J. Physiol.* 584, 735–741. doi: 10.1113/jphysiol.2007.140160

Garcia-Rill, E., and Skinner, R. D. (1987). The mesencephalic locomotor region. I. Activation of a medullary projection site. *Brain Res.* 411, 1–12. doi: 10.1016/0006-8993(87)90675-5

Graham Brown, T. (1911). The intrinsic factors in the act of progression in the mammal. *Proc. R. Soc. B Biol. Sci.* 84, 308–319. doi: 10.1098/rspb.1911.0077

Grillner, S., and Lund, S. (1968). The origin of a descending pathway with monosynaptic action on flexor motoneurones. *Acta Physiol. Scand.* 74, 274–284. doi: 10.1111/j.1748-1716.1968.tb04236.x

Hammond, G. R. (1973). Lesions of pontine and medullary reticular formation and prestimulus inhibition of the acoustic startle reaction in rats. *Physiol. Behav.* 10, 239–243. doi: 10.1016/0031-9384(73)90304-1

Henley, K., and Morrison, A. R. (1974). A re-evaluation of the effects of lesions of the pontine tegmentum and locus coeruleus on phenomena of paradoxical sleep in the cat. *Acta Neurobiol. Exp.* 34, 215–232.

Hildebrand, D. G. C., Cicconet, M., Torres, R. M., Choi, W., Quan, T. M., Moon, J., et al. (2017). Whole-brain serial-section electron microscopy in larval zebrafish. *Nature* 545, 345–349. doi: 10.1038/nature22356

Humphries, M. D., Gurney, K., and Prescott, T. J. (2006). The brainstem reticular formation is a small-world, not scale-free, network. *Proc. R. Soc. B Biol. Sci.* 273, 503–511. doi: 10.1098/rspb.2005.3354

Humphries, M. D., Gurney, K., and Prescott, T. J. (2007). Is there a brainstem substrate for action selection? *Philos. Trans. R. Soc. London Ser. B Biol. Sci.* 362, 1627–1639. doi: 10.1098/rstb.2007.2057

Jankowska, E. (2008). Spinal interneuronal networks in the cat: elementary components. *Brain Res. Rev.* 57, 46–55. doi: 10.1016/j.brainresrev.2007.06.022

Jankowska, E., and Edgley, S. A. (2006). How can corticospinal tract neurons contribute to ipsilateral movements? A question with implications for recovery of motor functions. *Neuroscientist* 12, 67–79. doi: 10.1177/1073858405283392

Jankowska, E., Jukes, M., Lund, S., and Lundberg, A. (1967). The effect of DOPA on the spinal cord. 6. Half-centre organization of interneurones transmitting effects from the flexor reflex afferents. *Acta Physiol. Scand.* 70, 389–402. doi: 10.1111/j.1748-1716.1967.tb03637.x

Jordan, L. M. (1998). Initiation of locomotion in mammals. *Ann. N Y Acad. Sci.* 860, 83–93. doi: 10.1111/j.1749-6632.1998.tb09040.x

Jordan, L. M., Liu, J., Hedlund, P. B., Akay, T., and Pearson, K. G. (2008). Descending command systems for the initiation of locomotion in mammals. *Brain Res. Rev.* 57, 183–191. doi: 10.1016/j.brainresrev.2007.07.019

Juvin, L., Grätsch, S., Trillaud-Doppia, E., Gariépy, J. F., Büschges, A., and Dubuc, R. (2016). A specific population of reticulospinal neurons controls the termination of locomotion. *Cell Rep.* 15, 2377–2386. doi: 10.1016/j.celrep.2016.05.029

Kawahara, K., Mori, S., Tomiyama, T., and Kanaya, T. (1985). Discharges of neurons in the midpontine dorsal tegmentum of mesencephalic cat during locomotion. *Brain Res.* 341, 377–380. doi: 10.1016/0006-8993(85)91078-9

Kim, L. H., Sharma, S., Sharples, S. A., Mayr, K. A., Kwok, C. H. T., and Whelan, P. J. (2017). Integration of descending command systems for the generation of context-specific locomotor behaviors. *Front. Neurosci.* 11:581. doi: 10.3389/fnins.2017.00581

Kimmel, C. B. (1993). Patterning the brain of the zebrafish embryo. *Annu. Rev. Neurosci.* 16, 707–732. doi: 10.1146/annurev.neuro.16.1.707

Kita, T., and Kita, H. (2012). The subthalamic nucleus is one of multiple innervation sites for long-range corticofugal axons: a single-axon tracing study in the rat. *J. Neurosci.* 32, 5990–5999. doi: 10.1523/JNEUROSCI.5717-11.2012

Kupfermann, I., and Weiss, K. R. (1978). The command neuron concept. *Behav. Brain Sci.* 1, 3–10. doi: 10.1017/s0140525x00059057

Lawrence, D. G., and Kuypers, H. G. J. M. (1968a). The functional organization of the motor system in the monkey: I. The effects of bilateral pyramidal lesions. *Brain* 91, 1–14. doi: 10.1093/brain/91.1.1

Lawrence, D. G., and Kuypers, H. G. J. M. (1968b). The functional organization of the motor system in the monkey: II. The effects of lesions of the descending brain-stem pathways. *Brain* 91, 15–36. doi: 10.1093/brain/91.1.15

Leitner, D. S., Powers, A. S., and Hoffman, H. S. (1980). The neural substrate of the startle response. *Physiol. Behav.* 25, 291–297. doi: 10.1016/0031-9384(80)90219-x

Lemon, R. N. (2008). Descending pathways in motor control. *Annu. Rev. Neurosci.* 31, 195–218. doi: 10.1146/annurev.neuro.31.060407.125547

Le Ray, D., Juvin, L., Boutin, T., Auclair, F., and Dubuc, R. (2010). A neuronal substrate for a state-dependent modulation of sensory inputs in the brainstem. *Eur. J. Neurosci.* 32, 53–59. doi: 10.1111/j.1460-9568.2010.07276.x

Liang, H., Paxinos, G., and Watson, C. (2011). Projections from the brain to the spinal cord in the mouse. *Brain Struct. Funct.* 215, 159–186. doi: 10.1007/s00429-010-0281-x

Limousin, N., Dehais, C., Gout, O., Héran, F., Oudiette, D., and Arnulf, I. (2009). A brainstem inflammatory lesion causing REM sleep behavior disorder and sleepwalking (parasomnia overlap disorder). *Sleep Med.* 10, 1059–1062. doi: 10.1016/j.sleep.2008.12.006

Liu, Y. C., and Hale, M. E. (2017). Local spinal cord circuits and bilateral mauthner cell activity function together to drive alternative startle behaviors. *Curr. Biol.* 27, 697–704. doi: 10.1016/j.cub.2017.01.019

Llinas, R., and Terzuolo, C. (1964a). Mechanisms of supraspinal actions upon spinal cord activities. Reticular inhibitory mechanisms on alpha-extensor motoneurons. *J. Neurophysiol.* 27, 579–591. doi: 10.1152/jn.1964.27.4.579

Llinas, R., and Terzuolo, C. (1964b). Mechaniss of supraspinal actions upon spinal cord activities. Reticular inhibitory mechanisms upon flexor motoneurons. *J. Neurophysiol.* 28, 413–422. doi: 10.1152/jn.1965.28.2.413

Lu, J., Sherman, D., Devor, M., and Saper, C. B. (2006). A putative flip-flop switch for control of REM sleep. *Nature* 441, 589–594. doi: 10.1038/nature04767

Magoun, H. (1944). Bulbar inhibition and facilitation of motor activity. *Science* 100, 549–550. doi: 10.1126/science.100.2607.549

Magoun, H., and Rhines, R. (1946). An inhibitory mechanism in the bulbar reticular formation. *J. Neurophysiol.* 9, 165–171. doi: 10.1152/jn.1946.9.3.165

Marlinskii, V. V., and Voitenko, L. P. (1992). Participation of the medial reticular formation of the medulla oblongata in the supraspinal control of locomotor and postural activities in the guinea pig. *Neurosci. Behav. Physiol.* 22, 336–342. doi: 10.1007/bf01182876

Matsuyama, K., and Drew, T. (2000). Vestibulospinal and reticulospinal neuronal activity during locomotion in the intact cat. II. Walking on an inclined plane. *J. Neurophysiol.* 84, 2257–2276. doi: 10.1152/jn.2000.84.5.2257

Matsuyama, K., Mori, F., Kuze, B., and Mori, S. (1999). Morphology of single pontine reticulospinal axons in the lumbar enlargement of the cat: a study using the anterograde tracer PHA-L. *J. Comp. Neurol.* 410, 413–430. doi: 10.1002/(sici)1096-9861(19990802)410:3<413::aid-cne5>3.0.co;2-q

Matsuyama, K., Nakajima, K., Mori, F., Aoki, M., and Mori, S. (2004). Lumbar commissural interneurons with reticulospinal inputs in the cat: morphology and discharge patterns during fictive locomotion. *J. Comp. Neurol.* 474, 546–561. doi: 10.1002/cne.20131

Matsuyama, K., Ohta, Y., and Mori, S. (1988). Ascending and descending projections of the nucleus reticularis gigantocellularis in the cat demonstrated by the anterograde neural tracer, Phaseolus vulgaris leucoagglutinin (PHA-L). *Brain Res.* 460, 124–141. doi: 10.1016/0006-8993(88)91212-7

McClellan, A. D., and Grillner, S. (1984). Activation of 'fictive swimming' by electrical microstimulation of brainstem locomotor regions in an *in vitro* preparation of the lamprey central nervous system. *Brain Res.* 300, 357–361. doi: 10.1016/0006-8993(84)90846-1

Mitchell, E. J., McCallum, S., Dewar, D., and Maxwell, D. J. (2016). Corticospinal and reticulospinal contacts on cervical commissural and long descending propriospinal neurons in the adult rat spinal cord; evidence for powerful reticulospinal connections. *PLoS One* 11:e0155664. doi: 10.1371/journal.pone.0155664

Mori, S. (1987). Integration of posture and locomotion in acute decebrate cats and in a wake, freely moving cats. *Prog. Neurobiol.* 28, 161–195. doi: 10.1016/0301-0082(87)90010-4

Mori, S., Kawahara, K., Sakamoto, T., Aoki, M., and Tomiyama, T. (1982). Setting and resetting of level of postural muscle tone in decerebrate cat by stimulation of brain stem. *J. Neurophysiol.* 48, 737–748. doi: 10.1152/jn.1982.48.3.737

Mori, S., Matsui, T., Kuze, B., Asanome, M., Nakajima, K., and Matsuyama, K. (1998). Cerebellar-induced locomotion: reticulospinal control of spinal rhythm generating mechanism in cats. *Ann. N Y Acad. Sci.* 860, 94–105. doi: 10.1111/j.1749-6632.1998.tb09041.x

Mori, S., Nishimura, H., Kurakami, C., Yamamura, T., and Aoki, M. (1978). Controlled locomotion in the mesencephalic cat: distribution of facilitatory and inhibitory regions within pontine tegmentum. *J. Neurophysiol.* 41, 1580–1591. doi: 10.1152/jn.1978.41.6.1580

Mori, S., Ohta, Y., Matsuyama, K., and Takukuski, K. (1986). "The setting of postural muscle tone: its importance for behaviors in freely moving intact cats," in *Emotions: Neuronal and Chemical Control*, ed. Y. Oomura (Basel: Karger), 231–239.

Mouret, J., Delorme, F., and Jouvet, M. (1967). Lesions of the pontine tegmentum field. *Compt. Soc. Biol. Fil.* 161, 1603–1606.

Noga, B. R., Kettler, J., and Jordan, L. M. (1988). Locomotion produced in mesencephalic cats by injections of putative transmitter substances and antagonists into the medial reticular formation and the pontomedullary locomotor strip. *J. Neurosci.* 8, 2074–2086. doi: 10.1523/JNEUROSCI.08-06-02074.1988

Noga, B. R., Kriellaars, D. J., Brownstone, R. M., Jordan, L. M., Leiras, R., Velo, P., et al. (2003). Mechanism for activation of locomotor centers in the spinal cord by stimulation of the mesencephalic locomotor region mechanism for activation of locomotor centers in the spinal cord by stimulation of the mesencephalic locomotor region. *J. Neurophysiol.* 90, 1464–1478. doi: 10.1152/jn.00034.2003

Orlovskii, G. N. (1970). Work of the reticulo-spinal neurons during locomotion. *Biofizika* 15, 728–737.

Paxinos, G., and Franklin, B. (2008). *The Mouse Brain in Sterotaxic Coordinates.* 3rd Edn. Oxford: Academic Press.

Paxinos, G., Xu-Feng, H., Sengul, G., and Watson, C. (2012). "Organization of brainstem nuclei," in *The Huaman Nervous System*, eds J. K. Mai and G. Paxinos (Amsterdam: Elsevier Academic Press), 260–327.

Perreault, M. C., Drew, T., and Rossignol, S. (1993). Activity of medullary reticulospinal neurons during fictive locomotion. *J. Neurophysiol.* 69, 2232–2247. doi: 10.1152/jn.1993.69.6.2232

Perreault, M. C., and Glover, J. C. (2013). Glutamatergic reticulospinal neurons in the mouse: developmental origins, axon projections, and functional connectivity. *Ann. N Y Acad. Sci.* 1279, 80–89. doi: 10.1111/nyas.12054

Peterson, B. W. (1984). "The reticulospinal system and its role in the control of movement," in *Brainstem Control of Spinal Cord Function*, ed. C. D. Barnes (New York, NY: Academic Press), 27–86.

Peterson, B. W., Maunz, R. A., Pitts, N. G., and Mackel, R. G. (1975). Patterns of projection and branching of reticulospinal neurons. *Exp. Brain Res.* 23, 333–351. doi: 10.1007/bf00238019

Peterson, B. W., Pitts, N. G., Fukushima, K., and Mackel, R. (1978). Reticulospinal excitation and inhibition of neck motoneurons. *Exp. Brain Res.* 32, 471–489. doi: 10.1007/bf00239548

Prasada Rao, P. D., Jadhao, A. G., and Sharma, S. C. (1987). Descending projection neurons to the spinal cord of the goldfish, Carassius auratus. *J. Comp. Neurol.* 265, 96–108. doi: 10.1002/cne.902650107

Rhines, R., and Magoun, H. (1946). Brain stem facilitation of cortical motor response. *J. Neurophysiol.* 9, 219–229. doi: 10.1152/jn.1946.9.3.219

Riddle, C. N., Edgley, S. A., and Baker, S. N. (2009). Direct and indirect connections with upper limb motoneurons from the primate reticulospinal tract. *J. Neurosci.* 29, 4993–4999. doi: 10.1523/JNEUROSCI.3720-08.2009

Roseberry, T. K., Lee, A. M., Lalive, A. L., Wilbrecht, L., Bonci, A., and Kreitzer, A. C. (2016). Cell-type-specific control of brainstem locomotor circuits by basal ganglia. *Cell* 164, 526–537. doi: 10.1016/j.cell.2015.12.037

Rothwell, J. C. (2006). The startle reflex, voluntary movement, and the reticulospinal tract. *Suppl. Clin. Neurophysiol.* 58, 223–231. doi: 10.1016/s1567-424x(09)70071-6

Saper, C. B., Fuller, P. M., Pedersen, N. P., Lu, J., and Scammell, T. E. (2010). Sleep state switching. *Neuron* 68, 1023–1042. doi: 10.1016/j.neuron.2010.11.032

Sasaki, S., Isa, T., Pettersson, L. G., Alstermark, B., Naito, K., Yoshimura, K., et al. (2004). Dexterous finger movements in primate without monosynaptic corticomotoneuronal excitation. *J. Neurophysiol.* 92, 3142–3147. doi: 10.1152/jn.00342.2004

Sastre, J. P., Sakai, K., and Jouvet, M. (1981). Are the gigantocellular tegmental field neurons responsible for paradoxical sleep? *Brain Res.* 229, 147–161. doi: 10.1016/0006-8993(81)90752-6

Schenck, C. H., and Mahowald, M. W. (1995). A polysomnographically documented case of adult somnambulism with long-distance automobile driving and frequent nocturnal violence: parasomnia with continuing danger as a noninsane automatism? *Sleep* 18, 765–772. doi: 10.1093/sleep/18.9.765

Schepens, B. (2004). Independent and convergent signals from the pontomedullary reticular formation contribute to the control of posture and movement during reaching in the cat. *J. Neurophysiol.* 92, 2217–2238. doi: 10.1152/jn.01189.2003

Schmidt, B. J., and Jordan, L. M. (2000). The role of serotonin in reflex modulation and locomotor rhythm production in the mammalian spinal cord. *Brain Res. Bull.* 53, 689–710. doi: 10.1016/s0361-9230(00)00402-0

Shapovalov, A. (1972). Evolution of neuronal systems of suprasegmental motor control. *Neurophysiology* 4, 346–359. doi: 10.1007/bf01063005

Sherrington, C. S. (1898). Decerebrate rigidity and reflex coordination of movements. *J. Physiol.* 22, 319–332. doi: 10.1113/jphysiol.1898.sp000697

Shik, M. L., Severin, F. V., and Orlovskii, G. N. (1966). Control of walking and running by means of electrical stimulation of the midbrain. *Biofizika* 11, 659–666.

Shimamura, M., and Kogure, I. (1983). Discharge patterns of reticulospinal neurons corresponding with quadrupedal leg movements in thalamic cats. *Brain Res.* 260, 27–34. doi: 10.1016/0006-8993(83)90761-8

Shimamura, M., Kogure, I., and Wada, S. (1980). Three types of reticular neurons involved in the spinobulbo-spinal reflex of cats. *Brain Res.* 186, 99–113. doi: 10.1016/0006-8993(80)90258-9

Shimamura, M., Kogure, I., and Wada, S. I. (1982). Reticular neuron activities associated with locomotion in thalamic cats. *Brain Res.* 231, 51–62. doi: 10.1016/0006-8993(82)90006-3

Siegel, J. M., Nienhuis, R., Wheeler, R. L., McGinty, D. J., and Harper, R. M. (1981). Discharge pattern of reticular formation unit pairs in waking and REM sleep. *Exp. Neurol.* 74, 875–891. doi: 10.1016/0014-4886(81)90260-0

Sillar, K. T., Picton, L. D., and Heitler, W. J. (2016). *The Neuroethology of Predation and Escape.* 1st Edn. Oxford: Wiley-Blackwell.

Sinnamon, H. M. (1993). Preoptic and hypothalamic neurons and the initiation of locomotion in the anesthetized rat. *Prog. Neurobiol.* 41, 323–344. doi: 10.1016/0301-0082(93)90003-b

Sinnamon, H. M., and Stopford, C. K. (1987). Locomotion elicited by lateral hypothalamic stimulation in the anesthetized rat does not require the dorsal midbrain. *Brain Res.* 402, 78–86. doi: 10.1016/0006-8993(87)91049-3

Sivertsen, M. S., Perreault, M. C., and Glover, J. C. (2016). Pontine reticulospinal projections in the neonatal mouse: internal organization and axon trajectories. *J. Comp. Neurol.* 524, 1270–1291. doi: 10.1002/cne.23904

Skinner, R. D., and Garcia-Rill, E. (1984). The mesencephalic locomotor region (MLR) in the rat. *Brain Res.* 323, 385–389. doi: 10.1016/0006-8993(84)90319-6

Sprague, J. M., and Chamber, W. W. (1954). Control of posture by reticular formation and cerebellum in the intact, anesthetized and unanesthetized and in the decerebrated cat. *Am. J. Physiol.* 176, 52–64. doi: 10.1152/ajplegacy.1953.176.1.52

Stecina, K. (2017). Midbrain stimulation-evoked lumbar spinal activity in the adult decerebrate mouse. *J. Neurosci. Methods* 288, 99–105. doi: 10.1016/j.jneumeth.2017.06.015

Steeves, J. D., and Jordan, L. M. (1980). Localization of a descending pathway in the spinal cord which is necessary for controlled treadmill locomotion. *Neurosci. Lett.* 20, 282–288. doi: 10.1016/0304-3940(80)90161-5

Steeves, J. D., Sholomenko, G. N., and Webster, D. M. S. (1987). Stimulation of the pontomedullary reticular formation initiates locomotion in decerebrate birds. *Brain Res.* 401, 205–212. doi: 10.1016/0006-8993(87)91406-5

Szokol, K., Glover, J. C., and Perreault, M.-C. (2011). Organization of functional synaptic connections between medullary reticulospinal neurons and lumbar descending commissural interneurons in the neonatal mouse. *J. Neurosci.* 31, 4731–4742. doi: 10.1523/JNEUROSCI.5486-10.2011

Szokol, K., Glover, J. C., Perreault, M.-C., and Perreault, M.-C. (2008). Differential origin of reticulospinal drive to motoneurons innervating trunk and hindlimb muscles in the mouse revealed by optical recording. *J. Physiol.* 58621, 5259–5276. doi: 10.1113/jphysiol.2008.158105

Takakusaki, K., Chiba, R., Nozu, T., and Okumura, T. (2016). Brainstem control of locomotion and muscle tone with special reference to the role of the mesopontine tegmentum and medullary reticulospinal systems. *J. Neural Transm. (Vienna)* 123, 695–729. doi: 10.1007/s00702-015-1475-4

Takakusaki, K., Kohyama, J., Matsuyama, K., and Mori, S. (1993a). Synaptic mechanisms acting on lumbar motoneurons during postural augmentation induced by serotonin injection into the rostral pontine reticular formation in decerebrate cats. *Exp. Brain Res.* 93, 471–482. doi: 10.1007/bf00229362

Takakusaki, K., Matsuyama, K., Kobayashi, Y., Kohyama, J., and Mori, S. (1993b). Pontine microinjection of carbachol and critical zone for inducing postural atonia in reflexively standing decerebrate cats. *Neurosci. Lett.* 153, 185–188. doi: 10.1016/0304-3940(93)90318-f

Valencia Garcia, S., Brischoux, F., Clément, O., Libourel, P.-A., Arthaud, S., Lazarus, M., et al. (2018). Ventromedial medulla inhibitory neuron inactivation induces REM sleep without atonia and REM sleep behavior disorder. *Nat. Commun.* 9:504. doi: 10.1038/s41467-017-02761-0

Valls-Solé, J., Rothwell, J. C., Goulart, F., Cossu, G., and Muñoz, E. (1999). Patterned ballistic movements triggered by a startle in healthy humans. *J. Physiol.* 516, 931–938. doi: 10.1111/j.1469-7793.1999.0931u.x

Wilson, V. J., and Yoshida, M. (1969). Comparison of effects of stimulation of Deiters' nucleus and medial longitudinal fasciculus on neck, forelimb and hindlimb motoneurons. *J. Neurophysiol.* 32, 743–758. doi: 10.1152/jn.1969.32.5.743

Wilson, V. J., Yoshida, M., and Schor, R. H. (1970). Supraspinal monosynaptic excitation and inhibition of thoracic back motoneurons. *Exp. Brain Res.* 11, 282–295. doi: 10.1007/bf01474387

Yasargil, G. M., and Sandri, C. (1990). Topography and ultrastructure of commissural interneurons that may establish reciprocal inhibitory connections of the Mauthner axons in the spinal cord of the tench, Tinca tinca L. *J. Neurocytol.* 19, 111–126. doi: 10.1007/bf01188443

Zaaimi, B., Edgley, S. A., Soteropoulos, D. S., and Baker, S. N. (2012). Changes in descending motor pathway connectivity after corticospinal tract lesion in macaque monkey. *Brain* 135, 2277–2289. doi: 10.1093/brain/aws115

Zottoli, S. J. (1977). Correlation of the startle reflex and Mauthner cell auditory responses in unrestrained goldfish. *J. Exp. Biol.* 66, 243–254.

Conflict of Interest Statement: The authors declare that the research was conducted in the absence of any commercial or financial relationships that could be construed as a potential conflict of interest.

Copyright © 2018 Brownstone and Chopek. This is an open-access article distributed under the terms of the Creative Commons Attribution License (CC BY). The use, distribution or reproduction in other forums is permitted, provided the original author(s) and the copyright owner are credited and that the original publication in this journal is cited, in accordance with accepted academic practice. No use, distribution or reproduction is permitted which does not comply with these terms.

frontiers in Physiology

ORIGINAL RESEARCH
published: 17 July 2018
doi: 10.3389/fphys.2018.00881

Inspiratory-Activated Airway Vagal Preganglionic Neurones Excited by Thyrotropin-Releasing Hormone via Multiple Mechanisms in Neonatal Rats

Lili Hou[1,2,3], Min Zhang[1], Xingyi Zhang[1], Zhenwei Liu[1], Pengyu Zhang[1], Dongying Qiu[2,4,5], Lei Zhu[3] and Xin Zhou[1]**

[1] Department of Respiratory and Critical Care Medicine, Shanghai General Hospital, Shanghai Jiao Tong University, Shanghai, China, [2] Department of Neurobiology, School of Basic Medical Sciences, Fudan University, Shanghai, China, [3] Department of Respiratory Medicine, Zhongshan Hospital, Fudan University, Shanghai, China, [4] Department of Physiology and Pathophysiology, School of Basic Medical Sciences, Fudan University, Shanghai, China, [5] Department of Gerontology, Zhongshan Hospital, Fudan University, Shanghai, China

OPEN ACCESS

Edited by:
Brian R. Noga,
University of Miami, United States

Reviewed by:
Klaus Ballanyi,
University of Alberta, Canada
Stephen M. Johnson,
University of Wisconsin-Madison, United States

***Correspondence:**
Lei Zhu
tfzhu@126.com
Xin Zhou
zhouxin_rm@163.com

Specialty section:
This article was submitted to Respiratory Physiology, a section of the journal Frontiers in Physiology

Received: 03 March 2018
Accepted: 19 June 2018
Published: 17 July 2018

Citation:
Hou L, Zhang M, Zhang X, Liu Z, Zhang P, Qiu D, Zhu L and Zhou X (2018) Inspiratory-Activated Airway Vagal Preganglionic Neurones Excited by Thyrotropin-Releasing Hormone via Multiple Mechanisms in Neonatal Rats. Front. Physiol. 9:881. doi: 10.3389/fphys.2018.00881

The airway vagal preganglionic neurons (AVPNs) providing projections to intrinsic tracheobronchial ganglia are considered to be crucial to modulation of airway resistance in physiological and pathological states. AVPNs classified into inspiratory-activated AVPNs (IA-AVPNs) and inspiratory-inhibited AVPNs (II-AVPNs) are regulated by thyrotropin-releasing hormone (TRH)-containing terminals. TRH causes a direct excitatory current and attenuates the phasic inspiratory glycinergic inputs in II-AVPNs, however, whether and how TRH influences IA-AVPNs remains unknown. In current study, TRH regulation of IA-AVPNs and its mechanisms involved were investigated. Using retrogradely fluorescent labeling method and electrophysiology techniques to identify IA-AVPNs in brainstem slices with rhythmic inspiratory hypoglossal bursts recorded by a suction electrode, the modulation of TRH was observed with patch-clamp technique. The findings demonstrate that under voltage clamp configuration, TRH (100 nM) caused a slow excitatory inward current, augmented the excitatory synaptic inputs, progressively suppressed the inhibitory synaptic inputs and elicited a distinctive electrical oscillatory pattern (OP). Such a current and an OP was independent of presynaptic inputs. Carbenoxolone (100 μM), a widely used gap junction inhibitor, fully suppressed the OP with persistence of TRH-induced excitatory slow inward current and augment of the excitatory synaptic inputs. Both tetrodotoxin (1 μM) and riluzole (20 μM) functioned to block the majority of the slow excitatory inward current and prevent the OP, respectively. Under current clamp recording, TRH caused a slowly developing depolarization and continuously progressive oscillatory firing pattern sensitive to TTX. TRH increased the firing

frequency in response to injection of a square-wave current. The results suggest that TRH excited IA-AVPNs via the following multiple mechanisms: (1) TRH enhances the excitatory and depresses the inhibitory inputs; (2) TRH induces an excitatory postsynaptic slow inward current; (3) TRH evokes a distinctive OP mediated by gap junction.

Keywords: thyrotropin-releasing hormone, airway vagal preganglionic neuron, gap junction, oscillation, patch clamp, asthma

INTRODUCTION

Bronchial asthma, a type of common chronic airway disease worldwide, has prominent features of airway hyper-responsiveness, inflammation and excessive activation of cholinergic fibers to the trachea and bronchioles. The mechanisms of neural reflex pathways involved are regarded as very primary points in the process of this disease. In reflex pathways the AVPNs located in medulla oblongata conveying signals from brain to the intrinsic tracheobronchial ganglia are considered to be very crucial for regulating airway function either in diseased conditions or normal states (Haxhiu et al., 2005; McGovern and Mazzone, 2010).

Airway vagal preganglionic neurons have been mainly found in the external compact of nucleus ambiguus (eNA) via application of fluorescent tracer to the extrathoracic tracheal wall (Haselton et al., 1992; Haxhiu and Loewy, 1996; Kc et al., 2004; Chen Y. et al., 2007; Qiu et al., 2011; Chen et al., 2012a,b; Hou et al., 2012, 2015; Zhou et al., 2013; Ge et al., 2015; Guo et al., 2017; Yan et al., 2017). AVPNs in the eNA function as the main neurons which modulate cholinergic tone of airway smooth muscles as well as control the intrapulmonary airway resistance and tracheobronchial caliber (Haselton et al., 1992; Canning and Fischer, 2001; Yan et al., 2017). As shown in previous studies *in vivo* and *in vitro*, postganglionic neurons in intrinsic tracheobronchial ganglia have been identified as "phasic" neurons and "tonic" ones, the former firing in phase with inspiration and primarily projecting to tracheobronchial smooth muscles, and the latter firing tonically during expiration and primarily projecting to the intercartilaginous spaces (Baker, 1986; Mitchell et al., 1987; Myers et al., 1990; Myers, 1998). AVPNs in the eNA also exhibit different rhythmic changes of synaptic inputs in parallel with central inspiratory activities (Chen Y. et al., 2007; Qiu et al., 2011; Chen et al., 2012a,b; Hou et al., 2012, 2015; Zhou et al., 2013; Ge et al., 2015; Guo et al., 2017; Yan et al., 2017). Thus, two types of AVPNs are identified according to their different synaptic control during inspiratory phase: some neurons activated by phasic excitatory inputs are identified as IA-AVPNs, and others inhibited by phasic inhibitory inputs are separated as inspiratory-inhibited airway vagal preganglionic neurons (II-AVPNs) (Chen Y. et al., 2007; Qiu et al., 2011; Chen et al., 2012a,b; Hou et al., 2012; Zhou et al., 2013; Ge et al., 2015; Guo et al., 2017; Yan et al., 2017). Morphological and electrical studies have shown that excitatory and inhibitory synaptic inputs from various brain regions determine the excitability of AVPNs (Haxhiu et al., 1993, 2002, 2003, 2005, 2008; Kc et al., 2006; Wilson et al., 2007; Chen et al., 2012b; Hou et al., 2012; Zhou et al., 2013; Ge et al., 2015; Guo et al., 2017; Yan et al., 2017), although AVPNs are capable of generating synchronous electrical oscillatory pattern (OP), revealed by "activation of NMDA receptors" or "blockade of $GABA_A$ receptors" (Haxhiu et al., 1987, 2005; Moore et al., 2004).

Nerves containing TRH innervate the airway vagal motor neurons in the cNA (Iwase et al., 1992; Sun et al., 1995). Microinjection of TRH, a neuropeptide well-known to excite the respiratory neurons in the PBC, into the NA induces first decrease and then increase of the tracheal pressure (Iwase et al., 1992). TRH affects neurons in the NA of adult guinea pigs by three different ways: depolarization, causing membrane potential oscillations and enhancement of postinhibitory rebound (Johnson and Getting, 1992), indicating that TRH could mediate complex alternations of membrane characteristics in neurons of NA. As demonstrated by the previous study in our laboratory, II-AVPNs were excited by TRH via both postsynaptic and presynaptic mechanisms (Hou et al., 2012). It has been reported that IA-AVPNs differ from II-AVPNs in anatomical location and intrinsic properties (Chen Y. et al., 2007; Chen et al., 2012a). Thus TRH modulation of IA-AVPNs is perhaps distinct from that of II-AVPNs, so how TRH regulates IA-AVPNs still remains elusive. In the current study, IA-AVPNs in the eNA were retrogradely labeled using fluorescent dye and identified in rhythmically active brainstem slices. The influences of TRH on whole-cell current and membrane potential of IA-AVPNs were examined using patch clamp. The current experiment is performed to test the following hypothesis that TRH affects IA-AVPNs via multiple mechanisms in neonatal rats: (1) TRH enhances the excitatory and inhibits the inhibitory synaptic inputs; (2) TRH induces a direct postsynaptic slow inward current; (3) TRH evokes a distinctive OP mediated by gap junction.

Abbreviations: 4V, 4th ventricle; ACSF, artificial cerebral spinal fluid; AMPA, 2-amino-3-(5-methyl-3-oxo-1,2-oxazol-4-yl)propanoic acid; AP_5, D-2-amino-5-phosphonovalerate; CBX, carbenoxolone; AVPNs, airway vagal preganglionic neurons; cNA, the compact formation of the nucleus ambiguous; CNQX, 6-cyano-7-nitroquinoxaline-2,3-dione; DHPG, (RS)-3,5-dihydroxyphenylglycine; DMSO, dimethyl sulfoxide; DMV, dorsal motor nucleus of vagus; eNA, the external formation of the nucleus ambiguous; EPSCs, excitatory postsynaptic currents; EPSPs, excitatory postsynaptic potentials; GABA, γ-aminobutyric acid; IA-AVPNs, inspiratory-activated airway vagal preganglionic neurons; ICSs, inward current spikelets; IO, inferior olive; INaP, persistent sodium currents; K_{ATP}, ATP-sensitive potassium channels; NA, nucleus ambiguous; NMDA, *N*-methyl-D-aspartate; PBC, pre-Bötzinger complex; PY, pyramidal tract; QX314, lidocaine *N*-ethyl bromide; ROb, raphe obscurus nucleus; NTS, nucleus tractus solitarius; sp5, spinal trigeminal tract; Sp5I, spinal trigeminal nucleus, interpolar part; TBOA, DL-threo-β-benzyloxyaspartate; TRH, thyrotropin-releasing hormone; TTX, tetrodotoxin; XIIN, hypoglossal nucleus.

MATERIALS AND METHODS

Ethical Approval

The experiments were performed on 120 newborn rats. The protocol was approved by the Ethical Committee of Shanghai Medical College affiliated to Fudan University (No. 20110307-060) and by the Animal Care Committee of Shanghai General Hospital affiliated to Shanghai Jiao Tong University, the research was carried out in line with the guideline of "Guide for the Care and Use of Laboratory Animals" established by the National Institutes of Health.

Retrograde Fluorescent Labeling of AVPNs and Preparation of Brainstem Slices

The 3- to 4-day-old Sprague-Dawley rats (Shanghai Institute for Family Planning and Shanghai General Hospital) were anesthetized with inhalation of halothane (0.5 ml) and hypothermia, and then the AVPNs were labeled retrogradely by rhodamine which have been described in details in our previous studies (Chen Y. et al., 2007; Chen et al., 2012a; Hou et al., 2012). Briefly, the extra thoracic trachea was exposed via a ventral midline incision in the neck. The fluorescent tracer rhodamine (XRITC, Molecular Probes, 1% solution, 0.5 μl) was injected into the tracheal wall between the fourth and eighth tracheal cartilage using a glass pipette of which the tip diameter was 30 μm with a syringe through polyethylene tubing attached. 48 h later, the animal was recovered. Halothane was used again to anesthetize the animal deeply as described above and then was decapitated. The brainstem was dissected out under a dissection microscope and then was submerged into ice-cold (4°C) ACSF which included (in mM) NaCl 124, KCl 3.0, KH_2PO_4 1.2, $CaCl_2$ 2.4, $MgSO_4$ 1.3, $NaHCO_3$ 26, D-glucose 10. The solution was constantly bubbled with 95% O_2–5% CO_2 to keep a pH of 7.4. The final osmolarity of ACSF was adjusted to 320 mosm/L with sucrose. The brainstem was then fixed with a chuck and submerged with the same ACSF in the slicing chamber. The rostral end of the brainstem was set upward; the dorsal surface was glued to an agar block facing the razor. Transverse brainstem slices of 500–800 μm thickness with two hypoglossal rootlets in each side (Smith et al., 1991) were cut using a vibratome (Leica VT 1000S). The brainstem slice with rhythmic inspiratory bursts (Smith et al., 1991) was transferred into the recording chamber (0.6 ml volume) to be superfused with high potassium (10 mM) ACSF at 23 ± 0.5°C. The rostral cutting plane of the slice was set upward to identify fluorescently labeled neurons and record synaptic activities of IA-AVPNs by patch clamp. The flow rate was maintained at 8–11 ml/min.

Electrophysiological Recording

The AVPNs were first identified by their characteristic distribution in the eNA (Chen Y. et al., 2007; Chen et al., 2012a) and by presence of fluorescence with a 40×-water immersion objective lens. The patch pipettes which was filled with K^+ gluconate-dominated internal solution included (in mM): K^+ gluconate 150, HEPES 10, EGTA 10, $CaCl_2$ 1, and $MgCl_2$ 1; pH 7.3; 320 mosm/L. The holding voltage was normally set as −80 mV. In these recording conditions, only excitatory glutamatergic synaptic events were detectable, and the inhibitory synaptic currents mediated by chloride ion were minimized. When the IA-AVPN was clamped at −50 mV, both excitatory synaptic events manifesting inward currents and inhibitory synaptic events showing outward currents were detected. In some experiments, QX314 (lidocaine *N*-ethyl bromide, 2.0 mM) was put into the pipette solution to prevent activation of voltage-dependent sodium currents and slow inward rectifier (I_h) (Marchetti et al., 2003; Sharifullina et al., 2005) of the patched neuron. IA-AVPNs were defined as those that were inspiratorily activated, as manifested by the rhythmic inspiratory discharges under cell-attached configuration (holding voltage 0 mV), by the rhythmic inspiratory bursts of the EPSCs under voltage clamp, or by the rhythmic inspiratory depolarizing EPSPs with superimposed trains of action potentials under current clamp (Chen Y. et al., 2007; Chen et al., 2012a). In each slice experiment was performed only on one IA-AVPN.

To get better recording of spontaneous inhibitory postsynaptic currents (sIPSCs) in some experiments, KCl-dominated internal solution was put into the patch pipette (in mM: KCL, 150; HEPES, 10; EGTA, 2; ATP-Mg, 2; pH 7.3; 320 mosm/L). The patched AVPNs were all clamped at −80 mV. Under this holding potential, both glutamatergic excitatory synaptic currents and sIPSCs in IA-AVPNs as well as sIPSCs in II-AVPNs were recorded as inward currents. In order to separate IA-AVPNs from II-AVPNs, the antagonists of glutamate receptors (CNQX and AP5) were topically applied to the patched neurons with the PV830 Pneumatic Picopump pressure delivery system (World Precision Instruments, Sarasota, FL, United States). IA-AVPNs were identified as those whose inspiratory inward currents could be abolished reversibly by CNQX and AP5.

The patch-clamp signal was amplified with an Axopatch 700B amplifier (10 kHz sampling frequency; 3 kHz filter frequency), digitized with 1322A digidata, and collected with Clampex 9.2 software (Axon Instruments, United States). The inspiratory hypoglossal bursts were recorded from hypoglossal rootlets using a suction electrode, amplified with a BMA-931 bioamplifier (5 kHz sampling frequency; 10–1,000 HZ band pass; 20,000 times), and electronically integrated (τ = 200 ms) with an MA-1000 Moving Averager (CWE Inc., Ardmore, PA, United States) before recording in the computer.

Drug Application

Carbenoxolone and glibenclamide were dissolved in DMSO to make fresh stock solution of 100 mM and diluted to 100 μM in the bath to block gap junctions and inhibit ATP-sensitive potassium channels (K_{ATP}), respectively. TRH affects the neural activity of inspiratory neurons and increases the discharging frequency of hypoglossal nerves in newborn mouse brainstem slices at the concentration of 1–5 μM (Rekling et al., 1996). In nucleus ambiguus neurons, 100 nM TRH induced membrane potential oscillations (Johnson and Getting, 1992). Thus two concentrations of TRH (1 μM and 100 nM) were used in this study at first. Because there were no significant differences between the effects of TRH

on IA-AVPNs at these two concentrations, 100 nM was then used in this study. TRH was applied normally in the bath at 100 nM for 3–5 min. Strychnine (1 μM) and picrotoxin (40 μM) were used to block glycine receptors and $GABA_A$ (γ-aminobutyric acid) receptors, respectively. CNQX (50 μM) and D-2-amino-5-phosphonovalerate (AP_5; 50 μM) were used to block non-NMDA and NMDA-type glutamate receptors, respectively. When KCL-dominated internal solution was used to record synaptic currents, CNQX and AP5 were first topically applied to distinguish IA-AVPNs from II-AVPNs, and then were added into the perfusate to block EPSCs. In some experiments, TTX (1 μM) was included in the bath to prevent action potential generation and polysynaptic effects; riluzole (20 μM), to block persistent sodium currents (INaP). ACSF flowing into the chamber was all fresh and was not recycled. The drugs were purchased from Sigma-Aldrich (St. Louis, MO, United States).

Data Analysis

The hypoglossal bursts and the TRH-evoked fast oscillatory currents (FOCs) in IA-AVPNs were analyzed with Clampfit 9.2 (Axon Instrument, United States). Spontaneous or miniature synaptic currents, as well as the ICSs phase-locked to the rapid inward phase of FOCs, were analyzed with MiniAnalysis (version 4.3.1, Synaptosoft), with a minimally acceptable amplitude at 10 pA. Regression analysis was performed with Origin 8.0 (OriginLab Corporation, Northampton, MA, United States). The results were presented as means ± SEM, and statistically compared with paired or independent Student's *t*-test when appropriate. The significant difference was set at $P < 0.05$.

RESULTS

Identification of Inspiratory-Activated Airway Vagal Preganglionic Neurons (IA-AVPNs)

Inspiratory-activated airway vagal preganglionic neurons were first identified by the presence of fluorescence and by their characteristic distribution in the eNA, which is in the close ventral, ventrolateral and ventromedial vicinity of the cNA (Chen Y. et al., 2007; Chen et al., 2012a) (**Figures 1A,B**).

Inspiratory-activated airway vagal preganglionic neurons were defined as those that were activated during inspiratory phase and were manifested by the rhythmic inspiratory-related discharges under cell-attached configuration (**Figure 1C**), by the rhythmic bursts of EPSCs during inspiratory phase under voltage clamp recording (**Figures 2A,D**) or by the rhythmic inspiratory-related depolarizing EPSPs superimposed by trains of action potentials under current clamp recording data not shown. Inspiratory inhibited AVPNs (II-AVPNs) were further defined as those that were inspiratorily inhibited and were manifested by the rhythmic bursts of the inhibitory (outward) postsynaptic currents (IPSCs) during inspiratory phase at holding voltages more positive than −50 mV or by the rhythmic hyperpolarizing inhibitory postsynaptic potentials (IPSPs) during inspiratory phase under current clamp recording (Chen Y. et al., 2007; Chen et al., 2012a). IA-AVPNs were mostly found in the close ventrolateral vicinity and II-AVPNs were mostly found in the near ventral or ventral medial vicinity of the cNA. From 120 slices, a total of 136 AVPNs were identified and tested, of which 120 were IA-AVPNs (88.2%) and 16 were II-AVPNs (11.8%).

TRH Caused an Excitatory Slow Inward Current and Fast Oscillatory Currents (FOCs) in IA-AVPNs

Under voltage clamp, TRH (100 nM) increased baseline current noise and caused a slowly developing excitatory inward current (**Figure 2A**), which peaked within 3 min, with an average amplitude of 55.3 ± 19.7 pA (from 12 neurones). As the excitatory slow inward current developed, the baseline current generated a fast oscillatory change with respect to a steady level reached by TRH. This change was readily recognizable during the inspiratory intervals in all the 12 IA-AVPNs examined from 12 slices (**Figures 2B,C**), with an average cycle length of 201.2 ± 18.5 ms. In some (eight of twelve) IA-AVPNs, the change was also identifiable during the inspiratory phase (**Figures 2D,E**), with a significantly shorter cycle length of 90.1 ± 6.2 ms ($P < 0.05$ compared with the value during inter-inspiratory intervals; $n = 8$). The amplitude of this FOCs was relatively consistent in individual neurones, with an average of 38.3 ± 4.1 pA ($n = 12$). Each oscillatory cycle was composed of a rapid inward phase and a slower outward phase (**Figure 2C**). The rapid inward phase of each oscillatory cycle was superimposed by a bursting of EPSCs (**Figure 2C**), and the slower outward phase was superimposed by sporadically occurring EPSCs that were either relatively more frequent (**Figure 2C**) or very scarce (data not shown) in individual neurons. During TRH application the tonic EPSCs increased in the frequency (4.7 ± 0.9 HZ vs. 18.9 ± 2.6 HZ, $P < 0.05$, $n = 12$, Student's paired *t*-test, **Figures 2C,F**) and showed a rhythmic-like change synchronized with FOCs (**Figure 2C**). TRH increased the frequency of the inspiratory inward currents from 3.9 ± 0.6 to 7.6 ± 0.9 bursts/min ($P < 0.05$, $n = 12$, Student's paired *t*-test, **Figures 2A,G**) but bell-shaped inspiratory inward currents became very irregular due to TRH-induced FOCs, which made the amplitude and area incomparable with that in the absence of TRH (**Figure 2H**). Additionally, TRH significantly increased the frequency, peak amplitude and area of the hypoglossal inspiratory bursts (Rekling et al., 1996; Hou et al., 2012). The effects of TRH usually disappeared in about 5 min upon wash, and a second application of TRH at 10–20 min interval caused comparable responses.

Tetrodotoxin (TTX) Inhibited the TRH-Induced Excitatory Slow Inward Current and Prevented the Oscillatory Pattern

In five of the twelve IA-AVPNs examined above, TRH was also applied in the presence of TTX (1 μM) (**Figure 3A**). TTX abolished hypoglossal respiratory bursts and the phasic EPSCs during inspiratory bursts in IA-AVPNs, and significantly inhibited tonic EPSCs in both the frequency

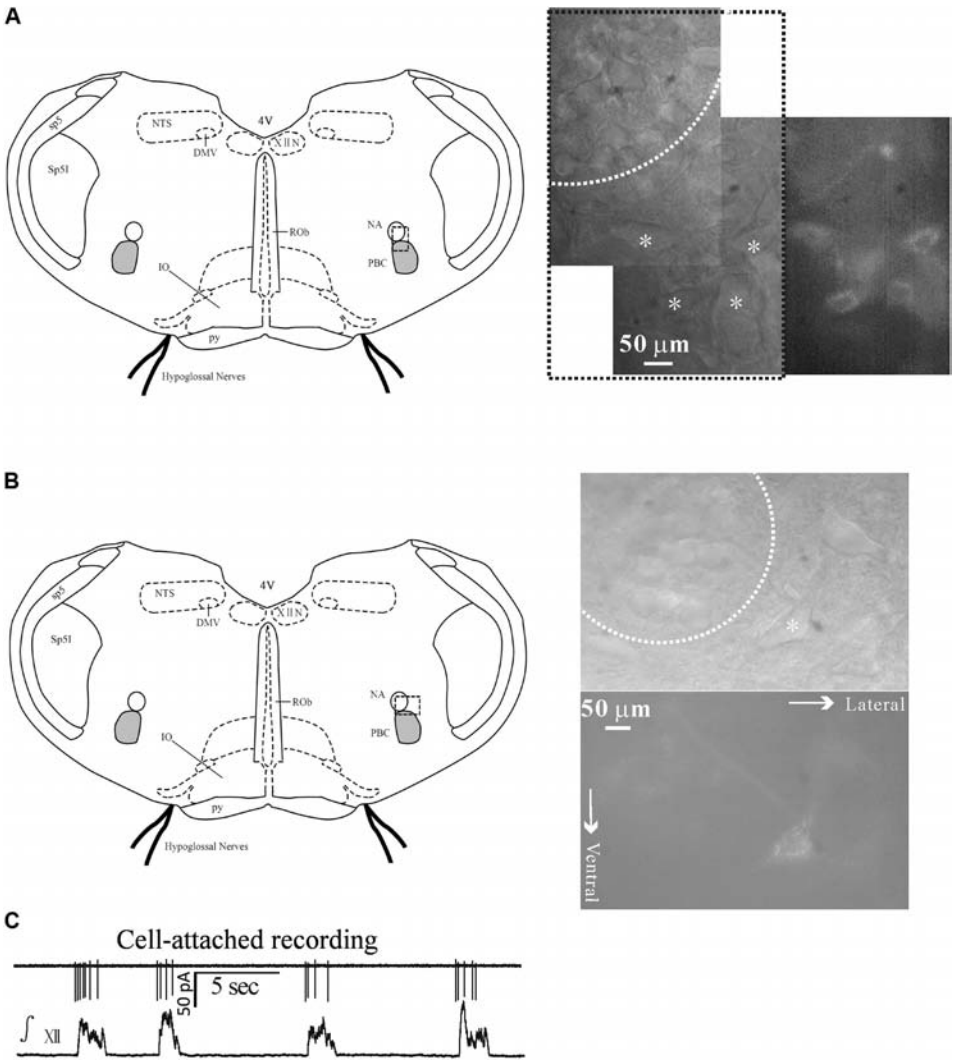


FIGURE 1 | Identification of inspiratory-activated airway vagal preganglionic neurons (IA-AVPNs) in the external formation of NA. **(A,B)** After application of rhodamine into extra-thoracic tracheal wall fluorescently labeled IA-AVPNs (marked by *) in the ventrolateral medulla were mostly in the ventrolateral, and occasionally in the ventral or ventromedial vicinity (not shown) of the compact portion (dashed circle) of the nucleus ambiguus (NA). Note these cells were larger in size compared with those within the compact portion of the NA, and were typically multipolar or spindle-like. The dashed frames in the schematic figures of the medullary slices indicate the areas from which photos were taken under infrared or fluorescent illumination. **(C)** IA-AVPNs in the ventrolateral vicinity of the NA mostly exhibited trains of inspiratory-related discharges under cell-attached configuration and were identified as inspiratory IA-AVPNs. ∫ XII, integrated hypoglossal activity; XIIN, hypoglossal nucleus; NTS, nucleus tractus solitarius; DMV, dorsal motor nucleus of vagus; sp5, spinal trigeminal tract; Sp5I, spinal trigeminal nucleus, interpolar part; PBC, pre-Bötzinger complex; ROb, raphe obscurus nucleus; py, pyramidal tract; 4V, 4th ventricle.

(from 6.9 ± 2.2 to 0.7 ± 0.03 Hz; $P < 0.05$, $n = 5$; pared Student's t-test) and the amplitude (from 61.1 ± 7.3 to 43.7 ± 1.5 pA; $P < 0.05$, $n = 5$; pared Student's t-test). Under this condition TRH did not cause any change of miniature EPSCs (mEPSCs), neither in the frequency nor in the amplitude (**Figures 3B–F**), and did not cause FOCs in any of these five IA-AVPNs (**Figure 3B**). The TRH-induced excitatory slow inward current was significantly inhibited (**Figure 3B**), from a control of 61.9 ± 16.2 pA to 19.0 ± 7.2 pA in the presence of TTX ($P < 0.05$; $n = 5$). All the mEPSCs were abolished by CNQX (50 μM) at the end of the experiments.

The TRH-Induced Excitatory Slow Inward Current and the Oscillatory Pattern (OP) in the IA-AVPNs Were Largely Independent of Their Inputs From Chemical Synapses

Tetrodotoxin blocked the TRH-induced enhancement of tonic EPSCs, significantly reduced the amplitude of the excitatory slow inward current and prevented the FOCs. These results raised such possibilities as in the absence of TTX TRH-induced enhancement of EPSCs might be critical in the generation of FOCs and might also contribute to the significantly larger

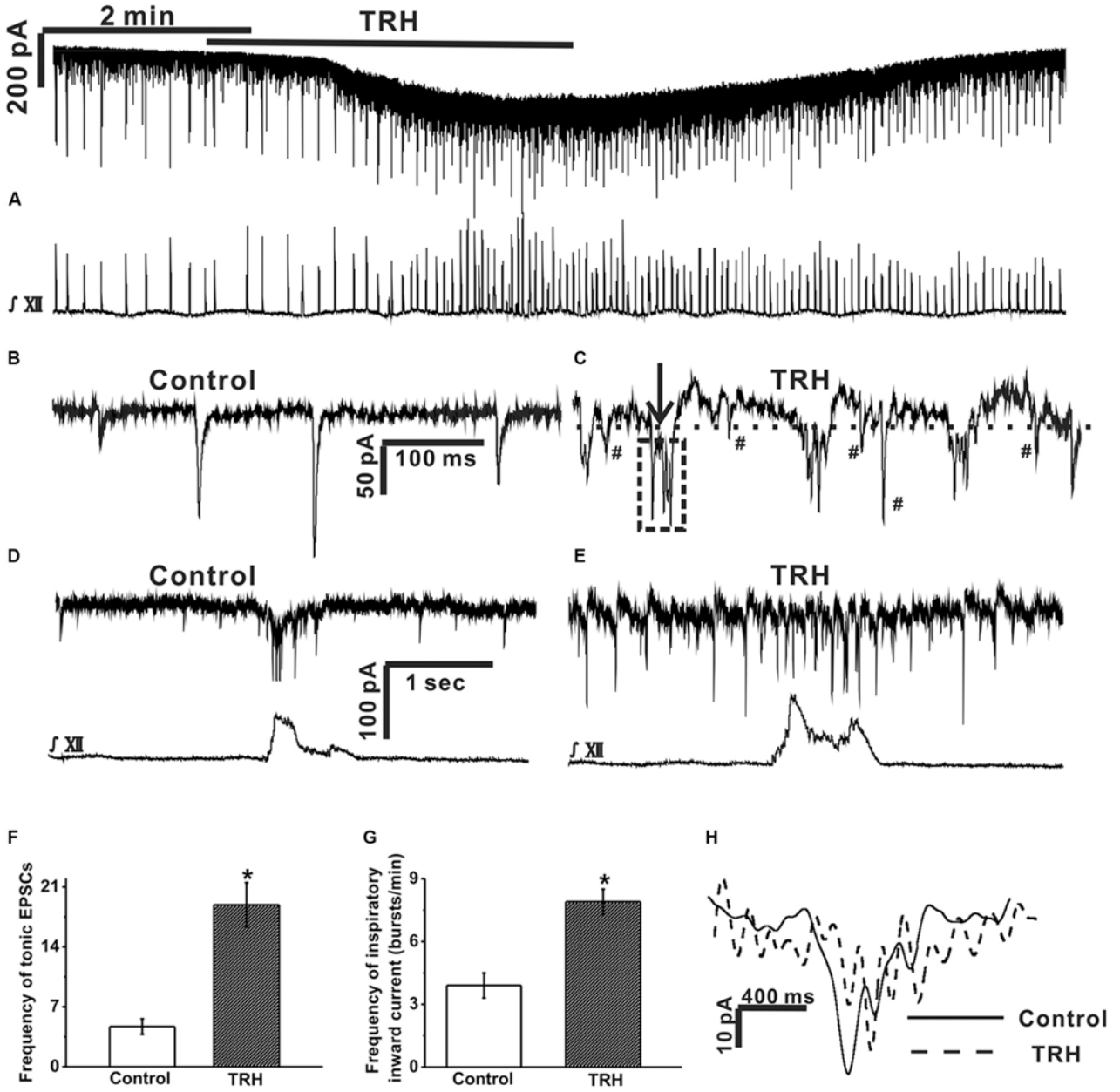


FIGURE 2 | TRH caused an excitatory slow inward current and fast oscillatory currents in the inspiratory-activated airway vagal preganglionic neurons (IA-AVPNs). **(A)** Simultaneous recording of an IA-AVPN under voltage clamp (upper panel) and the hypoglossal respiratory bursts (lower panel), showing that TRH application caused a slow excitatory inward current in this IA-AVPN and increased the frequency and the intensity of the hypoglossal respiratory bursts. **(B,C)** Selected traces of the tonic EPSCs captured from **(A)** during control **(B)** and during TRH application **(C)** are shown in an enlarged scale. The dashed horizontal line in **(C)** indicates the range of the slower outward phase and the arrow shows a typical rapid inward phase of FOCs. The tonic EPSCs show a rhythmic-like change (the box in dashed line) synchronous with the FOCs during TRH application **(C)**. EPSCs (marked by #) occurred during the slower outward phase. The scale bars in **(B)** also applies to **(C)**. **(D,E)** The phasic EPSCs during control **(D)** and TRH-induced FOCs in a different IA-AVPN were also identifiable during inspiratory phase **(E)** with a shorter cycle length. The scale bars in **(D)** also applies to **(E)**. **(F)** Summarized data for the frequency of tonic EPSCs in average (n = 12). **(G)** Summarized data for the frequency of phasic inspiratory inward currents in average (n = 12). **(H)** Comparison of bell-shaped inspiratory inward currents in **(D)** (during control) and in **(E)** (during application of TRH). *$P < 0.05$, Student's paired t-test.

excitatory slow inward current via summation. To test these possibilities, TRH was applied to IA-AVPNs pre-exposed to CNQX (50 μM) and AP_5 (50 μM) (**Figure 4A**). CNQX and AP5 blocked all the EPSCs and abolished hypoglossal respiratory bursts (**Figures 4B,C**). Under this condition TRH (100 nM) caused an excitatory slow inward current of 54.4 ± 11.9 pA (n = 36), which was not significantly different from that obtained in the twelve IA-AVPNs unexposed to CNQX and

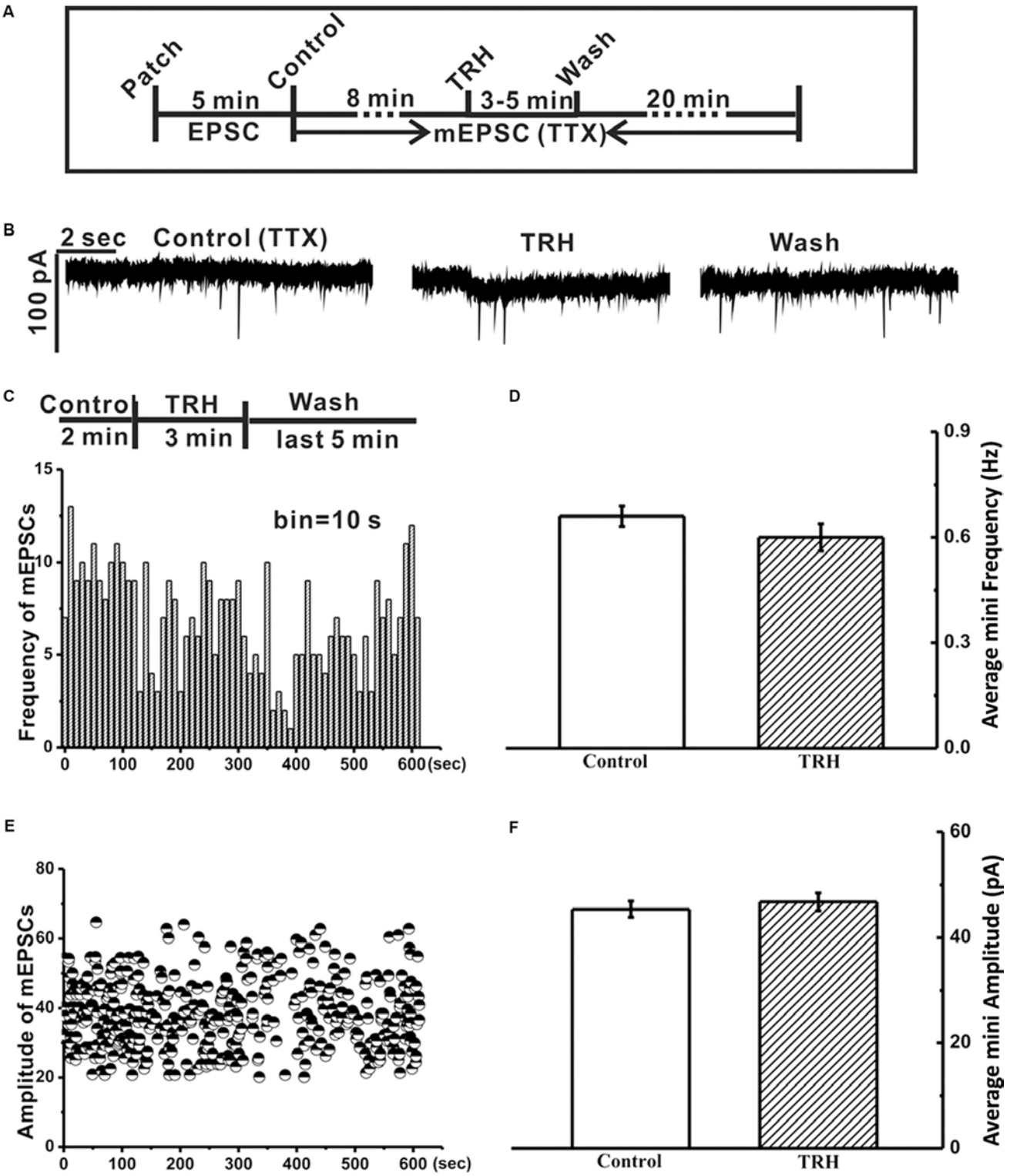


FIGURE 3 | Tetrodotoxin (TTX) inhibited the TRH-induced excitatory slow inward current and prevented generation of FOCs in IA-AVPNs. **(A)** A time axis in this experimental protocol. After TTX was applied for 8 min, TRH was globally applied into the bath for 3–5 min, followed by a 20 min wash with ACSF including TTX. **(B)** Representative mEPSCs recorded under control (left panel), during application of TRH (middle panel), and after 20 min wash (right panel) from an IA-AVPN. **(C,E)** Frequency histogram **(C)** and running amplitude of mEPSCs **(E)** in a representative IA-AVPN, showing TRH caused little alteration in both frequency and amplitude of mEPSCs. **(D,F)** Summarized data of the frequency **(D)** and amplitude **(F)** of mEPSCs in average in IA-AVPNs (n = 5).

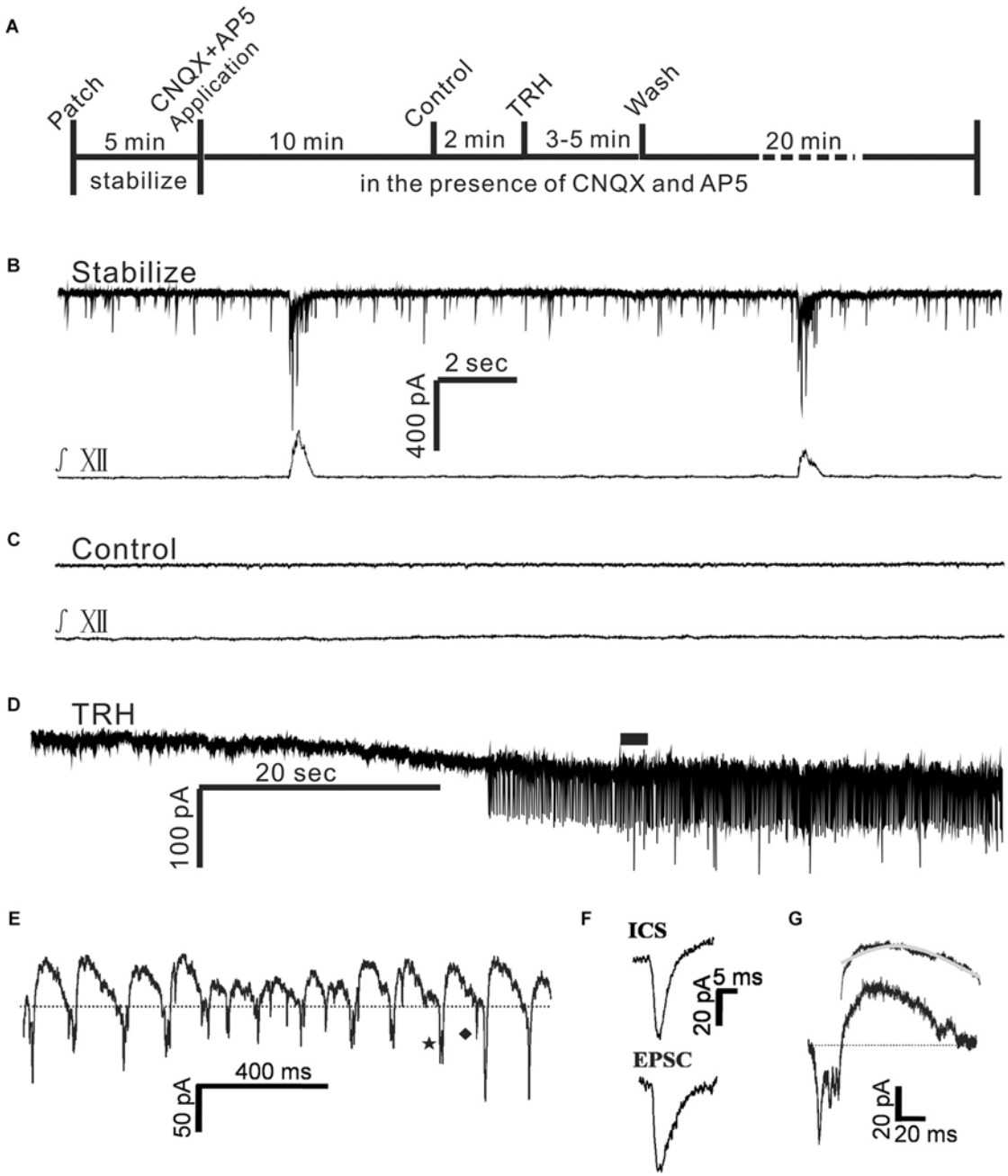


FIGURE 4 | TRH induced an excitatory slow inward current and oscillatory pattern (OP) in IA-AVPNs in the pre-incubation of CNQX and AP5. **(A)** A time axis in this experimental protocol. TRH was globally applied to the patched neuron for 3–5 min after control recording in the presence of CNQX and AP5, followed by a 20 min wash with ACSF including CNQX and AP5. **(B,C)** A representative stabilized recording trace of IA-AVPNs before **(B)** and during bath application of CNQX and AP5 **(C)**. **(D)** TRH induced the excitatory slow inward current and OPs in the presence of CNQX and AP5. **(E)** OPs indicated in **(D)** by the filled bar. Dashed line shows the slower outward phase superimposed by inward current spikelets (ICSs, a typical one indicated by ♦) and the rapid inward phase of FOCs coincident with single or multiple phase-locked ICSs (a typical one indicated by ★). **(F)** Comparison of the kinetics of the ICSs with the EPSCs, showing that the EPSCs had a longer decay time. **(G)** The time course of an oscillatory cycle, showing a rapid inward phase coincident with multiple ICSs and a slower outward phase. The bi-exponential outward phase averaged from 120 oscillatory cycles and the fitted curve (gray) is shown on the top.

AP5 ($P > 0.05$; independent Student's t-test). Interestingly, in all these 36 IA-AVPNs pre-incubation of CNQX and AP5, TRH still exclusively triggered the FOCs (**Figures 4D,E**). Moreover, the rapid inward phase of each oscillatory cycle was still accompanied by single or multiple phase-locked ICSs, and the slower outward phase was also superimposed by sporadically occurring ICSs (**Figure 4E**). FOCs and ICSs formed the OP. Noteworthily, our finding showed that TRH caused an initial

increase (three neurons, as is exemplified in **Figure 5B**) or no changes (one neuron, data not shown) in the frequency and/or amplitude of sIPSCs (**Figure 5A**). However, TRH caused progressive declination of sIPSCs in the frequency and amplitude with its prolonged application, which was accompanied by the occurrence of OPs in all the examined neurons (**Figures 5B–F**). TRH caused no changes in the frequency and amplitude of mIPSCs (data not shown). In order to investigate the effect of IPSCs in the generation of OP, in 13 of these 36 IA-AVPNs, picrotoxin (40 μM) and strychnine (1 μM) were also added into the bath to block sIPSCs before TRH application. Importantly, neither the cycle length nor the amplitude of the TRH-evoked oscillatory currents in these 13 neurones was significantly different from those obtained in IA-AVPNs untreated with

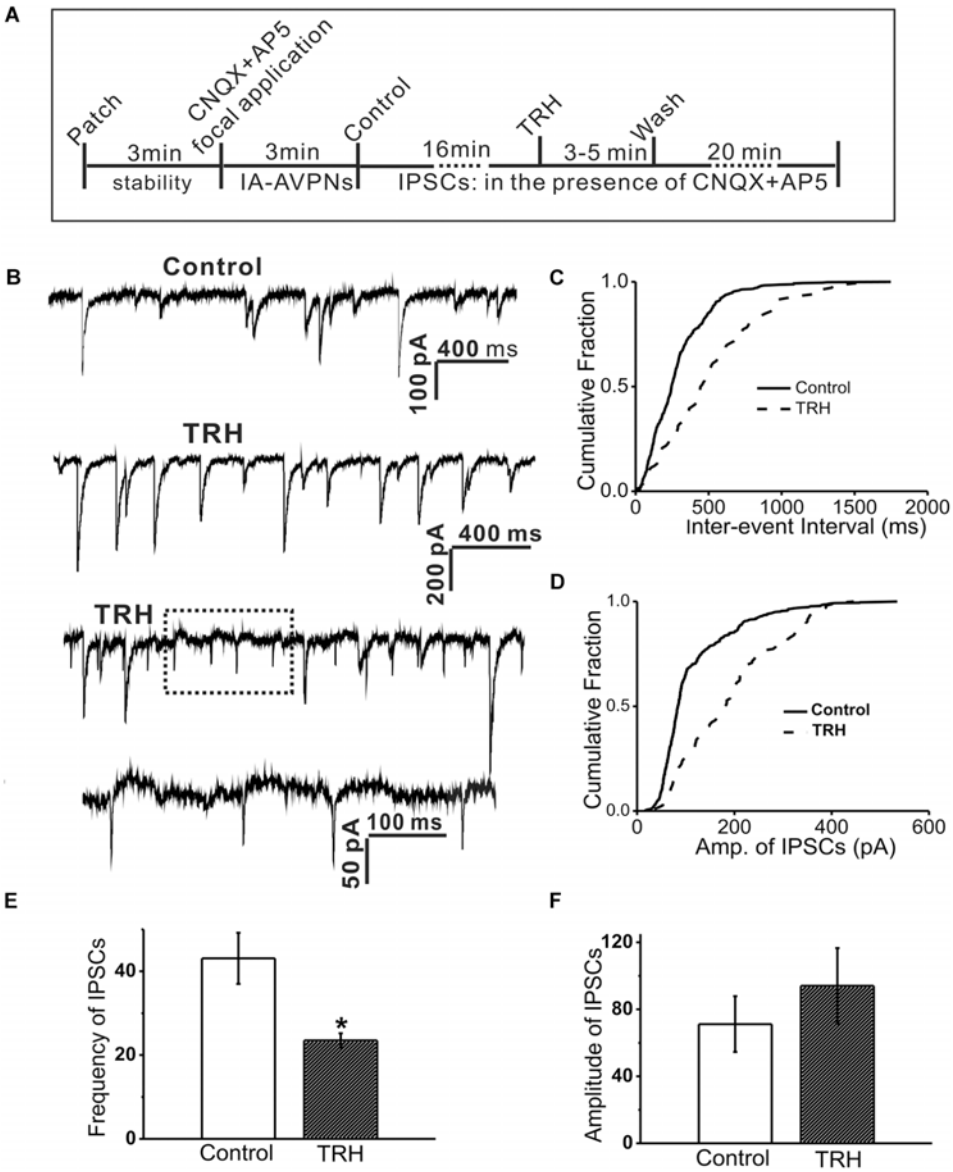


FIGURE 5 | TRH inhibited the frequency and amplitude of spontaneous inhibitory postsynaptic currents (sIPSCs) in IA-AVPNs and simultaneously induced OPs. **(A)** A time axis in this experimental protocol. After IA-AVPN was identified by focal application of CNQX and AP5, the baseline control was recorded in the bath application of CNQX and AP5. TRH was then globally applied to the patched neuron for 3–5 min, followed by a 20 min wash with ACSF including CNQX and AP5. **(B)** A representative recording of control (the first trace) and during application of TRH (the second and third trace), showing that TRH caused an initial increase in the frequency and amplitude (the second trace), and then decreased the frequency and amplitude accompanied by the occurrence of OPs (the third trace). The dashed box in the third trace is shown in an enlarged time scale (the fourth trace). The scale bars in the first trace also applicable to the third trace. **(C,D)** Cumulative plots of IPSCs intervals **(C)** and amplitude **(D)** of IPSCs during control (solid line) and the period of TRH-induced OPs (dashed line; plotted from the same IA-AVPN in **B**). Note that TRH induced a rightward shift in both the inter-event interval and the amplitude distribution curve, indicating decreases in the frequency and increases in the amplitude, respectively. **(E,F)** Summarized data for the frequency **(E)** and amplitude **(F)** of IPSCs in average ($n = 4$). $^*P < 0.05$, Student's paired t-test.

picrotoxin and strychnine (n = 23). The data were thus pooled together when analyzed. These results demonstrated that the inputs from the chemical synapses were less likely to be involved in the generation of TRH-induced OP and suggest that the summation of the TRH-enhanced tonic EPSCs might contribute little, if any, to the TRH-induced excitatory slow inward current.

In the presence of CNQX and AP_5 both the cycle length and the amplitude of the TRH-evoked FOCs were quite consistent in the individual neurones. Among different neurones, the frequency ranged from 3.8 to 9.5 Hz (6.4 ± 0.2 Hz; n = 36), and the amplitude ran from 20 to 50 pA (meanly 40.4 ± 2.7 pA; n = 36). The average amplitude of the TRH-induced FOCs in the IA-AVPNs pre-exposed to CNQX and AP_5 (n = 36) was not significantly different from that in those unexposed to CNQX and AP_5 (n = 12; $P > 0.05$). Furthermore, the rapid inward phase of the FOCs was usually accompanied by one to four ICSs, of which the amplitude was relatively consistent in individual neurons but ranged from 20 to 120 pA (46.5 ± 2.3 pA; n = 36) among different neurones. Compared with the tonic EPSCs during control recording, ICSs had a comparable rise time (1.3 ± 0.1 ms for ICSs, n = 12; 1.4 ± 0.2 ms for EPSCs, n = 6; $P > 0.05$, independent Student's t-test), and a significantly shorter decay time (2.4 ± 0.1 ms for ICSs, n = 12; 4.9 ± 0.4 ms for EPSCs, n = 6; $P < 0.05$, independent Student's t-test). A comparison was made by average of the difference in the kinetics of ICSs and tonic EPSCs (**Figure 4F**). The outward phase of the FOCs presented a bi-exponential time course, as indicated in the inset to the top of **Figure 4G**, in which a comparison was made of the average (n = 120) and the bi-exponentially fitted outward currents (gray). Properties of EPSCs in the absence of TRH during the inspiratory intervals and the inward phase of FOCs as well as ICSs induced by TRH in the presence of CNQX and AP5 were compared in **Table 1**.

In the majority (21 out of 36) of IA-AVPNs to which TRH was applied in the pre-incubation of CNQX and AP5, QX-314 (2 mM) was included in the pipette solution to block activation of voltage-dependent sodium currents and I_h. The cycle length and amplitude of the TRH-evoked FOCs, as well as the amplitude of the TRH-induced excitatory slow inward current in these neurones, was not significantly different from those obtained IA-AVPNs without intracellular QX-314 (values not shown). These data were thus pooled together when analyzed. The results suggested that the blockade of the voltage-dependent sodium channels from the inside of individual neurones under recording cannot prevent the occurrence of the FOCs as well as the concurrent ICSs, and has little effect on the excitatory slow inward current. Thus, it is likely that TRH-induced OP in IA-AVPNs are synchronized group activity, other than the activity of those under recording.

TRH-Induced OPs Were Insensitive to Membrane Potential

To test if TRH-induced FOCs as well as the coincident ICSs in IA-AVPNs were network-based activities, holding potential was changed under voltage-clamp recording. In the four IA-AVPNs examined from four slices, once the slow inward current evoked by TRH was in a steady level, the membrane potential was shifted from −100 mV to +30 mV. The cycle length of FOCs and the amplitude of ICSs were both unaltered at four different levels of membrane potentials (n = 4, **Figure 6**). Moreover, OPs couldn't be reversed by the very positive commanded potential of +30 mV in the presence of CNQX, AP5, picrotoxin and strychnine. In this experiment, the pipette solution contained QX-314. Similar voltage shifts didn't induce OPs in the absence of TRH (data not shown, n = 8).

The TRH-Induced OP Were Prevented by Gap Junction Blocker Carbenoxolone (CBX)

Since inspiratory motor neurones in the NA have been reported to be gap junction coupled (Rekling and Feldman, 1997), TRH-induced FOCs as well as the coincident ICSs in IA-AVPNs might be related to gap junction. To test this possibility CBX (100 μM) was added in the bath after the first TRH application, both in the normally perfused IA-AVPNs (n = 5) and in those pre-exposed to CNQX and AP_5 (n = 7). Under both circumstances, 30 min presence of CBX prevented completely the occurrence of the OPs during a subsequent TRH application. However, CBX did not significantly alter the amplitude of the TRH-induced excitatory slow inward current, neither in the normally perfused IA-AVPNs (63.6 ± 17.9 before vs. 56.8 ± 19.3 pA after CBX; $P > 0.05$; n = 5) nor in the IA-AVPNs pre-exposed to CNQX and AP_5 (55.8 ± 20.9 before vs. 56.6 ± 26.1 pA after CBX; $P > 0.05$; n = 7). A comparison was made of the TRH-induced excitatory slow inward current in a representative IA-AVPN in the absence and in the presence of CBX (**Figures 7A,B**)

In the normally perfused IA-AVPNs, CBX application inhibited gradually, and abolished finally the hypoglossal inspiratory bursts in a 3–60 min period, and also eventually abolished the bursting EPSCs. TRH was usually applied within the initial 10 min after the disappearance of the bursting EPSCs, under which TRH increased the frequency of the tonic EPSCs from 1.2 ± 0.3 to 5.6 ± 1.4 Hz ($P < 0.05$; n = 5), and also increased the amplitude from 32.2 ± 2.4 to 56.1 ± 4.4 pA ($P < 0.05$; n = 5). In three of these five IA-AVPNs, TRH caused rhythmic bursting of EPSCs (**Figures 7C–E**), which were coincident with the temporarily restored hypoglossal inspiratory bursts (not shown). At the end of the experiment, EPSCs induced by TRH in the presence of CBX were abolished by CNQX and AP5. These results indicated that TRH is capable of enhancing the EPSCs in IA-AVPNs, and that in the TRH-application experiments performed in the normally perfused IA-AVPNs without CBX, TRH-enhanced EPSCs include both those caused by enhanced glutamate release and those of ICSs coincident with the FOCs.

Additionally, the tonic EPSCs were slowly decreased in frequency and amplitude during CBX application. Since CBX was applied before the second application of TRH at varied time lengths, the CBX-induced gradual changes of tonic EPSCs were not statistically compared.

TABLE 1 | Comparision of properties of FOCs, ICSs and glutamatergic EPSCs in IA-AVPNs in the presence of CNQX, AP5, strychnine and picrotoxin.

	Amplitude (pA)	Rise time (ms)	Decay time (ms)	Frequency (Hz)	*n*
EPSCs	39.5 ± 1.3	1.4 ± 0.2	4.9 ± 0.4	6.2 ± 1.2 Hz	6
ICSs	41.5 ± 4.3	1.3 ± 0.1	2.4 ± 0.1*	6.9 ± 3.2 Hz	12
FOCs	41.9 ± 3.7	2.07 ± 0.3$	3.22 ± 0.4☆	4.7 ± 0.3 Hz$	12

*$P < 0.05$ from EPSCs, $^{\$}P < 0.05$ from EPSCs or ICSs, $^{☆}P < 0.05$ from ICSs.

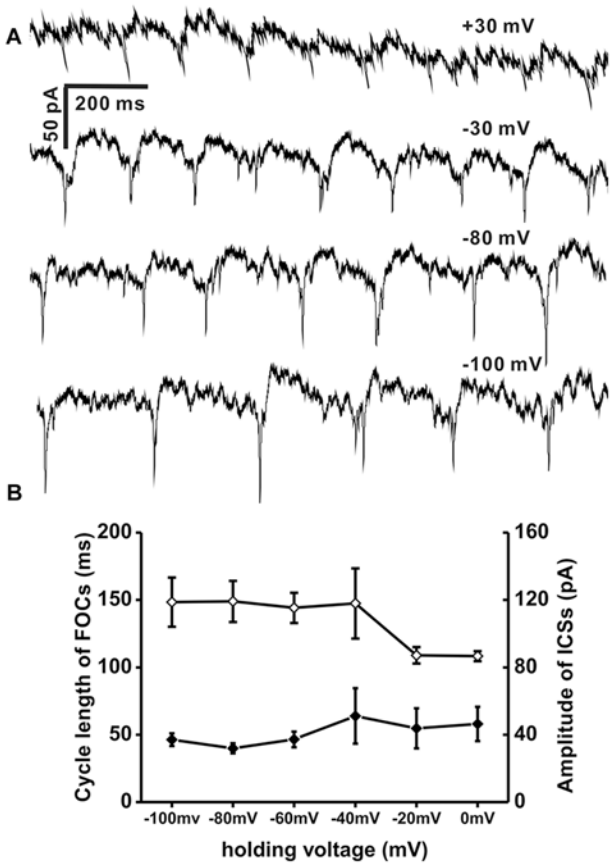


FIGURE 6 | OPs induced by TRH were insensitive to membrane potential. **(A)** A representative recording of OPs recorded at four different levels of holding voltage (values showed above each recording trace) of the same IA-AVPN in the presence of CNQX, AP5, strychnine and picrotoxion, showing that insensitivity of OP cycle length as well as amplitude in ICSs to membrane potential. Pipette solution included QX314 (2 mM). **(B)** Average plots of cycle length of FOCs (◇; left vertical scale; $n = 4$) and amplitude of ICSs (◆; right vertical scale, $n = 4$). QX314 was put into the electrodes in the process of recording.

Riluzole Decreased the Amplitude of TRH-Induced Excitatory Slow Inward Current and Prevented OPs

Since the summation of TRH-enhanced EPSCs contributed little to the TRH-induced excitatory slow inward current, its inhibition by TTX might be mediated by a direct postsynaptic mechanism, possibly via blockade of the persistent sodium current (INaP), because the blockade of voltage-gated sodium transient with intracellular QX-314 exerted little effect on this current. To test the mechanism, riluzole (20 μM) was added in the bath after the first TRH application to the IA-AVPNs pre-exposed to CNQX and AP_5; consequently, riluzole alone caused no change of the baseline current in IA-AVPNs. However, 10 min presence of riluzole inhibited significantly the TRH-induced excitatory slow inward current from 51.1 ± 24.3 pA of control to 19.3 ± 10.6 pA ($P < 0.05$; $n = 7$). In four of seven IA-AVPNs, the excitatory slow inward current was actually abolished by riluzole (**Figures 7F,G**). Interestingly, riluzole also completely prevented the occurrence of OPs in these seven IA-AVPNs (**Figure 7G**). These results suggested that activation of INaP might be involved in the generation of both the excitatory slow inward current and the OPs during TRH application.

Importantly, K_{ATP} inhibitor glybenclamide was reported to block the oscillatory currents triggered by the activation of metabotrophic glutamate receptors in hypoglossal motor neurones (Sharifullina et al., 2005). In the current study, therefore, the effect of glybenclamide (100 μM) was tested on the TRH-induced changes in the IA-AVPNs pre-exposed to CNQX and AP_5; consequently, glybenclamide had no effect neither on the TRH-evoked OPs nor on the excitatory slow inward current ($n = 3$; data not shown).

TRH Depolarized IA-AVPNs, Causing Continuous or Synchronized Firing Under Current Clamp, Both in the Absence and in the Pre-incubation of CNQX and AP_5

To test how TRH affects the firing behavior of IA-AVPNs, TRH was also applied under current clamp, both in normally perfused IA-AVPNs and in those pre-exposed to CNQX and AP5. Under current clamp configuration, the IA-AVPNs showed rhythmic depolarization and action potential firing during inspiratory phase under normal perfusion. Application of 100 nM TRH induced a slowly developing depolarization of 5–25 mV (14.2 ± 3.1 mV; $n = 5$), and the discharge of the IA-AVPNs became continuous, with significantly decreased action potential amplitude (from 70.4 ± 3 mV to 53.1 ± 5 mV; $P < 0.05$, $n = 5$) and significantly increased action potential duration (from 4.7 ± 0.1 to 6.2 ± 0.2 ms; $P < 0.05$, $n = 5$). A typical experiment is exhibited in **Figures 8A–D**. In the pre-incubation of CNQX and AP5, which silenced all the IA-AVPNs (**Figure 9A**), TRH application (100 nM) caused a similar slowly developing depolarization, and exclusively caused continuous discharge ($n = 5$). A typical experiment is exhibited in **Figure 8F**.

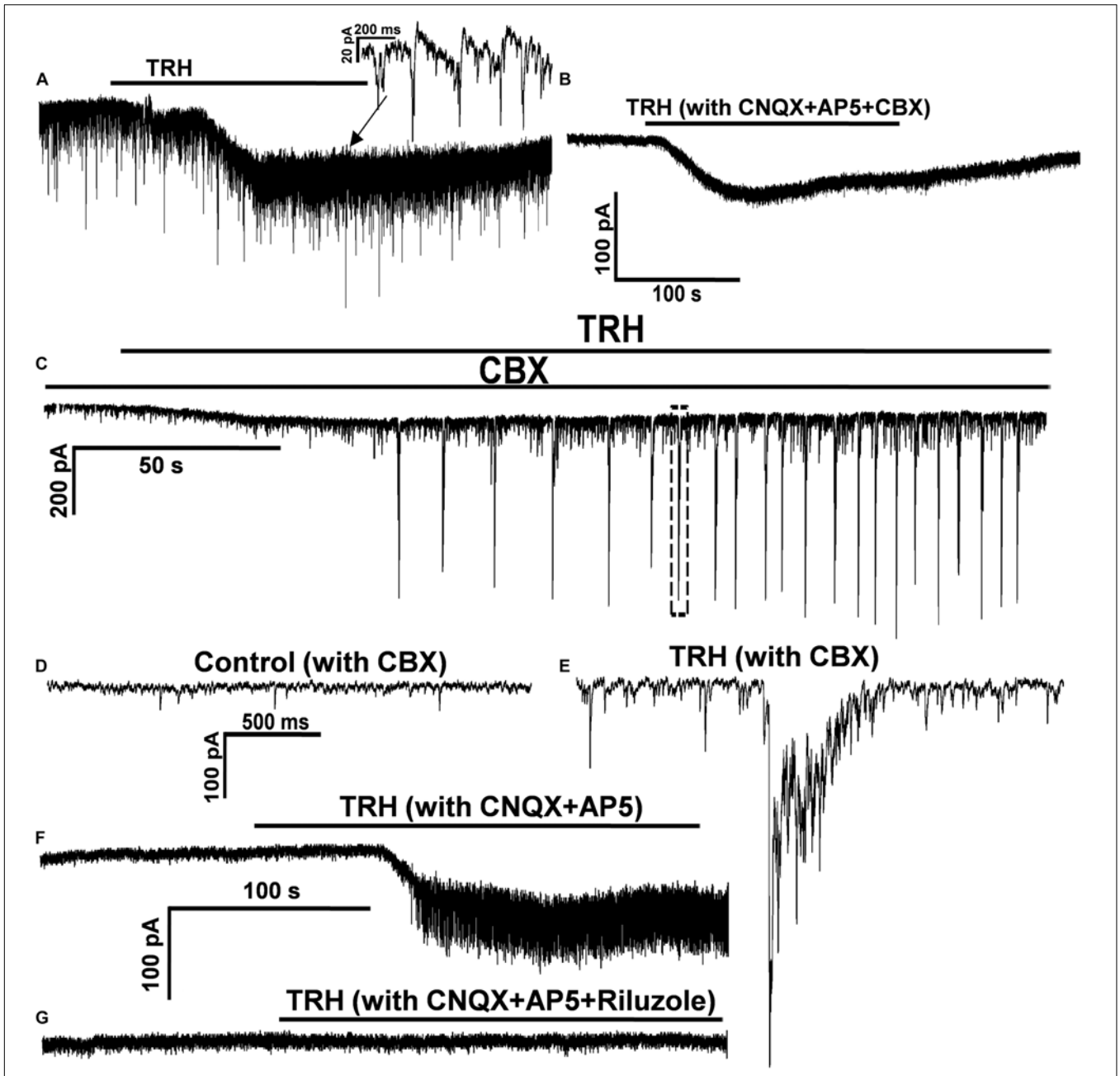


FIGURE 7 | CBX prevented the TRH-evoked oscillatory pattern, and TRH enhanced the EPSCs in the presence of CBX. **(A)** In a representative IA-AVPNs under normal perfusion TRH caused an excitatory slow inward current and evoked OPs. OPs was also evoked in this neurone in the pre-incubation of CNQX and AP5 (not shown). **(B)** In the same neurone in **(A)** CBX prevented OPs without altering the excitatory slow inward current. **(C)** In the presence of CBX, TRH increased the frequency and the amplitude of the tonic EPSCs, and evoked rhythmic bursts of the EPSCs that were coincident with the restored hypoglossal bursts (not shown). **(D,E)** The EPSCs captured from **(C)** before **(D)** and during (**E**: from the dashed box in **C**) TRH application are shown in an enlarged scale. **(F,G)** In a representative IA-AVPNs the TRH-induced OPs and the excitatory slow inward current **(F)** were completely blocked by pre-incubation of 20 μM riluzole **(G)**.

In two IA-AVPNs when the membrane potential was depolarized to a level more positive than −30 mV, the discharge ceased both under normally perfused condition and in the pre-incubation of CNQX and AP_5. The cessation of discharge was obviously because of the inactivation of the voltage-gated sodium channels by over depolarization. When the membrane potential was manually repolarised to a level equal or more negative to the level before TRH application, via injection of a hyperpolarizing current of 10–50 pA, the shape of the action potentials became relatively normal. Under the manually re-polarized condition, moreover, the IA-AVPNs showed fast oscillatory depolarizing potentials, and sporadic action potentials was loaded on the

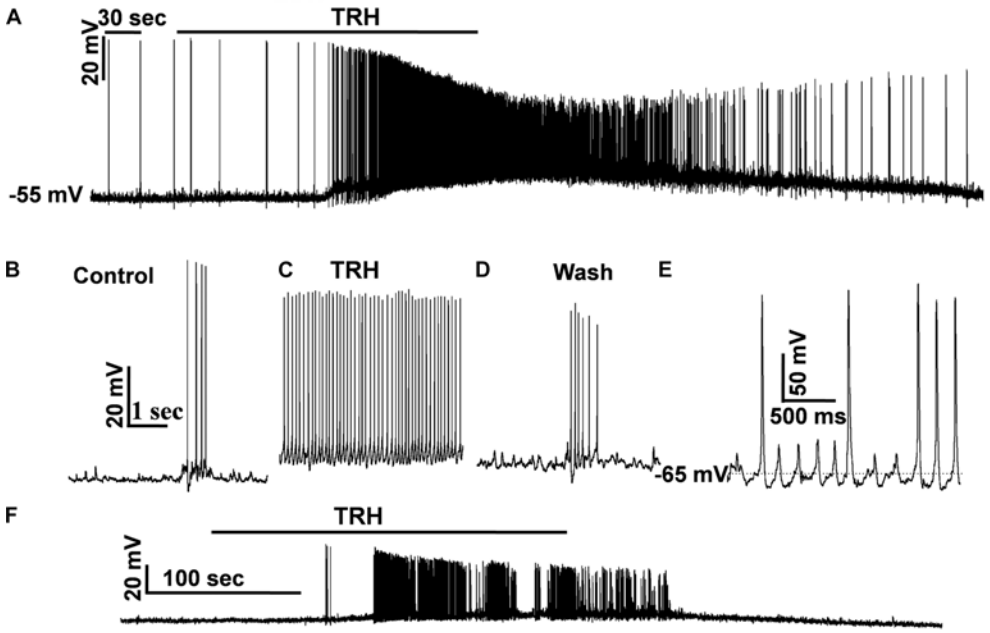


FIGURE 8 | TRH caused continuous firing of the IA-AVPNs and induced increases in firing frequency under current clamp. **(A)** TRH caused depolarization and continuous firing in a representative IA-AVPN. Note the amplitude decrease of action potentials. **(B–D)** Recording of the same IA-AVPN as in **(A)** in an enlarged scale, showing the rhythmic inspiratory depolarization and the superimposed trains of action potentials during control **(B)**, the continuous firing during TRH application **(C)**, and recovery **(D)**. **(E)** The rhythmic oscillatory potentials and the superimposed action potentials when the IA-AVPNs were manually re-polarized during TRH application. **(F)** TRH caused depolarization and continuous firing in a representative IA-AVPN pre-exposed to CNQX and AP_5.

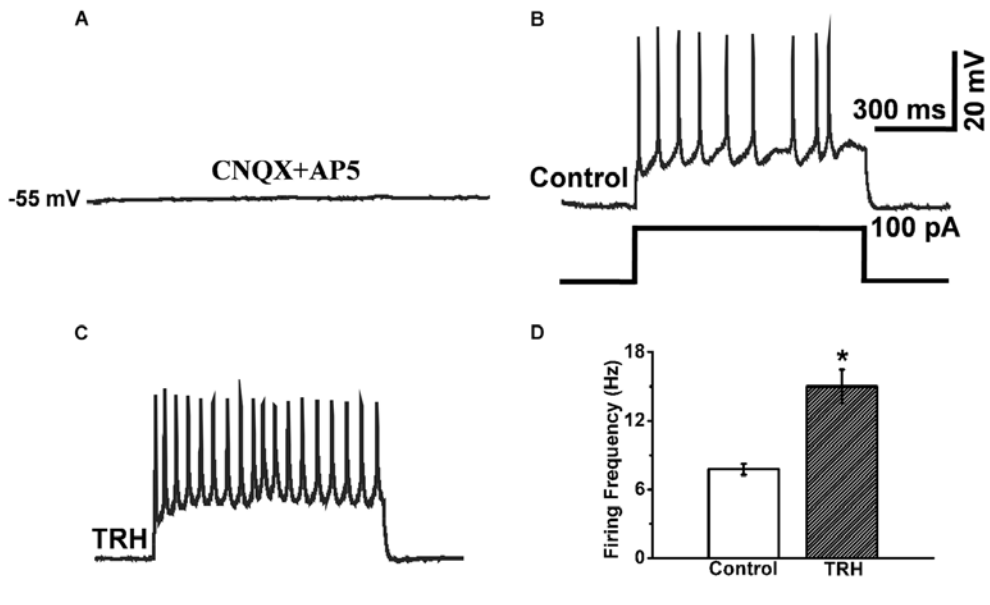


FIGURE 9 | TRH induced increases in instantaneous firing frequency responses to 100 pA depolarizing current. **(A)** In the pre-exposed to CNQX and AP5, an IA-AVPN was silent. **(B)** Injection of 100 pA current induced repetitive instantaneous firing. **(C)** Application of TRH increased the firing frequency in the same neuron in **(B)**. **(D)** Summarized data for the frequency of firing frequency ($n = 4$). $^*P < 0.05$, Student's paired *t*-test.

peak of some of these fast oscillatory depolarizing potentials (**Figure 8E**), of which the cycle length was identical to that of FOCs under voltage clamp.

In the pre-incubation of CNQX and AP5, the IA-AVPN was silent (**Figure 9A**), and injection of a square-wave current (100 pA) induced repetitive firing (**Figure 9B**). Under this

condition, TRH significantly increased firing frequency from 7.75 ± 0.48 Hz to 15 ± 1.47 Hz (n = 4) (**Figures 9C,D**). In the pre-incubation of TTX, TRH didn't cause any significant depolarization and failed to elicit firing behavior of IA-AVPNs. Under such circumstances, injection of a depolarizing current didn't trigger oscillatory depolarizing potentials (n = 3, data not shown).

DISCUSSION

The current study exhibits seven main findings:, (1) TRH caused an excitatory slow inward current and the OPs in IA-AVPNs, which were largely independent of their presynaptic inputs; (2) gap junction blocker CBX prevented the TRH-evoked OPs, but had little impact on the excitatory slow inward current; (3) in the presence of CBX, which blocked the hypoglossal respiratory rhythm and inspiratory bursting EPSCs, TRH enhanced the tonic EPSCs and restored the hypoglossal respiratory bursts in some slices; (4) TRH progressively decreased the frequency of the tonic sIPSCs coincident with the occurrence of OPs and had no influence on mIPSCs; (5) TRH-induced OPs were insensitive to membrane potential; (6) TTX and riluzole completely prevented the TRH-evoked OPs in IA-AVPNs, each of them also inhibiting a large proportion of the excitatory slow inward current; and (7) TRH depolarized IA-AVPNs, causing continuous or synchronized discharge under current clamp, both with and without perfusion of CNQX and AP_5; TRH increased firing frequency responses to input wave-forms.

In general, alterations of a baseline current in the pre-incubation of TTX reveal a postsynaptic mechanism. In IA-AVPNs, an excitatory slow inward current that was inhibited but not completely prevented by TTX during perfusion of TRH, suggesting that TRH had a postsynaptic effect. These results demonstrate that IA-AVPNs have TRH receptors, supporting the previous findings that TRH-containing terminals projected to respiratory motor neurons in NA (Iwase et al., 1992; Sun et al., 1995). In IA-AVPNs, TRH triggered a CBX-sensitive OPs, which was consistent with a previous report that inspiratory motor neurons in NA were coupled by gap junctions (Rekling et al., 2000). The finding also suggests that the generation of the TRH-evoked OPs in IA-AVPNs is a network-based, other than a single-neuron-based, behavior. TRH increased the frequency and the amplitude of the tonic EPSCs in IA-AVPNs in the presence of CBX, and in some slices restored the hypoglossal respiratory bursts and bursting EPSCs that had been abolished by CBX. These results suggest that TRH can have an excitatory stimulation on the glutamatergic inputs of IA-AVPNs, possibly via actions on the pre-terminal sites of the precedent glutamatergic neurons; and that TRH might also be of crucial importance in the respiratory rhythmogenesis via actions on glutamatergic rhythmogenesis neurons.

Thyrotropin-releasing hormone decreased the frequency of sIPSCs accompanied by the occurrence of OPs but didn't affect mIPSCs, indicating that presynaptic release of inhibitory transmitters was inhibited, in which perhaps two mechanisms involved. One possibility is that the propagation of action potential in the inhibitory neurons preceding the IA-AVPNs determines the presynaptic release of inhibitory transmitters. Once TTX eliminated action potentials mentioned above, TRH had no impact on the release of inhibitory transmitters by just targeting at the terminals of these inhibitory neurons. The other possibility is that OPs induced by TRH affect presynaptic release of inhibitory transmitters. Combined with enhancement of excitatory synaptic inputs induced by TRH, the possible significance of these findings lie in unveiling not only the imbalance of excitatory and inhibitory activities (Moore et al., 2004; Haxhiu et al., 2005) but also the generation of OPs contributes to abnormal activation of IA-AVPNs.

Blockade of chemical synaptic inputs of the IA-AVPNs could not prevent the TRH-evoked OPs. Nicotine and arginine vasopressin applied to the normally perfused IA-AVPNs enhanced the tonic EPSCs and the inspiratory bursting EPSCs, but did not evoke the OPs (Zhou et al., 2013; Yan et al., 2017). These findings suggest that presynaptic inputs are not the underlying cause for the TRH-evoked OP. However, in the normally perfused IA-AVPNs the TRH-evoked OPs had a significantly shorter cycle length during the inspiratory phase compared with that during inspiratory intervals. This finding suggests that the inspiratory-enhanced glutamate release, although cannot trigger the OP alone during inspiratory intervals, might have a promoting effect on this pattern during the inspiratory phase.

Oscillatory currents have been reported to be evoked in the hypoglossal motoneurons by NMDA, nicotine, TBOA (a selective blocker of glutamate transporter), or DHPG (an agonist of group I metabotropic glutamate receptors) (Sharifullina et al., 2008; Cifra et al., 2009). In the current study, TRH-evoked OPs shared some similar properties with the oscillatory currents evoked in the hypoglossal motoneurons, such as blockade by CBX or riluzole, and they also showed some quite different properties, as indicated by the evidence that TRH-evoked OP was independent of the inputs from chemical synapses, sensitive to TTX and resistant to glybenclamide. Whereas the oscillatory currents in the hypoglossal motoneurons evoked by nicotine, DHPG, or TBOA were enhanced by AMPA and blocked by CNQX and K_{ATP} inhibitors (Sharifullina et al., 2005; Cifra et al., 2009). Additionally, both the hypoglossal motoneurons and respiratory rhythmogenesis neurons have been reported to be linked by gap junctions (Rekling and Feldman, 1997; Rekling et al., 2000; Sharifullina et al., 2005). In the current study, TRH caused continuous discharge in IA-AVPNs, while the rhythm of the hypoglossal bursts was maintained. These results suggest that neither in the respiratory rhythmogenesis neurons nor in the hypoglossal motoneurons TRH caused persisted or oscillatory-like excitation, and OPs in IA-AVPNs is a rather specific response of these neurons to TRH. Gap junction couplings existed in the IA-AVPNs are of critical importance in the generation of OPs. This was supported by previous studies that gap junctions were identified between AVPNs in the rostral nucleus ambiguous (Rekling and Feldman, 1997) and were recorded in single IA-AVPNs located in eNA (Chen Y.H. et al., 2007). In the propagation of oscillatory currents, gap junction coupling involves a few HMs (Mazza et al., 1992; Sharifullina et al., 2005).

Perhaps gap junctions in IA-AVPNs also involve several neurons in the propagation of TRH-induced OPs. As a limitation, the current study doesn't use the method of paired patch clamp recording of two IA-AVPNs to clarify it, although CBX inhibits OPs on all the examined single-recorded neurons.

Thyrotropin-releasing hormone increased the bell-shaped inspiratory inward currents in the frequency and induced OPs during inspiratory bursts. In view of the rhythmic activation of inspiratory EPSCs, obviously IA-AVPNs receive synaptic inputs from neuronal network of inspiratory rhythmic generation, e.g., pre-BötC (PBC), or the synaptic inputs mentioned above happen to be the rhythm-generated origin. These are consistent with previous studies that TRH activated respiratory neurons in PBC (Rekling et al., 1996; Ruangkittisakul et al., 2006). In our recent study, gap junction couplings could also be activated by central inspiratory activity during inspiratory phase (Hou et al., unpublished paper). The location of the IA-AVPNs in this study are eNA region, within which the PBC neurons locate. Thus, it makes sense to postulate that gap junctions between IA-AVPNs and PBC neurons might contribute to the generation of OPs during inspiratory phase. Future studies are required to address the question as to whether IA-AVPNs are coupled via gap junctions with PBC neurons. Although we couldn't provide precise morphological locus of gap junctions at present, it seems that gap junctions here don't locate at axo-axonal coupling (Schmitz et al., 2001; Sharifullina et al., 2005). This view is supported by the current finding that the cycle length of FOCs is insensitive to membrane potential in a single recorded IA-AVPN in this study. The spikelets induced in hippocampal slice neurons originating from axo-axonal electrical coupling would be inhibited by hyperpolarizing the soma (Schmitz et al., 2001), which was inconsistent with the present findings. Therefore, it is reasonable to infer gap junctions here might locate on somatic-dendritic couplings. Additionally, although we can't completely rule out the probability that the generation of OPs originates from currents of nearby unclamped neurons, the resistance of input resistance to depolarization or hyper-polarization (from −100 mV to +30 mV) makes it impossible.

Both excitatory slow inward current and OPs induced by TRH were depressed by riluzole (20 μM). This finding indicates that persistent sodium current might play a crucial role in the generation of OPs due to its high sensitivity to riluzole (<10 μM) (Bellingham, 2011). However, riluzole was reported to have a wide-ranging neural effects (Bellingham, 2011), including inhibition of voltage-gated Ca^{2+} current (Bellingham, 2013) and augment of Ca^{2+}-dependent potassium current (Beltran-Parrazal and Charles, 2003), etc. It is unlikely that riluzole in this study suppresses presynaptic glutamate release (He et al., 2002; Pace et al., 2007; Rammes et al., 2008; Bellingham, 2013) or blocks ionotropic glutamate receptor postsynaptically (Bellingham, 2013) as OPs evoked by TRH is independent of chemical synapses, although other non-specific effects couldn't be excluded at present.

It is noted that AVPNs involved in the modulation of lower airway caliber experience developmental changes (Kohn et al., 2009). Especially, as a very crucial factor in the generation of TRH-induced OPs, gap junctions exist not only in inspiratory motoneurons of newborn mouse (Rekling and Feldman, 1997) and neonatal rats (Chen Y.H. et al., 2007), but also in vagal motoneurons in the nucleus ambiguus of adult animals (Lewis, 1994). To our knowledge, gap junction is made up of connexins (Cx). Cx 26 and Cx32, two important components of Cx, were expressed in PBC neurons, and both of them exhibit developmental variations (Solomon et al., 2001). Unfortunately, there is very little information on the expression and developmental changes of gap junctions in IA-AVPNs in the previous literatures. Therefore, it is not known whether OPs in this study could be induced by TRH in adult rats. This issue needs further investigations.

The inspiratory oscillations have been proved in previous studies to play significant roles in facilitating neural output at respiratory motor neurons levels (Huang et al., 1996; Funk and Parkis, 2002; Parkis et al., 2003). In this study, current clamp experiments showed that the IA-AVPNs were overall excited by TRH. Obviously, OPs contributed to increasing firing frequency of IA-AVPNs via the rapid inward phase of FOCs and multiple ICSs. ICSs in this study are likely to be caused by gap-junction communication among neighboring neurons due to their properties and sensitivity to CBX. Increase of such gap-junction communication involve in the synchronization of motor neurons (Kepler et al., 1990; Haxhiu et al., 2005; Sharifullina et al., 2005), although electrical coupling is also demonstrated to reduce motor-neural synchrony in the previous study (Bou-Flores and Berger, 2001). Thus ICSs are likely to play vital roles in the synchronization of IA-AVPNs. Funk et al. documented that the oscillations, especially high frequency oscillations of motor neurons, have high correlations with that of their respective nerves (Funk and Parkis, 2002). Accordingly, it makes reasonable to infer that OPs of IA-AVPNs are possibly synchronized with the oscillations of vagus nerves or airway smooth muscles they innervate. Therefore, OPs of IA-AVPNs might form functional basis for synchronous activation of airway smooth muscles. In addition, because the cycle length of FOCs was insensitive to membrane potentials, the neuronal output was likely to be constrained to the cycle length. Consequently, the emergence of this kind of fast oscillatory depolarizing potentials under current clamp might prevent excessive excitation of IA-AVPNs.

It is not exactly known how TRH induced the excitatory inward current and triggered FOCs in the IA-AVPNs. Based on the current findings, it is likely that TRH first activated of INaP and then opened gap junctions in IA-AVPNs. It seems that INaP contribute to the excitatory slow inward current. The slow outward phase of FOCs might due to the activation of some potassium channels, although TRH could inhibit acid-sensitive TASK channels in locus coeruleus noradrenergic neurons (Ishibashi et al., 2009). Once IA-AVPNs were depolarized to the threshold they fired action potentials, which were then synchronized by opened gap junctions and were detected as OPs in individual IA-AVPNs. The ion channel mechanisms of mediating the rapid inward phase and slow outward phase merit further investigations.

The physiological or pathological significance of the TRH-induced OPs in IA-AVPNs remains unknown. It has been demonstrated that activation of AVPNs by antidiuretic hormone might participate in psychological stress-induced asthma exacerbations in our previous study (Hou et al., 2017). In the previous animal experiment, the central release of TRH after cold stress was seven folds of the control level (Fiedler et al., 2006). Since cold stress is a well-recognized factor in inducing or accelerating asthma, it is likely that the TRH-induced OPs in IA-AVPNs contributes to the genesis or exacerbation of asthma. Network-based OPs mediated by gap junction in this study might be very crucial in the synchronization of IA-AVPNs. Changes in central mechanisms affecting such synchronization might lead to bronchoconstrictive asynchrony. For example, the imbalance of such synchronization might result in a fact that some bronchial branches nearly totally closed but others stay normal when asthma attacks. Alleviation of airway inflammation and airway hyperactivity by inhaled CBX had also been reported (Ram et al., 2009). Thus, ion channel blockers that can inhibit the TRH-induced the slow excitatory currents and block the triggering of the OP might function as promising candidates to prevent and treat asthma.

CONCLUSION

In current study, TRH enhances the excitatory inputs, decreases the inhibitory inputs, induces a slow postsynaptic excitatory inward current and triggers an OP mediated by gap junction, all of which contribute to the excitation of IA-AVPNs.

AUTHOR CONTRIBUTIONS

LH, LZ, and XZo designed the research. LH, MZ, XZa, ZL, PZ, and DQ performed the research. LH, MZ, XZa, LZ, and XZo analyzed the data. LH wrote the paper. LH, LZ, and XZo revised the paper.

FUNDING

This study was supported by the NSFC grant (81300020) to LH, the Young Physician Assistant Training Program of Shanghai and the Excellent Young Physician Assistant Training Program of Shanghai General Hospital affiliated to Shanghai Jiao Tong University to LH.

REFERENCES

Baker, D. G. (1986). Parasympathetic motor pathways to the trachea: recent morphologic and electrophysiologic studies. *Clin. Chest Med.* 7, 223–229.

Bellingham, M. C. (2011). A review of the neural mechanisms of action and clinical efficiency of riluzole in treating amyotrophic lateral sclerosis: what have we learned in the last decade? *CNS Neurosci. Ther.* 17, 4–31. doi: 10.1111/j.1755-5949.2009.00116.x

Bellingham, M. C. (2013). Pre- and postsynaptic mechanisms underlying inhibition of hypoglossal motor neuron excitability by riluzole. *J. Neurophysiol.* 110, 1047–1061. doi: 10.1152/jn.00587.2012

Beltran-Parrazal, L., and Charles, A. (2003). Riluzole inhibits spontaneous Ca2 + signaling in neuroendocrine cells by activation of K + channels and inhibition of Na + channels. *Br. J. Pharmacol.* 140, 881–888. doi: 10.1038/sj.bjp.0705491

Bou-Flores, C., and Berger, A. J. (2001). Gap junctions and inhibitory synapses modulate inspiratory motoneuron synchronization. *J. Neurophysiol.* 85, 1543–1551. doi: 10.1152/jn.2001.85.4.1543

Canning, B. J., and Fischer, A. (2001). Neural regulation of airway smooth muscle tone. *Respir. Physiol.* 125, 113–127. doi: 10.1016/S0034-5687(00)00208-5

Chen, Y., Hou, L., Zhou, X., Qiu, D., Yuan, W., Zhu, L., et al. (2012a). Inspiratory-activated and inspiratory-inhibited airway vagal preganglionic neurons in the ventrolateral medulla of neonatal rat are different in intrinsic electrophysiological properties. *Respir. Physiol. Neurobiol.* 180, 323–330. doi: 10.1016/j.resp.2011.12.014

Chen, Y., Li, M., Liu, H., and Wang, J. (2007). The airway-related parasympathetic motoneurones in the ventrolateral medulla of newborn rats were dissociated anatomically and in functional control. *Exp. Physiol.* 92, 99–108. doi: 10.1113/expphysiol.2006.036079

Chen, Y., Wang, L., Zhou, X., Ge, D., Yuan, W., and Wang, J. (2012b). Agonist of 5-HT1A/7 receptors but not that of 5-HT2 receptors disinhibits tracheobronchial-projecting airway vagal preganglionic neurons of rats. *Neuroscience* 207, 78–87. doi: 10.1016/j.neuroscience.2012.01.047

Chen, Y. H., Hou, L. L., and Wang, J. J. (2007). Selective revealing of gap junction currents in single inspiratory tracheal motor neurons. *Sheng Li Xue Bao* 59, 770–776.

Cifra, A., Nani, F., Sharifullina, E., and Nistri, A. (2009). A repertoire of rhythmic bursting produced by hypoglossal motoneurons in physiological and pathological conditions. *Philos. Trans. R. Soc. Lond. B. Biol. Sci.* 364, 2493–2500. doi: 10.1098/rstb.2009.0071

Fiedler, J., Jara, P., Luza, S., Dorfman, M., Grouselle, D., Rage, F., et al. (2006). Cold stress induces metabolic activation of thyrotrophin-releasing hormone-synthesising neurones in the magnocellular division of the hypothalamic paraventricular nucleus and concomitantly changes ovarian sympathetic activity parameters. *J. Neuroendocrinol.* 18, 367–376. doi: 10.1111/j.1365-2826.2006.01427.x

Funk, G. D., and Parkis, M. A. (2002). High frequency oscillations in respiratory networks: functionally significant or phenomenological? *Respir. Physiol. Neurobiol.* 131, 101–120. doi: 10.1016/S1569-9048(02)00041-1

Ge, D., Yan, X., Guo, Y., Chen, X., Guan, R., Chen, Y., et al. (2015). Activation of alpha1-adrenoceptors facilitates excitatory inputs to medullary airway vagal preganglionic neurons. *J. Appl. Physiol.* 119, 686–695. doi: 10.1152/japplphysiol.00045.2015

Guo, Y., Yan, X., Chen, X., He, D., Zeng, M., Chen, Y., et al. (2017). Corticotropin-releasing hormone modulates airway vagal preganglionic neurons of Sprague-Dawley rats at multiple synaptic sites via activation of its type 1 receptors: implications for stress-associated airway vagal excitation. *Neuroscience* 355, 101–112. doi: 10.1016/j.neuroscience.2017.04.049

Haselton, J. R., Solomon, I. C., Motekaitis, A. M., and Kaufman, M. P. (1992). Bronchomotor vagal preganglionic cell bodies in the dog: an anatomic and functional study. *J. Appl. Physiol.* 73, 1122–1129. doi: 10.1152/jappl.1992.73.3.1122

Haxhiu, M. A., Deal, E. C. Jr., Norcia, M. P., van Lunteren, E., and Cherniack, N. S. (1987). Effect of N-methyl-D-aspartate applied to the ventral surface of the medulla on the trachea. *J. Appl. Physiol.* 63, 1268–1274. doi: 10.1152/jappl.1987.63.3.1268

Haxhiu, M. A., Jansen, A. S., Cherniack, N. S., and Loewy, A. D. (1993). CNS innervation of airway-related parasympathetic preganglionic neurons: a transneuronal labeling study using pseudorabies virus. *Brain Res.* 618, 115–134. doi: 10.1016/0006-8993(93)90435-p

Haxhiu, M. A., and Loewy, A. D. (1996). Central connections of the motor and sensory vagal systems innervating the trachea. *J. Auton. Nerv. Syst.* 57, 49–56. doi: 10.1016/0165-1838(95)00092-5

Haxhiu, M. A., Kc, P., Balan, K. V., Wilson, C. G., and Martin, R. J. (2008). Modeling of sleep-induced changes in airway function: implication for nocturnal worsening of bronchial asthma. *Adv. Exp. Med. Biol.* 605, 469–474. doi: 10.1007/978-0-387-73693-8_82

Haxhiu, M. A., Kc, P., Moore, C. T., Acquah, S. S., Wilson, C. G., Zaidi, S. I., et al. (2005). Brain stem excitatory and inhibitory signaling pathways regulating bronchoconstrictive responses. *J. Appl. Physiol.* 98, 1961–1982. doi: 10.1152/japplphysiol.01340.2004

Haxhiu, M. A., Kc, P., Neziri, B., Yamamoto, B. K., Ferguson, D. G., and Massari, V. J. (2003). Catecholaminergic microcircuitry controlling the output of airway-related vagal preganglionic neurons. *J. Appl. Physiol.* 94, 1999–2009. doi: 10.1152/japplphysiol.01066.2002

Haxhiu, M. A., Yamamoto, B. K., Dreshaj, I. A., and Ferguson, D. G. (2002). Activation of the midbrain periaqueductal gray induces airway smooth muscle relaxation. *J. Appl. Physiol.* 93, 440–449. doi: 10.1152/japplphysiol.00752.2001

He, Y., Zorumski, C. F., and Mennerick, S. (2002). Contribution of presynaptic Na(+) channel inactivation to paired-pulse synaptic depression in cultured hippocampal neurons. *J. Neurophysiol.* 87, 925–936. doi: 10.1152/jn.00225.2001

Hou, L., Zhou, X., Chen, Y., Qiu, D., Zhu, L., and Wang, J. (2012). Thyrotropin-releasing hormone causes a tonic excitatory postsynaptic current and inhibits the phasic inspiratory inhibitory inputs in inspiratory-inhibited airway vagal preganglionic neurons. *Neuroscience* 202, 184–191. doi: 10.1016/j.neuroscience.2011.12.003

Hou, L., Zhou, X., Zhang, M., Liu, Z., and Zhang, G. (2015). Effects of Methyleugenol on central respiratory drive to inspiratory-activated airway vagal preganglionic neurons. *Zhonghua Yi Xue Za Zhi* 95, 933–937. doi: 10.3760/cma.j.issn.0376-2491.2015.12.014

Hou, L., Zhu, L., Zhang, M., Zhang, X., Zhang, G., Liu, Z., et al. (2017). Participation of antidiuretic hormone (adh) in asthma exacerbations induced by psychological stress via pka/pkc signal pathway in airway-related vagal preganglionic neurons (AVPNs). *Cell. Physiol. Biochem.* 41, 2230–2241. doi: 10.1159/000475638

Huang, W. X., Cohen, M. I., Yu, Q., See, W. R., and He, Q. (1996). High-frequency oscillations in membrane potentials of medullary inspiratory and expiratory neurons (including laryngeal motoneurons). *J. Neurophysiol.* 76, 1405–1412. doi: 10.1152/jn.1996.76.3.1405

Ishibashi, H., Nakahata, Y., Eto, K., and Nabekura, J. (2009). Excitation of locus coeruleus noradrenergic neurons by thyrotropin-releasing hormone. *J. Physiol.* 587, 5709–5722. doi: 10.1113/jphysiol.2009.181420

Iwase, M., Shioda, S., Nakai, Y., Iwatsuki, K., and Homma, I. (1992). TRH regulation of tracheal tension through vagal preganglionic motoneurons. *Brain Res. Bull.* 29, 821–829. doi: 10.1016/0361-9230(92)90150-V

Johnson, S. M., and Getting, P. A. (1992). Excitatory effects of thyrotropin-releasing hormone on neurons within the nucleus ambiguus of adult guinea pigs. *Brain Res.* 590, 1–5. doi: 10.1016/0006-8993(92)91074-O

Kc, P., Karibi-Ikiriko, A., Rust, C. F., Jayam-Trouth, A., and Haxhiu, M. A. (2006). Phenotypic traits of the hypothalamic PVN cells innervating airway-related vagal preganglionic neurons. *Respir. Physiol. Neurobiol.* 154, 319–330. doi: 10.1016/j.resp.2006.01.006

Kc, P., Mayer, C. A., and Haxhiu, M. A. (2004). Chemical profile of vagal preganglionic motor cells innervating the airways in ferrets: the absence of noncholinergic neurons. *J. Appl. Physiol.* 97, 1508–1517. doi: 10.1152/japplphysiol.00282.2004

Kepler, T. B., Marder, E., and Abbott, L. F. (1990). The effect of electrical coupling on the frequency of model neuronal oscillators. *Science* 248, 83–85. doi: 10.1126/science.2321028

Kohn, A. Z., Hoxha, Z., Balan, K. V., Martin, R. J., Haxhiu, M. A., Wilson, C. G., et al. (2009). Developmental changes in brainstem neurons regulating lower airway caliber. *Pediatr. Res.* 65, 509–513. doi: 10.1203/PDR.0b013e31819da270

Lewis, D. I. (1994). Dye-coupling between vagal motoneurones within the compact region of the adult rat nucleus ambiguus, in-vitro. *J. Auton. Nerv. Syst.* 47, 53–58. doi: 10.1016/0165-1838(94)90065-5

Marchetti, C., Taccola, G., and Nistri, A. (2003). Distinct subtypes of group I metabotropic glutamate receptors on rat spinal neurons mediate complex facilitatory and inhibitory effects. *Eur. J. Neurosci.* 18, 1873–1883. doi: 10.1046/j.1460-9568.2003.02924.x

Mazza, E., Núñez-Abades, P. A., Spielmann, J. M., and Cameron, W. E. (1992). Anatomical and electrotonic coupling in developing genioglossal motoneurons of the rat. *Brain Res.* 598, 127–137. doi: 10.1016/0006-8993(92)90176-A

McGovern, A. E., and Mazzone, S. B. (2010). Characterization of the vagal motor neurons projecting to the Guinea pig airways and esophagus. *Front. Neurol.* 1:153. doi: 10.3389/fneur.2010.00153

Mitchell, R. A., Herbert, D. A., Baker, D. G., and Basbaum, C. B. (1987). In vivo activity of tracheal parasympathetic ganglion cells innervating tracheal smooth muscle. *Brain Res.* 437, 157–160. doi: 10.1016/0006-8993(87)91537-X

Moore, C. T., Wilson, C. G., Mayer, C. A., Acquah, S. S., Massari, V. J., and Haxhiu, M. A. (2004). A GABAergic inhibitory microcircuit controlling cholinergic outflow to the airways. *J. Appl. Physiol.* 96, 260–270. doi: 10.1152/japplphysiol.00523.2003

Myers, A. C. (1998). Ca2+ and K+ currents regulate accommodation and firing frequency in guinea pig bronchial ganglion neurons. *Am. J. Physiol.* 275, L357–364. doi: 10.1152/ajplung.1998.275.2.L357

Myers, A. C., Undem, B. J., and Weinreich, D. (1990). Electrophysiological properties of neurons in guinea pig bronchial parasympathetic ganglia. *Am. J. Physiol.* 259, L403–409. doi: 10.1152/ajplung.1990.259.6.L403

Pace, R. W., Mackay, D. D., Feldman, J. L., and Del Negro, C. A. (2007). Role of persistent sodium current in mouse preBotzinger Complex neurons and respiratory rhythm generation. *J. Physiol.* 580, 485–496. doi: 10.1113/jphysiol.2006.124602

Parkis, M. A., Feldman, J. L., Robinson, D. M., and Funk, G. D. (2003). Oscillations in endogenous inputs to neurons affect excitability and signal processing. *J. Neurosci.* 23, 8152–8158. doi: 10.1523/JNEUROSCI.23-22-08152.2003

Qiu, D., Hou, L., Chen, Y., Zhou, X., Yuan, W., Rong, W., et al. (2011). Beta-asarone inhibits synaptic inputs to airway preganglionic parasympathetic motoneurons. *Respir. Physiol. Neurobiol.* 177, 313–319. doi: 10.1016/j.resp.2011.05.010

Ram, A., Singh, S. K., Singh, V. P., Kumar, S., and Ghosh, B. (2009). Inhaled carbenoxolone prevents allergic airway inflammation and airway hyperreactivity in a mouse model of asthma. *Int. Arch. Allergy Immunol.* 149, 38–46. doi: 10.1159/000176305

Rammes, G., Zieglgansberger, W., and Parsons, C. G. (2008). The fraction of activated N-methyl-D-aspartate receptors during synaptic transmission remains constant in the presence of the glutamate release inhibitor riluzole. *J. Neural Transm.* 115, 1119–1126. doi: 10.1007/s00702-008-0059-y

Rekling, J. C., Champagnat, J., and Denavit-Saubie, M. (1996). Thyrotropin-releasing hormone (TRH) depolarizes a subset of inspiratory neurons in the newborn mouse brain stem in vitro. *J. Neurophysiol.* 75, 811–819. doi: 10.1152/jn.1996.75.2.811

Rekling, J. C., and Feldman, J. L. (1997). Bidirectional electrical coupling between inspiratory motoneurons in the newborn mouse nucleus ambiguus. *J. Neurophysiol.* 78, 3508–3510. doi: 10.1152/jn.1997.78.6.3508

Rekling, J. C., Shao, X. M., and Feldman, J. L. (2000). Electrical coupling and excitatory synaptic transmission between rhythmogenic respiratory neurons in the preBotzinger complex. *J. Neurosci.* 20:RC113. doi: 10.1523/JNEUROSCI.20-23-j0003.2000

Ruangkittisakul, A., Schwarzacher, S. W., Secchia, L., Poon, B. Y., Ma, Y., Funk, G. D., et al. (2006). High sensitivity to neuromodulator-activated signaling pathways at physiological [K+] of confocally imaged respiratory center neurons in on-line-calibrated newborn rat brainstem slices. *J. Neurosci.* 26, 11870–11880. doi: 10.1523/JNEUROSCI.3357-06.2006

Schmitz, D., Schuchmann, S., Fisahn, A., Draguhn, A., Buhl, E. H., Petrasch-Parwez, E., et al. (2001). Axo-axonal coupling: a novel mechanism for ultrafast neuronal communication. *Neuron* 31, 831–840. doi: 10.1016/S0896-6273(01)00410-X

Sharifullina, E., Ostroumov, K., Grandolfo, M., and Nistri, A. (2008). N-methyl-D-aspartate triggers neonatal rat hypoglossal motoneurons in vitro to express rhythmic bursting with unusual Mg2+ sensitivity. *Neuroscience* 154, 804–820. doi: 10.1016/j.neuroscience.2008.03.010

Sharifullina, E., Ostroumov, K., and Nistri, A. (2005). Metabotropic glutamate receptor activity induces a novel oscillatory pattern in neonatal rat hypoglossal motoneurones. *J. Physiol.* 563, 139–159. doi: 10.1113/jphysiol.2004.079509

Smith, J. C., Ellenberger, H. H., Ballanyi, K., Richter, D. W., and Feldman, J. L. (1991). Pre-Botzinger complex: a brainstem region that may generate respiratory rhythm in mammals. *Science* 254, 726–729. doi: 10.1126/science.1683005

Solomon, I. C., Halat, T. J., El-Maghrabi, R., and O'Neal, M. H. III. (2001). Differential expression of connexin26 and connexin32 in the pre-Botzinger

complex of neonatal and adult rat. *J. Comp. Neurol.* 440, 12–19. doi: 10.1002/cne.1366

Sun, Q. J., Pilowsky, P., and Llewellyn-Smith, I. J. (1995). Thyrotropin-releasing hormone inputs are preferentially directed towards respiratory motoneurons in rat nucleus ambiguus. *J. Comp. Neurol.* 362, 320–330. doi: 10.1002/cne.903620303

Wilson, C. G., Akhter, S., Mayer, C. A., Kc, P., Balan, K. V., Ernsberger, P., et al. (2007). Allergic lung inflammation affects central noradrenergic control of cholinergic outflow to the airways in ferrets. *J. Appl. Physiol.* 103, 2095–2104. doi: 10.1152/japplphysiol.01182.2006

Yan, X., Chen, X., Guo, Y., He, D., Chen, Y., Xia, C., et al. (2017). Arginine vasopressin alters both spontaneous and phase-locked synaptic inputs to airway vagal preganglionic neuron via activation of v1a receptor: insights into stress-related airway vagal excitation. *Front. Cell. Neurosci.* 11:12. doi: 10.3389/fncel.2017.00012

Zhou, X., Chen, Y., Ge, D., Yuan, W., and Wang, J. (2013). Nicotine enhances both excitatory and inhibitory synaptic inputs to inspiratory-activated airway vagal preganglionic neurons. *Exp. Physiol.* 98, 67–80. doi: 10.1113/expphysiol.2012.066589

Conflict of Interest Statement: The authors declare that the research was conducted in the absence of any commercial or financial relationships that could be construed as a potential conflict of interest.

Copyright © 2018 Hou, Zhang, Zhang, Liu, Zhang, Qiu, Zhu and Zhou. This is an open-access article distributed under the terms of the Creative Commons Attribution License (CC BY). The use, distribution or reproduction in other forums is permitted, provided the original author(s) and the copyright owner(s) are credited and that the original publication in this journal is cited, in accordance with accepted academic practice. No use, distribution or reproduction is permitted which does not comply with these terms.

frontiers in Physiology

PERSPECTIVE
published: 02 August 2018
doi: 10.3389/fphys.2018.01021

Post-stroke Hemiplegic Gait: New Perspective and Insights

Sheng Li[1,2]*, *Gerard E. Francisco*[1,2] *and Ping Zhou*[1,2,3]

[1] Department of Physical Medicine and Rehabilitation, University of Texas Health Science Center, Houston, TX, United States, [2] TIRR Memorial Hermann Research Center, TIRR Memorial Hermann, Houston, TX, United States, [3] Guangdong Work Injury Rehabilitation Center, Guangzhou, China

Walking dysfunction occurs at a very high prevalence in stroke survivors. Human walking is a phenomenon often taken for granted, but it is mediated by complicated neural control mechanisms. The automatic process includes the brainstem descending pathways (RST and VST) and the intraspinal locomotor network. It is known that leg muscles are organized into modules to serve subtasks for body support, posture and locomotion. Major kinematic mechanisms are recognized to minimize the center of gravity (COG) displacement. Stroke leads to damage to motor cortices and their descending corticospinal tracts and subsequent muscle weakness. On the other hand, brainstem descending pathways and the intraspinal motor network are disinhibited and become hyperexcitable. Recent advances suggest that they mediate post-stroke spasticity and diffuse spastic synergistic activation. As a result of such changes, existing modules are simplified and merged, thus leading to poor body support and walking performance. The wide range and hierarchy of post-stroke hemiplegic gait impairments is a reflection of mechanical consequences of muscle weakness, spasticity, abnormal synergistic activation and their interactions. Given the role of brainstem descending pathways in body support and locomotion and post-stroke spasticity, a new perspective of understanding post-stroke hemiplegic gait is proposed. Its clinical implications for management of hemiplegic gait are discussed. Two cases are presented as clinical application examples.

Keywords: gait, stroke, hemiparesis, spasticity, botulinum toxin, motor recovery

OPEN ACCESS

Edited by:
Mikhail Lebedev,
Duke University, United States

Reviewed by:
Alexey Goltsov,
Abertay University, United Kingdom
Hu Zhou,
Shanghai Institute of Materia Medica (CAS), China

***Correspondence:**
Sheng Li
sheng.li@uth.tmc.edu

Specialty section:
This article was submitted to Systems Biology, a section of the journal Frontiers in Physiology

Received: *25 April 2018*
Accepted: *10 July 2018*
Published: *02 August 2018*

Citation:
Li S, Francisco GE and Zhou P (2018) Post-stroke Hemiplegic Gait: New Perspective and Insights. Front. Physiol. 9:1021. doi: 10.3389/fphys.2018.01021

INTRODUCTION

Stroke is a leading cause of serious long-term disability (Benjamin et al., 2017). Walking dysfunction occurs in more than 80% of stroke survivors (Duncan et al., 2005). Despite of rehabilitation efforts, 25% of all stroke survivors have residual gait impairments that require full physical assistance before hospital discharge (Hendricks et al., 2002). Consequently, gait impairments cause difficulties in performing activities of daily living and mobility. Gait abnormality is characterized by a pronounced clinical presentation of gait asymmetry, as compared to healthy people (Olney and Richards, 1996; Richards and Olney, 1996). Stroke survivors usually have decreased stance phase and prolonged swing phase of the paretic side. Further, the walking speed is decreased and the stride length is shorter (Perry and Burnfield, 2010). These gait abnormalities along with muscle weakness place stroke survivors at a high risk of falls (Dobkin, 2005; Batchelor et al., 2012). Falls usually occur during walking in community-dwelling stroke survivors (Hyndman et al., 2002). Thus, improving walking safety and speed is the major goal for stroke survivors to prevent falls and to improve quality of life (Olney and Richards, 1996; Dobkin, 2005).

Walking is a phenomenon that is taken for granted by healthy individuals but requires an extremely complex process of neuromusculoskeletal control. Activation of muscles in lower limbs, trunk, and upper limbs in a certain spatiotemporal pattern is required to ensure appropriate joint positions to support and advance the body weight in different phases of gait cycles. In most situations, human walking at a comfortable speed on the level surface is primarily mediated by brainstem and spinal mechanisms (Dietz, 1996; Nielsen, 2003). However, supraspinal control adds complexity and flexibility of gait control and gait versatility to meet dynamic environmental needs and challenges (Dietz, 1996; Nielsen, 2003). Spasticity and paresis are main motor impairments after stroke (Li, 2017). In the context of spastic hemiparesis, muscles are weak and spastic and at different levels of impairments involving different regions of the upper limb, trunk and lower limb on one side. As a result, a wide spectrum of gait abnormalities is seen clinically.

In this article, major kinematic determinants and neural control of normal human gait are briefly reviewed from a historical perspective. Current findings of post-stroke hemiplegic gait as a result of altered neural control are then summarized. Based on recent advances on pathophysiology of muscle weakness and spasticity after stroke, a new perspective of understanding post-stroke hemiplegic gait is proposed. Its clinical implications for management of hemiplegic gait are discussed.

MAJOR KINEMATIC DETERMINANTS OF NORMAL HUMAN GAIT

For a biomechanical and kinesiological point of view, human walking can be described as progression of alternating weight-bearing limbs. As such, the displacement of the center of gravity (COG) of the whole-body is viewed as the end result of all muscle forces acting upon the body during the progression. During normal level walking, the body COG follows a smooth regular curve in the three-dimensional space. The peak-to-peak amplitudes are ∼5 cm in the vertical and mediolateral planes, respectively Saunders et al. (1953). Using a hypothetical bipedal compass gait model and elementary geometrical arguments, Saunders et al. (1953) proposed six kinematic mechanisms that contribute to the efficient progress of the whole-body COG in the three dimensional space. These mechanisms are termed as six major determinants of human gait. They include pelvic rotation in the transverse plane, pelvic tilt in the coronal plan, knee flexion in the stance phase, foot and knee mechanisms and lateral displacement of the pelvis (hip adduction). This concept of major determinants was originally proposed to understand and manage pathological gait after orthopedic disorders, such as a fused hip joint (Saunders et al., 1953). From a historical perspective, major determinants of human gait are the fundamental concepts in understanding control of human gait and providing a foundation for clinical application of gait analysis. Although individual muscle activities (electromyography, EMG), joint kinematics, and ground reaction force were not available in the original "compass gait" model that permits only hip flexion and extension during walking, these determinants were able to explain the minimization of COG displacement well.

The conclusion of six determinants of human gait has been challenged in a number of studies (Gard and Childress, 1997, 1999; Croce et al., 2001; Kuo, 2007; Hayot et al., 2013). In the most recent study (Lin et al., 2014), Lin et al. quantitatively assessed the contribution of each determinant to the COG displacement over a gait cycle in young and healthy people. Using an "influence coefficient" concept, they found that hip flexion, stance knee flexion, and ankle-foot interaction significantly minimized the COG displacement in the sagittal plane; hip adduction and pelvic tilt are the main determinants of the mediolateral COG displacement in the coronal plane; however, pelvic rotation and pelvic tilt do not significantly affect the vertical COG displacement. Overall, there is general agreement between Saunders et al.'s classic article and this study with comprehensive quantitative kinematic data of individual joints. It is confirmatory that pelvic girdle movements (pelvic tilt, hip flexion, and adduction) contribute significantly to the displacement of COG in the three-dimensional space during walking.

NEURAL CONTROL OF NORMAL HUMAN GAIT

The above kinematic mechanisms are not able to account for a near perfect kinematic trajectory during human walking on a level surface, however. The distal part of the foot in the swing phase is lifted only 1–2 cm with <4 mm step-to-step variations (Winter, 1992). This displacement is enough to prevent stumbling, but not more than necessary. This remarkable precision of the foot position in the swing phase is determined by and the end result of coordinated activation of muscles from the lower extremities directly and of trunk and arm muscles indirectly. The number of different combinations of muscle activations that lead to the same foot position is almost infinite, i.e., the problem of motor redundancy (Bernstein, 1967). As suggested by Bernstein (1967), the brain may only control the endpoint, i.e., the foot position in this case, while allowing considerable flexibility for specific muscle activities. Using this fundamental approach, the muscle activities are not controlled individually. They are allowed to have a large range of flexibility as long as they are all scaled to each other to ensure the endpoint: the foot position within a desired range. These muscles are coordinated and organized into functional groups. They are often referred as muscle synergies or modules (Ting and McKay, 2007; Drew et al., 2008).

Different modules are described according to their biomechanical functions to the whole limb or the whole body during different types of locomotor functions, such as balance control or walking (Beyaert et al., 2015). There are five modules that are sufficient to perform sub-tasks of walking (Neptune et al., 2009). Module 1 includes gluteus medius, vasti, and rectus femoris muscles, primarily contributing to body support in early stance. Module 2 (soleus and gastrocnemius) is

activated during both body support and propulsion in late stance. Module 3 (rectus femoris and tibialis anterior) acts to decelerate the leg in early and late swing, as well as to generate energy to the trunk throughout the swing phase. Module 4 mainly consists of the hamstring muscles. Activation of these muscles decelerates the ipsilateral leg prior to heel strike. Module 3 and Module 5 (iliopsoas) act together to accelerate the ipsilateral leg forward in early swing. These modules represent a general repertoire of motor actions that can be recruited in a variety of combinations and at different times for different locomotion and balance control needs, as well as for voluntary, rhythmic and reactive locomotor behaviors (McGowan et al., 2010; Allen and Neptune, 2012; Beyaert et al., 2015).

Extensive neural structures and pathways are involved in the process of gait control, including the spinal cord, brainstem, cerebellum, basal ganglia, limbic system, and cerebral cortex, as well as their interactions with the environment (see review Nielsen, 2003; Beyaert et al., 2015). Briefly, the above motor modules are largely controlled by the spinal cord and brainstem under regulating control of the cerebellum. More specifically, the pontine medullary reticular formation (PMRF) and vestibular nuclei provide body support and balance control, thus providing an upright posture against gravity by activating trunk and lower extremity extensor muscles. The additional neurons in the PMRF activate the spinal locomotor network under influence of the mesencephalic locomotor region and subthalamic locomotor region or cerebellum. Activation of this network allows rhythmic locomotor activity. These structures constitute automatic processes by simultaneously controlling body support, balance and rhythmic locomotor activity. However, locomotion occurs only when this automatic process is initiated "volitionally" or "emotionally." The volitional process involves the cerebral cortex while an emotional process involves the limbic system. The basal ganglia influence volitional, emotional and automatic processes through its interactions with the cerebral cortex, limbic system, and brainstem, respectively. Furthermore, real-time sensory feedback via visual signals, vestibular, and proprioceptive signals is crucial for locomotor adaptation. In summary, walking is mainly a result of automatic process, involving the spinal cord and brainstem mechanisms. It is usually achieved and maintained without conscious awareness and cognitive processing.

ALTERED NEURAL CONTROL AND PATHOMECHANICS OF POST-STROKE HEMIPLEGIC GAIT

Neural control mechanisms are altered in stroke survivors with walking dysfunction. As compared to normal healthy controls, stroke survivors have fewer modules during walking (Clark et al., 2010). In their study (Clark et al., 2010), Clark and colleagues analyzed modules based on EMG signals from eight leg muscles in 55 subjects with chronic stroke and in 20 controls. Most of affected legs had only just two or three modules. These modules were merged from the modules observed in control subjects, thus less independent neural control for affected leg. Furthermore, the authors reported that the number of simplified modules was correlated to preferred walking speed, speed modulation, step length asymmetry, and propulsive asymmetry. In other words, stroke survivors with fewer modules on the paretic limb walk more slowly and demonstrate more gait asymmetry (Routson et al., 2014).This modification of modular organization likely reflects the central nervous system's response to muscle weakness and lack of voluntary muscle control on the affected side to improve body support and locomotion. In addition to simplified modular organization, abnormal muscle synergies and spastic synergistic activation patterns are often resulted as well (Kline et al., 2007; Finley et al., 2008). For example, Finley et al. demonstrated a reflex-mediated coupling between hip flexion and knee extension in stroke survivors (Finley et al., 2008). As a result of abnormal patterns of muscle activation, joint positions are altered at rest and joint movements are coupled during walking.

A full spectrum of gait abnormality is observed clinically, depending on the level of muscle weakness, severity of spasticity, compensatory mechanisms, and their interactions. Primarily due to muscle strength on the paretic side, there is a hierarchy of gait impairments. According to walking speeds which correspond to muscle weakness, stroke survivors are classified into four groups with different features of gait impairments (Mulroy et al., 2003). They are: Fast walker, Moderate walker, Slow-Extended walker (circumductory gait), and Slow-Flexed walker.

In the Fast walker group, a stroke survivor has ∼44% of a normal walking speed. There is a lack of heel rise in the terminal stance, due to inadequate plantarflexor (PF) muscle strength. Otherwise, discriminating gait events are within normal limits. Knee hyperextension in the stance phase is observed to compensate for lack of heel rise so that the body can roll forward onto the forefoot. As such, the step length is compromise secondary to lack of transition of momentum from the unaffected limb.

A typical Moderate walker has ∼21% of a normal walking speed. The stroke survivor is able to walk without any assistance. The plantar flexor muscles on the paretic side are further weakened. There are some weakness in hip extensors (gluteus maximum) and knee extensors (quadriceps muscle). Along with weakness, Gluteus maximum muscles, quadriceps, and plantarflexors start to show spastic responses to quick stretch. As a result, excessive knee flexion and hip flexion occur at the mid stance phase. Due to the lack of pre-swing forward progression over the toe rocker, ankle plantar flexion, knee flexion, and heel-off are inadequate in the terminal stance. However, the survivor is still able to achieve a neutral foot position for clearance in the mid swing phase.

In the Slow-Extended walker group, quadriceps muscles are further weakened, and are not able to support the knee during the stance phase. Though weak, the gluteus maximus muscle is still strong enough to retract the femur into knee hyperextension to support the body. There are also some plantarflexors contracture and spasticity to provide necessary ankle stability. During the swing phase, there is persistent gluteus maximum and ankle plantarflexor spasticity. Hip hiking and leg circumduction occur

for foot clearance. Stroke survivors in this group usually require assistive devices to walk. The walking speed is further decreased at ∼11% of a normal speed.

In the Slow-Flexed walker group, the gluteus maximus muscle is weakened further to the extent that it is not able to retract the femur to stabilize the knee. Strength limitation across hip, knee and ankle joints leaves stroke survivors with the boardline walking ability. In the mid stance, there is excessive hip and knee flexion, ankle dorsiflexion, and trunk forward leaning. This posture persists in the swing phase with assistance. The assisted walking speed is at about 10% of a normal speed.

PATHOPHYSIOLOGY OF HEMIPARESIS AND SPASTICITY AFTER STROKE

Spasticity and muscle weakness (i.e., spastic paresis) are the primary motor impairments and impose significant challenges for patient care. Spasticity is estimated to be present in about 20–40% of stroke survivors (Zorowitz et al., 2013). Clinically, post-stroke spasticity is easily recognized as a phenomenon of velocity-dependent increase in tonic stretch reflexes ("muscle tone") with exaggerated tendon jerks, resulting from hyperexcitability of the stretch reflex (Lance, 1980). Based on decades of animal studies and recent human research (Brown, 1994; Gracies, 2005; Nielsen et al., 2007; Mukherjee and Chakravarty, 2010; Burke et al., 2013; Stecco et al., 2014; Li and Francisco, 2015), there are advances in understanding the pathophysiology of spasticity and its relation with paresis (Li and Francisco, 2015; Li, 2017). A brief summary is presented here. In a stroke survivor with spastic hemiplegia, damages occur to the motor cortices and their descending corticospinal tract (CST). These damages cause muscle weakness (usually hemiparesis) immediately after stroke, including upper extremity, trunk, and lower extremity muscles on the affected side. On the other hand, neuroplasticity occurs after stroke as well. Due to lesions of corticobulbar pathways accompanied with lesion of motor cortices and/or descending CST, bulbospinal hyperexcitability develops due to loss of supraspinal inhibition. This is mainly a phenomenon of disinhibition, or unmasking effects. There are several potential candidates, including reticulospinal (RST), vestibulospinal (VST), and rubrospinal projections (Miller et al., 2014; Li and Francisco, 2015; Owen et al., 2017). Medial RST hyperexcitability appears to be the most likely mechanism related to post-stroke spasticity (Li and Francisco, 2015). RST hyperexcitability provides unopposed excitatory descending inputs to spinal stretch reflex circuits, resulting in elevated excitability of spinal motor neurons. This adaptive change can account for most clinical findings on spasticity, for example, exaggerated stretch reflex, velocity-dependent resistance to stretch, muscle overactivity, or spontaneous firings of motor units. Spasticity usually leads to a synergistic pattern of activation during standing and walking, e.g., flexor synergy in the upper extremity and extensor synergy in the lower limb (Francisco and Li, 2016). The inter-limb activation coupling between upper and lower extremities is also reported (Kline et al., 2007).

A NEW PERSPECTIVE FOR UNDERSTANDING HEMIPLEGIC GAIT

These recent advances in understanding the pathophysiology of spasticity and its relations to muscle weakness can help us better understand hemiplegic gait in stroke survivors. Given the disinhibited brainstem descending pathways (RST and VST) are linked to post-stroke spasticity, reorganization of modular control, and spastic synergistic activation, a new perspective for understanding hemiplegic gait is schematically illustrated in **Figure 1**. Muscle weakness is primarily a result of damage to motor cortices and their descending CST after stroke. Muscle strength, especially knee extensor strength determines gait independence (Akazawa et al., 2017). Disinhibited brainstem descending pathways (RST and VST) are hyperexcitable. These descending projections are diffuse and the activated muscles are organized into fewer modules or motor synergies that provide body support and posture stability and locomotion (Nielsen, 2003; Beyaert et al., 2015). In addition, they also mediate spasticity and spastic synergistic patterns. The most commonly observed abnormal patterns include flexor synergies in the upper extremity and extensor synergies in the lower extremity. These spastic activations also lead to abnormal coupling within a limb (Finley et al., 2008) and between limbs (Kline et al., 2007). The interactions among muscle weakness, spasticity, and spastic activations act on the trunk, pelvis and the legs. Mechanical consequences of these interactions are the clinically observed gait impairments. They are exemplified in the stereotypical hemiplegic gait. It is usually described as hip extension, adduction, and medial rotation, knee extension, ankle plantar flexion, and inversion. The spastic muscles are synergistically activated into hip and knee extension during the stance phase of walking. The abnormal activation does not allow the hip and knee to flex for foot clearance. To compensate for these impairments, stroke survivors usually hike hip and circumduct the affected leg during the swing phase for foot clearance. As such it is known as a "circumductory gait." Depending on the severity of weakness and spasticity, and the degree of involvement (focal, regional, or extensive), a wide spectrum of gait impairments are clinically observed, as described above.

IMPLICATIONS FOR MANAGEMENT OF HEMIPLEGIC GAIT

Improving walking safety and speed is the major goal for gait rehabilitation for stroke survivors to prevent falls and subsequently to improve quality of life (Olney and Richards, 1996; Dobkin, 2005). A multi-modality interdisciplinary approach is usually employed and encouraged to bring the maximum clinical outcomes for stroke survivors. Gait rehabilitation programs include muscle strength training, task-specific gait training, treadmill training, electromechanical and robot-assisted gait training, functional electrical stimulations, ankle foot orthoses (AFOs), virtual reality, mental practice with motor imagery, and botulinum toxin injection of spastic muscles (Verma et al., 2012; Tenniglo et al., 2014; Beyaert et al., 2015;

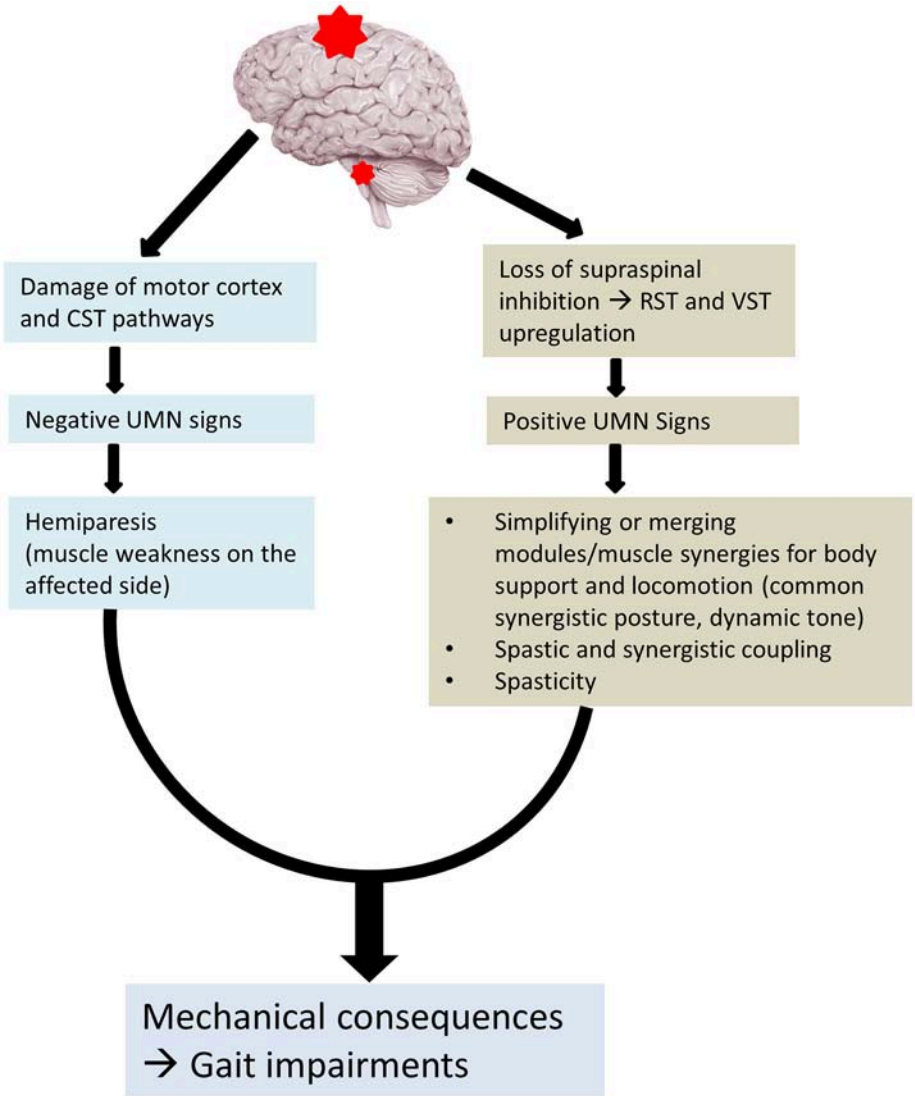


FIGURE 1 | Altered neural control for post-stroke gait. CST, corticospinal tract; RST, reticulospinal tract; VST, vestibulospinal tract.

Hsu et al., 2017; Jacinto and Reis Silva, 2018). The proposed new perspective also has clinical implications to improve management of hemiplegic gait. A few areas are discussed here as examples.

Spastic Kinetic Chain and Orthotic Management

As outlined above and in **Figure 1**, gait abnormality is a mechanical consequence of altered neural control after stroke. Abnormal joint posture during the stance phase represents the net result of interactions between ground reaction force and activation of spastic paretic muscles. For example, inadequate quadriceps support often results in a unique joint abnormality during the stance phase, i.e., greater knee flexion in the Moderate walker group. This knee position places the ground reaction force further anterior to the ankle joint, posterior to the knee joint, and anterior to the hip joint. In response to the increased moment imposed to each joint of the kinetic chain, spastic activation of gluteus muscles to assist hip extension, of quadriceps muscles to assist knee extension, and of ankle plantarflexors and invertors to assist ankle dorsiflexion and stabilization. For such a spastic kinetic chain, bracing with ankle-foot-orthosis to decrease ankle dorsiflexion angle is likely effective in changing the vector of ground reaction force (Owen, 2010). The forces required for maintaining joint position at each joint are reduced, and body support and joint stability are improved.

Muscle Selection for Botulinum Toxin Therapy

Botulinum toxin therapy is often used for spasticity management of leg muscles to improve gait (Esquenazi et al., 2015; Baker et al., 2016). Botulinum toxin (BoNT) acts to block presynaptic

release of acetylcholine at the neuromuscular junction, therefore, intramuscular injection of BoNT can lead to spasticity reduction (Jahn, 2006). Due to this, BoNT injection also results in muscle weakness. As stated above, increased spasticity of quadriceps is likely to be part of synergistic activation for body support and posture stabilization. Quadriceps strength and support determines walking independence (Akazawa et al., 2017). Though quadriceps spasticity is often linked to knee joint stiffness, judicious consideration of treatment for spasticity is required because of the side effect of muscle weakness from BoNT. Another common observation is that stroke survivors have ankle plantarflexion and ankle inversion. Intramuscular EMG exams may detect spontaneous motor unit activation potentials (MUAPs) in most relevant muscles, such as tibialis posterior, gastrocnemius, soleus, tibialis anterior, extensor hallux longus muscles, i.e., spasticity (Mottram et al., 2009, 2010; Chang et al., 2013). It is not surprising to detect spasticity in all of these muscles, given diffused activation of brainstem descending pathways. The clinical presentation of ankle plantarflexion and ankle inversion suggests that this abnormality is primarily caused by tibialis posterior, gastrocnemius, and soleus, or spasticity of these muscles overrides spasticity of tibialis anterior and extensor halluces longus muscles. Not all muscles with spasticity need botulinum toxin injection in this case. Rather, selection of muscles is based on mechanical consequences of spastic muscles and their relation to ankle and foot positioning during walking.

Muscles for Pelvis and Posture Control

Major kinematic determinants were originally proposed to explain contributions of individual joints (pelvic movement, hip, knee, and ankle joints) to minimize the COG displacement. The purpose was to understand human gait in general and to explain gait abnormality after orthopedic disorders in particular, such as hip joint fusion. As mentioned above, these kinematic determinants were in general validated by the modern instrumented gait analysis. Even though three out of six kinematic determinants involve pelvic movement, EMG studies are almost limited to leg muscles. Only one muscle (gluteus maximus) related to pelvic movement is commonly studied (Perry and Burnfield, 2010). The neural control mechanisms (brainstem-spinal network) involve trunk muscles and other pelvic movement related muscles as well. Post-stroke spastic hemiparesis could involve all muscles on the affected side. Depending on clinical presentations, these pelvic muscles could be the primary contributors of the gait impairments (**Figure 2**). Two cases are presented here to highlight the importance of spastic latissimus dorsi muscle and gluteus medius and tensor fasciae latae (TFL) muscles in post-stroke gait control. Written informed consent was obtained for scientific publication from both patients.

Case 1

A 62 year old right-handed female suffered right middle cerebral artery ischemic stroke 6 years ago with a residual left spastic hemiplegia. She was able to ambulate without any assistive device at a moderate walking speed. She presented with a mild



FIGURE 2 | (A,B) A stroke survivor with spasticity that resulted in dramatic trunk lateral flexion and hip hiking before and after botulinum toxin injections; **(C,D)** A stroke survivor with spasticity that resulted in dynamic hip adduction and pelvic anterior rotation before and after botulinum toxin injection. See text for details.

circumductory gait. Lateral trunk flexion to the left side and her left hip hiking were prominent and constant during walking. According to its spread origin of latissimus dorsi muscle from inferior 3–4 ribs, low thoracic spine, lumbar spine and iliac crest, and its insertion to the intertubercular groove of the humerus, a spastic latissimus dorsi muscle was viewed to be responsible for this patient's abnormal posture during walking, including pelvic vertical elevation in the coronal plane, trunk lateral flexion, shoulder adduction, and internal rotation (**Figure 2A**). A total of 150 units of onabotulinumtoxin A were injected into this muscle under ultrasound imaging guidance. Trunk lateral flexion and pelvic elevation were much improved at 6 weeks after injection. As shown on **Figure 2B**, pelvic vertical elevation was decreased from 19 to 9° after injection.

Case 2

A 27 year old right handed female had a history of stroke after a traumatic brain injury 20 years ago which resulted in right spastic hemiplegia. She received botulinum toxin injections several times in the first 3 years after the accident. At a seated or supine position, she only had very mild muscle weakness in the right upper and lower extremities with minimum to negligible spasticity. The chief complaint was that her right toes were hitting the left toes during the mid-swing phase, i.e., problematic right hip internal rotation and adduction secondary to dynamic tone (**Figure 2C**). According to possible pathomechanics, dynamic spasticity in right anterior gluteus medius and TFL muscles could cause excessive anterior rotation of the pelvis in the transverse plane and hip internal rotation, while hip adductor spasticity contributes further to hip adduction. A total of 200 units of incobotulinumtoxin A were injected to these muscles under ultrasound imaging guidance (75 units to gluteus medius, 50 units to TFL, and 75 units to hip adductors). Improved walking posture in the follow up visit at 6 weeks after injection validated the pathomechanics analysis (**Figure 2D**).

CONCLUDING REMARKS

Given the disinhibited brainstem descending pathways (RST and VST) are linked to post-stroke spasticity, reorganization of modular control, and spastic synergistic activation, a new perspective for understanding hemiplegic gait is proposed. This new perspective highlights post-stroke hemiplegic gait impairments as mechanical consequences of altered neural control mechanisms of human gait. Hemiplegic gait is not a result of isolated skeletal muscular disorder, as often seen after orthopedic disorders. In clinical observational analysis, muscle weakness, spasticity, and spastic activation on the paretic arm, trunk and leg need to be taken into consideration. This new perspective also advances clinical management strategies as outlined above. However, these are examples and cases. They need to be validated in future laboratory and clinical studies.

AUTHOR CONTRIBUTIONS

SL developed the initial version of the manuscript and created the figures. GF and PZ critically revised the manuscript and contributed substantially to the manuscript development. All authors read and approved the final manuscript.

FUNDING

This study was supported in part by NIH NICHD/NCMRR R21HD087128, R21HD090453.

REFERENCES

Akazawa, N., Okawa, N., Tamura, K., and Moriyama, H. (2017). Determining the cut-off value for knee extensor strength for identifying independence in gait in chronic stroke survivors. *J. Rehabil. Med.* 49, 765–767. doi: 10.2340/16501977-2279

Allen, J. L., and Neptune, R. R. (2012). Three-dimensional modular control of human walking. *J. Biomech.* 45, 2157–2163. doi: 10.1016/j.jbiomech.2012.05.037

Baker, R., Esquenazi, A., Benedetti, M. G., and Desloovere, K. (2016). Gait analysis: clinical facts. *Eur. J. Phys. Rehabil. Med.* 52, 560–574.

Batchelor, F. A., MacKintosh, S. F., Said, C. M., and Hill, K. D. (2012). Falls after stroke. *Int. J. Stroke* 7, 482–490. doi: 10.1111/j.1747-4949.2012.00796.x

Benjamin, E. J., Blaha, M. J., Chiuve, S. E., Cushman, M., Das, S. R., Deo, R., et al. (2017). Heart disease and stroke statistics-2017 update: a report from the American Heart Association. *Circulation* 135, e146–e603. doi: 10.1161/CIR.0000000000000485

Bernstein, N. A. (1967). *The Co-ordination and Regulation of Movements*. Oxford: T. Pergamon Press.

Beyaert, C., Vasa, R., and Frykberg, G. E. (2015). Gait post-stroke: pathophysiology and rehabilitation strategies. *Neurophysiol. Clin.* 45, 335–355. doi: 10.1016/j.neucli.2015.09.005

Brown, P. (1994). Pathophysiology of spasticity. *J. Neurol. Neurosurg. Psychiatry* 57, 773–777. doi: 10.1136/jnnp.57.7.773

Burke, D., Wissel, J., and Donnan, G. A. (2013). Pathophysiology of spasticity in stroke. *Neurology* 80, S20–S26. doi: 10.1212/WNL.0b013e31827624a7

Chang, S. H., Francisco, G. E., Zhou, P., Rymer, W. Z., and Li, S. (2013). Spasticity, weakness, force variability, and sustained spontaneous motor unit discharges of resting spastic-paretic biceps brachii muscles in chronic stroke. *Muscle Nerve* 48, 85–92. doi: 10.1002/mus.23699

Clark, D. J., Ting, L. H., Zajac, F. E., Neptune, R. R., and Kautz, S. A. (2010). Merging of healthy motor modules predicts reduced locomotor performance and muscle coordination complexity post-stroke. *J. Neurophysiol.* 103, 844–857. doi: 10.1152/jn.00825.2009

Croce, U. D., Riley, P. O., Lelas, J. L., and Kerrigan, D. C. (2001). A refined view of the determinants of gait. *Gait Posture* 14, 79–84. doi: 10.1016/S0966-6362(01)00128-X

Dietz, V. (1996). Interaction between central programs and afferent input in the control of posture and locomotion. *J. Biomech.* 29, 841–844. doi: 10.1016/0021-9290(95)00175-1

Dobkin, B. H. (2005). Rehabilitation after Stroke. *N. Engl. J. Med.* 352, 1677–1684. doi: 10.1056/NEJMcp043511

Drew, T., Kalaska, J., and Krouchev, N. (2008). Muscle synergies during locomotion in the cat: a model for motor cortex control. *J. Physiol.* 586, 1239–1245. doi: 10.1113/jphysiol.2007.146605

Duncan, P. W., Zorowitz, R., Bates, B., Choi, J. Y., Glasberg, J. J., Graham, G. D., et al. (2005). Management of adult stroke rehabilitation care. a clinical practice guideline. *Stroke* 36, e100–e143. doi: 10.1161/01.STR.0000180861.54180.FF

Esquenazi, A., Moon, D., Wikoff, A., and Sale, P. (2015). Hemiparetic gait and changes in functional performance due to OnabotulinumtoxinA injection to lower limb muscles. *Toxicon* 107, 109–113. doi: 10.1016/j.toxicon.2015.08.004

Finley, J. M., Perreault, E. J., and Dhaher, Y. Y. (2008). Stretch reflex coupling between the hip and knee: implications for impaired gait following stroke. *Exp. Brain Res.* 188, 529–540. doi: 10.1007/s00221-008-1383-z

Francisco, G. E., and Li, S. (2016). *Spasticity. Physical Medicine and Rehabilitation, 5th Edn*, ed D. X. CIfu (Philadelphia, PA: Elsevier), 487–489.

Gard, S. A., and Childress, D. S. (1997). The effect of pelvic list on the vertical displacement of the trunk during normal walking. *Gait Posture* 5, 233–238. doi: 10.1016/S0966-6362(96)01089-2

Gard, S. A., and Childress, D. S. (1999). The influence of stance-phase knee flexion on the vertical displacement of the trunk during normal walking. *Arch. Phys. Med. Rehabil.* 80, 26–32. doi: 10.1016/S0003-9993(99)90303-9

Gracies, J. M. (2005). Pathophysiology of spastic paresis. II: Emergence of muscle overactivity. *Muscle Nerve* 31, 552–571. doi: 10.1002/mus.20285

Hayot, C., Sakka, S., and Lacouture, P. (2013). Contribution of the six major gait determinants on the vertical center of mass trajectory and the vertical ground reaction force. *Hum. Mov. Sci.* 32, 279–289. doi: 10.1016/j.humov.2012.10.003

Hendricks, H. T., van Limbeek, J., Geurts, A. C., and Zwarts, M. J. (2002). Motor recovery after stroke: a systematic review of the literature. *Arch. Phys. Med. Rehabil.* 83, 1629–1637. doi: 10.1053/apmr.2002.35473

Hsu, C. J., Kim, J., Roth, E. J., Rymer, W. Z., and Wu, M. (2017). Forced use of the paretic leg induced by a constraint force applied to the nonparetic leg in individuals poststroke during walking. *Neurorehabil. Neural Repair* 31, 1042–1052. doi: 10.1177/1545968317740972

Hyndman, D., Ashburn, A., and Stack, E. (2002). Fall events among people with stroke living in the community: circumstances of falls and characteristics of fallers. *Arch. Phys. Med. Rehabil.* 83, 165–170. doi: 10.1053/apmr.2002.28030

Jacinto, L. J., and Reis Silva, M. (2018). Gait analysis in the context of spasticity management. *Biosyst. Biorobot.* 19, 471–487. doi: 10.1007/978-3-319-72736-3_31

Jahn, R. (2006). Neuroscience. A neuronal receptor for botulinum toxin. *Science* 312, 540–541. doi: 10.1126/science.1127236

Kline, T. L., Schmit, B. D., and Kamper, D. G. (2007). Exaggerated interlimb neural coupling following stroke. *Brain* 130, 159–169. doi: 10.1093/brain/awl278

Kuo, A. D. (2007). The six determinants of gait and the inverted pendulum analogy: a dynamic walking perspective. *Hum. Mov. Sci.* 26, 617–656. doi: 10.1016/j.humov.2007.04.003

Lance, J. W. (1980). "Symposium synopsis," in *Spasticity: Disordered Motor Control*, eds R. G. Feldman, R. R. Young, and W. P. Koella (Chicago, IL: Year Book Medical Publishers), 485–494.

Li, S. (2017). Spasticity, motor recovery, and neural plasticity after stroke. *Front. Neurol.* 8:120. doi: 10.3389/fneur.2017.00120

Li, S., and Francisco, G. (2015). New insights into the pathophysiology of post-stroke spasticity. *Front. Hum. Neurosci.* 9:192. doi: 10.3389/fnhum.2015.00192

Lin, Y. C., Gfoehler, M., and Pandy, M. G. (2014). Quantitative evaluation of the major determinants of human gait. *J. Biomech.* 47, 1324–1331. doi: 10.1016/j.jbiomech.2014.02.002

McGowan, C. P., Neptune, R. R., Clark, D. J., and Kautz, S. A. (2010). Modular control of human walking: adaptations to altered mechanical demands. *J. Biomech.* 43, 412–419. doi: 10.1016/j.jbiomech.2009.10.009

Miller, D. M., Klein, C. S., Suresh, N. L., and Rymer, W. Z. (2014). Asymmetries in vestibular evoked myogenic potentials in chronic stroke survivors with spastic hypertonia: evidence for a vestibulospinal role. *Clin. Neurophysiol.* 125, 2070–2078. doi: 10.1016/j.clinph.2014.01.035

Mottram, C. J., Suresh, N. L., Heckman, C. J., Gorassini, M. A., and Rymer, W. Z. (2009). Origins of abnormal excitability in biceps brachii motoneurons of spastic-paretic stroke survivors. *J. Neurophysiol.* 102, 2026–2038. doi: 10.1152/jn.00151.2009

Mottram, C. J., Wallace, C. L., Chikando, C. N., and Rymer, W. Z. (2010). Origins of spontaneous firing of motor units in the spastic-paretic biceps brachii muscle of stroke survivors. *J. Neurophysiol.* 104, 3168–3179. doi: 10.1152/jn.00463.2010

Mukherjee, A., and Chakravarty, A. (2010). Spasticity mechanisms–for the clinician. *Front. Neurol.* 1:149. doi: 10.3389/fneur.2010.00149

Mulroy, S., Gronley, J., Weiss, W., Newsam, C., and Perry, J. (2003). Use of cluster analysis for gait pattern classification of patients in the early and late recovery phases following stroke. *Gait Posture* 18, 114–125. doi: 10.1016/S0966-6362(02)00165-0

Neptune, R. R., Clark, D. J., and Kautz, S. A. (2009). Modular control of human walking: a simulation study. *J. Biomech.* 42, 1282–1287. doi: 10.1016/j.jbiomech.2009.03.009

Nielsen, J. B. (2003). How we walk: central control of muscle activity during human walking. *Neuroscientist* 9, 195–204. doi: 10.1177/1073858403009003012

Nielsen, J. B., Crone, C., and Hultborn, H. (2007). The spinal pathophysiology of spasticity–from a basic science point of view. *Acta Physiol.* 189, 171–180. doi: 10.1111/j.1748-1716.2006.01652.x

Olney, S. J., and Richards, C. (1996). Hemiparetic gait following stroke. Part I: Characteristics. *Gait Posture* 4, 136–148. doi: 10.1016/0966-6362(96)01063-6

Owen, E. (2010). The importance of being earnest about shank and thigh kinematics especially when using ankle-foot orthoses. *Prosthet. Orthot. Int.* 34, 254–269. doi: 10.3109/03093646.2010.485597

Owen, M., Ingo, C., and Dewald, J. P. A. (2017). Upper extremity motor impairments and microstructural changes in bulbospinal pathways in chronic hemiparetic stroke. *Front. Neurol.* 8:257. doi: 10.3389/fneur.2017.00257

Perry, J., and Burnfield, J. M. (2010). *Gait Analysis: Normal and Pathological Function, 2nd Edn*. Thorofare, NJ: SLACK Incorporated.

Richards, C. L., and Olney, S. J. (1996). Hemiparetic gait following stroke. Part II: recovery and physical therapy. *Gait Posture* 4, 149–162. doi: 10.1016/0966-6362(96)01064-8

Routson, R. L., Kautz, S. A., and Neptune, R. R. (2014). Modular organization across changing task demands in healthy and poststroke gait. *Physiol. Rep.* 2:e12055. doi: 10.14814/phy2.12055

Saunders, J. B., Inman, V. T., and Eberhart, H. D. (1953). The major determinants in normal and pathological gait. *J. Bone Joint Surg. Am.* 35-A, 543–558. doi: 10.2106/00004623-195335030-00003

Stecco, A., Stecco, C., Raghavan, P. (2014). Peripheral mecahnisms contributing to spasticity and implications for treatment. *Curr. Phys. Med. Rehabil. Rep.* 2, 121–127. doi: 10.1007/s40141-014-0052-3

Tenniglo, M. J., Nederhand, M. J., Prinsen, E. C., Nene, A. V., Rietman, J. S., and Buurke, J. H. (2014). Effect of chemodenervation of the rectus femoris muscle in adults with a stiff knee gait due to spastic paresis: a systematic review with a meta-analysis in patients with stroke. *Arch. Phys. Med. Rehabil.* 95, 576–587. doi: 10.1016/j.apmr.2013.11.008

Ting, L. H., and McKay, J. L. (2007). Neuromechanics of muscle synergies for posture and movement. *Curr. Opin. Neurobiol.* 17, 622–628. doi: 10.1016/j.conb.2008.01.002

Verma, R., Arya, K. N., Sharma, P., and Garg, R. K. (2012). Understanding gait control in post-stroke: implications for management. *J. Bodyw. Mov. Ther.* 16, 14–21. doi: 10.1016/j.jbmt.2010.12.005

Winter, D. A. (1992). Foot trajectory in human gait: a precise and multifactorial motor control task. *Phys. Ther.* 72, 45–56. doi: 10.1093/ptj/72.1.45

Zorowitz, R. D., Gillard, P. J., and Brainin, M. (2013). Poststroke spasticity: sequelae and burden on stroke survivors and caregivers. *Neurology* 80, S45–S52. doi: 10.1212/WNL.0b013e3182764c86

Conflict of Interest Statement: The authors declare that the research was conducted in the absence of any commercial or financial relationships that could be construed as a potential conflict of interest.

Copyright © 2018 Li, Francisco and Zhou. This is an open-access article distributed under the terms of the Creative Commons Attribution License (CC BY). The use, distribution or reproduction in other forums is permitted, provided the original author(s) and the copyright owner(s) are credited and that the original publication in this journal is cited, in accordance with accepted academic practice. No use, distribution or reproduction is permitted which does not comply with these terms.

frontiers in Cellular Neuroscience

ORIGINAL RESEARCH
published: 29 August 2018
doi: 10.3389/fncel.2018.00285

TASK1 and TASK3 Are Coexpressed With ASIC1 in the Ventrolateral Medulla and Contribute to Central Chemoreception in Rats

Xia Wang[1†], *Ruijuan Guan*[1†], *Xiaomei Zhao*[1], *Danian Zhu*[1], *Nana Song*[2*] *and Linlin Shen*[1,3*]

[1]*Department of Physiology and Pathophysiology, School of Basic Medical Sciences, Fudan University, Shanghai, China,* [2]*Division of Nephrology, Zhongshan Hospital, Fudan University, Shanghai, China,* [3]*Shanghai Key Laboratory of Medical Imaging Computing and Computer-Assisted Intervention, Fudan University, Shanghai, China*

The ventrolateral medulla (VLM), including the lateral paragigantocellular nucleus (LPGi) and rostral VLM (RVLM), is commonly considered to be a chemosensitive region. However, the specific mechanism of chemoreception in the VLM remains elusive. Acid-sensing ion channels (ASICs), a family of voltage-independent proton-gated cation channels, can be activated by an external pH decrease to cause Na^+ entry and induce neuronal excitability. TWIK-related acid-sensitive potassium channels (TASKs) are members of another group of pH-sensitive channels; in contrast to AISICs, they can be stimulated by pH increases and are inhibited by pH decreases in the physiological range. Our previous study demonstrated that ASICs take part in chemoreception. The aims of this study are to explore whether TASKs participate in the acid sensitivity of neurons in the VLM, thereby cooperating with ASICs. Our research demonstrated that TASKs, including TASK1 and TASK3, are colocalized with ASIC1 in VLM neurons. Blocking TASKs by microinjection of the non-selective TASK antagonist bupivacaine (BUP), specific TASK1 antagonist anandamide (AEA) or specific TASK3 antagonist ruthenium red (RR) into the VLM increased the integrated phrenic nerve discharge (iPND), shortened the inspiratory time (Ti) and enhanced the respiratory drive (iPND/Ti). In addition, microinjection of artificial cerebrospinal fluid (ACSF) at a pH of 7.0 or 6.5 prolonged Ti, increased iPND and enhanced respiratory drive, which were inhibited by the ASIC antagonist amiloride (AMI). By contrast, microinjection of alkaline ACSF decreased iPND and respiratory drive, which were inhibited by AEA. Taken together, our data suggest that TASK1 and TASK3 are coexpressed with ASIC1 in the VLM. Moreover, TASK1 and TASK3 contribute to the central regulation of breathing by coordinating with each other to perceive local pH changes; these results indicate a novel chemosensitive mechanism of the VLM.

Keywords: TASK1, TASK3, ventrolateral medulla, pH-sensitive, chemoreception

OPEN ACCESS

Edited by:
Mikhail Lebedev,
Duke University, United States

Reviewed by:
Klaus Ballanyi,
University of Alberta, Canada
Donald C. Bolser,
University of Florida, United States

***Correspondence:**
Nana Song
song.nana@zs-hospital.sh.cn
Linlin Shen
llshen@shmu.edu.cn

[†]*These authors have contributed equally to this work*

Received: *04 December 2017*
Accepted: *10 August 2018*
Published: *29 August 2018*

Citation:
Wang X, Guan R, Zhao X, Zhu D, Song N and Shen L (2018) TASK1 and TASK3 Are Coexpressed With ASIC1 in the Ventrolateral Medulla and Contribute to Central Chemoreception in Rats. Front. Cell. Neurosci. 12:285. doi: 10.3389/fncel.2018.00285

INTRODUCTION

Central chemoreceptors sense changes of H^+ concentration ($[H^+]$) in cerebrospinal fluid (CSF), play an important role in respiratory regulation and contribute to acid-base homeostasis. It is generally considered that chemoreceptors in the central nervous system (CNS) mainly detect CO_2, while carotid bodies (peripheral chemoreceptors) detect PCO_2 in the blood (Goridis and Brunet, 2010). CO_2 can be dissolved in CSF and penetrates membranes readily to generate H_2CO_3, which decomposes to H^+ and HCO_3^-. Therefore, the physiological stimulation of the central chemoreceptor is H^+ in the CSF and local extracellular fluid. It has been reported that chemoreceptors exist in many brain areas including raphe, retrotrapezoid nucleus (RTN), ventrolateral medulla (VLM), locus coeruleus (LC) and the nucleus of tractus solitaries (NTS). Among these chemosensitive areas, VLM is considered to specialize in central chemoreception (Millhorn and Eldridge, 1986). However, the mechanism of chemoreception by VLM neurons remains elusive. pH-sensitive ion channels, including acid-sensing ion channels (ASICs) and TWIK-related acid-sensitive potassium channels (TASKs), establish a new paradigm to study the chemosensory mechanism of the CNS. Molecular analysis has shown that ASICs contribute to the capacity of afferent neurons to monitor acidosis (Holzer, 2009). Our previous study also found that ASIC1 in the VLM contributes to chemoreception and the regulation of respiration (Song et al., 2016). However, it is unclear whether TASKs participate in central chemoreception.

TASKs are characterized by "leak" K^+ currents and play key roles in maintaining the rest membrane potential by adjusting the action potential duration and modulating the response to synaptic inputs (Honoré, 2007). TASKs are also pH-sensitive, which can be by inhibited by acidification and activated by alkalization. Among the three TASK subunits, TASK1 and TASK3 are widely expressed throughout the brain, including in the VLM and raphe nuclei (Washburn et al., 2002, 2003). These subunits are sensitive to extracellular protons with different sensitivities and contribute to the regulation of neuronal excitability (Bayliss et al., 2015). The pK value of TASK1 ranges from pH 7.3 to 7.5, and that of TASK3 ranges from pH 6.5 to 6.7 (Duprat et al., 2007). Their pH sensitivities are used to differentiate TASK1 from TASK3 (Hartness et al., 2001; Czirják and Enyedi, 2002; Washburn et al., 2003). TASKs in serotonergic raphe neurons exert pH and anesthetic sensitivity *in vitro* (Washburn et al., 2002). Inhibition of the TASKs by extracellular acidosis leads to an increased excitability of brainstem respiratory neurons (Duprat et al., 2007). Extracellular alkalization decreases the excitability of neurons expressing TASKs (Berg et al., 2004). In addition, they play a major functional role in the respiratory rhythm generation of the pre-Bötzinger complex (Koizumi et al., 2010). TASK1 and TASK3 appear to serve specific and distinct roles in chemoreception and respiratory control (Buehler et al., 2017).

It seems that both TASKs and ASICs are involved in the pH sensitivity of chemosensitive neurons in the CNS. However, the colocalization of TASKs and ASICs in chemosensitive neurons has not been addressed, and little is known about the cooperation of these two types of channels in respiratory regulation. In the current study, we hypothesized that TASKs and ASIC1 are coexpressed in the VLM and cooperate in the central control of respiration. In our present study, we found both ASIC1 and TASKs (1 and 3) expressed in the VLM of rats. We then investigated the role of ASIC1 and TASKs (1 and 3) in chemoreception. Our data showed that ASIC1 and TASKs (1 and 3) were colocalized in VLM neurons. The microinjection of different TASKs blockers, including a non-selective antagonist bupivacaine (BUP), a specific TASK1 antagonist anandamide (AEA) and a specific TASK3 antagonist ruthenium red (RR), into the VLM facilitated phrenic nerve discharge (PND). In addition, the microinjection of artificial CSF (ACSF) at a pH of 7.0 or 6.5 increased integrated PND (iPND), Inspiratory time (Ti) and respiratory drive, which were inhibited by the ASIC antagonist, amiloride (AMI). Contrarily, the microinjection of alkaline ACSF decreased iPND and respiratory drive, and this effect was attenuated by AEA. Our research indicated that TASKs and ASICs contribute to the central regulation of breathing by coordinating with each other to cause the perception of local pH changes. This investigation will help to establish a new understanding of the pH-sensing mechanism of chemosensitive neurons in the VLM.

MATERIALS AND METHODS

Animals

Male Sprague–Dawley rats (250–350 g, aged 3–4 months) were obtained from Shanghai Jiesijie Experimental Animal Co. Ltd. (Shanghai, China). All animals were kept in a room under a 12-h light-dark cycle, an ambient temperature of 22 ± 0.5°C and a relative humidity of 60 ± 2%. Food and water were given freely. The animal experiments were conducted in strict accordance with the US National Institutes of Health Guidelines for the Care and Use of Laboratory Animals and were approved by the Ethics Committee of Experimental Research, Shanghai Medical College, Fudan University. A total of 58 adult rats were used in this study. Maximal efforts were undertaken to minimize the number of animals and their suffering.

Drug Application

A nonselective ASIC inhibitor, AMI (Sigma Aldrich, St. Louis, MO, USA); a non-selective TASK antagonist, BUP (Sigma Aldrich, St. Louis, MO, USA); and a specific TASK3 antagonist, RR (Sigma Aldrich, St. Louis, MO, USA) were freshly prepared in ACSF immediately before administration. A specific TASK1 antagonist, AEA (Sigma Aldrich, St. Louis, MO, USA), was prepared in ethanol. The ACSF solutions were prepared at different pHs (8.0, 7.4, 7.0, 6.5, and 6.0). ACSF containing (mM) NaCl 130, $NaHCO_3$ 26, KCl 5, $CaCl_2$ 2.6, $MgSO_4$ 1.2, NaH_2PO_4 1.6, glucose 11 and sucrose 10 at pH 7.4 and ethanol served as the vehicle and volume controls.

Immunohistochemistry

Adult Sprague-Dawley rats were anesthetized with urethane (1 $g.kg^{-1}$) and perfused through the left ventricle with normal

saline followed by 4% paraformaldehyde. After perfusion, the medullary was dissected, transferred to graded sucrose solutions (20% and 30%) until sinking and were cut into coronal sections at 25-μm thickness using a Leica freezing microtome. The slides were washed with 0.01 M PBS and blocked in 1% BSA for 1 h at room temperature. After blocking, the slides were incubated with a primary antibody against TASK1 or TASK3 (Alomone Laboratory, Israel, 1:100) diluted in 0.01 M PBS, and the controls were incubated with 0.01 M PBS without primary antibody overnight. The reaction was then detected using a Boshide avidin-biotin-HRP complex (ABC) immunohistochemical kit (Wuhan, China). Slices were dried in the drying oven and mounted with coverslips after dehydration and rendering transparent and were then observed and photographed under a microscope.

Immunofluorescence Technique

Slides were washed with 0.01 M PBS and then blocked with a 5% mixture of donkey and goat serum for 1 h at room temperature. After blocking, the slides were incubated with primary antibodies against TASK1 (Alomone Laboratory, Israel, 1:100), TASK3 (Alomone Laboratory, Israel, 1:100) and ASIC1 (Santa Cruz Biotechnology, Dallas, TX, USA, 1:100), Neurofilament-H (Abcam, Cambridge, MA, USA) which were diluted in 0.01 M PBS, overnight. After washing, the slides were incubated with goat anti rabbit IgG conjugated with cy3, donkey anti goat IgG conjugated with FITC, rabbit anti mouse IgG conjugated with DY light 405 (1:100, Beyotime Institute of Biotechnology, Haimen, China) for 1 h in the dark. The slides were then mounted in antifading medium (Beyotime Institute of Biotechnology), and fluorescence was detected using a Zeiss LSM confocal laser system.

Phrenic Nerve Discharge Recording

PND was recorded with platinum bipolar electrodes, which were amplified (filters set at 5.0 kHz) using a Polygraph System (NIHON KOHDEN) and digitized using a SMUP system (SMUP-E, Shanghai Medical College, Fudan University). The experiments were started after the phrenic activity was stabilized (approximately 30 min). The iPND was obtained as a moving average of the phrenic signal. Ti was averaged over 30 s. The value of each iPND and the period of Ti reflected the respiratory drive.

Microinjection

Rats were held in stereotaxic frames with their heads inclined forward at 45 degrees to the level of the dorsal surface of the brain stem after anesthetization. A stainless steel needle was used to unilaterally microinject 0.1 μL into the VLM (12.3 mm posterior, 2.2 mm lateral, and 10 mm dorsal from the bregma). At the end of the experiment, 2% pontamine sky blue was microinjected into the same injection point. The brains were then removed and fixed in 10% formalin solution. After 48 h, the brain stem was coronally sectioned (30 μm) and stained with neutral red to determine the injection site. Data was discarded, if injection site was out of VLM.

Statistical Analysis

Data are expressed as the means ± SD. The significance of differences among the groups was evaluated using the Student *t*-test or a one-way ANOVA test. A value of $p < 0.05$ was considered statistically significant.

RESULTS

Distribution of TASK1 and TASK3 in Rat VLM

The localization of TASK1 and TASK3 immunopositive cells was determined in the VLM of rats (**Figure 1**). According to rat brain atlases, TASK1-ir and TASK3-ir cells are mainly localized in the VLM, including the rostroventrolateral reticular nucleus (RVL) and the lateral paragigantocellular nucleus (LPGi).

Colocalization of TASK1 and TASK3 in VLM Neurons

To detect whether TASK1 and TASK3 are localized in VLM neurons, TASK1-ir and TASK3-ir cells were measured in rat VLM by double immunofluorescence. TASK1 and TASK3 were colocalized with neurofilaments, the biomarker for neurons. Furthermore, TASK1 and TASK3 were colocalized in VLM (**Figure 2**).

Coexpression of ASIC1 and TASK1 or TASK3 in VLM Neurons

We have previously shown that ASIC1 is expressed in VLM neurons and contribute to respiratory regulation (Song et al., 2016). Thus, we wondered whether ASIC1 is coexpressed with TASK1 or TASK3 in VLM neurons. Immunofluorescence was applied to observe the coexpression of ASIC1 and TASK1 or TASK3. Our data showed that ASIC1 was coexpressed with TASK1 and with TASK3 in VLM neurons (**Figure 3**).

The Effects of Non-selective TASK Antagonists on Respiration

To test whether TASKs in the VLM are involved in respiration that is controlled by the respiratory center, the non-selective TASK antagonist BUP was applied. BUP was known to block TASK1 and TASK3 channels (Kindler et al., 1999).We microinjected BUP (200 μM) into the VLM to observe the consequent changes of PND and iPND (**Figure 4A**). Microinjection of BUP triggered significant changes in iPND, Ti and respiratory drive (integrating the value of iPND/Ti). The iPND value was increased by approximately 35% from 1.08 ± 0.11 to 1.45 ± 0.15 arbitrary units ($p < 0.01$, $n = 6$, **Figure 4C**). The respiratory drive was also increased from 1.05 ± 0.07 to 1.56 ± 0.12 ($p < 0.01$, $n = 6$, **Figure 4D**). However, Ti was shortened from 0.36 ± 0.02 to 0.31 ± 0.02 s ($p < 0.05$, $n = 6$, **Figure 4B**). Additionally, the injection spot was confirmed by histological staining (**Figure 4E**). These results indicate that the inhibition of TASKs in VLM neurons leads to cell depolarization by decreasing K^+ efflux, thus stimulating respiration.

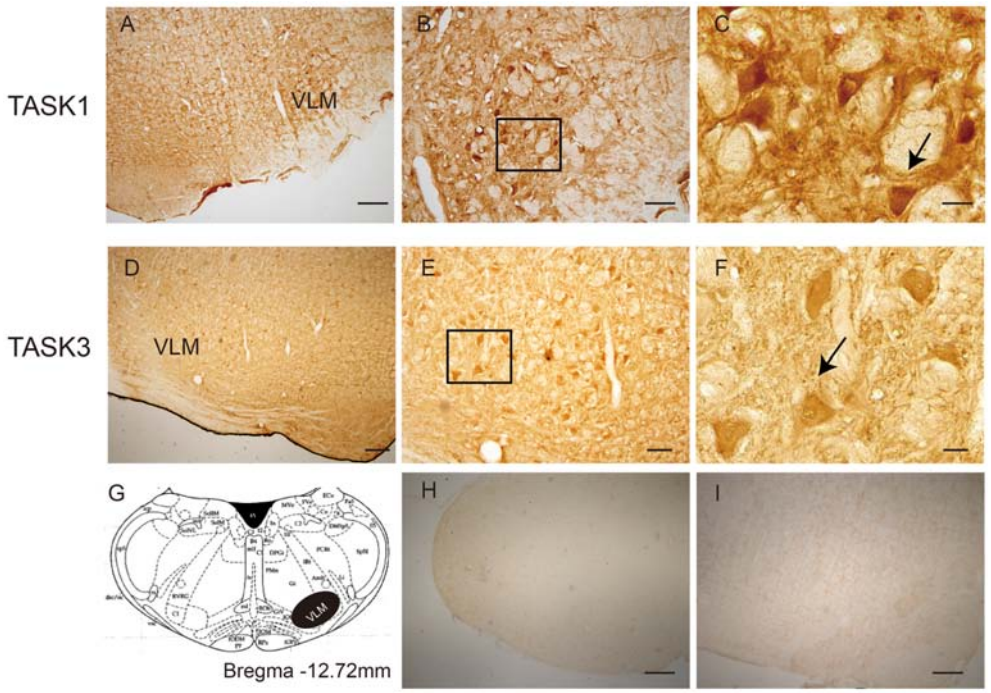


FIGURE 1 | The location of TWIK-related acid-sensitive potassium channel 1 and 3 (TASK1 and 3)-positive cells in the ventrolateral medulla (VLM) of SD rats. **(A)** TASK1-positive cells were located in the VLM of rats. **(B,C)** represent high-power visual fields of the area shown in **(A)**, showing a detailed view of TASK1-positive cells in the VLM. **(D)** TASK3-positive cells in the VLM of rats. **(E,F)** represent high-power visual fields of the area shown in **(D)**, showing a detailed view of TASK3-positive cells in the VLM. **(G)** Coronal diagram of the rat medulla; the area shown in black represents the distribution of TASK1 and TASK3. Cell morphology is indicated by the arrows shown in **(C,F)**. **(H–I)** Negative control. Scale bar: 200 μm **(A,D,H,I)**; 80 μm **(B,E)** and 20 μm **(C,F)**.

The Effects of TASK1 and TASK3 Selective Antagonists on Respiration

To determine the effects of TASK1 and TASK3 on respiration, we blocked TASK1 using AEA and blocked TASK3 using RR. It was reported that AEA was widely applied as TASK1 inhibitor (Maingret et al., 2001). RR was recently found to selectively inhibit TASK3 with little or no effect on TASK-1 (Berg et al., 2004). Microinjection of AEA (100 μM) increased iPND and respiratory drive from 0.97 ± 0.04 to 1.61 ± 0.15 ($p < 0.01$, $n = 5$, **Figures 5A,D**) and from 0.97 ± 0.04 to 1.69 ± 0.16 ($p < 0.001$, $n = 5$, **Figure 5E**), respectively. Ti was shortened from 0.31 ± 0.03 to 0.27 ± 0.03 s ($p < 0.05$, $n = 5$, **Figures 5C**). RR (10 μM) increased iPND from 1.07 ± 0.06 to 1.29 ± 0.07 ($p < 0.001$, $n = 5$, **Figures 5B,G**), enhanced respiratory drive from 1.07 ± 0.09 to 1.48 ± 0.12 ($p < 0.05$, $n = 5$, **Figure 5H**), and shortened Ti from 0.36 ± 0.02 to 0.31 ± 0.02 s ($p < 0.05$, $n = 5$, **Figure 5F**). Together, these results suggest that both TASK1 and TASK3 in the VLM are involved in the central regulation of respiration. Furthermore, inhibition of TASK1 and TASK3 in rat VLM stimulated breathing that is controlled by the respiratory center.

The Effect of ACSF With Different pH Values on Respiration

It has been reported that TASKs are sensitive to changes in extracellular proton chemoreception and that the inhibition of TASKs by extracellular acidosis leads to increased excitability of brainstem respiratory neurons (Duprat et al., 1997; Bayliss and Barrett, 2008). Conversely, activation by alkalization exerts an inhibitory effect. ASICs have been reported to be involved in the pH sensitivity in the CNS and are voltage-insensitive, proton-gated cation channels that are activated by extracellular acidification (Waldmann et al., 1997). AMI is widely used as a non-selective ASIC inhibitor (Waldmann et al., 1997; Baron and Lingueglia, 2015). We first microinjected ACSF at acidic pH (7.4, 7.0 and 6.5) into the VLM of rats and observed the resulting changes of respiratory activation (**Figures 6A–C**). Microinjection at pH 7.0 and 6.5 caused significant increases in iPND, Ti and respiratory drive, which were inhibited by AMI (**Figures 6D–F**). To explore the effect of TASK activation on respiration, we microinjected alkaline ACSF (pH 8.0) and found that alkaline ACSF triggers decreases of iPND and respiratory drive, which were inhibited by AEA (**Figures 7A,B,C,E,F**). However, microinjection of alkaline ACSF had no significant effect on Ti (**Figure 7D**).

DISCUSSION

The central chemoreflex is essential to the maintenance of circulatory acid-base homeostasis by adjusting the activity of breathing. However, the mechanism of chemoreflex has

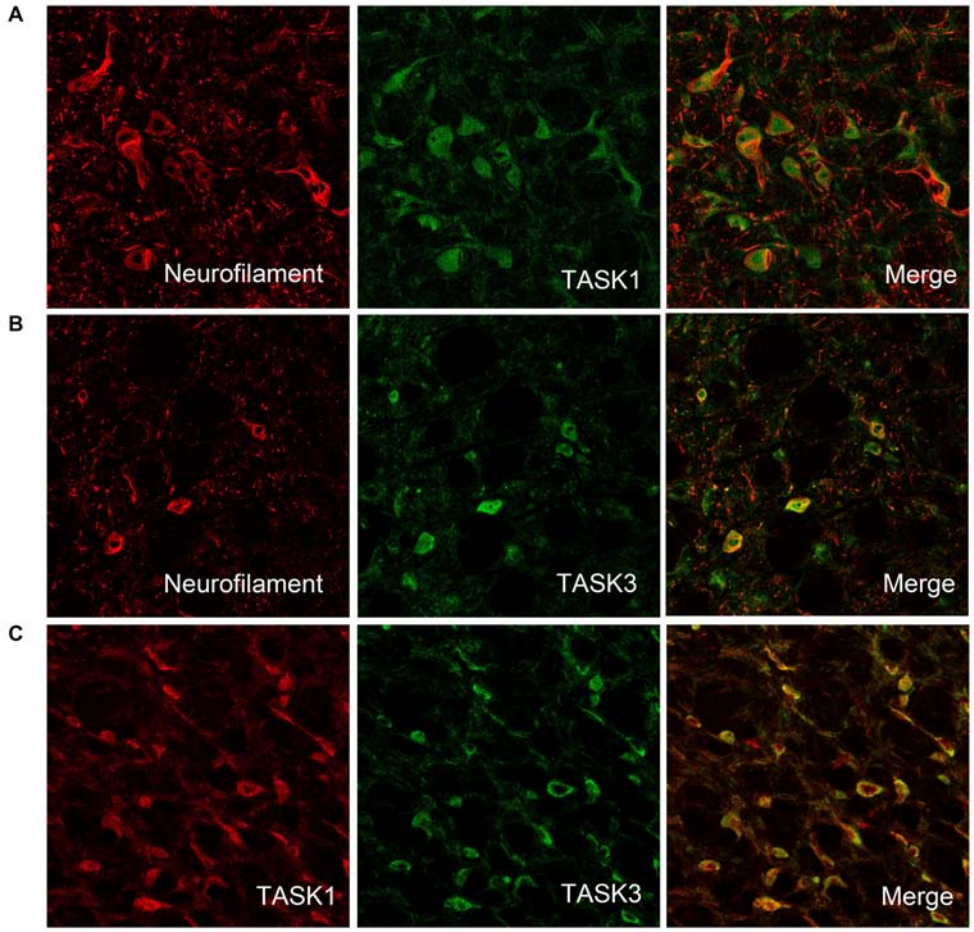


FIGURE 2 | TASK1 and TASK3 are expressed and colocalized in VLM neurons. **(A,B)** Representative confocal photomicrograph showing the colocalization of TASK1-ir and TASK3-ir (green) with neurofilament-ir (red) in the VLM. **(C)** Representative confocal photomicrograph showing the colocalization of TASK1 (red) and TASK3 (green) in the VLM. Original magnification, 200×.

remained unclear until now. Our previous study demonstrated that ASICs are expressed on the neurons of chemosensitive areas such as the lateral hypothalamus and VLM and contribute to respiratory regulation. In the present study, we focused on the role of another class of pH-sensitive ion channels, TASKs, in breathing regulation and their cooperation with ASICs in the central chemosensory system. We found that TASK1 and TASK3 are expressed in the VLM of rats. TASK1 and TASK3 cooperate with ASIC1 to participate in the central regulation of respiration. This might be the chemosensitive mechanism of the VLM.

The expression of TASKs in brain stem has been reported previously (Talley et al., 2001; Berg et al., 2004). TASK1 is expressed in the facial nucleus, ambiguous nucleus, hypoglossal nucleus and LC (Sirois et al., 2000; Bayliss et al., 2001), and TASK3 is expressed in the nucleus of the solitary tract, raphes and LC (Talley et al., 2001). ASICs, especially ASIC1 and ASIC2a, are widely expressed in the CNS (García-Añoveros et al., 1997; Waldmann et al., 1997; Alvarez de la Rosa et al., 2003). It has been reported that ASIC1 in NTS mediates chemosensitivity and is involved in the control of breathing (Huda et al., 2012). Acidification of the LH can stimulate breathing via the activation of ASIC1a on orexin neurons (Song et al., 2012). However, little is known about the coexpression of ASIC1 and TASKs (1 and 3) in the CNS. In the present study, we first examined the expression of TASK1 and TASK3 by localizing TASK1- and TASK3-positive cells in the VLM by immunohistochemistry. TASK1 and TASK3 subunits are colocalized with most serotonergic dorsal and caudal raphe neurons and with noradrenergic cells of the LC (Talley et al., 2001; Washburn et al., 2002). According to the immunofluorescence results, TASK1 and TASK3 coexpression were detected in the VLM, which indicates that heteromeric TASKs may also be involved in central chemoreception. Furthermore, ASIC1, which can be activated by extracellular acidification, was found to be coexpressed with TASK1 and TASK3, suggesting that TASKs may cooperate with ASIC1 and thereby participate in central respiratory regulation. The VLM neurons serve as central chemoreceptors mediating respiratory responses to hypoxia and/or hypercapnia (Wakai et al., 2015) Therefore, these morphological results lay the foundation for

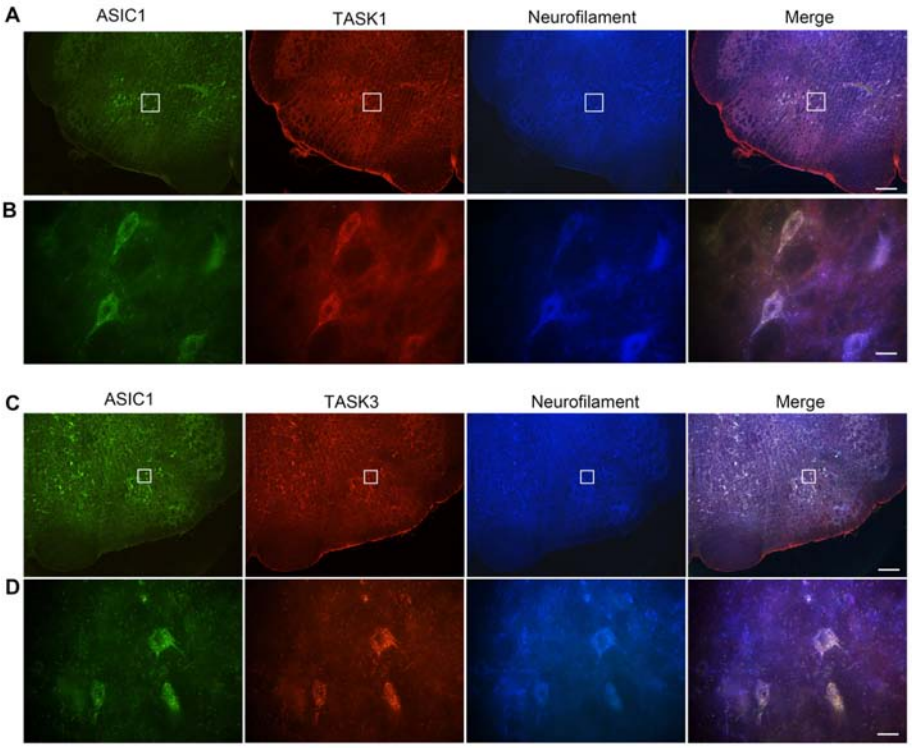


FIGURE 3 | Acid-sensing ion channel 1 (ASIC1), TASK1 and TASK3 are expressed and colocalized in the VLM neurons of adult rats. **(A)** Representative confocal photomicrographs showing the colocalization of ASIC1-ir (green), TASK1-ir (red) and neurofilament-H (blue) in the VLM. **(B)** Representative high power visual field of the area shown in **(A)**. **(C)** Representative confocal photomicrographs showing the colocalization of ASIC1-ir (green), TASK3-ir (red) and neurofilament-H (blue) in the VLM. **(D)** Representative high power visual field of the area shown in **(C)**. **(A–C)** Scale bar = 200 μm; **(B,D)** scale bar = 20 μm.

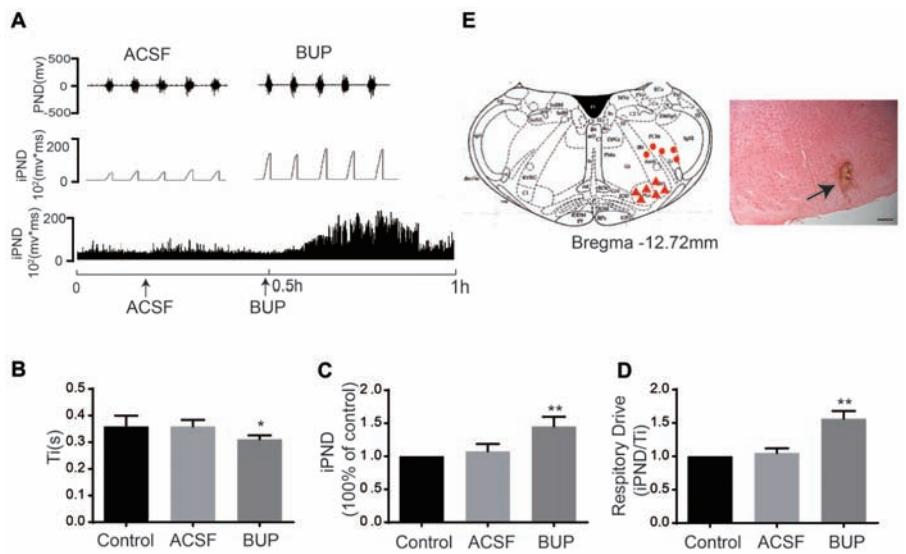


FIGURE 4 | The non-selective TASKs antagonist, bupivacaine (BUP) stimulated respiration of rats. **(A)** The phrenic nerve discharge (PND) was recorded from the same animal. The unilateral microinjection of 200 μM BUP into the VLM increased PND and integrated PND (iPND). The microinjection of artificial cerebrospinal fluid (ACSF; pH 7.4) served as a control. **(B)** Inspiratory time (Ti) was decreased by BUP injection. **(C)** Group data showing the effects of BUP on iPND. **(D)** Responses of the respiratory drive. Note that BUP stimulated respiration (*$p < 0.05$, **$p < 0.01$ relative to control; $n = 6$). **(E)** Histological staining with neutral red: the sky blue spot indicates the injection site in the VLM, and the injection plot was confirmed by comparison with the Bregma −12.72 mm coronal diagram in the Paxinos and Watson stereotaxic atlas of the rat brain. In the diagram, red arrowheads represent the injection points and dots signify injection points out of VLM.

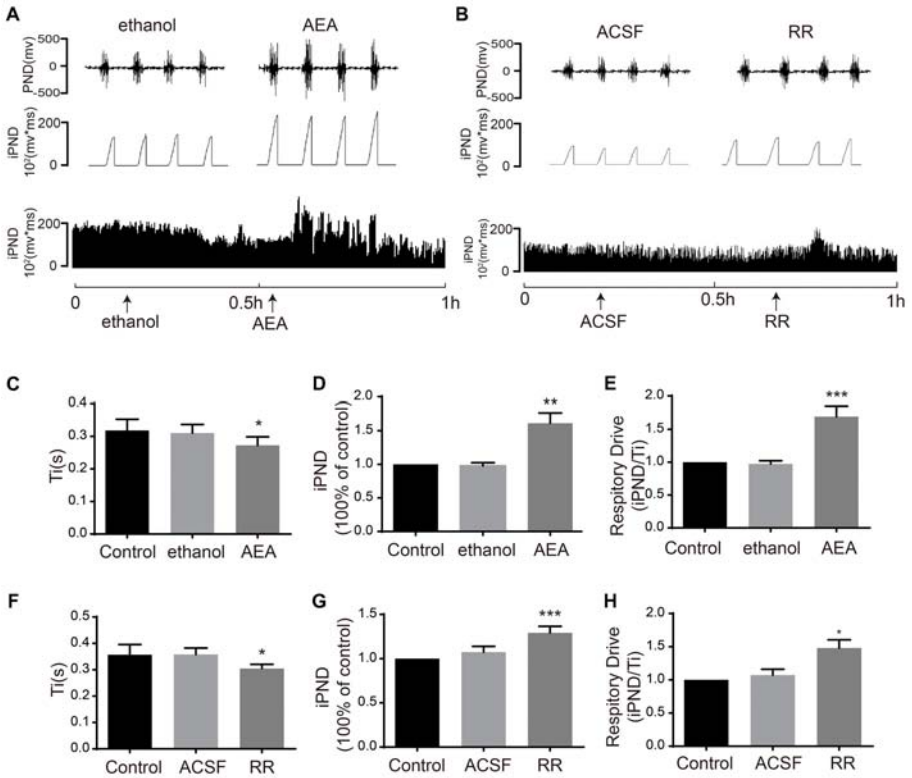


FIGURE 5 | TASK1 antagonist, anandamide (AEA) and TASK3 antagonist, ruthenium red (RR) stimulated the respiration of rats. **(A,B)** The PND was recorded from the same animal. The unilateral microinjection of 100 μM AEA and 10 μM RR into the VLM increased PND and iPND. The microinjection of ethanol and ACSF (pH 7.4) served as a control. **(C–F)** Ti was decreased by AEA and RR injection. **(D–G)** Group data showing the effects of AEA and RR on iPND. **(E–H)** Responses of the respiratory drive. Note that AEA and RR stimulated respiration, $^{*}p < 0.05$, $^{**}p < 0.01$, $^{***}p < 0.001$ relative to control; $n = 5$.

exploring the function of ASIC1 and TASKs (1 and 3) in the brainstem.

Recent studies have shown that TASK1 and TASK3 subunits generate a pH-sensitive and weakly rectifying K^+ current, which is critical for regulating the resting membrane potential and the excitability of respiration-related neurons (Duprat et al., 1997; Buckler et al., 2000; Kim et al., 2000; Bayliss et al., 2015). TASK1 and TASK3 are responsible for the pH sensitivity of serotonergic neurons in the dorsal and caudal raphe of mice (Washburn et al., 2002). *In vivo*, hypoxic and acidic responses are partially blunted in TASK1 and TASK3 knockout mice (Trapp et al., 2008). In the carotid body, TASK1 plays a key role in the control of ventilation peripherally in mice (Trapp et al., 2008). Despite these findings, the role of TASKs in the VLM in central respiratory regulation has not been reported yet. We determined the role of TASK1 and TASK3 in the central regulation of breathing by PND recording. TASK1 and TASK3 are both inhibited by local anesthetics, including BUP (Kindler et al., 1999; Kim et al., 2000). It has been demonstrated that TASK1 is directly inhibited by the AEA (Maingret et al., 2001), and TASK3 is selectively blocked by RR (Czirják and Enyedi, 2002). Therefore, a non-selective antagonist, BUP, a specific TASK1 antagonist, AEA, and a specific TASK3 antagonist, RR, were applied in an animal experiment. We found that the microinjection of BUP, AEA and RR stimulated breathing by increasing PND and iPND, shortened Ti, and enhanced respiratory drive, suggesting that the inhibition of TASK1 and TASK3 in VLM neurons blocked the background K^+ current, which contributes to producing the action potential and increases the excitability of inspiratory neurons. However, neither RR nor AEA are specific for TASKs channels. This is a shortcoming of the study. RR is a non-selective inhibitor of transient receptor potential (TRP) channels and AEA is agonist of both cannabinoid (CB) receptors and TRP channels (Watanabe et al., 2003; Kopczyńska, 2007). Indeed, it has been reported that CB receptors and TRP channels cooperate with each other in breathing regulation. Intravenous injection of AEA induced depression of breathing can be prevented by the CB1 antagonist AM281 (Kopczyńska, 2007; Iring et al., 2017). TRPV2 channel was found to be expressed in VLM (Nedungadi et al., 2012). However, TRPV2 channel is mainly stretch and thermo sensitive. TRPV1 is acidic sensitive, which can be activated by low pH. Our current study found that microinjection of either agonist (AEA) or antagonist (RR) of TRP channels into VLM stimulates breathing. Thus, we speculate that it is unlikely TRP take part in regulation of breathing by neurons of the VLM. Ordinarily, activation of CB receptors reduces neuronal excitability (den Boon et al., 2012). But, we found that microinjection of the agonist of CB receptors, AEA into the

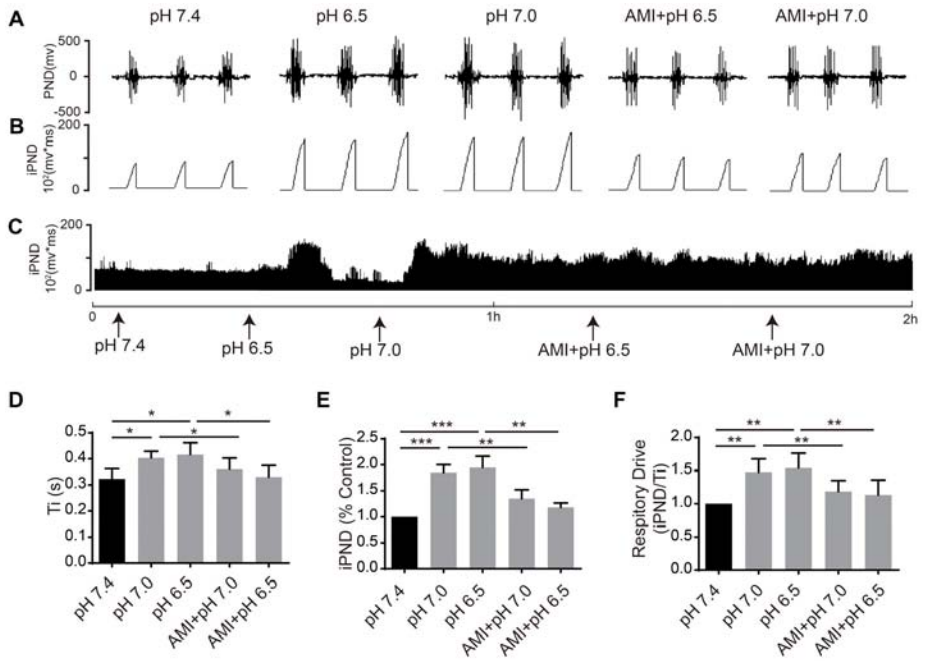


FIGURE 6 | ASIC antagonists attenuated the stimulatory effect of acidification on respiration in rat VLM. **(A–C)** The unilateral microinjection of 0.1 μL ACSF (pH 7.4, 7.0 and 6.5) into the VLM increased raw PND **(A)** and iPND **(B,C)**. AMI pre-treatment (100 μM) blocked this effect. The microinjection of ACSF (pH 7.4) served as a control. **(D–F)** Statistical data showing the effects of alkalization and AMI on Ti **(D)**, iPND **(E)** and respiratory drive **(F)**. $*p < 0.05$, $**p < 0.01$, $***p < 0.001$, $n = 6$.

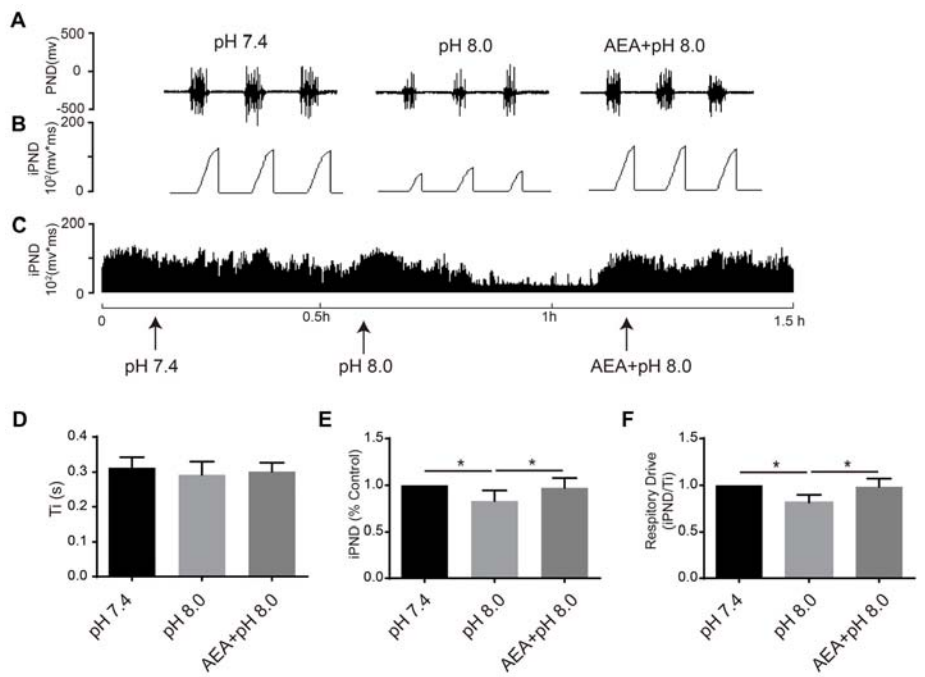


FIGURE 7 | TASK1 antagonists attenuated the subdued effect of alkalization on respiration in the rat VLM. **(A–C)** The unilateral microinjection of 0.1 μL ACSF (pH 8.0) into the VLM decreased raw PND **(A)** and iPND **(B,C)**. TASK1 antagonist AEA pre-treatment (100 μM) blocked this effect. The microinjection of ACSF (pH 7.4) served as a control. **(D–F)** Statistical data showing the effects of different levels of alkalization and AEA on Ti **(D)**, iPND **(E)** and respiratory drive **(F)**. $*p < 0.05$, $n = 6$.

VLM activated breathing. Thus, we consumed that it is unlikely the activation of CB receptor medicated respiratory regulation. However, there is no direct evidence to rule out the role of CB receptors and TRP channels in VLM mediated respiratory regulation. Further investigations are needed to explore the roles of TASKs channels in the central regulation of breathing.

It has been well documented that central respiratory chemoreceptors are located in the medullary raphe, nucleus tractus solitarius, VLM and hypothalamus (Funk, 2010). VLM, including RVL and LPGi, is a putative site for central chemoreception, (Corcoran et al., 2009). However, the specific pH sensing mechanism remains controversial. Therefore, we focused on the effect of ASIC1 and TASKs in the VLM on chemoreception.

TASKs are inhibited by extracellular acidification (Bayliss et al., 2003; Bayliss and Barrett, 2008; Enyedi and Czirják, 2010). The pH sensitivities of heterodimeric TASKs (1 and 3) and TASK1 (pK ∼7.4) are closer to the physiological range than that of TASK-3 (pK ∼6.8; Berg et al., 2004; Duprat et al., 2007). Thus, the acid-induced inhibition of TASK channel activity enhances nerve excitability. In addition to TASKs, ASICs have been reported to be involved in the pH sensitivity in the CNS; ASICs are voltage-insensitive, proton-gated cation channels that are activated by extracellular acidification (Waldmann et al., 1997). ASIC1 activation causes the entry of Na^+ and a little Ca^{2+}, which leads to the polarization and excitability of neurons. Because of the similar pKa values of TASK3 and ASIC1a and their coexpression in the VLM, we think that these proteins may work together to participate in respiratory regulation by central chemosensitive neurons. AMI is widely used to block ASICs and can reversibly inhibit ASICs (Champigny et al., 1998; Baron and Lingueglia, 2015). To investigate whether TASKs (1 and 3) and ASIC1 contribute to chemoreception in rats, we microinjected ACSF at pH values from 7.4 to lower pH levels dose-dependently in the absence and presence of AMI into VLM to observe the change of PND. Our results showed that the microinjection of ACSF at pH 7.0 and 6.5 obviously prolonged Ti, increased iPND, and enhanced respiratory drive. AMI inhibited this effect. On the contrary, the microinjection of ACSF at pH 8.0 decreased iPND and respiratory drive, which were inhibited by AEA. However, alkaline ACSF had no significant effect on Ti. One possible reason is that TASK1 and TASK3 exhibit different pH sensitivity. TASK-1 is activated strongly by alkalization pH over 7.3 (Duprat et al., 1997; Bayliss et al., 2001, 2015), whereas, TASK3 is nearly fully activated at pH 7.3, and additional alkalization has little effect on TASK-3 currents (Rajan et al., 2000; Bayliss et al., 2015). The results indicated that activation of TASK-1 may have minor effect on Ti. However, further studies are needed to explore the roles of TASKs in regulation of breathing.

Based on the data presented above, the inhibition of TASK1 and TASK3 in the VLM under physiological conditions stimulates respiration. The acidification of the VLM led to PND enhancement, which was caused by ASIC1 activation. The alkalization of the VLM reduced PND, which was mainly caused by TASK1 activation. This result indicates that ASIC1 and TASKs (1 and 3) coexist in the chemosensitive neurons of VLM and coordinate with each other to sense local pH fluctuations; this may be one of the mechanisms by which central chemosensitive neurons respond to pH changes.

In summary, extracellular pH is a critical signal in the central regulation of breathing. In the present study, we have shown that TASKs including TASK1 and TASK3 are expressed in the VLM of rats and are coexpressed with ASIC1 in VLM neurons. Furthermore, we have shown that local acidification of the VLM can stimulate respiration, mainly via ASIC1. Local alkalization weakens respiration, mainly via TASK1. Our findings support the notion that ASIC1, TASK1 and TASK3 are expressed on neurons in the VLM and participate in the chemical regulation of respiration in response to extracellular pH change under physiological conditions.

AUTHOR CONTRIBUTIONS

XW performed the *in vivo* and some of the *in vitro* experiments and prepared the manuscript. RG conducted some of the *in vitro* experiments. XZ and DZ analyzed some of the data. NS and LS designed the experiments and revised the manuscript.

FUNDING

This work was funded by a grant from the National Natural Science Foundation of China (Nos. 81470203 and 81500048).

REFERENCES

Alvarez de la Rosa, D., Krueger, S. R., Kolar, A., Shao, D., Fitzsimonds, R. M., and Canessa, C. M. (2003). Distribution, subcellular localization and ontogeny of ASIC1 in the mammalian central nervous system. *J. Physiol.* 546, 77–87. doi: 10.1113/jphysiol.2002.030692

Baron, A., and Lingueglia, E. (2015). Pharmacology of acid-sensing ion channels–Physiological and therapeutical perspectives. *Neuropharmacology* 94, 19–35. doi: 10.1016/j.neuropharm.2015.01.005

Bayliss, D. A., and Barrett, P. Q. (2008). Emerging roles for two-pore-domain potassium channels and their potential therapeutic impact. *Trends Pharmacol. Sci.* 29, 566–575. doi: 10.1016/j.tips.2008.07.013

Bayliss, D. A., Barhanin, J., Gestreau, C., and Guyenet, P. G. (2015). The role of pH-sensitive TASK channels in central respiratory chemoreception. *Pflugers Arch.* 467, 917–929. doi: 10.1007/s00424-014-1633-9

Bayliss, D. A., Sirois, J. E., and Talley, E. M. (2003). The TASK family: two-pore domain background K^+ channels. *Mol. Interv.* 3, 205–219. doi: 10.1124/mi.3.4.205

Bayliss, D. A., Talley, E. M., Sirois, J. E., and Lei, Q. (2001). TASK-1 is a highly modulated pH-sensitive 'leak' K^+ channel expressed in brainstem respiratory neurons. *Respir. Physiol.* 129, 159–174. doi: 10.1016/s0034-5687(01)00288-2

Berg, A. P., Talley, E. M., Manger, J. P., and Bayliss, D. A. (2004). Motoneurons express heteromeric TWIK-related acid-sensitive K^+ (TASK) channels containing TASK-1 (KCNK3) and TASK-3 (KCNK9) subunits. *J. Neurosci.* 24, 6693–6702. doi: 10.1523/JNEUROSCI.1408-04.2004

Buckler, K. J., Williams, B. A., and Honore, E. (2000). An oxygen-, acid- and anaesthetic-sensitive TASK-like background potassium channel in rat arterial chemoreceptor cells. *J. Physiol.* 525, 135–142. doi: 10.1111/j.1469-7793.2000.00135.x

Buehler, P. K., Bleiler, D., Tegtmeier, I., Heitzmann, D., Both, C., Georgieff, M., et al. (2017). Abnormal respiration under hyperoxia in TASK-1/3 potassium channel double knockout mice. *Respir. Physiol. Neurobiol.* 244, 17–25. doi: 10.1016/j.resp.2017.06.009

Champigny, G., Voilley, N., Waldmann, R., and Lazdunski, M. (1998). Mutations causing neurodegeneration in *Caenorhabditis elegans* drastically alter the pH

sensitivity and inactivation of the mammalian H^+-gated Na^+ channel MDEG1. *J. Biol. Chem.* 273, 15418–15422. doi: 10.1074/jbc.273.25.15418

Corcoran, A. E., Hodges, M. R., Wu, Y., Wang, W., Wylie, C. J., Deneris, E. S., et al. (2009). Medullary serotonin neurons and central CO_2 chemoreception. *Respir. Physiol. Neurobiol.* 168, 49–58. doi: 10.1016/j.resp.2009.04.014

Czirják, G., and Enyedi, P. (2002). TASK-3 dominates the background potassium conductance in rat adrenal glomerulosa cells. *Mol. Endocrinol.* 16, 621–629. doi: 10.1210/mend.16.3.0788

den Boon, F. S., Chameau, P., Schaafsma-Zhao, Q., van Aken, W., Bari, M., Oddi, S., et al. (2012). Excitability of prefrontal cortical pyramidal neurons is modulated by activation of intracellular type-2 cannabinoid receptors. *Proc. Natl. Acad. Sci. U S A* 109, 3534–3539. doi: 10.1073/pnas.1118167109

Duprat, F., Lauritzen, I., Patel, A., and Honore, E. (2007). The TASK background K_2P channels: chemo- and nutrient sensors. *Trends Neurosci.* 30, 573–580. doi: 10.1016/j.tins.2007.08.003

Duprat, F., Lesage, F., Fink, M., Reyes, R., Heurteaux, C., and Lazdunski, M. (1997). TASK, a human background K^+ channel to sense external pH variations near physiological pH. *EMBO J.* 16, 5464–5471. doi: 10.1093/emboj/16.17.5464

Enyedi, P., and Czirják, G. (2010). Molecular background of leak K^+ currents: two-pore domain potassium channels. *Physiol. Rev.* 90, 559–605. doi: 10.1152/physrev.00029.2009

Funk, G. D. (2010). The 'connexin' between astrocytes, ATP and central respiratory chemoreception. *J. Physiol.* 588, 4335–4337. doi: 10.1113/jphysiol.2010.200196

García-Añoveros, J., Derfler, B., Neville-Golden, J., Hyman, B. T., and Corey, D. P. (1997). BNaC1 and BNaC2 constitute a new family of human neuronal sodium channels related to degenerins and epithelial sodium channels. *Proc. Natl. Acad. Sci. U S A* 94, 1459–1464. doi: 10.1073/pnas.94.4.1459

Goridis, C., and Brunet, J. F. (2010). Central chemoreception: lessons from mouse and human genetics. *Respir. Physiol. Neurobiol.* 173, 312–321. doi: 10.1016/j.resp.2010.03.014

Hartness, M. E., Lewis, A., Searle, G. J., O'Kelly, I., Peers, C., and Kemp, P. J. (2001). Combined antisense and pharmacological approaches implicate hTASK as an airway O_2 sensing K^+ channel. *J. Biol. Chem.* 276, 26499–26508. doi: 10.1074/jbc.M010357200

Holzer, P. (2009). Acid-sensitive ion channels and receptors. *Handb. Exp. Pharmacol.* 194, 283–332. doi: 10.1007/978-3-540-79090-7_9

Honoré, E. (2007). The neuronal background K2P channels: focus on TREK1. *Nat. Rev. Neurosci.* 8, 251–261. doi: 10.1038/nrn2117

Huda, R., Pollema-Mays, S. L., Chang, Z., Alheid, G. F., McCrimmon, D. R., and Martina, M. (2012). Acid-sensing ion channels contribute to chemosensitivity of breathing-related neurons of the nucleus of the solitary tract. *J. Physiol.* 590, 4761–4775. doi: 10.1113/jphysiol.2012.232470

Iring, A., Hricisák, L., and Benyó, Z. (2017). CB1 receptor-mediated respiratory depression by endocannabinoids. *Respir. Physiol. Neurobiol.* 240, 48–52. doi: 10.1016/j.resp.2017.02.011

Kim, Y., Bang, H., and Kim, D. (2000). TASK-3, a new member of the tandem pore K^+ channel family. *J. Biol. Chem.* 275, 9340–9347. doi: 10.1074/jbc.275.13.9340

Kindler, C. H., Yost, C. S., and Gray, A. T. (1999). Local anesthetic inhibition of baseline potassium channels with two pore domains in tandem. *Anesthesiology* 90, 1092–1102. doi: 10.1097/00000542-199904000-00024

Koizumi, H., Smerin, S. E., Yamanishi, T., Moorjani, B. R., Zhang, R., and Smith, J. C. (2010). TASK channels contribute to the K^+-dominated leak current regulating respiratory rhythm generation *in vitro*. *J. Neurosci.* 30, 4273–4284. doi: 10.1523/JNEUROSCI.4017-09.2010

Kopczyńska, B. (2007). The contribution of VR1 and CB1 receptors and the role of the afferent vagal pathway in modelling of cardio-respiratory effects of anandamide in rats. *Life Sci.* 80, 1738–1745. doi: 10.1016/j.lfs.2007.01.062

Maingret, F., Patel, A. J., Lazdunski, M., and Honore, E. (2001). The endocannabinoid anandamide is a direct and selective blocker of the background K^+ channel TASK-1. *EMBO J.* 20, 47–54. doi: 10.1093/emboj/20.1.47

Millhorn, D. E., and Eldridge, F. L. (1986). Role of ventrolateral medulla in regulation of respiratory and cardiovascular systems. *J. Appl. Physiol.* 61, 1249–1263. doi: 10.1152/jappl.1986.61.4.1249

Nedungadi, T. P., Dutta, M., Bathina, C. S., Caterina, M. J., and Cunningham, J. T. (2012). Expression and distribution of TRPV2 in rat brain. *Exp. Neurol.* 237, 223–237. doi: 10.1016/j.expneurol.2012.06.017

Rajan, S., Wischmeyer, E., Xin, L. G., Preisig-Muller, R., Daut, J., Karschin, A., et al. (2000). TASK-3, a novel tandem pore domain acid-sensitive K^+ channel. An extracellular histiding as pH sensor. *J. Biol. Chem.* 275, 16650–16657. doi: 10.1074/jbc.M000030200

Sirois, J. E., Lei, Q., Talley, E. M., Lynch, C. R., and Bayliss, D. A. (2000). The TASK-1 two-pore domain K^+ channel is a molecular substrate for neuronal effects of inhalation anesthetics. *J. Neurosci.* 20, 6347–6354. doi: 10.1523/jneurosci.20-17-06347.2000

Song, N., Guan, R., Jiang, Q., Hassanzadeh, C. J., Chu, Y., Zhao, X., et al. (2016). Acid-sensing ion channels are expressed in the ventrolateral medulla and contribute to central chemoreception. *Sci. Rep.* 6:38777. doi: 10.1038/srep38777

Song, N., Zhang, G., Geng, W., Liu, Z., Jin, W., Li, L., et al. (2012). Acid sensing ion channel 1 in lateral hypothalamus contributes to breathing control. *PLoS One* 7:e39982. doi: 10.1371/journal.pone.0039982

Talley, E. M., Solorzano, G., Lei, Q., Kim, D., and Bayliss, D. A. (2001). Cns distribution of members of the two-pore-domain (KCNK) potassium channel family. *J. Neurosci.* 21, 7491–7505. doi: 10.1523/JNEUROSCI.21-19-07491.2001

Trapp, S., Aller, M. I., Wisden, W., and Gourine, A. V. (2008). A role for TASK-1 (KCNK3) channels in the chemosensory control of breathing. *J. Neurosci.* 28, 8844–8850. doi: 10.1523/JNEUROSCI.1810-08.2008

Wakai, J., Takamura, D., Morinaga, R., Nakamuta, N., and Yamamoto, Y. (2015). Differences in respiratory changes and Fos expression in the ventrolateral medulla of rats exposed to hypoxia, hypercapnia and hypercapnic hypoxia. *Respir. Physiol. Neurobiol.* 215, 64–72. doi: 10.1016/j.resp.2015.05.008

Waldmann, R., Champigny, G., Bassilana, F., Heurteaux, C., and Lazdunski, M. (1997). A proton-gated cation channel involved in acid-sensing. *Nature* 386, 173–177. doi: 10.1038/386173a0

Washburn, C. P., Bayliss, D. A., and Guyenet, P. G. (2003). Cardiorespiratory neurons of the rat ventrolateral medulla contain TASK-1 and TASK-3 channel mRNA. *Respir. Physiol. Neurobiol.* 138, 19–35. doi: 10.1016/s1569-9048(03)00185-x

Washburn, C. P., Sirois, J. E., Talley, E. M., Guyenet, P. G., and Bayliss, D. A. (2002). Serotonergic raphe neurons express TASK channel transcripts and a TASK-like pH- and halothane-sensitive K^+ conductance. *J. Neurosci.* 22, 1256–1265. doi: 10.1523/jneurosci.22-04-01256.2002

Watanabe, H., Vriens, J., Prenen, J., Droogmans, G., Voets, T., and Nilius, B. (2003). Anandamide and arachidonic acid use epoxyeicosatrienoic acids to activate TRPV4 channels. *Nature* 424, 434–438. doi: 10.1038/nature01807

Conflict of Interest Statement: The authors declare that the research was conducted in the absence of any commercial or financial relationships that could be construed as a potential conflict of interest.

Copyright © 2018 Wang, Guan, Zhao, Zhu, Song and Shen. This is an open-access article distributed under the terms of the Creative Commons Attribution License (CC BY). The use, distribution or reproduction in other forums is permitted, provided the original author(s) and the copyright owner(s) are credited and that the original publication in this journal is cited, in accordance with accepted academic practice. No use, distribution or reproduction is permitted which does not comply with these terms.

frontiers in Behavioral Neuroscience

ORIGINAL RESEARCH
published: 04 September 2018
doi: 10.3389/fnbeh.2018.00199

Differential Dopamine D1 and D3 Receptor Modulation and Expression in the Spinal Cord of Two Mouse Models of Restless Legs Syndrome

*Samantha Meneely[1], Mai-Lynne Dinkins[1], Miki Kassai[1], Shangru Lyu[2], Yuning Liu[2], Chien-Te Lin[1,3], Kori Brewer[4], Yuqing Li[2,5] and Stefan Clemens[1]**

[1] Department of Physiology, Brody School of Medicine, East Carolina University, Greenville, NC, United States, [2] Department of Neurology, College of Medicine, University of Florida, Gainesville, FL, United States, [3] East Carolina Diabetes and Obesity Institute, Brody School of Medicine, East Carolina University, Greenville, NC, United States, [4] Department of Emergency Medicine, Brody School of Medicine, East Carolina University, Greenville, NC, United States, [5] Wuxi Medical School, Jiangnan University, Wuxi, China

Restless Legs Syndrome (RLS) is often and successfully treated with dopamine receptor agonists that target the inhibitory D3 receptor subtype, however there is no clinical evidence of a D3 receptor dysfunction in RLS patients. In contrast, genome-wide association studies in RLS patients have established that a mutation of the *MEIS1* gene is associated with an increased risk in developing RLS, but the effect of *MEIS1* dysfunction on sensorimotor function remain unknown. Mouse models for a dysfunctional D3 receptor (D3KO) and Meis1 (Meis1KO) were developed independently, and each animal expresses some features associated with RLS in the clinic, but they have not been compared in their responsiveness to treatment options used in the clinic. We here confirm that D3KO and Meis1KO animals show increased locomotor activities, but that only D3KO show an increased sensory excitability to thermal stimuli. Next we compared the effects of dopaminergics and opioids in both animal models, and we assessed D1 and D3 dopamine receptor expression in the spinal cord, the gateway for sensorimotor processing. We found that Meis1KO share most of the tested behavioral properties with their wild type (WT) controls, including the modulation of the thermal pain withdrawal reflex by morphine, L-DOPA and D3 receptor (D3R) agonists and antagonists. However, Meis1KO and D3KO were behaviorally more similar to each other than to WT when tested with D1 receptor (D1R) agonists and antagonists. Subsequent Western blot analyses of D1R and D3R protein expression in the spinal cord revealed a significant increase in D1R but not D3R expression in Meis1KO and D3KO over WT controls. As the D3R is mostly present in the dorsal spinal cord where it has been shown to modulate sensory pathways, while activation of the D1Rs can activate motoneurons in the ventral spinal cord, we speculate that D3KO and Meis1KO represent two complementary animal models for RLS, in which the mechanisms of sensory (D3R-mediated) and motor (D1R-mediated) dysfunctions can be differentially explored.

Keywords: RLS animal models, dopamine, D1 receptor, D3 receptor, Meis1, sensorimotor function, spinal cord

OPEN ACCESS

Edited by:
Brian R. Noga,
University of Miami, United States

Reviewed by:
Patrick John Whelan,
University of Calgary, Canada
Nicola B. Mercuri,
Università degli Studi di Roma Tor Vergata, Italy

***Correspondence:**
Stefan Clemens
clemenss@ecu.edu

Received: *21 December 2017*
Accepted: *13 August 2018*
Published: *04 September 2018*

Citation:
Meneely S, Dinkins M-L, Kassai M, Lyu S, Liu Y, Lin C-T, Brewer K, Li Y and Clemens S (2018) Differential Dopamine D1 and D3 Receptor Modulation and Expression in the Spinal Cord of Two Mouse Models of Restless Legs Syndrome. Front. Behav. Neurosci. 12:199. doi: 10.3389/fnbeh.2018.00199

INTRODUCTION

Background on RLS

Restless Legs Syndrome (RLS) is a highly prevalent (5–10% of the population, Ghorayeb and Tison, 2010; Earley et al., 2011), but also underappreciated aging-associated neurological sensorimotor disorder that severely disrupts sleep and affects quality of life. First described in 1685 (Willis, 1685) and clinically confirmed in the mid-twentieth century (Ekbom, 1944, 1945, 1960), RLS is a clinical disorder in which overlapping genetic risk factors may play a role in the emergence of the symptoms (Trenkwalder et al., 2016). Genome-wide association studies in RLS patients have established several chromosome loci associated with RLS, notably *MEIS1* and *BTBD9* (Stefansson et al., 2007; Winkelmann et al., 2007), of which a point mutation in the *MEIS1* gene has the highest odd ratios with RLS (Winkelmann, 2008; Schormair et al., 2011, 2017; Winkelmann et al., 2011). Meis1 plays a role in the early development of the nervous system (Spieler et al., 2014; Marcos et al., 2015), and is essential to specify cell fates and differentiation patterns along the proximodistal axis of the limbs (Mercader et al., 1999, 2009). Intriguingly, a dysfunction of the *MEIS1* homolog in *C. elegans* is associated with an altered projection phenotype of dopamine neurons (M. Aschner, Albert Einstein College of Medicine, personal communication), suggesting a possible interaction between *MEIS1* and dopamine (DA) function.

RLS is often and successfully treated with DA receptor agonists that target the inhibitory D2-like receptor subtype, in particular D3 (Stiasny et al., 2000; Ferri et al., 2010; Manconi et al., 2011a; Garcia-Borreguero et al., 2016), and it has been suggested that a dysfunction of the descending A11 DA system in the hypothalamus may be involved in RLS by predominantly affecting the D3R system (Clemens et al., 2006; Lanza et al., 2017). There exist three DA receptors that mediate inhibitory actions via G*i*-coupled pathways (D2, D3, and D4), and the D3R subtype has a very high affinity to DA (Robinson et al., 1994; Cote and Kuzhikandathil, 2014). Yet despite the efficacy of the D3R compounds in treating RLS symptoms, there is no clinical evidence of A11 dysfunction in patients (Earley et al., 2009). However, a dysfunction of the DA system has been linked to altered iron homeostasis or iron-deficient diet (Dowling et al., 2011; Klinker et al., 2011; Dauvilliers and Winkelmann, 2013; Earley et al., 2014).

Animal Models of RLS

Mouse models for a dysfunctional D3 receptor (D3KO) and Meis1 (Meis1KO) were developed independently (Accili et al., 1996), and each animal expresses some features associated with RLS in the clinic. Both D3KO and Meis1KO express increased locomotor activity (Accili et al., 1996; Salminen et al., 2017), but only D3KO show an increased sensory excitability both in the isolated spinal cord (Clemens and Hochman, 2004) and *in vivo* (Keeler et al., 2012). The thermal pain withdrawal reflex depends on spinal cord circuits that can be recruited experimentally to assess compromised function of the underlying neural networks, both with the spinal cord and extending into the periphery. The previously reported increased excitability of the D3KO mouse to thermal stimuli suggests a possible role of C-fiber mediated pathways that convey altered sensations from deep within the muscle tissue (Clemens et al., 2006; Keeler et al., 2012). Further, as recent data suggest that the inhibitory D3 receptor can form functional heteromeric dimers with the excitatory D1 receptor (Marcellino et al., 2008), it is conceivable that the increased excitability observed in D3KO may be the result of an increased expression of the excitatory dopamine D1 receptor (D1R) (Brewer et al., 2014).

We here compared the effects of dopaminergic treatment on spinal reflexes as a tool to assess sensorimotor function (Eccles and Lundberg, 1959; Nielsen, 2004; Barriere et al., 2005) in Meis1KO and D3KO animal models, and we assessed D1R and D3R expressions the spinal cord, the gateway for sensorimotor processing. We found that Meis1KO share most of the tested behavioral properties with their wild type (WT) controls, including the modulation of the thermal pain withdrawal reflex by morphine, L-DOPA and D3 receptor (D3R) agonists and antagonists. However, Meis1KO and D3KO also shared behavioral similarities when tested with D1 receptor (D1R) agonists and antagonists, while the matching WTs were unresponsive to these drugs. Subsequent Western blot analyses of D1R and D3R protein expression in the spinal cord revealed a significant increase in D1R expression in Meis1KO and D3KO over the WT controls, while D3R expression was not significantly different across all 3 groups. Our data show that changes in spinal D1R expression and behavioral responses to D1R compounds are similar between Meis1KO and D3KO, while the increased sensitivity at baseline is present only in D3KO. We provide a model that separates D3KO and Meis1KO into two complimentary models of RLS that represent sensory and motor dysfunctions, respectively.

METHODS

Animals

All experimental procedures were approved by the Institutional Animal Care and Use Committees at East Carolina University and University of Florida, and were fully compliant with the National Institutes of Health guide for the care and use of Laboratory animals (NIH Publications No. 80-23). All efforts were made to minimize the number of animals used, and a total of 55 male mice (age range ∼9–12 months) were tested in this study. Behavioral testing was performed on *Meis1* heterozygous knockout mice (*Meis1*+/Δ, Meis1KO, $n = 15$) and their appropriate wild-type (WT) controls (C57BL/6J, $n = 12$), dopamine D3 receptor knockout mice (D3KO; strain B6.129S4-Drd3^{tm1dac}/J (stock # 002958, Jackson Laboratory, Bar Harbor, ME), $n = 13$) and their appropriate WT controls (C57BL/6J, $n = 15$) (Clemens and Hochman, 2004; Brewer et al., 2014). *Meis1 loxP mice* were from Drs. Copeland and Sadek (Kocabas et al., 2012), and Meis1+/Δ were generated by crossing *Meis1 loxP* with Emx1-cre mice (Guo et al., 2000). *Emx1* expresses in testis germ cells, so that when germ cells contain both *Emx1*-cre and *Meis1 loxP*, cre-mediated recombination occurs and leads to a deletion of the *loxP*-flanked sequence. Male mice heterozygous for both *Meis1 loxP* and *Emx1*-cre were then bred

with WT female mice. The deletion of *Meis1* gene occurred during the development and *Meis1*+/Δ mice were derived. Finally, *Meis1*+/Δ mice were crossed with WT mice to generate experimental mice. Animals were housed with free access to food, water, and enrichments under a 12-h light/dark cycle at room temperature.

Behavioral Assessments–Hargreaves

Behavioral testing procedures have been described in detail recently (Keeler et al., 2012; Brewer et al., 2014). Thermal withdrawal latencies (Hargreaves' method) were obtained in each cohort by using the IITC plantar analgesia meter (IITC Series 8, IITC Inc., Woodland Hills, CA). Experiments were performed between 9 am and 1 pm, to minimize the circadian variation. The week before testing started, animals were acclimated on 3–4 days to the experimental room and the Hargreave's system, by placing them individually into the Plexiglas cubicles for an average of 2 h. In week 1 of the testing period, we tested the effects of vehicle injections (0.9% NaCl, i.p., ∼90–120 μl per animal). Animals were tested 5 times per session, with resting periods for each individual animal between tests of 5–10 min. Stimulation cut-off for each test was set to 30 s test duration, to prevent the possibility of a heat-induced injury. Once initiated, recording sessions for all 5 trials lasted no longer than 60–90 min for all animals tested that day. After vehicle assessments, we subsequently compared all drug effects (i.p. injections, injection volumes matching the vehicle volumes) against the data obtained after the respective vehicle injections in each animal cohort. We started the tests 1 h after vehicle or drug injections. Each drug test was separated from the next drug treatment by an at least 3-day recovery period, to minimize any potential drug interactions possibly skewing the latency measurements. After ∼5–6 weeks, we again tested the responses to vehicle injections in two cohorts and found no significant differences from the values obtained at baseline (data not shown).

Behavioral Assessments–Locomotor Activity

Spontaneous locomotor activities were recorded for Meis1KO and their WT controls with a VersaMax Legacy open field apparatus connected to a computerized Digiscan System (Accuscan Instruments, Inc. OH), and for D3KO and their controls with a TSE LabMaster System (TSE Systems, Chesterfield, MO). Infrared sensors were used to record ambulatory activity in the X-Y plane). Counts across all these axes were summed to give total ambulatory activity. Meis1KO and their WT controls were monitored for 7 days. Only the data from the last 4 days were pooled and analyzed. For D3KO and their controls, after 2 days of acclimation, data were collected for 2 consecutive days to calculate locomotor activity.

Compounds Tested

We tested the effects of levodopa (L-DOPA, 10 mg/kg, Acros Organics, Geel, Belgium), the D3 receptor agonist, pramipexole (0.5 mg/kg, ApexBio Technology LLC, Houston, TX), the D3 receptor antagonist, SB277011-A (10 mg/kg, Abcam Cambridge, MA), the D1 agonist, SKF 38393 (10 mg/kg, Tocris, Ellisville, MO), the D1 receptor antagonist, SCH 39166 (5 mg/kg, Tocris, Ellisville, MO), and morphine (morphine sulfate salt pentahydrate, 2 mg/kg, Sigma-Aldrich St. Louis, MO). Drug concentrations were chosen based on previous publications by others and us (Acquas and Di Chiara, 1999; Williams et al., 2006; Brewer et al., 2014; Solís et al., 2015; Dinkins et al., 2017)

Tissue Harvesting and Protein Isolation

Mice were deeply anesthetized with isoflurane and decapitated before spinal cords were dissected out, immediately placed in RNAlater (Thermo Fisher Scientific, Waltham, MA), and stored at −20°C until use. Spinal cords were homogenized in 1 ml of RIPA buffer with protease and phosphatase inhibitors (0.12 ml/ml RIPA buffer, Sigma-Aldrich #P2714 and 0.012 ml/ml of RIPA buffer, Sigma-Aldrich #P5726 St. Louis, MO, respectively). The homogenized spinal cords were centrifuged (13,000 rpm, 4°C, 15 min), and supernatants were aliquoted and stored individually at −80°C. Following homogenization, standard protein concentrations were established with a Bradford protein assay (Quickstart Bradford reagent, Bio-Rad #500205), and plates were read on an Epoch Microplate Spectrophotometer (BioTek, Winooski, VT) at 595 nm using the Gen5.1 software package (BioTek, Winooski, VT).

Western Blot

For Western blots, 30 μg of each lumbar spinal cord protein samples were denatured using 2x Laemmli buffer containing 5% β-mercaptoethanol and 1% SDS at 95°C for 10 min and loaded onto a 12% Criterion™ TGX Stain-Free™ Protein Gel (#5678045, Bio-Rad, Hercules, CA) and run ∼45 min at 200 V. The proteins were transferred to a low fluorescent PVDF membrane using Trans-Blot® Turbo™ RTA Midi LF PVDF Transfer Kit (#170-4275, Bio-Rad, Hercules, CA). Membranes were probed with the primary antibodies and with secondary antibodies (LI-COR, Lincoln, NE) by the iBind™ Flex Western Device (SLF2000, Thermo Fisher, Waltham, MA) based on sequential Lateral Flow (SLF) technology using iBind™ Flex Fluorescent Detection (FD) Solution Kit (SLF 2019, Thermo Fisher, Waltham, MA). Membranes were imaged with an Odyssey imaging system (Odyssey Clx, LI-COR, Lincoln, NE).

Antibodies

The primary antibodies used for Western blot to detect receptor-specific protein expression were: anti-dopamine receptor D1 (Abcam 78021, 1:500 Cambridge, MA) and anti-dopamine receptor D3 (Abcam 42114, 1:1,000 Cambridge, MA). The secondary antibodies used were goat anti-rabbit 680RD (925-68071, 1:4,000, LI-COR Biosciences, Lincoln, NE) and goat anti-mouse 680RD (925-68070, 1:4,000, LI-COR Biosciences, Lincoln, NE).

Statistical Analysis

Following the experiments, behavioral data were transferred and stored in Excel format, then analyzed and plotted offline with SigmaPlot (Version 11, SPSS Science, San Jose, California). For statistical comparisons, we employed parametric or non-parametric comparisons as appropriate when comparing

multiple groups (One-Way ANOVA, RM ANOVA, or ANOVA on Ranks) with appropriate *post-hoc* comparisons (Holms-Sidak, Dunn's); *t*-tests or paired *t*-tests were used for comparison between two sets of data (treatment against respective control vehicle treatment only). Significance levels were set at $p < 0.05$. For Western blot analysis, images were analyzed with ImageStudio and ImageJ (1.50i National Institutes of Health, USA) and statistical analyses were performed with SigmaPlot 11.0.

RESULTS

Thermal Pain Withdrawal Latencies Under Baseline Conditions

We first tested and compared pain withdrawal latency responses in Meis1KO and D3KO lines under baseline conditions (after sham injection, i.p., 0.9% NaCl, 100 µl/30 g), and compared them to their respective controls. Meis1KO and their respective controls were tested as two independent cohorts. In cohort 1 the average WT latency was 10.2 ± 1.1 s, while Meis1KO latencies were 10.2 ± 0.5 s ($p = 0.97$, $n = 7$ each, power: 0.05). In cohort 2 (tested about 1 year later) the average WT latency was 6.6 ± 0.4 s, while Meis1KO latencies were 6.7 ± 0.9 s ($p = 0.92$, $n = 6$ [WT] and $n = 7$ [Meis1KO], power: 0.05). Thus despite the difference between the two Meis1KO cohorts and their WT controls, there was no effect within each cohort between WT and knockout. In contrast, individual withdrawal latencies in D3KO ranged per trial from 4.8 to 11.1 s, (average: 8.5 ± 0.24 s, $n = 7$) while the latencies of their respective WTs (WT_{D3KO}) ranged from 5.9 to 13.7 s (average: 6.5 ± 0.33 s, $n = 7$). A *t*-test comparison revealed that the difference between WT_{D3KO} and D3KO was significant ($p < 0.001$, power: 0.99).

To illustrate the effect of the genotype alone on thermal pain withdrawal reflex latencies, we normalized the WT_{meis1} response to 100% and compared them with the effects in the genetically modified animals (**Figure 1**). We found that pain withdrawal latencies of Meis1KO and their respective controls (WT_{meis1}) were not significantly different from each other (WT_{meis1}: 99.9 ± 6.1% S.E. $n = 13$, Meis1KO: 101 ± 6.7 % S.E., $n = 14$, $p = 0.97$, *t*-test, power: 0.5), while those of D3KO were significantly reduced over their respective WTs (WT_{D3KO}: 99.99 ± 2.8%; D3KO: 77.3 ± 3.9%, S.E., $p < 0.001$, *t*-test, both: $n = 7$, power: 0.99).

Morphine Modulation of Withdrawal Latencies

While opioids are commonly used for treating chronic neuropathic pain, they have also become a treatment of choice in dopamine agonist-refractory RLS (Trenkwalder et al., 2015; Gemignani et al., 2016). As we have previously shown that the D3KO mouse expresses a morphine-tolerant phenotype if treated with low doses of morphine (Brewer et al., 2014), we next addressed the question if the Meis1KO mouse follows the WT or the D3KO phenotype when challenged with morphine (**Figure 2**). In Meis1KO cohort 1, WT withdrawal latencies increased from 6.8 ± 0.45 s to 9.1 ± 1.2 s ($n = 6$), while responses of Meis1KO increased from 6.3 ± 1.2 s to 10.1 ± 1.1 s ($n = 7$). Similarly, in cohort 2, WT withdrawal latencies increased from 6.5 ± 1.2 s to 9.3 ± 1.9 s ($n = 5$), while responses of Meis1KO increased from 6.3 ± 0.6 s to 7.9 ± 1.9 s ($n = 7$). After normalization to each WT_{meis1} control, the data are as follows: WT_{meis1}; Ctrl: 99.3 ± 7.1%; after treatment: 132.5 ± 14.8%, $p = 0.08$, paired *t*-test, $n = 11$, power: 0.83, **Figure 2A1**; Meis1KO; Ctrl: 99.2 ± 5.7%; after treatment: 143 ± 16.6%, $p = 0.024$, paired *t*-test, $n = 14$, power: 0.59, **Figure 2A2**. For WT_{D3KO} the raw data were as follows; Ctrl: 8.3 ± 0.3 s; after treatment: 11.4 ± 0.6 s ($n = 7$), while D3KO were not responsive to 2 mg/kg morphine (Ctrl: 6.6 ± 0.4 s; after treatment: 6.1 ± 0.4 s, $n = 7$). After normalization to the pre-treatment control, the data for WT_{D3KO} are: 99.8 ± 2.8%; after treatment: 137.1 ± 7%, $p = 0.002$, paired *t*-test, power: 0.99; **Figure 2B1**. In contrast, normalized the data for the D3KO are: Ctrl 100.6 ± 5%; after treatment: 95.1 ± 6.6%, $p = 0.62$, paired *t*-test, power: 0.05, **Figure 2B2**). Together, these data suggest that WT_{meis1}, WT_{D3KO}, and Meis1KO animals respond similar to morphine, while D3KO are not affected.

Dopaminergic Modulation of Withdrawal Latencies

Dopaminergics are the first line of therapy in the treatment of RLS symptoms, and they can cover a range from L-DOPA to highly specific D3 receptor agonists. We therefore sought to first test the effects of L-DOPA on thermal withdrawal latencies in the different animal strains before testing the effects of the more selective receptor agonists and antagonists. We found that treatment with 10 mg/kg L-DOPA did not significantly alter withdrawal latencies in WT controls, Meis1KO or D3KO (data not shown).

We next tested the effects of the D3-receptor preferring agonist, pramipexole (PPX, **Figures 3**, **4**). In WT_{meis1}, treatment with PPX (0.5 mg/kg) increased withdrawal latencies from 100.2 ± 6.6% to 144.4 ± 13.7%, ($p = 0.008$, paired *t*-test, $n = 11$, power: 0.81, **Figure 3A1**; raw data for WT_{meis1} cohort 1: Ctrl 6.1 ± 0.7 s, PPX 9.6 ± 1.3 s, $n = 6$; cohort 2: Ctrl 7.2 ± 0.5 s; PPX: 8.6 ± 0.9 s, $n = 5$). In Meis1KO, the PPX treatment also led to a significant increase in withdrawal latencies from 100.1 ± 8.9% to 131.3 ± 12.3% ($p = 0.017$, paired *t*-test, $n = 14$, power: 0.65, **Figure 3A2**; raw data for Meis1KO cohort 1: Ctrl 6.7 ± 0.9 s, PPX 9.1 ± 1.2 s, $n = 7$; cohort 2: Ctrl 7.2 ± 0.9 s; PPX: 7.8 ± 1 s, $n = 7$). The effect of PPX was similar in the WT of the D3KO mice (WT_{D3KO}) to the effect observed in WT_{meis1} and Meis1KO, but it did not alter the responses in the D3KO. In WT_{D3KO}, withdrawal latencies rose significantly from 100 ± 6.3% (Ctrl) to 204.8 ± 9% (PPX, $p < 0.001$, paired *t*-test, $n = 8$, power: 1.0, **Figure 3B1**). In contrast, PPX did not have any significant effect in D3KO (Ctrl: 100 ± 5.6%, PPX: 108.4 ± 5.6%, $p = 0.47$, *t*-test, $n = 6$, power: 0.5, **Figure 3B2**). The raw data were as follows: WT_{D3KO}; Ctrl 6.6 ± 0.5 s, PPX 12.9 ± 1.8 s, $n = 8$; D3KO; Ctrl 9.3 ± 0.6 s; PPX: 10.1 ± 0.8 s, $n = 9$.

Additionally, treatment with the D3 receptor antagonist, SB 277011, significantly decreased withdrawal latencies in Meis1KO

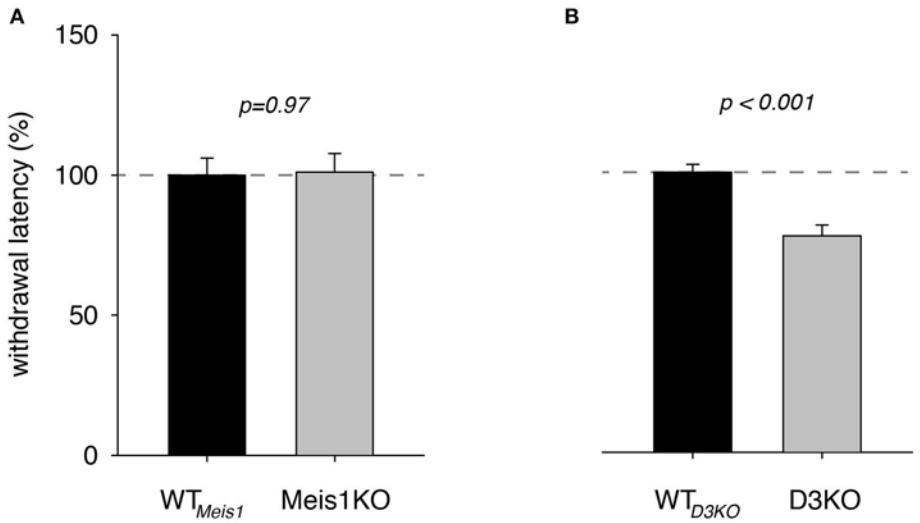


FIGURE 1 | Thermal pain withdrawal latencies under vehicle (control) conditions. **(A)** Normalized representation of data from Meis1KO mice and their respective WT controls (WT_{meis1}). WT_{meis1} latencies (black bar) were similar to those of Meis1KO (gray bar). **(B)** Normalized representation of data from D3KO animals and respective WT controls (WT_{D3KO}). WT_{D3KO} latencies (black bar) were significantly higher than those of the D3KO (gray bar).

but not D3KO (**Figure 4**). In Meis1KO, withdrawal latencies dropped from 99.5 ± 6.3% (Ctrl) to 78.5 ± 4.4% (SB277, $p = 0.004$, $n = 7$, paired t-test, power: 0.96, **Figure 4A**). However, we did not observe any significant effect in D3KO mice (Ctrl: 99.9 ± 5.3%, SB277: 92.8 ± 3.6%, $p = 0.28$, $n = 6$, paired t-test, power: 0.09, **Figure 4B**). The raw data were as follows: Meis1KO; Ctrl 7.2 ± 0.6 s, SB277 5.2 ± 0.2 s, $n = 7$; D3KO; Ctrl 7.9 ± 0.3 s; SB277: 7.8 ± 0.2 s, $n = 6$. Overall, treatment with the D3 receptor modulators led to similar effects in WT and Meis1KO and contrasted those in D3KO.

As recent findings from our lab point to a possible involvement of the D1 receptor in the face of D3 dysfunction (Brewer et al., 2014) or prolonged D3R agonist exposure (Dinkins et al., 2017), we next tested the effects of the D1 receptor agonist, SKF 38393 (SKF, **Figure 5**). We found that treatment with SKF had no significant effect in WT_{meis1} animals (Ctrl: 99.9 ± 8.2%; SKF: 92 ± 6.4%, $p = 0.77$, paired t-test, $n = 5$, power: 0.05, **Figure 5A1**), while the same treatment led to significant decrease of withdrawal latencies in Meis1KO (Ctrl: 99.9 ± 8.2%; SKF: 82.4 ± 5.7%, $p = 0.001$, paired t-test, $N = 7$, power: 0.98, **Figure 5A2**). The raw data were as follows: WT_{Meis1}; Ctrl 6.6 ± 0.3 s, SKF 6.2 ± 0.5 s; Meis1KO; Ctrl 6.9 ± 0.5 s; SKF: 5.4 ± 0.3 s.

In WT_{D3KO} animals, SKF effects were similar to WT_{meis1} (Ctrl: 100.1 ± 6.6%, SKF: 92.2 ± 5.9%, $p = 0.37$, $n = 5$, power: 0.051, **Figure 5B1**), while the responses in D3KO were similar to those in Meis1KO (Ctrl: 99.8 ± 3.9%, SKF: 71.6 ± 3.6%, $p < 0.001$, $n = 6$, power: 1.0, **Figure 5B2**). The raw data were as follows: WT_{D3KO}; Ctrl 16.8 ± 1.9 s, SKF 14 ± 1.2 s; D3KO; Ctrl 8.4 ± 0.9 s; SKF: 5.9 ± 0.8 s. In contrast to the D1 receptor agonist SKF 38393, the D1 receptor antagonist, SCH 39166, displayed no differential effects in WT controls, Meis1KO or D3KO animals (WT_{Meis1} animals: Ctrl: 100.3 ± 7.2%, SCH: 102.3 ± 12%, $p = 0.89$, paired t-test, $n = 5$, power: 0.05, Meis1KO: Ctrl: 100.3 ± 6.9%, SCH: 110.6 ± 11%, $p = 0.4$, paired t-test, $n = 7$, power: 0.05; D3KO: Ctrl: 99.7 ± 5.5%, SCH: 111.6 ± 8.8%, $p = 0.3$, paired t-test, $n = 6$, power: 0.07). Taken together, the results of these dopaminergic modulators suggest that D3 receptor-mediated actions affect WT and Meis1KO similarly, while activation of D1 receptor signaling pathways exert similar effects in Meis1KO and D3KO but not WTs.

D1R and D3R Protein Expression in the Lumbar Spinal Cord of WT, Meis1KO, and D3KO Animals

As treatments with D3- and D1 receptor-preferring agonists and antagonists respectively led to different outcomes, we next tested if the expression of these dopamine receptor subtypes was differentially regulated in Meis1KO and D3KO over WT (**Figures 6**, **7**). We found that D3 receptor protein expression did not significantly differ between WT_{Meis1}, Meis1KO, and D3KO (WT: 99.1 ± 3.5%; Meis1KO: 128.7 ± 8.5%; D3KO: 126.5 ± 11.5%, $p = 0.16$, One-Way ANOVA; **Figure 6**). Note that the D3KO expresses a dysfunctional D3 receptor that is not embedded into the membrane (Clemens et al., 2005). In contrast to the D3 receptor, when we probed for D1 receptor expression in the spinal cord, we found significantly increased D1 receptor protein levels in both Meis1KO and D3KO over WT controls (WT: 99.9 ± 8.4%; Meis1KO: 158.4 ± 13.5%; D3KO: 162 ± 12%, $p = 0.003$, One-Way ANOVA, **Figure 7**).

Increased Locomotor Activity in Meis1KO And D3KO Animals

As the pharmacological and Western blot data suggested a role of the D1 receptor system in the control of spinal cord function, and as D1 receptor activation can recruit spinal cord networks

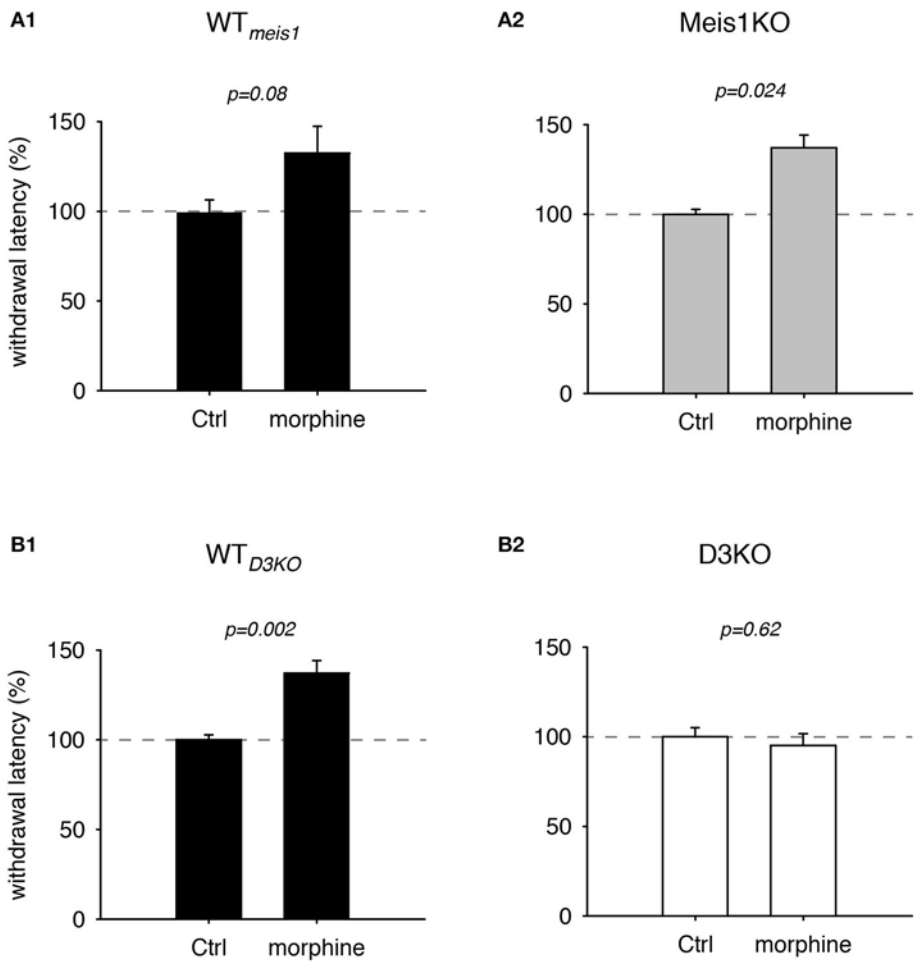


FIGURE 2 | Thermal pain withdrawal latencies of WT, Meis1KO, and D3KO under sham (Ctrl) and morphine conditions. **(A1)** Normalized representation of data from WT_{meis1} animals. Morphine significantly increased withdrawal latencies. **(A2)** Normalized representation of data from the pooled Meis1KO animals. As in WT_{meis1}, morphine significantly increased withdrawal latencies. **(B1)** Normalized representation of data from WT_{D3KO} animals. Morphine significantly increased withdrawal latencies. **(B2)** Normalized representation of data from D3KO animals. Unlike in both WT lines and Meis1KO, morphine had no effect on withdrawal latencies in D3KO.

to generate locomotor-like activities, we next tested if Meis1KO and D3KO show altered locomotor activities over their respective WT controls (**Figure 8**). We found that Meis1KO exhibited significantly increased locomotor activities compared to their WT (WT_{meis1}: 86.1 ± 13.7 m/day, $n = 7$; Meis1KO: 399.7 ± 35.5 m/day, $n = 8$, $p < 0.001$, t-test, power: 1.0), and that D3KO showed a similar significant increase over their WT controls (WT_{D3KO}: 343.2. ± 41.3 m/day, $n = 16$; D3KO: 587 ± 120 m/day, $n = 8$, $p = 0.035$, t-test, power: 0.48).

DISCUSSION

Here we compared thermal pain withdrawal latencies in two animal models of RLS, D3KO, and Meis1KO mice against wild type (WT) controls under different drug treatment conditions. We found that, under baseline conditions (sham), withdrawal latencies of WT and Meis1KO were similar, while those of D3KO were decreased, suggesting heightened excitability in these animals to a thermal stimulus and confirming earlier *in vivo* and *in vitro* studies (Keeler et al., 2012). DA acts via both excitatory (D1 and D5 receptor) and inhibitory (D2, D3, and D4 receptor) receptor subtypes, and D3KO animals express increased locomotor and rearing activities, indicating an inhibitory role of the D3 receptor in the control of these motor behaviors (Accili et al., 1996). Moreover, while present in all laminae of the spinal cord (Zhu et al., 2007), the D3 receptor is most densely expressed in the dorsal horn (Levant, 1998), suggesting a strong modulatory effect of D3 receptor-mediated pathways in this sensory area of the cord. Further, the lack of function of the inhibitory D3 receptor in the isolated spinal cord *in vitro* was sufficient to increase the number or large-reflex spinal reflex amplitudes when compared to WT controls (Clemens and Hochman, 2004). Similar to D3KO, Meis1KO show a pattern of hyperactivity but contrary to D3KO, express no significant nociceptive differences in a hotplate test (Salminen et al., 2017). This is consistent with our findings under baseline

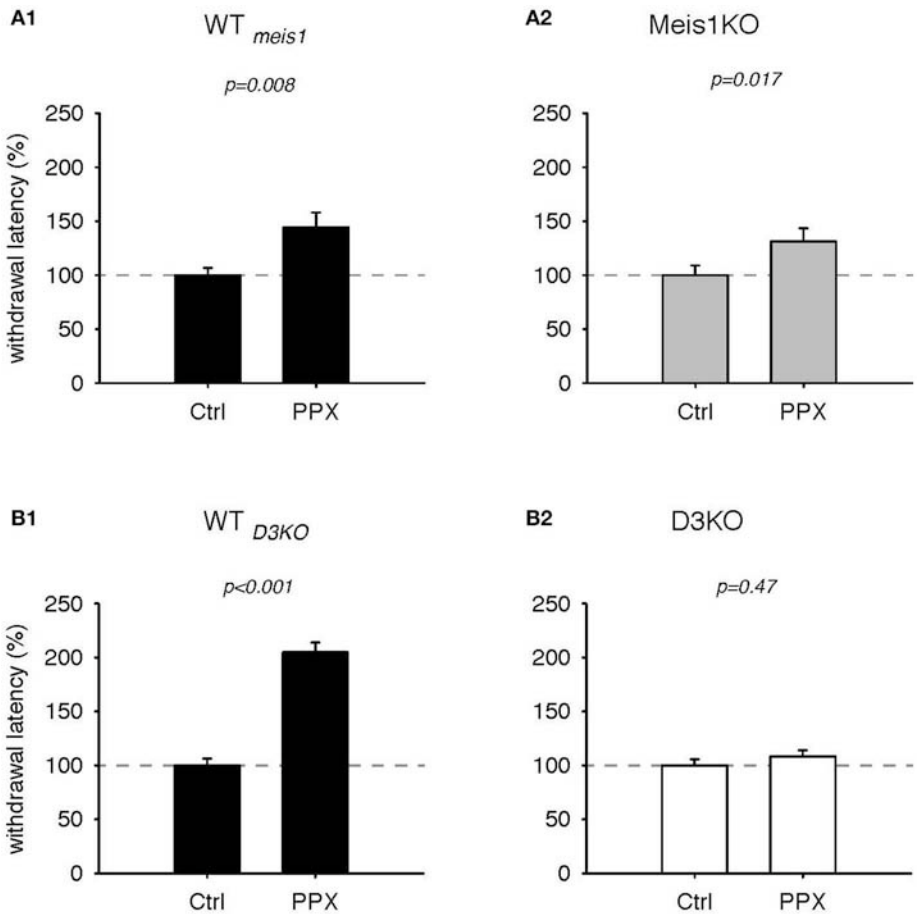


FIGURE 3 | Thermal pain withdrawal latencies of WT, Meis1KO, and D3KO before and after D3 receptor agonist (PPX) treatment. **(A1)** Normalized representation of data from WT_{meis1} animals. PPX significantly increased withdrawal latencies. **(A2)** Normalized representation of data from the Meis1KO animals. As in WT_{meis1}, PPX significantly increased withdrawal latencies. **(B1)** Normalized representation of data from WT_{D3KO} animals. PPX significantly increased withdrawal latencies. **(B2)** Normalized representation of data from D3KO animals. Unlike in both WT lines and Meis1KO, the D3 receptoer agonist PPX had no effect on withdrawal latencies in D3KO.

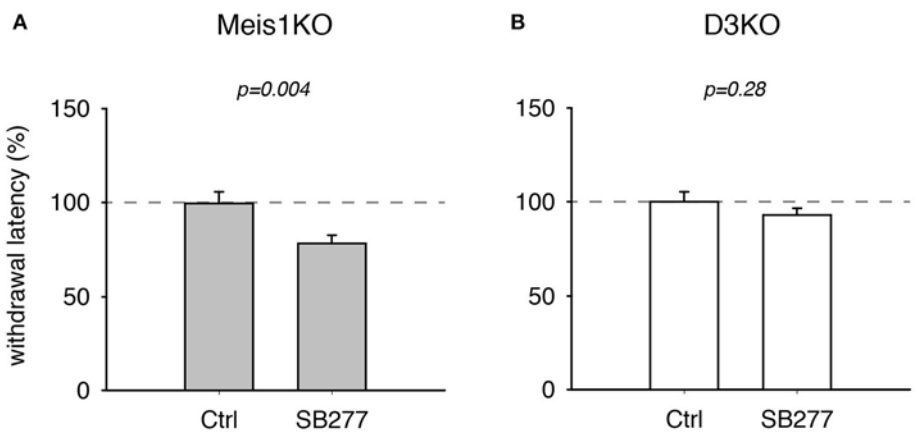


FIGURE 4 | Thermal pain withdrawal latencies of Meis1KO and D3KO before and after treatment with the D3R antagonist SB 277011. **(A)** In Meis1KO, SB277 significantly decreased withdrawal latencies. **(B)** In D3KO, treatment with SB277 did not lead to any significant changes in withdrawal latencies.

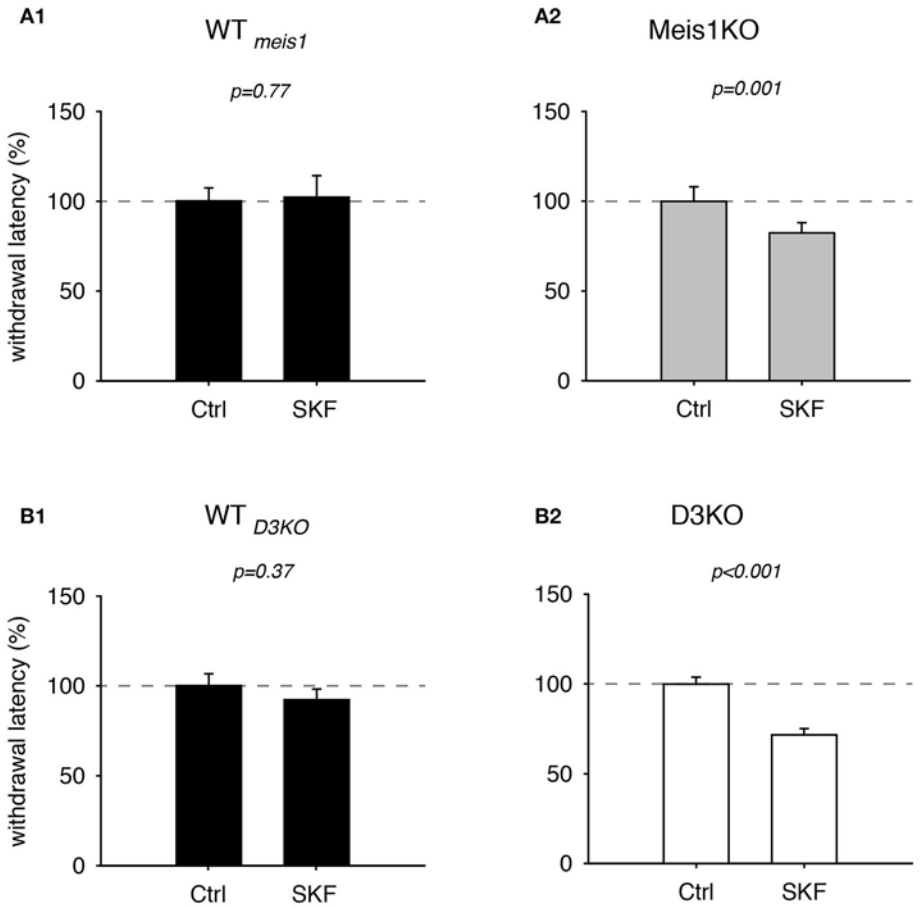


FIGURE 5 | Thermal pain withdrawal latencies of WT, Meis1KO, and D3KO before and after D1 receptor agonist (SKF) treatment. **(A1)** Normalized representation of data from WT_{meis1} animals. SKF did not have a significant effect on withdrawal latencies. **(A2)** Normalized representation of data from the Meis1KO animals. SKF significantly increased withdrawal latencies. **(B1)** Normalized representation of data from WT_{D3KO} animals. SKF did not significantly alter withdrawal latencies in WT_{D3KO}. **(B2)**. Normalized representation of data from D3KO animals. As in Meis1KO, the D1 receptor agonist significantly decreased withdrawal latencies in D3KO.

conditions where Meis1KO and WT express similar withdrawal thermal pain latencies, whereas reflex latencies are decreased in D3KO (**Figure 1**).

Effects of Morphine

Opioids are powerful modulators of nociceptive pathways, and we have shown previously that low morphine exposure (at 2 mg/kg, i.p.) was unsuccessful in modulating thermal pain withdrawal reflexes in D3KO and that this effect could be mimicked by acutely blocking D3 receptors in the isolated WT spinal cord preparation (Brewer et al., 2014). There, we also reported that the lack of a morphine effect in the D3KO animal was associated with an increased expression of the D1 receptor subtype in the spinal cord. While we did not perform other behavioral tests on pain (i.e. von Frey testing for mechanical pain), we confirmed the earlier D3KO findings here. We also found that Meis1KO and WT respond to morphine similarly (**Figure 2**). These data suggest that their opioid receptor pathways are alike, and preliminary Western blots indicate that the protein expression of the phosphorylated MOR is similar between WT and Meis1KO, but significantly increased in D3KO (data not shown). We are currently assessing if those receptor changes are found systemwide in the CNS or whether they are confined to specific (dorsal or ventral) areas of the spinal cord.

Effects of L-Dopa

We used L-DOPA (levodopa) as the immediate precursor of DA, to test the effects of raised DA levels on sensorimotor function in the three animal lines but observed no clear effect in either animal line. While L-DOPA plays an important modulatory role in controlling, at least temporarily, RLS symptoms (Akpinar, 1982; Paulus and Schomburg, 2006; Stiasny-Kolster et al., 2013), it can exert differential effects on monosynaptic and oligo- or polysynaptic nociceptive and non-nociceptive reflexes, where it depresses monosynaptic reflexes of flexors but not extensors, but also depresses transmission in nociceptive flexor reflex pathways (Schomburg and Steffens, 1998). There are several not mutually exclusive scenarios that may explain lack of any significant effect in our experiments: i) we only tested L-DOPA at a single dose of 10 mg/kg thus it is possible that lower or higher doses

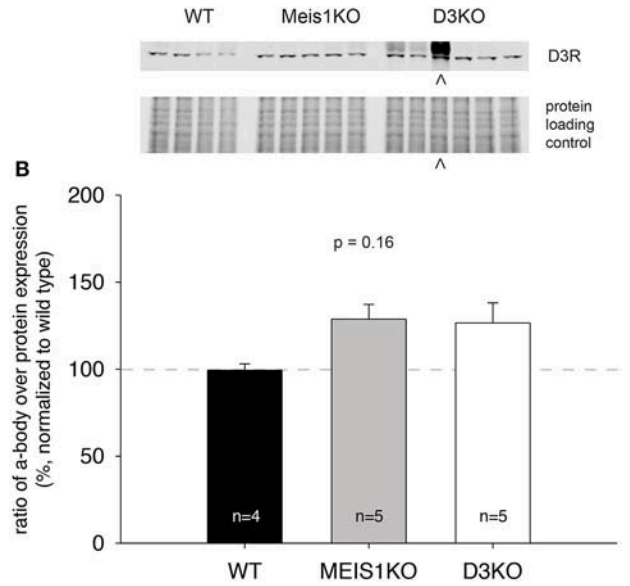


FIGURE 6 | D3R expression in the lumbar spinal cord. **(A)**. Western blot of D3R protein expression in the spinal cord. Top: D3R protein band; bottom: protein loading control. **(B)**. Quantification of D3R protein expression in the spinal cord, normalized to protein loading control / lane. D3R expression was not significantly altered in Meis1KO and D3KO animals. ∧: D3KO lanes that were excluded from the subsequent analysis.

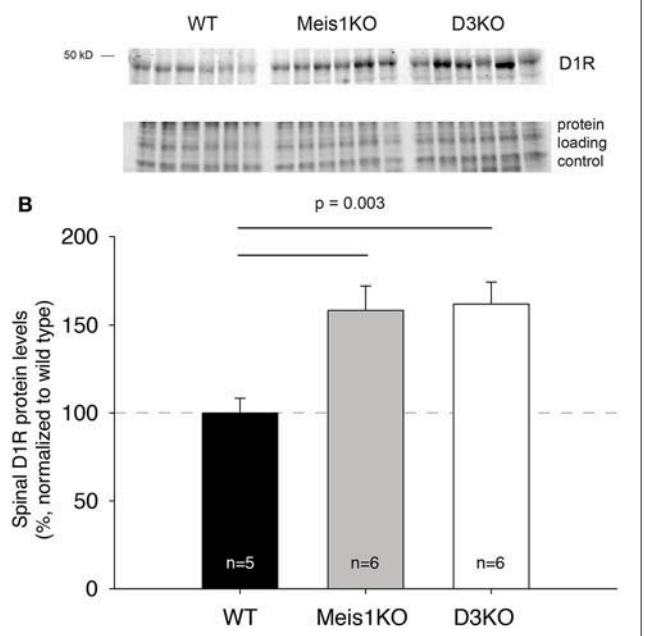


FIGURE 7 | D1R expression in the lumbar spinal cord. **(A)** Western blot of D1R protein expression in the spinal cord. Top: D1R protein band; bottom: protein loading control. **(B)** Quantification of D1R protein expression in the spinal cord, normalized to protein loading control / lane. D1R expression was significantly increased in Meis1KO and D3KO over WT animals.

would have yielded different results. However, doses of less than 10 mg/kg have been sufficient to provide behavioral effects and induce L-DOPA-induced dyskinesia in 6-hydroxydopamine lesioned mice (Lundblad et al., 2004). ii) Increasing dopamine levels with L-DOPA does not necessarily target the different DA receptor subtypes similarly. It is conceivable that high-affinity D3 receptor-activated inhibitory pathways compete with low-affinity D1 receptor-activated excitatory pathways, resulting in a net zero effect of this drug. iii), L-DOPA may act on the different components of sensory pain pathways differently; for example, in high spinal cats the onset of reflex facilitation induced by noxious radiant heat and mediated by Aϑ fibers is delayed after injection of L-DOPA, while the late component persisted (Schomburg et al., 2011).

Effects of D3R and D1R Agonists and Antagonists

While the conversion of L-DOPA to DA can lead to an activation of both inhibitory and excitatory receptor subtypes, we hypothesize that our findings reflect a strong influence of the D3 receptor in mediating the behavioral responses tested. The D3 receptor has a very high affinity to DA (Cote and Kuzhikandathil, 2014), thus an initial DA increase will primarily (but not exclusively) mediate an inhibitory response that should be missing in the D3KO. Both D3 and D1 receptors are expressed in the lumbar spinal cord (Zhu et al., 2007), and DA can

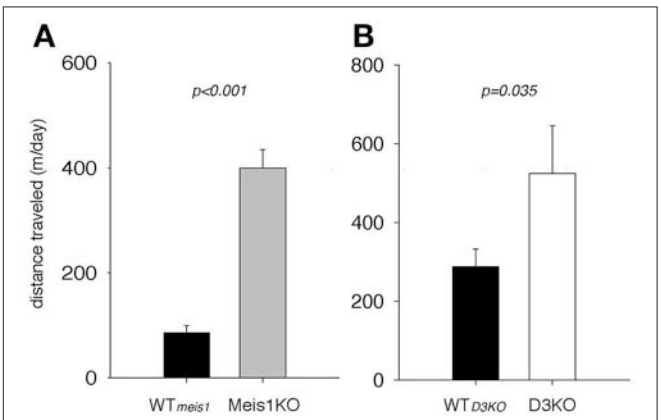


FIGURE 8 | Spontaneous locomotor activities of Meis1KO and D3KO and their respective controls. **(A)** Meis1KO. Meis1KO displayed significantly increased locomotor activities per 24 h over their WT controls (WT_{Meis1}). **(B)** Similar to Meis1KO, D3KO animals ran significantly longer distances per day over their controls (WT_{D3KO}).

up- or downregulate cellular and network functions in a dose-dependent manner (Missale et al., 1998; Thirumalai and Cline, 2008; Clemens et al., 2012). Current DA-based RLS treatment options center around D3 receptor agonists (Ferini-Strambi et al., 2016; Ferré et al., 2017), but their effect is reduced over time and can cause a worsening of the symptoms (augmentation)

(Allen et al., 2011; García-Borreguero and Williams, 2011; Earley et al., 2017; Trenkwalder et al., 2017). While we have previously shown that D3 receptor agonists and antagonists can oppositely regulate spinal reflex amplitudes (SRAs) of WT *in vitro* while they do not alter SRAs in D3KO (Clemens and Hochman, 2004), we here wanted to test how these neuromodulators act *in vivo*, and how their effects compare with the Meis1KO animals (**Figure 4**). Treatment with both D3 receptor modulators (agonist pramipexole; PPX, and antagonist SB277011-A; SB277) led to nearly identical outcomes in WT and Meis1KO respectively, and had, as expected, no effect in the D3KO. In WT and Meis1KO, PPX had a strong analgesic effect that was counteracted by SB277, suggesting a similar role for the D3 receptor in modulating the thermal nociceptive pathway in these two animal strains. As the D3 receptor in the spinal cord is most prominently expressed in the sensory neurons of the dorsal horn (Levant, 1998), it is tempting to speculate that reduced DA levels at this sensory interface in the evening or at night (Carlsson et al., 1980; Sowers and Vlachakis, 1984) might reduce descending inhibitory control and thus contribute to the emergence of the circadian symptoms in RLS ("urge to move"). Of particular note is that such a reduced functional state of the D3 receptor in the dorsal horn could also arise independent of circadian DA levels, either by Meis1-dependent compromised projections of descending DA fibers from the A11 nucleus (M. Aschner, personal communication) or with the normal aging-related gradual decline of DA levels (Haycock et al., 2003) and a subsequent reduction in the expression levels of inhibitory G*i*-coupled DA receptors (Mesco et al., 1991; Valerio et al., 1994). As with the circadian DA fluctuations, low DA levels would first affect the D3R and thus reduce overall DA-mediated inhibition. The D3KO animal then could serve as a model to specifically assess the mechanisms that follow a D3 receptor dysfunction in the sensory part of the spinal cord.

In contrast to D3 receptor modulators, the effects of the D1 receptor agonist was similar between Meis1KO and D3KO, but had no effect in WT. We suspect that the increase in spinal D1R protein expression (discussed below) may be the component that drives this behavioral outcome. We here confirmed that both Meis1KO and D3KO animals express increased locomotor activities (Accili et al., 1996; Salminen et al., 2017), and there is ample evidence that, in the isolated spinal cord preparation, D1R agonists can activate the central pattern generator (CPG) for locomotion (Kiehn and Kjaerulff, 1996) (Starr and Starr, 1993; Lapointe and Guertin, 2008; Urs et al., 2011; Sharples et al., 2015). As the locomotor CPG is contained to the ventral aspect of the thoraco-lumbar spinal cord (Kjaerulff and Kiehn, 1996; Kiehn, 2006, 2016) and the D1 receptor is more strongly expressed in ventral than sensory areas of the spinal cord (Zhu et al., 2007), D1 receptor-mediated actions may predominantly target motor-related over sensory functions in the spinal cord. Intriguingly, periodic limb movements during sleep (PLMS) are often associated with RLS (Wetter and Pollmächer, 1997; Moore et al., 2014; Li et al., 2016), and PLMS scores are regularly used to quantify RLS severity (Happe et al., 2001; Manconi et al., 2011b; Winkelmann et al., 2017). The similar responsiveness of Meis1KO and the D3KO to the D1 receptor modulators and their heightened motor activity suggest that the excitability of the spinal CPG may be upregulated in these animals, possibly via a D1 receptor-dependent beta-arrestin 2/phospho-ERK signaling complex that selectively mediates the locomotor CPG (Urs et al., 2011), which then could provide a target to understand the development of PLMS in future mechanistic studies.

D3R and D1R Protein Expression in the Spinal Cord

All DA receptor-mRNAs are expressed in the neurons of the rodent spinal cord (Zhu et al., 2007), although it is unclear if this translates also to proteins similarly, and if it is also the case in primates and man. For example, in non-human primates the D1 receptor is missing in the cord (Barraud et al., 2010), however its functions may be compensated for by the D5 receptor subtype, which also activates adenylyl cyclase (Missale et al., 1998). Using standard Western blot techniques, we tested for D3 receptor and D1 receptor protein expression in the lumbar spinal cord of the three animal models tested behaviorally. While we found no significant difference in D3 receptor expression across WT, Meis1KO and D3KO (**Figure 6**), we observed a significant upregulation of D1 receptor protein expression in Meis1KO and D3KO over WT (**Figure 7**). While present at relatively low levels in the spinal cord (Zhu et al., 2007), quantitative autoradiography has revealed that the D3 receptor is predominantly expressed in the dorsal horn (Levant, 1998), where it is in a prime position to modulate sensory pathways. In contrast, D1 receptor activation is regularly used to induce fictive locomotion in the isolated spinal cord preparation (Lapointe and Guertin, 2008; Han and Whelan, 2009; Sharples et al., 2015), suggesting a strong influence of the D1 receptor system to activate these more ventrally located circuits. Thus an increase in the availability or activation of D1 receptors in D3KO animals could explain an increase in an overall increase in the overall excitability and activity, similar to that observed with normal aging (Keeler et al., 2016).

The presence of a D3 receptor protein in the D3KO may appear unexpected, but the D3KO mouse used in our studies is not a genetic knockout of the D3 receptor; rather it is a targeted mutation of the D3 receptor gene in the second intracellular loop of the predicted protein sequence that prevents the incorporation of the D3R into the membrane (Accili et al., 1996). While this mutation does not preclude the transcription and translation of the D3 receptor, it prevents its insertion into the cell membrane (Zhu et al., 2008), rendering it functionally inactive (Clemens and Hochman, 2004). The lack of a difference between WT and Meis1KO supports the behavioral effects of the D3 receptor compounds and underlines the similarities between these two models with regard to the modulation of their sensory circuits.

In contrast to the D3 receptor data, the results of the D1 receptor protein expression point to a similarity of Meis1KO and D3KO, but not with either of them and the WT. We have shown previously that D3KO express not only decreased thermal pain withdrawal latencies but also an increased spinal D1 receptor protein expression (Brewer et al., 2014), and it is possible that in these animals a lack of synergistic D1-D3 receptor intra-membrane receptor-receptor interactions may account for the

underlying mechanism that is responsible for this behavioral outcome (Marcellino et al., 2008). However, our data do not completely answer the question if there is a spatial component to the differences in D3 receptor and D1 receptor protein expression in the cord between the two genetically-modified animals and their WT controls. While we performed our Western blot experiments on lumbar spinal segments only, we did not anticipate the outcome that point to potential differential changes in sensory and motor circuits, and hence did not further dissect out and differentiate the outcomes between ventral versus dorsal aspects within those segments.

The Caveat of Using Dopaminergics *in vivo* to Test Sensorimotor Circuits in the Spinal Cord

Descending DA projections to and the presence of DA receptors in the spinal cord are well established (Holstege et al., 1996; van Dijken et al., 1996; Levant, 1998; Zhu et al., 2007), yet we cannot exclude the possibility that any of the drugs tested may have triggered changes in descending pathways, which in turn altered spinal reflex circuit excitabilities. Possible alternate approaches to test whether the DA effects are systemwide or truly spinal, which was beyond the scope of this study, would be to test the modulatory effects of these compounds in acutely anesthetized and spinalized animals, or by employing intrathecal drug delivery or conditional knockout approaches. In fact, data from a preliminary study, in which a D3 receptor-specific blocker was applied intrathecally, indicate that such an intrathecal approach alone can alter locomotor patterns and spinal D1 receptor expression (Jensen et al., 2014).

D3KO and Meis1KO–Complementary Models of RLS?

Figure 9 presents a comparative model, in which we summarize baseline properties, behavioral responses to the drugs tested, and D1 and D3 receptor protein expression data between WT, Meis1KO, and D3KO. WT and Meis1KO are similar with regard to sensory excitability at baseline (sham), their behavioral responses to morphine and D3 receptor modulators, and the expression levels of the spinal D3 receptor. Importantly, WT are different from D3KO with regard to baseline, opioid response, D1 receptor modulators, and D1 receptor expression. While Meis1KO and D3KO differ from each other in baseline and opioid response, they react similarly to D1 receptor modulators, and they express similarly increased D1 receptor protein expression levels in the lumbar spinal cord. As Meis1KO show at baseline only an increased locomotor activity, but normal sensory excitability, and as locomotor circuits are located in the ventral

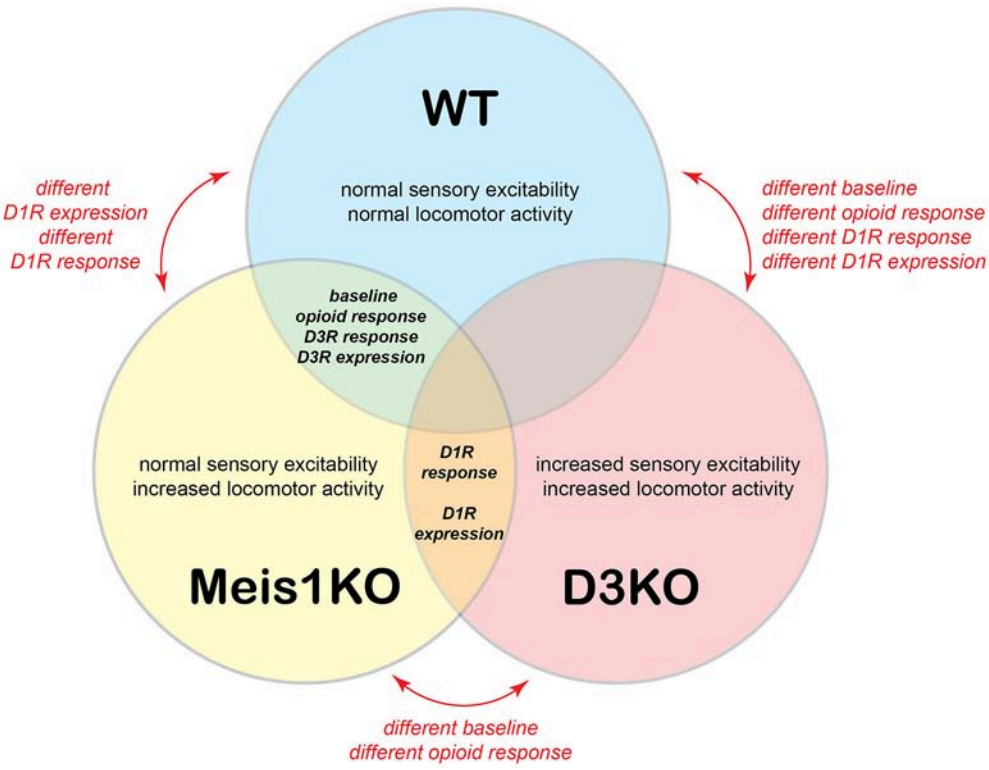


FIGURE 9 | Model of relationships between WT, Meis1KO, and D3KO animals. WT and Meis1KO share a similar baseline under control conditions, respond similarly to opioids, and have a similar D3R expression in the spinal cord. However, they differ in their responses to D1R modulators. WT and D3KO have different baselines under control conditions and respond differently to opioids, D3R, and D1R modulators. Meis1KO and D3KO have different baselines under control conditions, but respond similarly to D1R modulators, and have similar D1R expression levels in the spinal cord.

horn of the spinal cord, we posit that the Meis1KO mouse may serve as a model to specifically explore the mechanisms affiliated with the motor-related aspects of RLS (i.e. PLMS). In contrast, the increased sensory excitability and locomotor activity in D3KO suggest that both sensory and motor circuits are functionally upregulated in the spinal cord of this mouse, and that this model may be used to examine the impact of both sensory and motor pathways affiliated with RLS.

AUTHOR CONTRIBUTIONS

SM, M-LD, SL, YunL, C-TL, and MK performed the experiments. SM, M-LD, MK, C-TL, and SC analyzed the data. SC and YuqL designed the experiments. SM, KB, YuqL, and SC wrote the manuscript. SM, M-LD, MK, SL, YunL, YuqL, C-TL, KB, YL, and SC approved of the manuscript.

ACKNOWLEDGMENTS

Funding support for this study was provided in part by a National Institute of Health grant (R01NS082244), the Office of Research and Graduate Studies at East Carolina University, the Restless Legs Syndrome Foundation, and the Department of Physiology at the Brody School of Medicine. We thank B. and M. Neuhaus for their help with designing the model diagram, Drs. Neal G. Copeland and Hesham A. Sadek for providing the Meis1 loxP mice, and Kelly Dexter for breeding and genotyping the Meis1KO mice.

REFERENCES

Accili, D., Fishburn, C. S., Drago, J., Steiner, H., Lachowicz, J. E., Park, B. H., et al. (1996). A targeted mutation of the D3 dopamine receptor gene is associated with hyperactivity in mice. *Proc. Natl. Acad. Sci. U. S. A.* 93, 1945–1949. doi: 10.1073/pnas.93.5.1945

Acquas, E., and Di Chiara, G. (1999). Local application of SCH 39166 reversibly and dose-dependently decreases acetylcholine release in the rat striatum. *Eur. J. Pharmacol.* 383, 275–279. doi: 10.1016/S0014-2999(99)00660-3

Akpinar, S. (1982). Treatment of restless legs syndrome with levodopa plus benserazide. *Arch Neurol.* 39:739. doi: 10.1001/archneur.1982.00510230065027

Allen, R. P., Ondo, W. G., Ball, E., Calloway, M. O., Manjunath, R., Higbie, R. L., et al. (2011). Restless legs syndrome (RLS) augmentation associated with dopamine agonist and levodopa usage in a community sample. *Sleep Med.* 12, 431–439. doi: 10.1016/j.sleep.2011.03.003

Barraud, Q., Obeid, I., Aubert, I., Barriere, G., Contamin, H., McGuire, S., et al. (2010). Neuroanatomical study of the A11 diencephalospinal pathway in the non-human primate. *PLoS ONE* 5:e13306. doi: 10.1371/journal.pone.0013306

Barriere, G., Cazalets, J. R., Bioulac, B., Tison, F., and Ghorayeb, I. (2005). The restless legs syndrome. *Prog Neurobiol.* 77, 139–165. doi: 10.1016/j.pneurobio.2005.10.007

Brewer, K. L., Baran, C. A., Whitfield, B. R., Jensen, A. M., and Clemens, S. (2014). Dopamine D3 receptor dysfunction prevents anti-nociceptive effects of morphine in the spinal cord. *Front. Neural Circuits.* 8, 62-01 62–10. doi: 10.3389/fncir.2014.00062

Carlsson, A., Svennerholm, L., and Winblad, B. (1980). Seasonal and circadian monoamine variations in human brains examined post mortem. *Acta Psychiatr. Scand. Suppl.* 280, 75–85. doi: 10.1111/acps.1980.61.s280.75

Clemens, S., Belin-Rauscent, A., Simmers, J., and Combes, D. (2012). Opposing modulatory effects of D1- and D2-like receptor activation on a spinal central pattern generator. *J. Neurophysiol.* 107, 2250–2259. doi: 10.1152/jn.00366.2011

Clemens, S., and Hochman, S. (2004). Conversion of the modulatory actions of dopamine on spinal reflexes from depression to facilitation in D3 receptor knock-out mice. *J. Neurosci.* 24, 11337–11345. doi: 10.1523/JNEUROSCI.3698-04.2004

Clemens, S., Rye, D., and Hochman, S. (2006). Restless legs syndrome: revisiting the dopamine hypothesis from the spinal cord perspective. *Neurology* 67, 125–130. doi: 10.1212/01.wnl.0000223316.53428.c9

Clemens, S., Sawchuk, M. A., and Hochman, S. (2005). Reversal of the circadian expression of tyrosine-hydroxylase but not nitric oxide synthase levels in the spinal cord of dopamine D3 receptor knockout mice. *Neuroscience* 133, 353–357. doi: 10.1016/j.neuroscience.2005.03.002

Cote, S. R., and Kuzhikandathil, E. V. (2014). *In vitro* and *in vivo* characterization of the agonist-dependent D3 dopamine receptor tolerance property. *Neuropharmacology* 79, 359–367. doi: 10.1016/j.neuropharm.2013.11.023

Dauvilliers, Y., and Winkelmann, J. (2013). Restless legs syndrome: update on pathogenesis. *Curr. Opin. Pulm. Med.* 19, 594–600. doi: 10.1097/MCP.0b013e328365ab07

Dinkins, M.-L., Lallemand, P., and Clemens, S. (2017). Long-term treatment with dopamine D3 receptor agonists induces a behavioral switch that can be rescued by blocking the dopamine D1 receptor. *Sleep Med.* 40, 47–52. doi: 10.1016/j.sleep.2017.10.001

Dowling, P., Klinker, F., Stadelmann, C., Hasan, K., Paulus, W., and Liebetanz, D. (2011). Dopamine D3 receptor specifically modulates motor and sensory symptoms in iron-deficient mice. *J. Neurosci.* 31, 70–77. doi: 10.1523/JNEUROSCI.0959-10.2011

Earley, C. J., Allen, R. P., Connor, J. R., Ferrucci, L., and Troncoso, J. (2009). The dopaminergic neurons of the A11 system in RLS autopsy brains appear normal. *Sleep Med.* 10, 1155–1157. doi: 10.1016/j.sleep.2009.01.006

Earley, C. J., Allen, R. P., and Hening, W. (2011). Restless legs syndrome and periodic leg movements in sleep. *Handb. Clin. Neurol.* 99, 913–948. doi: 10.1016/B978-0-444-52007-4.00015-1

Earley, C. J., Connor, J., Garcia-Borreguero, D., Jenner, P., Winkelman, J., Zee, P. C., et al. (2014). Altered Brain iron homeostasis and dopaminergic function in Restless Legs Syndrome (Willis-Ekbom Disease). *Sleep Med.* 15, 1288–1301. doi: 10.1016/j.sleep.2014.05.009

Earley, C. J., Uhl, G. R., Clemens, S., and Ferre, S. (2017). Connectome and molecular pharmacological differences in the dopaminergic system in restless legs syndrome (RLS): plastic changes and neuroadaptations that may contribute to augmentation. *Sleep Med.* 31, 71–77. doi: 10.1016/j.sleep.2016.06.003

Eccles, R. M., and Lundberg, A. (1959). Supraspinal control of interneurones mediating spinal reflexes. *J. Physiol.* 147, 565–584. doi: 10.1113/jphysiol.1959.sp006262

Ekbom, K. A. (1944). Asthenia crurum pasasthetica (irritable legs). *Acta Med. Scand.* 118, 197–209. doi: 10.1111/j.0954-6820.1944.tb17800.x

Ekbom, K. A. (1945). Restless legs syndrome. *Acta Med. Scand.* 158, 4–122.

Ekbom, K. A. (1960). Restless legs syndrome. *Neurology* 10, 868–873. doi: 10.1212/WNL.10.9.868

Ferini-Strambi, L., Marelli, S., and Galbiati, A. (2016). Clinical pharmacology and efficacy of rotigotine (Neupro(R) patch) in the treatment of restless leg syndrome. *Expert Opin. Drug Metab. Toxicol.* 12, 967–975. doi: 10.1080/17425255.2016.1194393

Ferré, S., Earley, C., Gulyani, S., and Garcia-Borreguero, D. (2017). In search of alternatives to dopaminergic ligands for the treatment of restless legs syndrome: iron, glutamate, and adenosine. *Sleep Med.* 31, 86–92. doi: 10.1016/j.sleep.2016.08.019

Ferri, R., Manconi, M., Arico, D., Sagrada, C., Zucconi, M., Bruni, O., et al. (2010). Acute dopamine-agonist treatment in restless legs syndrome: effects on sleep architecture and NREM sleep instability. *Sleep* 33, 793–800. doi: 10.1093/sleep/33.6.793

Garcia-Borreguero, D., Silber, M., Winkelman, J. W., B. H., and Bainbridge, J., Buchfuhrer, M. J., et al. (2016). Guidelines for the first-line treatment of restless legs syndrome/Willis–Ekbom disease, prevention and treatment of dopaminergic augmentation: a combined task force of the IRLSSG, EURLSSG, and the RLS-foundation. *Sleep Med.* 211, 1–11. doi: 10.1016/j.sleep.2016.01.017

García-Borreguero, D., and Williams, A. M. (2011). Dopaminergic augmentation of restless legs syndrome: the scope of the problem. *Sleep Med.* 12, 425–426. doi: 10.1016/j.sleep.2011.03.004

Gemignani, F., Melpignano, A., Milioli, G., Riccardi, S., and Parrino, L. (2016). Restless legs syndrome: a new entity of neuropathic pain? Treatment with prolonged release oxycodone/naloxone combination. *J. Parkinson. Restless Legs Syndrome.* 6, 23–27. doi: 10.2147/JPRLS.S77560

Ghorayeb, I., and Tison, F. (2010). Restless legs syndrome epidemiology. *Presse Med.* 39, 564–570. doi: 10.1016/j.lpm.2009.08.006

Guo, H., Hong, S., Jin, X. L., Chen, R. S., Avasthi, P. P., Tu, Y. T., et al. (2000). Specificity and efficiency of Cre-mediated recombination in Emx1-Cre knock-in mice. *Biochem. Biophys. Res. Commun.* 273, 661–665. doi: 10.1006/bbrc.2000.2870

Han, P., and Whelan, P. J. (2009). Modulation of AMPA currents by D(1)-like but not D(2)-like receptors in spinal motoneurons. *Neuroscience* 158, 1699–1707. doi: 10.1016/j.neuroscience.2008.11.040

Happe, S., Klösch, G., Saletu, B., and Zeitlhofer, J. (2001). Treatment of idiopathic restless legs syndrome (RLS) with gabapentin. *Neurology* 57, 1717–1719. doi: 10.1212/WNL.57.9.1717

Haycock, J. W., Becker, L., Ang, L., Furukawa, Y., Hornykiewicz, O., and Kish, S. J. (2003). Marked disparity between age-related changes in dopamine and other presynaptic dopaminergic markers in human striatum. *J. Neurochem.* 87, 574–585. doi: 10.1046/j.1471-4159.2003.02017.x

Holstege, J. C., Van Dijken, H., Buijs, R. M., Goedknegt, H., Gosens, T., and Bongers, C. M. (1996). Distribution of dopamine immunoreactivity in the rat, cat and monkey spinal cord. *J. Comp. Neurol.* 376, 631–652. doi: 10.1002/(SICI)1096-9861(19961223)376:4<631::AID-CNE10>3.0.CO;2-P

Jensen, A. M., Salvad,è, A., Samir, S., Morales, G., Manconi, M., and Clemens, S. (2014). *Block of Dopamine D3 Receptors Induces Hind Limb Movements During Sleep and is Accompanied by an Increase in Spinal D1 Receptor Protein Expression*. Program No 14822. Washington, DC: Society for Neuroscience, Online.

Keeler, B. E., Baran, C. A., Brewer, K. L., and Clemens, S. (2012). Increased excitability of spinal pain reflexes and altered frequency-dependent modulation in the dopamine D3-receptor knockout mouse. *Exp. Neurol.* 238, 273–283. doi: 10.1016/j.expneurol.2012.09.002

Keeler, B. E., Patel, M. M., Lallemand, P., de Castro Brás, L. E., and Clemens, S. (2016). Opposing aging-related shift of excitatory dopamine D1and inhibitory D3 receptor protein expression in striatum and spinal cord. *J. Neurophysiol.* 115, 363–369. doi: 10.1152/jn.00390.2015

Kiehn, O. (2006). Locomotor circuits in the mammalian spinal cord. *Annu. Rev. Neurosci.* 29, 279–306. doi: 10.1146/annurev.neuro.29.051605.112910

Kiehn, O. (2016). Decoding the organization of spinal circuits that control locomotion. *Nat. Rev. Neurosci.* 17, 224–238. doi: 10.1038/nrn.2016.9

Kiehn, O., and Kjaerulff, O. (1996). Spatiotemporal characteristics of 5-HT and dopamine-induced rhythmic hindlimb activity in the *in vitro* neonatal rat. *J. Neurophysiol.* 75, 1472–1482. doi: 10.1152/jn.1996.75.4.1472

Kjaerulff, O., and Kiehn, O. (1996). Distribution of networks generating and coordinating locomotor activity in the neonatal rat spinal cord *in vitro*: a lesion study. *J. Neurosci.* 16, 5777–5794. doi: 10.1523/JNEUROSCI.16-18-05777.1996

Klinker, F., Hasan, K., Dowling, P., Paulus, W., and Liebetanz, D. (2011). Dopamine D(3) receptor deficiency sensitizes mice to iron deficiency–related deficits in motor learning. *Behav. Brain Res.* 220, 358–361. doi: 10.1016/j.bbr.2011.02.022

Kocabas, F., Zheng, J., Thet, S., Copeland, N. G., Jenkins, N. A., DeBerardinis, R. J., et al. (2012). Meis1 regulates the metabolic phenotype and oxidant defense of hematopoietic stem cells. *Blood* 120, 4963–4972. doi: 10.1182/blood-2012-05-432260

Lanza, G., Bachmann, C. G., Ghorayeb, I., Wang, Y., Ferri, R., and Paulus, W. (2017). Central and peripheral nervous system excitability in restless legs syndrome. *Sleep Med.* 31, 49–60. doi: 10.1016/j.sleep.2016.05.010

Lapointe, N. P., and Guertin, P. A. (2008). Synergistic effects of D1/5 and 5-HT1A/7 receptor agonists on locomotor movement induction in complete spinal cord-transected mice. *J. Neurophysiol.* 100, 160–168. doi: 10.1152/jn.90339.2008

Levant, B. (1998). Differential distribution of D3 dopamine receptors in the brains of several mammalian species. *Brain Res.* 800, 269–274. doi: 10.1016/S0006-8993(98)00529-0

Li, X., Allen, R. P., Earley, C. J., Liu, H., Cruz, T. E., Edden, R. A., et al. (2016). Brain iron deficiency in idiopathic restless legs syndrome measured by quantitative magnetic susceptibility at 7 tesla. *Sleep Med.* 22, 75–82. doi: 10.1016/j.sleep.2016.05.001

Lundblad, M., Picconi, B., Lindgren, H., and Cenci, M. A. (2004). A model of L-DOPA-induced dyskinesia in 6-hydroxydopamine lesioned mice: relation to motor and cellular parameters of nigrostriatal function. *Neurobiol. Dis.* 16, 110–123. doi: 10.1016/j.nbd.2004.01.007

Manconi, M., Ferri, R., Zucconi, M., Clemens, S., Giarolli, L., Bottasini, V., et al. (2011b). Preferential D2 or preferential D3 dopamine agonists in restless legs syndrome. *Neurology* 77, 110–117. doi: 10.1212/WNL.0b013e3182242d91

Manconi, M., Ferri, R., Zucconi, M., Clemens, S., Rundo, F., Oldani, A., et al. (2011a). Effects of acute dopamine-agonist treatment in restless legs syndrome on heart rate variability during sleep. *Sleep Med.* 12, 47–55. doi: 10.1016/j.sleep.2010.03.019

Marcellino, D., Ferré, S., Casado, V., Cortes, A., Le Foll, B., Mazzola, C., et al. (2008). Identification of dopamine D1-D3 receptor heteromers. Indications for a role of synergistic D1-D3 receptor interactions in the striatum. *J. Biol. Chem.* 283, 26016–26025. doi: 10.1074/jbc.M710349200

Marcos, S., González-Lázaro, M., Beccari, L., Carramolino, L., Martin-Bermejo, M. J., Amarie, O., et al. (2015). Meis1 coordinates a network of genes implicated in eye development and microphthalmia. *Development* 142, 3009–3020. doi: 10.1242/dev.122176

Mercader, N., Leonardo, E., Azpiazu, N., Serrano, A., Morata, G., Martinez, C., et al. (1999). Conserved regulation of proximodistal limb axis development by Meis1/Hth. *Nature* 402, 425–429. doi: 10.1038/46580

Mercader, N., Selleri, L., Criado, L. M., Pallares, P., Parras, C., Cleary, M. L., et al. (2009). Ectopic Meis1 expression in the mouse limb bud alters P-D patterning in a Pbx1-independent manner. *Int. J. Dev. Biol.* 53, 1483–1494. doi: 10.1387/ijdb.072430nm

Mesco, E. R., Joseph, J. A., Blake, M. J., and Roth, G. S. (1991). Loss of D2 receptors during aging is partially due to decreased levels of mRNA. *Brain Res.* 545, 355–357. doi: 10.1016/0006-8993(91)91314-Q

Missale, C., Nash, S. R., Robinson, S. W., Jaber, M., and Caron, M. G. (1998). Dopamine receptors, from structure to function. *Physiol. Rev.* 78, 189–225. doi: 10.1152/physrev.1998.78.1.189

Moore, H.t, Winkelmann, J., Lin, L., Finn, L., Peppard, P., and Mignot, E. (2014). Periodic leg movements during sleep are associated with polymorphisms in BTBD9, TOX3/BC034767, MEIS1, MAP2K5/SKOR1, and PTPRD. *Sleep* 37, 1535–1542. doi: 10.5665/sleep.4006

Nielsen, J. B. (2004). Sensorimotor integration at spinal level as a basis for muscle coordination during voluntary movement in humans. *J. Appl. Physiol.* 96, 1961–1967. doi: 10.1152/japplphysiol.01073.2003

Paulus, W., and Schomburg, E. D. (2006). Dopamine and the spinal cord in restless legs syndrome: does spinal cord physiology reveal a basis for augmentation? *Sleep Med Rev.* 10, 185–196. doi: 10.1016/j.smrv.2006.01.004

Robinson, S. W., Jarvie, K. R., and Caron, M. G. (1994). High affinity agonist binding to the dopamine D3 receptor: chimeric receptors delineate a role for intracellular domains. *Mol. Pharmacol.* 46, 352–356.

Salminen, A. V., Garrett, L., Schormair, B., Rozman, J., Giesert, F., Niedermeier, K. M., et al. (2017). Meis1: effects on motor phenotypes and the sensorimotor system in mice. *Dis. Model. Mech.* 10, 981–991. doi: 10.1242/dmm.030080

Schomburg, E. D., Dibaj, P., and Steffens, H. (2011). Role of L-DOPA in spinal nociceptive reflex activity: higher sensitivity of Adelta versus C fibre-evoked nociceptive reflexes to L-DOPA. *Physiol Res.* 60, 701–703. Available online at: http://www.biomed.cas.cz/physiolres/pdf/60/60_701.pdf

Schomburg, E. D., and Steffens, H. (1998). Comparative analysis of L-DOPA actions on nociceptive and non-nociceptive spinal reflex pathways in the cat. *Neurosci. Res.* 31, 307–316. doi: 10.1016/S0168-0102(98)00058-3

Schormair, B., Plag, J., Kaffe, M., Gross, N., Czamara, D., Samtleben, W., et al. (2011). MEIS1 and BTBD9: genetic association with restless leg syndrome in end stage renal disease. *J. Med. Genet.* 48, 462–466. doi: 10.1136/jmg.2010.087858

Schormair, B., Zhao, C., Bell, S., Tilch, E., Salminen, A. V., Putz, B., et al. (2017). Identification of novel risk loci for restless legs syndrome in genome-wide

association studies in individuals of European ancestry: a meta-analysis. *Lancet Neurol.* 16, 898–907. doi: 10.1016/S1474-4422(17)30327-7

Sharples, S. A., Humphreys, J. M., Jensen, A. M., Dhoopar, S., Delaloye, N., Clemens, S., et al. (2015). Dopaminergic modulation of locomotor network activity in the neonatal mouse spinal cord. *J. Neurophysiol.* 113, 2500–2510. doi: 10.1152/jn.00849.2014

Solís, O., Garcia-Montes, J. R., Gonzalez-Granillo, A., Xu, M., and Moratalla, R. (2015). Dopamine D3 Receptor Modulates l-DOPA-Induced Dyskinesia by Targeting D1 Receptor-Mediated Striatal Signaling. *Cereb. Cortex.* 27, 435–446. doi: 10.1093/cercor/bhv231

Sowers, J. R., and Vlachakis, N. (1984). Circadian variation in plasma dopamine levels in man. *J. Endocrinol. Invest.* 7, 341–345. doi: 10.1007/BF03351014

Spieler, D., Kaffe, M., Knauf, F., Bessa, J., Tena, J. J., Giesert, F., et al. (2014). Restless legs syndrome-associated intronic common variant in Meis1 alters enhancer function in the developing telencephalon. *Genome Res.* 24, 592–603. doi: 10.1101/gr.166751.113

Starr, M. S., and Starr, B. S. (1993). Facilitation of dopamine D1 receptor- but not dopamine D1/D2 receptor-dependent locomotion by glutamate antagonists in the reserpine-treated mouse. *Eur. J. Pharmacol.* 250, 239–246. doi: 10.1016/0014-2999(93)90387-W

Stefansson, H., Rye, D. B., Hicks, A., Petursson, H., Ingason, A., Thorgeirsson, T. E., et al. (2007). A genetic risk factor for periodic limb movements in sleep. *N. Engl. J. Med.* 357, 639–647. doi: 10.1056/NEJMoa072743

Stiasny, K., Wetter, T. C., Trenkwalder, C., and Oertel, W. H. (2000). Restless legs syndrome and its treatment by dopamine agonists. *Parkinsonism Relat. Disord.* 7, 21–25. doi: 10.1016/S1353-8020(00)00041-9

Stiasny-Kolster, K., Pfau, D. B., Oertel, W. H., Treede, R. D., and Magerl, W. (2013). Hyperalgesia and functional sensory loss in restless legs syndrome. *Pain* 154, 1457–1463. doi: 10.1016/j.pain.2013.05.007

Thirumalai, V., and Cline, H. T. (2008). Endogenous dopamine suppresses initiation of swimming in prefeeding zebrafish larvae. *J. Neurophysiol.* 100, 1635–1648. doi: 10.1152/jn.90568.2008

Trenkwalder, C., Allen, R., Hogl, B., Paulus, W., and Winkelmann, J. (2016). Restless legs syndrome associated with major diseases: a systematic review and new concept. *Neurology* 86, 1336–1343. doi: 10.1212/WNL.0000000000002542

Trenkwalder, C., Canelo, M., Lang, M., Schroeder, H., Kelling, D., Berkels, R., et al. (2017). Management of augmentation of restless legs syndrome with rotigotine: a 1-year observational study. *Sleep Med.* 30, 257–265. doi: 10.1016/j.sleep.2015.10.006

Trenkwalder, C., Winkelmann, J., Inoue, Y., and Paulus, W. (2015). Restless legs syndrome-current therapies and management of augmentation. *Nat. Rev. Neurol.* 11, 434–445. doi: 10.1038/nrneurol.2015.122

Urs, N. M., Daigle, T. L., and Caron, M. G. (2011). A dopamine D1 receptor-dependent beta-arrestin signaling complex potentially regulates morphine-induced psychomotor activation but not reward in mice. *Neuropsychopharmacology* 36, 551–558. doi: 10.1038/npp.2010.186

Valerio, A., Belloni, M., Gorno, M. L., Tinti, C., Memo, M., and Spano, P. (1994). Dopamine D2, D3, and D4 receptor mRNA levels in rat brain and pituitary during aging. *Neurobiol. Aging.* 15, 713–719. doi: 10.1016/0197-4580(94)90053-1

van Dijken, H., Dijk, J., Voom, P., and Holstege, J. C. (1996). Localization of dopamine D2 receptor in rat spinal cord identified with immunocytochemistry and *in situ* hybridization. *Eur. J. Neurosci.* 8, 621–628. doi: 10.1111/j.1460-9568.1996.tb01247.x

Wetter, T. C., and Pollmächer, T. (1997). Restless legs and periodic leg movements in sleep syndromes. *J. Neurol.* 244, S37–45. doi: 10.1007/BF03160570

Williams, S., Mmbaga, N., and Chirwa, S. (2006). Dopaminergic D1 receptor agonist SKF 38393 induces GAP-43 expression and long-term potentiation in hippocampus *in vivo*. *Neurosci. Lett.* 402, 46–50. doi: 10.1016/j.neulet.2006.03.075

Willis, T. (1685). *Of the Diseases of the Brain and the Genus Nervosum*. London, UK: The London Practice of Physick. Bassett and Crooke.

Winkelmann, J. (2008). Genetics of restless legs syndrome. *Curr. Neurol. Neurosci. Rep.* 8, 211–216. doi: 10.1007/s11910-008-0033-y

Winkelmann, J., Czamara, D., Schormair, B., Knauf, F., Schulte, E. C., Trenkwalder, C., et al. (2011). Genome-wide association study identifies novel restless legs syndrome susceptibility loci on 2p14 and 16q12.1. *PLoS Genet.* 7:e1002171. doi: 10.1371/journal.pgen.1002171

Winkelmann, J., Schormair, B., Lichtner, P., Ripke, S., Xiong, L., Jalilzadeh, S., et al. (2007). Genome-wide association study of restless legs syndrome identifies common variants in three genomic regions. *Nat. Genet.* 39, 1000–1006. doi: 10.1038/ng2099

Winkelmann, J., Schormair, B., Xiong, L., Dion, P. A., Rye, D. B., and Rouleau, G. A. (2017). Genetics of restless legs syndrome. *Sleep Med.* 31, 18–22. doi: 10.1016/j.sleep.2016.10.012

Zhu, H., Clemens, S., Sawchuk, M., and Hochman, S. (2007). Expression and distribution of all dopamine receptor subtypes (D1 - D5) in the mouse lumbar spinal cord: a real-time polymerase chain reaction and non-autoradiographic *in situ* hybridization study. *Neuroscience* 149, 885–897. doi: 10.1016/j.neuroscience.2007.07.052

Zhu, H., Clemens, S., Sawchuk, M., and Hochman, S. (2008). Unaltered D1, D2, D4, and D5 dopamine receptor mRNA expression and distribution in the spinal cord of the D3 receptor knockout mouse. *J. Comp. Physiol. A Neuroethol. Sens. Neural Behav. Physiol.* 194, 957–962. doi: 10.1007/s00359-008-0368-5

Conflict of Interest Statement: The authors declare that the research was conducted in the absence of any commercial or financial relationships that could be construed as a potential conflict of interest.

Copyright © 2018 Meneely, Dinkins, Kassai, Lyu, Liu, Lin, Brewer, Li and Clemens. This is an open-access article distributed under the terms of the Creative Commons Attribution License (CC BY). The use, distribution or reproduction in other forums is permitted, provided the original author(s) and the copyright owner(s) are credited and that the original publication in this journal is cited, in accordance with accepted academic practice. No use, distribution or reproduction is permitted which does not comply with these terms.

frontiers in Neuroscience

ORIGINAL RESEARCH
published: 26 September 2018
doi: 10.3389/fnins.2018.00667

Parameters of Surface Electromyogram Suggest That Dry Immersion Relieves Motor Symptoms in Patients With Parkinsonism

German G. Miroshnichenko[1], Alexander Yu Meigal[2], Irina V. Saenko[3], Liudmila I. Gerasimova-Meigal[4], Liudmila A. Chernikova[5], Natalia S. Subbotina[6], Saara M. Rissanen[1] and Pasi A. Karjalainen[1]*

[1] Biosignal Analysis and Medical Imaging Group, Department of Applied Physics, Faculty of Science and Forestry, University of Eastern Finland, Kuopio, Finland, [2] Laboratory for Novel Methods in Physiology, Institute of High-Tech Biomedical Solutions, Petrozavodsk State University, Petrozavodsk, Russia, [3] Laboratory of Gravitational Physiology of Sensorimotor System, Department of Sensorimotor Physiology and Countermeasure, Institute of BioMedical Problems, Russian Academy of Sciences, Moscow, Russia, [4] Department of Human and Animal Physiology, Physiopathology, Histology, Petrozavodsk State University, Petrozavodsk, Russia, [5] Department of Neurorehabilitation and Physiotherapy, Research Center of Neurology, Russian Academy of Medical Sciences, Moscow, Russia, [6] Department of Neurology, Psychiatry, and Microbiology, Petrozavodsk State University, Petrozavodsk, Russia

OPEN ACCESS

Edited by:
Brian R. Noga, University of Miami, United States

Reviewed by:
Domenico Caputo, Università degli Studi di Roma La Sapienza, Italy
Le Li, First Affiliated Hospital of Sun Yat-sen University, China
Roberto Merletti, Politecnico di Torino, Italy

***Correspondence:**
German G. Miroshnichenko
germanmi@uef.fi

Specialty section:
This article was submitted to Neural Technology, a section of the journal Frontiers in Neuroscience

Received: *13 March 2017*
Accepted: *05 September 2018*
Published: *26 September 2018*

Citation:
Miroshnichenko GG, Meigal AY, Saenko IV, Gerasimova-Meigal LI, Chernikova LA, Subbotina NS, Rissanen SM and Karjalainen PA (2018) Parameters of Surface Electromyogram Suggest That Dry Immersion Relieves Motor Symptoms in Patients With Parkinsonism. Front. Neurosci. 12:667. doi: 10.3389/fnins.2018.00667

Dry immersion (DI) is acknowledged as a reliable space flight analog condition. At DI, subject is immersed in water being wrapped in a waterproof film to imitate microgravity (μG). Microgravity is known to decrease muscle tone due to deprivation of the sensory stimuli that activate the reflexes that keep up the muscle tone. In contrary, parkinsonian patients are characterized by elevated muscle tone, or rigidity, along with rest tremor and akinesia. We hypothesized that DI can diminish the elevated muscle tone and/or the tremor in parkinsonian patients. Fourteen patients with Parkinson's disease (PD, 10 males, 4 females, 47–73 years) and 5 patients with vascular parkinsonism (VP, 1 male, 4 females, 65–72 years) participated in the study. To evaluate the effect of DI on muscles' functioning, we compared parameters of surface electromyogram (sEMG) measured before and after a single 45-min long immersion session. The sEMG recordings were made from the biceps brachii muscle, bilaterally. Each recording was repeated with the following loading conditions: with arms hanging freely down, and with 0, 1, and 2 kg loading on each hand with elbows flexed to 90°. The sEMG parameters comprised of amplitude, median frequency, time of decay of mutual information, sample entropy, correlation dimension, recurrence rate, and determinism of sEMG. These parameters have earlier been proved to be sensitive to PD severity. We used the Wilcoxon test to decide which parameters were statistically significantly different before and after the dry immersion. Accepting the $p < 0.05$ significance level, amplitude, time of decay of mutual information, recurrence rate, and determinism tended to decrease, while median frequency and sample entropy of sEMG tended to increase after the DI. The most

statistically significant change was for the determinism of sEMG from the left biceps with 1 kg loading, which decreased for 84% of the patients. The results suggest that DI can promptly relieve motor symptoms of parkinsonism. We conclude that DI has strong potential as a rehabilitation method for parkinsonian patients.

Keywords: parkinsonism, dry immersion, microgravity, rehabilitation, electromyogram, nonlinear dynamics, auto-mutual information, determinism

1. INTRODUCTION

Parkinson's disease (PD) is acknowledged as one of the major neurological problems due to its epidemiology (de Lau and Breteler, 2006), numerous motor and non-motor symptoms, and functional disability (Alves et al., 2005) in PD patients. From the patients' viewpoint, PD causes dramatic decrease in their safety, wellbeing, and quality of life (Boersma et al., 2016; Fan et al., 2016). From the society's viewpoint, PD patients have increased need for healthcare, which imposes notable economical burden on them, their families, and state (Noyes et al., 2006). PD is characterized by a classic triad of motor symptoms, which include rest tremor, elevated muscle tone, or rigidity, and akinesia. Motor symptoms worsen over time but respond to dopamine replenishment therapy (The Parkinson Study Group, 2004), deep brain stimulation (Vaillancourt et al., 2004), and transcranial magnetic stimulation (Zhu et al., 2015). Still, despite these medical therapies, PD patients develop progressive disability (Alves et al., 2005).

Varied physical interventions have been tried in an effort to find efficient, easy-to-perform, and no costly methods for rehabilitation of PD patients (Tomlinson et al., 2014). The techniques already tested include, e.g., resistance training (Scandalis et al., 2001), robotic-assisted therapy (Picelli et al., 2014), training by means of virtual reality (Yen et al., 2011), whole-body vibration (Ebersbach et al., 2008), and dancing (de Dreu et al., 2015). Also, such exotic therapies as Yoga (Ni et al., 2016), Tai Chi (Zhou et al., 2015), and music therapy (Bukowska et al., 2016) are reported to exert a positive effect on some symptoms of PD. Still, there is a strong need in a rehabilitation technique with a more clear link to pathophysiological mechanisms of parkinsonism. We assume that an unloading technique could be a relevant candidate. Indeed, various unloading techniques, such as weight support (Miyai et al., 2000) and water-related techniques, e.g., aquatic physical therapy (Katsura et al., 2010; Vivas et al., 2011; Volpe et al., 2014) have been reported to improve performance in PD patients.

The phenomenon of muscle tone appears as a commonly used, though often misunderstood concept (Needle et al., 2014). Muscle tone is defined as either the resistance of muscle being passively lengthened (Gordon, 1990), "state of readiness" (Davis et al., 2011), or unconscious "low-level steady-state muscle contraction at rest" (Needle et al., 2014). This prompts that muscle tone is comprised of several distinct components: (1) physical inertia of extremity, (2) the non-reflexive (mechanical-elastic) component, (3) peripheral reflexive muscle contraction, and (4) central neural mechanisms (Katz and Rymer, 1989; Ward, 2000; Needle et al., 2014). The non-reflexive component of muscle tone originates from intrinsic tension between molecules and cells and, correspondingly, it can be measured as a set of viscoelastic characteristics of the skeletal muscle (Demangel et al., 2017). The peripheral reflexive component of muscle tone originates from overactive tonic stretch reflex. On the level of CNS muscle tone is triggered and mediated through the reticular formation, brain stem, cerebellum, extrapyramidal pathways, with modifications from basal ganglia, gamma-motoneurones, and, finally, contraction of intrafusal fibers, which stretch spindle sensory organs, thus initiating activity of alpha-motoneurones via the stretch reflex (Needle et al., 2014). This reflexive activity is aimed at maximizing muscle responsiveness under stressful conditions (Davis et al., 2011). Inhibition from the cortical structures is needed to optimize muscle tone (Guyton and Hall, 2011). Due to complex origins, muscle tone has two different connotations in clinical and research practice. In clinics, muscle tone is used as an easy-to-do bedside measure performed with clinical scales, while for research purposes electromyography (EMG) is useful to assess muscle tone (Ward, 2000).

Two distinct types of exaggerated muscle tone—spasticity and rigidity—are known. Spasticity is hypertonicity caused by misbalance of supraspinal inhibitory and excitatory inputs directed to the spinal cord, leading to a state of disinhibition of the stretch reflex on one side of a joint (Dietz and Sinkjaer, 2007; Trompetto et al., 2014). Instead, rigidity is clinically defined as muscle hypertonicity that persists through the entire range of passive movement on both sides of a particular joint. Also, "unwilled" firing of slow-type motor units might be an important factor in the genesis of rigidity, which is seen as excessive EMG at rest (Cantello et al., 1995). Spasticity is very common in patients with the upper motoneurone lesion (stroke), cerebral palsy and multiply sclerosis (Rivelis and Morice, 2018), while rigidity is the characteristic of patients with Parkinson's disease (PD) and has distinctly different neurophysiological mechanisms (Baradaran et al., 2013).

It is well-known from space physiology that muscle tone in healthy subjects (cosmonauts/astronauts) dramatically decreases within even 1 day in real microgravity on orbit (Kozlovskaya et al., 1988). Tremor is also modified under conditions of space flight (Gallasch et al., 1994). Namely, frequency and amplitude of tremor decrease under weightlessness, presumably due to switch of main source of sensory information from load-dependent muscle reception to position-dependent joint reception (Gallasch et al., 1994). Therefore, we suppose that pathologically elevated muscle tone (rigidity) and tremor may be relieved in PD

patients with the help of ground-based analog microgravity techniques. There are few microgravity analog environments: (i) dry immersion (DI), (ii) bed rest, (iii) parabolic airplane flight, (iv) free fall machine, (v) weight support. Among these, DI provides the best microgravity analog due to the following physical factors: (i) supportlessness, (ii) physical inactivity, (iii) whole-body hydrostatic compression (Navasiolava et al., 2011; Watenpaugh, 2016; Demangel et al., 2017).

Effects of DI on the viscoelastic component of muscle tone in healthy subjects are usually seen after 3 days staying at DI (Demangel et al., 2017). However, some studies have demonstrated a much faster effect of analog microgravity on muscles. For example, Schneider et al. (2015) have shown that muscle stiffness changes even after a few seconds of parabolic flight at zero G. Also, Cronin et al. (2016) have demonstrated that muscle spasticity has decreased after 5 min of water immersion due to diminished reflexivity. These data promise that even a short-term DI session, which would be more suitable for older people and PD patients, could exert rehabilitation effect on the motor system. Indeed, the program of several DI sessions with the same patient group as here has been recently reported to exert positive effect on some clinical metrics of PD patients, including scores of depressive mood, UPDRS-III (Unified Parkinson's disease rating scale, motor part), and the rigidity subtotal of the UPDRS-III (Meigal et al., 2018). Tremor subtotal of the UPDRS-III has also decreased, though insignificantly. Still, to date, no instrumented measurement has been conducted to evaluate the effect of a single one DI session on muscle function in PD patients.

Surface electromyography (sEMG) is an affordable, noninvasive, and high-throughput way to get information about muscle functioning. sEMG has been extensively used to examine either normal motor functioning or movement disorders in humans (Farina et al., 2014). Such classical parameters of sEMG as amplitude and spectral frequency allow some estimation of motor unit number and synchronization (Sturman et al., 2005). In recent years, recurrence quantification analysis, entropy and fractal analysis of sEMG provided additional insight in the underlying motor strategies. These parameters characterize a signal in terms of regularity, predictability and self-similarity (Riley and van Orden, 2005). Indeed, nonlinear dynamics based parameters of sEMG surpass the traditional spectral frequency metrics in detection of, for example, fatigue (Sung et al., 2008; Boccia et al., 2016). The nonlinear dynamics based parameters have already been applied for diagnostics of parkinsonism with promising results (Rissanen et al., 2008, 2011; Meigal et al., 2009; Ruonala et al., 2018). They also proved sensitive to neuroleptic-induced parkinsonism in patients with schizophrenia (Meigal et al., 2015). Taken together, nonlinear dynamics based parameters allow quantifying motor unit synchronization and estimating number of independent oscillators generating sEMG (Sturman et al., 2005). Thus, among cardinal motor symptoms of PD, tremor is most reliably characterized by sEMG parameters due to their sensitivity to "hidden rhythms" on electromyogram (Meigal et al., 2013; Oung et al., 2015). In contrary, muscle tone and, presumably, rigidity, are better described by the kinematic parameters collected by wearable inertial sensors (Sáchez-Ferro et al., 2016; di Biase et al., 2018) or by viscoelasticity parameters (Schneider et al., 2015). By using sEMG, rigidity can be seen at best as excessive muscle activity at rest condition (Cantello et al., 1995).

Several studies provide information on the characteristics of sEMG in healthy subjects during analog microgravity. For example, under the condition of 1–8 weeks bed rest, such sEMG parameters as amplitude, median frequency, muscle fiber conduction velocity, and entropy substantially decrease (Portero et al., 1996; Mulder et al., 2009; Cescon and Gazzoni, 2010; Buehring et al., 2011; Fu et al., 2016). Usually, bed rest experiments last for several weeks to simulate space flights of varied duration and lead to substantial impairment in muscle performance, structure, and fiber content (Watenpaugh, 2016). In that respect, bed rest, especially in its most perfect form (with 6° head tilt below horizontal) is likely not reliable for rehabilitation purposes. In contrast, the condition of dry immersion induces microgravity-specific modifications in skeletal muscles much faster than does the bed rest condition (Navasiolava et al., 2011; Watenpaugh, 2016; Demangel et al., 2017). Earlier it has been shown that even a 5 min period of water immersion in waterproof trousers can decrease peripheral reflex excitability after returning to dry land in both healthy controls and post-stroke patients (Cronin et al., 2016). That can be considered as a promise of non-pharmaceutical method of decreasing hyperreflexivity following stroke (Cronin et al., 2016). As such, the condition of short-term dry immersion can be regarded as a potentially reliable method to decrease excessive muscle tone also in PD patients, though neurophysiology of muscle rigidity and spasticity is clearly different.

Therefore, we hypothesize that application of a single one short-term session of DI can diminish tremor and muscle rigidity in PD patients seen as decreased amplitude and modified nonlinear dynamics based parameters of sEMG.

2. PATIENTS AND METHODS

2.1. Patients

The general inclusion criteria for the patients were that they had an earlier diagnosis of either Parkinson's disease (PD) or vascular parkinsonism (VP). The exclusion criteria are listed in **Table 1**. Twenty-six patients were clinically examined for participation in this study. Seven of the twenty-six patients were excluded because of elevated blood pressure or extrasystoles on their ECG before a pilot immersion. The remaining 19 of the 26 patients underwent the 15 min pilot dry immersion and further participated in the study. Six of the nineteen patients had controlled arterial hypertension (II–III stage). All the 19 patients gave their informed signed consent before the dry immersion.

Of the 19 patients, 14 had PD (10 males, 4 females, 47–73 years) and 5 had VP (1 male, 4 females, 65–72 years). Their anthropological data, medication, and disease characteristics: duration, form, stage of PD according to Hoehn and Yahr Rating Scale, and Unified Parkinson's disease Rating Scale (UPDRS) are presented in **Table 2**. All PD patients were recruited through the Department of Neurology, Psychiatry, and Microbiology, Petrozavodsk State University (Petrozavodsk,

TABLE 1 | Exclusion criteria for the patients.

Exclusion reason	Exclusion criteria
Masking or modification of parkinsonian symptoms	Other neurological disorder or injury that interferes motor function
	Osteoporosis
	Recent spinal fracture
	Metabolic disease (e.g., hyperthyreosis, diabetes)
Dry immersion absolute contraindications	Epilepsy
	Mental disorders
	Administration of muscle relaxants
	Cerebral palsy
Dry immersion relative contraindications (these pathologies are allowable during dry immersion when controlled properly, but we still excluded patients who had them)	Hypovolemia
	Myoma of uterus
	Atrial fibrillation
	Hemorrhage of various etiology
	Lung diseases in acute stage
	Oncologic problems
	Myocardial infarction
	Blood clotting disorders (e.g., phlebothrombosis or thrombophlebitis)

Russian Federation). This study was approved by Medical Ethic Committee of PetrSU and Ministry of health care and social development of Republic of Karelia.

2.2. Dry Immersion Procedure

For analog microgravity we utilized the medical system for imitation of weightlessness (MEDSIM, Institute of BioMedical Problems, Moscow, Russia). MEDSIM (**Figure 1**) appears as a bathtub filled with 2 m^3 of fresh water. The bathtub is covered by a thin waterproof film of a large size, which allows wrapping subject's body. On the bathtub floor, a motor driven raising platform is mounted. At the initial point the platform is positioned above the water level, enabling the subject to lie down on the film. When a dry immersion procedure starts, the platform lowers down into the water so that the subject stays immersed inside the bathtub wrapped in the film with face and upper part of thorax floating on the water surface. For further details of dry immersion (DI) physics and procedure see Navasiolava et al. (2011).

The patients were instructed to take their medicines at the same time (usually at 7 AM) to standardize conditions of DI and medication. The DI procedure started almost at the same time for each patient (at 9:30 a.m., ±10 min due to differences in time required for blood pressure stabilization). The temperature of water in the DI bathtub was set at 32°C, and it was also filtered and aerated. Before the procedure, the patients visited toilet to urinate, because DI has strong diuretic effect, and drunk a glass of fresh water (200 mL). Then the patients were allowed to adapt to experimental conditions for 10–15 min, lying on the platform wrapped in a cotton sheet to prevent body cooling. By the 10th min blood pressure (UA-767, A&D Company Ltd., Japan) was measured. If blood pressure was not higher than 140/80 mm Hg, the DI procedure was started. The patients were immersed in water in supine position for 45 min, with opportunity to stop the procedure by demand or clinical indications, which were ECG and blood pressure. ECG (Poly-Spectr VNS, Neirosoft Ltd., Ivanovo, Russia) was monitored in lead II to control heart rate and search for extrasystoles. Blood pressure was measured every 15 min (at 15th, 30th, and 45th min).

2.3. Measurements of Surface Electromyogram

The study corresponds to a common pre/post design: we compared surface electromyogram (sEMG) samples before and after a single dry immersion procedure. For our measurements, we used EMG device Neuro-MEP-4 and electrodes from Neurosoft Ltd. (Ivanovo, Russia). We measured sEMG bilaterally from *biceps brachii* muscle. The skin over the muscles was carefully cleaned with a cotton alcohol swab prior to electrodes placement. Abrasive products were not applied to prepare the skin because most of the subjects were older people. Due to the old age, many subjects also had obesity and big skin folds on their arms, which was the reason to choose bipolar plate-mounted electrodes, which have two relevant features. First, they provide closer positioning to the muscle due to their protruding leads. Second, they can be mounted by wrapping adhesive band around the arm, which prevents sliding of the electrode over the muscle. The electrodes were covered with conductive gel (Unimax, Geltek-Medica Company, Moscow, Russia) and applied to the muscle belly longitudinally between the innervation zone and cubital fossa. The electrodes were fixed with adhesive plaster to make sure that sEMG would be recorded from the same sites before and after the immersion. The electrodes were not removed between the pre- and post-immersion measurements. Reference electrode in the form of fabric wrist strap was moistened and attached to the right wrist. Prior to the testing, the subjects were carefully instructed to perform the test correctly, and they were allowed to practice shortly in order to get accustomed with the EMG device and the experimental setting. They were also allowed to warm up their muscles by performing several elbow flexions and extensions. Then we measured sEMG during a submaximal quasi-isometric holding test (Meigal et al., 2012). The recordings were made in standing position in four loading conditions: (1) with arms hanging freely along the trunk, (2) holding elbows flexed to 90° (forearm directed forward and parallel to floor) with palm open and directed upwards (0 kg), (3) with 1 kg, and (4) 2 kg load on each palm. Before each isometric holding, the patient was allowed to rest for a few seconds, after which the next load was introduced. In summary, for each patient we considered 2 body sides and 4 loading conditions and made the measurements before and after the immersion session, which made up at most 16 recordings per patient. Due to technical problems during the measurement, the recording from patient 3: 2 kg after the DI session and the recording from patient 9: 0 kg after the DI session were missing (the patients numbers are from **Table 2**).

Features and settings of the EMG device and properties of the electrodes were the following. The electrodes (Neurosoft

TABLE 2 | Information about the patients.

No.	Age (yr)	Gender	Height (cm), weight (kg)	Disease duration (yr)	UPDRS/ UPDRS-III	Stage by H & Y	Disease & symptoms	Antiparkinsonian medication
1	62	M	180, 69	7	70 / 37	2	PD, T	Piribedil 200 mg Levodopa 400 mg Carbidopa 62.5 mg Rasagiline 1.56 mg Amantadine 100 mg Entocapone 200 mg
2	64	F	160, 81	4	68 / 25	2	PD, T	Piribedil 20 mg Levodopa 250 mg Benserasid 62.5 mg
3	72	F	154, 66	8	98 / 48	2	VP, T	No medication (never administered)
4	68	M	169, 83	9	49 / 33	2.5	VP, T	Levodopa 975 mg Carbidopa 87.5 mg Amantadine 300 mg Piribedil 150 mg Benserasid 25 mg
5	71	M	170, 51	8	43 / 28	2	PD, T	Trihexyphenidyl 6 mg
6	68	F	164, 90	3	59 / 42	2.5	VP, T	Levodopa 225 mg Benserasid 25 mg Carbidopa 12.5 mg Piribedil 75 mg
7	73	M	172, 61	8	85 / 47	3	PD, T	Piribedil 100 mg Rasagiline 1.56 mg Levodopa 250 mg Carbidopa 25 mg
8	62	F	169, 81	4	41 / 26	2	PD, T	No medication (for 1 year*)
9	57	M	178, 63	6	65 / 48	2.5	PD, T	Piribedil 50 mg Amantadine 200 mg Levodopa 250 mg Carbidopa 25 mg
10	66	F	160, 67	2	21 / 13	2	VP, T	Levodopa 250 mg Carbidopa 25 mg Trihexyphenidyl 6 mg
11	66	F	156, 53	7	82 / 45	2	PD, T	Levodopa 250 mg Carbidopa 25 mg
12	53	M	171, 81	5	49 / 38	1.5	PD, AR	Piribedil 150 mg Amantadine 200 mg
13	70	M	176, 74	2	79 / 49	3	PD, T	Trihexyphenidyl 4 mg
14	68	M	167, 78	3	60 / 32	2	PD, AR	Levodopa 250 mg Carbidopa 25 mg Pramipexol 50 mg
15	66	F	172, 66	4	57 / 25	3	PD, AR	Levodopa 375 mg Carbidopa 37.5 mg Piribedil 50 mg
16	47	M	182, 81	3	45 / 16	3	PD, AR	No medication (for 1 month*)
17	58	M	170, 60	N/A	75 / 37	3	PD, T	Levodopa 300 mg Benserasid 75 mg Amantadine 200 mg

(Continued)

TABLE 2 | Continued

No.	Age (yr)	Gender	Height (cm), weight (kg)	Disease duration (yr)	UPDRS/ UPDRS-III	Stage by H & Y	Disease & symptoms	Antiparkinsonian medication
18	69	M	179, 69	4	60 / 32	3	PD, T	Piribedil 100 mg Levodopa 250 mg Carbidopa 25 mg
19	65	F	152, 78	7	51 / 15	1	VP, AR	Levodopa 500 mg Benserasid 100 mg Pramipexole 3 mg Amantadine 200 mg

*PD, Parkinson's disease; VP, vascular parkinsonism; UPDRS, Unified Parkinson's disease Rating Scale; UPDRS-III, UPDRS motor part III; H & Y, Hoehn and Yahr Rating Scale; T, tremor; AR, akinesia and rigidity; *these patients abandoned their therapy themselves.*



FIGURE 1 | The condition of dry immersion. © PetrSU/L. Gerasimova-Meigal.

Ltd., Ivanovo, Russia) were made of tin, disk-shaped (8 mm in diameter), with 20 mm spacing between the electrode centers. Input impedance was not less than 200 MΩ, and the measured impedance after electrode placement was not more 10 MΩ. The gain of differential amplifiers was set to 328, the ADC span was ±5 V, the ADC resolution was 16 bits, the peak-to-peak input-referred noise was not more than 5 μV, and the common mode rejection ratio (CMRR) was not less than 100 dB. Each sEMG recording was 3.5 s (70,000 samples) long. The sampling frequency was set to 20 kHz. The 50 Hz notch filter was enabled. The frequency bandwidth was 20–1,000 Hz, and the filters had 3 dB attenuation at the cutoff frequencies. The filters frequency responses corresponded to 1st order high-pass and 2nd order low-pass Butterworth filters.

2.4. Preprocessing of Surface Electromyogram

Data processing and analysis were made using Matlab software (MathWorks Inc., Natick, USA). Preprocessing of the data consisted of removal of power line interference, low-pass filtering, and detrending. Despite of the 50 Hz notch filter in the EMG device, we discovered sharp peaks at multiples of 50 Hz in the spectra of some sEMG recordings, so we applied Fourier interpolation (Mewett et al., 2004) to all the recordings in their frequency domain. The amplitudes in ±1 Hz range around the multiples of 50 Hz were replaced by interpolated values from the line drawn through two points adjacent to the range, while the phases were kept the same. The low-pass filtering was performed using a 14th order elliptic filter designed with Matlab `design` function (passband frequency 420 Hz, stopband frequency 500 Hz, passband ripple $2 \cdot 10^{-6}$ dB, stopband attenuation 80 dB, passband exact match). The filter was applied in both forward and reverse directions to avoid phase distortion. Then the recordings were detrended using the smoothness priors method (Tarvainen et al., 2002) to remove possible movement artifacts. The smoothness priors method is based on regularized least squares and operates as a time-varying FIR high-pass filter with the cutoff frequency gradually changing to zero near the beginning and the end of a signal. Higher values of the only parameter λ correspond to lower cutoff frequencies. We used $\lambda = 10^5$, which corresponds to attenuation of -40 dB at 10 Hz in the middle of a signal sampled at 20 kHz.

2.5. Parameters of Surface Electromyogram

2.5.1. Amplitude and Spectral Parameters

We calculated amplitude (root mean square) of the recordings and median frequency of power spectrum of the recordings. The power spectrum was calculated as Welch periodogram with segment length of 1 s and 50% segment overlap. The segments spectrum was obtained using fast Fourier transform (Matlab `fft` function). Hann window was applied to the segments prior to the spectrum calculation to eliminate spectrum distortion because of nonzero values at the segments edges.

2.5.2. Time Delay Embedding Transformation of Surface Electromyogram

In the nonlinear dynamics based analysis, it is assumed that the examined system is governed by a set of free variables, which follow a trajectory in their space. When the original free variables are unobtainable, the trajectory is replaced by a surrogate obtained from one-dimensional time series. This

procedure is called phase space reconstruction and is justified by the embedding theorem (Mañé, 1981; Takens, 1981). As our sEMG recordings were one-dimensional, we applied the time delay embedding transformation to reconstruct the phase space trajectory. The one-dimensional sEMG time series $\{x_1, x_2, ..., x_n\}$ was transformed to sequences of vectors in m-dimensional space as in Equation (1).

$$X_i = (x_i, x_{i+L}, x_{i+2L}, ..., x_{i+(m-1)L})^T \quad (1)$$

The L parameter is called time lag. With properly chosen m and L parameters, the reconstruction produces a smooth m-dimensional trajectory that preserves some features of the presumed original trajectory in a space of free variables of the examined system.

L was chosen with the help of mutual information (MI) as advised by Celucci et al. (2003). The MI of a signal and the same signal shifted backwards in time on τ sampling periods was calculated with τ varying from 1 to 500 sampling periods, which produced a dependence MI(τ) for each sEMG recording. To calculate the MI of real-valued signals, we used the algorithm of Fraser and Swinney (1986). We slightly tuned the algorithm: recordings duration was not truncated to the nearest power of two, and the recursive splitting of the histogram bins was stopped when the number of points in a bin was less or equal to a preset value 547, which maximized smoothness of the MI(τ) dependencies. First minimum of MI(τ) (MI decay time) was converted to milliseconds and used as a separate signal parameter, and L was chosen as median MI decay time ($L = 54$ sampling periods). We used median instead of mean because the Kolmogorov-Smirnov test showed that the distribution of MI decay time was not normal.

We used false nearest neighbors (FNN) method to choose m (Kennel et al., 1992; Celucci et al., 2003). The dependence FNN(m) was calculated with m varying from 1 to 15, then the embedding dimension was chosen as the point where for all the recordings FNN dropped to 1% of the initial value or lower ($m = 6$).

2.5.3. Correlation Dimension and Sample Entropy

Correlation dimension was chosen as the slope of linear segment of the sEMG correlation integral in double logarithmic scale (Grassberger and Procaccia, 1983). The correlation integral was calculated with Theiler window $W_{CD} = 270$ ($W_{CD} = (m-1)L$, Gao and Zheng (1994)). We calculated sample entropy (Richman and Moorman, 2000) using Euclidean interpoint distances and the tolerance distance $r_{SampEn} = 1.15$. The measurements were normalized to unit standard deviation prior to the sample entropy calculation. The tolerance distance r_{SampEn} was fitted to maximize the difference between the maximum and minimum values of sample entropy. This fitting, on the one hand, does not imply any assumptions about the effect of dry immersion on sample entropy. On the other hand, it increases the differences of sample entropy between the recordings and, therefore, the potential of sample entropy to distinguish muscles' states.

2.5.4. Recurrence Quantification Analysis

Recurrence quantification analysis (RQA) parameters were calculated from recurrence plots (Marwan et al., 2007) of the recordings. Recurrence plot (Rec) is a tool for visualization of m-dimensional phase space trajectories on a plane. Rec is a square matrix of ones (black points) and zeros (white points) with a column i and a row j corresponding to the trajectory points X_i and X_j. Rec(i, j) is equal to one if the corresponding trajectory points X_i and X_j are not further apart from each other than the threshold distance ε and is equal to zero otherwise. Since consecutive ($i - j < W$) trajectory points tend to be close to each other, their proximity is not informative and is typically not shown on Rec, which produces a white strip along the main diagonal of Rec. Thus, Rec shows the periods of time when the trajectory passes close by its previous locations, which may be movement parallel to an earlier trajectory segment (diagonal lines) or enveloping movement perpendicularly to the segment (vertical lines). RQA quantifies the diagonal and vertical lines (we only quantified the diagonal lines). The recordings were normalized on mean Euclidean interpoint distance $\|X_i - X_j\|$, $i - j > 0$ prior to the RQA. Then we calculated recurrence rate (share of black points of Rec) and determinism (share of black points those form diagonal lines with the length not less than l_{min}). The auxiliary parameters ε, W, and minimum diagonal line length l_{min} were fitted to maximize the span of determinism similarly to sample entropy ($\varepsilon = 0.7$, $W = 270$, $l_{min} = 86$). However, in contrary to sample entropy, determinism may take saturated values 0 and 100%, which renders some sEMG recordings indistinguishable by their determinism because they share the same saturated value of it. Therefore, we fitted the auxiliary parameters so that to avoid the saturated values. We also limited the minimum index difference W so that $W \geq W_{CD}$.

2.6. Statistical Analysis

The statistical analysis was performed separately for each body side, each loading condition, and each parameter (2 sides × 4 conditions × 7 parameters = 56 statistical tests). The pre-immersion recordings from patients 3 and 4 those did not have the post-immersion counterpart were discarded from the statistical analysis. We used the Wilcoxon test to compare the parameters values before and after the dry immersion. This test quantifies within-subject differences for repeated measures. The reason to use a nonparametric test was that the distributions of the differences were not normal in most of the cases; the normality was tested using the Kolmogorov-Smirnov test. The p-values from the Wilcoxon test were compared to the significance level 0.05. We did not apply any correction for multiple comparisons because we had only one research question of whether dry immersion relieves motor symptoms, which are seen by sEMG in parkinsonian patients, so all the comparisons were complementary.

3. RESULTS

The general finding was that the post-immersion values of the surface electromyogram (sEMG) parameters tended to be different comparing to the pre-immersion values, excluding the

correlation dimension. See the **Tables 3**, **4** for median values and interquartile ranges of the parameters before and after the dry immersion, and for the percentages of patients for whom the parameters increased or decreased after the dry immersion. In the **Tables 3**, **4**, the 2 pre-immersion recordings with missing post-immersion counterpart are not considered.

See **Figure 2** for changes of the determinism for each patient. One can trace the tendency of determinism to decrease, which is more visible for the left biceps. For half of the patients (No. 2, 4, 8, 10, 11, 12, 14, 16, and 18), the determinism of recordings from the left biceps decreased no matter of the loading. What comes to the right biceps, the determinism values were often close to those for the left biceps, and the determinism changes were approximately parallel to those for the left biceps, although some exceptions occured, especially for the "arms down" loading. One may also consider that the changes near the bottom limit of determinism (patients No. 5, 11, 17, 19: "arms down" loading) are not very informative since determinism inherently cannot decrease below zero. See **Figure 3** for general picture of changes of the amplitude, the median frequency, and the determinism. As for the determinism, the tendency of the amplitude to decrease and the tendency of the median frequency to increase were apparent for the left biceps only, so the pictures for the right biceps are not shown. See **Figure 4** for an example of sEMG before and after the immersion. One can visually observe the drop of signal regularity and hence determinism.

The statistical analysis revealed that the following changes of the sEMG parameters were statistically significant. The amplitude decreased for both arms with the "arms down" loading and for the left arm with the 1 and 2 kg loadings. The median frequency increased for the left arm with the 1 and 2 kg loadings. Mutual information decay time decreased for the left arm with the 0 and 2 kg loadings. Sample entropy increased for both arms with the "arms down" loading and for the left arm with the 1 kg loading. Recurrence rate decreased for both arms with the "arms down" loading and for the left arm with the 1 kg loading. Determinism decreased for both arms with the "arms down" loading and for the left arm with the 1 and 2 kg loadings. The most statistically significant ($p = 0.00084$) change was for the determinism from the left biceps with 1 kg loading, which decreased for 16 out of 19 patients.

As regards the multiplicity of the statistical tests applied, the number of their results with $p < 0.05$ was enough to make an overall conclusion that sEMG parameters changed after the dry immersion. Indeed, if all the null hypotheses had been true then we would have had $p < 0.05$ for 5% of the hypotheses, but we had $p < 0.05$ for 32% of the hypotheses.

4. DISCUSSION

The key hypothesis of this study postulated that a single one dry immersion (DI) exerts effect on the motor system in parkinsonian patients. Surface electromyogram (sEMG) signal during isometric contraction was assumed to be indicative of such effect. The major outcome of the present study was that the parameters of sEMG signal in parkinsonian patients indeed modified in the direction of improvement under a single DI session. Generally, we found that the amplitude and mutual information decay time of sEMG had decreased, while spectral frequencies had increased right after DI session. Among nonlinear dynamics based sEMG parameters, sample entropy had increased, while percent of determinism and recurrence rate had decreased after DI session. Correlation dimension proved insensitive to DI.

On one hand, the amplitude of sEMG is known to correlate with the number of active motor units and their firing rate (Farina et al., 2004). On the other hand, the rigidity in parkinsonian patients is often seen as "unwilled" muscle tension generated by uncontrolled firing of low-threshold (slow) motor units at rest (Cantello et al., 1995; Rossi et al., 1996). Therefore, we assume that lowered amplitude of sEMG in parkinsonian patients after DI session found in the present study may be attributed to decreased recruitment of these unconsciously active motor units, either at rest condition or under loading. Two neurophysiological mechanisms may have contributed to the decrease of sEMG amplitude after DI session.

First, sEMG amplitude may have decreased due to attenuation of the reflexive component of muscle tone. Such immersion-induced attenuation of the stretch reflex has been characteristic for another type of exaggerated muscle tone (spasticity) (Cronin et al., 2016). Similarly, in healthy subjects under a program of DI the reflex component of muscle tone has been diminished due to deprivation of excitatory tonic stimuli from the pacinian corpuscles of sole (Kozlovskaya et al., 1988; Navasiolava et al., 2011). In our recent study we have found that the rigidity subscore has indeed decreased under the program of short-term DI sessions (Meigal et al., 2018). However, the non-reflexive (mechano-elastic) component of muscle tone may also have contributed to the decrease of rigidity score. Further studying of the stretch reflex and viscoelasticity of muscles in PD patients under DI is needed to evaluate their contribution to hypotonic effect of DI.

Second, as muscle tone appears as muscle state of readiness to contraction (Davis et al., 2011) triggered by brainstem, basal ganglia, cerebellum, and cortical circuits in stressful conditions, we assume that central neural mechanisms might also have been involved in sEMG amplitude decreasing in PD patients during DI session. That is in good line with our earlier finding that after a program of DI the score of depression has significantly decreased (Meigal et al., 2018). As such, the DI condition has probably exerted its action on muscle hypertonicity (rigidity) via lowering the level of anxiety and thus relieving disinhibition of the stretch reflex. In an earlier study, Koryak (2002) have shown that electrically evoked maximal tetanic contraction force decreased by 8.2 after 7 days of DI, which suggests that most of the force loss was due to a reduction in motor drive. This supports the supraspinal application of DI action on sEMG parameters in PD patients. Similar decrease of central activation reflected in lower sEMG amplitude has been recently reported for the condition of hyperthermia (Coletta et al., 2018).

However, the amplitude of sEMG has decreased under DI at all loading conditions. That raises the question of whether sEMG amplitude in PD patients has decreased during DI due

TABLE 3 | Amplitude (RMS), median frequency, and mutual information (MI) decay time of surface electromyogram before and after the dry immersion (DI).

Muscle	Load	Electromyogram parameter	Median (IQR) before the DI	Median (IQR) after the DI	Drop (%)	Rise (%)	No change (%)	*p*-value
Right	Arms	Amplitude (μV)	1.7 (1.3, 2.1)	1.2 (0.66, 2.3)	79	21	0	0.024*
arm	down	Median frequency (Hz)	73 (36, 107)	90 (74, 111)	42	58	0	0.15
biceps		MI decay time (ms)	4.2 (3.7, 7.2)	3.9 (2.4, 6)	58	37	5	0.21
	0 kg	Amplitude (μV)	15 (8, 25)	12 (8, 19)	67	33	0	0.18
		Median frequency (Hz)	96 (85, 101)	96 (89, 108)	44	56	0	0.25
		MI decay time (ms)	3 (2.6, 3.5)	2.7 (2.5, 3.1)	61	39	0	0.053
	1 kg	Amplitude (μV)	29 (15, 36)	21 (14, 40)	47	53	0	0.57
		Median frequency (Hz)	97 (87, 102)	101 (90, 105)	42	58	0	0.15
		MI decay time (ms)	2.7 (2.6, 3)	2.7 (2.5, 3)	52	37	11	0.32
	2 kg	Amplitude (μV)	34 (19, 56)	36 (21, 49)	50	50	0	0.88
		Median frequency (Hz)	95 (84, 100)	100 (85, 105)	28	72	0	0.053
		MI decay time (ms)	2.7 (2.5, 3.1)	2.6 (2.5, 3.1)	56	33	11	0.13
Left	Arms	Amplitude (μV)	1.6 (0.99, 2.9)	0.91 (0.53, 1.7)	79	21	0	0.016*
arm	down	Median frequency (Hz)	74 (27, 123)	114 (34, 175)	32	68	0	0.084
biceps		MI decay time (ms)	4 (2, 11)	2 (1.4, 6.7)	63	26	11	0.062
	0 kg	Amplitude (μV)	14 (8, 21)	11 (4, 19)	78	22	0	0.071
		Median frequency (Hz)	104 (90, 112)	109 (96, 139)	39	61	0	0.064
		MI decay time (ms)	2.5 (2.4, 3)	2.3 (1.8, 3.1)	83	17	0	0.011*
	1 kg	Amplitude (μV)	24 (12, 33)	20 (7, 30)	68	32	0	0.024*
		Median frequency (Hz)	98 (88, 110)	108 (92, 130)	26	74	0	0.036*
		MI decay time (ms)	2.6 (2.3, 3)	2.4 (2, 2.9)	68	21	11	0.055
	2 kg	Amplitude (μV)	30 (16, 48)	24 (9, 36)	78	22	0	0.0029*
		Median frequency (Hz)	99 (82, 110)	111 (86, 125)	22	78	0	0.0057*
		MI decay time (ms)	2.7 (2.3, 3.3)	2.3 (2, 3)	72	28	0	0.02*

The picture of individual changes of a parameter is described with the percentages of patients for whom the parameter decreased (Drop), increased (Rise), or did not change. The p-values are the results of assessment of a parameter changes using the Wilcoxon test.
$p < 0.05$; IQR, interquartile range.

to inhibition of uncontrolled firing of "unwilled" motor units, or due to inhibition of voluntarily recruited motor units. The decrease of sEMG amplitude at loading was bigger in comparison with the decrease at the non-loading condition when arms were hanging down. Therefore, we assume that at loading conditions, besides these abnormally active "unwilled" motor units, some normally recruited motor units were also inhibited by DI. Passive heating has been already shown to inhibit spontaneous rest activity of motor units in PD patients (Meigal and Lupandin, 2005).

As for the nonlinear dynamics based sEMG parameters, several earlier studies have shown that in PD patients their values significantly differ from those in healthy controls. In particular, percent of recurrence rate and determinism of sEMG was higher in the PD group, while entropy and correlation dimension were lower in comparison to old and young healthy controls (Fattorini et al., 2005; Meigal et al., 2009). High percent of determinism reflects appearance of "recurrent fragments" on sEMG similar to one another, which is argued to originate from increased synchronization of motor units firing (Fattorini et al., 2005). In turn, such increased regularity of sEMG in PD indicates presence of mechanical tremor (Meigal et al., 2012). That is in line with growth of the spectral frequency of sEMG under certain loading conditions revealed in the present study, which may be associated with decreased synchronization of motor units (Fattorini et al., 2005). Therefore, shift of determinism and recurrence rate of sEMG after a single one DI session in the direction of lower values may be indicative of diminished synchronization of motor units firing and, hence, temporary inhibition of parkinsonian tremor. In our recent study we observed decrease of tremor score in some PD patients (Meigal et al., 2018). Still, direct accelerometric measurements are needed to validate that effect in a single DI session.

However, motor unit synchronization during muscle contraction is not a uniform phenomenon. Several forms of motor unit synchronization have been demonstrated (McAuley and Marsden, 2000). The first one is short-term synchronization (STS) that occurs within short time period (around 5 ms) as reflected with a narrow peak in the cross-correlogram (Kirkwood et al., 1982). The STS may either arise from the common axonal inputs to pairs of motoneurones (Sears and Stagg, 1976; Nordstrom et al., 1992) or be just an epiphenomenon of firing rate characteristics (Kline and de Luca, 2016). The other form of synchronization is long-term (or broad-peak) one (LTS) that

TABLE 4 | Nonlinear dynamics based parameters of surface electromyogram before and after the dry immersion (DI).

Muscle	Load	Electromyogram parameter	Median (IQR) before the DI	Median (IQR) after the DI	Drop (%)	Rise (%)	*p*-value
Right	Arms	Sample entropy	0.89 (0.73, 0.97)	0.96 (0.84, 1)	16	84	0.0089*
arm	down	Correlation dimension	6 (5.6, 6.2)	6 (5.5, 6.1)	53	47	0.81
biceps		Recurrence rate (%)	11 (10, 16)	10 (9, 14)	89	11	0.0089*
		Determinism (%)	36 (21, 67)	20 (11, 54)	84	16	0.0079*
	0 kg	Sample entropy	0.9 (0.84, 0.92)	0.92 (0.85, 0.95)	33	67	0.18
		Correlation dimension	5.7 (5.2, 6.3)	5.6 (5.2, 5.8)	67	33	0.23
		Recurrence rate (%)	11 (10, 13)	10 (10, 13)	56	44	0.42
		Determinism (%)	49 (44, 60)	46 (37, 62)	56	44	0.1
	1 kg	Sample entropy	0.92 (0.87, 0.95)	0.92 (0.82, 0.94)	53	47	0.97
		Correlation dimension	6 (5.5, 6.4)	6.1 (5.6, 6.6)	42	58	0.57
		Recurrence rate (%)	10 (10, 13)	11 (10, 13)	47	53	0.69
		Determinism (%)	53 (41, 60)	51 (41, 61)	58	42	0.49
	2 kg	Sample entropy	0.93 (0.88, 0.95)	0.94 (0.89, 0.95)	50	50	0.88
		Correlation dimension	6.2 (5.7, 6.5)	5.7 (5, 6.2)	72	28	0.2
		Recurrence rate (%)	10 (9, 12)	10 (9, 12)	44	56	0.4
		Determinism (%)	44 (42, 53)	41 (38, 58)	67	33	0.33
Left	Arms	Sample entropy	0.89 (0.69, 0.97)	0.95 (0.88, 1)	26	74	0.0048*
arm	down	Correlation dimension	5.9 (5.6, 6.2)	6 (5.9, 6.3)	37	63	0.44
biceps		Recurrence rate (%)	12 (10, 17)	10 (9, 13)	68	32	0.018*
		Determinism (%)	42 (19, 76)	27 (8, 43)	84	16	0.0062*
	0 kg	Sample entropy	0.92 (0.71, 0.96)	0.94 (0.81, 0.98)	28	72	0.085
		Correlation dimension	5.8 (5.5, 6.2)	5.9 (5.6, 6.2)	39	61	0.53
		Recurrence rate (%)	11 (10, 15)	11 (10, 15)	50	50	0.78
		Determinism (%)	46 (35, 58)	39 (26, 65)	78	22	0.11
	1 kg	Sample entropy	0.93 (0.85, 0.96)	0.96 (0.92, 0.99)	21	79	0.0033*
		Correlation dimension	6 (5.7, 6.2)	5.8 (5.6, 6.4)	53	47	0.69
		Recurrence rate (%)	11 (9, 12)	10 (9, 12)	68	32	0.049*
		Determinism (%)	40 (36, 53)	36 (23, 40)	84	16	0.00084*
	2 kg	Sample entropy	0.94 (0.91, 0.96)	0.96 (0.93, 0.98)	39	61	0.11
		Correlation dimension	5.9 (5.5, 6.5)	5.9 (5.6, 6.4)	44	56	0.78
		Recurrence rate (%)	10 (9, 12)	10 (9, 11)	44	56	0.81
		Determinism (%)	42 (34, 48)	35 (27, 43)	78	22	0.0065*

The picture of individual changes of a parameter is described with the percentages of patients for whom the parameter decreased (Drop) or increased (Rise). The p-values are the results of assessment of a parameter changes using the Wilcoxon test.
$p < 0.05$; IQR, interquartile range.

occurs within broader time band (> 20 ms) (Kirkwood et al., 1982; Freund, 1983). LTS comes into play when a large group of motoneurons starts to respond synchronically to a periodic synaptic input either of supraspinal or segmentary afferent origins (Kirkwood et al., 1982). Also, a tuned (or external) synchronization may arise when common inputs to a pair of motoneurones are themselves driven by a common input (McAuley and Marsden, 2000).

In PD, large part of motor units present specific firing pattern in a form of rhythmical groups of discharges (doublets and, occasionally, triplets). These groups are separated with longer interspike intervals and are associated with 4–6 Hz clustering on sEMG (Baker et al., 1992; Lupandin et al., 1993; Glendinning and Enoka, 1994). This pattern of firing is believed to largely contribute to generation of tremor in PD (Christakos et al., 2009). Doublets may also be associated with LTS that is seen as broad periodic correlations on cross-correlogram (Baker et al., 1992). As follows from these studies, both motor units synchrony and paired/tripled discharges may be responsible for greater values of determinism of sEMG in PD patients. STS has been shown to be greater in PD patients than in normal subjects but no evidence has been found that the higher incidence of STS in PD is a result of lower discharge rates of motor units or 4–6 Hz tremor that is the characteristic of PD patients (Baker et al., 1992).

Sample entropy has increased in some instances after the DI session. According to recent findings, sample entropy is higher when the motor units fire with higher variability of interspike intervals (Hwang et al., 2017).

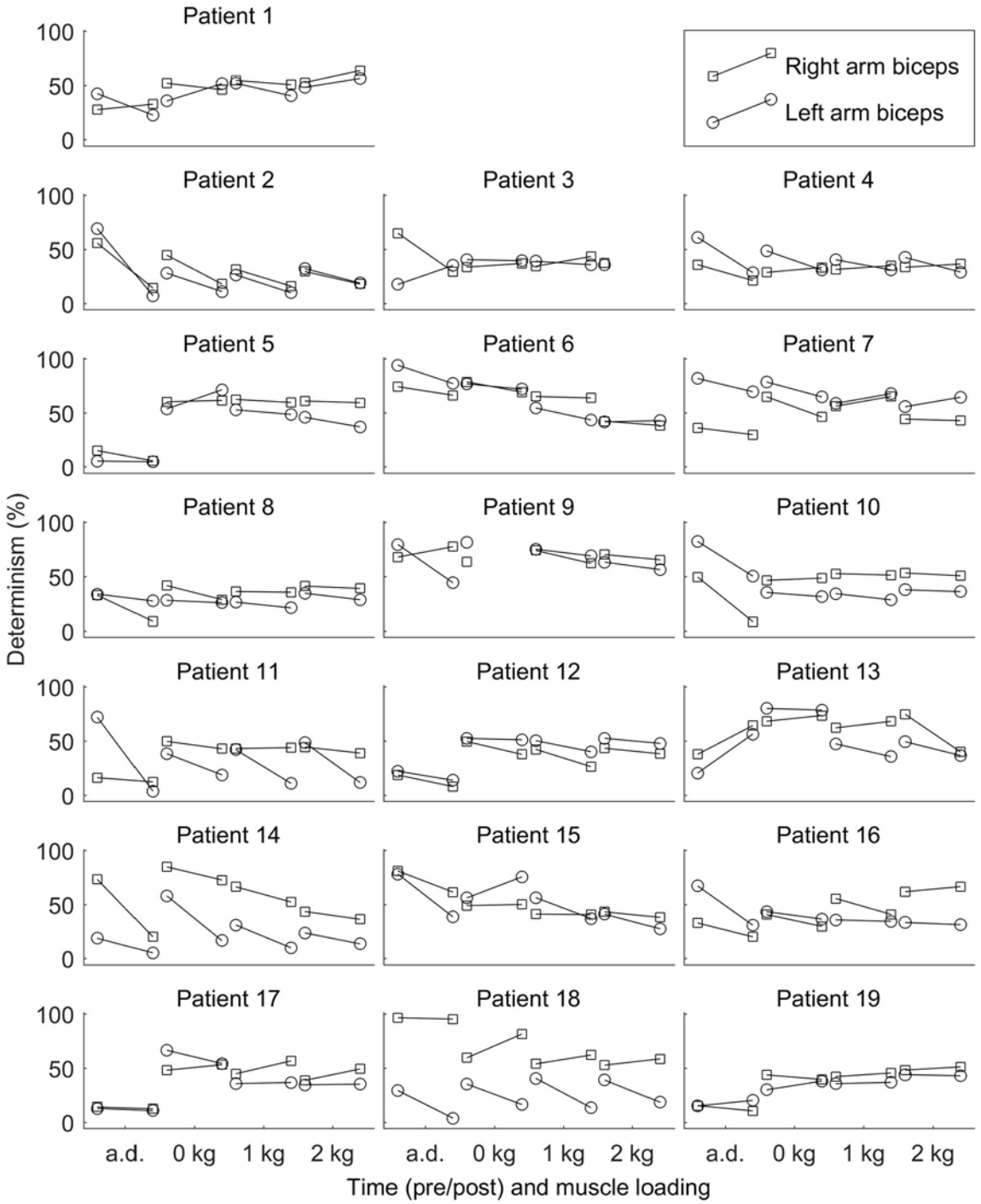


FIGURE 2 | Determinism of surface electromyogram for each patient before and after the dry immersion. The determinism tends to decrease after the dry immersion. Loading conditions are the following: arms down with no load (*a.d.*); 0, 1, and 2 kg loading on each hand with elbow being flexed to 90°.

The mutual information (MI) decay time, or first minimum of auto-mutual information function, quantifies how quickly information about a signal is lost as a function of time delay. MI decay time measures information transmission between a signal and its time shifted counterpart (Jeong et al., 2001) and, consequently, predictability of the signal (Ramanand et al., 2010). Also, MI decay time is regarded as a relevant estimator of irregularity of signal (Escudero et al., 2009). Though MI time decay has been already applied to measure information transmission within electroencephalographic signal (Jeong et al.,

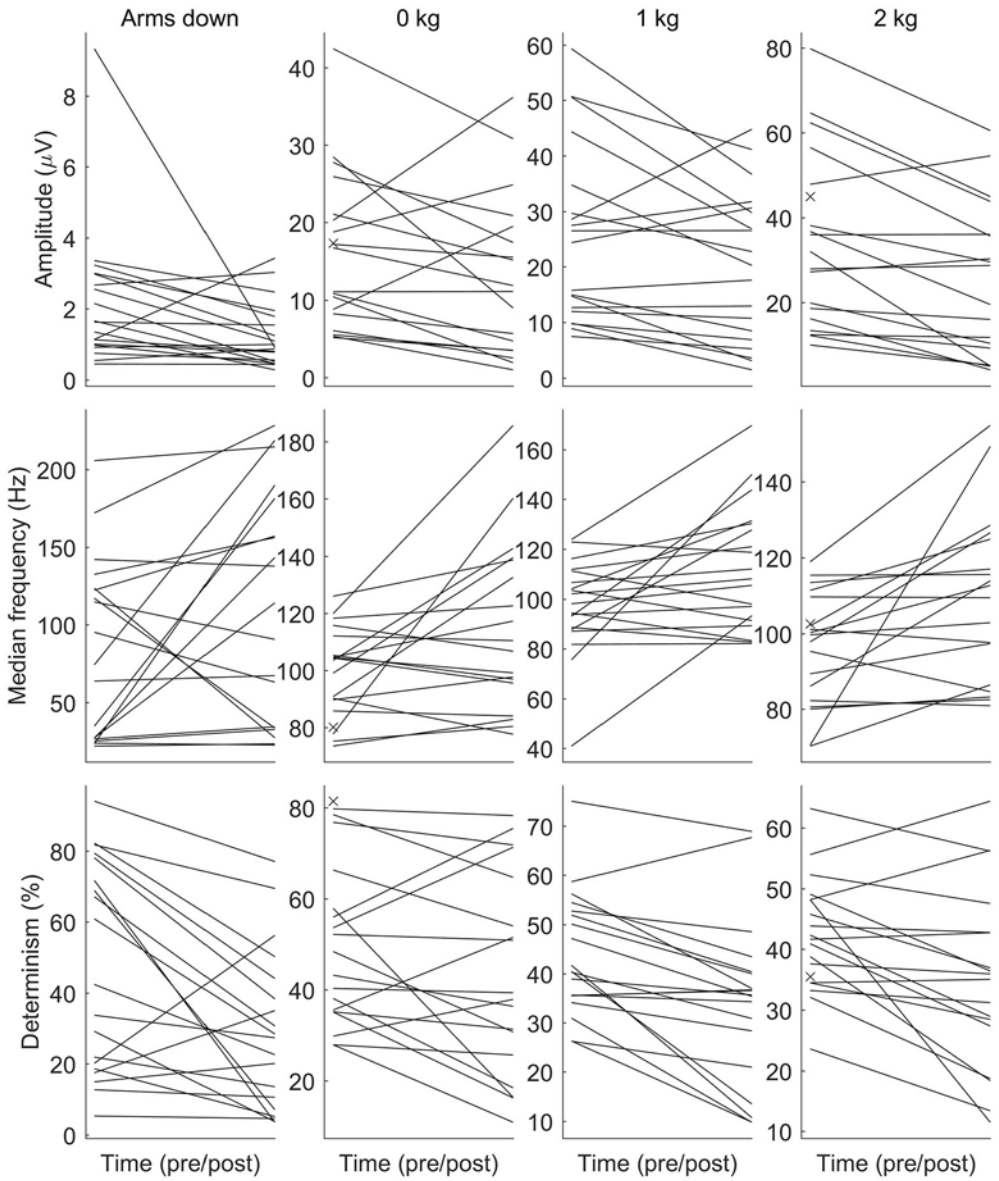


FIGURE 3 | The amplitude (RMS), the median frequency, and the determinism of surface electromyogram before and after the dry immersion. The amplitude and the determinism tend to decrease, while the median frequency tends to increase after the dry immersion. Each patient is denoted by a line. Each subplot corresponds to a combination of a parameter (the row) and a loading (the column). Loading conditions are the following: arms down without any load (*Arms down*); *0/1/2 kg* loading on each hand with elbow being flexed to 90°. The muscle is the biceps of the left arm. The pre-immersion values are marked with crosses when the post-immersion counterpart is missing.

2001; Ramanand et al., 2010) and heart rate (Hoyer et al., 2005), to the best of our knowledge it has not yet been used to characterize sEMG. Correspondingly, neurophysiology behind MI decay time for sEMG has not yet been well understood. In our study, the MI decay time lasted from 1 to 13 ms, and it had tendency to decrease after DI session. Visual inspection of sEMG records showed that those with lower MI decay time values had shorter turns of sEMG curve, while those with higher values of MI decay time had longer turns (see **Figure 4**). Therefore, we assume that MI decay time may correlate with average duration of signal turns or longer patterns those are typical for a particular sEMG recording. Also, duration of MI decay time overlaps with that of STS. That prompts hypothetic association between these two parameters, because STS has been shown to be characteristic of PD patients (Baker et al., 1992). As such, we speculate that DI might decrease STS during DI session.

From several studies it is known that percent of determinism of sEMG responds to certain anti-PD therapies. For example, under dopaminergic anti-PD treatment percent of determinism

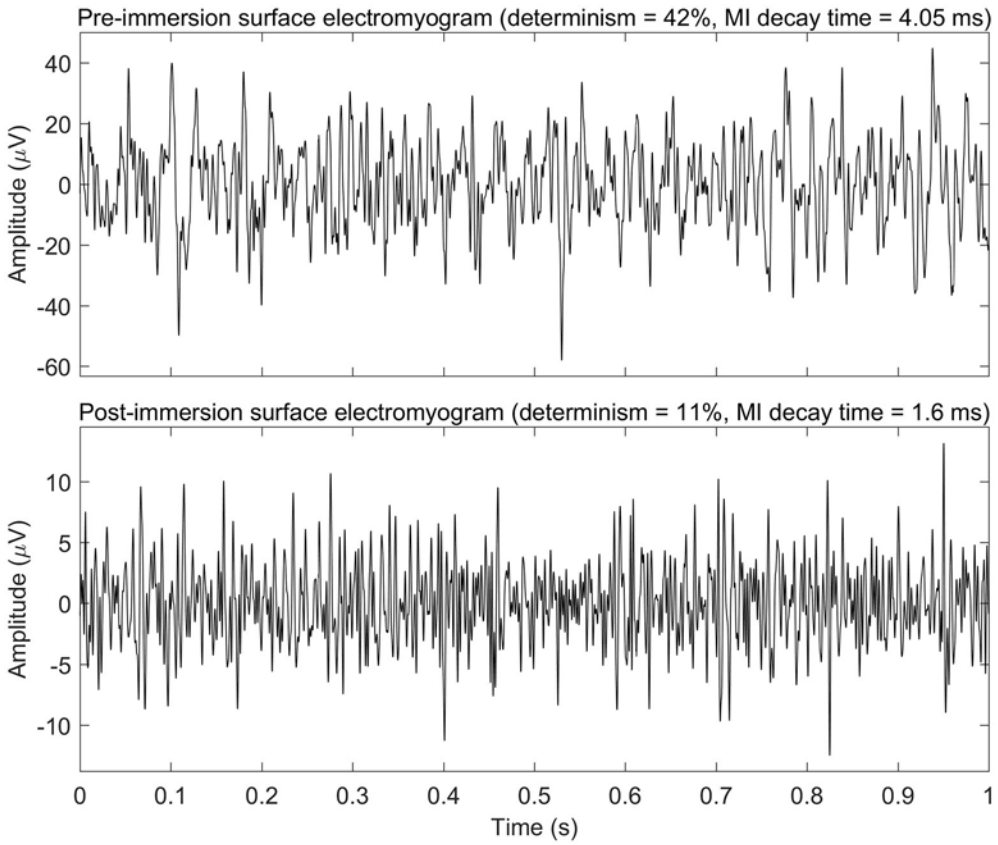


FIGURE 4 | Example of surface electromyogram before and after the dry immersion procedure (patient No. 11 in **Table 2**; 1 kg loading; left arm). Only first second of the electromyograms is shown. This example demonstrates drop of amplitude, mutual information (MI) decay time, and determinism of electromyogram signal after the dry immersion. MI decay time may be linked to typical duration of turns of electromyogram, and determinism may be linked to regularity of electromyogram.

of sEMG is decreased in comparison with the off-medication state (Rissanen et al., 2008; Ruonala et al., 2018). Similarly, after deep brain stimulation, sEMG signal characteristics turned more similar to the signal characteristics of the healthy controls (Rissanen et al., 2011). That is in good line with the result of the present study. We found only a few corresponding papers on the amount of motor unit synchrony after taking anti-PD medicine. In one, short-term synchrony was found to be irresponsible to taking levodopa (Baker et al., 1992). Therefore, we assume that analog microgravity induced by DI modulates the nonlinear dynamics based parameters of sEMG of parkinsonian patients by decreasing the long-term form of motor unit synchronization. We cannot exclude possible influence of DI also on the amount of motor unit doublets.

The most reliable neural site for effects of DI on motor unit synchrony and, hence, determinism of sEMG, presumably is located supraspinally, because (i) the above mentioned anti-PD therapies act directly on brain structures, and (ii) there is large corpus of data supporting the idea of supraspinal location of oscillatory circuits those generate the characteristic PD tremor (Timmermann et al., 2003). However, DI might also exerted certain peripheral action due to its well-documented unloading effect on muscles. We did not find corresponding data on nonlinear dynamics based parameters of sEMG during muscle contraction under the condition of real spaceflight. As for the physiological tremor, it is modified in the direction of lower frequency (as low as 4 Hz) and decreased amplitude by the 3rd day of space flight, presumably due to switch of main source of sensory information from load-dependent muscle reception to position-dependent joint reception (Gallasch et al., 1994). Thus, one may expect growth of regularity and decrease of amplitude of sEMG under the condition of real spaceflight. However, growth of determinism of sEMG was not the case in the present study. Several significant distinctions from real spaceflight condition could be figured out that probably contributed to such discrepancy. First, in our study, duration of analog microgravity was too short to induce the above said effect of microgravity on tremor. Second, arms under DI were not deprived of force-induced muscle afferent inputs. Additionally, in the present study, unlike to space based experiments, sEMG was collected under normal gravity, both before and after the session of DI. Thus, the condition of DI despite of its strong similarity with real microgravity cannot provide its absolute emulation.

The present study demonstrated large variance of sEMG parameters that might be associated with heterogeneity of clinical forms and severity of parkinsonism. Earlier, we demonstrated that percent of determinism of sEMG positively correlates with the UPDRS (part III) (Meigal et al., 2009) and tremor acceleration characteristic (Meigal et al., 2012). It means that with growing severity of PD tremor becomes more regular, while sEMG becomes more apparently clustered. We did not correlate percent of determinism of sEMG with the form of PD earlier, nor in this study due to insufficient number of parkinsonian patients with akinetic-rigid form. Further studies should have aimed on that.

4.1. Loading Conditions

In the present study the most readily seen modifications of sEMG parameters were the characteristic of the condition when arms were freely hanging down without any load. Earlier we found that the most significant differences between PD and control groups were observed when no additional loading was placed on hands during the isometric elbow flexion task (Meigal et al., 2009). We concluded that additional loading applied on hands most likely revealed "regular" postural muscle tonus. In a way, under loading, sEMG of parkinsonian patients may have become more "normal" in comparison to the unloading condition. However, the results for the condition with arms freely hanging down should be treated with caution, because the sEMG amplitude was comparable to typical level of the noise generated on a fully relaxed biceps (Piervirgili et al., 2014).

4.2. Limitations

The major methodological limitation in the present study was small number of subjects who met all inclusion criteria ($n = 19$). Such relatively small number of parkinsonian patients and big number of factors (disease duration, clinical form, stage of disease, age, sex, medication) presumably affecting the outcome restricted opportunities of statistical analysis. Earlier experiments with younger subjects showed that the most effect of microgravity on muscle tone is observed by 2 h of staying of healthy subjects under the DI environment (Navasiolava et al., 2011). In this study, average age of patients was around 65 years. That restricts their tolerance to the DI procedure, mostly for the reason of urge to urinate and, in some instances, due to unstable blood pressure. Also, staying in DI reportedly provokes some compensated neurological signs (Navasiolava et al., 2011). In older subjects, especially neurologically ill, such hidden symptoms may have taken place. However, a 45 min long DI session was still enough to exert effect on sEMG parameters in parkinsonian patients.

In that study we omitted measuring UPDRS scores right after the DI session due to highly probable inference of cardiovascular factors, such as DI-induced decrease of blood pressure and orthostatic reactions, on motor signs (gait, postural reactions, muscle tone) in PD patients. From our earlier study we know that muscle rigidity subtotal of UPDRS-III score and, to lesser degree, tremor subtotal, decrease across the program of DI (Meigal et al., 2018). In further studies, it would be wise to correlate sEMG parameters with clinical symptoms and scales that characterize parkinsonian patients for better understanding of the association between sEMG and motor symptoms. The idiopathic Parkinson's disease and vascular parkinsonism must be compared in their compliance to DI therapy. Additionally, it would be of interest to trace the net effect of several, rather than one, DI sessions on sEMG.

4.3. In Conclusion

The results presented here provide promising evidence that such analog microgravity environment as dry immersion exerts significant influence on the motor system in parkinsonian patients, as it is seen from surface electromyogram modification after a single short-term dry immersion session. The major outcome of the study was that the amplitude, mutual information decay time, recurrence rate, and determinism of surface electromyogram decreased whereas median frequency and sample entropy, in contrast, increased right after dry immersion. This evidences decreased rigidity and weakened tremor seen as synchronicity of motor unit activity.

AUTHOR CONTRIBUTIONS

GM has contributed by data analysis and interpretation, and by writing of the manuscript. AM has contributed by the research conception, design of the work, data acquisition and interpretation, and by writing of the manuscript. IS and LC have contributed by the research conception, design of the work, and by critical revision of the manuscript. LG-M has contributed by design of the work, data acquisition, and by writing of the manuscript. NS has contributed by design of the work, data acquisition, and by critical revision of the manuscript. SR and PK have contributed by data analysis and interpretation, and by critical revision of the manuscript. All the authors have read and approved the manuscript before the publication and agree to be accountable for all aspects of the research.

FUNDING

This study was financially supported by the University of Eastern Finland Doctoral Project funding to GM, by the Ministry of Higher Education and Science of Russian Federation (grants #761 and #17.7302.2017/VU to AM), and by Petrozavodsk State University Strategic Development Program (grant AAAA-A16-116093010011-5 to AM).

ACKNOWLEDGMENTS

We would like to thank CSC - IT CENTER FOR SCIENCE LTD. (Espoo, Finland) for giving us access to Taito supercluster, which helped to process our data rapidly.

REFERENCES

Alves, G., Wentzel-Larsen, T., Aarsland, D., and Larsen, J. P. (2005). Progression of motor impairment and disability in Parkinson disease: a population-based study. *Neurology* 65, 1436–1441. doi: 10.1212/01.wnl.0000183359.50822.f2

Baker, J. R., Davey, N. J., Ellaway, P. H., and Friediland, C. L. (1992). Short-term synchrony of motor unit discharge during weak isometric contraction in Parkinson's disease. *Brain* 115, 137–154. doi: 10.1093/brain/115.1.137

Baradaran, N., Tan, S. N., Liu, A., Ashoori, A., Palmer, S. J., Wang, Z. J., et al. (2013). Parkinson's disease rigidity: relation to brain connectivity and motor performance. *Front. Neurol.* 4:67. doi: 10.3389/fneur.2013.00067

Boccia, G., Dardanello, D., Beretta-Piccoli, M., Cescon, C., Coratella, G., Rinaldo, N., Barbero, M., et al. (2016). Muscle fiber conduction velocity and fractal dimension of EMG during fatiguing contraction of young and elderly active men. *Physiol. Meas.* 37, 162–174. doi: 10.1088/0967-3334/37/1/162

Boersma, I., Jones, J., Carter, J., Bekelman, D., Miyasaki, J., Kutner, J., et al. (2016). Parkinson disease patients' perspectives on palliative care needs: what are they telling us? *Neurol. Clin. Pract.* 6, 209–219. doi: 10.1212/CPJ.0000000000000233

Buehring, B., Belavý, D. L., Michaelis, I., Gast, U., Felsenberg, D., and Rittweger, J. (2011). Changes in lower extremity muscle function after 56 days of bed rest. *J. Appl. Physiol.* 111, 87–94. doi: 10.1152/japplphysiol.01294.2010

Bukowska, A. A., Krężałek, P., Mirek, E., Bujas, P., and Marchewka, A. (2016). Neurologic music therapy training for mobility and stability rehabilitation with Parkinson's disease – a pilot study. *Front. Hum. Neurosci.* 9:710. doi: 10.3389/fnhum.2015.00710

Cantello, R., Gianelli, M., Civardi, C., and Mutani, R. (1995). Parkinson's disease rigidity: EMG in a small hand muscle at "rest". *Electroencephalogr. Clin. Neurophysiol.* 97, 215–222. doi: 10.1016/0013-4694(95)93574-Q

Celucci, C. J., Albano, A. M., and Rapp, P. E. (2003). Comparative study of embedding methods. *Phys. Rev. E* 67:066210. doi: 10.1103/PhysRevE.67.066210

Cescon, C., and Gazzoni, M. (2010). Short term bed-rest reduces conduction velocity of individual motor units in leg muscles. *J. Electromyogr. Kines.* 20, 860–867. doi: 10.1016/j.jelekin.2010.03.008

Christakos, C. N., Erimaki, S., Anagnostou, E., and Anastasopoulos, D. (2009). Tremor-related motor unit firing in Parkinson's disease: implications for tremor genesis. *J. Physiol.* 587, 4811–4827. doi: 10.1113/jphysiol.2009.173989

Coletta, N. A., Mallette, M. M., Gabriel, D. A., Tyler, C. J., and Cheung, S. S. (2018). Core and skin temperature influences on the surface electromyographic responses to an isometric force and position task. *PLoS ONE* 13:e0195219. doi: 10.1371/journal.pone.0195219

Cronin, N. J., Valtonen, A. M., Waller, B., Pöyhönen, T., and Avela, J. (2016). Effects of short term water immersion on peripheral reflex excitability in hemiplegic and healthy individuals: a preliminary study. *J. Musculoskel. Neuron.* 16, 58–62. Available online at: http://www.ismni.org/jmni/pdf/63/V16I1_09CRONIN.pdf

Davis, J. R., Horslen, B. C., Nishikawa, K., Fukushima, K., Chua, R., Inglis, J. T., et al. (2011). Human proprioceptive adaptations during states of height-induced fear and anxiety. *J. Neurophysiol.* 106, 3082–3090. doi: 10.1152/jn.01030.2010

de Dreu, M. J., Kwakkel, G., and van Wegen, E. E. H. (2015). Partnered dancing to improve mobility for people with Parkinson's disease. *Front. Neurosci.* 9:444. doi: 10.3389/fnins.2015.00444

de Lau, L. M. L., and Breteler, M. M. B. (2006). Epidemiology of Parkinson's disease. *Lancet Neurol.* 5, 525–535. doi: 10.1016/S1474-4422(06)70471-9

Demangel, R., Treffel, L., Py, G., Brioche, T., Pagano, A. F., Bareille, M.-P., et al. (2017). Early structural and functional signature of 3-day human skeletal muscle disuse using the dry immersion model. *J. Physiol.* 595, 4301–4315. doi: 10.1113/JP273895

di Biase, L., Summa, S., Tosi, J., Taffoni, F., Marano, M., Rizzo, A. C., et al. (2018). Quantitative analysis of bradykinesia and rigidity in Parkinson's disease. *Front. Neurol.* 9:121. doi: 10.3389/fneur.2018.00121

Dietz, V., and Sinkjaer, T. (2007). Spastic movement disorder: impaired reflex function and altered muscle mechanic. *Lancet Neurol.* 6, 725–733. doi: 10.1016/S1474-4422(07)70193-X

Ebersbach, G., Edler, D., Kaufhold, O., and Wissel, J. (2008). Whole body vibration versus conventional physiotherapy to improve balance and gait in Parkinson's disease. *Arch. Phys. Med. Rehabil.* 89, 399–403. doi: 10.1016/j.apmr.2007.09.031

Escudero, J., Hornero, R., and Absolo, D. (2009). Interpretation of the auto-mutual information rate of decrease in the context of biomedical signal analysis. Application to electroencephalogram recordings. *Physiol. Meas.* 30, 187–199. doi: 10.1088/0967-3334/30/2/006

Fan, J.-Y., Chang, B.-L., and Wu, Y.-R. (2016). Relationships among depression, anxiety, sleep, and quality of life in patients with Parkinson's disease in Taiwan. *Parkinson's Dis.* 2016:4040185. doi: 10.1155/2016/4040185

Farina, D., Merletti, R., and Enoka, R. M. (2004). The extraction of neural strategies from the surface EMG. *J. Appl. Physiol.* 96, 1486–1495. doi: 10.1152/japplphysiol.01070.2003

Farina, D., Merletti, R., and Enoka, R. M. (2014). The extraction of neural strategies from the surface EMG: an update. *J. Appl. Physiol.* 117, 1215–1230. doi: 10.1152/japplphysiol.00162.2014

Fattorini, L., Felici, F., Filligoi, G. C., Traballesi, M., and Farina, D. (2005). Influence of high motor unit synchronization levels on non-linear and spectral variables of the surface EMG. *J. Neurosci. Methods* 143, 133–139. doi: 10.1016/j.jneumeth.2004.09.018

Fraser, A. M., and Swinney, H. L. (1986). Independent coordinates for strange attractors from mutual information. *Phys. Rev. A* 33, 1134–1140. doi: 10.1103/PhysRevA.33.1134

Freund, H. J. (1983). Motor unit and muscle activity in voluntary motor control. *Physiol. Rev.* 63, 387–436. doi: 10.1152/physrev.1983.63.2.387

Fu, A., Wang, C., Qi, H., Li, F., Wang, Z., He, F., et al. (2016). Electromyography-based analysis of human upper limbs during 45-day head-down bed-rest. *Acta Astronaut.* 120, 260–269. doi: 10.1016/j.actaastro.2015.12.007

Gallasch, E., Kozlovskaya, I., Löscher, W. N., Konev, A., and Kenner, T. (1994). Arm tremor and precision of hand force control in a short and long term flight on the Mir-Space-Station. *Acta Astronaut.* 33, 49–55. doi: 10.1016/0094-5765(94)90108-2

Gao, J. and Zheng, Z. (1994). Direct dynamical test for deterministic chaos and optimal embedding of a chaotic time series. *Phys. Rev. E* 49, 3807–3814. doi: 10.1103/PhysRevE.49.3807

Glendinning, D. S., and Enoka, R. M. (1994). Motor unit behavior in Parkinson's disease. *Phys. Ther.* 74, 61–70. doi: 10.1093/ptj/74.1.61

Gordon, J. (1990). "Disorders of motor control," in *Key Issues in Neurological Physiotherapy*, eds L. Ada and C. Canning (London: Heinemann), 35.

Grassberger, P., and Procaccia, I. (1983). Characterization of Strange Attractors. *Phys. Rev. Lett.* 50, 346–349. doi: 10.1103/PhysRevLett.50.346

Guyton, A. C., and Hall, J. E. (2011). *Textbook of Medical Physiology, 12th Edn*. Philadelphia, PA: Saunders Elsevier.

Hoyer, D., Pompe, B., Chon, K. H., Hardraht, H., Wicher, C., and Zwiener, U. (2005). Mutual information function assesses autonomic information flow of heart rate dynamics at different time scales. *IEEE Trans. Biomed. Eng.* 52, 584–592. doi: 10.1109/TBME.2005.844023

Hwang, I.-S., Lin, Y.-T., Huang, W.-M., Yang, Z.-R., Hu, C.-L., and Chen, Y.-C. (2017). Alterations in neural control of constant isometric contraction with the size of error feedback. *PLoS ONE* 12:e0170824. doi: 10.1371/journal.pone.0170824

Jeong, J., Gore, J. C., and Peterson, B. S. (2001). Mutual information analysis of the EEG in patients with Alzheimer's disease. *Clin. Neurophysiol.* 112, 827–835. doi: 10.1016/S1388-2457(01)00513-2

Katsura, Y., Yoshikawa, T., Ueda, S.-Y., Usui, T., Sotobayashi, D., Nakao, H., et al. (2010). Effects of aquatic exercise training using water-resistance equipment in elderly. *Eur. J. Appl. Physiol.* 108, 957–964. doi: 10.1007/s00421-009-1306-0

Katz, R. T., and Rymer, W. Z. (1989). Spastic hypertonia: mechanisms and measurement. *Arch. Phys. Med. Rehabil.* 70, 144–155.

Kennel, M. B., Brown, R., and Abarbanel, H. D. I. (1992). Determining embedding dimension for phase-space reconstruction using a geometrical construction. *Phys. Rev. A* 45, 3403–3411. doi: 10.1103/PhysRevA.45.3403

Kirkwood, P. A., Sears, T. A., Tuck, D. L., and Westgaard, R. H. (1982). Variations in the time course of the synchronization of intercostal motoneurones in the cat. *J. Physiol.* 327, 105–135. doi: 10.1113/jphysiol.1982.sp014223

Kline, J. C., and de Luca, C. J. (2016). Synchronization of motor unit firings: an epiphenomenon of firing rate characteristics not common inputs. *J. Neurophysiol.* 115, 178–192. doi: 10.1152/jn.00452.2015

Koryak, Y. A. (2002). Surface action potential and contractile properties of the human triceps surae muscle: effect of 'dry' water immersion. *Exp. Physiol.* 87, 101–111. doi: 10.1113/eph8702301

Kozlovskaya, I., Dmitrieva, I., Grigorieva, L., Kirenskaya, A., and Kreidich, Yu. (1988). "Gravitational mechanisms in the motor system. Studies in real and

simulated weightlessness," in *Stance and Motion: Facts and Concepts*, eds V. S. Gurfinkel, M. E. Ioffe, J. Massion, and J. P. Roll (Boston, MA: Springer), 37–48.

Lupandin, Yu. V., Antonen, E. G., and Meigal, Yu. A. (1993). The patterns of bioelectrical activity of motor units in different forms of parkinsonism. *Zh. Nevrol. Psikhiatr. Im. S. S. Korsakova* 93, 30–34.

Mañé, R. (1981). "On the dimension of the compact invariant sets of certain nonlinear maps," in *Dynamical Systems and Turbulence, Lecture Notes in Mathematics*, vol. 898, eds D. A. Rand and L.-S. Young (Warwick: Springer-Verlag), 230–242.

Marwan, N., Romano, M. C., Thiel, M., and Kurths, J. (2007). Recurrence plots for the analysis of complex systems. *Phys. Rep.* 438, 237–329. doi: 10.1016/j.physrep.2006.11.001

McAuley, J. H., and Marsden, C. D. (2000). Physiological and pathological tremors and rhythmic central motor control. *Brain* 123, 1545–1567. doi: 10.1093/brain/123.8.1545

Meigal, A., Gerasimova-Meigal, L., Saenko, I., and Subbotina, N. (2018). Dry immersion as a novel physical therapeutic intervention for rehabilitation of Parkinson's disease patients: a feasibility study. *Phys. Med. Rehab. Kuror.* doi: 10.1055/a-0577-5139

Meigal, A., and Lupandin, Y. (2005). "Thermoregulation-dependent component" in pathophysiology of motor disorders in Parkinson's disease? *Pathophysiology* 11, 187–196. doi: 10.1016/j.pathophys.2005.02.001

Meigal, A., Miroshnichenko, G., Kuzmina, A., Rissanen, S., Georgiadis, S., and Karjalainen, P. (2015). Nonlinear parameters of surface EMG in schizophrenia patients depend on kind of antipsychotic therapy. *Front. Physiol.* 6:197. doi: 10.3389/fphys.2015.00197

Meigal, A. Yu., Rissanen, S., Tarvainen, M., Georgiadis, S. D., Karjalainen, P. A., Airaksinen, O., et al. (2012). Linear and nonlinear tremor acceleration characteristics in patients with Parkinson's disease. *Physiol. Meas.* 33, 395–412. doi: 10.1088/0967-3334/33/3/395

Meigal, A. Yu., Rissanen, S., Tarvainen, M., Kajalainen, P. A., Iudina-Vassel, I. A., Airaksinen, O., et al. (2009). Novel parameters of surface EMG in patients with Parkinson's disease and healthy young and old controls. *J. Electromyogr. Kines.* 19, e206–e213. doi: 10.1016/j.jelekin.2008.02.008

Meigal, A. Yu., Rissanen, S. M., Tarvainen, M. P., Airaksinen, O., Kankaanpää, M., and Karjalainen, P. A. (2013). Non-linear EMG parameters for differential and early diagnostics of Parkinson's disease. *Front. Neurol.* 4:135. doi: 10.3389/fneur.2013.00135

Mewett, D. T., Reynolds, K. J., and Nazeran, H. (2004). Reducing power line interference in digitised electromyogram recordings by spectrum interpolation. *Med. Biol. Eng. Comput.* 42, 524–531. doi: 10.1007/BF02350994

Miyai, I., Fujimoto, Y., Ueda, Y., Yamamoto, H., Nozaki, S., Saito, T., et al. (2000). Treadmill training with body weight support: its effect on Parkinson's disease. *Arch. Phys. Med. Rehabil.* 81, 849–852. doi: 10.1053/apmr.2000.4439

Mulder, E. R., Gerrits, K. H. L., Kleine, B. U., Rittweger, J., Felsenberg, D., de Haan, A., et al. (2009). High-density surface EMG study on the time course of central nervous and peripheral neuromuscular changes during 8 weeks of bed rest with or without resistive vibration exercise. *J. Electromyogr. Kines.* 19, 208–218. doi: 10.1016/j.jelekin.2007.04.002

Navasiolava, N. M., Custaud, M.-A., Tomilovskaya, E. S., Larina, I. M., Mano, T., Gauquelin-Koch, G., et al. (2011). Long-term dry immersion: review and prospects. *Eur. J. Appl. Physiol.* 111, 1235–1260. doi: 10.1007/s00421-010-1750-x

Needle, A. R., Baumeister, J., Kaminski, T. W., Higginson, J. S., Farquhar, W. B., and Swanik, C. B. (2014). Neuromechanical coupling in the regulation of muscle tone and joint stiffness. *Scand. J. Med. Sci. Sports* 24, 737–748. doi: 10.1111/sms.12181

Ni, M., Signorile, J. F., Mooney, K., Balachandran, A., Potiaumpai, M., Luca, C., et al. (2016). Comparative effect of power training and high-speed yoga on motor function in older patients with Parkinson disease. *Arch. Phys. Med. Rehabil.* 97, 345–354.e15. doi: 10.1016/j.apmr.2015.10.095

Nordstrom, M. A., Fuglevand, A. J., and Enoka, R. M. (1992). Estimating the strength of common input to human motoneurons from the cross-correlogram. *J. Physiol.* 453, 547–574. doi: 10.1113/jphysiol.1992.sp019244

Noyes, K., Liu, H., Li, Y., Holloway, R., and Dick, A. W. (2006). Economic burden associated with Parkinson's disease on elderly Medicare beneficiaries. *Mov. Disord.* 21, 362–372. doi: 10.1002/mds.20727

Oung, Q. W., Muthusamy, H., Lee, H. L., Basah, S. N., Yaacob, S., Sarillee, M., et al. (2015). Technologies for assessment of motor disorders in Parkinson's disease: a review. *Sensors* 15, 21710–21745. doi: 10.3390/s150921710

Picelli, A., Tamburin, S., Passuello, M., Waldner, A., and Smania, N. (2014). Robot-assisted arm training in patients with Parkinson's disease: a pilot study. *J. NeuroEng. Rehabil.* 11, 1–4. doi: 10.1186/1743-0003-11-28

Piervirgili, G., Petracca, F., and Merletti, R. (2014). A new method to assess skin treatments for lowering the impedance and noise of individual gelled Ag-AgCl electrodes. *Physiol. Meas.* 35, 2101–2118. doi: 10.1088/0967-3334/35/10/2101

Portero, P., Vanhoutte, C., and Goubel, F. (1996). Surface electromyogram power spectrum changes in human leg muscles following 4 weeks of simulated microgravity. *Eur. J. Appl. Physiol. O.* 73, 340–345. doi: 10.1007/BF02425496

Ramanand, P., Bruce, M. C., and Bruce, E. N. (2010). Mutual information analysis of EEG signals indicates age-related changes in cortical interdependence during sleep in middle-aged vs. elderly women. *J. Clin. Neurophysiol.* 27, 274–284. doi: 10.1097/WNP.0b013e3181eaa9f5

Richman, J. S., and Moorman, J. R. (2000). Physiological time-series analysis using approximate entropy and sample entropy. *Am. J. Physiol. Heart Circ. Physiol.* 278, H2039–H2049. doi: 10.1152/ajpheart.2000.278.6.H2039

Riley, M. A., and van Orden, G. C., editors (2005). *Tutorials in Contemporary Nonlinear Methods for the Behavioral Science*. Available online at: https://www.nsf.gov/pubs/2005/nsf05057/nmbs/nmbs.pdf (Accessed June 21, 2018).

Rissanen, S. M., Kankaanpää, M., Meigal, A., Tarvainen, M. P., Nuutinen, J., Tarkka, I. M., et al. (2008). Surface EMG and acceleration signals in Parkinson's disease: feature extraction and cluster analysis. *Med. Biol. Eng. Comput.* 46, 849–858. doi: 10.1007/s11517-008-0369-0

Rissanen, S. M., Kankaanpää, M., Tarvainen, M. P., Novak, V., Novak, P., Hu, K., et al. (2011). Analysis of EMG and acceleration signals for quantifying the effects of deep brain stimulation in Parkinson's disease. *IEEE Trans. Biomed. Eng.* 58, 2545–2553. doi: 10.1109/TBME.2011.2159380

Rivelis, Y., and Morice, K. (2018). "Spasticity," in *StatPearls [Internet]*. Treasure Island: StatPearls Publishing. Available online at: https://www.ncbi.nlm.nih.gov/books/NBK507869/ (Updated June 19, 2018).

Rossi, B., Siciliano, G., Carboncini, M. C., Manca, M. L., Massetani, R., Viacava, P., et al. (1996). Muscle modifications in Parkinson's disease: myoelectric manifestations. *Electroencephalogr. Clin. Neurophysiol.* 101, 211–218. doi: 10.1016/0924-980X(96)94672-X

Ruonala, V., Pekkonen, E., Airaksinen, O., Kankaanpää, M., Karjalainen, P. A., and Rissanen, S. M. (2018). Levodopa-induced changes in electromyographic patterns in patients with advanced Parkinson's disease. *Front. Neurol.* 9:35. doi: 10.3389/fneur.2018.00035

Sáchez-Ferro, Á., Elshehabi, M., Godinho, C., Salkovic, D., Hobert, M. A., Domingos, J., et al. (2016). New methods for the assessment of Parkinson's disease (2005 to 2015): a systematic review. *Movement Disord.* 31, 1283–1292. doi: 10.1002/mds.26723

Scandalis, T. A., Bosak, A., Berliner, J. C., Helman, L. L., and Wells, M. R. (2001). Resistance training and gait function in patients with Parkinson's disease. *Am. J. Phys. Med. Rehabil.* 80, 38–43. doi: 10.1097/00002060-200101000-00011

Schneider, S., Peipsi, A., Stokes, M., Knicker, A., and Abeln, V. (2015). Feasibility of monitoring muscle health in microgravity environments using Myoton technology. *Med. Biol. Eng. Comput.* 53, 57–66. doi: 10.1007/s11517-014-1211-5

Sears, T. A., and Stagg, D. (1976). Short-term synchronization of intercostal motoneurone activity. *J. Physiol.* 263, 357–381. doi: 10.1113/jphysiol.1976.sp011635

Sturman, M. M., Vaillancourt, D. E., and Corcos, D. M. (2005). Effects of aging on the regularity of physiological tremor. *J. Neurophysiol.* 93, 3064–3074. doi: 10.1152/jn.01218.2004

Sung, P. S., Zurcher, U., and Kaufman, M. (2008). Gender differences in spectral and entropic measures of erector spinae muscle fatigue. *J. Rehabil. Res. Dev.* 45, 1431–1440. doi: 10.1682/JRRD.2007.11.0196

Takens, F. (1981). "Detecting strange attractors in turbulence," in *Dynamical Systems and Turbulence, Lecture Notes in Mathematics*, vol. 898, eds D. A. Rand and L.-S. Young (Berlin; Heidelberg: Springer-Verlag), 366–381.

Tarvainen, M. P., Ranta-aho, P. O., and Karjalainen, P. A. (2002). An advanced detrending method with application to HRV analysis. *IEEE Trans. Biomed. Eng.* 49, 172–175. doi: 10.1109/10.979357

The Parkinson Study Group (2004). Levodopa and the progression of Parkinson's disease. *N. Engl. J. Med.* 351, 2498–2508. doi: 10.1056/NEJMoa033447

Timmermann, L., Gross, J., Dirks, M., Volkmann, J., Freund, H.-J., and Schnitzler, A. (2003). The cerebral oscillatory network of parkinsonian resting tremor. *Brain* 126, 199–212. doi: 10.1093/brain/awg022

Tomlinson, C. L., Herd, C. P., Clarke, C. E., Meek, C., Patel, S., Stowe, R., et al. (2014). Physiotherapy for Parkinson's disease: a comparison of techniques. *Cochrane Db. Syst. Rev.* 6:CD002815. doi: 10.1002/14651858.CD002815.pub2

Trompetto, C., Marinelli, L., Mori, L., Pelosin, E., Currà, A., Molfetta, L., et al. (2014). Pathophysiology of spasticity: implications for neurorehabilitation. *Biomed. Res. Int.* 2014:354906. doi: 10.1155/2014/354906

Vaillancourt, D. E., Prodoehl, J., Metman, L. V., Bakay, R. A., and Corcos, D. M. (2004). Effects of deep brain stimulation and medication on bradykinesia and muscle activation in Parkinson's disease. *Brain* 127, 491–504. doi: 10.1093/brain/awh057

Vivas, J., Arias, P., and Cudeiro, J. (2011). Aquatic therapy versus conventional land-based therapy for Parkinson's disease: an open-label pilot study. *Arch. Phys. Med. Rehabil.* 92, 1202–1210. doi: 10.1016/j.apmr.2011.03.017

Volpe, D., Giantin, M. G., Maestri, R., and Frazzitta, G. (2014). Comparing the effects of hydrotherapy and land-based therapy on balance in patients with Parkinson's disease: a randomized controlled pilot study. *Clin. Rehabil.* 28, 1210–1217. doi: 10.1177/0269215514536060

Ward, A. B. (2000). Assessment of muscle tone. *Age Ageing* 29, 385–386. doi: 10.1093/ageing/29.5.385

Watenpaugh, D. E. (2016). Analogs of microgravity: head-down tilt and water immersion. *J. Appl. Physiol.* 120, 904–914. doi: 10.1152/japplphysiol.00986.2015

Yen, C. Y., Lin, K. H., Hu, M. H., Wu, R. M., Lu, T. W., and Lin, C. H. (2011). Effects of virtual reality-augmented balance training on sensory organization and attentional demand for postural control in people with Parkinson disease: a randomized controlled trial. *Phys. Ther.* 91, 862–874. doi: 10.2522/ptj.20100050

Zhou, J., Yin, T., Gao, Q., and Yang, X. C. (2015). A meta-analysis on the efficacy of tai chi in patients with Parkinson's disease between 2008 and 2014. *Evid. Based Compl. Alt.* 2015:593263. doi: 10.1155/2015/593263

Zhu, H., Lu, Z., Jin, Y., Duan, X., Teng, J., and Duan, D. (2015). Low-frequency repetitive transcranial magnetic stimulation on Parkinson motor function: a meta-analysis of randomised controlled trials. *Acta Neuropsychiatr.* 27, 82–89. doi: 10.1017/neu.2014.43

Conflict of Interest Statement: The authors declare that the research was conducted in the absence of any commercial or financial relationships that could be construed as a potential conflict of interest.

Copyright © 2018 Miroshnichenko, Meigal, Saenko, Gerasimova-Meigal, Chernikova, Subbotina, Rissanen and Karjalainen. This is an open-access article distributed under the terms of the Creative Commons Attribution License (CC BY). The use, distribution or reproduction in other forums is permitted, provided the original author(s) and the copyright owner(s) are credited and that the original publication in this journal is cited, in accordance with accepted academic practice. No use, distribution or reproduction is permitted which does not comply with these terms.

frontiers in Behavioral Neuroscience

REVIEW
published: 28 September 2018
doi: 10.3389/fnbeh.2018.00175

The Role of Long Noncoding RNAs in Central Nervous System and Neurodegenerative Diseases

*Chang-Wei Wei, Ting Luo, Shan-Shan Zou and An-Shi Wu**

Department of Anesthesiology, Beijing Chao-Yang Hospital, Capital Medical University, Beijing, China

Long noncoding RNAs (lncRNAs) refer to a group of noncoding RNAs (ncRNAs) that has a transcript of more than 200 nucleotides in length in eukaryotic cells. The lncRNAs regulate gene expression at epigenetic, transcriptional, and post-transcriptional levels by multiple action modes. In this review, we describe the diverse roles reported for lncRNAs, and discuss how they could mechanistically be involved in the development of central nervous system (CNS) and neurodegenerative diseases. Further studies on the function of lncRNAs and their mechanism will help deepen our understanding of the development, function, and diseases of the CNS, and provide new ideas for the design and development of some therapeutic drugs.

Keywords: long noncoding RNAs, central nervous system, neurodegenerative diseases, regulatory mechanism, gene expression

INTRODUCTION

Over the past decade, the extensive applications of second-generation sequencing technology have led to the discovery of tens of thousands of RNA transcripts that have similar properties to mRNAs, but are not translated into proteins. Long noncoding RNA (lncRNA) is a kind of noncoding RNA (ncRNA), with a length of longer than 200 nucleotides, that lacks a significant open reading frame (ORF) encoding a protein (Sun and Kraus, 2015). The central nervous system (CNS) is the most highly evolved and sophisticated biological system. The development of the CNS is a complex arrangement of stem cells, growth/differentiation factors, transcription factors, and epigenetic control. It consists of a large number of neuronal and glial cell subtypes distributed in rigorous and precise regions, forming a dynamic neural network that responds to internal signals and external stimuli and then is responsible for mediating the complex functional repertoire of the CNS including performing higher level functions, for example, cognition and behavior (Graff and Mansuy, 2008). As one of the most abundant ncRNA classes, lncRNAs are derived from different locations in the genome for transcription and are highly expressed in the brain (Mercer et al., 2008; Qureshi et al., 2010). The role of lncRNAs has been validated in brain development, neuronal function, maintenance, and differentiation.

Neurodegenerative diseases are associated with multiple clinical manifestations, brain pathologies, and health consequences (Quan et al., 2017). They include relatively well-known conditions like Alzheimer's disease (AD), Parkinson's disease (PD), and Huntington's disease (HD). In particular, AD and PD are a group of typically late-onset, progressive disorders that lead to cognitive and/or movement disorders (Peden and Ironside, 2012). Although drug therapy and/or surgery can delay the progression of these diseases, most neurodegenerative diseases remain untreatable. In addition, neurodegenerative diseases represent an increasing financial burden on health care systems, which attempt to respond to an aging population. Therefore, there is an

OPEN ACCESS

Edited by:
Ioan Opris,
University of Miami, United States

Reviewed by:
Neha Nagpal,
Boston Children's Hospital, United States
Timothy J. Jarome,
Virginia Tech, United States

****Correspondence:***
An-Shi Wu
wuanshi880923@163.com

Received: *09 March 2018*
Accepted: *27 July 2018*
Published: *28 September 2018*

Citation:
Wei C-W, Luo T, Zou S-S and Wu A-S (2018) The Role of Long Noncoding RNAs in Central Nervous System and Neurodegenerative Diseases. Front. Behav. Neurosci. 12:175. doi: 10.3389/fnbeh.2018.00175

urgent need to develop methods for preventing or curing neurodegenerative diseases. Some efforts carried out by the scientific community revealed important insights into the molecular bases of these disease, but the specific mechanism remains unknown. Increasing evidence has suggested that lncRNAs are involved in the pathogenesis of neurodegenerative diseases (Johnson, 2012; Briggs et al., 2015; Riva et al., 2016). This review summarizes data on lncRNA expression in the central nervous system (CNS) and neurodegenerative diseases and focuses on the role of some specific lncRNAs, which may provide new insights into our understanding of the etiology and pathophysiology of the neurodegenerative diseases.

BIOLOGY OF lncRNAs

Definition of lncRNAs

Genomewide analysis of the eukaryotic transcriptome revealed that up to 90% of the human genome IS transcribed. However, the GENCODE-annotated exon of the protein-encoding gene covers only 2.94% of the genome, while the rest are ncRNAs (Djebali et al., 2012). Noncoding transcripts are further divided into house-keeping ncRNAs and regulatory ncRNAs. House-keeping ncRNAs include ribosomes, metastasis, small nuclei, and small nucleolar RNA. Regulatory ncRNAs are generally divided into two classes based on nucleotide length. Those <200 nucleotides are commonly referred to as short/small ncRNAs, including microRNAs (miRNAs), small interfering RNAs, and Piwi-related RNAs, and those >200 nucleotides are known as lncRNAs (Nagano and Fraser, 2011).

The lncRNA transcripts are partially similar to messenger RNAs (mRNAs) as they are frequently transcribed by RNA polymerase II, contain classical splice sites (GU/AG), have an mRNA-like structure that contains intron and exon structures, exhibit alternative splicing, no open reading frame (ORF) in the sequence, and are associated with the same types of histone modifications as protein-coding genes (PCGs)(Ponting et al., 2009). They also have a specific secondary structure that provides multiple sites for protein binding or the specific binding between DNA and RNA by the principle of base pair complementarity. The main sources of lncRNAs are from PCG-related regions (Magistri et al., 2012), gene regulatory regions (Hung et al., 2011; Mercer et al., 2011), and specific chromosomal regions (Azzalin et al., 2007). The lncRNA was originally thought to be the "noise" of genomic transcription and as not having biological functions. However, recent studies have shown that lncRNAs can regulate gene expression at epigenetic, transcriptional, and post-transcriptional levels, and participate in X-chromosome silencing, genome imprinting, and chromatin modification, transcriptional activation, and many other important biological processes (Singh and Prasanth, 2013; Goff and Rinn, 2015; Kazemzadeh et al., 2015). Until now, only very few lncRNAs have been validated by experiment, while most of the lncRNAs have been annotated via bioinformatics and still need further experimental verification.

Expression and Sequence Conservation of lncRNAs

In 2002, Japanese scientists revealed that in large-scale sequencing of a mouse full-length complementary DNA (cDNA) library, a large number of ncRNA transcripts were identified (Okazaki et al., 2002). However, due to lack of functional annotation, these RNA transcripts did not attract the attention of researchers during subsequent periods. Not until 2007 did the situation change. Rinn et al. in Stanford University reported a 2.2-Kb functional lncRNA gene (Hox transcript antisense intergenic RNA, *HOTAIR*) (Rinn et al., 2007). It was found that *HOTAIR* could interact with the protein complex polycomb, which can modify chromatin, inhibit the transcription of the *Hox* gene, and regulate the growth and development of organisms. In 2008, Mercer et al. used *in situ* hybridization to identify the expression of a large amount of lncRNAs in mouse brain (Mercer et al., 2008). The expression levels of these lncRNAs are associated with specific neuroanatomical locations, cell types, and subcellular locations. For example, *Evf2* is mainly expressed in the ventral forebrain. The tissue-specific expression of lncRNAs also includes *Hox* transcript antisense intergenic RNA myeloid1 (*HOTAIRM1*), which is specifically expressed in the bone marrow (Zhang et al., 2009) and *Msx1* antisense RNA (*Msx1-AS* RNA), which is expressed only in differentiated teeth and bone cells (Coudert et al., 2005). The expression level of *Msx1-AS* RNA is negatively correlated with the content of Msx1 protein (Babajko et al., 2009).

The lncRNAs can appear in different subcellular structures, and the proportion of those lncRNAs located in the nucleus is the largest. For example, lncRNA *MEN ε/β* is mainly located in the nucleus, and is an important component of nuclear substructure paraspeckles (Sasaki et al., 2009; Sunwoo et al., 2009). Furthermore, metastasis-associated lung adenocarcinoma transcript 1 (*MALAT-1*) and nuclear-enriched abundant transcript 1 (*Neat1*) are localized mainly in the nuclear speckle of the nucleus, and are associated with the cleavage of RNA precursors (Hutchinson et al., 2007; Tripathi et al., 2010). In addition, Cesana et al. reported that *linc-MD1* is mainly expressed in the cytoplasm of differentiated muscle cells, and regulates the differentiation of skeletal muscles as a competing endogenous RNA (ceRNA) (Cesana et al., 2011). In 2011, Rackham et al. first identified three lncRNAs (*lncND5*, *lncND6,* and *lncCytb*) encoded by mitochondrial genome DNA in the analysis of high-throughput sequencing data (Rackham et al., 2011). This shows that lncRNAs may exist in many subcellular structures. Hence, special subcellular localization plays an important role in the biological function of lncRNAs.

The sequence conservation of lncRNAs is low. The sequence similarity is close to the intron region of the PCG, lower than 70% in humans and mice, and slightly lower than that in the 5′UTR or 3′UTR of genes (Pang et al., 2006). It was revealed in some studies that low sequence conservation did not affect the functional conservation of lncRNAs. Illustrated by the examples of *Xist* and *HOTAIR* expressed in mammals, although they are not highly conservative in sequence, the roles in X chromosome dosage compensation and epigenetic silencing are

the same (Braidotti et al., 2004; Pauler et al., 2005). In addition, some lncRNAs with high sequence homology have also been found such as *MALAT1* and *Neat1* (Nakagawa et al., 2012; Zhang et al., 2012).

THE lncRNAs IN CNS DEVELOPMENT

The CNS development is a complex and stereotyped process that requires the precise spatiotemporal regulation of pluripotent stem cell proliferation and differentiation. Neurons are able to change their set of synaptic connections and the relative strength of each of these connections over time in response to sensory experience and other environmental cues. The dynamic expression of lncRNAs plays an important role in controlling these processes **(Table 1)**.

Molecular Mechanisms of lncRNAs in Cell Proliferation and Differentiation

A study has revealed that approximately 40% of lncRNAs are distributed in the CNS (equivalent to 4,000–20,000 lncRNA genes) (Briggs et al., 2015). It may be that brain complexity requires more regulatory RNA to maintain normal brain development and function. The lncRNAs are involved in the regulation of the proliferation and development of the nervous system, and enable the nervous system to proliferate and differentiate according to normal time and spatial orders (Amaral et al., 2013).

The lncRNAs are involved in the differentiation of embryonic cells into neural cells during the embryonic period (Klattenhoff et al., 2013). A genetic analysis of the embryo revealed that lncRNAs are closely associated with the coding genes involved in neuronal differentiation and cell morphological maintenance, such as brain-derived neurotrophic factor (*BDNF*), developing brain homeobox 1 (*DBX1*), neuron–glia-related cell-adhesion molecule (*Nrcam*), etc. (Lv et al., 2013). Studies on neural stem cells revealed that lncRNAs are involved in regulating the differentiation of stem cells into neural cells (Ng et al., 2012; Antoniou et al., 2014; Ramos et al., 2016). For example, Ng *et al.* revealed that *lncRNA-ES1*, *lncRNA-ES2,* and *lncRNA-ES* are associated with the maintenance and differentiation of neural stem cells. Guttman et al. discovered at least 1,000 conserved intergenic lncRNAs genes by analyzing the chromatin of mouse neurons (including neural precursor cells) in 2009; they also primarily hypothesized and verified the role of lncRNAs in the maintenance of embryonic stem cells (Guttman et al., 2009). Subsequently, functional genomic analysis revealed that these intergenic lncRNA genes were not only involved the differentiation of mouse ventral forebrain-derived neural stem cells, but also in brain aging, mouse hippocampal development, differentiation of gamma aminobutyric acid (GABA)-ergic neurons, oligodendrocyte myelination, and the calcineurin-dependent signaling pathway, by regulating the expression of some important genes (Mercer et al., 2010).

A recent study has revealed that lncRNAs are associated with PCGs in neural development and play an important role in maintaining the intrinsic morphology and characteristics of neurons (Roberts et al., 2014). For example, the sex-determining region Y-box 2 (*Sox2*) is an important regulator of neural stem cell differentiation and nerve growth. *Sox2OT* encodes a sense-orientation transcript that overlaps with the *Sox2*. The genomic proximity of *Sox2OT* and *Sox2* suggested a possible regulatory role for *Sox2OT* in the neural stem cell differentiation and regeneration of neural cells.

The lncRNAs and Synaptic Plasticity

Synaptic plasticity is the basis of learning and memory and plays a key role in maintaining the stability of the nerve pathway. Some studies found that many lncRNAs might be involved in the regulation of synaptic plasticity (Leal et al., 2014; Panja and Bramham, 2014; Maag et al., 2015). Angelman syndrome (AS) is caused by the deletion of or an inactivating mutation in the maternal E3 ubiquitin ligase (*UBE3A*) gene and is characterized by intellectual disability, severe developmental delays, and speech impairment (Mabb et al., 2011). Furthermore, due to the expression of lncRNA *UBE3A-ATS*, the paternal allele of *UBE3A* undergoes silencing. A study found that hippocampal long-term potentiation (LTP) is defective in the AS-mutant mouse model (Jiang et al., 1998). Similar plasticity deficits may be the cause of learning disabilities observed in AS patients. This important role of *UBE3A-ATS* in neuronal function highlights the possible role of lncRNA in memory formation, while further studies on the role of other lncRNAs in these processes are necessary. The normal development of gamma-aminobutyric acid-ergic (GABAergic) inhibitory interneurons in the hippocampus is the key to learning in embryonic and adult brains. The *Evf-2* lncRNA, which transcribed from the Dlx-5/6 ultraconserved region, is essential for GABAergic neuron development. The *Evf-2* acts through the Dlx-2 transcriptional coactivator to increase the transcriptional activity of Dlx-5/6 and glutamate decarboxylase 1 (Gad1 required for the conversion of glutamate to GABA) (Colasante et al., 2008), and then regulates the gene expression of GABAergic interneurons in the developing mouse brain. The *Evf-2* silencing leads to abnormal synaptic activity in mice through abnormal formation of GABAergic circuits in the hippocampus and dentate gyrus (Bond et al., 2009).

In neurons, local protein synthesis in synaptodendritic microdomains has been implicated in the growth and plasticity of synapses. The lncRNA brain cytoplasmic 200 (*BC200*) is selectively located in the dendrites of postsynaptic neurons, and regulates local protein synthesis by blocking transcription initiation, thereby, controlling signal transduction (Kondrashov et al., 2005). In addition, *BC1* is an lncRNA located in the dendrites of neurons, which is a specific repressor of translation. Experimental use of internal ribosome entry mechanisms and sucrose density gradient centrifugation showed that BC1-mediated repression targets translation at the level of initiation. Specifically, *BC1* RNA inhibited formation of the 48S preinitiation complex, i.e., recruitment of the small ribosomal subunit to the mRNA (Wang et al., 2002). After that, the authors demonstrated that the lack of *BC1* could induce nerve overexcitation (Wang et al., 2005).

Neurons can change their connections when they face changes in the environment. Alterations in components of ion channels or signal proteins may affect neuronal excitability or neuronal

TABLE 1 | Molecular mechanisms of lncRNA in neuronal differentiation and synaptogenesis.

lncRNAs	Biological function	Molecular mechanisms	References
RMST	Promotes neuronal differentiation	The RMST interacts with *SOX2* to regulate neurogenic genes including *ASCL1* and *DLX1*	Ng et al., 2013; Lee et al., 2017
Linc-Brn1b	Specifies cortical NSPC fate and regulates area patterning and layer formation of mouse neocortex	Deletion of the linc-*Brn1b* locus leads to significant decrease in Brn1 expression	Sauvageau et al., 2013; Wang et al., 2017
Tuna	Regulates pluripotency and neural differentiation of ESCs	*TUNA* formed a complex with three pluripotency-related RNA-binding proteins, PTBP1, hnRNP-K, and NCL	Lin et al., 2014
Gomafu	Controls retinal development; Dysregulated in schizophrenia	*Gomafu/Miat* regulates splicing of neuronal genes, including *DISC1, ERRB4*, and *WNT7B*, probably via association with splicing factors SF1, SRSF1, and QKI	Briggs et al., 2015; Wang et al., 2017
KCNA2-AS	Regulates neuronal firing properties	It dynamically downregulates expression of the *KCNA2* potassium channel subunit	Zhao et al., 2013
BDNF-AS	Depletion of BDNF-AS promotes neuronal outgrowth adult neurogenesis; BDNF-AS modulates synaptic function	*BDNF-AS* negatively regulates BDNF expression by recruiting EZH2 (a PRC2 core component) in response to neuronal depolarization	Modarresi et al., 2012
Malat1	Promotes dendrite maturation and synaptogenesis in cultured hippocampal neurons	*Malat1* associates with SR family splicing factors to control expression of synaptic molecules including Nlgn1 and SynCAM1	Wang et al., 2017
BC1/BC200	Regulates synaptic excitability	Controls the translational repression of specific target mRNAs within synapses through a mechanism involving direct recruitment of translational machineries	Zhong et al., 2009

RMST, rhabdomyosarcoma 2 associated transcript; ASCL1, achaete-scute family bHLH transcription factor 1; DLX1, distal-less homeobox 1; Tuna, TCL1 upstream neural differentiation-associated RNA; PTBP1, polypyrimidine tract binding protein 1; hnRNP-K, heterogeneous nuclear ribonucleoprotein K; NCL, nucleolin; DISC1, disrupted in schizophrenia 1; EZH2, enhancer of zeste 2 polycomb repressive complex 2 subunit; PRC2, proteasome component 2.

function. For example, the magnitude of the action potential can be affected by changing the subunit stoichiometry of potassium channels. Potassium voltage-gated channel subfamily A member 2 (*KCNA2*) is a major potassium channel subunit, and its expression is regulated by overlapping antisense RNA when facing peripheral nerve injury or neuralgia. In a healthy rat model, *KCNA2* antisense (*KCNA2-AS*) is expressed in few dorsal root ganglia (DRG) neurons (<20% of DRG), and *KCNA2* is expressed in most DRG neurons. However, in the face of peripheral nerve injury, a large amount of *KCNA2-AS* is induced by transcription factor myeloid zinc finger 1 in DRG neurons. *In vivo* and *in vitro* experiments have revealed that the overexpression of *KCNA2-AS* could decrease KCNA2 mRNA and protein content. The mechanism may be that it binds with competing DNA- or RNA-binding factors, thereby, regulating the expression of *KCNA2* (Zhao et al., 2013). This regulation alters the function of DRG neurons. Therefore, *KCNA2-AS* can respond to peripheral nerve damage by altering synaptic plasticity. The lncRNA *NEAT1* provides a scaffolding function in the nucleus that releases regulatory proteins after neuronal activation to finetune excitatory responses and correlate with pathological seizure states. In addition, downregulation of lncRNA *NEAT1* results in changes in the expression of multiple gene transcripts involved in ion channel function following neuronal activation (Barry et al., 2017).

The BDNF is a class of secreted growth factors that are essential for neuronal growth, synaptic plasticity, and participation in learning and memory processes (Leal et al., 2014; Ninan, 2014; Zagrebelsky and Korte, 2014). The BDNF is an important growth factor, not only being regulated by miRNA, but also regulated by lncRNA. Dissection of the human BDNF locus revealed that antisense transcription of the *BDNF* gene from anti-BDNF (*BDNF-AS*, also annotated as *BDNF-OS*) in the brain takes place to form dsRNA duplexes with BDNF mRNA. Inhibition of *BDNF-AS* by antagoNAT *in vivo* or siRNA *in vitro* both resulted in increased *BDNF* mRNA and protein levels, which promoted neurite outgrowth and maturation, suggesting that anti-BDNF plays an important role in *BDNF* function (Lipovich et al., 2012; Modarresi et al., 2012). Further studies revealed that *BDNF-AS* inhibits *BDNF* transcription by recruiting the zeste homolog 2 (EZH2) and polycomb suppression complex 2 (PRC2) enhancers to the *BDNF* promoter region (Pruunsild et al., 2007).

The lncRNA *Gomafu* is widely expressed in the brain, (Mercer et al., 2008) and has recently been shown to modulate alternative splicing of the schizophrenia-associated genes *DISC1* and *ERBB4* (Barry et al., 2014). Since deletion of *Erbb4* in mice enhances LTP in the hippocampus, it is important to determine whether *Gomafu*-regulated splice isoforms affect normal synaptic plasticity (Pitcher et al., 2008; Shamir et al., 2012). In addition, lncRNA *MALAT1* mediates spinal cord maturation and synapse formation by recruiting splicing factors. In cultured hippocampal neurons, knock-down of Malat1 reduces synaptic density, whereas overexpression leads to autonomous increase in cells at synaptic density (Bernard et al., 2010).

These findings suggest that lncRNAs can regulate the synaptic plasticity, and thus, the fidelity of cognitive and memory

processes by dynamically monitoring and integrating multiple transcriptional and post-transcriptional events.

THE ROLE OF LNCRNAS IN NEURODEGENERATIVE DISEASES

The lncRNAs have broad-spectrum functions in the normal brain development and function maintenance. It is not surprising that dysregulation of lncRNAs might play a pivotal role in neurodegenerative diseases. This view has been reinforced by the identification of a growing number of lncRNAs that directly regulate the expression of genes associated with neurodegenerative disorders, including AD, PD, HD, respectively.

The Correlation of lncRNAs and Alzheimer's Disease

The AD is a neurodegenerative disease with cognitive decline as the main clinical manifestation. Its pathological mechanism has not been completely understood to date. The main pathological characteristic of AD is the progressive disease of neurons accompanied by the loss of neurons, senile plaques (SPs), and neurofibrillary tangles (Dewachter et al., 2000; Ghosal et al., 2009). Senile plaques mainly consist of β-amyloid (Aβ). Amyloid precursor protein was abnormally cleaved by β-amyloid precursor protein cleaving enzyme 1 (BACE1) to produce Aβ. The excessive accumulation of Aβ produces neurotoxicity. The *BACE1-AS* is an lncRNA transcribed from the antisense strand of the *BACE1* gene, which is highly expressed in the brain of patients with AD. A study revealed that the expression of *BACE1-AS* was significantly increased under extracellular stimulation, such as $A\beta_{42}$ (Faghihi et al., 2008). However, *BACE1-AS* does not inhibit the transcription of mRNA by forming dimers through binding with the coding genes as general natural antisense transcripts (NATs). In contrast, *BACE1-AS* covers the binding site of *miR-485-5p* on *BACE1* mRNA, thereby, silencing the inhibition of *miR-485-5p* on BACE1 mRNA and increasing the stability of *BACE1* mRNA (Faghihi et al., 2010). This leads to the production of more $A\beta_{42}$ and an increase in the formation of SPs in the brain in AD patients, aggravating the development of the disease. Feng et al. found that the level of the *BACE1* is increased in the plasma of AD patients and that it has a high specificity (88%) for AD, indicating *BACE1* may be a potential candidate biomarker to predict AD (Feng et al., 2018). Recently, Yang et al., investigated the hippocampal expression patterns of dysregulated lncRNAs in a rat model of AD through microarray (Yang et al., 2017). The authors identified a total of 315 lncRNAs and 311 mRNAs significantly dysregulated in the AD model, such as *BC158567, MRAK050857, Mrak033976*, etc. These differentially expressed genes are involved in synaptic transmission regulation, cholinergic regulation, and CNS neuron differentiation, all of which are important in learning and memory, as well as the development of AD. Furthermore, the dysregulated lncRNAs in the AD group are involved in the neuroactive ligand–receptor interaction, the renin–angiotensin system, axon guidance, and the PI3K–Akt, MAPK, and mTOR signaling pathways. Among these, the PI3K–Akt, MAPK, and mTOR signaling pathways play important roles in long-term learning and memory.

The BC200 RNA is selectively located in neuronal synapses, which regulates the synthesis of proteins surrounding the postsynaptic membrane. Mus et al. revealed that the expression of *BC200* RNA was significantly downregulated in the prefrontal cortical area in normal elderly subjects (49–86 years old, by autopsy), and was significantly increased in the brain of AD patients. Further studies have revealed that the distribution of *BC200* RNA in the brain of AD patients has changed. The *BC200* RNA in the brain of AD patients is located in the perinuclear area in the cluster, instead of the synaptic terminals. Hence, it loses its regulatory function on proteins surrounding the postsynaptic membrane. The overexpression and error spatial localization of *BC200* RNA may excessively inhibit the synthesis of cytoplasmic proteins, thereby, aggravating the pathological changes of AD (Mus et al., 2007).

The *17A* is also an lncRNA that has been recently discovered. It is located in intron 3 of the G protein-coupled receptor-51 (*GRP51*) gene, regulates the production of *GRP51* variable transcript, and inhibits the canonical transcription of GAGA(B2) receptors, thereby, significantly affecting the GABA-B signaling pathway. The inflammatory reaction in the brain in AD patients can activate the expression of *17A*. This increases the secretion of Aβ and the Aβ42/Aβ40 ratio, aggravating the progress of the disease (Massone et al., 2011). Another lncRNA *51A* overlapping with *SORL1* (antisense) was also shown to affect Aβ formation and upregulated in AD (Ciarlo et al., 2013).

In addition, neurotrophic factors (NTFs) play an important role in maintaining nervous system function. The expression level of *BDNF* is significantly changed in neurodegenerative diseases, psychosis, and neurodevelopmental disorders (Lu et al., 2013, 2014; Song et al., 2015). The inhibition of *BDNF-AS* expression can increase the expression of BDNF in the brain, which has a wide prospect for the treatment of neurodegenerative diseases. Glial cell-derived neurotrophic factor opposite strand (*GDNFOS*) is transcribed from the antisense strand of the GDNF gene. A study revealed that there was a difference in the expression of GDNFOS subunit in AD brains compared with normal brains, but the underlying mechanisms remain unknown at present (Airavaara et al., 2011). Furthermore, another study found that *Sox2OT* and *1810014B01Rik* could serve as biomarkers in the early and late stages of neurodegenerative diseases (Arisi et al., 2011). Tremendous efforts have been put into their translational applications by identifying specific lncRNAs that are changed in Alzheimer's disease in order to provide biomarkers and better illustrate molecular pathways.

The Correlation Between lncRNAs and Parkinson's Disease

Parkinson's disease (PD) is a neurodegenerative disease that commonly occurs in the elderly. Its pathological characteristic is the degeneration of dopaminergic neurons in the substantia nigra-striatum system, which decreases dopamine secretion, resulting in a series of extrapyramidal responses. The maintenance of mitochondrial homeostasis plays an important

role in the progression of PD (Moreira et al., 2010; Jin et al., 2014; Luo et al., 2015). Gene studies revealed that PD family-related genes such as *α-synuclein, parkin*, PTEN-induced putative kinase 1 (*PINK1*), *DJ-1,* and leucine-rich repeat kinase 2 (*LRRK2*) were closely related to mitochondrial function (Puspita et al., 2017). Endogenous *PINK1* is localized in the mitochondrial membrane and plays an important role in energy metabolism in neurons and muscle cells. In addition, *PINK1* can also inhibit the release of cytochrome C from mitochondria and decrease the occurrence of apoptosis. The inhibition or overexpression of *PINK1* can lead to abnormal mitochondrial morphology and affect the release of dopamine, resulting in behavior defects (Petit et al., 2005). Study found that lncRNA *NEAT1* was significantly upregulated in the midbrain of PD mice, and that lncRNA *NEAT1* promoted MPTP-induced autophagy in PD by stabilizing PINK1 protein (Yan et al., 2018). Noncoding antisense PTEN-induced putative kinase 1 (*naPINK1*) is an lncRNA transcribed from the antisense strand of the *PINK1* gene, which can stabilize the expression of the *PINK1* variable transcript *svPINK1*. The silencing of *naPINK1* leads to the decrease in *svPINK1* in neurons. This suggests that the PD process can be improved by regulating the *PINK1* locus (Scheele et al., 2007).

Ubiquitin carboxy-terminal hydrolase L1 (*Uchl1)* is a neuron-restricted protein acting as a de-ubiquitinating enzyme or a monoubiquitin stabilizer. The *UCHL1* gene mutations have been discovered to be related to familial PD and the oxidative inactivation of Uchl1 protein has been reported in PD and AD brains (Choi et al., 2004). The *Uchl1-AS* is a nuclear-enriched lncRNA that is transcribed antisense to the mouse *Uchl1*. The *Uchl1-AS* increases the protein synthesis of UCHL1 at the post-transcriptional level and then regulates the progression of PD (Carrieri et al., 2015). Furthermore, the activity of *Uchl1-AS* is controlled by the signaling pathway. The *Uchl1* mRNA is mainly localized in the cytoplasm, while *Uchl1-AS* is abundant in the nucleus of dopaminergic neurons. Interestingly, the mTOR inhibitor-Rapamycin treatment resulted in the induction of Uchl1 protein by association of shuttling *Uchl1-AS* from the nucleus to the cytoplasm, suggesting that the interaction between Uchl1–ncRNA–mTOR may be critical for PD development (Carrieri et al., 2012; Vucićević et al., 2014).

Correlation Between lncRNAs and Huntington's Disease

Huntington's disease (HD) is a rare autosomal dominant inherited neurodegenerative disease. Its pathological change is the loss of neurons in the striatum and cortex in brain. There is a CAG repetitive sequence in exon 1 of its pathogenic gene huntingtin (*HTT*), which encodes polyglutamine. The excessive repeat amplification of CAG in the gene-coding region induces the prolongation of the polyglutamine chain in protein, thereby inducing lesions (Aziz et al., 2011; De Souza and Leavitt, 2015). The *HTT* can regulate the nuclear translocation of transcription inhibiting factor RE-1 silencing transcription factor (REST), which is also known as neuron-restrictive silencer factor (NRSF)(Shimojo, 2008). Mutation in HTT leads to the abnormal nuclear/interstitial translocation of REST/NRSF, thereby, inducing the abnormal expression of the downstream target gene of REST/NRSF, including PCGs and ncRNA. Through studies on the expression profile of brain tissue in HD patients, Johnson et al. revealed that the expression of *HAR1* lncRNA in striatum decreased significantly, and the main cause was that REST inhibited *HAR1* transcription by locating in the *HAR1* locus *via* the specific DNA regulatory element (Johnson et al., 2010). Chung et al. discovered an lncRNA-*HTTAS* transcribed from the antisense strand of *HTT*. This has two types of transcripts: *HTTAS-v1* (exons 1 and 3) and *HTTAS-v2* (exons 2 and 3), where exon 1 contains repeated gene loci. Cell level verification results revealed that the overexpression of *HTTAS-v1* could significantly decrease the transcription level of *HTT*, while *HTT* transcription level significantly increased after *HTTAS-v1* was disrupted by siRNA. Furthermore, *HTTAS-v1* expression was found to be downregulated in frontal cortex of HD patients, and this strongly suggests that the change in *HTTAS* may play a certain role in the progress of HD (Chung et al., 2011).

The lncRNA *TUG1* has been shown to be a direct downstream target of p53, which is known to be upregulated in HD itself. Therefore, *TUG1* appears to be a pro-survival factor in neurons. The upregulation we observed in HD - probably through p53 activation–actually acts against mutHTT cytotoxicity (Khalil et al., 2009). The *NEAT1* is a nuclear-enrich lncRNA that is essential for the formation and maintenance of paraspeckles, which are subnuclear bodies found in mammalian cells (Clemson et al., 2009). Sunwoo et al. found that the levels of *NEAT1* were increased in R6/2 mice and HD patients. In order to determine the biological effects of *NEAT1* on neuronal survival, the authors transfected neuro2A cells with the *NEAT1* short isotype vector and subjected them to H2O2-induced damage. The *NEAT1* transfected cells showed enhanced viability under oxidative stress, confirming that upregulation of *NEAT1* contributes to neuroprotective mechanisms against neuronal damage rather than pathology of neurodegenerative diseases (Sunwoo et al., 2017). It has been reported that *MEG3* is a REST target and is dynamically expressed during neurodevelopment and associated with PRC2 chromatin regulators. This supporting *MEG3* might be participating in chromatin regulation, noncoding transcription, and neurodevelopment in HD (Johnson, 2012). Although functional studies on *DGCR5* have not been performed, the fact that this neuro-specific disease-related transcript is directly targeted by REST suggests that it has important functions in the human nervous system (Sutherland et al., 1996; Johnson, 2012).

Summary of lncRNAs in Neurodegenerative Diseases

An increasing number of studies report on lncRNAs as being implicated in neurodegenerative diseases, including AD, PD, and HD (**Table 2**).

The roles of *BACE1-AS* lncRNA have been widely defined in AD. The *BACE1-AS* levels are upregulated in AD brains,

TABLE 2 | Dysregulated lncRNAs in neurodegenerative diseases.

lncRNAs	Direction of change	Relative disease	Biological function	References
Sox2OT	Up	AD, PD	Regulate cotranscribed *Sox2* gene expression to down neurogenesis.	Arisi et al., 2011; Shimozaki, 2014
BC200	up(Soma) down(Dentritic)	AD, PD	Modulate local proteins in postsynaptic dendritic micro-domains to maintenance of long-term synaptic plasticity.	Lukiw et al., 1992; Mus et al., 2007; Vucićević et al., 2014; Luo and Chen, 2016
BACE1-AS	up	AD	Increase *BACE1* mRNA stability resulting in additional Aβ42 generation through a post-transcriptional feed-forward mechanism.	Faghihi et al., 2008; Liu et al., 2014
NAT-Rad18	up	AD	Down the expression of DNA repair protein Rad18 resulting in the neuron being more sensitive to apoptosis.	Parenti et al., 2007
NDM29	up	AD	Promotes Aβ secretion with increased Aβ42/ Aβ40 ratio, expression induced by inflammatory processes.	Massone et al., 2012
51A	up	AD	Promotes the alternative splicing of *SORL1* and increases Aβ formation.	Ciarlo et al., 2013; Tan et al., 2013; Luo and Chen, 2016
17A	up	AD	Impair GABAB signaling pathway by decreasing *GABAB R2* transcription.	Massone et al., 2011
GDNFOS	Dysregulated/ differences in tissue expression patterns	AD	Modulate the expression of endogenous *GDNF* in human brain.	Airavaara et al., 2011
naPINK1	up	PD	Stabilize the *svPINK1,* resulting in disturbed mitochondrial respiratory chain, and then increase the sensitivity to apoptosis.	Chiba et al., 2009; Sai et al., 2012
PINK1-AS	-	PD	Positively regulates the stability of *svPINK1* transcript.	Scheele et al., 2007
UCHL1-AS	-	PD	Positively regulates *UCHL1* mRNA translation.	Carrieri et al., 2012, 2015
HAR1	down	HD	Necessary for retinal development, the function with HD not be mentioned.	Johnson et al., 2010; Johnson, 2012
HTT-AS	down	HD	*HTTAS-v1* specifically reduces endogenous *HTT* transcript levels.	Chung et al., 2011
MEG3	down	HD	Binds the PCR2 epigenetic silencing complex.	Johnson, 2012

AD, Alzheimer's disease; PD, Parkinson's disease; HD, Huntington's disease; Sox2OT, Sox2 overlapping transcript; BACE1-AS, β-site amyloid precursor protein cleaving enzyme 1 antisense; GDNFOS, glial cell derived neurotrophic factor opposite strand; HAR1, human accelerated region 1; HTT-AS, Huntingtin antisense; PINK1-AS, PTEN induced putative kinase 1 antisense; UCHL1-AS, ubiquitin C-terminal hydrolase L1 antisense; MEG3, maternally expressed 3; NDM29, Neuroblastoma Differentiation Marker 29.

where *BACE1-AS* acts by stabilizing BACE1 mRNA, thereby, increasing BACE1 protein content and Aβ42 formation. While lncRNA *BC200, 17A, BC158567, MRAK050857, Mrak033976, BDNF-AS, Sox2OT,* and *1810014B01Rik* are also involved in AD. In PD, the lncRNA *UCHL1-AS1* acts by directly promoting translation of UCHL1 protein leading to perturbation of the ubiquitin–proteasome system. Different lncRNAs, such as *naPINK1, NEAT1 PINK1-AS, BC200,* and *Sox2OT*, were found to be dysregulated in their expression also in PD. Several studies reported altered expression levels of known lncRNAs *HTT-AS, TUG1, NEAT1, MEG3,* and *DGCR5* in the brains of HD patients. The emerging role of lncRNAs in neurodegenerative diseases suggests that their dysregulation may trigger neuronal death through an unexplored RNA-based regulatory mechanism that needs to be further investigated.

CHALLENGES AND PERSPECTIVES

With the continuous deepening of gene regulation research and the emergence of more biological methods, lncRNA function and mechanism will be further elucidated.

This relatively poorly characterized class of RNAs, with little or no coding capacity, has been implicated in the growth and development of the nervous system, the differentiation of neurons, synaptic plasticity, and the occurrence and progress of many diseases. Although many studies have been performed in clinical patients using various disease models, the exact role and impact of lncRNAs in disease pathogenesis still remain obscure. At present, there are still challenges for our understanding of lncRNAs.

Our lack of understanding of the molecular mechanisms of lncRNA action makes it particularly difficult for us to recognize the biological function of lncRNA. As we move forward from the annotation of lncRNAs to more emphasis on molecular function and biology, we still do not fully understand the biological significance of lncRNAs as a group. We need better tools to track lncRNA localization across the genome, monitor lncRNA interactions with proteins and nucleic acids, and determine the structure and elucidate the key structure–function relationships of lncRNAs, especially how they interact with proteins. Furthermore, unlike PCGs with systemic functional annotation systems, the lack of an annotation system for lncRNA function makes it difficult to evaluate computational algorithms for functional prediction. Finally, is it useful to find lncRNAs in neurodegenerative diseases? Two major long-term challenges in disease research are (a) the development of noninvasive diagnostic methods for

monitoring the progression of neurodegenerative diseases, and (b) the development of treatments to cure and reverse disease processes.

In fact, more and more attention has been paid to lncRNAs as potential targets for disease biomarkers or therapeutic strategies. Indeed, several commercial entities targeting lncRNAs (such as OPKO-CURNA and RaNA therapeutic agents) have been developed to design and develop oligonucleotide therapeutics for the treatment of neurodegenerative diseases (Qureshi and Mehler, 2013). Hereby, further investigation into the role of lncRNAs will provide a better understanding of how the brain functions and how diseases develop, and lead to greater insights into further therapeutic development for neurodegenerative diseases based on manipulations of lncRNA functions.

AUTHOR CONTRIBUTIONS

C-WW substantial contributions to the conception and design of the work, the acquisition, analysis, interpretation of data for the work. C-WW drafting the work and revising it critically for important intellectual content. A-SW final approval of the version to be published. TL and S-SZ agreement to be accountable for all aspects of the work in ensuring that questions related to the accuracy and integrity of any part of the work are appropriately investigated and resolved.

FUNDING

This work was supported by the National Natural Science Foundation of China (No. 81371199, 81771139).

REFERENCES

Airavaara, M., Pletnikova, O., Doyle, M. E., Zhang, Y. E., Troncoso, J. C., and Liu, Q. R. (2011). Identification of novel GDNF isoforms and cis-antisense GDNFOS gene and their regulation in human middle temporal gyrus of Alzheimer disease. *J. Biol. Chem.* 286, 45093–45102. doi: 10.1074/jbc.M111.310250

Amaral, P. P., Dinger, M. E., and Mattick, J. S. (2013). Non-coding RNAs in homeostasis, disease and stress responses: an evolutionary perspective. *Brief. Funct. Genomics* 12, 254–278. doi: 10.1093/bfgp/elt016

Antoniou, D., Stergiopoulos, A., and Politis, P. K. (2014). Recent advances in the involvement of long non-coding RNAs in neural stem cell biology and brain pathophysiology. *Front. Physiol.* 5: 155. doi: 10.3389/fphys.2014.00155

Arisi, I., D'Onofrio, M., Brandi, R., Felsani, A., Capsoni, S., Drovandi, G., et al. (2011). Gene expression biomarkers in the brain of a mouse model for Alzheimer's disease: mining of microarray data by logic classification and feature selection. *Biochim. Biophys. Acta* 24, 721–738. doi: 10.3233/JAD-2011-101881

Aziz, N. A., van Belzen, M. J., Coops, I. D., Belfroid, R. D., and Roos, R. A. (2011). Parent-of-origin differences of mutant HTT CAG repeat instability in Huntington's disease. *Eur. J. Med. Genet.* 54, e413–e418. doi: 10.1016/j.ejmg.2011.04.002

Azzalin, C. M., Reichenbach, P., Khoriauli, L., Giulotto, E., and Lingner, J. (2007). Telomeric repeat containing RNA and RNA surveillance factors at mammalian chromosome ends. *Science* 318, 798–801. doi: 10.1126/science.1147182

Babajko, S., Petit, S., Fernandes, I., Meary, F., LeBihan, J., Pibouin, L., et al. (2009). Msx1 expression regulation by its own antisense RNA: consequence on tooth development and bone regeneration. *Cells Tissues Organs* 189, 115–121. doi: 10.1159/000151748

Barry, G., Briggs, J. A., Hwang, D. W., Nayler, S. P., Fortuna, P. R., Jonkhout, N., et al. (2017). The long non-coding RNA NEAT1 is responsive to neuronal activity and is associated with hyperexcitability states. *Sci. Rep.* 7:40127. doi: 10.1038/srep40127

Barry, G., Briggs, J. A., Vanichkina, D. P., Poth, E. M., Beveridge, N. J., Ratnu, V. S., et al. (2014). The long non-coding RNA Gomafu is acutely regulated in response to neuronal activation and involved in schizophrenia-associated alternative splicing. *Mol. Psychiatry* 19, 486–494. doi: 10.1038/mp.2013.45

Bernard, D., Prasanth, K. V., Tripathi, V., Colasse, S., Nakamura, T., Xuan, Z., et al. (2010). A long nuclear-retained non-coding RNA regulates synaptogenesis by modulating gene expression. *EMBO J.* 29, 3082–3093. doi: 10.1038/emboj.2010.199

Bond, A. M., Vangompel, M. J., Sametsky, E. A., Clark, M. F., Savage, J. C., Disterhoft, J. F., et al. (2009). Balanced gene regulation by an embryonic brain ncRNA is critical for adult hippocampal GABA circuitry. *Nat. Neurosci.* 12, 1020–1027. doi: 10.1038/nn.2371

Braidotti, G., Baubec, T., Pauler, F., Seidl, C., Smrzka, O., Stricker, S., et al. (2004). The Air noncoding RNA: an imprinted cis-silencing transcript. *Cold Spring Harb. Symp. Quant. Biol.* 69, 55–66. doi: 10.1101/sqb.2004.69.55

Briggs, J. A., Wolvetang, E. J., Mattick, J. S., Rinn, J. L., and Barry, G. (2015). Mechanisms of long non-coding RNAs in mammalian nervous system development, plasticity, disease, and evolution. *Neuron* 88, 861–877. doi: 10.1016/j.neuron.2015.09.045

Carrieri, C., Cimatti, L., Biagioli, M., Beugnet, A., Zucchelli, S., Fedele, S., et al. (2012). Long non-coding antisense RNA controls Uchl1 translation through an embedded SINEB2 repeat. *Nature* 491, 454–457. doi: 10.1038/nature11508

Carrieri, C., Forrest, A. R., Santoro, C., Persichetti, F., Carninci, P., Zucchelli, S., et al. (2015). Expression analysis of the long non-coding RNA antisense to Uchl1 (AS Uchl1) during dopaminergic cells' differentiation *in vitro* and in neurochemical models of Parkinson's disease. *Front. Cell. Neurosci.* 9:114. doi: 10.3389/fncel.2015.00114

Cesana, M., Cacchiarelli, D., Legnini, I., Santini, T., Sthandier, O., Chinappi, M., et al. (2011). A long noncoding RNA controls muscle differentiation by functioning as a competing endogenous RNA. *Cell* 147, 358–369. doi: 10.1016/j.cell.2011.09.028

Chiba, M., Kiyosawa, H., Hiraiwa, N., Ohkohchi, N., and Yasue, H. (2009). Existence of Pink1 antisense RNAs in mouse and their localization. *Cytogenet. Genome Res.* 126, 259–270. doi: 10.1159/000251963

Choi, J., Levey, A. I., Weintraub, S. T., Rees, H. D., Gearing, M., Chin, L. S., et al. (2004). Oxidative modifications and down-regulation of ubiquitin carboxyl-terminal hydrolase L1 associated with idiopathic Parkinson's and Alzheimer's diseases. *J. Biol. Chem.* 279, 13256–13264. doi: 10.1074/jbc.M314124200

Chung, D. W., Rudnicki, D. D., Yu, L., and Margolis, R. L. (2011). A natural antisense transcript at the Huntington's disease repeat locus regulates HTT expression. *Hum. Mol. Genet.* 20, 3467–3477. doi: 10.1093/hmg/ddr263

Ciarlo, E., Massone, S., Penna, I., Nizzari, M., Gigoni, A., Dieci, G., et al. (2013). An intronic ncRNA-dependent regulation of SORL1 expression affecting Abeta formation is upregulated in post-mortem Alzheimer's disease brain samples. *Dis. Model. Mech.* 6, 424–433. doi: 10.1242/dmm.009761

Clemson, C. M., Hutchinson, J. N., Sara, S. A., Ensminger, A. W., Fox, A. H., Chess, A., et al. (2009). An architectural role for a nuclear noncoding RNA: NEAT1 RNA is essential for the structure of paraspeckles. *Mol. Cell* 33, 717–726. doi: 10.1016/j.molcel.2009.01.026

Colasante, G., Collombat, P., Raimondi, V., Bonanomi, D., Ferrai, C., Maira, M., et al. (2008). Arx is a direct target of Dlx2 and thereby contributes to the tangential migration of GABAergic interneurons. *J. Neurosci.* 28, 10674–10686. doi: 10.1523/JNEUROSCI.1283-08.2008

Coudert, A. E., Pibouin, L., Vi-Fane, B., Thomas, B. L., Macdougall, M., Choudhury, A., et al. (2005). Expression and regulation of the Msx1 natural antisense transcript during development. *Nucleic Acids Res.* 33, 5208–5218. doi: 10.1093/nar/gki831

De Souza, R. A., and Leavitt, B. R. (2015). Neurobiology of Huntington's disease. *Curr. Top. Behav. Neurosci.* 22: 81–100. doi: 10.1007/7854_2014_353

Dewachter, I., van Dorpe, J., Spittaels, K., Tesseur, I., Van Den Haute, C., Moechars, D., et al. (2000). Modeling Alzheimer's disease in transgenic mice: effect of age and of presenilin1 on amyloid biochemistry and pathology in APP/London mice. *Exp. Gerontol.* 35, 831–841. doi: 10.1016/S0531-5565(00)00149-2

Djebali, S., Davis, C. A., Merkel, A., Dobin, A., Lassmann, T., Mortazavi, A., et al. (2012). Landscape of transcription in human cells. *Nature* 489, 101–108. doi: 10.1038/nature11233

Faghihi, M. A., Modarresi, F., Khalil, A. M., Wood, D. E., Sahagan, B. G., Morgan, T. E., et al. (2008). Expression of a noncoding RNA is elevated in Alzheimer's disease and drives rapid feed-forward regulation of beta-secretase. *Nat. Med.* 14, 723–730. doi: 10.1038/nm1784

Faghihi, M. A., Zhang, M., Huang, J., Modarresi, F., Van der Brug, M. P., Nalls, M. A., et al. (2010). Evidence for natural antisense transcript-mediated inhibition of microRNA function. *Genome Biol.* 11:R56. doi: 10.1186/gb-2010-11-5-r56

Feng, L., Liao, Y. T., He, J. C., Xie, C. L., Chen, S. Y., Fan, H. H., et al. (2018). Plasma long non-coding RNA BACE1 as a novel biomarker for diagnosis of Alzheimer disease. *BMC Neurol.* 18:4. doi: 10.1186/s12883-017-1008-x

Ghosal, K., Vogt, D. L., Liang, M., Shen, Y., Lamb, B. T., and Pimplikar, S. W. (2009). Alzheimer's disease-like pathological features in transgenic mice expressing the APP intracellular domain. *Proc. Natl. Acad. Sci. U.S.A.* 106, 18367–18372. doi: 10.1073/pnas.0907652106

Goff, L. A., and Rinn, J. L. (2015). Linking RNA biology to lncRNAs. *Genome Res.* 25, 1456–1465. doi: 10.1101/gr.191122.115

Graff, J., and Mansuy, I. M. (2008). Epigenetic codes in cognition and behaviour. *Behav. Brain Res.* 192, 70–87. doi: 10.1016/j.bbr.2008.01.021

Guttman, M., Amit, I., Garber, M., French, C., Lin, M. F., Feldser, D., et al. (2009). Chromatin signature reveals over a thousand highly conserved large non-coding RNAs in mammals. *Nature* 458, 223–227. doi: 10.1038/nature07672

Hung, T., Wang, Y., Lin, M. F., Koegel, A. K., Kotake, Y., Grant, G. D., et al. (2011). Extensive and coordinated transcription of noncoding RNAs within cell-cycle promoters. *Nat. Genet.* 43, 621–629. doi: 10.1038/ng.848

Hutchinson, J. N., Ensminger, A. W., Clemson, C. M., Lynch, C. R., Lawrence, J. B., and Chess, A. (2007). A screen for nuclear transcripts identifies two linked noncoding RNAs associated with SC35 splicing domains. *BMC Genomics* 8:39. doi: 10.1186/1471-2164-8-39

Jiang, Y. H., Armstrong, D., Albrecht, U., Atkins, C. M., Noebels, J. L., Eichele, G., et al. (1998). Mutation of the Angelman ubiquitin ligase in mice causes increased cytoplasmic p53 and deficits of contextual learning and long-term potentiation. *Neuron* 21, 799–811. doi: 10.1016/S0896-6273(00)80596-6

Jin, H., Kanthasamy, A., Ghosh, A., Anantharam, V., Kalyanaraman, B., and Kanthasamy, A. G. (2014). Mitochondria-targeted antioxidants for treatment of Parkinson's disease: preclinical and clinical outcomes. *Biochim. Biophys. Acta* 1842, 1282–1294. doi: 10.1016/j.bbadis.2013.09.007

Johnson, R. (2012). Long non-coding RNAs in Huntington's disease neurodegeneration. *Neurobiol. Dis.* 46, 245–254. doi: 10.1016/j.nbd.2011.12.006

Johnson, R., Richter, N., Jauch, R., Gaughwin, P. M., Zuccato, C., Cattaneo, E., et al. (2010). Human accelerated region 1 noncoding RNA is repressed by REST in Huntington's disease. *Physiol. Genomics* 41, 269–274. doi: 10.1152/physiolgenomics.00019.2010

Kazemzadeh, M., Safaralizadeh, R., and Orang, A. V. (2015). LncRNAs: emerging players in gene regulation and disease pathogenesis. *J. Genet.* 94, 771–784. doi: 10.1007/s12041-015-0561-6

Khalil, A. M., Guttman, M., Huarte, M., Garber, M., Raj, A., Rivea Morales, D., et al. (2009). Many human large intergenic noncoding RNAs associate with chromatin-modifying complexes and affect gene expression. *Proc. Natl. Acad. Sci. U.S.A.* 106, 11667–11672. doi: 10.1073/pnas.0904715106

Klattenhoff, C. A., Scheuermann, J. C., Surface, L. E., Bradley, R. K., Fields, P. A., Steinhauser, M. L., et al. (2013). Braveheart, a long noncoding RNA required for cardiovascular lineage commitment. *Cell* 152, 570–583. doi: 10.1016/j.cell.2013.01.003

Kondrashov, A. V., Kiefmann, M., Ebnet, K., Khanam, T., Muddashetty, R. S., and Brosius, J. (2005). Inhibitory effect of naked neural BC1 RNA or BC200 RNA on eukaryotic *in vitro* translation systems is reversed by poly(A)-binding protein (PABP). *J. Mol. Biol.* 353, 88–103. doi: 10.1016/j.jmb.2005.07.049

Leal, G., Comprido, D., and Duarte, C. B. (2014). BDNF-induced local protein synthesis and synaptic plasticity. *Neuropharmacology* 76(Pt C), 639–656. doi: 10.1016/j.neuropharm.2013.04.005

Lee, S., Seo, H. H., Lee, C. Y., Lee, J., Shin, S., Kim, S. W., et al. (2017). Human long noncoding RNA regulation of stem cell potency and differentiation. *Stem Cells Int.* 2017: 6374504. doi: 10.1155/2017/6374504

Lin, N., Chang, K. Y., Li, Z., Gates, K., Rana, Z. A., Dang, J., et al. (2014). An evolutionarily conserved long noncoding RNA TUNA controls pluripotency and neural lineage commitment. *Mol. Cell* 53, 1005–1019. doi: 10.1016/j.molcel.2014.01.021

Lipovich, L., Dachet, F., Cai, J., Bagla, S., Balan, K., Jia, H., et al. (2012). Activity-dependent human brain coding/noncoding gene regulatory networks. *Genetics* 192, 1133–1148. doi: 10.1534/genetics.112.145128

Liu, T., Huang, Y., Chen, J., Chi, H., Yu, Z., Wang, J., et al. (2014). Attenuated ability of BACE1 to cleave the amyloid precursor protein via silencing long noncoding RNA BACE1AS expression. *Mol. Med. Rep.* 10, 1275–1281. doi: 10.3892/mmr.2014.2351

Lu, B., Nagappan, G., Guan, X., Nathan, P. J., and Wren, P. (2013). BDNF-based synaptic repair as a disease-modifying strategy for neurodegenerative diseases. *Nat. Rev. Neurosci.* 14, 401–416. doi: 10.1038/nrn3505

Lu, B., Nagappan, G., and Lu, Y. (2014). BDNF and synaptic plasticity, cognitive function, and dysfunction. *Handb. Exp. Pharmacol.* 220: 223–250. doi: 10.1007/978-3-642-45106-5_9

Lukiw, W. J., Handley, P., Wong, L., and Crapper McLachlan, D. R. (1992). BC200 RNA in normal human neocortex, non-Alzheimer dementia (NAD), and senile dementia of the Alzheimer type (AD). *Neurochem. Res.* 17, 591–597. doi: 10.1007/BF00968788

Luo, Q., and Chen, Y. (2016). Long noncoding RNAs and Alzheimer's disease. *Clin. Interv. Aging* 11: 867–872. doi: 10.2147/CIA.S107037

Luo, Y., Hoffer, A., Hoffer, B., and Qi, X. (2015). Mitochondria: a therapeutic target for Parkinson's disease?. *Int. J. Mol. Sci.* 16, 20704–20730. doi: 10.3390/ijms160920704

Lv, J., Liu, H., Huang, Z., Su, J., He, H., Xiu, Y., et al. (2013). Long non-coding RNA identification over mouse brain development by integrative modeling of chromatin and genomic features. *Nucleic Acids Res.* 41, 10044–10061. doi: 10.1093/nar/gkt818

Maag, J. L., Panja, D., Sporild, I., Patil, S., Kaczorowski, D. C., Bramham, C. R., et al. (2015). Dynamic expression of long noncoding RNAs and repeat elements in synaptic plasticity. *Front. Neurosci.* 9: 351. doi: 10.3389/fnins.2015.00351

Mabb, A. M., Judson, M. C., Zylka, M. J., and Philpot, B. D. (2011). Angelman syndrome: insights into genomic imprinting and neurodevelopmental phenotypes. *Trends Neurosci.* 34, 293–303. doi: 10.1016/j.tins.2011.04.001

Magistri, M., Faghihi, M. A., St Laurent, G. III., and Wahlestedt, C. (2012). Regulation of chromatin structure by long noncoding RNAs: focus on natural antisense transcripts. *Trends Genet.* 28, 389–396. doi: 10.1016/j.tig.2012.03.013

Massone, S., Ciarlo, E., Vella, S., Nizzari, M., Florio, T., Russo, C., et al. (2012). NDM29, a RNA polymerase III-dependent non coding RNA, promotes amyloidogenic processing of APP and amyloid beta secretion. *Biochim. Biophys. Acta* 1823, 1170–1177. doi: 10.1016/j.bbamcr.2012.05.001

Massone, S., Vassallo, I., Fiorino, G., Castelnuovo, M., Barbieri, F., Borghi, R., et al. (2011). 17A, a novel non-coding RNA, regulates GABA B alternative splicing and signaling in response to inflammatory stimuli and in Alzheimer disease. *Neurobiol. Dis.* 41, 308–317. doi: 10.1016/j.nbd.2010.09.019

Mercer, T. R., Dinger, M. E., Sunkin, S. M., Mehler, M. F., and Mattick, J. S. (2008). Specific expression of long noncoding RNAs in the mouse brain. *Proc. Natl. Acad. Sci. U.S.A.* 105, 716–721. doi: 10.1073/pnas.0706729105

Mercer, T. R., Qureshi, I. A., Gokhan, S., Dinger, M. E., Li, G., Mattick, J. S., et al. (2010). Long noncoding RNAs in neuronal-glial fate specification and oligodendrocyte lineage maturation. *BMC Neurosci.* 11:14. doi: 10.1186/1471-2202-11-14

Mercer, T. R., Wilhelm, D., Dinger, M. E., Solda, G., Korbie, D. J., Glazov, E. A., et al. (2011). Expression of distinct RNAs from 3' untranslated regions. *Nucleic Acids Res.* 39, 2393–2403. doi: 10.1093/nar/gkq1158

Modarresi, F., Faghihi, M. A., Lopez-Toledano, M. A., Fatemi, R. P., Magistri, M., Brothers, S. P., et al. (2012). Inhibition of natural antisense transcripts *in vivo* results in gene-specific transcriptional upregulation. *Nat. Biotechnol.* 30, 453–459. doi: 10.1038/nbt.2158

Moreira, P. I., Zhu, X., Wang, X., Lee, H. G., Nunomura, A., Petersen, R. B., et al. (2010). Mitochondria: a therapeutic target in neurodegeneration. *Biochim. Biophys. Acta* 1802, 212–220. doi: 10.1016/j.bbadis.2009.10.007

Mus, E., Hof, P. R., and Tiedge, H. (2007). Dendritic BC200 RNA in aging and in Alzheimer's disease. *Proc. Natl. Acad. Sci. U.S.A.* 104, 10679–10684. doi: 10.1073/pnas.0701532104

Nagano, T., and Fraser, P. (2011). No-nonsense functions for long noncoding RNAs. *Cell* 145, 178–181. doi: 10.1016/j.cell.2011.03.014

Nakagawa, S., Ip, J. Y., Shioi, G., Tripathi, V., Zong, X., Hirose, T., et al. (2012). Malat1 is not an essential component of nuclear speckles in mice. *RNA* 18, 1487–1499. doi: 10.1261/rna.033217.112

Ng, S. Y., Bogu, G. K., Soh, B. S., and Stanton, L. W. (2013). The long noncoding RNA RMST interacts with SOX2 to regulate neurogenesis. *Mol. Cell* 51, 349–359. doi: 10.1016/j.molcel.2013.07.017

Ng, S. Y., Johnson, R., and Stanton, L. W. (2012). Human long non-coding RNAs promote pluripotency and neuronal differentiation by association with chromatin modifiers and transcription factors. *EMBO J.* 31, 522–533. doi: 10.1038/emboj.2011.459

Ninan, I. (2014). Synaptic regulation of affective behaviors; role of BDNF. *Neuropharmacology* 76(Pt C), 684–695. doi: 10.1016/j.neuropharm.2013.04.011

Okazaki, Y., Furuno, M., Kasukawa, T., Adachi, J., Bono, H., Kondo, S., et al. (2002). Analysis of the mouse transcriptome based on functional annotation of 60,770 full-length cDNAs. *Nature* 420, 563–573. doi: 10.1038/nature01266

Pang, K. C., Frith, M. C., and Mattick, J. S. (2006). Rapid evolution of noncoding RNAs: lack of conservation does not mean lack of function. *Trends Genet.* 22, 1–5. doi: 10.1016/j.tig.2005.10.003

Panja, D., and Bramham, C. R. (2014). BDNF mechanisms in late LTP formation: a synthesis and breakdown. *Neuropharmacology* 76(Pt C), 664–676. doi: 10.1016/j.neuropharm.2013.06.024

Parenti, R., Paratore, S., Torrisi, A., and Cavallaro, S. (2007). A natural antisense transcript against Rad18, specifically expressed in neurons and upregulated during beta-amyloid-induced apoptosis. *Eur. J. Neurosci.* 26, 2444–2457. doi: 10.1111/j.1460-9568.2007.05864.x

Pauler, F. M., Stricker, S. H., Warczok, K. E., and Barlow, D. P. (2005). Long-range DNase I hypersensitivity mapping reveals the imprinted Igf2r and Air promoters share cis-regulatory elements. *Genome Res.* 15, 1379–1387. doi: 10.1101/gr.3783805

Peden, A. H., and Ironside, J. W. (2012). Molecular pathology in neurodegenerative diseases. *Curr. Drug Targets* 13, 1548–1559. doi: 10.2174/138945012803530134

Petit, A., Kawarai, T., Paitel, E., Sanjo, N., Maj, M., Scheid, M., et al. (2005). Wild-type PINK1 prevents basal and induced neuronal apoptosis, a protective effect abrogated by Parkinson disease-related mutations. *J. Biol. Chem.* 280, 34025–34032. doi: 10.1074/jbc.M505143200

Pitcher, G. M., Beggs, S., Woo, R. S., Mei, L., and Salter, M. W. (2008). ErbB4 is a suppressor of long-term potentiation in the adult hippocampus. *Neuroreport* 19, 139–143. doi: 10.1097/WNR.0b013e3282f3da10

Ponting, C. P., Oliver, P. L., and Reik, W. (2009). Evolution and functions of long noncoding RNAs. *Cell* 136, 629–641. doi: 10.1016/j.cell.2009.02.006

Pruunsild, P., Kazantseva, A., Aid, T., Palm, K., and Timmusk, T. (2007). Dissecting the human BDNF locus: bidirectional transcription, complex splicing, and multiple promoters. *Genomics* 90, 397–406. doi: 10.1016/j.ygeno.2007.05.004

Puspita, L., Chung, S. Y., and Shim, J. W. (2017). Oxidative stress and cellular pathologies in Parkinson's disease. *Mol. Brain* 10:53. doi: 10.1186/s13041-017-0340-9

Quan, Z., Zheng, D., and Qing, H. (2017). Regulatory roles of long non-coding RNAs in the central nervous system and associated neurodegenerative diseases. *Front. Cell. Neurosci.* 11:175. doi: 10.3389/fncel.2017.00175

Qureshi, I. A., Mattick, J. S., and Mehler, M. F. (2010). Long non-coding RNAs in nervous system function and disease. *Brain Res.* 1338c, 20–35. doi: 10.1016/j.brainres.2010.03.110

Qureshi, I. A., and Mehler, M. F. (2013). Long non-coding RNAs: novel targets for nervous system disease diagnosis and therapy. *Neurotherapeutics* 10, 632–646. doi: 10.1007/s13311-013-0199-0

Rackham, O., Shearwood, A. M., Mercer, T. R., Davies, S. M., Mattick, J. S., and Filipovska, A. (2011). Long noncoding RNAs are generated from the mitochondrial genome and regulated by nuclear-encoded proteins. *RNA* 17, 2085–2093. doi: 10.1261/rna.029405.111

Ramos, A. D., Attenello, F. J., and Lim, D. A. (2016). Uncovering the roles of long noncoding RNAs in neural development and glioma progression. *Neurosci. Lett.* 625, 70–79. doi: 10.1016/j.neulet.2015.12.025

Rinn, J. L., Kertesz, M., Wang, J. K., Squazzo, S. L., Xu, X., Brugmann, S. A., et al. (2007). Functional demarcation of active and silent chromatin domains in human HOX loci by noncoding RNAs. *Cell* 129, 1311–1323. doi: 10.1016/j.cell.2007.05.022

Riva, P., Ratti, A., and Venturin, M. (2016). The Long Non-coding RNAs in neurodegenerative diseases: novel mechanisms of pathogenesis. *Curr. Alzheimer Res.* 13, 1219–1231. doi: 10.2174/1567205013666160622112234

Roberts, T. C., Morris, K. V., and Wood, M. J. (2014). The role of long non-coding RNAs in neurodevelopment, brain function and neurological disease. *Philos. Trans. R. Soc. Lond. B Biol. Sci.* 369:20130507. doi: 10.1098/rstb.2013.0507

Sai, Y., Zou, Z., Peng, K., and Dong, Z. (2012). The Parkinson's disease-related genes act in mitochondrial homeostasis. *Neurosci. Biobehav. Rev.* 36, 2034–2043. doi: 10.1016/j.neubiorev.2012.06.007

Sasaki, Y. T., Ideue, T., Sano, M., Mituyama, T., and Hirose, T. (2009). MENepsilon/beta noncoding RNAs are essential for structural integrity of nuclear paraspeckles. *Proc. Natl. Acad. Sci. U.S.A.* 106, 2525–2530. doi: 10.1073/pnas.0807899106

Sauvageau, M., Goff, L. A., Lodato, S., Bonev, B., Groff, A. F., Gerhardinger, C., et al. (2013). Multiple knockout mouse models reveal lincRNAs are required for life and brain development. *Elife* 2: e01749. doi: 10.7554/eLife.01749

Scheele, C., Petrovic, N., Faghihi, M. A., Lassmann, T., Fredriksson, K., Rooyackers, O., et al. (2007). The human PINK1 locus is regulated *in vivo* by a non-coding natural antisense RNA during modulation of mitochondrial function. *BMC Genomics* 8:74. doi: 10.1186/1471-2164-8-74

Shamir, A., Kwon, O. B., Karavanova, I., Vullhorst, D., Leiva-Salcedo, E., Janssen, M. J., et al. (2012). The importance of the NRG-1/ErbB4 pathway for synaptic plasticity and behaviors associated with psychiatric disorders. *J. Neurosci.* 32, 2988–2997. doi: 10.1523/JNEUROSCI.1899-11.2012

Shimojo, M. (2008). Huntingtin regulates RE1-silencing transcription factor/neuron-restrictive silencer factor (REST/NRSF) nuclear trafficking indirectly through a complex with REST/NRSF-interacting LIM domain protein (RILP) and dynactin p150 Glued. *J. Biol. Chem.* 283, 34880–34886. doi: 10.1074/jbc.M804183200

Shimozaki, K. (2014). Sox2 transcription network acts as a molecular switch to regulate properties of neural stem cells. *World J. Stem Cells* 6, 485–490. doi: 10.4252/wjsc.v6.i4.485

Singh, D. K., and Prasanth, K. V. (2013). Functional insights into the role of nuclear-retained long noncoding RNAs in gene expression control in mammalian cells. *Chromosome Res.* 21, 695–711. doi: 10.1007/s10577-013-9391-7

Song, J. H., Yu, J. T., and Tan, L. (2015). Brain-derived neurotrophic factor in Alzheimer's disease: risk, mechanisms, and therapy. *Mol. Neurobiol.* 52, 1477–1493. doi: 10.1007/s12035-014-8958-4

Sun, M., and Kraus, W. L. (2015). From discovery to function: the expanding roles of long noncoding RNAs in physiology and disease. *Endocr. Rev.* 36, 25–64. doi: 10.1210/er.2014-1034

Sunwoo, H., Dinger, M. E., Wilusz, J. E., Amaral, P. P., Mattick, J. S., and Spector, D. L. (2009). MEN epsilon/beta nuclear-retained non-coding RNAs are up-regulated upon muscle differentiation and are essential components of paraspeckles. *Genome Res.* 19, 347–359. doi: 10.1101/gr.087775.108

Sunwoo, J. S., Lee, S. T., Im, W., Lee, M., Byun, J. I., Jung, K. H., et al. (2017). Altered expression of the long noncoding RNA NEAT1 in Huntington's disease. *Mol. Neurobiol.* 54, 1577–1586. doi: 10.1007/s12035-016-9928-9

Sutherland, H. F., Wadey, R., McKie, J. M., Taylor, C., Atif, U., Johnstone, K. A., et al. (1996). Identification of a novel transcript disrupted by a balanced translocation associated with DiGeorge syndrome. *Am. J. Hum. Genet.* 59, 23–31.

Tan, L., Yu, J. T., Hu, N., and Tan, L. (2013). Non-coding RNAs in Alzheimer's disease. *Mol. Neurobiol.* 47, 382–393. doi: 10.1007/s12035-012-8359-5

Tripathi, V., Ellis, J. D., Shen, Z., Song, D. Y., Pan, Q., Watt, A. T., et al. (2010). The nuclear-retained noncoding RNA MALAT1 regulates alternative splicing by modulating SR splicing factor phosphorylation. *Mol. Cell* 39, 925–938. doi: 10.1016/j.molcel.2010.08.011

Vucićević, D., Schrewe, H., and Orom, U. A. (2014). Molecular mechanisms of long ncRNAs in neurological disorders. *Front. Genet.* 5:48. doi: 10.3389/fgene.2014.00048

Wang, A., Wang, J., Liu, Y., and Zhou, Y. (2017). Mechanisms of long non-coding RNAs in the assembly and plasticity of neural circuitry. *Front. Neural Circuits* 11:76. doi: 10.3389/fncir.2017.00076

Wang, H., Iacoangeli, A., Lin, D., Williams, K., Denman, R. B., Hellen, C. U., et al. (2005). Dendritic BC1 RNA in translational control mechanisms. *J. Cell Biol.* 171, 811–821. doi: 10.1083/jcb.200506006

Wang, H., Iacoangeli, A., Popp, S., Muslimov, I. A., Imataka, H., Sonenberg, N., et al. (2002). Dendritic BC1 RNA: functional role in regulation of translation initiation. *J. Neurosci.* 22, 10232–10241. doi: 10.1523/JNEUROSCI.22-23-10232.2002

Yan, W., Chen, Z. Y., Chen, J. Q., and Chen, H. M. (2018). LncRNA NEAT1 promotes autophagy in MPTP-induced Parkinson's disease through stabilizing PINK1 protein. *Biochem. Biophys. Res. Commun.* 496, 1019–1024. doi: 10.1016/j.bbrc.2017.12.149

Yang, B., Xia, Z. A., Zhong, B., Xiong, X., Sheng, C., Wang, Y., et al. (2017). Distinct hippocampal expression profiles of long non-coding RNAs in an Alzheimer's disease model. *Mol. Neurobiol.* 54, 4833–4846. doi: 10.1007/s12035-016-0038-5

Zagrebelsky, M., and Korte, M. (2014). Form follows function: BDNF and its involvement in sculpting the function and structure of synapses. *Neuropharmacology* 76(Pt C), 628–638. doi: 10.1016/j.neuropharm.2013.05.029

Zhang, B., Arun, G., Mao, Y. S., Lazar, Z., Hung, G., Bhattacharjee, G., et al. (2012). The lncRNA Malat1 is dispensable for mouse development but its transcription plays a cis-regulatory role in the adult. *Cell Rep.* 2, 111–123. doi: 10.1016/j.celrep.2012.06.003

Zhang, X., Lian, Z., Padden, C., Gerstein, M. B., Rozowsky, J., Snyder, M., et al. (2009). A myelopoiesis-associated regulatory intergenic noncoding RNA transcript within the human HOXA cluster. *Blood* 113, 2526–2534. doi: 10.1182/blood-2008-06-162164

Zhao, X., Tang, Z., Zhang, H., Atianjoh, F. E., Zhao, J. Y., Liang, L., et al. (2013). A long noncoding RNA contributes to neuropathic pain by silencing Kcna2 in primary afferent neurons. *Nat. Neurosci.* 16, 1024–1031. doi: 10.1038/nn.3438

Zhong, J., Chuang, S. C., Bianchi, R., Zhao, W., Lee, H., Fenton, A. A., et al. (2009). BC1 regulation of metabotropic glutamate receptor-mediated neuronal excitability. *J. Neurosci.* 29, 9977–9986. doi: 10.1523/JNEUROSCI.3893-08.2009

Conflict of Interest Statement: The authors declare that the research was conducted in the absence of any commercial or financial relationships that could be construed as a potential conflict of interest.

Copyright © 2018 Wei, Luo, Zou and Wu. This is an open-access article distributed under the terms of the Creative Commons Attribution License (CC BY). The use, distribution or reproduction in other forums is permitted, provided the original author(s) and the copyright owner(s) are credited and that the original publication in this journal is cited, in accordance with accepted academic practice. No use, distribution or reproduction is permitted which does not comply with these terms.

frontiers in Neural Circuits

ORIGINAL RESEARCH
published: 11 October 2018
doi: 10.3389/fncir.2018.00086

Optogenetic Activation of A11 Region Increases Motor Activity

*Kathrin Koblinger[1,2], Céline Jean-Xavier[1,2], Sandeep Sharma[1,2], Tamás Füzesi[1,3], Leanne Young[1,2], Shane E. A. Eaton[1,2], Charlie Hong Ting Kwok[1,2], Jaideep Singh Bains[1,3] and Patrick J. Whelan[1,2,3]**

[1] Hotchkiss Brain Institute, University of Calgary, Calgary, AB, Canada, [2] Department of Comparative Biology and Experimental Medicine, University of Calgary, Calgary, AB, Canada, [3] Department of Physiology and Pharmacology, University of Calgary, Calgary, AB, Canada

Limbic brain regions drive goal-directed behaviors. These behaviors often require dynamic motor responses, but the functional connectome of limbic structures in the diencephalon that control locomotion is not well known. The A11 region, within the posterior diencephalon has been postulated to contribute to motor function and control of pain. Here we show that the A11 region initiates movement. Photostimulation of channelrhodopsin 2 (ChR2) transfected neurons in A11 slice preparations showed that neurons could follow stimulation at frequencies of 20 Hz. Our data show that photostimulation of ChR2 transfected neurons in the A11 region enhances motor activity often leading to locomotion. Using vGluT2-reporter and vGAT-reporter mice we show that the A11 tyrosine hydroxylase positive (TH) dopaminergic neurons are vGluT2 and vGAT negative. We find that in addition to dopaminergic neurons within the A11 region, there is another neuronal subtype which expresses the monoenzymatic aromatic L-amino acid decarboxylase (AADC), but not TH, a key enzyme involved in the synthesis of catecholamines including dopamine. This monoaminergic-based motor circuit may be involved in the control of motor behavior as part of a broader diencephalic motor region.

Keywords: spinal cord, dopamine, descending, motor activity, locomotion control

OPEN ACCESS

Edited by:
Brian R. Noga,
University of Miami, United States

Reviewed by:
Aaron M. Lambert,
Harvard University, United States
Shuichi Ueda,
Dokkyo Medical University, Japan
Shawn Hochman,
Emory University, United States

***Correspondence:**
Patrick J. Whelan
whelan@ucalgary.ca

Received: *12 March 2018*
Accepted: *21 September 2018*
Published: *11 October 2018*

Citation:
Koblinger K, Jean-Xavier C, Sharma S, Füzesi T, Young L, Eaton SEA, Kwok CHT, Bains JS and Whelan PJ (2018) Optogenetic Activation of A11 Region Increases Motor Activity. Front. Neural Circuits 12:86. doi: 10.3389/fncir.2018.00086

INTRODUCTION

Activation of the posterior hypothalamus, zona incerta or lateral hypothalamus can elicit a variety of motor behaviors, including locomotion (Shik and Orlovsky, 1976; Sinnamon et al., 1984; Sławińska and Kasicki, 1995; Young et al., 2009). A general finding was that the activity evoked from these areas was more complicated than the one elicited from motor regions of the brainstem (Mori et al., 1989), including the mesencephalic locomotor region and the medullary reticular formation (Kim et al., 2017). For example, stimulation of the lateral hypothalamus can result in varied responses ranging from feeding to predatory attack depending on context (Stuber and Wise, 2016; Kim et al., 2017). In this work, we focus on targeting diencephalic areas of the brain containing monoaminergic cells, with the goal of understanding their multifaceted motor function.

Dahlström and Fuxe (1964) identified a series of dopaminergic nuclei named A8-16. Some of these are well linked with motor functions such as the substantia nigra pars compacta (A9), while the role of others have been less well described. One of these nuclei is the A11 region which is located in the posterior diencephalon abutting the third ventricle (Björklund and Skagerberg, 1979; Barraud et al., 2010; Koblinger et al., 2014; Sharples et al., 2014). These neurons are non-canonical dopaminergic cells which lack the dopamine reuptake transporter in mouse (DAT) (Koblinger et al., 2014; Yip et al., 2017). The A11 cell group appears to be evolutionarily conserved from zebrafish (Ryu et al., 2007; Lambert et al., 2012) to mammals (Barraud et al., 2010). The broader connectome of the A11 has been under investigation; however, it has been shown to receive inputs from the parabrachial nucleus, infralimbic cortex, and the bed nucleus of the stria terminalis (Abrahamson and Moore, 2001; Qu et al., 2006). One of the primary efferent targets of the A11 is the spinal cord – sending collaterals at regular intervals into the gray matter, and has been proposed to be the primary source of spinal dopamine (Björklund and Skagerberg, 1979; Commissiong et al., 1979; Skagerberg and Lindvall, 1985). While the functions of the A11 are not fully understood, it appears to have both anti-nociceptive and pro-nociceptive properties (Fleetwood-Walker et al., 1988; Megat et al., 2018), pathologically it has been associated with Restless Legs Syndrome (RLS) (Clemens et al., 2006), and 6-OHDA lesions of the area are associated with an increase in motor function (Qu et al., 2007) possibly by actions on dopamine receptor type 3 (D_3) receptors (Clemens and Hochman, 2004; Qu et al., 2007).

One way in which A11 projections could control motor circuits is through direct modulation of spinal circuits, and indeed a sizable literature suggests that dopamine modulates the activity of motoneurons and interneurons within the lumbar spinal cord (Barrière et al., 2004; Madriaga et al., 2004; Han et al., 2007; Humphreys and Whelan, 2011; Gozal et al., 2014; Sharples et al., 2015; Sharples and Whelan, 2017). Specifically, dopamine can alter the frequency and pattern of locomotor activity, by increasing spiking frequency robustly, and decreasing both the first spike latency and after hyperpolarization amplitude (Han et al., 2007). The premotoneuronal excitatory drive onto motoneurons is also increased since dopamine can potentiate AMPA transmission in motoneurons by acting on D_1 receptors (Han and Whelan, 2009), and increase mEPSC frequency in motoneurons (Han et al., 2007). Finally, recent evidence suggests that dopamine acts on the sodium pump in motoneurons to directly increase an ultra-slow hyperpolarization (Picton et al., 2017). In sum, dopamine can modulate spinal motor function through an array of modulatory mechanisms. The larger family of monoamines (Kiehn et al., 1999; Madriaga et al., 2004; Liu and Jordan, 2005) and trace amines (Gozal et al., 2014; Hochman, 2015), can also sculpt the pattern of activity evoked from spinal cord circuits. Sources of these monoamines include supraspinal projections (Schmidt and Jordan, 2000; Sławińska et al., 2014).

Given the effects of monoamines on spinal motor circuits, this led to our hypothesis that activation of the A11 region in the freely behaving adult mouse would lead to changes in motor behavior. We found that photostimulation of the A11 region elicits motor behavior, and that dopamine neurons lacking DAT are present in the region (Ugrumov, 2009). Part of this work was reported in an abstract and in a mini-symposium (Koblinger et al., 2015; Whelan, 2017).

MATERIALS AND METHODS

Ethics Statement

All animal experiments were approved by the University of Calgary Health Sciences Animal Care Committee (Protocol: AC15-0016), following the Canadian Council for Animal Care guidelines. Animals were housed in a double-barrier facility for breeding.

Animals

TH-IRES-Cre knock-in mice were used (a gift from Dr. Antoine Adamantidis, Universität Bern, Switzerland – source; EM: 00254;B6.129X1-Thtm1(cre)Te/Kieg; European Mouse Mutant Archive) as well as DAT-IRES-Cre knock-in mice were obtained from Jackson labs [B6.SJL-Slc6a3tm1.1(cre)Bkmn/J]. Reporter mice were purchased from Jackson labs [tdTomato mice: B6.Cg-Gt(ROSA)26Sortm14(CAG-TdTomato)Hze/J (Ai14)]. vGluT2-Cre-tdTomato (gift from Dr. Marie-Claude Perreault, Slc17a7-IRES2-CRE, Jackson labs) and vGAT-ChR2-eYFP [B6.Cg-Tg(Slc32a1-COP4*H134R/EYFP)8Gfng/J, Jackson labs] mice were also used. We then crossed the different lines to obtain TH-IRES-Cre homozygous, TH-IRES-Cre tdTomato, and DAT-IRES-Cre tdTomato heterozygous mice. Pairs of homozygous TH-IRES-Cre (male), DAT-IRES-Cre (female) or Ai14 (male or female) genotypes were mated, and the resulting heterozygous TH-IRES-Cre; Ai14 and DAT-IRES-Cre; Ai14 male offspring were used in subsequent experiments. All mice were genotyped with DNA extracted from ear notches using the Kapa mouse genotyping kit (Kapa Biosystems, Wilmington, MA, United States) according to manufacturer's instructions. TH-IRES-Cre mice were genotyped using mixed primer PCR employing TH-IRES-Cre-F (CCTGGTCTGGACACAGTGC), TH-WT-F (CAAGCACTGAGTGCCATTAGC) and TH-Com-R (AGAGGCCAGGAACACTCCTG). Amplification of wild-type genomic DNA yielded a 298 bp PCR product whereas amplification from the mutant locus yielded a 453 bp PCR product. Genotyping of the TH-IRES-tdTomato and DAT-IRES-Cre mice was performed similarly, using the primers recommended by the supplier (Jackson Labs, Bar Harbor, ME, United States). Mice were housed on a 12:12 h light:dark schedule (lights on at 07:00 – off at 19:00) with *ad libitum* access to food and water. All behavioral experiments were performed in male mice between 8 and 16 weeks old.

Validation of TH-IRES-Cre Mice via Real Time qPCR

Total RNA was isolated from TH-IRES-Cre;CAG-LSL-tdTomato mouse microdissected brain regions (n = 7) A13, A11, and substantia nigra/ventral tegmental area (SN/VTA)

using the RNeasy lipid tissue mini kit (Qiagen, Hilden, Germany) following manufacturer's recommendations. Reverse transcription was performed using the Superscript VILO IV kit (Thermo Fisher, Waltham, MA, United States). For the negative control groups, all components except the reverse transcriptase were included in the reaction mixtures. The primers for real time qPCR were mGAPD-F (GTGAAGGTCGGTGTGAACG) and mGAPD-R (TCGT TGATGGCAACAATCTC); TH-F (CCCAAGGGCTT CAGAAGAGC) and TH-R (ATCCTCGATGAGACTCTGCC); Cre-F (ACGCACTGATTTCGACCAGGTTCG) and Cre-R (CATTCTCCCACCGTCAGTACGTGAG). Real time qPCR was performed with PowerUp SYBR green master mix (Thermo Fisher, Waltham, MA, United States) and mouse GAPDH was utilized as the reference gene. The running protocol extended to 45 cycles in fast mode consisting of 95°C for 1 s, 60°C for 30 s using a Quantstudio 3 instrument (Thermo Fisher, Waltham, MA, United States). Standard curve experiments using control mouse brain RNA were determined using a 5 log range of cDNA concentrations yielding efficiencies ranging from 90 to 110% (Bustin et al., 2009). Control reactions and those containing cDNA from the various brain regions were performed with 10 ng of template per reaction. PCR specificity was checked by dissociation curve analysis. Template controls yielded no detectable fluorescence. The relative mRNA abundance of TH and Cre in each sample were normalized to the abundance of GAPDH mRNA.

Optogenetics

Under isoflurane anesthesia (1.5 %), mice were secured in a stereotaxic apparatus (Stoelting Co., Wood Dale, IL, United States), and glass capillaries were lowered into the brain of TH-IRES-Cre or TH-IRES-Cre; Ai14 mice (AP −2.3 mm; ML −0.1 mm from the bregma; DV −2.9 mm from the dura). Recombinant AAV carrying a fluorescently tagged channelrhodopsin 2, ChR2-eYFP (Addgene plasmid 20298, pAAV-EF1a-double floxed-hChR2(H134R)-eYFP-WPRE-HGHpA; titre: 3×10^{12} GC/ml; Virus Vector Core, UNC, Lot # AV4844B) or eYFP (Addgene plasmid 20296, pAAV-EF1a-double floxed-eYFP-WPRE-HGHpA; 4×10^{12} GC/ml; Virus Vector Core, UNC, Lot # AV4842C) were pressure injected using the Nanoject II apparatus (Drummond Scientific Company, Broomall, PA, United States). 210 nl of the virus were injected bilaterally, with a total volume of 420 nl per mouse.

Mice were returned to their home cage and left for at least 14 days to allow for transfection of the viral construct into A11 neurons. For optogenetic experiments, mono-fiber optic cannulas were stereotactically implanted into the A11 area (MF2.5-FLT, Doric, Quebec, QC, Canada) (AP −2.3 mm; ML, −0.1 mm from the bregma; DV −2.7 mm from the dura). Fiber optic cannulas were secured in place using dental cement (Metabond, Parkell, Brentwood, NY, United States and Dentsply, York, PA, United States). Mice were allowed to recover for at least 3 days before behavioral testing. We performed *post hoc* histology to confirm $A11^{ChR2}$ transfection and ferrule placement.

Whole Cell Patch Experiments

In a separate series of experiments, we measured inward currents and spike activity using *in vitro* slice preparations to examine the effectiveness of $A11^{ChR2}$ transfection. Young male TH-IRES-Cre; Ai14 mice (4–6 weeks postnatal) were deeply anesthetized with isoflurane and decapitated. Brains were then rapidly removed and immersed in 4°C slicing solution containing, in mM: 87 NaCl, 2.5 KCl, 0.5 $CaCl_2$, 7 $MgCl_2$, 25 $NaHCO_3$, 25 D-glucose, 1.25 NaH_2PO_4, 75 sucrose saturated with 95% O_2/5% CO_2. 250 μm coronal sections were obtained using a vibratome (Leica), and allowed to recover for 1 + h in 95% O_2/5% CO_2 saturated, 30°C artificial cerebrospinal fluid (aCSF) containing (in mM): 126 NaCl, 2.5 KCl, 26 $NaHCO_3$, 2.5 $CaCl_2$, 1.5 $MgCl_2$, 1.25 NaH_2PO_4, 10 glucose. All recordings took place in aCSF at 30–32°C perfused at a rate of 1 mL/min, with DNQX (10 μM, Tocris) or picrotoxin (100 μM, Sigma) applied via perfusion pump. Neurons were visualized with an upright microscope fitted with differential interference contrast and epifluorescence optics (UVICO, Rapp OptoElectronic) and camera (AxioCam MRm). Borosilicate pipettes (3–5 MΩ) were filled with internal solution containing (in mM) 108 K-gluconate, 2 $MgCl_2$, 8 Na-gluconate, 8 KCl, 1 K_2-EGTA, 4 K_2-ATP, 0.3 Na_3-GTP, 10 mM HEPES, 0.2 Alexa-488 hydrazide and 10 mg/mL biocytin. A fiber optic cable (105 μm core diameter) was placed 1–2 mm from the A11 using a manipulator to deliver light from a laser (473 nm, OptoGeni 473, IkeCool Corporation). Light intensity was measured by a Photodiode Power Sensor (Thorlabs). Maximally, 2.5 mW light was delivered to the tissue. Signals were amplified (Multiclamp 700B, Molecular Devices), low pass filtered at 1 kHz, digitized at 10 kHz (Digidata 1322, Molecular Devices, San Jose, CA, United States), and recorded (pClamp 9.2, Molecular Devices) for offline analysis of evoked or spontaneous synaptic currents (Clampfit, Molecular Devices; MiniAnalysis, Synaptosoft).

Behavior

For *in vivo* experiments the light source (473 nm, LRS-0473-GFM, Laserglow Technologies, Toronto, ON, Canada) was connected to an implanted ferrule with a fiber optic cable (200 μm core diameter, Doric Lenses, Quebec City, QC, Canada). The laser was controlled by TTL pulses delivered using a Master 8 pulse stimulator (A.M.P.I., Jerusalem, Israel). The blue light was delivered for 3 min (20 Hz, 10 ms pulse width, 15 mW).

Each mouse was tested for 9 min (3 min pre, 3 min light, 3 min post) for five consecutive days. Behavior was recorded using a vertically mounted video camera and *post hoc* analyzed with the TopScan video tracking software (Clever Sys Inc., Reston, VA, United States). For c-Fos immunolabelling, animals were sacrificed 2 h after light stimulation. Behavioral testing was performed in a 70 cm × 70 cm × 50 cm high open field chamber with opaque walls. Each mouse was habituated to the chamber for 3 days for 1 h per day before testing. On test days, mice were habituated for 30 min before testing and trials were performed at the same time of day. Mice were transferred to and from a behavioral testing room for day-to-day testing. Mice were housed singly in standard cages (SafeSeal Plus Mouse Green Line

GM500, Techniplast, Italy, 501 cm^2 floor) with no environmental enrichment.

The Clever Sys tracking software divided movement into three categories:

(1) Immobility/No movement: Immobility is defined by both speed and motion measures (animal body change in consecutive frames expressed as a percentage). Immobility bouts over 15 successive frames were estimated when speed was <60 mm/s and the change in motion was <1% change in animal body position.
(2) In Place Activity: Animal stays in one place with some observed activity such as grooming, sniffing, stretching, rearing, but the animal is not immobile.
(3) Locomotion. Distance traveled: The mouse physically moves or displaces itself from one location to another with a minimum prescribed speed of greater than 60 mm/s and a minimum distance of 100 mm. Locomotor bouts: the number of times animal moves from one place to another place. If the animal continuously moves, it is counted as one single bout. Locomotor duration: the amount of time the mouse spends in locomotion.

Immunohistochemistry

Mice were sacrificed with isoflurane (2%) and transcardially perfused with phosphate-buffered saline (PBS), followed by 10% formalin in PBS. Brains were placed in 10% formalin for 12 h followed by 30% sucrose phosphate buffer (PB) for cryoprotection. 30 μM coronal brain sections were obtained using a cryostat (Leica CM1850 UV, Leica Biosystems, Richmond Hill, ON, Canada). The sliced brain sections were collected in a staggered fashion and placed into four consecutive wells. Rinses were performed before and between incubations with 0.1 M PBS, followed by one 20 min wash in Tris-buffered saline containing Triton (TBSt; pH 7.4, with 0.1% TritonX-100). Sections were incubated in blocking solution (5% donkey and 5% goat serum in PBS) for 1 h, and blocking solution was used in subsequent antibody incubations. The primary antibodies used were rabbit anti-TH, sheep anti-TH (1:1000, Abcam Inc., Toronto, ON, Canada), chicken anti-GFP (1:1000, Aves Laboratories, Tigard, OR, United States), rabbit anti-c-Fos (1:1000, EMD Millipore, Billerica, MA, United States), rabbit anti-RFP (1:5000, Rockland Immunochemicals Inc, Limerick, PA, United States) and rabbit anti-AADC (1:250, Novus Biologicals, Littleton, CO, United States). The secondary antibodies used were Alexa-564-conjugated donkey anti-rabbit, Alexa-488-conjugated donkey anti-sheep, Alexa-488-conjugated goat anti-chicken, Alexa-647-conjugated donkey anti-sheep (1:1000, Molecular Probes, Burlington, ON, Canada), biotinylated donkey anti-rabbit and Cy3-conjugated streptavidin (1:500, Jackson Immuno Research, West Grove, PA, United States). Free-floating brain sections were then mounted onto Superfrost^{TM} slides, coated with Vectashield^{TM} (H-1000, Vector, Burlingame, CA, United States) and cover-slipped. Fluorescent images were collected using the following microscopes; Nikon Eclipse C1si spectral confocal microscope, Nikon A1R MP+ and Olympus BX51. The objectives used were 4X (NA 0.13), 20X PLAN APO DIC (NA 0.75), 20X PLAN FLUOR (NA 0.75), 60X PLAN APO IR (NA 1.27) for Nikon Eclipse C1si spectral confocal microscope. The lasers used were centered on 488 nm (515/30 nm emission filter) and 561 (590/50 nm emission filter). The objectives used were 10X DIC L N1 (NA 0.30), 20X PLAN FLUOR MImm DIC N2 (NA 0.75), 60X PLAN APO IR WI DIC N2 (1.27) for the Nikon A1R MP+ microscope. The lasers used were centered at 403 nm, (450 nm emission filter) 488 nm (525 nm emission filter), and 562 nm (595 nm emission filter), respectively using pinhole radius of 12.7–21.5 microns on Nikon A1R MP+ microscope. The 20X images were taken with z-step 0.5 or 1 μm, 60X with z-step 0.15 μm. Stacked images were acquired by averaging four frames with a resolution of 1024 × 1024 or 512 × 512. Some images were acquired using a Panoramic FLASH II digital slide scanner (3DHISTECH inc., provided by Quorum Technologies) equipped with a Lumencor SPECTRA light source and PCO.edge sCMOS camera. Off-line image processing included maximal intensity projections conducted using NIS-Elements Advanced Research Version 4.10 as well as adjustments of brightness and contrast in Adobe Photoshop. Cell counting was accomplished by a person blinded to the study using ImageJ (NIH Image, Bethesda, MD, United States). We counted five sections containing the area of interest per animal.

Data Analysis and Statistics

Statistical analyses were performed in GraphPad Prism 6. Unpaired Student's *t*-tests were conducted comparing between two independent groups (e.g., $A11^{eYFP}$ vs. $A11^{ChR2}$). When assumptions of normality were violated, a Mann–Whitney test was performed instead of a *t*-test. A two-way repeated measures analysis of variance (ANOVA) was conducted to examine changes between two groups (i.e., $A11^{eYFP}$ vs. $A11^{ChR2}$) across time. When a significant main effect or interaction was found, Tukey *post hoc* comparisons were conducted. When assumptions of normality were violated on the ANOVA, non-parametric Friedman tests were done with a Dunn's multiple comparison tests when significant main effects were found. Repeated measures one-way ANOVA (RM-ANOVA) tests were conducted to examine changes within a group (i.e., $A11^{eYFP}$ vs. $A11^{ChR2}$) in different conditions (before, during, just after light-activation of the A11). When a significant main effect or interaction was found, Bonferroni multiple *post hoc* comparisons tests were conducted. Data are reported as the mean ± standard deviation (SD) and $P < 0.05$ values were considered significant. When data did not pass normality tests, the median is reported with 25–75% ranges. When histograms were used (**Figure 6**) both the median and mode were used to report data.

RESULTS

Classes of Cells Within the A11 Region

We used a viral approach to identify classes of cells within the A11. The viral transfection efficiency was confirmed by injecting an AAV-DIO-ChR2-eYFP construct into A11 region in TH-IRES-Cre-tdTomato reporter mice (**Figures 1A–C**, $n = 4$). We found that 96% (SD = 1.7%) of ChR2-eYFP neurons expressed

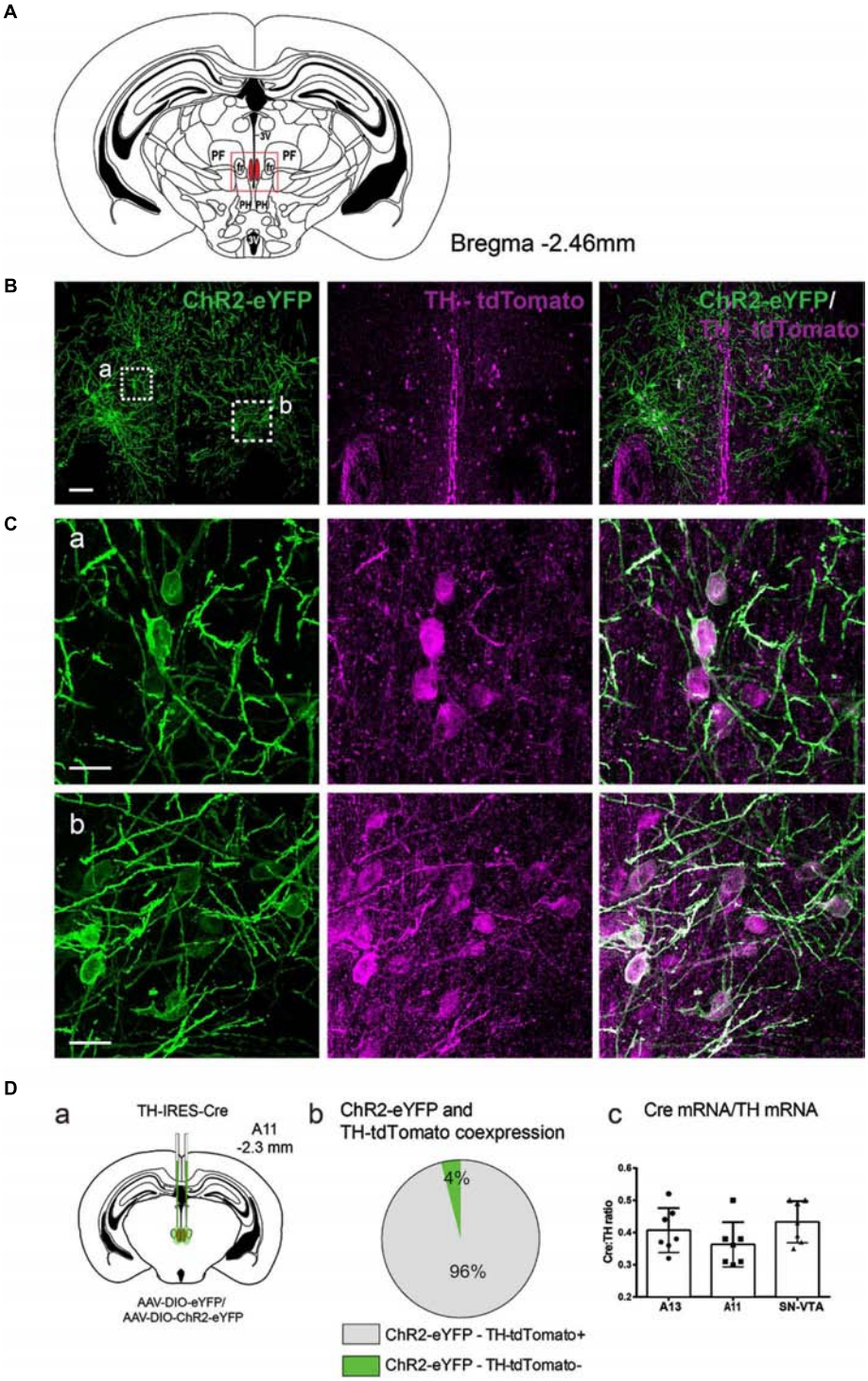


FIGURE 1 | Anatomical characterization of TH-IRES-Cre A11 neurons following transfection with AAV-DIO-ChR2-eYFP. **(A)** Diagram showing the middle region of the A11 area in the mouse (Bregma –2.46). The red frame represents the area where representative micrographs were taken. 3V, third ventricle; PF, parafascicular thalamic nucleus; fr, fasciculus retroflexus; PH, posterior hypothalamic nucleus. **(B)** TH-IRES-Cre tdTomato mice expressing channelrhodopsin-2 – enhanced yellow fluorescent protein (ChR2-eYFP) in A11. Confocal image showing A11 neurons expressing ChR2-eYFP bilaterally (stitched image consisting of 4 20X images). Scale bar 100 μm. **(C)** Higher magnification (60X zoom) of boxed areas **(a,b)** in **B**, Scale bar 20 μm. **(Da)** Schematic map showing the injection site of virus with the Cre-dependent ChR2 construct tagged with ChR2-eYFP or eYFP alone into the A11 of TH-IRES-Cre mice. **(Db)** Pie graph showing that 96% of ChR2-eYFP positive cells in A11 co-express tdTomato ($n = 4$). **(Dc)** Quantitative real-time PCR analysis of ratio of Cre mRNA to that of TH mRNA in A13, A11 and substantia nigra/ventral tegmental area (SN/VTA) brain regions.

TH-tdTomato (**Figure 1D**) in the A11 region. To confirm that Cre expression levels correlated with the expression levels of endogenous TH, real time qPCR analyses were performed on RNA isolated from TH-expressing brain regions A13 (A), A11 (B), and SN/VTA (C) (**Figure 1D**). Expression of TH and Cre, respectively, were normalized to the expression of the reference gene GAPDH. The normalized expression of Cre was consistently lower than that of TH, with levels ranging from 36 to 43%, depending on the brain region. All of the animals analyzed were heterozygous for the Cre transgene so the expected result was that Cre mRNA levels would be 50% of TH mRNA levels. Based on these results we expect that Cre mRNA levels will be close to TH mRNA levels in homozygous TH-IRES-Cre mice. Next, we confirmed in TH-IRES-Cre mice that the viral injections were restricted to the A11 region. **Figure 2** shows that the expression of ChR2-eYFP^{+} was spatially restricted to neurons from the A11 region (**Figure 2A**) following Cre-dependent viral expression. Other neighboring TH expressing regions, like the VTA, substantia nigra pars compacta and A13 did not show evidence of eYFP reporter expression (**Figures 2Ac,Ba–c,Ca–c**, respectively).

Next, we examined the co-localization of TH^{+}-IR cells with A11^{ChR2} cells to identify the neurotransmitter phenotype of the cells transfected within the A11 region of TH-IRES-Cre mice. Similar to recent reports (Lammel et al., 2015) we found that 54% of A11^{ChR2} expressing cells were co-localized with TH^{+}-IR (n = 4, ChR2 mean = 132, SD = 32.01, TH^{+}-IR mean = 105.5, SD = 11.03; co-localizing mean = 71.75, SD = 15.97, data not shown). In our previous work, we established that the large diameter cells which constitute the A11 region in mice are a non-canonical class of dopaminergic neurons that lack the Dopamine Transporter (DAT) (Koblinger et al., 2014) which was replicated in a report that used a DAT-GFP reporter line (Yip et al., 2017). We further confirmed these findings using our DAT-Cre-tdTomato reporter line (data not shown). We then tested for non-classical types of monoaminergic cells within the A11 region. These neurons only express the AADC enzyme and can produce various monoamines and trace amines (Ugrumov, 2009). We found evidence for AADC cells lacking TH in the A11 region (**Figure 3**) which suggest the presence of putative D-cells in the A11 region (Jaeger et al., 1983). In TH-tdTomato^{+} mice, we found that 35% of TH-tdTomato^{+}/TH^{-}-IR neurons were also AADC^{+} in the A11 region (n = 5, TH-tdTomato^{+}/TH^{-}-IR mean = 185.8, SD = 129.1, TH-tdTomato^{+}/TH^{-}-IR/AADC^{+} mean = 64.4, SD = 38.14; **Figure 3**). Taken together these results suggest that approximately 70% of transfected cells are capable of releasing dopamine and other monoamines such as serotonin (5-HT) or trace amines.

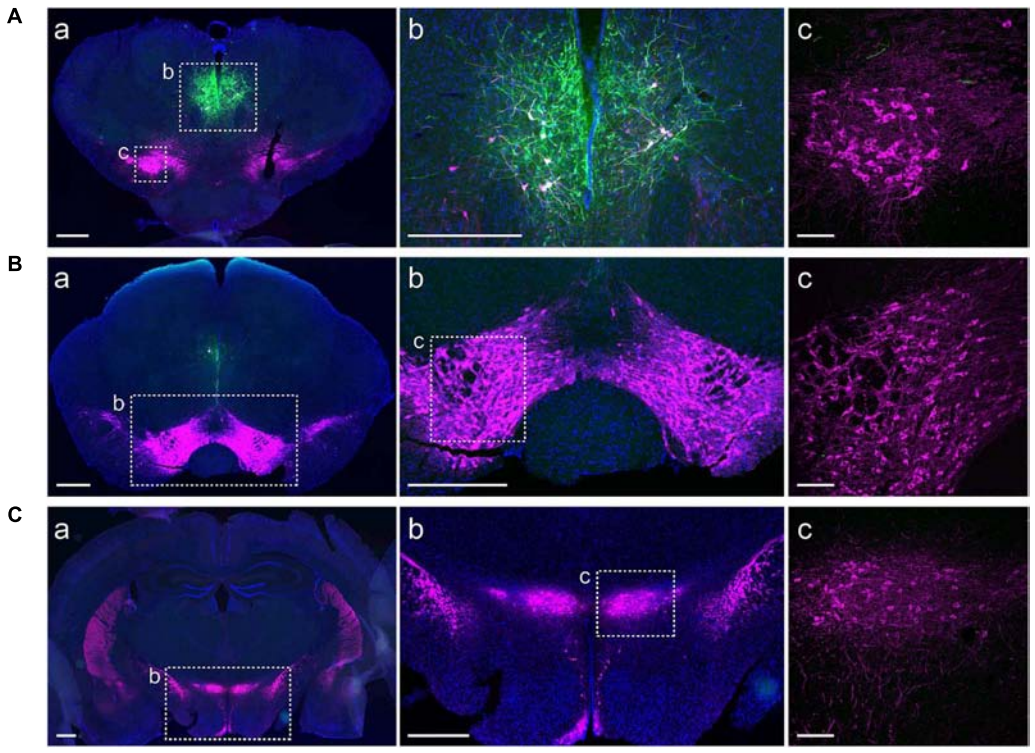


FIGURE 2 | ChR2-eYFP expression is restricted to A11 area. Immunohistochemistry targeted against eYFP (green) and TH (magenta) showing restricted ChR2-eYFP expression to A11. **(Aa,b)** ChR2-eYFP expression in A11 following Cre-dependent viral expression (DAPI, blue was used to label the cell nuclei). **(Ac)** Higher magnification (20X) of boxed TH^{+}-IR neurons in substantia nigra pars compacta. **(Ba,b,c)** No ChR2-eYFP expression in the ventral tegmental area (VTA). **(Ca,b,c)** No ChR2-eYFP expression in A13. Images **(Aa,b, Ba,b, Ca,b)** acquired with Olympus slide scanner 20X magnification, scale bar 500 μm; **(Ac, Bc, Cc)** Higher magnification confocal images of boxed area in **b (Ab, Bb, Cb)**, scale bar 100 μm.

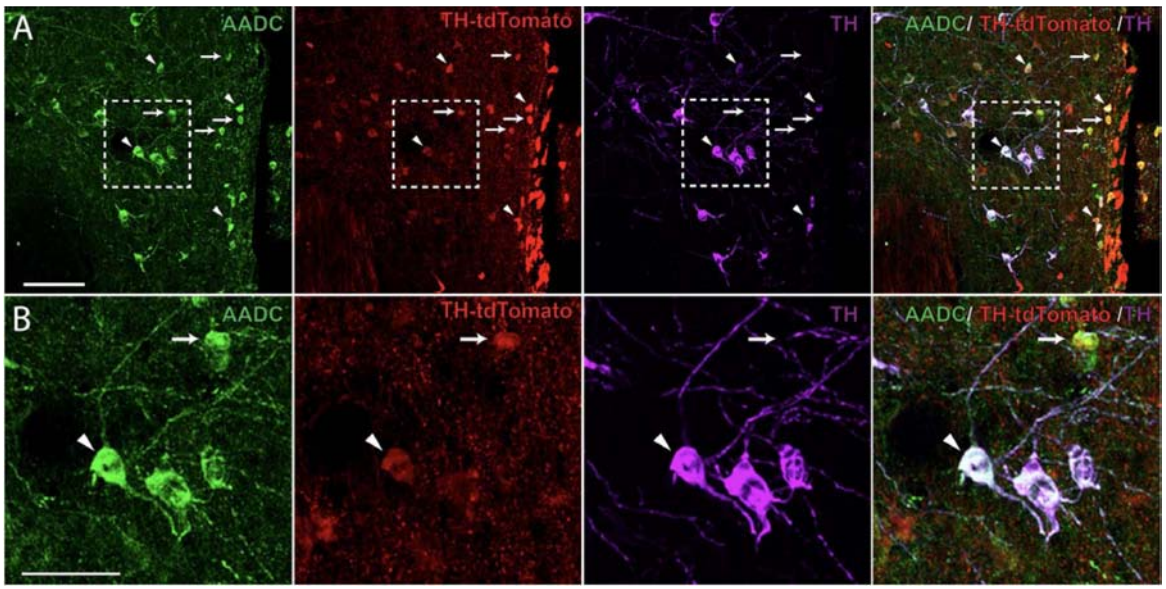


FIGURE 3 | Aromatic L-amino acid decarboxylase (AADC) expression in A11 TH-IR neurons. **(A)** Immunohistochemistry targeted against AADC (green) and TH^+-IR (magenta) as well as native TH-tdtomato (red) expression showing that a proportion of A11 TH-tdTomato$^+$/TH$^-$-IR neurons were also $AADC^+$ in TH-IRES-Cre tdTomato mice. 20X magnification, scale bar 100 μm. **(B)** Enlarged image showing $AADC^+$/TH-tdTomato$^+$/TH$^-$-IR (arrows) and $AADC^+$/TH-tdTomato$^+$/TH^+-IR neurons (arrowheads). 20X magnification, scale bar 50 μm.

Since there is evidence of localization of dopamine with co-transmitters such as peptides, glutamate or GABA, we asked whether co-localization of dopamine neurons in the A11 with GABA or glutamate could be detected. **Figure 4** illustrates there is evidence of a small number of $vGluT2^+$ cells within the A11 region. However, there was no $vGluT2^+$-TH^+-IR co-localization in the A11 region, compared to the arcuate nucleus of hypothalamus (**Figures 4A,B**). While vGluT2 was the most likely target subpopulation we also examined Allen Brain Atlas data and found strong expression of vGluT3, however, no evidence for vGluT1 staining in the A11 vicinity was found. Our data indicates a lack of vGAT colocalization in TH^+ -IR neurons of A11 (**Figures 4C,D**). We did see evidence for some $vGAT^+$ somata within the A11 region.

Photostimulation of the A11 Region Increases Motor Activity

Given that the viral injections were restricted to the A11 region, we tested the feasibility of using TH-IRES-Cre mice as a tool to photostimulate A11 neurons.

First, we tested, using brain slices, if the $A11^{ChR2}$-cells could elicit sodium (Na^+) spikes or currents following photostimulation. Pulses of blue light (473 nm) were delivered via an optical fiber, which successfully elicited photocurrents in $A11^{ChR2}$ cells (**Figure 5**). We also determined that trains of Na^+ spikes were reliably elicited at frequencies up to 20 Hz (**Figure 5Dc**), which was the frequency we adopted for *in vivo* studies.

We then asked whether light pulses directed to the A11 region *in vivo* could also successfully activate $A11^{ChR2}$-cells. We implanted a fiber optic cannula unilaterally 0.1 mm lateral to the midline just above A11 region to bilaterally stimulate A11. We photostimulated both $A11^{ChR2}$ or $A11^{eYFP}$ mice at 20 Hz for 3 min (same parameters as for behavior), sacrificed them 2 h later to allow for c-Fos expression and prepared brain slices to probe for c-Fos^+-expression, which is increased in neurons following depolarization (**Figures 5A,B**). We found that in 10 animals (ChR2 $n = 5$, eYFP $n = 5$) $A11^{ChR2}$-cells were more likely to be also c-Fos^+ compared to cells infected with control $eYFP^+$ construct (**Figure 5C**, ChR2 $n = 5$, eYFP $n = 5$, $U = 0$, $P = 0.004$, Mann–Whitney test). These data suggest that the $A11^{ChR2}$-cells can be photo-activated *in vitro* and *in vivo* and that the neurons from the A11 region that are infected with control $eYFP^+$ construct are not activated by the same light stimulation parameters.

Next, we addressed the functional role of A11 neuronal activation in freely moving mice. We assessed movement in the open field test in animals expressing $A11^{ChR2}$ or in $A11^{eYFP}$. The mice were habituated to the open field for 1 h daily for 3 days and then tested for a fixed period on each of five consecutive days. Prior to testing, mice were habituated to the open field for 30 min with optical fibers attached. We recorded baseline activity 3 min prior to light activation, directly followed by 3 min of 20 Hz, 10 ms pulse width of light (473 nm) and 3 min of post-light activation (**Figure 6A**).

In the $A11^{ChR2}$ cohort only, qualitatively we noticed that animals reacted immediately to the light by changing behavior in a variety of ways (e.g., postural changes, starting to groom, turning, sniffing, stretching, and rearing but the animal is neither locomoting nor immobile). Collectively, these behaviors were quantified as changes in "in-place activity." When we compared

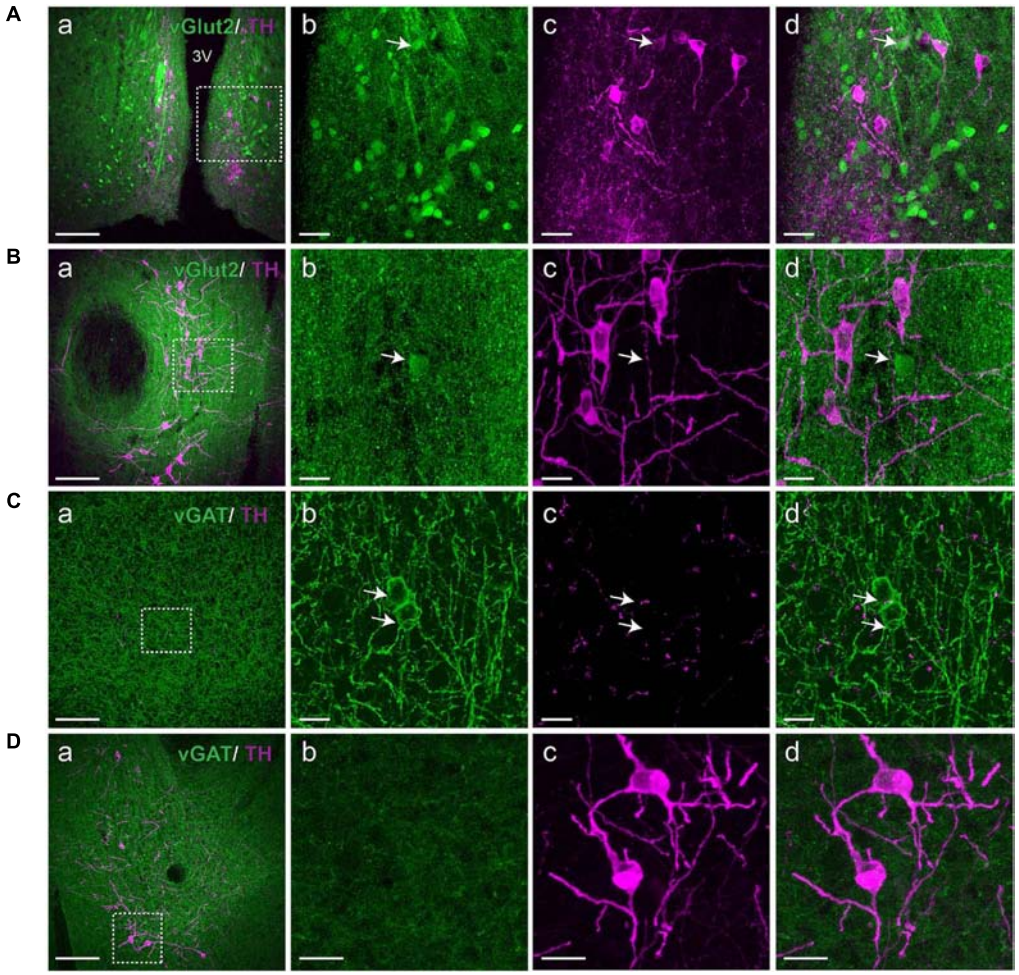


FIGURE 4 | A11 TH$^+$-IR neurons lack vGluT2 and vGAT expression. **(A,B)** Immunohistochemistry targeted against TH (magenta) in a vGluT2-reporter (green) mouse. (Aa) vGluT2 expressing neurons are plentiful in the arcuate nucleus of hypothalamus, scale bar 200 μm. **(Ab–d)** Higher magnification of boxed area **(Aa)**, Scale bar 20 μm. vGluT2 is present in the arcuate nucleus of hypothalamus which served as a positive control. Arrow indicates a double positive TH$^+$-IR A11 neuron expressing vGluT2. **(Ba)** TH$^+$-IR neurons in A11 region, scale bar 200 μm. **(Bb–d)** Higher magnification of boxed area **(Ba)**, scale bar 10 μm. We observed a few vGluT2 expressing neurons in the A11 region but these neurons lacked TH$^+$-IR (arrow). **(C,D)** Immunohistochemistry targeted against TH (magenta) in a vGAT-reporter (green) mouse. **(Ca)** Large number of vGAT expressing GABAergic interneurons are observed in cortex, scale bar 200 μm. **(Cb–d)** Higher magnification of boxed area **(Ca)**, scale bar 10 μm. Arrows indicate GABAergic interneurons expressing vGAT and TH$^+$-IR fibers and puncta are also observed. **(Da)** TH$^+$-IR neurons in A11 region, scale bar 200 μm. **(Db–d)** Higher magnification of boxed area **(Da)**, scale bar 10 μm. TH$^+$-IR neurons in A11 region lack any vGAT expression.

the effect of light between the groups (A11^{ChR2} and A11^{eYFP}, baseline corrected; difference = value - baseline) we found significant differences between the groups for in place activity (A11^{ChR2} $n = 16$, 803 ± 741 mm; A11^{eYFP} −391 ± 503 mm; $n = 7$, $U = 11$, $P = 0.0007$, Mann–Whitney test; data not shown).

These animals would then generally begin to locomote after engaging in these activities (see **Supplementary Video 1**). When we further examined these changes in the A11^{ChR2} cohort, photostimulation increased the distance traveled by 86.0% (**Figure 6C**; $n = 16$, $Q = 18.9$, $P < 0.0001$, Friedman test) and the total number of locomotor bouts by 75.6% (**Figure 6D**; $n = 16$, $Q = 16.6$, $P = 0.0002$, Friedman test, see methods for definitions). In contrast, this was not observed in the A11^{eYFP} control group (**Figure 6C**, $n = 7$, Q = 2.0, $P = 0.5$; **Figure 6D**, $n = 7$, $Q = 1.5$, $P = 0.5$, Friedman test). When we compared the effect of light between the groups (A11^{ChR2} and A11^{eYFP}, baseline corrected, difference = value - baseline) we found significant differences for the following parameters: locomotion (A11^{ChR2} $n = 16$, 1551 ± 1503 mm; A11^{eYFP} −149 ± 665 mm; $n = 7$, $U = 10$, $P = 0.0005$, Mann–Whitney test), and bouts of locomotion (A11^{ChR2}, $n = 16$, 1.88 ± 4.09 bouts; A11^{eYFP}, −3.18 ± 3.36 bouts; $n = 7$, $U = 13$, $P = 0.001$, Mann–Whitney test). We did not observe an effect of day [2-way ANOVA with repeated measures, $F(4.6) = 0.04$, $P = 1$].

Next, we determined the latency for changes in movement behavior after photostimulation. For this, we averaged the data (distance in mm) into 10 s bins and set a threshold (mean of the pre-light distance traveled over 3 min, + two times SD) for

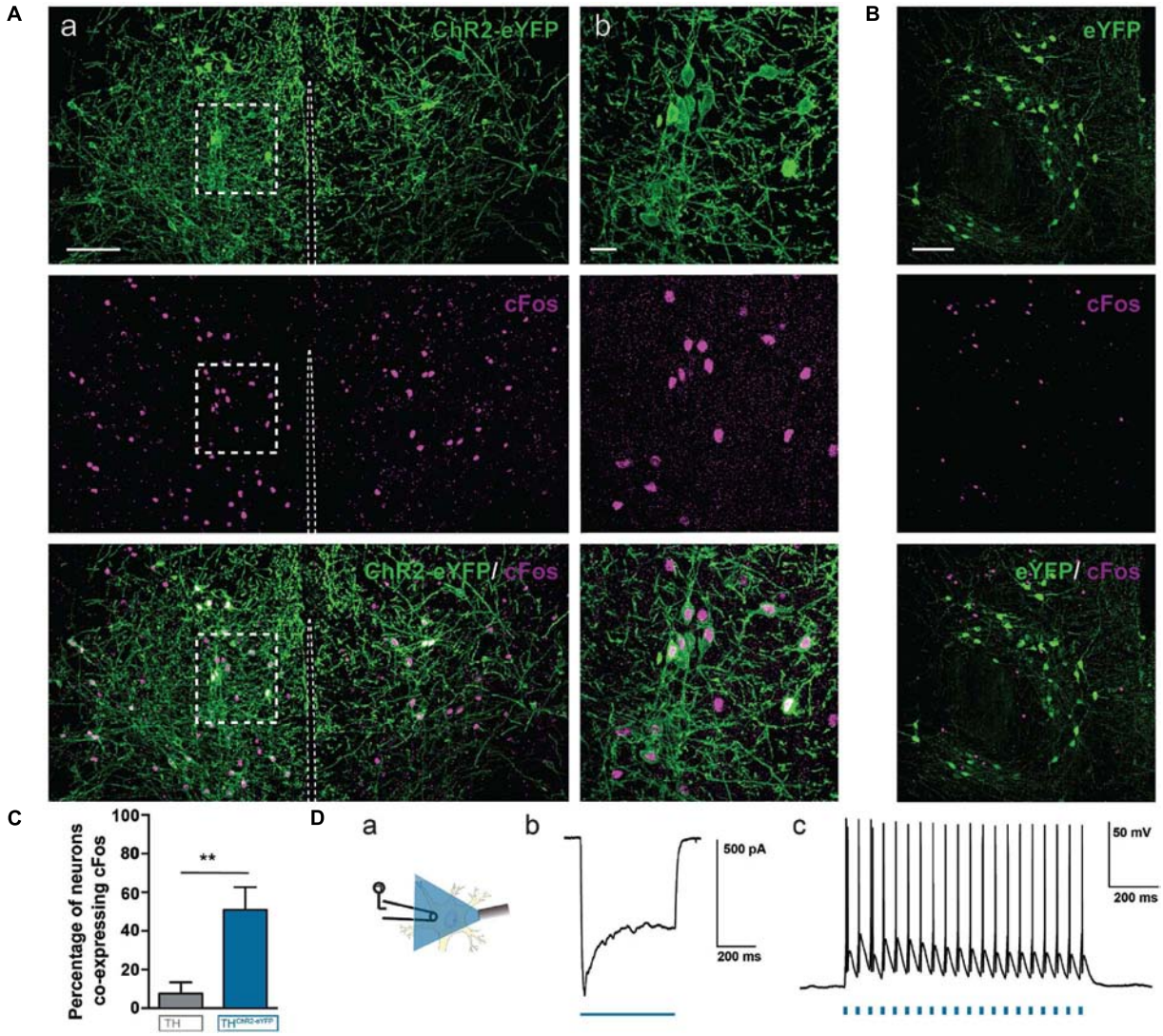


FIGURE 5 | Photostimulation of A11 cells induces c-Fos protein expression in A11 ChR2-eYFP neurons *in vivo* and action potentials *in vitro*. ChR2-eYFP expressing (n = 4) mice and eYFP control (n = 4) mice were stimulated with 473 nm light at 15 mW with 20 Hz, 10 ms pulses, 2 h prior to sacrifice. **(Aa)** A11 neurons from ChR2-eYFP light stimulated mouse (stitched image consisting of 4 20X images; scale bar 100 μm). **(Ab)** Higher magnification (60X zoom) of boxed area (scale bar 20 μm). **(B)** Photostimulation of A11 eYFP neurons (no ChR2) *in vivo* does not result in significant co-localization of c-Fos in A11-eYFP$^+$ cells (scale bar 100 μm). **(C)** Bar graph summarizing changes in the percentage of neurons co-expressing c-Fos in ChR2-eYFP (n = 4) versus eYFP (n = 4). **(D)** Real-time optical stimulation with 473 nm light reliably elicits spikes in A11 neurons *in vitro*. Example of a photocurrent recorded in voltage-clamp mode, elicited by 473 nm blue light **(Db)**. Trains of light pulses (10 ms pulse-width) at 20 Hz frequency evoked spike activity **(Dc)**. **(Da)** Schematic showing approach. $^{**}P < 0.01$.

each individual trial and determined the latency of crossing the threshold. We examined all trials (n = 80, all days, all animals) and found that 87.3% of the A11^{ChR2} trials crossed threshold during light activation with a median latency of 40 s (25–75% percentile 20–80, **Figure 6E**). In contrast, only 38.2% of the A11^{eYFP} mice trials (n = 35, all days, all animals) crossed threshold with a median latency of 60 s (25–75% percentile 48–130 **Figure 6E**).

When we examined all photostimulation trials on a trial-to-trial basis, there was no significant correlation between basal locomotor activity and the light mediated effect (distance traveled (mm); r = −0.1, P = 0.1) due to variability in the data (mean = 43.80 mm, SD = 272.2, median = 2.6 mm). Taken together our data suggest that photostimulation of A11 affects both the movement during locomotion as well as the in-place activity.

DISCUSSION

Previous work has shown that the diencephalic A11 cell group contains neurons that project to the spinal cord and its effects are associated with pain control (Fleetwood-Walker et al., 1988), migraine (Charbit et al., 2009), cataplexy (Okura et al., 2004), and possibly a role in RLS (Clemens et al., 2006). Our work provides

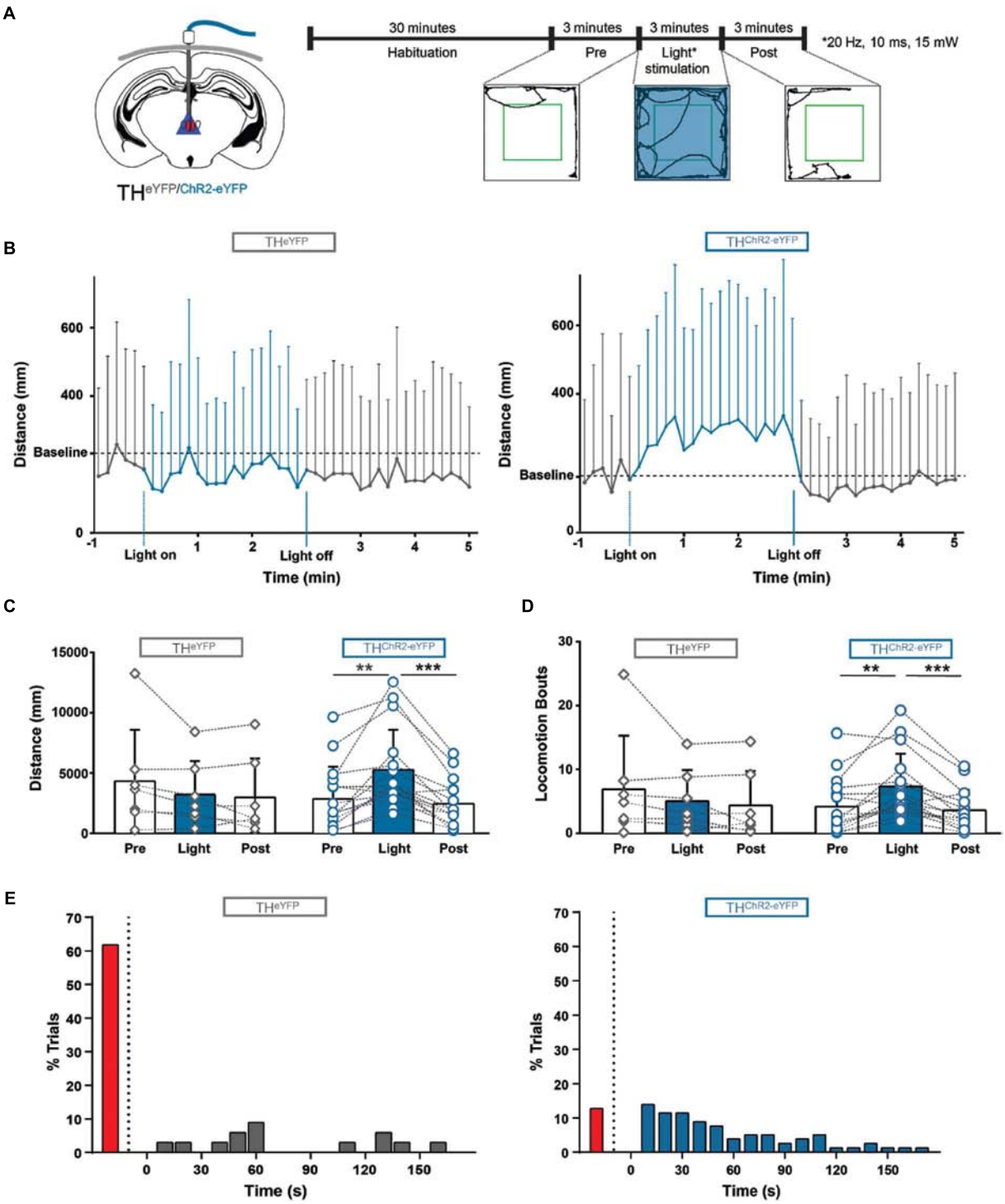


FIGURE 6 | Photostimulation of A11 in awake behaving mice initiates and modulates locomotion. **(A)** Schematic showing the implantation site of the light ferrule, along with a schematic of the experimental plan. **(B)** Locomotor distance was significantly increased during photostimulation in ChR2 animals compared to eYFP-control mice (averaged over 5 days). Baseline was corrected. **(C,D)** ChR2 mice displayed significantly more distance traveled **(C)** and locomotion bouts **(D)** during blue light stimulation compared with light-off conditions. There was no significant difference between the three conditions in eYFP control mice (n = 7) (average over 5 days). **(E)** 87.3% of ChR2 trials (blue bars) crossed the threshold during photostimulation while only 38.2% of the eYFP trials (gray bars) crossed the threshold (5 days, all trials), looking at individual trials the median time to cross the threshold was 40 s for ChR2 mice, and 60 s for eYFP mice. The red bars on the left of both graphs indicate the percentage of trials where the threshold was not crossed. These data suggest that photostimulation of A11 can initiate and modulate locomotion. $^{**}P < 0.01$; $^{***}P < 0.001$.

evidence that activation of A11 increases motor behavior, including locomotor and non-locomotor events. The A11 was shown to depress firing of dorsal horn neurons responding to noxious input (Fleetwood-Walker et al., 1988; Taniguchi et al., 2011), through a D_2 receptor-mediated mechanism (Tamae et al., 2005). Similar effects on trigeminal nociception have been also reported (Abdallah et al., 2015). But dopamine has also been shown to be pro-nociceptive through D_5 receptors expressed in the spinal cord (Megat et al., 2018). This complex sensorimotor role is shared with other monoamines such as 5-HT and noradrenaline (Schmidt and Jordan, 2000; Millan, 2002), and is partly dependent on the diversity of monoamine receptor subtypes. Indeed, this sensorimotor modulation may be related to expression of movement as hypothesized for RLS (Clemens et al., 2006). As outlined below, dopamine's actions on motor circuits are also diverse. This points to a role in both pain and motor function where the actions of dopamine can modulate multiple circuits within the spinal cord to fine-tune sensorimotor function. A further diversity of A11 actions could be linked to the sex of the animals. Our work used male mice and it is possible that results in females may differ, since work in rats has shown a sexual dimorphism in the A11 descending projections (Pappas et al., 2008, 2010) and recent work show spinal D_5 receptors in the dorsal horn contributing to hyperalgesia in male but not female mice (Megat et al., 2018). Since male rats have a greater density of A11 fibers in the ventral horn it is possible that A11 stimulation in males would show greater motor effects compared to females.

Mode of Action

Our previous work established that in mice, the A11 is primarily dopaminergic but lacks DAT (Koblinger et al., 2014) which has also been confirmed using DAT reporter mice (Yip et al., 2017). In the A11 system, this DAT^- mechanism may increase synaptic dopamine concentration, augmenting dopamine's actions within the spinal cord.

Data from the neonatal rat and mouse shows that bath application of dopamine restricted to the thoracolumbar spinal region modulates fictive locomotor patterns (Kiehn and Kjaerulff, 1996; Jiang et al., 1999; Whelan et al., 2000; Barrière et al., 2004; Christie and Whelan, 2005; Gordon and Whelan, 2006; Humphreys and Whelan, 2012; Sharples et al., 2015; Sharples and Whelan, 2017). This dopamine-evoked excitation of mammalian spinal locomotor circuits occurs through $D_{1/5}$ receptors (Maitra et al., 1993; Seth et al., 1993; Barrière et al., 2004; Madriaga et al., 2004; Gordon and Whelan, 2006; Han et al., 2007) although a role for $D_{2/3/4}$ receptors exists (Humphreys and Whelan, 2012). In particular, $D_{1/5}$ receptors appear to enhance the stability of ongoing locomotion but $D_{2/3/4}$ receptors appear to contribute to a slowing of the rhythm (Sharples et al., 2015), and may access part of the pattern generator through recurrent collaterals (Humphreys and Whelan, 2012). In adult spinalized mice, D_1 receptors appear to contribute more than D_5 receptors to locomotion, based on the use of D_5 receptors KO mice (Lapointe et al., 2009). Since this study used a mixed cohort of male and female mice, and recent evidence suggests that D_5 receptors are present in higher numbers in the spinal cord of male mice (Megat et al., 2018), a role for D_5 receptors in locomotion cannot be excluded. Dopamine fibers projecting from the diencephalon (A11 region) are present in the ventral horn of the mouse adult spinal cord, an area where dopamine receptors and motor circuits are located (Yoshida and Tanaka, 1988; Weil-Fugazza and Godefroy, 1993; Qu et al., 2006; Zhu et al., 2007). The release of dopamine and its metabolites occurs in the ventral horn of neonatal rats during fictive locomotion (Jordan and Schmidt, 2002) and in the spinal cord of adult rats following walking (Gerin and Privat, 1998). Moreover, administration of D_1 agonists in adult mice with a complete thoracic injury elicited bouts of stepping (Lapointe et al., 2009). Finally, the critical role played by dopamine transmission in locomotion is highlighted by the fact that L-DOPA-elicited air stepping in intact neonatal rats is blocked by intrathecally introduced dopamine receptor antagonists (Sickles et al., 1992; McCrea et al., 1997). Work by several groups (Fleetwood-Walker et al., 1988; Taniguchi et al., 2011) has shown that stimulation of A11 in adult animals has effects on nociception, acting both pre- and post-synaptically on neurons within the dorsal horn of the spinal cord (Taniguchi et al., 2011), and inhibited by dopaminergic antagonists. Taken together, these data suggest that A11 activation can influence spinal cord circuits via dopamine, and dopamine can have several actions on spinal motor circuits.

Like many nuclei the A11 is known to project to other areas of the brain, including the amygdala, prefrontal cortex (Takada et al., 1988; Takada, 1990, 1993), and dorsal raphe (Peyron et al., 1995). Indeed diencephalon-specific pathways to the brainstem, including the medullary reticular formation and the mesencephalic locomotor region have been shown in the past (Sinnamon and Stopford, 1987; Sinnamon et al., 1987). We expect therefore that the A11 connectome is more extensive than has been published. Therefore while spinal cord connections may be responsible for the observed effects, A11 collaterals projecting to other brain regions may also be involved. Within the A11 we found neurons that were positive for vGluT2 and negative for vGAT. But we did not find cells that co-localized dopamine and vGluT2. However, vGluT3 neurons are found in the A11 vicinity (Allen Brain Atlas) so it is possible that dopamine neurons could still contain glutamate. Our data show some $vGAT^+$ positive neurons in the A11 region, agreeing with data from the Allen Brain Atlas, and we saw no $vGAT^+$-TH^+-IR neurons.

Effects on Motor Activity

We found that photostimulation of the A11 region produced immediate responses that, although varied, always led to locomotion. The delay in the initiation of locomotion is consistent with early reports of stimulation of this region (Mori et al., 1989; Sławińska and Kasicki, 1995). There are several possibilities for this delay. The A11 network may form a reverberating positive-feedback local network resulting in an increase in spike output over time, and the fact that vGluT2 neurons are in the A11 region point to this being a possibility. We do not feel that the delay may be due to fast inhibitory neurons being recruited since our data do not show $vGAT^+$ somata within the A11. On the other hand, low concentrations of dopamine

bind to high-affinity $D_{2/3/4}$ receptors, producing inhibition. At higher dopamine concentrations, expected with prolonged spiking within the A11, a switch to excitation could occur (Clemens et al., 2012). Alternatively, an interesting observation is that within the isolated spinal cord preparation of the rodent, bath application of dopamine produces a delayed activation of the network often being an order of magnitude slower compared to 5-HT application (Gozal et al., 2014). An action of dopamine on trace amine receptors (TAAR1) has been proposed to account for this delay in the rat (Bunzow et al., 2001; Gozal et al., 2014) and a similar mechanism operating *in vivo* could partly account for the delays noted here. A component of the A11 cells activated were presumably D-cells (Jaeger et al., 1983), which lack TH but contain AADC, based on the Allen Brain Atlas, and our own work. Little is known about the storage and release of dopamine (or other transmitters) from these cells. Work by Weihe et al. (2006) shows evidence of hypothalamic $AADC^+/TH^-$ cells that lack VMAT2. Therefore neurotransmitter release from D-cells likely occurs differently from the standard vesicular-based dopamine release. Recent evidence shows that the hypothalamic neurons containing glutamate, GABA, and dopamine cells can be subdivided into 62 distinct subpopulations where neuropeptides are co-localized in a distinct manner (Romanov et al., 2017). While our data show that the A11 contains a small number of vGluT2 neurons we did not see any co-expression with TH^+ neurons, but vGluT3 expression was not tested here, and is observed in the A11 region, therefore glutamate co-localization in TH^+ neurons may still be possible. Our RT-PCR data showed that the levels of Cre mRNA are between 36 and 41% of TH mRNA in heterozygous TH-tdTomato mice, which is close to our expectations of 50% levels. Slightly lower levels of Cre mRNA may be due to the possibility that the locus of TH transcription is more active than the locus of Cre transcription. On the other hand, this supports the idea of active transcription of TH mRNA in the absence of the translation of TH protein which was highlighted in a recent report (Meng et al., 2018). In this regard, we feel that future attempts using other techniques such as double fluorescent in situ hybridization or single cell RNA-seq may provide additional insights on molecular and cellular diversity in phenotypes of TH cells in the A11. The most conservative interpretation of our data is that at a minimum 54% of ChR2-TH^+ neurons were dopaminergic, and a possibility remains that this percentage could be higher. Since we did not observe co-localization of vGAT or vGluT2 with TH^+-IR, we conclude that the stimulated population includes mainly dopaminergic neurons, D-cells, and an undefined neuronal population.

CONCLUSION

This is the first study to show that stimulation of the A11 has pro-locomotory effects. This adds to the hypothesized role of the A11 in RLS (Clemens et al., 2006; Qu et al., 2006, 2007), where patients suffer from an uncontrolled desire to move their limbs associated with modulation of D_3 receptors in the spinal cord (Maitra et al., 1993). Further clues to the role of the A11 in motor control will require selective activation and inactivation of spinally projecting axons to differentiate direct from indirect actions on spinal cord functions. Given the robust effects of dopamine on modulation of spinal circuits (Sharples et al., 2014) this would be an interesting target to investigate. A11 forms one of many nuclei in the diencephalon and midbrain that have motor effects and connect with nuclei in the brainstem and spinal cord (Kim et al., 2017; Brownstone and Chopek, 2018; Gatto and Goulding, 2018; Sharma et al., 2018). A more complete understanding of their role will require parallel recording and stimulation of these distinct regions during complex motor behavior.

AUTHOR CONTRIBUTIONS

KK performed the experiments, analyzed the data, and wrote and edited the paper. CJ-X participated in performing experiments, analyzed data, edited the paper, and participated in experimental design. SS participated in performing experiments, edited the paper, and participated in experimental design. TF edited the paper, analyzed the data, and participated in performing experiments. LY, SEAE, and CHTK performed experiments, analyzed data, and edited the paper. JB participated in experiment design and edited the paper. PW conceived the experiments, supervised the research, and edited and wrote the paper.

ACKNOWLEDGMENTS

We acknowledge grant support from the Canadian Institutes of Health Research and from the HALO initiative, HBI. KK and LY received studentship support from Alberta Innovates Health Solutions; KK also received support from the Fong studentship (Hotchkiss Brain Institute) and Eyes High (University of Calgary). We acknowledge technical assistance from Ms. Jillian Ejdrygiewicz, Ms. Claude Veillette, and Ms. Michelle Tran. We also acknowledge technical support from the RUN/HBI-AMP Core Microscopy, the HALO Behavioral Facility, and Dr. Frank Visser from the Molecular Core Facility at the University of Calgary. We acknowledge assistance from Dr. Luis de Lecea's lab (Stanford University) in ferrule implantation. The TH-IRES-Cre mice were a kind gift from Dr. Antoine Adamantidis (Universität Bern). The vGluT2 mice were a kind gift from Dr. Marie-Claude Perreault (Emory University).

SUPPLEMENTARY MATERIAL

The Supplementary Material for this article can be found online at: https://www.frontiersin.org/articles/10.3389/fncir.2018.00086/full#supplementary-material

VIDEO 1 | Photostimulation of $A11^{ChR2}$ mouse during the open field test.

REFERENCES

Abdallah, K., Monconduit, L., Artola, A., Luccarini, P., and Dallel, R. (2015). GABAAergic inhibition or dopamine denervation of the A11 hypothalamic nucleus induces trigeminal analgesia. *Pain* 156, 644–655. doi: 10.1097/j.pain.0000000000000091

Abrahamson, E. E., and Moore, R. Y. (2001). The posterior hypothalamic area: chemoarchitecture and afferent connections. *Brain Res.* 889, 1–22. doi: 10.1016/S0006-8993(00)03015-8

Barraud, Q., Obeid, I., Aubert, I., Barrière, G., Contamin, H., Mcguire, S., et al. (2010). Neuroanatomical study of the A11 diencephalospinal pathway in the non-human primate. *PLoS One* 5:e13306. doi: 10.1371/journal.pone.0013306

Barrière, G., Mellen, N., and Cazalets, J.-R. (2004). Neuromodulation of the locomotor network by dopamine in the isolated spinal cord of newborn rat. *Eur. J. Neurosci.* 19, 1325–1335. doi: 10.1111/j.1460-9568.2004.03210.x

Björklund, A., and Skagerberg, G. (1979). Evidence for a major spinal cord projection from the diencephalic A11 dopamine cell group in the rat using transmitter-specific fluorescent retrograde tracing. *Brain Res.* 177, 170–175. doi: 10.1016/0006-8993(79)90927-2

Brownstone, R. M., and Chopek, J. W. (2018). Reticulospinal systems for tuning motor commands. *Front. Neural Circuits* 12:30. doi: 10.3389/fncir.2018.00030

Bunzow, J. R., Sonders, M. S., Arttamangkul, S., Harrison, L. M., Zhang, G., Quigley, D. I., et al. (2001). Amphetamine, 3,4-methylenedioxymethamphetamine, lysergic acid diethylamide, and metabolites of the catecholamine neurotransmitters are agonists of a rat trace amine receptor. *Mol. Pharmacol.* 60, 1181–1188. doi: 10.1124/mol.60.6.1181

Bustin, S. A., Benes, V., Garson, J. A., Hellemans, J., Huggett, J., Kubista, M., et al. (2009). The MIQE guidelines: minimum information for publication of quantitative real-time PCR experiments. *Clin. Chem.* 55, 611–622. doi: 10.1373/clinchem.2008.112797

Charbit, A. R., Akerman, S., Holland, P. R., and Goadsby, P. J. (2009). Neurons of the dopaminergic/calcitonin gene-related peptide A11 cell group modulate neuronal firing in the trigeminocervical complex: an electrophysiological and immunohistochemical study. *J. Neurosci.* 29, 12532–12541. doi: 10.1523/JNEUROSCI.2887-09.2009

Christie, K. J., and Whelan, P. J. (2005). Monoaminergic establishment of rostrocaudal gradients of rhythmicity in the neonatal mouse spinal cord. *J. Neurophysiol.* 94, 1554–1564. doi: 10.1152/jn.00299.2005

Clemens, S., Belin-Rauscent, A., Simmers, J., and Combes, D. (2012). Opposing modulatory effects of D1- and D2-like receptor activation on a spinal central pattern generator. *J. Neurophysiol.* 107, 2250–2259. doi: 10.1152/jn.00366.2011

Clemens, S., and Hochman, S. (2004). Conversion of the modulatory actions of dopamine on spinal reflexes from depression to facilitation in D3 receptor knock-out mice. *J. Neurosci.* 24, 11337–11345. doi: 10.1523/JNEUROSCI.3698-04.2004

Clemens, S., Rye, D., and Hochman, S. (2006). Restless legs syndrome: revisiting the dopamine hypothesis from the spinal cord perspective. *Neurology* 67, 125–130. doi: 10.1212/01.wnl.0000223316.53428.c9

Commissiong, J. W., Gentleman, S., and Neff, N. H. (1979). Spinal cord dopaminergic neurons: evidence for an uncrossed nigrospinal pathway. *Neuropharmacology* 18, 565–568. doi: 10.1016/0028-3908(79)90102-3

Dahlström, A., and Fuxe, K. (1964). Evidence for the existence of monoamine-containing neurons in the central nervous system. I. Demonstration of monoamines in the cell bodies of brain stem neurons. *Acta Physiol. Scand. Suppl.* 232, 1–55.

Fleetwood-Walker, S. M., Hope, P. J., and Mitchell, R. (1988). Antinociceptive actions of descending dopaminergic tracts on cat and rat dorsal horn somatosensory neurones. *J. Physiol.* 399, 335–348. doi: 10.1113/jphysiol.1988.sp017084

Gatto, G., and Goulding, M. (2018). Locomotion control: brainstem circuits satisfy the need for speed. *Curr. Biol.* 28, R256–R259. doi: 10.1016/j.cub.2018.01.068

Gerin, C., and Privat, A. (1998). Direct evidence for the link between monoaminergic descending pathways and motor activity: II. A study with microdialysis probes implanted in the ventral horn of the spinal cord. *Brain Res.* 794, 169–173. doi: 10.1016/S0006-8993(98)00278-9

Gordon, I. T., and Whelan, P. J. (2006). Monoaminergic control of cauda-equina-evoked locomotion in the neonatal mouse spinal cord. *J. Neurophysiol.* 96, 3122–3129. doi: 10.1152/jn.00606.2006

Gozal, E. A., O'Neill, B. E., Sawchuk, M. A., Zhu, H., Halder, M., Chou, C.-C., et al. (2014). Anatomical and functional evidence for trace amines as unique modulators of locomotor function in the mammalian spinal cord. *Front. Neural Circuits* 8:134. doi: 10.3389/fncir.2014.00134

Han, P., Nakanishi, S. T., Tran, M. A., and Whelan, P. J. (2007). Dopaminergic modulation of spinal neuronal excitability. *J. Neurosci.* 27, 13192–13204. doi: 10.1523/JNEUROSCI.1279-07.2007

Han, P., and Whelan, P. J. (2009). Modulation of AMPA currents by D(1)-like but not D(2)-like receptors in spinal motoneurons. *Neuroscience* 158, 1699–1707. doi: 10.1016/j.neuroscience.2008.11.040

Hochman, S. (2015). Metabolic recruitment of spinal locomotion: intracellular neuromodulation by trace amines and their receptors. *Neural Regen. Res.* 10, 1940–1942. doi: 10.4103/1673-5374.169625

Humphreys, J., and Whelan, P. (2011). Dopamine exerts activation dependent modulation of spinal locomotor circuits in the mouse. *J. Neurophysiol.* 108, 3370–3381. doi: 10.1152/jn.00482.2012

Humphreys, J. M., and Whelan, P. J. (2012). Dopamine exerts activation-dependent modulation of spinal locomotor circuits in the neonatal mouse. *J. Neurophysiol.* 108, 3370–3381. doi: 10.1152/jn.00482.2012

Jaeger, C. B., Teitelman, G., Joh, T. H., Albert, V. R., Park, D. H., and Reis, D. J. (1983). Some neurons of the rat central nervous system contain aromatic-L-amino-acid decarboxylase but not monoamines. *Science* 219, 1233–1235. doi: 10.1126/science.6131537

Jiang, Z., Carlin, K. P., and Brownstone, R. M. (1999). An in vitro functionally mature mouse spinal cord preparation for the study of spinal motor networks. *Brain Res.* 816, 493–499. doi: 10.1016/S0006-8993(98)01199-8

Jordan, L. M., and Schmidt, B. J. (2002). Propriospinal neurons involved in the control of locomotion: potential targets for repair strategies? *Prog. Brain Res.* 137, 125–139. doi: 10.1016/S0079-6123(02)37012-2

Kiehn, O., and Kjaerulff, O. (1996). Spatiotemporal characteristics of 5-HT and dopamine-induced rhythmic hindlimb activity in the in vitro neonatal rat. *J. Neurophysiol.* 75, 1472–1482. doi: 10.1152/jn.1996.75.4.1472

Kiehn, O., Sillar, K. T., Kjaerulff, O., and McDearmid, J. R. (1999). Effects of noradrenaline on locomotor rhythm–generating networks in the isolated neonatal rat spinal cord. *J. Neurophysiol.* 82, 741–746. doi: 10.1152/jn.1999.82.2.741

Kim, L. H., Sharma, S., Sharples, S. A., Mayr, K. A., Kwok, C. H. T., and Whelan, P. J. (2017). Integration of descending command systems for the generation of context-specific locomotor behaviors. *Front. Neurosci.* 11:581. doi: 10.3389/fnins.2017.00581

Koblinger, K., Füzesi, T., Ejdrygiewicz, J., Krajacic, A., Bains, J. S., and Whelan, P. J. (2014). Characterization of a11 neurons projecting to the spinal cord of mice. *PLoS One* 9:e109636. doi: 10.1371/journal.pone.0109636

Koblinger, K., Jean-Xavier, C., Ejdrygiewicz, J., Fuzesi, T., Bains, J. S., and Whelan, P. J. (2015). "A11 optogenetic stimulation elicits locomotor activity in mice," in *Conference Society for Neuroscience*, Chicago, IL.

Lambert, A. M., Bonkowsky, J. L., and Masino, M. A. (2012). The conserved dopaminergic diencephalospinal tract mediates vertebrate locomotor development in zebrafish larvae. *J. Neurosci.* 32, 13488–13500. doi: 10.1523/JNEUROSCI.1638-12.2012

Lammel, S., Steinberg, E. E., Földy, C., Wall, N. R., Beier, K., Luo, L., et al. (2015). Diversity of transgenic mouse models for selective targeting of midbrain dopamine neurons. *Neuron* 85, 429–438. doi: 10.1016/j.neuron.2014.12.036

Lapointe, N. P., Rouleau, P., Ung, R.-V., and Guertin, P. A. (2009). Specific role of dopamine D1 receptors in spinal network activation and rhythmic movement induction in vertebrates. *J. Physiol.* 587, 1499–1511. doi: 10.1113/jphysiol.2008.166314

Liu, J., and Jordan, L. M. (2005). Stimulation of the parapyramidal region of the neonatal rat brain stem produces locomotor-like activity involving spinal 5-HT7 and 5-HT2A receptors. *J. Neurophysiol.* 94, 1392–1404. doi: 10.1152/jn.00136.2005

Madriaga, M. A., McPhee, L. C., Chersa, T., Christie, K. J., and Whelan, P. J. (2004). Modulation of locomotor activity by multiple 5-HT and dopaminergic receptor subtypes in the neonatal mouse spinal cord. *J. Neurophysiol.* 92, 1566–1576. doi: 10.1152/jn.01181.2003

Maitra, K. K., Seth, P., Thewissen, M., Ross, H. G., and Ganguly, D. K. (1993). Dopaminergic influence on the excitability of antidromically activated Renshaw

cells in the lumbar spinal cord of the rat. *Acta Physiol. Scand.* 148, 101–107. doi: 10.1111/j.1748-1716.1993.tb09538.x

McCrea, A. E., Stehouwer, D. J., and van Hartesveldt, C. (1997). Dopamine D1 and D2 antagonists block L-DOPA-induced air-stepping in decerebrate neonatal rats. *Brain Res. Dev. Brain Res.* 100, 130–132. doi: 10.1016/S0165-3806(97)00027-8

Megat, S., Shiers, S., Moy, J. K., Barragan-Iglesias, P., Pradhan, G., Seal, R. P., et al. (2018). A critical role for dopamine d5 receptors in pain chronicity in male mice. *J. Neurosci.* 38, 379–397. doi: 10.1523/JNEUROSCI.2110-17.2017

Meng, D., Li, H.-Q., Deisseroth, K., Leutgeb, S., and Spitzer, N. C. (2018). Neuronal activity regulates neurotransmitter switching in the adult brain following light-induced stress. *Proc. Natl. Acad. Sci. U.S.A.* 115, 5064–5071. doi: 10.1073/pnas.1801598115

Millan, M. J. (2002). Descending control of pain. *Prog. Neurobiol.* 66, 355–474. doi: 10.1016/S0301-0082(02)00009-6

Mori, S., Sakamoto, T., Ohta, Y., Takakusaki, K., and Matsuyama, K. (1989). Site-specific postural and locomotor changes evoked in awake, freely moving intact cats by stimulating the brainstem. *Brain Res.* 505, 66–74. doi: 10.1016/0006-8993(89)90116-9

Okura, M., Fujiki, N., Kita, I., Honda, K., Yoshida, Y., Mignot, E., et al. (2004). The roles of midbrain and diencephalic dopamine cell groups in the regulation of cataplexy in narcoleptic Dobermans. *Neurobiol. Dis.* 16, 274–282. doi: 10.1016/j.nbd.2004.02.008

Pappas, S. S., Behrouz, B., Janis, K. L., Goudreau, J. L., and Lookingland, K. J. (2008). Lack of D2 receptor mediated regulation of dopamine synthesis in A11 diencephalospinal neurons in male and female mice. *Brain Res.* 1214, 1–10. doi: 10.1016/j.brainres.2008.03.010

Pappas, S. S., Tiernan, C. T., Behrouz, B., Jordan, C. L., Breedlove, S. M., Goudreau, J. L., et al. (2010). Neonatal androgen-dependent sex differences in lumbar spinal cord dopamine concentrations and the number of A11 diencephalospinal dopamine neurons. *J. Comp. Neurol.* 518, 2423–2436. doi: 10.1002/cne.22340

Peyron, C., Luppi, P. H., Kitahama, K., Fort, P., Hermann, D. M., and Jouvet, M. (1995). Origin of the dopaminergic innervation of the rat dorsal raphe nucleus. *Neuroreport* 6, 2527–2531. doi: 10.1097/00001756-199512150-00019

Picton, L. D., Nascimento, F., Broadhead, M. J., Sillar, K. T., and Miles, G. B. (2017). Sodium pumps mediate activity-dependent changes in mammalian motor networks. *J. Neurosci.* 37, 906–921. doi: 10.1523/JNEUROSCI.2005-16.2016

Qu, S., Le, W., Zhang, X., Xie, W., Zhang, A., and Ondo, W. G. (2007). Locomotion is increased in a11-lesioned mice with iron deprivation: a possible animal model for restless legs syndrome. *J. Neuropathol. Exp. Neurol.* 66, 383–388. doi: 10.1097/nen.0b013e3180517b5f

Qu, S., Ondo, W. G., Zhang, X., Xie, W. J., Pan, T. H., and Le, W. D. (2006). Projections of diencephalic dopamine neurons into the spinal cord in mice. *Exp. Brain Res.* 168, 152–156. doi: 10.1007/s00221-005-0075-1

Romanov, R. A., Zeisel, A., Bakker, J., Girach, F., Hellysaz, A., Tomer, R., et al. (2017). Molecular interrogation of hypothalamic organization reveals distinct dopamine neuronal subtypes. *Nat. Neurosci.* 20, 176–188. doi: 10.1038/nn.4462

Ryu, S., Mahler, J., Acampora, D., Holzschuh, J., Erhardt, S., Omodei, D., et al. (2007). Orthopedia homeodomain protein is essential for diencephalic dopaminergic neuron development. *Curr. Biol.* 17, 873–880. doi: 10.1016/j.cub.2007.04.003

Schmidt, B. J., and Jordan, L. M. (2000). The role of serotonin in reflex modulation and locomotor rhythm production in the mammalian spinal cord. *Brain Res. Bull.* 53, 689–710. doi: 10.1016/S0361-9230(00)00402-0

Seth, P., Gajendiran, M., Maitra, K. K., Ross, H. G., and Ganguly, D. K. (1993). Evidence for D1 dopamine receptor-mediated modulation of the synaptic transmission from motor axon collaterals to Renshaw cells in the rat spinal cord. *Neurosci. Lett.* 158, 217–220. doi: 10.1016/0304-3940(93)90268-P

Sharma, S., Kim, L. H., Mayr, K. A., Elliott, D. A., and Whelan, P. J. (2018). Parallel descending dopaminergic connectivity of A13 cells to the brainstem locomotor centers. *Sci. Rep.* 8:7972. doi: 10.1038/s41598-018-25908-5

Sharples, S. A., Humphreys, J. M., Jensen, A. M., Dhoopar, S., Delaloye, N., Clemens, S., et al. (2015). Dopaminergic modulation of locomotor network activity in the neonatal mouse spinal cord. *J. Neurophysiol.* 113, 2500–2510. doi: 10.1152/jn.00849.2014

Sharples, S. A., Koblinger, K., Humphreys, J. M., and Whelan, P. J. (2014). Dopamine: a parallel pathway for the modulation of spinal locomotor networks. *Front. Neural Circuits* 8:55. doi: 10.3389/fncir.2014.00055

Sharples, S. A., and Whelan, P. J. (2017). Modulation of rhythmic activity in mammalian spinal networks is dependent on excitability state. *eNeuro* 4:ENEURO.0368-16.2017. doi: 10.1523/ENEURO.0368-16.2017

Shik, M. L., and Orlovsky, G. N. (1976). Neurophysiology of locomotor automatism. *Physiol. Rev.* 56, 465–501. doi: 10.1152/physrev.1976.56.3.465

Sickles, A. E., Stehouwer, D. J., and van Hartesveldt, C. (1992). Dopamine D1 and D2 antagonists block L-dopa-elicited air-stepping in neonatal rats. *Brain Res. Dev. Brain Res.* 68, 17–22. doi: 10.1016/0165-3806(92)90243-P

Sinnamon, H. M., Ginzburg, R. N., and Kurose, G. A. (1987). Midbrain stimulation in the anesthetized rat: direct locomotor effects and modulation of locomotion produced by hypothalamic stimulation. *Neuroscience* 20, 695–707. doi: 10.1016/0306-4522(87)90120-5

Sinnamon, H. M., Lee, S. H., Adams, D. B., and Stopford, C. K. (1984). Locomotor stepping elicited by electrical stimulation of the lateral hypothalamus requires an ipsilateral descending pathway. *Physiol. Behav.* 33, 209–215. doi: 10.1016/0031-9384(84)90101-X

Sinnamon, H. M., and Stopford, C. K. (1987). Locomotion elicited by lateral hypothalamic stimulation in the anesthetized rat does not require the dorsal midbrain. *Brain Res.* 402, 78–86. doi: 10.1016/0006-8993(87)91049-3

Skagerberg, G., and Lindvall, O. (1985). Organization of diencephalic dopamine neurones projecting to the spinal cord in the rat. *Brain Res.* 342, 340–351. doi: 10.1016/0006-8993(85)91134-5

Sławińska, U., and Kasicki, S. (1995). Theta-like rhythm in depth EEG activity of hypothalamic areas during spontaneous or electrically induced locomotion in the rat. *Brain Res.* 678, 117–126. doi: 10.1016/0006-8993(95)00174-O

Sławińska, U., Miazga, K., and Jordan, L. M. (2014). The role of serotonin in the control of locomotor movements and strategies for restoring locomotion after spinal cord injury. *Acta Neurobiol. Exp.* 74, 172–187.

Stuber, G. D., and Wise, R. A. (2016). Lateral hypothalamic circuits for feeding and reward. *Nat. Neurosci.* 19, 198–205. doi: 10.1038/nn.4220

Takada, M. (1990). The A11 catecholamine cell group: another origin of the dopaminergic innervation of the amygdala. *Neurosci. Lett.* 118, 132–135. doi: 10.1016/0304-3940(90)90266-C

Takada, M. (1993). Widespread dopaminergic projections of the subparafascicular thalamic nucleus in the rat. *Brain Res. Bull.* 32, 301–309. doi: 10.1016/0361-9230(93)90191-D

Takada, M., Li, Z. K., and Hattori, T. (1988). Single thalamic dopaminergic neurons project to both the neocortex and spinal cord. *Brain Res.* 455, 346–352. doi: 10.1016/0006-8993(88)90093-5

Tamae, A., Nakatsuka, T., Koga, K., Kato, G., Furue, H., Katafuchi, T., et al. (2005). Direct inhibition of substantia gelatinosa neurones in the rat spinal cord by activation of dopamine D2-like receptors. *J. Physiol.* 568, 243–253. doi: 10.1113/jphysiol.2005.091843

Taniguchi, W., Nakatsuka, T., Miyazaki, N., Yamada, H., Takeda, D., Fujita, T., et al. (2011). In vivo patch-clamp analysis of dopaminergic antinociceptive actions on substantia gelatinosa neurons in the spinal cord. *Pain* 152, 95–105. doi: 10.1016/j.pain.2010.09.034

Ugrumov, M. V. (2009). Non-dopaminergic neurons partly expressing dopaminergic phenotype: distribution in the brain, development and functional significance. *J. Chem. Neuroanat.* 38, 241–256. doi: 10.1016/j.jchemneu.2009.08.004

Weihe, E., Depboylu, C., Schütz, B., Schäfer, M. K.-H., and Eiden, L. E. (2006). Three types of tyrosine hydroxylase-positive CNS neurons distinguished by dopa decarboxylase and VMAT2 co-expression. *Cell. Mol. Neurobiol.* 26, 659–678. doi: 10.1007/s10571-006-9053-9

Weil-Fugazza, J., and Godefroy, F. (1993). Dorsal and ventral dopaminergic innervation of the spinal cord: functional implications. *Brain Res. Bull.* 30, 319–324. doi: 10.1016/0361-9230(93)90259-E

Whelan, P., Bonnot, A., and O'Donovan, M. J. (2000). Properties of rhythmic activity generated by the isolated spinal cord of the neonatal mouse. *J. Neurophysiol.* 84, 2821–2833. doi: 10.1152/jn.2000.84.6.2821

Whelan, P. J. (2017). *Uncovering Parallel Pathways for Movement Control. Program No. 267.06. 2017 Neuroscience Meeting Planner*. Washington, DC: Society for Neuroscience.

Yip, S. H., York, J., Hyland, B., Bunn, S. J., and Grattan, D. R. (2017). Incomplete concordance of dopamine transporter Cre (DATIREScre)-mediated recombination and tyrosine hydroxylase immunoreactivity in the mouse forebrain. *J. Chem. Neuroanat.* 90, 40–48. doi: 10.1016/j.jchemneu.2017.12.002

Yoshida, M., and Tanaka, M. (1988). Existence of new dopaminergic terminal plexus in the rat spinal cord: assessment by immunohistochemistry using anti-dopamine serum. *Neurosci. Lett.* 94, 5–9. doi: 10.1016/0304-3940(88)90261-3

Young, C. K., Koke, S. J., Kiss, Z. H., and Bland, B. H. (2009). Deep brain stimulation of the posterior hypothalamic nucleus reverses akinesia in bilaterally 6-hydroxydopamine-lesioned rats. *Neuroscience* 162, 1–4. doi: 10.1016/j.neuroscience.2009.04.053

Zhu, H., Clemens, S., Sawchuk, M. A., and Hochman, S. (2007). Expression and distribution of all dopamine receptor subtypes (D(1)-D(5)) in the mouse lumbar spinal cord: a real-time polymerase chain reaction and non-autoradiographic in situ hybridization study. *Neuroscience* 149, 885–897. doi: 10.1016/j.neuroscience.2007.07.052

Conflict of Interest Statement: The authors declare that the research was conducted in the absence of any commercial or financial relationships that could be construed as a potential conflict of interest.

Copyright © 2018 Koblinger, Jean-Xavier, Sharma, Füzesi, Young, Eaton, Kwok, Bains and Whelan. This is an open-access article distributed under the terms of the Creative Commons Attribution License (CC BY). The use, distribution or reproduction in other forums is permitted, provided the original author(s) and the copyright owner(s) are credited and that the original publication in this journal is cited, in accordance with accepted academic practice. No use, distribution or reproduction is permitted which does not comply with these terms.

frontiers in Neuroscience

ORIGINAL RESEARCH
published: 30 October 2018
doi: 10.3389/fnins.2018.00775

Electroacupuncture Inhibits Visceral Nociception via Somatovisceral Interaction at Subnucleus Reticularis Dorsalis Neurons in the Rat Medulla

Lingling Yu[1,2], Liang Li[2], Qingguang Qin[2], Yutian Yu[2], Xiang Cui[2], Peijing Rong[2] and Bing Zhu[2]**

[1] Department of Neurology, Tongji Hospital, Tongji Medical College, Huazhong University of Science and Technology, Wuhan, China, [2] Institute of Acupuncture and Moxibustion, China Academy of Chinese Medical Sciences, Beijing, China

Electroacupuncture (EA) is an efficacious treatment for alleviating visceral pain, but the underlining mechanisms are not fully understood. This study investigated the role of medullary subnucleus reticularis dorsalis (SRD) neurons in the effects of EA on visceral pain. We recorded the discharges of SRD neurons extracellularly by glass micropipettes on anesthetized rats. The responses characteristics of SRD neurons to different intensities of EA (0.5, 1, 2, 4, 6, and 8 mA, 0.5 ms, and 2 Hz) on acupoints "Zusanli" (ST 36) and "Shangjuxu" (ST 37) before and during noxious colorectal distension (CRD) were analyzed. Our results indicated that SRD neurons responded to either a noxious EA stimulation ranging from 2 to 8 mA or to noxious CRD at 30 and 60 mmHg by increasing their discharge frequency at an intensity-dependent manner. However, during the stimulation of both CRD and EA, the increasing discharges of SRD neurons induced by CRD were significantly inhibited by 2–8 mA of EA. Furthermore, SRD neurons can encode the strength of EA, where a positive correlation between current intensity and the magnitude of neuronal responses to EA was observed within 2–6 mA. Yet, the responses of SRD neurons to EA stimulation reached a plateau when EA exceeded 6 mA. In addition, 0.5–1 mA of EA had no effect on CRD-induced nociceptive responses of SRD neurons. In conclusion, EA produced an inhibiting effect on visceral nociception in an intensity-dependent manner, which probably is due to the somatovisceral interaction at SRD neurons.

Keywords: electroacupuncture, visceral pain, colorectal distension, subnucleus reticularis dorsalis, analgesia

OPEN ACCESS

Edited by:
Ioan Opris,
University of Miami, United States

Reviewed by:
Guang-Yin Xu,
Soochow University, China
Man Li,
Huazhong University of Science and Technology, China

****Correspondence:***
Peijing Rong
drrongpj@163.com
Bing Zhu
zhubing@mail.cintcm.ac.cn

Specialty section:
This article was submitted to Autonomic Neuroscience, a section of the journal Frontiers in Neuroscience

Received: *28 August 2018*
Accepted: *05 October 2018*
Published: *30 October 2018*

Citation:
Yu L, Li L, Qin Q, Yu Y, Cui X, Rong P and Zhu B (2018) Electroacupuncture Inhibits Visceral Nociception via Somatovisceral Interaction at Subnucleus Reticularis Dorsalis Neurons in the Rat Medulla. Front. Neurosci. 12:775. doi: 10.3389/fnins.2018.00775

INTRODUCTION

Visceral pain is one of the most common symptoms in patients with gastrointestinal disorders (Sach et al., 2002). It is usually associated with impaired health-related quality of life and a significant health care burden (Chang, 2004; Spiegel et al., 2004). Electroacupuncture (EA) therapy is an effective analgesic by delivering of electrical current to acupoints via acupuncture needles connected to an electrical stimulator (Zhao, 2008). Many behavioral studies have confirmed that EA stimulation exerts good effects on rats with acute or chronic visceral hyperalgesia (Qi and Li, 2012; Wang et al., 2012). In addition, EA therapy has been proven to be effective in treating visceral

pain in long–term follow–up clinical trials (MacPherson et al., 2017). It is generally accepted that EA analgesia is an integrative process of afferent impulses between pain regions and acupoints at convergence neurons and this process involves different levels of central structures, such as spinal dorsal horn (Rong et al., 2005), nucleus tractus solitarius (Liu et al., 2014) and periaqueductal gray (Wang et al., 2014). However, the involvement of other convergence neurons in EA analgesia is still unknown.

Accumulating evidence suggests that subnucleus reticularis dorsalis (SRD), the caudal-most aspect of the medulla, plays an important role in the transmission and modulation of nociceptive information (Villanueva et al., 1996). Neurons within SRD are not only activated exclusively by somatic noxious stimuli (mechanical, thermal, or chemical noxious stimuli) applied to widespread areas of the body (Villanueva et al., 1988, 1990), but also respond to noxious visceral stimuli (Roy et al., 1992). Owing to the widespread nociceptive convergence, SRD neurons might contribute to the processing of visceral nociception. In fact, SRD has been verified as a critical region in the pain-inhibiting effect of diffuse noxious inhibitory controls (DNIC) (Bouhassira et al., 1992; Villanueva and Le Bars, 1995). In order to explore the role of SRD neurons in the effects of EA on visceral nociception, the response characteristics of SRD neurons to different intensities of EA before and during noxious CRD was observed and investigated in the present study.

MATERIALS AND METHODS

Animals Preparations

Thirty eight male Sprague–Dawley rats, weighing 220–280 g, were purchased from the Laboratory Animal Center of China Academy of Military Medical Sciences [License number: SCXK–(Military)–2016–0024]. This study was carried out in accordance with the recommendations of the Guideline on the Humane Care and Use of Laboratory Animals issued by the Ministry of Science and Technology of the People's Republic of China in 2006. The protocol was approved by the CACMS Animal Ethics Committee (No. 20160218). Rats were housed in standard laboratory conditions under artificial 12 h light/dark cycle and at an ambient temperature of 22 ± 0.5. Food and water were available *ad libitum*. After an overnight fast of 12 h, rats were deeply anesthetized with 10% urethane (1.0–1.2 g/kg) and artificially ventilated through a tracheal cannula. Body temperature was maintained at 37 ± 0.5 by means of a feedback controlled homoeothermic heating blanket system.

Colorectal Distension

Visceral nociceptive stimulus was generated by noxious CRD. Briefly, A 6 cm balloon was gently inserted into descending colon at 4 cm depth through the anus. During the recording sessions, the balloon in the colon was consecutively inflated with air to produce pressure and the intracolonic pressure was monitored with a pressure transducer. The pressure of CRD stimulation applied to rats was 30 and 60 mmHg. In order to prevent possible sensitization triggered by overstimulation of the colorectum, the interval between two CRD stimulations was at least 10 min.

Recordings

Rats were mounted in a stereotaxic frame with the head fixed in a ventroflexed position by means of a metallic bar cemented to the skull. The caudal medulla was exposed by removing the overlying musculature, atlantooccipital membrane, and dura mater.

Unitary extracellular recordings were made with glass micropipettes (8–12 MΩ) filled with a mixture of 2% pontamine sky blue dye and 0.1 M of natrium aceticum. Micropipettes were inserted on the right side of the medulla, 1.0–2.0 mm caudal to the obex, and 0.5–l.5 mm lateral to the midline.

Single unit activities were fed into a window discriminator and displayed on an oscilloscope screen. The output of the window discriminator and amplifier were fed into a data acquisition system developed by ADInstrument (Power Lab) through a personal computer and Chart 5.0 was used to compile histograms and waveform files for further analysis.

Electroacupuncture

The rats were treated with EA via a pair of non-insulated acupuncture needles. The needles were inserted into the skin 3 mm apart at the right side of the acupoints "Zusanli" (ST36) and "Shangjuxu" (ST37), which is located in the ipsilateral side of the inserted location of micropipettes. The needles were then connected to an electrical stimulator (88–102G, Nihon Kohden). During a 30 s EA session, intensities of 0.5, 1, 2, 4, 6, and 8 mA were applied in random order. The duration and frequency of electrical stimulation were set at 0.5 ms and 2 Hz.

Experimental Procedure

(1) After locating a neuron with stable discharges, noxious (pinch) and innocuous (brush) skin stimuli were used to identify the targeted neurons. Since SRD neurons were excited by noxious stimulation to widespread areas of the body including foot, tail and finger, but did not response to innocuous stimuli, we first observed neuronal response to pinch and brush stimulation to foot, tail and finger to identify SRD neurons. Only the neurons that can be excited by pinch stimulation to widespread areas of the body characterized as SRD neurons and were used for further study.

(2) Second, responses of SRD neurons to different intensities of single EA stimulation were compared. The baseline activity was recorded for 5 s, then followed by 10 s EA stimulation, then another 5 s recovery of neuronal discharge was recorded after EA stimulation had stopped.

(3) Third, responses of SRD neurons to graded intensities of CRD stimulation were observed. The baseline activity was recorded for 10 s, followed by 10 s CRD stimulation, then another 10 s of recovery of neuronal discharge was recorded after CRD had stopped.

(4) Fourth, the responses of SRD neurons to different intensities of EA during CRD were observed. A standard conditioned recording procedure was administered for 60 s. Recording of 5 s baseline activities and 5 s recovery neuronal activities were acquired before and after 50 s CRD recording

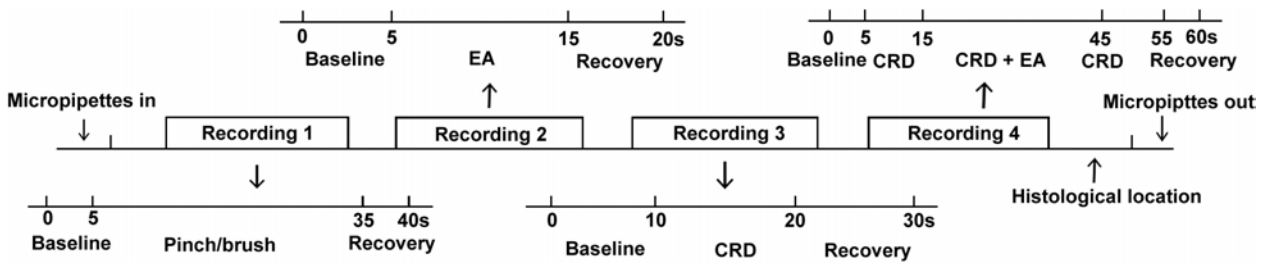


FIGURE 1 | Timeline of experimental prodedure.

procedure. During the CRD recording procedure, an initial 10 s response of neuron activities to CRD were recorded, 30 s of EA stimulation was administrated and the response of neurons to both EA and CRD was recorded, followed by recording of 10 s of responses to CRD.

The interval between any two stimulations was at least 10 min. The timeline of recording protocol was presented in **Figure 1**.

Histological Location

After single unit recordings, the recording sites were marked by electrophoretic deposition of pontamine sky blue and checked by HE coloration. Locations of the recording sites were then determined with reference to the rat brain atlas.

Data Collection and Statistical Analysis

Neuronal discharges per second (identified as $\bar{X} \pm SE\%$) were calculated with PowerLab, Chart 5.0, and SPSS13.0. One way ANOVA and linear regression analyses were used for statistical purposes. $P < 0.05$ was deemed statistically significant.

RESULTS

General Characteristics of SRD Neurons on Medulla

A total of 68 units were recorded within medulla, among which 82.35%(56/68) were characterized as SRD neurons with a "whole body receptive field." Other neuronal types, such as spinal nucleus of trigeminal, were not considered in this paper. Examination of the rat brain slices verified that the recording sites (n = 12) were located in the dorsomedial part of the SRD (**Figure 2**).

SRD neurons could be characterized by their response to mechanical and electrical stimuli, our initial approach is to identify these neurons by their responses to pinch and brush stimuli at various part of the rat's body, which was defined as conditional noxious and innocuous mechanical stimuli. As presented in **Figure 3**, SRD neurons that were recorded responded to noxious pinch stimulation of the foot, tail and finger with increasing neuronal discharges (**Figures 3A–C**), but did not respond to innocuous bursting stimulation of the foot, tail and finger (**Figures 3D–F**).

Effects of EA With Different Intensities on SRD Neurons Before CRD

The neuronal response to graded EA stimulation at acupoints ST 36 and ST 37 was observed on 7 SRD neurons. An individual example of neuronal discharges evoked by graded intensity of

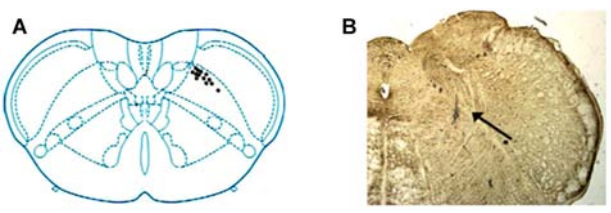


FIGURE 2 | Location of SRD neurons in the medulla. **(A)** Locations of recording sites were marked according to the brain atlas of the rat. **(B)** An individual example showing the location of an SRD neuron marked by pontamine sky blue. Blue dye represents the sites, as indicated by an arrow.

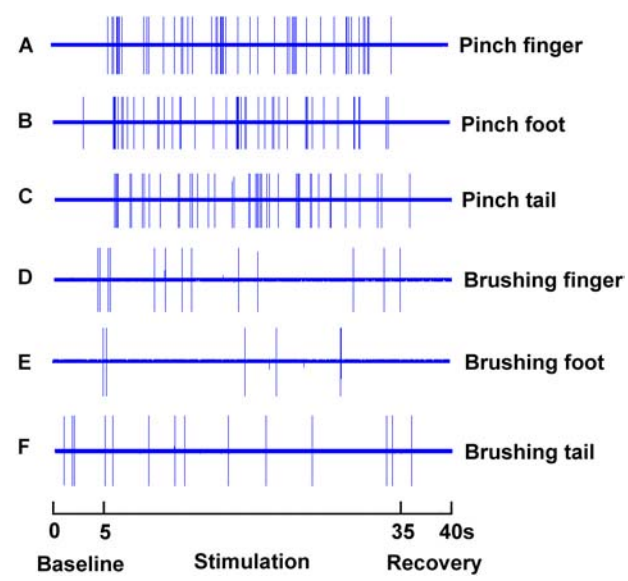


FIGURE 3 | Response characteristics of SRD neurons to innocuous and noxious stimuli. SRD neurons increased neuronal discharges to noxious pinch stimuli of the finger **(A)**, foot **(B)**, and tail **(C)**, but they did not response to innocuous brush stimuli of the finger **(D)**, foot **(E)**, and tail **(F)**.

EA stimulation is presented in **Figure 4**. We found that SRD neurons did not respond to low intensity of EA stimulation (0.5–1 mA), but were significantly activated by high intensity of EA stimulation (2–8 mA). After EA stimulation, the average discharge frequency of SRD neurons was significantly increased from 0.08 ± 0.06 spikes/s at baseline to 1.78 ± 0.42 spikes/s (2 mA), 5.47 ± 0.65 spikes/s (4 mA), 8.89 ± 0.65 spikes/s (6 mA) and 9.03 ± 0.92 spikes/s (8 mA) ($P < 0.05$). There is also a

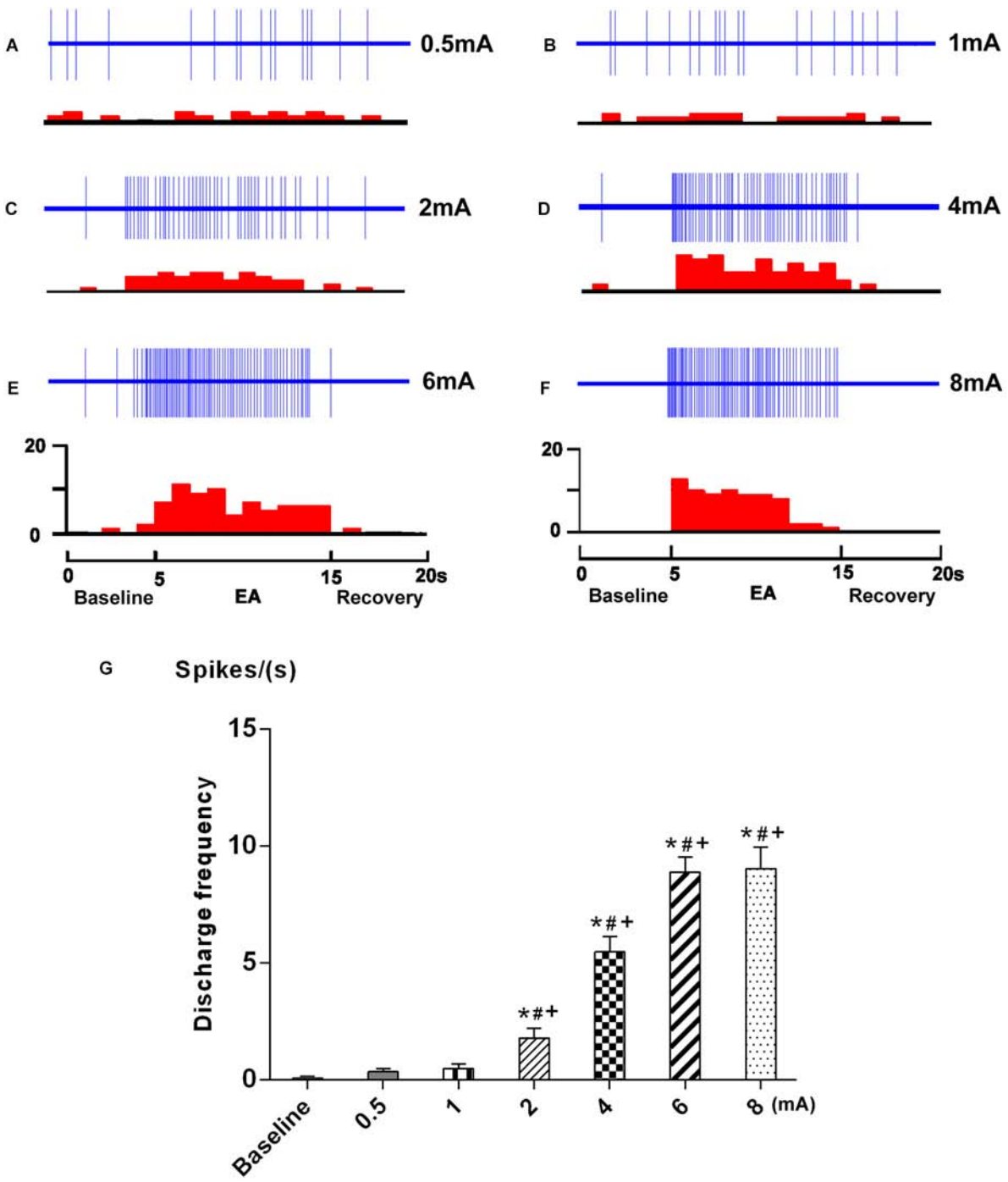


FIGURE 4 | Response characteristics of SRD neurons to graded EA. **(A–F)** Representative examples showing the responses of SRD neuron to graded EA stimulation. The upper rows show the unit discharges at different stimulations and the lower rows show these discharges in histogram. EA (Electroacupuncture) **(G)** A histogram showing the dicharges of SRD neurons ($n = 7$) were significantly activated by EA at 2–8 mA. $^{*}p < 0.05$ compared with baseline; $^{\#}p < 0.05$ compared with 0.5 mA EA; $^{+}p < 0.05$ compared with 1 mA EA.

significant difference between the effects of high intensity of EA (2–8 mA) and low intensity of EA (0.5–1 mA) ($P < 0.05$).

Furthermore, SRD neurons increased their discharges linearly when the intensity of current was raised from 2 to 6 mA; Further increased the current beyond 6 mA resulted in a plateau effect on neuronal responses. These observations indicated that SRD neurons responsed to noxious EA stimuli, and could encode the intensity of EA stimuli within a specific range.

Effects of EA With Different Intensities on the Discharges of SRD Neurons During CRD

In this experiment, we examined 7 SRD neurons on their reactions to CRD stimulation. As showed in **Figure 5**, SRD neurons responsed to 30–60 mmHg CRD with increasing discharge rates. After the stimulation of 30 mmHg CRD, the average discharges of SRD neurons were significantly increased from 0.96 ± 0.32 spikes/s at baseline to 2.97 ± 0.32 spikes/s ($P < 0.001$); when CRD was set at 60 mmHg, the average discharges of SRD neurons were increased to 11.87 ± 0.79 spikes/s($P < 0.001$). This indicates that noxious CRD stimulation could activate the activity of SRD neurons and of significant dose–effect relation.

During the stimulation of 60 mmHg CRD, the response of SRD neurons to different intensities of EA was observed. As illustrated in **Figure 6**, the increased discharges of SRD neurons induced by CRD could be inhibited by EA at 2–8 mA. However, low intensity of EA (0.5–1 mA) had no significant inhibitory effect on CRD induced noxious discharges of SRD neurons.

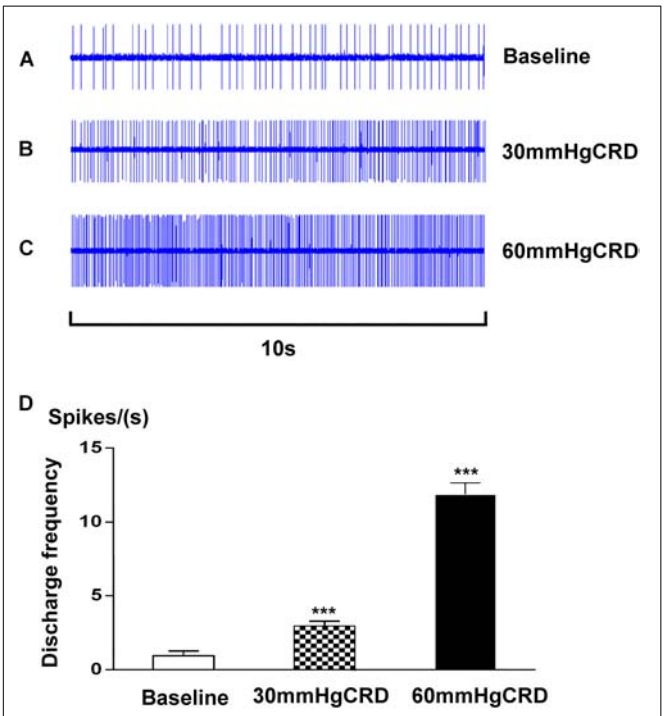


FIGURE 5 | Response characteristics of SRD neurons to graded CRD. **(A–C)** Representative examples showing the responses of SRD neuron to 30–60 mmHg CRD stimulation. **(D)** Cumulative results showing the discharges of SRD neurons ($n = 7$) were significantly activated by 30–60 mmHg CRD stimulation. ***$p < 0.001$ compared with baseline.

When the intensity of the current was set at 2 mA, EA produced a slight, but significant inhibition on the discharges of SRD neurons. The average discharges decreased from 13.02 ± 1.15 spikes/s of CRD to 9.51 ± 0.98 spikes/s, with an inhibiting percentage of 29.91 ± 6.24% ($P < 0.05$, $n = 7$). There is also a significantly difference between the effects of 2 mA EA and 0.5 mA EA ($P < 0.05$), as well as 2 mA EA and 1 mA EA ($P < 0.05$).

When the intensity of the current was set at 4 mA, EA produced a moderate inhibition, the average discharges of SRD neurons decreased from 12.63 ± 1.02 spikes/s of CRD to 5.84 ± 0.74 spikes/s, with an inhibiting percentage of 57.59 ± 4.25 % ($P < 0.05$, $n = 7$). There is also a significantly difference between the effects of 4 mA EA and 0.5 mA EA ($P < 0.05$), as well as 4 mA EA and 1 mA EA ($P < 0.05$).

When the intensity of the current was set at 6 mA, EA produced a stronger inhibition, the average discharges of SRD neurons decreased from 13.15 ± 1.08 spikes/s of CRD to 2.30 ± 0.88 spikes/s, with an inhibiting percentage of 83.36 ± 6.31 % ($P < 0.05$, $n = 7$). There is also a significantly difference between the effects of 6 mA EA and 0.5 mA EA ($P < 0.05$), as well as 6 mA EA and 1 mA EA ($P < 0.05$).

When the intensity of EA was set at 8 mA, EA still produced a strong inhibition, yet this inhibitory effects of EA on the noxious responses of SRD neurons had reached a plateau. After EA, the average discharges of SRD neurons decreased from 13.39 ± 1.02 spikes/s of CRD to 3.65 ± 1.13 spikes/s, with a inhibiting percentage of 73.00 ± 8.14 % ($P < 0.05$, $n = 7$). Although there is also a significantly difference between the effects of 8 mA EA and 0.5 mA EA ($P < 0.05$), as well as 8 mA EA and 1 mA EA ($P < 0.05$). There is no significantly difference between the effects of 8 mA EA and 6 mA EA.

These results indicated that the noxious responses of SRD neurons to CRD could be inhibited by EA in an intensity dependent manner, but such an inhibiting effect of EA reached a plateau when the current exceeded 6 mA.

DISCUSSION

Although EA has been practiced in China since the early 1950s and is widely used for analgesia in clinic, the mechanisms of EA analgesia on visceral pain are not fully understood. In this study, we explored the role of SRD in EA analgesia on visceral pain. Our results demonstrated that the activities of SRD neurons were activated by either a single noxious CRD or 2–8 mA of EA stimulation by increasing their spontaneous discharges. However, the increased discharges of SRD neurons resulted from the stimulation of noxious CRD could be inhibited by 2–8 mA of EA stimulation. These results suggest that visceral nociception could be inhibited by EA via somatovisceral interaction onto SRD neurons.

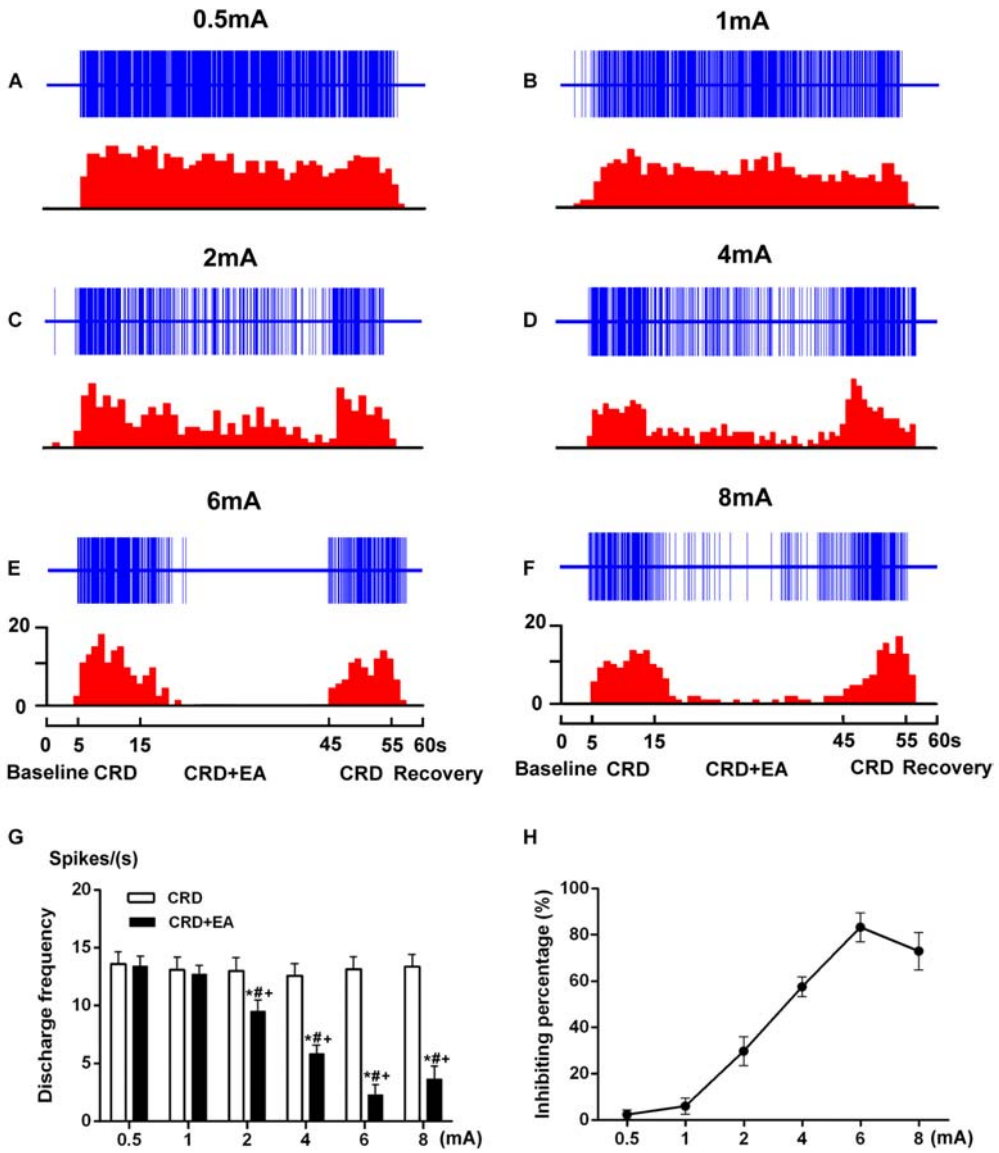


FIGURE 6 | Response characteristics of SRD neurons to different intensities of EA during CRD. **(A–F)** Representative examples showing a decrease in discharges of SRD neurons during the CRD + EA sequence was elicited by EA at 2–8 mA. The upper rows show the unit discharges at different stimulations and the lower rows show these discharges in histogram. Note: CRD (Colorectal distention), CRD + EA (CRD plus EA). **(G)** This histogram shows that CRD induced discharges of SRD neurons were inhibited by EA at 2–8 mA. Data consists of the average spikes per second (mean ± SEM). $^{*}p < 0.05$ compared with CRD; $^{\#}p < 0.05$ compared with 0.5 mA EA; $^{+}p < 0.05$ compared with 1 mA EA. **(H)** This stimulus–response curve shows the percentage of inhibition induced by EA. A positive linear relationship between intensity and inhibition percentage of inhibition was observed within 2–6 mA ($Y = 10.79 \log X + 3.387$, $P < 0.001$). Further increased the intensity to 8 mA induced a significant decrease in inhibition percentage.

The antinociceptive effects of EA on visceral nociception were observed on acupoints ST 36 and ST 37. According to traditional acupuncture theory, the two acupoints are lower confluent acupoint of the meridians of stomach and large intestine, and are used for the treatment of gastrointestinal disease. It has been confirmed by animal experiments that EA and acupuncture stimulation applied at acupoints ST 36 and ST 37 exerts good effects on rats with acute visceral hyperalgesia induced by acetic acid (Qi et al., 2016, 2018) and CRD (Rong et al., 2005). In addition, ST 36 has a specific effect on CRD–induced changes in blood pressure, abnormal electrogastrogram and gastric tension (Chen et al., 2011). In the present study, we observed that noxious EA stimulation of ST 36 and ST 37 is effective in inhibiting visceral nociception at SRD level. Together with previous studies, these findings provide evidence for the efficacy of ST 36 and ST 37 in treating visceral gastrointestinal pain.

SRD could play a specific role in processing nociceptive information. It was a well delimited area within the caudal most aspect of the medulla. Previous electrophysiological studies had clearly demonstrated the response properties of neurons

within SRD to somatic and visceral inputs. The great majority of neurons within SRD did not exhibit spontaneous activity, but these neurons were activated exclusively by thermal, mechanical, and electrical noxious stimulation on any part of the body surface, thus exhibiting a "whole body" receptive field (Villanueva et al., 1988, 1990). In addition, SRD neurons also responded to noxious visceral stimulation (Li et al., 2013; Yu et al., 2014). Similarly, the present study observed the activation responses of SRD neurons evoked by noxious pinch stimulation applied to the foot, tail and finger, and also by noxious CRD stimulation and high intensity of EA stimulation within 2–8 mA. However, SRD neurons did not response to innocuous brush stimulation nor to low intensity of EA stimuli within 0.5–1 mA. Interestingly, the threshold of the intensity for Aδ–and C–fiber activation evoked by EA stimulation was approximately 1.68 ± 0.53 mA and 4.78 ± 0.45 mA, respectively (Zhu et al., 2004). Therefore, EA with the intensity of 2–8 mA could be identified as noxious stimulation. This indicated that SRD neurons have similar characteristics of responses to EA stimulation as to other somatic stimulation, receive solely noxious information.

EA achieves analgesic effects on visceral pain via somatovisceral interactions between pain regions and acupoints at different level of central nervous system. The inhibition of visceral nociception induced by acupuncture has been observed at spinal wide dynamic range neurons in our previous study (Rong et al., 2005). However, the inhibition was abolished by blockade of the central descending pathway, indicating that the effects of EA on visceral nociception may not only modulate by spinal level, but many others in supraspinal center. Accumulating evidences showed that the occurrence of a reciprocal connection between dorsal reticular structure and spinal neurons (Villanueva et al., 1991; Almeida et al., 1993). SRD is an important structure in spino-reticulo-spinal loop, which implicated in the modulating of ascending noxious information (Almeida et al., 1993). In this study, we clearly demonstrated that the nociceptive response of SRD neurons induced by noxious CRD stimulation could be inhibited by EA stimulation within the intensity of 2–8 mA. Because SRD neurons receive only noxious inputs, the nociceptive responses of SRD neurons were not affected by EA stimulation within the intensity of 0.5–1 mA. Our findings provide evidence for the interaction of visceral and EA inputs onto SRD neurons. Together with previous electrophysiological studies (Bing et al., 1991), we reasoned that SRD may be involved in EA analgesia on visceral pain by means of spino-reticulo-spinal feed-back mechanism.

The mechanisms underlying EA induced segmental and extrasegmental analgesia are differ. Electrophysiological studies on somatic pain have shown that segmental analgesia of homotopic EA stimulation can be elicited by the activation of Aβ- and part of Aδ – fibers, whereas extrasegmental analgesia of heterotopic EA stimulation is only effective with intensities strong enough to excite Aδ–or C–fibers (Xu et al., 2003; Zhu et al., 2004; Xin et al., 2016). It is very likely that SRD neurons are involved in the mechanism of the widespread extrasegmental antinociceptive effects of EA.

When the intensity of EA increased to noxious range, EA stimulation produced apparent inhibition of the nociceptive responses in the SRD neurons. The widespread extrasegmental analgesia induced by noxious EA stimuli can also be illustrated by DNIC that was proposed by Le Bars et al. (1979a). DNIC refer to the phenomena that noxious response of convergent neurons of the dorsal horn and/or medullary dorsal horn was inhibited by heterotopic noxious stimuli (Cadden et al., 1983; Cadden and Morrison, 1991). SRD has been verified as an important supraspinal relay in DNIC. Similar to the response properties of SRD neurons, DNIC is triggered only by A δ–and C–fibers (Le Bars et al., 1979b). The arrival of nociceptive inputs to medulla can activate SRD neurons and trigger DNIC function, and then trigger a negative feedback to nociceptive signals (Le Bars, 2002). Actually, 2 Hz EA exert analgesic effect on chronic pain by improve DNIC function (Yuan et al., 2018).

We also found that there is a positive relationship between current intensity and the magnitude of neuronal responses to EA within 2–6 mA, while the responses of SRD neurons to EA reached a plateau beyond 6 mA. The encoding property of SRD neurons to EA closely resembles the encoding property of SRD neurons to electrical stimuli (Villanueva et al., 1989). SRD neurons can encode the intensity of electrical stimuli, especially within the noxious range (Villanueva et al., 1989, Gall et al., 2000), For instance, they responded to the graded intensity of electrical stimuli in the range of 1.5–6.0 mA (Villanueva et al., 1989). However, we must point out that if the electrical current is strong enough to excite C–fibers, EA treatment will inevitably cause unbearable pain in clinical practice. As such, if the intensity of EA exceeds a certain range, this treatment is not suitable for analgesia in patients. The present results show that 6 mA may be sufficient to elicit the optimal analgesic effects on visceral pain rats.

CONCLUSION

The present study emphasizes the important role of SRD neurons in EA analgesia on visceral pain. In normal state, the spontaneous activity of SRD neurons could be activated by EA within 2–8 mA. However, during CRD, the nociceptive responses of SRD neurons could be inhibited by EA within 2–8 mA. In summary, we speculated that the transmission of visceral nociceptive could be inhibited by EA via somatovisceral interaction at SRD neurons.

AUTHOR CONTRIBUTIONS

LY, LL, and QQ performed the experiments. BZ designed the experiments. LY and YY analyzed the data and drafted the manuscript. All the authors discussed the results, reviewed the final manuscript, and approved it for the publication.

FUNDING

This work was funded by National Natural Science Foundation of China (No. 81403475) and the Fundamental Research Funds for the Central Public Welfare Research Institutes (Nos. ZZZD16001 and ZZ10-006).

REFERENCES

Almeida, A., Tavares, I., Lima, D., and Coimbra, A. (1993). Descending projections from the medullary dorsal reticular nucleus make synaptic contacts with spinal cord lamina I cells projecting to that nucleus: an electron microscopic tracer study in the rat. *Neuroscience* 55, 1093–1106. doi: 10.1016/0306-4522(93)90323-8

Bing, Z., Villanueva, L., and Le Bars, D. (1991). Acupuncture-evoked responses of subnucleus reticularis dorsalis neurons in the rat medulla. *Neuroscience* 44, 693–703. doi: 10.1016/0306-4522(91)90088-6

Bouhassira, D., Villanueva, L., Bing, Z., and le Bars, D. (1992). Involvement of the subnucleus reticularis dorsalis in diffuse noxious inhibitory controls in the rat. *Brain Res.* 595, 353–357. doi: 10.1016/0006-8993(92)91071-L

Cadden, S. W., and Morrison, J. F. (1991). Effects of visceral distension on the activities of neurones receiving cutaneous inputs in the rat lumbar dorsal horn; comparison with effects of remote noxious somatic stimuli. *Brain Res.* 558, 63–74. doi: 10.1016/0006-8993(91)90714-7

Cadden, S. W., Villanueva, L., Chitour, D., and Le Bars, D. (1983). Depression of activities of dorsal horn convergent neurones by propriospinal mechanisms triggered by noxious inputs; comparison with diffuse noxious inhibitory controls (DNIC). *Brain Res.* 275, 1–11. doi: 10.1016/0006-8993(83)90412-2

Chang, L. (2004). Review article: epidemiology and quality of life in functional gastrointestinal disorders. *Aliment. Pharmacol. Ther.* 20(Suppl. 7), 31–39. doi: 10.1111/j.1365-2036.2004.02183.x

Chen, S. P., Gao, Y. H., Wang, J. Y., and Liu, J. L. (2011). Effects of electroacupuncture at different points on colorectal distention-induced changes in blood pressure, electrogastrogram, gastric tension and gastric blood flow. *J. Tradit. Chin. Med.* 31, 360–366. doi: 10.1016/S0254-6272(12)60019-3

Gall, O., Villanueva, L., Bouhassira, D., and Le Bars, D. (2000). Spatial encoding properties of subnucleus reticularis dorsalis neurons in the rat medulla. *Brain Res.* 873, 131–134. doi: 10.1016/S0006-8993(00)02524-5

Le Bars, D. (2002). The whole body receptive field of dorsal horn multireceptive neurones. *Brain Res. Brain Res. Rev.* 40, 29–44. doi: 10.1016/S0165-0173(02)00186-8

Le Bars, D., Dickenson, A. H., and Besson, J. M. (1979a). Diffuse noxious inhibitory controls (DNIC). I. Effects on dorsal horn convergent neurones in the rat. *Pain* 6, 283–304. doi: 10.1016/0304-3959(79)90049-6

Le Bars, D., Dickenson, A. H., and Besson, J. M. (1979b). Diffuse noxious inhibitory controls (DNIC). II. Lack of effect on non-convergent neurones, supraspinal involvement and theoretical implications. *Pain* 6, 305–327.

Li, L., Yu, L., Rong, P., Ben, H., Li, X., Zhu, B., et al. (2013). Visceral nociceptive afferent facilitates reaction of subnucleus reticularis dorsalis to acupoint stimulation in rats. *Evid. Based Complement. Alternat. Med.* 2013:931283. doi: 10.1155/2013/931283

Liu, K., Gao, X. Y., Li, L., Ben, H., Qin, Q. G., Zhao, Y. X., et al. (2014). Neurons in the nucleus tractus solitarius mediate the acupuncture analgesia in visceral pain rats. *Auton. Neurosci.* 186, 91–94. doi: 10.1016/j.autneu.2014.08.004

MacPherson, H., Tilbrook, H., Agbedjro, D., Buckley, H., Hewitt, C., and Frost, C. (2017). Acupuncture for irritable bowel syndrome: 2-year follow-up of a randomised controlled trial. *Acupunct. Med.* 35, 17–23. doi: 10.1136/acupmed-2015-010854

Qi, D., Wu, S., Zhang, Y., and Li, W. (2016). Electroacupuncture analgesia with different frequencies is mediated via different opioid pathways in acute visceral hyperalgesia rats. *Life Sci.* 160, 64–71. doi: 10.1016/j.lfs.2016.06.025

Qi, D. B., and Li, W. M. (2012). Effects of electroacupuncture on expression of c-fos protein and N-methyl-D-aspartate receptor 1 in the rostral ventromedial medulla of rats with chronic visceral hyperalgesia. *Zhong Xi Yi Jie He Xue Bao* 10, 416–423. doi: 10.3736/jcim20120410

Qi, D. B., Zhang, S. H., Zhang, Y. H., Wu, S. Q., and Li, W. M. (2018). A rat model for studying electroacupuncture analgesia on acute visceral hyperalgesia. *Exp. Anim.* 67, 51–61. doi: 10.1538/expanim.17-0063

Rong, P. J., Zhu, B., Huang, Q. F., Gao, X. Y., Ben, H., and Li, Y. H. (2005). Acupuncture inhibition on neuronal activity of spinal dorsal horn induced by noxious colorectal distention in rat. *World J. Gastroenterol.* 11, 1011–1017. doi: 10.3748/wjg.v11.i7.1011

Roy, J. C., Bing, Z., Villanueva, L., and Le Bars, D. (1992). Convergence of visceral and somatic inputs onto subnucleus reticularis dorsalis neurones in the rat medulla. *J. Physiol.* 458, 235–246. doi: 10.1113/jphysiol.1992.sp019415

Sach, J., Bolus, R., Fitzgerald, L., Naliboff, B. D., Chang, L., and Mayer, E. A. (2002). Is there a difference between abdominal pain and discomfort in moderate to severe IBS patients? *Am. J. Gastroenterol.* 97, 3131–3138. doi: 10.1111/j.1572-0241.2002.07110.x

Spiegel, B. M., Gralnek, I. M., Bolus, R., Chang, L., Dulai, G. S., Mayer, E. A., et al. (2004). Clinical determinants of health-related quality of life in patients with irritable bowel syndrome. *Arch. Intern. Med.* 164, 1773–1780. doi: 10.1001/archinte.164.16.1773

Villanueva, L., Bing, Z., Bouhassira, D., and Le Bars, D. (1989). Encoding of electrical, thermal, and mechanical noxious stimuli by subnucleus reticularis dorsalis neurons in the rat medulla. *J. Neurophysiol.* 61, 391–402. doi: 10.1152/jn.1989.61.2.391

Villanueva, L., Bouhassira, D., Bing, Z., and Le Bars, D. (1988). Convergence of heterotopic nociceptive information onto subnucleus reticularis dorsalis neurons in the rat medulla. *J. Neurophysiol.* 60, 980–1009. doi: 10.1152/jn.1988.60.3.980

Villanueva, L., Bouhassira, D., and Le Bars, D. (1996). The medullary subnucleus reticularis dorsalis (SRD) as a key link in both the transmission and modulation of pain signals. *Pain* 67, 231–240. doi: 10.1016/0304-3959(96)03121-1

Villanueva, L., Cliffer, K. D., Sorkin, L. S., Le Bars, D., and Willis, W. D. Jr. (1990). Convergence of heterotopic nociceptive information onto neurons of caudal medullary reticular formation in monkey (Macaca fascicularis). *J. Neurophysiol.* 63, 1118–1127. doi: 10.1152/jn.1990.63.5.1118

Villanueva, L., de Pommery, J., Menetrey, D., and Le Bars, D. (1991). Spinal afferent projections to subnucleus reticularis dorsalis in the rat. *Neurosci. Lett.* 134, 98–102. doi: 10.1016/0304-3940(91)90517-W

Villanueva, L., and Le Bars, D. (1995). The activation of bulbo-spinal controls by peripheral nociceptive inputs: diffuse noxious inhibitory controls. *Biol. Res.* 28, 113–125.

Wang, K., Xiang, X. H., Qiao, N., Qi, J. Y., Lin, L. B., Zhang, R., et al. (2014). Genomewide analysis of rat periaqueductal gray-dorsal horn reveals time-, region- and frequency-specific mRNA expression changes in response to electroacupuncture stimulation. *Sci. Rep.* 4:6713. doi: 10.1038/srep06713

Wang, S. J., Yang, H. Y., and Xu, G. S. (2012). Acupuncture alleviates colorectal hypersensitivity and correlates with the regulatory mechanism of TrpV1 and p-ERK. *Evid. Based Complement. Alternat. Med.* 2012:483123. doi: 10.1155/2012/483123

Xin, J., Su, Y., Yang, Z., He, W., Shi, H., Wang, X., et al. (2016). Distinct roles of ASIC3 and TRPV1 receptors in electroacupuncture-induced segmental and systemic analgesia. *Front. Med.* 10:465–472. doi: 10.1007/s11684-016-0482-7

Xu, W. D., Zhu, B., Rong, P. J., Bei, H., Gao, X. Y., and Li, Y. Q. (2003). The pain-relieving effects induced by electroacupuncture with different intensities at homotopic and heterotopic acupoints in humans. *Am. J. Chin. Med.* 31, 791–802. doi: 10.1142/s0192415x03001478

Yu, L. L., Li, L., Rong, P. J., Zhu, B., Qin, Q. G., Ben, H., et al. (2014). Changes in responses of neurons in spinal and medullary subnucleus reticularis dorsalis to acupoint stimulation in rats with visceral hyperalgesia. *Evid. Based Complement. Alternat. Med.* 2014:768634. doi: 10.1155/2014/768634

Yuan, X.-C., Zhu, B., Jing, X.-H., Xiong, L.-Z., Wu, C.-H., Gao, F., et al. (2018). Electroacupuncture potentiates cannabinoid receptor-mediated descending inhibitory control in a mouse model of knee osteoarthritis. *Front. Mol. Neurosci.* 11:112. doi: 10.3389/fnmol.2018.00112

Zhao, Z. Q. (2008). Neural mechanism underlying acupuncture analgesia. *Prog. Neurobiol.* 85, 355–375. doi: 10.1016/j.pneurobio.2008.05.004

Zhu, B., Xu, W. D., Rong, P. J., Ben, H., and Gao, X. Y. (2004). A C-fiber reflex inhibition induced by electroacupuncture with different intensities applied at homotopic and heterotopic acupoints in rats selectively destructive effects on myelinated and unmyelinated afferent fibers. *Brain Res.* 1011, 228–237. doi: 10.1016/j.brainres.2004.03.034

Conflict of Interest Statement: The authors declare that the research was conducted in the absence of any commercial or financial relationships that could be construed as a potential conflict of interest.

The reviewer ML declared a shared affiliation, with no collaboration, with one of the authors, LY, to the handling editor at time of review.

Copyright © 2018 Yu, Li, Qin, Yu, Cui, Rong and Zhu. This is an open-access article distributed under the terms of the Creative Commons Attribution License (CC BY). The use, distribution or reproduction in other forums is permitted, provided the original author(s) and the copyright owner(s) are credited and that the original publication in this journal is cited, in accordance with accepted academic practice. No use, distribution or reproduction is permitted which does not comply with these terms.

frontiers in Physiology

ORIGINAL RESEARCH
published: 08 January 2019
doi: 10.3389/fphys.2018.01860

Upregulation of AT_1 Receptor Mediates a Pressor Effect Through ROS-SAPK/JNK Signaling in Glutamatergic Neurons of Rostral Ventrolateral Medulla in Rats With Stress-Induced Hypertension

Liping Jiang[1†], Xuan Zhou[1†], Hongyu Yang[1], Ruijuan Guan[1], Yanlei Xin[1], Jijiang Wang[1], Linlin Shen[1], Danian Zhu[1], Shulan Ma[2] and Jin Wang[1*]*

[1] Department of Physiology and Pathophysiology, School of Basic Medical Sciences, Fudan University, Shanghai, China,
[2] Training Center of Medical Experiments, School of Basic Medical Sciences, Fudan University, Shanghai, China

OPEN ACCESS

Edited by:
Brian R. Noga,
University of Miami, United States

Reviewed by:
Tomoyuki Kuwaki,
Kagoshima University, Japan
Eric Lazartigues,
LSU Health Sciences Center New Orleans, United States

***Correspondence:**
Shulan Ma
slma@fudan.edu.cn
Jin Wang
wangjin@shmu.edu.cn

[†] These authors have contributed equally to this work

Specialty section:
This article was submitted to Autonomic Neuroscience, a section of the journal Frontiers in Physiology

Received: 25 July 2018
Accepted: 11 December 2018
Published: 08 January 2019

Citation:
Jiang L, Zhou X, Yang H, Guan R, Xin Y, Wang J, Shen L, Zhu D, Ma S and Wang J (2019) Upregulation of AT_1 Receptor Mediates a Pressor Effect Through ROS-SAPK/JNK Signaling in Glutamatergic Neurons of Rostral Ventrolateral Medulla in Rats With Stress-Induced Hypertension. Front. Physiol. 9:1860. doi: 10.3389/fphys.2018.01860

The present study examined whether angiotensin II (Ang II) mediates the pressor effect through nicotinamide adenine dinucleotide phosphate (NADPH) oxidase-derived reactive oxygen species (ROS)-mitogen-activated protein kinase (MAPK) signaling in the glutamatergic neurons of the rostral ventrolateral medulla (RVLM) in stress-induced hypertensive rats (SIHR). The SIHR model was established using electric foot-shocks combined with noises for 15 days. We observed that Ang II type 1 receptor (AT_1R) and the glutamatergic neurons co-localized in the RVLM of SIHR. Furthermore, glutamate levels in the intermediolateral column of the spinal cord were higher in SIHR than in controls. Microinjection of Ang II into the RVLM of SIHR activated stress-activated protein kinase/Jun N-terminal kinase (SAPK/JNK), extracellular signal-regulated protein kinase (ERK) 1/2, and p38MAPK. Compared with controls, the activation of SAPK/JNK, ERK1/2, p38MAPK, and ROS in the RVLM were higher in SIHR, an effect that was blocked by an NADPH oxidase inhibitor (apocynin) and an AT_1R antagonist (candesartan). RVLM microinjection of apocynin or a SAPK/JNK inhibitor (SP600125), but not an ERK1/2 inhibitor (U0126) or a p38MAPK inhibitor (SB203580), decreased AT_1R mRNA and mean arterial blood pressure (MABP) in SIHR. The increase of AT_1R protein expression and MABP was inhibited by intracerebroventricular infusion (ICV), for 14 days, of SP600125, but not U0126 or SB203580 in SIHR. We conclude that Ang II modulates the pressor effect through AT_1R-dependent ROS-SAPK/JNK signaling in glutamatergic neurons in the RVLM of SIHR.

Keywords: angiotensin II type 1 receptor, stress-induced hypertension, glutamatergic neurons, rostral ventrolateral medulla, NAPDH oxidase-ROS-SAPK/JNK signaling

Abbreviations: aCSF, artificial cerebrospinal fluid; Ang II, angiotensin II; AP-1, activator protein-1; APO, apocynin; AT_1R, angiotensin II type 1 receptors; BP, blood pressure; CAN, candesartan; FISH, fluorescence *in situ* hybridization; Glu, glutamate; HR, heart rate; ICV, intracerebroventricular; IML, intermediolateral column; MABP, mean arterial blood pressure; ROS, reactive oxygen species; RVLM, rostral ventrolateral medulla; SBP, systolic blood pressure; SHR, spontaneously hypertensive rats; SIH, stress-induced hypertension; SIHR, stress-induced hypertensive rats.

INTRODUCTION

Hypertension is a silent killer worldwide and an outcome of a convoluted interaction between genetic and environmental factors. The psychosocial stress caused by the fast-paced lifestyle of modern society, is an important risk factor for hypertension. Chronic stress leads to the generation of stress-induced hypertension (SIH) (Xia et al., 2008; Xiao et al., 2013; Zhang et al., 2013). Angiotensin II (Ang II) has important effects on the central modulation of cardiovascular activities. Ang II modulates sympathetic functions acting on a diverse range of receptors such as Ang II type 1 receptor (AT_1R) and type 2 receptor (AT_2R); the pressor effect of Ang II mainly results from the activation of AT_1R (Reja et al., 2006).

Oxidative stress is caused by the imbalance between free radicals and antioxidants—an essential factor in hypertension. It has been indicated that nicotinamide adenine dinucleotide phosphate (NADPH) oxidase-derived reactive oxygen species (ROS), particularly superoxide anions ($O_2^{\cdot -}$), are crucial intracellular messengers within Ang II signaling pathways (Hanna et al., 2002; Ushio-Fukai and Alexander, 2004). Ang II can upregulate mRNA and protein expression of NADPH oxidase subunits and augment production of ROS (Hausding et al., 2013; Wakui et al., 2013; Ding et al., 2015; Minas et al., 2015). In addition, ROS have been reported to participate in the modulation of sympathetic activities (Wang et al., 2002; Gao et al., 2004; Campese et al., 2005). NADPH oxidase-derived ROS act as essential intracellular messengers to activate downstream signaling molecules, including mitogen-activated protein kinase (MAPK) and transcriptional factors (Zhang et al., 2007; Bae et al., 2011; Lassegue et al., 2012). It is reported that Ang II activates stress-activated protein kinase/Jun N-terminal kinase (SAPK/JNK), extracellular signal-regulated protein kinase 1/2 (ERK1/2), and p38MAPK, which are critical protein kinases for gene expression and cell growth (Omura et al., 2005). A previous study demonstrated that chronic Ang II infusion elevated NADPH oxidase subunit protein expression, ROS production, as well as p38MAPK activation, leading to hypertension in Sprague Dawley rats (Bao et al., 2007).

The rostral ventrolateral medulla (RVLM) has an important impact on the maintenance of sympathetic activities. It is widely accepted that the neurons in the RVLM provide downward impulses to the sympathetic preganglionic neurons in the intermediolateral column (IML) of the spinal cord, which projects the sympathetic nerves that dominate the heart and blood vessels (Xiang et al., 2014). Our previous studies suggested that Ang II might activate glutamatergic neurons in the RVLM, resulting in the enhancement of blood pressure (BP) in Wistar and spontaneously hypertensive rats (SHR) (Hu et al., 2002). Moreover, AT1R, an angiotensin converting enzyme, mRNA and protein expression were significantly higher in the RVLM in stress-induced hypertensive rats (SIHR) compared with control rats (Du et al., 2013). It has been shown that the elevated glutamatergic inputs to the RVLM contribute to increased BP and sympathetic activities in Goldblatt hypertension (Carvalho et al., 2003) and spontaneous hypertension (Zha et al., 2013). However, the cellular and molecular mechanisms underlying the central roles of Ang II in SIHR remain to be identified. Therefore, this study evaluated the hypothesis that Ang II mediates pressor response through AT1R-dependent NADPH oxidase derived-ROS-MAPK signaling pathways in the glutamatergic neurons of the RVLM of SIHR.

MATERIALS AND METHODS

Animals

Adult male Sprague-Dawley rats (200–220 g) were randomly housed (5 per cage) at room temperature (22–27°C), on a 12/12 h light/dark schedule, and allowed free access to food and water. All experimental procedures were approved by the Animal Use and Care Committee of Shanghai Medical College, Fudan University and were performed in strict accordance with the guidelines of the National Institutes Health Guide for the Care and Use of Laboratory Animals.

Stress-Induced Hypertension Model

Rats were randomly allocated into normotension (control) and stressed-induced hypertension (SIH) groups. The SIH model was created as described in our previous studies (Xia et al., 2008; Xiao et al., 2013; Zhang et al., 2013). Briefly, the rats of SIH group were placed in a cage with a grid floor and received 2-h random electric foot-shocks paired with interval noise stimulation, twice daily, for 15 days. The control rats received the same treatment excluding the stressful stimuli. Systolic blood pressure (SBP) in conscious rats was measured using the tail-cuff method at 2 h after stress and obtaining the average of three measurements. The criterion for hypertension in this experiment was determined as an SBP greater than 140 mmHg. After the 15-day stimulation period, the rats in the SIH group with an SBP less than 140 mmHg were removed from the follow-up experiments.

MABP Measurements

After endotracheal intubation, the right carotid artery of each rat was cannulated to monitor BP continuously using a polygraph (Model SMUP-A, Department of Physiology and Pathophysiology, Shanghai Medical College of Fudan University, Shanghai, China). The heart rate (HR) was derived automatically from the BP phasic wave. During the experiment, the rectal temperature of rats was kept at 37 ± 0.5°C using a thermostat.

RVLM Microinjections

Similar to the procedures reported previously (Xiao et al., 2013), the rats were anesthetized with urethane/α-chloralose (urethane 0.75 g/kg; α-chloralose 70 mg/kg) intraperitoneally, and the bilaterally microinjection of test agents to the RVLM was performed with a micropipette (40–70 μm internal diameter) attached to a 0.5 μl microsyringe (Hamilton). The RVLM was located 0.8 mm from the first anterior branch of the hypoglossal nerve, 1.9 mm lateral, and 0.7 mm deeper toward the ventral surface. As a routine, a total volume of 50 nl was delivered to each side of the RVLM over 30 s to allow for complete diffusion of the test agents. The RVLM injection was verified by the presence of a transient pressor response (MABP

greater than 15 mmHg) to an L-glutamate (2 nmol/50 nl) microinjection (Ross et al., 1984). Ang II, AT_1R antagonist candesartan, and NADPH oxidase inhibitor apocynin, were purchased from Sigma-Aldrich (St. Louis, MO, United States). The SAPK inhibitor SP600125, ERK1/2 inhibitor U0126, and p38MAPK inhibitor SB203580 were obtained from Sigma-Aldrich (St. Louis, MO, United States). Artificial cerebrospinal fluid (aCSF) or 1% dimethyl sulphoxide (the solvent of SP600125, U0126, or SB203580) was used as a vehicle control. To avoid the confounding effects of drug interactions, each animal received only one pharmacological treatment. After the experiments, 50 nl of pontamine sky blue was injected through the micropipette to confirm the position (rostroventrolateral reticular nucleus, lateral paragigantocellular nucleus).

Fluorescence *in situ* Hybridization (FISH)

The staining procedure was performed with an enhanced sensitive FISH detection kit (Servicebio, China). Six-micron cryosections were prepared ahead of time. We applied proteinase K (20 μg/ml) on the slice for 5 min to expose the nucleic acid and then washed the slides three times with 0.5M PBS. Following incubation with hybridization buffer at 37°C for 2 h, the slides were incubated with 50 μl of 8 ng/ul 5′,3′ double CY3-labeled RNA (VGLUT2 mRNA) detection probe and 5′,3′ double FAM-labeled RNA (AT_1R mRNA) detection probe (TSINGKE, China) in the same buffer at 37°C overnight. After the samples were washed with different concentrations of SSC buffers. After three 5 min washes in PBS for the last time, the slides were detected under a Nikon Ni-U microscope (Nikon, Japan) and pictures were collected.

Intracerebroventricular (ICV) Infusion

Anesthetized rats were fixed in a stereotaxic apparatus (NeruoStar, United States). After the bregma was identified, an ICV cannula was implanted for the infusion of the inhibitors, as described previously (Dange et al., 2014). Once the anterior fontanel was identified, an ICV cannula was implanted into the right lateral cerebral ventricle 0.8 mm caudal to bregma, 1.5 mm lateral to the bregma, and 3.8 mm ventral to the zero level (Pan et al., 2007). The cannula was fixed to the cranium using dental acrylic and two stainless steel screws. The pump body was implanted subcutaneously. The rats underwent a 14-day ICV infusion of the SAPK/JNK inhibitor (SP600125), ERK1/2 inhibitor (U0126), p38MAPK inhibitor (SB203580) (0.5 μl/hr, 0.6 mmol/L), NADPH oxidase inhibitor APO (0.5 μl/hr, 0.45 mmol/L) (Fang et al., 2013), or aCSF via osmotic micro-pumps (Alzet, Cupertino, CA, United States). The position of the cannula in the lateral cerebral ventricle was confirmed by the staining of all four ventricles after injection of 5 μl of evans blue dye at the end of the experiments.

Intermediolateral Column (IML) Microdialysis

After making an incision in the back to expose the T8 level of the thoracic segment and then removing the bone and meningeal membrane to expose the spinal cord surface, the microdialysis probe was inserted into the T8 spinal cord 0.45 mm lateral to the midline and 0.9 mm below the dorsal surface. The tip of the probe was in the IML. The probe was perfused (2 μl/min) with aCSF using a microdialysis pump (BASi, United States). Each dialysate sample was harvested for 10 min at a volume of 20 μl.

High-Performance Liquid Chromatography (HPLC)

Amino acids of dialysate samples were separated using reverse-phase HPLC (Waters 1525, United States) and fluorescence detection (Waters 2475, United States) with a reverse-phase column (C18, ultrasphere octadecyl silane). The derivatized reagent consisted of 5 ml of absolute ethanol, 5 ml of 0.1 mol/L sodium tetraborate, 27 mg of orthophthaldialdehyde (Sigma-Aldrich, St. Louis, MO, United States), and 40 μl of β-mercaptoethanol (Sigma-Aldrich, St. Louis, MO, United States). The sample (20 μl) was mixed with the derivatized reagent (10 μl) for 90 s and then injected into the HPLC system. The mobile phase, which contained 63% 0.1 mol/L KH_2PO4, 35% methanol, and 2% tetrahydrofuran, flowed through the system with a flow rate of 1.0 ml/min. The temperature of the column was 35°C. The excitation and emission wave lengths were 330 and 450 nm, respectively. For each sample, the analysis time was not more than 10 min.

Collection of Tissue Samples From the RVLM

On the 15th day, or after microinjections, rats were euthanized and their brains were removed and frozen on dry ice. Both sides of the ventrolateral medulla covering the RVLM (0.5–2.5 mm rostral to the obex and 1.4–2.4 mm lateral to the midline and medial to the spinal trigeminal tract) were dissected using a stainless steel micropunch (1 mm internal diameter) (Chan et al., 2007). Medullary tissues were stored at –80°C prior to protein analysis.

Western Blot Analysis

The samples of brain tissues were homogenized in RIPA lysis buffer with protease or phosphatase inhibitor (Roche, Basel, Switzerland) and then centrifuged (12000 rpm, 15 min, 4°C) to obtain supernatants. The total protein concentration of the supernatants was determined using the BCA assay kit (Pierce). Samples were loaded and separated on the SDS–PAGE gel (40 μg per well). The protein was transferred to the PVDF membrane (Millipore, MA, United States), which was incubated overnight with primary antibodies at 4°C and then probed with the corresponding secondary antibody. The primary antibodies were as follows: rabbit anti-AT_1R antibody (1:800 dilution, Abcam, MA, United States) (Czikora et al., 2015; Wang et al., 2018), rabbit anti-SAPK/JNK antibody, mouse anti-phospho-SAPK/JNK antibody, mouse anti-ERK1/2 antibody, rabbit anti-phospho-ERK1/2 antibody, rabbit anti-p38MAPK antibody, rabbit anti-phospho-p38MAPK antibody and rabbit anti-β-tublin antibody (1:1000 dilution, Cell Signaling Technology, Danvers, MA, United States). The membranes were detected by an ECL-Plus detection kit (Tiangen, Beijing, China),

and scanned using Image Quant LAS 4000 (GE Healthcare Life Sciences, CT, United States). The images were quantified using the ImageJ densitometry system.

Measurement of ROS in the RVLM

The lucigenin-enhanced chemiluminescence assay was adopted to detect the ROS production in the RVLM (Chan et al., 2005). RVLM was homogenized in PBS (20 mM, pH 7.4) containing EDTA (0.01 mM). The homogenate was centrifuged at 1200 × *g* for 10 min at 4°C and the supernatant was collected for ROS assay. Background chemiluminescence in a 2-ml buffer mixed with lucigenin (5 μmol/L) was detected for 5 min. Adding 100 μl supernatant, the chemiluminescence was detected for 30 min at room temperature. The production of ROS was determined and expressed as average light units per minute per milligram of protein.

Immunohistochemistry

The procedure for immunohistochemistry was described previously (Peng et al., 2009). One section from every six serial sections was picked up, with a total of five sections in each animal. Tissue sections were deparaffinized, rehydrated by graded ethanol series, pre-incubated with 5% BSA for an hour, and then incubated with mouse anti-phospho-SAPK/JNK antibody (1:50 dilution, Cell Signaling Technology, Danvers, MA, United States), rabbit anti-phospho-ERK1/2 antibody (1:200 dilution, Cell Signaling Technology, Danvers, MA, United States), or rabbit anti-phospho-p38MAPK antibody (1:400 dilution, Cell Signaling Technology, Danvers, MA, United States) at 4°C overnight. The sections were washed three times with PBS and then incubated with corresponding secondary antibodies. The color reaction was carried out with HRP-linked polymer detection system.

Quantitative Real-Time PCR

The total RNA was extracted from lung tissues using TRIzol Reagent (Invitrogen Corporation, CA, United States). First-strand cDNA was synthesized and amplified from 0.5 μg of total RNA using the ReverTra Ace qPCR RT Kit (Toyobo, Tokyo, Japan). Then the mRNA levels of AT_1R were measured by quantitative real-time PCR (iCyler iQ Real-time PCR Detection System, Bio-Rad Laboratories Inc., United States) using SYBR Green Real-time PCR Master Mix (Toyobo, Japan) in a total volume of 20 μL. Glyceraldehyde-3-phosphate dehydrogenase (GAPDH) was used as an internal standard to normalize the expression level of each mRNA. Primers were designed by Sangon Biotech (Shanghai, China). The target gene names and their primer sequences were shown as follows: forward primer 5′-CCCAAGTCCACACATCAAAG-3′, reverse primer 5′-GCAAGGCAGACTGTATGGAA-3′ for AT_1R; and forward primer 5′-AAGGTGGTGAAGCAGGCGGC-3′, reverse primer 5′-GAGCAATGCCAGCCCCAGCA-3′ for GAPDH. The PCR amplification consisted of 40 cycles of denaturation (94°C, 15 s), annealing (60°C, 30 s) and extension (72°C, 30 s). All the samples were assayed in one essay in our study. The relative quantification of gene expression was analyzed from the measured threshold cycles (CT) by using the $2-\Delta\Delta Ct$ method in the experiment.

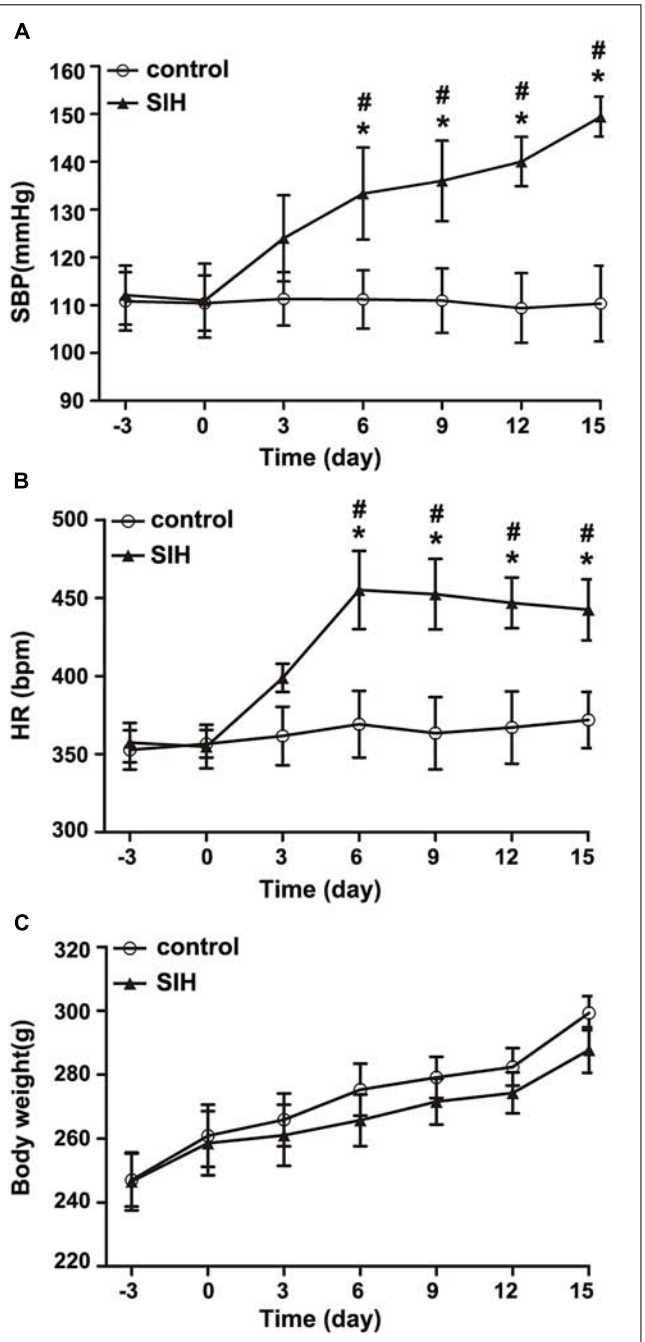


FIGURE 1 | The changes of systolic blood pressure (SBP) **(A)**, heart rate (HR) **(B)**, and body weight **(C)** in stress-induced hypertension (SIH) and control group. $n = 10$, $^*P < 0.05$ vs. control (Student's *t*-test); $^{\#}P < 0.05$ vs. baseline (paired *t*-test) (third day prior to stress).

Statistical Analysis

All of the data are presented as mean ± standard error (SE). Student's *t*-test, paired *t*-test, or analysis of variance (ANOVA) was performed as appropriate. Statistical analyses were performed using Statistical Package for the Social Sciences (SPSS) version 16.0. A $P < 0.05$ was considered statistically significant.

RESULTS

The Systolic Blood Pressure (SBP) and Heart Rate (HR) of the Stressed Rats Increase in a Time-Dependent Manner

Systolic blood pressure and HR of the stressed rats significantly increased from the 6th day compared with the control rats ($^*P < 0.05$). SBP and HR of stressed rats was also significantly different from the 6th day compared with baseline (3rd day prior to stress) ($^\#P < 0.05$), and stayed stable at a high level around the 15th day (**Figures 1A,B**). However, there was no discernible difference in body weight between the SIH and control group (**Figure 1C**).

AT_1R and VGLUT2 Co-localize in the RVLM and the Release of Glutamate Increases in the IML of SIHR

Figure 2A showed that AT_1R and VGLUT2 co-localized in the RVLM of SIHR, suggesting that AT_1R expressed in the glutamatergic neurons. To establish that the development of SIH is associated with the actions of glutamatergic neurons in the RVLM, we examined the concentration of amino acid neurotransmitters in the IML. We found the release of glutamate (Glu) neurotransmitter increased in SIHR (**Figure 2C**) than in the control rat (**Figure 2B**) ($n = 8$, $P < 0.05$, **Figure 2D**). These data reveal that the activated glutamatergic neurons of the RVLM release more glutamate neurotransmitter to the IML of SIHR.

Exogenous Ang II Activates SAPK/JNK, ERK1/2 and p38MAPK in the RVLM of SIHR

As **Figure 3** shows, SAPK/JNK, ERK1/2, and p38MAPK phosphorylation in the RVLM were much higher in SIHR than in control rats. RVLM microinjection of Ang II (50 pmol) increased SAPK/JNK, ERK1/2, and p38MAPK phosphorylation in SIHR at 15 min after application, and lasted at least 30 min; while total SAPK/JNK, ERK1/2, or p38MAPK levels were unchanged (**Figures 3A–C**).

Antagonist of AT_1R Decreases ROS Production and SAPK/JNK, ERK1/2, and p38MAPK Phosphorylation in the RVLM of SIHR

The production of ROS was significantly higher in the RVLM of SIHR (**Figure 4A**). Furthermore, the enhancement of ROS production and SAPK/JNK, ERK1/2, and p38MAPK phosphorylation were discernibly blunted (**Figures 4B,C**) by administration of candesartan (2 nmol, an AT_1R antagonist) to the RVLM, bilaterally. However, there was no discernible change elicited by microinjection of PD123319 (2 nmol, an AT_2R antagonist) to the RVLM, bilaterally (data not shown). These findings implicate that stress elevates phosphorylation of SAPK/JNK, ERK1/2, and p38MAPK and activates MAPK pathway via AT_1R.

NADPH Oxidase Inhibitor Inhibits the Activation of MAPK in the RVLM of SIHR

Bilateral administration of NADPH oxidase inhibitor APO (2 nmol) significantly inhibits SAPK/JNK, ERK1/2, or p38MAPK activation in the RVLM of SIHR (**Figures 5A–D**). These findings suggest that NADPH oxidase-derived ROS might be an upstream signaling molecule within the MAPK pathway.

Inhibitor of SAPK, but Not ERK1/2 or p38MAPK, Inhibits AT_1R Expression in the RVLM of SIHR

Both RT-PCR and Western blot studies showed that APO or SAPK inhibitor SP600125 led to a profound decrease in AT_1R mRNA and protein expression in the RVLM of SIHR, whereas ERK1/2 inhibitor U0126 or p38MAPK inhibitor SB203580 did not demonstrate a significant effect in AT_1R mRNA and protein expression in the RVLM of SIHR (**Figures 6A,B**).

Inhibitors of NADPH Oxidase and SAPK Decreased MABP of SIHR

Bilateral microinjection of the APO (2 nmol) or the SAPK inhibitor SP600125 (500 nmol) into the RVLM decreased MABP of SIHR. However, administration of the ERK1/2 inhibitor U0126 (500 nmol) or p38MAPK inhibitor SB203580 (500 nmol) into the RVLM did not obviously change the MABP of SIHR (**Figure 6C**). There was no obvious change in the HR of SIHR. In addition, microinjection of SP600125, U0126, or SB203580 into regions adjacent to the RVLM had no discernible change in the MABP or HR of SIHR. ICV infusion of the APO (0.45 mmol/L) or SP600125 (0.6 mmol/L) for 14 days decreased MABP in the SIHR, whereas U0126 (0.6 mmol/L) or SB203580 (0.6 mmol/L) did not obviously change the MABP of SIHR (**Figure 6D**).

DISCUSSION

Hypertension is a major risk factor for cardiovascular and cerebrovascular diseases, which affects over one billion individuals worldwide (Wu et al., 2015; Mills et al., 2016). SIH caused by chronic and excessive stress, is inflicted on an increasing number of people, including young adults. Therefore, it is necessary to understand the mechanism underlying SIH. The SIHR model is established by electric foot-shocks combined with interval noises (Xia et al., 2008; Xiao et al., 2013; Zhang et al., 2013). The present experiment revealed that this chronic stress in rats led to an increase in BP, implying the successful establishment of an SIHR model.

In the current study, we examined the roles of AT_1 R on cardiovascular modulation and the effects of NADPH oxidase-derived ROS-MAPK signaling in the glutamatergic neurons of the RVLM in SIHR. The primary findings of the present study are: (1) AT_1R expressed in the glutamatergic neurons of the RVLM of SIHR and the glutamate in the IML of the spinal cord is higher in SIHR than that in control rats. (2) Exogenous Ang II activates SAPK/JNK, ERK1/2, and p38MAPK in the RVLM of SIHR. AT_1R antagonist and NADPH oxidase inhibitor reduce the enhanced

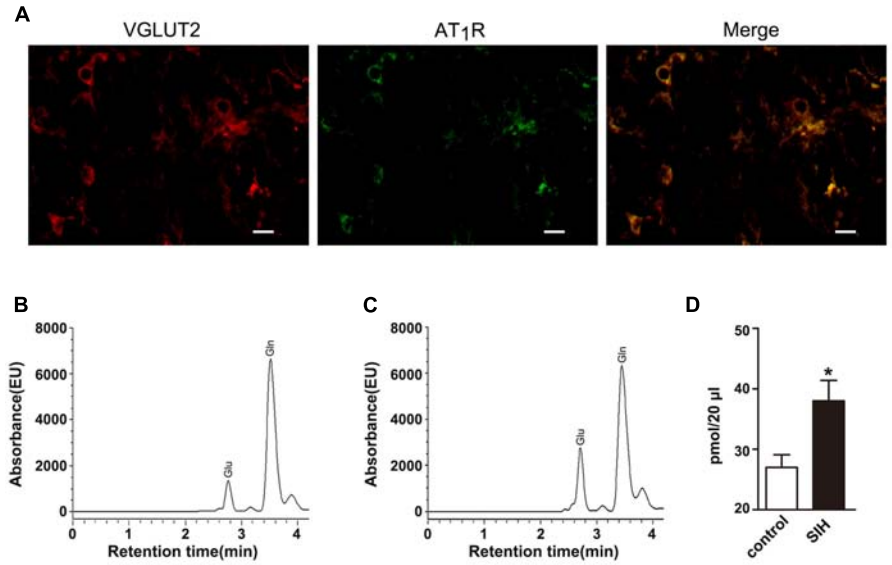


FIGURE 2 | Localization of AT_1R and VGLUT2 in the rostral ventrolateral medulla (RVLM) of SIH rat **(A)** and chromatogram of amino acids in the IML in control **(B)** and SIH rats **(C)** the red (cy3), green (FAM) areas represented the staining of glutamatergic neurons and AT_1R, respectively. Scale bars = 25 μm. The baseline release of glutamate increased in SIH rats compared with control rats **(D)**. $n = 8$, $^*P < 0.05$ vs. control (Student's *t*-test). Glu, glutamate; Gln, glutamine.

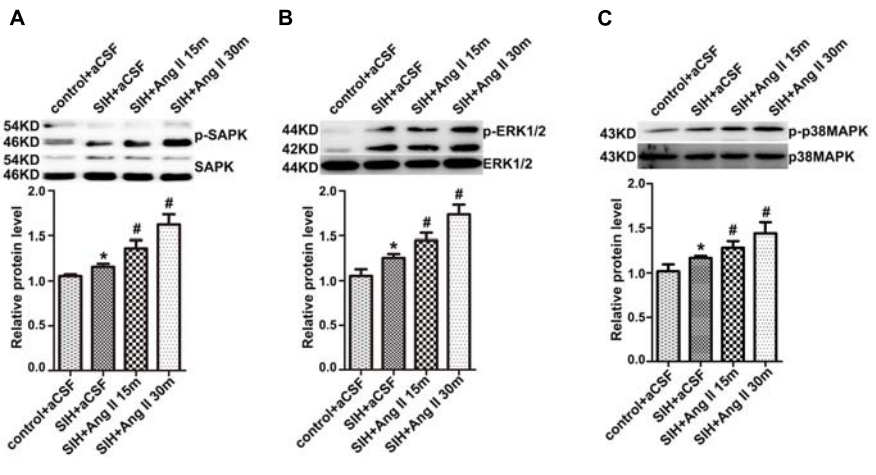


FIGURE 3 | The protein levels of phosphorylation or total SAPK/JNK **(A)**, ERK1/2 **(B)**, and p38MAPK **(C)** in the RVLM in the SIH group 15 and 30 min after RVLM microinjection of Ang II (50 pmol). Densitometry values were determined as indicated. $n = 4$, $^*P < 0.05$ vs. control; $^{\#}P < 0.05$ vs. SIH (one-way ANOVA with Tukey *post hoc* test).

production of ROS and the activation of SAPK/JNK, ERK1/2, and p38MAPK in the RVLM of SIHR. (3) Injection of the SAPK/JNK inhibitor, but not the p38MAPK or the ERK1/2 inhibitor, into the RVLM significantly decreases expression of AT_1R mRNA and MABP in SIHR. ICV infusion of the SAPK/JNK inhibitor for 14 days, but not the p38MAPK or the ERK1/2 inhibitor, significantly decreases the expression of AT_1R protein and MABP in SIHR.

First, we identified that AT_1R in glutamatergic neurons played a crucial role in the pathogenesis of SIH. Fluorescence *in situ* hybridization (FISH) analysis showed that the AT_1R and VGLUT2 co-localized in the RVLM of SIHR, which indicated that the activity that Ang II bands to AT_1R in the RVLM, is connected to the glutamatergic neurons. A majority of the glutamatergic neurons were co-localized with AT_1R in the RVLM of Wistar rats and SHR (Hu et al., 2002). In hypertensive Dahl salt-sensitive rats, the elevated BP response to AT_1R activation in the hypothalamic paraventricular nucleus (PVN) has been shown to be partly regulated by increased glutamate receptor activation (Gabor and Leenen, 2012). Ang II infusion increases co-localization of $gp91^{phox}$-containing NADPH oxidase and glutamate N-methyl-D-aspartate receptor (NMDAR) NR_1 subunit in the dendrites of PVN neurons, and augments baseline and NMDAR-induced production of ROS in PVN

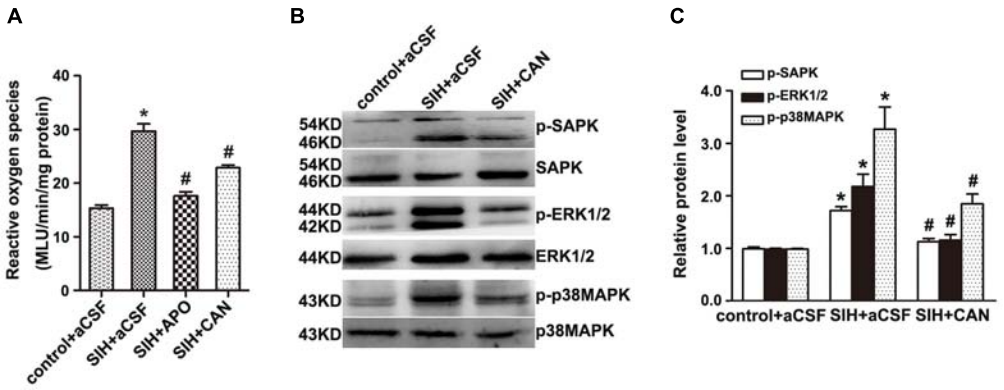


FIGURE 4 | Effects of candesartan (CAN) on the production of Reactive oxygen species (ROS) and phosphorylation of SAPK/JNK, ERK1/2, and p38MAPK in the RVLM in SIH and control groups. The production of ROS in the RVLM detected at 20 min after microinjection of apocynin APO (2 nmol) or CAN (2 nmol) into the RVLM **(A)**; $n = 6$. The protein levels of phosphorylated SAPK/JNK, ERK1/2, and p38MAPK were detected 30 min after microinjection of CAN (2 nmol) into the RVLM, bilaterally **(B,C)**; $n = 4$. $^{*}P < 0.05$ vs. control + aCSF; $^{\#}P < 0.05$ vs. SIH + aCSF (one-way ANOVA with Tukey *post hoc* test).

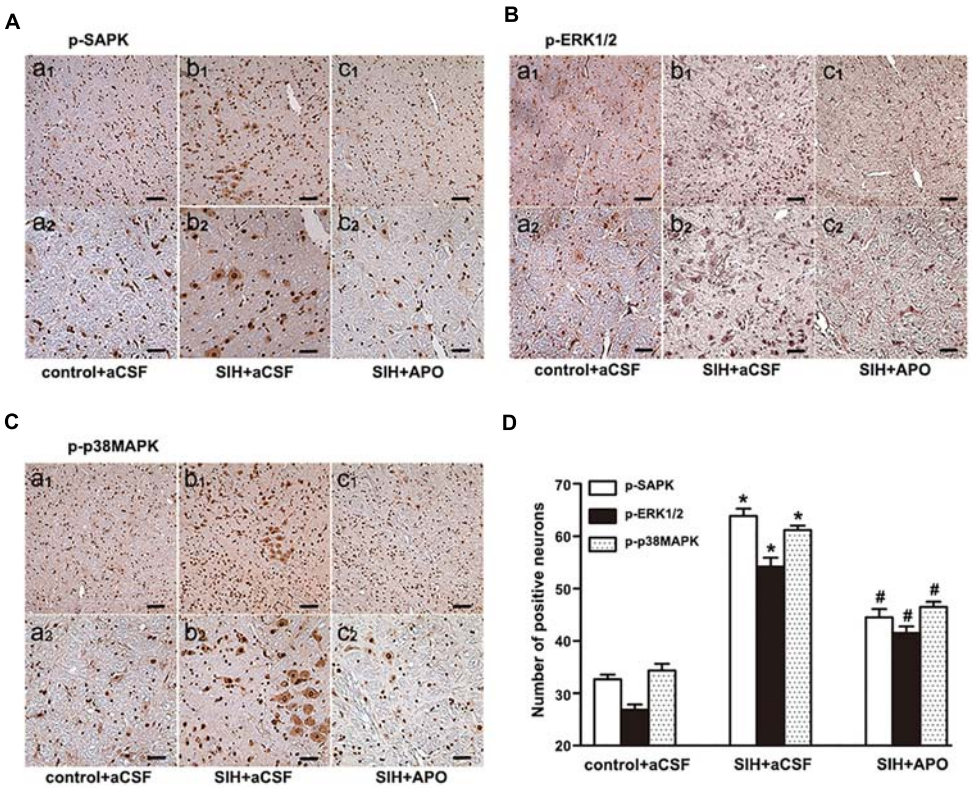


FIGURE 5 | Effects of APO on MAPK activation in the RVLM in the SIH and control group. Immunohistochemistry for p-SAPK/JNK **(A)**, p-ERK1/2 **(B)**, or p-p38MAPK **(C)** in control and SIH groups treated with or without APO **(D)**. Scale bars = 50 μm in a1, b1, c1; 25 μm in a2, b2, c2. $n = 4$, $^{*}P < 0.05$ vs. control + aCSF; $^{\#}P < 0.05$ vs. SIH + aCSF (one-way ANOVA with Tukey *post hoc* test).

cells and spinally projecting PVN neurons (Wang et al., 2013). Our findings provide evidence that AT_1R expressed in the glutamatergic neurons of the RVLM in SIHR, indicating that Ang II might evoke the activation of glutamatergic neurons via AT_1R in the RVLM of SIHR. Furthermore, HPLC analysis showed that the glutamate was increased in the IML of spinal cord. It has been shown that projections from the RVLM to the IML of spinal cord dominate preganglionic neurons resulting in the elevated BP and HR (Guyenet, 2006; Oshima et al., 2008). Our previous studies determined that Ang II-induced glutamate release in the spinal cord might arise from the AT_1R-containing glutamatergic spinally projecting neurons in the RVLM of SHR

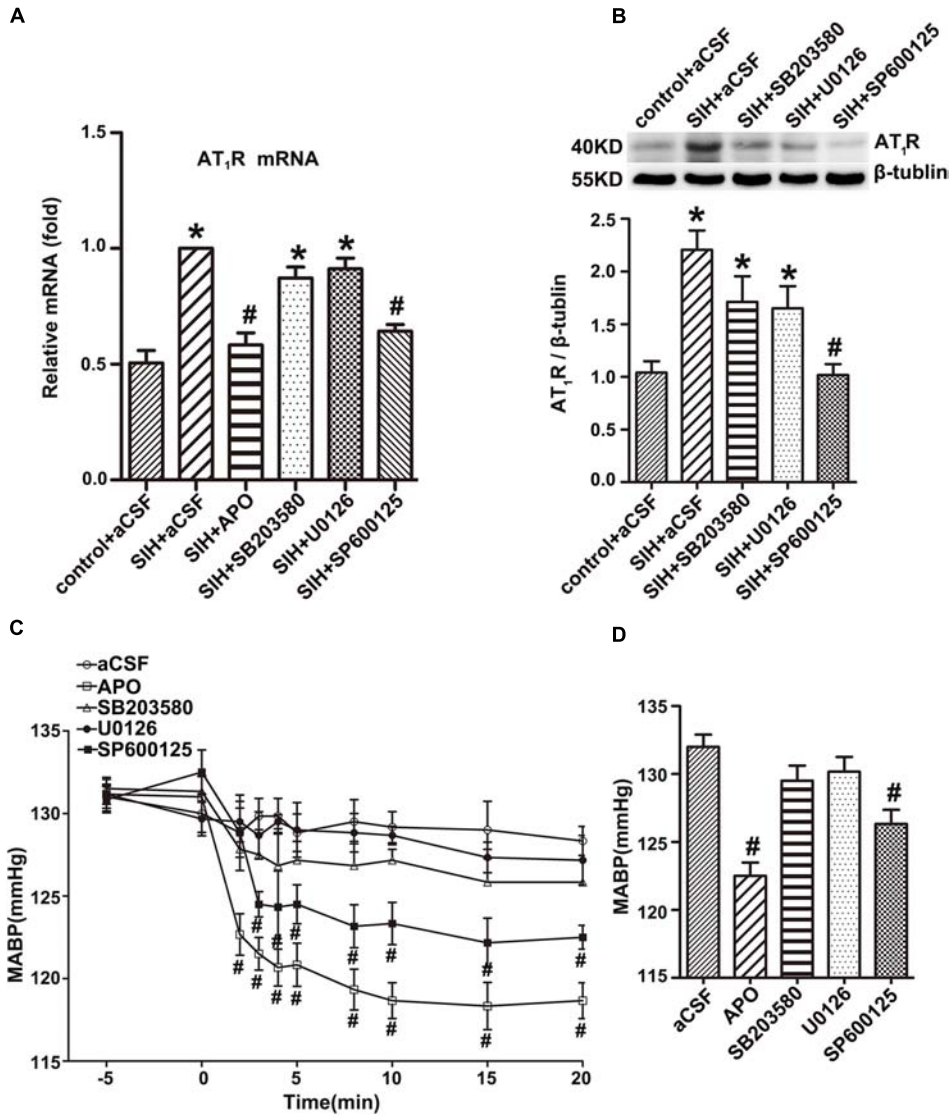


FIGURE 6 | Effects of the inhibitors of nicotinamide adenine dinucleotide phosphate (NADPH) oxidase, SAPK/JNK, ERK1/2, and p38MAPK on AT_1R expression in the RVLM and Mean arterial blood pressure (MABP) in rats with SIH. The mRNA levels of AT_1R in the RVLM ($n = 4$) **(A)**, and change in MABP ($n = 6$) **(C)** in response to microinjection of APO (2 nmol), SP600125 (500 nmol), U0126 (500 nmol), or SB203580 (500 nmol) into the RVLM of rats with SIH. Representative gels or densitometric analysis of AT_1R protein in the RVLM ($n = 5$) **(B)**, and change in MABP ($n = 6$) **(D)** of SIH group after intracerebroventricular infusion (ICV) of aCSF, APO (0.45 mol/L), SP600125 (0.6 mol/L), U0126 (0.6 mol/L), or SB203580 (0.6 mol/L) for 14 days in stress-induced hypertensive rats (SIHR). $^*P < 0.05$ vs. control + aCSF; $^\#P < 0.05$ vs. SIH + aCSF (one-way ANOVA with Tukey *post hoc* test, **A,B,D**; Student's *t*-test, **C**).

(Hu et al., 2002). Our present findings implicate that, in SIHR, the glutamatergic neurons of the RVLM are activated, which are associated with the binding of Ang II to AT_1R, and the further release of more glutamate neurotransmitter into the IML through projection fibers. The vesicular glutamate transporters (VGLUTs), capable of specifically packaging glutamate into presynaptic vesicles and promoting glutamate release (Liguz-Lecznar and Skangiel-Kramska, 2007), comprise three members, wherein VGLUT1 and VGLUT2 are considered as specific markers of canonical glutamatergic neurons. Additionally, VGLUT2-immunoreactivities were widely observed in the lower brainstem (Vigneault et al., 2015).

Chronic infusion of Ang II into the brain of normal rabbits resulted in sympathoexcitation and increased oxidative stress, as well as an upregulation of several of the protein subunits of NADPH oxidase, which have shown to be inhibited by losartan (Gao et al., 2005). In a study performed in rabbits with chronic heart failure, central administration of losartan, superoxide dismutase mimetic tempol, or NADPH oxidase inhibitor APO, reduced sympathetic nerve activity and oxidative stress (Gao et al., 2004). What is more, other models demonstrated similar findings, such as cardiac diastolic dysfunction (Li et al., 2013) and nitric oxide inhibition induced-hypertension (Rincón et al., 2015). In our experiments, ICV infusion for 14 days

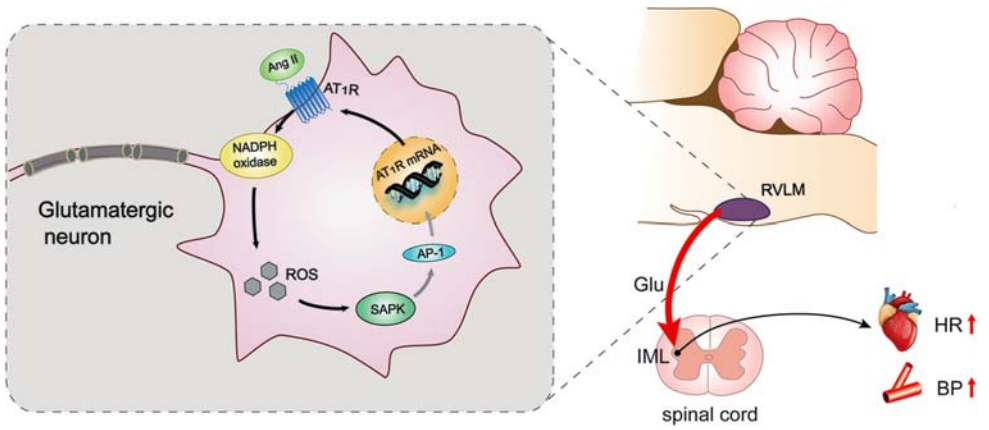


FIGURE 7 | Schematic diagram showing the mechanism by which AT_1R mediates pressor effect in the glutamatergic neurons of the RVLM of SIHR. Ang II triggers the activation of NADPH oxidase derived ROS-SAPK pathway via AT_1R in the glutamatergic neurons of the RVLM of SIHR, then may activate activator protein (AP)-1 to evoke gene transcription and increase AT_1R expression, which promotes the release of glutamate in the IML and eventually increases BP and HR.

or RVLM microinjection of NADPH oxidase inhibitor APO obviously decreased MABP in the SIHR. These results implicate that AT_1R and oxidative stress elicited by NADPH oxidase have an important effect on the regulation of sympathetic activities.

Secondly, we observed that the MAPK pathway was activated in SIHR and, specifically, that Ang II activated the MAPK pathway via AT_1R. The current data show that SAPK/JNK, ERK1/2, and p38MAPK phosphorylation in the RVLM were significantly higher in SIHR than in control rats. Additionally, exogenous Ang II application to the RVLM causes this increase in SAPK/JNK, ERK1/2, and p38MAPK phosphorylation in SIHR. The enhanced activation of MAPKs has been observed in pulmonary arterial hypertension and spontaneous hypertension (Cao et al., 2014; Awad et al., 2016). Importantly, we found that the activation of SAPK/JNK, ERK1/2, and p38MAPK in the RVLM was significantly inhibited by bilateral microinjection of AT_1R antagonist candesartan, which can cross the blood-brain barrier easily.

Our findings might not be consistent with previous studies noting that in normal rats, Ang II elicited ERK1/2 and p38MAPK phosphorylation, whereas SAPK/JNK was not activated in normal rats (Chan et al., 2005). The difference between the current study and these previous results is that SAPK/JNK, ERK1/2, and p38MAPK phosphorylation induced by Ang II administration may be related to the specialty of the current SIH model. Chronic and excessive stress can activate not only ERK1/2 and p38MAPK, but also the stress related proteins SAPK/JNK, to regulate sympathetic activity further.

Thirdly, we demonstrated that NADPH oxidase-derived ROS is the upstream messenger that mediated SAPK/JNK, ERK1/2, and p38MAPK activation induced by Ang II binding to AT_1R in the RVLM of SIHR. We identified that the production of ROS enhanced in SIHR compared with control rats. Microinjections of AT_1R antagonist candesartan and NADPH oxidase inhibitor APO into the RVLM partially inhibited ROS production and SAPK/JNK, ERK1/2, and p38MAPK phosphorylation in SIHR. APO also inhibited the elevation of MABP in SIHR. A previous study suggested that NADPH oxidase-derived ROS mediated the Ang II-evoked pressor effect via p38MAPK activation in the RVLM of normal rats (Chan et al., 2005). The present study suggests that in the RVLM of SIHR, NADPH oxidase-derived ROS has a crucial effect on SAPK/JNK, ERK1/2, and p38MAPK activation elicited by endogenous Ang II.

Finally, we noted that SAPK/JNK activation in the RVLM had important effects on AT_1R expression and the modulation of pressor response. The enhancement of AT_1R mRNA expression and MABP in SIHR were attenuated by the bilateral microinjection of SAPK/JNK inhibitor SP600125, but not ERK1/2 inhibitor U0126, or p38MAPK inhibitor SB203580. Besides, ICV infusion of the SAPK/JNK inhibitor, not ERK1/2, or p38MAPK inhibitor for 14 days decreased AT_1R protein expression and MABP in the SIHR, Our previous study demonstrated that endogenous Ang II production was increased in SIHR and AT_1R expression in the RVLM was much higher in SIHR than in control rats (Du et al., 2013). Hence, we suggested that SAPK/JNK played a major role in regulating the pressor effect.

The AT_1R expression was enhanced in the RVLM of normal rabbits infused with Ang II and rabbits with heart failure (Gao et al., 2005; Liu et al., 2006). It has been reported that Ang II induces MAPK signaling to upregulate AT_1R in PVN and contributes to AT_1R-mediated sympathetic excitation in heart failure (Wei et al., 2008). Ang II activates diverse nuclear transcription factors, such as activator protein-1 (AP-1) (Jia et al., 2008), some of which participate in AT_1R gene transcription. There was some evidence that Ang II promoted the upregulated transcription of AT_1R by oxidant stress and AP-1 activation in the intact brain of rabbits and cultured neuronal cells (Liu et al., 2008). The enhancement of AP-1 upregulated AT_1R expression in the RVLM of rabbits with heart failure, which was activated by the SAPK/JNK pathway (Liu et al., 2006). Furthermore, Ang II-evoked ERK1/2 phosphorylation also functioned in central sympathetic activities via transcription regulation. For example, the PKCb/NADPH

oxidase/ERK1/2/CREB/c-fos signaling cascade modulates the long-term pressor effect induced by Ang II in the RVLM of normal rats (Chan et al., 2007). Our present findings indicate that SAPK/JNK, but not ERK1/2 or p38MAPK, has a crucial effect on the modulation of pressor response and AT_1R expression in the RVLM of SIHR. The findings reveal that Ang II upregulates its own receptors via positive feedback involving the AT_1R-ROS-SAPK/JNK pathway (**Figure 7**).

Overall, the present data show that AT_1R localizes in the glutamatergic neurons of the RVLM of SIHR. This localization results in the release of glutamate into the IML of the spinal cord, leading to the pressor response in SIHR. Further, the NADPH oxidase-ROS-SAPK/JNK pathway has an essential impact on the actions of glutamatergic neurons and promotes the expression of AT_1R in the RVLM of SIHR. Thus, this study reveals that Ang II modulates pressor effect through AT_1R-dependent activation of SAPK/JNK by NADPH oxidase-derived ROS in the glutamatergic neurons of the RVLM in SIHR. One limitation of the present study is that we didn't examine the expression of AP-1 and the role of AP-1 in SIHR, although it has been reported that AP-1 activation might participate in the upregulation of AT_1R in heart failure. This interesting possibility in SIHR will be investigated in our future study.

AUTHOR CONTRIBUTIONS

JinW designed the work. LJ, XZ, RG, and YX performed the experiments. XZ, JinW, and SM wrote the manuscript. HY drew the figures. JinW, JijW, LS, and DZ interpreted the data.

FUNDING

This study was supported by the National Natural Science Foundation of China (No. 31371155).

ACKNOWLEDGMENTS

We would like to thank Editage (www.editage.com) for English language editing.

REFERENCES

Awad, K. S., West, J. D., de Jesus, P. V., and MacLean, M. (2016). Novel signaling pathways in pulmonary arterial hypertension (2015 Grover Conference Series). *Pulm. Circ.* 6, 285–294. doi: 10.1086/688034

Bae, Y. S., Oh, H., Rhee, S. G., and Yoo, Y. D. (2011). Regulation of reactive oxygen species generation in cell signaling. *Mol. Cells* 32, 491–509. doi: 10.1007/s10059-011-0276-3

Bao, W., Behm, D. J., Nerurkar, S. S., Ao, Z., Bentley, R., Mirabile, R. C., et al. (2007). Effects of p38 MAPK inhibitor on angiotensin II-dependent hypertension, organ damage, and superoxide anion production. *J. Cardiovasc. Pharmacol.* 49, 362–368. doi: 10.1097/fjc.0b013e318046f34a

Campese, V. M., Shaohua, Y., and Huiquin, Z. (2005). Oxidative stress mediates angiotensin II-dependent stimulation of sympathetic nerve activity. *Hypertension* 46, 533–539. doi: 10.1161/01.hyp.0000179088.57586.26

Cao, Y., Zhang, Y., Wang, N., and He, L. (2014). Antioxidant effect of imperatorin from angelica dahurica in hypertension via inhibiting NADPH oxidase activation and MAPK pathway. *J. Am. Soc. Hypertens.* 8, 527–536. doi: 10.1016/j.jash.2014.04.006

Carvalho, T. H. F., Bergamaschi, C. T., Lopes, O. U., and Campos, R. R. (2003). Role of endogenous angiotensin II on glutamatergic actions in the rostral ventrolateral medulla in goldblatt hypertensive rats. *Hypertension* 42, 707–712. doi: 10.1161/01.hyp.0000086524.35251.2D

Chan, S. H., Hsu, K. S., Huang, C. C., Wang, L. L., Ou, C. C., and Chan, J. Y. (2005). NADPH oxidase-derived superoxide anion mediates angiotensin II-induced pressor effect via activation of p38 mitogen-activated protein kinase in the rostral ventrolateral medulla. *Circ. Res.* 97, 772–780. doi: 10.1161/01.res.0000185804.79157.C0

Chan, S. H., Wang, L. L., Tseng, H. L., and Chan, J. Y. (2007). Upregulation of AT1 receptor gene on activation of protein kinase C beta/nicotinamide adenine dinucleotide diphosphate oxidase/ERK1/2/c-fos signaling cascade mediates long-term pressor effect of angiotensin II in rostral ventrolateral medulla. *J. Hypertens.* 25, 1845–1861. doi: 10.1097/hjh.0b013e328217b286

Czikora, I., Feher, A., Lucas, R., Fulton, D. J., and Bagi, Z. (2015). Caveolin-1 prevents sustained angiotensin II-induced resistance artery constriction and obesity-induced high blood pressure. *Am. J. Physiol. Heart Circ. Physiol.* 308, H376–H385. doi: 10.1152/ajpheart.00649.2014

Dange, R. B., Agarwal, D., Masson, G. S., Vila, J., Wilson, B., Nair, A., et al. (2014). Central blockade of TLR4 improves cardiac function and attenuates myocardial inflammation in angiotensin II-induced hypertension. *Cardiovasc. Res.* 103, 17–27. doi: 10.1093/cvr/cvu067

Ding, K., Wang, Y., Jiang, W., Zhang, Y., Yin, H., and Fang, Z. (2015). Qian yang yu yin granule-containing serum inhibits angiotensin II-induced proliferation, reactive oxygen species production, and inflammation in human mesangial cells via an NADPH oxidase 4-dependent pathway. *BMC Complement. Altern. Med.* 15:81. doi: 10.1186/s12906-015-0619-2

Du, D., Chen, J., Liu, M., Zhu, M., Jing, H., Fang, J., et al. (2013). The effects of angiotensin II and angiotensin-(1-7) in the rostral ventrolateral medulla of rats on stress-induced hypertension. *PLoS One* 8:e70976. doi: 10.1371/journal.pone.0070976

Fang, X., Shu, G., Yu, J., Wang, L., Yang, J., Zeng, Q., et al. (2013). The anorexigenic effect of serotonin is mediated by the generation of NADPH oxidase-dependent ROS. *PLoS One* 8:e53142. doi: 10.1371/journal.pone.0053142

Gabor, A., and Leenen, F. H. H. (2012). Cardiovascular effects of angiotensin II and glutamate in the PVN of dahl salt-sensitive rats. *Brain Res.* 1447, 28–37. doi: 10.1016/j.brainres.2012.01.060

Gao, L., Wang, W., Li, Y. L., Schultz, H. D., Liu, D., Cornish, K. G., et al. (2004). Superoxide mediates sympathoexcitation in heart failure: roles of angiotensin II and NAD(P)H oxidase. *Circ. Res.* 95, 937–944. doi: 10.1161/01.res.0000146676.04359.64

Gao, L., Wang, W., Li, Y. L., Schultz, H. D., Liu, D., Cornish, K. G., et al. (2005). Sympathoexcitation by central ang II: roles for AT1 receptor upregulation and NAD(P)H oxidase in RVLM. *Am. J. Physiol. Heart Circ. Physiol.* 288, H2271–H2279. doi: 10.1152/ajpheart.00949.2004

Guyenet, P. G. (2006). The sympathetic control of blood pressure. *Nat. Rev. Neurosci.* 7, 335–346. doi: 10.1038/nrn1902

Hanna, I. R., Taniyama, Y., Szocs, K., Rocic, P., and Griendling, K. K. (2002). NAD(P)H oxidase-derived reactive oxygen species as mediators of angiotensin II signaling. *Antioxid. Redox. Signal.* 4, 899–914. doi: 10.1089/152308602762197443

Hausding, M., Jurk, K., Daub, S., Kröller-Schön, S., Stein, J., Schwenk, M., et al. (2013). CD40L contributes to angiotensin II-induced pro-thrombotic state, vascular inflammation, oxidative stress and endothelial dysfunction. *Basic Res. Cardiol.* 108:386. doi: 10.1007/s00395-013-0386-5

Hu, L., Zhu, D., Yu, Z., Wang, J. Q., Sun, Z., and Yao, T. (2002). Expression of angiotensin II type 1 (AT1) receptor in the rostral ventrolateral medulla in rats. *J. Appl. Physiol.* 92, 2153–2161. doi: 10.1152/japplphysiol.00261.2001

Jia, G., Cheng, G., Gangahar, D. M., and Agrawal, D. K. (2008). Involvement of connexin 43 in angiotensin II-induced migration and proliferation of saphenous vein smooth muscle cells via the MAPK-AP-1 signaling pathway. *J. Mol. Cell. Cardiol.* 44, 882–890. doi: 10.1016/j.yjmcc.2008.03.002

Lassegue, B., San, M. A., and Griendling, K. K. (2012). Biochemistry, physiology, and pathophysiology of NADPH oxidases in the cardiovascular system. *Circ. Res.* 110, 1364–1390. doi: 10.1161/circresaha.111.243972

Li, Y. Q., Li, X. B., Guo, S. J., Chu, S. L., Gao, P. J., Zhu, D. L., et al. (2013). Apocynin attenuates oxidative stress and cardiac fibrosis in angiotensin II-induced cardiac diastolic dysfunction in mice. *Acta Pharmacol. Sin.* 34, 352–359. doi: 10.1038/aps.2012.164

Liguz-Lecznar, M., and Skangiel-Kramska, J. (2007). Vesicular glutamate transporters (VGLUTs): the three musketeers of glutamatergic system. *Acta Neurobiol. Exp.* 67, 207–218.

Liu, D., Gao, L., Roy, S. K., Cornish, K. G., and Zucker, I. H. (2006). Neuronal angiotensin II type 1 receptor upregulation in heart failure: activation of activator protein 1 and jun N-terminal kinase. *Circ. Res.* 99, 1004–1011. doi: 10.1161/01.res.0000247066.19878.93

Liu, D., Gao, L., Roy, S. K., Cornish, K. G., and Zucker, I. H. (2008). Role of oxidant stress on AT1 receptor expression in neurons of rabbits with heart failure and in cultured neurons. *Circ. Res.* 103, 186–193. doi: 10.1161/circresaha.108.179408

Mills, K. T., Bundy, J. D., Kelly, T. N., Reed, J. E., Kearney, P. M., Reynolds, K., et al. (2016). Global disparities of hypertension prevalence and control: a systematic analysis of population-based studies from 90 countries. *Circulation* 134, 441–450. doi: 10.1161/circulationaha.115.018912

Minas, J. N., Thorwald, M. A., Conte, D., Vázquez-Medina, J., Nishiyama, A., and Ortiz, R. M. (2015). Angiotensin and mineralocorticoid receptor antagonism attenuates cardiac oxidative stress in angiotensin II-infused rats. *Clin. Exp. Pharmacol. Physiol.* 42, 1178–1188. doi: 10.1111/1440-1681.12473

Omura, T., Yoshiyama, M., Matsumoto, R., Kusuyama, T., Enomoto, S., Nishiya, D., et al. (2005). Role of c-jun NH2-terminal kinase in G-protein-coupled receptor agonist-induced cardiac plasminogen activator inhibitor-1 expression. *J. Mol. Cell. Cardiol.* 38, 583–592. doi: 10.1016/j.yjmcc.2005.01.008

Oshima, N., Kumagai, H., Onimaru, H., Kawai, A., Pilowsky, P. M., Iigaya, K., et al. (2008). Monosynaptic excitatory connection from the rostral ventrolateral medulla to sympathetic preganglionic neurons revealed by simultaneous recordings. *Hypertens. Res.* 31, 1445–1454. doi: 10.1291/hypres.31.1445

Pan, Y. X., Gao, L., Wang, W. Z., Zheng, H., Liu, D., Patel, K. P., et al. (2007). Exercise training prevents arterial baroreflex dysfunction in rats treated with central angiotensin II. *Hypertension* 49, 519–527. doi: 10.1161/01.hyp.0000256955.74461.93

Peng, J., Wang, Y. K., Wang, L. G., Yuan, W. J., Su, D. F., Ni, X., et al. (2009). Sympathoinhibitory mechanism of moxonidine: role of the inducible nitric oxide synthase in the rostral ventrolateral medulla. *Cardiovasc. Res.* 84, 283–291. doi: 10.1093/cvr/cvp202

Reja, V., Goodchild, A. K., Phillips, J. K., and Pilowsky, P. M. (2006). Upregulation of angiotensin AT1 receptor and intracellular kinase gene expression in hypertensive rats. *Clin. Exp. Pharmacol. Physiol.* 33, 690–695. doi: 10.1111/j.1440-1681.2006.04420.x

Rincón, J., Correia, D., Arcaya, J. L., Finol, E., Fernández, A., Pérez, M., et al. (2015). Role of angiotensin II type 1 receptor on renal NAD(P)H oxidase, oxidative stress and inflammation in nitric oxide inhibition induced-hypertension. *Life Sci.* 124, 81–90. doi: 10.1016/j.lfs.2015.01.005

Ross, C. A., Ruggiero, D. A., Park, D. H., Joh, T. H., Sved, A. F., Fernandez-Pardal, J., et al. (1984). Tonic vasomotor control by the rostral ventrolateral medulla: effect of electrical or chemical stimulation of the area containing C1 adrenaline neurons on arterial pressure, heart rate, and plasma catecholamines and vasopressin. *J. Neurosci.* 4, 474–494. doi: 10.1523/JNEUROSCI.04-02-00474.1984

Ushio-Fukai, M., and Alexander, R. W. (2004). Reactive oxygen species as mediators of angiogenesis signaling: role of NAD (P)H oxidase. *Mol. Cell. Biochem.* 264, 85–97. doi: 10.1023/B:MCBI.0000044378.09409.b5

Vigneault, E., Poirel, O., Riad, M., Prud'Homme, J., Dumas, S., Turecki, G., et al. (2015). Distribution of vesicular glutamate transporters in the human brain. *Front. Neuroanat.* 9:23. doi: 10.3389/fnana.2015.00023

Wakui, H., Dejima, T., Tamura, K., Uneda, K., Azuma, K., Maeda, A., et al. (2013). Activation of angiotensin II type 1 receptor-associated protein exerts an inhibitory effect on vascular hypertrophy and oxidative stress in angiotensin II-mediated hypertension. *Cardiovasc. Res.* 100, 511–519. doi: 10.1093/cvr/cvt225

Wang, G., Coleman, C. G., Chan, J., Faraco, G., Marques-Lopes, J., Milner, T. A., et al. (2013). Angiotensin II slow-pressor hypertension enhances NMDA currents and NOX2-dependent superoxide production in hypothalamic paraventricular neurons. *Am. J. Physiol. Regul. Integr. Comp. Physiol.* 304, R1096–R1106. doi: 10.1152/ajpregu.00367.2012

Wang, H. D., Johns, D. G., Xu, S., and Cohen, R. A. (2002). Role of superoxide anion in regulating pressor and vascular hypertrophic response to angiotensin II. *Am. J. Physiol. Heart Circ. Physiol.* 282, H1697–H1702. doi: 10.1152/ajpheart.00914.2001

Wang, M., Chen, D., Chen, L., Cao, G., Zhao, H., Liu, D., et al. (2018). Novel inhibitors of the cellular renin-angiotensin system components, poricoic acids, target Smad3 phosphorylation and Wnt/β-catenin pathway against renal fibrosis. *Br. J. Pharmacol.* 175, 2689–2708. doi: 10.1111/bph.14333

Wei, S. G., Yu, Y., Zhang, Z. H., Weiss, R. M., and Felder, R. B. (2008). Mitogen-activated protein kinases mediate upregulation of hypothalamic angiotensin II type 1 receptors in heart failure rats. *Hypertension* 52, 679–686. doi: 10.1161/hypertensionaha.108.113639

Wu, L., He, Y., Jiang, B., Sun, D., Wang, J., Liu, M., et al. (2015). Trends in prevalence, a wareness, treatment and control of hypertension during 2001-2010 in an urban elderly population of China. *PLoS One* 10:e0132814. doi: 10.1371/journal.pone.0132814

Xia, C., Shao, C., Xin, L., Wang, Y., Ding, C., Wang, J., et al. (2008). Effects of melatonin on blood pressure in stress-induced hypertension in rats. *Clin. Exp. Pharmacol. Physiol.* 35, 1258–1264. doi: 10.1111/j.1440-1681.2008.05000.x

Xiang, H. B., Liu, C., Liu, T. T., and Xiong, J. (2014). Central circuits regulating the sympathetic outflow to lumbar muscles in spinally transected mice by retrograde transsynaptic transport. *Int. J. Clin. Exp. Pathol.* 7, 2987–2997.

Xiao, F., Jiang, M., Du, D., Xia, C., Wang, J., Cao, Y., et al. (2013). Orexin A regulates cardiovascular responses in stress-induced hypertensive rats. *Neuropharmacology* 67, 16–24. doi: 10.1016/j.neuropharm.2012.10.021

Zha, Y. P., Wang, Y. K., Deng, Y., Zhang, R. W., Tan, X., Yuan, W. J., et al. (2013). Exercise training lowers the enhanced tonically active glutamatergic input to the rostral ventrolateral medulla in hypertensive rats. *CNS Neurosci. Ther.* 19, 244–251. doi: 10.1111/cns.12065

Zhang, C., Xia, C., Jiang, M., Zhu, M., Zhu, J., Du, D., et al. (2013). Repeated electroacupuncture attenuating of apelin expression and function in the rostral ventrolateral medulla in stress-induced hypertensive rats. *Brain Res. Bull.* 97, 53–62. doi: 10.1016/j.brainresbull.2013.05.013

Zhang, G. X., Lu, X. M., Kimura, S., and Nishiyama, A. (2007). Role of mitochondria in angiotensin II-induced reactive oxygen species and mitogen-activated protein kinase activation. *Cardiovasc. Res.* 76, 204–212. doi: 10.1016/j.cardiores.2007.07.014

Conflict of Interest Statement: The authors declare that the research was conducted in the absence of any commercial or financial relationships that could be construed as a potential conflict of interest.

Copyright © 2019 Jiang, Zhou, Yang, Guan, Xin, Wang, Shen, Zhu, Ma and Wang. This is an open-access article distributed under the terms of the Creative Commons Attribution License (CC BY). The use, distribution or reproduction in other forums is permitted, provided the original author(s) and the copyright owner(s) are credited and that the original publication in this journal is cited, in accordance with accepted academic practice. No use, distribution or reproduction is permitted which does not comply with these terms.

frontiers in Human Neuroscience

CLINICAL TRIAL
published: 21 January 2019
doi: 10.3389/fnhum.2018.00533

Non-invasive High Frequency Median Nerve Stimulation Effectively Suppresses Olfactory Intensity Perception in Healthy Males

Ashim Maharjan[1], *Mei Peng*[2] *and Yusuf O. Cakmak*[1,3,4]*

[1]*Department of Anatomy, School of Biomedical Sciences, University of Otago, Dunedin, New Zealand,* [2]*Department of Food Science, University of Otago, Dunedin, New Zealand,* [3]*Brain Health Research Centre, Division of Sciences, University of Otago, Dunedin, New Zealand,* [4]*Medical Technologies Centre of Research Excellence, Auckland, New Zealand*

Median nerve stimulation (MNS) had been performed in the existing literature to alleviate symptoms of nausea and vomiting. The observed facilitative effects are thought to be mediated by the vagal pathways, particularly the vagus nerve (VN) brainstem nuclei of the dorsal motor nucleus of vagus and nucleus tractus solitarius (DMV-NTS). Sense of smell is one of the major sensory modalities for inducing vomiting and nausea as a primary defense against potentially harmful intake of material. This study aimed to test effects of non-invasive, high and low frequency MNS on human olfactory functioning, with supplementary exploration of the orbitofrontal cortex (OFC) using near-infrared spectroscopy (NIRS). Twenty healthy, male, adults performed supra-threshold odor intensity tests (labeled magnitude scale, LMS) for four food-related odorant samples (presented in three different concentrations) before and after receiving high-, low frequency MNS and placebo (no stimulation), while cortical activities in the OFC was monitored by the NIRS. Data of the NIRS and LMS test of separate stimulation parameters were statistically analyzed using mixed-model analysis of variance (ANOVA). Only the high frequency MNS showed effects for suppressing the intensity perception of the moderate concentration of Amyl Acetate (p:0.042) and strong concentration of Isovaleric Acid (p:0.004) and 1-Octen-3-ol (p:0.006). These behavioral changes were coupled with significant changes in the NIRS recordings of the left (p:0.000) and right (p:0.003) hemispheric orbitofrontal cortices. This is the first study that applied non-invasive, high frequency MNS to suppress the supra-threshold odor ratings of specific concentrations of odors. The vagal networks are potential relays of MNS to influence OFC. Results from the current article implore further research into non-invasive, high frequency MNS in the investigation of its modulatory effects on olfactory function, given its potential to be used for ameliorating nausea and malnutrition associated with various health conditions.

Keywords: median nerve stimulation, near-infrared spectroscopy, orbitofrontal cortex, olfaction, labeled magnitude scale, non-invasive electrostimulation, nausea and vomiting

OPEN ACCESS

Edited by:
Mikhail Lebedev,
Duke University, United States

Reviewed by:
Peter Herman,
Yale University, United States
Alessandro Tonacci,
Istituto di Fisiologia Clinica (IFC), Italy

***Correspondence:**
Yusuf O. Cakmak
yusuf.cakmak@otago.ac.nz

Received: *05 August 2018*
Accepted: *17 December 2018*
Published: *21 January 2019*

Citation:
Maharjan A, Peng M and Cakmak YO (2019) Non-invasive High Frequency Median Nerve Stimulation Effectively Suppresses Olfactory Intensity Perception in Healthy Males. Front. Hum. Neurosci. 12:533. doi: 10.3389/fnhum.2018.00533

INTRODUCTION

Sense of smell, in combination with vision and taste, are essential contributors to inducing nausea or vomiting as the primary defense against dangerous or contaminated food (Andrews, 1992). The link between odor and nausea even dates back to the Roman empire where invaders were thought to give off a nauseating odor, caused by the use of rancid butter as hair ointment (Classen et al., 1994). Nausea and vomiting are one of the most frequently reported symptoms in clinical settings due to the wide range of conditions including medications, motion sickness, infections, hormonal disorders, pregnancy, central nervous system disorders, psychiatric disorders, anesthesia, and cardiovascular dysfunctions (Andrews, 1992; Babic and Browning, 2014; Lee and Fan, 2015). Furthermore, nausea and vomiting often coincide with a loss of appetite. For those who suffer from this cluster of symptoms for a long term, such as patients who undergo chemotherapy treatment, their quality of life can be substantially affected (Guerdoux-Ninot et al., 2016). Despite its high prevalence and numerous causes, the treatment options for nausea with medication are not highly effective and can also have side effects (Lee and Fan, 2015). Median nerve stimulation (MNS) is one of the alternative approaches that are being explored in the current literature to reduce nausea and vomiting.

MNS was initially performed using manual acupuncture on the median nerve (MN) [a traditional Chinese method using Neiguan acupuncture point (pericardium meridian of acupuncture point 6; PC-6)]. Over the past couple of decades, MNS has advanced from manual acupuncture techniques (Napadow et al., 2009; Bai et al., 2010; Lee and Fan, 2015) to electroacupuncture (EA) which is a modification of the acupuncture technique using electrical current (Spiegel et al., 1999; Chen et al., 2003; Tatewaki et al., 2005; Lee and Fan, 2015). A popular form of MNS in the current literature is the use of transcutaneous electrical nerve stimulation (TENS; Zatorre et al., 1992; Urasaki et al., 1998; Ferretti et al., 2007; Lee and Fan, 2015). In the current literature, MNS is used to treat gastrointestinal diseases (Diehl, 1999; Wang et al., 2000; Chang et al., 2001; Takahashi, 2006; Xu et al., 2006) and alleviating symptoms of nausea and vomiting in clinical settings that includes post-surgery/chemotherapy, pregnancy or motion sickness (Xu et al., 2006; Dhond et al., 2008; Ren et al., 2010; Zotelli et al., 2014).

In the existing literature, MNS has been used to alleviate symptoms of nausea and vomiting, effects that are thought to occur through the vagal pathways (Chen et al., 2003; Tada et al., 2003; Tatewaki et al., 2005; Xu et al., 2006; Bai et al., 2010; Ren et al., 2010; Takahashi, 2011; Zotelli et al., 2014; Lee and Fan, 2015). The use of low frequency (10–25 Hz) MNS has also demonstrated a positive control of gastric mobility *via* increased gastric emptying and the ability to regulate gastric dysthymia (Chen et al., 2003; Tatewaki et al., 2005; Xu et al., 2006). As the vagus nerve (VN) is recognized as the sole contributor to the control of gastric acid secretion and mobility, this tantalizes VN and MNS interactions. In both animal models and human studies, MNS has displayed the ability to modulate the VN (Ouyang et al., 2002; Chen et al., 2003; Xu et al., 2006; Takahashi, 2011). In a previous article by Ouyang et al. (2002), low frequency MNS accelerated gastric emptying of liquids and improved gastric slow-wave rhythmicity. Modulation of gastric function using MNS was also absent after vagotomy in animal models (Noguchi and Hayashi, 1996; Xu et al., 2006). This supports the notion that the potential pathway of MNS on gastric functions are through the dorsal motor nucleus of vagus-Nucleus Tractus Solitarius (DMV-NTS), both of which are VN brainstem nuclei (Ruggiero et al., 1998; Cakmak, 2006; Imai et al., 2008).

In a previous article by our group (Maharjan et al., 2018), non-invasive and high frequency auricular VN electrostimulation improved olfactory performance in the supra-threshold test. However, to date, the MNS' potential effects on olfactory function *via* its interactions with vagal nerve networks has not been explored yet. Therefore, this study aimed to observe the effects of non-invasive MNS on olfactory sensory function using a labeled magnitude scale (LMS) test in healthy, male, adults under high and low frequencies of electrostimulation with supplementary exploration of the orbitofrontal cortex (OFC) using near-infrared spectroscopy (NIRS).

METHODS

Participants

Twenty Caucasian-male, healthy, non-smokers (age range = 22–32 years, mean: 25.05 years, standard deviation: 2.36 years) participated in the current study. Prior to the study, each participant was asked not to consume any food or non-water beverages for 2 h prior to the experiments. They were also instructed to refrain from applying any fragrance product/s on the day of the experiment. All participants gave an informed, written consent to participate in the experiment, in accordance with the Declaration of Helsinki and met the exclusion criteria set for the experiment (non-smoker, in a healthy condition and were of NZ-European descent). The experiment was approved by the Otago Human Participants Ethics Committee (Reference: H16/148) and registered to the Australian New Zealand clinical trials registry (ANZCTR; registration ID: ACTRN12617000034336, Clinical trial name: MODOLF).

Labeled Magnitude Scale (LMS) Test

The LMS test is a widely-used psychophysical scaling method for quantifying intensity perception of sensory stimuli (Green et al., 1993, 1996). The LMS is composed of seven verbal labels arranged according to the geometric means of their rated magnitude which ranges from 0 to 100 ("no sensation"-0, "barely detectable"-1.4, "weak"-6.1, "moderate"-17.2, "strong"-35.4, "very strong"-53.3, "strongest imaginable"-100). Following previous protocols (Green et al., 1993, 1996; Kalva et al., 2014), the current study tested responses to four different odors—two "pleasant" odors [Citral (CAS number: 5392-40-5; purity: 99%, Sigma-Aldrich, St. Louis, MO, USA)—commonly described as citrus and Amyl Acetate (CAS number: 628-63-7;

purity: 99%, Sigma-Aldrich, St. Louis, MO, USA)—commonly described as banana] and two "unpleasant" odors [Isovaleric Acid (CAS number: 503-74-2; purity: 99%, Sigma-Aldrich, St. Louis, MO, USA)—commonly described as cheese and 1-Octen-3-ol (CAS number: 3391-86-4; purity: 99%, Sigma-Aldrich, St. Louis, MO, USA)—commonly described as mushroom]—with three different concentrations for each odor. Specifically, these odors included Citral (2 ppm, 20 ppm, 200 ppm), 1-Octen-3-ol (3 ppm, 18 ppm, 108 ppm), Amyl Acetate (1.5 ppm, 15 ppm, 150 ppm) and Isovaleric acid (4 ppm, 28 ppm, 196 ppm). All odors were diluted in distilled water. The selection of these concentrations underwent four stages of bench-top testing (n = 6–10) which were performed to differentiate three concentrations (weak, moderate and strong) for each odorant. Participants used the LMS scale to rate each concentration of each odor in the bench-top testing stages. After four stages of bench-top testing, the use of specific concentrations for each odor matched the ratings (weak, moderate and strong) in the LMS to a satisfactory level. All results of bench-top testing are provided in **Supplementary Table S1**.

An additional screening criterion used in the initial studies of the LMS test (Green et al., 1996) was also included to ensure that each participant could differentiate weak, moderate and strong concentrations of each odor (Citral, Amyl Acetate, Isovaleric Acid, 1-Octen-3-ol). In this instance, we used Ethyl-butyrate (CAS number: 105-54-4; purity: 99%, Sigma-Aldrich, St. Louis, MO, USA) using 1.25 ppm as weak concentration, 13.69 ppm as moderate concentration and 150 ppm as strong concentration. These concentrations of Ethyl-butyrate also underwent four stages of bench-top testing (**Supplementary Table S1**). This odor was chosen as it was distinct from the odors used in the testing phase of the current study. Before the start of the pre-stimulation and post-stimulation LMS, each participant was given a separate set of glass lidded bottles with an example of a weak and strong concentration of an independent odor distinct to the testing odors (Ethyl-butyrate: weak-1.25 ppm and strong-150 ppm). Each concentration of all four odors was presented in a 240-ml glass lidded bottles. To sample an odorant, the subject was asked to place the glass bottle approximately 2 cm away from the nose and inhale within a 2–3 s window. Separate sets of randomized numeral labeled bottles were used for pre-stimulation and post-stimulation LMS. Each concentration was presented once (in both pre-stimulation LMS and post-stimulation LMS), in a randomized order that was counterbalanced for each stage (pre- and post-stimulation LMS) across all participants. 30 s inter-stimulus interval was present between the presentation of each odor. The participants' response on the LMS was measured using the software "Compusense" (Compusense Cloud, Version 8.8.6766.17069, Compusense Inc., Guelph, ON, Canada).

Application of Median Nerve Stimulation (MNS)

Non-invasive MNS was applied to the participant using "TENS ECO-2" (SCHWA-MEDICO, 35630 Ehringshausen, Germany) by the experimenter, using TENS for all three different parameters—high frequency MNS (80 Hz), low frequency MNS (10 Hz) and placebo (no stimulation but the electrodes were still attached). TENS in the current experiment was performed with the use of two pairs of disposable rubber electrode-pads, placed on the MN region of the left forearm, with the cathode being 3 cm proximal to the anode (**Figure 1b**), similar to previous studies using MNS with TENS (Urasaki et al., 1998; Ferretti et al., 2007). The TENS intensity was adjusted to obtain a tingling sensation over the MN territory of the palm and visible flexion response of index and/or middle finger (and/or thumb). This indicated the stimulation of the sensory and motor fibers of the MN in each stimulation session. In addition, the stimulation intensity was also kept to a comfortable range for the participant to ensure there was no perception of pain. The strength of the MNS (amplitude) was between 8 mA and 15 mA and the pulse bandwidth was 180 μS width bipolar square waveform.

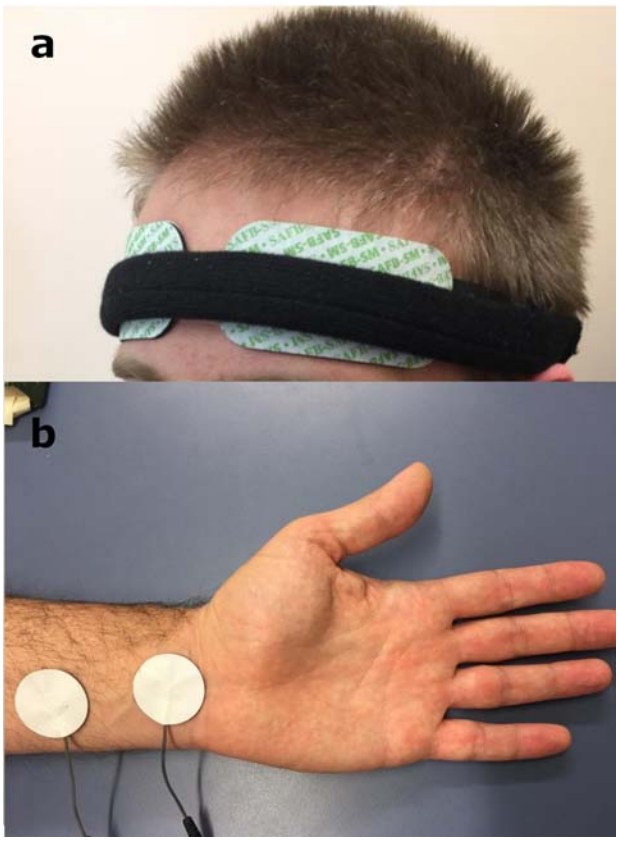


FIGURE 1 | (a) Near-infrared spectroscopy (NIRS) electrodes set up on the forehead of the participant. **(b)** The location of the non-invasive median nerve stimulation (MNS) using the pair of disposable rubber electrode-pads on the MN region of the left forearm. Written informed consent was obtained from the participant for the publication of this image (**Supplementary Figure S1**).

Procedure

Each participant was given a brief introduction to all the stages of the experiment and were instructed to attend

three, 30–45-min sessions with at least 24-h apart. The experimental room was an isolated environment with air conditioning, allowing for a consistent temperature (23 ± 1°C) in the absence of any olfactory or visual stimuli representing food or distractions. The participants were instructed not to sniff during the olfactory tests to eliminate the potential effects of sniffing itself during the olfactory tests and NIRS recordings. The participant was seated directly opposite to the experimenter. A consent form and exclusion criteria sheet were signed to qualify the participants for the study. A brief explanation of the full experimental process and the olfactory test (LMS) were given to the participant. Pre-stimulation, LMS was performed for 10–15 min, followed directly by the allocated stimulation parameter for 10 min (high frequency MNS, low frequency MNS or placebo) that was delegated randomly for each participant. Lastly, post-stimulation, LMS (10–15 min) was performed directly after the allocated stimulation parameter (**Figure 2**). This study followed a double-blind design.

Figure 2 details the experimental design of the current study. A within-participant design was enforced. In each session, participants were randomly assigned to one of the three experimental conditions: high frequency MNS, low frequency MNS or placebo. The order of experimental conditions was counterbalanced across the participants. In addition to the exclusion criteria put in place to ensure that all participants were in healthy condition for the experiment, University of Pennsylvania Smell Identification Test (UPSIT) odor identification test (OIT; Sensonics International, Haddon Heights, NJ, USA) and odor discrimination/memory test (ODMT; Sensonics International, Haddon Heights, NJ, USA) were performed by each participant, after the placebo session. The results from these olfactory tests were compared to that of previous studies (Doty et al., 1984, 1995; Choudhury et al., 2003) to ensure that all participants met the standard for normative, healthy response in healthy, adult, male subjects.

Near-Infrared Spectroscopy (NIRS)

NIRS (COVIDIEN INVOS OXIMETER, Model 5100C-PA, Mansfield, MA, USA) was performed in the current study to measure participants' activity from the OFC. This INVOS (*in vivo* Optical Spectroscopy)-NIRS model is a clinically validated and FDA approved device, used in over 600 peer-reviewed articles and three randomized controlled trials

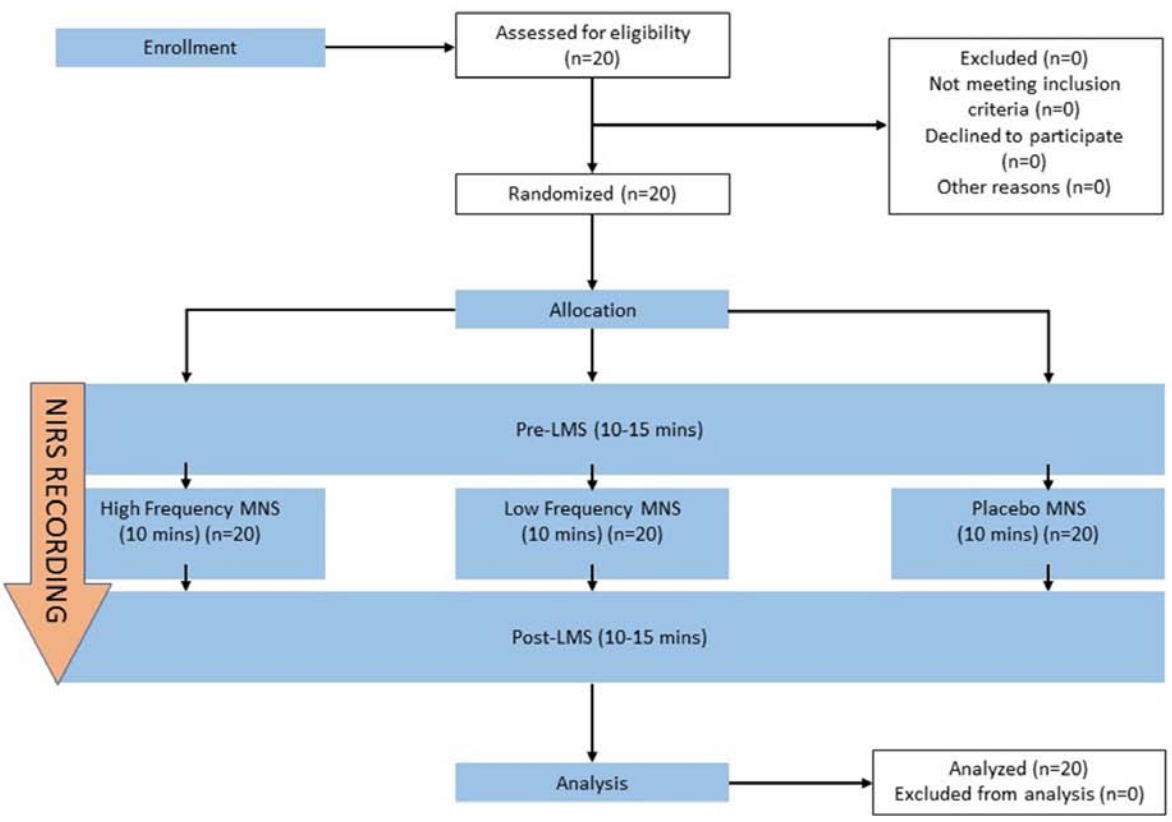


FIGURE 2 | Schematic sequence of each stage of the current study. The sequence of the experimental stages includes pre-stimulation labeled magnitude scale (Pre-LMS), allocated stimulation parameter (high frequency MNS, low frequency MNS, placebo) and post-stimulation (Post-LMS). A brief 5-min introduction, prior to the experiment comprised of obtaining participant's consent and device set up. MNS, LMS, NIRS recordings from both hemispheres of the orbitofrontal cortex (OFC) were recorded simultaneously across all stages of the experiment (Pre-LMS, allocated stimulation parameter, Post-LMS) for all participants.

(Harrer et al., 2010; Edmonds et al., 2016, 2017). The setup of this device is shown in **Figure 1a**. In the existing literature, several studies have demonstrated the efficiency of the NIRS in monitoring the activation of the OFC under olfactory stimulus (Hongo et al., 1995; Cho et al., 1998; Edmonds et al., 1998; Ishimaru et al., 2004; Harada et al., 2006; Kobayashi et al., 2012). With the aid of fMRI localization, olfactory expression was understood to be present in the lateral and anterior orbito-frontal gyri of the frontal lobe. With this knowledge, several studies have recorded from the orbito-frontal region using NIRS techniques and found that oxygenated hemoglobin (HbO_2) concentration increased only over the orbito-frontal region during olfactory stimulation (Ishimaru et al., 2004; Harada et al., 2006; Kobayashi et al., 2012).

INVOS-NIRS facilitates non-invasive method of monitoring regional tissue oxygenation (oxy- and deoxyhemoglobin) by using the modified Beer-Lambert law for light attenuation changes through the illuminated tissue (relating to optical density to chromophore concentration). INVOS-NIRS measures the red pigment of hemoglobin molecules within the red blood cells which is understood to have the highest light absorption of the wavelengths (730 and 810 nm; Edmonds et al., 2004; Covidien, 2013). The INVOS-NIRS system sensors used two near-infrared light sources at two different wavelengths (730 and 810 nm) and two photodiode detectors at a distance to observe the oxygen-hemoglobin saturation of the tissues beneath the sensors. The sensor's light emitting diode sends light to either a proximal or distal detector in a parabolic path, which allows the processing of separate data of shallow and deep optical signals. With the use of an algorithm of subtraction of the short vs. long travel distance of the light, INVOS-NIRS enables high spatial resolution (effective localization of the area of measurement) and enables the elimination of skin and scalp data (Hongo et al., 1995; Edmonds et al., 2004; Covidien, 2013). With the wavelengths of 730–810 nm, it is worth mentioning that melanin and water also behave as chromophores, but fortunately, INVOS-NIRS has shown in the existing literature that recordings have been unaffected by normal skin pigmentation in adults (Misra et al., 1998; Damian and Schlosser, 2007).

By measuring regional hemoglobin oxygen saturation (rSO_2), the INVOS-NIRS system provides absolute, real time data accuracy from the cortex with the use of multi-sensors within the same sensor and is empirically validated in human subjects (Hongo et al., 1995; Cho et al., 1998; Edmonds et al., 1998, 2004; Roberts et al., 1998; Higami et al., 1999; Singer et al., 1999; Yao et al., 2001; Alexander et al., 2002; Iglesias et al., 2003). rSO_2 reflects the balance between cerebral oxygen supply and demand, measuring the continuous local brain oxygen balance in a non-invasive approach (Cho et al., 1998; Edmonds et al., 1998, 2004; Blas et al., 1999; Janelle et al., 2002; Prabhune et al., 2002; Casati et al., 2005; Harada et al., 2006).

Unlike other systems that only assesses venous or arterial blood, the current study used the clinically validated and FDA approved INVOS-NIRS, which measures a 3:1 ratio of venous and arterial blood. This algorithm was calibrated using blood samples with the assumption that 25% of the blood within the sample volume being arterial while 75% of the blood within the sample volume was venous (Edmonds et al., 2004) This represented a venous-blood saturation (venous-weighted percent of rSO_2-$VWrSO_2$%) which can be used to provide real-time data about the balance (or imbalance) of oxygen supply/demand. Thus, this reflects venous oxygen reserve (VOR; oxygen remaining from extraction of associated tissues and vital organs) providing accurate measurement of site-specific tissue oxygenation (Blas et al., 1999; Janelle et al., 2002; Prabhune et al., 2002; Casati et al., 2005). In the current literature, reduction in VOR is considered a warning sign of developing pathology or deteriorating patient condition with reports of 20%–25% from baseline or rSO_2 of 40–50 considered to be cause of concern in association with neurologic dysfunction and other adverse outcomes (Hongo et al., 1995; Cho et al., 1998; Edmonds et al., 1998, 2004; Roberts et al., 1998; Higami et al., 1999; Singer et al., 1999; Yao et al., 2001; Alexander et al., 2002; Iglesias et al., 2003; Murkin et al., 2007; Ballard et al., 2012; Vretzakis et al., 2013).

The current study also used disposable electrodes for each participant to ensure highest hygiene and data quality, in addition to using a rigid head band to stabilize the electrodes and the cables that are attached to the electrodes (**Figure 1a**). We measured from the forehead region (**Figure 1a**) to avoid issues regarding hair or hair follicles that can produce excessive photon scattering in INVOS-NIRS resulting in artificial low rSO_2 (Oriheula-Espina et al., 2010). Furthermore, this forehead region is the routine zone of cerebral oximetry monitoring by INVOS-NIRS and has FDA validated approval for the use of this device for cerebral monitoring (Prabhune et al., 2002; Casati et al., 2005; Edmonds et al., 2017). INVOS-NIRS system also provides a reliable signal strength index (SSI) for stable recordings with each channel showing a 5-unit bar scale system. Any signal over 1 bar indicates a stable recording to generate an accurate $VWrSO_2$ (%) recording [Chapter 6.4.16 and 11.7.4 in the INVOS-NIRS 5100c manual (Covidien, 2013)]. In the current study, we ensured that the SSI bar was at the highest signal (5/5 SSI) throughout all of the recordings. We only enrolled healthy participants in the current study to eliminate potential pathological artifacts (cranial bone anomalies, frontal sinus inflammation or dyshemoglobinemia; Gopinath et al., 1995; de Letter et al., 1998; Madsen et al., 2000; McRobb et al., 2011) as well as maintaining a consistent room temperature and position of participant throughout the experiment to avoid any potential anomalies with the INVOS-NIRS measurements. With the INVOS-NIRS recordings, each section of the experiment (**Figure 2**), was mapped to ensure that each stage of the experiment had an average (mean) recording of $VWrSO_2$ (representing VOR) for each participant from the left and the right hemispheres of the OFC.

Data Analysis

Data from the NIRS device was transferred to the INVOS software which accommodated data presentation. We used average (mean) recordings of $VWrSO_2$ (%) data of specific time periods marked for each segment of each session which was in line with the previous research (Cho et al., 1998; Murkin et al., 2007). To insure that the baseline

TABLE 1 | Pre-stimulation results of the repeated-measures analysis of variance (ANOVA) that assessed the potential difference (if any) of the labeled magnitude scale (LMS) test and the near-infrared spectroscopy (NIRS; $VWrSO_2$%) data in all stimulation parameters [high frequency median nerve stimulation (MNS), low frequency MNS and placebo].

Olfactory test and NIRS recordings (h = hemisphere)	Stimulation parameter (H-High, L-Low, P-Placebo)	Mean	SD	*F*-Value	*p*-value
Pre-S LMS Mod AA	H	16.2225	12.8618	0.910	0.411
	L	13.4375	9.7741		
	P	17.3500	12.3399		
Pre-S LMS Str VA	H	22.8375	16.9355	0.015	0.985
	L	22.2125	20.4004		
	P	22.7275	22.4596		
Pre-S LMS Str Octen	H	29.9650	23.4717	0.821	0.448
	L	27.8775	21.0517		
	P	32.3925	21.2645		
Left-h $VWrSO_2$ at Pre-S LMS	H	70.9675	9.3354	2.259	0.118
	L	70.8867	8.8145		
	P	72.7027	9.5207		
Right-h $VWrSO_2$ at Pre-S LMS	H	72.9550	7.5862	1.049	0.360
	L	71.2606	8.0289		
	P	72.7104	9.7302		

SD, standard deviation; LMS score ranges, 0–100; NIRS, 0–100%; H, high frequency MNS; L, low frequency MNS; P, placebo condition; left-h, left hemisphere; right-h, right hemisphere; mod AA, moderate concentration of Amyl Acetate; Str VA, Strong concentration of Isovaleric Acid; Str Octen, Strong concentration of 1-Octen-3-ol; Pre-S, Pre-Stimulation.

activity was consistent across all three different stimulation parameters for LMS and LMS-NIRS data, repeated-measures analysis of variance (ANOVA) was also applied to the data that was obtained at the pre-stimulation stage (**Table 1**). Mixed-model ANOVA was applied to data obtained from each stimulation parameters (i.e., high frequency MNS, low frequency MNS and placebo) for assessing $VWrSO_2$ (%) changes in separate hemispheric OFC (independent variable: left and right) across stages of the experiment (repeated-measures variable: pre-stimulation LMS, stimulation parameter and post-stimulation LMS). For the LMS data, mixed-model ANOVA (repeated-measures variable: pre-stimulation LMS, post-stimulation LMS; independent variables: stimulation, odor, concentration) were performed to assess differences between the scores before and after stimulation for all three parameters (high frequency MNS, low frequency MNS, and placebo). *Post hoc* test, based on simple effects tests with Bonferroni correction, was applied to understand any significance at *p*-value of 0.05. All the analyses were performed using SPSS (IBM SPSS Statistics, Ver. 20, St Leonards, NSW, Australia).

RESULTS

Pre-screening Olfactory Test Results—Odor Identification Test (OIT) and Odor Discrimination/Memory Tests (ODMT)

Half of the 20 participants displayed values of Mild Microsmia (30–33 out of 40 in OIT) while the other half of the participants displayed values of Normosmia (34–40 out of 40 in OIT). None of the participants in the current study displayed total anosmia which was the exclusion criteria for the current study and therefore, all participants presented olfactory performances in OIT to a standard held in line with the existing olfactory research (Doty et al., 1984, 1995). All participants scored between 8 and 12 out of 12 in the ODMT which corresponds to healthy ranges, in line with existing literature (Doty et al., 1984, 1995; Choudhury et al., 2003; Doty, 2003). In this context, all participants were qualified to take part in the current study.

Labeled Magnitude Scale (LMS) Test Results

Inspection of changes in LMS scores of all participants (n = 20) between the pre-stimulation and post-stimulation stages in all three stimulation parameters (high frequency MNS, low frequency MNS and placebo) suggested significant differences for only the high frequency MNS (**Figure 3**). Specifically, significant post-stimulation declines were evident for moderate concentration of Amyl Acetate (*post hoc* pair wise analysis with Bonferroni, pre-stimulation-post-stimulation, p:0.042, *Partial Eta Squared*: 0.006, low size effect), strong concentration of Isovaleric Acid (*post hoc* pairwise analysis with Bonferroni, pre-stimulation-post-stimulation, p:0.004, *Partial Eta Squared*: 0.012, low size effect) and strong concentration of 1-Octen-3-ol (*post hoc* pairwise analysis with Bonferroni, pre-stimulation-post-stimulation, p:0.006, *Partial Eta Squared*: 0.011, low size effect). Ratings for moderate concentration of Amyl Acetate, strong concentration of Isovaleric Acid and strong concentration of 1-Octen-3-ol were reduced in the post-stimulation LMS stage in comparison to the pre-stimulation LMS stage after high frequency MNS. Notably, there were no significant differences between the pre-stimulation and post-stimulation LMS stages in all concentrations of Citral, weak and strong concentrations of Amyl Acetate, and weak and moderate concentrations of Isovaleric Acid and 1-Octen-3-ol after high frequency MNS. Under low frequency MNS and placebo conditions, no significant changes were observed for

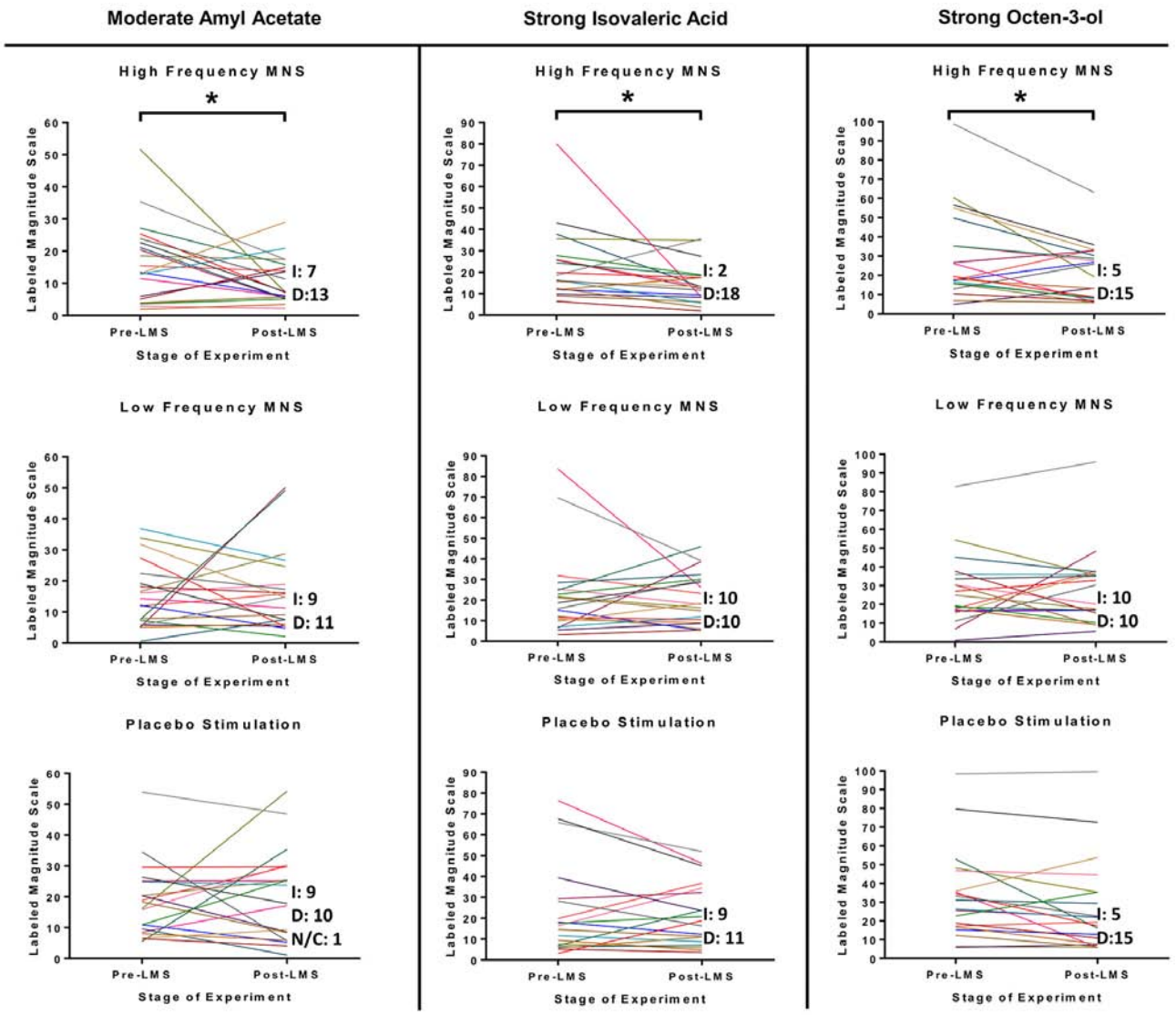


FIGURE 3 | LMS test results for moderate concentration of Amyl Acetate, strong concentration of Isovaleric Acid and strong concentration of 1-Octen-3-ol from each participant before and after each stimulation parameter (high frequency MNS, low frequency MNS and placebo). Each participant's scores, before (Pre-S LMS) and after (Post-S LMS) each of the stimulation parameters (high frequency MNS, low frequency MNS and placebo), for the LMS (LMS scores range = 0–100). Each colored line represents one case (total cases = 20). Letter "I" corresponds to cases that increased LMS test score in Post-S LMS in comparison to Pre-S LMS, letter "D" corresponds to cases that decreased LMS test score in Post-S LMS in comparison to Pre-S LMS and letters "N/C" corresponds to no change in LMS test score in Post-S LMS in comparison to Pre-S LMS. *Statistically significant ($p < 0.05$).

any odor in any of the different concentrations (**Supplementary Figures S2–S6**).

All Stage NIRS Data Analysis

Individual results from each participant's ($n = 20$) recording of $VWrSO_2$ (%) from the left and right hemispheres of the OFC is displayed in **Figure 4**. Significant differences across the three stages (pre-stimulation LMS, MNS/placebo, post-stimulation LMS) of $VWrSO_2$ (%) recordings were only present in the high frequency MNS parameter in both hemispheres of the OFC (left hemisphere: p:0.000, *Partial Eta Squared*: 0.463-large effect size; right hemisphere: p:0.003, *Partial Eta Squared*: 0.270-large effect size). *Post hoc* pairwise analysis with Bonferroni correction indicated that in the left and right hemispheres of the OFC, there were significant differences in $VWrSO_2$ (%) recordings between the pre-stimulation and stimulation stages (left hemisphere p:0.000; right hemisphere p:0.016) and pre-stimulation and post-stimulation stages (left hemisphere p:0.000; right hemisphere p:0.002). There were no significant differences between the left and the right hemispheric recordings of the OFC (p:0.592). The NIRS recordings of $VWrSO_2$ (%) increased in the stimulation and post-stimulation stages in comparison to the pre-stimulation stage in both hemispheres.

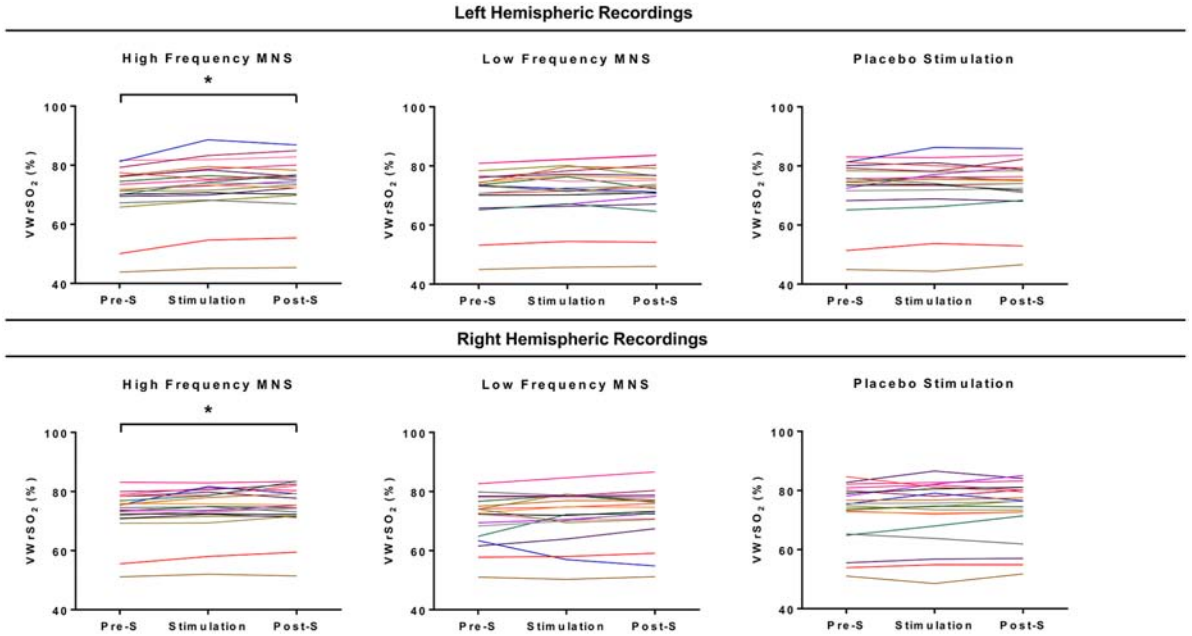


FIGURE 4 | Each of the participant's recordings for all three stages of the experiment (pre-stimulation LMS, stimulation parameter, post-stimulation LMS) for each stimulation parameter (high frequency MNS, low frequency MNS and placebo) from both the left and right hemispheres of the OFCs, measuring venous oxygen reserve ($VWrSO_2$%) using NIRS. Each colored line represents one case (total cases = 20). *Statistically significant ($p < 0.05$).

Pre-stimulation, Intergroup Differences of Labeled Magnitude Scale (LMS) and Respective Near-Infrared Spectroscopy (NIRS) Recordings From Orbitofrontal Cortices (OFC) Convergent and Divergent Co-transmission

Table 1 displays the results of the repeated-measures ANOVA that assessed the potential differences (if any were present) in the significant results from the LMS test (pre-stimulation vs. post-stimulation) and the NIRS recordings ($VWrSO_2$%) in all of the three different stimulation parameters (high frequency MNS, low frequency MNS, placebo) at the pre-stimulation stage of testing. As indicated in **Table 1**, there is no significant differences in the pre-stimulation stage for all significant results of the LMS test (moderate concentration of Amyl Acetate, strong concentration of Isovaleric Acid and strong concentration of 1-Octen-3-ol) and NIRS ($VWrSO_2$%) recordings under any of the stimulation parameters for both hemispheres of the OFC.

DISCUSSION

Studies of MNS in the existing literature have primarily focused on the cortical activation of primary (S-I) and secondary (S-II) somatosensory cortex (Spiegel et al., 1999; Nihashi et al., 2005; Napadow et al., 2009; Zhang et al., 2012; Zotelli et al., 2014), improvement of gastric function (Ouyang et al., 2002; Chen et al., 2003; Tatewaki et al., 2005; Xu et al., 2006; Takahashi, 2011) and alleviating symptoms associated with nausea and vomiting (Tatewaki et al., 2005; Xu et al., 2006; Bai et al., 2010; Takahashi, 2011; Zhang et al., 2012; Zotelli et al., 2014; Lee and Fan, 2015). As the VN is the key contributor towards gastric acid secretion and mobility, the modulation of gastric function by MNS addressed a potential interaction between MNS and VN. This interaction is supported in animal models and human studies (Ouyang et al., 2002; Chen et al., 2003; Xu et al., 2006; Takahashi, 2011). In the current literature, low frequency MNS has indicated several functions in regards to gastric mobility that includes accelerated gastric emptying of liquids and improved gastric slow-wave rhythmicity (Ouyang et al., 2002), effects absent after vagotomy (Noguchi and Hayashi, 1996; Xu et al., 2006). In a previous article by our group (Maharjan et al., 2018), non-invasive and high frequency auricular VN electrostimulation improved olfactory performance in the supra-threshold test. This indicated that high frequency, VN stimulation (VNS) can modulate olfactory function with its neural connections (**Figure 5**). In the context of modulation of olfactory function with high frequency VNS in our previous study and the existing literature on MNS' effects on changes in gastric mobility and secretion [which is also driven by the DMV and viscerosensory VN-NTS and subsequently to the insula-olfactory networks (**Figure 5**)] (Ruggiero et al., 1998; Cakmak, 2006; Imai et al., 2008; Mayer, 2011), we conceptualized that high frequency MNS may have a modulatory effect on olfactory function.

On the other hand, to date, MNS studies primarily used low frequencies (1.5–25 Hz). MNS with low frequencies (1.5–4.0 Hz) showed maximal activation of the S-I and S-II in animals models (Gyngell et al., 1996) and humans studies (Ibáñez et al., 1995)

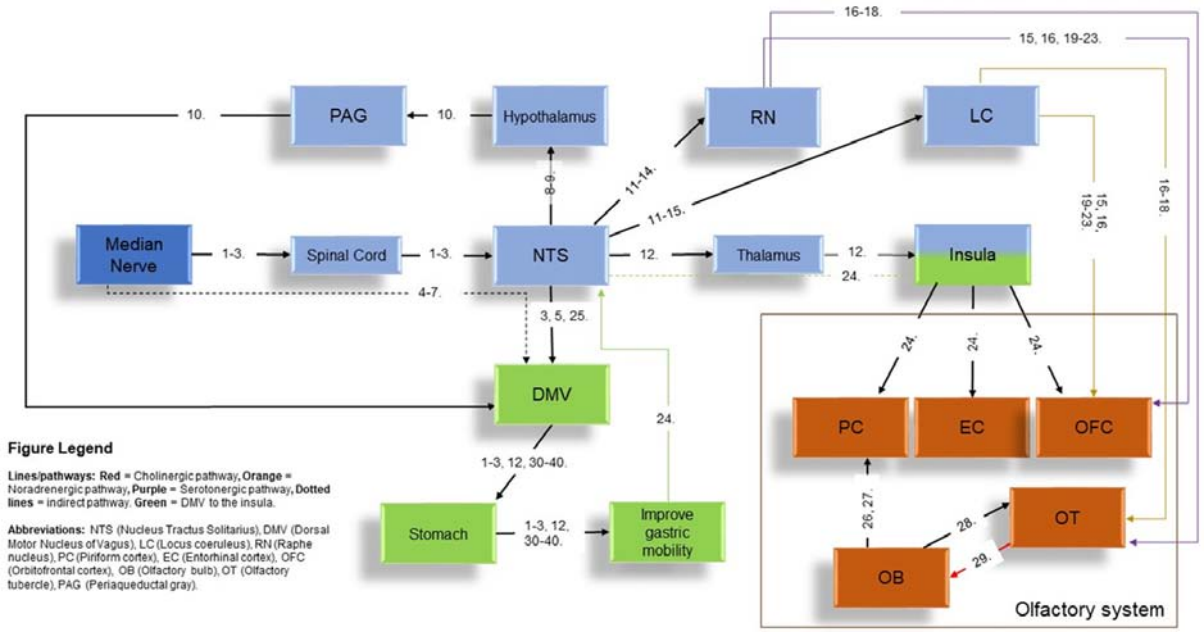


FIGURE 5 | The potential pathways to the olfactory network *via* MNS. Figure legend in the image indicates all abbreviations and the type of pathways (represented by different colors) present in the current diagram. Structures in color "blue" refer to the indirect stimulation of the vagus nerve (VN) pathway using MNS to the olfactory network while structures in color "green" refer to the stimulation of the Nucleus Tractus Solitarius-dorsal motor nucleus of vagus (NTS-DMV; VN brainstem nucleus) and subsequent interactions with the insula to the olfactory network *via* MNS. Orange structures represent the structures of the main olfactory system. Numbers in the figures represent references provided in a separate document in **Supplementary Table S2**. Abbreviations of structures are given in the Figure Legend on the bottom-left corner of the diagram.

while the use of 5 Hz resulted in an absence of activation in the S-I and the use of 15–30 Hz only had effects on some of the participants in the enrolled study (Puce et al., 1995). MNS using 0.5–1 Hz in conjunction with fMRI techniques in human subjects have found increased default network interconnectivity, greater connectivity between sensorimotor networks (Dhond et al., 2008) and increased activation of posterior insula, hypothalamus and cerebellum (Bai et al., 2010). Furthermore, low frequencies MNS of 10–25 Hz have been used on the modulation of gastric function (Noguchi and Hayashi, 1996; Ouyang et al., 2002; Xu et al., 2006; Imai et al., 2008). Low frequencies (1–25 Hz) have also been performed to alleviate symptoms of nausea and vomiting in animal models (Ouyang et al., 2002; Chen et al., 2003) and human studies (Xu et al., 2006; Bai et al., 2010). The use of MNS in higher frequencies (50 Hz) was only explored in a single study and resulted in reduced activation of the S-I in comparison to the use of lower frequencies of MNS (Davis et al., 1995). In the current study, the use of low frequency MNS (10 Hz) did not show any significant changes in the supra-threshold odor rating in the LMS test. This indicates that it is possible that the suppression of nausea and vomiting with MNS could be acting through different cortical structures that excludes the OFC and potentially separate mechanisms from the sense of smell for alleviating symptoms of nausea and vomiting. This requires further exploration in future research, coupled with the investigation of high frequency MNS in the alleviation of symptoms associated with nausea and vomiting as it could have stronger effects in comparison to low frequency MNS.

Results of the present study demonstrated that non-invasive high frequency MNS can reduce olfactory intensity ratings of the moderate concentration of Amyl Acetate, strong concentration of Isovaleric Acid and 1-Octen-3-ol in healthy participants. In contrast, non-invasive low frequency MNS and placebo groups did not show any effects on modulating olfactory sensory ratings in the LMS test. These results were also supported by statistically significant increase of $VWrSO_2$ (%) in the NIRS recordings in both hemispheres of the OFC only under high frequency MNS but not in the low frequency stimulation or placebo conditions. This is the first study that indicates that MNS under high frequency stimulation can suppress odor intensity ratings of specific concentrations of several odors in combination with the increased and simultaneous activation in the OFCs in both hemispheres. The previous study by our group (Maharjan et al., 2018) demonstrated that non-invasive high frequency (80 Hz) electrostimulation of the auricular VN can improve the performance of supra-threshold test in healthy, adult male participants. This improvement in supra-threshold olfactory function was also supported by a significant improvement of $VWrSO_2$ (%) in the NIRS recordings only in the right hemisphere (Maharjan et al., 2018). In the present study, high frequency electrostimulation (80 Hz) of the MN suppressed the supra-threshold function of odor intensity ratings in the healthy volunteers with the bilateral improvement of

$VWrSO_2$ (%) in the NIRS recordings in both hemispheres. Both studies' outcomes underlined the significance of high frequency (80 Hz) electrostimulation on modulating the olfactory function and also indicated the potential contribution of the OFC that accompanies the significant results from the supra-threshold olfactory tests in both studies with $VWrSO_2$ (%) recordings.

Although both electrostimulation techniques were capable of modulating olfactory supra-threshold function in healthy humans, use of 80 Hz electrostimulation on two different nerves modulated the supra-threshold olfactory function in opposite directions. In this context, it is worth to note the lateralization of the OFC for olfactory function. The right OFC, along with the right piriform cortex, is associated with increased activation during higher-order processing of smell sensation in comparison to the left hemispheric counterparts (Zatorre et al., 1992; Jones-Gotman and Zatorre, 1993; Hummel et al., 1995). This functional lateralization of OFC may explain the underlying mechanism of the opposite effects obtained with MNS vs. auricular VNS with high frequency (80 Hz) electrostimulation. The "smell image" may also be another factor that may contribute the suppression of olfactory function with high frequency MNS in the present study. It has been reported that each odor has been coded with its integrating senses in the brain. The smell image is described as an unconscious perception, influenced by multi-sensory inputs (including vision, sound, somatosensory-touch, taste and smell), contributing to our perception of smell that arises from the sub modalities of the somatosensory system (Shepherd, 2006). In the current study, use of high frequency MNS of 80 Hz may potentially decrease the activation of S-I (as a component of smell image) as in the reports of 50 Hz MNS study (Davis et al., 1995) and this may lead to the suppression of the smell image.

In the present study, weak, moderate and strong concentrations of 4 odors (Citral, Isovaleric Acid, Amyl Acetate and 1-Octen-3-ol) have been used. The results demonstrated that high frequency (80 Hz) MNS was capable of olfactory supra-threshold suppression for moderate concentration of Amyl Acetate, strong concentration of Isovaleric Acid and strong concentration of 1-Octen-3-ol. However, this effect was not present for the remainder. Effects on different concentrations of odors *via* MNS were not completely surprising as different odorants and different concentrations of each odorant can activate different sets of olfactory receptors (ORs; Kajiya et al., 2001; Buck, 2004). This suggests that effects of MNS could be as early as the encoding stage of olfactory processing. To confirm this hypothesis, future studies could use a combination of calcium imaging and electrophysiological techniques (Touhara, 2002) or single-cell reverse transcription-polymerase chain reaction techniques (Kajiya et al., 2001) in rodent models and explore if the specific ORs that are expressed under the concentrations of odors in the current study are suppressed after high frequency MNS. NIRS recording of the OFC was performed in the current study as it has been indicated in the existing literature that presentation of olfactory stimuli is represented in this region of the cortex (Ishimaru et al., 2004; Harada et al., 2006; Kobayashi et al., 2012). However, to understand how and what part of the neural olfactory system is affected by MNS (in this particular instance, high frequency MNS), investigations of the full neural circuitry of connections that MNS propagates to before reaching the OFC is necessary. This includes the potential pathways that MNS entails to reach the olfactory regions of the cortex/sub-cortex that is indicated in **Figure 5**. This could be performed in future investigations using magneto encephalography or fMRI, observing the neurocircuitry that is associated with MNS and specific olfactory tests. In particular, it would help address why high frequency MNS only had an effect on specific concentrations of odors in the present study.

The networks that relays the effects of MNS to the olfactory networks is potentially acting through the vagal brainstem nuclei. NTS is a recipient of direct neural inputs from the afferent (sensory) vagus as well as the direct and indirect inputs from the pharyngeal, glossopharyngeal and trigeminal nerves, the spinal tract, the area postrema, the hypothalamus, the cerebellum and vestibular/labyrinthine systems as well as the cerebral cortex, all of which play important roles in regulation of medullary reflexes controlling nausea and vomiting (Babic and Browning, 2014). These shared effects by all corresponding nerves is thought to intersect at the NTS, which is considered a focal point of neuroanatomical intersection center for pathways associated with the peripheral and cranial nerves of the scalp, face, auricular and body (van der Kooy et al., 1984; Ruggiero et al., 2000; Cakmak, 2006). MNS relays to the NTS (Noguchi and Hayashi, 1996; Zhang et al., 2002; Tada et al., 2003; Guan and Wu, 2005; Cakmak, 2006; Imai et al., 2008; Wang et al., 2015) where afferents for locus coeruleus (LC; Chandler et al., 2014) and raphe nucleus (RN) are present (Sawchenko, 1983; Ruggiero et al., 2000; Mello-Carpes and Izquierdo, 2013; Frangos et al., 2015). LC and RN, can innervate the olfactory tubercle (OT) using noradrenergic and serotonergic fibers respectively (Solano-Flores et al., 1980; Guevara-Guzman et al., 1991; Wesson and Wilson, 2011). Both of these structures can project to the OFC, directly or through the OT (Kannan and Yamashita, 1985; Mooney et al., 1987; Ikemoto, 2007; Price, 2010; Wesson and Wilson, 2011; Chandler et al., 2014; Zhou et al., 2015). LC and RN can also be stimulated through an indirect stimulation through the NTS using MNS (**Figure 5**). In addition, MNS could also follow the pathway from the NTS to the insula, which can activate the primary olfactory centers (piriform cortex-PC and entorhinal cortex-EC) and OFC (Mayer, 2011). Therefore, MNS could influence the OT, OFC and OB, *via* the LC, RN and insula (**Figure 5**).

In addition to the neuroanatomical insights, findings from the current study also give practical supports to use MNS as a way to ameliorate nausea symptoms in patients. Drawing evidence from interviews with cancer patients, it has been identified that some strong smells (e.g., shaving cream) and food-related smells (e.g., cooked meat, frying food) can trigger or aggravate nauseas, which aversively impact on patients' food intake (McGreevy et al., 2014; Olver et al., 2014). The current study found that MNS can effectively suppress the intensity perception of three of the four food-related odor compounds. Notably, two of these odorants are generally described by the population as unpleasant (i.e., cheese, mushroom; Ventanas et al., 2010; Mcrae et al., 2013). It is known from the previous literature that OFC is not

only responsible for sensory integration, but also for assigning reward values to sensory stimulus (Rolls et al., 2003). The current finding indicates that the unpleasant odorants may be more susceptible to the modulatory effect of MNS. Although more research is needed to confirm whether MNS has differentiating effects on pleasant and unpleasant odor groups, its noticeable effects on Isovaleric Acid and 1-Octen-3-ol are promising for future investigations in the use of MNS on suppressing nausea-triggering olfactory perceptions. This non-invasive approach can particularly help cancer patients who commonly experience the cluster of symptoms associated with nausea, vomiting and loss of appetite (Guerdoux-Ninot et al., 2016).

The current study has some limitations. In the present study, only acute effects of high- and low frequency MNS were tested and chronic effects of MNS should also be investigated in future studies. The LMS test was selected for testing supra-threshold intensity perception due to its common applications in studying chemical senses. However, the LMS test procedure did not allow to observe odor-specific responses due to the presentation of stimuli without rigorous time controls. Future studies should replicate the current experimental design with different supra-threshold olfactory tests and with the use of a more accurate odor delivery system (such as a neuroimaging-compatible olfactometer). In addition, the use of NIRS techniques in the current experiment measured only the OFC ($VWrSO_2$%). fMRI or magneto encephalography approaches would be useful to clarify the modulation of olfactory networks by MNS. It should also be reiterated that the current study only included healthy male participants. Female participants were excluded from the study because olfactory functioning fluctuates across menstrual cycles, which could introduce biases with the current repeated-measures design. Building on the positive findings from the current study, future studies can examine effects on female cohorts incorporating calibration of menstrual cycles in the experimental design. The last but not the least, the significant results were obtained with the conservative approach of Bonferroni correction in the present study and we also provided the effect size analysis of significant results for future meta-analysis. The effect size analysis indicated low effect size for the significant LMS results and large effect size for the significant NIRS results. It's worth to note that low effect size for significant LMS results which are correlated with large effect size in NIRS (cortical data) do not clarify or indicate a weak or strong behavioral effect of MNS in the present study design. The clinical significance or clinical usability of MNS should be investigated in future studies with behavioral designs.

In conclusion, the present research investigated the potential role of MNS using high and low frequencies on olfactory intensity perception in healthy, adult, male participants, with supplementary exploration of the OFC. The present study indicated for the first time in human research that non-invasive high frequency MNS is able to modulate human olfactory functioning, accompanied by observation of increased activation in bilateral hemispheres of the OFC. Future studies should explore effects of MNS with high- and low frequencies on separate olfactory functioning, such as odor recognition, odor memory and odor identification, in combination with functional neuroimaging techniques, in order to understand the modulatory effect of MNS on specific olfactory-related neural circuitries.

AUTHOR CONTRIBUTIONS

YC: concept idea. YC and MP: project design. AM, YC and MP: performing experiments and data collection statistical analysis and preparation of final manuscript. MP and AM: interpretation of the results. YC and AM: draft manuscript.

FUNDING

This work was supported by the University of Otago, School of Biomedical Sciences, Dean's Bequest Fund.

SUPPLEMENTARY MATERIAL

The Supplementary Material for this article can be found online at: https://www.frontiersin.org/articles/10.3389/fnhum.2018.00533/full#supplementary-material

REFERENCES

Alexander, J. C., Knonenfeld, M. A., and Dance, G. R. (2002). Reduced postoperative length of stay may result from using cerebral oximetry monitoring to guide treatment. *Annu. Thorac. Surg.* 73:s373. doi: 10.1016/s0003-4975(01)03537-8

Andrews, P. L. R. (1992). Physiology of nausea and vomiting. *Br. J. Anaesth.* 69, 2S–19S. doi: 10.1093/bja/69.supplement_1.2S

Babic, T., and Browning, K. N. (2014). The role of vagal neurocircuits in the regulation of nausea and vomiting. *Eur. J. Pharmacol.* 5, 38–47. doi: 10.1016/j.ejphar.2013.08.047

Bai, L., Yan, H., Li, N., Qin, W., Chen, P., Liu, P., et al. (2010). Neural specificity of acupuncture stimulation at pericardium 6: evidence from an fMRI study. *J. Magn. Reson. Imaging* 31, 71–77. doi: 10.1002/jmri.22006

Ballard, C., Jones, E., Gauge, N., Aarsland, D., Nilsen, O. B., Saxby, B. K., et al. (2012). Optimised anaesthesia to reduce post operative cognitive decline (POCD) in older patients undergoing elective surgery, a randomised controlled trial. *PLoS One* 7:e37410. doi: 10.1371/journal.pone.0037410

Blas, M. L., Lobato, E. B., and Martin, T. (1999). Noninvasive infrared spectroscopy as a monitor of retrograde cerebral perfusion during deep hypothermia. *J. Cardiothorac. Vasc. Anesth.* 13, 244–245. doi: 10.1016/s1053-0770(99)90114-3

Buck, L. B. (2004). Olfactory receptors and odor coding in mammals. *Nutr. Rev.* 62, S184–S188. doi: 10.1111/j.1753-4887.2004.tb00097.x

Cakmak, Y. O. (2006). Epilepsy, electroacupuncture and the nucleus of the solitary tract. *Acupunct. Med.* 24, 164–168. doi: 10.1136/aim.24.4.164

Casati, A., Fanelli, G., Pietropaoli, P., Proietti, R., Tufano, R., Danelli, G., et al. (2005). Continuous monitoring of cerebral oxygen saturation in elderly patients undergoing major abdominal surgery minimizes brain exposure to potential hypoxia. *Anaesth. Analg.* 101, 740–747. doi: 10.1213/01.ane.0000166974.96219.cd

Chandler, D. J., Gao, W.-J., and Waterhouse, B. D. (2014). Heterogeneous organization of the locus coeruleus projections to prefrontal and motor cortices. *Proc. Natl. Acad. Sci. U S A* 111, 6816–6821. doi: 10.1073/pnas.1320827111

Chang, X., Yan, J., Yi, S., Lin, Y., and Yang, R. (2001). The affects of acupuncture at sibai and neiting acupoints on gastric peristalsis. *J. Tradit. Chin. Med.* 21, 286–288.

Chen, J. D. Z., Qian, L., Ouyang, H., and Yin, J. (2003). Gastric electrical stimulation with short pulses reduces vomiting but not dysrhythmias

in dogs. *Gastroenterology* 124, 401–409. doi: 10.1053/gast.2003.50048

Cho, H., Nemoto, E. M., Yonas, H., Balzer, J., and Sclabassi, R. J. (1998). Cerebral monitoring by means of oximetry and somatosensory evoked potentials during carotid endarterectomy. *J. Neurosurg.* 89, 533–538. doi: 10.3171/jns.1998.89.4.0533

Choudhury, E. S., Moberg, P., and Doty, R. L. (2003). Influences of age and sex on a microencapsulated odor memory test. *Chem. Senses* 28, 799–805. doi: 10.1093/chemse/bjg072

Classen, C., Howes, D., and Synnott, A. (1994). *Aroma: The Cultural History of Smell* 1st Edn. London: Routledge.

Covidien. (2013). *Operations Manual INVOS System, Model 5100C.* Mansfield, MA: 15 Hampshire Street.

Damian, M. S., and Schlosser, R. (2007). Bilateral near infrared spectroscopy in space-occupying middle cerebral artery stroke. *Neurocrit. Care* 6, 165–173. doi: 10.1007/s12028-007-0010-3

Davis, K. D., Wood, M. L., Crawley, A. P., and Mikulis, D. J. (1995). fMRI of human somatosensory and cingulate cortex during painful electrical nerve stimulation. *Neuroreport* 7, 321–325. doi: 10.1097/00001756-199512000-00077

de Letter, J. A., Sie, T. H., Moll, F. L., Algra, A., Eikelboom, B. C., and Ackerstaff, G. A. (1998). Transcranial cerebral oximetry during carotid endarterectomy: agreement between frontal and lateral probe measurements as compared with an electroencephalogram. *Cardiovasc. Surg.* 6, 373–377. doi: 10.1016/s0967-2109(98)00020-9

Dhond, R. P., Yeh, C., Park, K., Kettner, N., and Napadow, V. (2008). Acupuncture modulates resting state connectivity in default and sensorimotor brain networks. *Pain* 136, 407–418. doi: 10.1016/j.pain.2008.01.011

Diehl, D. L. (1999). Acupuncture for gastrointestinal and hepatobiliary disorders. *J. Altern. Complement. Med.* 5, 27–45. doi: 10.1089/acm.1999.5.27

Doty, R. L. (2003). *The Odor Discrimination/Memory TestTM Administration Manual.* 2nd Edn. Haddon Heights, NJ: Sensonics, Inc.

Doty, R. L., McKeown, D. A., Lee, W. W., and Shaman, P. (1995). A study of the test-retest reliability of 10 olfactory tests. *Chem. Senses* 20, 645–656. doi: 10.1093/chemse/20.6.645

Doty, R. L., Shaman, P., and Dann, M. (1984). Development of the university of pennsylvania smell identification test: a rapid quantitative olfactory function test for the clinic. *Physiol. Behav.* 32, 489–502. doi: 10.1016/0031-9384(84)90269-5

Edmonds, H. L. Jr., Gordon, E. K., and Levy, W. J. (2016). "Central nervous system monitoring," in *Kaplan's Cardiac Anesthesia*, 7th Edn. ed. J. A. Kaplan (Philadelphia: Elsevier Saunders), 466–495.

Edmonds, H. L. Jr., Ganzel, B. L., and Austin, E. H. III. (2004). Cerebral oximetry for cardiac and vascular surgery. *Semin. Cardiotorac. Vasc. Anesth.* 8, 147–166. doi: 10.1177/108925320400800208

Edmonds, H. L. Jr., Isley, M. R., and Balzer, J. (2017). "A guide to central nervous system near-infrared spectroscopic monitoring," in *Neuromonitoring for the Anesthesiologist and Other Health Care Providers*, 2nd Edn. eds. A. Koht, T. B. Sloan and R. Toleikis (New York, NY: Springer), 205–217.

Edmonds, H. L., Singer, I., Sehic, A., and Strickland, T. J. (1998). Multimodality neuromonitoring for neurocardiology. *J. Interv. Cardiol.* 11, 197–204. doi: 10.1111/j.1540-8183.1998.tb00119.x

Ferretti, A., Babiloni, C., Arienzo, D., Del Gratta, C., Rossini, P. M., Tartaro, A., et al. (2007). Cortical brain responses during passive nonpainful median nerve stimulation at low frequencies (0.5–4 Hz): an fMRI study. *Hum. Brain Mapp.* 28, 645–653. doi: 10.1002/hbm.20292

Frangos, E., Ellrich, J., and Komisaruk, B. R. (2015). Non-invasive access to the vagus nerve central projections via electrical stimulation of the external ear: fMRI evidence in humans. *Brain Stimul.* 8, 624–636. doi: 10.1016/j.brs.2014.11.018

Gopinath, S. P., Robertson, C. S., Contant, C. F., Narayan, R. K., Grossman, R. G., and Chance, B. (1995). Early detection of delayed traumatic intracranial hematomas using near-infrared spectroscopy. *J. Neurosurg.* 83, 438–444. doi: 10.3171/jns.1995.83.3.0438

Green, B. G., Dalton, P., Cowart, B., Shaffer, G., Rankin, K., and Higgins, J. (1996). Evaluating the 'labeled magnitude scale' for measuring sensations of taste and smell. *Chem. Senses* 21, 323–334. doi: 10.1093/chemse/21.3.323

Green, B. G., Shaffer, G. S., and Gilmore, M. M. (1993). Derivation and evaluation of a semantic scale of oral sensation magnitude with apparent ratio properties. *Chem. Senses* 18, 683–702. doi: 10.1093/chemse/18.6.683

Guan, Y. H., and Wu, X. P. (2005). The influence of electroacupunturing Neiguan on the content of ET, TXB2, and 6-Keto-PGF1a in acute myocardial ischemia rabbits. *Hu Bei Zhong Yi Xue Yuan Xue Bao* 7, 13–14.

Guerdoux-Ninot, E., Kilgour, R. D., Janiszewski, C., Jarlier, M., Meuric, J., Poirée, B., et al. (2016). Meal context and food preferences in cancer patients: results from a French self-report survey. *Springerplus* 5:810. doi: 10.1186/s40064-016-2538-1

Guevara-Guzman, R., Garcia-Diaz, D. E., Solano-Flores, L. P., Wayner, M. J., and Armstrong, D. L. (1991). Role of the paraventricular nucleus in the projection from the nucleus of the solitary tract to the olfactory bulb. *Brain Res. Bull.* 27, 447–450. doi: 10.1016/0361-9230(91)90140-f

Gyngell, M. L., Bock, C., Schmitz, B., Hoehn-Berlage, M., and Hossmann, K. A. (1996). Variation of functional MRI signal in response to frequency of somatosensory stimulation in α-chloralose anesthetized rats. *Magn. Reson. Med.* 36, 13–15. doi: 10.1002/mrm.1910360104

Harada, H., Tanaka, M., and Kato, T. (2006). Brain olfactory activation measured by near-infrared spectroscopy in humans. *J. Laryngol. Otol.* 120, 638–643. doi: 10.1017/s002221510600123x

Harrer, M., Waldenberger, F. R., Weiss, G., Folkmann, S., Gorlitzer, M., Moidl, R., et al. (2010). Aortic arch surgery using bilateral antegrade selective cerebral perfusion in combination with near-infrared spectroscopy. *Eur. J. Cardiothorac. Surg.* 38, 561–567. doi: 10.1016/j.ejcts.2010.03.016

Higami, T., Kozawa, S., Asada, T., Obo, H., Gan, K., Iwahashi, K., et al. (1999). Retrograde cerebral perfusion versus selective cerebral perfusion as evaluated by cerebral oxygen saturation during aortic arch reconstruction. *Annu. Thorac. Surg.* 67, 1091–1096. doi: 10.1016/s0003-4975(99)00135-6

Hongo, K., Kobayashi, S., Okudera, H., Hokama, M., and Nakagawa, F. (1995). Noninvasive cerebral optical spectroscopy: depth-resolved measurements of cerebral haemodynamics using indocyanine green. *Neurol. Res.* 17, 89–93. doi: 10.1080/01616412.1995.11740293

Hummel, T., Pauli, E., Schüler, P., Kettenmann, B., Stefan, H., and Kobal, G. (1995). Chemosensory event-related potentials in patients with temporal lobe epilepsy. *Epilepsia* 36, 79–85. doi: 10.1111/j.1528-1157.1995.tb01670.x

Ibáñez, V., Deiber, M. P., Sadato, N., Toro, C., Grissom, J., Woods, R. P., et al. (1995). Effects of stimulus rate on regional cerebral blood flow after median nerve stimulation. *Brain* 118, 1339–1351. doi: 10.1093/brain/118.5.1339

Iglesias, I., Murkin, J. W., Bainbridge, D., and Adams, S. (2003). Monitoring cerebral oxygen saturation significantly decreases postoperative length of stay: a prospective randomized blinded study. *Heart Surg. Forum* 6:204.

Ikemoto, S. (2007). Dopamine reward circuitry: two projection systems from the ventral midbrain to the nucleus accumbens-olfactory tubercle complex. *Brain Res. Rev.* 56, 27–78. doi: 10.1016/j.brainresrev.2007.05.004

Imai, K., Ariga, H., Chen, C., Mantyh, C., Pappas, T. N., and Takahashi, T. (2008). Effects of electroacupuncture on gastric motility and heart rate variability in conscious rats. *Auton. Neurosci.* 138, 91–98. doi: 10.1016/j.autneu.2007.11.003

Ishimaru, T., Yata, T., Horikawa, K., and Hatanaka, S. (2004). Near-infrared spectroscopy of the adult human olfactory cortex. *Acta Otolaryngologica. Suppl.* 6489, 95–98. doi: 10.1080/03655230410017751

Janelle, G. M., Mnookin, S., Gravenstein, N., Martin, T. D., and Urdaneta, F. (2002). Unilateral cerebral oxygen desaturation during emergent repair of a DeBakey type 1 aortic dissection: potential aversion of a major catastrophe. *Anesthesiology* 96, 1263–1265. doi: 10.1097/00000542-200205000-00033

Jones-Gotman, M., and Zatorre, R. J. (1993). ORMT in humans. *Brain Cogn.* 22, 182–198.

Kajiya, K., Inaki, K., Tanaka, M., Haga, T., Kataoka, H., and Touhara, K. (2001). Molecular bases of odor discrimination: reconstitution of olfactory receptors that recognize overlapping sets of odorants. *J. Neurosci.* 21, 6018–6025. doi: 10.1523/JNEUROSCI.21-16-06018.2001

Kalva, J. J., Sims, C. A., Puentes, L. A., Snyder, D. J., and Bartoshuk, L. M. (2014). Comparison of the hedonic general labeled magnitude scale with the hedonic 9-point scale. *J. Food Sci.* 79, S239–S245. doi: 10.1111/1750-3841.12342

Kannan, H., and Yamashita, H. (1985). Connections of neurons in the region of the nucleus tractus solitarius with the hypothalamic paraventricular nucleus: their possible involvement in neural control of the cardiovascular system in rats. *Brain Res.* 329, 205–212. doi: 10.1016/0006-8993(85)90526-8

Kobayashi, E., Karaki, M., Touge, T., Deguchi, K., Ikeda, K., Mori, N., et al. (2012). "Olfactory assessment using near-infrared spectroscopy," in *2012 ICME International Conference on Complex Medical Engineering (CME)* (Kobe, Japan: IEEE), 517–520.

Lee, A., and Fan, L. T. Y. (2015). Stimulation of the wrist acupuncture point PC6 postoperative nausea and vomiting. *Cochrane Database Syst. Rev.* 11:CD003281. doi: 10.1002/14651858.CD003281.pub4

Madsen, P. L., Skak, C., Rasmussen, A., and Secher, N. H. (2000). Interference of cerebral near-infrared oximetry in patients with icterus. *Anesth. Analg.* 90, 489–493. doi: 10.1213/00000539-200002000-00046

Maharjan, A., Wang, E., Peng, M., and Cakmak, Y. O. (2018). Improvement of olfactory function with high frequency non-invasive auricular electrostimulation in healthy humans. *Front. Neurosci.* 12:225. doi: 10.3389/fnins.2018.00225

Mayer, E. A. (2011). Gut feelings: the emerging biology of gut-brain communication. *Nat. Rev. Neurosci.* 12, 453–466. doi: 10.1038/nrn3071

McGreevy, J., Orrevall, Y., Belqaid, K., Wismer, W., Tishelman, C., and Bernhardson, B. M. (2014). Characteristics of taste and smell alterations reported by patients after starting treatment for lung Cancer. *Support. Care Cancer* 22, 2635–2644. doi: 10.1007/s00520-014-2215-2

Mcrae, J. F., Jaeger, S. R., Bava, C. M., Beresford, M. K., Hunter, D., Jia, Y., et al. (2013). Report identification of regions associated with variation in sensitivity to food-related odors in the human genome. *Curr. Biol.* 23, 1596–1600. doi: 10.1016/j.cub.2013.07.031

McRobb, C., Walczak, R., Lawson, S., Lodge, E., Lockhart, N., and Bandarenko, I. I. I. R. (2011). Carboxyhemoglobinemia in a pediatric cardiopulmonary bypass patient derived from a contaminated unit of allogenic blood. *Perfusion* 26, 302–307. doi: 10.1177/0267659111406993

Mello-Carpes, P. B., and Izquierdo, I. (2013). The nucleus of the solitary tract→nucleus paragigantocellularis→locus coeruleus→CA1 region of dorsal hippocampus pathway is important for consolidation of object recognition memory. *Neurobiol. Learn. Mem.* 100, 56–63. doi: 10.1016/j.nlm.2012.12.002

Misra, M., Stark, J., Dujovny, M., Wildman, R., and Ausman, J. I. (1998). Transcranial cerebral oximetry in random normal subjects. *Neurol. Res.* 20, 137–141. doi: 10.1080/01616412.1998.11740496

Mooney, K. E., Inokuchi, A., Snow, J. B. Jr., and Kimmelman, C. P. (1987). Projections from the ventral tegmental area to the olfactory tubercle in the rat. *Otolaryngol. Head Neck Surg.* 96, 151–157. doi: 10.1177/019459988709600207

Murkin, J. M., Adams, S. J., Novick, R. J., Quantz, M., Bainbridge, D., Iglesias, I., et al. (2007). Monitoring brain oxygen saturation during coronary bypass surgery: a randomized, prospective study. *Anesth. Analg.* 104, 51–58. doi: 10.1213/01.ane.0000246814.29362.f4

Napadow, V., Dhond, R. P., Kim, J., LaCount, L., Vangel, M., Harris, R. E., et al. (2009). Brain encoding of acupuncture sensation—coupling on-line rating with fMRI. *Neuroimage* 47, 1055–1065. doi: 10.1016/j.neuroimage.2009.05.079

Nihashi, T., Naganawa, S., Sato, C., Kawai, H., Nakamura, T., Fukatsu, H., et al. (2005). Contralateral and ipsilateral responses in primary somatosensory cortex following electrical median nerve stimulation—an fMRI study. *Clin. Neurophysiol.* 116, 842–848. doi: 10.1016/j.clinph.2004.10.011

Noguchi, E., and Hayashi, H. (1996). Increases in gastric acidity in response to EA stimulation of hindlimb of anesthetized rats. *Jpn. J. Physiol.* 46, 53–58. doi: 10.2170/jjphysiol.46.53

Olver, I. N., Eliott, J. A., and Koczwara, B. (2014). A qualitative study investigating chemotherapy-induced nausea as a symptom cluster. *Support. Care Cancer* 22, 2749–2756. doi: 10.1007/s00520-014-2276-2

Oriheula-Espina, F., Leff, D. R., James, D. R. C., Darzi, A. W., and Yang, G. Z. (2010). Quality control and assurance in functional near infrared spectroscopy (fNIRS) experimentation. *Phys. Med. Biol.* 55, 3701–3724. doi: 10.1088/0031-9155/55/13/009

Ouyang, H. U. I., Yin, J., Wang, Z., Pasricha, P. J., Chen, J. D. Z., Yin, J., et al. (2002). Electroacupuncture accelerates gastric emptying in association with changes in vagal activity. *Am. J. Gastroint. Liver Physiol.* 282, 390–396. doi: 10.1152/ajpgi.00272.2001

Prabhune, A., Sehic, A., Spence, P. A., Church, T., and Edmonds, H. L. Jr. (2002). Cerebral oximetry provides early warning of oxygen delivery failure during cardiopulmonary bypass. *J. Cardiothorac. Vasc. Anesth.* 16, 204–206. doi: 10.1053/jcan.2002.31069

Price, J. L. (2010). "Olfactory higher centers anatomy," in *Encyclopedia of Neuroscience*, ed. L. R. Squire (London: Elsevier Ltd), 129–136. doi: 10.1016/B978-008045046-9.01692-2

Puce, A., Constable, T., Luby, M. L., McCarthy, G., Nobre, A. C., Spencer, D. D., et al. (1995). Functional magnetic resonance imaging of sensory and motor cortex: comparison with electrophysiological localization. *J. Neurosurg.* 83, 262–270. doi: 10.3171/jns.1995.83.2.0262

Ren, Y., Bai, L., Feng, Y., Tian, J., and Li, K. (2010). Investigation of acupoint specificity by functional connectivity analysis based on graph theory. *Neurosci. Lett.* 482, 95–100. doi: 10.1016/j.neulet.2010.06.091

Roberts, K. W., Crnkowic, A. P., and Linneman, L. J. (1998). Nearinfrared spectroscopy detects critical cerebral hypoxia during carotid endarterectomy in awake patients. *Anesthesiology* 9:A933. doi: 10.1097/00000542-199809160-00038

Rolls, E. T., Kringelbach, M. L., and de Araujo, I. E. T. (2003). Different representations of pleasant and unpleasant odours in the human brain. *Eur. J. Neurosci.* 18, 695–703. doi: 10.1046/j.1460-9568.2003.02779.x

Ruggiero, D. A., Anwar, S., Kim, J., and Glickstein, S. B. (1998). Visceral afferent pathways to the thalamus and olfactory tubercle: behavioral implications. *Brain Res.* 799, 159–171. doi: 10.1016/s0006-8993(98)00442-9

Ruggiero, D. A., Underwood, M. D., Mann, J. J., Anwar, M., and Arango, V. (2000). The human nucleus of the solitary tract: visceral pathways revealed with an "*in vitro*" postmortem tracing method. *J. Auton. Nerv. Syst.* 79, 181–190. doi: 10.1016/s0165-1838(99)00097-1

Sawchenko, P. E. (1983). Central connections of the sensory and motor nuclei of the vagus nerve. *J. Auton. Nerv. Syst.* 9, 13–26. doi: 10.1016/0165-1838(83)90129-7

Shepherd, G. M. (2006). Smell images and the flavour system in the human brain. *Nature* 444, 316–321. doi: 10.1038/nature05405

Singer, I., Dawn, B., Edmonds, H. Jr., and Stickland, T. J. (1999). Syncope is predicted by neuromonitoring in patients with ICDs. *Pacing Clin. Electrophysiol.* 22, 216–222. doi: 10.1111/j.1540-8159.1999.tb00336.x

Solano-Flores, L. P., Aguilar-Baturoni, H. U., and Guevara-Aguilar, R. (1980). Locus coeruleus influences upon the olfactory tubercle. *Brain Res. Bull.* 5, 383–389. doi: 10.1016/s0361-9230(80)80008-6

Spiegel, J., Tintera, J., Gawehn, J., Stoeter, P., and Treede, R. D. (1999). Functional MRI of human primary somatosensory and motor cortex during median nerve stimulation. *Clin. Neurophysiol.* 110, 47–52. doi: 10.1016/s0168-5597(98)00043-4

Tada, H., Fujita, M., Harris, M., Tatewaki, M., Nakagawa, K., Yamamura, T., et al. (2003). Neural mechanism of acupuncture-induced gastric relaxations in rats. *Dig. Dis. Sci.* 48, 59–68. doi: 10.1023/A:1021730314068

Takahashi, T. (2006). Acupuncture for functional gastrointestinal disorders. *J. Gastroenterol.* 41, 408–417. doi: 10.1007/s00535-006-1773-6

Takahashi, T. (2011). Mechanism of acupuncture on neuromodulation in the gut—a review. *Neuromodulation* 14, 8–12. doi: 10.1111/j.1525-1403.2010.00295.x

Tatewaki, M., Strickland, C., Fukuda, H., Tsuchida, D., Hoshino, E., Pappas, T. N., et al. (2005). Effects of acupuncture on vasopressin-induced emesis in conscious dogs. *Am. J. Physiol. Regul. Integr. Comp. Physiol.* 288, 401–408. doi: 10.1152/ajpregu.00344.2004

Touhara, K. (2002). Odor discrimination by G protein-coupled olfactory receptors. *Microsc. Res. Tech.* 58, 135–141. doi: 10.1002/jemt.10131

Urasaki, E., Wada, S., Yasukouchi, H., and Yokota, A. (1998). Effect of transcutaneous electrical nerve stimulation (TENS) on central nervous system amplification of somatosensory input. *J. Neurol.* 245, 143–148. doi: 10.1007/s004150050194

van der Kooy, D., Koda, L. Y., McGinty, J. F., Gerfen, C. R., and Bloom, F. E. (1984). The organization of projections from the cortex, amygdala, and hypothalamus to the nucleus of the solitary tract in rat. *J. Comp. Neurol.* 224, 1–24. doi: 10.1002/cne.902240102

Ventanas, S., Mustonen, S., Puolanne, E., and Tuorila, H. (2010). Odour and flavour perception in flavoured model systems: influence of sodium chloride, umami compounds and serving temperature. *Food Qual. Prefer.* 21, 453–462. doi: 10.1016/j.foodqual.2009.11.003

Vretzakis, G., Georgopoulou, S., Stamoulis, K., Tassoudis, V., Mikroulis, D., Giannoukas, A., et al. (2013). Monitoring of brain oxygen saturation (INVOS) in a protocol to direct blood transfusions during cardiac surgery: a prospective randomized clinical trial. *J. Cardiothorac. Surg.* 8, 145–154. doi: 10.1186/1749-8090-8-145

Wang, S., Ren, L., Jia, L., Gu, Z., Fan, X., Chen, W., et al. (2015). Effect of acupuncture at Neiguan (PC 6) on cardiac function using echocardiography in myocardial ischemia rats induced by isoproter-enol. *J. Tradit. Chin. Med.* 35, 653–658. doi: 10.1016/s0254-6272(15)30155-2

Wang, Z., Qian, L., Ueno, T., and Chen, J. (2000). Mechanisms of various gastric electrical stimulations. *Gastroenterology* 118: A669. doi: 10.1016/S0016-5085(00)84814-3

Wesson, D. W., and Wilson, D. A. (2011). Sniffing out the contributions of the olfactory tubercle to the sense of smell: hedonics, sensory integration, and more? *Neurosci. Biobehav. Rev.* 35, 655–668. doi: 10.1016/j.neubiorev.2010.08.004

Xu, S., Hou, X., Zha, H., Gao, Z., Chen, Y., and Zhang, J. D. Z. (2006). Electroacupuncture accelerates solid gastric emptying and improves dyspeptic symptoms in patients with functional dyspepsia. *Dig. Dis. Sci.* 51, 2154–2159. doi: 10.1007/s10620-006-9412-x

Yao, F. S. F., Tseng, C. C., Woo, D., Huang, S. W., and Levin, S. K. (2001). Maintaining cerebral oxygen saturation during cardiac surgery decreased neurological complications. *Anesthesiology* 95:A152.

Zatorre, R. J., Jones-Gotman, M., Evans, A. C., and Meyer, E. (1992). Functional localization and lateralization of human olfactory cortex. *Nature* 360, 339–340. doi: 10.1038/360339a0

Zhang, G., Yin, H., Zhou, Y.-L., Han, H.-Y., Wu, Y.-H., Xing, W., et al. (2012). Capturing amplitude changes of low-frequency fluctuations in functional magnetic resonance imaging signal: a pilot acupuncture study on NeiGuan (PC6). *J. Altern. Complement. Med.* 18, 387–393. doi: 10.1089/acm.2010.0205

Zhang, F. B., Zhou, Y. P., Wang, Y. L., and Wang, K. M. (2002). Effect of electroacupuncture on blood free radicals, ET and CGRP contents in rats with acute myocardial ischemia. *Acupunct. Res.* 27, 192–196.

Zhou, J., Jia, C., Feng, Q., Bao, J., and Luo, M. (2015). Prospective coding of dorsal raphe reward signals by the orbitofrontal cortex. *J. Neurosci.* 35, 2717–2730. doi: 10.1523/JNEUROSCI.4017-14.2015

Zotelli, V. L. R., Grillio, C. M., and de Sousa Mda, L. (2014). Nausea control by needling at acupuncture point neiguan (PC6) during an intraoral impression-taking procedure. *J. Acupunct. Meridian Stud.* 7, 318–323. doi: 10.1016/j.jams.2014.04.009

Conflict of Interest Statement: The authors declare that the research was conducted in the absence of any commercial or financial relationships that could be construed as a potential conflict of interest.

Copyright © 2019 Maharjan, Peng and Cakmak. This is an open-access article distributed under the terms of the Creative Commons Attribution License (CC BY). The use, distribution or reproduction in other forums is permitted, provided the original author(s) and the copyright owner(s) are credited and that the original publication in this journal is cited, in accordance with accepted academic practice. No use, distribution or reproduction is permitted which does not comply with these terms.

frontiers in Human Neuroscience

ORIGINAL RESEARCH
published: 02 April 2019
doi: 10.3389/fnhum.2019.00098

Adjustment of Synchronization Stability of Dynamic Brain-Networks Based on Feature Fusion

Haifang Li, Rong Yao, Xiaoluan Xia, Guimei Yin, Hongxia Deng and Pengfei Yang*

College of Information and Computer, Taiyuan University of Technology, Taiyuan, China

When the brain is active, the neural activities of different regions are integrated on various spatial and temporal scales; this is termed the synchronization phenomenon in neurobiological theory. This synchronicity is also the main underlying mechanism for information integration and processing in the brain. Clinical medicine has found that some of the neurological diseases that are difficult to cure have deficiencies or abnormalities in the whole or local integration processes of the brain. By studying the synchronization capabilities of the brain-network, we can intensively describe and characterize both the state of the interactions between brain regions and their differences between people with a mental illness and a set of controls by measuring the rapid changes in brain activity in patients with psychiatric disorders and the strength and integrity of their entire brain network. This is significant for the study of mental illness. Because static brain network connection methods are unable to assess the dynamic interactions within the brain, we introduced the concepts of dynamics and variability in a constructed EEG brain functional network based on dynamic connections, and used it to analyze the variability in the time characteristics of the EEG functional network. We used the spectral features of the brain network to extract its synchronization features and used the synchronization features to describe the process of change and the differences in the brain network's synchronization ability between a group of patients and healthy controls during a working memory task. We propose a method based on the fusion of traditional features and spectral features to achieve an adjustment of the patient's brain network synchronization ability, so that its synchronization ability becomes consistent with that of healthy controls, theoretically achieving the purpose of the treatment of the diseases. Studying the stability of brain network synchronization can provide new insights into the pathogenic mechanism and cure of mental diseases and has a wide range of potential applications.

Keywords: EEG, working memory, EEG dynamic brain network, brain network synchronization stability, brain network synchronization adjustment and control

OPEN ACCESS

Edited by:
Mikhail Lebedev,
Duke University, United States

Reviewed by:
Axel Hutt,
German Weather Service, Germany
Arthur Bikbaev,
Leibniz Institute for Neurobiology (LG), Germany

****Correspondence:***
Haifang Li
lihaifang@tyut.edu.cn

Received: *28 July 2018*
Accepted: *04 March 2019*
Published: *02 April 2019*

Citation:
Li H, Yao R, Xia X, Yin G, Deng H and Yang P (2019) Adjustment of Synchronization Stability of Dynamic Brain-Networks Based on Feature Fusion. Front. Hum. Neurosci. 13:98. doi: 10.3389/fnhum.2019.00098

INTRODUCTION

The brain is a complex system that exhibits various subsystems on different spatial and temporal scales. These subsystems are recurrent networks, that is, very large clusters of neurons that repeatedly interact with each other. Individual neurons are microscopic and change at a different time rate than macroscopic neural populations. After Babloyantz et al. (1986) first used nonlinear

dynamics theory to study EEG signals in 1985, research on EEG signals rapidly entered the era of nonlinear dynamics. Various theories and methods of nonlinear dynamics have opened up new possibilities for analyzing EEG data. Eliasmith et al. (2012) presented a 2.5 million neuron model of the brain (called "Spaun") that bridged this gap by exhibiting many different behaviors. The model is presented by only visual image sequences, and it draws all its responses with a physically modeled arm. Although simplified, the model captures many aspects of neuroanatomy, neurophysiology, and psychological behavior.

Hutt (2010) studied the main characteristics of a single neuron and its interactions by establishing a standard mathematical model and applied the model to explain experimental results from the delayed feedback system of weak electric fish and from electroencephalography (EEG). Liley et al. (2002) used nonlinear differential equations based on the human brain's physiological structure and medical anatomy to define a mathematical model of brain neuron clusters in states of both excitement and inhibition. With the establishment of neuron models, neuroscientists have conducted extensive and in-depth studies on neural network dynamics using various neuronal models to try to reveal the hidden secrets of the brain (Stam et al., 2007; Liu et al., 2008, 2014; De Han et al., 2009; Sun et al., 2009; Bartolomei et al., 2010; Skidmore et al., 2011).

Currently, many studies (Zhao et al., 2008; Qun, 2009; Gao et al., 2014b; Ruizhen et al., 2017) have shown that when the brain is active, the neural activities of different regions are integrated on a variety of spatial and temporal scales; this is known as the synchronization phenomenon in neurobiological theory. Synchronization is the basic mechanism for information integration and processing. Clinical medicine studies have shown that some of the neurological diseases that are difficult to cure have deficiencies or abnormalities in the whole or local integration process of the brain. Scientists have discovered a variety of synchronous behaviors in the neuronal system. The results of these studies show that the synchronization behavior of neuronal firing not only affects daily learning, brain memory, calculation, and motor control but can also be used to explain some neurological diseases such as epilepsy and Parkinson's disease.

The human brain is a complex network. Synchronization capability is an important indicator of complex networks. Therefore, brain network synchronization research has gradually attracted the attention of brain scientists and has made great advances. For example, Ma et al. (2014) and Hongli et al. (2013) found that the synchronization of the brain network of Alzheimer's patients was lower than that of a control group. Hou et al. (Dong et al., 2014; Feng-Zhen et al., 2014) analyzed the brain network of epilepsy patients using the network connectivity index to understand whether the brain network of patients with epilepsy is different from a normal brain network, and also investigated the brain electrical signal synchronization of patients with cerebral infarction. Rosário et al. (2015) proposed a new brain network edge association method that involves motif synchronization, primarily by calculating the number of occurrences of certain patterns between any two time-series to provide information about the degree and direction of synchronization between two nodes in the network. Sakkalis et al. (2013) used amplitude square coherence, phase synchronization estimation, and robust nonlinear state space generalized synchronization assessment methods to calculate the synchrony between all the pairs of channels in alcohol addiction patients. The experimental results showed that, during a rehearsal procedure, the alcohol addiction patients showed a loss of synchrony and an impaired lateralization of the brain activity.

Although previous studies have used synchrony to study neurodegenerative diseases, most of the current studies about the differences in brain function between patients with mental disorders and normal subjects investigated traditional features of brain network properties (node degree, mean-clustering-coefficient, global-efficiency, small-world attributes, etc.) (Micheloyannis et al., 2006; Zhang et al., 2013a,b, 2015; Müller et al., 2018). Researching these traditional features can clearly aid in understanding the topological characteristics of the brain network, but these features do not fully reflect the structure of the brain network. As a result, clinicians cannot find a unique and effective index for determining the specific diagnosis that a subject should receive. The spectral properties of complex networks (Li and Zhang, 1997; Xiao, 2012; Sato and Iwai, 2014; Liu and Shen, 2017) can provide a comprehensive measure of the global structure of the network. Any change in a local attribute feature is reflected in changes in the spectrum.

Therefore, to find more significant indicators of the differences between mental patients and healthy controls, we built a brain network based on complex network theory, used the spectral features of the brain network to identify the synchronization characteristics, and used the synchronous features to characterize the patients and the healthy controls. Thus, we studied the process by which the brain's synchronization ability changed during the working memory process and its difference between the two groups. We also proposed a method based on fusing traditional features and spectral features to adjust the synchronization ability of the brain networks of patients so that their synchronization ability will be consistent with those of healthy controls. Theoretically we can achieve the goal of treating diseases. Studying brain network synchronization can help to more clearly explain the dynamic process of the collective behavior of a large number of nodes in a complex brain network and may be able to prevent the harm that comes from some types of synchronizations. Thus, this research may provide a new direction for studying the pathological mechanisms of brain diseases. The brain network mechanisms of healthy controls and patients have very important practical significance and academic value.

The paper is organized as follows: Section EEG Dataset Description and Preprocessing briefly describes the dataset of EEG signals employed in our research. Section Methods presents information about the methods used in this study, including constructing the brain-network, extracting synchronization features, and synchronizing optimization algorithms. Section Experimental Results and Analysis provides the experiments undertaken in the framework of the study, the experimental procedures used, and the experimental results obtained. Finally, section Limitations describes the conclusions derived from the study and some thoughts, with regard to future work.

EEG DATASET DESCRIPTION AND PREPROCESSING

EEG Dataset Description

The dataset used in this work was task state EEG data. The experimental paradigm used the modified Sternberg's SMST (Manoach et al., 1999) (short-term memory scanning task) paradigm (see **Figure 1**) The dataset included 34 psychiatric (in this study we used schizophrenic) patients and 34 healthy people (controls), none of whom had any record of drug abuse or diagnosis of neuropsychiatric disease in the past 6 months. The age range of the patient group was 20–51 years old, and the average age was (40.1 ± 11.1) years old; the healthy control group age range was 21–58 years old, and the average age was (37.1 ± 13.8) years old. Age, sex, and education level did not differ significantly between the two groups. All the members of both groups had normal vision or corrected visual acuity, had no color disturbance, and were right-handed (Zhao et al., 2011).

Data Preprocessing

Data collection was completed at a hospital psychiatry research center on a NeuroScan 64-lead EEG acquisition device. The sampling frequency was 500 Hz, the impedance was kept below 5 kΩ, the ground electrode was AFz, and the reference electrode was physically connected to the left and right mastoids. The vertical electro-oculogram recording was from electrodes placed above and below the left eye, and the horizontal electro-oculogram recording was from electrodes placed on the right eyelid margin (Stam et al., 2007).

The preprocessing was performed on the EEGLab (https://sccn.ucsd.edu/eeglab/download.php) platform on Matlab, which converted the reference data of the original data, removing the electrooculogram, filtering, segmenting, and removing artifacts to yield noiseless and clean EEG data. An average reference electrode was selected as the reference electrode, and the low-pass and high-pass noise were removed by filtering in the range of 0.5–50 Hz. The ocular electrical artifacts in the data were removed using the negative entropy-based FastICA method (Joyce et al., 2010; Jiaqing et al., 2018). Compared with the traditional blind source separation algorithm, this method does not require the ocular electrical signal as the reference electrode, avoiding the mixing of new noise during the EE signal acquisition process and reducing the collection workload. In addition, volume conduction can affect the output of synchronization measures when using EEG signals, because EEG is bipolar by nature. This means that EEG signals are composed of a difference between an electrode of interest and a reference (Guevara et al., 2005; Peraza et al., 2012). We used surface Laplacian transform methods (Matlab toolbox CSD) (Kayser and Tenke, 2006a,b) to eliminate the mixing effect of volume conduction. During the data acquisition process the data were labeled as S1–S10, in which S1–S5 represented the encoding phases, S6–S8 represented the maintenance phases, and S9–S10 represented the retrieval phases (see **Figure 2**). The data were filtered and retained by θ (4–7 Hz), α (7–14 Hz), β1 (14–20 Hz), β2 (for 20–30 Hz), and γ (30–40 Hz) signals in five frequency bands. From these data, 20 segments were selected from the different frequency bands in the different stages, and each was spliced. Duration of the EEG trajectory in the encoding, maintenance, and retrieval phases were 100 s, 60 s, and 50 s, respectively.

METHODS

Unweighted Complex Dynamic Brain-Networks Construction

In the experiment, 60 scalp electrode channels were selected as the nodes of the brain network. The phase-locking value (PLV) coherence function was chosen for the edges of the network. This function was used to calculate the correlation between two electrode channels to form a 60 × 60 PLV correlation matrix. PLV can separate phase and amplitude components. Because EEG data can be affected by transient amplitude changes such as eye movements, PLV is quite suitable for this data. This paper uses a wavelet transform to extract phase information. The short time Fourier transform (STFT) method uses a sliding window to intercept the signal and performs a Fourier transform on the signal in the window to obtain the spectrum formula of the signal at any time (1), where STFT of *f(t)*: computed for each window centered at $t = t'$; t' is the time parameter; μ is the frequency parameter; *f(t)* is the signal to be analyzed; $W(t - t')$ is the windowing function.

$$STFT(t', \mu) = \int f(t)\, W(t - t') e^{-j2\pi\mu t} dt \tag{1}$$

Specifically, the PLV definition (Xu et al., 2014) is Equation (2), where N represents the number of brain network nodes (In

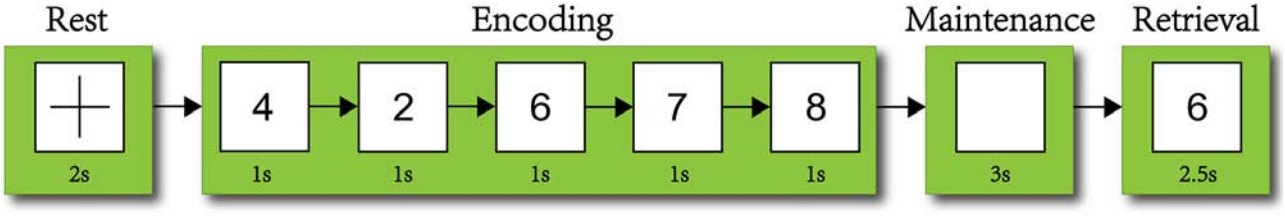


FIGURE 1 | Short-term memory scanning task (SMTS) paradigm. Subjects needed to remember the numbers appearing on the screen during the encoding stage and recall these during the maintenance stage. Finally, in the retrieval stage, the subjects were required to determine whether the number had appeared by searching their memory.

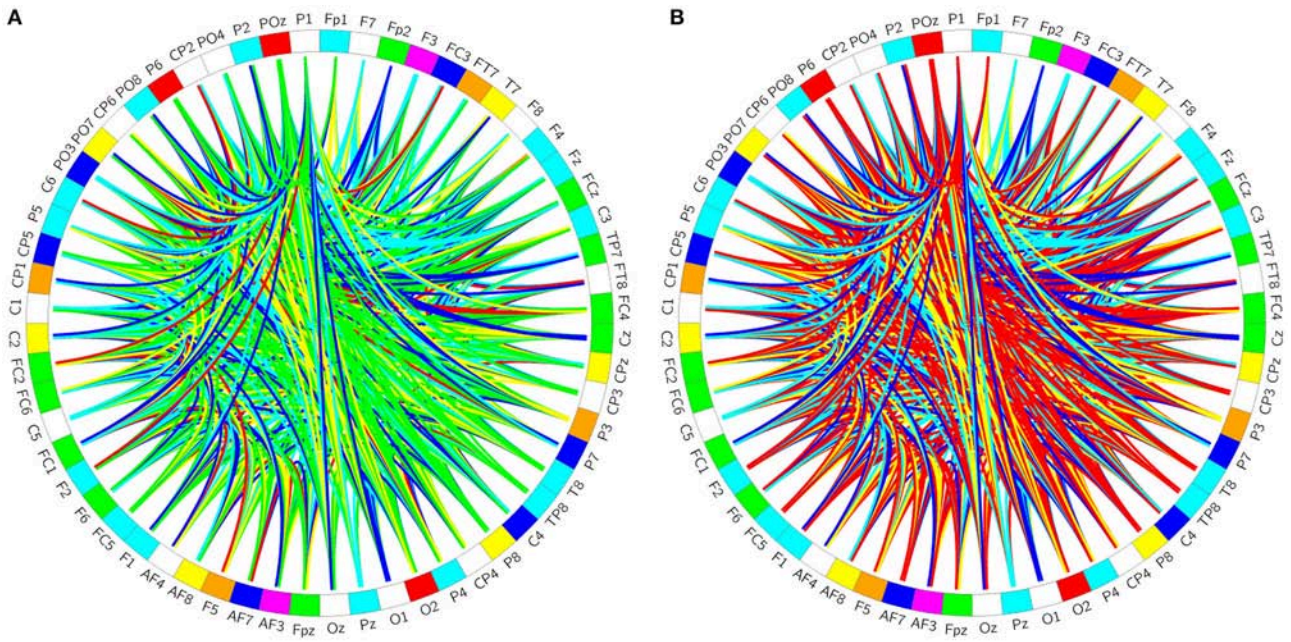


FIGURE 2 | Brain-network. **(A)** Represents the healthy controls, **(B)** represents the patients.

this paper $N = 60$); $\Delta\ \varphi_n(t) = \varphi_x(t) - \varphi_y(t)$ represents the phase difference between the two channel time-frequency points t; and PLV ϵ [0,1].

$$PLV\ (t) = \frac{1}{N}\left|\sum_{n=1}^{N} exp(j(\triangle\Phi_n(t)))\right| \tag{2}$$

The study of dynamic functional networks or time-varying brain function networks is an emerging field in brain function connection research. Its purpose is to study the dynamic nature or variability of functional connections over time. It has been applied to the analysis and diagnosis of brain diseases in fMRI and has in EEG signal analysis. Common methods for studying time-varying functional connections include important transfer point detection, time-frequency decomposition methods, and time window methods (Rosário et al., 2015). Of these, the sliding time window method is currently the most widely used. Existing research found that the brain network clearly shows time-variability and dynamics even over a short period of time and that the size of the time window is related to changes in the topological properties of the brain network (Sakkalis et al., 2013). The time window selected for the PLV cannot be too large. If it is too large, the signal may not be reasonably stable during this time period. Therefore, referring to existing research in a PLV phase synchronicity measurement study (Yi et al., 2014) and existing related research (Gysels and Celka, 2004; Gao et al., 2014a; Bola et al., 2015), we selected a sliding time window (step size of 0.04 s) in the range of 0.04–0.48 s. To determine the size of the PLV sliding time window, the classification accuracy of the network attributes was calculated within a given range of 0.04–0.48 s. The classification accuracy between the groups was determined. The final time window was determined to be 0.12 s.

The experiment was related to previous research on the small-world characteristics of the human brain (Guo et al., 2013). The sparsity range chosen was 30 to 40% with a step size of 2%; the network was constructed separately for each of the 20 trials. The networks for the 34 patients and 34 healthy controls were constructed separately for the encoding, maintenance, and retrieval stages and for the alpha and theta bands. A total of 48,960 brain networks were constructed.

Brain-Network Feature Extraction

The traditional features of brain networks are usually attributes of the network and include global attributes and local attributes (Guo et al., 2013). Our experiment calculated four local attributes, which were degree, inference, clustering coefficient, and local efficiency, and six global attributes, which were global efficiency, modularity index, positive and negative matching degree, feature path length, average clustering coefficient, and average local efficiency. The feature extraction in this research included two stages: The first stage extracted the distinctive features from the traditional features; the second stage extracted the features of the brain network spectrum; and spectral feature calculations provided the synchronization features.

The first stage:

A. Extraction of significant differences from global features

We compared the global attribute values between the patient group and the healthy controls in the same frequency band and at the same sparsity in the same stage. We used the Kolmogorov-Smirnov (KS) test ($P < 0.05$) to indicate that the node difference

between the patients' brain networks and those of the healthy controls was significant. A significant difference attribute was put into a support vector machine (SVM) classifier as a feature. Based on an analysis of the classification result, a global attribute with a significant difference at a specific stage and a specific frequency band was selected.

B. Extraction of significant differences and nodes from local attributes

To characterize the overall level of a property Y over a given sparsity range (Guo et al., 2013; Hao, 2013), these two papers from our research group used the area under the curve (AUC) to characterize the value of the entire sparsity range Y^{AUC} in the selected sparsity range. Its definition is shown in formula (3), where ΔS represents the space between the sparse upper bound Sn and the lower bound S1 span, which is the step size for the change in sparseness. In this study, the upper bound Sn was 40%, the next S1 was 30%, and the step size ΔS was 2%.

$$Y^{AUC} = \sum_{k=1}^{n-1} [Y(S_k) + Y(S_{k-1})] \times \Delta S/2 \quad (3)$$

In our current experiment, the sparsity range was fused by calculating the AUC. Throughout the entire sparsity range, we identified the nodes that had significant differences between the patients and the healthy controls. We tested the AUC value of each subject's local attribute value in the sparsity range at a certain stage and a certain frequency band. Then, we selected the local attribute AUC value splicing of the significant difference node as a feature to classify, and obtained locally significant attributes and significant nodes that differed significantly between the patients and healthy controls.

The second stage extracted the brain network spectrum characteristics and calculated the brain network synchronization characteristics according to section Synchronization Criteria. The spectral features of a network generally refer to the set of all the eigenvalues of the Laplacian matrix.

Synchronization Criteria

Network synchronization is a very common and important nonlinear phenomenon. There are many different types of network synchronization, such as common constant synchronization, phase synchronization, generalized synchronization, etc. Identical synchronization is defined as:

Definition 1:

Let $x_i(t, X_0)$ be a solution of the complex dynamic network

$$\dot{x} = f(x_i) + g_i(x_1, x_2, x_3, \ldots x_N), \quad i = 1, 2, \ldots, N \quad (4)$$

where $X_0 = \left(\left(x_1^0\right)^T, \left(x_2^0\right)^T, \ldots, \left(x_N^0\right)^T,\right)^T \in R^{N^*N}$, $f: D \to R^n$ and $g_i: D \times D \to R^n (i = 1, 2, \ldots, N)$ are all continuously differentiable , $D \subseteq R^n$,and meet $g(x_1, x_2, \ldots, x_n) = 0$. There is any non-empty open set $C \subseteq F$ in the domain, which can make any $x_i(t, X_0) \in F$ and

$$\lim_{t\to\infty} \|x_i(t, X_0) - s_i(t, X_0)\| = 0 \; i = 1, 2, \ldots, N$$

for any $x_i^0 \in C, i = 1, 2, \ldots, N$ and $t \geq 0, i = 1, 2, \ldots, N$, where $s_i(t, X_0)$ is an effective solution space of equation $\dot{x} = f(x)$, and $X_0 \in F$, then the complex dynamics network can reach the identity synchronous steady state, and $C \times \ldots \times C$ is called the synchronous area of the complex dynamic network.

Identical synchronization is a common phenomenon of network synchronization, which shows that all nodes in the network are in the same state at a particular time point. In Definition 1, $s(t, X_0)$ is the synchronous steady state of the network, and $x_1 = x_2 = \ldots = x_N$ is the synchronization manifold of the network state space; that is, each physical oscillator tends to be in a described state when a network is synchronized.

Definition 2:

In 1998, Pecora and Carroll (Pecora and Carroll, 1990; Kashtan and Alon, 2005) studied the stability of the synchronization of linear coupled networks and developed the main stability function discrimination method. In 2002, Wang and Chen (Lü and Guanrong, 2005; Jin-Hu, 2010; Gao et al., 2014b; Zhou et al., 2014) studied the problem of the synchronization stability of coupled oscillators in a continuous system and proposed a dynamic network consisting of N identical vibrators whose dynamic equation is:

$$\dot{x_i} = f(x_i) - c\sum_{j=1}^{N} l_{ij} H(x_j) \quad , i = 1, 2, \ldots\ldots N \quad (5)$$

where $x_i = (x_{i1}, x_{i2}, \ldots, x_{in})^T \in R^N$ are the node's state variable; $\mathbf{x_i} = \mathbf{f(x_i)}$ describes the state of a single node when there is no coupling; c is the strength of the brain network coupling that has been constructed; H is a node state variable indicating which variables are passed between the coupled nodes; **L** is the Laplacian matrix of the brain network; $\mathbf{l_{ij}}$ is the matrix element of L and contains the information of the network topology.

When the coupling matrix is a Laplacian matrix:If L is a positive semidefinite symmetric matrix and the row sum is 0, then the eigenvalue of L satisfies the following when the network remains connected:

①matrix L has only one eigenvalue with a multiplicity of 1 and its corresponding eigenvector is

$(1,1,1,1 \ldots \ldots 1)^T$

②The remaining N-1 eigenvalues of the matrix L are positive real numbers, that is: $0 = \lambda 1 < \lambda 2 \leq \lambda 3 \leq \lambda 4 \leq \ldots\ldots\ldots \leq \lambda N$。

Definition 3:

When the coupling matrix L satisfies Definition 2, the synchronization ability of the network can be expressed by the spectral features of the coupling matrix L. According to the different situations of the synchronization area, a dynamic network (Definition 2) can be divided into two categories. One (type 1) is that the synchronization field of the network is semi-unbounded, and its synchronization ability passes through the minimum non-zero spectral feature λ2 of the corresponding Laplacian matrix L. The larger the value of λ2, the stronger the synchronization ability. The other type (type 2) is that the synchronization domain of the network is bounded, and

its synchronization capability can be characterized by the ratio R of the maximum non-zero spectral characteristics of the corresponding Laplacian matrix L to the smallest non-zero spectral features. The smaller the value of R, the stronger the synchronization capability.

Note:

$$R = \lambda N/\lambda 2 \tag{6}$$

Proof:

Construct a brain network of experimental datasets and compute the spectral features of the L-matrix. The experimental results shown in **Figure 3** show that the spectral features of the brain network were all positive. The data verification used in this paper satisfies the synchronization criterion condition type 2. That is, the synchronization ability of the network can be measured by calculating the parameter R.

Defining the Coupling Formula L*

Currently, the adjustment of the synchronization capability of complex network power systems (Wigand et al., 2015; Hongyue et al., 2017; Ruizhen et al., 2017) is mainly based on the network topology, adaptive synchronization control of dynamic equations, and network coupling methods. Considering the particularity of a brain network in the practical application process, that is, that the brain network structure is not easy to change and that the dynamic system is more complex and difficult to control, we here propose a method based on the fusion of traditional features and spectral features to achieve the ability of brain network synchronization for patients. In theory, adjusting a disease brain network so that it is synchronized with that of normal people could be a way to treat the disease.

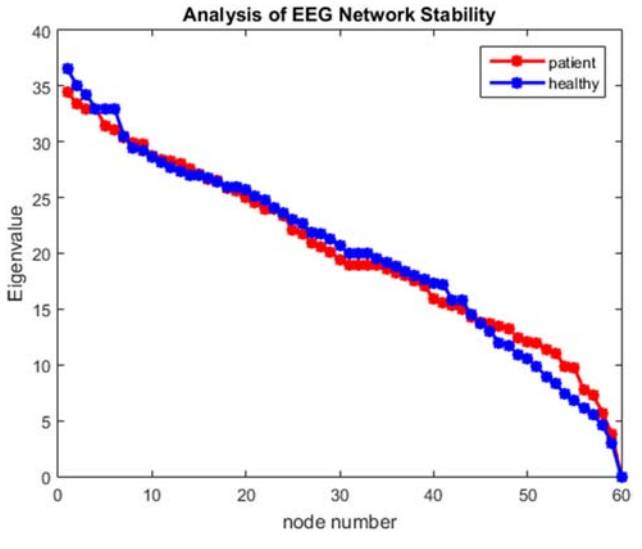


FIGURE 3 | EEG Working memory data Laplacian eigenvalue spectrum (descending order) diagram.

The definition of the T&S(Traditional and Spectral)coupling matrix $\mathbf{L}^*$equationis:

$$L^* = L * G \tag{7}$$

where matrix L is the original Laplacian matrix of the complex network dynamics equation, which represents the network spectrum characteristics. Matrix G is the distinctive feature of the extracted brain network.

Formula (7) can be written as formula (8):

$$l_{ij}^* = l_{ij}^* g_i^{aa} * g_j^{bb} \tag{8}$$

Where ∀ aa, bbϵ R, we can adjust the parameters aa, bb to enhance or weaken the synchronization ability of the network. The combinations of parameters aa, bb are: ① parameters aa, bb are both positive; ② parameters aa, bb are one positive and one negative; ③ parameters aa, bb are both negative.

Define the T&S coupling matrix $\mathbf{L}^*$ [Equation (7)], If the T&S coupling matrix $\mathbf{L}^*$ satisfies definition 3 of section Synchronization Criteria,

which is:

$\mathbf{L}^*$ is a positive semidefinite symmetric matrix;

$\mathbf{L}^*$ line sum is 0;

Then the synchronization capability of the brain network is the ratio R of the spectral features of the T&S coupling matrix $\mathbf{L}^*$.

Mathematical proof:

① If the matrix $\mathbf{L}^*$ is a real symmetric matrix know all eigenvalues of $\mathbf{L}^*$ are real numbers;

② If the matrix $\mathbf{L}^*$ is a positive semi-definite matrix know all eigenvalues of $\mathbf{L}^*$ are positive or 0;

③The following only proves that the matrix $\mathbf{L}^*$ satisfies the row sum to 0;

Proof:

Write formula (7) as a matrix:

$$L^* = L * G^{aa} * G^{bb} \tag{9}$$

Where

$G = diag\{k_1, k_2 \ldots . k_N\}$ is a diagonal matrix composed of a distinctive feature of the brain network.

TABLE 1 | Extracted nodes that showed differences in encoding/alpha/sparsity 34%.

ELECTRODE NUMBER—ELECTRODE NAME		
59-POZ	3-FP2	51-PO3
58-P2	60-P1	29-Pz
36-AF4	57-PO4	31-FPz
16-Cz	22-TP8	17-CPz
15-FC4	27-O2	28-O1
35-AF8	43-FC6	5-FC3
9-F4	10-Fz	11-FCz
13-TP7	14-FT8	32-AF3

TABLE 2 | The average Pearson correlation coefficient for the 10 healthy controls.

Normal/Encoding/Alpha	NO.1	NO.2	NO.3	NO.4	NO.5	NO.6	NO.7	NO.8	NO.9	NO.10	AVE
Assortativity	0.59	0.20	0.57	0.237	0.571	0.059	0.602	0.326	0.549	0.152	0.385
Mean-Clustering-Coef	**0.79**	**0.531**	**0.567**	**0.259**	**0.697**	**0.834**	**0.824**	**0.595**	**0.718**	**0.588**	**0.6105**
Transitivity	**0.82**	**0.546**	**0.566**	**0.595**	**0.701**	**0.703**	**0.653**	**0.666**	**0.544**	**0.795**	**0.6588**
Global-Efficiency	**−0.769**	**−0.430**	**−0.554**	**−0.708**	**−0.718**	**−0.787**	**−0.787**	**−0.572**	**−0.892**	**−0.852**	**−0.7069**
Modularity	−0.234	0.163	−0.378	−0.337	0.369	0.063	0.549	−0.405	0.114	−0.484	−0.0579
Mean-Path-Length	**0.774**	**0.530**	**0.754**	**0.717**	**0.709**	**0.797**	**0.789**	**0.633**	**0.899**	**0.906**	**0.774**

Bold indicates that the conclusion is drawn from the bold part.

The sum of all elements in the i-th row of matrix L^* is:

$$L_J{}^* = \sum_{i=1,j\neq i}^{N} L_{ij} g_i^{aa} * g_j^{bb} = \left(\sum_{i=1,j\neq i}^{N} L_{ij} g_i^{aa}\right) * g_j^{bb}$$
$$= \left(\sum_{i=1,j\neq i}^{N} L_{ij} g_i^{aa} - \left(\sum_{i=1,i\neq j}^{N} L_{ij} g_j^{-aa} g_i^{aa} g_j^{aa}\right)\right) * g_j^{bb}$$
$$= \sum_{i=1,i\neq j}^{N} L_{ij} g_i^{aa} g_j^{bb} - \sum_{i=1,i\neq j}^{N} L_{ij} g_i^{aa} g_j^{bb} = 0 \quad (10)$$

Through mathematics and experiments (**Figure 3**) prove: When the network remains connected, the spectral features of $\mathbf{L}^*$satisfy: (1) The matrix $\mathbf{L}^*$has only one eigenvalue with a multiplier of 1 and its corresponding eigenvector (1,1,1,1, … … 1)^T; (2) The remaining N-1 eigenvalues of the matrix $\mathbf{L}^*$are positive real numbers, that is: $0 = \lambda 1 < \lambda 2 \leq \lambda 3 \leq \lambda 4 \leq \ldots\ldots\ldots \leq \lambda N$.

EXPERIMENTAL RESULTS AND ANALYSIS

Experiment 1:Brain-Network Significant Difference Features and Node Extraction

Experiment 1 investigated the encoding stage.

①Using the method of feature extraction described in section Brain-Network Feature Extraction, the distinctive features obtained in the first stage extraction included: assortativity (depending on the trend of nodes in the network, it can be divided into an assortative or disassortative network. Assortative means that a node tends to be connected to its similar node; otherwise, the network is said to be disassortative), mean-clustering-coefficient, transitivity (transitivity is the ratio of "triangles to triplets" in the network), global efficiency, modulus, and mean path length (in the current study, we reanalyzed EEG data from our previous publications Liting et al., 2017; Yuchi et al., 2017).

②We calculated the Pearson correlation coefficient of the features extracted from the first stage and the second stage and identified the features that were strongly correlated. We randomly selected 10 normal subjects and 10 patients with 7 significant differences in characteristics and used their network spectral characteristics (R) to calculate the Pearson correlation coefficients (**Tables 2**, **3**). **Table 1** shows the nodes that differed significantly between the patient and healthy controls, as identified using the KS test.

Tables 2, **3** show that there was a strong positive correlation between the synchronization of the brain network and the mean-clustering-coefficient, transitivity, mean path length, and node degree and that there was a strong negative correlation with global efficiency.

The criteria for evaluating the Pearson correlation coefficient are: (1) 0.8–1.0 means that the two are highly correlated; (2) 0.6–0.8 means that the two are significantly correlated; (3) 0.4–0.6 means that the two are mildly correlated (4) 0.2–0.4 means that the two are weakly related; (5) 0.0–0.2 means that the two are very weakly related.

Experiment 2:Brain-Network Synchronization Stability Analysis

Differences in Synchronous Processing

In this process, 20 brain networks were constructed for each subject's 20 trial EEG signals and were used to extract the synchronization features (R) of the brain network's spectral features. The patients and healthy controls could be represented by their synchronization features and by the time required to reach the initial synchronization. The process by which brain synchronization occurs during memory processing differs between healthy subjects and patients. **Table 4** is the range of changes in the mean values of the synchronization characteristics for the 34 patients and 34 healthy controls in the encoding, maintenance, and retrieval stages; **Figure 4** is the initial synchronization of the time chart for the 10 patients and 10 healthy controls who were randomly selected during the encoding, maintenance, and retrieval stages; **Table 5** shows the mean and variance at the initial synchronization in **Figure 4**.

Table 4 shows that there was a significant difference in the synchronization between the patients and the healthy controls in the encoding phase and that the patient's synchronization ability was stronger than that of the normal subjects. This may be because patients have cognitive impairments in memory and their thinking and speech are often confused. Therefore, they showed considerable differences from the healthy controls in the encoding phase of working memory. An analysis of **Table 5** shows that the normal subjects achieved synchronization earlier than the patients.

Determining Significant Differences in the Synchronization Stability of Area S

A. Discovering-significant-differences-in-area-s

The PLV binary matrix corresponding to 48,960 brain networks constructed using data from the patients and the healthy controls is shown in **Figures 5A–C** shows the difference significant area, S, a mathematical representation of the difference between

TABLE 3 | The average Pearson correlation coefficient for the 10 patients' group.

Patient/Encoding/Alpha	NO.1	NO.2	NO.3	NO.4	NO.5	NO.6	NO.7	NO.8	NO.9	NO.10	AVE
Assortativity	0.25	0.32	0.29	0.275	0.683	0.847	0.314	0.383	0.545	0.604	0.4522
Mean-Clustering-Coef	**0.59**	**0.814**	**0.683**	**0.745**	**0.773**	**0.818**	**0.844**	**0.819**	**0.545**	**0.668**	**0.730**
Transitivity	**0.57**	**0.667**	**0.581**	**0.551**	**0.774**	**0.804**	**0.851**	**0.823**	**0.716**	**0.703**	**0.65883**
Global-Efficiency	**−0.735**	**−0.801**	**−0.530**	**−0.582**	**−0.804**	**−0.898**	**−0.841**	**−0.830**	**−0.885**	**−0.829**	**−0.7736**
Modularity	−0.285	0.092	−0.379	−0.119	−0.154	−0.062	−0.551	0.486	−0.150	−0.174	−0.1295
Mean-Path-Length	**0.667**	**0.802**	**0.635**	**0.709**	**0.804**	**0.797**	**0.848**	**0.839**	**0.902**	**0.826**	**0.667**

Bold indicates that the conclusion is drawn from the bold part.

TABLE 4 | Comparison of synchronization differences between healthy controls and patients.

NORMAL GROUP AND PATIENT GROUP R-MEAN		
	Normal	**Patient**
Encoding	**5–19**	**5–8**
Maintenance	5–13	5–8
Retrieval	5–8	5–8

Bold indicates that the conclusion is drawn from the bold part.

5a and 5b; **Figure 5D** is a brain electrode position diagram corresponding to a 5c S region in the brain map.

Comparing the differences (**Figures 5A,B**) we found that the significant differences in the brain network between normal subjects and patients were located in the S region (**Figure 5C**). The specific manifestations were as follows: The normal controls' S-area connections were tightly organized and the patients' S-area connections were sparsely disordered. This is likely because psychiatric (specifically schizophrenic in this study) patients have cognitive impairments in memory, and their thinking and speech are often confused. Therefore, in memory processing, the connections between the brain regions of the brains of the psychiatric patients were disorganized, but the brain connections of the normal controls showed obvious signs of organization.

From the above analysis, we concluded that the area that was significantly different between the patients and the healthy controls was region S, so the corresponding brain area was primarily located in the occipital lobe.

B. Regional-s-synchronization-stability-analysis

Using the information about the significant difference node (**Table 1**) extracted in Experiment1: Brain-Network Significant Difference Features and Node Extraction the coupling between a certain node in the brain network and the other nodes was removed, and the synchronous characteristics R of brain networks that were randomly selected from the patients and healthy controls (if the other subject conditions were kept constant) were the same. The subjects were compared based on the order of magnitude (**Figure 6**). In **Figure 6**, the abscissa represents the decoupling node number (the electrode corresponding to the node number in **Table 6**), and the ordinate represents the synchronization eigenvalue of the brain network after decoupling.

Figure 6 shows that, in the encoding stage, when node numbers 59, 3, 51, 58, 60, ..., 9, 10, 11 were successively removed, the trends of the patients and the healthy controls in the **Figure 6A** were similar to those in **Figure 6B**. Particularly when the node numbers 16, 22, 17, 15, 27, 28 were sequentially removed, the synchronicity between the patient and the normal person increased. In addition, the node numbers 16, 22, 17, 15, 27, 28 all belong to the red area S, and the ability to remove these nodes one at a time was enhanced. The data shown in **Figure 6** also indicate that, as the density of the red zone S edge decreased, the synchronization ability was stronger, and as the edge density increased, the worse the synchronization ability became (**Figures 5A,B** as healthy controls).

Without changing the coupling relationship of the red region S (**Figure 5C**), the effect of the influence on the synchronization ability of the brain network was observed by enhancing the edge strength of the red region S. **Figures 7A,B** show the changes in the synchronization ability of the red region S edge strengths of the 20 brain networks of a specific patient and a specific individual from the healthy controls from 1, 1.5...3.5 times (In the encoding phase, we chose a period of consecutive 100 s for each participant, constructing a brain network every 5 s).

It can be seen from **Figure 7** that for the same edge strength, the change in the synchronization ability between the patients and the healthy controls exhibited opposite trends and tended to be uniform; the strength of the internal bridging of S is more obvious. However, if the edge strength was too great, it simultaneously reduced the ability of the healthy subjects' network and the patients' network to synchronize.

Experiment 3: Synchronization Stability and Brain-Network Adjustment

From the analysis of the differences in the synchronization ability of the brain network between the patients and healthy controls in section Experiment 2:Brain-Network synchronization stability analysis, we found that the two groups differed considerably in their brains' synchronization ability and that these differences are concentrated in the local area S. That is, the smaller the S edge density, the stronger the synchronization ability. To achieve the goal of curing disease, this section primarily discusses the theory of complex network synchronization control to explore ways in which a patient's brain network could be given a certain "treatment" that would make the patient's synchronization ability consistent with the synchronization ability of normal people.

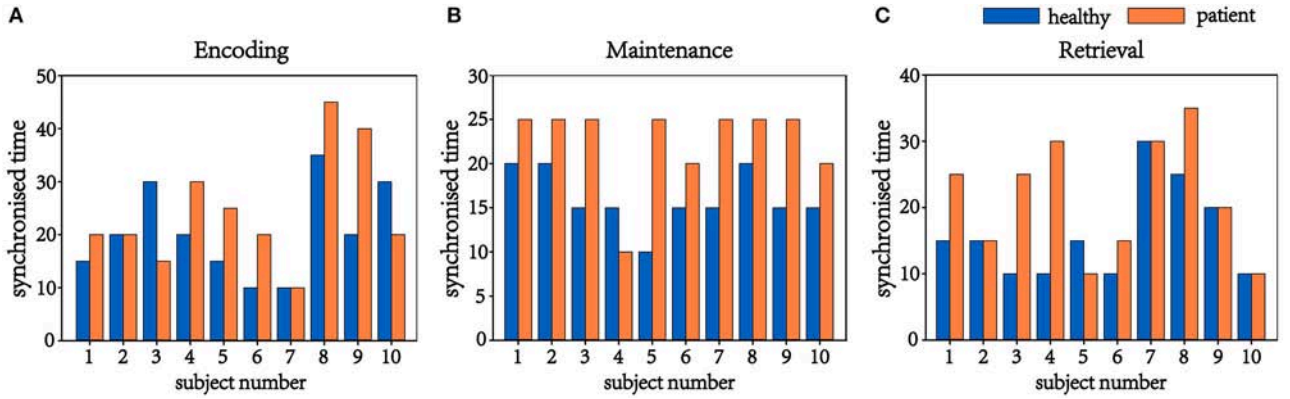


FIGURE 4 | Time of initial synchronization in the healthy controls and the patients. **(A)** is the encoding stage, **(B)** is the maintenance stage, and **(C)** is the retrieval stage.

TABLE 5 | Time to initial synchronization in patients and healthy controls.

Subject	Stage/band (alpha)	Average value (ms)	Standard deviation (ms)
Patients	Encoding	27	9.798
	Maintenance	26.5	10.259
	Retrieval	22	7.810
Normal	Encoding	18	6.782
	Maintenance	21	5.385
	Retrieval	15.5	6.874

This section proposes a method based on the fusion of traditional features and spectral features to achieve the adjustment of the patient's brain network synchronization ability, so that its synchronization ability would be consistent with normal subjects, theoretically achieving the purpose of treatment of diseases. Applying the T&S coupling formula defined in section Defining the Coupling Formula $\mathbf{L}^*$, the patient's brain network synchronization ability could be adjusted by selecting appropriate values of the T&S coupling matrix $\mathbf{L}^*$ parameters aa or bb. The feasibility and validity of the method were verified by specific data.

Coupling Matrix L^*Parameter Selection

The experiment investigated the patients' brain networks. Based on the results of the Pearson correlation coefficient calculation in section Experiment1:Brain-Network Significant Difference Features and Node Extraction, the clustering coefficient of the matrix G and the mean path length were used to adjust the brain's synchronization ability. **Figure 8** shows the change in the synchronization ability of the patient's brain network when the matrix G takes the clustering coefficient; **Figure 9** shows the synchronization stability of the brain network when the matrix G takes the path length. The abscissa indicates the value of the parameter bb, and the ordinate indicates the corresponding brain network synchronization feature value. The parameters chosen in the experiment were arbitrary and have no practical meaning. Other values could also be selected.

Adjustment-A

Figure 8A shows the result when the parameters aa and bb are both positive; 8b shows the result when parameter aa is negative and bb is positive; 8c shows the result when the parameters aa and bb are both negative.

In **Figure 8A**, when the parameters aa and bb are positive numbers, the results are as follows: When parameter bb is fixed, the network synchronization capability is proportional to the value of parameter aa; when parameter aa is constant, the synchronization capability of the network has an anti-proportional relationship to the value of parameter bb.

In **Figure 8B**, when parameter aa is negative and bb is positive, the network synchronization capability changes are more complex. When parameter aa < -1.5, the trend of the network synchronization capability is exactly the same as that in graph c. When the parameter aa> -1.5, the synchronization trend of the network is exactly the same as that in graph a.

In **Figure 8C**, when the parameters aa and bb are both negative numbers, the results are as follows: When parameter bb is fixed, the network synchronization ability is inversely proportional to the value of parameter aa. When parameter aa is constant, the network synchronization ability increases with parameter bb and then decreases, and the network synchronization ability gradually changes to become consistent with the original synchronization capabilities.

Adjustment-B

Figure 9A shows the results when the parameters aa and bb are both positive; 9b shows the results when parameter aa is negative and bb is positive; 9c shows the results when parameters aa and bb are both negative.

In **Figure 9A**, when the parameters aa and bb are both positive, the results are as follows: When parameter bb is fixed, the network synchronization capability is directly proportional to the value of parameter aa; when parameter aa is fixed, the synchronization capability of the network is directly proportional

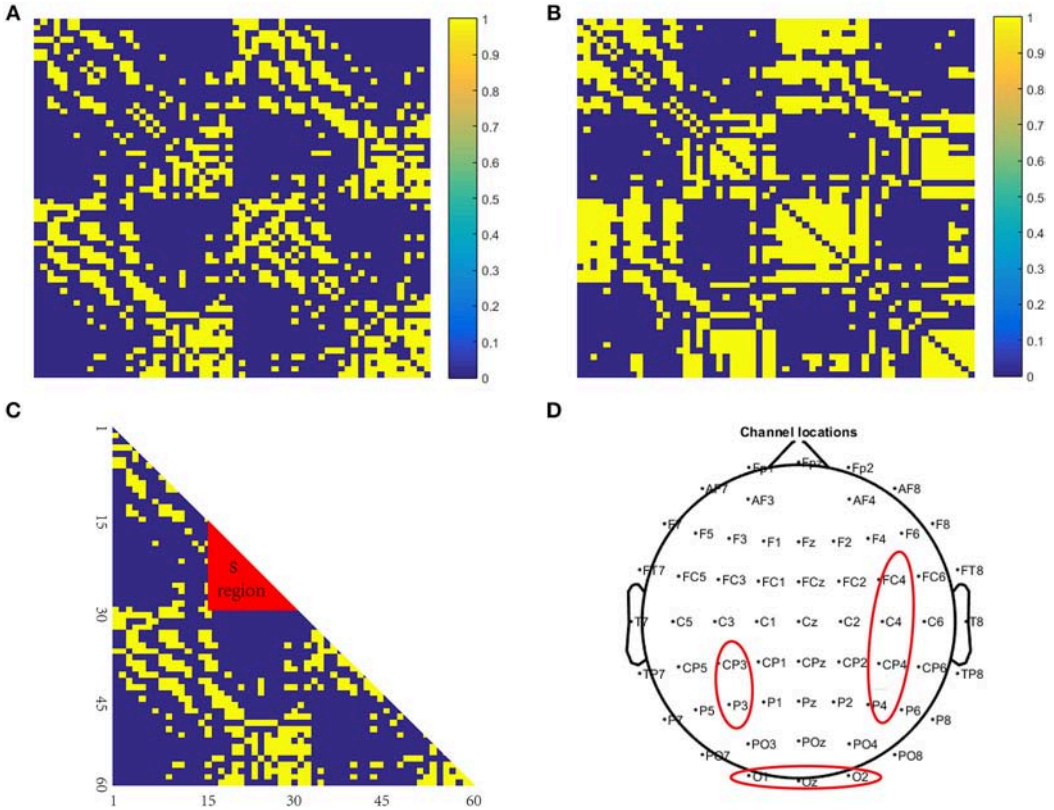


FIGURE 5 | Brain network structure. **(A)** is a binary matrix constructed using the healthy controls; **(B)** is a binary matrix constructed using the patient subjects; **(C)** is the difference significant area S, a mathematical representation of **(A,B,D)** is a brain electrode position diagram corresponding to a **(C)** S region in the brain map.

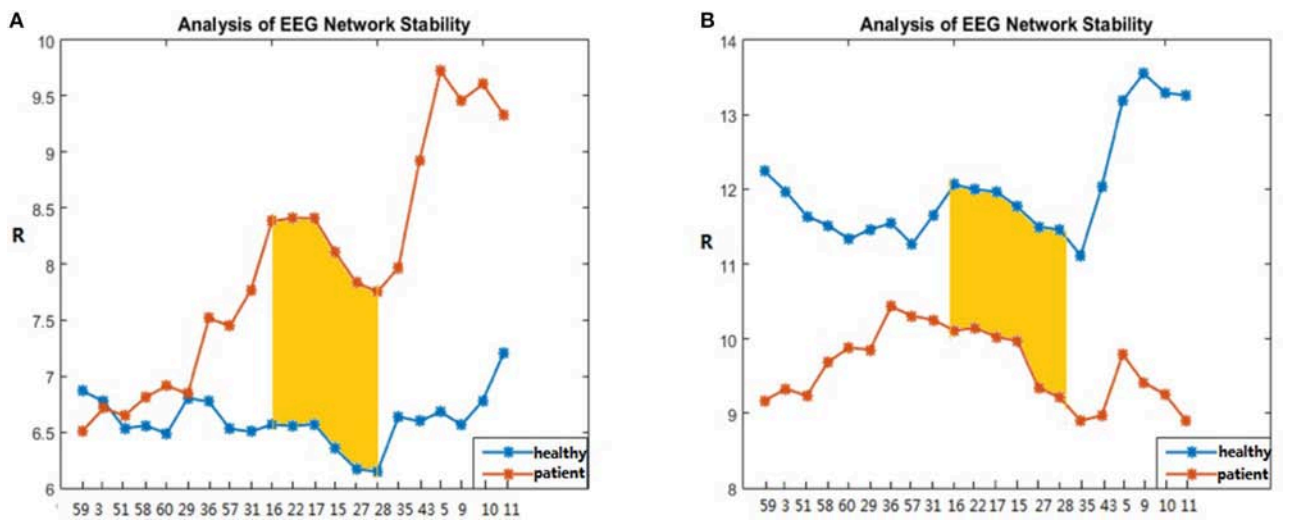


FIGURE 6 | R-value changes with the coupling of the S area in patients and healthy controls. The patient subject graphed here was #6 and the healthy control subject was #4 in **(A)**, and the patient subject graphed in **(B)** was #4 and the healthy control subject was #6.

to the value of parameter bb. This shows that, when the coupling matrix selects the path length as the "weighted" mode, the network synchronization capability is proportional to the values of the parameters aa and bb.

In **Figure 9B**, when parameter aa is negative and bb is positive, the results are as follows: When parameter bb is fixed, the network synchronization capability is directly proportional to the value of parameter aa; when parameter aa is fixed,

TABLE 6 | EEG signal 64 electrode name numbering table.

Ele-No.	EN	Ele-No.	EN	Ele-No.	EN	Ele-No.	EN	Ele-No.	EN
1	Fp1	14	FT8	27	O2	40	F2	53	CP6
2	F7	15	FC4	28	O1	41	FC1	54	PO8
3	Fp2	16	Cz	29	Pz	42	C5	55	P6
4	F3	17	CPz	30	Oz	43	FC6	56	CP2
5	FC3	18	CP3	31	Fpz	44	FC2	57	PO4
6	FT7	19	P3	32	AF3	45	C2	58	P2
7	T7	20	P7	33	AF7	46	C1	59	POz
8	F8	21	T8	34	F5	47	CP1	60	P1
9	F4	22	TP8	35	AF8	48	CP5	61	VEOU
10	Fz	23	C4	36	AF4	49	P5	62	VEOL
11	FCz	24	P8	37	F1	50	C6	63	HEOL
12	C3	25	CP4	38	FC5	51	PO3	64	HEOR
13	TP7	26	P4	39	F6	52	PO7		

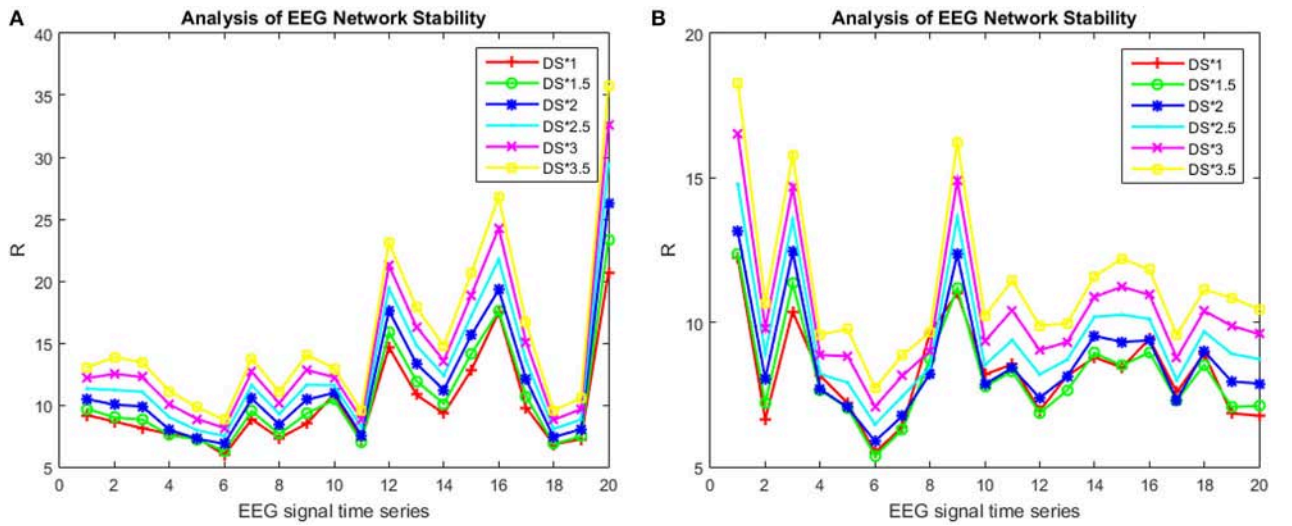


FIGURE 7 | *R*-value changes with the strength of the S area in patients and healthy controls. The patient subject graphed here was #6 in **(A)** and the healthy control subject was #4 in **(B)**.

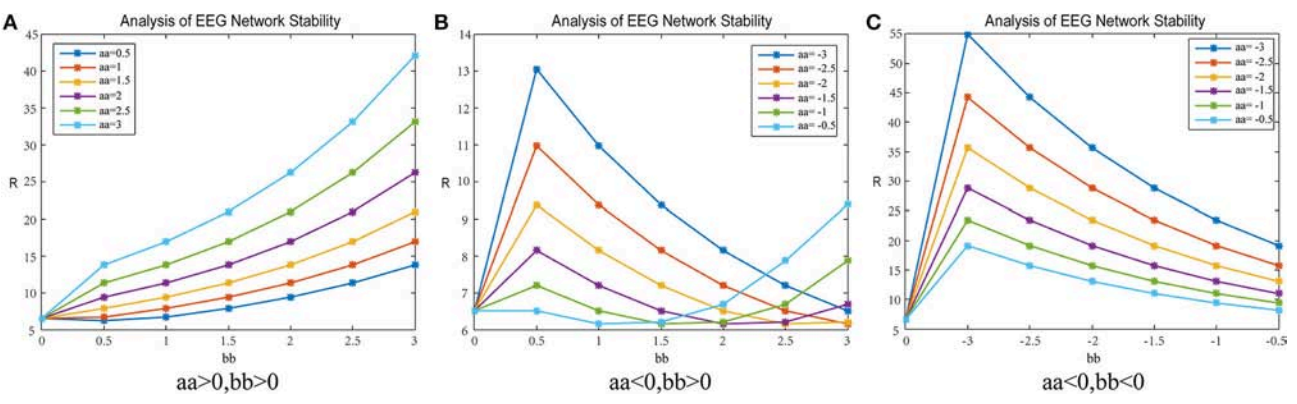


FIGURE 8 | *R*-value changes in a patient subject. Matrix G represents mean-clustering-coef and the data are from patient #6. **(A)** shows the parameters aa, bb are positive. **(B)** shows the parameter aa is negative, bb is positive. **(C)** shows the parameter aa, bb are negative.

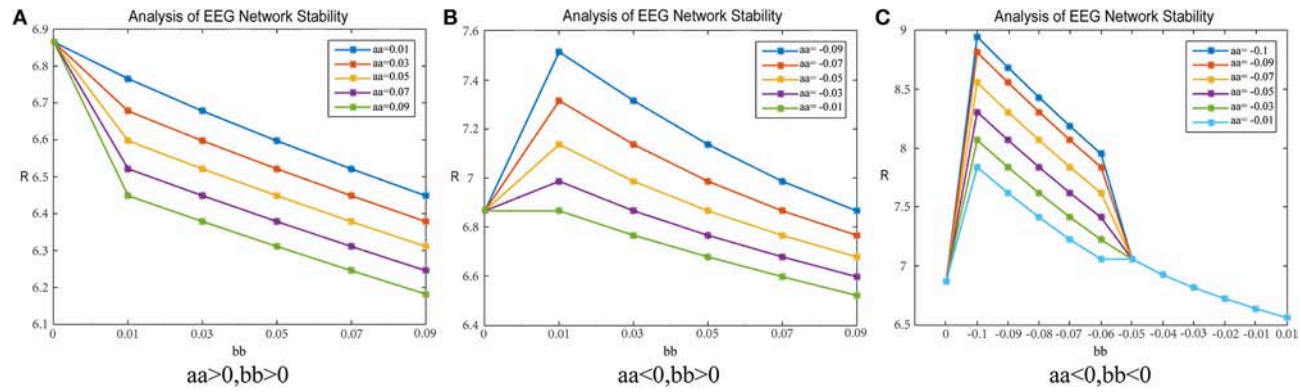


FIGURE 9 | *R*-value changes in a healthy subject. Matrix G represents mean-path-length and the data are from patient #6. **(A)** shows the parameters aa, bb are positive. **(B)** shows the parameter aa is negative, bb is positive. **(C)** shows the parameter aa, bb are negative.

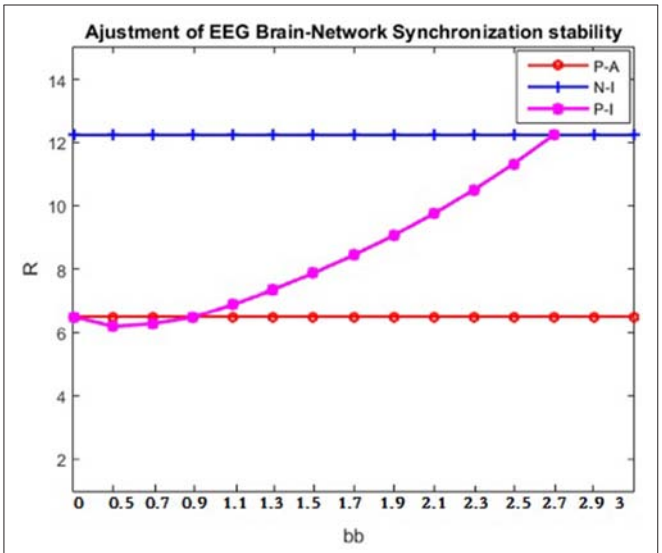


FIGURE 10 | Adjustment of patient's brain- network synchronization ability. The data are from patient #6 and healthy control subject number #4. The abscissa is the value of parameter bb, and the ordinate is the corresponding brain network synchronization feature value. P-A indicates the synchronization ability of the patient after the brain network adjustment; P-I indicates the synchronization ability of the patient before the brain network adjustment; N-I indicates normal synchronization ability.

the relationship between the synchronization capability of the network and the value of the parameter bb is first weakened and then enhanced to match the initial synchronization ability. After weakening, the enhancement tends to be consistent with the original synchronization ability.

In **Figure 9C**, when parameters aa and bb are negative, the network synchronization capability changes are more complex. When parameter bb is fixed and bb < -0.05, the synchronization capability of the network is proportional to the value of parameter aa; when parameter bb is fixed and bb > -0.05, the network synchronization capability is enhanced and does not change with parameter aa; when parameter aa is constant, the synchronization capability of the network decreases with an increase in parameter bb, and then the enhancement gradually changes to become stronger than the original synchronization capability.

Adjusting the Patient Synchronization Stability

Based on the conclusions in Coupling Matrix L ^* Parameter Selection, the best values of parameters aa and bb could be selected to be applied to the patient, so that the synchronization ability of the brain network of a patient and the brain synchronization ability of a normal person would tend to be consistent. Next, the clinician would refer to the equivalent of **Figure 8A** to identify the parameter transformation and would select aa $= 0.5$. The patient's brain network synchronization ability would finally be adjusted using parameter bb (**Figure 10**). In **Figure 10**, it can be seen that when aa $= 0.5$ and bb $= 2.5$, the patient's synchronization ability should be consistent with that of a normal person. In this way, the goal of curing disease can theoretically be achieved.

LIMITATIONS

The current study involved several limitations that should be considered. First, the effect of offline processing of EEG traces on brain network dynamics synchronization was not considered, so it is unclear how the synchronization differences obtained in an offline analysis of the EEG can pave a way for the treatment of unspecified neuropsychiatric diseases. In addition, EEG signals recorded from the scalp surface are generally highly correlated. Each channel is a linear mixture of concurrently active brain and non-brain electrical sources, whose activities are volume conducted to the scalp electrodes with broadly overlapping patterns (Nunez et al., 1997). Therefore, we used surface Laplacian transform methods to eliminate the mixed effect of volume conduction (Makeig et al., 1996; Jung et al., 2001; Delorme et al., 2012). Also, our study did not provide specific values for the parameters aa and bb, so the values of aa and bb were arbitrarily chosen. The purpose was only to verify the validity of the T&S coupling formula proposed in this study. As

for its application in clinical trials, it may be necessary to correlate the aa and bb parameters with certain biological characteristics of the human body (such as blood flow). Consequently, we should pay more attention to these aspects and add related experiments in future research.

CONCLUSION

In this study, a brain network was constructed based on complex network theory. The synchronization characteristics of the brain network were calculated using the spectral features of the brain network. The synchronization process characterizes the differences and changes in the brain network synchronization ability between a patient and healthy subjects during the process of making memories. Our experiments showed that the synchronization of aa differed significantly between the patients and the healthy controls and that this synchronization is concentrated in the S region. In addition, these experiments further indicated that the effect of S on the synchronization ability in this S region was that the density of the S region was smaller, and the synchronization ability was stronger. To achieve the purpose of treating patients, we proposed a method based on the fusion of traditional features and spectral features to achieve the adjustment of a patient's brain network synchronization ability. The KS test, SVM classification, and other methods were used to extract traditional features and nodes that showed significant differences; we designed a T&S coupling method that fuses traditional features with spectral features and selects the appropriate parameter values aa or bb to adjust the patient's brain network synchronization capabilities. The data validated the feasibility of the method and theoretically achieved the purpose of treating disease. This study has only theoretically explored the treatment of disease through algorithms and has not been clinically applied. In the future, we will try to explore animal (rat) susceptibility factors, clinical manifestations, skull characteristics, and prognosis in depth, and we hope to find feasible measures (such as physical therapy) that can adjust these features.

ETHICS STATEMENT

All subjects were given written informed consent in accordance with the Declaration of Helsinki.

AUTHOR CONTRIBUTIONS

RY performed the experiment and completed the manuscript. XX, GY, HD, and PY provided suggestions for this study. HL provided the guidance throughout the study. HL had full access to all of the data in the study and takes responsibility for its integrity and the accuracy of the data analysis. All the authors have read through the manuscript, approved it for publication, and declared no conflict of interest.

FUNDING

This study Natural Science Foundation of China (61472270, 61873178, and 61876124) and the Natural Science Foundation of Shanxi (201801D121135). The sponsors had no role in the design or execution of the study, the collection, management, analysis, and interpretation of the data, or the preparation, review, and approval of the manuscript. This manuscript has not been published or presented elsewhere in part or in entirety and is not under consideration by any another journal.

ACKNOWLEDGMENTS

The authors also thank Rhoda E. Perozzi Ph.D. for linguistic assistance during the preparation of this manuscript and thank the reviewers for helpful comments.

REFERENCES

Babloyantz, A., Salazar, J. M., and Nicolis, C. (1986). Evidence of chaotic dynamics of brain activity during the sleep cycle. *Phys. Lett. A*. 111, 152–156. doi: 10.1016/0375-9601(85)90444-X

Bartolomei, F., Bosma, I., Klein, M., Baayen, J. C., Reijneveld, J. C., Postma, T. J., et al. (2010). How do brain tumors alter functional connectivity? A magnetoencephalography study. *Digest World Core Med. J.* 59, 128–138. doi: 10.1002/ana.20710

Bola, M., Gall, C., and Sabel, B. A., (2015). Disturbed temporal dynamics of brain synchronization in vision loss. *Cortex* 67, 134–146. doi: 10.1016/j.cortex.2015.03.020

De Han, W., Pijnenburg, Y. A., and Strijers, R. L. (2009). Functional neural network analysis in fronto temporal dementia and Alzheimer's disease using EEG and graph theory. *BMC Neuro sci.* 10:101. doi: 10.1186/1471-2202-10-101

Delorme, A., Palmer, J., Onton, J., Oostenveld, R., and Makeig, S., (2012). Independent EEG sources are dipolar. *PLoS ONE* 7:e30135. doi: 10.1371/ journal.pone.0030

Dong, Z. Q., Hou, F. Z., Dai, J. F., and Liu, X. F. (2014). An improved synchronous algorithm based on Kendall for analyzing epileptic brain network. *Acta Phys. Sinica. Chin. Ed.* 63, 208705–208705. doi: 10.7498/aps.63.208705

Eliasmith, C., Stewart, T. C., Choo, X., Bekolay, T., DeWolf, T., Tang, Y., et al. (2012). A large-scale model of the functioning brain. *Science* 338, 1202–1205. doi: 10.1126/science.1225266

Feng-Zhen, H., Jia-Fei, D., Xin-Feng, L., and Xiao-Lin, H. (2014). Phase synchrony in the cerebral infarction electroencephalogram based on the degree of network-links. *Acta Phys. Sinica.* 63, 257–264. doi: 10.7498/aps.63.040506

Gao, X., Cao, H., Ming, D., Qi, H., Wang, X., Wang, X., et al. (2014a). Analysis of EEG activity in response to binaural beats with different frequencies. *Int. J. Psychophysiol.* 94, 399–406. doi: 10.1016/j.ijpsycho.2014.10.010

Gao, X., Huang, J., Liu, S., Li, Y., Li, H., Li, L. et al. (2014b). Research on mechanisms of low temperature for blocking excessive synchronization discharge *in vitro* epilepsy model. *Chongqing Med.* 43, 2319–2322. doi: 10.3969/j.issn.1671-8348.2014.18.020

Guevara, R., Velazquez, J. L., Nenadovic, V., Wennberg, R., Senjanovic, G., and Dominguez, L. G. (2005). Phase synchronization measurements using electroencephalographic recordings: what can we really say about neuronal synchrony?[J]. *Neuroinformatics* 3, 301–313. doi: 10.1385/NI:3:4:301

Guo, H., Cao, X., and Liu, Z. (2013). Machine learning classifier using abnormal brain network topological metrics in major depressive

disorder. *Neuroreport* 24, 51–51. doi: 10.1097/WNR.0b013e32835ca23a

Gysels, E., and Celka, P. (2004). Phase synchronization for the recognition of mental tasks in a brain-computer interface. *IEEE Trans. Neural Syst. Rehabil. Eng. A Public. IEEE Eng. Med. Biol. Soc.* 12:406. doi: 10.1109/TNSRE.2004.838443

Hao, G. (2013). *Analysis and Classification of Abnormal Topological Properties of Resting Brain Function Network in Depression.* Taiyuan University of Technology, Taiyuan, Shanxi.

Hongli, L. I., Jiang, W., Bin, D., and Xile, W. (2013). Analysis of mutual information and synchronism for epileptic EEG signals. *J. Comput. Eng. Appl.* 49, 19–192. doi: 10.3778/j.issn.1002-8331.1205-0234

Hongyue, Z., Suogang, W., and Shuping, T. (2017). Study on functional brain network of schizophrenia p50 sensory gating based on granger causality. *Space Med. Med. Eng.* 30, 203–207. doi: 10.16289/j.cnki.1002-0837.2017.03.009

Hutt, A. (2010). Oscillatory activity in excitable neural systems. *Contemp. Phys.* 51, 3–16. doi: 10.1080/00107510903293710

Jiaqing, L. I., Haifang, L. I., Yifan, B., Guimei, Y., and Liting, S. (2018). Research on recognizing and removing ocular artifact automatically from EEG signals. *Comput. Eng. Appl.* 54, 148–152. doi: 10.3778/j.issn.1002-8331.1702-0267

Jin-Hu, L. (2010). Synchronization of complex networks and consensus of complex multi-agent systems. *Complex Syst. Complex. Sci.* 57, 50–52. doi: 10.3969/j.issn.1672-3813.2010.02.013

Joyce, C. A., Gorodnitsky, I. F., and Kutas, M. (2010). Automatic removal of eye movement and blink artifacts from EEG data using blind component separation. *Psychophysiology* 41, 313–325. doi: 10.1111/j.1469-8986.2003.00141.x

Jung, T. P., Makeig, S., McKeown, M. J., Bell, A. J., Lee, T. W., and Sejnowski, T. J., (2001). Imaging brain dynamics using independent component analysis. *Proc. IEEE* 89, 1107–1122. doi: 10.1109/5.939827

Kashtan, N., and Alon, U. (2005). Spontaneous evolution of modularity and network motifs. *Proc. Natl. Acad. Sci. U.S.A.* 102, 13773–13778. doi: 10.1073/pnas.0503610102

Kayser, J., and Tenke, C. E. (2006a). Principal components analysis of Laplacian waveforms as a generic method for identifying ERP generator patterns: I. Evaluation with auditory oddball tasks. *Clin. Neurophysiol.* 117, 348–368. doi: 10.1016/j.clinph.2005.08.034

Kayser, J., and Tenke, C. E. (2006b). Principal components analysis of Laplacian waveforms as a generic method for identifying ERP generator patterns: II. Adequacy of low-density estimates. *Clin. Neurophysiol.* 117, 369–380. doi: 10.1016/j.clinph.2005.08.033

Li, J. S., and Zhang, X. D. (1997). A new upper bound for eigenvalues of the Laplacian matrix of a graph[J]. *Linear Algebr. Appl.* 265, 93–100. doi: 10.1016/S0024-3795(96)00592-7

Liley, D. T., Cadusch, P. J., and Dafilis, M. P. (2002). A spatially continuous mean field theory of electrocortical activity. *Network* 13, 67–113. doi: 10.1080/net.13.1.67.113

Liting, S., Guimei, Y., Shuping, T., Yanli, Z., Jinguo, Z., Dong, L., et al. (2017). Properties analysis of working memory EEG functional network in schizophrenia. *Comput. Eng. Appl.* 53, 25–30. doi: 10.3778/j.issn.1002-8331.1703-0114

Liu, Y., Liang, M., Zhou, Y., He, Y., Hao, Y., Song, M., et al. (2008). Disrupted small-world networks in schizophrenia. *Brain* 131, 945–961. doi: 10.1093/brain/awn018

Liu, Y., and Shen, J. (2017). Some results on the sum of the normalized Laplacian eigenvalues of graphs. *Adv. Math.* 46, 848–856. doi: 10.3969/j.issn.1000-5641.2010.01.003

Liu, Y., Yu, C., Zhang, X., Liu, J., Duan, Y., Alexander-Bloch, A. F., et al. (2014). Impaired long distance functional connectivity and weighted network architecture in Alzheimer's disease. *Cerebral Cortex.* 24, 1422–1435. doi: 10.1093/cercor/bhs410

Lü, J., and Guanrong, C. (2005). A time-varying complex dynamical network model and its controlled synchronization criteria. *IEEE Trans. Autom. Control* 50, 841–846. doi: 10.1109/TAC.2005.849233

Ma, C. C., Liu, A. J., Liu, A. H., Zhou, X. Y., and Zhou, S. N. (2014). Electroencephalogram global field synchronization analysis: a new method for assessing the progress of cognitive decline in Alzheimer's disease. *Clin. Eeg. Neurosci.* 45, 98–103. doi: 10.1177/1550059413489669

Makeig, S., Bell, A. J., Jung, T.-P., and Sejnowski, T. J. (1996). Independent component analysis of electroencephalographic data. Adv. *Neural Inform. Process. Syst.* 8, 145–151

Manoach, D. S., Press, D. Z., Thangaraj, V., Searl, M. M., Goff, D. C., Halpern, E., et al. (1999). Schizophrenic subjects activate dorsolateral prefrontal cortex during a working memory task, as measured by fMRI. *Biol. Psychiatry* 45:1128–1137. doi: 10.1016/S0006-3223(98)00318-7

Micheloyannis, S., Pachou, E., Stam, C. J., Vourkas, M., Erimaki, S., and Tsirka, V. (2006). Using graph theoretical analysis of multi channel EEG to evaluate the neural efficiency hypothesis. *Neurosci. Lett.* 402, 273–277. doi: 10.1016/j.neulet.2006.04.006

Müller, V., Sänger, J., and Lindenberger, U. (2018). Hyperbrain network properties of guitarists playing in quartet. *Ann. N. Y. Acad. Sci.* 1423, 198–210. doi: 10.1111/nyas.13656

Nunez, P. L., Srinivasan, R., Westdorp, A. F., Wijesinghe, R. S., Tucker, D. M., Silberstein, R. B., et al. (1997). EEG coherency: I: statistics, reference electrode, volumeconduction,Laplacians,corticalimaging,andinterpretationatmultiple scales. *Electroencephalogr. Clin. Neurophysiol.* 103, 499–515. doi: 10.1016/S0013-4694(97)00066-7

Pecora, L. M., and Carroll, T. L. (1990). Synchronization in chaotic systems. *Phys. Rev. Lett.* 64, 821–824. doi: 10.1103/PhysRevLett.64.821

Peraza, L. R., Asghar, A. U., Green, G., and Halliday, D. M. (2012). Volume conduction effects in brain network inference from electroencephalographic recordings using phase lag index[J]. *J. Neurosci. Methods* 207, 189–199. doi: 10.1016/j.jneumeth.2012.04.007

Qun, Z. (2009). On the study methods of electroencephalograph synchronization. *J. Biomed. Eng.* 26, 1353–1357. doi: 10.3321/j.issn:1001-5515.2009.06.040

Rosário, R. S., Cardoso, P. T., Muñoz, M. A., Montoya, P., and Miranda, J. G. V. (2015). Motif-Synchronization: A new method for analysis of dynamic brain networks with EEG. *Phys. A Stat. Mech. Appl.* 439, 7–19. doi: 10.1016/j.physa.2015.07.018

Ruizhen, Z., Yinan, T., Yuhan, S., Huanhuan, Z., and Mengya, W. (2017). Apparent receptor dynamics analysis of hippocampal excitatory synaptic transmission in rats and its application. *J. Gannan Med. College* 36, 103–106. doi: 10.3969/j.issn.1002-0217.2017.02.001

Sakkalis, V., Oikonomou, T., and Tsiaras, V. (2013). Graph-theoretic indices of evaluating brain network synchronization: application in an alcoholism paradigm. *Neuromethods* 91, 159–169. doi: 10.1007/7657_2013_62

Sato, H., and Iwai, T. (2014). Optimization algorithms on the Grassmann manifold with application to matrix eigenvalue problems. *Jpn. J. Ind. Appl. Math.* 31, 355–400. doi: 10.1007/s13160-014-0141-9

Skidmore, F., Korenkevych, D., Liu, Y., He, G., Bullmore, E., and Pardalos, P. M. (2011). Connectivity brain networks based on wavelet correlation analysis in Parkinson fMRI data. *Neurosci. Lett.* 499, 47–51 doi: 10.1016/j.neulet.2011.05.030

Stam, C. J., Jones, B. F., Nolte, G., Breakspear, M., and Scheltens, P. (2007). Small-world networks and functional connectivity in Alzheimer's disease. *Cerebral Cortex.* 17, 92–99. doi: 10.1093/cercor/bhj127

Sun, Y., Dai, Z., Li, J., Collinson, S. L., and Sim, K. (2009). Connectome alterations in schizophrenia. *Neuroimage* 47, S157–S157. doi: 10.1016/S1053-8119(09)71653-2

Wigand, M., Kubicki, M., Clemm von Hohenberg, C., Leicht, G., Karch, S., Eckbo, R., et al.. (2015). Auditory verbal hallucinations and the interhemispheric auditory pathway in chronic schizophrenia. *World J. Biol. Psychiatry* 16, 31–44. doi: 10.3109/15622975.2014.948063

Xiao, C. (2012). *Research on Quasi-Laplace Matrix Eigenvalues of Graphs.* University of Electronic Science and Technology, Chengdu, Sichuan.

Xu, B., Fu, Y., Shi, G., Yin, X., Wang, Z., Li, H., et al. (2014). Enhanced performance by time-frequency-phase feature for EEG-based BCI systems. *Sci. World J.* 2014:420561. doi: 10.1155/2014/420561

Yi, W., Qiu, S., Wang, K., Qi, H., Zhang, L., Zhou, P., et al. (2014). Evaluation of EEG Oscillatory patterns and cognitive process during simple and compound limb motor imagery. *PLoS ONE* 9:e114853. doi: 10.1371/journal.pone.0114853

Yuchi, L. I., Haifang, L. I., Dan, J., Guimei, Y., and Keyou, H. (2017). Phase synchronization analysis of emotional EEG based on complex network theory. *Comput. Eng. Appl.* 53, 230–235. doi: 10.3778/j.issn.1002-8331.1604-0007

Zhang, Y., Guo, D., Cheng, K., Yao, D., and Xu, P. (2015). The graph theoretical analysis of the sssvep harmonic response networks. *Cogn. Neurodyn.* 9, 305–315. doi: 10.1007/s11571-015-9327-3

Zhang, Y., Xu, P., Guo, D., and Yao, D. (2013b). Prediction of ssvep-based bci performance by the resting-state eeg network. *J. Neural Eng.* 10:066017. doi: 10.1088/1741-2560/10/6/066017

Zhang, Y., Xu, P., Huang, Y., Cheng, K., and Yao, D. (2013a). Ssvep response is related to functional brain network topology entrained by the flickering stimulus. *PLoS ONE* 8:e72654. doi: 10.1371/journal.pone.0072654

Zhao, L., Wang, B., and Yao, D. (2008). Research on analytical methods of phase synchronization in EEG. *Sheng Wu Yi Xue Gong Cheng Xue Za Zhi.* 25, 250–254. doi: 10.3321/j.issn:1001-5515.2008.02.005

Zhao, Y. L., Tan, S. P., Yang, F. D., Wang, L. L., Feng, W. F., Chan, R. C., et al. (2011). Dysfunction in different phases of working memory in schizophrenia: evidence from ERP recordings. *Schizophrenia Res.* 133, 112–119. doi: 10.1016/j.schres.2011.09.017

Zhou, T., Zhang, Z.-K., Chen, G.-R., Wang, X.-F., Shi, D.-H., Di, Z.-R., et al. (2014). The opportunities and challenges of complex networks research. *J. Univ. Electron. Sci. Technol. China.* 43, 1–5. doi: 10.3969/j.issn.1001-0548.2014.01.001

Conflict of Interest Statement: The authors declare that the research was conducted in the absence of any commercial or financial relationships that could be construed as a potential conflict of interest.

Copyright © 2019 Li, Yao, Xia, Yin, Deng and Yang. This is an open-access article distributed under the terms of the Creative Commons Attribution License (CC BY). The use, distribution or reproduction in other forums is permitted, provided the original author(s) and the copyright owner(s) are credited and that the original publication in this journal is cited, in accordance with accepted academic practice. No use, distribution or reproduction is permitted which does not comply with these terms.

frontiers in Systems Neuroscience

ORIGINAL RESEARCH
published: 14 November 2019
doi: 10.3389/fnsys.2019.00069

Activation of Brainstem Neurons During Mesencephalic Locomotor Region-Evoked Locomotion in the Cat

*Ioan Opris[1], Xiaohong Dai[2], Dawn M. G. Johnson[1†], Francisco J. Sanchez[1], Luz M. Villamil[1], Songtao Xie[1†], Cecelia R. Lee-Hauser[1], Stephano Chang[1], Larry M. Jordan[2] and Brian R. Noga[1]**

[1] The Miami Project to Cure Paralysis, Department of Neurological Surgery, University of Miami Miller School of Medicine, Miami, FL, United States, [2] Department of Physiology, Spinal Cord Research Centre, University of Manitoba, Winnipeg, MB, Canada

OPEN ACCESS

Edited by:
James W. Grau,
Texas A&M University, United States

Reviewed by:
David Magnuson,
University of Louisville, United States
Simon Arthur Sharples,
University of St Andrews,
United Kingdom

***Correspondence:**
Brian R. Noga
bnoga@miami.edu

†Present address:
Dawn M. G. Johnson,
National Institute of Mental Health,
Bethesda, MD, United States
Songtao Xie,
Department of Chemical and Natural Gas Engineering, Texas A&M University – Kingsville, Kingsville, TX, United States

Received: 23 July 2019
Accepted: 31 October 2019
Published: 14 November 2019

Citation:
Opris I, Dai X, Johnson DMG, Sanchez FJ, Villamil LM, Xie S, Lee-Hauser CR, Chang S, Jordan LM and Noga BR (2019) Activation of Brainstem Neurons During Mesencephalic Locomotor Region-Evoked Locomotion in the Cat.
Front. Syst. Neurosci. 13:69.
doi: 10.3389/fnsys.2019.00069

The distribution of locomotor-activated neurons in the brainstem of the cat was studied by c-*Fos* immunohistochemistry in combination with antibody-based cellular phenotyping following electrical stimulation of the mesencephalic locomotor region (MLR) – the anatomical constituents of which remain debated today, primarily between the cuneiform (CnF) and the pedunculopontine tegmental nuclei (PPT). Effective MLR sites were co-extensive with the CnF nucleus. Animals subject to the locomotor task showed abundant *Fos* labeling in the CnF, parabrachial nuclei of the subcuneiform region, periaqueductal gray, locus ceruleus (LC)/subceruleus (SubC), Kölliker–Fuse, magnocellular and lateral tegmental fields, raphe, and the parapyramidal region. Labeled neurons were more abundant on the side of stimulation. In some animals, *Fos*-labeled cells were also observed in the ventral tegmental area, medial and intermediate vestibular nuclei, dorsal motor nucleus of the vagus, n. tractus solitarii, and retrofacial nucleus in the ventrolateral medulla. Many neurons in the reticular formation were innervated by serotonergic fibers. Numerous locomotor-activated neurons in the parabrachial nuclei and LC/SubC/Kölliker–Fuse were noradrenergic. Few cholinergic neurons within the PPT stained for *Fos*. In the medulla, serotonergic neurons within the parapyramidal region and the nucleus raphe magnus were positive for *Fos*. Control animals, not subject to locomotion, showed few *Fos*-labeled neurons in these areas. The current study provides positive evidence for a role for the CnF in the initiation of locomotion while providing little evidence for the participation of the PPT. The results also show that MLR-evoked locomotion involves the parallel activation of reticular and monoaminergic neurons in the pons/medulla, and provides the anatomical and functional basis for spinal monoamine release during evoked locomotion. Lastly, the results indicate that vestibular, cardiovascular, and respiratory centers are centrally activated during MLR-evoked locomotion. Altogether, the results show a complex pattern of neuromodulatory influences of brainstem neurons by electrical activation of the MLR.

Keywords: mesencephalic locomotor region, cuneiform nucleus, pedunculopontine nucleus, fictive locomotion, reticulospinal, monoamine, choline acetyltransferase, activity-dependent labeling

INTRODUCTION

Of the various higher brain centers that elicit locomotion when stimulated, the MLR, a key, phylogenetically preserved, regulatory node within the supraspinal locomotor circuit controlling spinal locomotor neurons (Shik et al., 1966, 1967; Grillner et al., 2008; Jordan et al., 2008), is increasingly looked at as a target for improving locomotion (freezing-of-gait) in Parkinson's disease (PD) and after spinal cord injury (SCI). The anatomical equivalent of this physiologically defined region was originally thought to be the CnF (Shik et al., 1966) and subsequent work confirmed this conclusion (Mori et al., 1989, 1992; Grillner et al., 1997; Jordan, 1998; Jordan and Sławińska, 2014; Takakusaki et al., 2016). The nearby cholinergic PPT has also been suggested to be the primary component of the MLR (Garcia-Rill et al., 1986, 1987, 2011). Recent optogenetic and chemogenetic experiments, however, have cast doubt on the role of the cholinergic PPT neurons in the initiation of locomotion (Lee et al., 2014; Roseberry et al., 2016; Capelli et al., 2017; Kroeger et al., 2017; Caggiano et al., 2018; Josset et al., 2018). Rather, these studies emphasize the key role for glutamatergic neurons, especially in CnF and SubCnF regions, for initiating locomotion and suggest that cholinergic neurons may only have a role in the modulation of ongoing locomotor activity or play a role in non-locomotor functions of the MLR.

The MLR does not directly project to the spinal cord but rather activates spinal neurons controlling locomotion (Noga et al., 1995, 2003; Dai et al., 2005) by activation of reticulospinal (RS) neurons in the brainstem (Shik et al., 1967; Orlovskii, 1970; Shefchyk et al., 1984; Garcia-Rill and Skinner, 1987; Noga et al., 1988, 1991, 2003). These in turn descend through the ventral funiculus (Steeves and Jordan, 1984; Noga et al., 1991, 2003). This pathway, considered to be the "command pathway" for the initiation of locomotion (Shik et al., 1967; Jordan, 1998), activates spinal locomotor neurons, in part, by the release of glutamate (Douglas et al., 1993; Hägglund et al., 2010). Such results are supported by optogenetic studies in the mouse, which were used to stimulate glutamatergic RS neurons within the lateral paragigantocellular (LPGi) nucleus (Capelli et al., 2017). Photo-stimulation of these neurons evokes short-latency high-speed locomotion, while ablation of this population significantly reduces the speed of glutamatergic MLR-evoked locomotion. LPGi neurons receive a predominant glutamatergic input from the CnF (Capelli et al., 2017). Glutamatergic RS neurons expressing the transcription factors Lhx3 and/or Chx10 within the MedRF that are activated during locomotion and receive anatomical inputs from the MLR have also been described (Bretzner and Brownstone, 2013), supporting this concept.

In addition to RS command neurons, there is evidence that monoaminergic neurons may play a key role in the activation of spinal locomotor networks. For example, intravenous administration of noradrenergic and serotonergic precursors produces reflex discharges that resemble locomotion (Jankowska et al., 1967; Viala and Buser, 1969). Since then, many studies have shown that monoaminergic drugs may evoke or modulate locomotion in spinally injured cats (Barbeau and Rossignol, 1991; Kiehn et al., 1992; Marcoux and Rossignol, 2000), rats (Cazalets et al., 1992; Kiehn and Kjærulff, 1996; Feraboli-Lohnherr et al., 1999; Sqalli-Houssaini and Cazalets, 2000; Antri et al., 2002), and mice (Christie and Whelan, 2005). Since MLR stimulation produces a similar effect as seen with L-DOPA administration to the spinal cord, it was suggested that the MLR activates a noradrenergic descending system which controls the spinal locomotor generating network (Grillner and Shik, 1973). This idea is supported by the presence of catecholamine-containing neurons in the vicinity of the MLR (Steeves et al., 1976), the demonstration of direct projections from the MLR to the monoaminergic nuclei (Edwards, 1975; Steeves and Jordan, 1984; Sotnichenko, 1985) and the observation that both noradrenergic (Rasmussen et al., 1986) and serotonergic neurons are rhythmically active during overground or treadmill locomotion (Veasey et al., 1995). Recent work in our laboratory has now shown that during MLR-evoked locomotion, spinal monoamine release is widespread and modulated on a timescale of seconds, in tandem with centrally generated locomotion (Noga et al., 2017). While this release is observed during MLR-evoked locomotion, it is not obligatory since depletion of spinal NE or 5-HT does not abolish the MLR's ability to evoke locomotion (Steeves et al., 1980).

To enable MLR-evoked locomotion the activity within brainstem microcircuits must be modulated. In this study we aimed to identify the brainstem neurons activated by electrical stimulation of the MLR as this method is the current clinical standard for targeted stimulation of deep brain structures. MLR sites were identified by their low electrical thresholds and best locomotor responses to stimulation. In the first series of experiments, we documented the distribution of locomotor-activated neurons within the mesencephalon, pons, and medulla using c-*Fos* immunohistochemistry (IHC) (Herdegen and Leah, 1998) as an activity-dependent marker of induced locomotion (Huang et al., 2000; Dai et al., 2005; Noga et al., 2009, 2011). To gain perspective on cells potentially generating locomotor movements, i.e., those that are centrally activated in the absence of peripheral afferent feedback, we used the fictive locomotion preparation in which animals are paralyzed by neuromuscular blockade and locomotor activity is monitored

Abbreviations: 4, trochlear nucleus; 5M, motor trigeminal nucleus; 5SL, laminar spinal trigeminal nucleus; 5SP, spinal trigeminal nucleus; 5ST, spinal trigeminal tract; 7, facial nucleus; 7G, genu of the facial nerve; 7N, facial nerve; AMB, nucleus ambiguus; BC, brachium conjunctivum; bcm, marginal nucleus of the brachium conjunctivum; CI, inferior central nucleus; CnF, cuneiform nucleus; CU, cuneate nucleus; dmnV, dorsal motor nucleus of the vagus; DRG, dorsal root ganglion; FF, fields of Forel; FTC, central tegmental field; FTG, gigantocellular tegmental field; FTL, lateral tegmental field; FTM, magnocellular tegmental field; FTP, paralemniscal tegmental field; GR, gracile nucleus; IC, inferior colliculus; IO, inferior olive nucleus; KF, Kölliker–Fuse nucleus; LC, locus ceruleus; LDT, laterodorsal tegmental nucleus; LLD, dorsal nucleus of the lateral lemniscus; LRI, lateral reticular nucleus internal division; LRN, lateral reticular nucleus; MedRF, medial reticular formation; MLR, mesencephalic locomotor region; NRM, nucleus raphe magnus; NRO, nucleus raphe obscurus; NRP, nucleus raphe pallidus; NTS, nucleus tractus solitarii; P, pyramidal tract; PAG, periaqueductal gray; PPR, post-pyramidal nucleus of the raphe; PPT, pedunculopontine tegmental nucleus; RFN, retrofacial nucleus; RVLM, rostral ventrolateral medulla; SC, superior colliculus; SO, superior olivary nucleus; SubC, subceruleus; SubCnF, subcuneiform region; TB, trapezoid body; VIN, inferior vestibular nucleus; VLN, lateral vestibular nucleus; VMN, medial vestibular nucleus; VRG, ventral respiratory group; VTA, ventral tegmental area.

by electroneurogram (ENG) recordings from peripheral nerves. Animals subject to treadmill locomotion, with consequent phasic, sensory feedback were also examined for comparative purposes. In a second series of experiments, *Fos*+ cells were inspected for co-localization with either dopamine-beta-hydroxylase (DβH), 5-hydroxytryptamine (5-HT), or choline acetyltransferase (ChAT) to determine whether noradrenergic, serotonergic, or cholinergic neurons are activated during MLR-evoked fictive locomotion. The results reveal the anatomical correlate of the MLR, the target descending locomotor pathway neurons and provide evidence for a central coupling of locomotor, vestibular, respiratory, and cardiovascular networks during locomotion. Preliminary results have been reported (Noga et al., 2008).

MATERIALS AND METHODS

Animal Preparation

Experimental procedures were approved by the local University IACUC committees in accordance with the National Institute of Health guidelines (NIH Publications No. 80-23; revised 1996). The number of animals used, and their pain and distress, were minimized. Experiments were performed on 10 adult female cats weighing between 1.9 and 4.3 kg subject to precollicular–postmammillary decerebration. Experimental procedures for treadmill and fictive locomotion experiments were as described previously (Dai et al., 2005; Noga et al., 2009). For fictive locomotion experiments, nerves to one flexor and extensor muscle supplying each of the hindlimbs and forelimbs were dissected, bilaterally, and mounted in tunnel electrodes. The head of each animal was fixed in a Transvertex headframe. In treadmill-locomotion (TL-1) and treadmill-control (TC-1 and TC-2) experiments, all four limbs were free to step on a treadmill belt, and the hindquarters were suspended by a sling under the abdomen. In fictive-locomotion (FL-1,2,3) and fictive-control (FC-1,2,3,4) experiments, the animals were suspended with all four limbs pendant. **Table 1** summarizes the procedural details of animals included in the present study.

Stimulation and Recording

The experimental setup is illustrated in **Figure 1**. Following a recovery period from the decerebration of 1.5–3 h, 4-limbed locomotion was evoked by electrical stimulation of the MLR (1.0 ms square wave pulses, 15–20 Hz) using monopolar stimulating electrodes (SNE-300; David Kopf Instruments, Tujunga, CA, United States) as previously described (Noga et al., 2009, 2011). Electrodes were stereotaxically inserted into the mesopontine tegmentum at an area bounded by posterior (P) 1–3 and lateral (L) 3.0–5.0 mm and included the CnF, bcm within the SubCnF region, and the PPT. Electrodes were typically advanced slowly while stimulating, thus limiting the stimulation of unrelated sites, until the optimal locomotor response was obtained. Thresholds were then tested. If no response was noted or if stimulation strength was high, the electrode was repositioned, and the procedure repeated. Final position was determined by the best locomotor response (greatest ENG amplitudes presenting in locomotor-like rhythms) provided by the lowest threshold at the specified frequency and pulse width. Tract coordinates and electrode depth were noted. In some experiments, electrodes were repositioned in small incremental steps and responses to electrical stimulation at the same strength (slightly above predetermined thresholds) were examined (**Figure 2**) as a further validation of the threshold test results. During the experiment, the strength of stimulation was adjusted to a level which was suitable to maintain locomotion for prolonged periods. Locomotion was monitored by visual confirmation of weight support and walking on the treadmill (treadmill experiments: belt speed: ∼0.46 m/s) or from ENG recordings (fictive locomotion experiments). Representative ENG activity was obtained from the bouts of locomotion throughout the stimulation period (**Figures 1B**, **2**). The ENG signals were amplified with AC-coupled amplifiers (bandwidth 300 Hz to 10 kHz), rectified and low-pass filtered (10 or 20 ms

TABLE 1 | Animals and experimental procedures.

ID	Study	Total time locomotion (min)	Time end of stim to perfusion (h)	Time decerebration to perfusion (h)	IHC procedures	Previous study designation
FL-1	1	157	1	9	DAB (Fos)	FL-1†
FL-2	1	210	1	9	DAB (Fos)	FL-2†
FL-3	2	262	1	10	Fluorescence (Fos, DβH, ChAT, 5-HT)	LC-1††
FC-1	1	<1	6	8.5	DAB (Fos)	FC-1†
FC-2	1	<1	6	8.5	DAB (Fos)	FC-2†
FC-3	1	No stim	–	9	DAB (Fos)	FC-4†
FC-4	2	<1	8	10	Fluorescence (Fos, DβH, ChAT, 5-HT)	C††
TL-1	1	322	1	9	DAB (Fos)	TL-1†
TC-1	1	<1	7	8.5	DAB (Fos)	TC-1†
TC-2	1	No stim	–	9	DAB (Fos)	TC-2†

Animals are assigned into different groups: fictive locomotion (FL); treadmill locomotion (TL); fictive control (FC); and treadmill control (TL). †*Dai et al. (2005) and* ††*Noga et al. (2009, 2011).*

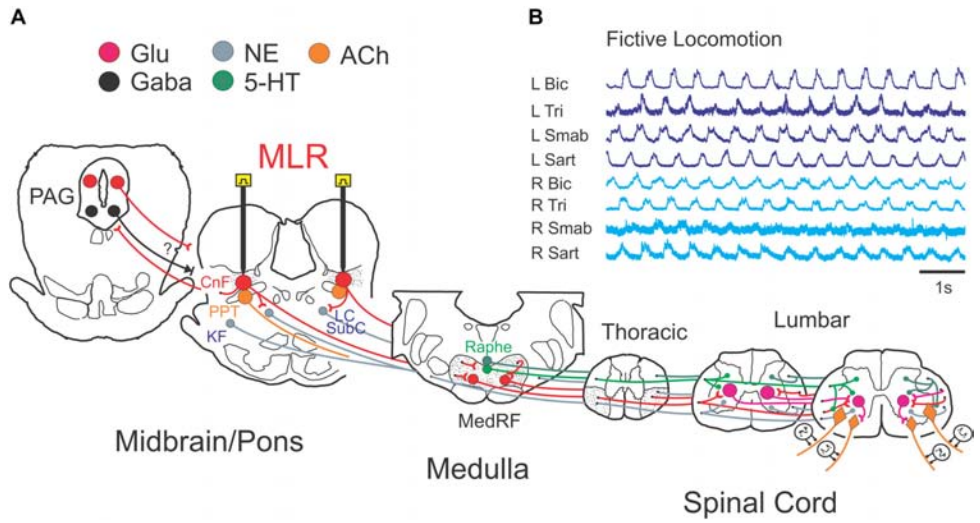


FIGURE 1 | Experimental schema illustrating the brainstem network involved in neuromodulation of locomotor command with stimulation of the MLR. **(A)** Schematic diagram of the brainstem showing the putative anatomical correlates of the MLR, the cuneiform (CnF), and pedunculopontine tegmental (PPT) nuclei, and their putative target neurons within the midbrain/pons and medulla: the periaqueductal gray (PAG), the glutamatergic reticulospinal (RS) neurons within the medial reticular formation (MedRF), the noradrenergic nuclei locus ceruleus (LC), subceruleus (SubC) and Kölliker–Fuse (KF), and the serotonergic nuclei (Edwards, 1975; Steeves and Jordan, 1984; Sotnichenko, 1985). Axons of RS, noradrenergic and serotonergic neurons innervate locomotor central pattern generator neurons (Steeves and Jordan, 1980; Noga et al., 2003, 2009, 2011, 2017). The projections of neurons releasing the neurotransmitters glutamate (Glu), acetylcholine (ACh), noradrenaline (NE), serotonin (5-HT), and gamma-aminobutyric acid (GABA) are depicted across the major relays in locomotion control. **(B)** Example of fictive locomotor activity as monitored by electroneurogram (ENG) recordings from peripheral nerves from all limbs. R, right; L, left; Bic, biceps brachii; Tri, triceps brachii; Smab, semimembranosus/anterior biceps, Sart, sartorius.

time constant), and subsequently digitized through a 1 MHz, 16 channel analog-to-digital converter (12 bit) at 2–4 kHz using customized software (Spinal Cord Research Centre, University of Manitoba, Canada).

Tissue Perfusion

In all of the experiments reported here, there was an 8.5–10 h interval between decerebration and perfusion to reduce *Fos* expression resulting from surgical procedures (**Table 1**). At the end of each locomotor experiment, after a 1 h interval with no-stimulation and immediately prior to perfusion, a small electrolytic lesion was made to mark the MLR stimulation site(s). Animals were re-anesthetized with either halothane or sodium pentobarbital (30 mg/kg) and perfused transcardially with normal saline (0.3 ml/g of animal weight) containing 0.1% $NaNO_2$ and 100 units/ml heparin, followed by 4% paraformaldehyde, 0.2% picric acid, in 0.1 M phosphate-buffered saline (PBS, 4°C), pH 7.4 (1 ml/g of animal weight). The brainstems were removed, post-fixed in the fixative solution for 5 h, and cryoprotected by washing in a solution containing 25% sucrose, 10% glycerol, and 0.001% sodium azide in 0.1 M phosphate buffer for several days.

Immunohistochemistry

The immunohistochemical analysis was carried out on brainstem tissue obtained from animals described in our previous publications on MLR-evoked spinal cord *Fos* expression (Dai et al., 2005; Noga et al., 2009, 2011). **Table 1** summarizes the designations (animal ID) for the present study and from previous studies. Frozen tissue sections of 20 (Dai et al., 2005) or 30 μm (Noga et al., 2009, 2011) thickness were sectioned in a sagittal or coronal plane with a sliding microtome and collected in 0.1 M PBS. To optimize immunohistochemical procedures, a small group of sections were randomly collected from the brainstem segments and a primary antibody dilution series performed. In addition, for the pre-adsorption control, cat tissue sections were incubated only with pre-immuno serum without the primary antibodies. Immunoreactivity was totally absent after omission of all primary antibodies. Controls conducted for double labeling demonstrated no cross-reactivity between primary antibodies and inappropriate secondary antibodies. Selected serial sections of the brainstem were processed to label c-*Fos* nuclear protein alone or co-localized with either DβH, 5-HT, or ChAT to identify activated noradrenergic, serotonergic, or cholinergic brainstem neurons. Two experimental protocols were followed. In Study 1, examining the distribution of activated neurons, *Fos* was stained using diaminobenzidine (DAB) IHC (Dai et al., 2005). Sections were incubated for 72 h in sheep polyclonal anti-*Fos* IgG (Cambridge Research Biochemical) 1:2,000. In Study 2, we examined the distribution of *Fos*-activated noradrenergic, serotonergic, or cholinergic neurons. Cells were stained for *Fos*, and either DβH, 5-HT, or ChAT using fluorescent immunohistochemical techniques (Noga et al., 2009, 2011). Sections were incubated 48 h in rabbit polyclonal anti-*Fos* IgG (PC38-100U: Oncogene Research Products/Calbiochem, San Diego, CA, United States) 1:2,500. Sections were then incubated for 48 h in either mouse monoclonal anti-DβH IgG (MAB308: Chemicon International, Temecula, CA, United States) 1:500, rat

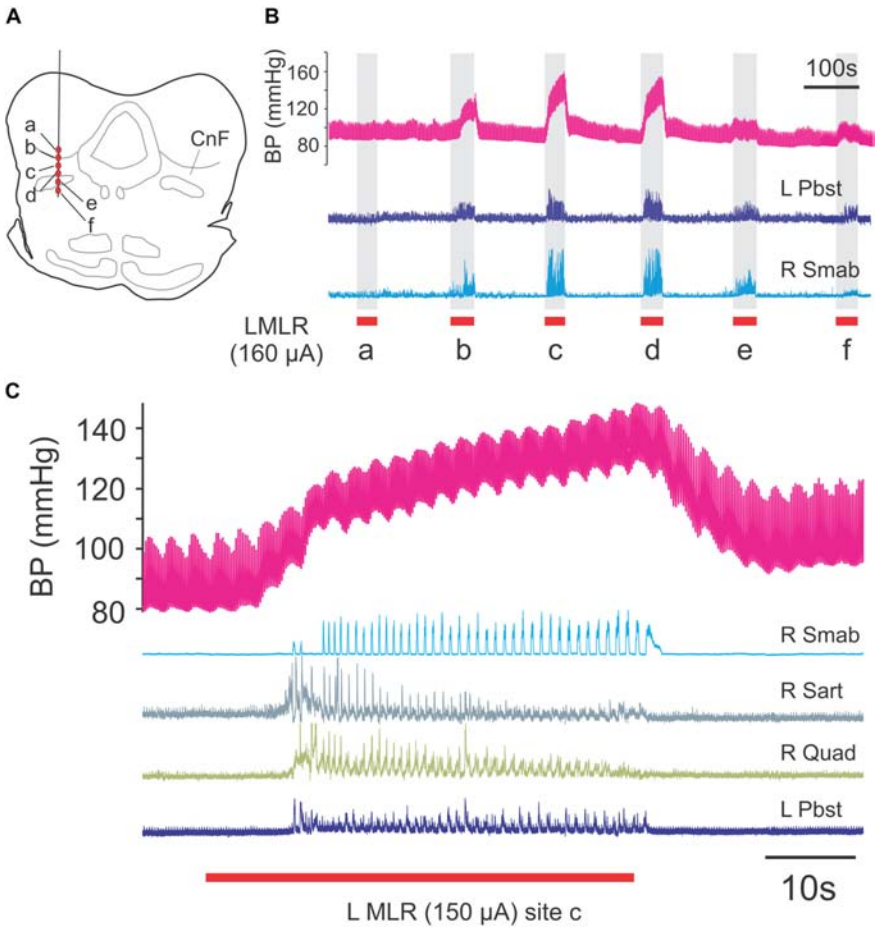


FIGURE 2 | Mapping of locomotor responses to electrical stimulation of the MLR and surrounding region of the midbrain. Stimulation of CnF and SubCnF sites **(A)** produces largest locomotor and pressor responses **(B)** in neuromuscular paralyzed and artificially ventilated decerebrate cats. Note reduced ENG responses in ventral stimulation locations. Locomotion monitored by electroneurogram recordings from hindlimb peripheral nerves. Blood pressure responses measured from indwelling catheter (carotid artery). **(C)** Locomotor and pressure responses to stimulation of site *c*. Low amplitude pressor responses (~0.4 Hz) result from artificial respiration of the animal. R, right; L, left; Pbst: posterior biceps/semitendinosus; Smab, semimembranosus/anterior biceps; Sart, sartorius; Quad, quadriceps.

monoclonal anti-5-HT IgG (MAB352: Chemicon International, Temecula, CA, United States) 1:100, or goat polyclonal anti-ChAT IgG (AB144P: Millipore) 1:100. Each secondary antibody was conjugated to a different fluorophore (Molecular Probes-Invitrogen, Carlsbad, CA, United States): Alexa 488 (green) for *Fos* (1:500; goat anti-rabbit, A-11008), Alexa 594 (red) for DβH (1:500; goat anti-mouse, A-11005), Alexa 594 for 5-HT (1:200; goat anti-rat; A-11007), and Alexa 594 for ChAT (1:200; donkey anti-goat).

Data Analysis and Interpretation

Anatomical landmarks from sagittal or coronal brainstem sections were identified using an atlas of the cat brainstem (Berman, 1968). The location of the stimulation sites were determined from depth measurements taken from the surface of the IC of the electrode along the reconstructed electrode tracks and also from a small electrolytic lesions made in the MLR prior to perfusion. For DAB experiments, sections were examined under a light microscope, and cellular architecture, as well as locations of labeled cells, were drawn using a camera lucida. For co-localization experiments, sections were examined with Zeiss Axioline microscopes using fluorescence microscopy. Cells were mapped using Neurolucida software. Cell counts were done using stereologic cell counting methods (Stereo Investigator 5.0, Microbrightfield Bioscience, Inc., Williston, VT, United States) giving estimates of cell number per sections and or nuclei. Cell positions of labeled neurons were determined by reconstruction of individual images of each section at 10× power. Confocal microscopy (Zeiss LSM510, with Ar multiline and HeN1 564) was used for high power examination of the three-dimensional structure of selected cells. Noradrenergic, cholinergic, and serotonergic cells were scanned in a series of optical sections and three-dimensional reconstructions were digitized. Serotonergic innervation of *Fos*-labeled reticular neurons (Di Prisco et al., 1994; Antri et al., 2008) was assessed using criteria previously established for spinal locomotor activated neurons (Noga et al., 2009).

RESULTS

Locomotion was evoked by stimulation of the MLR for a period of 2.5–5.5 h in four animals (FL-1, FL-2, FL-3, and TL-1; **Table 1**). In three animals (FL-1, FL-2, and TL-1), MLR stimulation was confined to one side (Study 1). In FL-3, both sides were stimulated during the testing period (Study 2). Control animals received the same surgical procedures as the locomotor test animals, except that they were not subject to the full locomotor task. Most control animals (FC-1, FC-2, FC-4, and TC-1) could produce locomotion with MLR stimulation but were only briefly stimulated. Sub-optimal sites were stimulated only briefly during the search for low threshold sites (see the section "Materials and Methods"), limiting their possible contribution to overall *Fos* expression. Two animals (FC-3 and TC-2) were neither stimulated nor had stimulating electrodes inserted.

Study 1: *Fos*-Labeled Cells in the Brainstem

Sagittal sections of the brainstems from two fictive locomotion animals (FL-1 and FL-2), one treadmill locomotion (TL-1), and five control animals (FC-1–3, TC-1, and TC-2) were stained for *Fos* using the DAB method and examined under the microscope. Representative photomicrographs illustrating the appearance of *Fos*-labeled neurons in the CnF and the SubCnF region (bcm) from FL-2 cat are shown in **Figure 3A**.

Locomotor Experiments

In animals subject to the locomotion protocol, the best locomotor responses were observed with stimulation within the CnF and SubCnF region (bcm), dorsal to the BC (**Figure 2**). At the frequencies used (15–20 Hz), the response produced by stimulation in more ventral sites including the BC and/or PPT was either of lower amplitude or consisted of erratic or tonic nerve activity. Stimulation of the MLR invariably increased blood pressure during the stimulation period, the amplitude of which was highest during stimulation of the best locomotor points (**Figure 2**). Stimulation strengths adjusted to maintain locomotor bouts over long periods of time ranged between 50 and 160 μA.

The distribution of *Fos*-labeled neurons from three locomotor animals is presented in **Figures 3** (FL-2) and 4 (FL-1 and TL-1). Overall, the distribution of labeled cells within fictive and treadmill locomotor animals was similar, indicating that *Fos* expression is governed more by the central drive than by afferent feedback. Labeled neurons were observed in several brainstem nuclei and were typically greater in number on the side of stimulation. (1) CnF: large numbers of cells were labeled in the CnF on the side of stimulation (*insets*, **Figures 3**, **4**). Fewer cells

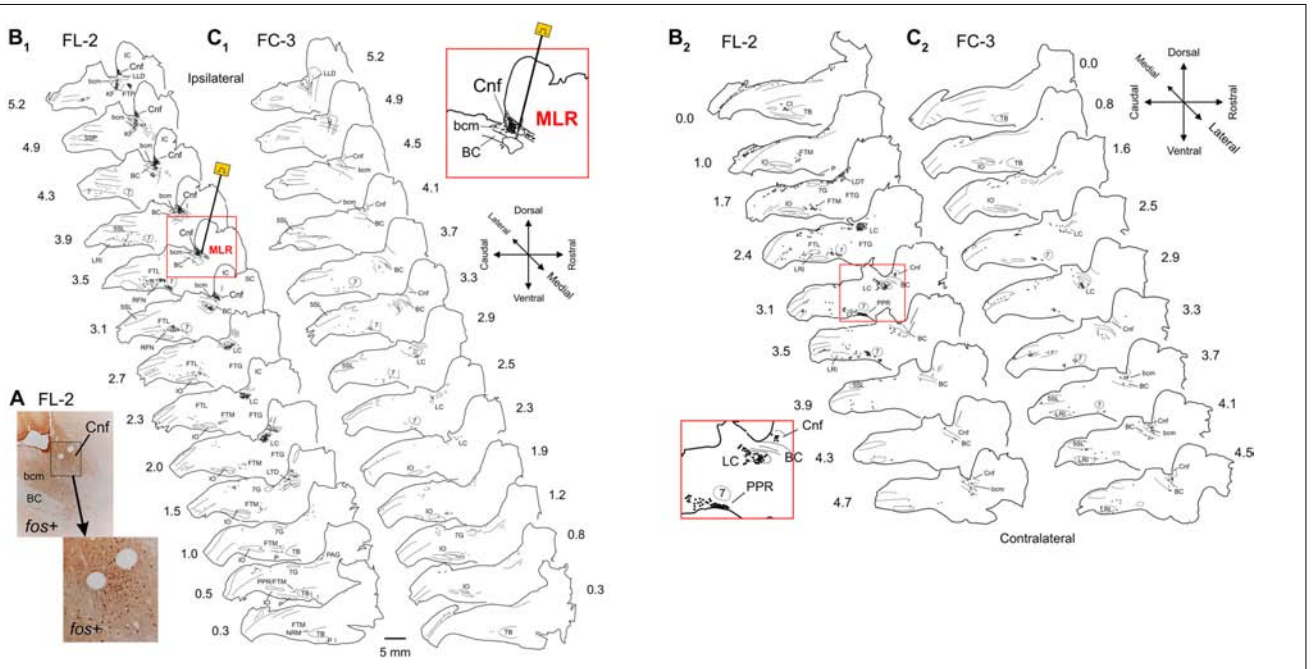


FIGURE 3 | Distribution of *Fos* labeled neurons in the brainstem of a MLR-evoked fictive locomotor cat compared to non-locomotor control cat.
(A) Photomicrographs illustrating the appearance of *Fos* labeled neurons near the stimulation electrode in the CnF and SubCnF region. Inset: higher magnification image of indicated area. **($B_{1,2}$,$C_{1,2}$)** Camera lucida drawings showing distribution of *Fos* immunoreactive neurons in brainstem of fictive locomotor cat FL-2 and non-locomotor control cat FC-3, respectively. Images in **(B_1)** and **(B_2)** show distribution on side ipsilateral and contralateral to the stimulating electrode (indicated in sagittal section at 3.5 mm from midline), respectively. Images in **(C_1)** and **(C_2)** show distribution on right and left sides of the brainstem, respectively. Note dense labeling within the CnF, the bcm of the SubCnF region, the locus ceruleus (LC), the lateral tegmental field (FTL), the magnocellular tegmental field (FTM), and the parapyramidal region (PPR). Labeling was more robust on side of stimulation. Control animals show relatively low numbers of labeled cells. Each diagram includes all labeled cells from single sections at the indicated levels. Each dot represents one labeled cell in this and other figures. Insets: higher magnification of MLR stimulation site in **(B_1)** (lateral 3.5 mm) and LC/FTL/PPR region in **(B_2)** (contralateral 3.1 mm). Anatomical structures labeled in this and other figures are listed under Abbreviations.

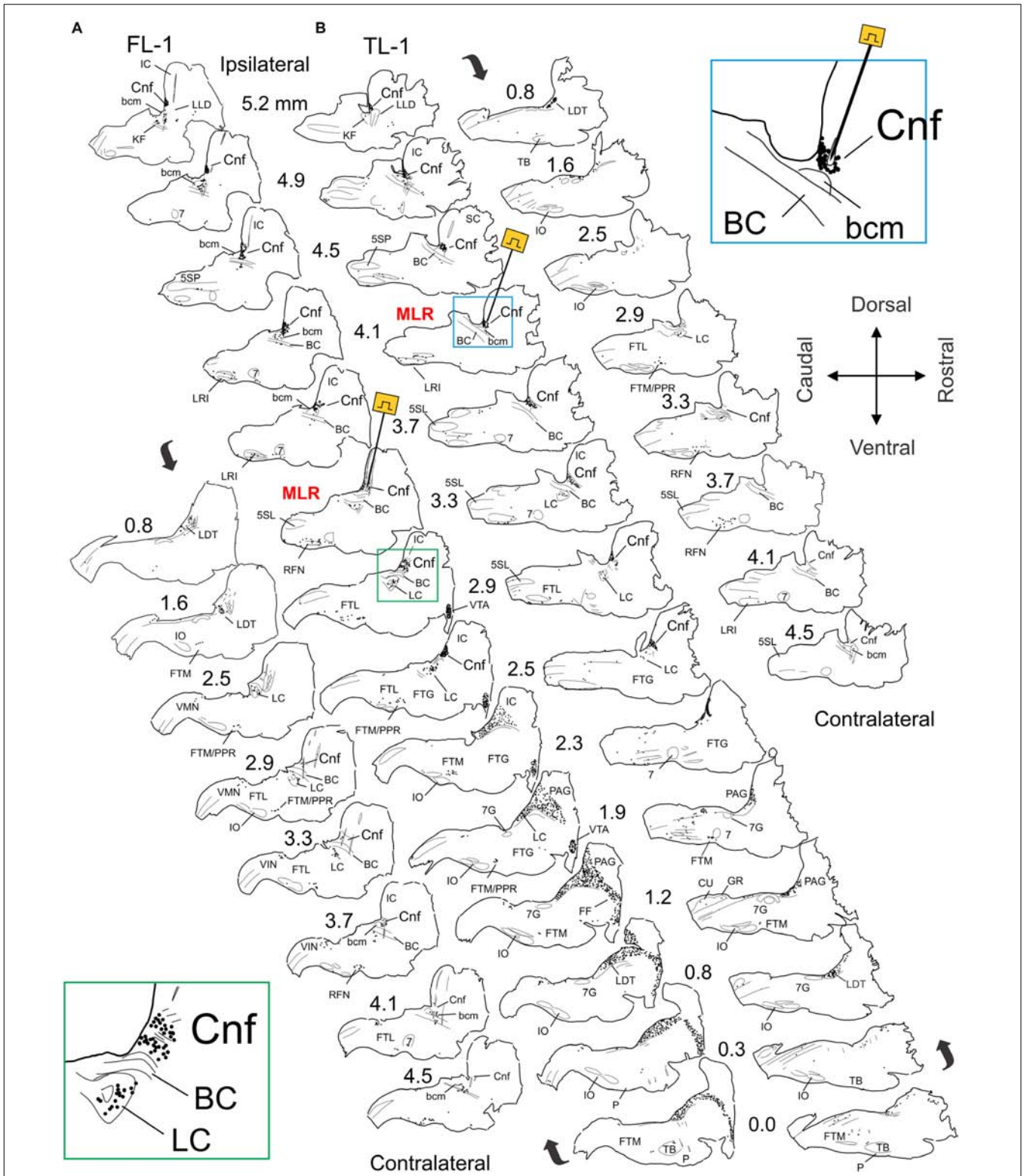


FIGURE 4 | Distribution of *Fos* labeled neurons in the brainstem of MLR-evoked fictive locomotor cat 1 (FL-1) and treadmill locomotor cat 1 (TL-1). **(A,B)** Camera lucida drawings showing distribution of *Fos* immunoreactive neurons in brainstem. Site of MLR stimulation electrodes indicated in sagittal sections at 3.3 and 4.1 mm lateral to midline for FL-1 **(A)** and TL-1 **(B)**, respectively. Note dense labeling within the CnF, bcm, the laterodorsal tegmental nucleus (LDT), the LC, the FTL, the FTM, and the PPR in both animals. Strong labeling was also observed in the periaqueductal gray (PAG) and ventral tegmental area (VTA) of FL-1 and less so in the PAG of TL-1. Labeling was more robust on side of stimulation. Insets: higher magnification of CnF/LC region in FL-1 (**A:** ipsilateral 2.9 mm) and MLR stimulation site in TL-1 (**B:** lateral 3.5 mm).

were observed in the contralateral CnF (e.g., FL-1; **Figure 4**). (2) bcm: cells in the bcm of the SubCnF region were labeled in all animals. (3) LC: cells in the LC were labeled bilaterally in all locomotor cats (**Figure 4**, *inset*). (4) KF: labeled cells were found bilaterally in the area of the KF. (5) PPT: a small group of labeled cells located rostral to the bcm and KF, in lateral sections on the side of stimulation (lateral L4.3–5.2) was seen in cat FL-2 (**Figure 3B**$_1$) but not cats FL-1 and TL-1 (**Figure 4**). *Fos*+ neurons were also observed more caudally in an area medial and ventral to the BC. The phenotype(s) of these neurons is not clear without ChAT immunostaining (Garcia-Rill et al., 1987) and cells in this area overlap with cells of the LC. (6) Laterodorsal tegmental nucleus (LDT): *Fos*+ cells were observed in the LDT on the ventromedial border of the caudal ventrolateral PAG in all locomotor animals (**Figure 3B**$_1$ – L0.5–1.5 and **Figures 4A,B** – L0.8–1.2). (7) PAG: many *Fos*-labeled neurons of the ipsilateral PAG were labeled at-level and rostral to the site of stimulation in FL-Cat1 (**Figures 3B1,2**, **4A,B**). A small number of cells within the PAG of TL-1 was also labeled. (8) FF: a column of *Fos*+ cells extended rostrally and ventrally from the PAG (**Figure 4A** – L0–1.2) through the central gray and the FF toward the VTA of FL-1. (9) The VTA of Tsai was labeled on the side of stimulation of cat FL-1 (**Figures 3B1,2**, **4A,B** – L1.9–2.9). It was not possible to evaluate the contralateral VTA since tissue along the cut edge of the brain (decerebration) was contaminated with blood cells. (10) FTL: numerous cells were labeled bilaterally in the FTL (L4.0–2.0) in all locomotor animals (**Figures 3B**, **4A,B**). Most cells were located in an area bounded rostrally by the facial nucleus (7N), caudally by the LRI, and ventrally by the inferior olivary nucleus (IO) (**Figure 3B**$_2$, *inset*). Few, if any, cells were found in the LRI or the trigeminal nuclei (5SL and 5SP). Around L3, the length of this cell column shortened and was concentrated in the medulla near the ponto-medullary junction. The labeled cells in this area overlapped the areas occupied by the AMB and the RFN. (11) FTM: *Fos*-labeled cells were found bilaterally in an area immediately caudal to the TB and rostral to the IO from about L0.5 to 2.0 at the ponto-medullary junction in all locomotor animals. Some labeled cells also appeared in an area just dorsal to the TB. Cells toward the midline were in the region of the NRM and obscurus (NRO). (12) Dorsal medulla: a small group of cells located bilaterally in the dorsal medulla was labeled in locomotor cats (**Figures 3B**, **4A,B**). Most of the cells were located in the area of the NTS, the dmnV, and the vestibular nuclei (VLN) (VIN, VMN) (L1–3.5). (13) CU and GR: a few labeled neurons were observed in the CU and GR of TL-1 (**Figure 4B**, L1.2) but not in FL-1 and FL-2. (14) Central canal: a strip of labeled neurons were observed surrounding the central canal in caudal brainstem sections of FL-2 (**Figure 3B**$_1$) but was not observed in FL-1 and TL-1.

Non-locomotor Control Experiments

Limited labeling in the various brainstem nuclei was seen in control animals, including those that were stimulated only briefly to ensure that the brainstem health was comparable to locomotor animals. Many hours elapsed between this brief locomotor bout and perfusion (**Table 1**) to minimize *Fos* expression in the Control animals. Labeling was not observed in the CnF nucleus of FC-3 (**Figures 3C1,2**), the non-stimulated control, although sparse labeling was seen in the bcm. This animal was representative of the other fictive locomotion cats and showed higher numbers of labeled cells in comparison to treadmill control animals (**Figure 5A**). The increased numbers of cells in the fictive-control animals as compared with the treadmill-control animals is most likely due to the additional sensory input produced by the nerve dissection surgery and placement of the animals in the spinal frame.

Comparisons of the Number of Labeled Cells in Locomotor and Control Animals

Fos labeling in the brainstem, MedRF, and LC of locomotor animals was much higher than that seen in their respective controls (**Figure 5**). In locomotor animals, the total number of labeled cells was highest in FL-1. This was primarily due to the large number of labeled cells within the PAG, although there was a scattering of labeled cells in the PAG of TL-1 (**Figure 4**: 1.9 and 1.2 lateral to midline). Inspection of panels from **Figures 3**, **4** show that the number of labeled cells was also greater on the side of stimulation than on the opposite, unstimulated side. This is shown for the LC of locomotor animals in **Figure 5C**.

Study 2: Phenotyping of *Fos*-Labeled Cells in the Brainstem

A second set of experiments were done combining *Fos* IHC with staining for either DβH, ChAT, or 5-HT to identify noradrenergic, cholinergic, and serotonergic neurons, respectively. As in Study 1 animals, the best locomotor responses were obtained with stimulation within the CnF and SubCnF region (bcm), dorsal to the BC. Four-limbed locomotion was evoked by stimulation of both sides of the brainstem, either separately or together to maintain locomotor bouts lasting upward of 100 min at a time for a total of 262 min. Stimulation in more ventral sites failed to induce coordinated locomotion and instead evoked erratic or tonic nerve activity. The brainstem viability was comparable in control (FC-4) and locomotor (FL-3) cats since the control animal was also capable of four-limbed locomotion, but was stimulated only briefly (∼1 min), 8 h before perfusion.

DβH/*Fos* Immunohistochemistry

Dopamine-beta-hydroxylase IHC was used to quantify the number of noradrenergic neurons in midbrain and pons activated during MLR-evoked lcocomotion. Numerous noradrenergic neurons were observed in the LC, SubC, and KF of both locomotor and control animals. Noradrenergic neurons were medium-sized oval, fusiform, or round (**Figures 6A–D**). Maps of *Fos*- and/or DBH-stained neurons within the brainstems of locomotor and control cats are illustrated in **Figures 6E,F**.

Locomotor experiment

As observed in Study 1 animals, abundant *Fos*-labeled neurons were observed in the CnF (sites of stimulation), the bcm or SubCnF region, FTC, PAG, LDT, LC, SubC, and KF of cat FL-3. *Fos*+ cells were generally symmetrically distributed in this bilaterally stimulated animal. Fewer neurons were labeled in the

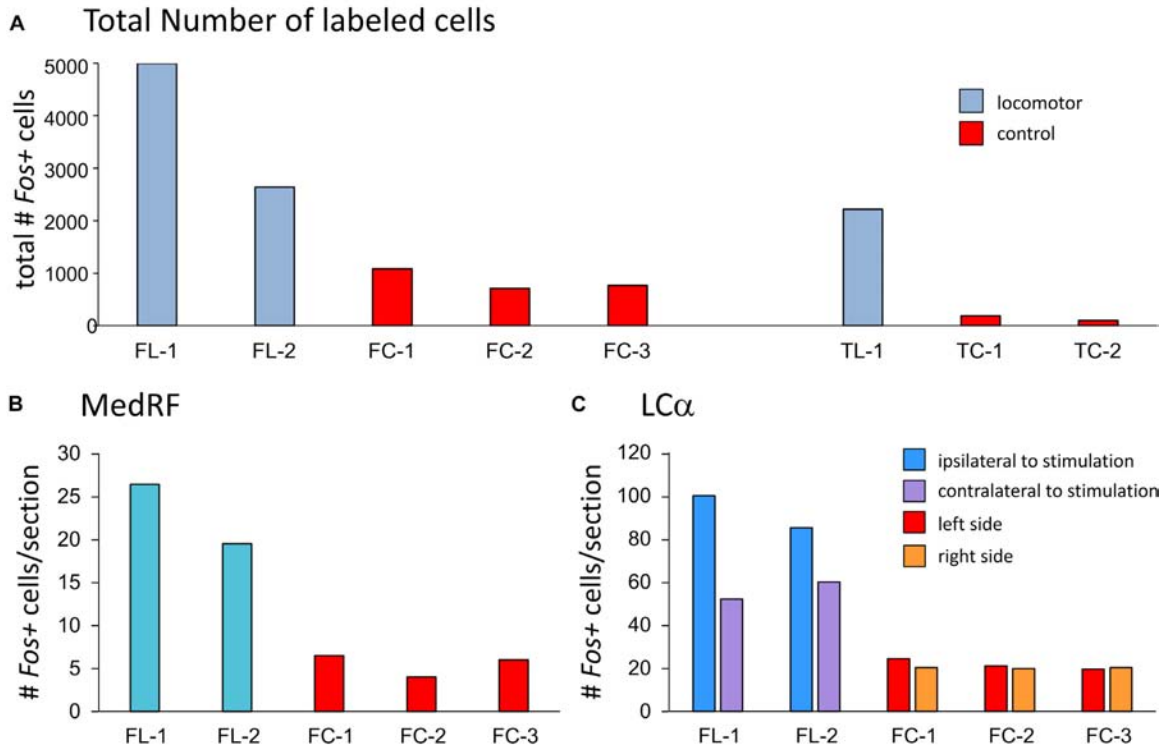


FIGURE 5 | Comparisons of numbers of *Fos*-labeled cells within the brainstem, MedRF, and locus ceruleus alpha (LCα) of MLR-evoked locomotor and control cats. The total number of labeled cells in both fictive and treadmill locomotor animals exceeds that observed in respective control animals **(A)**. Likewise, the number of *Fos*+ cells/section within the MedRF **(B)** and LCα **(C)** was consistently much higher that observed in control animals. The number of *Fos*-labeled cells/section in the LCα was higher on the side of stimulation.

superior (SC) and IC pontine FTL and FTG (**Figure 6E** – P4 and P5). Large numbers of *Fos*+ neurons in the LC/SubC and KF stained positive for DβH (**Figures 6A–D**), indicating that many of the Fos+ labeled cells in the LC region in Study 1 were likely noradrenergic (**Figure 5C**). While the majority of *Fos*+ noradrenergic neurons were located 1–2 mm away from the sites of stimulation, a scattering of *Fos*+ noradrenergic neurons were also observed in the parabrachial region nearer to the electrode stimulation site, as reported previously (Steeves et al., 1976).

Non-locomotor control

Like Study 1, few *Fos*-labeled cells were observed in the control animal (**Figure 6F**) than in the locomotor animal (**Figure 6E**). Furthermore, relatively few noradrenergic neurons in the control animal showed *Fos* expression. Interestingly, *Fos* co-expression in some sections was slightly higher on the side of the stimulation used to demonstrate that the control animal was capable of MLR-evoked locomotion.

Distribution of Fos-labeled DβH neurons

The rostro-caudal distribution of *Fos*+ cells observed in the brainstem of locomotor (FL-3) and control (FC-4) cats is illustrated in **Figure 7A**. In FL-3, the greatest number of *Fos*+ cells was found between P0.5 and P3.3, with a peak at P1.6 near the MLR stimulation site located at P1.8 (note that the electrolytic lesion used to mark the stimulation sites likely resulted in an underestimate of the number of *Fos*+ cells at that level). This represented a 6–144-fold increase in the number of *Fos*+ cells compared to the control animal. At more caudal levels (P3.7–5.0), the number of *Fos*-labeled neurons in the locomotor animal was 3–10 times greater than the control. The number of *Fos* immunoreactive noradrenergic neurons was also dramatically increased in the locomotor animal compared to the control (**Figure 7B**). The largest number of *Fos*+/DβH cells in FL-3 was found between P2.25 and P4.0 and peaked at P3.3 where all three noradrenergic nuclei (LC, SubC, and KF) were present. Between P2 and P4, ∼75–100% of noradrenergic cells showed *Fos* co-expression. In contrast, relatively few noradrenergic neurons between P2-4 showed *Fos* labeling in the control animal (0–37%).

ChAT/*Fos* Immunohistochemistry

Choline acetyltransferase IHC was used to quantify the number of cholinergic neurons in midbrain and pons activated during MLR-evoked locomotion. Numerous cholinergic neurons were observed in the PPT, LDT, trochlear (4), and motor trigeminal (5M) nuclei of both locomotor and control animals. The neurons were medium-sized, irregular multipolar shaped. Photomicrographs taken from single sections through the LDT and PPT of cat FL-3 are illustrated in **Figures 8A–D**. Maps of *Fos*- and/or ChAT-stained neurons within the brainstems of locomotor and control cats are

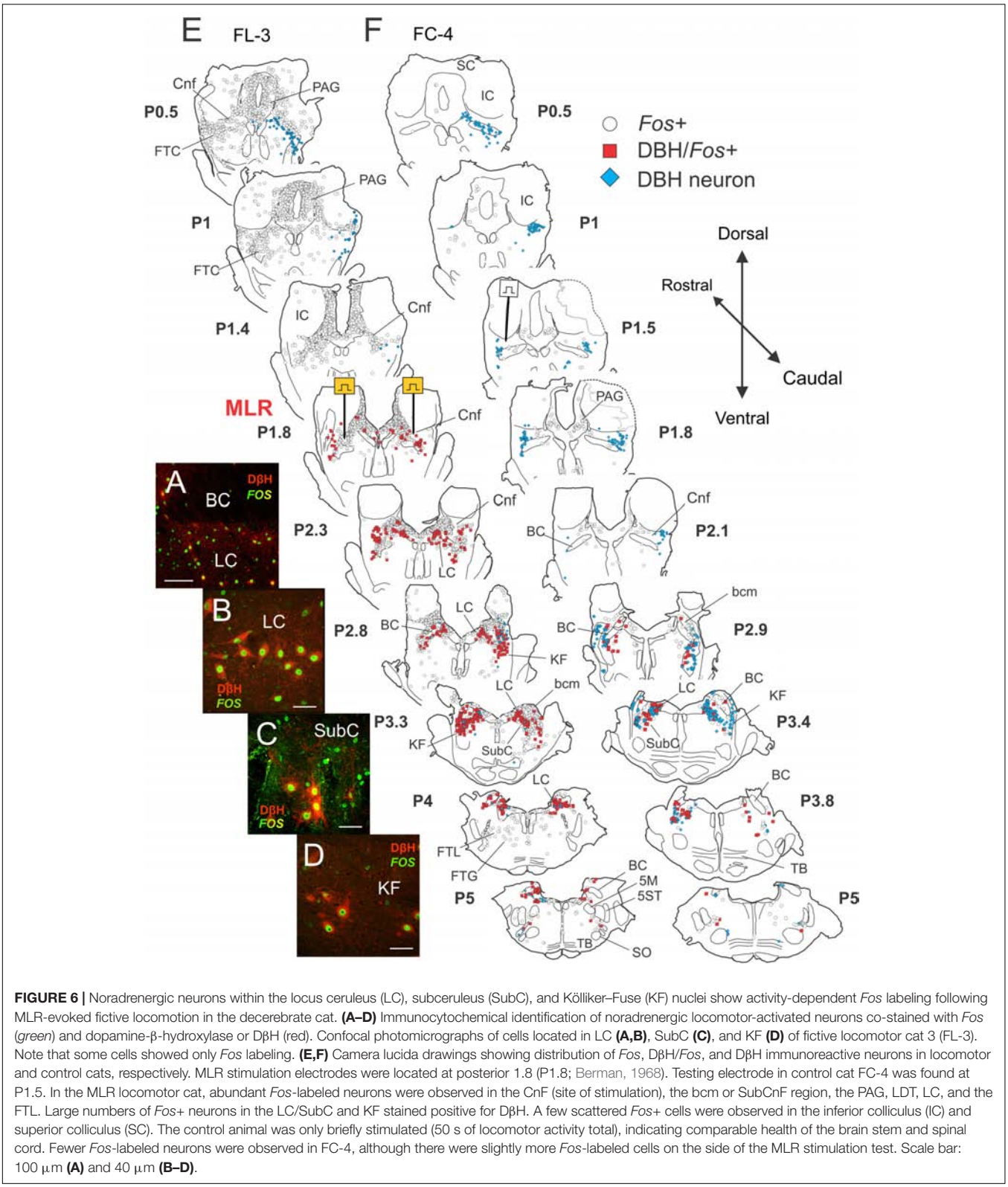


FIGURE 6 | Noradrenergic neurons within the locus ceruleus (LC), subceruleus (SubC), and Kölliker–Fuse (KF) nuclei show activity-dependent *Fos* labeling following MLR-evoked fictive locomotion in the decerebrate cat. **(A–D)** Immunocytochemical identification of noradrenergic locomotor-activated neurons co-stained with *Fos* (*green*) and dopamine-β-hydroxylase or DβH (red). Confocal photomicrographs of cells located in LC **(A,B)**, SubC **(C)**, and KF **(D)** of fictive locomotor cat 3 (FL-3). Note that some cells showed only *Fos* labeling. **(E,F)** Camera lucida drawings showing distribution of *Fos*, DβH/*Fos*, and DβH immunoreactive neurons in locomotor and control cats, respectively. MLR stimulation electrodes were located at posterior 1.8 (P1.8; Berman, 1968). Testing electrode in control cat FC-4 was found at P1.5. In the MLR locomotor cat, abundant *Fos*-labeled neurons were observed in the CnF (site of stimulation), the bcm or SubCnF region, the PAG, LDT, LC, and the FTL. Large numbers of *Fos*+ neurons in the LC/SubC and KF stained positive for DβH. A few scattered *Fos*+ cells were observed in the inferior colliculus (IC) and superior colliculus (SC). The control animal was only briefly stimulated (50 s of locomotor activity total), indicating comparable health of the brain stem and spinal cord. Fewer *Fos*-labeled neurons were observed in FC-4, although there were slightly more *Fos*-labeled cells on the side of the MLR stimulation test. Scale bar: 100 μm **(A)** and 40 μm **(B–D)**.

illustrated in **Figures 8E,F**. At their most rostral location, PPT neurons were observed more ventrolaterally within the tegmentum. Caudally, PPT neurons were observed loosely scattered around or ventral to the BC in areas occupied by noradrenergic neurons stained in other adjacent sections (**Figures 6E,F**).

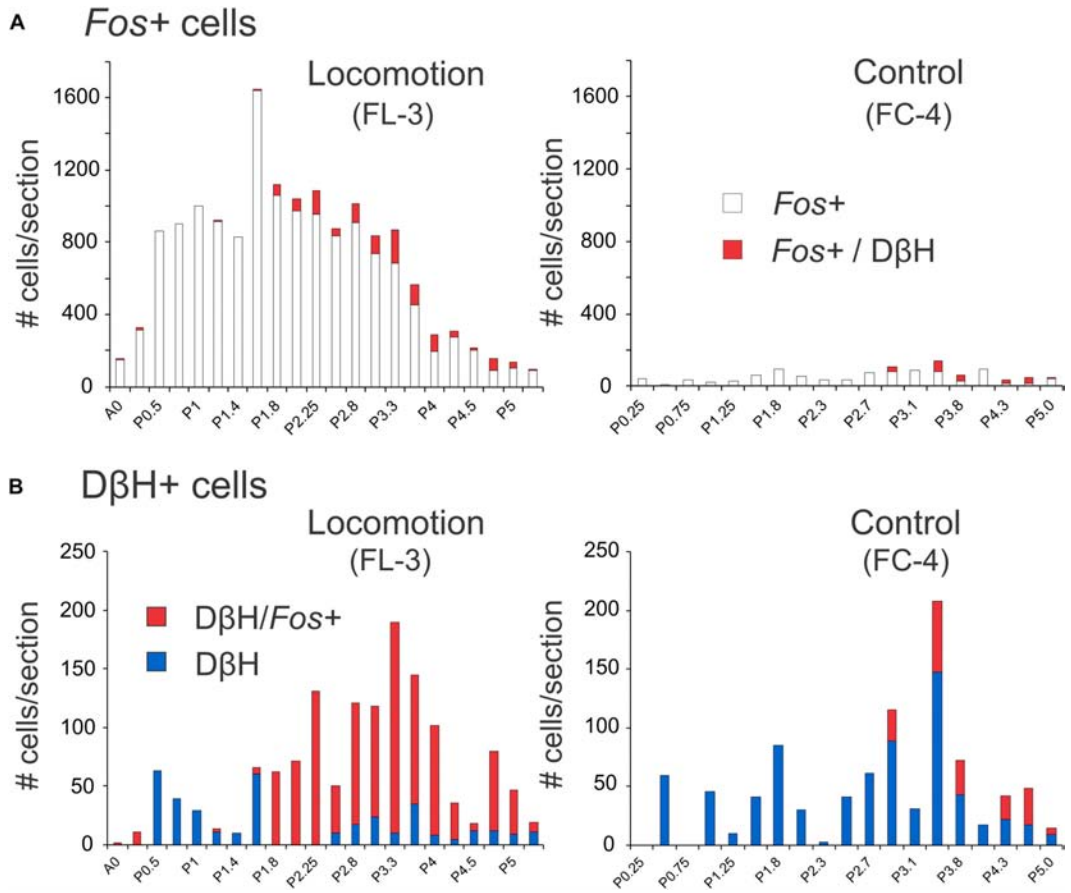


FIGURE 7 | Distribution of *Fos*+ neurons with or without co-labeling with DβH in the midbrain and pons following bilateral stimulation of the MLR. **(A)** The number of *Fos*-labeled cells increased tremendously in FL-3 compared to the non-locomotor control animal (FC-4). **(B)** Noradrenergic neurons showed dramatic increases in *Fos* expression in the locomotor animal. Numeration includes all labeled cells from single sections at the indicated levels.

Locomotor experiment

As observed in sections stained for *Fos* and DβH (**Figures 6E,F**), a large number of *Fos*-labeled neurons were observed in the CnF (sites of stimulation), bcm, PPT, FTC, PAG, LDT, LC, SubC, and KF. Caudally, a few neurons were labeled in the FTL and FTG (**Figure 8E** – P5.5 and P6). Relatively few cholinergic PPT neurons, however, stained positive for *Fos* (**Figure 8E**). Cholinergic PPT neurons were located ventral to sites producing the best locomotor response to electrical stimulation. In the LDT, a number of cholinergic neurons also stained positive for *Fos*. This group of cells accounted for about 50% of the double-labeled cholinergic neurons in the locomotor animal. Cholinergic motoneurons in cranial nerve nuclei [trochlear nucleus (4) and motor trigeminal nucleus (5M)] did not stain for *Fos*.

Non-locomotor control

As before, fewer *Fos*-labeled cells were observed in the control animal (**Figure 8F**) than in the fictive locomotor animal (**Figure 8E**). Likewise, few PPT cholinergic neurons showed *Fos* co-expression although there were a number of double labeled cells in the LDT. As in locomotor animals, no motor nuclei (4 and 5M) were double labeled.

Distribution of Fos-labeled ChAT neurons

The rostro-caudal distribution of ChAT and/or *Fos*+ cells in control and locomotor animals is shown in **Figure 9**. In FL-3, *Fos*+ cells peaked at P1.7 near the MLR stimulation sites (lesion visible at this level). This represented an approximately eightfold increase compared to the control. At more caudal levels (∼P2.4–4.2), the number of *Fos*-labeled neurons showed a two to sevenfold increase in the locomotor cat. The number of *Fos*-immunoreactive cholinergic neurons was slightly increased in the locomotor animal (**Figure 9B**), the increase split between cholinergic neurons in the PPT and LDT. This increase was much less than that observed for noradrenergic neurons within the same area (**Figure 7B**).

5-HT/*Fos* Immunohistochemistry

Numerous serotonergic neurons were observed in the NRM, pallidus (NRP), obscurus (NRO), and PPR of locomotor and control animals. Photomicrographs of serotonergic and non-serotonergic reticular (FTM) neurons taken from single sections of the brainstem of cat FL-3 are illustrated in **Figures 10A–D**. Serotonergic neurons were medium-sized, oval, or fusiform and in the PPR, were intermingled with

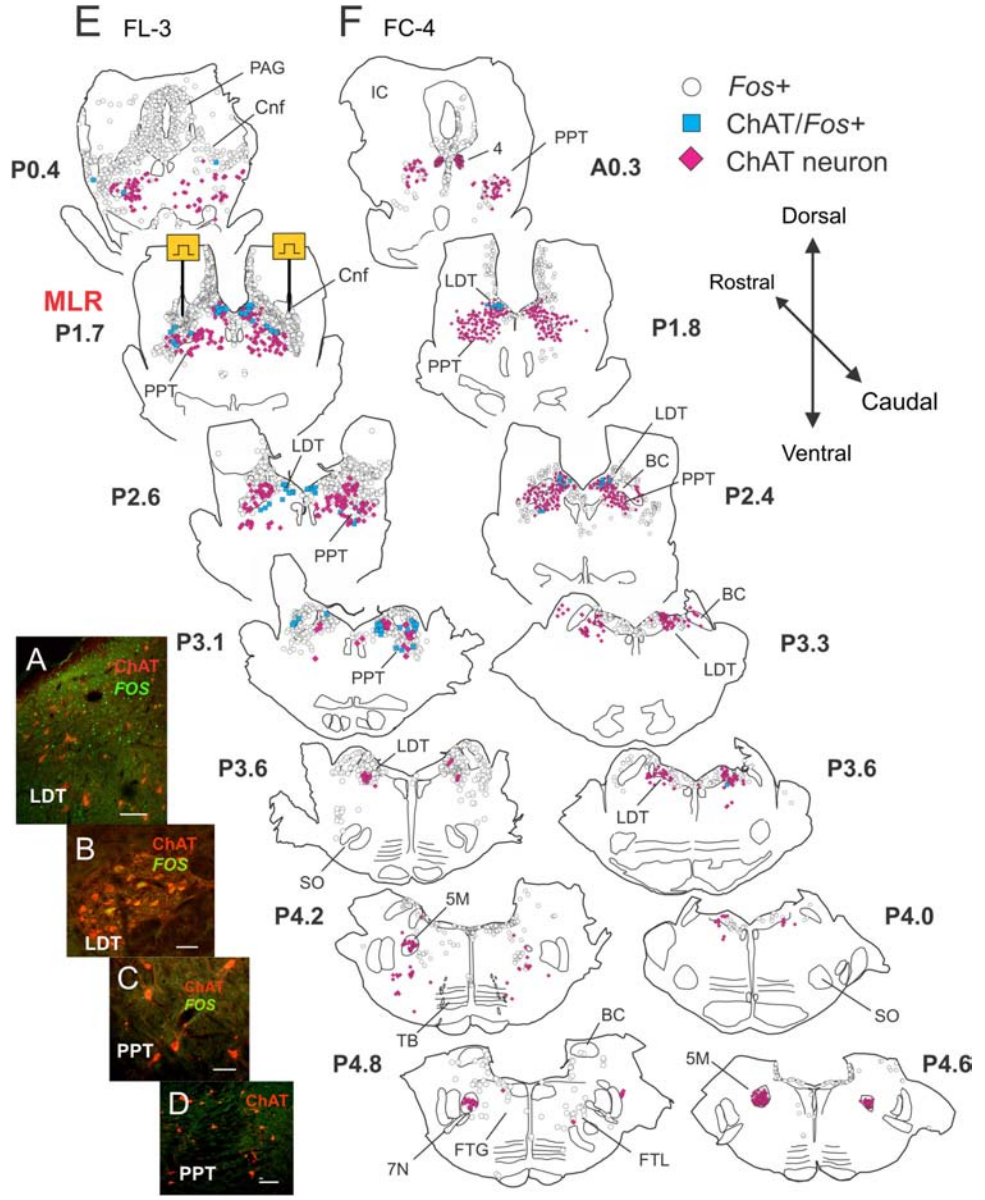


FIGURE 8 | Few cholinergic cells in midbrain and pons show activity dependent *Fos* labeling following MLR-evoked fictive locomotion in the decerebrate cat. **(A–D)** Confocal photomicrographs demonstrating *Fos* (*green*) and/or choline acetyltransferase (ChAT, *red*) immunoreactive cells in the brainstem between levels P0-5. Micrographs taken of cells located in the LDT **(A,B)** or PPT **(C,D)** of fictive locomotor cat FL-3. Few ChAT neurons in the PPT showed *Fos* labeling. **(E,F)** Camera lucida drawings showing distribution of *Fos*, ChAT/*Fos*, and ChAT immunoreactive neurons in locomotor FL-3 and control FC-4 cats, respectively. MLR stimulation sites, marked electrolytically, were located at approximately P1.7 (Berman, 1968) in FL-3. As in **Figure 4**, the MLR locomotor cat show abundant *Fos*-labeled neurons were observed in the CnF, bcm, PAG, LDT, LC, SubC, and the FTL. Some cholinergic neurons in the PPT and LDT (about equal numbers) showed *Fos* labeling although many non-cholinergic neurons in these areas also showed *Fos* expression. Relatively few *Fos*+ neurons were observed in the control animal. Scale bar: 100 μm **(A,D)** and 50 μm **(B,C)**.

other non-serotonergic neurons. In all areas of the medulla, serotonergic fibers formed a dense network surrounding many *Fos*-stained neurons (**Figure 10D**) and many cells in reticular and other areas appeared to be innervated by them (Noga et al., 2009). Maps of *Fos* and/or 5-HT stained neurons within the brainstems of locomotor and control cats are illustrated in **Figures 10E,F**.

Locomotor experiment

Many *Fos*-labeled cells were observed in the pons and medulla (P5.5–P14) following the locomotor task (**Figure 10E**). The distribution of these neurons was mostly symmetrical in this bilaterally stimulated animal. Abundant *Fos*-labeled neurons were found in the FTM, dorsal to the TB, and pyramids in a region laterally bounded by the superior olive (SO) and

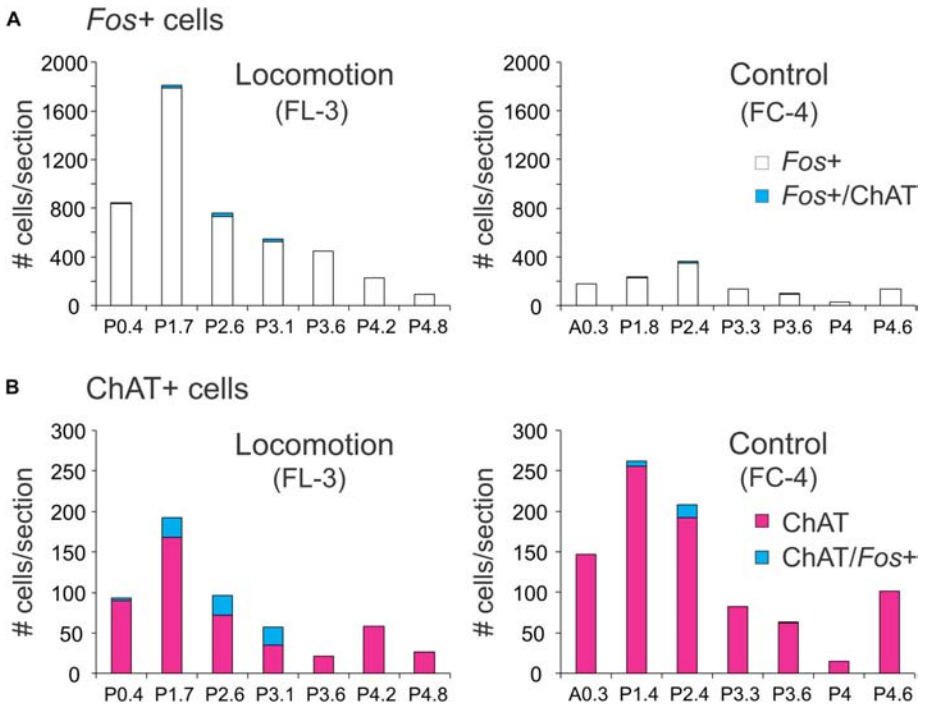


FIGURE 9 | Distribution of *Fos*+ neurons with or without co-labeling with ChAT in the midbrain and pons following bilateral stimulation of the MLR. **(A)** The number of *Fos*-labeled cells increased tremendously compared to the non-locomotor control animal. Relatively few *Fos*+ neurons were cholinergic. **(B)** Comparison of cholinergic neurons with or without *Fos* expression in the locomotor and control animals. Numeration includes all labeled cells from single sections at the indicated levels.

facial motor nucleus (7M). Relatively fewer cells were labeled in the FTG and more dorsally located FTL in this rostral area. This pattern of activated neurons corresponded with the MLR termination pattern described by Steeves and Jordan (1984). At the P8.5 level and caudally, ventrally located *Fos*+ neurons were found extending more laterally in the FTL. Numerous *Fos*+ neurons were also observed in the VMN and the VIN in rostral and caudal medulla. Relatively few labeled cells were observed within the lateral VLN. In caudal areas of the medulla, at the level of the inferior olivary nuclei (IO), large numbers of *Fos*+ cells were observed in the NTS of the dorsal respiratory group (DRG), the RFN of the VRG, the LRN, the RVLM, and the dmnV. Moderate labeling was observed in the FTM in caudal areas and scattered labeling of neurons were seen in the FTG. A small number of *Fos*+ cells was found within or bordering the AMB. Several serotonergic neurons in NRM were double labeled with *Fos*. Laterally, a large number of the serotonergic neurons within the PPR were also positive for *Fos* (P8.5).

Non-locomotor control

Like that observed in Study 1, maps constructed from brainstem segments in the control (FC-4) animal showed relatively few *Fos*-labeled neurons (**Figure 10F**). The difference between the control (**Figure 10F**) and fictive locomotor animals (**Figure 10E**) was striking. No serotonergic neurons in the control animal showed *Fos* labeling.

Distribution of Fos-labeled 5-HT neurons

The rostro-caudal distribution of 5-HT and/or *Fos*+ cells for control and locomotion experiments is shown in **Figure 11**. In the locomotor animal, the number of *Fos*+ cells/section found between P5.5 and P14 ranged from 250 to 684 and peaked at the P11 level in the caudal medulla (**Figure 11A**). In contrast, the number of *Fos*+ neurons/section in the control animal ranged between 7 and 64 neurons. At the peak level, this represented an approximately 34-fold increase in the number of *Fos*+ neurons in the locomotor animal compared to control. At other levels this increase ranged from 8- to 43-fold. Serotonergic immunoreactive boutons were found in close contact with many of these *Fos*+ neurons (**Figure 11A**). Overall, the percentage of *Fos*+ cells contacted by serotonergic fibers was ∼60% (**Figure 7B**) with a range between 25 and 83%. The number of *Fos*-immunoreactive serotonergic neurons was increased in the locomotor animal compared to control (**Figure 11B**). The largest number of *Fos*+/5-HT cells was found at P8.5 at the level of the NRM and PPR. At this level, 38.5% of serotonergic neurons expressed *Fos* protein. In contrast, no serotonergic neurons between P5.5 and P14 in the control animal expressed *Fos*.

Overview of labeled cells in locomotor and control animals – Study 2

The distribution of brainstem *Fos*+ neurons in control and animals subject to MLR-evoked fictive locomotion is plotted in **Figure 12**.

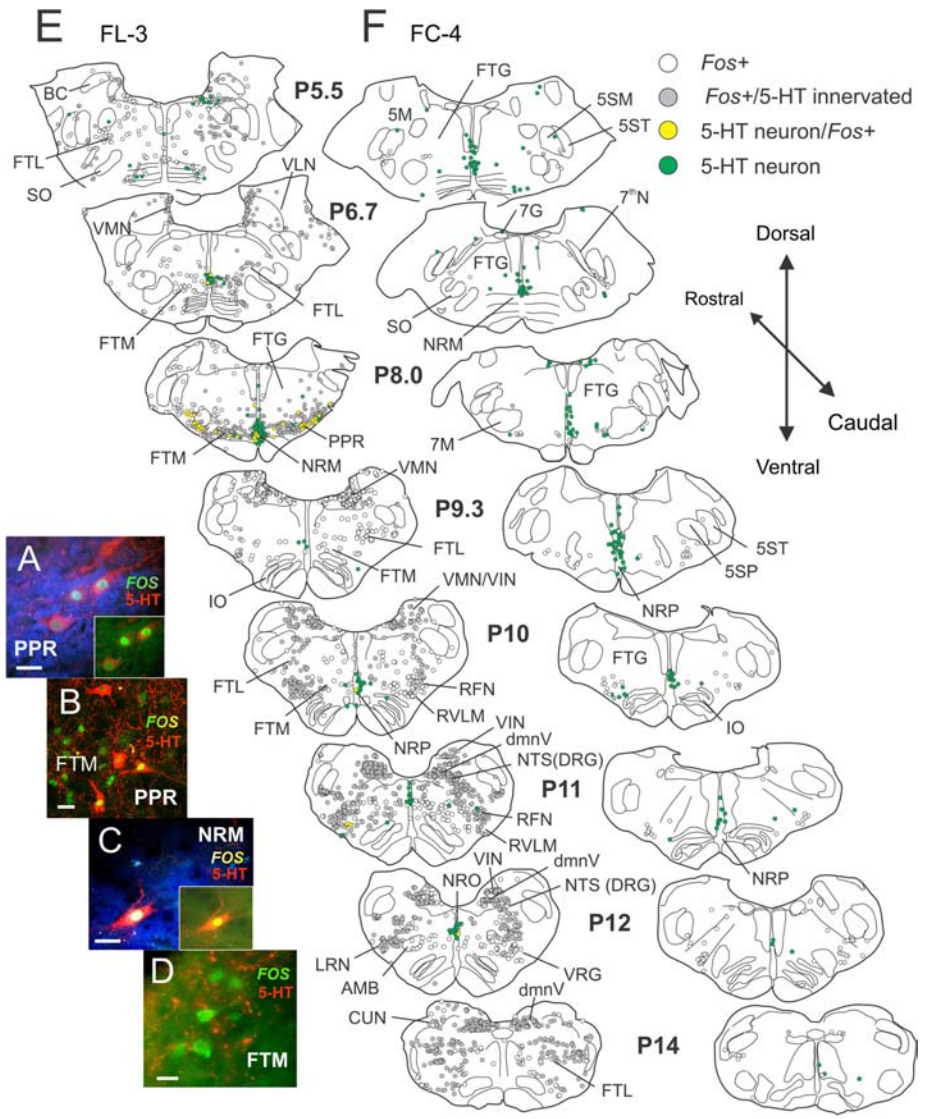


FIGURE 10 | Locomotor activated pontomedullary neurons: serotonergic cells within the raphe and parapyramidal region show activity-dependent *Fos* labeling following MLR-evoked fictive locomotion in the decerebrate cat. **(A–D)** Confocal photomicrographs of locomotor-activated neurons from FL-3 showing *Fos* nuclear labeling (*green*) with and without cytoplasmic co-localization of 5-HT (*red*). Photomicrographs taken from FTM, PPR, and nucleus raphe magnus (NRM). Micrographs enhanced (blue background) in **(A)** and **(C)** to better illustrate fine serotonergic fibers and varicosities in surrounding neuropil (insets show original micrographs). Note that *Fos*+ cells in the FTM (and other regions of the reticular formation) are surrounded by a dense network of serotonergic fibers, likely making close contacts with the neurons. **(E,F)** Camera lucida drawings of single sections between posterior levels P5.5–14 showing distribution of *Fos*, 5-HT/*Fos*+, and 5-HT immunoreactive neurons in locomotor FL-3 and control FC-4 cats, respectively. *Fos* neurons with serotonergic contacts (gray) are indicated. In the MLR locomotor cat, abundant *Fos*-labeled neurons were observed in the FTM, FTL, PPR, NRM, medial vestibular nucleus (VMN), inferior vestibular nucleus (VIN), dorsal motor nucleus of the vagus (dmnV), rostral ventrolateral medulla (RVLM) and the nucleus tractus solitarii (NTS), and retrofacial nucleus (RFN) of the dorsal respiratory and ventral respiratory groups (DRG and VRG), respectively. Many locomotor-activated neurons in the PPR and NRM were positive for 5-HT. Few *Fos*+ neurons were observed in the control animal. Scale bar: 20 μm **(A–C)**; 10 μm **(D)**.

DISCUSSION

General Observations and Limitations of the Study

In the present experiments we have documented the location of brainstem neurons activated during MLR-evoked locomotion in the precollicular–postmammillary decerebrate cat and examined their correspondence to serotonergic, noradrenergic, and cholinergic phenotypes. Fictive locomotion experiments were conducted to determine the activation pattern produced from centrally driven locomotor pathways. Due to the nature of these experiments, most of the data presented in this study is on individual animals, with some minor differences seen between animals; however, the differences demonstrated between

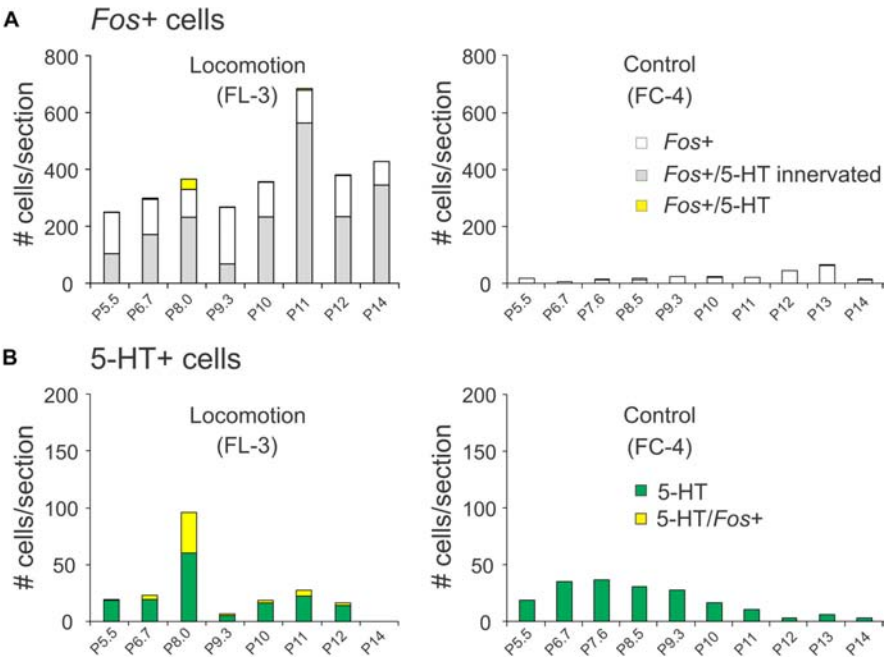


FIGURE 11 | Distribution of *Fos*+ neurons with or without co-labeling with 5-HT in the pons/medulla following bilateral stimulation of the MLR. **(A)** The number of *Fos*-labeled cells increased tremendously compared to the non-locomotor control animal. A small number of *Fos*+ neurons were serotonergic. **(B)** Comparison of serotonergic neurons with or without *Fos* expression in the locomotor and control animals. Most serotonergic neurons within the PPR were positive for *Fos*. Numeration includes all labeled cells from single sections at the indicated levels.

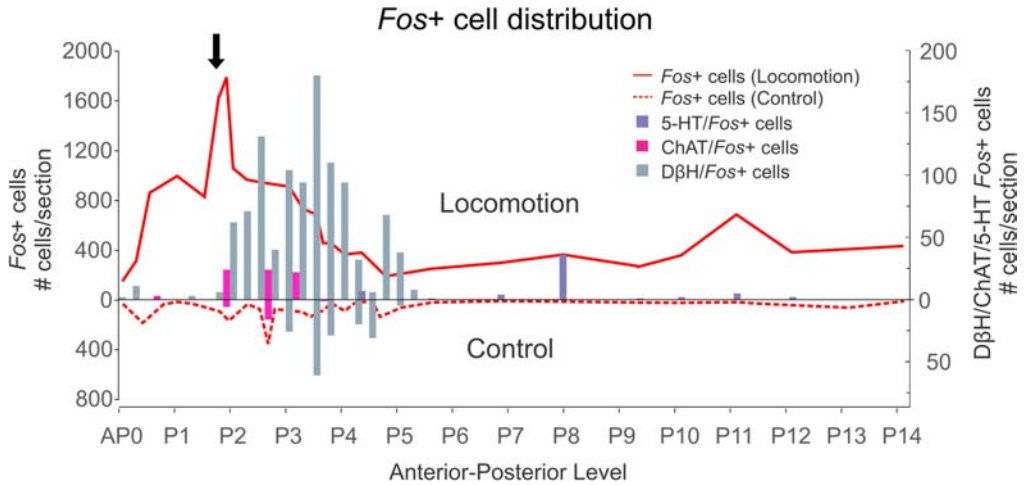


FIGURE 12 | *Fos*+ cell distribution within brainstem following MLR-evoked fictive locomotion. Numeration includes all labeled cells from single sections at the indicated AP levels. The numbers of activated neurons in locomotor and control animals are indicated above and below the *X*-axis, respectively. Scale bar for noradrenergic, cholinergic, and serotonergic neurons indicated on right side of diagram. MLR stimulation level is indicated by *arrow*. Data from FL-3 and FC-4.

MLR-stimulated and control animals was strongly significant. The results provide evidence in support of the idea that the anatomical equivalent of the MLR is the CnF and/or SubCnF region rather than the cholinergic PPT (Jordan, 1998; Takakusaki et al., 2016). Furthermore, it shows that MLR stimulation activates both reticular and monoaminergic neurons in parallel, providing anatomical and functional validation for centrally mediated monoaminergic neuromodulation of spinal locomotor circuitry during evoked locomotion (Noga et al., 2009, 2011, 2017). Lastly, the results also show that MLR stimulation activates neurons within vestibular, cardiovascular, and respiratory areas. Overall, these results demonstrate a complex neuromodulation

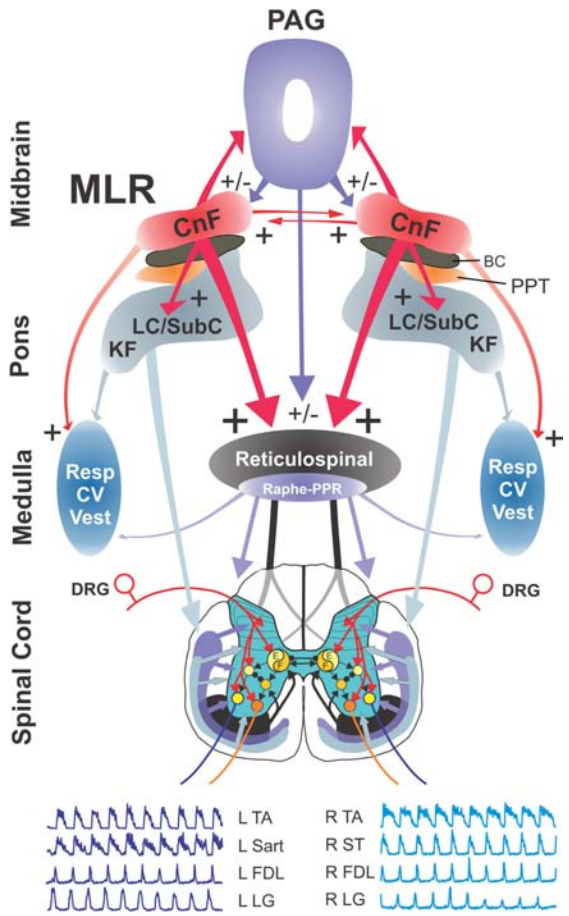


FIGURE 13 | Model of brainstem pathways for initiation of locomotion in the cat. Relationships between the various components of the pathway activated by the MLR, the spinal central pattern generator for locomotion (CPG), and their output motoneurons for bilateral hindlimb locomotion. The model incorporates parallel activation of descending RS and neuromodulatory pathways originating in the catecholaminergic and serotonergic nuclei of the pons and medulla, in addition to the facilitation of cardiorespiratory and vestibular centers during locomotion. Glutamatergic neurons within the CnF and SubCnF region form the primary phenotype for initiation and control of locomotion (Caggiano et al., 2018; Josset et al., 2018). Glutamatergic PPT neurons may contribute to the initiation of low speed locomotion (Caggiano et al., 2018) although this is disputed (Josset et al., 2018). Cholinergic neurons do not initiate locomotion but may play a modulatory role for ongoing locomotion (Roseberry et al., 2016; Caggiano et al., 2018; Josset et al., 2018) possibly by their effects on other brainstem output neurons. RS neurons of the magnocellular reticular formation, which form the final common motor pathway of the brainstem, relay the central command for initiation of locomotion to the spinal locomotor central pattern generator ultimately activating hindlimb motoneurons (Shefchyk et al., 1984; Noga et al., 2003; Jordan et al., 2008). The model also incorporates known projections between CnF/MLR nuclei on each side of the midbrain (Edwards, 1975; Steeves and Jordan, 1984). At the spinal level, flexor (F) and extensor (E) components of the locomotor pattern generator are activated/modulated by descending bilateral RS and monoaminergic projections as well as by crossed excitatory (►) and inhibitory (●) segmental projections from the generator opposite to it. Details of the rhythm and pattern components of the locomotor generator are omitted to emphasize general interconnections between them and their target neurons. Electroneurograms: FDL, flexor digitorum longus; LG, lateral gastrocnemius; Sart, sartorius; ST, semitendinosus; TA, tibialis anterior. R, right; L, left.

pattern of brainstem neurons that integrate the kinematic, dynamic, and metabolic facets of locomotor activity induced by electrical stimulation.

Mesencephalic Locomotor Region

Historically, two adjacent nuclei, the CnF and the PPT, have been proposed as putative structural correlates of the MLR and two schools of thought have emerged in support of one or the other nucleus. Much of the preclinical literature, including Shik et al. (1966) original description, has supported the more dorsally located CnF, where electrical mapping studies consistently show it to promote locomotion (Takakusaki et al., 2003). Others have favored the more ventral, cholinergic cell-containing PPT (Garcia-Rill et al., 1986, 1987, 2011), despite its more varied electrical mapping results (Takakusaki et al., 2003, 2016). Data from the present study are discussed below with respect to this and other recent studies of this area of the midbrain.

Cuneiform Nucleus and the Sub-Cuneiform Region

The lowest electrical threshold sites for initiation of locomotion in the present study were found within the boundaries of the CnF nucleus and SubCnF region, thereby defining the MLR (see also Takakusaki, 2008, 2013; Takakusaki et al., 2016). Extensive labeling of neurons in these sites was observed, the majority of which are likely glutamatergic (Mena-Segovia et al., 2009; Wang and Morales, 2009). Cells in these areas are consistently labeled in studies examining locomotor activated neurons with *Fos* IHC (e.g., Silveira et al., 1995; Brudzynski and Wang, 1996; Iwamoto et al., 1996; Lamprea et al., 2002; Ferreira-Netto et al., 2005). Recent optogenetic studies show that glutamatergic CnF neurons are capable of initiating locomotion at short latencies, through a range of gait patterns and speeds (Roseberry et al., 2016; Capelli et al., 2017; Caggiano et al., 2018; Josset et al., 2018). Importantly, it is glutamatergic mesencephalic reticular formation neurons, including regions of the CnF, SubCnF, and PPT, that are activated during treadmill locomotion and which may code for locomotor speed (Roseberry et al., 2016; Caggiano et al., 2018). Cholinergic neurons, in contrast are characterized by repetitive, slow firing (Takakusaki et al., 1996). In non-human primates, rhythmically active cells are preferentially located in more dorsal CnF and SubCnF locations than tonically activated ones (Goetz et al., 2016). These latter cells are located within a region with higher densities of choline acetyl transferase labeled (cholinergic) neurons, corresponding to the PPT. GABAergic CnF neurons (Mena-Segovia et al., 2009; Wang and Morales, 2009) cannot initiate locomotion and rather, block locomotion when activated (Roseberry et al., 2016). If they were activated by electrical stimulation in the present study, their influence was overcome by activation of other neurons.

Pedunculopontine Tegmental Nucleus and Other Cholinergic Nuclei

The classically defined cholinergic PPT nucleus has long been considered a component of the MLR (Garcia-Rill et al., 1986, 1987, 2011) but the role of cholinergic PPT neurons in locomotion is controversial. In the present study, we examined neuronal *Fos* expression in the area encompassing

the PPT and the adjacent cholinergic nucleus, LDT. Cholinergic neurons of the PPT and LDT were distributed within the mesopontine tegmentum as described previously (Jones and Beaudet, 1987). These neurons were not co-extensive with the low threshold locomotor producing sites within the CnF and SubCnF. Based on the known anatomical projections of the CnF and SubCnF (Steeves and Jordan, 1984; Caggiano et al., 2018) and on anticipated but limited current spread, stimulation of these low threshold MLR sites would be expected to activate some cells within this area of the tegmentum. However, relatively few cholinergic PPT/LDT neurons were activated compared to non-cholinergic *Fos*+ neurons (**Figures 8E**, **9**). Overall, this data support the growing body of evidence that cholinergic neuron activation does not play a principal role in MLR-evoked locomotion. This is consistent with our study showing that cholinergic antagonists fail to block MLR-evoked locomotion in decerebrate cats (Jordan et al., 2014) and data from Takakusaki et al. (2016) showing that electrical stimulation of PPT results in a muscarinic-sensitive motor inhibition. Selective deletion of the vesicular acetylcholine transporter also does not abolish open field locomotion nor affect locomotor coordination but may result in hyperactivity and balance problems in mature animals (Janickova et al., 2017). The results are also consistent with recent studies in rodents which show that optogenetic stimulation of cholinergic PPT neurons does not elicit locomotion in stationary animals (Roseberry et al., 2016; Caggiano et al., 2018; Josset et al., 2018). Cholinergic neurons may, however, modulate ongoing locomotion, producing accelerating (Roseberry et al., 2016) or decelerating effects on locomotor speed (Caggiano et al., 2018; Josset et al., 2018). This modulation is unlikely to result from co-release of glutamate or GABA (Roseberry et al., 2016; see also Wang and Morales, 2009) and could be the result of cholinergic action on neurons of the substantia nigra pars compacta (SNc) and VTA (see the section "Ascending Pathways") (Dautan et al., 2016; Xiao et al., 2016), CnF (Jin et al., 2016), and/or reticular formation (Tebēcis, 1973; Shiromani et al., 1990; Smetana et al., 2010). Within the LDT, a small, but similar number of cholinergic neurons also stained positive for *Fos* (**Figures 8A,B,E**). The LDT is thought to play a role in arousal, eye movements, learning and reward, visual orienting, and sensory-motor patterns, possibly via projections to the VTA and SNc (Wang and Morales, 2009; for review, see Martinez-Gonzalez et al., 2011).

Non-cholinergic neurons within the PPT, LDT, and adjacent area (Jones and Beaudet, 1987; Usunoff et al., 2003; Wang and Morales, 2009) were also activated by electrical stimulation of the MLR. Photo-activation of glutamatergic PPT neurons is reported to induce low-speed locomotion from rest in a subset of trials (∼50%), but with long onset latency and requiring high frequency (50 Hz) stimulation (Caggiano et al., 2018). This has led to the suggestion that glutamatergic PPT neurons may be involved in explorative locomotor behavior (Caggiano et al., 2018). In support of this suggestion, these authors have shown that both the CnF and the PPT glutamatergic neurons project predominantly ipsilaterally, to locomotor areas of the MedRF (Noga et al., 2003). In a different study, however, glutamatergic PPT cell activation not only failed to initiate locomotion, it also decelerated and stopped ongoing locomotion (Josset et al., 2018; see also Takakusaki et al., 2016). Partial or complete lesions of the PPT (affecting all neuronal types) also fail to result in gait deficits (Gut and Winn, 2015) indicating that such modulatory effects on locomotion are likely compensated for by other modulatory systems. Further careful electrophysiological studies are needed to establish the role for the PPT.

Although more concentrated within the rostral pole of the PPT (Pienaar et al., 2017), GABAergic PPT neurons cannot initiate locomotion and rather, block locomotion when activated (Roseberry et al., 2016; Caggiano et al., 2018). If they were activated by electrical stimulation in the present study, their influence was minimal.

Ascending Pathways

Fos expression was elevated in the ipsilateral PAG (**Figure 4A**), an important mediator of defensive behavior including escape locomotion (Koutsikou et al., 2017). More ventrally, labeling was observed within the FTC, FF, and VTA in a sagittaly continuous band of activated neurons. Bilateral MLR stimulation produced symmetrical *Fos* expression (**Figures 6E**, **8E**) within the PAG and FTC, and may be the activation pattern for rectilinear locomotion with balanced bilateral MLR activity (Noga and Opris, 2017b; see the section "Asymmetry in Brainstem Circuits"). This functional connectivity is consistent with anterograde tracer studies targeting the MLR and/or the CnF nucleus (Edwards, 1975; Edwards and de Olmos, 1976; Steeves and Jordan, 1984; Sotnichenko, 1985). The strong interconnection of the CnF, PAG (Edwards and de Olmos, 1976; Mantyh, 1983; Steeves and Jordan, 1984; Sotnichenko, 1985; Ferreira-Netto et al., 2005; Dampney et al., 2013; Caggiano et al., 2018), and the limbic system (see Koutsikou et al., 2017) indicates that the MLR plays an important role in the integration of complex motor behaviors related to defensive behavior (Sinnamon, 1993; Jordan, 1998).

Neurons within the VTA showed increased *Fos* activity (**Figure 4A**). The VTA contains dopaminergic neurons involved in goal-directed behavior and reinforcement-learning (Wise, 2004). It receives a direct input from non-catecholaminergic neurons of the PAG (Suckow et al., 2013) and from cholinergic and glutamatergic neurons of the PPT and LDT (Mena-Segovia and Bolam, 2017). Stimulation of cholinergic PPT terminals within the VTA activates dopaminergic neurons and transiently increases locomotor activity (Dautan et al., 2016). In contrast, LDT cholinergic neuron activation decreases locomotion (Dautan et al., 2016) and results in reward reinforcement (Xiao et al., 2016). These differential effects are likely due to actions on different neurons within the VTA. PPT glutamatergic neurons also increase arousal and drive motivated behavior via ascending projections, in part to the VTA (Kroeger et al., 2017; Yoo et al., 2017).

Descending Pathways

Reticular Formation

The major output pathway of the brainstem for activation of locomotor circuits is the RS pathway originating in the rostral

medulla (Orlovskii, 1970; Garcia-Rill et al., 1983; Shefchyk et al., 1984; Steeves and Jordan, 1984; Garcia-Rill and Skinner, 1987; Noga et al., 1988, 1991, 2003). In the present study, neurons in the nucleus reticularis magnocellularis (FTM) were the primary reticular neurons activated in this region, dorsal to the TB and pyramids. Relatively few neurons were labeled in the FTG, although more posteriorly we observed labeling within the FTL (**Figure 10**; P9.3) which gradually merged with areas corresponding to the cardiorespiratory regions of the caudal medulla (see the section "Coupling of Neuronal Networks"). An asymmetrical activation pattern was observed with unilateral stimulation of the MLR (**Figures 3–5**), mirroring the anatomical projection pattern of the MLR (Steeves and Jordan, 1984). The implications of this pattern are discussed below (see the section "Asymmetry in Brainstem Circuits").

One candidate RS neuron mediating MLR-evoked locomotion is the Lhx3/Chx10-expressing neuron in the mouse (Bretzner and Brownstone, 2013). These neurons are glutamatergic, are targets of MLR (CnF) projections, support tonic repetitive firing, project to the spinal cord, and are activated (express *Fos*) during wheel running or treadmill locomotion. They are found in the ventral and α (FTM in the cat) parts of the gigantocellular reticular nuclei (together termed α/vGRN or GiA/GiV). Optogenetic studies in mice have shown that activation of glutamatergic neurons within the LPGi, a caudal subgroup of the magnocellular nucleus, can also trigger continuous locomotion (Capelli et al., 2017). Neurons in this area harbor terminals of MLR (CnF/PPT) efferents and express *Fos* after locomotion (Capelli et al., 2017). Some neurons in this lateral subdivision of the FTM caudal to 7M were also labeled in the present study. However, MLR (CnF) projections in the cat do not extend much more caudally than 7M (Steeves and Jordan, 1984), indicating that activation of reticular neurons at more caudal levels may be indirect, via local circuits within the brainstem (Shimamura et al., 1980). Further studies are needed to clarify whether there are species differences that may account for these discrepancies (see also Caggiano et al., 2018).

Interestingly, a large percentage of the MedRF neurons were innervated by serotonergic fibers. Such innervation of variously sized cells in the reticular formation has been described before (Kobayashi et al., 1994; see also Gao and Mason, 1997; Viana Di Prisco) as well as for vestibular (Halberstadt and Balaban, 2003) and cardio-respiratory neurons (see the section "Coupling of Neuronal Networks"). The serotonergic innervation of RS neurons may thus provide the basis for a neuromodulatory influence of 5-HT on brainstem circuits (Takakusaki et al., 1993), in addition to its effects on spinal circuits for locomotion (see Schmidt and Jordan, 2000).

Monoaminergic Neurons

As discussed in the section "Introduction," monoamines play a key role in the activation of spinal locomotor networks. The present study now confirms that monoaminergic neurons are activated during MLR-evoked locomotion (**Figures 6**, **10**), with increased activity-dependent labeling of both catecholaminergic neurons of the LC, SubC, and KF nuclei and serotonergic neurons of the NRM and PPR. These nuclei are the primary source of the monoaminergic innervation of the spinal cord (Westlund et al., 1982; Clark and Proudfit, 1991a,b; Jones and Light, 1992). Monoaminergic neurons are likely activated by direct projections from the CnF and/or MLR (Edwards, 1975; Steeves and Jordan, 1984; Sotnichenko, 1985). Furthermore, both cerulear (Rasmussen et al., 1986) and raphe neurons are rhythmically active during overground locomotion (Veasey et al., 1995; Jacobs et al., 2002) and stimulation of the PPR in the neonatal rat also produces serotonergic receptor-dependent locomotor-like activity (Liu and Jordan, 2005). Taken together with our observation that stimulation of the MLR results in the spinal release of 5-HT and NE (Noga et al., 2017), these results provide the anatomical basis for the central control of locomotor activity by 5-HT and NE, in the absence of peripheral afferent feedback from moving limbs. Thus, in addition to RS command neurons (see the section "Reticular Formation"), monoaminergic neurons comprise a major component of the central descending pathways controlling locomotion.

Coupling of Neuronal Networks

Cells in other brainstem nuclei show increased activity-dependent labeling following MLR-evoked locomotion. These include nuclei of cardiovascular, respiratory, and vestibular systems (**Figure 10**). Several studies have demonstrated that locomotor and respiratory rhythms are centrally coupled (DiMarco et al., 1983; Millhorn et al., 1987; Perségol et al., 1988; Kawahara et al., 1989, 1993; Ezure and Tanaka, 1997). Respiratory and cardiovascular networks are also coupled through peripheral feedback (Iwamoto et al., 1996) and/or central interconnections between the different pattern generators (Dick et al., 2009; Le Gal et al., 2014). Here we present functional and anatomical evidence for a central coupling of locomotor, respiratory, and cardiovascular networks (DiMarco et al., 1983; Eldgridge et al., 1985; Bell, 2006; Wienecke et al., 2015) as well as activation of neurons within the medial VLN following stimulation of the MLR. While most of the nuclei of the cardiovascular, respiratory, and vestibular systems in the cat are not directly innervated by the CnF/MLR (Edwards, 1975; Steeves and Jordan, 1984), other nuclei receiving projections from the MLR (e.g., monoaminergic system, see below) may act as intermediaries to modulate their activity.

Respiratory Nuclei

In the present study, stimulation of the MLR increased *Fos* expression in nuclei involved in respiratory control, including neurons in the NTS, RFN, and LRN of the dorsal and VRGs. Other nuclei that may modulate respiratory activity under specific conditions also showed increased *Fos* expression in the present study. These included neurons within the raphe/PPR region, LC, SubC, KF, PPT, and PAG. Although respiratory responses to MLR stimulation were not monitored in these animals, previous work has shown that stimulation of the hypothalamic and MLRs facilitate respiration (Eldgridge et al., 1981; DiMarco et al., 1983; Millhorn et al., 1987; Kawahara et al., 1989; Ezure and Tanaka, 1997). Serotonergic neurons from the raphe nuclei and parapyramidal region project to the

dorsal (Voss et al., 1990) and ventral respiratory column and may also contribute to central chemoreception and respiratory control (Ribas-Salgueiro et al., 2005; DePuy et al., 2011; Morinaga et al., 2019). Evidence of their involvement in control of breathing in the present study comes from the observation that serotonin-immunoreactive boutons were found in close apposition to many of these neurons (see also Voss et al., 1990). LC and KF nuclei are also involved in the control of breathing (Dutschmann and Herbert, 2006; Gargaglioni et al., 2010; Dutschmann and Dick, 2012; Barnett et al., 2018). Effects are likely mediated by noradrenergic (Magalhães et al., 2018) or glutamatergic projections (in the case of the KF) (Herbert et al., 1990; Ezure and Tanaka, 2006; Yokota et al., 2007; Geerling et al., 2017). The major source of cholinergic innervation of the brainstem regions controlling breathing is from the PPT and LDT (Kubin and Fenik, 2004) and neurons from these nuclei may thus have contributed to the activation of medullary respiratory-related neurons in the present experiments (Chatonnet et al., 2003). Lastly, respiratory activity may be modulated by the PAG; indirectly through its projections to the CnF (from the dlPAG); or directly by projections to the parabrachial complex, midline medulla, and VRG (from the dmPAG, lPAG, and vlPAG; see Dampney et al., 2013).

Cardiovascular Nuclei

Stimulation of the MLR invariably increased blood pressure (**Figure 2**) and *Fos* expression in nuclei associated with cardiovascular regulation (**Figure 10**). Consistent with this observation, stimulation of the CnF in the anesthetized rat increases arterial blood pressure in the absence of locomotion. The effect on blood pressure may be mediated by activation of sympathoexcitatory neurons in the RVLM (Verberne, 1995), catecholaminergic neurons of the KF/parabrachial complex and LC (Lam et al., 1996; Shafei and Nasimi, 2011), the dorsal PAG (Lam et al., 1996), and/or serotonergic neurons of the caudal raphe nuclei (Lam and Verberne, 1997; DePuy et al., 2011). Neurons within the parapyramidal region also project to cardiovascular-related nuclei (NTS) and may increase mean arterial blood pressure, independent of the RVLM (Helke et al., 1989). Interestingly, cholinergic systems may counteract the pressor effect of CnF stimulation by acting directly on nuclei known to produce hypotension (Shafei et al., 2013). Lastly, a role of the dorsolateral (sympathoexcitatory) and ventrolateral (inhibitory) PAG in the regulation of cardiovascular function has also been demonstrated (e.g., Carrive and Bandler, 1991; Lovick, 1992; Subramanian and Holstege, 2014) possibly via the FTM, raphe nuclei (Gao et al., 1997; Hermann et al., 1997), RVLM, or CnF (see Dampney et al., 2013).

Vestibular Nuclei

Vestibular signals are important in the regulation of balance (Shinoda et al., 2006) and contribute to cardiovascular and respiratory regulation during movement (McCall et al., 2017). In the present study, *Fos* labeling was observed in the VMN and VIN, areas important for stabilization of the head during movement (Cullen, 2012). Relatively few neurons within the lateral VLN were labeled. Orientation and movement of the head in the walking cat are active processes but reflexes appear to play only a partial role in determining head movement during walking, indicating that signals from the centrally generated locomotor synergy must be the main drivers for head movements (Zubair et al., 2016). In contrast, although vestibulospinal neurons within the VLN are rhythmically active during locomotion (Orlovsky, 1972; Matsuyama and Drew, 2000), their rhythmic activity likely reflects hindlimb and labyrinthine inputs during walking (Arshian et al., 2014) rather than centrally generated activity. Supporting this, bilateral lesions of the VLN in decerebrate cats do not interrupt MLR-evoked locomotion (Jell et al., 1985). The VLN are not directly innervated by projections of the MLR (Steeves and Jordan, 1984). Possible sources of activation of these nuclei (reviewed by McCall et al., 2017) in the reduced paralyzed preparation may include cerebellar (fastigial) nuclei (Takakusaki et al., 2016) or spinal interneurons (Noga et al., 2009, 2011) signaling locomotor activity. Interestingly, afferent inputs that may contribute to the vestibulo-cardiovascular and respiratory reflex relayed through the VMN and VIN originate in the medullary and pontine reticular formation, LRN, and raphe nuclei (Jian et al., 2005) and it is possible that activity in these nuclei from centrally driven locomotor inputs (this study; Zubair et al., 2016) could, via the VLN, further enhance cardiovascular and respiratory center activation (Stocker et al., 1997) in addition to those nuclei described above.

Asymmetry in Brainstem Circuits

As revealed in the present study, unilateral stimulation of the MLR produced an asymmetrical activation of brainstem neurons with *Fos* expression more commonly observed on the side of stimulation (**Figures 3–5**) even though bilateral locomotor activity was observed. This distribution reflects the anatomical projections of the MLR which are mostly uncrossed through the parabrachial region to the MedRF (Steeves and Jordan, 1984; see also Edwards, 1975; Sotnichenko, 1985). The results are consistent with the functional asymmetry of the RS output revealed by localized reversible cooling of the spinal cord in the decerebrate cat during fictive locomotion (Noga et al., 1995). Furthermore, they are consistent with electrophysiological studies which show that the majority of activated RS neurons project through the ventral funiculus on the same side as the stimulated MLR (Garcia-Rill and Skinner, 1987) to terminate on ipsilateral lumbar spinal neurons in the intermediate zone and ventral horn (Holstege and Kuypers, 1982; Capelli et al., 2017). Although fewer, projections from the MLR to the contralateral reticular formation (Steeves and Jordan, 1984; Capelli et al., 2017) and contralaterally/bilaterally projecting RS neurons (Peterson et al., 1975; Garcia-Rill and Skinner, 1987) likely account for the activation of RS neurons on the side opposite to stimulation [this study; Noga et al., 1995; see Humphries et al. (2006, 2007) for a discussion of intrinsic reticular network connections]. Finally, crossed spinal (Holstege and Kuypers, 1982; Kausz, 1991) or segmental pathways (Jankowska and Noga, 1990; Kjaerulff and Kiehn, 1997;

Kremer and Lev-Tov, 1997; Matsuyama et al., 2004a) likely also contribute to the generation of bilateral locomotor activity with unilateral stimulation of the MLR. In such a way, secondary projection systems compensate for the anatomical asymmetry of the primary MLR projection. Thus, the spinal activation pattern produced by unilateral MLR stimulation is essentially symmetrical (Dai et al., 2005). While this experimental situation reveals the complex projections within brainstem and spinal cord, spontaneous locomotion likely would provide a more balanced descending output to the spinal locomotor centers (Noga and Opris, 2017b), reflective of the pattern of activation observed within the brainstem (**Figures 6**, **8**, **10**) and spinal cord (Noga et al., 2009, 2011) produced with bilateral MLR stimulation. In this situation, forward or rectilinear locomotion likely occurs through bilaterally symmetric commands transmitted by the MLR and RS pathways. In contrast, during turning movements, an asymmetric command may be generated and transmitted along RS pathways to modulate CPGs on one side. Such a command would need to overwhelm compensatory mechanisms from contralaterally projecting RS neurons and segmental commissural neurons (Noga et al., 2003; Matsuyama et al., 2004a). A theoretical model in mammals for symmetry breaking of rectilinear locomotion by adjusting the level of activity of components of the descending locomotor pathway has been presented (Noga and Opris, 2017b). In that model, steering of locomotor activity may be achieved by temporarily adjusting the balance of MLR and/or RS outputs – in essence, creating an asymmetrical drive on either side of the brainstem. Evidence in favor of such an organization at the RS level for steering of locomotor activity has recently been presented (Oueghlani et al., 2018).

Descending Pathway for Initiation of Locomotion

A new model of the descending pathway for the control of locomotion (after Noga et al., 2017) is presented in **Figure 13**, with the MLR representing a central node in the control of locomotion by higher brain centers. Data presented in the present study indicate that the anatomical locus of the MLR is the CnF/SubCnF region of the midbrain. Little evidence is found to support the participation of cholinergic neurons in the initiation of locomotion by electrical stimulation of this region, although a modulatory role of locomotor activity is possible (Roseberry et al., 2016; Caggiano et al., 2018; Josset et al., 2018). This is consistent with recent optogenetic studies that show that initiation of locomotor activity is primarily, if not exclusively, the result of activation of glutamatergic neurons within the CnF and SubCnf (Roseberry et al., 2016; Caggiano et al., 2018; Josset et al., 2018). The MLR is reciprocally connected with the contralateral MLR (Steeves and Jordan, 1984; Bayev et al., 1988) possibly facilitating/coordinating descending signal output on both sides of the brainstem, and with the PAG (Mantyh, 1983; Bayev et al., 1988; Sandner et al., 1992; Ferreira-Netto et al., 2005; Dampney et al., 2013; Caggiano et al., 2018) which may be important for the mediation of rapid defensive decision making or the mediation of locomotion during pursuit. Electrical stimulation of the MLR activates three primary brainstem targets affecting locomotor circuits within the spinal cord: RS, ceruleospinal and raphespinal. RS neurons located within the MedRF (FTM) comprise the primary "command pathway" for the initiation of locomotion (Shik et al., 1966, 1967; Orlovskii, 1970; Jordan, 1991; Noga et al., 2003). Glutamatergic RS neurons in this region activate spinal locomotor neurons (e.g., Douglas et al., 1993; Hägglund et al., 2010; Bretzner and Brownstone, 2013; Capelli et al., 2017). Activation of noradrenergic (LC, SubC, and KF) and serotonergic (NRM and PPR) neurons within the pons and medulla results in the rapid, widespread release of the neuromodulators NE and 5-HT in the spinal cord during locomotion (Noga et al., 2017). Central respiratory (Resp), cardiovascular (CV), and vestibular (Vest) neurons are also activated by MLR stimulation, either directly or indirectly (Voss et al., 1990; Nasimi et al., 2012; Damasceno et al., 2014), likely in anticipation of the increased metabolic and postural demands associated with locomotion. Additionally, MLR stimulation activates neurons within the PAG, an area important for mediating defensive behaviors (Deng et al., 2016).

The RS neurons of the MedRF (FTM) also have multiple inputs in addition to the MLR (Steeves and Jordan, 1984; Garcia-Rill and Skinner, 1987; Bretzner and Brownstone, 2013). They are innervated by the ipsilateral SLR (Sinnamon and Stopford, 1987; Takakusaki et al., 2016), the contralateral cerebellar locomotor region (Mori et al., 1998), the PAG (Mantyh, 1983; Dampney et al., 2013), the motor cortex via corticoreticular pathways (Matsuyama et al., 2004b), as well as various sensory systems (e.g., visual, auditory, and vestibular) (Furigo et al., 2010; Miller et al., 2017). Thus locomotion may be initiated by activation of the RF directly, bypassing the MLR (Shik et al., 1966; Noga et al., 1988; Mori et al., 1998; Bretzner and Brownstone, 2013; Capelli et al., 2017) or modulated by activation of sensory or neuromodulatory inputs to the RF (Antri et al., 2008; Smetana et al., 2010; Noga and Opris, 2017a,b; Oueghlani et al., 2018). The neuronal circuit selected for goal-directed locomotion may depend upon the behavioral context (Sinnamon, 1993), whether locomotion is required for either exploration, foraging, or defense (see Jordan, 1998; Takakusaki, 2008).

DATA AVAILABILITY STATEMENT

The datasets generated for this study are available on request to the corresponding author.

ETHICS STATEMENT

The animal study was reviewed and approved by the University of Miami IACUC.

AUTHOR CONTRIBUTIONS

BN and LJ: conceptualization, supervision, and funding acquisition. BN, LJ, DJ, XD, and LV: methodology. BN, DJ, and XD: investigation. XD, IO, DJ, FS, LV, CL-H, and SX: formal

analysis. BN, XD, IO, and LV: visualization. BN, XD, IO, and SC: writing – original draft. BN, LJ, IO, and SC: writing – review and editing.

FUNDING

This work was supported by the National Institutes of Health (NIH) Grants R01 NS046404 and R56NS46404-6A1 to BN, the State of Florida and the Miami Project to Cure Paralysis, and a Medical Research Council Grant to LJ, a Rick Hansen Man in Motion Legacy Fund Studentship to XD, and a research fellowship from the Neurosurgery Research and Education Foundation (NREF) to SC (GR010471).

ACKNOWLEDGMENTS

The authors would like to thank B. Frydel for assistance in the use of StereoInvestigator and Neurolucida Systems and M. Riesgo, J. R. Douglas, and A. Pinzon for assistance during some of the experiments.

REFERENCES

Antri, M., Auclair, F., Albrecht, J., Djeudjang, N., and Dubuc, R. (2008). Serotonergic modulation of sensory transmission to brainstem reticulospinal cells. *Eur. J. Neurosci.* 28, 655–667. doi: 10.1111/j.1460-9568.2008.06368.x

Antri, M., Orsal, D., and Barthe, J.-Y. (2002). Locomotor recovery in the chronic spinal rat: effects of long-term treatment with a 5-HT2 agonist. *Eur. J. Neurosci.* 16, 467–476. doi: 10.1046/j.1460-9568.2002.02088.x

Arshian, M. S., Hobson, C. E., Catanzaro, M. F., Miller, D. J., Puterbaugh, S. R., Cotter, L. A., et al. (2014). Vestibular nucleus neurons respond to hindlimb movement in the decerebrate cat. *J. Neurophysiol.* 111, 2423–2432. doi: 10.1152/jn.00855.2013

Barbeau, H., and Rossignol, S. (1991). Initiation and modulation of the locomotor pattern in the adult chronic spinal cat by noradrenergic, serotonergic and dopaminergic drugs. *Brain Res.* 546, 250–260. doi: 10.1016/0006-8993(91)91489-n

Barnett, W. H., Jenkin, K. S. E., Milsom, W. K., Paton, J. F., Abdala, A. P., Molkov, Y. I, et al. (2018). The Kölliker–Fuse nucleus orchestrates the timing of expiratory abdominal nerve bursting. *J. Neurophysiol.* 119, 401–412. doi: 10.1152/jn.00499.2017

Bayev, K. V., Beresovskii, V. K., Kebkalo, T. G., and Savoskina, L. A. (1988). Afferent and efferent connections of brainstem locomotor regions: study by means of horseradish peroxidase transport technique. *Neuroscience* 26, 871–891. doi: 10.1016/0306-4522(88)90106-6

Bell, H. J. (2006). Respiratory control at exercise onset: an integrated systems perspective. *Resp. Physiol. Neurobiol.* 152, 1–15. doi: 10.1016/j.resp.2006.02.005

Berman, A. (1968). *The Brainstem of the Cat*. Madison, WI: The University of Wisconsin press.

Bretzner, F., and Brownstone, R. M. (2013). Lhx3-Chx10 reticulospinal neurons in locomotor circuits. *J. Neurosci.* 33, 14681–14692. doi: 10.1523/jneurosci.5231-12.2013

Brudzynski, S. M., and Wang, D. (1996). C-fos immunohistochemical localization of neurons in the mesencephalic locomotor region in the rat brain. *Neuroscience* 75, 793–803. doi: 10.1016/0306-4522(96)00284-9

Caggiano, V., Leiras, R., Goñi-Erro, H., Masini, D., Bellardita, C., Bouvie, R. J., et al. (2018). Midbrain circuits that set locomotor speed and gait selection. *Nature* 553, 455–460. doi: 10.1038/nature25448

Capelli, P., Pivetta, C., Esposito, M. S., and Arber, S. (2017). Locomotor speed control circuits in the caudal brainstem. *Nature* 551, 373–377. doi: 10.1038/nature24064

Carrive, P., and Bandler, R. (1991). Control of extracranial and hindlimb blood flow by the midbrain periaqueductal grey of the cat. *Exp. Brain Res.* 84, 599–606. doi: 10.1007/BF00230972

Cazalets, J. R., Sqalli-Houssaini, Y., and Clarac, F. (1992). Activation of the central pattern generators for locomotion by serotonin and excitatory amino acids in neonatal rat. *J. Physiol.* 455, 187–204. doi: 10.1113/jphysiol.1992.sp019296

Chatonnet, F., Boudinot, E., Chatonnet, A., Taysse, L., Daulon, S., Champagnat, J., et al. (2003). Respiratory survival mechanisms in acetylcholinesterase knockout mouse. *Eur. J. Neurosci.* 18, 1419–1427. doi: 10.1046/j.1460-9568.2003.02867

Christie, K. J., and Whelan, P. J. (2005). Monoaminergic establishment of rostrocaudal gradients of rhythmicity in the neonatal mouse spinal cord. *J. Neurophysiol.* 94, 1554–1564. doi: 10.1152/jn.00299.2005

Clark, F. M., and Proudfit, H. K. (1991a). The projection of locus coeruleus neurons to the spinal cord in the rat determined by anterograde tracing combined with immunocytochemistry. *Brain Res.* 538, 231–245. doi: 10.1016/0006-8993(91)90435-x

Clark, F. M., and Proudfit, H. K. (1991b). The projection of noradrenergic neurons in the A7 catecholamine cell group to the spinal cord in the rat demonstrated by anterograde tracing combined with immunocytochemistry. *Brain Res.* 547, 279–288. doi: 10.1016/0006-8993(91)90972-x

Cullen, K. E. (2012). The vestibular system: multimodal integration and encoding of self-motion for motor control. *Trends Neurosci.* 35, 185–196. doi: 10.1016/j.tins.2011.12.001

Dai, X., Noga, B. R., Douglas, J. R., and Jordan, L. M. (2005). Localization of spinal neurons activated during locomotion using the *c-fos* immunohistochemical method. *J. Neurophysiol.* 93, 3442–3452. doi: 10.1152/jn.00578.2004

Damasceno, R. S., Takakura, A. C., and Moreira, T. S. (2014). Regulation of the chemosensory control of breathing by kölliker–Fuse neurons. *Am. J. Physiol. Regul. Integr. Comp. Physiol.* 307, R57–R67. doi: 10.1152/ajpregu.00024.2014

Dampney, R. A. L., Furlong, T. M., Horiuchi, J., and Iigaya, K. (2013). Role of dorsolateral periaqueductal grey in the coordinated regulation of cardiovascular and respiratory function. *Auton. Neurosci.* 175, 17–25. doi: 10.1016/j.autneu.2012.12.008

Dautan, D., Souza, A. S., Huerta-Ocampo, I., Valencia, M., Assous, M., Witten, I. B., et al. (2016). Segregated cholinergic transmission modulates dopamine neurons integrated in distinct functional circuits. *Nat. Neurosci.* 19, 1025–1033. doi: 10.1038/nn.4335

Deng, H., Xiao, X., and Wang, Z. (2016). Periaqueductal gray neuronal activities underlie different aspects of defensive behaviors. *J. Neurosci.* 36, 7580–7588. doi: 10.1523/JNEUROSCI.4425-15.2016

DePuy, S. D., Kanbar, R., Coates, M. B., Stornetta, R. L., and Guyenet, G. (2011). Control of breathing by raphe obscurus serotonergic neurons in mice. *J. Neurosci.* 31, 1981–1990. doi: 10.1523/JNEUROSCI.4639-10.2011

Di Prisco, G. V., Dubuc, R., and Grillner, S. (1994). 5-HT innervation of reticulospinal neurons and other brainstem structures in lamprey. *J. Comp. Neurol.* 342, 23–34. doi: 10.1002/cne.903420104

Dick, T. E., Baekey, D. M., Paton, J. F. R., Lindsey, B. G., and Morris, K. F. (2009). Cardio-respiratory coupling depends on the pons. *Resp. Physiol. Neurobiol.* 168, 76–85. doi: 10.1016/j.resp.2009.07.009

DiMarco, A. F., Romaniuk, J. R., Von Euler, C., and Yamamoto, Y. (1983). Immediate changes in ventilation and respiratory pattern associated with onset and cessation of locomotion in the cat. *J. Physiol.* 343, 1–16. doi: 10.1113/jphysiol.1983.sp014878

Douglas, J. R., Noga, B. R., Dai, X., and Jordan, L. M. (1993). The effects of intrathecal administration of excitatory amino acid agonists and antagonists on the initiation of locomotion in the adult cat. *J. Neurosci.* 13, 990–1000. doi: 10.1523/JNEUROSCI.13-03-00990.1993

Dutschmann, M., and Dick, T. E. (2012). Pontine mechanisms of respiratory control. *Compr. Physiol.* 2, 2443–2469. doi: 10.1002/cphy.c100015

Dutschmann, M., and Herbert, H. (2006). The Kölliker–Fuse nucleus gates the postinspiratory phase of the respiratory cycle to control inspiratory off-switch and upper airway resistance in rat. *Eur. J. Neurosci.* 24, 1071–1084. doi: 10.1111/j.1460-9568.2006.04981.x

Edwards, S. B. (1975). Autoradiographic studies of the projections of the midbrain reticular formation: descending projections of nucleus cuneiformis. *J. Comp. Neurol.* 161, 341–358. doi: 10.1002/cne.901610306

Edwards, S. B., and de Olmos, J. S. (1976). Autoradiographic studies of the projections of the midbrain reticular formation: ascending projections of nucleus cuneiformis. *J. Comp. Neurol.* 165, 417–432. doi: 10.1002/cne.901650403

Eldgridge, F. L., Millhorn, D. E., Kiley, J. P., and Waldrop, T. G. (1985). Stimulation by central command of locomotion, respiration and circulation during exercise. *Resp. Physiol.* 59, 313–337. doi: 10.1016/0034-5687(85)90136-7

Eldgridge, F. L., Millhorn, D. E., and Waldrop, T. G. (1981). Exercise hyperpnea and locomotion: parallel activation from the hypothalamus. *Science* 211, 844–846. doi: 10.1126/science.7466362

Ezure, K., and Tanaka, I. (1997). Convergence of central respiratory and locomotor rhythms onto single neurons of the lateral reticular nucleus. *Exp. Brain Res.* 113, 230–242. doi: 10.1007/BF02450321

Ezure, K., and Tanaka, I. (2006). Distribution and medullary projection of respiratory neurons in the dorsolateral pons of the rat. *Neuroscience* 141, 1011–1023. doi: 10.1016/j.neuroscience.2006.04.020

Feraboli-Lohnherr, D., Barthe, J. Y., and Orsal, D. (1999). Serotonin-induced activation of the network for locomotion in adult spinal rats. *J. Neurosci. Res.* 55, 87–98. doi: 10.1002/(SICI)1097-4547(19990101)55

Ferreira-Netto, C., Borelli, K. G., and Brandão, M. L. (2005). Neural segregation of Fos-protein distribution in the brain following freezing and escape behaviors induced by injections of either glutamate or NMDA into the dorsal periaqueductal gray of rats. *Brain Res.* 1031, 151–163. doi: 10.1016/j.brainres.2004.10.044

Furigo, I. C., De Oliveira, W. F., De Oliveira, A. R., Colmoli, E., Baldo, M. V. C., Mota-Ortiz, S. R., et al. (2010). The role of the superior colliculus in predatory hunting. *Neuroscience* 165, 1–15. doi: 10.1016/j.neuroscience.2009.10.004

Gao, K., Kim, Y.-H. H., and Mason, P. (1997). Serotonergic pontomedullary neurons are not activated by antinociceptive stimulation in the paeriaqueductal gray. *J. Neurosci.* 17, 3285–3292. doi: 10.1523/JNEUROSCI.17-09-03285.1997

Gao, K., and Mason, P. (1997). Somatodendritic and axonal anatomy of intracellularly labeled serotonergic neurons in the rat medulla. *J. Comp. Neurol.* 389, 309–328. doi: 10.1002/(sici)1096-9861(19971215)389:2<309::aid-cne9>3.3.co;2-d

Garcia-Rill, E., Houser, C. R., Skinner, R. D., Smith, W., and Woodward, D. J. (1987). Locomotion-inducing sites in the vicinity of the pedunculopontine nucleus. *Brain Res. Bull.* 18, 731–738. doi: 10.1016/0361-9230(87)90208-5

Garcia-Rill, E., Simon, C., Smith, K., Kezunovic, N., and Hyde, J. (2011). The pedunculopontine tegmental nucleus: from basic neuroscience to neurosurgical applications: arousal from slices to humans: implications for DBS. *J. Neural Transm.* 118, 1397–1407. doi: 10.1007/s00702-010-0500-x

Garcia-Rill, E., and Skinner, R. D. (1987). The mesencephalic locomotor region. II. Projections to reticulospinal neurons. *Brain Res.* 411, 13-20. doi: 10.1016/0006-8993(87)90676-7

Garcia-Rill, E., Skinner, R. D., Conrad, C., Mosley, D., and Campbell, C. (1986). Projections of the mesencephalic locomotor region in the rat. *Brain Res. Bull.* 17, 33–40. doi: 10.1016/0361-9230(86)90158-9

Garcia-Rill, E., Skinner, R. D., and Fitzgerald, J. A. (1983). Activity in the mesencephalic locomotor region during locomotion. *Exp. Neurol.* 82, 609-622. doi: 10.1016/0014-4886(83)90084-5

Gargaglioni, L. H., Hartzler, L. K., and Putnam, R. W. (2010). The locus coeruleus and central chemosensitivity. *Respir. Physiol. Neurobiol.* 173, 264–273. doi: 10.1016/j.resp.2010.04.024

Geerling, J. C., Yokota, S., Rukhadze, I., Roe, D., and Chamberlin, N. L. (2017). Kölliker–Fuse GABAergic and glutamatergic neurons project to distinct targets. *J. Comp. Neurol.* 525, 1844–1860. doi: 10.1002/cne.24164

Goetz, L., Piallat, B., Bhattacharjee, M., Mathieu, H., David, O., and Chabardès, S. (2016). On the role of the pedunculopontine nucleus and mesencephalic reticular formation in locomotion in nonhuman primates. *J. Neurosci.* 36, 4917–4929. doi: 10.1523/JNEUROSCI.2514-15.2016

Grillner, S., Georgopoulos, A. P., and Jordan, L. M. (1997). "Selection and initiation of motor behavior," in *Neurons, Network and Motor Behavior*, eds P. S. G. Stein, A. I. Selverston, and D. G. Stuart, (Cambridge, MA: MIT Press), 3–19.

Grillner, S., and Shik, M. L. (1973). On the descending control of the lumbosacral spinal cord from the "mesencephalic locomotor region". *Acta Physiol. Scand.* 87, 320–333. doi: 10.1111/j.1748-1716.1973.tb05396.x

Grillner, S., Wallén, P., Saitoh, K., Kozlov, A., and Robertson, B. (2008). Neural bases of goal-directed locomotion in vertebrates – an overview. *Brain Res. Rev.* 57, 2–12. doi: 10.1016/j.brainresrev.2007.06.027

Gut, N. K., and Winn, P. (2015). Deep brain stimulation of different pedunculopontine targets in a novel rodent model of Parkinsonism. *J. Neurosci.* 35, 4792–4803. doi: 10.1523/jneurosci.3646-14.2015

Hägglund, M., Borgius, L., Dougherty, K. J., and Kiehn, O. (2010). Activation of groups of excitatory neurons in the mammalian spinal cord or hindbrain evokes locomotion. *Nat. Neurosci.* 13, 246–252. doi: 10.1038/nn.2482

Halberstadt, A. L., and Balaban, C. D. (2003). Organization of projections from the raphe nuclei to the vestibular nuclei in rats. *Neuroscience* 120, 573–594. doi: 10.1016/S0306-4522(02)00952-1

Helke, C. J., Thor, K. B., and Sasek, C. A. (1989). Chemical neuroanatomy of the parapyramidal region of the ventral medulla in the rat. *Prog. Brain Res.* 81, 17–28. doi: 10.1016/S0079-6123(08)61997-4

Herbert, H., Moga, M. M., and Saper, C. B. (1990). Connections of the parabrachial nucleus with the nucleus of the solitary tract and the medullary reticular formation in the rat. *J. Comp. Neurol.* 293, 540–580. doi: 10.1002/cne.902930404

Herdegen, T., and Leah, J. D. (1998). Inducible and constitutive transcription factors in the mammalian nervous system: control of gene expression by Jun, Fos, and Krox, and CREB/ATF proteins. *Brain Res. Rev.* 28, 370–490. doi: 10.1016/s0165-0173(98)00018-6

Hermann, D. M., Luppi, P.-H., Peyron, C., Hinckel, P., and Jouvet, M. (1997). Afferent projections to the rat nuclei raphe magnus, raphe pallidus and reticularis gigantocellularis pars α demonstrated by iontophoretic application of choleratoxin (subunit b). *J. Chem. Neuroanat.* 13, 1–21. doi: 10.1016/S0891-0618(97)00019-7

Holstege, G., and Kuypers, H. G. (1982). The anatomy of the brain stem pathways to the spinal cord in a cat. A labelled amino acid tracing study. *Prog. Brain Res.* 57, 145–175. doi: 10.1016/S0079-6123(08)64128-X

Huang, A., Noga, B. R., Carr, P. A., Fedirchuk, B., and Jordan, L. M. (2000). Spinal cholinergic neurons activated during locomotion: localization and electrophysiological characterization. *J. Neurophysiol.* 83, 3537–3547. doi: 10.1152/jn.2000.83.6.3537

Humphries, M. D., Gurney, K., and Prescott, T. J. (2006). The brainstem reticular formation is a small-world, not scale-free, network. *Proc. R. Soc. B Biol. Sci.* 273, 503–511. doi: 10.1098/rspb.2005.3354

Humphries, M. D., Gurney, K., and Prescott, T. J. (2007). Is there a brainstem substrate for action selection? *Philos. Trans. R. Soc. Lond. Ser. B Biol. Sci.* 362, 1627–1639. doi: 10.1098/rstb.2007.2057

Iwamoto, G. A., Wappel, S. M., Fox, G. M., Buetow, K. A., and Waldrop, T. G. (1996). Identification of diencephalic and brainstem cardiorespiratory areas activated during exercise. *Brain Res.* 726, 109–122. doi: 10.1016/0006-8993(96)00303-4

Jacobs, B. L., Martín-Cora, F. J., and Fornal, C. A. (2002). Activity of medullary serotonergic neurons in freely moving animals. *Brain Res. Rev.* 40, 45–52. doi: 10.1016/S0165-0173(02)00187-X

Janickova, H., Rosborough, K., Al-Onaizi, M., Kljakic, O., Guzman, M. S., Gros, R., et al. (2017). Deletion of the vesicular acetylcholine transporter from pedunculopontine/laterodorsal tegmental neurons modifies gait. *J. Neurochem.* 140, 787–798. doi: 10.1111/jnc.139.10

Jankowska, E., Jukes, M. G. M., Lund, S., and Lundberg, A. (1967). The effect of DOPA on the spinal cord. VI. Half-centre organization of interneurons transmitting effects from the flexor reflex afferents. *Acta Physiol. Scand.* 70, 389–402. doi: 10.1111/j.1748-1716.1967.tb03637.x

Jankowska, E., and Noga, B. R. (1990). Contralaterally projecting lamina VIII interneurons in middle lumbar segments in the cat. *Brain Res.* 535, 327–330. doi: 10.1016/0006-8993(90)91618-Q

Jell, R. M., Elliot, C., and Jordan, L. M. (1985). Initiation of locomotion from the mesenecephalic locomotor region: effects of selective brainstem lesions. *Brain Res.* 328, 121–128. doi: 10.1016/0006-8993(85)91330-7

Jian, B. J., Acernese, A. W., Lorenzo, J., Card, J. P., and Yates, B. J. (2005). Afferent pathways to the region of the vestibular nuclei that participates in

cardiovascular and respiratory control. *Brain Res.* 1044, 241–250. doi: 10.1016/j.brainres.2005.03.010

Jin, X., Schwabe, K., Krauss, J. K., and Alam, M. (2016). The anterior and posterior pedunculopontine tegmental nucleus are involved in behavior and neuronal activity of the cuneiform and entopeduncular nuclei. *Neuroscience* 322, 39–53. doi: 10.1016/j.neuroscience.2016.02.016

Jones, B. E., and Beaudet, A. (1987). Distribution of acetylcholine and catecholamine neurons in the cat brainstem: a choline acetyltransferase and tyrosine hydroxylase immunohistochemical study. *J. Comp. Neurol.* 261, 15–32. doi: 10.1002/cne.902610103

Jones, S. L., and Light, A. R. (1992). Serotonergic medullary raphespinal projection to the lumbar spinal cord in the rat: a retrograde immunohistochemical study. *J. Comp. Neurol.* 322, 599–610. doi: 10.1002/cne.903220413

Jordan, L. M. (1991). "Brainstem and spinal cord mechanisms for the initiation of locomotion," in *Neurobiological Basis of Human Locomotion*, eds M. Shimamura, S. Grillner, and V. R. Edgerton, (Tokyo: Japan Scientific Societies Press), 3–20.

Jordan, L. M. (1998). Initiation of locomotion in mammals. *Ann. N. Y. Acad. Sci.* 860, 83–93. doi: 10.1111/j.1749-6632.1998.tb09040.x

Jordan, L. M., Liu, J., Hedlund, P. B., Akay, T., and Pearson, K. G. (2008). Descending command systems for the initiation of locomotion in mammals. *Brain Res. Rev.* 57, 183–191. doi: 10.1016/j.brainresrev.2007.07.019

Jordan, L. M., McVagh, J. R., Noga, B. R., Cabaj, A. M., Majczyński, H., Sławińska, U., et al. (2014). Cholinergic mechanisms in spinal locomotion – potential target for rehabilitation approaches. *Front. Neural Circuits* 8:132. doi: 10.3389/fncir.2014.00132

Jordan, L. M. J., and Sławińska, U. (2014). "The brain and spinal cord networks controlling locomotion," in *Neuronal Networks in Brain Function, CNS Disorders, and Therapeutics*, eds C. L. Faingold, and H. Blumenfeld, (Amsterdam: Elsevier Inc.), 215–233. doi: 10.1016/b978-0-12-415804-7.00017-4

Josset, N., Roussel, M., Lemieux, M., Lafrance-Zoubga, D., Rastqar, A., and Bretzner, F. (2018). Distinct contributions of mesencephalic locomotor region nuclei to locomotor control in the freely behaving mouse. *Curr. Biol.* 28, 884–901. doi: 10.1016/j.cub.2018.02.007

Kausz, M. (1991). Arrangement of neurons in the medullary reticular formation and raphe nuclei projecting to thoracic, lumbar and sacral segments of the spinal cord in the cat. *Anat. Embryol.* 183, 151–163. doi: 10.1007/BF00174396

Kawahara, K., Nakazono, Y., Yamauchi, Y., and Miyamoto, Y. (1989). Coupling between respiratory and locomotor rhythms during fictive locomotion in decerebrate cats. *Neurosci. Lett.* 103, 326–330. doi: 10.1016/0304-3940(89)90121-3

Kawahara, K., Yoshioka, T., Yamauchi, Y., and Niizeki, K. (1993). Heart beat fluctuation during fictive locomotion in decerebrate cats: locomotor-cardiac coupling of central origin. *Neurosci. Lett.* 150, 200–202. doi: 10.1016/0304-3940(93)90535-S

Kiehn, O., Hultborn, H., and Conway, B. A. (1992). Spinal locomotor activity in acutely spinalized cats induced by intrathecal application of noradrenaline. *Neurosci. Lett.* 143, 243–246. doi: 10.1016/0304-3940(92)90274-b

Kiehn, O., and Kjærulff, O. (1996). Spatiotemporal characteristics of 5-HT and dopamine-induced rhythmic hindlimb activity in the *in vitro* neonatal rat. *J. Neurophysiol.* 75, 1472–1482. doi: 10.1152/jn.1996.75.4.1472

Kjaerulff, O., and Kiehn, O. (1997). Crossed rhythmic synaptic input to motoneurons during selective activation of the contralateral spinal locomotor network. *J. Neurosci.* 17, 9433–9447. doi: 10.1523/JNEUROSCI.17-24-09433.1997

Kobayashi, Y., Matsuyama, K., and Mori, S. (1994). Distribution of serotonin cells projecting to the pontomedullary reticular formation in the cat. *Neurosci. Res.* 20, 43–55. doi: 10.1016/0168-0102(94)90021-3

Koutsikou, S., Apps, R., and Lumb, B. M. (2017). Top down control of spinal sensorimotor circuits essential for survival. *J. Physiol.* 595, 4151–4158. doi: 10.1113/JP273360

Kremer, E., and Lev-Tov, A. (1997). Localization of the spinal network associated with generation of hindlimb locomotion in the neonatal rat and organization of its transverse coupling system. *J. Neurophysiol.* 77, 1155–1170. doi: 10.1152/jn.1997.77.3.1155

Kroeger, D., Ferrari, L. L., Petit, G., Mahoney, C. E., Fuller, P. M., Arrigoni, E., et al. (2017). Cholinergic, glutamatergic, and GABAergic neurons of the pedunculopontine tegmental nucleus have distinct effects on sleep/wake behavior in mice. *J. Neurosci.* 37, 1352–1366. doi: 10.1523/JNEUROSCI.1405-16.2016

Kubin, L., and Fenik, V. (2004). Pontine cholinergic mechanisms and their impact on respiratory regulation. *Resp. Physiol. Neurobiol.* 143, 235–249. doi: 10.1016/j.resp.2004.04.017

Lam, W., Gundlach, A. L., and Verberne, A. J. (1996). Increased nerve growth factor inducible-A gene and c-fos messenger RNA levels in the rat midbrain and hindbrain associated with the cardiovascular response to electrical stimulation of the mesencephalic cuneiform nucleus. *Neuroscience* 71, 193–211. doi: 10.1016/0306-4522(95)00450-5

Lam, W., and Verberne, A. J. M. (1997). Cuneiform nucleus stimulation-induced sympathoexcitation: role of adrenoceptors, excitatory amino acid and serotonin receptors in rat spinal cord. *Brain Res.* 757, 191–201. doi: 10.1016/S0006-8993(97)00201-1

Lamprea, M. R., Cardenas, F. P., Vianna, D. M., Castilho, V. M., Cruz-Morales, S. E., and Brandão, M. L. (2002). The distribution of fos immunoreactivity in rat brain following freezing and escape responses elicited by electrical stimulation of the inferior colliculus. *Brain Res.* 950, 186–194. doi: 10.1016/s0006-8993(02)03036-6

Le Gal, J. P., Juvin, L., Cardoit, L., Thoby-Brisson, M., and Morin, D. (2014). Remote control of respiratory neural network by spinal locomotor generators. *PLoS One* 9:e89670. doi: 10.1371/journal.pone.0089670

Lee, A. M., Hoy, J. L., Bonci, A., Wilbrecht, L., Stryker, M. P., and Niell, C. M. (2014). Identification of a brainstem circuit regulating visual cortical state in parallel with locomotion. *Neuron* 83, 455–466. doi: 10.1016/j.neuron.2014.06.031

Liu, J., and Jordan, L. M. (2005). Stimulation of the parapyramidal region of the neonatal rat bran stem produces locomotor-like activity involving spinal 5-HT7 and 5-HT2A receptors. *J. Neurophysiol.* 94, 1392–1404. doi: 10.1152/jn.00136.2005

Lovick, T. A. (1992). Inhibitory modulation of the cardiovascular defense response by the ventrolateral periaqueductal grey matter in rats. *Exp. Brain Res.* 89, 133–139. doi: 10.1007/BF00229010

Magalhães, K. S., Spiller, P. F., da Silva, M. P., Kuntze, L. B., Paton, J. F. R., Machado, B. H., et al. (2018). Locus Coeruleus as a vigilance centre for active inspiration and expiration in rats. *Sci. Rep.* 8:15654. doi: 10.1038/s41598-018-34047-w

Mantyh, P. W. (1983). Connections of midbrain periaqueductal gray in the monkey. II. Descending efferent projections. *J. Neurophysiol.* 49, 582–594. doi: 10.1152/jn.1983.49.3.582

Marcoux, J., and Rossignol, S. (2000). Initiating or blocking locomotion in spinal cats by applying noradrenergic drugs to restricted lumbar spinal segments. *J. Neurosci.* 20, 8577–8585. doi: 10.1523/JNEUROSCI.20-22-08577.2000

Martinez-Gonzalez, C., Bolam, J. P., and Mena-Segovia, J. (2011). Topographical organization of the pedunculopontine nucleus. *Front. Neuroanat.* 5:22. doi: 10.3389/fnana.2011.00022

Matsuyama, K., and Drew, T. (2000). Vestibulospinal and reticulospinal neuronal activity during locomotion in the intact cat. I. Walking on a level surface. *J. Neurophysiol.* 84, 2237–2256. doi: 10.1152/jn.2000.84.5.2237

Matsuyama, K., Kakajima, K., Mori, F., Aoki, M., and Mori, S. (2004a). Lumbar commissural interneurons with reticulospinal inputs in the cat: morphology and discharge patterns during fictive locomotion. *J. Comp. Neurol.* 474, 546–561. doi: 10.1002/cne.20131

Matsuyama, K., Mori, F., Nakajima, K., Drew, T., Aoki, M., and Mori, S. (2004b). Locomotor role of the corticoreticular-reticulopinal-spinal interneuronal system. *Prog. Brain Res.* 143, 239–249. doi: 10.1016/S0079-6123(03)43024-0

McCall, A. A., Miller, D. M., and Yates, B. J. (2017). Descending influences on vestibulospinal and vestibulosympathetic reflexes. *Front. Neurol.* 27:8. doi: 10.3389/fneur.2017.00112

Mena-Segovia, J., and Bolam, J. P. (2017). Rethinking the pedunculopontine nucleus: from cellular organization to function. *Neuron* 94, 7–18. doi: 10.1016/j.neuron.2017.02.027

Mena-Segovia, J., Micklem, B. R., Nair-Roberts, R. G., Ungless, M. A., and Bolam, J. P. (2009). GABAergic neuron distribution in the pedunculopontine nucleus defines functional subterritories. *J. Comp. Neurol.* 515, 397–408. doi: 10.1002/cne.22065

Miller, D. M., DeMayo, W. M., Bourdages, G. H., Wittman, S. R., Yates, B. J., and McCall, A. A. (2017). Neurons in the pontomedullary reticular formation receive converging inputs from the hindlimb and labyrinth. *Exp. Brain Res.* 235, 1195–1207. doi: 10.1007/s00221-017-4875-x

Millhorn, D. E., Eldridge, F. L., Waldrop, T. G., and Kiley, J. P. (1987). Diencephalic regulation of respiration and arterial pressure during actual and fictive locomotion in cat. *Circ. Res.* 61, I53–I59.

Mori, S., Matsui, T., Kuze, B., Asanome, M., Nakajima, K., and Matsuyama, K. (1998). Cerebellar-induced locomotion: reticulospinal control of spinal rhythm generating mechanism in cats. *Ann. N. Y. Acad. Sci.* 860, 94–105. doi: 10.1111/j.1749-6632.1998.tb09041.x

Mori, S., Matsuyama, K., Kohyama, J., Kobayashi, Y., and Takakusaki, K. (1992). Neuronal constituents of postural and locomotor control systems and their interactions in cats. *Brain Dev.* 14, S109–S120.

Mori, S., Sakamoto, T., Ohta, Y., Takakusaki, K., and Matsuyama, K. (1989). Site-specific postural and locomotor changes evoked in awake, freely moving intact cats by stimulating the brainstem. *Brain Res.* 505, 66–74. doi: 10.1016/0006-8993(89)90116-9

Morinaga, R., Nakamuta, N., and Yamamoto, Y. (2019). Serotonergic projections to the ventral respiratory column from raphe nuclei in rats. *Neurosci. Res.* 143, 20–30. doi: 10.1016/j.neures.2018.05.004

Nasimi, A., Shafei, M. N., and Alaei, H. (2012). Glutamate injection into the cuneiform nucleus in rat, produces correlated single unit activities in the Kolliker–Fuse nucleus and cardiovascular responses. *Neuroscience* 223, 439–446.

Noga, B. R., Fortier, P. A., Kriellaars, D. J., Dai, X., Detillieux, G. R., and Jordan, L. M. (1995). Field potential mapping of neurons in the lumbar spinal cord activated following stimulation of the mesencephalic locomotor region. *J. Neurosci.* 15, 2203–2217. doi: 10.1523/JNEUROSCI.15-03-02203.1995

Noga, B. R., Johnson, D. M. G., Riesgo, M. I., and Pinzon, A. (2009). Locomotor-activated neurons of the cat. I. Serotonergic innervation and co-localization of 5-HT7, 5-HT2A and 5-HT1A receptors in the thoraco-lumbar spinal cord. *J. Neurophysiol.* 102, 1560–1576. doi: 10.1152/jn.91179.2008

Noga, B. R., Johnson, D. M. G., Riesgo, M. I., and Pinzon, A. (2011). Locomotor-activated neurons of the cat. II. Noradrenergic innervation and co-localization with NEα1A or NEα2B receptors in the thoraco-lumbar spinal cord. *J. Neurophysiol.* 105, 1835–1849. doi: 10.1152/jn.00342.2010

Noga, B. R., Kettler, J., and Jordan, L. M. (1988). Locomotion produced in mesencephalic cats by injections of putative transmitter substances and antagonists into the medial reticular formation and the pontomedullary locomotor strip. *J. Neurosci.* 8, 2074–2086. doi: 10.1523/JNEUROSCI.08-06-02074.1988

Noga, B. R., Kriellaars, D. J., Brownstone, R. M., and Jordan, L. M. (2003). Mechanism for activation of locomotor centers in the spinal cord by stimulation of the mesencephalic locomotor region. *J. Neurophysiol.* 90, 1464–1478. doi: 10.1152/jn.00034.2003

Noga, B. R., Kriellaars, D. J., and Jordan, L. M. (1991). The effect of selective brainstem or spinal cord lesions on treadmill locomotion evoked by stimulation of the mesencephalic or pontomedullary locomotor regions. *J. Neurosci.* 11, 1691–1700. doi: 10.1523/JNEUROSCI.11-06-01691.1991

Noga, B. R., and Opris, I. (2017a). "The hierarchical circuit for executive control of movement (Chapter 5),". in *Physics of the Mind and Brain Disorders: Integrated Neural Circuits Supporting the Emergence of Mind*, eds I. Opris, and M. R. Casanova (New York, NY: Springer Series in Cognitive and Neural Systems).

Noga, B. R., and Opris, I. (2017b). "From symmetry to symmetry-breaking in locomotion (Chapter 8)," in *Physics of the Mind and Brain Disorders: Integrated Neural Circuits Supporting the Emergence of Mind*, eds I. Opris, and M. R. Cassanova (New York, NY: Springer Series in Cognitive and Neural Systems), 155–174. doi: 10.1007/978-3-319-29674-6_7

Noga, B. R., Turkson, R. P., Xie, S., Taberner, A., Pinzon, A., and Hentall, I. D. (2017). Monoamine release in the cat lumbar spinal cord during fictive locomotion evoked by the mesencephalic locomotor region. *Front. Neural Circuits* 11:59. doi: 10.3389/fncir.2017.00059

Noga, B. R., Xie, S., Sanchez, F. J., and Blythe, A. D. (2008). Activity-dependent labelling of brainstem monoaminergic and non-monoaminergic neurons during mesencephalic locomotor region evoked fictive locomotion in the cat. *Soc. Neurosci. Abstr.* 34:576.

Orlovskii, G. N. (1970). Relations between reticulospinal neurons and locomotor regions of the brainstem. *Biofizika* 15, 171–177.

Orlovsky, G. N. (1972). Activity of vestibulospinal neurons during locomotion. *Brain Res.* 46, 85–98. doi: 10.1016/0006-8993(72)90007-8

Oueghlani, Z., Simonnet, C., Cardoit, L., Courtland, G., Cazalets, J.-R., Morin, D., et al. (2018). Brainstem steering of locomotor activity in the newborn rat. *J. Neurosci.* 38, 7725–7740. doi: 10.1523/JNEUROSCI.1074-18.2018

Perségol, L., Jordan, M., Viala, D., and Fernandez, C. (1988). Evidence for central entrainment of the medullary respiratory pattern by the locomotor pattern in the rabbit. *Exp. Brain Res.* 71, 153–162. doi: 10.1007/BF00247530

Peterson, B. W., Maunz, R. A., Pitts, N. G., and Mackel, R. (1975). Patterns of projection and branching of reticulospinal neurons. *Exp. Brain Res.* 23, 333–351. doi: 10.1007/BF00238019

Pienaar, I. S., Vernon, A., and Winn, P. (2017). The cellular diversity of the pedunculopontine nucleus: relevance to behavior in health and aspects of Parkinson's disease. *Neuroscientist* 23, 415–431. doi: 10.1177/1073858416682471

Rasmussen, K., Morilak, D. A., and Jacobs, B. L. (1986). Single unit activity of locus coeruleus neurons in the freely moving cat. I. During naturalistic behaviors and in response to simple and complex stimuli. *Brain Res.* 371, 324–334. doi: 10.1016/0006-8993(86)90370-7

Ribas-Salgueiro, J. L., Gaytán, S. P., Ribas, J., and Pásaro, R. (2005). Characterization of efferent projections of chemosensitive neurons in the caudal parapyramidal area of the rat brain. *Brain Res. Bull.* 66, 235–248. doi: 10.1016/j.brainresbull.2005.05.014

Roseberry, T. K., Lee, A. M., Lalive, A. L., Wilbrecht, L., Bonci, A., and Kreitzer, A. C. (2016). Cell-type-specific control of brainstem locomotor circuits by basal ganglia. *Cell* 164, 526–537. doi: 10.1016/j.cell.2015.12.037

Sandner, G., Di Scala, G., Rocha, B., and Angst, M. J. (1992). C-fos immunoreactivity in the brain following unilateral electrical stimulation of the dorsal periaqueductal gray in freely moving rats. *Brain Res.* 573, 276–283. doi: 10.1016/0006-8993(92)90773-3

Schmidt, B. J., and Jordan, L. M. (2000). The role of serotonin in reflex modulation and locomotor rhythm production in the mammalian spinal cord. *Brain Res. Bull.* 53, 689–710. doi: 10.1016/s0361-9230(00)00402-0

Shafei, M. N., and Nasimi, A. (2011). Effect of glutamate stimulation of the cuneiform nucleus on cardiovascular regulation in anesthetized rats: role of the pontine Kolliker–Fuse nucleus. *Brain Res.* 1385, 135–143. doi: 10.1016/j.brainres.2011.02.046

Shafei, M. N., Niazmand, S., Enayatfard, L., Hosseini, M., and Daloee, M. H. (2013). Pharmacological study of cholinergic system on cardiovascular regulation in the cuneiform nucleus of rat. *Neurosci. Lett.* 549, 12–17. doi: 10.1016/j.neulet.2013.05.046

Shefchyk, S. J., Jell, R. M., and Jordan, L. M. (1984). Reversible cooling of the brainstem reveals areas required for mesencephalic locomotor region evoked treadmill locomotion. *Exp. Brain Res.* 56, 257–262. doi: 10.1007/BF00236281

Shik, M. L., Severin, F. V., and Orlovskii, G. N. (1966). Control of walking and running by means of electrical stimulation of the mid-brain. *Biofizika* 11, 659–666.

Shik, M. L., Severin, F. V., and Orlovskii, G. N. (1967). Structures of the brain stem responsible for evoked locomotion. *Fiziol. Zh. SSSR I M Sechenova* 53, 1125–1132.

Shimamura, M., Kogure, I., and Wada, S. (1980). Three types of reticular neurons involved in the spinobulbo-spinal reflex of cats. *Brain Res.* 186, 99–113. doi: 10.1016/0006-8993(80)90258-9

Shinoda, Y., Sugiuchi, Y., Izawa, Y., and Hata, Y. (2006). Long descending motor tract axons and their control of neck and axial muscles. *Prog. Brain Res.* 151, 527–563. doi: 10.1016/s0079-6123(05)51017-3

Shiromani, P. J., Lai, Y. Y., and Siegel, J. M. (1990). Descending projections from the dorsolateral pontine tegmentum to the paramedian reticular nucleus of the caudal medulla in the cat. *Brain Res.* 517, 224–228. doi: 10.1016/0006-8993(90)91030-K

Silveira, M. C. L., Sandner, G., Di Scala, G., and Graeff, F. G. (1995). C-fos immunoreactivity in the brain following electrical or chemical stimulation of the medial hypothalamus. *Brain Res.* 674, 265–274. doi: 10.1016/0006-8993(94)01451-m

Sinnamon, H. M. (1993). Preoptic and hypothalamic neurons and the initiation of locomotion in the anesthetized rat. *Prog. Neurobiol.* 41, 323–344. doi: 10.1016/0301-0082(93)90003-B

Sinnamon, H. M., and Stopford, C. K. (1987). Locomotion elicited by lateral hypothalamic stimulation in the anesthetized rat does not require the dorsal midbrain. *Brain Res.* 402, 78–86. doi: 10.1016/0006-8993(87)91049-3

Smetana, R., Juvin, L., Dubuc, R., and Alford, S. (2010).). A parallel cholinergic brainstem pathway for enhancing locomotor drive. *Nat. Neurosci.* 13, 731–738. doi: 10.1038/nn.2548

Sotnichenko, T. S. (1985). Differentiation of efferent projections of the medial (cuneiform nucleus) and lateral regions of the reticular formation in cat midbrain. *Neurophysiology* 17, 466–471. doi: 10.1007/bf01052183

Sqalli-Houssaini, Y., and Cazalets, J.-R. (2000). Noradrenergic control of locomotor networks in the in vitro spinal cord of the neonatal rat. *Brain Res.* 852, 100–109. doi: 10.1016/s0006-8993(99)02219-2

Steeves, J. D., and Jordan, L. M. (1980). Localization of a descending pathway in the spinal cord which is necessary for controlled treadmill locomotion. *Neurosci. Lett.* 20, 283-288. doi: 10.1016/0304-3940(80)90161-5

Steeves, J. D., and Jordan, L. M. (1984). Autoradiographic demonstration of the projections from the mesencephalic locomotor region. *Brain Res.* 307, 263-276. doi: 10.1016/0006-8993(84)90480-3

Steeves, J. D., Jordan, L. M., and Lake, N. (1976). The close proximity of catecholamine containing cells to the 'mesencephalic locomotor region' (MLR). *Brain Res.* 100, 663–670. doi: 10.1016/0006-8993(75)90166-3

Steeves, J. D., Schmidt, B. J., Skovgaard, B. J., and Jordan, L. M. (1980). The effect of noradrenaline and 5-hydroxytryptamine depletion on locomotion in the cat. *Brain Res.* 185, 349–362. doi: 10.1016/0006-8993(80)91073-2

Stocker, S. D., Steinbacher, B. C., Balaban, C. D., and Yates, B. J. (1997). Connections of the caudal ventrolateral medullary reticular formation in the cat brainstem. *Exp. Brain Res.* 116, 270–282. doi: 10.1007/PL00005755

Subramanian, H. H., and Holstege, G. (2014). Chapter 17 - The midbrain periaqueductal gray changes the eupneic respiratory rhythm into a breathing pattern necessary for survival of the individual and of the species. *Prog. Brain Res.* 212, 351–384. doi: 10.1016/B978-0-444-63488-7.00017-3

Suckow, S. K., Deichsel, E. L., Ingram, S. I., Morgan, M. M., and Aicher, S. A. (2013). Columnar distribution of catecholaminergic neurons in the ventrolateral periaqueductal gray and their relationship to efferent pathways. *Synapse* 67, 94–108. doi: 10.1002/syn.21624

Takakusaki, K. (2008). Forebrain control of locomotor behaviors. *Brain Res. Rev.* 57, 192–198. doi: 10.1016/j.brainresrev.2007.06.024

Takakusaki, K. (2013). Neurophysiology of gait: from the spinal cord to the frontal lobe. *Mov. Disord.* 28, 1483–1491. doi: 10.1002/mds.25669

Takakusaki, K., Chiba, R., Nozu, T., and Okumura, T. (2016). Brainstem control of locomotion and muscle tone with special reference to the role of the mesopontine tegmentum and medullary reticulospinal systems. *J. Neural Transm.* 123, 695–729. doi: 10.1007/s00702-015-1475-4

Takakusaki, K., Habaguchi, T., Ohtinata-Sugimoto, J., Saitoh, K., and Sakamoto, T. (2003). Basal ganglia efferents to the brainstem centers controlling postural muscle tone and locomotion: a new concept for understanding motor disorders in basal ganglia dysfunction. *Neuroscience* 119, 293–308. doi: 10.1016/S0306-4522(03)00095-2

Takakusaki, K., Kohyama, J., Masuyama, K., and Mori, S. (1993). Synaptic mechanisms acting on lumbar motoneurons during postural augmentation induced by serotonin injection into the rostral pontine reticular formation in decerebrate cats. *Exp. Brain Res.* 93, 471–482. doi: 10.1007/bf00229662

Takakusaki, K., Shiroyama, T., Yamamoto, T., and Kitai, S. T. (1996). Cholinergic and noncholinergic tegmental pedunculopontine projection neurons in rats revealed by intracellular labeling. *J. Comp. Neurol.* 371, 345–361. doi: 10.1002/(sici)1096-9861(19960729)371:3<345::aid-cne1>3.0.co;2-2

Tebēcis, A. K. (1973). Transmitters and reticulospinal neurons. *Exp. Neurol.* 40, 297–308. doi: 10.1016/0014-4886(73)90075-7

Usunoff, K. G., Itzev, D. E., Lolov, S. R., and Wree, A. (2003). Pedunculopontine tegmental nucleus. Part 1: cytoarchitecture, transmitters, development and connections. *Biomed. Rev.* 14, 95–120. doi: 10.14748/bmr.v14.111

Veasey, S. C., Fornal, C. A., Metzler, C. W., and Jacobs, B. L. (1995). Response of serotonergic caudal raphe neurons in relation to specific motor activities in freely moving cats. *J. Neurosci.* 15, 5346–5359. doi: 10.1523/JNEUROSCI.15-07-05346.1995

Verberne, A. J. M. (1995). Cuneiform nucleus stimulation produces activation of medullary sympathoexcitatory neurons in rats. *Am. J. Physiol.* 268, R752–R758. doi: 10.1152/ajpregu.1995.268.3.R752

Viala, D., and Buser, P. (1969). The effects of DOPA and 5-HTP on rhythmic efferent discharges in hind limb nerves in the rabbit. *Brain Res.* 12, 437–443. doi: 10.1016/0006-8993(69)90011-0

Voss, M. D., de Castro, D., Lipski, J., Pilowski, P. M., and Jiang, C. (1990). Serotonin immunoreactive boutons form close appositions with respiratory neurons of the dorsal respiratory group in the cat. *J. Comp. Neurol.* 295, 208–218. doi: 10.1002/cne.902950205

Wang, H. L., and Morales, M. (2009). Pedunculopontine and laterodorsal tegmental nuclei contain distinct populations of cholinergic, glutamatergic and GABAergic neurons in the rat. *Eur. J. Neurosci.* 29, 340–358. doi: 10.1111/j.1460-9568.2008.06576.x

Westlund, K. N., Bowker, R. M., Ziegler, M. G., and Coulter, J. D. (1982). Descending noradrenergic projections and their spinal terminations. *Prog. Brain Res.* 57:1982. doi: 10.1016/S0079-6123(08)64131-X

Wienecke, J., Enriquez Denton, M., Stecina, K., Kirkwood, P. A., and Hultborn, H. (2015). Modulation of spontaneous locomotor and respiratory drives to hindlimb motoneurons temporally related to sympathetic drives as revealed by Mayer waves. *Front. Neural Circ.* 9:1. doi: 10.3389/fncir.2015.00001

Wise, R. A. (2004). Dopamine, learning and motivation. *Nat. Rev. Neurosci.* 5, 483–494. doi: 10.1038/nrn1406

Xiao, C., Cho, J. R., Zhou, C., Treweek, J. B., Chan, K., McKinney, S. L., et al. (2016). Cholinergic mesopontine signals govern locomotion and reward through dissociable midbrain pathways. *Neuron* 90, 333–347. doi: 10.1111/jnc.13910

Yokota, S., Oka, T., Tsumori, T., Nakamura, S., and Yasui, Y. (2007). Glutamatergic neurons in the Kölliker–Fuse nucleus project to the rostral ventral respiratory group and phrenic nucleus: a combined retrograde tracing and in situ hybridization study in the rat. *Neurosci. Res.* 59, 341–346. doi: 10.1016/j.neures.2007.08.004

Yoo, J. H., Zell, V., Wu, J., Punta, C., Ramajayam, N., Shen, X., et al. (2017). Activation of pedunculopontine glutamate neurons is reinforcing. *J. Neurosci.* 37, 38–46. doi: 10.1523/JNEUROSCI.3082-16.2016

Zubair, H. N., Beloozerova, I. N., Sun, H., and Marlinski, V. (2016). Head movement during walking in the cat. *Neuroscience* 332, 101–120. doi: 10.1016/j.neuroscience.2016.06.031

Conflict of Interest: The authors declare that the research was conducted in the absence of any commercial or financial relationships that could be construed as a potential conflict of interest.

Copyright © 2019 Opris, Dai, Johnson, Sanchez, Villamil, Xie, Lee-Hauser, Chang, Jordan and Noga. This is an open-access article distributed under the terms of the Creative Commons Attribution License (CC BY). The use, distribution or reproduction in other forums is permitted, provided the original author(s) and the copyright owner(s) are credited and that the original publication in this journal is cited, in accordance with accepted academic practice. No use, distribution or reproduction is permitted which does not comply with these terms.

Advantages of publishing in Frontiers

OPEN ACCESS
Articles are free to read for greatest visibility and readership

FAST PUBLICATION
Around 90 days from submission to decision

HIGH QUALITY PEER-REVIEW
Rigorous, collaborative, and constructive peer-review

TRANSPARENT PEER-REVIEW
Editors and reviewers acknowledged by name on published articles

Frontiers
Avenue du Tribunal-Fédéral 34
1005 Lausanne | Switzerland

Visit us: www.frontiersin.org
Contact us: info@frontiersin.org | +41 21 510 17 00

REPRODUCIBILITY OF RESEARCH
Support open data and methods to enhance research reproducibility

DIGITAL PUBLISHING
Articles designed for optimal readership across devices

FOLLOW US
@frontiersin

IMPACT METRICS
Advanced article metrics track visibility across digital media

EXTENSIVE PROMOTION
Marketing and promotion of impactful research

LOOP RESEARCH NETWORK
Our network increases your article's readership